

**ELEVENTH INTERNATIONAL CONFERENCE
ON COMPOSITE MATERIALS**

**Gold Coast, Queensland, Australia
14th - 18th July 1997**

PROCEEDINGS

VOLUME III

**METAL MATRIX COMPOSITES
AND PHYSICAL PROPERTIES**

**Editor
Murray L. Scott**

**AUSTRALIAN COMPOSITE STRUCTURES SOCIETY
WOODHEAD PUBLISHING LIMITED**

TABLE OF CONTENTS

Metal Matrix Composites

Local Strain Fields in a Particulate Metal Matrix Composites Characterized by Object Grating Technique	1
<i>Y.L. Liu, G. Fischer</i>	
In Situ Tensile Observation of a Squeeze Casting SiC Whisker-6061AL Composite in Transmission Electron Microscope	10
<i>ZongRong Liu, DeZun Wang</i>	
Analysis on the Load Transfer to Misaligned Whiskers in Metal Matrix Composite	15
<i>Soon H. Hong, Kyung H. Chung</i>	
Microstructure of Titanium Dioxide(Rutile)/Pure Aluminum Composites	24
<i>Gen Sasaki, Isao Tsuchitori, Hideharu Fukunaga</i>	
The Interpretation of X-Ray Stress Measurements of Metal Matrix Composites Using Computer Modelling Techniques	32
<i>M.R. Watts, P.J. Withers</i>	
A Cost Effective Foundry Method for the Preparation of Structural Grade Discontinuously Reinforced AIMCs	43
<i>Varuzan M. Kevorkijan</i>	
Thermomechanical Behavior of Squeeze Cast SiC/Al Metal-Matrix Composites	53
<i>S. Elomari, M.D. Skibo, C. San Marchi, H. Richards</i>	
Reaction Hardening of TiO₂/Al Alloys Composites Stimulated by Doping	63
<i>Isao Tsuchitori, Toshio Fujii, Nobuyuki Fuyama, Hideharu Fukunaga</i>	
A Study of the Metal Flow Characteristics of Composite Sheets Formed by Powder Plating and Rolling	75
<i>Zhang Daiming, Sun Yong, Zhang Shuhong, Shi Qingnan</i>	
Surface MMCs on a Ti-6Al-4V Alloy Produced by Combining Laser Nitriding and Powder Alloying	80
<i>C. Hu, H. Xin, T.N. Baker</i>	
Graphite Reinforced Non Equilibrium Al-Mo Metal Matrix Composites	90
<i>Barbara A. Shaw, William C. Moshier, Robert G. Wendt</i>	
Electron Irradiation Induced Crystalline Amorphization at SiO₂ Surface Layer of SiC Particles in a SiCp/Al Composite	101
<i>Zhi Mei, Mingyuan Gu, Yi Liu, Renjie Wu</i>	
Joining Process of Alumina Borate Whiskers Reinforced Aluminum Composite	108
<i>J. Hu, W.D. Fei, Q.F. Xing</i>	
Resistance Brazing of SiCp/Al Composite	113
<i>J. Zhang, J. Yu, S. Meng, X.B. Zeng</i>	
Effect of Sintering Conditions on the Bond Strength of Roll Bonded Metal Laminate Composites	119
<i>Xing Kui Peng, Greg Heness, Wing Yiu Yeung</i>	
Effects of Process Parameters and Surface Conditioning on the Bonding Between MMC-Inserts and Matrix	126
<i>Sabine Hofmann, Eric Neussl, Peter R. Sahn</i>	

Design and Mechanical Properties of Continuous Fibre Reinforced MMC Bolt Connectors	134
<i>Eric Neussl, Sabine Hofmann, Peter R. Sahn, Jérôme Pora, Dominique Schuster</i>	
Hot Forging of a Suspension Arm Component in Al-MMC for Automotive Applications	143
<i>A. Forcellese, F. Gabrielli, S.M. Roberts, P.J. Withers</i>	
High Strain Rate Superplasticity of Ceramic Particulate Reinforced Aluminium Composites and the Fabrication Processing	154
<i>Tsunemichi Imai, Takeo Hikosaka, Gilles L'Esperance, Bande Hong, Daming Jiang</i>	
Fabrication and Properties Of Reaction Squeeze Cast (Al₂O₃.SiO₂+Ni)/Al Hybrid Metal Matrix Composites	164
<i>Sangsuck Kim, Sungmin Kang, Ik-Min Park, Sungjoon Kim, Ildong Choi</i>	
Lower Volume Fraction SiCp/Al Composites Fabricated by Squeeze Infiltration Casting	174
<i>Kung-Hsien Shue, Su-Jien Lin</i>	
Reaction Squeeze Cast Processing and Intermetallics Dispersed Aluminum Matrix Composites	182
<i>Hideharu Fukunaga, Gen Sasaki, Isao Tsuchitori, Toshio Fujii, Nobuyuki Fuyama</i>	
High Temperature Thermal Explosive Synthesis of Nickel/Nickel Aluminide Multilayer Composites	192
<i>Huabin Wang, Jie-Cai Han, Shanyi Du</i>	
Superplastic Forming of Aluminum Matrix Composite Sheets Reinforced by SiC Particles	198
<i>T. Ninomiya, H. Hira, N. Kanetake, T. Choh</i>	
Machining of Reinforced Aluminium and Magnesium	205
<i>K. Weinert, D. Biermann, M. Liedschulte</i>	
The Effect of a Slight Interfacial Reaction on the Mechanical Behaviour of Squeeze-Cast SiCp/6061 Al Composites	215
<i>Yan Cui, Lin Geng, Congkai Yao, Xiaoli Li</i>	
Influence of the Interface on the Creep Properties of the Carbon Fibre Reinforced Magnesium Alloy AS41	221
<i>Bernd Sommer, Karl Ulrich Kainer, Harry Berek</i>	
Strain Analysis of Interface of Composite Formed by PPR Method with Computer-Aided Techniques	230
<i>Zhang Shuhong, Zhang Daiming, Sun Yong, Shi Qingnan</i>	
Effects of the Interface on Local Versus Global Load Sharing Behavior in Metal Matrix Composites Under Longitudinal Tension	238
<i>B.S. Majumdar, T.E. Matikas, D.B. Miracle</i>	
Microstructure and Mechanical Properties of Al-4.5Wt.%Cu/10Vol.%SiCp Metal Matrix Composite Fabricated via Mechanical Alloying Technique	250
<i>J.K. Kek, L. Lu, M.O. Lai</i>	
The Effects of Interfacial Debonding and Work Hardening on the Fracture of Metal-Ceramic Laminates	260
<i>S.J. Howard, S.K. Pateras, T.W. Clyne</i>	
Effect of Squeeze Infiltration Speed on Infiltration Quality and Tensile Properties of Cast Saffil/AlCu4MgAg Composite	274
<i>S. Long, O. Beffort, L. Rohr, H.M. Flower</i>	

The Mechanical Properties of Particulate Reinforced Aluminum Alloy at Elevated Temperature	284
<i>J.H. Shyong, Y.M. Yeh, C.H. Huang, C.Y. Ma</i>	
Properties of Discontinuously Reinforced Copper Matrix Composites	294
<i>J. Goñi, D. Coupard, A. Garcia-Romero, M.C. Castro, J. Coletto, C. Foruria, J.F. Silvain</i>	
Effect of Reinforcement and Processing on Isothermal Creep Properties of Discontinuously Reinforced Aluminium Composites	300
<i>A.F. Whitehouse, H.M.A. Winand</i>	
The Bending Properties and Fracture Character of Directional Solidified Al₂O₃/Al-4.5Cu Composites	311
<i>Chu Shuangjie, Wu Renjie, Zhao Changzheng</i>	
Transverse Tensile Characterization of SiC/Ti-6242 Fiber-Reinforced MMC's with the Cruciform Sample Geometry	317
<i>D.B. Miracle, A.F. Kalton, T.W. Clyne</i>	
Fracture Toughness Evaluation of Hybrid Metal Matrix Composites	327
<i>J.I. Song, K.S. Han</i>	
Assessment of Microfracture Mechanisms in Al₂O₃/6061 Al and SiC/6061 Al Discontinuous Reinforced Composites	337
<i>J.P. Lucas, J.K. Park</i>	
Influence of SiC Particles Volume Fraction on Ductile Damage Process in Al-Si Metal Matrix Composites	348
<i>N. Bonora, F. Iacoviello, G.M. Newaz</i>	
An In Situ Study of Fatigue Crack Growth in Comral-85 at Ambient and Elevated Temperatures	356
<i>Greg Heness, Yiu-Wing Mai</i>	
Strength Degradation in Titanium Matrix Composites Exposed to Fatigue at Elevated Temperature	365
<i>David D. Robertson, Shankar Mall</i>	
Effect of the Interface on Crack Deflection and Fiber Bridging During Fatigue Crack Growth of SiC/Ti-6Al-4V Composites	374
<i>S.G. Warrier, B.S. Majumdar, D.B. Miracle</i>	
Synthesis of YBa₂Cu₃O_{7-x}/Ag Composite Superconductors by a Citric Acid SOL-Gel Method	384
<i>A.L. Juwono, S. Waluyo, S. Poertadji</i>	
Fabrication and Characterisation of Continuous Fibre Reinforced MoSi₂-Based Composites	391
<i>A.R. Bhatti, R.A. Shatwell</i>	
On the Role of Carbon Diffusion During Fiber/Matrix Reaction in SiC Fiber Reinforced Ti-Based MMCs	399
<i>S. Krishnamurthy, D.B. Miracle</i>	
Damage Accumulation and Fracture in Metal Matrix Composites	409
<i>J.D. Boyd, R.D. Evans, G. de Kleine, S. Tao</i>	
Rupture of 7075/Al₂O₃ Composites at High Temperature	418
<i>H.J. McQueen, E.V. Konopleva, G. Avramovic Cingara</i>	
Relations of the Mesoscopic Damage Mechanisms with the Macroscopic Properties of Metal Matrix Composites	429
<i>Chen Haoran, Su Xiaofeng</i>	

Synthesis and Compression Behaviour of Al₂O₃-Al₃Ti In Situ Intermetallic Matrix Composite	438
<i>Huaxin Peng, Ceng Liu, Dezun Wang</i>	
Effect of Interfacial Damage on Residual Tensile Strength for SCS6/Ti-15-3 Metal Matrix Composite	447
<i>Chitoshi Masuda, Yoshihisa Tanaka, Yu-Fu-Liu</i>	
Fully-Coupled Thermomechanical Analysis of Viscoplastic Composites Under Quasistatic and Dynamic Environments	457
<i>Eui-Sup Shin, Seung-Jo Kim, Yong Hyup Kim</i>	
The Failure Mechanism in Monofilament-Reinforced Titanium Under Axial Compression	467
<i>J.E. Spowart, T.W. Clyne</i>	
Superplastic Deformation Mechanisms for SiC Whisker And Particulate Reinforced Aluminium Composites	479
<i>K.C. Chan, B.Q. Han</i>	
Superplasticity of Ceramic Particulate Reinforced Magnesium Alloy Composites Fabricated by a Melt Stirring Method	486
<i>Suk-Won Lim, T. Imai, Y. Nishida, D. Jiang</i>	
Electrochemical Plating of Composite Coatings	495
<i>S. Steinhäuser, B. Wielage</i>	
SiCp - Al Composites Fabricated with a Modified Extrusion Method	505
<i>S. Kohara</i>	
Properties of Particle Reinforced Magnesium Alloys in Correlation with Different Particle Shapes	511
<i>F. Moll, K.U. Kainer</i>	
Fracture Behavior of Cast SiCp-Al Composites Under Elevated Temperature	520
<i>Daifeng Wang, Fengying Wu, Pengxing Li, Renjie Wu, Jingkun Guo</i>	
Squeeze Casting and Characterization of Al₂O₃p/ZL102 Composite Materials	527
<i>X.L. Guo, B.Y. Wu, J. Tao, S.L. Li</i>	
Cold Rolling of Particle Reinforced Aluminium Matrix Composite and Mechanical Properties	532
<i>N. Kanetake, T. Kaneko, T. Choh</i>	
An In-Situ Study of the Fracture Mechanisms of SiCw/AZ91 Magnesium Matrix Composites	539
<i>Mingyi Zheng, Kun Wu, Wencong Zhang, Min Zhao</i>	
Study on Fabrication Technique of Al₂O₃/Steel Composite Pipe by Centrifugal SHS Process	546
<i>Wei Canchun, Zhou Xiang, Tao Jie</i>	
High Temperature Compressive Deformation Behavior of SiCw/6061Al Composite at Liquid-Solid Dual Phase Zone	550
<i>L. Geng, J. Q. Hu, B. Liu</i>	
SiC Particles Volume Fraction Influence on Fatigue Crack Propagation in Al-Si Metal Matrix Composites	556
<i>F. Iacoviello, N. Bonora, L. Jaresovà, Z. Jonsta, L. Hyspeckà</i>	
Modelling and Experimental Characterisation of Phase Strain Evolution in 10vol% Al/SiC_w Composite During Thermo Mechanical Loading	565
<i>T. Lorentzen, Y.L. Liu</i>	

Synthesis and Characterization of Si- N=C=N Containing Preceramic Polymers	573
<i>Hai-Feng Hu, Zhao-Hui Chen, Chun-Xiang Feng, Chang-Rui Zhang, Yong-Cai Song, Jia-Yu Xiao, Zheng-Fang Xie, Wen-Wei Zheng, Zheng-Xiang Fan</i>	
Elastic Deformation Behaviors of Particulate Reinforced Composites	578
<i>Quan Gaofeng, Chai Donglang, Song Yujiu</i>	
Detection of Dislocations in Short Fibre Reinforced Magnesium Alloys by Non-Destructive Methods	585
<i>J. Kiehn, K.U. Kainer, Z. Trojanová, F. Chmelik, P. Lukác</i>	
Process and Tribological Behavior of 6061 Al/Gr.(p) Composites	597
<i>R.J. Chang, C.B. Lin</i>	
Hardness Property and Wear Resistance of ZN-AL/AL₂O₃p or SiCp Particulate Composite	607
<i>Tao Jie, Cui Yihua , Li Shunlin</i>	
A Study on the Microstructure of Alumina Borate Whisker Reinforced Aluminum Composite	612
<i>W.D. Fei, L.J. Yao, C.K. Yao</i>	
Cast Welding of Aluminum Alloy Reinforced with Alumina Material	617
<i>C.K Mu, C.B. Lin</i>	
The Effect of Squeeze Casting and Hot Extrusion Process on the Mechanical Properties of SiCp/Al Composites	627
<i>C.G. Kang, Y.H. Seo</i>	
Microstructure of LaB₆-ZrB₂ In Situ Composite Prepared by Electron Beam Heated Melting Methods	637
<i>Chang-Ming Chen, W.C. Zhou, L.T. Zhang, L.F. Cheng, Y.D. Xu</i>	
Nano-Structures of Pitch-Based Carbon Fibers and the Compatibility with Aluminium Matrix Composites	643
<i>Takakazu Suzuki</i>	
Preparation and the Properties of SiC/MoSi₂ Composites	653
<i>J.Pan, B.W. Liu, D.M. Yang, M.K. Surappa, Y. Zhuo</i>	
Models of Anodic Diffusion When Joining PSZ to Nickel	661
<i>Yu Wang, Robert G. Bathgate</i>	
The Influence of Solidification on the Interface of CF/Al-4.5 CU Composites	672
<i>Chu Shuangjie, Wu Renjie</i>	
The Sliding Wear Resistance Behavior of NiAl and SiC Particles Reinforced Aluminium Matrix Composites	678
<i>Rong Chen, Akira Iwabuchi, Tomoharu Shimizu, Hyung Seop Shin, Hidenobu Mifune</i>	
Fabrication of SiC-Reinforced AZ91D Magnesium-Based Composites	688
<i>Jason S.H. Lo, Graham J.C. Carpenter</i>	
Effect of Microstructure, Interface and on the Aging Behavior of A356 Al/SiC(p) Composites	698
<i>J.J. Yeh, L.D. Chen, C.B. Lin</i>	
The Influence of Heat Treatment on the Dry Sliding Wear Behaviour of Saffil-Reinforced AA6061 Composites	709
<i>H.C. How, T.N. Baker</i>	

Physical Properties

Moisture Absorption in Voided Polymer Composites	719
<i>L.M.P. Fellows, A.R. Chambers</i>	
Shielding Effects of Different Aspect Ratio of Aluminum Flakes in Conductive Plastics for Injection Molding Processes	727
<i>Huang-Lung Hung, Chao-Chang A. Chen, C.B. Lin, C.H. Liu, Tung-Han Chuang</i>	
Neutron Diffraction Study of the Co-Deformation Behavior of a Beryllium-Aluminium Composite	736
<i>David H. Carter, Mark A.M. Bourke</i>	
Generation of Electret State in Composite Polymeric Materials by Friction	746
<i>A.I. Sviridenok, A.F. Klimovich, V.N. Kestelman</i>	
The Flow Behaviour of Composites Containing Cut, Aligned Fibres	755
<i>D.T. Steel, W.J. Clegg</i>	
A Study on Thermo-Oxidative Stability of Non-MDA PMR Polyimide Composites	765
<i>Xiang Bao Chen, Ying Fu, Ping Li</i>	
The Application of Positron Annihilation Methods for Investigation and Testing of Composites	772
<i>S.A. Tishin, V.A. Tishin, V.N. Kestelman</i>	
Nonlinear Viscoelastic Characterization of Filled Elastomer Composites	781
<i>J.D. Brown, S.S. Sternstein, L. Yanyo</i>	
“Good Vibrations”, the Science and Application of Intrinsically Damped Composite Materials	792
<i>I.D. Grant, A. Lowe, S. Thomas</i>	

LOCAL STRAIN FIELDS IN PARTICULATE METAL MATRIX COMPOSITES CHARACTERIZED BY THE OBJECT GRATING TECHNIQUE

Y. L. Liu¹ and G. Fischer²

¹ *Materials Department, Risø National Laboratory,
Frederiksborgvej 399, P.O. Box 49, DK-4000 Roskilde, Denmark*

² *Quality Assurance Department, Dortmund University,
D-44227 Dortmund, Germany*

SUMMARY: This paper addresses the experimental characterization of local strain distribution in Al6061-10%Al₂O₃ and Al6061-20%Al₂O₃ particulate composites under deformation using the object grating technique. The maximum overall strain of the specimen deformed by bending or tension in SEM is 2-3%. The lateral resolution and strain measurement accuracy of this technique allow the local strain field associated with large particles to be characterized. Strain maps of particles of different geometries have been obtained and the effects of particle geometry on the constrained plastic flow in the matrix are analyzed and compared to FEM predictions.

KEYWORDS: metal matrix composite, object grating technique, deformation, local strain distribution, constrained plastic flow.

INTRODUCTION

The presence of the hard, plastically undeformable reinforcement in the ductile matrix changes radically the stress/strain fields in the vicinity of the reinforcement when a metal matrix composite (MMC) is strained. The characteristics of the stress/strain field are affected by geometry and distribution of the reinforcement. The study of the evolution of the local stress/strain fields is essential for improved understanding of the overall elastic and plastic response, and of the strengthening mechanisms of the composite. Numerical techniques such as FEM (Finite Element Model) have been widely used in recent years, where the phase geometry, thermomechanical properties of phases and non-uniform local stress and strain fields are easily accounted for in the simulation of overall mechanical response [1-3]. These models have been used successfully to make quantitative predictions about the overall stress-strain behaviour of such materials. On the local scale they demonstrate that the hydrostatic stresses lead to constrained plastic deformation. The degree of constraint is dependent on the geometrical shape and arrangement of reinforcement.

Various experimental techniques have been developed to characterize the local distribution of stress/strain in MMCs for comparison with FEM simulations. High energy synchrotron radiation [4] has been used to determine the local stress field in bulk material of a composite by measuring the lattice (elastic) strain of small volumes deep within the material. This technique provides the possibility of in-situ measurements, but the lateral resolution is low

(tens and hundreds of microns). TEM (Transmission Electron Microscopy) and EBSD (Electron BackScattered Pattern) have been used to determine the local dislocation density as a measure of the local plastic strain [5,6]. These methods have high lateral resolution in the order of microns or less. But the strain measure is indirect.

Object grating methods [7] have been used to characterize the strain fields on the bulk specimen surface of inhomogeneous materials in the past decades. To meet the new challenge of applying this technique to local strain investigation in particulate reinforced MMCs where both high lateral resolution and high accuracy of strain measurement are required, a more sophisticated object grating method has been developed [8,9]. This method combined with a stress-rig in a scanning electron microscope (SEM) allows the local strain distribution to be studied in-situ during deformation. The experimental procedure consists of: 1) the deposition of a grating on the polished specimen surface by photolithography, 2) deforming the specimen in a SEM by bending or tension, taking digital images at different stages of deformation, 3) image processing, and 4) computation of strain components. Finally the measured strains are plotted in 2D-strain maps.

With the aim to evaluate numerical predictions of the local behaviour, the MMC materials of Al6061 containing 10 or 20% Al_2O_3 particulates are investigated using this object grating technique. The maximum overall strain reached by bending or tension is 2-3%. In this paper, the characteristic strain field in the vicinity of the reinforcement particles revealed by this technique is described, the effects of particle geometry are analyzed and compared to FEM predictions.

EXPERIMENTAL

The materials Al6061-10% Al_2O_3 and Al6061-20% Al_2O_3 are supplied by Duralcan, USA. The as-received materials are in the form of extrusion rod. The measured mean particle size of Al_2O_3 is 6 - 8 μm , while the particle size distribution ranges from <5 μm to about 30 μm . Bending and tensile specimens (Fig.1) are machined from the extruded rods in such a way that the longitudinal axis of the specimen is parallel to the original extrusion direction.

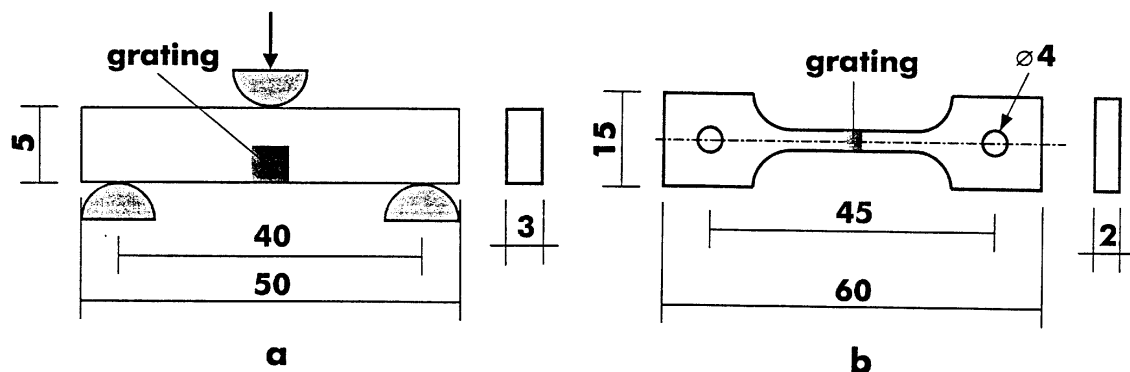


Fig. 1: Bending (a) and tensile (b) specimens.

The grating distance has to be chosen so that it remains sufficiently small in comparison to the smallest wavelength of the expected strain field. In this work grating distance of 1.5 μm is applied. The deposition of gold grating dots is described elsewhere [9].

The specimen is strained in a stress-rig (Raith GmbH, Dortmund) inside a JEOL 840 SEM. The loading is applied by the crosshead displacement at a constant speed of 50 mm/min, corresponding to a strain rate of 10^{-5} - 10^{-4} s $^{-1}$ in the case of tensile tests. A typical stress-strain curve recorded during tension is given in Fig. 2. For tensile tests the overall strain is recorded by an extensometer. The test is interrupted at various strains. Without unloading, digitized images of the area of interest are taken at each deformation step. Also digitized images before loading (as a reference image), and after final unloading are recorded.

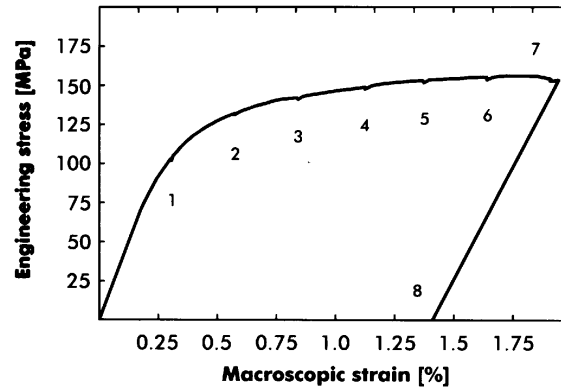


Fig. 2: Stress-strain curve recorded during tensile testing in SEM. 1-8 indicate the deformation steps where the load is held and the image is taken.

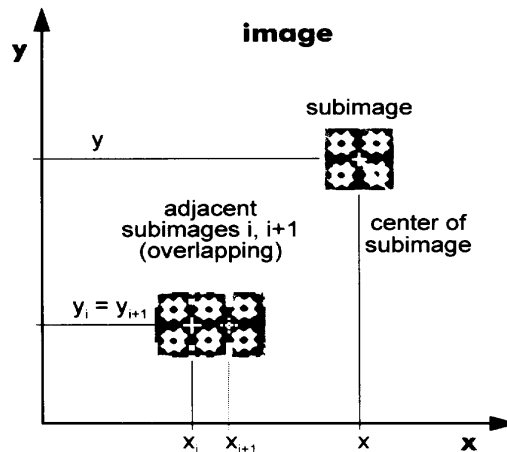


Fig. 3: Schematic drawing showing subimage, centre and overlapping of subimages.

The especially developed algorithm for image processing [8,9] divides the whole image into many subimages (Fig. 3). The algorithm is iteratively searching the best local and grey value transformation of each subimage in the deformed state to the corresponding subimage in the undeformed state. As a result, an average set of local transformation parameters for each subimage is calculated. The in-plane strain components ϵ_{xx} , ϵ_{yy} and ϵ_{xy} at the centre point of each subimage can be derived on the basis of these transformation parameters. The equivalent strain ϵ_{equ} is calculated as

$$\epsilon_{equ} = 2/3 (\epsilon_1 - \epsilon_2) \quad (1)$$

where ϵ_1 and ϵ_2 are principal strains. The mathematics for image processing and strain component calculations are given elsewhere [8,9]. Finally contours of strain ϵ_{equ} are plotted on the top of the deformed image to visualize the distribution of strain over the microstructural inhomogeneities.

RESULTS AND DISCUSSION

Strain Measure Accuracy and Lateral Resolution

All the strain measurements are performed on the surface of the specimen. One has to assume that there is no free-surface effect, so the obtained surface information has also a three-dimensional significance. The previous work [9] shows that the measured strain value while the load is held is a sum of elastic and plastic strains. Since the elastic strain value is very low and remains constant in the elastic-plastic region, the measured strain can be considered to represent the evolution of the plastic strain.

The algorithm determines the displacement of the subimage centre with subpixel accuracy (0.2 - 0.3 pixel) (see Fig. 3). With a subimage size of 64 pixel, accuracy for strain measure is therefore estimated to be in the range of 0.3 to 0.5 % [9]. The improvement in strain accuracy compared with that of the algorithm used by other authors [7] is significant. The latter [7] extracts the individual dots and gives an accuracy of about 1 pixel to determine the displacement of the centre of each dot.

The lateral resolution is improved with decreasing grating distance and subimage size [9]. The presently used grating distance of 1.5 μm is practically the smallest grating distance which can be made on the surface of this type of material by means of photolithography. For statistical reasons a least number of grey level edges within a subimage is needed to secure the measuring accuracy. The selection of the subimage size is therefore a compromise between lateral resolution (a small subimage is wanted) and strain accuracy (a large subimage is preferred). In the present work, a combination of the grating distance of 1.5 μm and the subimage size of 64x64 pixel (2.5x2.5 μm) is used. Generally the local strain field around particles greater than 10 - 15 μm can be characterized [9].

Characterization of Local Strain Fields

With the aim of making a comparison with FEM simulations which are based on ideal arrays of reinforcement, the particles of interest in the experiment are selected as follows: they are close to a regular shape and reasonably isolated.

Al6061-20%Al₂O₃

The first set of experiments is carried out using bending specimens of Al6061-20%Al₂O₃. Due to the high volume concentration of the Al₂O₃ particles and the small particle spacing (calculated value 13 μm), it is very difficult, if not impossible, to find an isolated particle. Typical microstructure is shown in Fig. 4 where a large particle (about 20 x 30 μm) is surrounded by many small particles at rather small particle spacing. The shape of the large particle is irregular and it is not aligned with the loading direction. A series of strain maps of this area at different deformation steps has been obtained, of which two examples are shown in Fig. 4 (a) and (b). The overall strain of these two deformation steps is 1.7 and 3.3%, respectively. (The overall strain is taken as the mean ϵ_{equ} value over the whole image area).

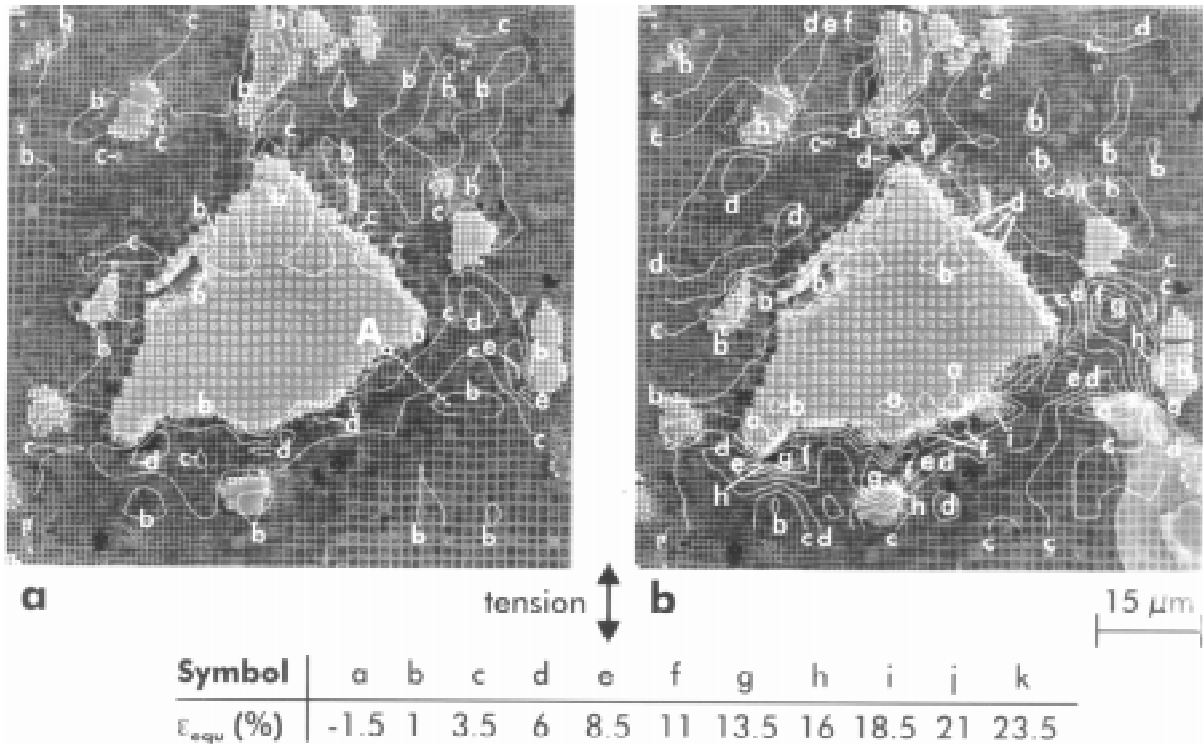


Fig. 4: Strain maps of Al6061-20%Al₂O₃ specimen deformed by bending at overall strains of (a) 1.7% and (b) 3.3%..

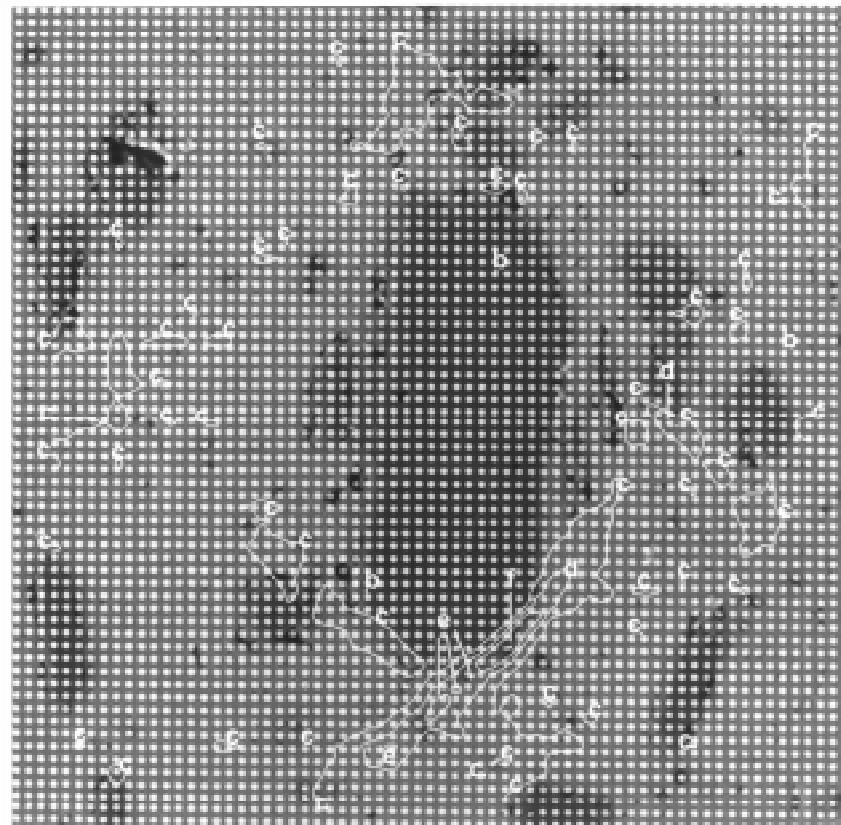
The characteristic information about the strain field one can obtain from the strain maps in Fig. 4 is:

- 1) A systematic development of the strain field with the increasing overall strain can be visualized.
- 2) The strain in the Al₂O₃ particles is lower than 1% in the whole deformation process studied, apart from a few exceptions in which the strain line of 1% penetrates into the particles. This agrees with the fact that the Al₂O₃ particles are not plastically deformable.
- 3) The deformation introduces large strain gradients in the matrix region close to the reinforcement particles.
- 4) Strain localization has different origins. The occurrence of high strain localization in the matrix may be related to the sharp corner of particle or to a given particle distribution [1-3, 5]. However, the present microstructural examination shows that high strain peaks are often associated with micro-voids/cracks [9]. In the studied composites these micro-defects are possibly present in the initial state, and new micro-defects may develop at the early stage of deformation. It is therefore important to distinguish the strain localization caused by the particle geometry and by the presence of micro-voids/cracks. Examples of strain localization of the latter type can be seen in Fig. 4(b), such as the strain contour lines of i and h near the interface in the lower part of the figure. Similarly the high strain contour lines (> 1%) within the particle are often found to be associated with micro-cracks of the particle.

Al6061-10%Al₂O₃

Further experiments are carried out by uniaxial tension of Al6061-10%Al₂O₃ specimens. The lower concentration of particles and the larger particle spacing in this material (calculated

particle spacing $18\ \mu\text{m}$) give rise to more possibilities of finding reasonably isolated particles. Two particles of different geometries are selected: one has an aspect ratio of ~ 3 and is aligned to the direction of tensile loading (Fig. 5(a)), whereas the other has an aspect ratio of ~ 1.5 and the axis of the particle is 45° to the direction of loading (Fig. 5(b)). These two particles will be referred as A and B, respectively in the following text. One must bear in mind that these observations are made on the specimen surface, which is only a cross section of the material. On the basis of Fig. 5, we assume that the shapes of particle A and B are close to the ideal shapes of an aligned cylinder and a double-cone, respectively. The cross section of the two ideal shapes is shown schematically in Fig. 6.



Loading \updownarrow 20 μm

Symbol	a	b	c	d	e	f	g	h	i	j	k
r_{max} [%]	-1	0	1	2	3	4	5	6	7	8	9

a

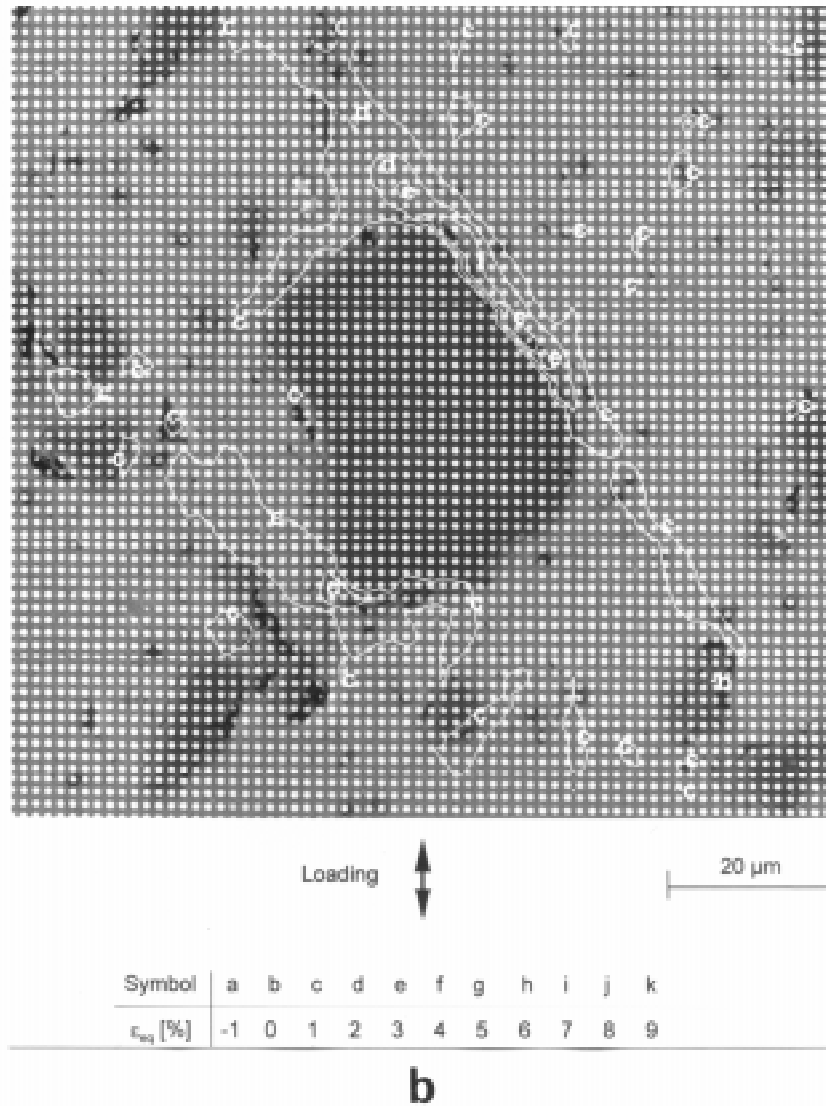


Fig. 5: Strain maps of Al6061-10%Al₂O₃ specimen deformed by tension at an overall strain of 0.4%. (a) particle A, and (b) particle B.

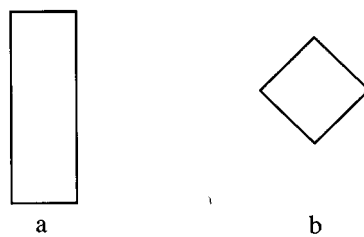


Fig. 6: Cross section of the ideal shapes. (a) aligned cylinder, and (b) double-cone.

The images of the areas which include the selected particles are taken at overall tensile strains of 0.4, 1.1, 3.1 and 4.6%. Immediately after the stage 4 (4.6%) the specimen fractures. This paper will concentrate on the study of strain distribution at a very early stage of deformation (strain of 0.4%) shown in Fig. 5 (a) and (b). The contour line of 1% follows the particle/matrix interface quite well implying that the strain map is a good description of the strain field around the particle.

Further investigation reveals that for both particles intense matrix plastic deformation occurs along a direction of about 45° to the tensile axis. But the extent of plastic flow is different. Consider the contour line of 1% (c line) in the two maps in Fig. 5, the matrix portion with a strain greater than this value forms three continuous bands along the 45° direction (which is parallel to the interface) for particle B (Fig. 5(b)). The scale of these bands is about $30\ \mu\text{m}$ long and $5\ \mu\text{m}$ wide. But for the particle A (Fig. 5(a)), the matrix region with a strain greater than 1% is small and discontinuous in most cases, only one long band can be seen in the lower-right part of the particle. This indicates that for the aligned particle with a higher aspect ratio (particle A), the plastic flow path is to a larger extent interrupted as compared to particle B.

FEM analysis made by Shen et al. [2] can be correlated with the present observations. The shapes of particles studied in this FEM work, among others, are cylinder and double-cone (Fig. 6). At an average axial strain of 0.5% under tensile loading, the plastic deformation bands in the matrix at 45° to the tensile axis are continuous for the double-cone particle, whereas this pattern is interrupted for the cylinder, particularly for the aligned cylinder with an aspect ratio greater than 1 (whisker) (Fig. 6 in [2]). As the ideal shapes of the aligned cylinder and the double-cone are assumed to be related to the shapes of particles A and B, respectively, the comparison between the FEM predictions and the experimental observations shows good qualitative agreement. It is understood that such effects of particle shape on the local plastic flow pattern within the matrix are caused by the differences in the level of hydrostatic stress and the differences in constrained plastic flow in the matrix [2].

In Fig. 5. it can also be seen that strain tends to be more concentrated at the end of particle A, but distributed more uniformly around the particle B. This is in agreement with TEM observations [5] where it is reported that the ends of an aligned whisker (aspect ratio 5) are particularly associated with early dislocation generation, while the dislocation structure around a particle (smaller aspect ratio) is more homogeneous. According to FEM predictions [2], the highest strain localization associated with the end and the sharp corner of an aligned whisker is about two times of that associated with a double-cone particle. However, this “sharp corner” effect has not been observed in the present experiment. The direct explanation for the disagreement is that the shape of studied particles in the real composites is more smooth and without sharp corners, by comparison with the assumptions in FEM calculations. The observed highest strain localization for both particles shown in Fig 5 is, independent of shape, at the level of 4% (contour line f in Fig. 5(a) and (b)), which is about 10 times the overall strain. The occurrence of such high strain localization may be associated with the early void initiation (see above), the chance of which may well be similar for both particles. The strain localization caused by void formation is so intense that the effect of the “sharp corner” of the aligned particle, if there is any, is likely to be concealed.

CONCLUSIONS

The newly developed object grating technique is a powerful tool for characterizing local strain fields in metal matrix composites in-situ during deformation in a SEM. The strain distribution in the matrix around particles greater than $10 - 15\ \mu\text{m}$ can be characterized. The accuracy of strain measurement is in the range of 0.3 - 0.5%. The development of the strain field in a low strain range of 2-3% can be followed. Strain maps of particles of different geometries in particulate composites Al6061-10%Al₂O₃ and Al6061-20%Al₂O₃ have been obtained at early stages of deformation by bending/tension. The effects of particle geometry on the constrained plastic flow in the matrix have been visualized. For the aligned particle with an aspect ratio of

3, the strain in the matrix tends to be more concentrated at the end of the particle and the 45° plastic flow pattern is often interrupted, whereas the strain around the 45° aligned particle with an aspect ratio close to 1 is more homogeneous and continuous plastic deformation bands are formed. The comparison with FEM predictions shows good qualitative agreement. However, the disagreement suggests that the very high constraint effect at the end and corner of an aligned cylinder predicted by FEM is an overestimation of the situation in the real material.

ACKNOWLEDGEMENTS

This work is supported by the German Research Foundation (DFG) and by the Danish research program MP²M “Centre for Materials Processing, Properties and Modelling”.

REFERENCES

1. Sørensen, N.J., Hansen, N. and Liu, Y.L., “On the Inelastic Behaviour of Metal Matrix Composites”, *Proceedings 15th Risø International Symposium on Materials Science*, Andersen, S.I., Bilde-Sørensen, J.B., Lorentzen, T., Pedersen, O.B. and Sørensen, N.J., Eds., Risø National Laboratory, Roskilde, Denmark, 1994, pp. 149-168.
2. Shen, Y.-L., Finot, M., Needleman, A. and Suresh, S., “Effective Plastic Response of Two-Phase Composites”, *Acta Metall. Mater.*, Vol. 43, No. 4, 1995, pp. 1701-1722.
3. Watt, D.F., Xu, X.Q. and Lloyd, D.J., “Effects of Particle Morphology and Spacing on the Strain Fields in a Plastically Deforming Matrix”, *Acta Mater.*, Vol. 44, No. 2, 1996, pp. 789-799.
4. Poulsen, H.F., Lorentzen, T., Feidenhans'l, R. and Liu, Y.L., “A Synchrotron X-ray diffraction Study of the Local Residual Strains Around a Single Inclusion in an Al/W Metal-Matrix Composite”, *Metall. Trans.*, Vol. 28A, 1997, pp. 237-243.
5. Barlow, C.Y. and Hansen, N., “Dislocation Configurations in Metal-Matrix Composites Correlated with Numerical Predictions”, *Acta Metall. Mater.*, Vol. 43, No. 10, 1995, pp. 3633-3648.
6. Wilkinson, A.J. and Dingley, D.J., “The Distribution of Plastic Deformation in a Metal Matrix Composite Caused by Straining Transverse to the Fibre Direction”, *Acta Metall. Mater.*, Vol. 40, No. 12, 1992, pp. 3357-3368.
7. Allais, L., Bornert, M., Bretheau, T. and Caldemaison, D., “Experimental Characterization of the Local Strain Field in a Heterogeneous Elastoplastic Material”, *Acta Metall. Mater.*, Vol. 42, No. 11, 1994, pp. 3865-3880.
8. Crostack, H.-A. and Fischer, G., *Beitrage zur eiektronenmikroskopischen Direktabbildung und Analyse von Oberflachen (BEDO) Vol.29*, in press, (1996).
9. Liu Y.L. and Fischer, G., “In-Situ Measurement of Local Strain in a Metal Matrix Composite by the Object Grating Technique”, *Scripta Mater.*, Vol. 36, No. 10, 1997, pp. 1187-1194.

IN SITU TENSILE OBSERVATION OF A SQUEEZE CASTING SiC WHISKER-6061Al COMPOSITE IN TRANSMISSION ELECTRON MICROSCOPE

ZongRong Liu and DeZun Wang

*National Defence Key Laboratory for precision Hot-Working
School of Materials Science and Engineering, Harbin Institute
of Technology, Harbin 150001, People's Republic of China.*

SUMMARY: The fracture process of a squeeze casting SiCw/6061Al composite has been observed using transmission electron microscopy (TEM) straining techniques. The results show that the crack initiation modes include: (1) cracking of the SiC whiskers; (2) decohesion of the SiCw-Al interfaces and (3) tearing of the matrix. The interaction between crack, dislocations and whisker has been examined in detail. The SiC whiskers in the SiCw/6061Al composite are major obstacles to the propagation of cracks. The SiCw/6061Al composite does not form the single major crack which results in the fracture of the composite, instead, the microcracks can only propagate and grow to a limited size. The failure of the specimen is caused by the abrupt linkage of cracks. A film of aluminum could be observed adhering to the exposed whiskers along the crack edge. This indicates that the SiCw-Al interfaces in the squeeze casting SiCw/6061Al composite is high strength bonded.

KEYWORDS: SiCw/6061Al composite, transmission electron microscopy (TEM) straining techniques, crack initiation, crack propagation, interaction between crack, dislocations and whisker

INTRODUCTION

Major restrictions on the application and dissemination of aluminum-matrix composite materials reinforced with SiC whiskers or particles have been their low ductility and fracture toughness. In recent years, its failure mechanisms have been studied by numerous investigations[1-4]. These mechanisms can be loosely grouped into four categories: (1) cracking of the whiskers or particles [1]; (2) decohesion of the SiC-Al interfaces; (3) fracture of the matrix [2,3] and (4) cracking of the precipitates and/or brittle particles in the matrix [4]. The dominant fracture mechanism of a SiC/Al composite depends on a variety of factors such as: (1) the composition of the matrix and the alloying element added; (2) the microstructure of the matrix; (3) the volume fraction, shape (short fibre, whisker, particulate and particle) and size of the SiC; (4) the spatial distribution of SiC; (5) the nature of the SiC-Al interfaces; (6) the fabrication technique and processing of the composite and (7) the heat treatment condition applied to the composite. Since the failure of a SiC/Al composite is influenced by so many factors and failure mechanisms mentioned above often coexist, it is difficult to categorize the fracture process in SiC/Al composite materials and to take effective measures to improve the ductility and toughness. Although the fracture process of SiC particle-Al (SiCp/Al) composites produced by powder metallurgy process have been extensively studied, related information on the squeeze casting SiC whisker-Al (SiCw/Al) composites is limited. The objective of the present paper is to investigate the fracture process

of a squeeze casting SiCw/6061Al composite using transmission electron microscopy (TEM) straining techniques. Compared with a previous work in which the initiation and growth of microcracks in a squeeze casting SiCw/99.75% Al has been examined in details [5], particular emphasis will be placed on the difference in fracture behavior of the SiCw/6061 from that of SiCw/99.75% Al.

EXPERIMENTAL PROCEDURE

The SiCw/6061Al composite was produced by a squeeze casting method. Using (-SiC whisker (of diameter 0.1~1.0 μm and length 30~100 μm) as the reinforcement and commercial 6061 aluminum alloy as the matrix. The volum fraction of SiCw is 23%. The TEM specimens were cut from as-cast billets and prepared by ion milling and then strained on the tensile stage in the TEM. The fracture process of the composite was observed in situ.

RESULTS AND DISCUSSION

Crack Initiation

Figures 1(a), (b) and (c) are microcracks caused by the cracking of SiC whisker, the decohesion of SiCw-Al interface and the tearing of the matrix in the SiC clustering region, respectively. The crack initiation sources are the same as that in the SiCw/99.75% Al composite [5]. However, the microcracks caused by the matrix cracking in the SiCw/6061Al can only grow to a limited size rather than propagate and form the major crack which leads to fracture of the specimen as that in the SiCw/99.75% Al.

Interaction Between Crack, Dislocations and Whisker

As shown in Figure 1(c), a distinct dislocation-free zone (DFZ) is present between the crack tip and the inverse pile up. The size of DFZ in the SiCw/6061Al is much smaller than that in aluminum. This may be due to the suppressing effect of the SiC to the movement of dislocations. Cell wall are often observed adjacent to SiC whiskers during the TEM experiments, see Figure 2. When a crack approaches to a whisker, the propagation of the crack often stopped and a pile up of dislocations concurs between the crack and the whisker. This indicates that SiC whiskers play an important role in impeding crack propagation. On the other hand, it is obvious that the piling up dislocations in front of SiC whiskers will also lead to stress concentration.

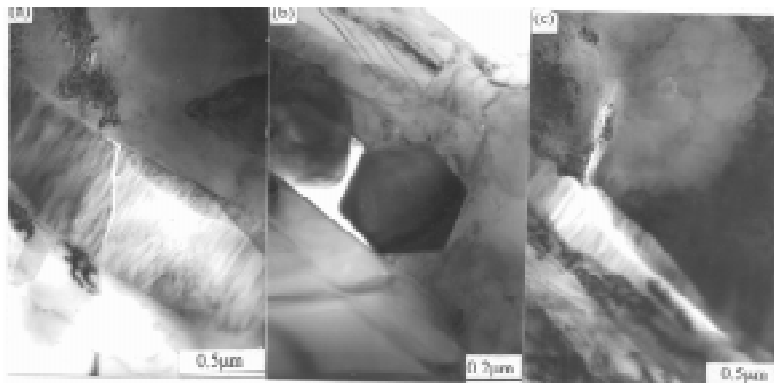


Fig.1: Microcrack initiation sources: (a) cracking of SiC whisker; (b) decohesion of SiC-Al interface and (c) tearing of the matrix

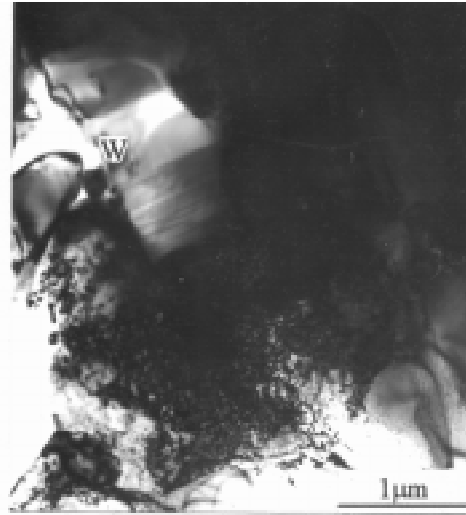


Fig.2: Interaction between a crack, dislocations and a whisker; the crack advancing by bypassing the whisker end

Fracture Mode

In the early stages of straining, many microcracks could be detected mainly in the matrix adjacent to SiC whiskers and in the matrix in the SiC clustering regions. These microcracks could only propagate and grow to a limited size, as shown in Figure 3(a). The cracking processes of the ligament between cracks are sequentially shown in Figures 4(a), (b), (c) and (d). The ligament cracks by shear fracture, and there is no substantial neckin before fracture. An interesting phenomenon can be found from the sequential TEM micrographs that a distinct turing of the ligament is occurred, which may be due to the shear stress applied to the ligament. The fracture mode of the SiCw/Al is different from that of the SiCw/99.75% Al [5] and the unaged SiCp/6061Al [6]: (1) the SiCw/6061Al composite does not form the single major crack which leads to the fracture of the specimen; (2) the local strain of the ligament between cracks after fracture is much smaller than that in the SiCw/99.75%Al and (3) the failure of the specimen is caused by the quick linkage of cracks (see Figure 3(b)). There may be two interpretations. Firstly, it is easier to result in stress concentration for SiC whiskers than SiC particles, and the matrix adjacent SiC whiskers is easier to crack. Secondly, they are more difficult for the stress concentration to relax and for the crack to propagate for the SiCw/6061Al relative to the SiCw/99.75%Al due to higher yield strength and work hardening rate of the former than that of the latter.

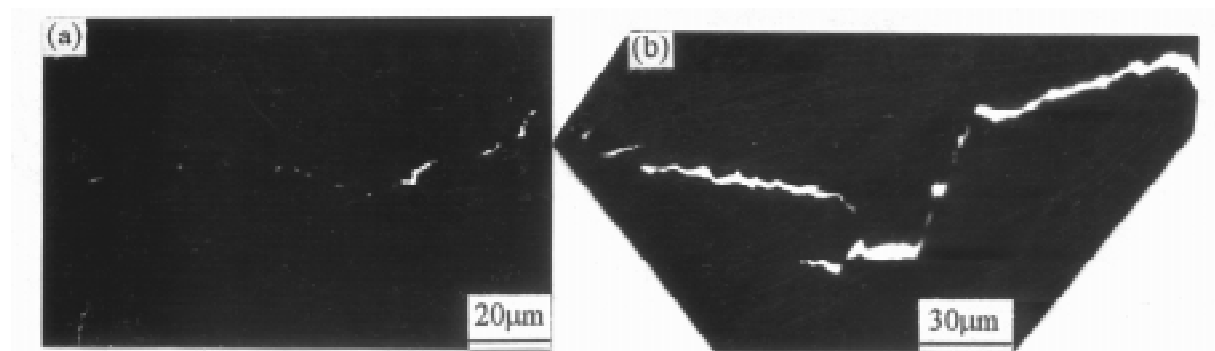


Fig.3: Fracture mode of the SiCw/6061Al composite, (b) showing the failure of the specimen is caused by the abrupt linkage of microcracks in (a)

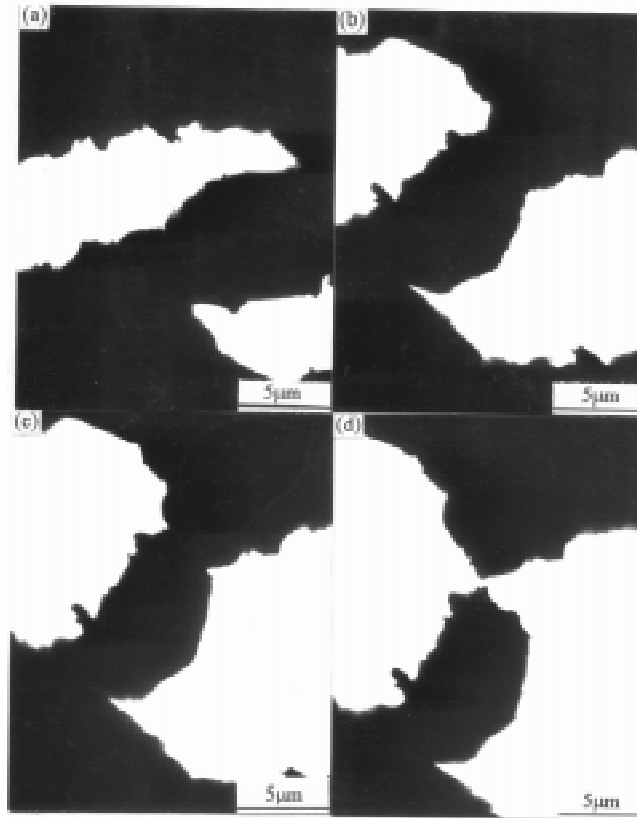
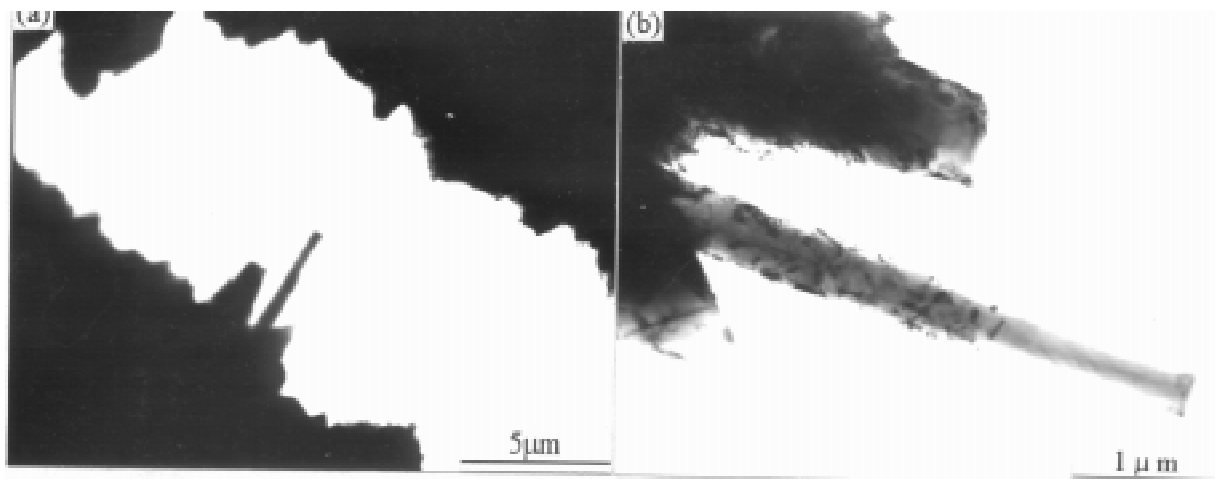


Fig.4: Sequential TEM micrographs showing fracture of the ligament between cracks

Fractured Surface

The TEM micrographs of the fractured surface in SiCw/6061Al composite are shown in Figure 5, in which (b) is at higher magnification than (a). A film of aluminum could



*Fig.5: TEM micrographs of the fractured surface in SiCw/6061Al composite.
(b) is at a higher magnification than (a)*

be observed adhering to the exposed whiskers along the crack edge. This indicates the bonding strength of the SiC-Al interfaces in the squeeze casting SiCw/6061Al is at least higher than the ultimate strength of 6061Al alloy. In addition, the quantity of the exposed whiskers along the crack path is far smaller than the average volume fraction of SiC whiskers

in the SiC/6061Al. This may be because that the formation of microcracks is dominated by the cracking of the matrix although there are three microcrack initiation sources detected as shown in Figure 1.

CONCLUSIONS

The SiCw-Al interfaces in the squeeze casting SiCw/6061Al composite is high strength bonded. The crack initiation modes include: (1) cracking of the SiC whiskers; (2) decohesion of the SiCw-Al interfaces and (3) tearing of the matrix. The SiC whiskers in the SiCw/6061Al composite are major obstacles to the propagation of cracks. The SiCw/6061Al composite does not form the single major crack which results in the fracture of the composite, instead, the microcracks can only propagate and grow to a limited size. The failure of the specimen is caused by the abrupt linkage of cracks.

ACKNOWLEDGMENT

The support of the National Nature Science Foundations, No. 59381002 and the foundation for young scientist with a newly conferred Ph.D in Harbin Institute of Technology, is gratefully acknowledged.

REFERENCES

1. Llorca, J., Martin, A., Ruiz, J. and Elices, M. "Particulate Fracture During Deformation of a Spray Formed Metal-Matrix Composite", *Metallurgical Transactions A*, Vol.24A, No.11, 1993, pp.1575-1588
2. Manoharan, M. and Lewandowski, J.J., "Effect of Reinforcement Size and Matrix Microstructure on the Fracture Properties of an Aluminum Metal Matrix Composite", *Materials Science and Engineering*, Vol.A150, No.1, 1992, pp.179-186.
3. Lee, C.S., Kim, Y.H., Lim T. and Han, K.S., "Dynamic Observation of Failure Processes in Al/SiCw Composite Materials", *Scripta Metallurgica et Materialia*, Vol.25, No.3, 1991, pp.613-618.
4. Kim, Y.H., Lee, S. and Kim, N., "Fracture Mechanisms of a 2124 Aluminum Matrix Composite Reinforced with SiC Whiskers", *Metallurgical Transactions A*, Vol.23A, No.9, 1992, pp.2589-2596.
5. Liu, Z.R., Wang, D.Z., Yao, Z.K., Yao, M., Liu, J. and Geng, L. "In Situ Transmission Electron Microscopy Observation of the Initiation and Growth of Microcracks in an SiC Whisker-Al Composite", *Materials Science and Engineering*, Vol.A189, No.12, 1994, pp.235-239.
6. Doong, S.H., Lee, T.C., Robertson, I.M. and Birnbaum, H.K., "Dynamic Studies of the Crack Initiation and Growth Mechanisms in Al/SiCp Composites", *Scripta Metallurgica*, Vol.23, No.8, 1989, pp.1413-1418.

ANALYSIS ON THE LOAD TRANSFER TO MISALIGNED WHISKERS IN METAL MATRIX COMPOSITE

Soon H. Hong¹ and Kyung H. Chung²

¹*Department of Materials Science and Engineering, Korea Advanced Institute of Science and Technology, 373-1 Kusung-dong, Yusung-gu, 305-701, Korea*

²*Automotive Part, Samsung Electro-Mechanics Co., 28 Block, Nocksan Industrial Complex, Songjeong-dong, Kangseo-ku, Pusan, 618-270, Korea*

SUMMARY: The load transfer mechanism from matrix to whiskers in metal matrix composite was investigated by analyzing the load transfer efficiency at whisker/matrix interfaces. The stress acting on the surface of a whisker was divided into two components, which are longitudinal and transverse to the whisker axis. The stress transferred on a whisker was calculated by solving the differential equations for force equilibrium in longitudinal and transverse directions. An effective aspect ratio was suggested as a new parameter indicating the load transfer efficiency of a misaligned whisker. The effective aspect ratio contributed from the whole distributed whiskers in metal matrix composites was formulated as a function of average aspect ratio and misalignment angle of whiskers. A generalized shear-lag model based on the analysis of the load transfer of misaligned whiskers predicted the tensile strengths of metal matrix composites more accurately than the modified shear-lag model.

KEYWORDS: metal matrix composites, whiskers, load transfer, generalized shear-lag model, effective aspect ratio, misalignment angle, interface

INTRODUCTION

The addition of SiC reinforcements in aluminum matrix results in an increase of mechanical properties, such as tensile strength, elastic modulus and creep resistance [1,2]. The increase of mechanical properties of metal matrix composites(MMCs) is explained by the two strengthening mechanisms. One is the strengthening mechanism due to the load transfer from soft matrix to rigid reinforcement [3]. The other is the strengthening mechanism by the increase of dislocation density due to the mismatch of thermal expansion coefficients between matrix and reinforcement [4]. The two strengthening mechanisms influence on the tensile strength of MMCs independently [4,5]. The effects of dislocation density on tensile strength were effectively formulated by Hall-Petch equation [5] or other equations [6,7]. The shear-lag model was proposed by Piggot [3] to analyze the load transfer effect of fibers in composite materials.

The shear-lag model was modified by Nardone and Prewo [8] into the form which takes into account the tensile load transfer from the matrix to the discontinuous reinforcement. The modified shear-lag model describes the strengthening of metal matrix composites more precisely than the shear-lag model, especially for the composites containing reinforcement with small aspect ratio. However, the modified shear-lag model often overestimates the

strengthening effect in longitudinal direction and underestimates in transverse direction [5]. This discrepancy in the strengthening effect is originated from the assumption of perfect alignment of reinforcement in the modified shear-lag model. In our previous works [9,10], the load transfer efficiency of misaligned whiskers was analyzed and could reasonably correlated with the creep behavior of metal matrix composites.

In this paper, a generalized shear-lag model was proposed through the theoretical modeling of the load transfer mechanism of misaligned whiskers in metal matrix composite. The tensile strengths of metal matrix composites were estimated by the proposed model and were compared with the measured tensile strengths in longitudinal and transverse directions.

THEORETICAL MODEL

Load Transfer on a Misaligned Whisker

In our previous investigations [9,10], the load transfer at the side surface of a whisker was analysed. When the aspect ratio of a whisker is relatively small, the load transfer contribution at the end surface of whisker need to be also considered. Therefore, the load transfer efficiency was analyzed considering the load transfer on both side surface and end surface of a misaligned whisker as shown in Fig.1.

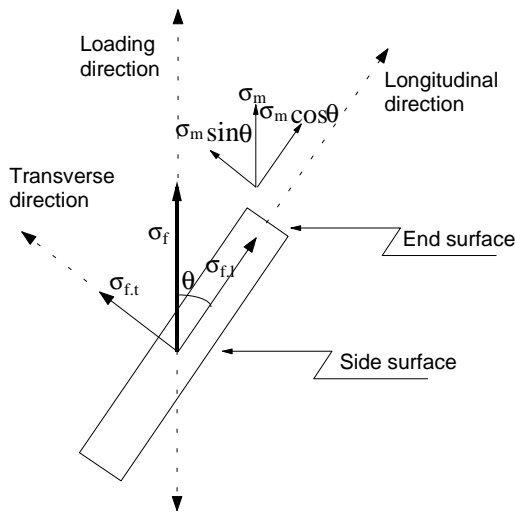


Fig.1 : The analysis of the stresses acting on a whisker aligned with misorientation angle θ from the loading axis

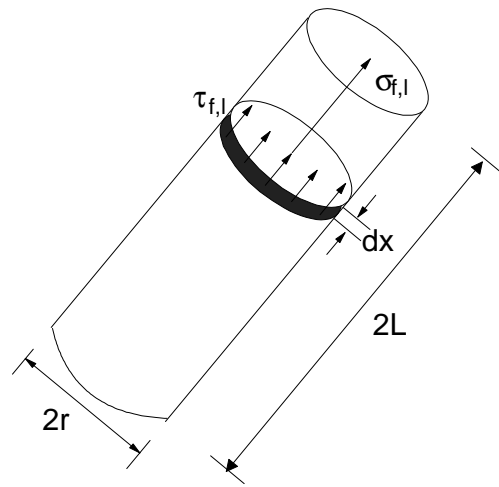


Fig.2: Schematic diagram showing the longitudinal stresses on thin slice of a misaligned whisker

As the differential longitudinal tensile stress, $d\sigma_{f,l}$, should balance with the shear stress on side surface of thin slice perpendicular to the longitudinal direction of a whisker with length $2L$ and diameter $2r$ as shown in Fig.2, a differential equation for the longitudinal stresses on whisker is derived as Eq.(1),

$$-d\sigma_{f,l} = \frac{2\tau_{f,l}}{r} dx \quad (1)$$

where $\tau_{i,l}$ is longitudinal shear stress on side surface of thin slice of whisker in Fig.2. Integration of Eq.(1) using a boundary condition, $\sigma_{f,l} = \sigma_m \cos\theta$ at $x = L$, gives following Eq.(2).

$$\sigma_{f,l} = \sigma_m \cos\theta + \frac{2\tau_{i,l}(L-x)}{r} \quad (2)$$

Then the average longitudinal tensile stress on a misaligned whisker is given as,

$$\bar{\sigma}_{f,l} = \sigma_m \cos\theta + \frac{\tau_{i,l} \cdot L}{r} \quad (3)$$

Assuming the longitudinal shear stress on whisker/matrix interface is one half of the tensile stress parallel to the interface, i.e. $\tau_{i,l} = \sigma_m \cos\theta/2$, the Eq.(3) can be expressed as,

$$\bar{\sigma}_{f,l} = \sigma_m \cos\theta + S \cdot \frac{\sigma_m \cos\theta}{2} \quad (4)$$

where S is aspect ratio, which is defined as L/r , of whisker.

At the same time, as the differential transverse tensile stress, $d\sigma_{f,t}$, should balance with the shear stress on side surface of a thin slice perpendicular to the transverse direction of whisker as shown in Fig.3, a force balance equation is derived as Eq.(5).

$$4Lr \cos^2 \phi (\tau_{i,t} + r\tau_{i,t}) d\phi = -d\sigma_{f,t} 4Lr \cos\phi \quad (5)$$

Then, a differential equation for the transverse stresses on whisker, $\sigma_{f,t}$, is given as Eq.(6),

$$-d\sigma_{f,t} = \left(1 + \frac{1}{S}\right) \cos\phi \cdot \tau_{i,t} \cdot d\phi \quad (6)$$

where $\tau_{i,t}$ is transverse shear stress on side surface of thin slice of whisker in Fig.3. Integration of Eq.(6) using a boundary condition, $\sigma_{f,t} = \sigma_m \sin\theta$ at $\theta = 90^\circ$, gives a following Eq.(7).

$$\sigma_{f,t} = \sigma_m \sin\theta + \left(1 + \frac{1}{S}\right) (1 - \sin\phi) \tau_{i,t} \quad (7)$$

To calculate the average transverse tensile stress on whiskers, the stress multiplied by the slice area, $(2L)(2r\cos\phi)$, was integrated from center to surface and then divided by the integrated area. Since the relative position, y , is represented as $r\sin\phi$, dy is substituted by $r\cos\phi d\phi$, the average transverse tensile stress acting on a whisker can be represented as Eq.(8),

$$\begin{aligned} \bar{\sigma}_{f,t} &= \frac{\int_0^{90} \sigma_{f,t} \cdot 4Lr \cos\phi \cdot r \cos\phi d\phi}{\int_0^{90} 4Lr \cos\phi \cdot r \cos\phi d\phi} \\ &= \sigma_m \cos\phi + \left(\frac{3\pi - 4}{3\pi}\right) \left(1 + \frac{1}{S}\right) \cdot \tau_{i,t} \end{aligned} \quad (8)$$

Assuming the shear stress on side surface is one half of the tensile stress on matrix, i.e. $\tau_{i,t} = \sigma_m \sin \theta / 2$, the Eq.(8) can be rewritten as following Eq.(9),

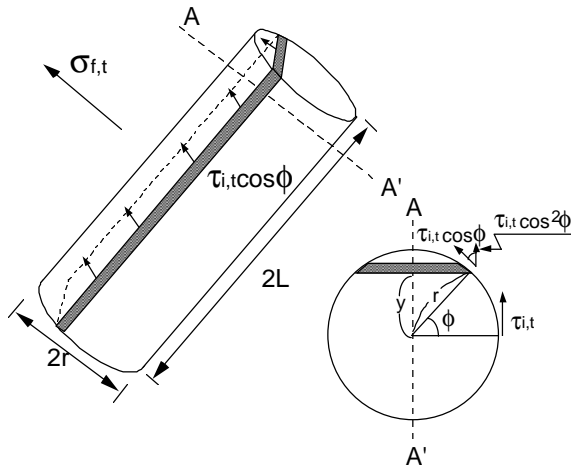


Fig.3: Schematic diagram showing the transverse stresses on thin slice of a misaligned whisker.

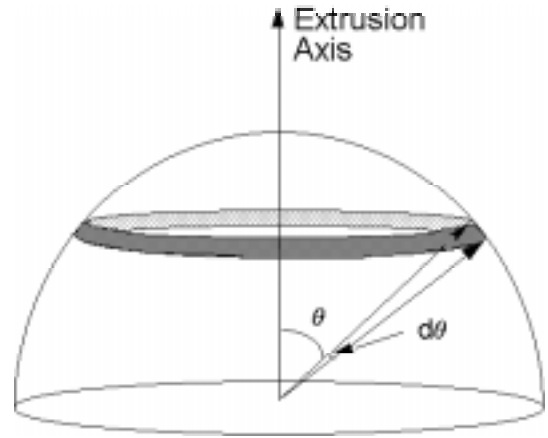


Fig.4: The schematic diagram showing the hemisphere for integration of distributed whiskers in composites.

$$\bar{\sigma}_{f,t} = \sigma_m \sin \theta + \left(\frac{3\pi - 4}{3\pi} \right) \left(1 + \frac{1}{S} \right) \frac{\sigma_m \sin \theta}{2} \quad (9)$$

The stress transferred on whisker along loading axis, σ_f , can be calculated by the vector summation of average longitudinal tensile stress and average transverse tensile stress as following,

$$\begin{aligned} \sigma_f &= \bar{\sigma}_{f,l} \cdot \cos \theta + \bar{\sigma}_{f,t} \cdot \sin \theta \\ &= \sigma_m \cos^2 \theta + \frac{S}{2} \sigma_m \cos^2 \theta + \sigma_m \sin^2 \theta + \left(\frac{3\pi - 4}{3\pi} \right) \left(1 + \frac{1}{S} \right) \frac{\sigma_m \sin^2 \theta}{2} \\ &= \sigma_m \left[1 + \frac{S}{2} \cos^2 \theta + \left(\frac{3\pi - 4}{3\pi} \right) \left(1 + \frac{1}{S} \right) \sin^2 \theta \right] + \sigma_m \end{aligned} \quad (10)$$

By using the rule-of-mixture for composites, a generalized shear-lag model is proposed to calculate the stress on composites with misaligned whiskers as following Eq.(11).

$$\begin{aligned} \sigma &= V_f \sigma_f + V_m \sigma_m \\ &= V_f \sigma_m \left[1 + \frac{S}{2} \cos^2 \theta + \left(\frac{3\pi - 4}{3\pi} \right) \left(1 + \frac{1}{S} \right) \frac{\sin^2 \theta}{2} \right] + V_m \sigma_m \\ &= V_f \sigma_m \frac{1}{2} \left[S \cos^2 \theta + \left(\frac{3\pi - 4}{3\pi} \right) \left(1 + \frac{1}{S} \right) \sin^2 \theta \right] + \sigma_m \end{aligned} \quad (11)$$

From the modified shear-lag model [8], the stress on composites with perfectly aligned whiskers is suggested as Eq.(12).

$$\sigma = V_f \sigma_m \frac{S}{2} + \sigma_m \quad (12)$$

Comparing Eq.(11) and Eq.(12), a new parameter named effective aspect ratio, S_{eff} , for a misaligned whisker is defined as following Eq.(13).

$$S_{\text{eff}} = S \cos^2 \theta + \left(\frac{3\pi - 4}{3\pi} \right) \left(1 + \frac{1}{S} \right) \sin^2 \theta \quad (13)$$

Load Transfer on Distributed Whiskers

The density of whiskers aligned with misorientation angle, θ , in extruded composite decreases exponentially with increasing θ [10,11]. Therefore, it is reasonable to assume that the whisker density function, $F(\theta)$, is expressed as following Eq.(14),

$$F(\theta) = A \cdot \exp(-K\theta) \quad (14)$$

where A and K are constants related to the degree of whisker alignment. The effective aspect ratio contributed by the whiskers aligned with misorientation angle between θ and $\theta+d\theta$, as shown in Fig.4, could be calculated as following equation.

$$dS_{\text{eff}} = S_{\text{eff}}(\theta) \cdot F(\theta) \cdot (2\pi \sin \theta) \cdot d\theta \quad (15)$$

Then, the effective aspect ratio contributed by the whole distributed whiskers along the longitudinal direction of composites is calculated as,

$$S_{\text{eff},l} = \int_0^{90} S_{\text{eff}}(\theta) \cdot F(\theta) \cdot 2\pi \sin \theta \cdot d\theta \quad (16)$$

On the other hand, the effective aspect ratio contributed by the whole distributed whiskers along the transverse direction of composite is calculated as Eq.(17) including the two geometrical angles, η and ϕ , shown in Fig.5.

$$S_{\text{eff},t} = 4 \int_0^{90} \int_0^{90} S_{\text{eff}}(\eta) \cdot F(\cos^{-1}(\sin \eta \cdot \cos \phi)) \cdot \sin \eta \cdot d\eta \cdot d\phi \quad (17)$$

The value of $S_{\text{eff},t}$ can be calculated numerically as a function of degree of alignment, K , and average aspect ratio, S , of whiskers.

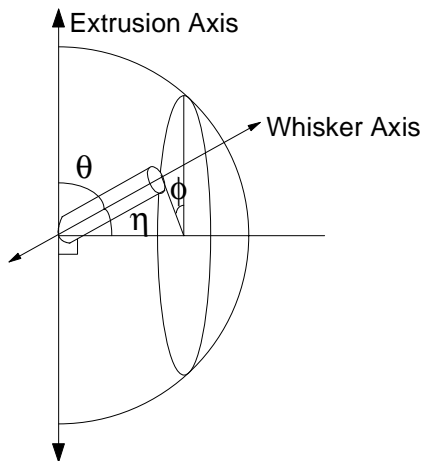


Fig.5: The schematic diagram showing the geometrical angles related to the alignment of a whisker

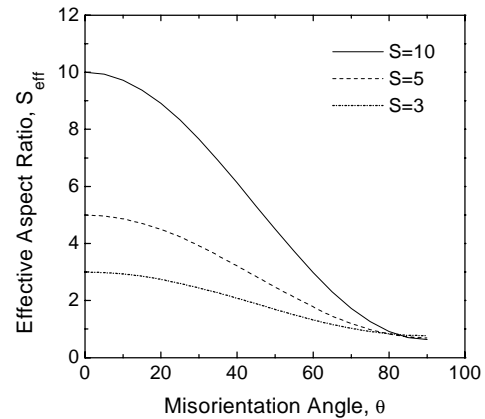


Fig.6: The variation of effective aspect ratio of a whisker with varying the misorientation angle, θ

RESULTS AND DISCUSSION

The calculated effective aspect ratio of a misaligned whisker using the Eq.(13) decreased rapidly with increasing the misorientation angle, θ , from 0° to 90° as shown in Fig.6. The effective aspect ratio of a whisker with larger aspect ratio decreased more rapidly than that with smaller aspect ratio with increasing the misorientation angle. The decrease in effective aspect ratio with increasing the misorientation angle in Fig.6 indicates that the load transfer efficiency decreases and the strengthening effect of misaligned whisker reduces with increasing the misorientation angle.

Fig.7 shows the variation of the effective aspect ratio with varying the aspect ratio of a misaligned whisker having misorientation angle θ . When the whisker is perfectly aligned parallel to the loading axis, i.e. the misorientation angle is 0° , the effective aspect ratio increased linearly with increasing the aspect ratio of whisker. When the misorientation angle is 45° , the effective aspect ratio increased non-linearly with increasing the aspect ratio and was smaller than that with misorientation angle of 0° . However, when the misorientation angle is 90° , i.e. the whisker is aligned perpendicular to the loading axis, the effective aspect ratio decreased with increasing the aspect ratio of whisker. This is because the end surface of whisker mainly contribute to the load transfer to whisker with misorientation angle of 90° and the fraction of end surface area decreased with increasing the aspect ratio.

Fig. 8 shows the variation of effective aspect ratios of distributed whiskers in longitudinal and transverse directions with varying the degree of alignment, K , when the average aspect ratio of whiskers is 3 and 10. The effective aspect ratio in longitudinal direction increased, while that in transverse direction decreased with increasing the K value. The effective aspect ratio was sensitively varied within the K value ranged from -10 to +10, while showed almost constant value when the K value above 10 or below -10. When the K value is 10, the amount of whiskers misaligned more than 30° was calculated only 0.5%. This indicates almost perfect alignment of whiskers when the K value is 10 or higher. As the most extruded metal matrix

composites showed K value less than 5, the effective aspect ratio was sensitively dependent on the degree of alignment in addition to the average aspect ratio of whiskers.

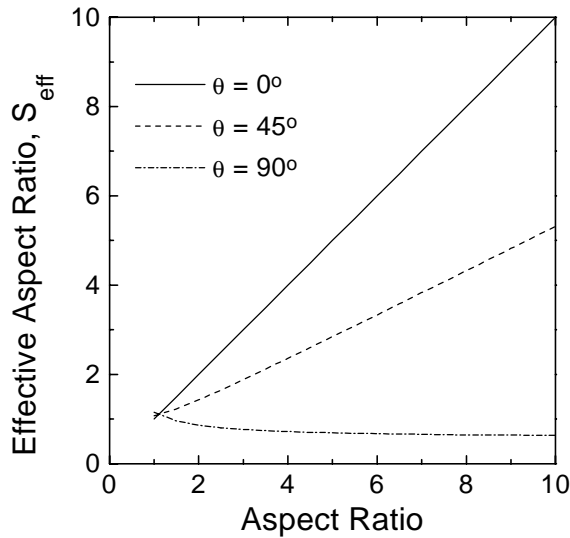


Fig. 7 : The variation of effective aspect ratio with varying the aspect ratio of a whisker with misorientation angle θ

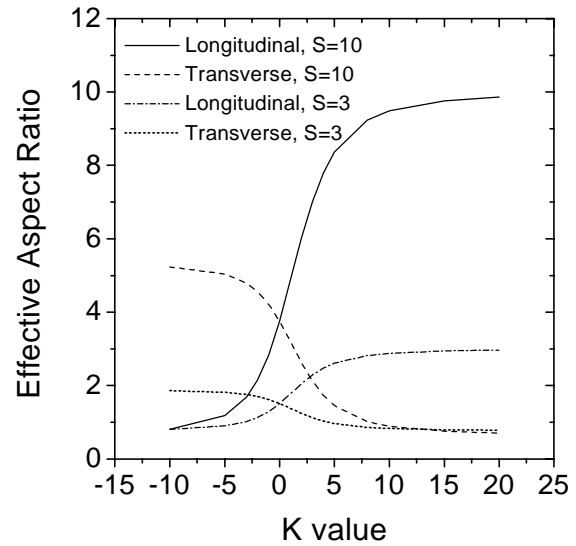


Fig.8: The variation of the effective aspect ratio of distributed whiskers in longitudinal and transverse directions with varying the degree of alignment, K , of distributed whisker.

The tensile strength of metal matrix composites along longitudinal and transverse directions can be represented by the generalized shear-lag model by substituting the effective aspect ratio, S_{eff} , into the aspect ratio, S , expressed as following equation,

$$\sigma_c = \sigma_m \left[V_f \cdot \frac{S_{\text{eff}}}{2} + V_m \right] \quad (18)$$

where σ_m is the average stress on matrix, and V_f and V_m are the volume fractions of whisker and matrix, respectively. To examine the validity of the concept on the generalized shear-lag model, the tensile strengths calculated from the Eq.(18) using the effective aspect ratios in longitudinal and transverse directions were compared with the measured tensile strengths[7] and calculated values by the modified shear-lag model. The average aspect ratio was assumed to be 4 as indicated in the paper, and the degree of whisker alignment, K , was assumed to be 4, which is a typical value for whiskers in extruded metal matrix composites. Table1 compares the measured tensile strengths of SiCw/Al composites with the calculated values based on both the generalized shear-lag model and the modified shear-lag model, respectively. The calculated tensile strengths from the generalized shear-lag model showed more similar values with the measured tensile strengths of SiCw/Al composites in longitudinal and transverse directions than those calculated from the modified shear-lag model. This indicates that the load transfer efficiency of whiskers was analyzed more accurately by the proposed generalized shear-lag model, which considers the load transfer at

side and end surface of misaligned whiskers, because the whiskers are not perfectly aligned in metal matrix composites.

Table 1: The measured and calculated tensile strengths of SiCw/Al composites in longitudinal and transverse directions.

		Measured Tensile Strength (MPa)	Calculated by Generalized Shear-lag Model (MPa)	Calculated by Modified Shear-lag Model (MPa)
20% SiCw/6061Al -T6	Longitudinal	447	472	500
	Transverse	409	402	393
	L/T Ratio	1.10	1.17	1.27
20% SiCw/2124Al -T6	Longitudinal	524	520	551
	Transverse	466	442	433
	L/T Ratio	1.12	1.18	1.27

CONCLUSIONS

The load transfer efficiency of a misaligned whisker was analyzed assuming that both the shear stresses on side surface and the normal stress on end surface of whisker contribute to the load transfer from matrix. Considering the load transfer contribution of distributed whiskers in composite, a new parameter of effective aspect ratio, S_{eff} , was proposed to represent the load transfer efficiency of misaligned whiskers in composites as a function of average aspect ratio and misalignment angle. A generalized shear-lag model was proposed as a function of effective aspect ratio to estimate the tensile strength of metal matrix composites. It is confirmed that the generalized shear-lag model estimate the tensile strength of SiCw/Al composites more accurately compared to the modified shear-lag model in longitudinal and transverse directions.

REFERENCES

1. T.G. Nieh and R.F. Karlak, "Hot-Rolled Silicon Carbide-Aluminium Composite", *Journal of Materials Science Letters*, Vol. 2, No. 3, 1983, 119-122.
2. D.J. Lloyd, "Particle Reinforced Aluminium and Magnesium Matrix Composite", *International Materials Reviews*, Vol. 39, No. 1, 1994, pp. 1-23.
3. M.R. Piggot, *Load Bearing Fiber Composites*, Pergamon Press Inc., 1980, pp. 62-82.

4. Y. Wu and E.J. Lavernia, "Strengthening Behavior of Particulate Reinforced MMCs", *Scripta Metallurgica et Materialis*, Vol. 27, No. 2, 1992, pp. 173-178.
5. V.C. Nardone, "Assesment of Models Used to Predict The Strength of Discontinuous Silicon Carbide Reinforced Aluminium Alloys", *Scripta Metallurgica et Metallurgica*, Vol. 21, No. 19, 1987, pp.1313-1318.
6. R.J. Arsenault, "The Strengthening of Aluminium Alloy 6061 by Fiber and Platelet Silicon Carbide", *Materials Science and Engineering*, Vol. 64, No.2, 1984, pp.171-181.
7. J. Sarkar, "Aspects of Strengthening and Work Hardening in Particulate Metal Matrix Composites", *Scripta Metallurgica et Materialia*, Vol. 32, No.1, 1995, pp.37-42.
8. V.C. Nardone and K.M. Prewo, "On The Strength of Discontinuous Silicon Carbide Reinforced Aluminium Composites", *Scripta Metallurgica*, Vol.20, No.1, 1986, pp.43-48.
9. S.H. Hong and K.H. Chung, "High Temperature Creep Behavior of Metal Matrix Composites", *Key Engineering Materials*, Vol. 104-107, 1995, pp.757-764.
10. S.H. Hong and K.H. Chung, "The Role of Reinforcement on High Temperature of SiC/2124Al Metal Matrix Composites", *Proceedings Tenth International Conference on Composite Materials*, Whistler, British Columbia, Canada, August 14-18, 1995, pp. 645-652.
11. R.K. Everett and R.J. Arsenault, *Metal Matrix Composites*, New York: Academic Press, 1991.

MICROSTRUCTURE OF TITANIUM DIOXIDE (RUTILE)/ PURE ALUMINUM COMPOSITES

Gen Sasaki¹, Isao Tuchitori² and Hideharu Fukunaga¹

¹*Department of Mechanical Engineering, Hiroshima University, 1-4-1 Kagamiyama Higashi-Hiroshima, Hiroshima, 739 Japan.*

²*Industrial Research Institute West of Hiroshima Prefecture, 2-10-1 Aga-minami, Kure, Hiroshima, 737 Japan.*

SUMMARY: The hardness of TiO₂/Al composites by squeeze casting is able to control easily by carrying out a heat treatment. The hardening of the composites is caused by Al₂O₃ and Al-Ti compounds reacted from TiO₂ and Al. For as-cast composites, TiO₂ particles are dispersed uniformly in Al matrix. On the other hand, the completely reacted composite is composed by the reaction products, and Al₂O₃ grains are dispersed uniformly. The interface between Al₂O₃ and Al-Ti compounds has a good coherent with little lattice mismatch. However, the crack propagate along Al₂O₃ and Al-Ti compound grains, so that the hardness of the composite seem to depend on the interface strength, strongly. In order to investigate the micromechanism that Na containing in TiO₂ particles decrease the temperature for TiO₂ and Al, Na was thermal doped to TiO₂ particles. Some structure changes are locally occurred on the surface of the particles, which seem to be a reaction site of TiO₂ and Al.

KEYWORDS: metal matrix composite, titanium dioxide, aluminum, squeeze casting, reaction hardening, transmission electron microscopy, interface, sodium

INTRODUCTION

Recently, the study on the composites prepared by utilizing a reaction between aluminum alloys and inorganic reinforcements is watched with great interest because of the hardness, strength and some other mechanical properties of which are able to be controlled by carrying out a heat treatment after or during fabrication. Many remarkable fabrication techniques, such as Lanxide method[1], XD process[1], VLS process[2] and spontaneous infiltration technique[3] have been studied. Squeeze casting method have great advantage for the productivity and the workability. Authors fabricated TiO₂/Al alloy composites by squeeze casting, and found that the hardness of the composites is controlled easily by heat-treatment[4]. TiO₂ reacts slowly with solid Al resulting Al₂O₃ and Al-Ti compounds during heat-treatment process[5]. This composite is the mixture of metal matrix and intermetallic compound matrix composite, so that the hardness and strength of the composite are superior than the usual metal matrix composite. The composites fabricated by the reaction process are able to obtain the high performance compounds under the low temperature and easy forming condition. But the microstructure of the composite and the change of the micromechanism by the reaction are unknown.

Pure TiO₂ particles do not react with solid Al, so that the composites are not able to be hardened by heat treatment. It is also reported that alkaline metal and alkaline earth metal elements containing in the practical grade TiO₂ particles lead to decrease in the reaction temperature[6]. Especially, the elements having large ionic diameter such as Na assist the reaction of Al and TiO₂ with calorification above 873K. But the micromechanism about the effect of Na element containing in the particles is also unknown.

In order to improve the mechanical properties for TiO₂/Al composites, an analysis to the microstructure and micromechanism of the reaction is needed. This study puts stress on issues the structure change in the composite during the reaction and the effect of Na element on the reaction process.

EXPERIMENTAL PROCEDURE

TiO₂ particles employed here were the rutile type with 0.3μm in diameter and its purity was 98.5% (practical grade, Wako Pure chemical Industry Ltd., Japan). In order to make clear the effect of Na element on the reactivity, the mixture of pure TiO₂ (99.9%, Wako Pure chemical Industry Ltd., Japan) and NaCO₃ powders was doped by ball milling (Pulverisette-5, Fritsch Ltd., Germany) and be heat-treated at 1373K for 3.6ks. Table 1 and Table 2 show the chemical compositions of practical grade TiO₂ particles and the impurity elements in high purity TiO₂ particles, respectively. In practical grade, 0.2 mass% NaO are contained. On the other hand, there is few Na content (7.8 mass ppm), and other alkaline and alkaline earth metal elements in high purity TiO₂ particles. The TiO₂ preform was fabricated by cold press forming with 0.3MPa and heat-treated at under 1373K for 1.8ks in atmosphere. The size of prepared preform is 30mm in diameter and 25mm in height and the volume fraction of TiO₂ is 40.5%. Pure Al (99.993%) was selected as the matrix and the composite was fabricated by a squeeze casting method at the molten metal temperature of 923K and preform temperature of 523K with the pressure of 100MPa. These parameters are almost the lowest temperature condition for the fabrication of a composite. Then the fabricated materials was heat-treated at a temperature between 773K and 1273K in atmosphere by the electric furnace. The microstructure and the reaction products were analyzed by transmission electron microscopy (TEM), scanning electron microscopy (SEM), energy dispersive X-ray spectroscopy (EDS) and X-ray diffraction analysis (XRD). TEM observation was carried out with JEOL/JEM4000EX for high resolution observation and JEOL/JEM2010 with EDS (NORAN/series II) for elemental analysis. SEM observation was carried out with HITACHI/S800.

Table 1. Chemical compositions of practical grade (85.5 mass%) TiO₂ particles.

(mass%)										
Al ₂ O ₃	ZnO	SiO ₂	P ₂ O ₅	Na ₂ O	Nb ₂ O ₅	SO ₂	ZrO ₂	K ₂ O	CaO	TiO ₂
2.71	1.03	0.56	0.19	0.2	0.15	0.08	0.047	0.01	0.005	bal.

Table 2. Impurity elements in high purity (99.9 mass%) TiO₂ particles.

(mass ppm)												
Al	Zn	Na	K	Ca	Fe	Ta	Cr	Ni	As	Pb	Mg	Ba
25.0	1.5	7.8	0.3	8.0	13.8	28.2	12.3	4.3	4.7	1.8	1.9	0.3

RESULTS AND DISCUSSION

Microstructure of Practical Grade TiO₂ Particles/Al Composite

Figure 1 is some TEM photographs showing the microstructure of TiO₂/Al composites. The compounds of the composite were identified by EDS analysis. Fig. 1(a) shows the as-cast TiO₂/Al composites, which hardness is Hv 210. TiO₂ particles are dispersed uniformly in the Al matrix. Fig. 1(b) shows the composite heat-treated at 833K for 3.0ks, which hardness is Hv 400. Under this heat-treatment condition, the composite consists of TiO₂, Al₂O₃ and Al₃Ti compounds. But Ti₃Al compound was not observed. Al₂O₃ exists at the surface of TiO₂ particles and among Al₃Ti compounds. Fig. 1(c) is taken from the heat-treated composite at 973K for 0.3ks, which hardness is Hv 760. TiO₂ and Al were not observed under this condition. It seems that TiO₂ and Al in the composite react completely. The composites consist of Al₂O₃ and Al-Ti composites, such as Al₃Ti and Ti₃Al compounds. Al₂O₃ grains are dispersed uniformly in Al-Ti matrix and are equiaxed in shape with 10-50 nm in diameter. It seems that TiO₂ particles react with Al resulting in Al₂O₃ and Al₃Ti at first and then TiO₂ react with Al₃Ti forming Al₂O₃ and Ti₃Al.

Figure 2 is an enlargement of fig. 1(a) showing the microstructure of the as-cast TiO₂/Al composite. The black-white contrasts are observed in TiO₂ particles (fig. 2(a)). Fig. 2(b) shows the lattice arrangement of TiO₂ particles. Lattices have some curvature and disappeared here and there. The broad black-white contrast is due to strain field. It seems that the lattice of TiO₂ particles is distorted by the high pressure of squeeze casting and the compression stress caused by the solidification of Al matrix. Fig. 2(c) shows the atomic arrangement of the interface between TiO₂

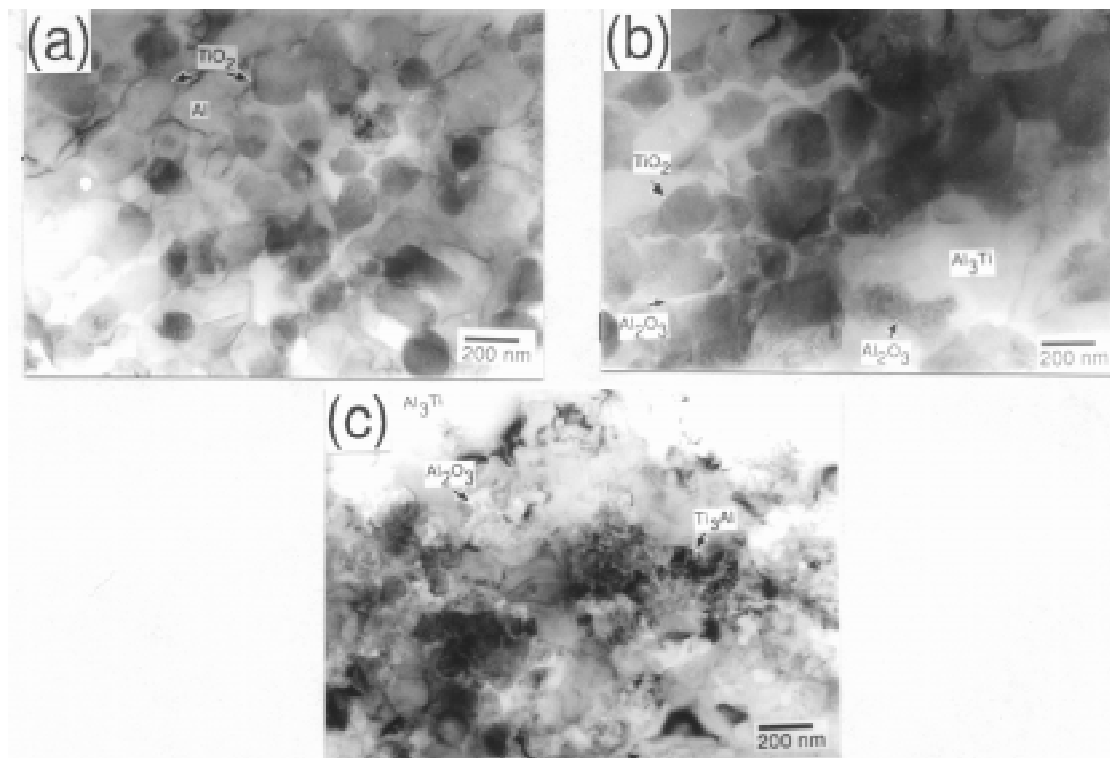


Figure 1. TEM images of TiO₂/Al composites. (a) As cast, (b) 833K-3.0ks heat treatment, (c) 973K-0.3ks heat treatment.

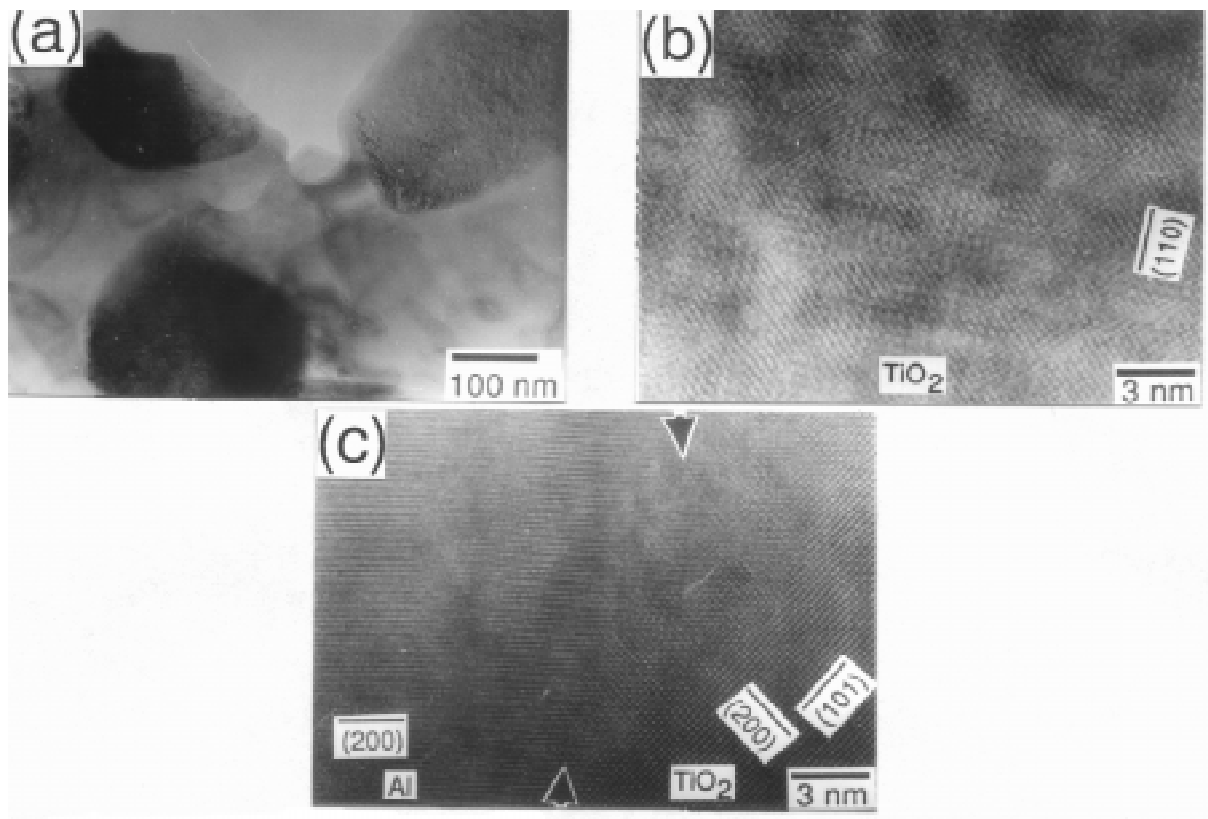


Figure 2. TEM images of as-cast TiO₂/Al composites. (a) microstructure of the composite, (b) High resolution image inside TiO₂ particles, (c) high resolution image of the interface between TiO₂ particles and Al matrix.

and Al. The lattices of TiO₂ and Al connect directly. There is not any reaction product between TiO₂ and Al. The accurate interface position is not able to decide because of the good coherent. It seems that there is a epitaxial growth of Al on TiO₂ particles during solidification after a squeeze casting. Figure 3 is a microstructure of heat-treated composite at 973K for 0.3ks.

Fig. (a) is a high resolution observation at the interface between Al₂O₃ grain and Al₃Ti compound. In the heat-treated TiO₂/Al composites, the interface between Al₂O₃ and Al-Ti compounds formed by the reaction of TiO₂ and Al has a good coherent with little lattice mismatch. Fig. (b) shows a crack propagation in the microstructure. The crack propagates almost straightly along Al₂O₃ and Al-Ti compound grains. It seem that the interface strengths between Al₂O₃ and Al-Ti compounds or between the Al-Ti compound themselves are weak. The hardness and strength of the composite depend on these interface strength, strongly.

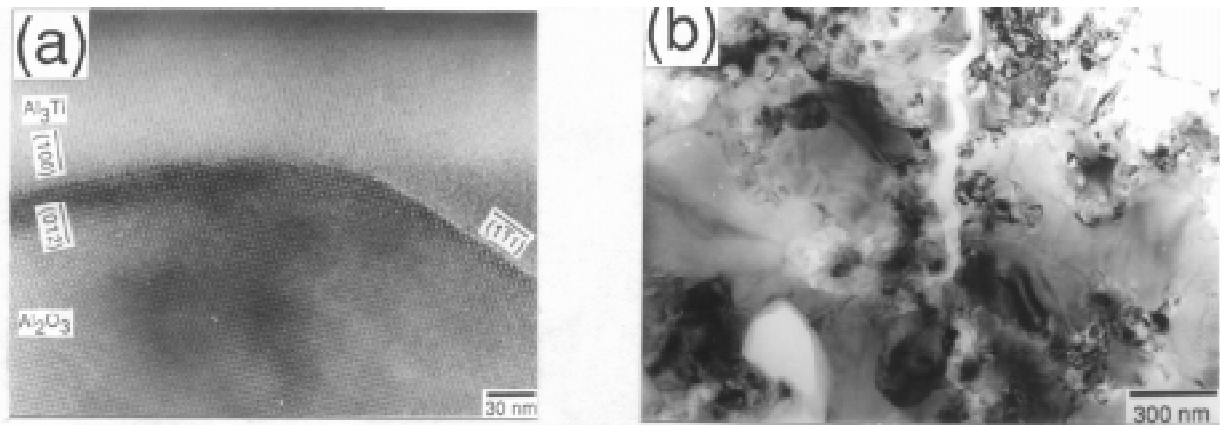


Figure 3. TEM images of heat-treated TiO_2/Al composite at 973K for 0.3ks. (a) high resolution image of the interface between Al_2O_3 and Al_3Ti compound (b) conventional image of the crack propagation.

Effect of Na Element in TiO_2 Particles

Na element in practical grade TiO_2 particles leads to a decrease in the reaction temperature during a heat treatment after the fabrication of the composites. In order to investigate this effect, Na element was doped to TiO_2 particles by ball milling. Figure 4 show that the microstructure of no-treated high purity TiO_2 particles (fig. 4(a)) and Na doped TiO_2 particles (fig. 4(b)). There is no difference for the morphology between Na doped and no-doped TiO_2 particles. Both the particles in fig. 4(a) and (b) are equiaxed in shape with about 300nm in diameter and have a straight surface. Table 3 is a EDS analysis of Na doped TiO_2 particles at the center and edge of the particle. At the center, the detected element was only Ti and O and the atomic ratio of Ti:O is about 1:2, which is equal to the composition of TiO_2 . At the edge, 0.28 at% Na element are detected. The EDS result illustrates that Na distributes only at the surface of the particle.

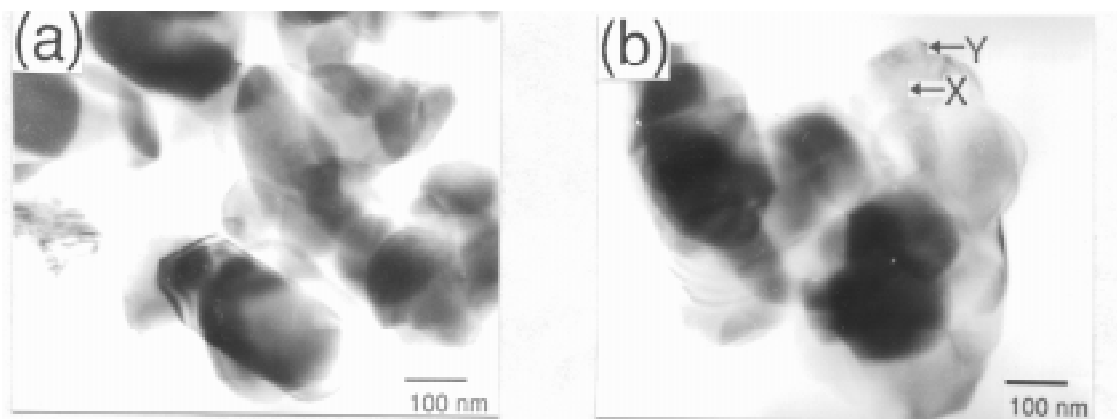


Figure 4. TEM images of high purity TiO_2 particles. (a) no-treated particle (b) Na doped particles.

(analyzed area : $\phi 3\text{nm}$)

Region	element (at%)		
	Ti	Na	O
X: Center	39.58	0.00	60.42
Y: Edge	31.51	0.28	68.21

Table 3. EDS analysis of Na doped TiO_2 particles in region X and Y shown in fig. 4 (b). Analyzed areas are 3nm in diameter.
(analyzed area : $\phi 3\text{nm}$)

Figure 5 is some high resolution images showing the microstructure of the interface. Fig. 5 (a) is the case of no-treated TiO_2 particle. There is an amorphous layer at the surface which is the contamination, such as organic matter. The surface structure shown in fig. 5 (b) are observed here and there in Na doped TiO_2 particle. By thermal doping Na to TiO_2 particles, an amorphous layer on the surface disappeared, and new structure layer generated. This New layer is 1-2nm in depth. The structure of it seem to be the complex oxide formed by Na and Ti. Some structure changes are locally occurred on the surface of the particles.

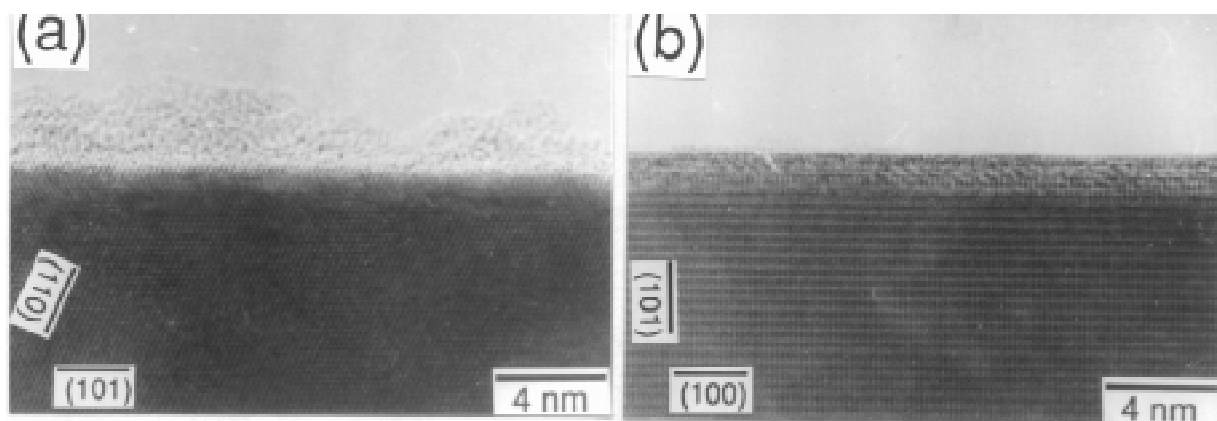


Figure 5. High resolution TEM images of the surface structure of TiO_2 particle. (a) No-treated TiO_2 particle (b) Na doped TiO_2 particle.

Figure 6 shows the microstructure of TiO_2/Al composite operated by SEM. TiO_2 particles employed here are the high purity grade (99.9%) with $5\mu\text{m}$ in diameter. Fig. 6(a) shows the no doped and as cast composite. TiO_2 particles are dispersed uniformly and the reaction products have not been observed. Fig. 6(b) is the no-doped and heat-treated composite at 873K for 86.4ks. The reaction products are observed at the interface between TiO_2 and Al. The white layers at the interface is Al_2O_3 which is formed by the reaction of TiO_2 and Al. Fig. 6(c) is the Na doped and heat-treated composite under the condition of 873K for 86.4ks. The reaction products are observed as the fine precipitates in TiO_2 particles. The reaction occurs

inside the TiO_2 particles. This phenomenon quite differ from that of the no-doped composite. Some structure changes are locally occurred on the surface of the TiO_2 particle and these areas become a reaction site of TiO_2 . Consequently, the reaction temperature is decreased and Al_2O_3 can be seen to precipitate inside the TiO_2 particles.

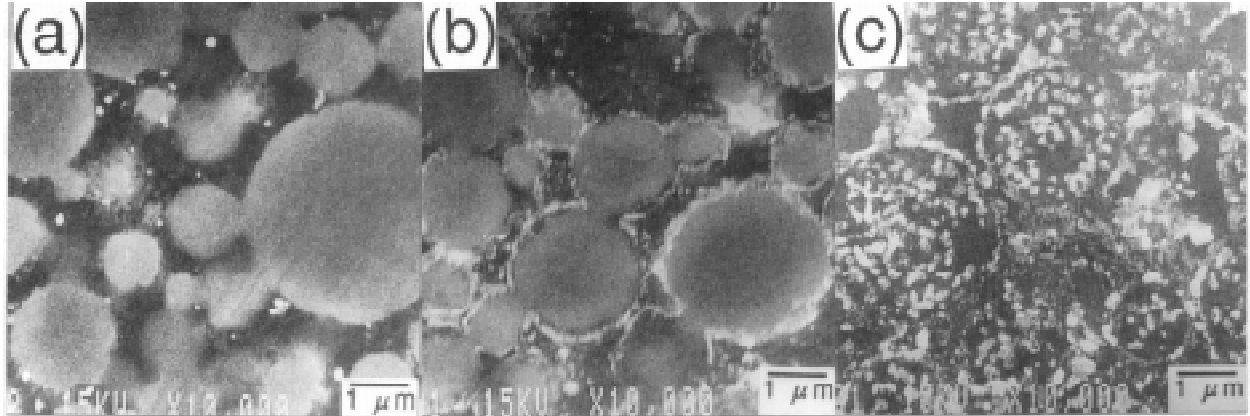


Figure 6. SEM images of the microstructure of TiO_2/Al composites. (a) As cast high purity TiO_2 composite (b) high purity TiO_2/Al composite with the heat treated under the condition of 873K for 86.4ks (c) Na doped TiO_2/Al composite heat treated under the condition of 873K for 86.4ks.

CONCLUSION

TiO_2/Al composites were fabricated by a squeeze casting and the changes of microstructure in the composite during the heat-treatment process were investigated. The mechanism of the stimulatory reaction by thermal doping Na to TiO_2 was analyzed.

- 1) For the as-cast TiO_2/Al composite, TiO_2 particles are dispersed uniformly in the matrix. There is not any reaction product between TiO_2 and Al. The lattice of TiO_2 particles is distorted by the high pressure of squeeze casting.
- 2) For the heat-treated TiO_2/Al composites, TiO_2 particles react with Al resulting in Al_2O_3 and Al-Ti compounds. The interface between Al_2O_3 and Al-Ti compounds has a good coherent with little lattice mismatch.
- 3) By thermal doping Na to TiO_2 particles, some structure changes are locally occurred on the surface of the particles in depth of 1nm. By heat-treating TiO_2/Al composite, Al_2O_3 formed inside TiO_2 particles. The spotty areas seem to be a reaction site of TiO_2 and Al, and the reaction temperature is decreased.

ACKNOWLEDGEMENTS

The authors are grateful to Mr. Yao L. J. of Hiroshima University for his help. This works is supported by a Grant-in-Aid (No. 08455312) from the Ministry of Education, Science, Sports and Culture of Japan and, performed under the inter-university cooperative research program of the Institute for Materials Research, Tohoku University.

REFERENCES

1. R.K. Everett and R.J. Arsenault, Metal Matrix Composites: Processing and Interface, Academic Press Ltd, San Diego, 1991.
2. H. Nakata, T.Choh and N. Kanetake, "Fabrication and mechanical properties of in situ TiCp/Al composites by the interfacial reaction between SiCp and liquid Al-Ti alloy", J. Japan Inst. Light Metals, Vol.43, No.3, 1993, pp. 152-158
3. H. Nakata, T.Choh and N. Kanetake, "Development of Spontaneous Infiltration-in situ Production Process for Fabrication of Particulate Reinforced Aluminum Composites", J. Japan Inst. Metals, Vol.58, No.7, 1994, pp.803-809
4. I. Tuchitori and H. Fukunaga, "Reaction Hardening of Particulate Titanium Dioxide (rutile)/ Aluminum Composites by Heat-Treatment", J. Japan. Inst. Metals, Vol.58, No.9, 1994, pp.1029-1035
5. I. Tuchitori and H.Fukunaga, "Process Control by Reaction Squeeze Casting for Intermetallic-strengthening of TiO₂/AL Composite", Proc. of ICCM9, Vol.2, 1993, pp. 906-912
6. I. Tuchitori, N. Morinaga and H. Fukunaga, "Effects of Mg and Si on Reaction Hardening of Particulate Titanium Dioxide (Rutile)/ Aluminum Composites", J Japan Inst. Metals, Vol.59, No.3, 1995, pp. 331-338

THE INTERPRETATION OF X-RAY STRESS MEASUREMENTS OF METAL MATRIX COMPOSITES USING COMPUTER MODELLING TECHNIQUES

M.R.Watts and P.J.Withers

Department of Materials Science and Metallurgy, University of Cambridge, Pembroke Street, Cambridge, CB2 3QZ, United Kingdom.

SUMMARY: In this paper the interpretation of X-ray measurements of stress based on the conventional $\sin^2\psi$ method is examined for metal matrix composites. While the biaxial assumption may be valid for macrostress distributions, its range of validity for materials such as composites which contain microstresses is not so clear. A finite element model has been constructed to simulate the relaxation of an internal thermal microstress distribution near the free surface. Analytical modelling has then been used to simulate the stress distribution, on the basis of which $\sin^2\psi$ plots have been produced. This work suggests that the biaxial stress assumption is valid over a shorter region than previously thought and that this has serious implications for the interpretation of X-ray measurements made on composites. These implications are examined for an Al/SiC metal matrix particulate composite system.

KEYWORDS: residual stresses, metal matrix composites, x-rays, finite element modelling, internal stresses, thermal stresses

INTRODUCTION

The fact that the normal stress across a free surface must be zero has long been exploited for the interpretation of X-ray stress measurements using the $\sin^2\psi$ method [1-3]. Of course this assumption is only strictly true at the surface, but since the penetration of X-ray radiation within metallic materials is limited to depths of only tens of microns, in many cases it is a fair assumption for the whole of the sampling volume. While this assumption may well have merit for single phase materials, the situation is not so clear for composites, which often contain microstresses between the phases, arising for example, from differences in thermal expansion coefficient, or from plastic deformation of the matrix phase. Previously, Nishioka et al. and Hanabusa et al. [4,5] attempted to calculate the rate at which the internal stresses fall off as the free surface is approached for a regular array of second phase particles. In this paper we use finite element modelling techniques to examine the rate of decay of the stress state near-surface for a randomly distributed reinforcing phase.

When the penetration depth is significantly less than the particle spacing a steep gradient is predicted indicative of a biaxial stress and when the penetration is greater than the particle

spacing, the gradient is shallow, indicative of the hydrostatic stress state typical of the bulk. Hanabusa et al. [5] found that using their model the $\sin^2\psi$ gradient is dependent upon the depth of penetration as a fraction of the particle spacing. Traditionally, it is assumed that if the $\sin^2\psi$ plot gives a straight line then the biaxial assumption is valid, because were the biaxial assumption to be invalid one would expect to find curvature of the $\sin^2\psi$ plot arising from the decreasing depth of penetration as the ψ angle increases. In practice it is extremely rare to obtain a perfect straight line. Loss of linearity is not uncommon for MMC's and is often ascribed to poor counting statistics. However, if the effect is caused through a breakdown in the biaxial assumption, then the stress state will be very poorly estimated. In this paper the severity of this problem is investigated by modelling the stress relaxation profile from the surface for a series of composites, and to use the profiles thus deduced to simulate the associated X-ray $\sin^2\psi$ profiles. As the results amply demonstrate, for Al based composites, the estimated microstresses can be seriously in error.

EXPERIMENTAL APPROACH

The $\sin^2\psi$ Method

In general X-ray stress measurements are made using the standard $\sin^2\psi$ method (Fig.1).

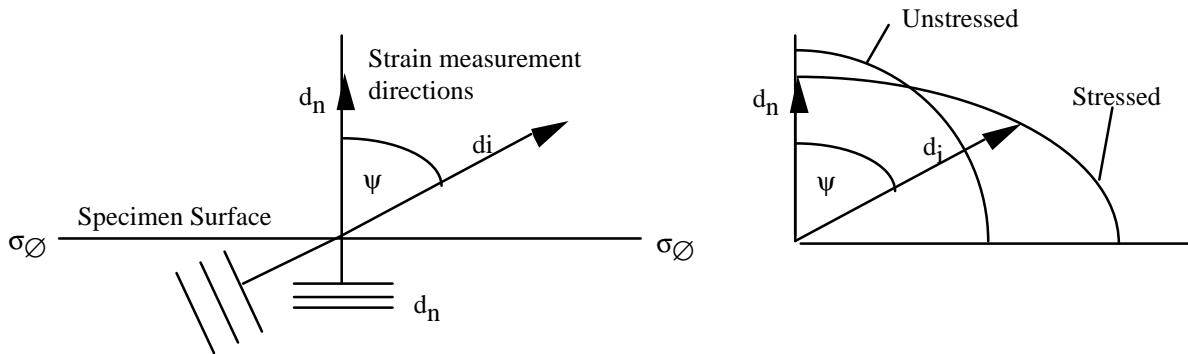


Figure 1: Schematic representations illustrating the variation in d with measurement angle ψ [1].

It can be shown that [1],

$$\epsilon_\psi - \epsilon_y = \frac{\sigma_\phi}{E} (1 + \nu) \sin^2 \psi \quad (1)$$

where ϵ_ψ is the strain at an angle ψ , and ϵ_y is the normal strain. This equation is the basis for the $\sin^2\psi$ method for the measurement of stress using X-rays. By rewriting Eqn 1 in terms of lattice parameter instead of strains, the following equation can be arrived at;

$$\sigma_\phi = \frac{E}{(1 + \nu) \sin^2 \psi} \left(\frac{d_i - d_n}{d_n} \right) \quad (2)$$

Using this equation, it is possible to calculate in-plane stresses without having to know the unstressed plane spacing, d_o since it is assumed that the error between d_o , d_i and d_n is small.

The Finite Element Model

To simulate experimental $\sin^2\psi$ plots, two types of computer model were used. The first, a finite element model, was used to model the composite in order to calculate the extent of relaxation of the microstress profile as a function of distance from the free surface. The second was used to calculate the X-ray $\sin^2\psi$ response that such stress variation would produce.

A 25,000 element model was constructed within ABAQUS™. To reduce computational complexity a two dimensional generalised plane strain model was employed. In effect this is equivalent to studying a randomly distributed array of fibres with their axes all lying parallel to the z-axis. Each particle was represented as a square comprising 5x5 square four noded elements. Overall, the model comprised 500 elements in the x-direction and 50 element layers in the y-direction (Fig. 2). The boundaries of the model were constrained to remain planar, except for the free surface at $y=0$, across which there was no constraint at all. The x-co-ordinate of each particle was chosen at random, but ensuring that no particles were touching. With respect to the through thickness (y) co-ordinate, the particles were placed such that each layer contained the same volume fraction of particles as the composite as a whole. This procedure was chosen to simulate a random particle distribution without the need for thousands of particles to overcome the fluctuations in the stress profile from sub-surface layer to layer arising from random fluctuations in the *number* of particles in each layer. Particle volume fractions of 5, 10 and 20% were studied simply by adding more and more particles using the above procedure. The use of square particles does lead to some level of stress concentration at particle corners not present if spheres were used, but this geometry has the advantage that it requires relatively few elements to capture the geometry and it simplifies the process of calculating the average phase stresses as a function of distance from the free surface. In order to generate sizeable thermal expansion misfit microstresses, a temperature drop of 400°C was applied across the whole composite, and it was assumed that there were no temperature gradients through the body of the material. Perfect elasticity and perfect bonding across the interface of the particle/matrix were also assumed. The particle and matrix regions were assigned material properties appropriate to silicon carbide and an aluminium alloy respectively (Table 1).

Once the stress field had been computed the stress profile with distance from the free surface was calculated by measuring the average phase stress in each layer. By doing this as a function of depth from the surface, it was possible to obtain a profile of the stress as it increased from the surface into the bulk of the material. Profiles such as those shown in Fig. 3 were produced for the stress in the x, y, and z-directions, as a function of depth (y) from the free surface.

Table 1: Material properties used in finite element modelling.

Material Property	Matrix (Aluminium, 2024)	Particles (Silicon Carbide)
Young's Modulus, E (GPa)	69	400
Poisson's Ratio, ν	0.34	0.17
CTE, α (10^{-6} K^{-1})	24	4.5

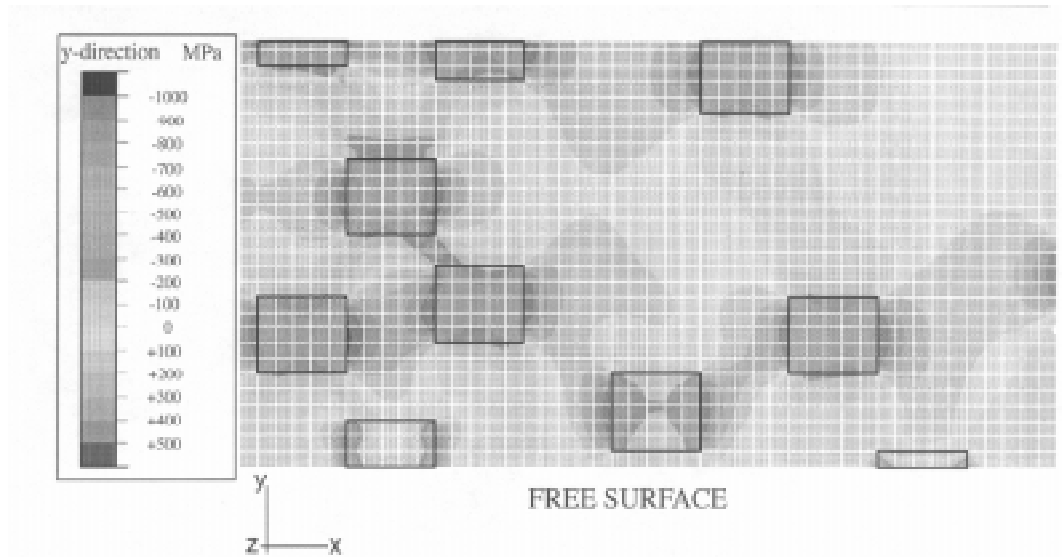


Figure 2: The stress distribution caused by cooling the composite by 400°C in a small part of the FE model.

Mathematica Simulation of X-ray $\text{Sin}^2\psi$ Curves

With the stress profile for the matrix and reinforcement phases calculated it is necessary to simulate the $\text{sin}^2\psi$ curves taking into account increasing attenuation with increasing depth. The elastic strain $\epsilon(y)$ in the direction ψ at a depth y can be calculated from the stress profiles, $\sigma_x(y)$, $\sigma_y(y)$ and $\sigma_z(y)$. For a given measurement direction ψ , the strain from each layer contributes to the overall diffraction peak according to:

$$\langle \epsilon_{\psi} \rangle = \frac{\int_0^{\infty} dI_D \cdot \epsilon}{\int_0^{\infty} dI_D} \quad \text{where} \quad dI_D = \frac{I_0 ab}{\sin(\theta + \psi)} \exp \left[-\mu y \left(\frac{1}{\sin(\theta + \psi)} + \frac{1}{\sin(\theta - \psi)} \right) \right] dy \quad (3)$$

where I_0 is the incident beam intensity, and a and b are constants. By using at least five ψ angles a plot of the strain versus $\text{sin}^2\psi$ can be obtained, which can then be compared to actual experimental plots.

RESULTS

Stress Relaxation Profiles

Fig. 3a-d shows the stress profiles obtained from finite element (FEA) models of the type shown in Fig. 2. As expected, and predicted by Hanabusa et al. [5], the stress components increase from the surface towards the bulk. As required of a free surface, the out-of-plane stress, σ_y , tends to zero as the surface is approached, as do the in-plane stresses. As one might expect, little change is observed the fibre direction.

Table 2: A comparison of residual stress levels predicted from Eshelby's method and FEM models. All the values quoted are in MPa.

Direction x and y	ESHELBY		FEM	
	Matrix	Fibre	Matrix	Fibre
5%	21.7	-415.0	22.2	-434
10%	44.0	-398.0	45.5	-409
20%	89.0	-360.0	90.8	-363
z				
5%	130.0	-2520	119	-2263
10%	232.0	-2080	206	-1847
20%	366.0	-1500	329	-1318

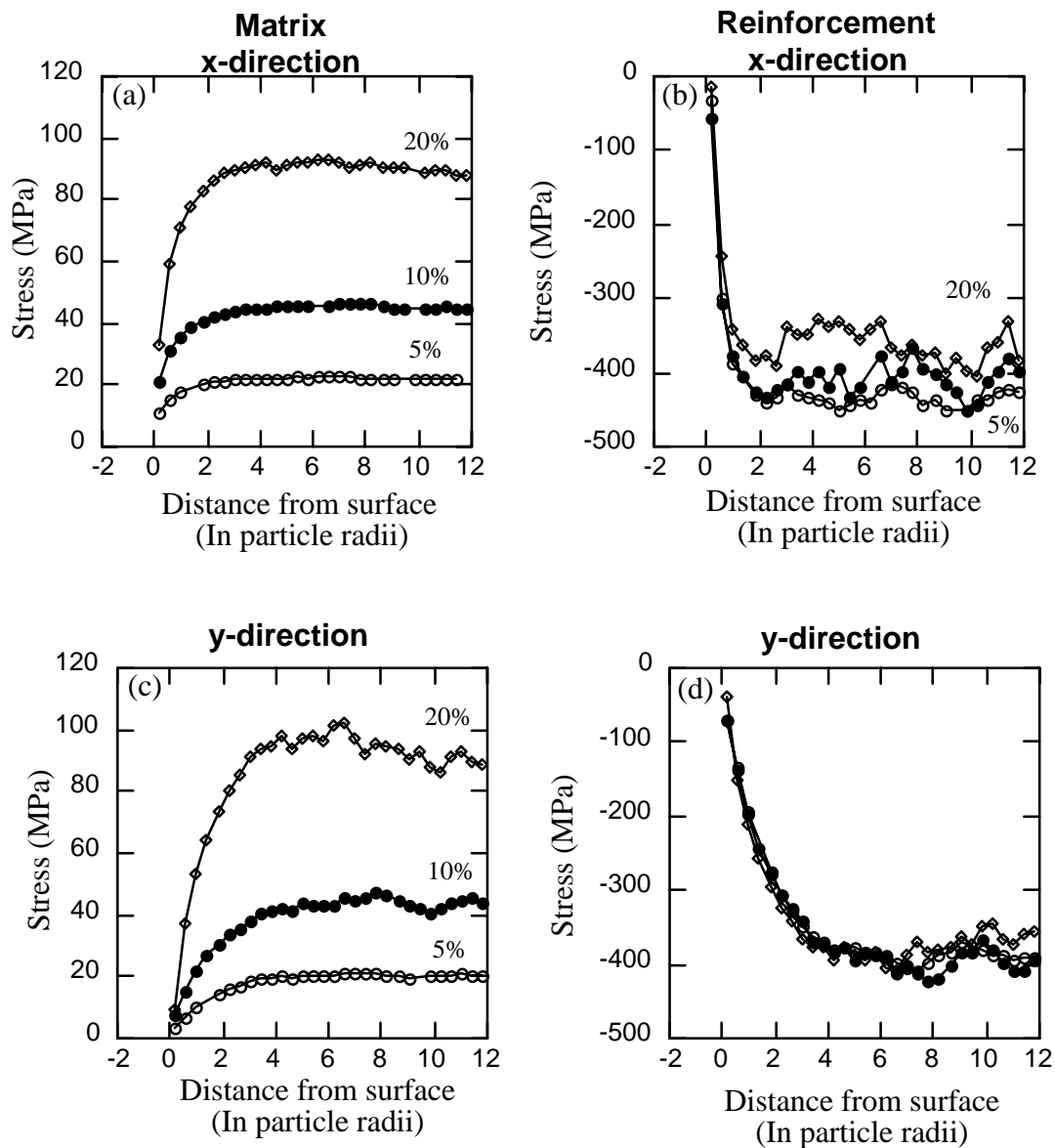


Figure 3a-d: The stress variation with distance from the free surface within the matrix and reinforcement, for 5, 10, and 20% reinforcement.

Far from the free surface, the results of the FEA are in very good agreement with the stresses predicted by a simple Eshelby analysis (see Table 2). Because the ‘fibre’ direction is not representative of particulate composites, the following discussion will focus primarily on changes in the x and y directions. A number of features should be noted; i) as the percentage of reinforcement increases, the stresses in the matrix increase greatly, while the stresses in the particles decrease slightly. ii) The stress reaches the bulk value more quickly in the in-plane direction (x) than in the out-of-plane direction. iii) While the rate at which the bulk value is reached is dependent on the particle spacing and volume fraction, it is more closely related to the particle size in that the rise in stress is almost identical for each reinforcement fraction.

DISCUSSION

The approach of Hanabusa et al. [5] predict the following responses for the 2D and 3D cases:

$$\sigma_y(y) = A(1 + ky)\exp(-ky)\cos ky \quad (4a)$$

$$\sigma_x(y) = A(1 - ky)\exp(-ky)\cos ky \quad (4b)$$

$$\sigma_{yy}(y) = A(1 + ky)\exp(-ky)\cos ky \cos kz \quad (5a)$$

$$\sigma_x(y) = \frac{A}{2} \left(1 + 2\nu - 2\sqrt{2} \frac{\pi y}{a} \right) \exp(-\sqrt{2}ky)\cos ky \cos kz \quad (5b)$$

with $k=2\pi/a$.

While the stress profiles are in qualitative agreement with the response predicted by Hanabusa et al. [5] for the two dimensional ‘particle’ (fibre) system, Fig. 4 shows that the stress field for the random array relaxes to zero at the surface over a much shorter distance. Furthermore, the observation that the $\sigma_x(y)$ and the $\sigma_y(y)$ stress components increase at approximately the same rate with depth irrespective of particle volume fraction (see Fig. 3) is in contrast to the predictions of Hanabusa et al. [5]. This is clear from the normalised plots (Fig. 5) which do not all fall onto a single curve as Eqns 4a and b would suggest they should.

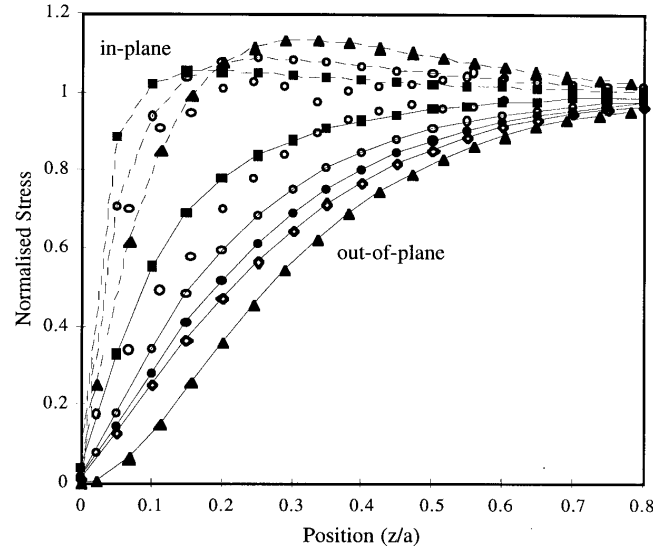


Figure 4: Predicted and experimental normalised 'particle' (fibre) stress profiles in the x and y -directions. The unconnected points correspond to the FE predictions of Fig. 3, and the symbols denoting the curves are the same as used in Fig. 3, 5% (open circles), 10% (closed circles), and 20% (open diamonds). Hanabusa's model is represented by solid triangles, and the representative area 5% area fraction curves denoted by solid squares.

The difference stems from the form of the stress field fluctuation assumed by Hanabusa et al. [5] in their theoretical treatment. Essentially, the approach is too simplistic to capture this effect in that it places a row of fibres at the surface and assumes the variation in normal stress to be sinusoidal prior to cutting the free surface. It is then, this sinusoidal variation which is reduced to zero when the free surface is formed. Consequently, the model for stress relaxation contains no information about the particle size or volume fraction. In reality the stress does not decay as a sine wave from the centre of each particle, instead the stress is found to be fairly uniform within the particle and changes rapidly within the matrix (Fig.2). Eshelby's approach is consistent with Lamé's relationship for the out-of-plane (hoop) stress, namely that it varies as $-P(r_0/r)^3$ away from each particle where r_0 is the particle diameter [6].

In an attempt to capture these aspects of the stress distribution we have extended the approach of Hanabusa et al. [5] whilst retaining a fairly simple analytical approach. We have approximated the stress variation as a step function, having the constant value P throughout each particle $|x| < r$, as predicted by the Eshelby formulation [6], and a constant value, $-P(1-f_a)/f_a$ throughout the matrix $r_0 < |x| < a/2$ where f_a is the area fraction across the cut surface. Whilst this oversimplifies the variation of stress within the matrix, it is a good approximation when f_a is small, and will provide the opposite bound to that provided by Hanabusa et al. [5]. This variation retains the advantage of being fairly simple to describe as a Fourier series. As a result the balancing force which must be applied at $y=0$ when the free surface is introduced is given by:

$$F_y = \sum_{n=1}^{\infty} A_n \sin(k_n x) \quad \text{and} \quad F_y = \sum_{n,m=1}^{\infty} A_n A_m \sin(k_n x) \sin(k_m z) \quad (6a \text{ and } b)$$

for fibres and particles respectively, with $A_n = A_0 (\sin(k_n r_0))/n$ and $k_n = 2\pi n/a$.

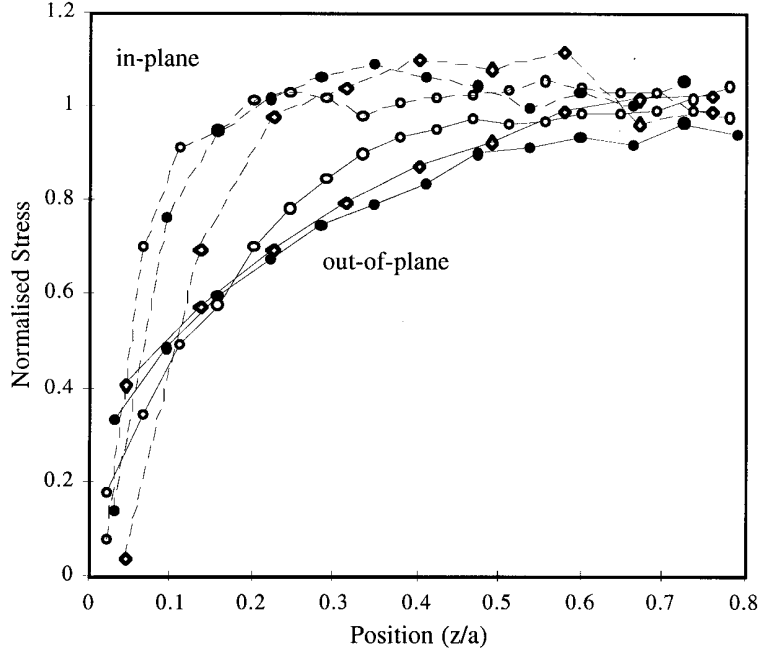


Figure 5: Normalised plots of the FE derived stress profiles. The markers used represent the same reinforcement percentages as those in Fig. 3 and 4. The out of plane (y) direction is shown by a solid line, and the x -direction by dashed line.

As a result, the stress which must be superimposed to ensure zero stress at the newly formed surface is a fourier series the components of which decay exponentially with distance from $y=0$. In order to calculate the net stress within the particle, the resulting equations must be averaged over the width of the particle ($|x| < r_o$), giving rise to the following equations:

$$\langle \sigma_y \rangle = \sum_{n=1}^{\infty} \frac{A_o a (1 + k_n y) \exp(-k_n y) \sin^2(k_n r_o)}{2\pi n^2 r} \quad (7a)$$

$$\langle \sigma_x \rangle = \sum_{n=1}^{\infty} \frac{A_o a (1 - k_n y) \exp(-k_n y) \sin^2(k_n r_o)}{2\pi n^2 r} \quad (7b)$$

$$\langle \sigma_y \rangle = \sum_{m,n=1}^{\infty} \frac{A_o^2 a^2 (1 + k_{mn} y) \exp(-k_{mn} y) \sin^2(k_n r_o) \sin^2(k_m r_o)}{(2\pi m n r)^2} \quad (8a)$$

$$\langle \sigma_x \rangle = \sum_{m,n=1}^{\infty} \frac{A_o^2 (k_n^2 + 2\nu k_m - k_{mn} k_n^2) \exp(-k_{nm} y) \sin^2(k_n r_o) \sin^2(k_m r_o)}{(k_{mn} m n r)^2} \quad (8b)$$

for fibres and particles respectively, with $k_{nm} = 2\pi \sqrt{(n^2 + m^2)}/a$. The stress profiles are shown in Fig. 4 alongside the FE results for the 5% composite. The results clearly show that the averaged series solution is in much better agreement than the simple method with the experimental results, although the rate of build up of the normal state is still slightly underestimated. It should be remembered that the approach is rather simplistic; it assumes that a surface force can be applied to a elastically homogeneous cross-section containing a stress profiles equivalent to that caused by an array of particles (fibres) spacing a . In common with the approach of Hanabusa et al. [5], the area fraction of particles (fibres) on the newly

created free surface is much greater than the volume fraction of reinforcement because of the periodic nature of the array. Consequently, although the stress is balanced over the cross-section, the phase stresses are quite different from if the section contained a fraction of reinforcing particles equivalent to the composite as a whole, i.e. $f_a = f$. This also has the effect of bringing the particles closer together than would be expected in a randomly distributed composite or for a less special cut through the periodic array. In order to account for this effect, results corresponding to an r_o/a ratio representative of a slice with $f_a = f$ for the 5% composite are also shown in Fig. 4.

While a cubic (square) array of particles (fibres) at this spacing would have a reinforcement content much greater than 5%, this regular arrangement could be thought of as representing a random slice through a randomly distributed system. Besides, the distribution of particles below the free surface ($y=0$) is not actively included in the model anyway. Other simplifications include the fact that the rate of change of stress from a free surface would be affected by the elastic heterogeneity. Nevertheless, the model does capture the effect of reinforcing volume fraction on the rate at which the bulk stress state is reached and is in fairly good agreement with the actual stress values, whilst retaining the simplicity of the approach pioneered by Hanabusa et al. [5]. In common with the FE results the rate of change of stress decreases with increasing volume fraction. The area fraction matched curve shows the greatest rate of change of stress, much greater than the original 5% curve. This is because the model predicts a strong sensitivity to f , only when the ratio r_o/a is small; hence the similarity of the 5, 10, and 20% curves. The FEA data can be seen to lie between the two 5% curves, but can be said to be closer to the new representative area curve, indicating that this approach may have merit, although further work is still needed to confirm this.

Simulation of X-ray $\text{Sin}^2\psi$ Curves

The FE results and the modelling approaches all show that the concept of using the $\text{sin}^2\psi$ technique to measure thermal micro residual stresses for the fibre-like composite in the transverse directions is fundamentally flawed. If the attenuation depth is much smaller than the microstructure of the reinforcement the normal stress state (σ_y) is zero over the sampling volume, but so too is the in-plane stress so that the $\text{sin}^2\psi$ gradient is zero and no stress would be inferred. If on the other hand, the penetration is large the bulk stress state is sampled and since the stresses two transverse directions (σ_x and σ_y) are equal, deep within the bulk, the $\text{sin}^2\psi$ technique would again record zero gradient, incorrectly suggesting a zero transverse stress component. Note however that it is possible to estimate the average axial fibre and matrix stresses (σ_z) since these stresses decrease only slightly as the surface is approached giving a relatively reliable measure of the stress. In this case the gradient would give σ_z under highly attenuating conditions and $\sigma_z - \sigma_y$ if the reinforcement separation is smaller than the penetration depth.

Given that the extended series approach to modelling the stress profiles is a fairly good predictor of the actual stresses evaluated using our 2D FE model, it would seem reasonable to assume that the 3D series solution is an acceptable approximation for the computationally more demanding 3D case for which it is very laborious to construct a model. The 3D series solution profiles are shown in Fig. 6. Here it can be seen that the predicted stress profiles for 5, 10, and 20% are essentially the same, indicating that except at low r_o/a ratios, the stress profile is dependent only upon a , as for Hanabusa's model. In the x-direction, again our

model shows a shift towards the surface with decreasing volume fraction. In both directions, our models show a greater rise in the stress than Hanabusa's model.

Optimised curve fits describing the stress profiles of the type shown in Fig. 6 were defined and used to simulate the $\sin^2\psi$ curves. In each case best fit straight lines have been used to estimate the phase stress results that would arise were biaxiality of stress assumed. The results are summarised in Table 3 for Cu and Cr radiation. Upon comparing the results with the stresses in the bulk it is clear the thermal mismatch stresses are significantly underestimated and, for Cu radiation, are even of the wrong sign relative to the bulk value.

It is believed that the incorrect sign is achieved because the $\sin^2\psi$ shifts upwards from near the triaxial to the biaxial curve as the penetration decreases with increasing ψ angle. This would record as a tensile gradient. This has been observed in the literature previously for X-ray measurements on Al-SiC particulate composites [7], although unexplained. A similar situation has been observed experimentally by the authors, where thermal micro-stresses were being measured. The lower penetration of Cr would tend to increase the level of biaxiality and this may be responsible for the correct sign of the Cr results. The table also shows that as the percentage of reinforcement gets larger the measured stress increases.

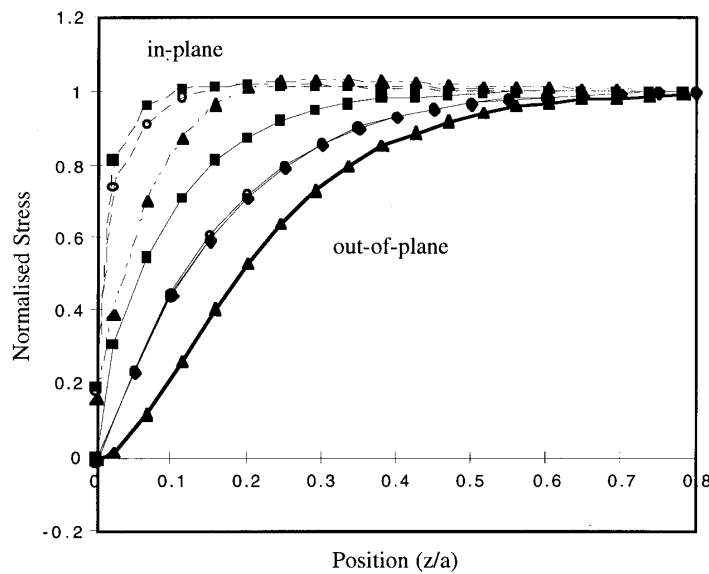


Figure 6: Predicted normalised particle stress profiles in the x and y-directions for a 3D arrangement of particles, spacing a. Markers are as in earlier Figs.

Table 3: Predicted stress results for the reinforcement calculated using the $\sin^2\psi$ criteria for the simulated stress profiles. All stresses are in MPa.

	20 μm (Cu radiation)	20 μm (Cr radiation)	Eshelby
5% in cut plane	6.4 \pm 5.7	-19.3 \pm 8.3	-415
5%	14.3 \pm 7.3	-16.0 \pm 8.1	-415
10%	15.6 \pm 6.8	-7.6 \pm 8.0	-398
20%	17.1 \pm 6.3	2.6 \pm 8.3	-360

CONCLUSIONS

- i) The stress in both the matrix and the reinforcement in a metal matrix composite increases to the bulk value at a much greater rate than predicted by Hanabusa et al. [5], and it is not only dependent upon the size of the particle, but also on the spacing.
- ii) The X-ray 'measurements' indicate that in the Al system, the assumption of a biaxial stress over the x-ray sampling volume is invalid. This could give rise to totally unreliable estimates of the microstress fields. Even using Cr radiation, little improvement is seen. It is expected that in other systems where the penetration is much lower, such as titanium metal matrix composites, that the use of these plots becomes much more useful, although further work will be needed before this can be confirmed.

ACKNOWLEDGEMENTS

Mr Watts is funded by EPSRC and the DRA.

REFERENCES

1. Cullity, B.D. "Measurement of Residual Stress." in *Elements Of X-Ray Diffraction.*, Addison-Wesley, 1978, pp.447-478.
2. Kurimura, T. and King, J.E. "Residual Stress Effects On Crack Initiation And Growth In Al/SiC MMCs." at *Fourth European Conference On Residual Stresses*, Cluny, France, 1996.
3. Holdway, P. and Bowen, A.W. "Surface And Near Surface Analysis Of Residual Stresses In Aluminium And Titanium Alloys - Examples Of The Case For X-Ray Diffraction." in *Measurement of Residual Stress Using Neutron Diffraction*. Eds. Hutchings, M.T. and Krawitz, A.D., 1, 1992, pp.461-471.
4. Nishioka, K., Hanabusa, T. and Fujiwara, H. "Theory Of The X-Ray Residual Stress Analysis." *Scripta Metallurgica* , Vol.8, 1974, pp.1349-1350.
5. Hanabusa, T., Nishioka, K. and Fujiwara, H. "Criterion For The Triaxial X-Ray Residual Stress Analysis." *Zeitschrift Fuer Metallkunde* , Vol.74, No.5, 1983, pp.307-313.
6. Clyne, T.W. and Withers, P.J. "An Introduction To Metal Matrix Composites." Cambridge, Cambridge University Press, 1993, pp 44-70
7. Arsenault, R.J. and Taya, M. "The Effects Of differences In Thermal Coefficients Of Expansion In SiC Whisker 6061 Aluminium Composite." at *Fifth International Conference On Composite Materials*, San Diego, California, USA, 1985, The Metallurgical Society, Eds; Harrigan, W.C., Strife, J. and Dhingra, A.K., pp.21-36.

A COST EFFECTIVE FOUNDRY METHOD FOR THE PREPARATION OF STRUCTURAL GRADE DISCONTINUOUSLY REINFORCED AIMCS

Varuzan M. Kevorkijan

Alpha and Omega in Composites, Lackova 139, 2341 Pekre, Slovenia

SUMMARY: In this work, it was demonstrated that the wetting between ceramic particles and molten metal can be activated by exothermic interfacial reactions (e.g. $\text{Si}+\text{C}\rightarrow\text{SiC}$ or $3\text{TiO}_2+3\text{C}+4\text{Al}\rightarrow3\text{TiC}+2\text{Al}_2\text{O}_3$). In this way, two methods of processing for introducing larger amounts of fine SiC particles into a Al alloy melt without rejection of the reinforcement, and without unwanted chemical reactions between the matrix and the reinforcement were developed. The introduction of fine (less than 6 μm) rounded-off SiC particles combined with a significant reduction in casting and extrusion defects caused by cost effective HIP treatment without encapsulation results in superior tensile properties. Moreover, in a defect-free composite, high aspect ratio reinforcements like SiC whiskers and platelets *can* be successfully used in order to improve the mechanical properties of final parts.

KEYWORDS: discontinuously reinforced metal matrix composites, liquid metal processing modes, wetting activated by exothermic interfacial reactions, hipping

INTRODUCTION

Recently, it was suggested by the author [1] that the wetting between ceramic particles and molten metal can be activated by exothermic interfacial reactions (e.g. $\text{Si}+\text{C}\rightarrow\text{SiC}$). In this way, a method of processing for introducing larger amounts of fine SiC particles into a Al alloy melt without rejection of the reinforcement, and without unwanted chemical reactions between the matrix and the reinforcement was presented.

Chemically treated fine SiC particles were first dispersed in a Si-Al melt (at 1473 K in vacuo). The wetting of SiC by the Si-Al melt was enhanced by exothermic chemical reaction between a carbon layer doped with MgO, previously deposited on the surface of the SiC particles, and the matrix. Improvements in fluidity was achieved by increasing the temperature of the melt. By using a very high Si content in the starting melt composition (60 wt. %), the formation of Al_4C_3 was inhibited even at high operating temperatures. When a sufficient concentration of SiC particles had been incorporated into the Si-Al melt, an Al-Mg alloy was carefully added at a controlled rate in a nitrogen atmosphere, so as to obtain the final eutectic composition. It was found that once dispersed, ceramic particles will not be rejected during the introduction of the second melt, if the process is performed with careful processing control. In this particular case, the processing control was performed by a specially designed

cooling regime and by using a nitrogen atmosphere. As a result, Al-SiC composites with 20 vol. % of SiC particles in the size range less than 6 μm were routinely prepared.

However, the effectiveness of the solution offered was still close to the existing commercial foundry procedures which operate with particles in the size range 10 to 20 μm . Moreover, a recent investigation performed by the same author has confirmed that the real improvement of mechanical properties of cast discontinuously reinforced metal matrix composites (DR MMC) achieved by introduction of fine or even high aspect ratio ceramic dispersoids is very modest. It was confirmed that the damage accumulation processes, caused by casting and extrusion defects, limit further improvement of the mechanical properties of cast MMCs, especially when fine ceramic particles with a high aspect ratio have been used for the reinforcement.

The aim of this work is twofold: (i) to confirm further that an exothermic interfacial reaction is a key factor in successful introduction of ceramic particles into a melt; and (ii) to demonstrate that the introduction of a sufficient concentration of fine ceramic particles and platelets with higher aspect ratio can result in a DR MMC with superior tensile properties, if the casting and extrusion defects are previously eliminated by HIP treatment.

EXPERIMENTAL PROCEDURES

Two types of β -SiC powders produced by low temperature carbothermal reduction (AP-1 consisting fine particles with a diameter range between 2-12 μm , and AP-2 consisting of coarser particles with about 20 μm mean diameter), commercially available M-Grade ART SiC whiskers and laboratory scale prepared SiC platelets (size range: 30-50 μm , thickness: 3-5 μm , aspect ratio 8-10, purity: max. 1000 ppm of metallic impurities, particulate content 5-10 wt%, oxygen 1.1 wt% and free carbon 0.53 wt%) were used in this study. Standard 356-T6 alloy was used in all experiments. Note that 356-T6 alloy has a nominal composition of 7 wt% of Si and 0.3 wt% of Mg.

SiC reinforcements used in this study were surface treated by the following procedures: **Coating SiC reinforcements with a carbon layer:** Phenolic resin and SiC reinforcements were first wet mixed in acetone. Then the acetone was evaporated with constant stirring in order to maintain the homogeneous distribution of species. The dry mixture was then pyrolyzed in flowing argon for 4h at 450°C to permit the formation of an amorphous carbon layer on the surface of the SiC reinforcements; **Coating the SiC reinforcements with a carbon layer doped with TiO₂:** Phenolic resin, SiC reinforcements and TiO₂ powder (99.9% pure, rutile, average particle size 1 μm) were wet-milled in ethanol for 24 h using alumina milling media. Using the same procedure as just described, SiC reinforcement were covered with an amorphous carbon layer doped with TiO₂. Note that in a separate set of experiments, the wetting tendency of the as received SiC reinforcements was also evaluated.

Both treated and untreated SiC reinforcements (except SiC reinforcement doped with TiO₂ + C) were first dispersed into the Si-Al melt at 1150°C in vacuo. The composition of the melt was usually 60 wt% Si - 40 wt% Al. The SiC reinforcement was introduced into the melt through a ceramic tube using a flow of carrier gas (argon with some additives). When a sufficient amount of SiC reinforcement was incorporated into the Si - Al melt, an Al alloy (Al-4wt%Mg) and pure Al were added at a controlled rate and under vigorous mixing

conditions in vacuo, or under a protective atmosphere, in order to achieve the 356-T6 alloy composition. SiC particles doped with $\text{TiO}_2 + \text{C}$ were dispersed directly into the Al alloy melt in an argon atmosphere. The volume fraction of different SiC reinforcements successfully incorporated in the Al 6061-T6 matrix is listed in Table 1.

The apparatus consisted of a graphite crucible surrounded by an induction heating coil. The mixing assembly consisted of a DC variable speed motor, the spindle and the dispersion impeller having the blades angled from about 15° to about 45° from a line perpendicular to the shaft. The crucible was provided with a protective cover and an inert gas or vacuum protection chamber.

Hot extrusion was carried out using a 4 MN (400 t) direct pilot extrusion press. Before extrusion, the samples were preheated in air to 420°C . The extrusion container was also preheated to 400°C and, before each pressing cycle, lubricated with an oil suspension of flaked graphite. The hot extrusion of samples was performed at a deformation ratio $\delta \approx 1:20$. Therefore, the resulting final diameter of the extruded bars was approximately 16 mm. A typical dependence between extrusion pressure and ram travel was obtained; starting with a higher peak pressure and continuing with a stable working (running) pressure. The peak pressure was 330 to 470 MPa (3.3 - 4.0 t/cm²). The extrusion speed was maintained as low as possible (4-10 mm/s) and regulated manually, depending on the extrudability of each individual sample.

HIP treatment (without encapsulation) of extruded specimens was performed in a HIP 2000 unit (National Forge, Belgium) using a graphite furnace. Typical experimental conditions were: temperature 30-50 K below the melting point of Al-Si-Mg alloy, argon pressure: 150-180 MPa, holding time: 1-2 hours. Samples for HIP treatment were cut parallel to the direction of extrusion from an extruded billet, and then machined on a lathe to a rod with diameter 50 mm and length 100 mm.

The mechanical properties investigated included Brinell and Vickers hardness tests and tensile tests performed at room temperature. The composite Brinell hardness (62.5 kgf, preload 10 kgf, sphere 2.5 mm) was measured at the centre of the samples and near the edges. Vickers microhardness measurements (20 gf load) were taken from the aluminium matrix. The average of three measurements is reported in Table 3.. The tensile tests were carried out in accordance with ASTM B557. Three parallel tensile tests for each specimen were performed. NonHIPped samples were first rough cut parallel to the direction of extrusion, directly from an extruded billet, using a carbide band saw, and then machined on a lathe using a tungsten carbide cutting tool. The HIPped and nonHIPped samples were sand cast first, and then machined on a lathe. The load versus strain, was measured using an extensometer and plotted. The measured yield strength (σ_y), ultimate tensile strength (σ_{uts}), and % elongation are reported in Table 3, along with values for unreinforced 356-T6 alloy.

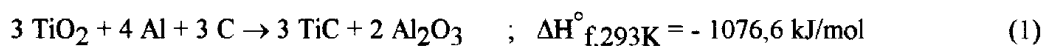
Extruded and HIPped material was also investigated in optical and scanning electron microscopes with regard to parameters such as SiC - distribution, surface tearing, grain size and primary constituents. However, these results will be published later.

RESULTS AND DISCUSSION

Table 1 summarizes the lowest experimentally monitored concentrations of SiC reinforcement which result in the spontaneous rejection of the reinforcing phase from the melt. In this way, the efficiency of the direct immersion of fine SiC reinforcements into an Al-Si melt was **quantitatively** compared with the potential of the new processing route. As described, the new processing route is based on the immersion of SiC reinforcements in a Si-Al melt and its further alloying with Al-Mg to the final eutectic composition.

The preliminary results in Table 1 show that, as expected, only a very limited level of uncoated fine SiC particulates can be successfully introduced into a melt. Rejection occurs spontaneously at a particulate concentration between 2-3 wt%. More promising results were obtained with fine SiC particles previously oxidised in air (at 1200°C for 1 h). In that case, 6-9 wt% of fine SiC particles could be successfully incorporated into the matrix prior to their spontaneous rejection. However, note that oxidation of fine SiC particles at 1200°C for 1 h changes their chemical composition dramatically. Thus, the wetting kinetics of strongly oxidised fine SiC particles in an Al melt are rather governed by the wetting tendency of the equivalent amorphous SiO₂ particulates. Using an exothermic reaction between carbon, previously deposited on the surface of SiC particles, and silicon in the melt, a high portion of ceramic filler can be successfully immersed, Table 1. For example, it was found that only 10-15 wt% uncoated fine SiC particles could be successfully incorporated into a Si melt without significant rejection. In contrast, under the same experimental conditions more than 30 wt% fine SiC particles covered by a carbon layer were successfully introduced into a Si melt, in accordance with the exothermic reaction between the carbon layer and silicon in the melt. The details of the reaction paths are not beyond the scope of this work [2]. However, it is important to note that the overall reaction is highly exothermic. Therefore, using a recently postulated model of the wetting process [3], one can conclude that an exothermic interfacial reaction which proceeds rapidly at the surface of the ceramic phase should enhance its wetting tendency.

Very recent experiments performed on SiC reinforcements covered with a TiO₂ + C layer strongly support this conclusion. Note that the reaction:



is very exothermic. As reported [4], this could result in a local rise in temperature of up to 2600 K. The reaction occurred at a temperature approximately 250 K higher than the melting point of Al (933.4 K). For details of the reaction mechanism see [4]. As evident from Table 1, approximately 25 vol% of fine SiC particles or SiC reinforcement with high aspect ratio were successfully introduced **directly** into the melt by the very exothermic chemical reaction between the melt and a mixture of TiO₂ and carbon deposited on the surface of SiC particles. This clearly confirms that an exothermic interfacial chemical reaction can significantly improve the immersion of ceramic particles into a melt.

Mechanical properties

An effort has been made to compare the mechanical properties of HIPped and nonHIPped Al-SiC composites prepared by liquid-metal processing. Types A-1 and A-2 are composites reinforced with low aspect ratio SiC particles (AP-1 SiC powder and AP-2 SiC powder with mean particle diameters of 10µm and 20µm , respectively). Type B are composites

reinforced with high aspect ratio ceramic fillers like SiC whiskers (B-1) or SiC platelets (B-2). Although there is significant scatter in some of the experimental data (especially in data generated using nonHIPped specimens), probably caused by the presence of casting defects, defects introduced by hot extrusion and differences in residual porosity at the interface, some general conclusions regarding the effect of the reinforcement and HIP treatment can be made.

Table 1: The concentration of SiC reinforcement which leads to the spontaneous rejection of ceramic dispersoids from the melt

Introduction of SiC phase directly to a Al-Si melt				Immersion of SiC phase to a Si-Al melt - the new processing route			
Type of reinforcement				Type of reinforcement			
AP-1	AP-2	whiskers	platelets	AP-1	AP-2	whiskers	platelets
Coating SiC with a carbon layer							
/	/	/	/	40-50 10-20	50-60 10-25	50-60 10-25	50 10-20
Coating SiC with a carbon layer doped with TiO ₂							
18	25	23	23	/	/	/	/
As received SiC phase							
1-2	2-3	1	1	20-30 5-8	25-35 5-7	25-35 5-6	20-30 3-5

*concentration in Si-Al melt, **concentration in final eutectic composition

Tensile data obtained from composites A-1 and A-2 containing a volume fraction of reinforcement from 0.10 to 0.20 and SiC particles of mean diameters from about 10µm to 20 µm indicates that the mechanical properties depend on both the size and volume fraction of the particles. However, it seems that the strength of nonHIPped particulate MMCs prepared by liquid metal is dependent most strongly on the volume fraction of reinforcement, with a weaker dependence on the particle size and aspect ratio.

The modulus of elasticity of the composites investigated increases with increasing reinforcement content. Again, in nonHIPped specimens the reinforcement content is the dominant factor in increasing the modulus of elasticity.

Based on collected experimental data, one can also conclude that the modulus appears to be insensitive to the type of reinforcement used. Note that in defect-free material prepared by P/M, several authors [5] reported that the modulus of particulate MMCs is much less than that of whisker MMC's due to the particulates much lower aspect ratio (≈1-2), and

therefore, their inability to pick up load from the matrix as effectively as the whiskers. Moreover, the variation in the elastic modulus of MMC's with the aspect ratio of the reinforcement has been also theoretically predicted [5]. According to this model, significant improvements in the elastic modulus should be obtained by increasing the aspect ratio of the reinforcement.

However, as reported [5], the model is very sensitive to the orientation of high aspect ratio particles with respect to the axis of measurement. The same author [5], using SiC platelets with different aspect ratios, reported that modulus values fall very rapidly with degree of platelet misorientation.

The results of the present investigation mostly confirm this conclusion. The values of UTS, YS and elongation measured in nonHIPped specimens are almost the same for both high aspect ratio composites (B-1 and B-2) and are only $\approx 10\%$ higher than for the corresponding particle reinforced composite (A-2). Moreover, there is no significant difference in mechanical properties between B-1 and B-2 grades and A-1 grade prepared by fine and, at least one order of magnitude cheaper, rounded-off SiC particles. Note that this effect could strongly affect the cost competitiveness of MMC's prepared by the liquid metal route and, consequently, the future market prospects for MMC commercialisation.

It seems that in MMCs prepared by casting the key factor which needs to be controlled is the successful immersion of fine SiC particles. The introduction of high cost, high aspect ratio particles not can improve the mechanical properties significantly.

Obviously, the presence of casting defects and defects caused by hot extrusion in the nonHIPped samples tested played a major role in the actual results obtained. Both high aspect ratio composites (B-1 and B-2) showed a significant amount of whisker and platelet fracture after extrusion, probably due to high loading and to the high selected aspect ratio of the reinforcements.

From these considerations, the mechanical properties in nonHIPped MMC's prepared via the liquid metal route are most strongly dependent on the volume fraction of reinforcement, with a somewhat weaker dependence on particle size, and are almost insensitive to the aspect ratio of the ceramic filler.

The results of Brinell hardness and Vickers microhardness tests are similar for both as extruded and annealed nonHIPped composites, Table 3. This fact suggest that dynamic recrystallization might have occurred during extrusion.

The Brinell hardness increased with the SiC volume fraction, as would be expected. For purposes of comparison, both hardness values of unreinforced A 356-T6 are also given. The hardness values presented in Table 3 indicate that even the hardness of cast Al-SiC composite is not strongly affected by the morphology and the aspect ratio of the reinforcing phase. Again, in nonHIPped specimens defects in the material seems to play the dominant role in the actual results obtained.

However, the immersion of fine SiC particles in an A356 matrix (using AP-1 SiC powder with a mean particle diameter less than $10\mu\text{m}$) resulted in some improvement of hardness. This suggests that by limiting the size of the particles and by improving their dispersion and alignment, it should be possible to improve the composite properties, even at a low aspect

ratio of the reinforcing phase. Moreover, the introduction of SiC platelets with an average particle size less than $10\mu\text{m}$, employed in order to minimize platelet fracture during extrusion, could result in significant improvement of the composite properties. Again, in addition to cost, some improvement of mechanical properties in nonHIPped specimens, caused by using a ceramic phase with higher aspect ratio, should be compared with the eventual increase of defects simultaneously introduced in this way.

Table 2 - Room temperature tensile properties of extruded and hipped MMCs based on an A356 alloy (T6 condition). Grade A-1: fine ($6\mu\text{m}$) SiC particles, Grade A-2: Coarser ($15\mu\text{m}$) SiC particles, Grade B-1: SiC whiskers, Grade B-2: platelets .

Extruded						
Composite	V_f	Aspect ratio	σ_y (MPa)	σ_{uts} (MPa)	E (GPa)	Elongation %
A-1	10	< 2	293	309	83	0.6
A-2	10	< 2	278	301	81	0.6
B-1	10	12	307	328	88	0.6
B-2	10	8-10	302	322	83	0.6
A-1	20	< 2	359	377	103	0.4
A-2	20	< 2	337	355	98	0.3
B-1	20	12	372	391	108	0.4
B-2	20	8-12	368	386	106	0.3
A356 (T6) unreinforced	/	/	205	280	76	6

Hipped						
Composite	V_f	Aspect ratio	σ_y (MPa)	σ_{uts} (MPa)	E (GPa)	Elongation %
A-1	10	< 2	320	351	109	0.8
A-2	10	< 2	318	335	93	0.8
B-1	10	12	465	475	168	0.7
B-2	10	8-10	467	481	173	0.7
A-1	20	< 2	438	465	136	0.5
A-2	20	< 2	431	461	124	0.4
B-1	20	12	593	565	212	0.4
B-2	20	8-12	595	562	226	0.4
A356 (T6) unreinforced	/	/	262	364	97	9

In contrast, inspection of the room temperature tensile properties of HIPped specimens (Table 2) showed a significant improvement in yield strength (σ_y), ultimate tensile strength (σ_{uts}) and modulus of elasticity (E). In HIPped specimens Brinell hardness and Vickers microhardness (Table 3) were also improved (in some cases it was doubled).

The improvement in tensile properties and hardness of HIPped specimens was more marked in specimens reinforced with a high volume fraction (20 vol%) of SiC whiskers and platelets (B-1 and B-2), i.e. in specimens with a high concentration of casting defects. Note that in

HIPped specimens a significant difference between the modulus of particulate MMCs with low aspect ratio (A-1, A-2) and MMCs with high aspect ratio (B-1, B-2) was found. A possible explanation is that in nonHIPped specimens the casting and extrusion defects masked the real correlation between the aspect ratio and modulus.

Hence, it seems that ceramic reinforcements with high aspect ratio, such as low cost SiC platelets prepared by $\beta \rightarrow \alpha$ phase transformation, can be effectively used in the liquid metal foundry route for the preparation of DR MMCs.

Table 3: Brinell and Vickers microhardness tests results

Composite	V_f (%)	Aspect ratio	Brinell hardness		Vickers microhardness	
			as extruded	annealed	as extruded	annealed
Extruded						
A-1	10	< 2	103±10	91±6	89±3	89±3
A-2	10	< 2	96±6	83±6	81±3	81±3
B-1	10	12	107±10	95±6	92±3	93±3
B-2	10	8-10	106±10	95±6	91±3	92±3
A-1	20	< 2	122±10	103±10	91±3	91±3
A-2	20	< 2	110±10	94±10	85±3	86±3
B-1	20	12	119±10	105±10	92±3	92±3
B-2	20	8-10	117±10	104±10	93±3	92±3
Hipped						
A-1	10	< 2	153±10	152±6	142±3	154±3
A-2	10	< 2	148±6	147±6	139±3	149±3
B-1	10	12	162±10	154±6	148±3	154±3
B-2	10	8-10	171±10	156±6	149±3	153±3
A-1	20	< 2	203±10	167±10	213±3	211±3
A-2	20	< 2	189±10	159±10	208±3	206±3
B-1	20	12	212±10	182±10	207±3	202±3
B-2	20	8-10	1214±10	189±10	202±3	202±3
A356 (T6)	/	/	112-144	98-127	109-141	106-147

In this way, it was recognised that the supplementing of conventional foundry method by HIP treatment, which reduces casting defects, offers a new commercial route for further cost effective production of cast DR MMCs with superior mechanical properties.

CONCLUSION

Two processing routes for introducing larger amounts of fine SiC particles into an Al alloy melt without rejection of the reinforcement, and without unwanted chemical reactions

between the matrix and the reinforcement were described. Both processes are based on an exothermic interfacial reaction, i.e. on the chemically activated wetting of ceramic dispersoids into a melt.

In the first processing route chemically treated fine SiC particles were first dispersed in a Si-Al melt (at 1200°C in vacuo). The wetting of SiC by liquid silicon was enhanced by chemical reaction between a carbon layer previously deposited on the surface of the SiC particles and the matrix. When a sufficient amount of SiC particles had been incorporated into the Si matrix, an Al alloy was carefully added at a controlled rate under vigorous stirring conditions and in a protective atmosphere, so as to obtain the final matrix composition of A 356 without SiC particle rejection. In this way, a processing route for the production of Al-SiC composites with 10-20 wt% of SiC particles in the size range less than 10µm was developed.

In the second processing route SiC reinforcements covered with a TiO₂+C layer were directly immersed into a Al alloy melt, introducing a very exothermic reaction between the melt and the surface reactants. In this way more than 25 vol % of fine SiC particles or SiC reinforcement with a high aspect ratio were successfully introduced into the melt. The process is also suitable for introducing other ceramic reinforcements such as AlN, Al₂O₃, etc. in molten light metals.

The extrusion tests performed showed that the cast MMCs, based on A356 alloy reinforced with silicon carbide particles, platelets or whiskers, can be extruded with good results following the same procedure as that for unreinforced aluminium.

A study of the influence of silicon carbide particle size, aspect ratio and volume fraction on room temperature tensile properties showed that, according to the strengthening mechanism, a higher volume fraction and a smaller particle size are beneficial to improving tensile strength, because of the reduction of space between the particles. On the other hand, because silicon carbide particles were introduced and dispersed into a molten aluminium alloy in liquid form by a mechanical stirring method, adding particles resulted in casting defects which deteriorate the properties of composites. In this way, the damage accumulation processes, caused by casting and extrusion defects, limit further improvement of the mechanical properties of nonHIPped cast MMCs based on high aspect ratio reinforcement. Because of this, use of costly reinforcement like SiC platelets or whiskers in nonHIPped cast MMCs seems unreasonable and not cost effective.

On the contrary, the elimination of casting and extrusion defects achieved by HIP treatment of specimens resulted in superior tensile properties. Moreover, in defect-free composites, it was found that high aspect ratio reinforcements like low cost SiC platelets can be successfully used in order to improve the mechanical properties of the final material. From the accumulated data it is also evident that the mechanical properties of the resulting composites matched the same characteristics of similar composites prepared via the PM route.

One can conclude that supplementing the conventional foundry method for DR MMCs by the low cost HIP technique results in DR MMCs with a very advanced quality/cost ratio and, therefore, it could represent an important market factor for further application of DR MMCs in the automotive sector.

REFERENCES

1. Kevorkijan, M. K. and Sustarsic, B., "The Introduction of Fine SiC Particles into a Molten Al Alloy Matrix: Application to MMCs Preparation via a Foundry Route", *Proceedings of the American Society for Composites - Tenth Technical Conference*, Santa Monica, California, USA, October 18-20, 1995, Composite Materials, Mechanics and Processing, Technomic, pp. 569-578.
2. Ness, J. N. and Page, T. F., "Microstructural Evolution in Reaction-Bonded Silicon Carbide", *Journal of Materials Science*, Vol. 21, 1986, pp. 1377-1397.
3. Kevorkijan, M. V. and Sustarsic, B., "The Introduction of Fine SiC Particles into a Molten Al alloy Matrix: Application to Composite Material Casting", *Metals, Alloys, Technologies*, Vol.29, No.5 - 6, 1995, pp. 447 - 454.
4. Choi, Y. and Rhee, S. W., "Reaction of TiO_2 - Al - C in the Combustion Synthesis of TiC - Al_2O_3 Composite", *Journal of the American Ceramic Society*, Vol. 78, No. 4, 1995, pp. 986 - 992.
5. Jain, M. K., Lloyd, D. J. and Tremblay, S. P., "Evaluation of Silicon Carbide Platelets in Metal Matrix Composites", *Proceedings of International Conference on Metal and Ceramic Matrix Composites*, Anaheim, California, February 19 - 22, 1990, Metal & Ceramic Matrix Composites: Processing, Modeling & Mechanical Behavior, Bhagat, R. B., Clauer, A. H., Kumar, P. and Ritter, A. M., Eds, pp. 549 - 560.

THERMOMECHANICAL BEHAVIOR OF SQUEEZE CAST SIC/AL METAL-MATRIX COMPOSITES

S. Elomari ¹, M. D. Skibo ², C. San Marchi ³ and H. Richards ¹

¹ *Spacecraft Engineering, Canadian Space Agency, Montreal, Canada*

² *MC-21 Incorporated, San Diego, CA 92121, USA*

³ *Department of Materials Science and Engineering, Massachusetts Institute of Technology, Cambridge, USA*

SUMMARY: Aluminum-matrix composites containing thermally oxidized SiC particles of controlled diameter ranging from 3 to 40 μm were successfully produced by vacuum assisted- high pressure infiltration. Their thermal expansion coefficients were measured between 25 and 500°C, and compared with the predictions of various theoretical models. The thermal expansion behavior of three-phase Al-SiC-SiO₂ composite show no significant deviation from the predictions of elastic analysis, since the measured CTEs lie within the elastic bounds derived by Schapery's analysis. The effect of particle size is quite evident in the pressure infiltrated composites reinforced with oxidized ceramic particulates. The larger the particles, the greater the thermal expansion of the composite. The observed behavior of these composites is discussed in terms of particle size, silica layer formed during oxidation, and thermal stresses developed as a result of the difference in the coefficient of thermal expansion between the reinforcement and the matrix.

KEYWORDS: metal-matrix, SiC particle, oxidation, squeeze casting, thermal expansion

INTRODUCTION

Advanced composites show considerable promise for applications where weight and volume are critical as, for example, in aircraft and space vehicles. Aluminum alloys reinforced with various ceramics such as SiC and Al₂O₃ (MMC) are gaining commercial importance. Although these composites are quite light they exhibit significant improvements in strength and elastic modulus [1-3], wear resistance [4], fatigue resistance [5] and damping capacity [6] in addition to high-temperature mechanical properties [7] and low thermal expansion [8].

The coefficient of thermal expansion of metal-matrix composites can be tailored by varying the nature, volume fraction and morphology of the reinforcement in the composite. A low CTE and high thermal conductivity are desirable for applications such as electronic heat sinks and space structures. Furthermore, a low density is desirable for aerospace applications, particularly electrical structural applications. Conventional metals for electronic packaging applications include Cu, Al, Ni-Fe alloys, and Cu-W and Cu-Mo blends; however, these materials do not meet the requirements in advanced electronic packaging applications for low CTE, high thermal conductivity, low density and low cost.

The limitations of conventional metallic materials have led to increased focus on SiC particle reinforced Aluminum-matrix composites as potential candidates for a variety of uses in

advanced electronic packaging. The SiC particulates, which are available in different structures from inexpensive raw material sources, exhibit low density ($d=3.2 \text{ g/cm}^3$), low CTE ($\alpha=4.7 \times 10^{-6} \text{ K}^{-1}$), high Young's modulus ($E=450 \text{ GPa}$), and a commercially available particle size range of 1 to 80 μm . The thermal conductivity, κ , of SiC is in the range 80 to 200 $\text{W}/(\text{m}\cdot\text{K})$, depending on purity and processing conditions. By contrast, pure Al has the following physical properties : $d=2.7 \text{ g/cm}^3$, $E=70 \text{ GPa}$, $\alpha=23 \times 10^{-6} \text{ K}^{-1}$, and $\kappa=180$ to 230 $\text{W}/(\text{m}\cdot\text{K})$.

The present investigation was undertaken with the objective of studying the thermal expansion behavior of isotropic metal-matrix composites reinforced with SiC particles. In this work, composites having a matrix of high purity aluminum containing oxidized SiC reinforcements ranging from 3 to 40 μm in size were successfully produced using the high pressure infiltration technique. The coefficient of thermal expansion (CTE) of the MMCs was measured between 25 and 500°C, and compared to the predictions of three theoretical models.

EXPERIMENTAL PROCEDURES

Metal-Matrix Composites Production by Squeeze Casting

The composites were fabricated by vacuum-assisted infiltration of a liquid metal into a porous preform under high pressure. The matrix was 99.9 pct initial purity aluminum from ALCOA™ (Trademark, Aluminum Company of America, Pittsburgh, PA, USA). Four SiC particulates from two suppliers with average diameters in the range 3 to 40 μm were used. Thickness of preform used in this study was 30 mm. The procedure of preform fabrication can be outlined as follows. First, SiC particles were packed by hand into a boat made of Fiberfrax™ board. Stirring by impeller was performed to establish a uniform particle distribution. Finally, oxidation of particles in air under programmed heating and isothermal conditions was carried out at 1300°C. The temperature in the hot zone was kept constant to within $\pm 1^\circ\text{C}$. As the preforms used in this study were fabricated with different particle sizes, the oxidation time was varied somewhat, ranging from two to four hours. Preforms were infiltrated with pure aluminum using the squeeze casting press shown in Fig.1.

The composite samples were cut along their length on a low-speed diamond saw with ethanol as a lubricant. Metallography was performed on the Al/SiC composites by grinding the samples with a 200 grit perforated diamond wheel. Samples were then polished using 15 μm , 6 μm and 3 μm Buehler Metadi™ (Lake Bluff, IL, USA) diamond suspension on a Buehler Metlap 10™ spiral polishing platens. Samples were washed with water and ethanol between polishing steps. Finally, samples were polished for approximately 10 minutes on Buehler Chemomet™ polishing cloth using Buehler Mastermet™ polishing compound. Scanning electron microscope examination of the polished composite was performed on a Jeol 840 microscope equipped with EDAX energy dispersive X-Ray analysis. The volume fractions of the SiC particles were measured using an IBAS2 image analyzer system attached to an optical microscope.

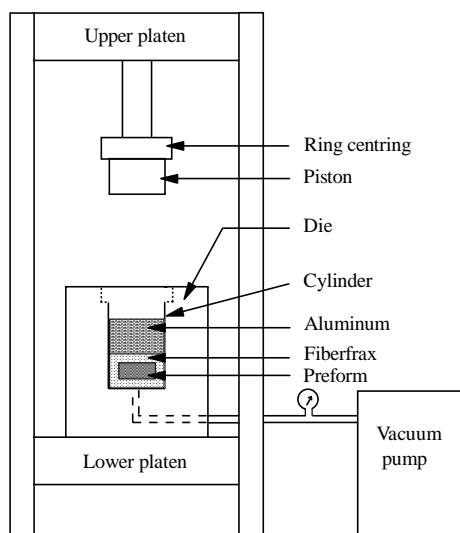


Fig. 1: Schematic of the pressure infiltration unit.

Measurement of Thermal Expansion

Specimens for CTE testing, 10 x 5 x 2 mm in size, were machined from the prepared MMC samples. Specimen surfaces were polished using 1 μm diamond paste. More than four samples of each composite were tested under each condition to verify reproducibility of the data. CTE measurements were performed from 25°C to 500°C at 5°C/min using a commercial thermal mechanical analysis equipment (model TMA 2940, Dupont, USA). The thicknesses of the samples were measured with increased sensitivity (0.1 μm) using the standard expansion probe. The data were obtained in the form of PLC (per cent linear change) versus temperature curve. TMA standard data analysis software was used to evaluate the coefficient of thermal expansion of the composites tested.

RESULTS

Composite Characterization

Fig. 2 shows SEM micrograph of polished section of the SiC/Al composite. Pressure infiltration of the oxidized preforms produced composites in which most of the material appeared to be free of porosity and microscopically homogeneous and thus, are expected to have isotropic properties. The SEM micrographs for the oxidized SiC particles, as compared to those of unoxidized particulates, showed that the SiC particles have been cemented together by the viscous silica glass formed by the oxidation reaction. The large reinforcements (20-40 μm) exhibited less coalescence than the other materials. The silicon carbide particulates showed extensive coarsening following this oxidation exposure and clear evidence of bonding of the particles by the glassy silica phase. After oxidation at 1300°C, even for periods of 2 hrs, the small particles of 3 μm in size were found to have fused into a bonded network as a result of the flow of the silica glass from particle to particle.

The volume fraction of silicon carbide in the composites was determined via image analysis. The average volume fraction of oxidized particles was 56 vol.%, regardless the size of ceramic particulate.

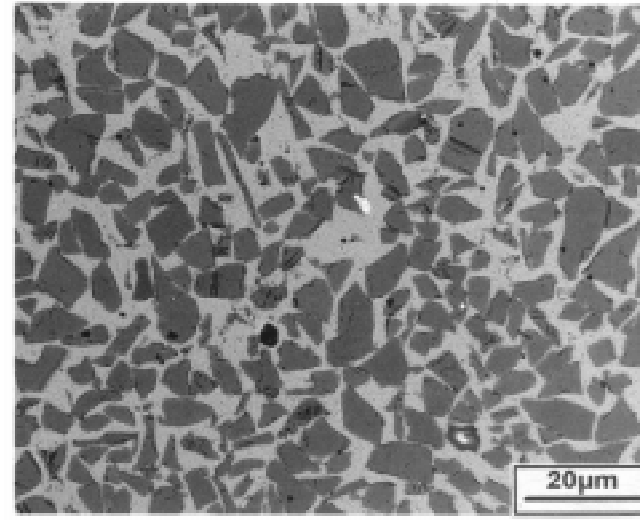


Fig. 2: Typical Microstructure of infiltrated SiC/Al metal-matrix composite.

Thermal Expansion

The results of the thermal expansion (expressed as a PLC), as a function of temperature, for the different composites, containing oxidized SiC particulates, are shown in Fig. 3. In general, the thermal cycling experiments produced no conclusive evidence of thermal ratcheting in any of the materials during two cycles. As shown in Fig.3, the effect of particle size is quite evident and the larger the particles, the greater is the thermal expansion at a particular temperature.

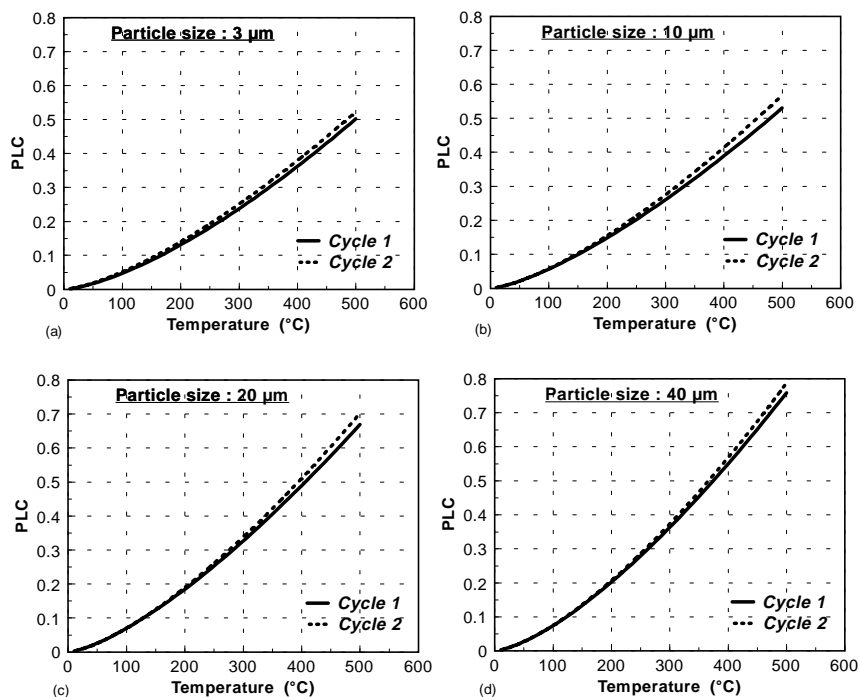


Fig. 3: Per cent linear change (PLC) versus temperature for composites reinforced with various oxidized SiC particle sizes: (a) 3 μm, (b) 10 μm, (c) 20 μm, and (d) 40 μm.

Fig. 4 shows the values of the coefficient of thermal expansion as a function of temperature for each of the composites tested. Note that the CTE is determined at intervals of 50°C based on the calculated slope fit between two selected temperatures. As expected from Fig.3, the larger oxidized particle reinforced composite shows consistently higher CTE than the composite containing smaller oxidized particles. It is evident for a given composite, that the CTE is decreased by the oxidation process. This is consistent with image analysis results which indicate a higher volume fraction of the composite reinforcement in the case of oxidized particles.

DISCUSSION

Theoretical Models

Several theoretical analyses have been presented in the literature which give expressions for the CTE of the metal-matrix composite; these are reviewed in Refs. [9,10]. Of these, the simplest and most used are those of Kerner, Schapery and Turner.

Kerner's Model

The Kerner model assumes that the reinforcement is spherical and wetted by a uniform layer of matrix; thus the CTE of the composite is stated to be identical with that of a volume element composed of a spherical reinforcement particle surrounded by a shell of matrix, both phases having the volume fractions present in the composite. This model gives the composite CTE as:

$$\alpha_c = \bar{\alpha} + V_p(1 - V_p)(\alpha_p - \alpha_m) \frac{K_p - K_m}{(1 - V_p)K_m + V_pK_p + (3K_pK_m / 4G_m)} \quad (1)$$

Where the rule of mixture is given by $\bar{\alpha} = (1 - V_p)\alpha_m + V_p\alpha_p$. K and G are the bulk and shear moduli, V is the volume fraction, and α is the coefficient of thermal expansion. The bulk modulus is calculated using the standard relationship :

$$K = \frac{E}{3(3 - E/G)} \quad (2)$$

b) Schapery's Model

Among the several formulae that have been suggested for the calculation of the thermal expansion coefficient of composite materials taking into account the stress interaction between components is that of Schapery who has derived the effective CTE of isotropic composites. By employing extremum principles of thermoelasticity, The CTE value can be written as

$$\alpha_c = \alpha_p + (\alpha_m - \alpha_p) \frac{(1/K_c) - (1/K_p)}{(1/K_m) - (1/K_p)} \quad (3)$$

Where α_c and K_c are the CTE and bulk modulus of the composite. Note that α_c depends on the volume fraction and phase geometry only through their effect on bulk modulus. This

equation provides an exact relation between composite CTE and bulk modulus. However, only upper and lower bounds of K_c are known in a given case (Hashin's bounds [11]), thus, this expression will provide only bounds on CTE. The lower bound on bulk modulus is

$$K_c^{(-)} = K_m + \frac{V_p}{\frac{1}{K_p - K_m} + \frac{V_m}{K_m + \frac{4}{3}G_m}} \quad (4)$$

The upper bound is obtained by interchanging indices m and p everywhere. Lower bound on K_c yields the upper bound on the composite CTE shown in equation (1) (and vice-versa). It is noteworthy that this upper bound of composite CTE was shown by Schapery to coincide with CTE value determined using Kerner's model. This is not surprising since Hashin's lower bound for bulk modulus is stated to be an exact result for elastic composite, in which the reinforcement is a sphere coated with a uniform layer of the matrix.

c) Turner's Model

The Turner model considered that an internal stress system on a mixture containing n phases is such that the stresses are nowhere sufficient to disrupt the composite, the sum of the internal forces can be equated to zero and an expression of the CTE of the composite is obtained.

$$\alpha_c = \frac{\sum_i^n \alpha_i V_i K_i}{\sum_i^n V_i K_i} \quad (5)$$

Where V is the volume fraction.

It is interesting to point out, none of the many models that have been proposed for calculating the CTE of a composite incorporates a dependence on particle size. Nevertheless, we have used the Turner, Schapery and Kerner expressions to see whether any of them fitted our results.

Theoretical Calculations of Three-phase Al-SiC-SiO₂ Composite CTE

The apparent influence of reinforcement particle size on the CTE may reflect differences in the relative amount of silicon oxide formed as particle size varies: with a roughly constant silica layer thickness, smaller particles feature more silica in proportion to SiC. To evaluate the influence of this effect, the CTE of composites of aluminum reinforced with silica-coated SiC was evaluated under the assumption that the reinforcement is spherical and coated with a uniform thickness of silica. So, considering V_p uncoated particles volume fraction, the number of particles, N, is $N = 6V_p / \pi d^3$, where d is the SiC particle size. The volume fraction of silica layer for thickness t is:

$$V_{SiO_2} = N \left[\frac{\pi}{6} (d + 2t)^3 - \frac{\pi}{6} (d)^3 \right] \quad (6)$$

and then we calculate the CTE change expected for different size particles and different thickness interface layer. The reinforcement CTE and bulk modulus were calculated for each particle size explored in this work, using the Kerner model, use of which is justified by the predominantly convex shape of the SiC reinforcement. Using these values for the reinforcement properties, elastic bounds for aluminum reinforced with silica-coated SiC were then calculated using Kerner's and Schapery's formulae (Eq. (1) and (3)). Finally, Turner's model was used to determine the CTE of three-phase Al-SiC-SiO₂ composite.

Numerical values of parameters used for the computation of predicted composite CTE using Eqs. (1), (2) and (4) are extracted from previous work [12,13]. The variation in Young's and shear moduli with temperature for pure aluminum was examined using Dynamic Mechanical Analysis (DMA), and a summary of the elastic constants evaluated is provided in Table 1.

Table 1: Properties of SiC, SiO₂ and pure Al.

T°C	SiC			SiO ₂			Pure Aluminum		
	E (GPa)	G (GPa)	CTE (μ/°C)	E (GPa)	G (GPa)	CTE (μ/°C)	E (GPa)	G (GPa)	CTE (μ/°C)
50	450	192	4.5	70.5	30.7	0.41	72.03	27.2	21.8
100	450	192	4.5	71.3	31.1	0.47	70.66	26.6	22.4
200	450	192	4.5	72.3	31.6	0.55	65.90	24.7	23.9
300	450	192	4.5	73.4	32.1	0.58	63.73	24.1	25.9
400	450	192	4.5	74.2	32.5	0.61	49.16	18.1	27.8
500	450	192	4.5	75.2	33.5	0.62	36.91	13.2	29.5

Comparison Between the Experimental and Theoretical Results

The comparison between the theoretical calculations and experimental results for the composites produced with preform oxidation is shown in Fig. 4. In the case of composites which contain larger oxidized particles (20 and 40 μm), the experimental CTEs agree well with the values predicted by the Schapery model at low temperatures (50-150°C), while the CTEs in 400-500°C temperature range, are relatively close to Kerner's predictions. On the 200-400°C range, the experimental CTEs show a rapid increase, and do not agree with any of the theories and this underlines the influence of matrix plasticity. On the other hand, CTE values measured on composites produced from oxidized preforms show no significant deviation from the predictions of elastic analysis, since these lie within the elastic bounds derived by Schapery's analysis. This feature was reported in previous work [14] on Duralcan Al₂O₃/6061 composites containing high volume fraction of reinforcement (40%). A good agreement with Kerner's model at high temperatures was found while the CTEs in the low-temperatures agreed relatively well with the values predicted by Schapery's equation.

The results in terms of particle size effect, indicate that the oxidized particles interact sufficiently strongly with the surrounding aluminum that they are able to modify the thermal expansion behavior of the bulk material. The greater the particle size, the higher is the thermal expansion. The more constraint in the composites reinforced with smaller oxidized

particulates is attributed to the interfacial zone where a layer of silica exists because of oxidation. Since the interfacial area is related to the particle size, the volume of the interfacial zone will depend on the particle size and accordingly, the CTE of the composites will vary with the reinforcement size. It is not surprising that very small particles, with their larger surface area, have a greater effect than large particles—as our own observations demonstrate. The measured CTE shows, for each composite type, similar variations with temperature, but with a slight decrease in the CTE value by about $10^{-6} \text{ }^\circ\text{C}^{-1}$, as the SiC particle size decreases from 40 to 3 μm . This effect of particle size is, as shown in Fig. 4, relatively well predicted by mechanical models using three phases composite system.

Recently, Ma et al. [15] have examined the effect of reinforcement size on the CTE of SiC/Al metal-matrix composite, in which the SiC particle sizes were 3.5, 10 and 20 μm . They reported no significant effect of particle size on the thermal behavior of the composites produced with SiC particles having undergone no oxidation treatment prior to the infiltration process.

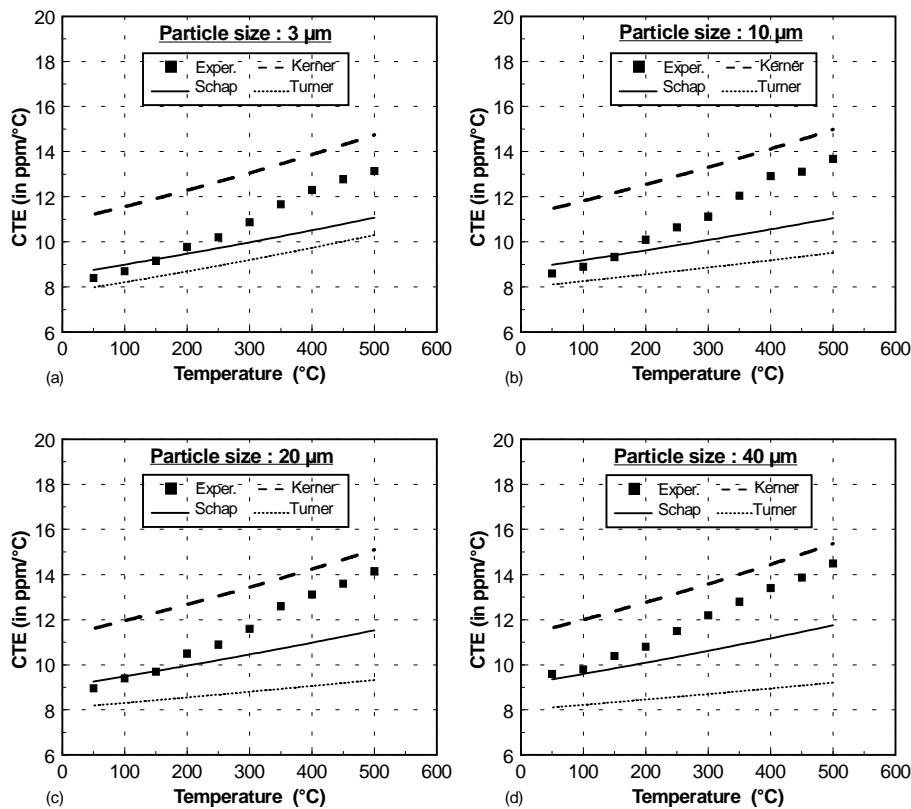


Fig. 4: Comparison of the measured CTE of infiltrated SiC/Al composites with the theoretical predictions.

The agreement of the high temperature CTE with the Kerner model prediction is not in agreement with published CTE values for highly loaded SiC particle reinforced aluminum composites, which have been found to agree with the Turner model above 40 vol% SiC [16]. However, Balch et al. [12], in 53 vol% SiC/Al composites produced by pressure infiltration, reported that the measured low-temperature CTE agreed fairly well with that predicted by the Turner model, while the CTE in the high temperature (175–325 $^\circ\text{C}$) were in a good agreement with the Kerner prediction. The authors interpreted these observations as being an effect of residual stresses and void volume change in the thermally cycled composites.

CONCLUSIONS

Several important conclusions can be drawn from this work :

1. Vacuum assisted-high pressure infiltration produced composites in which most of the material appeared to be free of porosity and of high quality.
2. The thermal expansion coefficients of pressure infiltrated metal-matrix composites lie within the elastic bounds derived by Schapery's analysis.
3. Oxidized SiC particles in the amount of 56 vol% decreased the CTE of aluminum from $25.2 \times 10^{-6} \text{ C}^{-1}$ to $12 \times 10^{-6} \text{ C}^{-1}$. In the case of composites which contain larger oxidized particles (20, 40 μm), the experimental CTEs agree well with the values predicted by the Schapery model at low temperatures (50-150°C), while the CTEs in 400-500°C temperature range, are relatively in agreement with Kerner's predictions.
4. The effect of particle size is quite evident and the larger the particles, the greater the thermal expansion of the composite.

ACKNOWLEDGMENTS

The authors are grateful to Professors Flemings and Mortensen (MIT) for the squeeze casting facilities used in this work. Also, we would like to thank Dr. Vukovich, Director of Spacecraft Engineering at the Canadian Space Agency for assistance and stimulating suggestions.

REFERENCES

1. M. J. Koczak, S. C. Khatri, J. E. Allison and M. G. Bader, "Fundamentals of Metal Matrix Composites", edited by S. Suresh, A. Mortensen and A. Needleman (Butterworth-Heinemann, Boston, 1993) 297.
2. S. Elomari, R. Boukhili, M. D. Skibo and J. Masounave, "Dynamic mechanical analysis of prestrained Metal-Matrix Composites", *Journal of Materials Science*, Vol. 30, 1995, pp. 3037-3044
3. Y. Flom and R. J. Arsenault, *Journal of Metals*, Vol. 38, 1986, p. 31.
4. F. A. Girod, J. M. Quenisset and R. Nashlain, *Composite Science & Technology*, Vol. 30, 1987, p. 155.
5. R. H. Jones, C. A. Lavender and M. T. Smith, *Scripta Metallurgica*, Vol. 21, 1987, p. 1565.
6. H. J. Heine, *Foundary Mgmt & technology*, Vol. 116, 1988, p. 25.
7. V. C. Nardone and J. R. Strife, *Metallurgical Transactions*, Vol. 18, 1987, p. 109.
8. Duralcan composites casting guidelines, "Duralcan composites-mechanical and physical property, Wrought composites, SI Units", 1992, Duralcan^{USA}, San Diego, CA, USA.
9. R. J. Vaidya and K. K. Chawla, *Composite Science & Technology*, Vol. 50, 1994, p. 13.

10. S. Elomari, R. Boukhili and D. J. Lloyd, "Thermal expansion behavior of prestrained metal-matrix composites", *Acta Materialia*, Vol. 44, No. 5, 1996, pp. 1873-1882.
11. R.A. Schapery, *Journal of Composite Materials*, Vol. 2, 1968, pp. 380-404.
12. D. K. Balch, V. J. Michaud, T. J. Fitzgerald, A. Mortensen, Y.L. Shen and S. Suresh, "Thermal Expansion of Metals Reinforced with Ceramic Particles and Microcellular", *Metallurgical and Materials Transactions*, in press, 1997.
13. O. V. Mazurin, M. V. Streltsina and T. P. Shvaiko-Shvaikovkaya, *Handbook of Glass Data*, Elsevier Inc., Oxford, 1983.
14. S. Elomari and D. J. Lloyd, "Thermal expansion behavior of Duralcan metal-matrix composites", ASM/TMS Materials week, Cincinnati, Ohio, 1996.
15. Z. Y. Ma, J. Bi, Y. X. Lu and Y. X. Gao, "Effect of SiC particulate size on properties and fracture behavior of SiCp/2024 Al composites", Proceedings of the The Ninth International Conference of Composite Materials (ICCM/9), Madrid, 12-16 July, 1993.
16. M. K. Premkumar, W. H. Hunt and R. R. Sawtell, *Journal of Metals*, Vol. 44, 1992, p. 24.

REACTION HARDENING OF TiO₂/AL ALLOYS COMPOSITES STIMULATED BY DOPING

Isao Tsuchitori¹, Toshio Fujii¹, Nobuyuki Fuyama¹ and Hideharu Fukunaga²

¹*Industrial Research Institute West of Hiroshima Prefecture,
2-10-1, Aga-Minami, Kure city, Hiroshima, 737, JAPAN*

²*Faculty of Engineering, Hiroshima University,
1-4-1, Kagamiyama, Higashi-Hiroshima, Hiroshima, 724, JAPAN*

SUMMARY: The reactivities of rutile type TiO₂/Al composites have been investigated for the purpose of defining the effects of some impurities in rutile type TiO₂ on the solid state reaction. Because such reaction in the composites is induced by impurity in reinforcement and is considered practically valuable. The reactivities of each TiO₂/Al composites, which are fabricated from pure Al and TiO₂ doped with alkali and alkali earth metal oxides respectively, have been examined by DSC. Doped Na, K, Rb and Cs except for Li caused the TiO₂/Al composites to react on the solid state. Otherwise, in the case of alkali earth metals, doped Ca, Sr and Ba except for Be and Mg effects on the reaction of the composites on the solid state. These results indicate that some elements which are large ionic radius, caused the reaction of the composites on the solid state. In addition, it is seemed that the exothermic reaction of the composites on the solid state is larger with increasing ionic radius of the dopants. These results reveal the possibility of reaction control between matrix alloy and reinforcement by doping. In other words, it is shown that new flexible MMC and the process, which harden by heat treatment are produced.

KEYWORDS: TiO₂, Al alloys, Metal matrix composites, Heat treatment, Reaction, Hardening, Doping, Al₂O₃, Al-Ti intermetallic

INTRODUCTION

Much attention on metal matrix composites has been recently paid to take advantage of the reaction between matrix alloy and reinforcement. The reaction has great potential to offer economically high performance composites. From the views, various kinds of fabrication procedure for the composites have been developed. They are divided into classes by the reactants states, e.g. liquid-liquid, liquid-solid, solid-solid and gas-liquid, and therefore, have various features. Some of them are practically applying for machine components, but a disadvantage of these composites is lower machinability. Because, most of these composites have been fabricated accompanying with the reaction, and resulting to include reaction products in it.

In the previous conferences, we have been proposed new composites which harden by heat treatment on the solid phase after they are fabricated by conventional squeeze casting[1]. In rutile type TiO_2/Al alloys system, three kinds composites had been obtained by squeeze casting due to the reactivity between reinforcement and matrix[2]. One of them is plain composites which particulate rutile type TiO_2 merely dispersed in Al alloys. It had been found that the composites hardened not only on the liquid phase, but also on the solid phase, and shown the commercial significance of the composites availed the reaction on solid phase, such as behavior of the hardenability, effects of alloy elements and some properties[3,4]. Furthermore, it has been found that the reaction of TiO_2/Al composites on the solid state is stimulated by a impurity in TiO_2 , which is Na[5]. In this work, the reactivities between TiO_2 and Al composites were investigated to research of the reaction mechanism and other effective elements as dopants.

EXPERIMENTAL PROCEDURE

Fabrication of TiO_2/Al composites

High purity rutile type TiO_2 (Wako Chem. Co., 99.9%) powder and Al(99.99%) were employed as reinforcement or matrix respectively. Chemical compositions of impurities in the TiO_2 are shown in Table 1. The particulate TiO_2 is very fine powder which the mean diameter is about $0.3 \mu\text{m}$ (Fig.1). For doping to reinforcement, alkali or alkali earth metal elements, which are Li, Na, K, Rb, Cs and Be, Mg, Ca, Sr, Ba, were added respectively to the TiO_2 powder as each element's oxide or carbonate. These employed additives are first grade reagents. Amount of each additive is slightly 0.3 mass% as each element's oxide, respectively. The TiO_2 powder was mixed with each additives by planetary ball mill. The each mixed TiO_2 powder was formed by cold press(0.3MPa) in die, and the shaped TiO_2 block($20 \times 50 \times \sim 17\text{mm}$) was fired at 1273 ~ 1473K. As some kinds of dopants to TiO_2 cause large shrinkage during sintering, the firing temperature was changed as being almost same Vf of reinforcement. Thus, the fabricated TiO_2 block as preform has 32.5 ~ 40.3% as volume fraction of TiO_2 and was located in the casting

Table 1: Impurity elements in high purity TiO_2 powder(99.9 mass%)

(mass ppm)

Al	Zn	Na	K	Ca	Fe	Ta	Cr	Ni	As	Pb	Mg	Ba
25.0	1.5	7.8	0.3	8.0	13.8	28.2	12.3	4.3	4.7	1.8	1.9	0.3

die. Subsequently, the composites were fabricated by squeeze casting under lower temperature condition. That is, preheating temperature of the preform and the die were less than 523K and pouring temperature of melt is less than 973K. Thus fabricated TiO_2/Al composites has not hardly reacted.

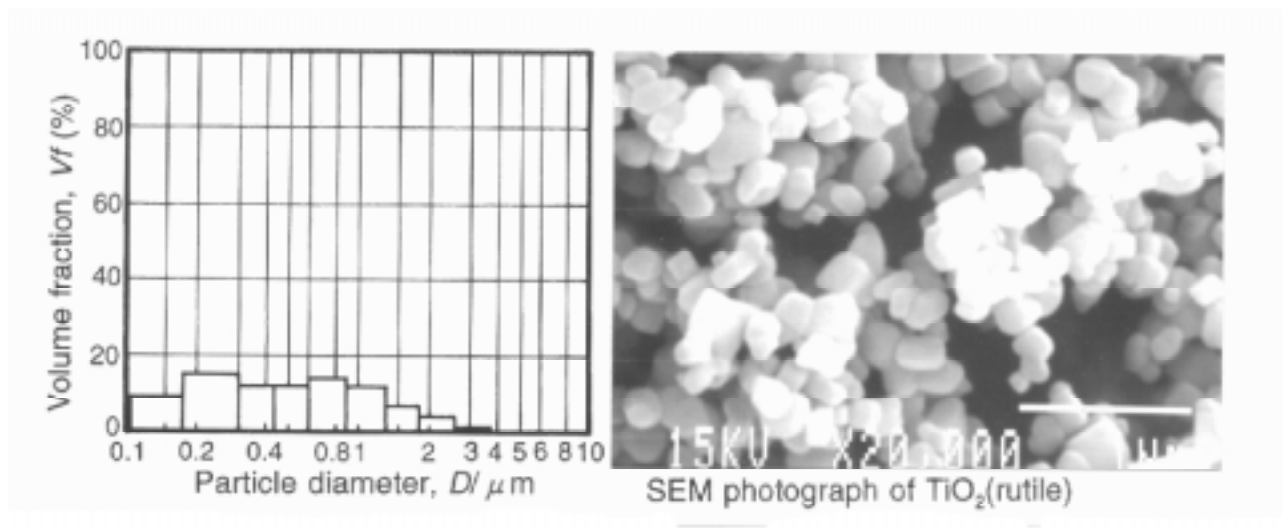


Fig 1: Particle size distribution and SEM image of rutile type high purity TiO_2 powder

Some Examination on Reactivity of the Composites

The specimens for thermal analysis are cut out from each composites and examined the reactivity on the solid state by DSC. The structures of each composites corresponding to proceeding of reaction were observed and analyzed by SEM-EDX, TEM-EDX and XRD. From the view of reaction mechanism, the amount of element Na was analyzed before and after dissolving case of TiO_2 by fluorescent X ray analysis. Fluoride solution was used as dissolving fluid The microstructure of TiO_2 observed by TEM from the view of seeing effect of the additives.

Furthermore, the interface between sintered TiO_2 and pure Al was examined with regard to interaction between reinforcement and matrix.

RESULTS AND DISCUSSION

Reactivities and Structures of the Doped TiO_2/Al Composites

DSC thermograms of each TiO_2/Al composites doped with alkali metal which is univalent are shown in Fig.2. The curves of Li_2O doped TiO_2/Al composites did not react on the solid state (arrow a). But, when Na_2O or K_2O doped TiO_2 , it shows that the composites indicate little peak on the solid state (arrow a) due to exothermic reaction. Then, in the case of Rb_2O , the peak is more define at the same temperature. Furthermore, Cs_2O doped TiO_2/Al composites reveal more greater peak. On the other hand, in the case of alkali earth metal elements which are divalent, DSC thermograms of each doped TiO_2/Al composites are shown in Fig.3. Although the curves of BeO or MgO doped TiO_2/Al composites did not react on the solid state (arrow a), one of CaO doped TiO_2/Al composites emerged little peak of exothermic reaction at the same temperature. When SrO doped TiO_2 , the composites appear sharp peak.

Then BaO doped TiO_2 , the composites show more large peak. From the results of Fig.2 and 3, the later element of atomic number on periodic table give rise to larger peak 'a' versus 'c' for exothermic reaction in each figure respectively. The tendency also corresponds to the order of ionic radius of each element.

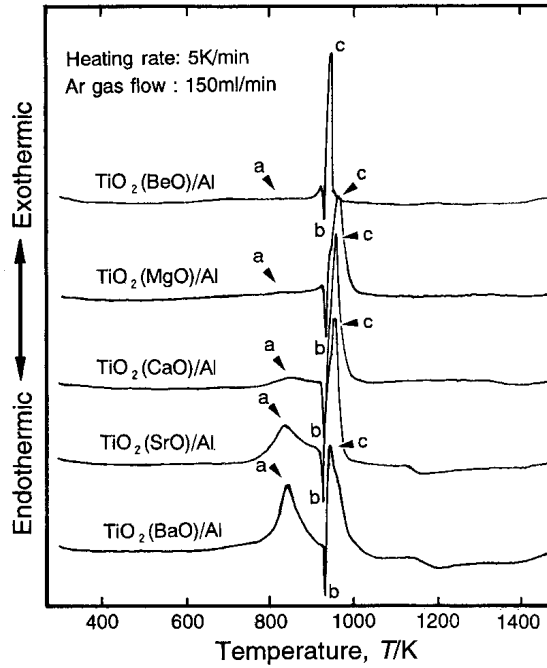


Fig. 2: DSC thermograms of TiO_2/Al composites doped with 0.3 mass% of alkali metal oxides.

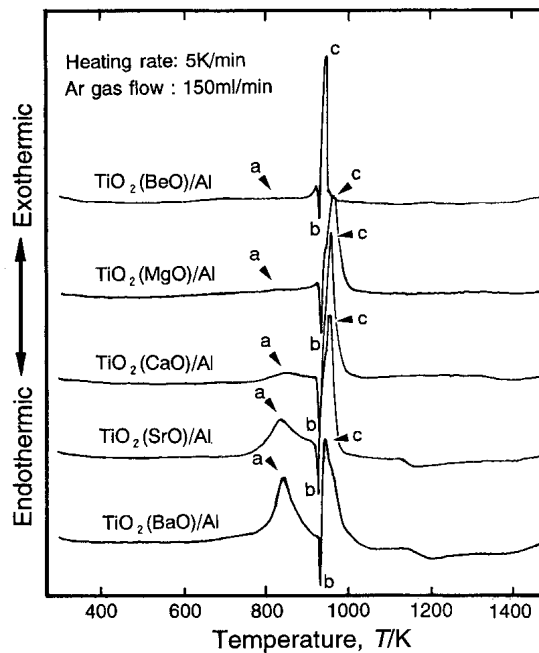


Fig. 3: DSC thermograms of TiO_2/Al composites doped with 0.3 mass% of alkali earth metal oxides.

For representative examples, XRD of BeO or Rb₂O doped TiO₂/Al composites after heat treatment on the solid state are shown in Fig.4. In the case of BeO, the XRD patterns does not change before and after heat treatment. However, in the case of Rb₂O, the main peak of Al₃Ti near one of Al appears after heat treatment on the XRD patterns. The Rb₂O doped TiO₂/Al composites actually hardened after heat treatment. Thus, TiO₂/Al composites proceed the reaction by heat treatment on the solid state.

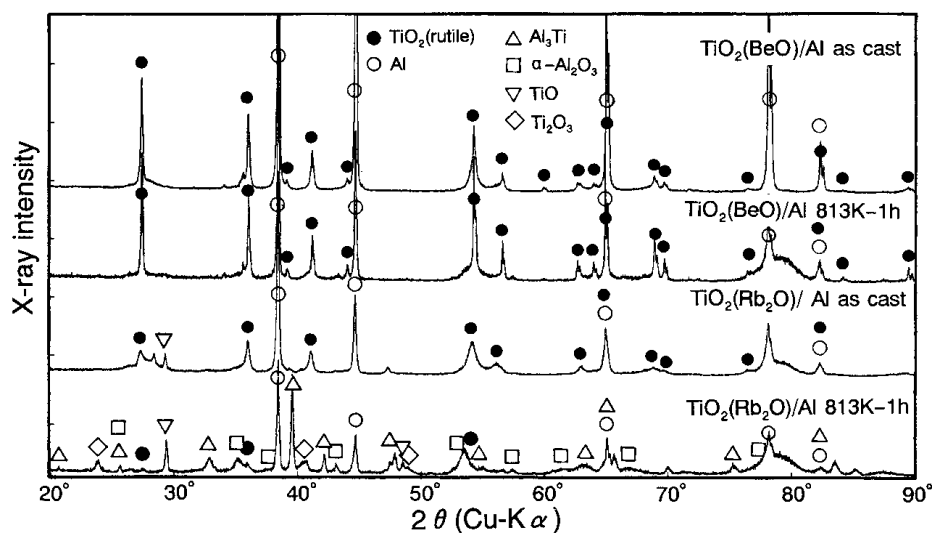


Fig. 4: XRD patterns of TiO₂/Al composites doped with small amount of BeO or Rb₂O before and after heat treatment. reaction by heat treatment on the solid state.

Fig.5 shows TEM structures and point analysis of Na₂O doped TiO₂/Al composites during reaction hardening. Point a or b in Al matrix contains small amount of Ti and O. Point c or d is thought to be in TiO₂ particle region. Al is slightly detected at point c and is considerably detected at point d. Al-Ti intermetallic may be produced at point d. In this way, every TiO₂ in the composites during reaction hardening contains somewhat Al. Therefore, it is thought that Al diffuses into TiO₂ comparatively. Since then, it is also revealed there is difference of proceeding of the reactions between each TiO₂ particles and matrix in the composites.

For the purpose of confirming the morphology of the reaction, SEM structures in TiO₂/Al composites during reaction hardening were observed (shown in Fig.6). When the reaction of the composites begin from (a) to (b), white crusty layer precipitates surround TiO₂ particle, and the layer thickness increases with time such as (c), (c'). The white layer is α-Al₂O₃ certainly from the results of XRD. But, the crusty α-Al₂O₃ did not develop into the core of TiO₂ particle, and the core seemed to be Al-Ti intermetallic.

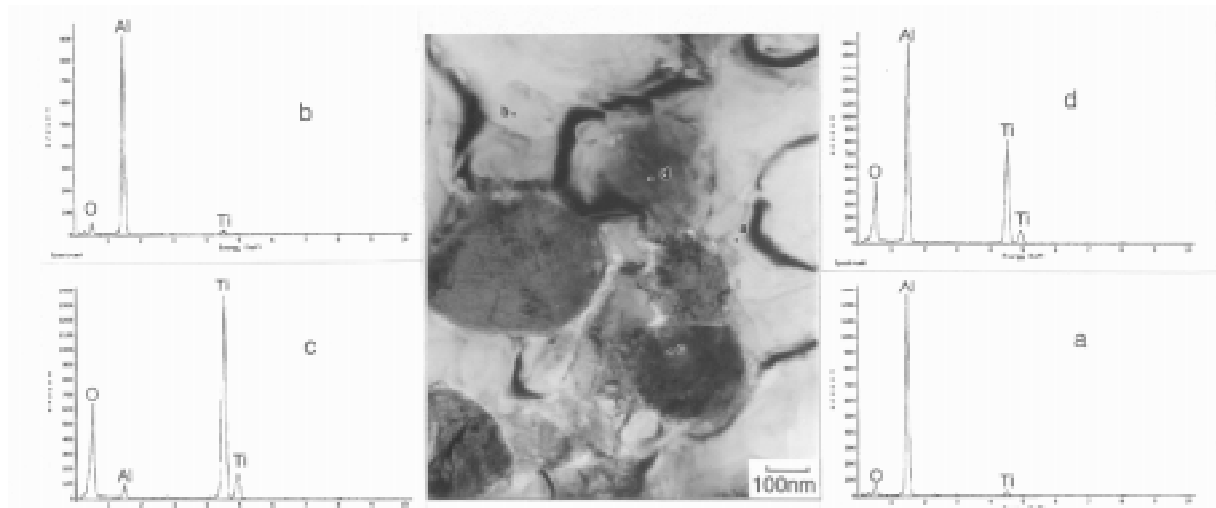


Fig. 5: Microstructure and point analysis at the respective locations of TiO_2/Al composites on the way of reaction hardening by TEM-EDX.

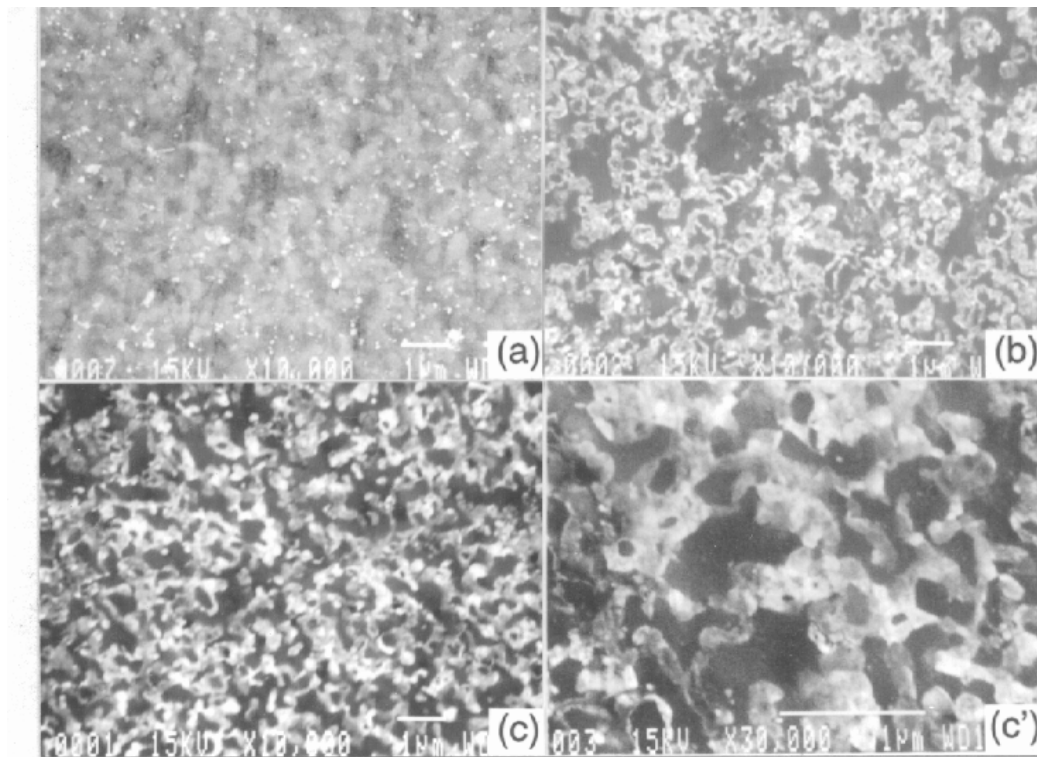


Fig. 6: SEM structures of practical grade TiO_2/Al composites. (a)As cast, (b)873K-10min, (c)873K-60min, (c')Magnified of (c).

Effects of Doping Element on Interaction

Interface constituted of sintered high purity TiO_2 or practical TiO_2 contained Na as impurity and Al was fabricated by squeeze casting, and the comparison of both interfaces after heat treatment on the solid state is shown in Fig.7. In the case of Na contained TiO_2 , TiO_2 side changes dark layer near the interface after heat treatment, though the interface does not change in the case of high purity TiO_2 . Fig. 8 shows XRD of the dark layer. The color changed dark layer is almost rutile type TiO_2 from the results. It is recognized that the dark

layer have electric conductivity too. Considering these results, it can be fairly certain that the dark layer is produced to be removed oxygen from TiO_2 . That is, TiO_2 has been partially reduced by Al. From these phenomena, it is indicated that either oxygen is easy to move in TiO_2 or Al is easy to diffuse into TiO_2 when TiO_2 contain a specific element such as Na.

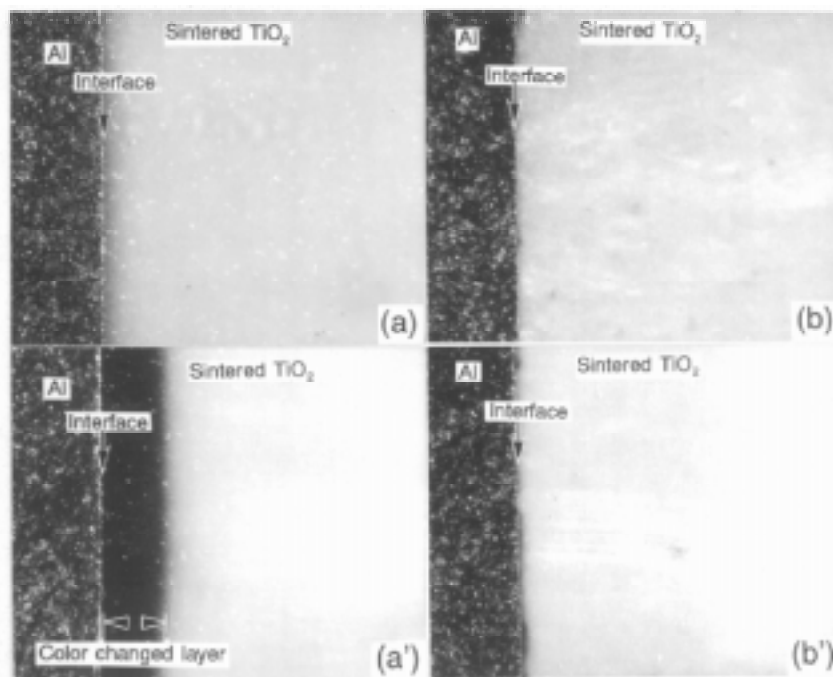


Fig. 7: Optical microstructures of interface between Al and sintered TiO_2 before and after heat treatment. (a) Practical grade TiO_2 - as cast, (a') Practical grade TiO_2 - after heat treatment (873K-120h), (b) High purity TiO_2 - as cast, (b') High purity TiO_2 - after heat treatment (873K-120h).

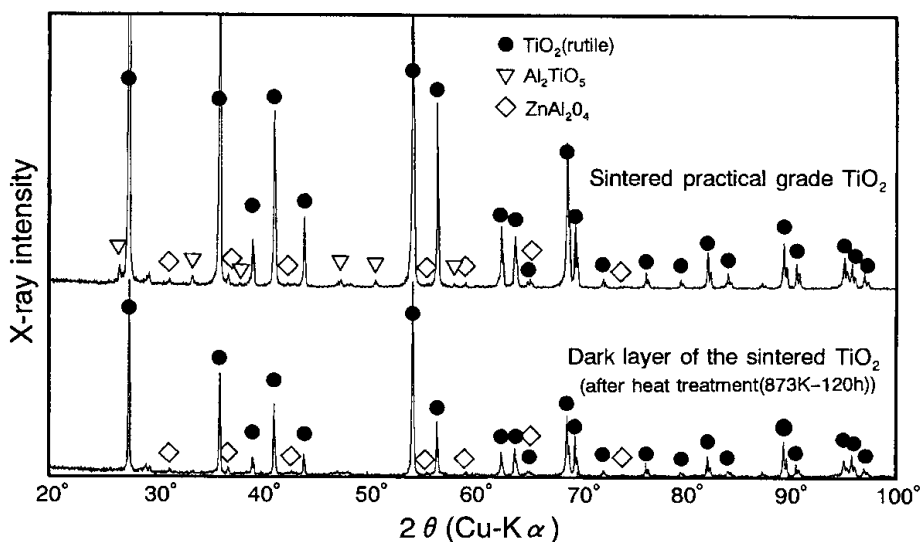


Fig. 8: XRD patterns of the dark layer of sintered practical grade TiO_2 bonded with Al after heat treatment.

Anyway, it is significant to find out where such specific element is located in TiO₂ from the view of reaction mechanism. When each specific element in Fig.2 and 3 doped TiO₂, Lattice parameter of TiO₂ was attempted to get by XRD. But the results corresponding to ionic radius of each element were not obtained. Table 2 shows the concentrations of case and core of TiO₂ particles which were doped with Na₂O. From the results, it is clear that Na exists near surface of TiO₂ particle. This can be extended in the case of alkali or alkali earth metal element from the phase diagrams.

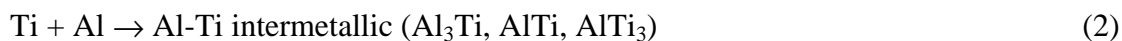
Table 2: Analysis of impurity oxide of case and core in TiO₂ particle.

Sample	Impurity oxide	Whole particle	After dissolution	Case (difference)
Doped TiO ₂	Na ₂ O	0.028	0.000	0.028

(mass%)

Reaction Mechanism

It has been reconfirmed that the high purity TiO₂ hardly react with Al by heat treatment on the solid state and specific element doped TiO₂ reacts. The reaction represents as follows equation from reaction products.



In equation (1), the change of freedom energy ‘ ΔG ’ gives negative ($\approx -173\text{kJ/mol}$) on the solid state ($\sim 873\text{K}$). Therefore, The reaction of equation (1) has to proceed, but not proceed actually (in the case of high purity TiO₂). However, it has been apparent when alkali or alkali earth metal element except for a part of them dopes into TiO₂, the reaction of the composite comes to proceed.

We shall discuss the reaction mechanism between specific element contained TiO₂ and Al on the solid state. In the high purity TiO₂/Al composites, the reaction occurred firstly at the interface, and does not almost proceed since. It was observed in the composites that Al₂O₃ is thin produced at the interface and Al-Ti intermetallic existed massively near the interface. The first reaction on the interface makes Al₂O₃. As the heat treatment is carried out on the solid state, Al or Ti have to diffuse through the Al₂O₃ so as to continue the reaction. It was reported that Ti could diffuse fast in Al₂O₃ relatively[6]. But, the self diffusion of Al in Al₂O₃ is extremely late at same temperature[7]. Accordingly, it is considered that the late diffusion retard the reaction between TiO₂ and Al.

However, when alkali or alkali earth metal element dopes TiO₂, it is predicted that oxide complex is produced to react with TiO₂ at surface, partially or overall. In fact, when the amount of dopant which is Na or Ba increased over 1 mass%, Na₂Ti₆O₁₃ or Ba₂Ti₉O₂₀ was detected by XRD, respectively. Thus, these oxide complexes could be also produced in relation to another dopants from phase diagram. Then the ion radius of the elements accelerated the reaction are large ($\geq 1\text{\AA}$) except for some dopants. Considering that these

dopants form substitutional solid solutions with TiO_2 is impossible, because cation radius which can be substituted for Ti ion limits to its 15% increment. Then, such large space does not indeed exist in interstitial of rutile structure in TiO_2 . Accordingly, The dopants accelerated the reaction can not consider to diffuse into TiO_2 particle. From these results, it is thought that alkali or alkali earth metal elements form thin film of oxide complex with TiO_2 at interface except for Li, Be, Mg.

These oxide complex constituted of each alkali or alkali earth metal element and TiO_2 is known to have a layer or tunnel structure. These cation are sited in interlayer or tunnel of the structures and can be easy to exchange another alkali or alkali earth metal cation. The oxide complexes react with Al furthermore, and ternary oxide complexes may be produced. The ternary oxide complexes have occasionally one dimensional ion conductor or super ion conductor, etc.[8]. Anyhow Al ion is thought to diffuse through such as the complex oxide easily.

Fig.9 shows schematic illustration of reaction mechanism. As above mentioned, in alkali or alkali earth metal element doped TiO_2/Al composites, the oxide complex layer which constituted of alkali or alkali earth metal element and Al, is produced partially on the TiO_2 . In site of direct contact interface between TiO_2 and Al, matrix Al reacts with TiO_2 to form Al_2O_3 as initial reaction by heat treatment on the solid state. In the site of oxide complex layer on the TiO_2 , matrix Al changes to Al ion to release electric charges on the interface. The Al ion diffuses fast through the complex oxide compared with through α - Al_2O_3 by the heat treatment and therefore, Al ion can attain to TiO_2 . Rutile structure of TiO_2 is known to have diffusion path in the direction of c axis. It had been reported that the diffusion rate of Li ion in the direction of c axis of rutile has 108 times compared with a or b axis[9]. It had been also reported that thus strong anisotropy of impurity diffusion in rutile had not only univalent ion such as Li, but also divalent or trivalent ion such as B, O, Ni, Co, Fe, Cr[10-13]. From the facts, Al ion (0.53 Å) which is smaller ion radius than one of Li (0.74 Å), is considered to diffuse to inner of TiO_2 . The maximum radius of void in rutile structure is reported as 0.77 Å by Wittke[10]. Diffused Al ion in TiO_2 reacts with O ion to form Al_2O_3 and to dissociate into Ti ion. For the development of the produced Al_2O_3 , O ions have to diffuse in TiO_2 . But O ions are difficult to diffuse because of the large ionic radius. Therefore, the growth of Al_2O_3 is so late, Al ions diffuse to inner of TiO_2 to nucleate and grow of Al_2O_3 . Then the dark layer observed in Fig.7 shows that TiO_2 is reduced partially. The apparatus activation energy is calculated 255.1 kJ/mol from DSC to use Augis and Bennet's method[14].

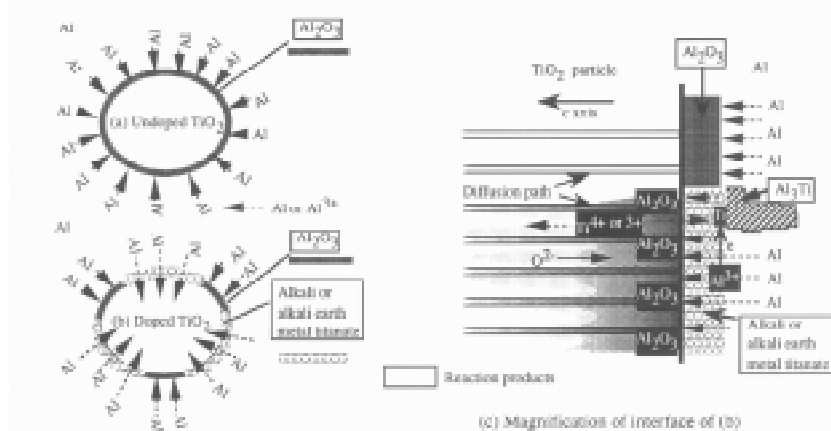


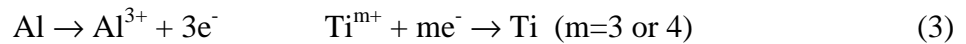
Fig. 9: Schematic illustrations of promoted reaction mechanism by impurity elements in TiO_2/Al composites.

As the value is closest to one of O ion in rutile type TiO₂[15], the reaction of TiO₂/Al composites on the solid state is considered to be controlled by the diffusion of O ion in TiO₂.

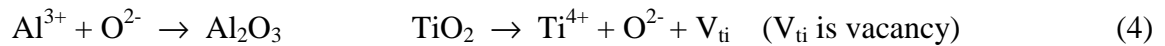
On the other hand, as the dissociated Ti ion is easy to diffuse through Al₂O₃, Ti ion received electric charge released from Al to form metal Ti on the interface. The Ti immediately dissolved in Al. Al-Ti intermetallic is produced because Ti is so late to diffuse in Al[16]. Thus Al-Ti intermetallic increases with proceeding the reaction and comes to occupy in matrix.

The following reactions proceed on the both interfaces.

On the interface of Al / oxide complex;



On the interface of Al₂O₃ / TiO₂;



The doping of Li, Be or Mg oxide to TiO₂ gives no effect on the solid reaction of TiO₂/Al composites. The ionic radius of Li, Be or Mg are 0.74 Å, 0.35 Å, 0.72 Å respectively and as above mentioned, the radius of the diffusion path in the direction of c axis of rutile is 0.77 Å. Therefore, when TiO₂ doped with each oxide of Li, Be or Mg was fired at 1273~1473K, the each ion is presumed to diffuse into TiO₂ through c axis of rutile structure. As a consequence, the oxide complex of the each elements and TiO₂ could not produced. The ionic radius of Na or Ca are 1.00 Å or 1.02 Å which are larger radius than 15% increment of 0.77 Å. Indeed, the another ions of alkali or alkali earth metal have larger radius with later elements in periodical table and oxide complex is produced.

Furthermore, it is thought that the magnitude of exothermic reaction on the composites on the solid state depends on volume diffusivities of Al ion in the oxide complex. When large ion sites in interlayer or tunnel of oxide complex, the interlayer or the tunnel is broadened and Ti-O₆ octahedron may be distorted to widen the lattice. Anyhow, Al ion is easy to pass through the oxide complex with larger ion sited in the interlayer or the tunnel.

Rutile type TiO₂/Al composites can harden by heat treatment on the solid state, which contained the specific elements in reinforcement. The reaction hardening is considered effects of ion diffusivity due to the oxide complex, their's structures and rutile structure.

CONCLUSION

In the reaction hardening of rutile type TiO₂/Al composites on the solid state, the reactivity of the composites in which each oxide of alkali or alkali earth metal elements was doped to TiO₂, was examined and the reaction mechanism was investigated. These results as follows;

- (1) TiO₂/Al composites shows exothermic reaction on the solid state which Na, K, Rb, Cs, Ca, Sr, Ba doped in the reinforcement except for Li, Be, Mg.
- (2) The exothermic reaction of the composites on the solid state appeared to be intensive with increasing ionic radius of the dopants.

- (3) The reaction mechanism of the composites on the solid state can be explained by the formation of titanate alkali or alkali earth metal oxide, their structures, the rutile structure and the diffusivity of each ion.

REFERENCES

1. Isao Tsuchitori and Hideharu Fukunaga, "High Performance Composites by Reaction Hardening in Titanium Di-Oxide /Aluminum Alloys System", Proceedings of the Tenth International Conference on Composite Materials (ICCM-10), Whistler, British Columbia, Canada, August 14-18, Vol. 2, 1995, pp.263-270.
2. Isao Tsuchitori and Hideharu Fukunaga, "Process Control by Reaction Squeeze Casting for Intermetallics-Strengthening of TiO₂/Al Composites", Proceedings of the Ninth International Conference on Composite Materials (ICCM-9), Madrid, 12-16 July, Vol. 2, 1993, pp. 906-912.
3. Isao Tsuchitori and Hideharu Fukunaga, "Reaction Hardening of Particulate Titanium Dioxide(rutile)/Aluminum Composites by Heat-Treatment", Journal of Japan Institute of Metals, Vol. 58, No. 9, 1994, pp. 1029-1035.
4. Isao Tsuchitori and Hideharu Fukunaga, "Effects of Mg and Si on Reaction Hardening of Particulate Titanium Dioxide(Rutile)/Aluminum Composites", Journal of Japan Institute of Metals, Vol. 59, No. 3, 1995, pp. 331-338.
5. Isao Tsuchitori and Hideharu Fukunaga, "Effect of Impurity Elements on Reaction of Reinforcement with Matrix in Rutile Type Titanium Oxide / Aluminum Composites", Journal of Japan Institute of Metals, Vol. 59, No. 12, 1995, pp. 1306-1314.
6. Yoshiaki Shida and Hiroyuki Anada, "Structure of Oxide of Binary Ti-Al Alloys formed in High Temperature Air", Journal of Japan Institute of Metals, Vol. 55, No. 6, 1991, pp. 690-695.
7. Kingery W.D., Bowen H.K. and Uhlmann D.R., "Introduction to Ceramics", Uchida Rokakuho LTD, Tokyo, 1981.
8. National Institute for research in Inorganic Materials, "Study on Alkali Titanate Metals", Research Report of National Institute for Research in Inorganic Materials Edition, Vol. 38, 1984.
9. Johnson O.W., "One-Dimensional Diffusion of Li in Rutile", Physical Review, Vol. 136, No. 1A, 1964, pp. A284-A290.
10. Wittke J.P., "Diffusion of Transition Metal Ions into Rutile(TiO₂)", Journal of The Electrochemical Society, Vol. 113, No. 2, 1966, pp. 193-194.
11. Steele J.L. and McCartney E.R., "Anisotropy of Diffusion in Rutile", NATURE, Vol. 222, No. 5, 1969, pp. 79.

12. Bogomolov V.N., "Anisotropy of The Diffusion of Oxygen and Boron in Rutile", Soviet Physics-Solid State, Vol. 5, 1964, pp. 1468-1469.
13. Haul R. and Dumbgen G., "Suerstoff-Selbstdiffision in Rutilkristallen", Physical Chemistry in Solids, Vol. 26, 1964, pp. 1-10.
14. Augis J.A. and Bennet J.E., "Calculation of The Avrami Parameters for Heterogeneous Solid State Reactions Using A Modification of The Kissinger Method", Journal of Thermal Analysis, Vol. 13, 1978, 283-292.
15. Venkatu D.A. and Poteat L.E., "Diffusion of Titanium in Single Crystal Rutile", Materials Science and engineering, Vol. 5, 1969/1970, pp. 258-262.
16. Grammatikakis J., Eftaxias K. and Hadjicontis V., "Interconnection of The Diffusion Coefficients of Various Elements in Aluminum", Journal of Physical Chemistry in Solids, Vol. 49, No. 10, pp. 1275-1277.

A STUDY OF THE METAL FLOW CHARACTERISTICS OF COMPOSITE SHEETS FORMED BY POWDER PLATING AND ROLLING

Zhang Daiming, Sun Yong, Zhang Shuhong, Shi Qingnan

Kunming University of Science and Technology Kunming 650093, Yunnan, P.R..China

ABSTRACT: This paper, beginning with a new technique of producing metal composite sheets, namely PPR technique, makes a study of the metal flow characteristics of the upper and lower surfaces of the workpiece and of the binding interface of the two metal layers in applying the technique to roll composite sheets. Findings prove that when a composite sheet is rolled, the flow of the metal in the cleaning between rolls along the horizontal direction of the workpiece is uneven; the flow rate of the metal depends on the forward slip rate, the latter being related with the surplus friction between the workpiece and the rolls. The final part is an attempt to present the concept of equivalent friction coefficient and derive equivalent coefficient by using the comparison expression among nip angle, neutral angle and forward slip.

KEYWORDS : sheet-composite rolling, metal flow, friction coefficient

INTRODUCTION

Powder plating rolling technique, called PPR for short, is a new technique of producing metal sheets. It is an invention patent of the writers. The main technological characteristic is that using a certain metal sheet as matrix, on whose surface another kind of metal or alloy is deposited with a unique technique and which is then rolled and treated with relevant technology treatment, a new metal composite sheet with unique property will be produced. This composite technique is best applied to producing multi-layer and thinner composite sheets. Because the state of both the upper surface and lower surface of the workpiece (shape, resistance, friction coefficient, etc.) is different in PPR process, the rolling process of PPR technique is a kind of asymmetrical rolling, research on which is seldom reported. We have made an experiment to study the metal flow characteristics and have explored the flow law of the metal and deforming characteristics of the workpiece when using PPR to roll composite sheets, This has laid a foundation for establishing the systematic theory of PPR technique.

EXPERIMENT

1. Test workpiece and rolling equipment

- (1) Matrix: $250 \times 50 \times 0.8$ mm common carbon steel, on the surface of which 0.5×0.5 grid lines were carved.
- (2) Surface composite layers: there were soft metal group and hard metal group (stainless steel) respectively.

1.1 Rolling equipment

Four-roll cold sheet mill.

1.2 Determination

- (1) After rolling, the composite layer were peeled and the changes in the matrix and the grid pitch were determined respectively.
- (2) Indentation was used to determine the forward slip quantity on the upper and lower surfaces of the workpiece.

2. The experiment results and analysis

2.1 Change in grids:

It can be seen from Fig. 1 that on the binding interface the grid was of square before deforming, and after deforming, it was still rectangular. No matter it was a soft metal or a hard metal, the change law of the grid was the same. This shows that:

- (1) On the binding interface of the two metal layers, form changes are even and constant.
- (2) On the binding interface of the two metal layers there is no relative slip, which is a prerequisite for the realization of composite rolling.
- (3) The study also shows that the change rate of grid pitch and rolling rate are of a direct proportion. It is in accord with percentage elongation.

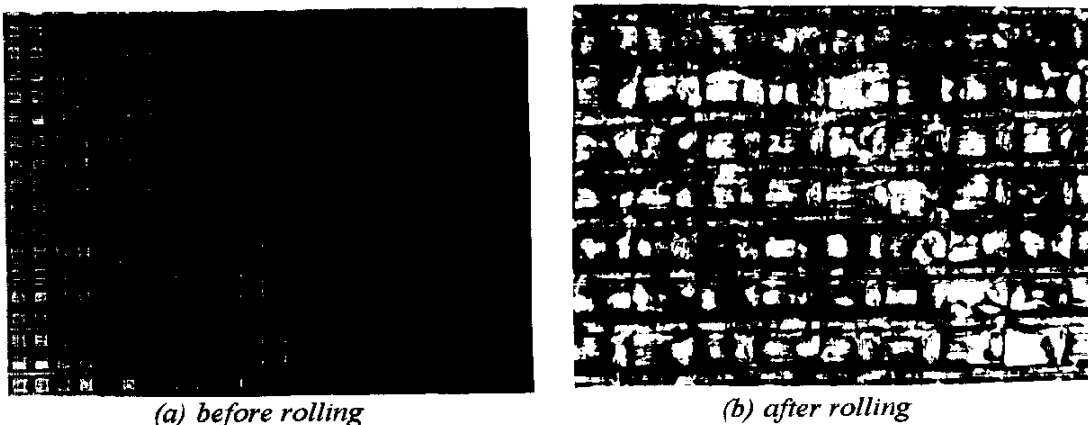


Fig. 1: Changes of surfaces grids of base material before and after rolling

2.2 The forward slip of the upper and lower surfaces

After rolling it was found that there was a significant difference between the forward slip value of the upper surface and that of the lower surface. The changes of forward slip value follow the following law:

(1) Forward slip increases with rolling rate (Fig. 2).

(2) Forward slip is related with the surface state of the workpiece. The different state of the workpiece causes the differences in the forward slip value of the upper and lower surfaces of the workpiece. Fig. 2 shows the different forward slip of the surfaces with different state under the same rolling rate.

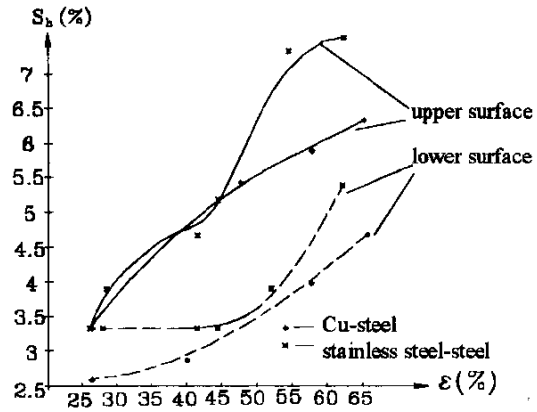


Fig. 2: Relation between forward slip and rolling rate

2.3 Forward slip and the horizontal pace

Fig. 3 shows the relationship between forward slip and measured horizontal velocity of workpiece. The horizontal velocity of workpiece increases with rolling rate, which is of a linear distribution.

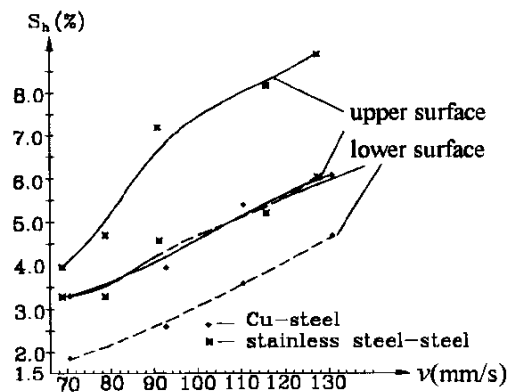


Fig. 3: Relation between forward velocity and the horizontal velocity of workpiece

DISCUSSIONS

Metal flow

The above experiment proves that when double-metal sheets are rolled, the height metal flow along the section of workpiece in the cleaning between the rolls is not even. Under the same rolling rate, on the side of workpiece's surface with smaller friction coefficient, the horizontal pace of the workpiece is bigger, conversely, when the horizontal pace is small, the pace of workpiece on the binding interface of the two metals is the same. The velocities of the upper and lower surfaces of workpiece are all bigger than the linear velocity of roll. The horizontal velocity of rolled composite sheet at the outlet of the cleaning between rolls is of a linear distribution in terms of thickness direction. It is this uneven deforming velocity that causes the inevitable bending of composite sheet in the rolling process (Fig. 4).

Forward slip

As mentioned above, in asymmetric rolling process, because forward slip value of the upper and lower surfaces of workpiece is different, the paces of the upper and lower surfaces of

workpiece is uneven, causing the bending of workpiece in the rolling process. It is thus evident that the effect of forward slip is very important in asymmetric rolling process, which should be paid attention to.

The effect of rolling rate on forward slip

As shown by Fig. 2, forward rate increases with rolling rate, which is due to the increase of height press of workpiece, causing the increase of deformation of workpiece horizontally and longitudinally, thus resulting in the increase of forward slip.

The effect of friction on forward slip

The forward slip expression formula is worked out through D. Deliston

$$S_n = \frac{\gamma^2}{h} R \quad (1)$$

In the formula γ --neutral angle

$$\gamma = \frac{\alpha}{2} \left(1 - \frac{\alpha}{2f} \right) \quad (2)$$

α ---nip angle, f ---friction coefficient.

It is thus clear that under the condition that rolling quantity and other technological parameters are the same the bigger the friction coefficient is, the bigger the forward slip value will be. This is due to the fact that the increase of friction coefficient will cause the increase of surplus friction, thus resulting in the increase of forward slip.

About friction coefficient

In sum, in the double-metal composite rolling process, a study of the deforming process of workpiece and rolling force is a study of surplus friction, or friction coefficient. In fact, in rolling composite sheets, the formulation of technological parameter and the ultimate quality control of products are related with friction coefficient. There are many factors affecting friction coefficient. At present there has not been a reliable method to determine the friction coefficient under rolling state. Because of the technological characteristics of PPR, it is more difficult to rationally determine the friction between the rolls and the workpiece. This is a problem to be solved in the asymmetric rolling process.

By contrary, forward slip value is easy to determine in asymmetric rolling process. Therefore the measured forward slip value can be employed to work out the friction coefficient in PPR process. To differentiate from real friction coefficient, the friction coefficient might as well be called equivalent friction coefficient f_s .

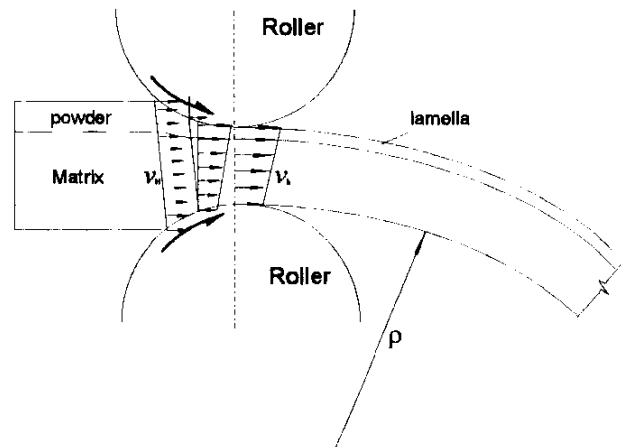


Fig. 4: Distribution chart of the horizontal velocity of workpiece after compositing

By using D. Deliston Forward Slip Formula and simplified neutral angle formula, and when nip angle is very small and proportion between the diameter (D) of the roll and the thickness of the rolled workpiece(h) $D/h \gg 1$, the calculation formula of equivalent coefficient f_s can be derived:

$$f_s = \frac{\alpha^3 R' \pm 2\alpha^2 \sqrt{S \cdot h \cdot R'}}{2\alpha^2 R' - 8 \cdot S \cdot h} \quad (3)$$

In the formula,

R'-----Taking into consideration the radius of the working roll after elastic flaser

S-----forward slip rate %, h-----thickness of rolled workpiece mm

Practical calculation confirms that the equivalent coefficient f_s can be worked out by using the formula (3), thus solving the calculation problem of rolling force theory of PPR.

CONCLUSIONS

- (1) When PPR is employed to roll metal composite sheets, there is no relative slip on the binding interface of the double-metal layers of the workpiece coming out of the deforming zone of rolling.
- (2) When double-metal composite sheets are rolled, the velocity of metal flow along the horizontal direction in the deforming zone is of linear distribution.
- (3) In the process of double-metal composite rolling, because of the effect of the surplus friction produced by different rolling state of the upper and lower surfaces of workpiece, the paces of the upper and lower surfaces of workpiece are different, resulting in the bending of workpiece.
- (4) Using the relation among forward slip, nip angle and friction coefficient, a relation formula to work out the friction coefficient in the asymmetrical rolling of sheets can be established, thus solving the theoretical calculation problem of rolling force in asymmetrical rolling in a better way.

ACKNOWLEDGMENT

This project is supported by the National Natural Science Foundation of China.

REFERENCES

1. Kiuchi and H. Yongmao, *4th International Steel Rolling Conference--The Science and Technology of Flat Rolling*, Beijing, Metallurgy Industry Press, 1990 (in Chinese)
2. Shi Q. N., Sun, Y., Zhang D. M., Zhang S. H., "A Study of Rolling Force in Composite Rolling Process with Metallic Powder and Metallic Sheets" *MSMM'96*, Beijing, 1996.

SURFACE MMCS ON A TI-6AL-4V ALLOY PRODUCED BY COMBINING LASER NITRIDING AND POWDER ALLOYING

C. Hu, H. Xin and T.N. Baker

*Metallurgy and Engineering Materials Group, Department of Mechanical Engineering
University of Strathclyde, Glasgow G1, UK*

SUMMARY: Laser processing, which normally involves gaseous alloying by combining laser melting with nitriding, has been developed to produce better surface properties. Surfaces having hardness >2000 (HV0.1) have been produced, but rarely in a crack-free alloy and then only with sheet < 7 mm thickness. The present work describes a combined alloying approach as an alternative to gaseous laser nitriding, with the aim of overcoming the cracking problem while providing better tribological properties than the untreated material. Several types of powder were preplaced on the surface prior to the laser nitriding. Abrasive wear testing was conducted to determine the improvement in the surface wear resistance after the nitriding plus powder alloying process. The microstructures developed in the laser processing were examined and the cracking tendencies studied for all the processed surfaces.

KEYWORDS: laser processing, Ti-6Al-4V alloy, hardness, wear resistance, nitriding, powder alloying, melt pool

INTRODUCTION

The application of titanium alloys which require good wear or erosion resistance has been restricted, despite their attractive strength to weight ratio, due to their poor tribological properties. Therefore, laser nitriding of titanium alloys has been extensively investigated with the aim of improving the surface properties [1-5]. The hardness was reported to reach 1800HV, when a commercial purity titanium alloy was treated by a CO₂ laser with a Gaussian energy distribution under a pure nitrogen environment [4]. The wear resistance significantly increased [2]. However, cracking on the nitrided surface was recognised as a critical problem in laser nitriding of titanium alloys [1-7]. The tendency to cracking has been found to relate to the processing conditions, the nitrogen concentration in the environment and the thickness of the specimen. Although the residual stress could be reduced and cracking eliminated when a dilute nitrogen environment was used for the processing [2-4, 6-7], the dilution of the nitrogen concentration equates to less effective tribological properties. For example, the surface laser nitriding of Ti-6Al-4V (Ti64) alloy using 100v%N gave a surface hardness greater than 850 HV, while that using 40v% had a value of ~650 HV [5].

Obviously, the titanium nitride formed during the process, on one hand, is the major phase to enhance the material surface properties, and on the other hand, is a cause of cracking as well as the rapid cooling rate in laser processing. The quantity of the titanium nitride formed in the melt

has a significant influence on the tendency to cracking. The purpose of the present work is to explore a new technique of combining laser nitriding and powder alloying to compensate the reduction of the surface properties due to the decrease in the amount of titanium nitrides in the melt when the quantity of the titanium nitride is controlled below a critical level to avoid cracking.

Four types of powders, or mixtures of powders, were chosen. These powders were preplaced on the surface prior to the laser scanning under a nitrogen environment. When the surface was melted by the laser, the preplaced powders dissolved, or partially dissolved into the melt and formed a phase or compound which enhanced the properties of the melt. If the powders partially dissolved, solid particles with a reduced size remained after the laser processing. These particles would also reinforce the surface and enhance the properties. The processed specimens were examined to characterise the microstructure, the hardness, the melt depth and the tendency to cracking. Since the thickness of the specimens has also an influence on the tendency to cracking, the effect of the specimen thickness in the nitriding plus powder alloying was also investigated. This is believed to be important in industrial applications where the thickness/size of the component to be treated must be considered.

EXPERIMENTAL WORK

A continuous CO₂ 5kW laser was used at AEA Technology, Culham, UK. The beam had an annular shape and the energy was uniformly distributed in an annular area when the beam was in a stationary state. In the spinning beam mode the radius of the spinning locus (r_s) was set at 2 mm and the velocity of the spinning at 1500 rpm for all the experiments in the present work. Single tracks were melted. The laser power q was set at 2.8 kW, the specimen velocity v at 5, 10 or 15 mm.s⁻¹. A Ti-6Al-4V alloy (IMI 318) was used as the base alloy to be nitrided. The specimens were ground with 600 grit paper and cleaned with methanol before painting and then laser nitrided. Four types of particles, SiC(7 μ m), a mixture of SiC (7 μ m, 50v%) and Ti-6Al-4V (45 μ m, 50v%) powders, ZrC (45 μ m) and ZrN (45 μ m), were used as a preplaced layer and processed by a spinning laser beam under a gas contained 40%N and 60%Ar with a gas flow of 10 l.min⁻¹. These powders were blended with an organic solution and painted on the surface. During the processing, the specimens were moved under the laser on a work table with the surfaces to be treated at a defocused distance (DFD) of 15 mm above the focal point. Three levels of the specimen thickness (4, 10 and 18 mm) were used, and the dimensions of the surface were 100 mm \times 100 mm.

The microstructure, the melt pool depth and the profile of the transverse section were examined on an optical microscope. The hardness of the surface was measured on the transverse section of the specimens using a Mitutoyo MVK-G1 microhardness tester with a load of 100g, and given as a function of the depth below the surface. Wear resistance of these processed specimens were determined using a pin-on disc device using a constant load of 4.9 N and a speed of 0.236 ms⁻¹. The wear specimens were cleaned in methanol and blown dry with air before testing against P600 SiC grit paper, which was replaced every 25 m during each test. Weight losses were measured after a known sliding distance by weighing the sample to an accuracy of 10⁻⁵g. All tests were carried out at room temperature in air under dry sliding conditions.

RESULTS AND DISCUSSION

Microstructure

The microstructure developed in the specimen preplaced with SiC powder followed by laser nitriding, is shown Fig.1. No solid SiC particles remained after the laser nitriding. This showed a good agreement with our previous work [8] that only the SiC particles greater than $50\mu\text{m}$ had a chance to remain in the solid state after the preplaced SiC surface was laser processed under an argon environment. Fine dendrites formed in the melt pool. The phases developed under argon were identified as TiC and Ti_5Si_3 [9]. The phases formed in the melt shown in Fig.1 could be different from these, or more complex compounds containing a certain content of nitrogen since a nitrogen environment was used in the present work.

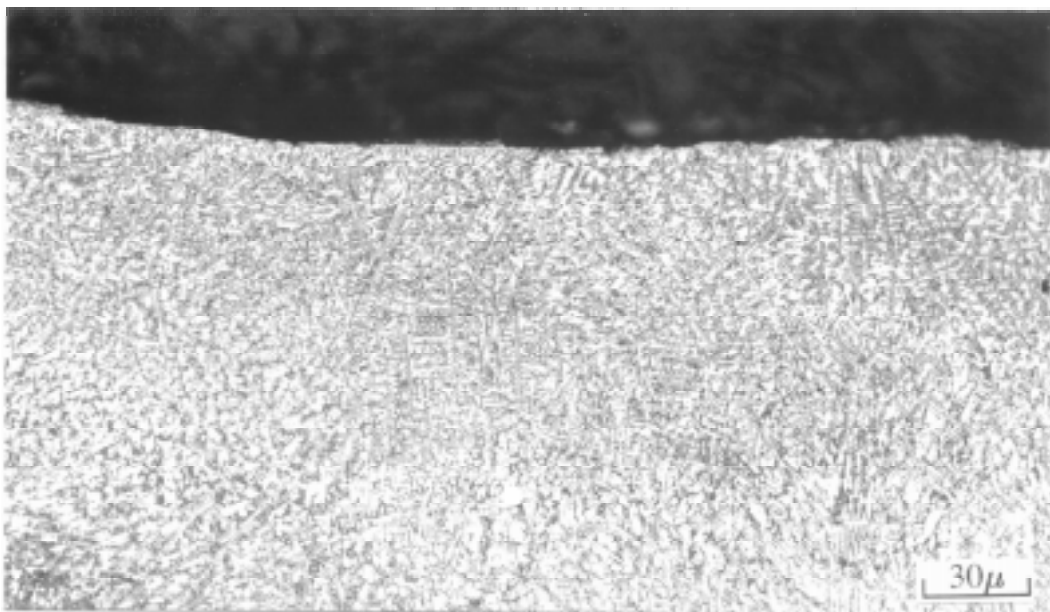


Fig.1 The microstructure developed in the 4 mm thick specimen preplaced with SiC powder and laser treated at 2.8 kW, 10 mms^{-1} .

The microstructure developed in the specimen preplaced with a mixture of SiC and Ti-6Al-4V alloy powders after laser nitriding shows similar features to those in Fig.1, except for a lower concentration of the dendrites formed in the melt pool. This is because less SiC was added into the melt shown in Fig.2 compared with that in Fig.1. A significant high concentration of nitrides formed in the top region of the melt in Fig.2, but the nitrides did not grow into a dendritic structure which was observed in a normal laser nitriding process [9]. It is considered that when SiC powder was preplaced on the surface, the preplaced layer separated the base alloy liquid from the nitrogen environment for a considerable time with respect to the liquid life-time, and therefore restricted the diffusion of nitrogen into the alloy melt pool. This resulted in fewer titanium nitrides forming in the melt shown in Fig.1 than that in Fig.2. In the case of the preplaced mixture of SiC and Ti64 powders, the Ti64 particles melted and were nitrided, but the nitrogen concentration in the melt was less than that in the melt developed on the surface without a preplaced layer. An insufficient concentration together with a high content of silicon and carbon in the liquid, resulted in a non-dendritic nitride layer formed in the top region of the melt.

Fig.3 shows the microstructure developed in the surface preplaced with ZrC powders. Large particles of ZrC (5-8 in the transverse section of the melt pool) remained after laser nitriding. The mean size of the particles of ZrC preplaced on the surface is 45 μ m. The size of the ZrC particle shown in Fig.3 is about 55 μ m, and no smaller ZrC particles were observed in the melt after the laser nitriding. This is in good agreement with our previous work [8] and indicates that a large size is required for the preplaced particle to remain undissolved after nitriding. The size required for the particle to remain undissolved also depends on the processing conditions. This can be seen clearly by comparing Fig.4 with Fig.5.

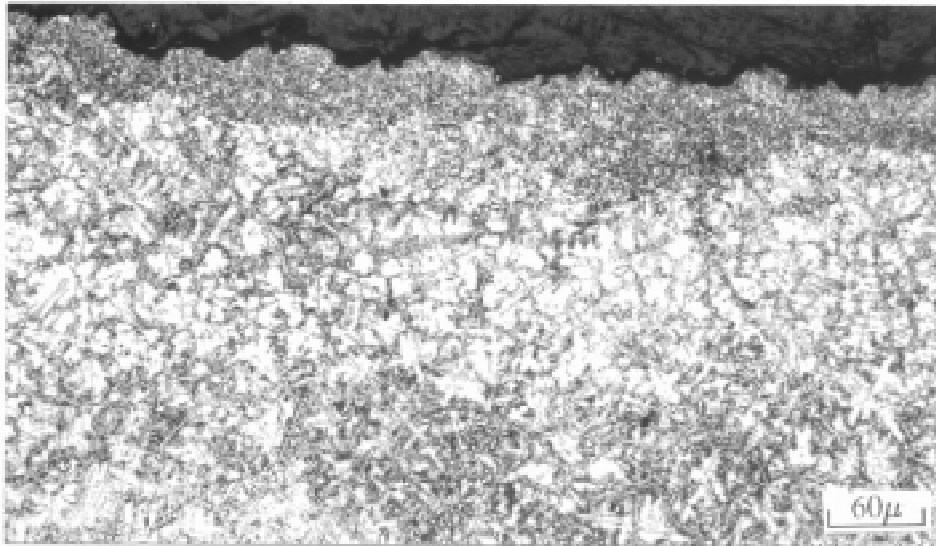


Fig.2 The microstructure developed in the 4 mm thick specimen preplaced with a mixture of SiC and Ti64 powders and laser treated at 2.8 kW, 5 mms⁻¹.

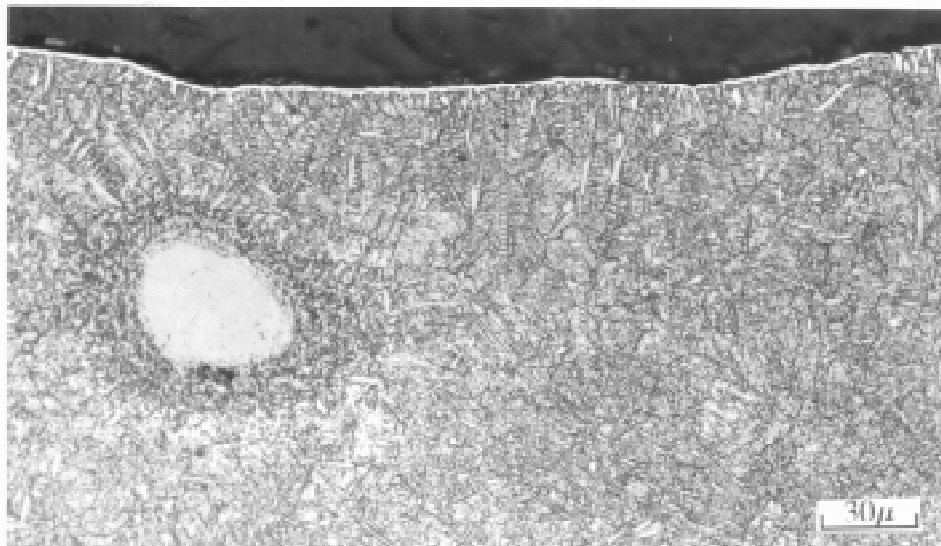


Fig.3 The microstructure developed in the 4 mm thick specimen preplaced with ZrC powder and laser treated at 2.8 kW, 5 mms⁻¹.

Both Figs.4 and 5 show the microstructures developed in the ZrN preplaced specimens but laser processed under different conditions. When a low specimen velocity was used, which gave a high laser energy density, no particles of ZrN remained in the melt, as shown in Fig.4. With a higher specimen velocity, the extent of the dissolution of these ZrN particles decreased, and some of the ZrN particles remained, but at a reduced size. This is shown in

Fig.5. Also it is seen in Fig.5 that the titanium nitrides near to the undissolved ZrN particles grew radially. This suggests that a nitrogen concentration gradient developed locally around the undissolved ZrN particles. A significant difference shown in Figs.4 and 5 from the previous figures is that a high concentration of titanium nitrides formed in the melts developed in the surfaces preplaced with ZrN particles. This must be attributed to a higher nitrogen concentration in the melt due to the dissolution of the ZrN particles. Typical titanium nitrides were observed in these two specimens as a thin continuous TiN (or more possibly $\text{TiN}_{0.8}$ [9]) layer formed at the top of the melt, and dendritic TiN grew from the continuous layer in a nearly perpendicular direction to the surface. It is interesting to note that at the top left corner of Fig.4, two continuous TiN layers formed in the melt which are likely to be branches from the original one. This is because the liquid melted in other areas was moved by the convective flow and filled the previously nitrated surface, due to the effect of overlapping of a spinning laser trace on the surface. Different sizes of $\text{TiN}_{0.3}$ needles (N) below the region of TiN (T) can be clearly seen in Figs.4 and 5.

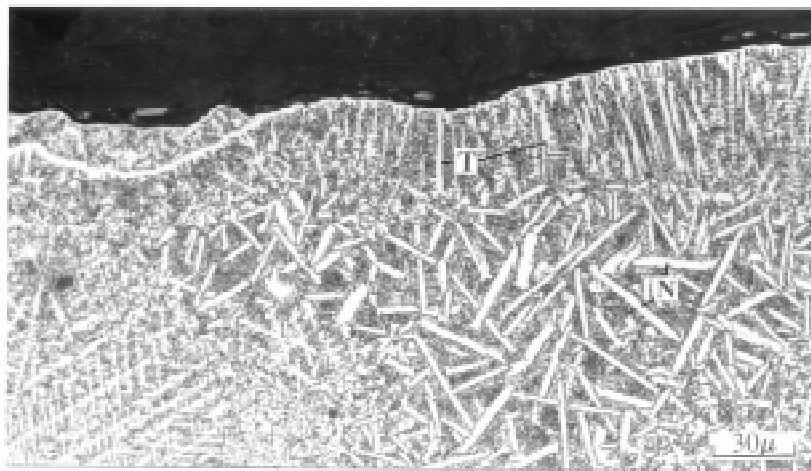


Fig 4 The microstructure developed in the 4 mm thick specimen preplaced with ZrN powder and laser treated at 2.8 kW, 5 mm s^{-1} .



Fig 5 The microstructure developed in the 4 mm thick specimen preplaced with ZrN powder and laser treated at 2.8 kW, 10 mm s^{-1} .

Cracking Tendency

No cracking was observed in the 4 mm thick specimens, but cracks did occur in all the 17 mm thick specimens. This indicates that the thickness of the specimen has a significant influence

on the tendency to cracking. When the same laser processing conditions were used, a thicker specimen absorbed a smaller energy per unit volume and resulted in a higher cooling rate during the solidification of the melt. The effect of the thickness of the specimen on the cracking in the present work is in good agreement with our previous work on laser gas nitriding of Ti64 alloy [10], where a thick specimen (18 mm) was observed to have a high tendency to cracking.

The cracking tendency in the specimens preplaced with different types of powders can be seen from the 10 mm thick specimens. No cracking was observed except in the ZrN preplaced specimens. This is shown in Fig.6. Obviously, the high cracking tendency in the ZrN preplaced specimens could be related to the high concentration of titanium nitrides formed in the melt. In other words, no matter whether the nitrogen content is introduced into the melt by gas nitriding or by preplacement of the powders containing nitrogen, a high concentration of nitrides formed in the melt resulted in a high tendency to cracking. Therefore, one or both of the followings reduced the tendency to cracking in the specimens preplaced with other powders. Firstly, the compounds formed in the specimens preplaced with non-N-containing powders are less brittle, and secondly the compounds have a lower melting point than the titanium nitrides, and reduced the temperature range over which the development of residual stresses during the solidification of the melt occurred. However, a further analysis of the phases formed in the melts is required before this conclusion can be verified.

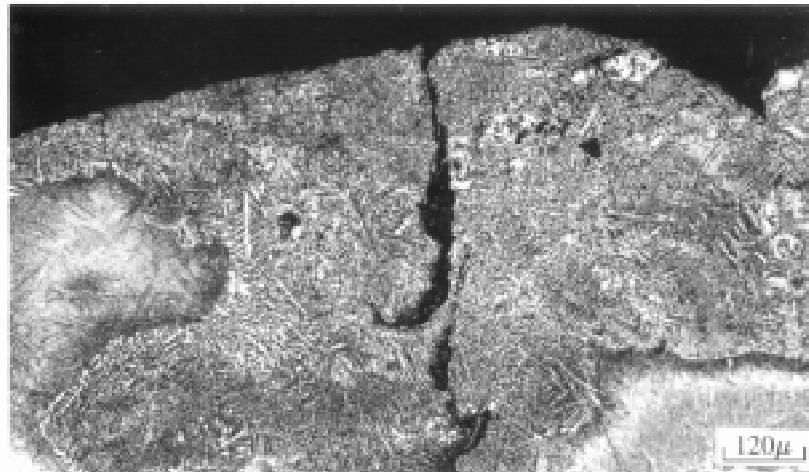


Fig.6 The microstructure developed in the 10 mm thick specimen preplaced with ZrN powder and laser treated at 2.8 kW, 10 mm^s⁻¹.

Melt Pool

There was no significant difference between the melt depths developed in the specimens preplaced with different powders. This is true even in the specimen preplaced with ZrN powder, in which a high concentration of titanium nitrides formed in the melt is considered to release a larger amount of heat than in the other specimens and therefore to develop a deeper melt. This may be explained by the fact that the heat of formation of the ZrN is -82.2 kcal/gmol, and that of TiN -73 kcal/gmol [11], and therefore the amount of heat released from the formation of TiN was only just sufficient to compensate that spent on the dissolution of ZrN when the same content of nitrogen in the preplaced powder is assumed.

Both the laser processing conditions and the thickness of the specimen have an influence on the melt depth. This is shown in Fig.7 for the SiC preplaced specimens of thickness 4, 10 and 17 mm at speeds 5, 10 and 15 mms^{-1} . The deepest position in the centre of the melt pool was measured for Fig.7. It can be seen that the thicker the specimen, the shallower the melt when the specimen speed is constant, and that the lower the speed, the deeper the melt pool for a given specimen. The relation between the specimen speed and the melt depth is linear. The influence of the specimen thickness is less significant when the thickness is greater than 10 mm. This is because when the specimen thickness is above a certain value, the specimen can be considered as a semi-infinite plate with respect to the heat flow developed by the laser beam. Therefore, melt pools developed in a semi-infinite plate under the same laser processing conditions are of constant depth.

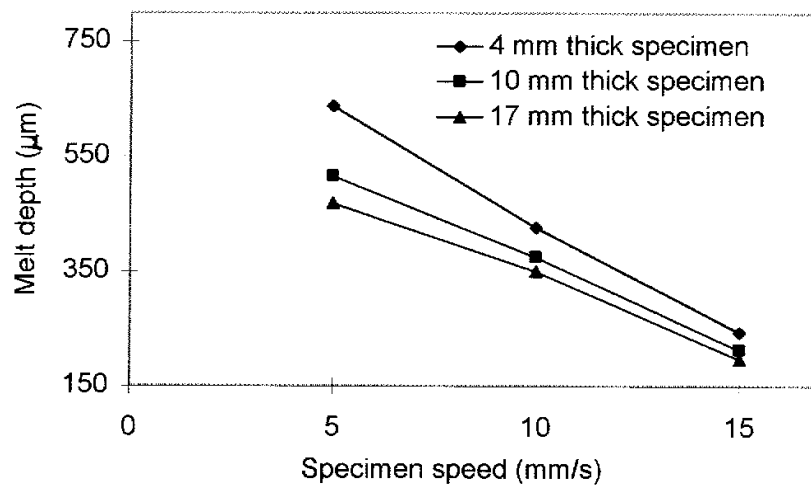


Fig.7 The relations between the melt depth, the specimen speed and thickness.

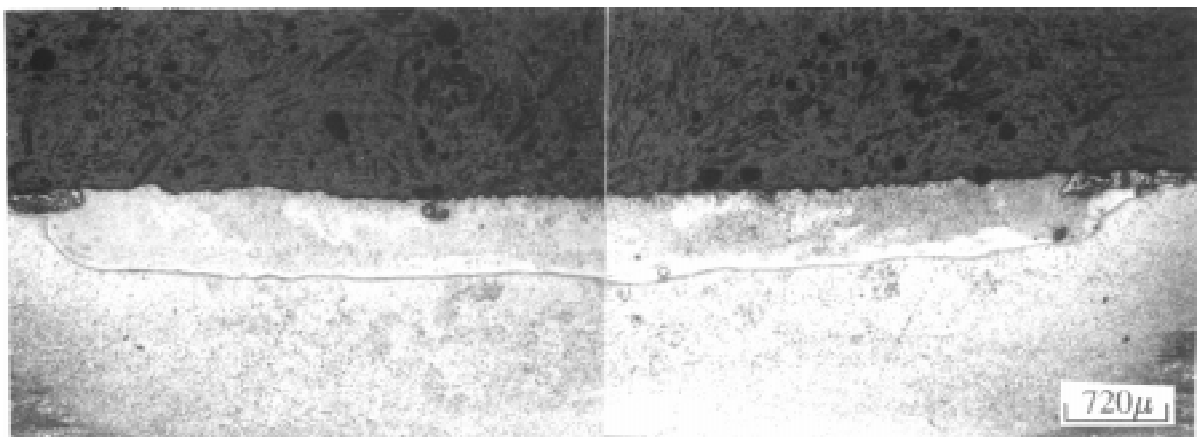


Fig.8 A uniformly thick smooth surface MMC layer produced in the 4 mm thick specimen preplaced with a mixture of SiC and Ti64 powders and laser treated at 2.8 kW, 5 mms^{-1} .

The profile of the melt pool can be controlled by laser processing conditions. Under specific processing conditions, a uniformly thick smooth surface MMC was produced. Fig.8 shows a melt pool developed on the specimen preplaced with a mixture of SiC and Ti64 powders. It was reported in our previous work [12] that the melt pool profile was affected not only by the laser processing conditions, but also by the laser modes (the shape and the energy distribution

of the beam), and that a spinning beam was the only mode possible to produce a uniformly deep melt layer in comparison with a stationary Gaussian or annular beam. Fig.8 shows a good agreement with our previous work.

Microhardness

Fig.9 shows a group of the hardness profiles measured in the melt pools developed in the 5 mm thick specimens, which were given as a function of the depth below the surface. The SiC preplaced specimen has a hardness of 1200 HV at the top of the surface and then the hardness decreases sharply with the depth below the surface until a value of 600HV was achieved at depth of 200 μm. The hardness continues to decrease with melt depth but at a relative low rate until a nearly constant value 450-500 HV at the bottom of the melt. Both the hardness in the SiC+Ti64 preplaced specimen and that in the ZrN preplaced specimen reached a value over 700 HV. The ZrC preplaced specimen shows the lowest hardness. This is due to the fact that some large ZrC particles remained in the specimen and the hardness was measured only in the matrix with a micro-hardness tester. In other words, if a hardness tester with a 10 kg load had been used for the measurement of the same bulk material, the hardness in the melt of the ZrC preplaced specimen might have shown a higher hardness than that shown in Fig.9.

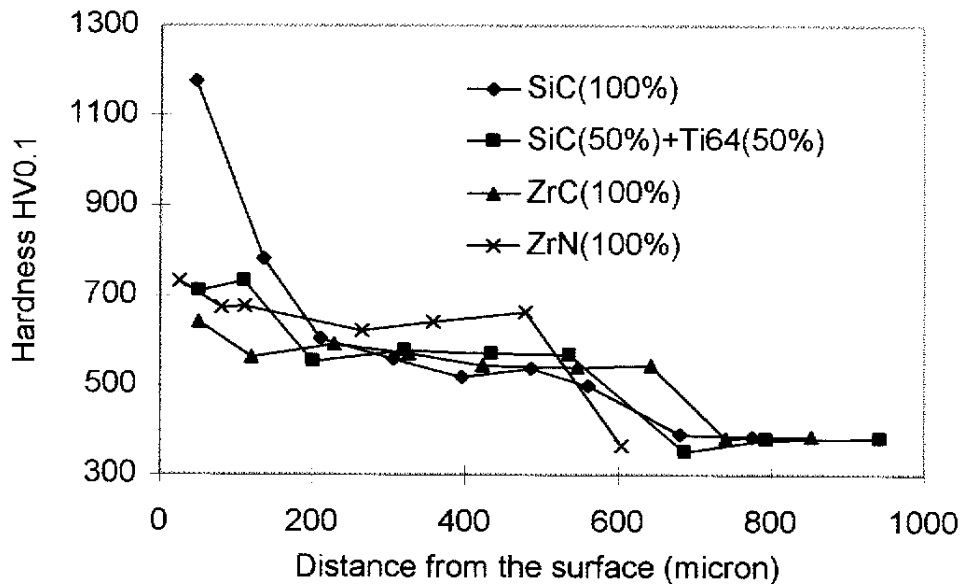


Fig.9 The hardness profiles of the surface layers developed in the 4 mm thick specimens.

Abrasive Wear Testing Results

The abrasive wear testing results are shown in Fig.10. A typical wear testing graph of the processed specimens consists of two periods of wearing: the wear in the surface layer and that in the base alloy after the surface layer was worn away. The wear graph of the base alloy is also presented in Fig.10 for comparison. All the laser processed specimens show a significant improvement in wear resistance in the surface layer, compared with that of the base alloy. As soon as the surface layer was worn away, the processed specimens had the same wear rate as that of the base alloy. A close relation between the hardness and the wear resistance can be clearly seen by comparing Fig.9 with Fig.10, i.e. the higher the hardness of the melt, the better the wear resistance. The specimen preplaced with SiC powder has the highest wear resistance. Therefore, to obtain a high wear resistant surface, a high hardness in a deep surface layer is

required with the harder phase being strongly bonded to the matrix. The undissolved ZrC and ZrN particles may have been detached and accelerated the wear rate by a three body wear mechanism.

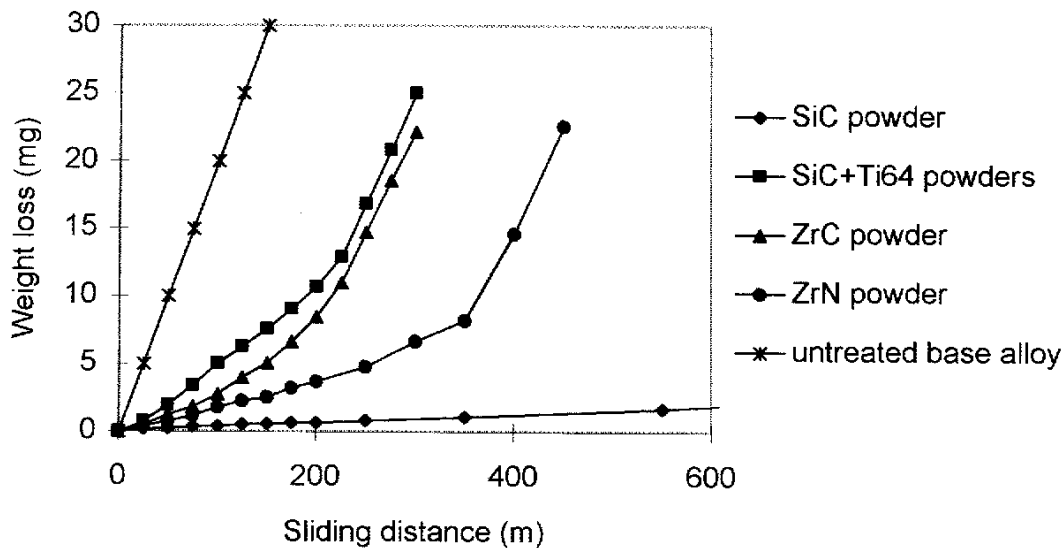


Fig.10 The wear testing results for the base alloy and the 4 mm thick processed specimens.

CONCLUSIONS

1. A process of combining CO₂ laser powder alloying and nitriding was investigated in the present work to produce a crack-free high wear resistant surface of Ti64 alloy. Four types of powders (SiC, SiC+Ti64, ZrC and ZrN) were chosen in this investigation.
2. The surface preplaced with ZrN powder after laser nitriding has a higher tendency to cracking than the surfaces preplaced with other three powders. This is because the nitrogen content in the ZrN powder increased the volume of the titanium nitrides formed in the melt which is a cause of the cracking.
3. The thickness of the specimen has a significant influence on the tendency to cracking. The thicker the specimen, the greater the tendency to cracking when all the other conditions are constant.
4. The specimen preplaced with SiC powder achieved the highest hardness (1200 HV) of the four specimens. This suggests that the surface hardness can be controlled by the quantity of the SiC powder in a mixture of powders of SiC and the base alloy.
5. The abrasive wear testing showed that the higher the hardness of the surface, the higher the wear resistance, when the hard phase was well bonded to the matrix.

ACKNOWLEDGEMENTS

The authors of this paper gratefully acknowledge a financial support from EPSRC, UK and an ORS grant for Mr H. Xin. Thanks are due to Dr J. Fieret and Mr R. Heath for their assistance with the operation of the laser.

REFERENCES

1. Walker, A., Folkes, J., Steen, W.M. and West, D.R.F., "Laser Surface Alloying of Titanium Substrates with Carbon and Nitrogen", *J. Surf. Eng.*, vol. 1, 1985, pp. 23-29.
2. Morton, P.H., Bell, T., Weisheit, A., Kroll, J., Mordike, B.L. and Sagoo, K., "Laser Gas Nitriding of Titanium and Titanium Alloys", *Surface Modification Technologies 5*, Sudarshan, T. S. and Braza, J. F., The Institute of Materials, 1992, pp. 593-609.
3. Mridha, S. and Baker, T.N., "Crack Free Hard Surface Produced by Laser Nitriding of Commercial Purity Titanium", *Mater. Sci. Eng.*, vol. A188, 1994, pp. 229-239.
4. Kloosterman, A.B. and Hosson, J.Th.M. De., "Microstructural Characterization of Laser Nitrided Titanium", *Scripta Metallurgica et Materialia*, vol. 33, 1995, pp. 567-573.
5. Hu, C., Mridha, S., Ubhi, H.S., Bowen, A.W. and Baker, T.N., "Hardness, Dendrite Population and Microstructure under Different Environments in the Laser Nitrided Ti-6Al-4V Alloy", *Titanium '95: Science and the Technology*, Blenkinsop, P.A., Evans, W.J., and Flower, H.M., The Institute of Materials, London, UK, vol. 3, 1996, pp. 2835-2842.
6. Bell, T., Bergmann, H.W., Lanagan, J., Morton, P.H. and Staines, A.M., "Surface Engineering of Titanium with Nitrogen", *J. Surf. Eng.* vol. 2, 1986, pp. 133-143.
7. Mridha, S. and Baker, T.N., "Surface Cracking in Laser-Nitrided Titanium of Commercial Purity and Possible ways of Reducing These Defects", *Proc. Ad. Mater.*, vol. 4, 1994, pp. 85-94.
8. Mridha, S., Hu, C., Ubhi, H.S., Holdway, P., Bowen, A.W. and Baker, T.N., "Characteristic Features of the MMC Layer Formed on Ti-6Al-4V (IMI318) Alloy Surface through Laser Treatment by Using SiC Powder Injection and Preplacement Techniques", *Titanium '95: Science and the Technology*, Blenkinsop, P.A., Evans, W.J. and Flower, H.M., The Institute of Materials, London, UK, Vol. 3, 1996, pp. 1959-1966.
9. Hu, C., Xin, H., Watson, L. M. and Baker, T.N., "Analysis of the Phases Developed in Laser Nitriding Ti64 Alloys", *Acta. Metall. Mater.*, submitted for publication.
10. Hu, C. and Baker, T. N., "Overlapping Laser Tracks to Produce a Continuous Nitrided Layer in Ti-6Al-4V Alloy", *J. Mater. Sci.*, submitted for publication.
11. R.C. Weast and M.J. Astle (eds), *Handbook of Chemistry and Physics (61th edition)*, CRC Press, Florida, USA, 1980.
12. Hu, C. and Baker, T.N., "Influence of the Beam Mode in Laser Processing to Create a Surface Ti-SiC_p MMC", *Proceedings of 5th International Conference on Improvement of Materials*, Liu, J., MATEC, Paris-Marne La Vallee, 1996, pp. 167-176.

GRAPHITE REINFORCED NONEQUILIBRIUM AL-MO METAL MATRIX COMPOSITES

Barbara A. Shaw ¹, William C. Moshier ², Robert G. Wendt ³

¹ *Department of Engineering Science and Mechanics, The Pennsylvania State University,
211 Hallowell Bldg., University Park, PA 16802, USA*

² *Global Solar Energy Incorporated, 12401 West 49th Avenue, Wheat Ridge, CO 80033, USA*

³ *Bettis Atomic Power Lab, PO Box 79, West Mifflin, PA 15122, USA*

SUMMARY: Poor corrosion resistance, fiber/matrix reaction-induced embrittlement, excessive thermal/strain hysteresis, and restricted processing capabilities are problems associated with graphite/aluminum MMCs. To alleviate these problems, this research investigated nonequilibrium alloying by sputter disposition.

Binary nonequilibrium Al-Cr, Al-Mo, Al-Ta, and Al-W alloys were successfully fabricated and evaluated. All Al-based alloys exhibited improved corrosion resistance over pure Al; Al-W and Al-Mo alloys showed marked increased resistance to pitting and galvanic corrosion.

An Al-17Mo alloy with pure Al surface foils and interlayers was chosen for processing into a composite. The best hot-pressed composites contained void contents exceeding 9% and processing damage of the Al surface foils exposed graphite fibers. SEM analysis of the pitted composite after anodic polarization in 0.1M NaCl revealed that diffusion bonding of the alloy coated fibers was not achieved; moreover, the alloy coating on the graphite fibers was apparently unchanged during diffusion bonding or polarization. The lack of diffusion bonding was disappointing, but the fact that the alloy coated fibers underwent no discernible degradation after polarization was very promising. An alternative consolidation approach, such as hot isostatic pressing without surface foils or using Al-Mo surface foils, could result in a fully consolidated, corrosion resistant composite.

KEYWORDS: graphite-reinforced metal matrix composites, nonequilibrium Al alloys, Al-based metal matrix composites, corrosion resistant composites

INTRODUCTION

Metal matrix composites (MMCs) have been intensively studied over the past thirty years due to their unique combination of stiffness and thermal stability. During this period, there have been many proposals to develop matrix alloys that are compatible with the reinforcing phase. However, for one reason or another, the technology has continued to focus on conventional alloys and fabrication practices. Although there have been tremendous advances in the field of composite materials, the basic technology remains similar to systems studied twenty years ago. This work represents the first program where new alloys are being developed for graphite reinforced composites that are tailored to a novel processing technology for manufacturing corrosion resistant graphite reinforced composites.

Graphite fiber reinforced aluminum metal matrix composites are susceptible to rapid

corrosion especially in chloride environments [1-16], which has, in part, limited the use of these materials in aircraft, spacecraft, and naval applications. Attempts have been made to improve the corrosion resistance of graphite/aluminum composites through the use of coatings or some other form of electrical isolation between the fiber and matrix [4,5,7,9], cathodic protection, or cathodic inhibitors [3,13]. However, each of these protection techniques often adversely affects composite properties and in the long term only delays pitting and subsequent galvanic interaction between the matrix and fiber. In addition, none of these corrosion prevention processes address the real problem -- poor corrosion resistance of the aluminum matrix, especially when coupled to graphite fibers in a chloride-containing environment. In this program, the approach was to develop a corrosion resistant matrix alloy more electrochemically compatible with graphite than pure Al or commercially available Al alloys.

One study of the corrosion of graphite/aluminum MMCs reported that these composites corroded at rates up to fifteen times greater than monolithic aluminum alloys in a sodium chloride (NaCl) electrolyte at room temperature [13]. Corrosion of conventionally processed graphite/aluminum composites is a result of pitting of the face sheet foils. Once these foils have been penetrated, corrosion is accelerated by the following mechanisms [4,5,13-16]:

- Residual microstructural chlorides within the composite at precursor wire interfaces increase and lead to rapid internal composite corrosion, and
- Exposure of the graphite fibers creates a galvanic couple with the aluminum matrix leading to rapid matrix dissolution.

One of the key problems leading to rapid corrosion of graphite/aluminum composites stems from the current state-of-the-art (SOA) manufacturing of graphite/aluminum MMCs, which introduces residual microstructural chlorides during the liquid metal infiltration (LMI) process [13,17-21].

A new process has been developed, and is in commercial practice, that does not rely on the titanium diboride coating or the cast aluminum matrix [21,22]. In this process, the matrix alloy is deposited onto each individual fiber by a physical vapor deposition (PVD) method such as sputtering. The very nature of the PVD process allows virtually any matrix alloy to be deposited on the graphite fibers.

Using the PVD approach, composite processing involves the following steps:

- Deposit metal alloy onto fibers using automated magnetron sputtering (a process developed at Naval Research Laboratory and now in commercial practice).
- Configure the flexible graphite fibers by automated processes such as filament winding, braiding, or weaving.
- Consolidate the composite by low temperature diffusion bonding or hot isostatic pressing (HIPing).

Sputtering of metal alloys onto graphite fibers has several potential advantages over the current liquid metal infiltration process used to fabricate graphite/aluminum composites. The three most significant advantages of the physical vapor deposition method of fabricating graphite/aluminum composites are that it eliminates unwanted reactions at the fiber/matrix interface [23-30], it minimizes thermal strain hysteresis [21], and sputter coated graphite fibers provide near-net shape processing capability.

EXPERIMENTAL DETAILS

Non-equilibrium Al-Mo, Al-W, Al-Cr, and Al-Ta alloys for the initial phases of the investigation were prepared by co-sputtering the two elements onto silicon single crystal wafers using a Denton Vacuum 602RS Loadlock Thin Film Deposition System. For the final phase of the investigation, a nonequilibrium Al-17 atomic % (a/o%) Mo alloy was deposited onto graphite fibers using a proprietary process developed at Cordec Incorporated. The temperature of the substrates was not controlled during deposition for either of the substrates.

Compositional analysis of the alloys was conducted using the inductively coupled plasma (ICP) technique. Alloy compositions reported in this paper as Al-xxMo correspond to Al alloys with a Mo concentration, in atomic percent, of xx percent. X-ray diffraction (XRD) of each alloy film was conducted to determine: 1) whether the solute was in solid solution in the aluminum, and 2) whether precipitation occurred after heat treating. In the initial phases of the research, the alloy coated Si wafers were heat treated at 400, 500 and 600° C for times of one, two and eight hours to assess stability of the alloys at anticipated processing temperatures.

In the initial phases of the research, anodic polarization experiments were conducted to assess the corrosion resistance of each of the alloys in chloride-containing environments (typically 0.1M NaCl) before and after heat treatment. Corrosion testing during the initial phases of the investigation also included galvanic corrosion experiments. In these experiments, the alloy coated Si substrates were coupled to graphite-fiber specimens in 0.1M NaCl solutions and the galvanic corrosion current was monitored as a function of time. Later phases of the research involved anodic polarization testing of single alloy coated fibers and consolidated composites in chloride solutions. In all of the anodic potentiodynamic polarization experiments, the alloys were allowed to stabilize for at least one hour prior to scanning the potential at a rate of 0.2 mV/s, or lower. Areas not to be tested on electrochemical specimens were masked with a room temperature curing marine epoxy paint. All electrochemical tests were conducted under ambient lab conditions in cells open to the atmosphere and potentials were measured versus a saturated calomel electrode (SCE).

RESULTS

Alloy Development Studies

In comparison to pure Al and commercial Al alloys, all of the alloys investigated in this study exhibited enhanced corrosion resistance. Figure 1 shows a comparison of representative anodic polarization curves for four of the alloys produced in this study to that of pure Al. The largest passive regions were noted for the Al-W and Al-Mo alloys. X-ray diffraction of as-deposited Al-Mo, Al-W, Al-Cr and Al-Ta alloy films revealed that the solute in all of the alloys was in solid solution with the Al (i.e., no precipitates were found). After heat treatment at 400° C only the Al-Mo and Al-W alloys remained precipitate free. The lack of precipitation in the Al-Mo and Al-W alloy systems, especially at the higher solute concentrations despite the high driving force for precipitation, was believed to be a result of the amorphous nature of these alloys. This early segment of the investigation clearly showed that the Al-W and the Al-Mo alloy systems provided the best combination of corrosion resistance and thermal stability at anticipated processing temperatures.

Since one of the possible applications for MMCs made with these nonequilibrium alloys is aerospace structures, alloy density was an important parameter in selecting the best alloy for use in subsequent phases of the investigation. Because of their combination of corrosion

resistance, thermal stability, and density, the Al-Mo alloy system was selected for further evaluation and optimization. The following are important factors in determining the optimal Al-Mo alloy composition: lack of precipitates and the presence of a nanocrystalline/amorphous structure for the alloy after heat treatment at anticipated consolidation temperatures; extent of the passive region in alloy anodic polarization curve; galvanic compatibility of the alloy with graphite; corrosion resistance of the alloy after heat treatment at anticipated consolidation temperatures; and alloy density.

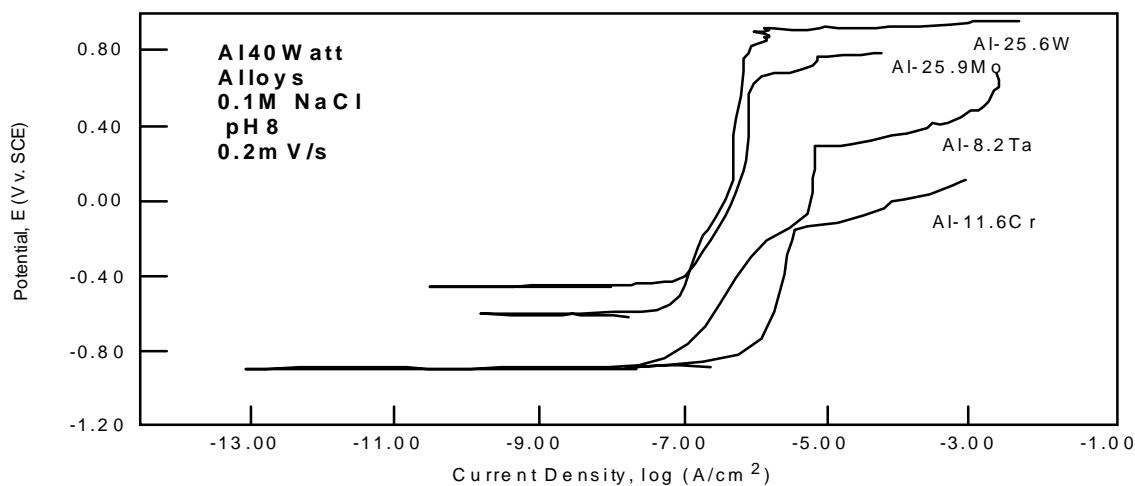


Fig. 1: Comparison of the anodic polarization behavior for the highest solute concentration Al nonequilibrium alloys in 0.1M NaCl under quiescent conditions.

X-ray Diffraction Studies

X-ray diffraction was conducted on both the as-sputtered and heat treated Al-Mo alloys to determine whether the Mo: 1) was in solid solution with the Al and readily available for enhancing corrosion resistance, or 2) had reacted with the Al to form Al_xMo_y precipitates. The as-deposited alloys showed no signs of precipitation. X-ray diffraction results for the heat-treated alloys are presented in Table 1. At the two higher Mo concentrations, the Al-Mo alloys exhibited no precipitates and a nanocrystalline/amorphous structure when heat treated at 400° C. Again, the lack of precipitation at the higher solute concentrations, despite the higher driving force for precipitation, was believed to be a result of the amorphous structure of the alloys.

Corrosion Evaluation

As Figure 1 revealed, the Al-Mo alloys exhibited significant passivity. This passivity was maintained in a variety of different chloride solutions over a wide range of pH and after galvanic coupling to either graphite, SiC, or TiB₂. A galvanic diagram for the Al-18Mo alloy coupled to various reinforcing materials in a variety of different chloride solutions is presented in Figure 2. This figure reveals that galvanic corrosion is controlled by the anodic metal dissolution reaction for the alloy rather than by the reduction of oxygen on the reinforcement material. Since the Al-18Mo alloy is passive in the crossover region for the two curves, low galvanic corrosion rates are predicted when this alloy is coupled to graphite. Current measurements in actual galvanic couple experiments, Figure 3, confirmed the galvanic diagram prediction and showed that low galvanic currents were also obtained after heat treatment of the alloy.

Table 1: Summary of Al-Mo Alloy structure as a function of heat treatment time and temperature

		Heat Treatment Temperature		
		400°C	500°C	600°C
Heat Treatment Time (h)	1	Al-11Mo, ppt Al-18Mo, Amorphous Al-23Mo, Amorphous	Al-11Mo, ppt Al-18Mo, ppt Al-23Mo, Amorphous	Al-11Mo, ppt Al-18Mo, ppt Al-23Mo, Amorphous
	2	Al-11Mo, ppt Al-18Mo, Amorphous Al-23Mo, Amorphous	Al-11Mo, ppt Al-18Mo, ppt Al-23Mo, Amorphous	Al-11Mo, ppt Al-18Mo, ppt Al-23Mo, Amorphous
	8	Al-11Mo, ppt Al-18Mo, Amorphous Al-23Mo, Amorphous	Al-11Mo, ppt Al-18Mo, ppt Al-23Mo, Amorphous	Al-11Mo, ppt Al-18Mo, ppt Al-23Mo, ppt

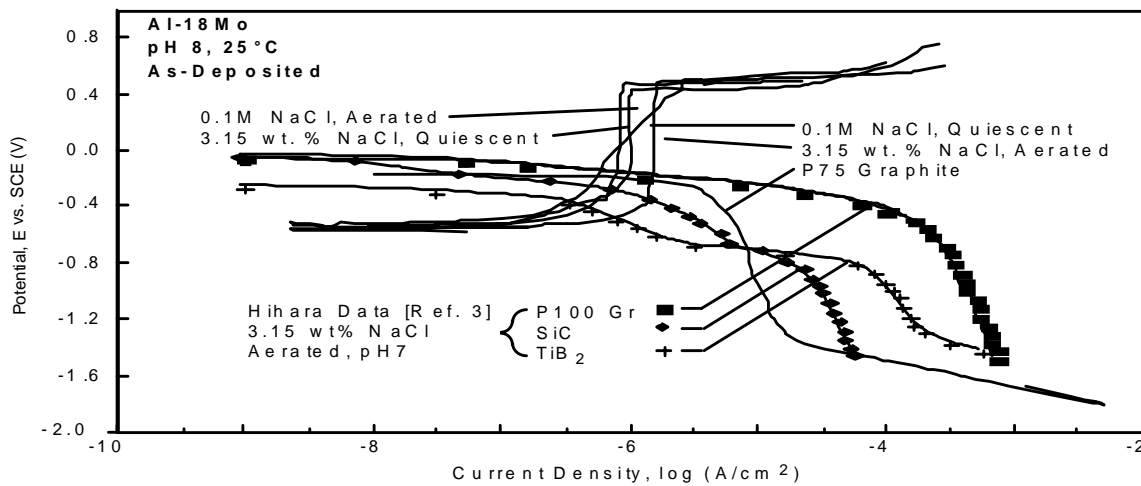


Fig. 2: Galvanic diagram created by overlaying the anodic polarization data for the Al-18 Mo alloy tested in quiescent 0.1M and 0.55M NaCl on the cathodic curves for P75 graphite, P100 graphite, SiC, and TiB₂. Cathodic data for P100 graphite, SiC and TiB₂ after Hihara and Latanision (16).

Coated Fiber Evaluation

Al with a Mo concentration greater than 11a/o Mo and less than, or equal to, 18 a/o Mo was targeted as the optimum alloy composition because these alloys showed promise for consolidation, they retained their enhanced corrosion resistance after heat treatment, and they minimized the impact of higher Mo concentrations on alloy density. Several fiber coating trials were conducted at Cordec Incorporated using a commercial in-line sputtering system designed for rapid deposition of alloys onto graphite fibers. Targets for this system were fabricated by inserting 99.9 % pure Mo plugs into 99.99 % pure Al plates. Alloy composition was controlled by modifying the area ratio of the Mo and Al. Both hollow cathode and planar cathode sputter deposition processes were investigated for depositing the Al-Mo alloy onto the graphite fibers. The hollow cathode process for applying the alloy resulted in uniform coating of the fibers; however, the Mo concentrations in the coatings were low and curling of the fibers made handling difficult. The planar cathode process resulted in

slightly less uniform coating of the fibers, but an Al-17Mo coating was easily produced and fibers coated with this process were easy to handle. A micrograph one of the fibers coated using the planar cathode process is presented in Figure 4.

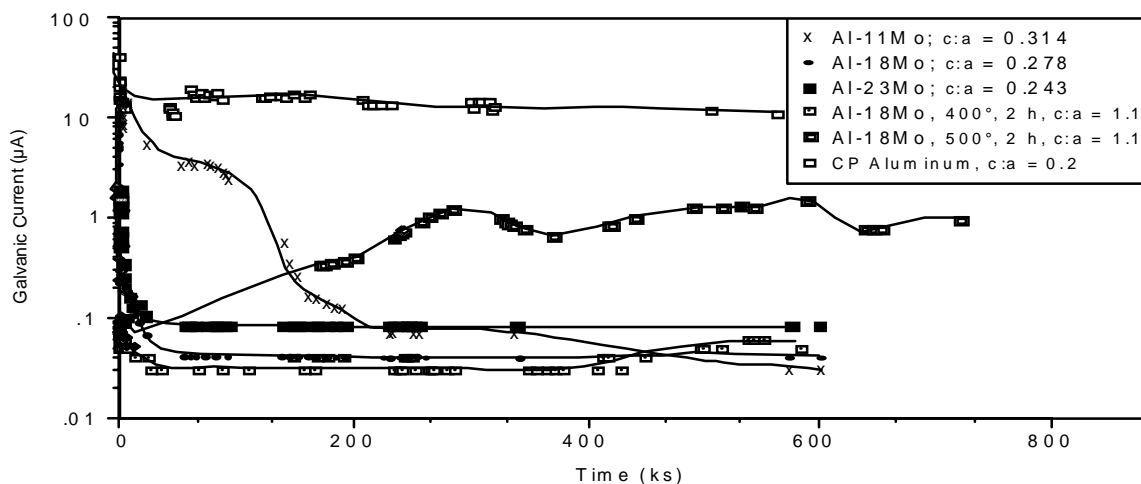


Fig. 3: Galvanic Current as a function of time for commercially pure Al and Al-18 Mo Alloys (as-deposited and heat treated) coupled to P75 graphite fibers in quiescent 0.1M NaCl, (at a pH of 8 and a temperature of 25° C). (Since the anodic area was 1 cm² the galvanic current equals the galvanic current density.)

Anodic polarization of a single coated fiber revealed a pitting potential of approximately -250 mV vs. SCE resulting in a passive range about half the size of the one obtained for the Al-18a/o Mo when it was deposited onto a Si substrate using the laboratory deposition system. The difference in polarization behavior was attributed to the columnar morphology of the Cordec Al-Mo deposit. While the polarization behavior of the single coated fibers was not nearly as good as the behavior of the alloy deposited onto Si, it was thought that this modest enhancement in corrosion resistance would be adequate enough and that consolidation of the alloy might result in further densification of the coating.

Composite Consolidation and Testing

Consolidation trials (via hot pressing) were conducted on the Al-17Mo alloy coated fibers at both Martin Marietta and Cordec Incorporated. For each consolidation trial, the preforms were created by unidirectional orientation of the coated fibers between Al interlayers and Al surface foils. The best consolidation was achieved on the Cordec specimen hot pressed at 550° C at a pressure of 8 ksi for 240 minutes.

Metallographic examination of the best Cordec composite revealed the presence of approximately 9 volume percent porosity and exposed graphite fibers at the composite surface. X-ray diffraction of the consolidated composite revealed the presence of precipitates. While the presence of precipitates was undesirable, it was not surprising in light of the higher than anticipated temperature needed for consolidation.

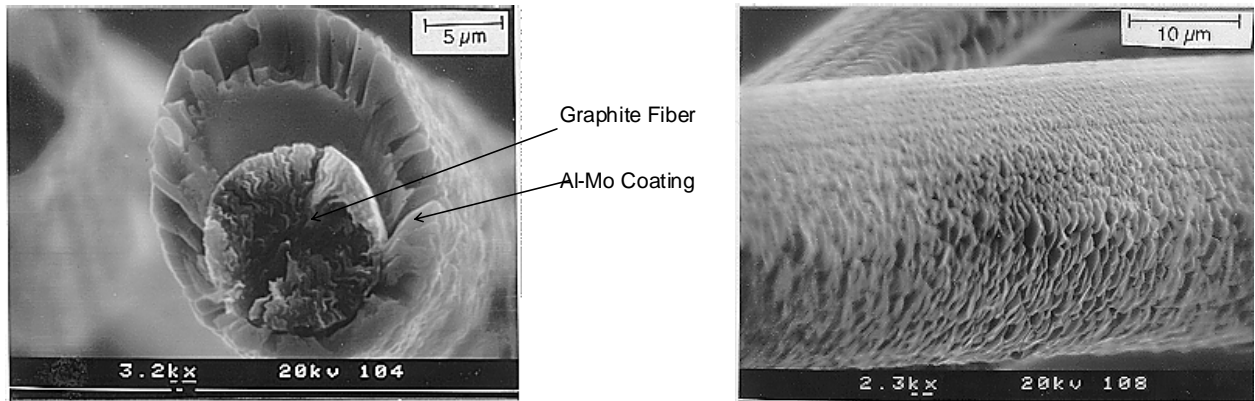


Fig. 4: Cross section of an Al-17 a/o Mo Alloy-Coated Graphite Fiber. The fiber was produced using a planar cathode sputtering system at Cordec Incorporated.

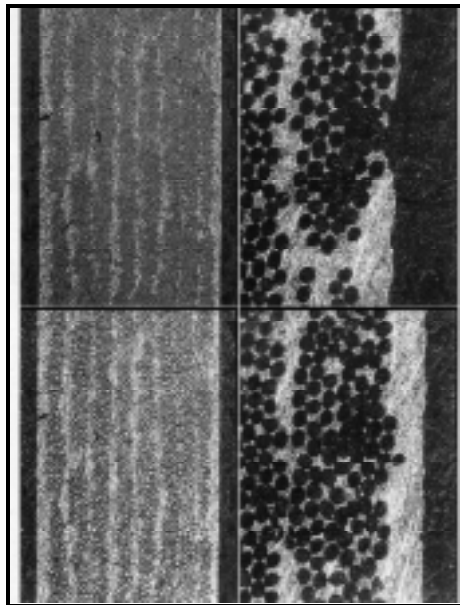


Fig. 5: Representative cross-sectional microstructures of corrosion resistant Al-14Mo/P120 Gr fiber composite.

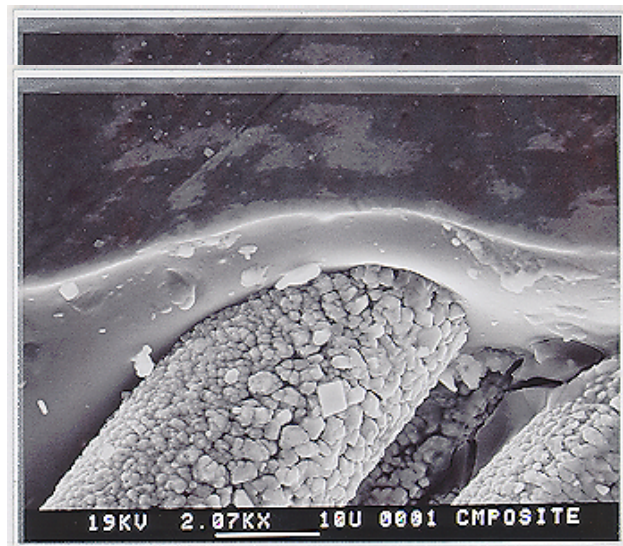


Fig. 6: SEM micrograph of composite after polarization in 0.1M NaCl revealing lack of consolidation of coated fibers

Anodic polarization experiments were conducted on the composite panels that were considered to have consolidated relatively well. Unfortunately, none of the polarization curves generated on the composite specimens in chloride-containing environments showed evidence of passive behavior. The poor anodic polarization performance of the alloy was not unexpected considering that the composite contained galvanic couples between pure Al, the Al-17Mo alloy, and the graphite fibers. In addition, SEM inspection of the composite after corrosion testing, Figure 6, clearly revealed that diffusion bonding of the coated fibers was far from complete. In fact, the alloy coating on the fiber surfaces appeared to have undergone little or no change during either the diffusion bonding process or potentiodynamic polarization.

SUMMARY

This research has clearly revealed that nonequilibrium Al-Mo, Al-W, Al-Ta, Al-Cr alloys exhibit significantly enhanced resistance to corrosion when compared to pure Al or any commercial aluminum alloy. For two of the alloys investigated in this program (the intermediate solute concentration Al-Mo and Al-W alloys) this significantly enhanced corrosion resistance was maintained at nominal composite consolidation temperatures (400°C). In addition to anodic potentiodynamic polarization testing, the enhanced corrosion resistance of these alloys was confirmed in long-term galvanic coupling experiments. Precipitation reactions in the intermediate solute concentration Al-Mo and Al-W alloys were retarded as a result of the nanocrystalline /amorphous nature of these sputter deposited alloys.

Commercial deposition of an Al-17Mo alloy on P120 graphite fibers yielded a very columnar deposit that maintained a degree of flexibility similar to that of the uncoated fibers. The breakdown potential for the Al-17Mo coated fiber was several hundred millivolts greater than that of pure Al (or any commercial Al alloy), but it was also several hundred millivolts less than that of the Al-18Mo alloy sputtered on planar substrates using a laboratory scale system at Martin Marietta. This difference in performance between the alloy deposited by Cordec on graphite fibers and the alloy deposited by Martin Marietta on planar substrates was a result of the morphology differences between the two deposits. The alloy film produced at Martin Marietta was smooth and dense; whereas, the Cordec deposit was rough and columnar. Rough columnar deposits, such as the one illustrated in Figure 4 for the Al-17Mo alloy on the P120 graphite fibers, have been shown to significantly degrade localized corrosion resistance [31]. Fortunately, the morphology of the deposit can be changed by optimizing the sputtering conditions. In this research, optimization of the sputtering process was not conducted because of the limited budget and because it was hoped that hot pressing would densify the alloy.

Consolidation of the alloy via hot pressing proved to be a more difficult task than anticipated. As a result of the relatively high melting temperature of the alloy (715° C), consolidation was far from complete at the temperature and pressure ranges available for hot pressing. Void concentrations greater than 9 volume %, lack of diffusion bonding of the alloy coated fiber within the composite, and the presence of pure aluminum surface foils and inter-layers all contributed to the poor corrosion performance of the hot-pressed composite. SEM examination of the composite after anodic polarization testing confirmed that diffusion bonding of the coated fibers was far from complete. In addition, this analysis revealed that little or no degradation of the coated fibers had taken place; instead, corrosion of the composite was confined to the Al surface foils and interlayers. As a result of the excellent corrosion behavior of the nonequilibrium Al-17 Mo matrix alloy under these conditions (despite its less than optimal morphology), it is believed that corrosion resistant graphite-reinforced composites could be produced with this alloy via hot-isostatic pressing (HIPing). To insure that the enhanced corrosion resistance of the nonequilibrium Al alloy is not compromised by corrosion of the pure Al surface foils or interlayers these composites should either be HIPed without surface foils or HIPed with vapor deposited Al-17 Mo surface foils.

CONCLUSIONS

- 1) Aluminum alloyed with W or Mo at atomic concentrations between 10 and 25 percent showed the best overall corrosion resistance of the alloys investigated in this program. This enhanced corrosion resistance was maintained after heat-treatment at nominal composite consolidation temperatures (400° C).

- 2) The most promising alloys for use in MMCs exhibited amorphous or short range ordering.
- 3) Intermediate concentration Al-Mo alloys (with Mo concentration between 11 and 18 at/o %) provide the best combination of corrosion resistance, thermal stability, and alloy density for use as a matrix metal in graphite reinforced composites.
- 4) Consolidation of the nonequilibrium Al-17 Mo coated wires will require higher pressures than those used in this study.
- 5) Production of a corrosion resistant graphite reinforced composite utilizing nonequilibrium Al-Mo alloys will require processing without surface foils and inter-layers or with vapor deposited surface foils and inter-layers of the same composition as the matrix alloy.

ACKNOWLEDGMENTS

The authors would like to acknowledge the Office of Naval Research (Dr. A.J. Sedriks) for their support of this research.

REFERENCES

1. Evans, J.M. and D.M. Braddick, *Corros. Sci.*, 1971, vol. 11, pp. 611-614.
2. Dull, D.L., W.C. Harrigan Jr., and M.F. Amateau, *Proceedings of Tri-service Corrosion of Military Equipment Conference*, F.H. Meyer, ed., Air Force Materials Laboratory Report AFML-TR-75-42, 1975, vol. 1, p. 399.
3. Crowe, C.R., Localized Corrosion Currents from Graphite Aluminum and Welded SiC/Al metal Matrix Composites, NRL Memorandum report 5415, Naval Research Laboratory, February, 1985.
4. Payer, J.H. and P.G. Sullivan, *Bicentennial of Materials*, Society for the Advancement of Material and Process Engineering, Azusa, CA, 1976 vol. 8, pp. 343-352.
5. Aylor, D.M. and R.M. Kain, ASTM STP 864 - Recent Advances in Composites in the US and Japan, Vinson and Taya, ed., American Society of Testing and Materials, Philadelphia, PA, 1985, pp. 632-647.
6. Trzaskoma, P.P., *Environmental Effects on Advanced Materials*, R.H. Jones and R.E. Ricker, ed., The Minerals, Metals, and Materials Society, Warrendale, PA, 1991, pp. 249-266.
7. Pfeifer, W.H. and W.J. Renton, ed., *American Institute of Aeronautics and Astronautics*, New York, NY, 1977, pp. 231-252.
8. Vassilaros, M.G., D.A. Davis, G.L. Steckel, and J.P. Gudas, *Proceeding of the 1980 Tri-Service Corrosion Conference*, vol. 2, U.S. Government Publication, 1980.
9. Aylor, D.M., R.J. Ferrara, and R.M. Kain, *Mater. Performance*, 1984, vol. 23, pp. 32-39.

10. Aylor, D.M. and P.J. Moran, *J. Electrochem. Soc.*, 1985, vol. 132, pp. 1277-2684.
11. Kendall, E.G. and D.L. Dull, National Technical Information Service, U.S. Department of Commerce, AD-777, p. 160, (1974).
12. Buonanno, M.A., R.M. Latanision, L.H. Hihara, and J.F. Chiang, Environmental Effects on Advanced Materials, R.H. Jones and R.E. Ricker, ed., The Minerals, Metals, and Materials Society, Warrendale, PA, 1991, pp. 267-282.
13. Hihara, L.H., Corrosion of Aluminum-Matrix Composites, Ph.D. Dissertation, Massachusetts Institute of Technology, (1985).
14. Hihara L.H. and R.M. Latanision, *Mater. Sci. Engineering A*, 1990, vol. 126, pp. 231-234.
15. Hihara L.H. and R.M. Latanison, *Corrosion*, 1991, vol. 47, pp. 335-340.
16. Hihara L.H. and R.M. Latanison, *Corrosion*, 1992, vol. 48, pp. 546-552.
17. Harrigan, W.C. and R.H. Flowers, Failure Modes in Composites IV, J.A. Cornie and F.W. Crossman, eds., The Minerals, Metals, and Materials Society, Warrendale, PA, 1977, pp. 319-335.
18. Toth, I.J., W.D. Brenthall, and G.D. Menke, Composites: State of the Art, J.W. Weeton and E. Scala, eds., The Minerals, Metals, and Materials Society, Warrendale, PA, 1971, pp. 139-207.
19. Meyerer, W., D. Kizer, S. Paprocki, Failure Modes in Composites IV, J.A. Cornie and F.W. Crossman, ed., The Minerals, Metals, and Materials Society, Warrendale, PA, 1977, pp. 319-335.
20. Amateau, M.F., *J. Composite Mat.*, 1976, vol. 10, pp 279-296.
21. Nardone, V.C. and J.R. Strife, United Technologies Research Center, Interim Report R89-917711-4, East Hartford, CT, July 1989.
22. Weimer, R.J., W.F. Henshaw, T.G. Casswell, B.D. Dickerson, J.P. Hickerson, and S.D. Shelton, Fabrication of Thin-Walled Seamless Tubes from Gr/Mg Precursor Tapes, Cordec Corporation, Lorton, VA, 1992.
23. Pepper, R.T. and R.A. Penty, *J. Composite Mat.*, 1974, vol. 8, pp. 29-37.
24. Baker, A.A., C. Shipman, and P.W. Jackson, *Fibre Science and Technology*, 1972, vol. 5, pp. 213-218.
25. Shorshorov, M.Kh., T.A. Chernyshova, and L.I. Kobeleva, ICCM-IV, T. Hayashi, K. Kawata, and S Umekawa, ed., Toyoka, 1982, pp. 1273-1279.
26. Arsenault, R.J. and C.S. Pande, *Scripta Metallurgica*, 1984, vol. 18, pp. 1131-1134.
27. Baker, S.J. and W. Bonfield, *J. of Mater. Sci.*, 1978, vol. 13, pp. 1329-1334.

28. Fu, L.-J., M. Schmerling, and H.L. Marcus, *Composite Materials: Fracture and Fatigue*, ASTM Special Publication 907, H.T. Hahn, ed., 1984, pp. 51-72.
29. Khan, I.H., *Metallurgical Transactions A*, 1976, vol. 7A, pp. 1281-1289.
30. Harrigan Jr., W.C., *Metallurgical Transactions A*, 1978, vol. 9A.
31. Gunier, A., *X-Ray Diffraction In Crystals, Imperfect Crystals and Amorphous Bodies*, W.H. Freeman and Company, San Francisco, CA, 1963, pp. 121-126.

ELECTRON IRRADIATION INDUCED CRYSTALLINE AMOPHIZATION AT SiO₂ SURFACE LAYER OF SiC PARTICLES IN A SiC_p/AL COMPOSITE

Zhi Mei¹, Mingyuan Gu², Yi Liu², Renjie Wu²

¹*Department of Materials, Huazhong University of Science & Technology, Wuhan, 430074, P.R.China*

²*State Key Lab of MMCs, Shanghai Jiao Tong University, Shanghai, P.R.China, 200030*

SUMMARY: The structures of surface SiO₂ layer of oxidized silicon carbide before and after compositing with aluminum matrix were studied by XRD and TEM. It is shown that the surface SiO₂ layer is crystalline when silicon carbide particles are oxidized at the temperature of 1100°C in the air. It will be amorphized under the irradiation of high energy electron beam after being compositing with aluminum matrix. It was found by EDX analysis that there existed a concentration gradient of aluminum across the SiO₂ layer. The amorphization mechanism of the SiO₂ layer was also discussed on the basis of qualitative thermodynamics and kinetic considerations.

KEYWORDS: amorphization, electron irradiation, induced, SiC particle, oxidization, SiO₂, surface layer, crystalline, aluminum matrix

INTRODUCTION

It is widely recognized that introducing an oxide layer (SiO₂) on the surface of SiC plays an important role in preventing SiC from being attacked by liquid Al, improving its wettability and also improving the fracture strain of the SiC_p/Al composites [1,2,3]. Nevertheless, as for the structure of surface oxidized layer of SiC particles, there exist different views. Some investigators believe that the oxidation of SiC below 1200°C produces amorphous silica [4,5], but according to other researchers' result [6], heat treatment of the SiC particulates in the temperature range of 800-1100°C produces a crystalline SiO₂ layer of tetragonal and hexagonal structures.

The purpose of this communication is to report a new observation concerned with *in situ* electron irradiation studies using transmission electron microscopy (TEM). In this particular case a crystalline to amorphous transformation is observed. Although the electron irradiation induced crystalline amorphization is well known in ionization-sensitive materials, so far it has not been observed to occur in such composite systems.

EXPERIMENTAL PROCEDURES

SiC particles used in this work is green α - SiC abrasives with an average diameter of 60 μm . The particles used were in an artificially oxidized condition. Oxidation was carried out in air at 1100⁰C for 10 hours using a Al₂O₃ crucible heated in an electric furnace. The phases formed after oxidization were identified by X-ray diffraction (XRD) using nickel-filtered Cu K α radiation.

The composite samples were manufactured by squeeze casting technology in the matrix of commercial pure aluminum. Transmission electron microscopes (PHILIPS CM 12, JEM-200CX) were used. The interface microstructure was examined by using bright field(BF) images, dark field(DF) images, selected area diffraction(SAD), electron energy loss spectroscopy(EELS) and energy dispersive X-ray spectroscopy(EDX). The TEM thin foils were prepared by ion milling at 12 degree with a voltage of 4 kv after mechanical polishing and dimpling.

RESULTS

The XRD result (Fig.1) shows that the oxidized SiC particles consist of two different phases identified as hexagonal α - SiC and pseudohexagonal SiO₂. Intensities of α - SiC peaks are much higher than those of the SiO₂. According to the oxidation process, it is reasonable to deduct that the oxidized SiC is composed of a SiC core and a SiO₂ surface shell. At this time, the SiO₂ phase is crystalline.

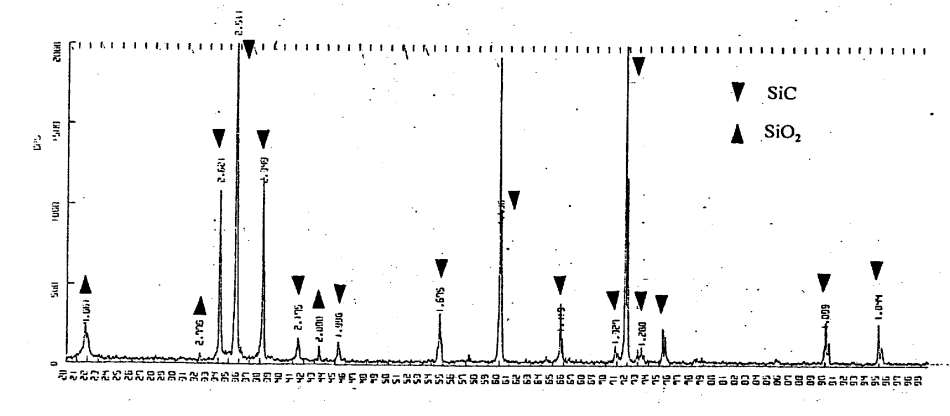


Fig.1 X-ray diffraction pattern of oxidized SiC

A layer of about 500 nm was observed on the surface of oxidized SiC at the Al/SiC interface (Fig.2a), and its diffraction pattern and corresponding dark field image were shown in Figs.2b, 2c. It is interesting to find that the layer becomes unstable under the radiation of high energy electron beam. Only after about two minutes the SAD pattern of the SiO₂ layer became a halo ring (Fig.3a) which is characteristic of an amorphous phase. Diffraction spots outside the halo ring are from aluminum matrix. It is a pity that a symmetric low index pattern of crystalline SiO₂ could not be obtained due to the rapid transformation from crystalline to

amorphous. Nevertheless, according to the indexing of the obtained diffraction pattern(Fig.2b), there exists some diffraction spots which corresponds strong X-ray diffraction peaks (such as $d=0.407$ nm) of the crystalline SiO_2 . Fig.3b is the morphology of the SiO_2 oxidation layer after irradiation of the electron beam for about two minutes. Compared with its morphology before the transformation (Fig.2a), the two contrasts under TEM are different. The SiO_2 layer before the transformation showed typical contrast variation with the tilt of the specimen. This indicates that the SiO_2 layer before irradiation are crystalline in nature. On the other hand, the SiO_2 layer after the transformation showed no distinct diffraction contrast at any orientation and its diffraction patterns typically consisted of only halo rings as shown in Fig.3a. The absence of any diffraction contrast indicates the presence of an amorphous phase.

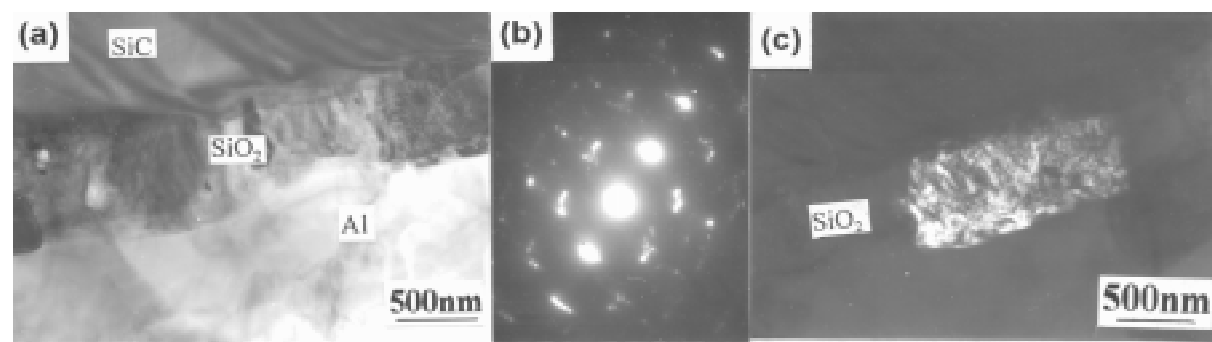


Fig.2 Morphology of SiO_2 layer at SiC/Al interface before the transformation
 (a)bright field image (b)diffraction pattern (c)dark field image

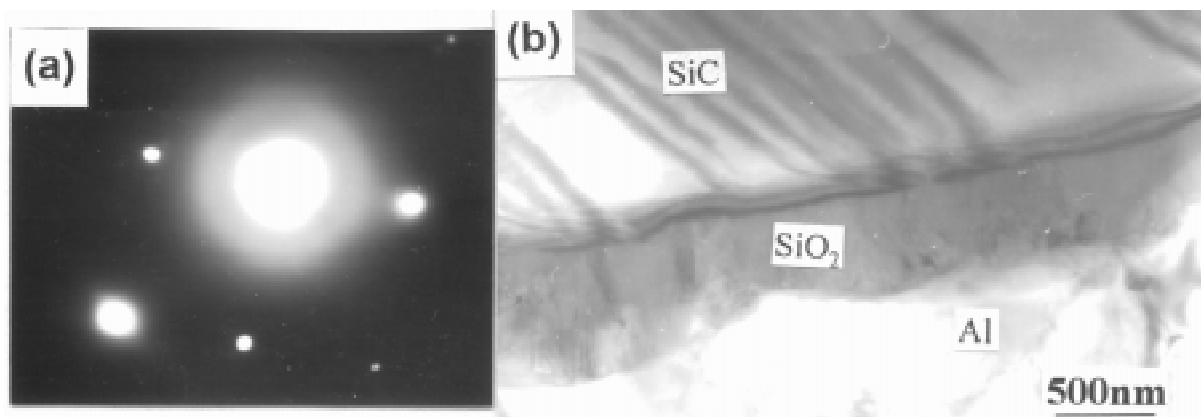


Fig.3 Morphology of SiO_2 layer at SiC/Al interface after the transformation
 (a)halo ring diffraction (b)bright field image

EELS analysis performed on the oxidized SiC shows a strong presence of O and Si peaks. Fig.4 shows the obtained electron energy loss spectrums of the amorphous layer. Comparing with Fig.5, we can see that the amorphous layer contains silicon element whose valence state is plus four and oxygen element whose valence state is negative two. So, we confirm the amorphous layer is amorphous SiO_2 layer. The EDX chemical analysis of the amorphous layer (Fig.6) was performed using a 100 nm diameter electron beam. We find that there exists a concentration gradient of aluminum. Obviously this is caused by the diffusion of aluminum.

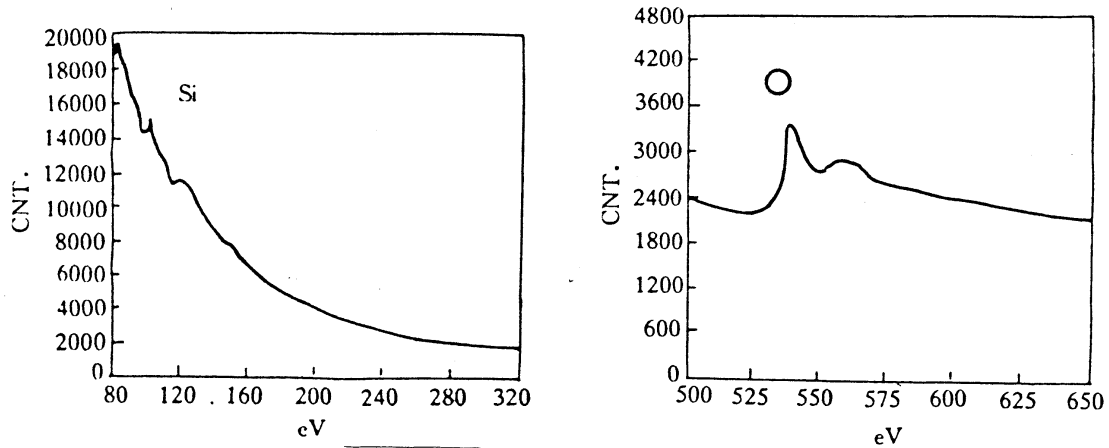


Fig.4 Electron energy loss spectrums of amorphous layer
(a) Silicon edge (b) Oxygen edge

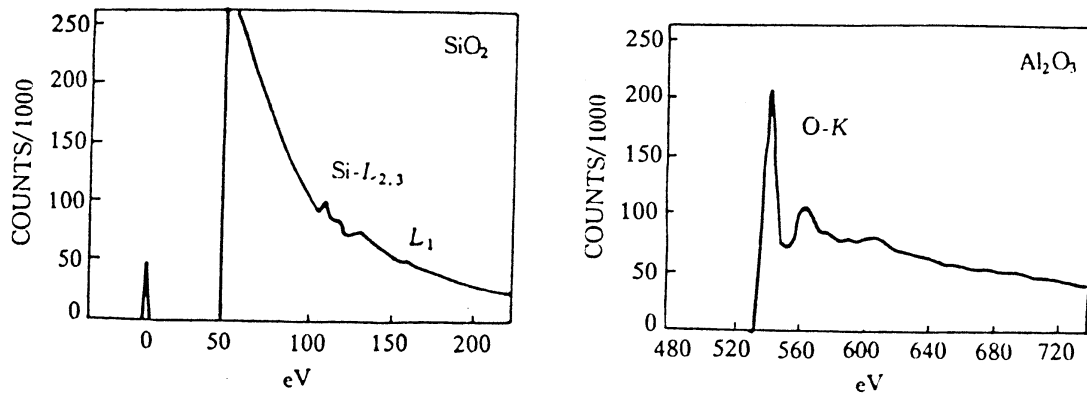


Fig.5 Standard electron energy loss spectrums
(a) Silicon L_{2,3} edge of SiO₂ (b) Oxygen K edge of Al₂O₃

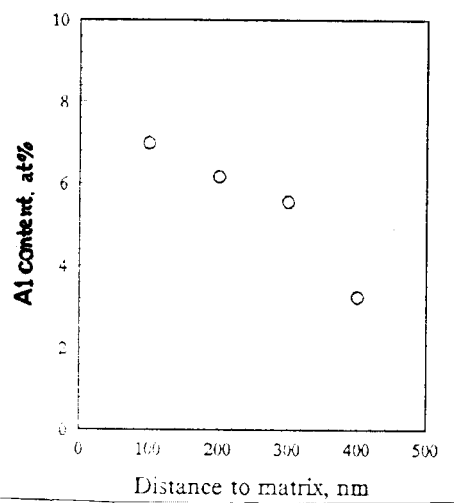


Fig.6 Concentration gradient of aluminum in the SiO₂ layer

From the above experimental results, it can be concluded that when SiC particles are heated at temperature of 1100°C, crystalline SiO₂ layer firstly forms. After the oxidized SiC particles were composited with commercial pure aluminum, the crystalline SiO₂ layer transforms to amorphous SiO₂ layer under the irradiation of high energy(200kv) electron beam. Due to the rapid transformation process, only by careful observation can the phenomenon be observed. Thus, the difference between X-ray diffraction result and electron diffraction result is explained. It helps to understand the combining mechanism of SiC and Al matrix.

DISCUSSION

The present results are interesting in the radiation damage field since the crystalline silica layer has been made amorphous with such mild damage conditions. A proper combination of thermodynamic and kinetic factors is necessary for amorphization to occur. The basic requirements for a crystal to glass transformation are [7]: (I) a large negative heat of mixing of the constituent elements and (II) a large disparity in the diffusivities of the elements involved in the transformation. Criteria (I) makes the glassy phase thermodynamically stable with respect to the crystalline reactants while criteria (II) kinetically favours growth of the amorphous phase as opposed to the crystalline products.

The strong Al-O, Si-O, Al-C and Si-C bond strengths suggest that these elements have large negative heats of mixing as binary systems. Therefore, it is proposed that in the Al/SiO₂/SiC system examined, the strong attraction between Al, C, Si and O results in an amorphous mixture of these elements that has a lower free energy than the Al and SiC crystals with a thin layer of silica in between. It is possible that O, which has a strong affinity for Al, Si and C, binds and stabilizes the amorphous phase. Formation of competing crystalline phases such as Al₄C₃ and Al₂O₃ which probably have higher thermodynamic stability than the Al-Si-C-O phase has to be kinetically suppressed in order for the amorphous phase to form.

Based on the results of this study, the following mechanism is proposed to explain the amorphization at the Al/SiO₂/SiC interface. At the manufacturing temperature of the SiC_p/Al composite, nascent Al comes into contact with the silica on the surface of SiC. As Al has a high affinity for C and O, while SiC is relatively stable, hence Al diffuses into the silica. Because manufacturing process is short and manufacturing temperature is not high enough, the diffusion process may not be fully carried out. When an energetic electron strikes an atom in the SiO₂ crystal, a substantial energy transfer occurs and the atom is displaced and set in motion. It in turn collides with other atoms setting up a displacement cascade during which many atoms are relocated in the lattice. The displacement process can be viewed as an isotropic random walk [8]. It was shown that radiation induced atomic mixing of a diffusion couple can be thought of as a very high temperature diffusion process(10⁴ K or so) which takes place in very short time intervals (10⁻¹¹-10⁻¹² second). The overall composition profile evolution is the result of many uncorrelated displacement spikes. So, the diffusion of aluminum is sped up. The presence of Al in the amorphous layer with the lack of Si or C diffusion into Al indicates that there is a large disparity in the diffusivities of the elements involved in the transformation.

Of course, when discussing amorphization process, the effects of the defects produced by the collision cascade can not be neglected. These defects include interstitial atom-vacancy pairs as well as other types of defects such as vacancy loops and possible chemical disordering by

irradiation, etc. The presence of such defects should destabilize crystalline solid solutions with respect to glass formation. All the above factors support the amorphization and hence the amorphous phase forms.

Much work remains to be done to find out the conditions (composition, temperature, dose rate, electron energy, etc) under which amorphization occurs. Fundamental insight into the atomic mechanisms of the amorphization is lacking in this preliminary work and will require extensive further experimentation.

CONCLUSIONS

XRD and TEM studies show that the surface SiO₂ layer is crystalline when SiC particles are oxidized at the temperature of 1100°C in the air, but it will be amorphized under the irradiation of high energy electron beam after composited with commercial pure aluminum matrix. The crystal to glass transformation is explained on the basis of qualitative thermodynamics and kinetic considerations.

ACKNOWLEDGEMENTS

This research has been supported by the Chinese National Natural Science Foundation and the State Key Lab of MMCs in Shanghai Jiao Tong University. The authors would like to thank Yu Chen for his help with the EELS studies and Dr. Qian Wang for helpful discussions.

REFERENCES

1. Ribes H, Suery M, L'esperance G, et al, "Microscopic Examination of the Interface Region in 6061-Al/SiC Composites Reinforced with As-received and Oxidized SiC Particles", *Metallurgical Transactions*, Vol.21A, 1990, pp.2489-2496
2. Salvo L, L'esperance G, Suery M, et al, "Interfacial Reactions and Age Hardening in Al-Mg-Si Metal Matrix Composites Reinforced with SiC Particles", *Materials Science and Engineering*, Vol.177A, 1994, pp.173-183
3. Mei Zhi, Gu Mingyuan, Jiang Weiji et al, "The Effect of Surface Oxidized Layer on the Interface of Silicon Carbide Particulate Reinforced Aluminum Matrix Composite", *Journal of Shanghai Jiao Tong University(in Chinese)*, Vol.30, Sup., 1996, pp.116-121
4. P.J.Jorgenson, M.E.Wadsworth and I.B.Cutler, "Oxidation of Silicon Carbide", *Journal of The American Ceramic Society*, Vol.42, No.12, 1959, pp.613-616
5. S.Sen, B.K.Dhindaw and D.M.Stefanescu, "Evaluation of Interface Stability and Melt-processing Techniques of Ni₃Al/SiC Particulate Composites", *Materials Science and Engineering*, Vol.174A, 1994, pp.207-214
6. Li Jianping, "The Study of the Microstructure of the SiCp/ZL101 Composite", *Journal of Xi'an Institute of Polytechnique(in Chinese)*, Vol.13, No.2, 1993, pp.79-82

7. P.L.Ratnaparkhi and J.M.Howe, "Characterization of A Diffusion-bonded Al-Mg Alloy/SiC Interface by High Resolution and Analytical Electron Microscopy", *Acta metallurgical et materials*, Vol.42, No.3, 1994, pp.811-815
8. William L.Johnson, "Thermodynamic and Kinetic Aspects of the Crystal to Glass Transformation in Metallic Materials", *Progress in Materials Science*, Vol.30, No.81, 1986, pp.42-126

JOINING PROCESS OF ALUMINA BORATE WHISKERS REINFORCED ALUMINUM COMPOSITE

J. Hu, W. D. Fei, Q. F. Xing

*Box 433, School of Materials Science and Engineering , Harbin Institute of Technology,
Harbin 150001, P. R. China*

SUMMARY: Alumina borate whisker reinforced aluminum composite which is considered as a advanced material with high properties and low cost. In this study, the joining processes was studied using alumina borate whisker reinforced aluminum-copper alloy composite in semi-solid state. The microstructure and the joint strengths of the joining interface were investigated. Both composites were connected directly with a wide aluminum band, no pore and crack can be found at the joining interface. The whiskers which exited at the jointing interface play a key role for the joining. The joint strengths is higher than matrix alloy. Moreover, the joint strength could be improved by T4 treatment. It was revolted that the composites could be successfully joined to themselves.

KEYWORDS: alumina borate whisker, aluminum matrix composite, semi-solid state, joining interface, joint strength.

INTRODUCTION

Metal matrix composites exhibit high specific strength, elastic modules and good high-temperature properties. These properties offer a wide application spectrum in aerospace industries and make them attractive materials for airframe and spacecraft structure. There are some problems which hinder the engineering application of MMCs in structure components: the high cost and the secondary procedures. Two steps are necessary for MMCs to achieve application in industry: the fabrication of MMCs and the secondary procedures, especially the joining of MMCs. Among the different secondary procedures for structure component fabrication, joining of MMCs is fundamental for the production of complex structures. Joining technologies are essential for practical application of MMCs[1]. The fabrication processes for MMCs are being overcome by many efforts, however, there has been litter study concerning joining processes of the materials. Thus, the paper aims to study these processes using alumina borate whiskers reinforced aluminum composite which is considered as a advanced material with high properties and low cost[2,3].

EXPERIMENTAL

The composite used in this study was an Al-Cu alloy reinforced by 20% volume fraction alumina borate whiskers. The chemical composition of matrix alloy is 4.5wt% Cu, 0.6wt% Mn, 0.15wt% Ti, 94.75wt% Al. The composite was fabricated by squeeze casting method. The dimension of the composite is $\phi 50 \times 25$ mm.

The to-be-jointed specimens were cut from the parent composite material, along the center line of the material. The joint form is butt joint. Its schematic diagram was shown in Fig.1.

Prior to be bonded, the specimens were treated as follows: First, the surfaces were mechanically grinded with silicon carbide papers up to 600 grade, then, they were chemically cleaned using a commercial deoxidant to reduce the alumina film thickness.

The joining experiment of the composites were carried out at the pressure of 110 MPa with the hold time of 3 min and 560 °C temperature at which the matrix is in semi-solid state.

The specimens blanks were cut from the different position of the butt joining interface of the material which had been joined for microstructure study, using scanning electron microscopy(SEM).

The tensile specimens of joining interface were studied both in the as-bonded state and in T4 heat treated state. The T4 treatment is at 540 °C for 8 hours. The direction selected for tensile specimen and the dimension of the specimen were shown in Fig.2.

The tests of bond strength were carried out using Instron-1186 type electron testing machine, at room temperature, with a speed of 0.5 mm/min.

RESULTS

From the microstructure of butt joining interface in Fig.3, it can be observed that a wide aluminum band exists at the interface, which was connected directly with both composites. The matrix band is continuous in the joint composite from top to bottom. The width of the matrix band is almost same. The unbonded part does not exist at the whole material. At the initial stage of butt joining process, the surfaces to be jointed were not connected directly and a small gap existed. In this case, the matrix and whiskers in the composite could not flow at the same time, the flow rate of matrix with the semi-solid state in the composite may be quicker than that of the motion or deformation of the surface to be jointed, so the matrix with semi-solid was squeezed from composites to break the oxide film of the to-be-jointed surface and formed the matrix band.

Fig.4 is the high magnification micrograph of butt joining interface, it can be found that litter whiskers exist at both of the interface and the aluminum band. The whiskers were broken during the joining process and moved along with the flowing matrix. The oxide film can easily be broken by these whiskers. The break oxide films and the existence of break whiskers at joining interface play an important role for joining process. In this case, the joint strength of the joining interface is higher than that of the matrix alloy. After T4 treated, the strength can be improved.

The joining interface was not break during tensile test, which revolted that the joint state is good. Moreover, no pore and crack can be found as shown in Fig.3 and Fig.4.

As discussion above, the joint process of the composite in semi-solid state can be concluded as follows: the first step is the formation of the semi-solid aluminum band. Because the to-be-jointed surface was unfair in micro-scale, the gaps should exist, during deformation of the composite, the aluminum alloy with semi-solid state can flow out from the surface, which

lead to the aluminum band formation with semi-solid state; the second step is the aluminum band solidification, which results in the joining of the two parts of the composite.

Because aluminum film at the to-be-joined surface can obstruct the joining of the composite, to break the aluminum film is very important for the joining process of the composite.

CONCLUSIONS

On the basis of the above analysis, the following conclusions were provided:

1. The alumina borate whiskers reinforced aluminum composite can be joined to themselves using butt joint in semi-solid. The joint state is good.
2. The joining strength of bonding interface is higher than that of matrix alloy, it could be improved by T4 treatment in butt joint.
3. The break of oxide films of the to-be-joined surface and the existence of whiskers in the jointed interface play a key role for the joining.

REFERENCES

1. A. Hirose, S. Fukumoto, and K. F. Kobayashi, Joining Processes for Structural applications of Continuous Fiber Reinforced MMCs”, *Metal Matrix Composites: key Engineering Materials Vols. 104-107* (1995) pp. 853-872.
2. K. Sugauma, T. Fujita, N. Suzuki and K. Nihara, “Aluminum Composites Reinforced with a New Aluminum Borate Whisker”, *Journal of Materials Science Letters*. 9 (1990) 633-635.
3. J. Hu, W. D. Fei, C. Li and C. K. Yao, “Interfacial Reaction in Alumina Borate Whisker Reinforced Aluminum Composite”, *Journal of Materials Science Letters*. 13 (1994) 1797- 1799.

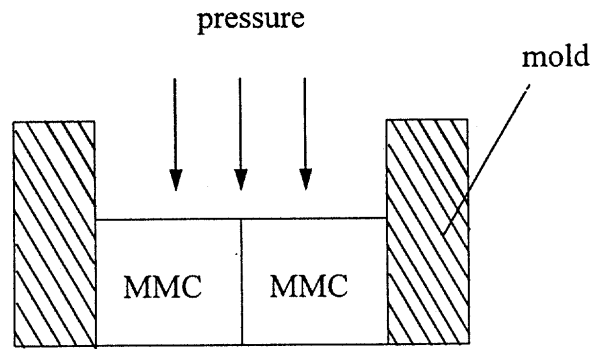


Fig.1 Schematic diagram joint form for the composite joining

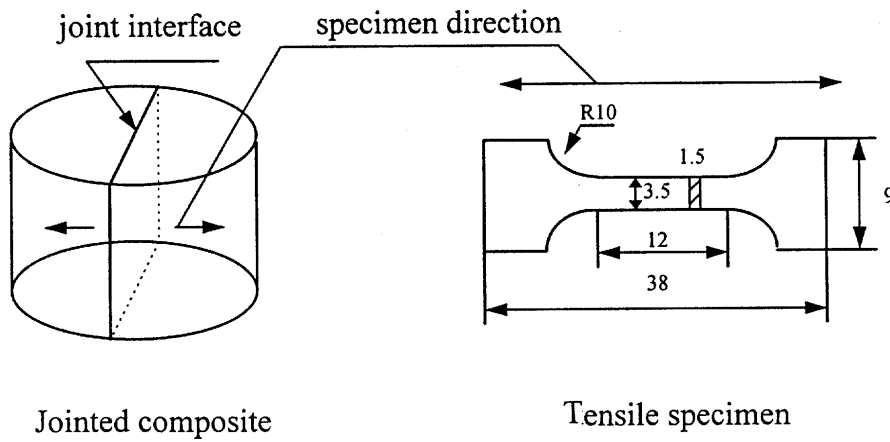


Fig. 2 Direction selected for tensile specimen and the dimension of the specimen

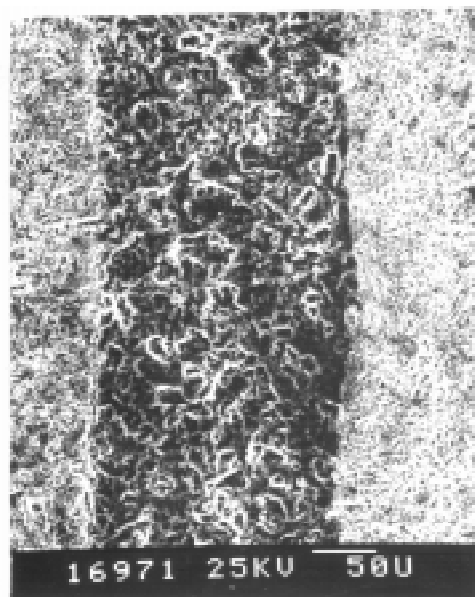


Fig.3 SEM micrograph of the jointed interface

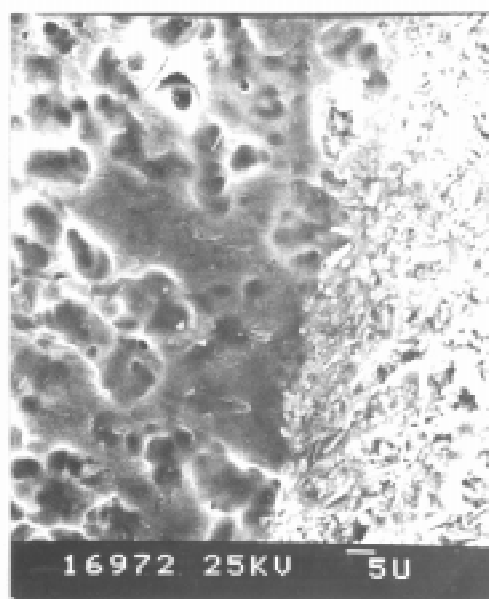


Fig. 4 Higher magnification SEM micrograph of the jointed interface

RESISTANCE BRAZING OF SiCp/Al COMPOSITE

J. Zhang¹, J. Yu¹, S. Meng² and X.B. Zeng¹

¹ *Analysis and Measuring Center, Harbin Institute of Technology,
Harbin 150001, P.R. China*

² *Beijing Spacecrafts, Chinese Academy of Space Technology,
Beijing 100080, P.R. China*

SUMMARY: The SiCp/Al composite plate was fabricated by powder metallurgy and rolling. Resistance brazing of the SiCp/Al composite was carried out by a Gleeble-1500 Thermal Mechanical Simulator. Al, Al-Zn-Mg-Si, Cu, Zn-Al and Zn-Sn-Cu were adopted as interlayer materials. The properties of the joint were measured and the microstructure was observed by electron microscope. It was found that the properties of the joints with interlayer of Al, Al-Zn-Mg-Si or Cu is lower, while the shear strength of the joint with a interlayer of Zn-Sn-Cu is 76 MPa, which is almost the same as the strength of the interlayer. Therefore, the effects of welding parameters (temperature, pressure and interlayer thickness) on the shear strength of the joint with the interlayer of Zn-Sn-Cu were studied in detail. The strength of the joint with a interlayer of Zn-Al is influenced by the composition of the agent for eliminating the oxide film on the composite surface, and especially, greatly depends on the welding parameters which is hardly controlled precisely.

KEYWORDS: silicon carbide, particle, aluminum, interlayer, brazing.

INTRODUCTION

Silicon carbide particle reinforced aluminum (SiCp/Al) composites have potential advantages such as high properties and low cost, and therefore have a strong application future in many fields. Many works have been done about the fabrication techniques, plastic deformation behavior, microstructure and properties of the SiCp/Al composites. However, welding technique of this composite is still a big problem which limits its applications in many aspects. The great difference of the physical and chemical properties between matrix and reinforcement in the SiCp/Al composite results in a low weldability of the SiCw/Al composite [1].

There are a few reports about the welding of the SiCp/Al composites [2,3], from which it can be seen that brazing is a feasible route for welding this composite. There are two main advantages of the brazing of the SiCp/Al composite: (1) there is a small damage to the matrix materials because of the low temperature during brazing; and (2) The brazing interlayer material will be melted and squeezed out of the welding seam together with the oxide film, which improves the wettability between the interlayer and matrix materials.

A resistance brazing route was adopted in this research for welding the SiCw/Al composite. The welded specimens can be heated at a very high speed, and a higher pressure can be applied, so a good bonding of the SiCw/Al composites can be expected.

MATERIALS AND EXPERIMENTAL PROCEDURES

The SiCp/Al composite was fabricated by powder metallurgy technique. The reinforcement is SiC particle with average diameter of 10 μ m, and the matrix is 2024Al. The SiCp/Al composites were joined by the resistance braze welding technique, and the effect of interlayer and welding parameter on the microstructure and shear strength of the joint was investigated. The microstructure and elemental distribution at the joints were observed and measured by EPMA, and the fracture surfaces were observed by SEM.

Table 1: Optimum shear strength of the joints with different interlayers

Interlayer material	Al	Al-Zn-Mg-Si	Cu	Zn-Sn-Cu	Zn-Al
Melting point (°C)	660	547~568	1083 (548)*	200~350	430~500
Shear strength (MPa)	33.5	13.5	<10	77.5	-

*:Melting point of Al-Cu eutectic alloy is 548 °C.

RESULTS AND DISCUSSION

On the one hand, in order not to damage the matrix composite, the welding temperature should not be higher than 505°C, which is the solidus temperature of 2024Al. On the other hand, the interlayer should be melted to get a tightly connect. Five kinds of materials (shown in Table 1) were adopted as the interlayer, while Al, Al-Zn-Mg-Si and Cu were found not suitable as the interlayer material in the resistance braze welding of the SiCp/Al composite. The most important reason is that the three kinds of materials can not be melted at the temperatures lower than 505°C.

When Al was used as interlayer material, the SiCp/Al composite was welded in the conditions that interlayer thickness of 10~60 μ m, temperatures of 460~540°C, pressure of 23~38MPa and time of 3s. After 20 times of welding tests in the condition within the parameter range above, it was found that the shear strength of the joint is very low, and the maximum value is 33.5MPa. Because the melting point of Al is too high to be melted at the temperatures from 460°C to 540°C, the interlayer can not be squeezed out of the welding seam, and therefore the oxide file can not eliminated, leading to a low joint strength. Fig.1 is the morphology of the joint and the distribution of Si and Al across the joint. It can be seen that there is a distinguished interface between the interlayer and matrix material (Fig.1a) and no elemental diffusion can be found (Fig.1b). This indicates that this joint is a kind of mechanical bonding, which results in a low shear strength of the joint.

When Al-Zn-Mg-Si was used as interlayer material, the SiCp/Al composite was welded in the conditions that interlayer thickness of 80~100 μ m, temperatures of 470~530°C, pressure of 16~32MPa and time of 2s. After 8 times of welding tests, it was found that the shear strength of the joint is even lower than that with Al interlayer, and the maximum value is only 13.5MPa. Although the melting point of Al-Zn-Mg-Si is lower than Al, it is still too high to be melted at the temperatures from 470°C to 530°C, which leads to a low joint strength because of the same reason. On the other hand, the plastic deformation of the Al-Zn-Mg-Si is more hard than that of Al, leading to a lower bonding strength compared with that of the joint with Al interlayer.

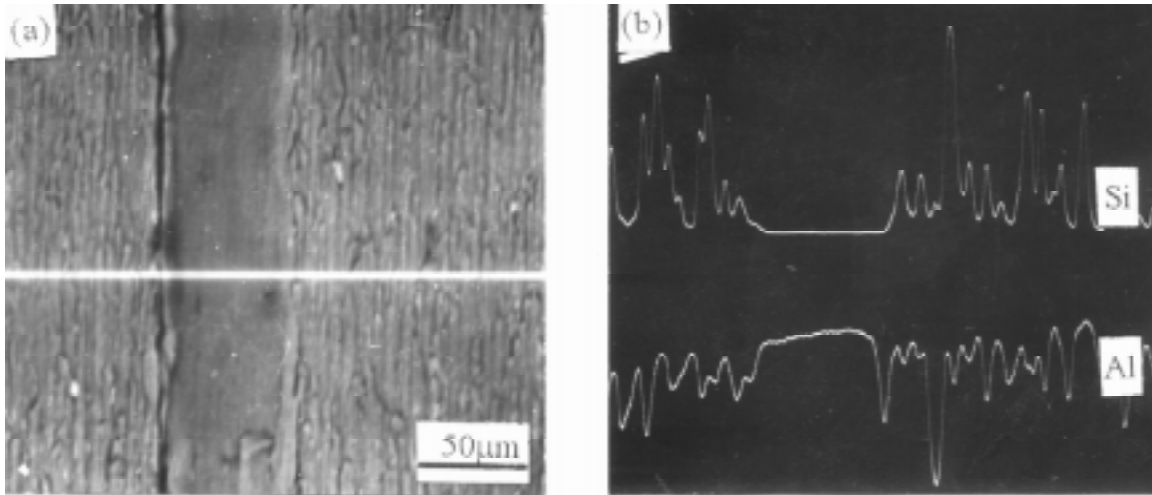


Fig.1: EPMA morphology (a) of the joint and the distribution of Si and Al (b) across the joint with a interlayer of Al.

When Cu was used as interlayer material, the SiCp/Al composite was welded in the conditions that interlayer thickness of 35~75µm, temperatures of 450~500°C, pressure of 25MPa and time of 2s. It was found that the shear strength of the joint is very low, and the maximum value is lower than 10MPa, which indicates that the SiCp/Al composite is almost not connected. If the Al-Cu eutectic alloy is formed at the interface between Cu interlayer and the SiCp/Al composite, the melting point of the Al-Cu eutectic alloy is only 548°C, and a good bonding may be formed in this case. However, no Al-Cu eutectic alloy is formed in this experimental condition, so the SiCp/Al composite can not be welded with Cu interlayer in this condition.

Zn-Sn-Cu alloy are the most desirable interlayer materials, and an optimum shear strength of 76 MPa was obtained.

The effect of welding parameters on the microstructure and shear strength of the joint with a Zn-Sn-Cu interlayer was studied. The shear strength of the joint firstly increases with increasing welding temperature from 370°C to 410°C and then gradually decrease from 420°C to 440°C, as shown in Fig.2. With increasing temperature, the flowability of the Zn-Sn-Cu alloy increases, which makes it easier for the interlayer material to be squeezed out of the welding seam together with the oxide film. So the shear strength of the joint increases with increasing temperature. However, when the temperature is higher than 420°C, the shear strength of the joint decreases with increasing temperature because of the more serious oxidization.

Fig.3 is fracture surfaces of the welded specimens with a 40µm thick Zn-Sn-Cu interlayer. Under a same pressure (15MPa), when the temperature is lower (370°C, as shown in Fig.3a) lots of area was broken between the interlayer and the matrix, because some oxide film can not be eliminated; while at higher temperature (410°C, as shown in Fig.3b), only a few area was broken at the interface, and most of the fracture takes place in the interlayer.

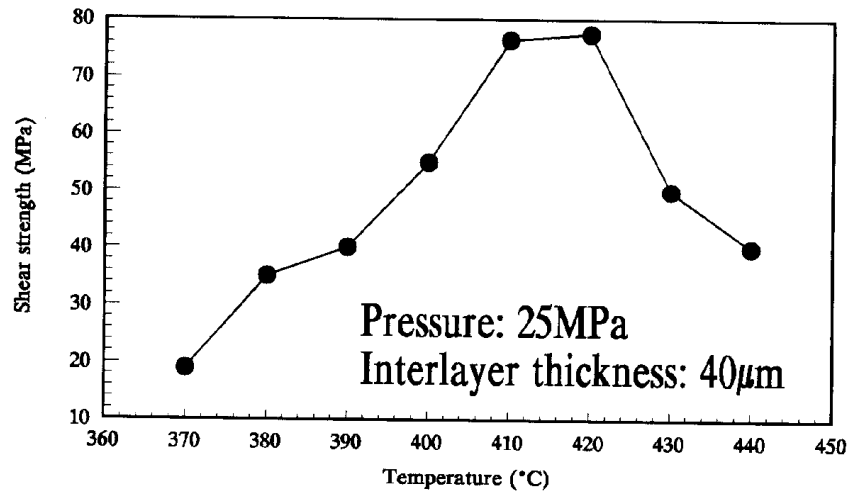


Fig. 2: Effect of welding temperature on the shear strength of the joint with a interlayer of Zn-Sn-Cu

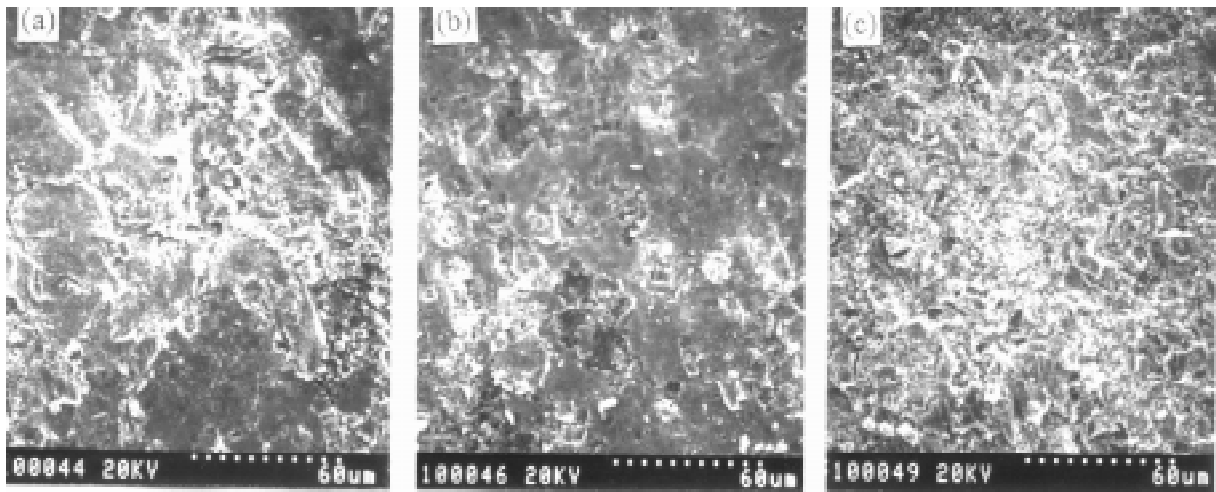


Fig. 3: SEM photographs of the fracture surface of the welded specimens with a 40µm thick Zn-Sn-Cu interlayer, (a) $T=370^{\circ}\text{C}$, $P=15\text{MPa}$; (b) $T=410^{\circ}\text{C}$, $P=15\text{MPa}$, (c) $T=410^{\circ}\text{C}$, $P=30\text{MPa}$.

With increasing welding pressure, the joint shear strength firstly increases from 12MPa to 25MPa, and becomes constant when the pressure is higher than 25MPa, as shown in Fig.4. With increasing pressure, more and more oxide film can be eliminated, and when the pressure is higher than 25MPa, all the fracture takes place in the interlayer, so the joint strength becomes constant. This analysis can be proved from the comparison between Fig.3b and Fig.3c.

Interlayer thickness is also a very important factor to influence the joint shear strength. From Fig.5 it can be seen that the joint shear strength decreases with increasing interlayer thickness from 40µm to 100µm. This is mainly because that with decreasing interlayer thickness the elemental diffusion becomes easier, and the diffusion bonding will contribute to the high joint strength.

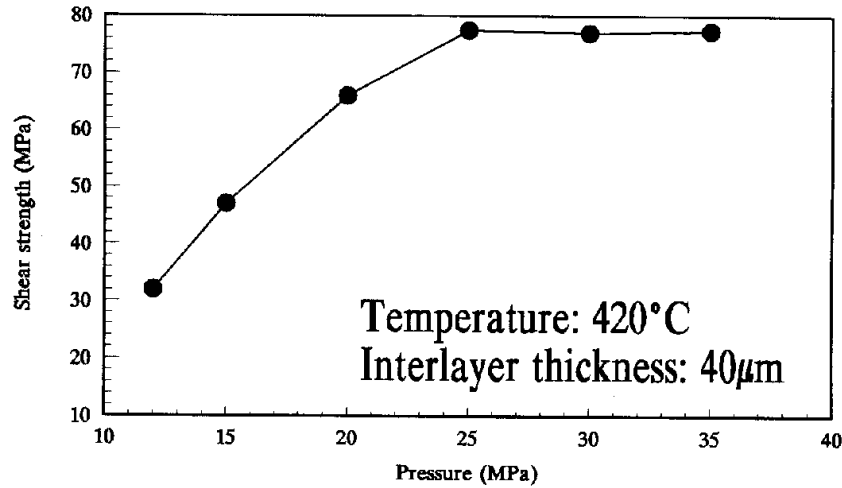


Fig. 4: Effect of welding pressure on the shear strength of the joint with a interlayer of Zn-Sn-Cu

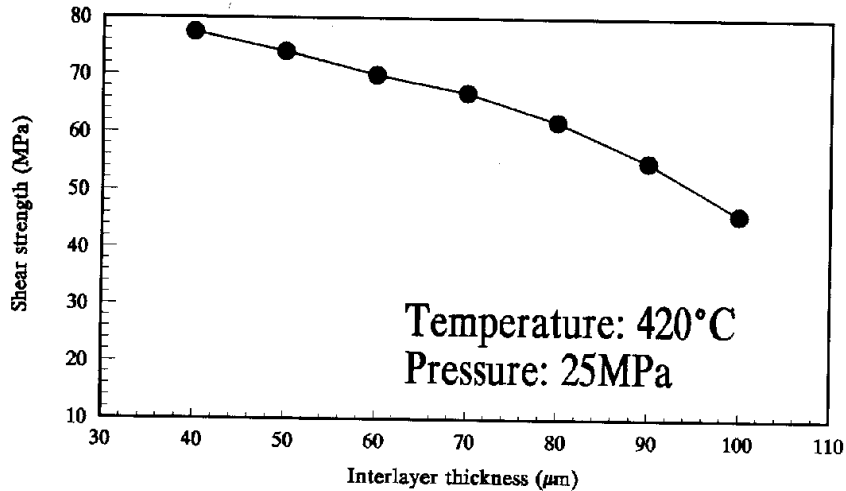


Fig.5: Effect of thickness of the Zn-Sn-Cu interlayer on the shear strength of the joint

An optimum shear strength of the joint was obtained by the resistance braze welding with a Zn-Sn-Cu interlayer (40µm in thickness) under the pressure of 25MPa at 420°C. At this condition, a good connect between SiCp/Al composite and the interlayer was obtained as shown in Fig.6(a). The elemental distribution shown in Fig.6(b) indicates that there is a little elemental diffusion at the interface, which leads to a higher bonding strength .

Zn-Al alloy was also adopted as the interlayer material for welding the SiCp/Al composite. The liquidus temperature is 500°C, which is only 5°C lower than the solidus temperature of 2024Al, so it is very difficult to precisely control the welding temperature. On the other hand, the strength of the joint with a interlayer of Zn-Al is greatly influenced by the composition of the agent for eliminating the oxide film on the composite surface. In this test, we can not get good result because of above reason and also because it is difficult to get very thin Zn-Al alloy film. However, it is believed that Zn-Al alloy is one of the most suitable interlayer material for welding the SiCp/Al composite.

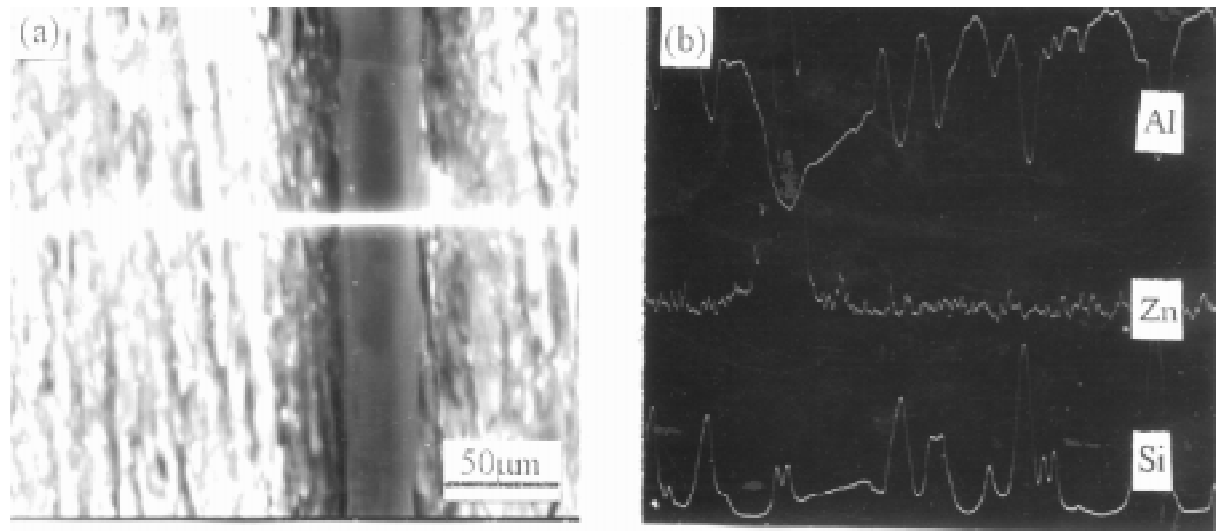


Fig.6: EPMA results of the joint: (a) morphology of the joint, (b) elemental distribution at the joint.

CONCLUSIONS

1. Al, Al-Zn-Mg-Si and Cu is not suitable for brazing the SiCp/Al composite. The joint strength is very low because the three kinds of materials can not be melted at the temperature lower than 505°C.
2. Zn-Sn-Cu alloy is suitable for the brazing of the SiCp/Al composite, and a shear strength of 76MPa was obtained, which reaches the strength of the interlayer.
3. The effect of welding parameters on the joint properties was studied with a interlayer of Zn-Sn-Cu alloy. The shear strength of the joint firstly increases with increasing welding temperature from 370°C to 410°C and then gradually decrease from 420°C to 440°C; with increasing welding pressure, the joint shear strength firstly increases from 12MPa to 25MPa, and becomes constant when the pressure is higher than 25MPa; the joint shear strength decreases with increasing interlayer thickness from to 40µm to 100µm.
4. The strength of the joint with a interlayer of Zn-Al is influenced by the composition of the agent for eliminating the oxide film on the composite surface, and especially, greatly depends on the welding parameters which is hardly controlled precisely.

REFERENCES

1. “What’s Being done to Weld Metal-Matrix Composite”, Welding Journal, June, 1991, pp. 65.
2. Devletion, J.H., “SiC/Al Metal Matrix Composite Welding by a Capacitor Discharge Process”, Welding Journal, June, 1987, pp. 33.
3. Guo, Y., “Brazing of Al-C Fiber Composite”, Journal of Welding, No.4, 1993, pp. 233 (in Chinese).

EFFECTS OF SINTERING CONDITIONS ON THE BOND STRENGTH OF ROLL BONDED METAL LAMINATE COMPOSITES

Xing Kui Peng, Greg Heness and WingYiu Yeung

*Department of Materials Science, University of Technology, Sydney
P. O. Box 123, Broadway, NSW 2007, Australia*

SUMMARY: Metal laminate composites of copper/aluminium were prepared by roll bonding at 430°C with a 60% rolling reduction. Post-rolling heat treatments were applied to the composite laminates to investigate the effect on the interface reaction between the bonded metals monitored. It was found that as the sintering temperature and duration increased, the interface of the metal laminates continued to grow to greater thickness. However growth of the interface did not always enhance the strength of the composites. Critical sintering conditions were found to exist for achieving the optimum bond strengths of the composites. It is evident that development of the optimum bond strength for the composites is related to the formation of the various intermetallic phases at the interface, determined by their energies of formation and the composition gradient across that interface. Development of the copper-rich porous structure, consisting of a Cu_9Al_4 phase, becomes dominant in the interface after sintering at high temperatures and/or prolonged periods. The porous structure is detrimental to the bonding of the metal laminates, leading to the observed low strengths. When aluminium-rich phases are developed during sintering at lower temperatures the bond strength of the laminate composites is increased.

KEYWORDS: metal laminate composites, sintering treatments, bond strength, intermetallic phases

INTRODUCTION

Advanced metal laminate composites have experienced rapid development in engineering applications in the past 30 years [1,2]. The composites usually possess high specific strengths, enhanced fatigue characteristics, improved wear performance and corrosion resistance, resulting in better service performance at reasonable manufacturing costs. Metal laminate composites can be manufactured by a number of methods and roll bonding is one of the major production methods commonly used in industry [3]. It is known that the bond strength and properties of the laminate composites are determined by several important processing parameters such as rolling temperature, deformation strain and sintering conditions. However the complex interface reaction of the metal laminates in the rolling and sintering processes which determine the bond strength of the composites are still not fully understood. In studying the formation of intermetallic phases at the interface of multilayer thin films, Jiang et al. [4] suggested that the interface reactions might be controlled by interfacial and grain boundary diffusion of the metallic elements in the area. Detail of the mechanism however has not been explored. The present paper reports results of a study of the effects of sintering conditions on the interface development and bond strength of the copper/aluminium laminate

composites. Examination of composition profile and formation of intermetallic phases across the interface of the metal laminates was performed. Relationship between the interface development and bond strength of the composites was studied.

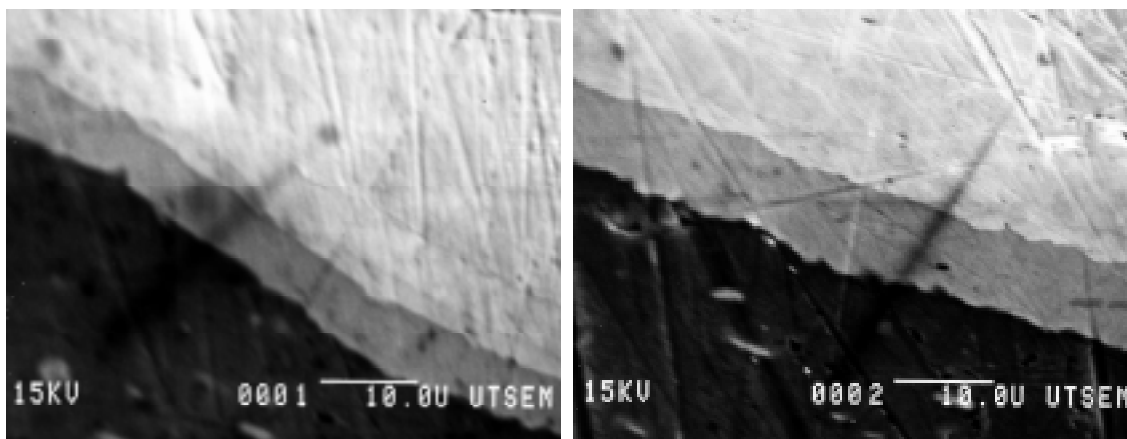
EXPERIMENTAL

Metal laminate composites of copper/aluminium were prepared by rolling, with a 60% reduction, at 430°C. Post-rolling heat treatments of the composites were employed at sintering temperatures from 350°C to 500°C for various periods to investigate the effect on interface reactions between the bonded metals. Bond strength of the composites was determined by peel tests conducted on samples of standard dimensions of 100 (L) x 10 (W) mm. Microstructure and interface morphology of the composites were examined using scanning electron microscopy (SEM). Composition profiles across the interface of the metal laminates were determined using energy dispersive X-ray spectroscopy (EDS) at 15 kV conducted in a scanning electron microscope. Thickness of the interface was determined as the distance between the 5%Cu/95%Al and 95%Cu/5%Al compositional boundaries in all the samples. Detection of the intermetallic phases at the interface of the laminate composites was carried out in a Siemens D5000 X-ray diffractometer using $\text{CuK}\alpha$ radiation at small scattering angles of $1^\circ - 3^\circ$.

RESULTS

The Effect of Sintering Time

A steady growth of the interface was evident in the specimens sintered at 450°C, as shown in the scanning electron micrographs of Figures 1a and 1b.



(a)

(b)

Figure 1. Scanning Electron Micrographs showing Interface Development after Sintering at 450°C for (a) 1.5 hours (b) 3.0 hours

Figure 2 shows that as the sintering time increased, thickness of the copper/aluminium interface continuously increased from 5.7 μm in the as-rolled condition to 28.6 μm after the samples were sintered for a period of 3 hours.

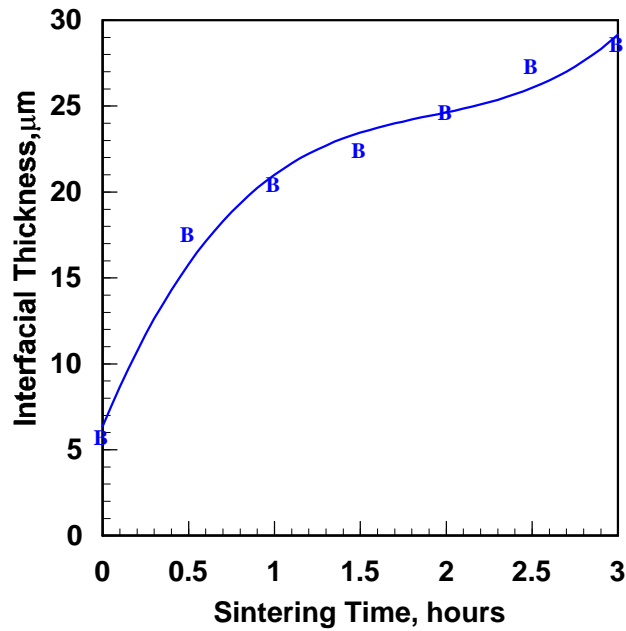


Figure 2. Growth of the Interfacial Thickness at 450°C for Different Times

Figure 3 shows, however, that the bond strength of the composites had not shown similar trends with growth of the interface.

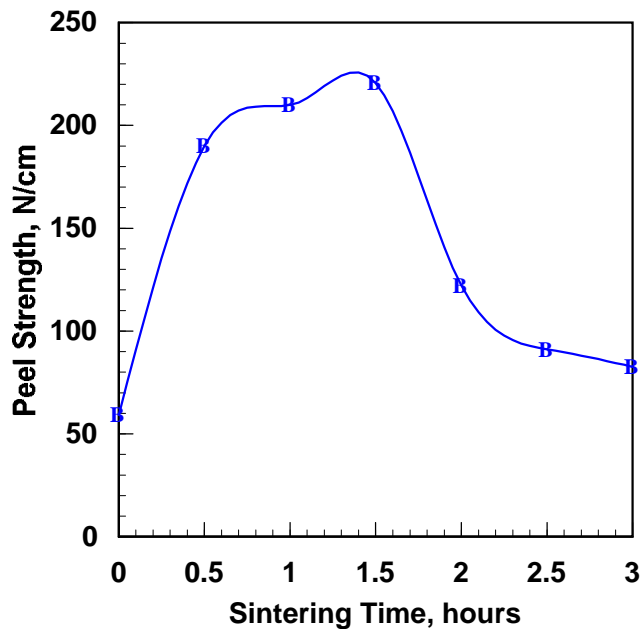


Figure 3 Variation of Peel Strength as a Function of Sintering Time at 450°C

As sintering time increased, the bond strength of the composites, measured by the peel test, increased from 59 N/cm in the as-rolled condition to a maximum of ~220 N/cm after a sintering of 1.5 hours and then substantially decreased to 83 N/cm after 3 hours as shown in

Figure 3, indicating the bonding of the metal laminates had been degraded after prolonged sintering. The results also reflect the complexity of the strength development of the composites and show no simple relationship between the interface growth and bond strength of the material.

The Effect of Sintering Temperature

The effect of sintering temperature on the bond strength of the laminates were investigated by heat treating the composites at temperatures from 350°C to 500°C for 0.5 and 2 hours. Figure 4 shows that as the sintering temperature increased, interface thickness increased for both conditions. After the samples were sintered for 0.5 hour, the interface of the metal laminates grew from a thickness of 8.2 μm at 350°C to 31.4 μm at 500°C. On the other hand, after sintered for 2 hours, thickness of the interface increased from 11.5 μm at 350°C to 33.8 μm at 500°C.

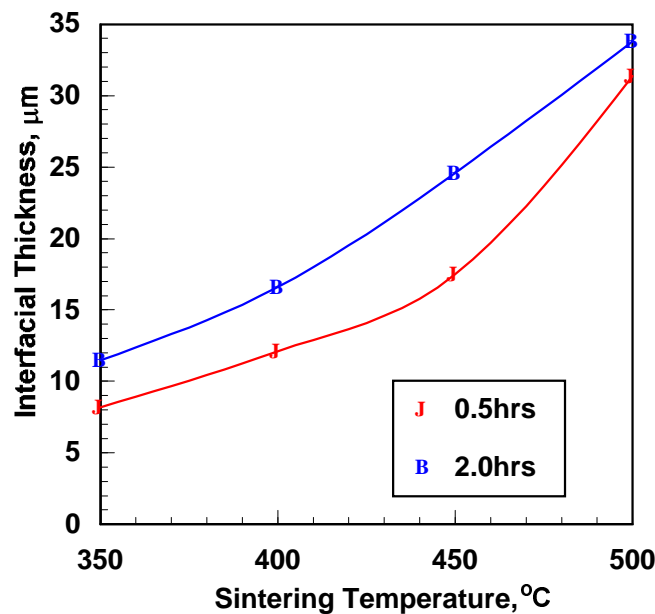


Figure 4. Interface Thickness as a Function of Sintering Temperature for Times of 0.5 and 2.0 Hours.

However an increase of the interface thickness did not always enhance the bond strength of the composites. After the samples were sintered for 0.5 hour, the peel strength of the samples increased from 192 N/cm at 350°C to a maximum of 216 N/cm at 400°C and decreased to a very low value of 17 N/cm at 500°C, Figure 5. In samples sintered for 2 hours, the peel strength increased from 141 N/cm at 350°C to a maximum of 186 N/cm at 400°C and then dropped to 10 N/cm at 500°C, Figure 5. The results indicated that the bonds of the metal laminates were significantly weakened after the composites were sintered at high temperatures.

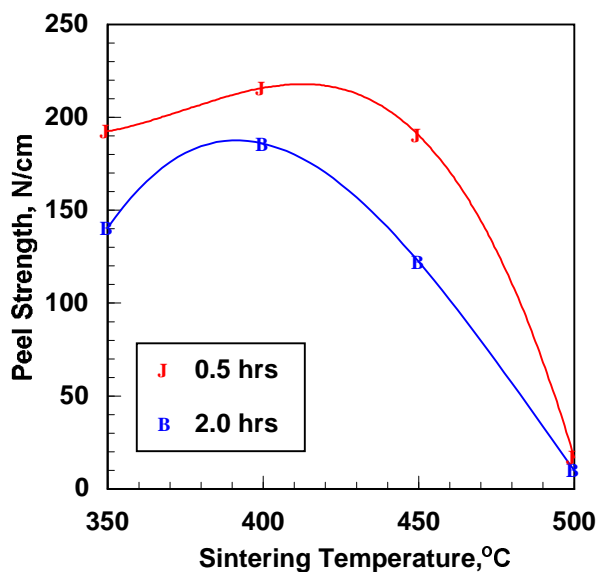


Figure 5 Variation of Peel Strength with Temperature for Sintering Times of 0.5 and 2.0 Hours.

Fractography

Fracture surfaces of the tested samples were examined to identify origins of failure. Scanning electron microscopy of the fracture surface of the composites showed substantially different microstructural development under various sintering conditions. A porous structure consisting of many voids was generally observed in samples of lower peel strength after sintering at high temperatures and/or prolonged durations. A typical structure of the porous interface after sintering at 500°C for 2 hours is shown in Figure 6a. For the stronger laminates cleavage facets were usually dominant with features as those shown in Figure 6b. In general, the porous structure contained a copper content above 85% whereas the faceted structure consisted of less than 75% copper, resulting in formation of different phases and structures at the interface. X-ray diffraction measurement confirmed existence of different intermetallic phases in the samples. Cu_9Al_4 was found to be a dominant phase in the structures of high copper whilst formation of CuAl_2 was evident in those of lower copper content.

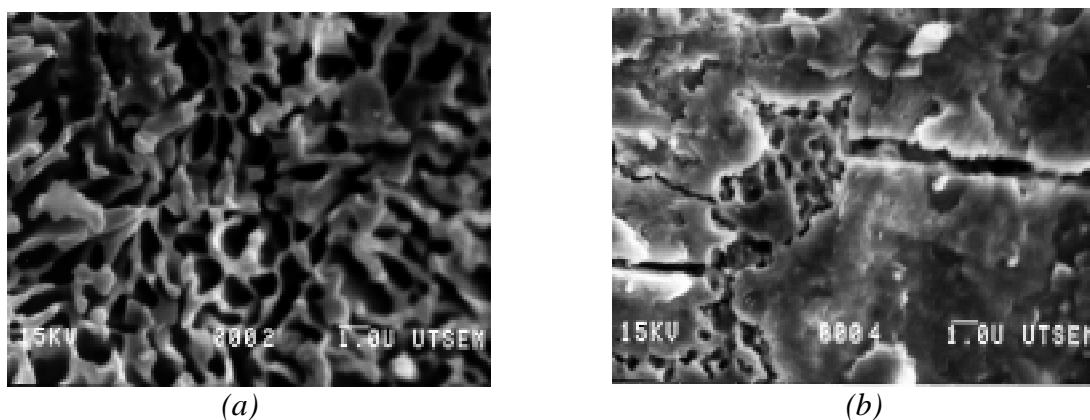


Figure 6 Scanning Electron Fractographs Showing the Structural Development after Sintering at (a) 500°C for 2 hours and (b) 400°C for 2 hours

DISCUSSION

Results of the present study show that a complex relationship exists between the interface development and bond strength of the composites in the sintering process. It was found that as the sintering temperature and/or duration increased, interface of the composites would continue to grow to greater thickness. However an increase of the interface thickness did not always enhance the strength of the composites. In general the peel strength of the composites initially rose to some maximum values and then dropped to low values after sintering at high temperatures for prolonged periods, indicating critical sintering conditions do exist for attaining optimum strengths of the composites. It is believed that development of the optimum strengths of the composites is related to the formation of various intermetallic phases at the interface area. Scanning electron microscopy on the fracture surface of the tested samples showed substantially different structures developed under various sintering conditions. A porous structure of higher copper content, as that shown in Figure 6a generally developed after sintering at a high temperature for a long period. Results of the peel tests showed that this porous structure was generally of low bond strength. X-ray diffraction measurement confirmed that Cu_9Al_4 was dominant in this structure. On the other hand, a cleavage facet structure was found to develop in the tested samples of high peel strength. The facet structure was usually of lower copper content with formation of CuAl_2 phase.

It is understood that both copper and aluminium atoms will be thermally activated in the sintering treatment. Moreover the diffusion rate of copper in aluminium is reported to be greater than that of aluminium in copper [5], thus creating a composition gradient of the metallic elements across the interface. Different intermetallic phases form across the interface of the composites. According to the phase equilibrium diagram of the copper-aluminium system [6], a copper-rich structure will then favour formation of Cu_9Al_4 - γ phase and as the copper content decreases, formation of CuAl_2 - θ phase will become possible. The EDS and X-ray diffraction measurements conducted in the present study confirmed the above phase development. It is recognised that with increasing sintering time, the volume of the copper-rich structure will increase because of the higher diffusion rate of copper atoms, thus increasing the volume of the porous structure. On the other hand, development of the Cu_9Al_4 and CuAl_2 phases will also be affected by their energies of formation. In a study of phase development of the copper-aluminium system, Jiang et al. [4] reported that the formation energies of Cu_9Al_4 and CuAl_2 are respectively 0.83 and 0.78 eV, showing that CuAl_2 may develop with lower activation energy. With a higher sintering temperature, the activation energy provided in the heating process is substantially increased, thus formation of Cu_9Al_4 becomes more viable at higher sintering temperatures. A comparison of the microstructures shown in Figures 6a and 6b shows a large difference in structure development between sintering at 400°C and 500°C, indicating the significant effect of sintering temperature on phase development at the interface. Development of a large volume of a porous structure at the interface will weaken the strength of the composites as reflected by the results obtained in the peel tests.

CONCLUSIONS

Interface development and bond strength of copper/aluminium metal laminate composites were examined in the present study. It was found that as the sintering temperature and duration increased, the interface of the metal laminates continued to become thicker. However, growth of the interface did not always enhance the strength of the composites. Critical sintering conditions for achieving optimum bond strengths of the composites were identified. It is believed that development of the optimum strengths of the composites is related to the formation of various intermetallic phases at the interface area that is in turn determined by the composition gradient across the interface of the composites and the formation energies of the various intermetallic phases. It is evident that development of the copper-rich porous structure of Cu_9Al_4 phase is detrimental to the bond strength of the laminates and formation of the aluminium-rich phases will enhance the strength of the composites as reflected by the results of the peel tests.

REFERENCES

1. Horvath, C. and Haynes, G., "Stainless Steel Claddings" *Automotive Engineering*, Vol. 99, 1991, pp.35-37.
2. Bittrich, J. and Fluegge, D., "Al-Cu Cladding Cables"., *Aluminium*, Vol. 21, 1984, pp.379-383.
3. Baboian, R. and Haynes, G., "Corrosion of Clad Metals" *ASM Metals Handbook*, Vol. 6, 1993, pp.887-890.
4. Jiang, H.G., Dai, J.Y., Tong, H.Y., Ding, B.Z., Song, Q.H. and Hu, Z.Q., "Interfacial Reactions on Annealing Cu/Al Multilayer Thin Films", *Journal of Applied Physics*, Vol. 74, 1993, pp.6165-6169.
5. Askill, J., *Tracer Diffusion Data for Metals, Alloys and Simple Oxides*, IFI Plenum, New York, 1970, p.31.
6. Lu, J.Q. and Yi, W.Z., *Metallurgical Equilibrium Diagrams of Binary Alloys*, Science and Technology Press, Shanghai, 1987, p.137.

EFFECTS OF PROCESS PARAMETERS AND SURFACE CONDITIONING ON THE BONDING BETWEEN MMC-INSERTS AND MATRIX

Sabine Hofmann, Eric Neussl, Peter R. Sahn

Geisserei-Institut, RWTH Aachen, Intzestr. 5, D-52072 Aachen, Germany

SUMMARY: The selective reinforcement by continuous fibres promises various new applications. Especially if high quality inserts are produced separately and embedded subsequently into a commercial casting. A systematic investigation to determine the appropriate process parameter for the embedding has been carried out.

KEYWORDS: CFRM, selective reinforcement, two-step process, insert, hybrid, interface

INTRODUCTION

The properties of CFRM (Continuous Fibre Reinforced Metals) especially containing light weight alloys based on aluminium and magnesium have attracted researchers and engineers alike. The vast majority of investigations carried out in the field of light metal MMCs with continuous fibre reinforcement has so far concentrated on pure Aluminium and Al-2%Cu as matrix materials. The main advantage being the chemical compatibility with the fibres and high gain of strength. However the mechanical properties transverse to the fibres and of the unreinforced material itself are poor. As this only allows for the application with full reinforcement and under one-dimensional loading, these material combinations are not suitable for the production of complex loaded components. Also the production of completely reinforced parts is restricted to few applications especially due to the high fibre costs [1].

Most components require a reinforcement only locally, where the exposure is most severe. The prerequisite being to select an alloy/fibre combination which fulfils at least the minimum property requirements in all areas. The use of commercial alloys is not feasible, due to the formation of second phase precipitates as well as brittle reaction products on the fibre-matrix interface. As this would result in stress peaks on the fibre surface and leads to the untimely failure of the MMC. Therefore alloy development is obligatory. The AlZnMg alloys are most suitable to make use of the reinforcement potential. They exhibit very high static strength and stiffness and are consequently highly interesting for a wide range of applications [2, 3].

A one step process for the production of MMCs has been developed and established at the Geisserei-Institut (*Foundry Institute*) in Aachen [3, 4]. This means that the mould is filled and the fibres are infiltrated in a single pressure assisted casting step [5]. Therefore the alloy composition of the reinforcement is the same as in the unreinforced sections. The alloy composition has to compromise the mechanical properties of the reinforced and the unreinforced material. Even though the results are very encouraging [6] the potential of

continuous fibre reinforced MMCs is not made use of and for many industrial applications [7] the embedding alloy cannot easily be modified.

For more flexibility in alloy composition a two step processing technique is more suitable for industrial series production. The two steps are the pre-fabrication of MMC-inserts and the subsequent embedding into a conventional casting, the fabrication of the so-called hybrid. The separate production of the reinforced section offers the advantage of adapting an alloy for optimum properties in the MMC inserts. The matrix alloy of the continuous fibre reinforced composites should be rather ductile than of high strength to provide a homogeneous load transfer between the fibres. In contrast the choice of the embedding alloy can be governed by the required service properties and the appropriate casting process. Commercially available high strength, corrosion resistant alloys can be selected for the second processing step. However, proper embedding of the fibre reinforced part in the embedding metal (secondary matrix) is imperative. The interface formed during the casting process has to be strong. This means especially the ability to transfer load from the unreinforced sections to the fibre reinforced part and to withstand shear. Metallurgical bonding between insert and surrounding casting is the objective. As for most applications the embedding alloy cannot be modified, the parameters, which are to be investigated are the parameters of the casting process and the surface treatment of the insert.

MMC-inserts can be surface conditioned for the embedding process by removal of oxide layers or by galvanic coatings. Alloy additives for the insert matrix can be selected and tried to enhance the metallurgical reaction while avoiding the formation of brittle phases at the interface during the embedding. But all these measures require a further production substep and consequently increase the production costs. The process parameters of the casting process are a more practicable approach to promote an easy embedding and maintain the good properties of both the fibre reinforced part and the secondary metal surrounding the insert. The specific parameters are the preheating temperature of the shell mould, the casting temperature and inert-gas pressure applied during the embedding casting. Mechanical testing and surface analysis provides the means of evaluation.

MATERIALS

The Insert

The selection of an appropriate alloy/fibre combination was based on the results of previous investigations [2] (Table 1). The composite was fabricated by a precision casting process developed at the Giesserei Institut in Aachen [2, 3]. The technique is based on the investment casting process which is well established for the manufacture of high quality cast components. High design flexibility is ensured by employing a filament winding technique known from fibre reinforced polymers. Infiltration of the molten aluminium alloy into the fibres is supported by inert gas pressurisation. The matrix alloy for the cylindrical MMC-specimens consists of 6% Zn, 1% Mg and balance aluminium. The continuous fibre reinforcement consists of 50 vol.% continuous fibres (type Sumitomo Altex) composed of 85% Al₂O₃ and 15% SiO₂. A typical cross section is shown in Figure 1. All rods were prepared with identical process parameters. The inserts were used in the as cast condition after machining by cutting and turning with diamond or hard metal cutting tools to the overall diameter of 8 mm.

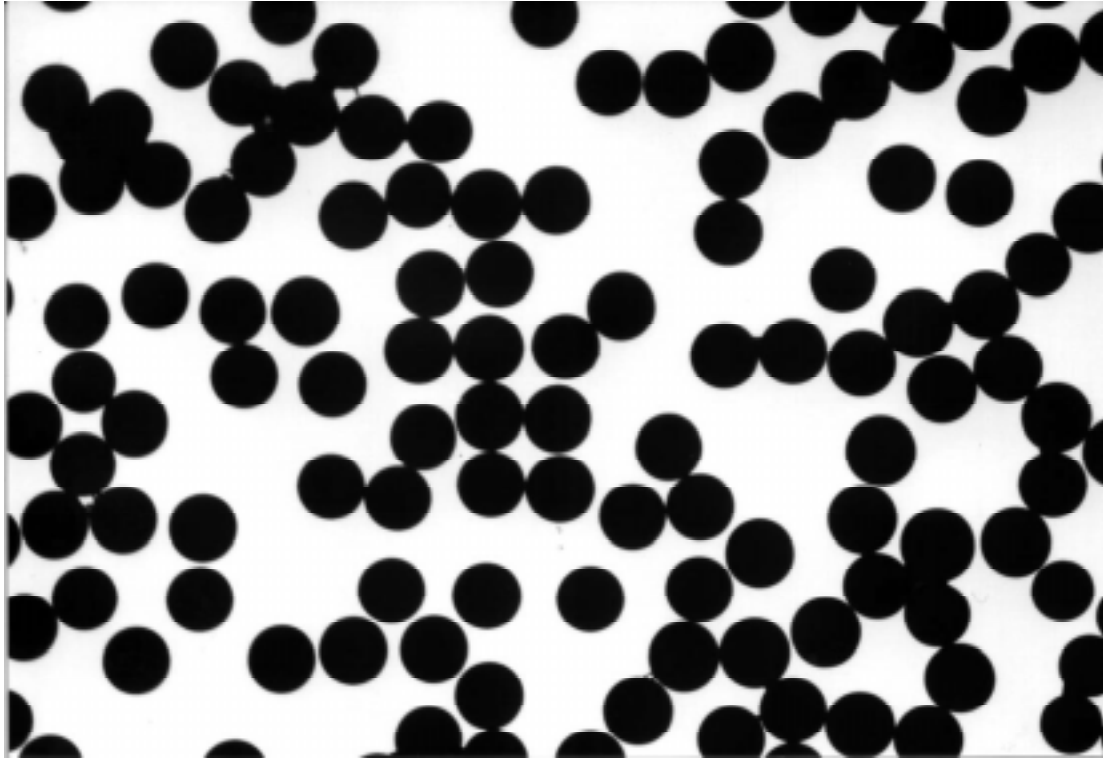


Fig. 1: A typical cross-section of a MMC rod with good fibre distribution

The Hybrid

A commercially available alloy A356 (Pantal7, Al-7%Si-0.3%Mg) was chosen for the unreinforced section (Table 1). The MMC rods were inserted into a deepening in the preheated ceramic shell mould and remained there for one hour before the alloy for the unreinforced section was cast around them. Three preheating temperatures for the shell moulds (300°C, 400°C and 500°C) were selected and the casting temperature was varied (700°C, 750°C and 800°C for each shell mould temperature). The pressure applied was 3 bar for all experiments. This makes a total of 9 parameter combinations. After the removal of the shell mould the specimens were sand blasted and solutionised at 538°C for 12 hours, water quenched and then aged at 154°C for 5 hours to produce a T6 temper. They were then cut and machined to the final test geometry (see Figure 2a and 2b). The cut-off sections were prepared for the microscopical investigation of the interface.

Table 1: Mechanical properties of the materials used

		UTS [MPa]	Elastic Modulus [GPa]	Density [g/cm ³]
Fibre	Sumitomo Altex	1800	210	3.3
Matrix I	Al-6%Zn-1%Mg	304	67.9	2.96
Insert	Matrix I + 50 vol.% fibres	970	140	3.13
Matrix II	Al-7%Si-0.3%Mg	230	71.5	2.68

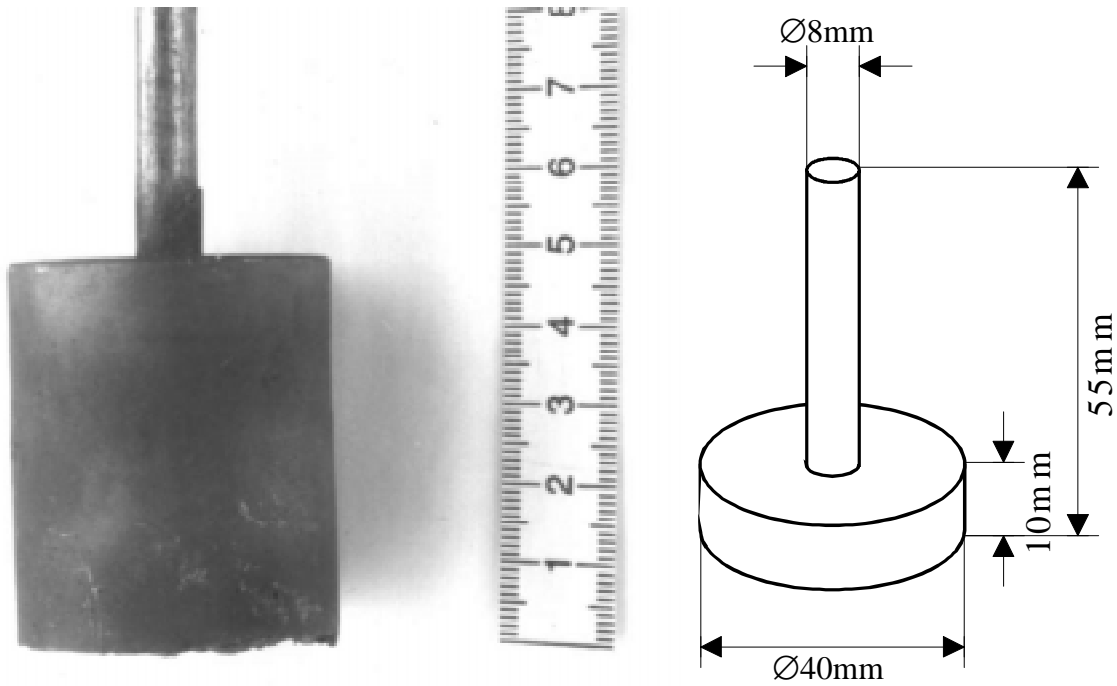


Fig. 2: (left) Geometry of cast hybrid, (right) and test specimen geometry

EXPERIMENTAL PROCEDURES

The pull out tests were carried out on a servohydraulic testing machine (Figure 3) in order to test the quality of the interface. A total number of 36 tests has been performed with a number of 4 specimens for each parameter combination. Load and dislocation have been measured. Furthermore, the specimens have been investigated by optical microscopy to determine the interface characteristics.

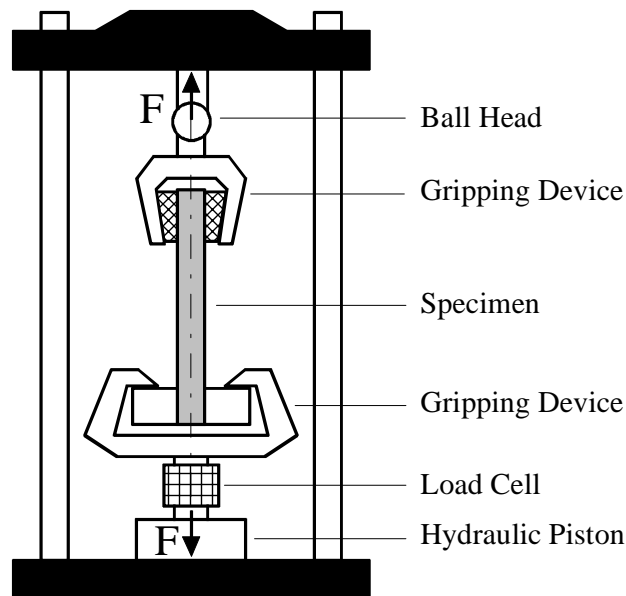


Fig. 3: Schematic drawing of the servohydraulic testing machine

RESULTS AND DISCUSSION

For the evaluation of the interface behaviour under shear load several sources of information were taken into account:

From the graphs the slope and the highest load value of the first linear section as it was found in most experiments and the maximum load value obtained were determined. The shear strength of the interface and the highest applicable shear load were calculated. Additionally the test specimens and the cut-off sections were investigated under a light microscope. No definite conclusion concerning the parameter-property-correlation could be drawn, therefore this evaluation will concentrate on the description of findings and on tendencies.

Interface Failure

Two main types of failure could be identified: Of the 36 specimens tested 20 failed because of MMC failure (Figure 4 left) (half of those near the gripping device and the other half close to or inside the hybrid zone), 15 because the insert was pulled out of the hybrid (Figure 4 right). One specimen showed no interfacial adhesion.

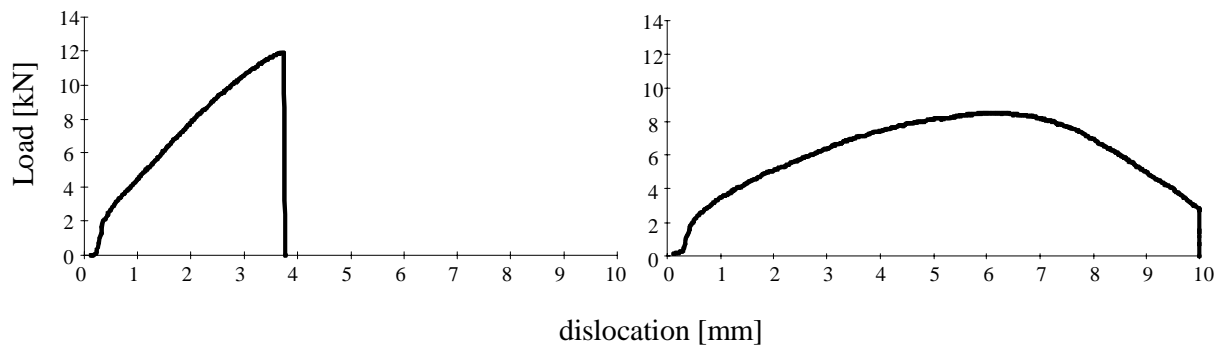


Fig. 4: The two main types of failure identified: (left) the specimen fails by MMC failure, (right) the insert is pulled out

It should be noted that with three specimens a mixture of both types was found. A sharp load-drop occurred, when the insert cracked inside the hybrid zone, but the interface friction was strong enough so the load increased again and the specimens finally failed by pull-out.

Shear Strength and Shear Load

The primal slope and maximum load before a kink or gradual change in slope occurs characterises the shear strength of the hybrid. The linear slope in the beginning varies very little. The mean value for all tests performed is an angle of 85.04° to the x-axis. The samples which exhibited the lowest interfacial adhesion also had the lowest maximum strength values and failed by pull-out. However the samples with the higher values exhibited all types of failure described above.

After the failing of the interface sliding effects take place. This is due to the friction between insert and embedding material. By this the applicable shear can be increased to at least 5-times the value for the interfacial shear strength, before the specimen fails. The applicable shear load was calculated from the maximum interface area. However, as no dislocation was

measured, it is not known how large the interfacial area accountable for the friction exactly is, the actual shear load values are even higher.

From the experiments it is not possible to present a conclusion on the correlation between process parameters, hybrid behaviour and the kind of failure that occurs. Even within a single set of process parameters the performance varies strongly. The maximum load values obtained range between 2.89 kN and 13.22 kN with a mean value of 8.24 kN, the mean interface shear strength being 6.26 N/mm². The best parameters according to the data measured are 400°C as preheating temperature of the shell mould of and 700°C as casting temperature. For these parameters the mean value of the 4 specimens was 11.72 kN for the maximum load and a shear strength of 9.26 N/mm². However, good values were also obtained with other parameter combinations.

Micro-optical Investigation

The micro-optical investigation revealed three different categories of interface (Figure 5):

- The interface is closed and of varying thickness, the interface precisely separates MMC and embedding alloy.
- Even though the interface layer is closed, it is washed away from the fibres and the presence of embedding alloy within the MMC can be identified by Si crystals. Under the microscope the cross section of some fibres appears to be elliptical because they are bend and no longer aligned.
- The interface is broken up and embedding alloy has penetrated into the MMC. In many cases channels of AlSiMg alloy leading into the interior of the MMC are clearly visible in the cross section.

Most test specimens comprise all three categories. Pores on the interface in differing size and quantity were present in samples of all temperature ranges.

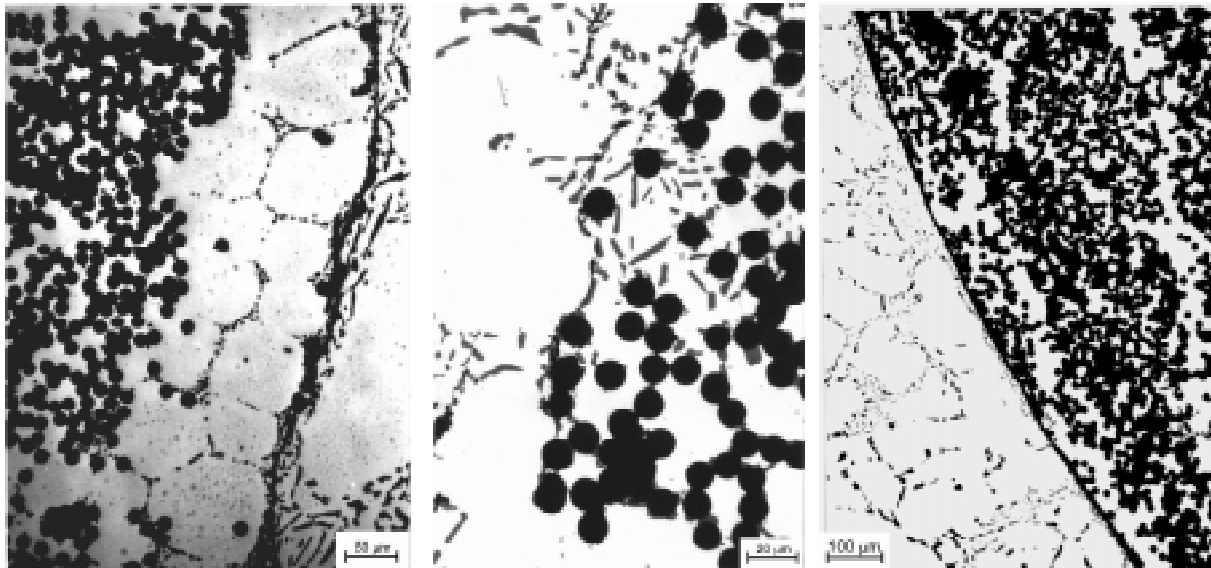


Fig. 5: (left) The oxide layer is broken up and embedding alloy can be found within the MMC region, (middle) the oxide layer is closed but is washed away from the fibres, Si crystals are visible inside, (right) the interface is closed with fibres straight to the interface

Figure 6 shows two specimens which had some of the top values and failed within the MMC. Yet the cross section is evidently divergent.

The specimen on the left (preheating temperature: 400°C, casting temperature: 700°C) has an interface clearly defined by a thin dark line. It is almost perfect with just some minor matrix channels and very few Si crystals within the MMC. The shear stress value of 10.39 N/mm² indicates good metallurgical bonding between insert and embedding material. Other test specimens with similar cross sections exhibited distinctly lower values. This means that the quality of the metallurgical bonding cannot be judged by micro-optical investigation.

The MMC insert of the specimen on the right (preheating temperature: 500°C, casting temperature: 750°C) is unmistakably deformed. In contrast to the specimen on the left the high values are not caused by good interface quality but rather because MMC and embedding alloy are meshed. This constitutes mechanical rather than metallurgical bonding. This was the case for all samples where the insert was hardly dislocated from the hybrid prior to MMC failure.

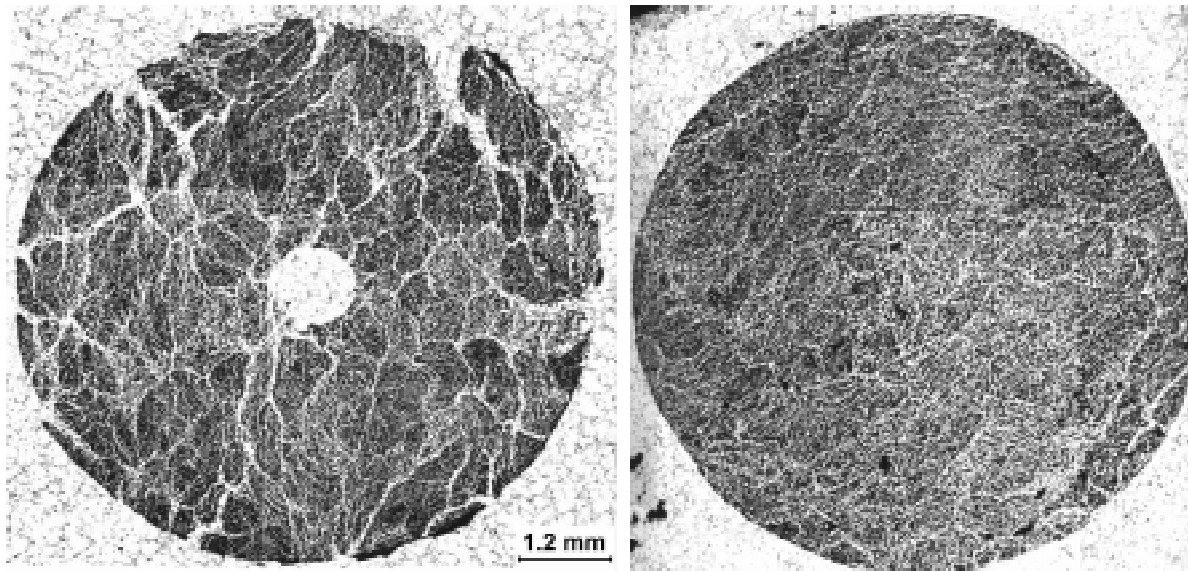


Fig 6: (left) almost perfect interface, MMC not damaged, (right) strongly deformed MMC insert and broken up interface

CONCLUSIONS

The micro optical investigation of the test specimens shows that there is no clear macroscopic interface between embedding alloy and MMC. Almost all specimens show areas where the oxide layer has been broken up or washed away from the fibres. The embedding material frequently penetrates into the MMC. This means that the strength values detected is a total of shear, dovetail and friction effects. The scatter of test results and the limited number of four test specimens produced with identical process parameters dose not allow to judge whether the control of process parameters is sufficient to guarantee proper embedding of an insert or which parameters are to be chosen. For a real components the load has to be transferred from the reinforcement to the unreinforced sections via sheer. The average interface sheer strength of 6.26 N/mm² seems to be insufficient for this purpose. The pressure applied during casting of the embedding alloy can be increased to improve the metallurgical bonding.

For the investigations presented in this paper an aluminium-silicon alloy was chosen for embedding of the MMC due to its popularity for high quality castings. Especially the combination of silicon containing matrix materials with a continuous fibre reinforcement is known to be disadvantageous [3]. Therefore the interface between reinforced and unreinforced sections should prevent the penetration of silicon into the MMC. Especially if silicon gets into contact with the fibres the advantageous mechanical properties of the composite are lost. However, almost all micrographs indicate that silicon finally has penetrated into the MMC. To avoid the penetration of silicon further developments should concentrate on how the interface can be sealed. Scanning electron microscopy of the shear surface as well as EDX analysis of the alloy composition across the interface area will be performed next.

Al test specimens have been T6 heat treatment to reach optimised mechanical properties of the embedding alloy. However, the influence of the heat treatment on the MMC and the interface quality needs further investigations.

A further improvement of the test device would be to introduce a displacement pick up into the gripping device so that the dislocation at the bottom of the insert can be measured as an additional data source.

Finally, if sufficient bonding cannot be achieved by parameter control surface coating should be considered, as there are chemical deoxidisation of surface or galvanic coatings.

REFERENCES

1. E. Neussl, M. Nolte, P.R. Sahn, "Mechanical Testing of Unidirectionally Reinforced Aluminium Alloys" ICCM/10 1995 p. 505ff
2. M. Nolte, E. Neussl, P.R. Sahn, "Near Net Shape Processing of Fibre Reinforced Aluminium", Advanced Structural Fibre Composites Vol. 7, 1995
3. M. Nolte, E. Neussl, P.R. Sahn, B. Hornung, "The Effect of Alloy Additions in Binary Al-alloys for Fibre MMCs Produced by Medium Pressure Casting", Euromat 1995
4. BREU-92-5258
5. Mortensen, I. Jin, Int. Mat. Rev. 37 (1992) p. 101-128
6. M. Nolte, E. Neussl, P.R. Sahn, C. Carré, B. Hornung, "Progress in the Development of Cost-Efficient MMCs with Selective Continuous Fibre Reinforcement" ICCM/10 1995 p.115ff
7. C. Carré, Y. Barbaux "Discontinuous Reinforced Aluminium Matrix Composites for Aerospace Applications -an Overview" ICCM/9 Madrid 1993

DESIGN AND MECHANICAL PROPERTIES OF CONTINUOUS FIBRE REINFORCED MMC BOLT CONNECTORS

Eric Neussl¹, Sabine Hofmann¹, Peter R. Sahn¹, Jérôme Pora², Dominique Schuster²

¹*Giesserei Institut, RWTH Aachen, Intzestr. 5, 52072 Aachen, Germany*

²*Aerospatiale, 12, rue Pasteur, 92152 Suresnes, France*

SUMMARY: An analytic model to predict the load distribution within the shoulder area of MMC bolt connectors has been developed and verified. This model predicts, that the specimen geometry has a significant influence on the stress distribution. The theoretic stress distribution and the experiments indicate that the failure of the component occurs as soon as a critical stress level in the face of the hole has been reached. For these investigations the detected critical stress level was 550 MPa. However, this value is significantly below the values measured by tensile tests of UTS = 970 MPa. This may be due to the more complex stress field in the component than in the tensile test specimen.

The theoretic model and the experiments show, that the applicable load can be reduced by 50% and more by use of an unfavourable component geometry. A comparison of the fatigue behaviour of fibre reinforced castings to unreinforced components, machined out of a aluminium 2024 sheet, shows the improvement that can be achieved by local fibre reinforcement.

KEYWORDS: continuous fibre reinforced MMC, aluminium matrix composites, selective reinforcement, bolt connector, fatigue behaviour

INTRODUCTION

Various production processes and material combinations for CFRMs (Continuous Fibre Reinforced Metals) have been investigated in the past. Especially light weight metals such as aluminium and magnesium have attracted researchers, and in several cases, encouraging mechanical properties have been obtained [1]. One potential candidate for application is an aluminium based Zn-Mg alloy reinforced with alumina or alumina-silica fibres.

A common means for fixation of components in aeronautics and also other applications, are bolt connectors. The bolt connection of an aileron to the wing is one example. Often large scale housings are fixed to other components by rather small connectors, so that the housing may be highly stressed locally. A potential application for CFRMs can be the local reinforcement of such highly stressed areas.

Within a project funded by the EC [2] a modified investment casting process has been developed [3], which allows the production of selectively fibre-reinforced castings. The investigated test specimens have all been produced at the *Giesserei-Institut (Foundry Institute)* by this process and the testing was performed by *Aerospatiale* and *Giesserei-*

Institut. First investigations of bolt connector specimens showed unsatisfactory strength values. For better understanding an analytic model has been developed to predict the load distribution in the shoulder area of such components. This model has been confirmed by tensile tests of various specimen geometries. Additional fatigue tests showed the potential for improvement by local fibre reinforcement.

These investigations have been performed with a Al-6%Zn-1%Mg matrix, selectively reinforced by 50 vol% „Altex“ Alumina-silica fibres. The mechanical properties of the constituents and the composite are listed in Table 1.

Table 1: Mechanical properties of the constituents, fibre and matrix, and of the 50 vol% unidirectionally reinforced composite ⁽¹⁾= own measurements on dog bone specimen geometry; ⁽²⁾= value given by the fibre producer).

	Al-Zn-Mg matrix ⁽¹⁾	Altex fibre ⁽²⁾	Composite ⁽¹⁾
Tensile strength [MPa]	300	1800	UTS = 970
E-Modulus [GPa]	74	210	E = 125; E _⊥ = 85
Strain to failure [%]	2 – 8	0.85	0.75 - 0.85
Density [g/cm ³]	2.95	3.3	3.1

THEORETIC LOAD DISTRIBUTION IN THE SHOULDER AREA OF BOLT CONNECTORS

All tests performed on bolt connector specimens (Fig. 1) showed a fracture in the shoulder area of the specimen. Therefore an analytic model to predict the load distribution within this area has been developed. To simplify the model some assumptions had to be made.

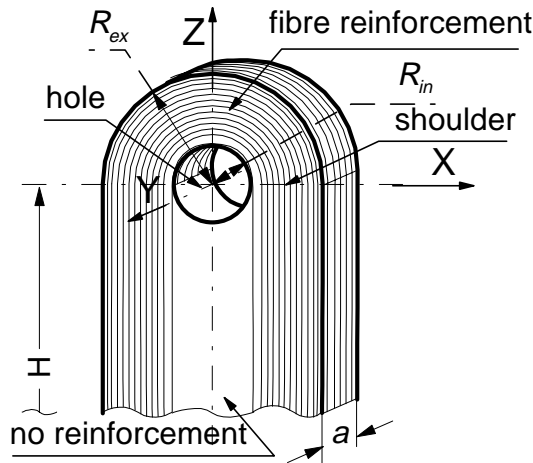


Fig.1: Example of selectively reinforced bolt connection geometry.

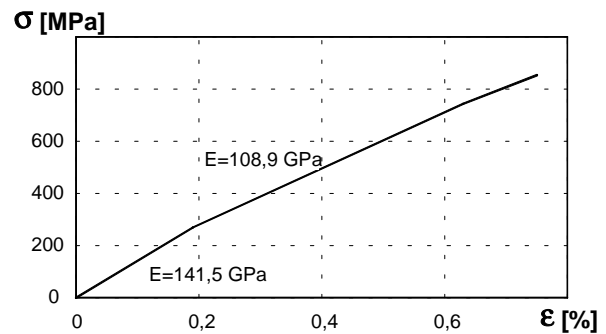


Fig.2: Typical stress-strain behaviour of unidirectional "Altex" fibre reinforced aluminium.

1. The stress-deformation correlation corresponds to the Hook's law until rupture of the specimen. The typical stress-strain behaviour of continuous ceramic fibre reinforced aluminium (Fig. 2) indicates the validity of this assumption, at least in direction of the reinforcement.

2. The stress distribution in y-direction is homogeneous.
3. A constant elongation Δl in the shoulder area of the specimen results in a peak stress of the internal fibres. This is due to the smaller circumference of internal compared to external fibres (Fig. 3).

$$\varepsilon_{ex} = \frac{2 \times \Delta l}{\pi \times R_{ex}} \quad \varepsilon_{in} = \frac{2 \times \Delta l}{\pi \times R_{in}}$$

with $R_{ex} > R_{in} \rightarrow \varepsilon_{in} > \varepsilon_{ex} \xrightarrow{\text{Hook's law}} \sigma_{in} > \sigma_{ex}$

4. The bolt creates compression in the face of the hole, which results in a further relaxation of the external fibres Δl_{\perp} . This is due to elastic deformations transverse to the fibre orientation (Fig. 4).

$$2 \times \Delta l_{\perp} = \pi \times R_{ex} - \pi \times R_{ex'} = \pi (R_{ex} - R_{ex'})$$

$$\Delta l_{\perp} = \frac{1}{2} \pi \times \lambda_{\perp} \tag{1}$$

Δl_{\perp} is given as soon as λ_{\perp} has been determined.

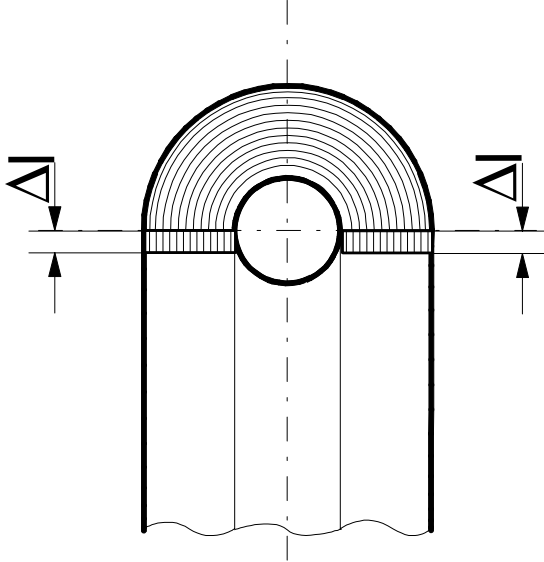


Fig.3: Linear elongation Δl in the shoulder area of the specimen

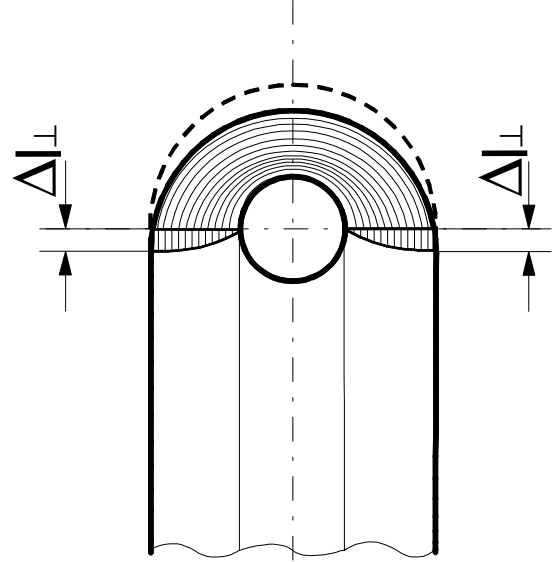


Fig.4: Relaxation Δl_{\perp} caused by compression in the face of the hole

5. Presuming the validity of Hook's law also transverse to the fibre orientation, it follows:

$$\sigma_{\perp}(r) = \varepsilon_{\perp}(r) \times E_{\perp} \quad \Leftrightarrow \quad \varepsilon_{\perp}(r) = \frac{\sigma_{\perp}(r)}{E_{\perp}} \tag{2}$$

6. A linear decrease of σ_{\perp} has been assumed, showing a maximum at the face of the hole and dropping to zero at the outside. This means:

$$\sigma_{\perp}(R_{in}) = \frac{2N}{(R_{ex} + R_{in}) \times a} \quad \text{and} \quad \sigma_{\perp}(R_{ex}) = 0$$

Herewith the stress $\sigma_{\perp}(r)$ transverse to the fibres results to:

$$\sigma_{\perp}(r) = \frac{2N}{(R_{ex}^2 - R_{in}^2) \times a} (R_{ex} - r) \quad (3)$$

The strain at the position r is given by the quotient of the infinitesimal relaxation $d\lambda_{\perp}$ versus the infinitesimal radius dr .

$$\varepsilon_{\perp}|_r = \frac{d\lambda_{\perp}}{dr}$$

In combination with Eqn 2 we get:

$$\begin{aligned} \frac{d\lambda_{\perp}}{dr} &= \frac{\sigma_{\perp}(r)}{E_{\perp}} \quad \Leftrightarrow \quad d\lambda_{\perp} = \frac{\sigma_{\perp}(r)}{E_{\perp}} dr \\ \lambda_{\perp}(r) &= \int_{R_{in}}^r \frac{\sigma_{\perp}(r)}{E_{\perp}} dr \\ \lambda_{\perp}(r) &= \frac{2N}{E_{\perp}(R_{ex}^2 - R_{in}^2)a} \left[R_{ex}(r - R_{in}) - \frac{1}{2}(r^2 - R_{in}^2) \right] \end{aligned} \quad (4)$$

The stress distribution in the shoulder area parallel to the fibres $\sigma_{\parallel}(r)$ can be calculated by overlapping the two effects, the linear elongation Δl in the shoulder area of the specimen and the relaxation Δl_{\perp} caused by compression in the face of the hole.

$$\sigma_{\parallel}(r) = \frac{2[\Delta l - \Delta l_{\perp}(r)]}{\pi \cdot r} E_{\parallel}$$

With Eqn 1 and 4 it follows:

$$\begin{aligned} \sigma_{\parallel}(r) &= \frac{2\Delta l - \pi \cdot \lambda_{\perp}(r)}{\pi \cdot r} E_{\parallel} \\ \sigma_{\parallel}(r) &= \frac{2\Delta l}{\pi \cdot r} E_{\parallel} - \frac{2N}{(R_{ex}^2 - R_{in}^2)a} \cdot \frac{E_{\parallel}}{E_{\perp}} \cdot \frac{1}{r} \cdot \left[R_{ex}(r - R_{in}) - \frac{1}{2}(r^2 - R_{in}^2) \right] \end{aligned}$$

It has to be considered that there is no relaxation of the fibres in the face of the hole.

$$\sigma_{\parallel}(r = R_{in}) = \sigma_{in} = \frac{2\Delta l}{\pi \cdot R_{in}} E_{\parallel}$$

Herewith we get:

$$\sigma_{\parallel}(r) = \sigma_{in} \cdot \frac{R_{in}}{r} - \frac{2N}{(R_{ex}^2 - R_{in}^2)a} \cdot \frac{E_{\parallel}}{E_{\perp}} \cdot \left[R_{ex} - \frac{1}{2}r + \frac{1}{r} \left(\frac{R_{in}^2}{2} - R_{ex} \cdot R_{in} \right) \right] \quad (5)$$

The integral of the stress $\sigma_{\parallel}(r)$ via the width of the shoulders must be in equilibrium with the load N applied by the bolt.

$$N = 2 \cdot \int_{R_{in}}^{R_{ex}} \sigma_{\parallel}(r) \cdot a \cdot dr$$

With Eqn 5 it follows:

$$\sigma_{in} = \frac{N}{2 \cdot a \cdot R_{in} \cdot \ln\left(\frac{R_{ex}}{R_{in}}\right)} \left\{ 1 + 2 \frac{E_{II}}{E_{\perp}} \left[\frac{1}{2} + \left(1 + \ln\left(\frac{R_{ex}}{R_{in}}\right) \right) \frac{\left(\frac{R_{ex}}{R_{in}} - 1\right)}{\left(\frac{R_{ex}}{R_{in}} + 1\right)} - \ln\left(\frac{R_{ex}}{R_{in}}\right) \cdot \frac{\left(\frac{R_{ex}}{R_{in}}\right)^2}{\left(\frac{R_{ex}}{R_{in}}\right)^2 - 1} \right] \right\} \quad (6)$$

Inserting Eqn 6 into Eqn 5 and after some additional transformations, we get:

$$\sigma_{II}(r) = \left\{ \left[\frac{1}{2 \ln\left(\frac{R_{ex}}{R_{in}}\right)} + \frac{E_{II}}{E_{\perp}} \cdot \left(\frac{1}{2 \ln\left(\frac{R_{ex}}{R_{in}}\right)} + \frac{1}{\ln\left(\frac{R_{ex}}{R_{in}}\right)} \cdot \frac{\left(\frac{R_{ex}}{R_{in}} - 1\right)}{\left(\frac{R_{ex}}{R_{in}} + 1\right)} \right) \right] \frac{1}{r} + \left[\frac{E_{II}}{E_{\perp}} \right] \cdot r - \left[\frac{2 \left(\frac{R_{ex}}{R_{in}} \cdot \frac{E_{II}}{E_{\perp}}\right)}{R_{in} \cdot \left(\left(\frac{R_{ex}}{R_{in}}\right)^2 - 1\right)} \right] \right\} \frac{N}{a}$$

The final structure of the equation is:

$$\sigma_{II}(r) = \left\{ A \cdot \frac{1}{r} + B \cdot r - C \right\} \cdot \frac{N}{a}$$

Obviously the specimen geometry, especially the quotient R_{ex}/R_{in} , has a decisive influence on the stress distribution in the shoulder area. The anisotropy of the material is represented by the quotient of the elastic modulus in fibre direction and transverse to it E_{II}/E_{\perp} . Furthermore the load applied N and the specimen geometry, represented by the width a and the internal radius R_{in} , influence the stress values.

For validation of the above equation three different specimen geometries have been produced and tested. The theoretic stress distribution for these geometries are shown in Fig.7.

TENSILE TEST RESULTS

The first specimen geometry investigated is shown in Fig.5 and has been produced and tested within a BritEuRam project. For comparison specimens of the same geometry have been machined out of a 2024 aluminium sheet. The tests showed that the tensile strength of the 2024 specimens is 390 MPa in average compared to 189 MPa for the composite (Fig.8).

The starting point for the theoretical and practical investigations on the influence of the specimen geometry on tensile strength, was to explain the low tensile strength values detected with geometry 1. The follow up investigations have been performed as university study in cooperation of *Institut für Leichtbau (Institute for light weight structures)* and *Giesserei Institut*. To facilitate the investigation and to minimise the material required, three small geometries have been selected (Table 2), showing always the same cross section of the shoulder area. With these geometries a significant variation of the relation R_{ex}/R_{in} has been achieved. The tensile tests have been performed on a servohydraulic test device. The applied load has been increased with a step width of 1000 N starting from zero until failure of the specimen. Additionally the strain of the external fibres have been recorded with strain gauges (Fig. 6). The average tensile strength, the external fibre stress and the resulting theoretic stress distribution are shown in Fig.7.

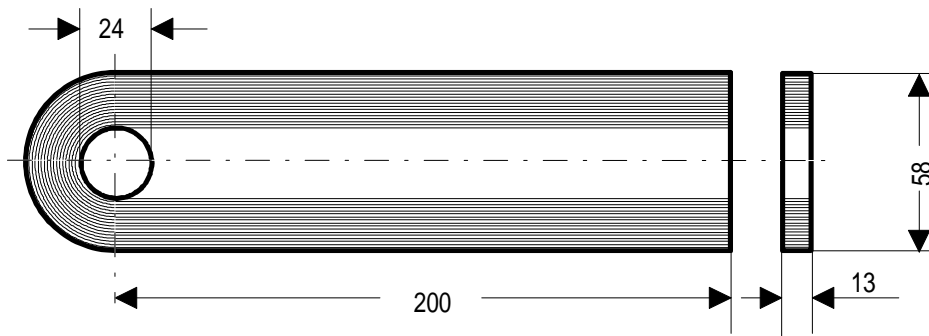


Fig 5: First investigated bolt connection geometry. For reinforcement the fibres are wound around a hole.

Table 2: Geometries, average tensile strength and external fibre stress values of the three small bolt connectors (see Fig.1).

	Specimen geometry		
	small	medium	large
a [mm]	4	4	4
H [mm]	80	80	80
R _{in} [mm]	2	3	6
R _{ex} [mm]	4.5	5.5	8.8
A = 2a*(R _{ex} -R _{in}) [mm ²]	20	20	20
R _{ex} / R _{in}	2.25	1.83	1.42
N [N]	4400	5500	8000
σ _{ex}	90	46	320

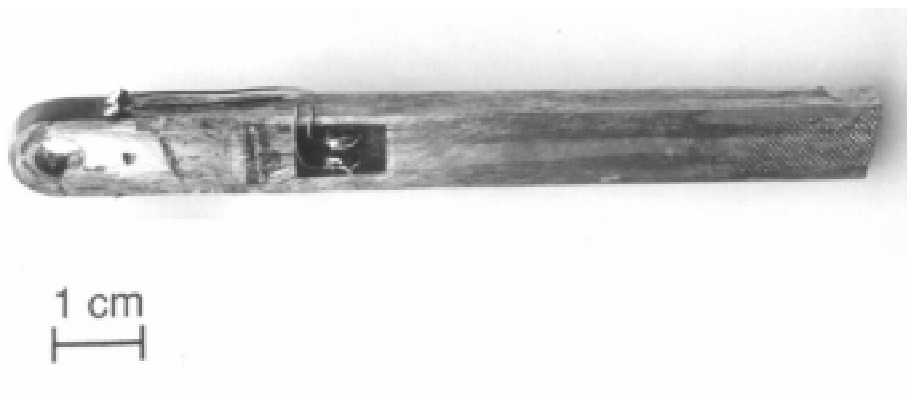


Fig. 6: Small specimen geometry equipped with strain gauges after tensile test.

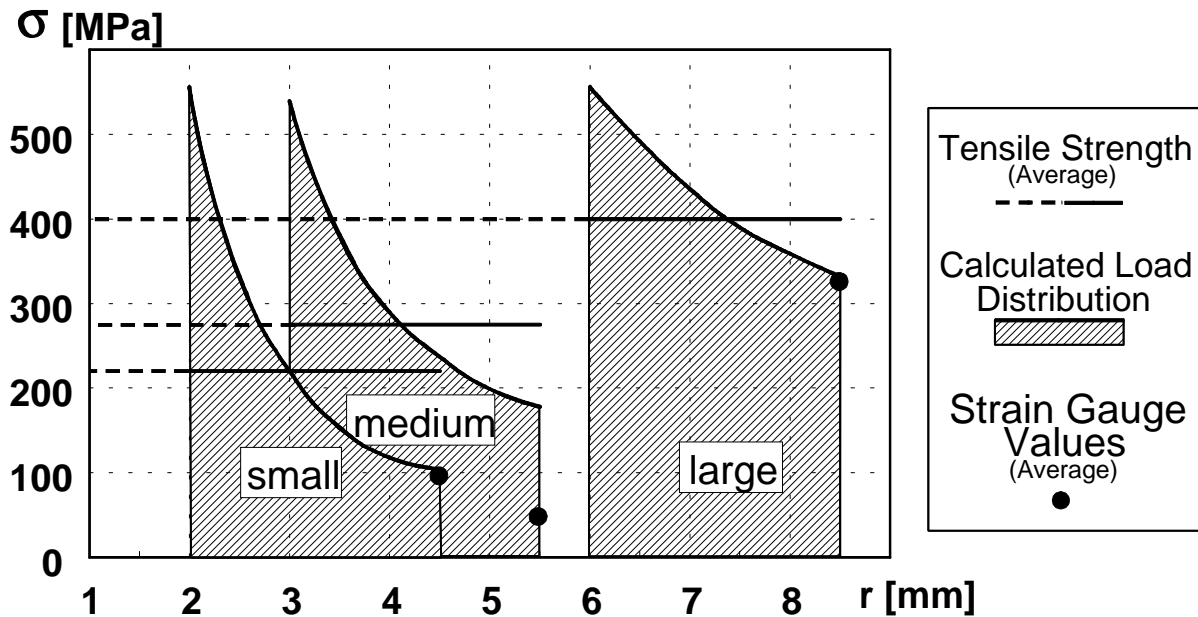


Fig.7: Average tensile strength, detected by the load cell of the servohydraulic test equipment, calculated stress distribution in the shoulder area of the specimen and average tensile stress of the external fibres, measured by strain gauges, for the three investigated geometries.

From Fig.7 it can be seen that the geometry has a significant influence on the load distribution and that with increasing R_{ex}/R_{in} ratio the average tensile strength decreases significantly. Even though the average tensile strength of the small specimen is much lower than of the large one, the peak stress in the face of the hole for all three specimens is similar. This indicates that once the critical stress level for the composite has been reached, a sudden failure of the specimen occurs. However, the peak level (550 MPa) of the bolt connector specimens is significantly lower than the values detected by tensile tests (970 MPa). The geometry 1 specimen has a even worse ratio of $R_{ex}/R_{in} = 2.42$ and therefore the average tensile strength is very low.

FATIGUE TEST RESULTS

Fatigue tests have been performed on specimens of geometry 1, reinforced with 50 vol.% „Altex“ fibres, made of the same Al-Zn-Mg alloy as used for tensile test specimens. Furthermore five components have been machined from 2024 T351 plates in order to compare the properties of fibre reinforced cast parts to those of a conventional wrought alloy, frequently used on aerospace structures. All the specimens have been tested on a MTS machine. Fatigue tests were conducted at $R = 0,1$ under a frequency of 10 Hertz. The test results are shown in Fig.8.

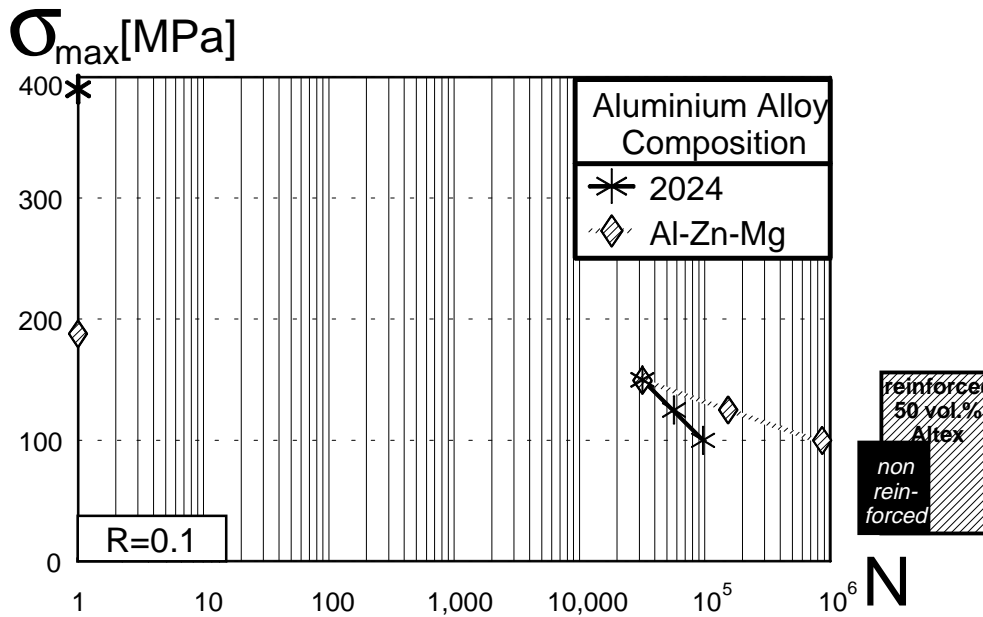


Fig.8: Tensile and fatigue test results of fibre reinforced castings and unreinforced machined specimen of geometry 1.

CONCLUSION AND OUTLOOK

The advantageous tensile properties of the composite (970 MPa) could not be transferred to the bolt connector geometry. This can be due to the more complex stress field in the component than in the tensile test specimen. The bolt creates compression transverse to the orientation of the fibre reinforcement. This effect is overlapped by an additionally tensile loading of the composite in fibre direction. Both stresses have their maximum in the face of the hole.

The specimen geometry influences the stress distribution in the shoulder area significantly. Compared to unreinforced aluminium the composite shows only limited stress relaxation's in the shoulder area, especially in the face of the hole, which results in a sudden failure of the component, as soon as a critical peak stress-level has been reached. This can be explained by the characteristic stress-strain of the ceramic fibre reinforcement, which is almost linear until failure. Therefore the tensile strength values of the composite component are rather low and a favourable geometry has a R_{ex} / R_{in} ratio close to 1. For unfavourable geometries the external sections of the component remain almost unloaded.

The fatigue tests show that, even though the tensile strength values of composite geometry 1 specimens are much lower than of unreinforced 2024, the fatigue behaviour can significantly be improved. Under a stress of 150 MPa, both materials present the same behaviour and for lower stresses longer fatigue lives have been observed on the composite. These results confirm the high fatigue potential of fibre reinforced aluminium castings.

There are two possibilities to reach a favourable stress distribution in the shoulder area of bolt connectors:

1. To design the component with a R_{ex}/R_{in} ratio close to 1
2. With increasing radius r a gradual increase of the composite stiffness would homogenise the stress distribution.

A gradual increase represents the theoretical optimum, but would be very difficult to realise. Therefore a step by step increase is more realistic. Specimens of geometry 1 are in preparation showing an unreinforced section in the centre followed up by an alumina-silica "Altex" reinforcement and a pure alumina "Nextel 610" reinforcement of the external section. Test results will be presented at the conference.

ACKNOWLEDGEMENTS

The authors would like to thank Prof. Dr.-Ing. H. Öry for his support to develop the theoretic stress distribution model. Furthermore we would like to thank the European Commission for there financial support, given within the project No. BREU-92-5258.

REFERENCES

1. Nolte, E. Neussl, P.R. Sahn, B. Hornung, "The Effect of Alloy Additions in Binary Al-alloys for Fibre MMCs Produced by Medium Pressure Casting", Euromat 1995
2. Project No. BREU-92-5258
3. M. Nolte, E. Neussl, P.R. Sahn, "Near Net Shape Processing of Fibre Reinforced Aluminium", Advanced Structural Fibre Composites Vol. 7, 1995

HOT FORGING OF A SUSPENSION ARM COMPONENT IN AL-MMC FOR AUTOMOTIVE APPLICATIONS

A. Forcellese¹, F. Gabrielli¹, S. M. Roberts², P. J. Withers²

¹*Department of Mechanics, University of Ancona, Via Brecce Bianche, 60131 Ancona, Italy*

²*Department of Materials Science & Metallurgy, University of Cambridge, Pembroke Street, Cambridge CB2 3QZ, UK*

SUMMARY: A procedure to establish the optimum hot forging conditions needed to produce a suspension arm component in Al-MMCs is proposed. Hot formability studies on Al-6061/Al₂O₃/10p composite were used to develop processing and stability maps. In the 'safe' region of the processing map, the most favourable forming window was defined as being over temperature and strain rate ranges of 450-500°C and 0.03-0.3 s⁻¹, respectively. These conditions were used to define the optimum forging parameters by FEM analysis. For the suspension arm geometry, a die speed of 18 mm/s, and initial die and billet temperatures of 450 and 500°C were found to best fit the nominal constraints of temperature and strain rate distributions in the workpiece imposed by the optimal processing window. Internal damage was then predicted using a critical strain rate model; hence, it was predicted that damage would be confined to a very small region, and an excellent agreement between processing and stability maps and the critical strain rate model was found. The validity of the proposed approach was confirmed by the experimental damage measurements.

KEYWORDS: Al-MMCs, damage model, FEM, forging, processing map, stability map

INTRODUCTION

In a climate of intense international competition, the efforts of the production industries in industrialised countries are devoted to improving the quality of their products in order to counter the strong competition deriving from industries in the developing countries where labour costs are much lower. At the same time, the manufactured products must evolve due to pressures deriving from more sophisticated markets, government regulations, etc. Such objectives can be reached by developing new materials, by applying innovative processing techniques and technologies, and using simulation methods that allow one to study the production process and to optimise the conditions.

In the automotive industry, a major target is the reduction in fuel car consumption and the associated reduction in harmful engine emissions. The replacement of traditional materials such as steels by lighter metals such as aluminium is desirable. However, aluminium is not sufficiently stiff or strong to be used in many situations and so reinforcement is necessary. Discontinuously reinforced aluminium alloy matrix composites (Al-MMCs) are among the most promising candidate materials for this purpose. However, such materials are difficult to form due to their intrinsic poor ductility deriving from the presence of the undeformable reinforcing phase,

usually SiC or Al₂O₃ particles. The presence of the reinforcement also makes the subsequent machining operations difficult. Consequently, the production of defect-free components is strongly dependent on the processing parameters. Forming conditions can be more easily optimised if models, that describe the evolution of damage, are developed.

The present paper aims to establish the optimum forging parameters needed to produce an automotive suspension arm component from Al-MMC. To this end, a combined approach based on both the processing and stability maps and the critical strain rate damage model is proposed.

THE DYNAMIC MATERIAL MODEL

Processing and stability maps are a helpful guide in the optimisation of metal-forming processes. They are based on a dynamic material model (DMM) [1-3] which considers metal-forming systems as energy manipulators; the power, generated by a source, is transmitted through the dies to the deforming material. This power is dissipated both by plastic work and dynamic processes occurring during deformation such as recovery, recrystallization, phase transformation, etc., and by damage mechanisms such as cavitation and cracking. In the DMM material behaviour is modelled in terms of power dissipated by metallurgical mechanisms defined as: $J = \sigma \dot{\epsilon}^m / (m+1)$, where σ is the equivalent stress, $\dot{\epsilon}$ is the equivalent strain rate and $m (= \partial \log \sigma / \partial \log \dot{\epsilon} |_{\epsilon, T})$ is the strain rate sensitivity coefficient. The maximum value of J is obtained when the deforming material acts as a linear dissipator (i.e. $m=1 \Rightarrow J_{\max} = \sigma \dot{\epsilon} / 2$). Under this condition, one-half of the power applied to the workpiece is dissipated by the operative deformation mechanisms. Usually $m < 1$ and $J < J_{\max}$. The capacity for power dissipation can be measured by the efficiency of dissipation (η) defined as [2]:

$$\eta = \frac{J}{J_{\max}} = \frac{2m}{m+1} \quad (1)$$

The higher η , the more effective are the processes occurring during deformation in dissipating power.

The temperature sensitivity of flow stress is taken into account by the entropy rate ratio (s) given by the relationship:

$$s = \frac{\dot{S}_{\text{sys}}}{\dot{S}_{\text{app}}} = \frac{1}{T} \left. \frac{\partial \ln \sigma}{\partial (1/T)} \right|_{\epsilon, \dot{\epsilon}} \quad (2)$$

where \dot{S}_{sys} is the rate of entropy produced by the system, \dot{S}_{app} is the rate of entropy applied to the system during deformation, ϵ is the equivalent strain and T is the absolute temperature.

Since damage mechanisms also contribute to the value of η , it is necessary to identify the 'safe' regions where no damage occurs, i.e. where the plastic flow is stable. The stability criteria derive from the theoretical requirement that the energy of the system decreases continuously. Besides the condition that m should be greater than 0, which is usually achieved under hot forming

conditions, and s should be greater than 1, derived from the observation that all the irreversible processes are associated with a net increase in entropy, the following relationships are used to identify the stable plastic flow regions [2]:

$$\left. \frac{\partial \eta}{\partial \log \dot{\epsilon}} \right|_{\epsilon, T} < 0 \quad (3)$$

$$\left. \frac{\partial s}{\partial \log \dot{\epsilon}} \right|_{\epsilon, T} < 0 \quad (4)$$

A high value of the strain rate sensitivity coefficient reduces the tendency for plastic flow localisation and hinders necking and shear band formation. Eqn 3 requires that, for stable plastic flow, the power dissipation efficiency must decrease with increasing strain rate, that is the strain rate sensitivity coefficient must decrease with increasing strain rate. In fact, if strain rate increases in a given region of the workpiece, the flow stress also increases owing to the positive m value. If m increases with increasing strain rate, flow stress undergoes a further increase. Such a strong increase in flow stress leads to a non-uniform stress field with marked plastic flow localisation. On the contrary, a decrease in m with increasing strain rate leads to a plastic flow condition that leads to a more uniform stress state in the deforming material. The stability criterion given by Eqn 4 requires that the rate at which entropy increases decreases with increasing strain rate. In reality, when the strain rate increases, flow softening due to adiabatic heating causes a decrease in flow stress. If the entropy rate ratio increases with increasing strain rate, a further decrease in flow stress will occur. Such a marked flow softening can lead to severe plastic flow localisation and adiabatic shear bands.

Eqn 1 defines the strain rate and temperature ranges with the highest capacity for power dissipation; Eqns 3 and 4 provide the necessary, but not sufficient, strain rate and temperature conditions for stable plastic flow. Such equations are probabilistic indicators of the intrinsic hot formability of a material. If they are not realised, the corresponding plastic flow instabilities can be reduced by a proper definition of the die geometry, i.e. by designing the die cavity so that a stress state characterised by a highly compressive hydrostatic stress component, or by reduced tensile stresses, is created in the workpiece.

THE CRITICAL STRAIN RATE MODEL

The dynamic material model neglects the micromechanics of a deforming composite material. We have developed a micromechanical criterion to establish whether the strain rate is sufficiently large for stress to accumulate within the reinforcing particles at the relevant temperature as a function of location within the workpiece. During plastic deformation load may be transferred from the plastically deforming matrix to the elastically deforming particles. If the misfit between the two phases is not relaxed the particle stress will rise and damage may occur. For large scale plasticity it has been shown that these particle stresses can be many times greater than the applied stresses [4]. If the deformation rate is high enough, or the temperature adequately low, then dislocations which approach the reinforcing particles will not be able to climb or by-pass them sufficiently quickly and the stress in the particle will build up drastically [5]. If, however, the deformation rate is less than the critical rate at that temperature then the dislocations will be able to by-pass the particles sufficiently quickly without a 'pile-up' effect so that the misfit strain is relaxed. This is the basis of the

Humphreys and Kalu model [6]. The successful implementation of the criterion depends on recognising the areas in which such a critical rate is exceeded. This in itself may indicate areas of potential damage, however, an important aspect is the extent to which the deformation rate exceeds the critical rate, since regions for which the strain rate is very large will tend to accumulate stress and hence damage more quickly than regions for which the strain rate is only slightly above the critical rate. As such the model developed reflects the rate of stress build up and hence damage accumulation simply by determining the difference between the actual strain rate and the critical strain rate. Whilst promising results can be obtained for most stages of the forging process using this condition alone it is not in itself sufficient. Zones exhibiting high strain rate levels, but in which the stress state is predominantly compressive, are found to exhibit little damage. On the other hand, one might expect damage to occur predominantly in regions for which at least one of the principal stresses is tensile. This does indeed appear to be so; in that the areas of observed damage appear to coincide with areas of tensile stress. The critical strain rate criterion has thus been augmented by a condition that requires the stress field to be tensile for damage to occur [7]. It is the combination of these simple criteria which enables the location of potential damage sites.

THE PROPOSED APPROACH

In our approach to metal-forming process design, the forming parameters are selected using as a guide the 'safe' region of the processing map characterised by the highest level of the power dissipation efficiency. The temperature and strain rate distributions within the workpiece, for a given die geometry, predicted by Finite Element Method (FEM) simulations using different forming parameters, are compared with the nominal ranges defined by the selected processing window. The parameters that best fit the constraints imposed by the processing window represent, in terms of intrinsic formability of the material, the conditions that minimise the probability of the occurrence of damage mechanisms.

The processing and stability maps, however, do not allow for any effect on damage arising from the internal stress state between matrix and particle caused by the deformation. In order to take into account such effects and to obtain a more accurate description of the material behaviour, the critical strain rate model can be implemented into a FEM code. The utilisation of a micromechanical damage model allows verification of whether the forming parameters selected on the basis of the material formability still ensure product integrity at the microstructural level.

Damage mechanisms occurring at low strain rates and high temperatures, such as diffusional void growth at the matrix-reinforcing particle interfaces in MMCs, are not considered by the critical strain rate model. Therefore, the forming parameters must be selected from the processing map window so that the lower limit of strain rate and the upper limit of temperature are not exceeded.

MATERIAL AND EXPERIMENTAL TECHNIQUES

Material

The particle-reinforced aluminium alloy matrix composite used in the present work is Al-6061/Al₂O₃/10p supplied by Duralcan Co., USA (Duralcan designation: W6A.10A). It was

produced by mixing 10 vol% of Al_2O_3 particles, having an average size of $7\ \mu\text{m}$, into molten AA 6061 aluminium alloy. After casting, billets were pre-homogenised at 570°C for 4 h and cooled at 200°C/h . They were then hot extruded into 55 and 80 mm diameter rods.

Compression Tests

The hot deformation behaviour of Al-6061/ Al_2O_3 /10p composite was studied by axisymmetric compression tests performed, using a servohydraulic computer-controlled testing machine, in the temperature and strain rate ranges of $350\text{-}500^\circ\text{C}$ and $0.001\text{-}1.16\ \text{s}^{-1}$, respectively. Cylindrical samples with an initial diameter of 12 mm and an initial height of 18 mm were obtained by EDM. The samples and the loading platens were heated before testing in a resistance furnace with a total heating time of 90 min, consistent with the industrial forging practice. An aqueous suspension of graphite (Renite S-28TM) was used to reduce the frictional effects at the workpiece-die interfaces. The equivalent stress-equivalent strain data were deduced from the load versus stroke data according to the relationships reported in reference [8]. The equivalent stress was corrected for the increase in friction and in temperature due to deformation induced heating (for $\dot{\epsilon} \geq 0.1\ \text{s}^{-1}$).

Forging Trials

The upper transversal arm (Fig. 1) of a multilink suspension for an automotive application was forged. The forging sequence consists of two steps: a preforming process in which the billet is bent followed by a closed-die forging that leads to the final shape.

Each extruded billet in Al-6061/ Al_2O_3 /10p, with a diameter of 55 mm and a length of 390 mm, was heated at 475°C for 2 h before preforming. After the first step each workpiece was heated at $500 \pm 10^\circ\text{C}$ for 2 h prior to closed-die forging. The temperature was checked using a pyrometer just before operation. The average upper and lower die temperatures were about 325°C and 320°C , respectively; these values were continuously monitored throughout the trials by embedded thermocouples. The optimum lubrication conditions were found to be a combination of Renite S-28TM sprayed between each operation, and animal grease mixed with lead oxide 'painted' on the dies every third or fourth forging. The forgings were obtained on a hydraulic press with a piston diameter of 1450 mm and a capacity of 5000 t at 300 bar. The average pressure was 180 bar and the pressing time was about 8 s; the die speed was about 18 mm/s.

The extent and location of damage in the crank section of the upper transversal arm was mapped using an image analysis technique based on optical microscope images. The very small size of voids and their location at the reinforcing particle-matrix interfaces, where Mg_2Si precipitates are also present, made the damage measurements very difficult. Damage was quantified by the ratio between the number of particles associated with voids and the total number of particles investigated (Pv%). A second damage parameter was given by the ratio between the number of voids per unit of area in the forging (N) and the number of voids per unit of area in the undeformed material (N_a) [9]. As such, the ratio N/N_a indicates the amount of damage accumulated during the process in terms of the damage prior to forging. The change in damage level is thus monitored, indicating the influence of the processing state on the observed damage.

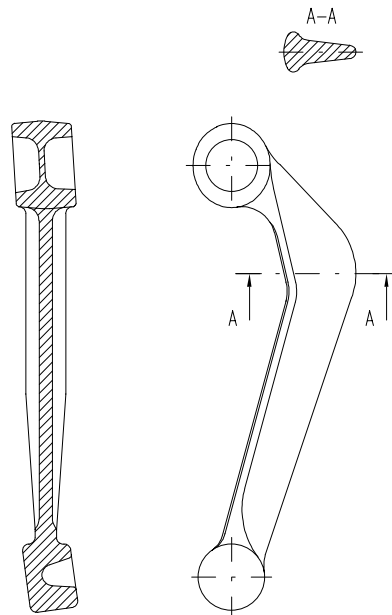


Fig. 1: The forged suspension arm component (length: 340 mm).

RESULTS AND DISCUSSION

Processing and Stability Maps

Equivalent stress-equivalent strain data for Al-6061/Al₂O₃/10p demonstrates a weak influence of strain and a strong influence of strain rate and temperature on flow stress [8], as typically observed in aluminium alloys. The data were used to calculate the strain rate sensitivity coefficient. At each strain and temperature, the $\log\sigma$ - $\log\dot{\epsilon}$ data were fitted using a third order regression; a dependency of the strain rate sensitivity coefficient on strain rate was also assumed. The map of the power dissipation efficiency, expressed in terms of strain rate and temperature, shows three different processing windows (Fig. 2):

- window I, in the temperature and strain rate ranges of about 350-400°C and 0.1-1.16 s⁻¹, characterised by the lowest power dissipation efficiency;
- window II, in the temperature and strain rate ranges of about 450-500°C and 0.03-0.3 s⁻¹, characterised by the highest power dissipation efficiency;
- window III, in the temperature and strain rate ranges of about 350-400°C and 0.001-0.003 s⁻¹, characterised by intermediate power dissipation efficiency values.

The occurrence of the plastic flow stability was assessed by Eqns 3 and 4. Eqn 3 is not satisfied in the temperature and strain rate ranges of about 430-500°C and 0.001-0.025 s⁻¹ (Fig. 3); this indicates a plastic flow instability. Such an unstable region can be attributed to the diffusional void growth at the matrix-particle interfaces that is the mechanism governing damage at low strain rates and high temperatures [10]. This causes a reduction in flow stress that decreases, for a given temperature, with increasing strain rate and, for a given strain rate, with decreasing temperature. This flow stress behaviour produces an increase in the strain rate sensitivity coefficient with increasing strain rate and, therefore, a non-uniform stress state leading to an instability in the plastic flow. This was confirmed by the occurrence of several very small voids at the reinforcing particle-matrix interfaces in the compression-tested samples deformed within the unstable plastic flow region [8].

The Definition of the Forging Parameters

The ‘safe’ region II ($T=450-500^{\circ}\text{C}$, $\dot{\epsilon} = 0.03-0.3 \text{ s}^{-1}$) in the processing map was used to select the nominal forming parameters of both preforming and forging operations for producing the upper transversal arm (Fig. 1) in Al-6061/Al₂O₃/10p composite. Since the stress and strain states

induced by the closed-die forging are more severe than those induced by the initial bending, the optimisation focused on the forging stage. Furthermore, due to the complexity of applying the critical strain rate model to the closed-die forging simulation with the available 3-D numerical codes, only the cross section across the crank of the suspension arm component was simulated (i.e. across A-A in Fig. 1). A plane strain approximation was made using the DEFORMTM 2-D code. The combination of the distortion due to the forming of the elbow followed by the subsequent closed-die operation in this section of the component suggests that the internal damage is expected to be the highest. For the suspension arm die geometry, a die speed of 18 mm/s, and initial die and billet temperatures of 450 and 500°C, respectively, are the forging parameters that best fit the nominal constraints of temperature and strain rate distributions within the workpiece imposed by the processing window II. As already mentioned, the forging parameters must be selected in order to avoid the damage mechanisms occurring at the low strain rates and high temperatures that are not taken into account by the critical strain rate model; such conditions were obtained by preventing the strain rate from falling below 0.03 s⁻¹ and the temperature rising above 500°C. The damage predicted by the critical strain rate model is shown in Fig. 4.a. It can be observed that a very small damaged area is expected in the region of the forging near the flash. This is due to the high $\dot{\epsilon}$ values in this region which exceed the upper limit of the reference range (0.3 s⁻¹) given by the window II of the processing map.

Validation of the Predictive Model

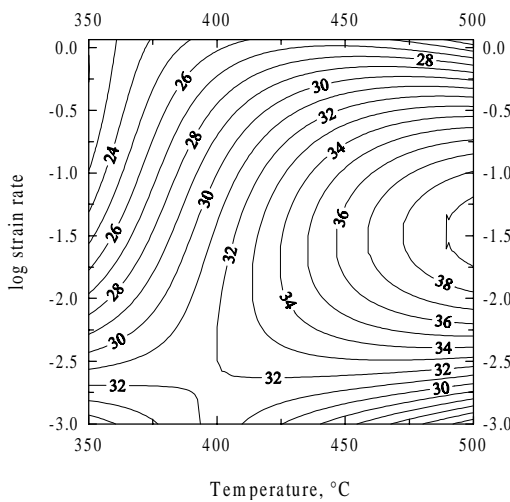


Fig. 2: Map showing the power dissipation efficiency contours for Al-6061/Al₂O₃/10p composite.

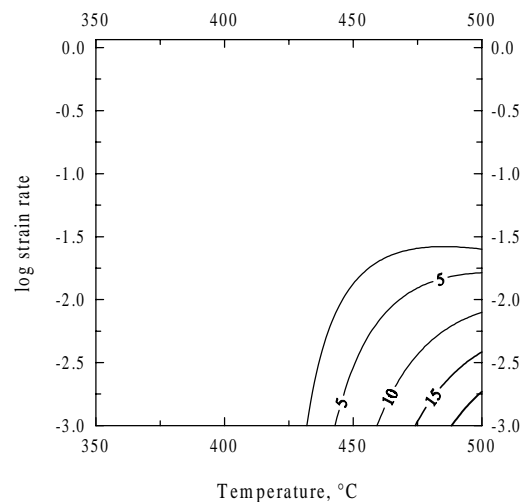


Fig. 3: Map showing the unstable plastic flow region ($\partial\eta / \partial\log\dot{\epsilon} > 0$) for Al-6061/Al₂O₃/10p composite.

In order to validate the predictive damage capability of the procedure based on both the processing and stability maps, and the critical strain rate model, the component was produced under conditions for which internal damage was expected to occur. Closed-die trials were carried out with a die temperature of about 320°C whilst the billet temperature (500°C) and the die speed (18 mm/s) were taken to be equal to the optimal values obtained in the previous section. The FEM simulation performed under these conditions has shown that the workpiece temperature varies from about 320 to 480°C. These conditions correspond to the processing window IV ($T=320-480^{\circ}\text{C}$, $\dot{\epsilon}=0.03-0.3\text{ s}^{-1}$). In this window, despite the plastic flow still being stable (Fig. 3), the probability of occurrence of internal damage is higher than in the window II. This is as a result of the level of the stability parameters of the Eqns 3 and 4 being closer to the instability condition than in window II. Moreover, the processing window IV is characterised by power dissipation efficiency values that are lower than those of the optimum window II; therefore, it can be assumed that the dynamic restoration mechanisms taking place under the temperature and strain rate conditions given by window IV are less effective in recovering ductility than those occurring under the conditions of window II. In the temperature and strain rate conditions given by the processing window IV the critical strain rate model successfully

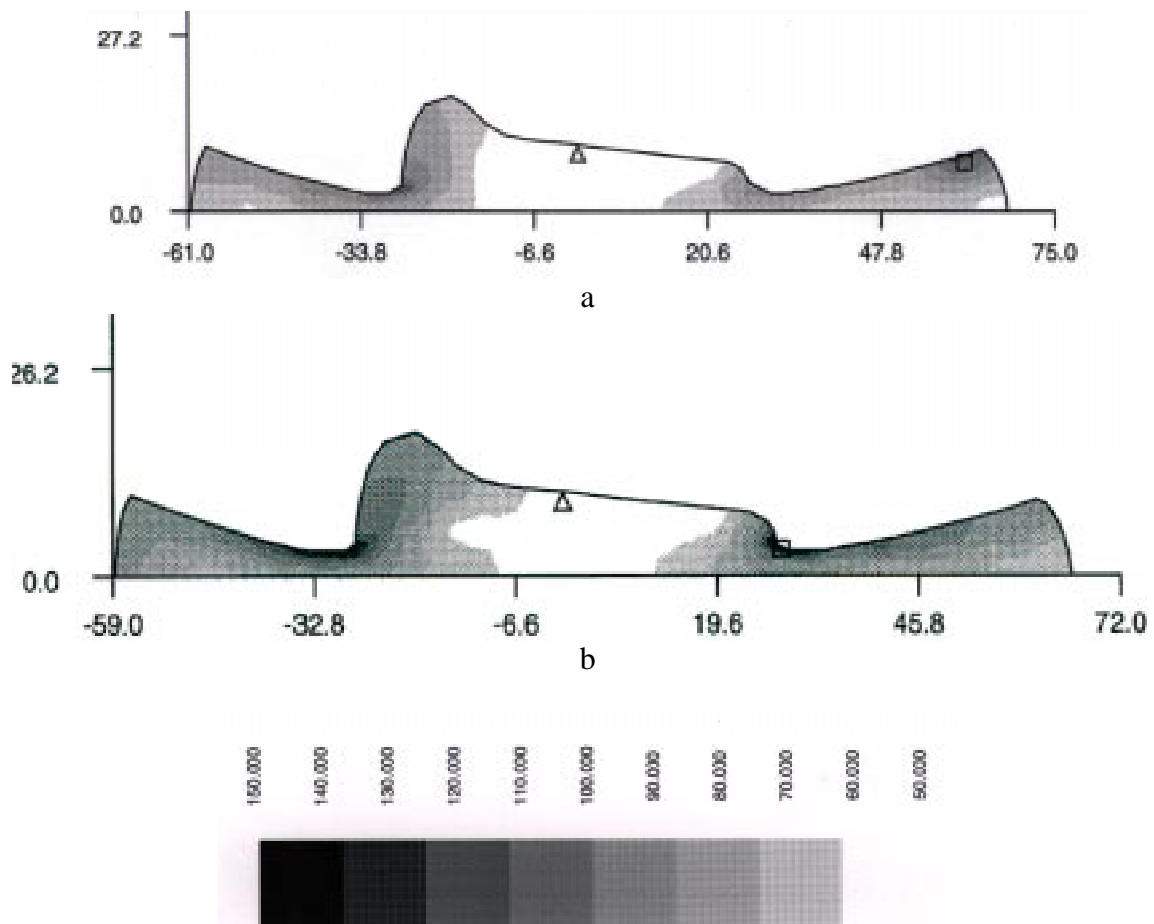


Fig. 4: Maps showing the propensity for damage as characterised by the strain rate/critical strain rate ratio for:

- a die speed of 18 mm/s, initial die and billet temperatures of 450 and 500°C;
- a die speed of 18 mm/s, initial die and billet temperatures of 320 and 500°C.

predicts internal damage in the flash area (Fig. 4.b). This behaviour is confirmed by the experimental damage measurements (Pv% and N/Na parameters) performed in different positions of the crank cross section of the upper transversal arm (Fig. 5), forged at an initial billet temperature of about 500°C, initial lower and upper die temperatures of about 325 and 320°C, respectively, with a die speed of 18 mm/s (Table I). Fig. 6 shows the comparison between measured and predicted damage: both the parameters used to ‘measure’ damage show the same behaviour. A strong correlation is observed between the measured and predicted damage values. The high level of damage in the regions B and G can be attributed to the high values of strain rate in the corners close to the flash. Such values were successfully predicted by the critical strain rate model. In regions C and D the primary cause of damage would appear to be the tensile stress. Whilst areas C and D were indicated by the critical strain rate model to be the next most susceptible to damage, the levels predicted are less satisfactory. As such the model is an excellent *indicator* of zones of likely damage in forgings but a more precise model is required to predict actual damage levels by position. To this end, a particle stress predictor model is under development [5].

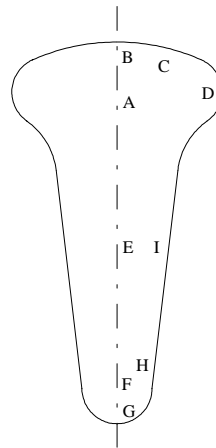


Fig. 5: Positions of the crank cross section of the suspension arm component where damage was measured.

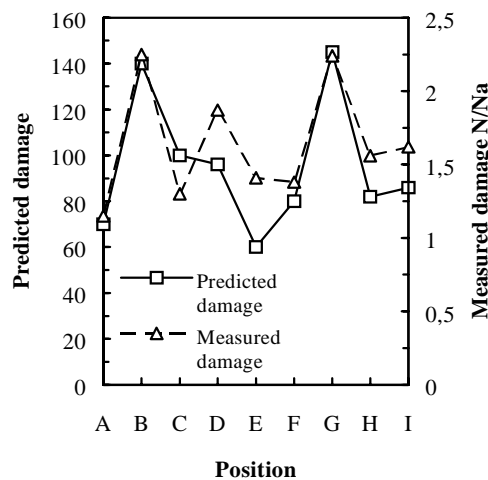


Fig. 6: Comparison between the predicted propensity for damage (arbitrary units) and the measured damage.

Table 1: Damage measured in different positions of the crank cross section of the suspension arm component.

Position	A	B	C	D	E	F	G	H	I
Pv%	18	35	16	27	17	17	30	23	22
N/Na	1.15	2.25	1.30	1.87	1.41	1.38	2.24	1.56	1.62

CONCLUSIONS

A combined procedure based on the processing and stability maps and the critical strain rate model for selecting the optimum parameters to forge a suspension arm component in Al-6061/Al₂O₃/10p composite was proposed. The processing and stability maps were shown to be a very effective guide for optimisation the choice of the forging parameters, in terms of billet and die temperatures and die speed. The utilisation of the critical strain rate damage model allows a more precise and safer choice of the forging conditions and a faster route to forge process design.

ACKNOWLEDGEMENTS

The present work has been carried out with funding from the BRITE-EURAM project “Forging of Aluminium Metal Matrix Composites for Automotive Applications” (Contract n. BRE2-CT92-0177). The authors would like to thank their partners on this project: Risø National Laboratory, Roskilde, Dk (H. Lilholt, T.M. Nilsson, Y.L. Lin), Alcan International Ltd, Banbury, UK (P. Enright, A. Owen, R. Grimes, R. Dickson), Stampal SpA, Caselette, I (G.L. Chiarmetta), U.E.S. Garringtons, Bromsgrove, UK (P. Williams), Centro Ricerche Fiat, Orbassano, I (C. Mus, A. Fuganti, L. Lorenzi), and UMIST, Manchester, UK (F.J. Humphreys, P.B. Prangnell, S.J. Barnes).

REFERENCES

1. Gegel, H.L., “Material Behaviour Modeling - An Overview”, *Proceedings Symposium on “Experimental Verification of Process Models”*, Metals Congress, C.C. Chen Ed., ASM, Metals Park, OH, September 21-23, 1983, pp. 3-32.
2. Prasad, Y.V.R.K., Gegel, H.L., Doraivelu, S.M., Malas, J.C., Morgan, J.T., Lark, K.A. and Barker D.R., “Modeling of Dynamic Material Behaviour in Hot Deformation: Forging of Ti-6242”, *Metallurgical Transaction*, Vol. 15A, 1984, pp.1883-1892.
3. Gegel H.L., Malas, J.C., Doraivelu, S.M. and Shende, V.A., “Modeling Techniques Used in Forging Process Design”, *Metals Handbook*, 9th Edition, ASM, Metals Park, OH, Vol. 14, 1987, pp. 417-438.
4. Withers, P.J., Lorentzen, T. and Stobbs W.M., “A Study of the Relation Between the Internal Stresses and the External Loading Response in Al/SiC Composites”, *Proceedings 7th International Conference on Composite Materials (ICCM-7)*, Beijing, China, 1989, Vol. 1, pp. 429-434.

5. Roberts, S.M., Kusiak, J., Withers, P.J., Barnes, S.J. and Prangnell, P.B., "Numerical Prediction of the Development of Particle Stress in Forging of Aluminium Metal Matrix Composites", *Journal of Materials Processing Technology*, Vol. 60, 1996, pp 711-718.
6. Humphreys, F.J. and Kalu, P.N., "Dislocation-Particle Interaction During High Temperature Deformation of Two-Phase Aluminium Alloys", *Acta Metallurgica*, Vol. 35, 1987, pp. 2815-2829.
7. Withers, P.J., Roberts, S.M. and Kusiak, J., "Computer Aided Design of Forged Metal Matrix Composite Component Microstructures", *Proceedings 4th International Conference on CAD of Advanced Materials and Technology (CADAMT '95)*, Tomsk, Russia, 1995.
8. De Sanctis, A.M., Evangelista, E. and Forcellese, A., "Assessment of the Forging Conditions of 6061/Al₂O₃/10p Using Processing Maps and Stability Criteria, *Key Engineering Materials*, Vol. 127-131, Part 1, Trans Tech Publications, 1997, pp. 525-532.
9. Barnes, S.J., Prangnell, P.B., Roberts, S.M. and Withers, P.J., "The Influence of Temperature on Microstructural Damage During Uniaxial Compression of Aluminium Matrix Composites", *Scripta Metallurgica*, Vol. 33, 1995, pp. 323-329.
10. Syu, D.-G.C. and Ghosh, A.K., "The Effect of Temperature on the Fracture Mechanism in 2014Al/15vol.%Al₂O₃ Composite", *Materials Science and Engineering*, Vol. A184, 1994, pp. 27-35.

HIGH STRAIN RATE SUPERPLASTICITY OF CERAMIC PARTICULATE REINFORCED ALUMINUM COMPOSITES AND THE FABRICATION PROCESSING

Tsunemichi Imai¹, Takeo Hikosaka², Gilles L'Esperance³, Bande Hong³, and Daming Jiang⁴

¹ National Industrial Research Institute of Nagoya, 1 Hirate-cho, Kita-ku, Nagoya 462, Japan

² Industrial Research Institute, Aichi Prefectural Government Nishishinwari, Hitotsuki-cho, Kariya City 448, Japan

³ Ecole polytechnique de Montreal, P.O.Box 6079, Station "A", Montreal (Quebec) Canada H3C 3A7

⁴ Harbin Institute of Technology, Harbin 150001, P.R.China

SUMMARY: Metal matrix composites (MMC) fabricated by a vortex method, squeeze casting and PM method have already been applied to automobile engine components, satellite components and even for semi-conductor packings. It is important to clarify deformation mechanism involved in high strain rate superplasticity (HSRS) which exhibits a total elongation of 250~600% at strain rates of about 0.1~10 s⁻¹ and to establish a cost-effective fabrication processing for HSRS materials.

An AlN/1N90 PM pure aluminum composite were hot-rolled after extrusion. The deformation mechanism of the HSRS were investigated. A maximum tensile elongation of about 200% of the AlN/1N90 Al composite was obtained in a strain rate range of 0.1~0.3 s⁻¹ and at 913K.

The results indicate that the optimum strain rate at which a maximum elongation is obtained is related to the fine grain size and that the primary deformation mechanism in HSRS is fine grain boundary sliding.

Effect of hot rolling condition on the superplastic characteristics of the SiCp/6061 Al alloy composite fabricated by a vortex method before squeeze casting and extrusion were examined. The composite was hot-rolled at 573K with a rolling strain per passes of 0.05~0.3 and exhibits a *m* value of 0.4~0.6 and a total elongation of 200~300% in the strain rate range of 0.08~1.3 s⁻¹ at 853K. The optimum rolling temperature to produce a *m* value of more than 0.4 and a total elongation of 300% were 573, 673 and 723K.

TEM observations indicate that the SiC/6061 Al composite has a grain size of about 2 μ m with dispersed fine dispersoids after hot rolling. There was no major microstructure variation during the superplastic deformation.

KEYWORDS: superplasticity, SiC, 6061 aluminum, composite, a vortex method, hot rolling

INTRODUCTION

High strain rate superplasticity (HSRS) in ceramic whisker or particulate reinforced aluminum alloy composites is expected to offer an efficiently near-net shape forming technique to automobile, aerospace, and even semi-conductor industries, since the HSRS composites usually exhibit a total elongation of 250~600% at a high strain rate of about $0.1\sim 10\text{ s}^{-1}$ [1-12] as shown in Table 1.

Metal matrix composites (MMC) fabricated by squeeze casting, a vortex method, compocasting, a powder metallurgical (P/M) method and spray deposition could produce HSRS. Among fabrication processing of MMC, casting processes such as squeeze casting, compocasting and a vortex method are cost effective so that composites fabricated by these processing methods have already been applied to automobile engine components, satellite components, and so on. A serious problem of cast aluminum alloy composites reinforced by relatively larger size ceramic particles is their low tensile ductility and fracture toughness at room temperature, since the composite just after being fabricated by a vortex method includes a lot of defects. Therefore, it is important to control fine microstructure for any aluminum alloy and ceramic system composites fabricated by casting processing and to produce the HSRS.

It has been pointed out that primary deformation mechanisms of the HSRS composites include grain boundary sliding, interfacial sliding at liquid phase and dynamic recrystallization because the decreasing of a grain size is related to the increasing of the optimum strain rate at which maximum total elongation of the HSRS composites is obtained and also the HSRS usually produces above or below solidus temperature of the matrix [1-12]. An interfacial sliding at liquid phase is expected to take an important role as accommodation mechanism to achieve larger elongation in the HSRS composites. It has not yet, however, made clear how interfacial sliding at liquid phase could promote the HSRS phenomena. It is necessary, therefore, to investigate effect of testing temperature on superplastic behavior of pure aluminum based composite to make clear deformation mechanism of HSRS.

The purpose of this study is to investigate effect of testing temperature on the HSRS in a AlN particulate reinforced 1N90 pure aluminum composites and to make clear the effect of hot rolling condition after extrusion and squeeze casting on HSRS behavior of a SiC particulate reinforced aluminum alloy composite fabricated by a vortex method. In addition, the deformation mechanism of the HSRS in the composite will also be discussed.

EXPERIMENTAL PROCEDURE

AlN particle (average particle size of $1.35\mu\text{m}$) and α -SiC particles (the average particle size of $0.6\mu\text{m}$, the chemical composition by weight%: 94.0SiC, 1.3SiO₂, 1.53Si, 1.05C, 0.09Fe, 0.02Al) were used as reinforcement material. Table 2 indicates chemical composition of AlN particle and 1N90 pure aluminum powder. Chemical compositions of 6061 aluminum alloy used as matrix and of the SiC/6061 Al composite fabricated by a vortex method are shown in Table 3. AlN/1N90 Al composite was sintered with the pressure of 200 MPa under 773K for 20 minutes and extruded with the extrusion ratio of 44 at 773K.

Table :1 Superplastic characteristics of aluminum matrix composites

Fabrication Processing	Materials *1	Vf*2	Temp. (K)	Strain rate(1/s)	Elongation (%)	m value	Ref.
PM+Ex	SiCw/2124	0.20	798	0.3	300	0.3	1
	Si3N4w/2124	0.20	798	0.2	250	0.5	2
	Si3N4w/6061	0.20	818	0.2	600	0.5	3
	Si3N4w/7064	0.20	798	0.8	160	0.34	4
	Si3N4p/6061	0.20	818	0.1	600	0.5	5
PM+Ex +Roll	AlNp/6061	0.15	873	0.1~1.0	300~500	0.5	6
	SiCp/6061	0.175	853	0.1	375	0.5	7
	AlNp/1N90	0.15	913	0.1	200	0.3	8
	TiCp/2014	0.15	818	0.8	200~300	0.23	9
	TiCp/6061	0.15	873	0.8	200	0.3	9
	TiB2p/6061	0.15	873	0.1~0.8	200	0.26	10
	TiB2p/2014	0.15	818	0.1~0.8	200	0.25	10
SQ+Ex	Si3N4w/6061	0.25	818	0.07	170	0.3	11
	Si3N4w/2024	0.27	773	0.17	175	0.5	12
	SiCw/7075	0.27	773	0.1	---	0.3	13
	SiCw/6061	0.20	823	0.17	300	0.3	14
	SiCw/2324	0.20	793	0.05	520	0.47	15
Vor+Ex	SiCp/2024	0.20	515	0.0004	685	0.4	16
Vor+SQ+Ex+Roll	SiCp/6061	0.20	853	0.2	200	0.3	17

Fabrication processing:SQ:Squeeze casting, Vor:Vortex method, Ex:Extrusion, Roll:Rolling, PM:Powder metallurgy

*1:w:whisker, p:particle, *2:Vf:volume fraction of reinforcement

Table 2 Chemical composition of 1N90 pure aluminum and AlN particle

materials	Fe	Si	Cu	Mg	Ni	Ti	Mn	Zn	O	N	C	d50
1N90	ppm 43	ppm 41	ppm 6	ppm 3	ppm 3	ppm 2	ppm 5	ppm 17	ppm			45
AlN	ppm 50	ppm 100							wt% 1	wt% 33.8	wt% 0.2	1.35

AlN:a carbothermal nitridation d_{50} (μm)

Table 3 Chemical composition of 6061 Al matrix and SiC/6061 Al composite

Materials	Si	Cu	Fe	Zn	Mg	Mn	Cr	Ti
6061	0.68	0.29	0.20	0.14	0.75	0.03	0.07	0.02
SiC/6061	*8.67	0.25	0.40	0.16	0.90	0.02	0.06	0.16

*:The Si content includes the value of SiC particle

(wt%)

Molten 6061 aluminum alloy heated at 1023K was stirred with the heated SiC particles and with 0.3wt%Ca and 0.15%Sb at a rotating speed of 500~700rpm in a crucible for 10.8Ksec. Also, 0.3wt%Mg was added to 6061 aluminum alloy of 40Kg to compensate for evaporation during stirring so that the final Mg content in the matrix became 0.90wt%. Ti was added as Al-5mass%Ti-B alloy. The volume fraction (V_f) of SiC particle was about 0.20. The as-cast composite was further forged at 1123K in air under an applied pressure of 100MPa by a squeeze casting machine in order to remove the defects.

Thermomechanical processing, including further hot rolling, was used to produce the HSRS composite. Hot rolling was carried out at 923K for AlN/1N90 Al PM composite. The hot extrusion for SiC/6061 Al composite was performed at 573 and 673K. Rolling strain per pass used 0.1 and the reheating time between each rolling pass was about 5 minutes. The final thickness of the hot-rolled composite was about 0.75mm (total strain was about 2.4). Tensile specimens with a 4mm gage width and a 5.5mm gage length were made. The AlN/1N90 Al composite were pulled at 873, 893, 913, 923K and the SiC/6061 Al composite was pulled at 853K and at strain rates ranging from 1×10^{-3} to 2 s^{-1} . The microstructure and fracture surface of the sample were examined by TEM and SEM.

RESULTS AND DISCUSSION

Microstructure

Fig.1 shows SEM microstructures of the SiC/6061 Al composites just after hot rolling. SiC particles are dispersed homogeneously in the hot-rolled SiC/6061 Al composites, although a vortex method is so difficult processing as to make fine SiC particles of $0.6\mu\text{m}$ disperse homogeneously and reinforcement-free aluminum alloy layer is present. The fact that SiC particles are dispersed along grain boundaries probably restrains grain growth during hot rolling.

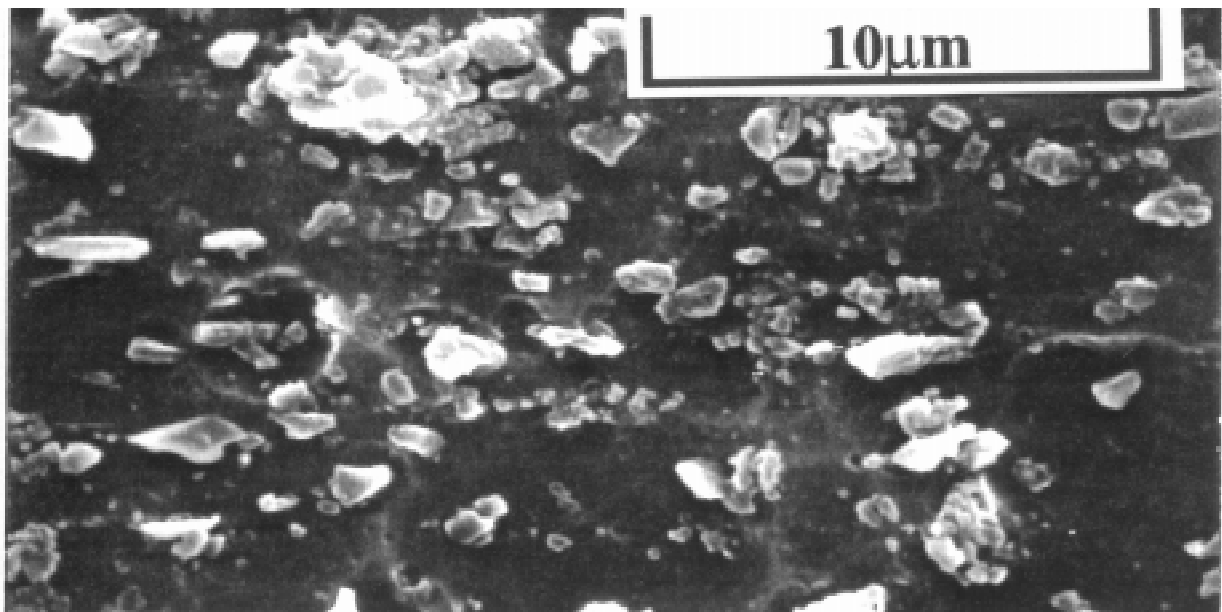


Fig.1: SEM microstructures of SiC/6061 Al composite.

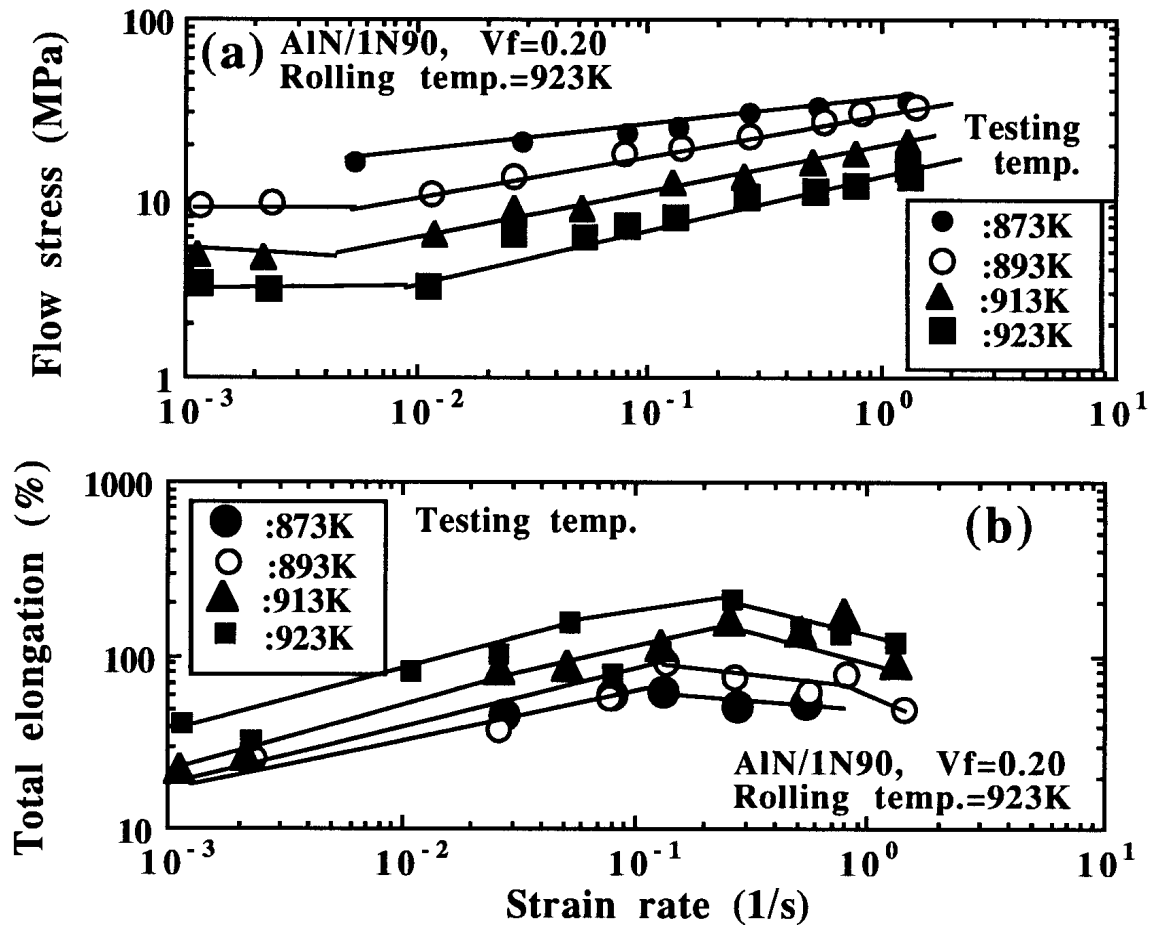


Fig.2: Superplastic characteristics of AlN/1N90 Al composite with $V_f=0.20$

HSRS of AlN/1N90 Al Composite

Flow stress (σ) and true strain rate ($\dot{\epsilon}$) in a superplastic material are related via the equation $\sigma = K\dot{\epsilon}^m$ where K is a constant, and m is the strain rate sensitivity value. The m value of a superplastic material is normally greater than 0.3 because a higher m value is expected to suppress neck formation and leads to high tensile elongation.

Superplastic characteristics of the AlN/1N90 Al composite with $V_f=0.20$ are shown in Fig.2(a), (b) as a function of testing temperature. The composite deformed at 873, 913 and 923K indicates the m value of about 0.3 in the strain rate range higher than $0.01 s^{-1}$ and also threshold stress appears in the strain rate range less than $0.01 s^{-1}$. The maximum tensile elongation of about 200% in the composite was obtained at the strain rate of about $0.3 s^{-1}$ and at 923K which is just below melting temperature of pure aluminum. At strain rates higher than $1.0 s^{-1}$, the elongation value of the AlN/1N90 Al composite deformed at 923K begins to decrease although the m value still keeps 0.3.

The results indicate that the AlN/1N90 pure aluminum composite made by a powder metallurgical method before extrusion and rolling could produce HSRS by grain boundary sliding.

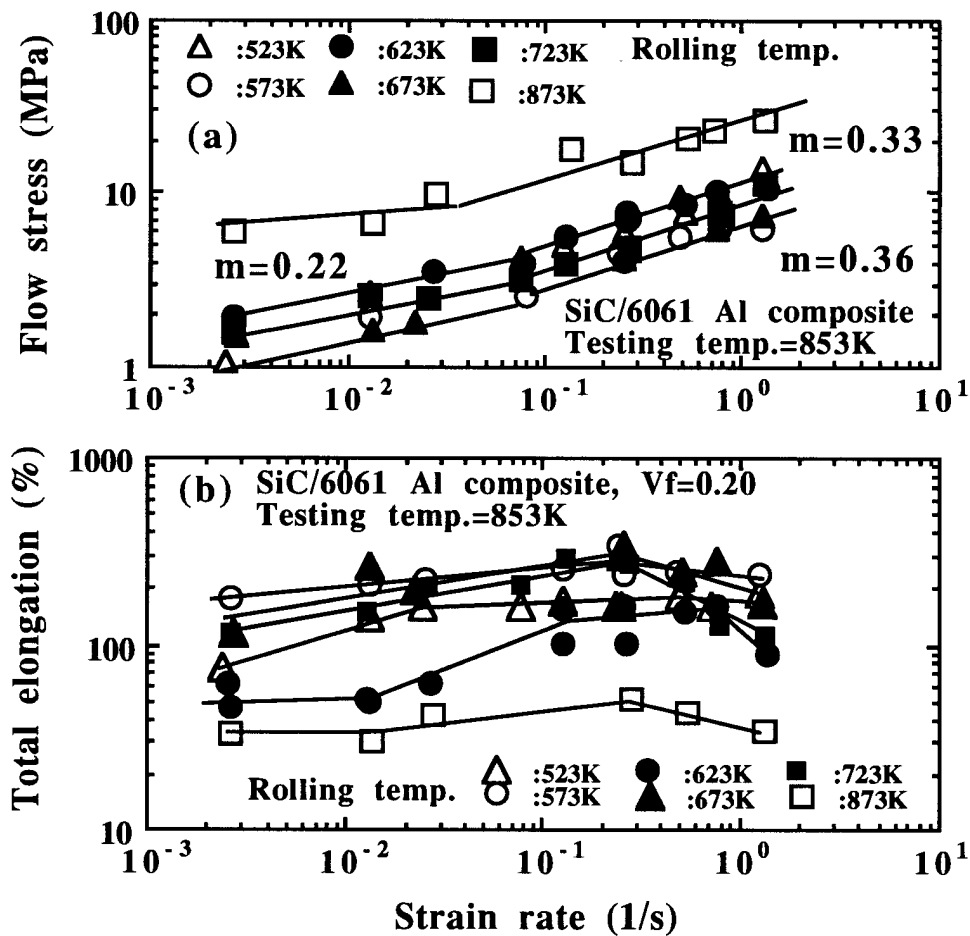


Fig.3: Effect of rolling temperature on (a) the flow stress and (b) on the total elongation of the SiC/6061 Al composite hot-rolled after extrusion and squeeze casting

Fig.3(a) shows the flow stress-strain rate relationship of the SiC/6061 Al composite fabricated by a vortex method and squeeze casting before extrusion and hot rolling as a function of rolling temperature. The flow stresses increase with increasing strain rate and the m value becomes more than 0.3 in the strain rate region from 0.1 to 1.3 s^{-1} . The flow stress in the case of 873K rolling became higher as compared with those of the composites hot-rolled below 723K because reaction between matrix and SiC may have occurred. The composites hot-rolled at 573 and 623K give lowest flow stresses. The composite made by the vortex method shows a lower m value of about 0.2 in the strain rates of less than 0.08 s^{-1} .

Total elongations of the SiC/6061 Al composites hot-rolled after extrusion, are shown in Fig. 3(b). The composites hot-rolled at 573, 623 and 723K exhibit 200~300% in the strain rate range of $0.01 \sim 0.8 \text{ s}^{-1}$. The total elongation of the composite hot-rolled at 873K decreases to less than 50% due to reaction with SiC particles. The lower total elongation of the composite hot-rolled at 523K and 623K might be related to damage produced near or at the interface during hot rolling. For rolling temperatures of 573, 673 and 723K, the highest elongation were obtained for a strain rate of about 0.1 s^{-1} .

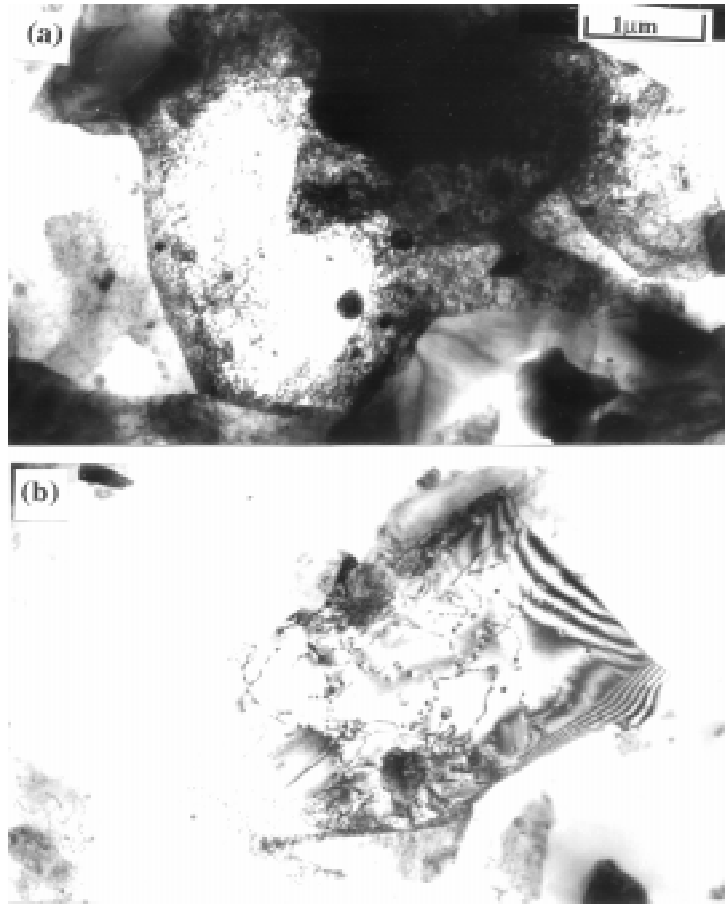


Fig.4: TEM microstructures of (a) the SiC/6061 aluminum alloy composite heated at 853K and (b) the SiC/6061 deformed superplastically

Deformation Mechanism of HSRS

Several possible deformation processes, including fine grain boundary sliding, interfacial sliding at liquid phase, and dynamic recrystallization, are expected to take place during HSRS. The m value of more than 0.3 at a relatively high strain rate of about $0.1s^{-1}$ in the AlN/1N90 Al composites indicates that the observed HSRS phenomena in the both composites occur predominantly by fine grain boundary sliding, since melting temperature of AlN/1N90 pure aluminum composite is 923.5K and the matrix in the AlN/1N90 Al composite hot-rolled after extrusion consists of a fine grain of about $2\mu m$. Fig.4(a) shows TEM microstructure of the SiC/6061 Al composite fabricated by a vortex method, squeeze casting before extrusion and rolling. TEM micrograph of the SiC/6061 Al composites in Fig.4(b) deformed superplastically indicate that the composite consists of a fine grain of about $2\mu m$ and the grain size is thought to be stable during and after superplastic deformation.

Fig.5 shows the fracture surfaces of the SiC/6061 Al composite ($\dot{\epsilon}=0.13s^{-1}$ and $e_f=342\%$) pulled at 853K. The fracture surface of the SiC/6061 Al composites shows a partially melted matrix and a lot of filaments. The solidus temperature of the SiC/6061 composite was 836K. The solidus and melting temperature of the composite decreases due to the Mg, Si, Cu segregation at grain boundaries [9-12], so that semi-solid phase is thought to exist at the interfaces between matrix and SiC particles during superplastic deformation at 853K. The filaments could be related to a semi-solidus phase at or near an interface of the composite

since this could be elongated significantly during hot rolling and superplastic deformation [9-12]. Table 3 indicates that the SiC/6061 Al composite made by a vortex method includes a lot of alloy elements which decrease the melting point of the aluminum alloy matrix. The diameters of the filaments in the SiC/6061 Al composite are very fine as the relative distance between the fine SiC with average particle size of $0.6\mu\text{m}$ is narrow. It is thought, therefore, that the interfacial sliding at the liquid phase contributes to HSRS in addition to grain boundary sliding.

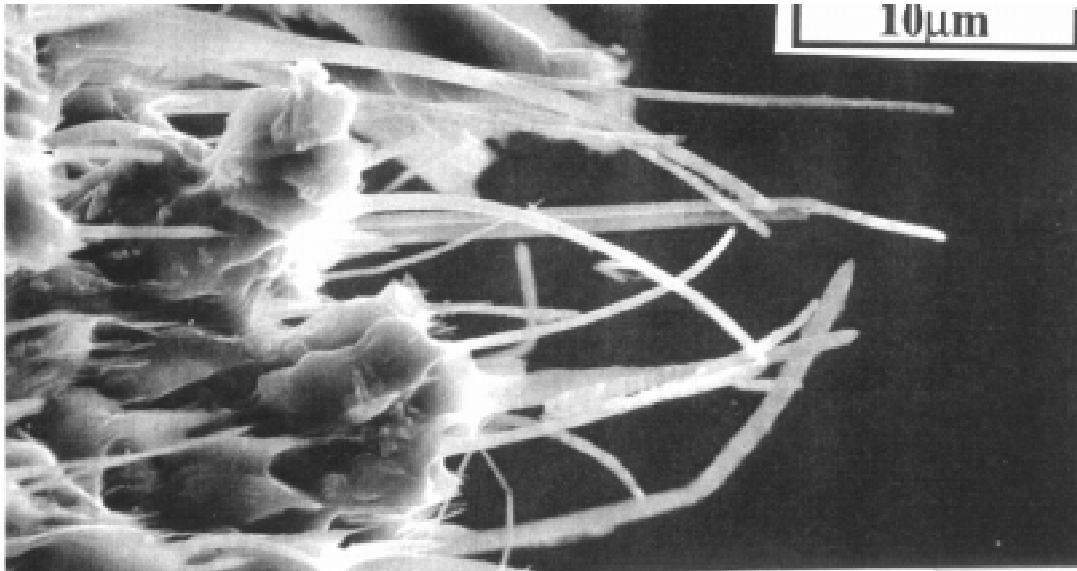


Fig.5: Fracture surface of the SiC/6061 aluminum alloy composite hot-rolled and extruded after vortex & squeeze castings

CONCLUSIONS

The superplastic characteristics of AlN/1N90 Al composite made by a powder metallurgical method and the SiC/6061 Al alloy composite fabricated by a vortex method before squeeze casting, hot-rolled after extrusion, were investigated.

- (1) The AlN/1N90 PM Al composite with $V_f=0.20$ indicates the m value of about 0.3 in the strain rate range higher than 0.01 s^{-1} at 873, 913 and 923K.
- (2) The maximum total elongation of about 200% in the AlN/1N90 PM Al composite with $V_f=0.20$ was obtained at the strain rate of about 0.3 s^{-1} and at 923K. The result indicates that in the case of AlN/1N90 Al composite, the HSRS could produce without help of interfacial sliding at liquid phase.
- (3) The SiC/6061 Al composites hot-rolled in rolling strain per passes of 0.1 and at 573K exhibits m values of 0.4~0.6 and total elongations of 200~300% at 853K in the strain rate of $0.08\sim 1.3\text{ s}^{-1}$.
- (4) The AlN/1N90 and the SiC/6061 Al composite has a fine grain of about $2\mu\text{m}$ and the fine grain size did not change after superplastic deformation.
- (5) The fracture surface of the SiC/6061 Al composite has a partially liquid phase and shows filaments. It is thought that in the case of the SiC/6061 Al composite, interfacial sliding at the liquid phase contributes to the HSRS in addition to grain boundary sliding in these composites.

REFERENCES

1. T.G.Nieh, C.A.Henshall and J.Wadsworth, "Superplasticity at High Strain Rate in A SiC Whisker Reinforced Al Alloy"*Scripta Metall.et Mat.*, Vol.18, No.12,1984, pp.1405-1408.
2. T.Imai, M.Mabuchi, Y.Tozawa and M. Yamada, "Superplasticity in β -silicon nitride whisker reinforced 2124 aluminum composite"*J.Mat.Sci.letters* vol.9, 1990, pp.255.
3. M.Mabuchi, T.Imai, K.Kubo, H.Higashi,Y.Obada and T.Tanimura, "Superplasticity in as-extruded Si₃N₄/6061 aluminum composites processed at a ratio of 100:1", *Materials Letters*, vol.11, 1991, pp.339.
4. T.Imai, G.L'Esperance & B.D.Hong, "High Strain rate Superplasticity of AlN Particulate Reinforced Aluminum Alloy Composites", *Scripta Metall. et Mat.*, Vol.31, No.3, 1994, pp.321-326.
5. M.Mabuchi, K.Higashi, Y.Okada, S. Tanimura, T.Imai and K.Kubo, "Very High Strain-Rate Superplasticity in a Particulate Si₃N₄/6061 Aluminum composite"*Scripta Metall. et Mat.* Vol.25, 1991, pp.2517.
6. T. Imai, G.L'Esperance, B.D.Hong & J.Kusui, "High Strain Rate Superplasticity of AlN and TiC particulate reinforced Aluminum Alloy Composites", *Proceedings of ECCM-6*, Edited by A.R.Bunsell, A.K.Kelly & A.Massianh, 1993, pp.533.
7. T.G.Nieh, T.Imai, J.Wadsworth and S.Kojima, "High Strain Rate Superplasticity of a Powder Metallurgy SiC Particulate Reinforced 6061 Al Composite(6061/SiC/17.5p) ", *Scripta Metall. et Mat.*, Vol.31, No.12 (1994)pp.1685-1690.
8. T.Imai, G.L'Esperance, B.D.Hong and S.Kojima, "High Strain Rate Superplasticity of AlN Particulate Reinforced 1N90 Pure Aluminum Composite"*Scripta Metall. et Mat.*, Vol.33, No.8, 1995, pp.1333-1338.
9. T. Imai, G. L'Esperance, B.D.Hong, Y.Tozawa, "Fabrication and properties of TiC particulate reinforced aluminum alloy composite foils"*J.Mat. Scie. Letters*, Vol.13, 1994, pp.963-965.
10. T. Imai, G. L'Esperance, B.D.Hong, Y.Tozawa, "High Strain Rate Superplasticity of TiB₂ Particulate Reinforced Aluminum Alloy Composites", *ibid*, Vol.14, 1995, pp.373-376.
11. I.Tochigi, T.Imai and K.Ai, "High Temperature Mechanical Properties of A β -Si₃N₄ whisker reinforced aluminum alloy composite produced by squeeze casting", *Scripta Metall. et Mat.*, Vol.32, No.11, 1995, pp.1801-1806.
12. Suk-Won Lim and Y.Nishida, "Superplasticity of Whisker Reinforced 2024 Aluminum Alloy Composites Fabricated by Squeeze casting"*Scripta Metall. et Mat.*, Vol.32, No.12, 1995, pp.1911-1915.

13. Suk-Won Lim and Y.Nishida, "High Strain Rate Superplasticity of Si₃N₄ Whisker Reinforced 7075 Alloy Matrix Composite Fabricated by Squeeze casting", *ibid.*, Vol.32, No.11, 1995, pp.1821-1825.
14. H.Xiaoxu, L.Qing, Ciki Yao and Y.Mei, "Superplasticity in a SiCw-6061 Al Composite"*J.Mat. Scie. Letters*, Vol.10, 1991, pp.964-966.
15. M.Kon, J.Kaneko and M.Sugamata, *J.Japan STP*, Vol, 35, 1994, pp.823-828.
16. J.Pilling, "Superplasticity in Aluminium Base Metal Matrix Composites, *Scripta Metall.*, Vol.13, No.8, 1989, pp.1375-1380.
17. T.Hikosaka, T.Imai, T.G.Hieh and J.Wadsworth, "High Strain Rate Superplasticity of A SiC Particulate Reinforced Aluminum Alloy Composites by A Vortex Method", *Scripta Metall. et Mat.*, Vol.31, No.9, 1994, pp.1181-1186.

FABRICATION AND PROPERTIES OF REACTION SQUEEZE CAST (AL₂O₃ • SiO₂+Ni)/AL HYBRID METAL MATRIX COMPOSITES

Sangsuck Kim¹, Sungmin Kang¹, Ikmin Park¹, Sungjoon Kim², Ildong Choi³

¹*Dept. of Metallurgical Engineering, Pusan National University, Pusan 609-735, Korea*

²*Korea Institute of Machinery and Materials, Changwon 641-010, Korea*

³*Dept. of Mat. Eng., Korea Maritime University, Pusan 606-791, Korea*

SUMMARY: Mechanical properties of (10%Al₂O₃ • SiO₂+5%Ni)/Al hybrid composites fabricated by the reaction squeeze casting were compared with those of (15%Al₂O₃ • SiO₂)/Al composites. Al-Ni intermetallic compounds (10~20 μm) formed by the reaction between nickel powder and molten aluminum were uniformly distributed in the Al matrix. These intermetallic compounds were identified as Al₃Ni using X-ray diffraction analysis and they resulted in beneficial effects on room and high temperature strength and wear resistance. Microhardness values of (10%Al₂O₃ • SiO₂+5%Ni)/Al hybrid composite were greater by about 100Hv than those of (15%Al₂O₃ • SiO₂)/Al composite. Wear resistance of (10%Al₂O₃ • SiO₂+5%Ni)/Al hybrid composites was superior to that of (15%Al₂O₃ • SiO₂)/Al composites regardless of the applied load. Tensile tests were carried out at room temperature and 300°C. While tensile and yield strength of (10%Al₂O₃ • SiO₂+5%Ni)/Al hybrid composites were greater at both temperature, strength drop at high temperature was much smaller in hybrid composites.

KEYWORD: reaction squeeze cast, hybrid MMC, wear resistance, room and high temperature strength

INTRODUCTION

The application of Al alloy metal matrix composites for automotive parts has been limited due to softening of Al matrix and interfacial reaction between matrix and reinforcement at the high temperature (more than 300°C)[1-2]. Recently the new reaction squeeze casting techniques have been proposed to overcome the deterioration of Al matrix at high temperatures. Intermetallic compounds formed by the reaction between aluminum melt and the metal powder (Fe,Cu,Ni) or the metal oxide powder (TiO₂, NiO) during the squeeze casting are very effective for improving the mechanical properties such as hardness, wear resistance, and high temperature strength[3-4].

Intermetallic compounds can be formed by the processes such as plasma arc melting, powder metallurgy, plastic deformation and reaction squeeze casting. Plasma arc melting is difficult to obtain a proper composition in the formation of Ti-Al type intermetallic compounds by the difference of melting point. Powder metallurgy is apt to contaminate the surface of the

powders by the oxygen adsorption. Plastic deformation must be performed at the high temperature and has difficulty in fabricating complicated shape. However, reaction squeeze casting which is newly applied to form intermetallic compounds has advantages of low cost, simple process, low product defects, mass producibility of near-net-shape parts, and save energy (form easily intermetallic compounds near the melting point of low melting metal).

In the present study, (10%Al₂O₃ • SiO₂+5%Ni)/Al hybrid composites were fabricated with reaction squeeze casting technique with a variation of pouring temperature of the pure aluminum melt. To understand the reaction characteristics, the differential thermal analysis of the reaction squeeze cast samples was performed. Microstructure has been analyzed by the SEM, XRD and mechanical properties such as bending strength, wear properties, elevated temperature properties have been characterized for the (10%Al₂O₃ • SiO₂+5%Ni)/Al hybrid composites. Microstructure and mechanical properties of (15%Al₂O₃ • SiO₂)/Al composites and Al have been also analysed for comparison.

EXPERIMENTAL

Pure aluminum (purity 99.9%) was chosen for matrix, Kaowool short fibers (amorphous structure with average dimensions of 2.8μm in diameter and 200°C in length, 47%Al₂O₃-53%SiO₂ : Isolite Co.) and pure nickel powders (purity 99.9%, 2-3 in diameter) were used as reinforcements for the fabrication of reaction squeeze cast (10%Al₂O₃ • SiO₂+5%Ni)/Al hybrid composites. The hybrid preforms were prepared by employing the vacuum suction method. The mixture of reinforcements, 3% silica colloidal inorganic binder and 2% starch organic binder was dispersed in distilled water and consolidated with vacuum suction method [5]. The aiming volume fraction of reinforcement in the preform (20 x 32 x 84 mm) was about 15% and preform was roughly controlled with vacuum suction pressure. Preforms were dried at room temperature for 3 days and at 110°C for 7 days. Reaction squeeze casting was carried out by pouring the molten aluminum of 750°C, 800°C, 850°C and 900°C into the hybrid preform placed in the mold preheated to 400°C. Preform was also preheated to 400°C to improve the wettability between matrix and reinforcements. After pouring molten aluminum, pressure of 35 MPa was applied within 7 seconds, and was held for 60 seconds. SEM, XRD and DTA analyses were carried out for the investigation of the microstructure. For the composites fabricated by pouring the molten aluminum of 800°C, microhardness test, three-point bending test, wear test, and tensile test were carried out to characterize the mechanical properties of composites.

RESULTS AND DISCUSSION

Microstructure

Figure 1(a) and 1(b) are SEM micrographs of the Al₂O₃ • SiO₂ and the Al₂O₃ • SiO₂ + Ni preform respectively. Regardless of the size of reinforcement in Figure 1(b), both reinforcements of Al₂O₃ • SiO₂ short fibers and Ni powders were uniformly distributed and thus preforms were successfully prepared by the vacuum suction method. Figure 2(a) and 2(b) show SEM microstructures of the (15%Al₂O₃ • SiO₂)/Al composite and the (10%Al₂O₃ • SiO₂+5%Ni)/Al hybrid composite fabricated from the preforms shown in Figure 1. Reinforcements in composites were uniformly distributed and revealed no casting defects.

SEM microstructure for the hybrid composites in Figure 2(b) revealed that Al-Ni intermetallic compounds(10~20 μm) formed by the reaction between nickel powder and molten aluminum.

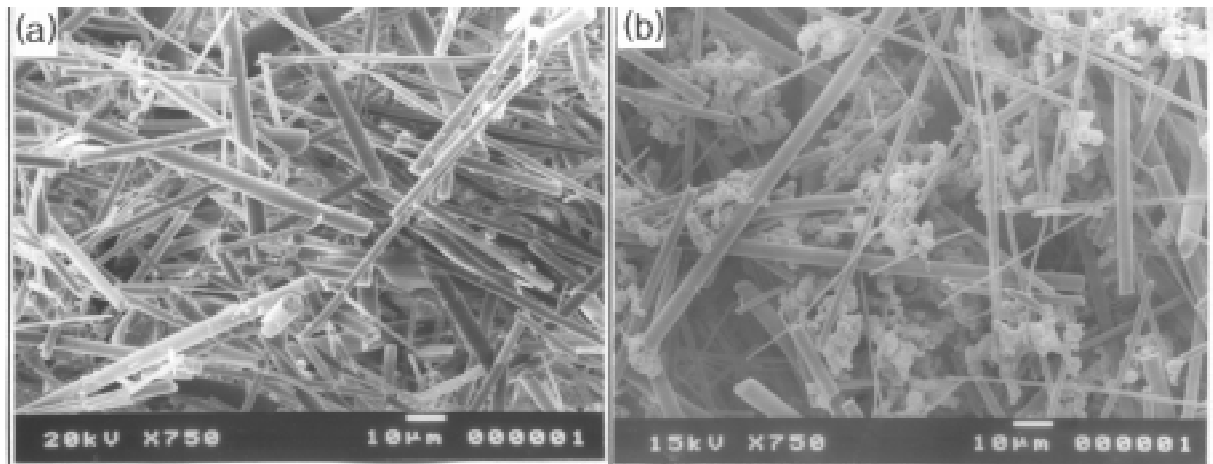


Figure 1. The preforms fabricated by the vacuum suction method with the reinforcement of (a) $\text{Al}_2\text{O}_3 \bullet \text{SiO}_2$ (b) $\text{Al}_2\text{O}_3 \bullet \text{SiO}_2 + \text{Ni}$

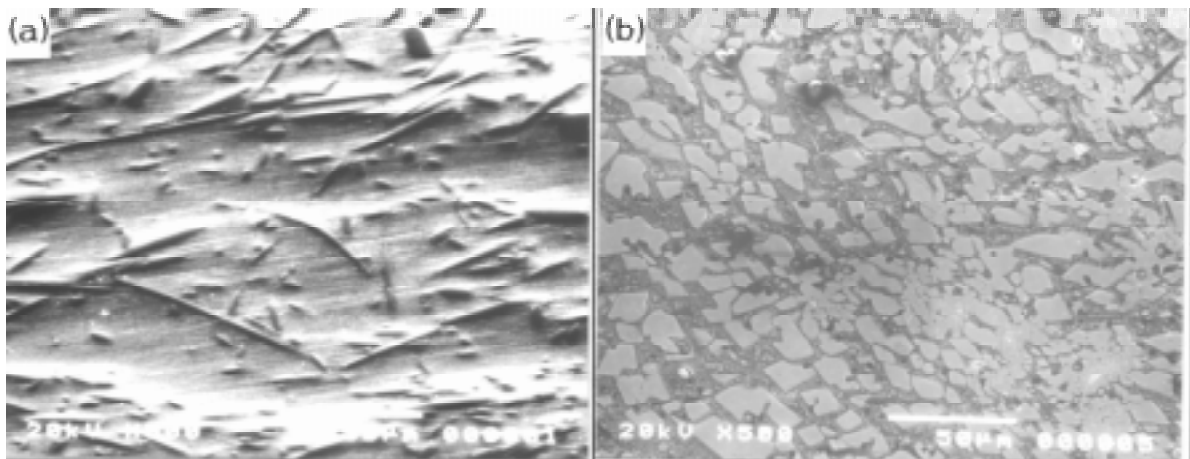


Figure 2. SEM microstructure of squeeze cast Al matrix composites. (a) $(15\% \text{Al}_2\text{O}_3 \bullet \text{SiO}_2)/\text{Al}$ (b) $(10\% \text{Al}_2\text{O}_3 \bullet \text{SiO}_2 + 5\% \text{Ni})/\text{Al}$

According to thermodynamics, the equation of the reaction between nickel powder and molten aluminum can be written as :



The phases Al_xNi_y can be Al_3Ni , Al_3Ni_2 and AlNi intermetallic compounds according to the reaction condition. The DTA curve of the $(10\% \text{Al}_2\text{O}_3 \bullet \text{SiO}_2 + 5\% \text{Ni})/\text{Al}$ hybrid composite is shown in Figure 3. There are two peaks related to phase transitions. The exothermic peak appearing in the range of $629\text{-}645^\circ\text{C}$ and $855\text{-}863^\circ\text{C}$ is related to the Al_3Ni and Al_3Ni_2 formation respectively. Detection of formation temperature for Al-Ni intermetallic compounds by using differential thermal analysis is coincide with the Al-Ni binary phase diagram[6]. However, the X-ray diffraction patterns of Figure 4 are identified with a major

portion of the Al_3Ni and free of other compounds regardless of the pouring temperature ($750^\circ C, 800^\circ C, 850^\circ C, 900^\circ C$) of the molten aluminum. The reason of this phenomenon could be explained by the formation temperature of the Al-Ni type intermetallic compounds. The Al_3Ni intermetallic compounds are formed more easily than the other compounds due to their lower formation temperature.

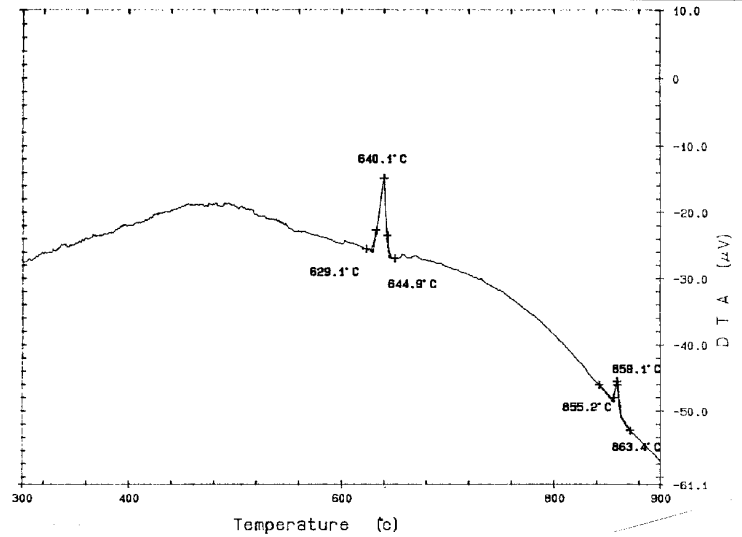


Figure 3. Differential thermal analysis scan for the $(10\%Al_2O_3 \bullet SiO_2+5\%Ni)/Al$ composites.

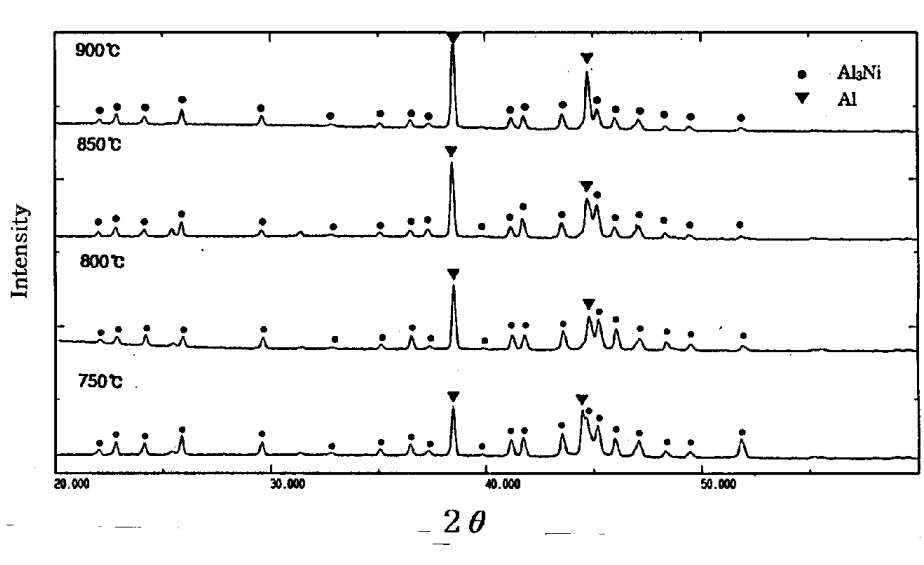


Figure 4. X-ray diffraction pattern of $(10\%Al_2O_3 \bullet SiO_2+5\%Ni)/Al$ composites according to pouring temperature of molten aluminum.

Mechanical properties

The results of the microhardness test and three-point bending test are summarized in Figure 5 for squeeze cast Al, $(15\%Al_2O_3 \bullet SiO_2)/Al$ composite and the $(10\%Al_2O_3 \bullet SiO_2+5\%Ni)/Al$ hybrid composite. Microhardness and bending strength of $(10\%Al_2O_3 \bullet SiO_2+5\%Ni)/Al$ hybrid composite are higher than those of $(15\%Al_2O_3 \bullet SiO_2)/Al$ composite 100Hv, 66 MPa, respectively. The enhancement of the bending strength is not as high as that of the

microhardness because the hybrid composite containing the intermetallic compounds is somewhat brittle as shown in the result of three-point bending test in Figure 6.

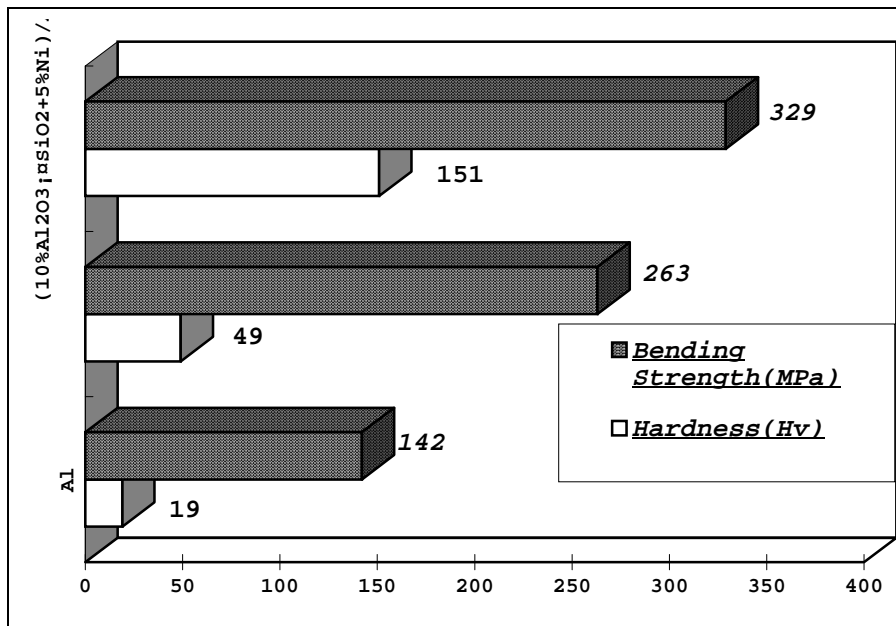


Figure 5. Hardness(Hv) and bending strength(MPa) of squeeze cast Al and Al matrix composites.

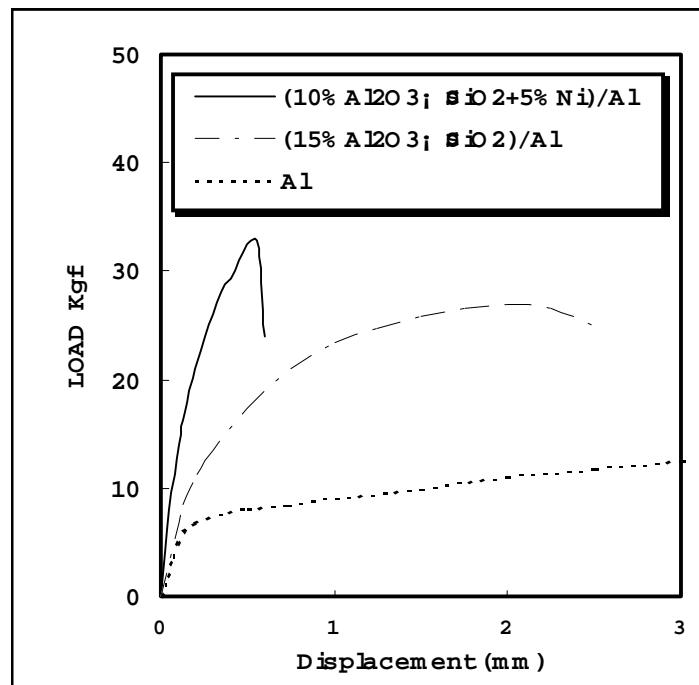


Figure 6. Load-Displacement curve of the Al and Al matrix composites with the three-point bending test.

Wear loss was measured employing a total sliding contact block-on-roller type wear testing machine with variations of applied load (42N, 66.5N, 91N) at ambient temperature under dry condition. Sliding speed was 0.64m/sec and sliding distance was set to 1000m which was long enough for the onset of the steady state wear. Wear tests were performed with block specimens (12.7 x 12.7 x 12.7 mm) against counterface ring of S45C steel (HRC=63, 60mm in diameter and 20mm in thickness). Figure 7 shows the wear loss of squeeze cast Al matrix, (15%Al₂O₃ • SiO₂)/Al composite and the (10%Al₂O₃ • SiO₂+5%Ni)/Al hybrid composite as a function of applied load at ambient temperature. As the applied load increased, for all specimens, the wear loss increased. Wear resistance of (10%Al₂O₃ • SiO₂+5%Ni)/Al hybrid composite is highly superior to that of (15%Al₂O₃ • SiO₂)/Al composites regardless of the applied load. In order to characterize the wear behavior observed in Figure 7, worn surfaces and wear debris collected at the end of wear experiment were examined. Figure 8 shows worn surfaces of the three specimens tested at 66.5N load. Worn surfaces of Al and (15%Al₂O₃ • SiO₂)/Al composites deformed severely by the softening of aluminum. On the other hand, worn surface of the (10%Al₂O₃ • SiO₂+5%Ni)/Al hybrid composites reveals the flat tracks with the crushed fine intermetallic compound particles on the worn surfaces. Conclusively speaking, wear resistance is likely to be increased due to the hard intermetallic compound particles. It was found that the shape of debris particles produced during wear tests coincided with the above features observed on worn surfaces as shown in Figure 9.

Tensile tests were utilized to evaluate the room and elevated temperature properties of the composites. All tensile-test data are summarized in Table 1 for the sake of quick reference. Tensile and yield strength of (10%Al₂O₃ • SiO₂+5%Ni)/Al hybrid composites are greater at both temperature (25°C,300°C), strength drop at 300°C is much smaller in hybrid composites.

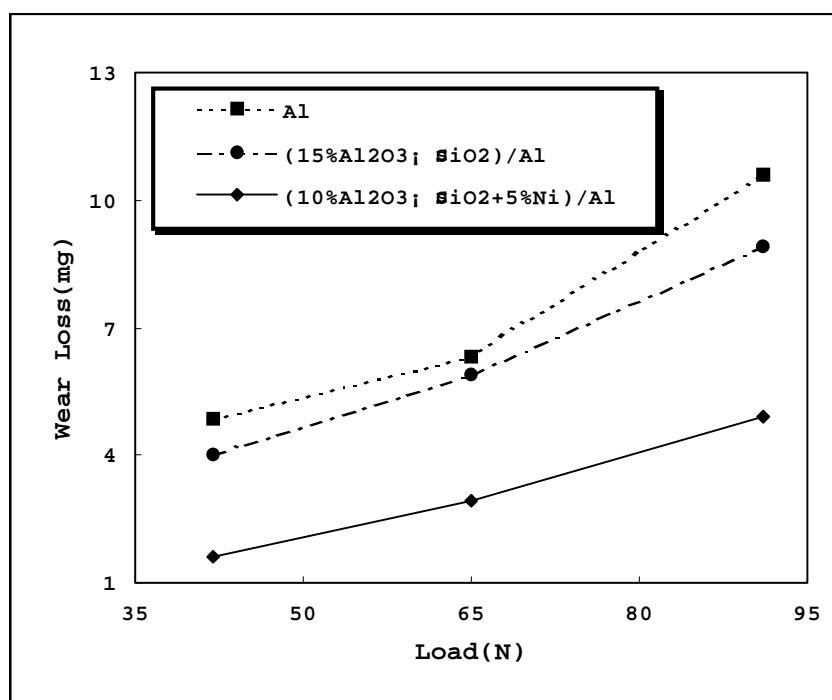
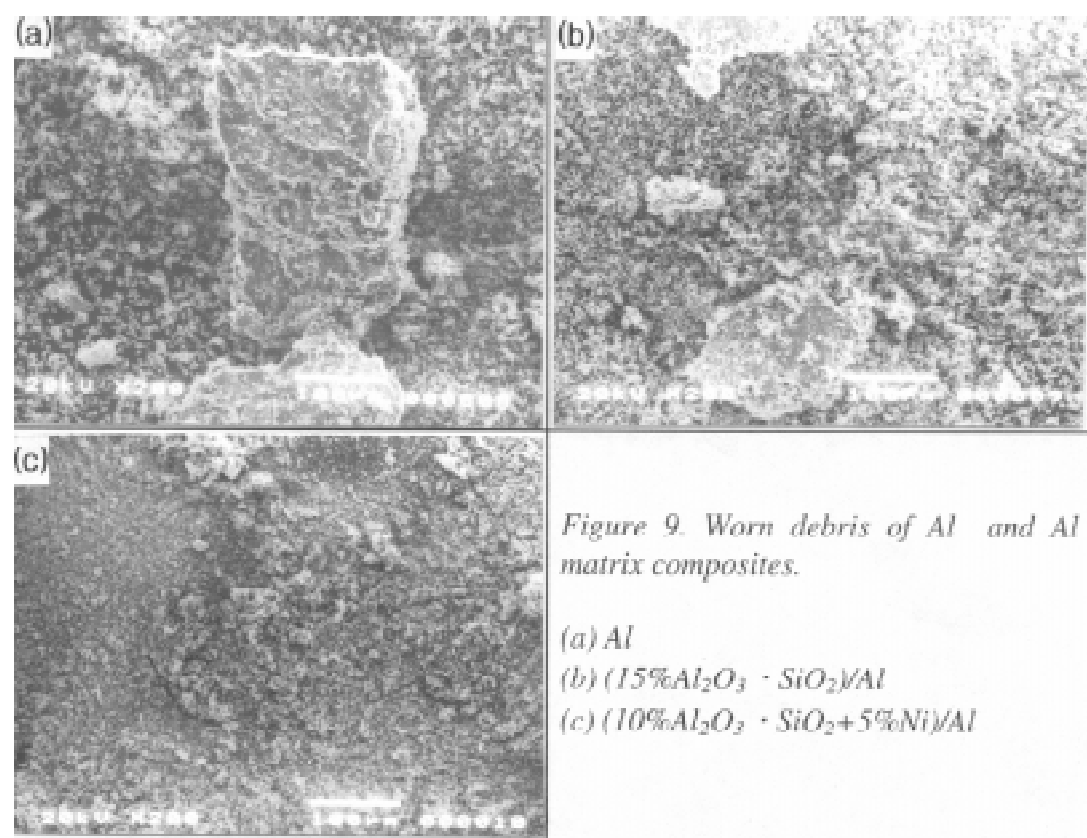
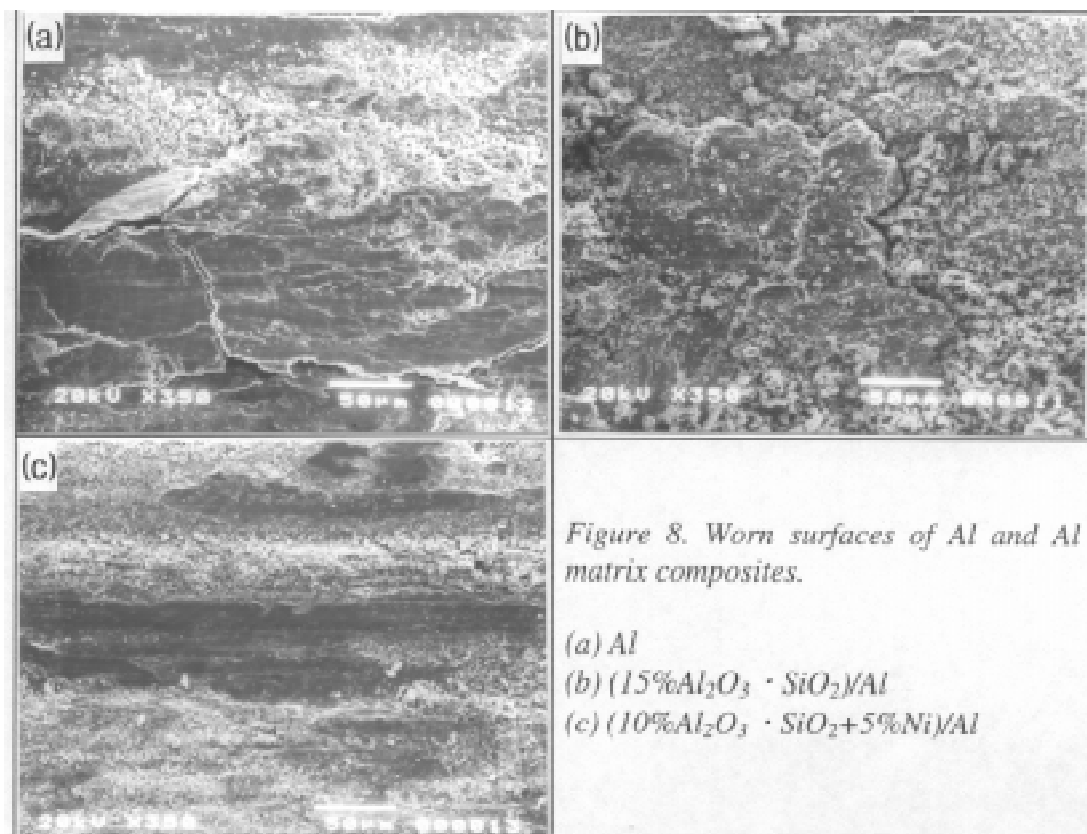


Figure 7. Wear loss of Al and Al matrix composites with variations of applied load.



The improvement of elevated temperature strength in hybrid composites is considered that the intermetallic compound particles act as barriers to the slip behavior of the aluminum matrix as schematically shown in Figure 10. This strengthening mechanism is similar to the conventional theory of grain-boundary strengthening in which the grain boundaries block the dislocation movement during plastic deformation. However, this effect of the intermetallic compound particles in the matrix is obviously much stronger than that of grain boundary [7].

Table 1. The results of tensile test of the Al matrix composites at the 25°C and 300°C.

Composites	(15%Al ₂ O ₃ • SiO ₂)/Al		(10%Al ₂ O ₃ • SiO ₂ +5%Ni)/Al	
	25	300	25	300
0.2% Y.S., MPa	83	52	130	123
U.T.S., MPa	118	89	135	130
Elongation, %	5	9	1.2	2.3

The differences in the high temperature fracture behaviors between the (15%Al₂O₃ • SiO₂)/Al composite and the (10%Al₂O₃ • SiO₂+5%Ni)/Al hybrid composite can be found in the SEM fractographs of Figure 11. Figure 11(a),(c) showing the overall feature of the ductile fracture which has mostly circular-shaped dimples and a number of short fibers distributed irregularly are to be pulled out. Figure 11(b),(d) exhibit the interfacial debonding between the intermetallic compound particles and Al matrix. It is considered that the interfacial debonding of matrix-intermetallic compounds particles plays an important role in the microcrack formation of hybrid composite. Therefore, (10%Al₂O₃ • SiO₂+5%Ni)/Al hybrid composite exhibited somewhat brittle fracture in comparison with (15%Al₂O₃ • SiO₂)/Al composite.

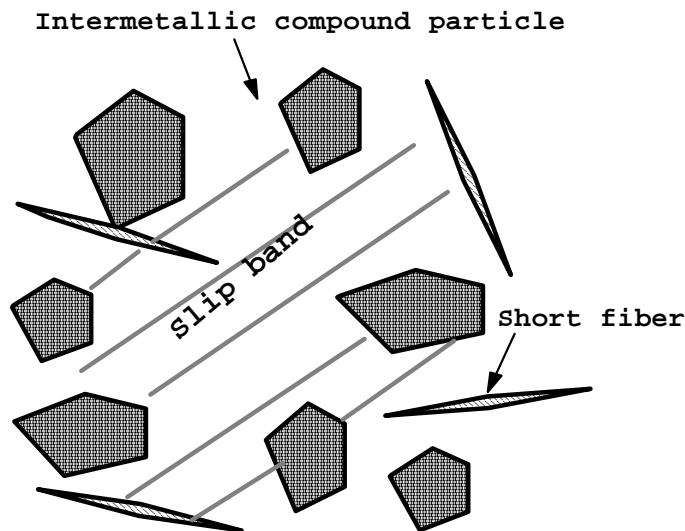


Figure 10. Schematic illustration showing the role of intermetallic compound particles for interfering slip behavior of the MMCs.

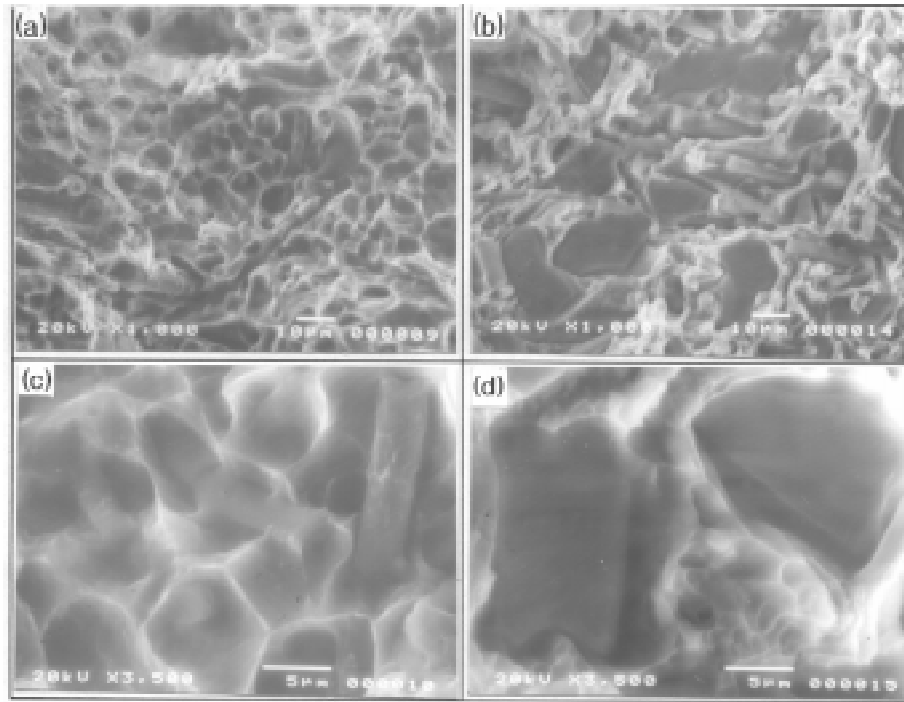


Figure 11. SEM fractographs of squeeze cast Al matrix composites tested at 300°C.
 (a) (15%Al₂O₃ • SiO₂)/Al (b) (10%Al₂O₃ • SiO₂+5%Ni)/Al
 (c) and (d) is magnification of (a),(b), respectively.

CONCLUSIONS

1. (10%Al₂O₃ • SiO₂+5%Ni)/Al hybrid composites were fabricated successfully by the reaction squeeze casting.
2. It was exhibited that a major portion of the Al₃Ni was formed regardless of the pouring temperature of the molten aluminum. The Al₃Ni intermetallic compounds are formed more easily than the other intermetallic compounds due to their lower formation temperature.
3. Microhardness and bending strength of (10%Al₂O₃ • SiO₂+5%Ni)/Al hybrid composite are higher than those of (15%Al₂O₃ • SiO₂)/Al composite 100Hv, 66MPa, respectively. And besides, wear resistance of (10%Al₂O₃ • SiO₂+5%Ni)/Al hybrid composite is highly superior to that of (15%Al₂O₃ • SiO₂)/Al composites regardless of the applied load. The enhancement of these mechanical properties is likely to be due to the hard intermetallic compound particles.
4. The improvement of elevated temperature strength is considered that the intermetallic compound particles act as barriers to the slip behavior of the aluminum matrix. Interfacial debonding between the matrix and intermetallic compound particles which was observed in the fractographs plays a role in the microcrack formation and, hence, (10%Al₂O₃ • SiO₂+5%Ni)/Al hybrid composite exhibited somewhat brittle behavior in comparison with (15%Al₂O₃ • SiO₂)/Al composite.

ACKNOWLEDGMENT

This work was supported by RASOM(CNU) and Ministry of Education Research Fund for Advanced Materials in 1996.

REFERENCES

1. I.M.Park, B.S.Kim, Bulletin of the Korean Inst. of Met. & Mat. vol.9, No.2, (1996),112-125
2. T.Blucher, "Discussion of a Liquid Metal Pressure Infiltration Process to Produce Metal Matrix Composites," J.Mat.Pross.Tech., 30 (1992), 381-390
3. H.Fukunaga and G.K. Yeoh, J. of Jpn. Soc. of Powd. and Powd. Met., 39(6) (1992), 459-463
4. I.Tsuchitori and H.Fukunaga, Proc. ICCM-10, Ceramic Matrix Composites and Other Systems, (2) (1993), 906-912
5. K.Kim et al, "Fabrication Processing and Properties of AZ91D Mg/9(Al_2O_3) • 2(B_2O_3) Metal Matrix Composites," Proc. of 3rd Asian Foundry Congress, ed. Z.H. Lee, C.P. Hong and M.H.Kim (Kyongju, Korea, 1995), 328-335
6. T.B.Massalski, Binary Phase Diagram, ASM, Metal Park, Ohio (1958), 174
7. Zhirui Wang and Ruby J. Zhang, Metall. Trans. A, 22A, (1991), 1585-1591

LOWER VOLUME FRACTION SiC_p/AL COMPOSITES FABRICATED BY SQUEEZE INFILTRATION CASTING

Kung-Hsien Shue and Su-Jien Lin

*Department of Materials Science and Engineering
National Tsing Hua University, Hsinchu, Taiwan, R.O.C.*

SUMMARY: The volume fraction of particulate reinforcement in an aluminum composite fabricated by squeeze infiltration casting is always about 50 vol% or higher. To make lower volume fraction composites (0-25 vol%), a mixed preform, composed of pure aluminum powder and SiC particles, was used and squeeze cast by a low melting-point alloy (AA383). Reinforcement macro-distribution uniformity and successful infiltration suggest that the suitable processing parameters are: melt temperature, 750°C; preform temperature, 515°C; infiltration pressure, 75 MPa; ram speed, 4 mm/s. Microstructure analysis shows that SiC_p distributed uniformly and no pore was observed for all the composites with various volume fraction or size of particulate reinforcement. The tensile properties of 85 μm SiC_p/Al/A383 composites (0-25 vol%) are better than that of A383 alloy though pure Al has a low strength. It is resulted from the refinement of silicon plates.

KEYWORDS: SiC_p/Al composites, squeeze casting, microstructures, tensile properties

INTRODUCTION

Metal matrix composites (MMCs) have been developed and applied as structural materials in aerospace and automobile industry for two decades because of their high specific strength, high specific stiffness, good elevated temperature properties, and better wear resistance [1-4]. Among these composites, short fiber and particulate reinforced aluminum matrix composites have maintained a lot of emphases recently because of their isotropic properties. Methods for the production of the particulate reinforced MMCs mainly involve liquid casting [5,6] and powder metallurgy [7]. Though liquid casting offers an advantage of high economic profit, many defects, such as gas porosity, oxide inclusions, clustering of the reinforcements, and intensive interfacial reaction between the reinforcements and the molten metal, incorporate with this products and result in the worse properties [8]. In other side, the powder metallurgy method offers the products good properties, however, the cost is expensive.

Squeeze casting [9-11] eliminates the gas porosity and interfacial reaction by a large pressure and rapid solidification rate, respectively, offering a combination of economic profit and good properties. However, only the composites with high and fixed volume fraction of the reinforcements can be obtained by a traditional squeeze casting. In our research, a mixed preform, composed of the reinforcements and pure aluminum powders, lowered the amount of the reinforcements in the composites. Squeeze casting this mixed preform by a lower

melting-point aluminum alloy obtained the composites containing lower and various volume fraction of the reinforcements.

EXPERIMENTAL PROCEDURES

Materials

Four different particle size of SiC_p: 85 μm (180 mesh), 35 μm (400 mesh), 15 μm (800 mesh), and 12 μm (1200 mesh), with a density of 3.22 g/cm³ were chosen as the reinforcements. The 40 μm (325 mesh) commercial pure aluminum powders with the purity of 99.7% was mixed with SiC_p to lower the amount of reinforcements in the preform. The lower melting-point A383 Al alloy, whose solidus temperature is 515⁰C and liquidus temperature is 585⁰C, was chosen as the casting matrix material. The chemical composition of AA383 Al alloy was obtained by the inductively coupled plasma-atomic emission spectrometer (ICP-AES) analysis and was Al-8.60 wt% Si-2.28 wt% Cu-0.14 wt% Fe.

Preforms

Various volume fractions of the reinforcements were determined by the mixing ratio of the amount of SiC_p to that of the pure aluminum powder. The proper amounts of the different particle-size SiC_p and the aluminum powder were well ball mixed for one hour and then cold compacted at a pressure of 5 MPa to be the SiC_p/Al mixed preform. Another preform, pure aluminum without reinforcements, was also prepared for comparison.

Squeeze Castings

The SiC_p/Al preform was preheated in the mold to 465 or 515⁰C. Molten A383 alloy at 685 or 750⁰C was poured into the mold and followed by the push action of the preheated ram. The pressure between 50 and 125 MPa was applied to squeeze the liquid A383 alloy into the preform at various ram speeds between 1-6 mm/s until the ram could no longer advance. After squeeze casting, the SiC_p/Al/A383 composites containing different volume fraction and particle size of the reinforcements were furnace cooled and obtained. Monolithic A383 alloy and Al/A383 alloys without reinforcements were also squeeze cast and compared to the composites.

Microstructure Observations

Optical microscopy (OM) and JEOL scanning electronic microscopy (SEM) were applied to investigate the microstructure of composites and the distribution of reinforcements. Volume fraction of SiC_p was obtained by a LECO image analysis system. Specimens for OM and SEM observations were prepared by conventional metallographic procedures up to 0.05 μm diamond powder polishing. The fracture surface of the tensile test specimens were analyzed by SEM.

Tensile Tests

Tensile tests were conducted using a materials testing system (MTS 810). Before test, the specimens were machined to a gauge size of 6.25 mm in width, 3 mm in thickness, and a gauge length of 25 mm. The surfaces of the specimens were polished to 600 mesh.

RESULTS AND DISCUSSION

Squeeze Castings

Table 1 The SiCp volume fractions of various locations in the 25 vol% 85 μm SiCp/Al/A383 composites fabricated by various squeeze pressures and ram speeds at 515 °C preform and 750 °C melt temperatures.

Location from Bottom (mm)	2	10	17	Average	Standard
Location from Side (mm)	0~25, 25~50	0~25, 25~50	0~25, 25~50	Value	Deviation
50 MPa, 2 mm/s	incomplete filtration				
75 MPa, 2 mm/s	27.66, 25.59	27.68, 32.43	25.65, 26.38	27.63	2.29
100 MPa, 2 mm/s	28.46, 24.99	28.82, 33.01	29.61, 29.02	28.98	2.34
125 MPa, 2 mm/s	26.90, 24.46	29.40, 31.91	27.76, 25.84	27.71	2.42
75 MPa, 1 mm/s	incomplete infiltration				
75 MPa, 3 mm/s	25.61, 23.30	28.80, 29.36	33.28, 28.20	28.09	3.11
75 MPa, 4 mm/s	26.25, 23.03	25.53, 26.33	24.84, 25.08	25.18	1.11
75 MPa, 5 mm/s	24.74, 23.08	30.47, 28.26	37.14, 29.91	28.93	4.53
75 MPa, 6 mm/s	30.15, 30.33	33.37, 29.78	38.06, 35.55	32.87	3.10

The 25 vol% 85 μm SiCp/Al/A383 alloy composites were used to check the optimum squeeze casting parameters. The preform and melt temperatures of squeeze casting were selected at 515 and 750°C, respectively, because too low temperature resulted in an incomplete infiltration. Table 1 exhibits the SiCp volume percentages of various locations in the 25 vol% 85 μm SiCp/Al/A383 composites fabricated under various squeeze pressures and ram speeds at 515°C preform and 750°C melt temperatures. Each datum is the average value of five 100x pictures of a location specimen. The infiltration was not complete when the squeeze pressure was only 50 MPa. The preform can be complete infiltrated as the squeeze pressure was increased to 75 MPa or more. The volume fraction and distribution uniformity of SiCp are almost the same for various squeeze pressure condition in the successful infiltrated composites. This means that the optimum squeeze pressure is 75 MPa from economic aspect.

For various ram speeds, Table 1 shows the optimum ram speed is 4 mm/s because it can result the most uniform distribution and the least volume percentage of SiCp. These suggest that the deformation of the preform under 4 mm/s ram speed is the smallest during squeeze casting processing. Darcy's law is usually used to describe a non-compressible fluid infiltrates the porous preform [12] and is

$$dP/dX = -(\mu/k)/V \quad (1)$$

where dP/dX is pressure gradient, μ is viscosity, k is permeability, and V is fluid velocity. Increasing ram speed increases the fluid velocity and decreases the fluid viscosity because the heat absorption by preform is increased. The former increases the pressure gradient, however, the latter decreases the pressure gradient. The degree of preform deformation is dependent on the pressure gradient. A higher pressure gradient will result in a severer deformation of preform. So that, to get a minimum distortion of preform and uniform SiCp distribution, a optimum ram speed should be selected. In this experiment, the optimum ram speed is 4 mm/s.

From above results, the suitable squeeze processing parameters are: 750°C melt temperature, 515 °C preform temperature, 75 MPa infiltration pressure, and 4 mm/s ram speed.

Microstructures

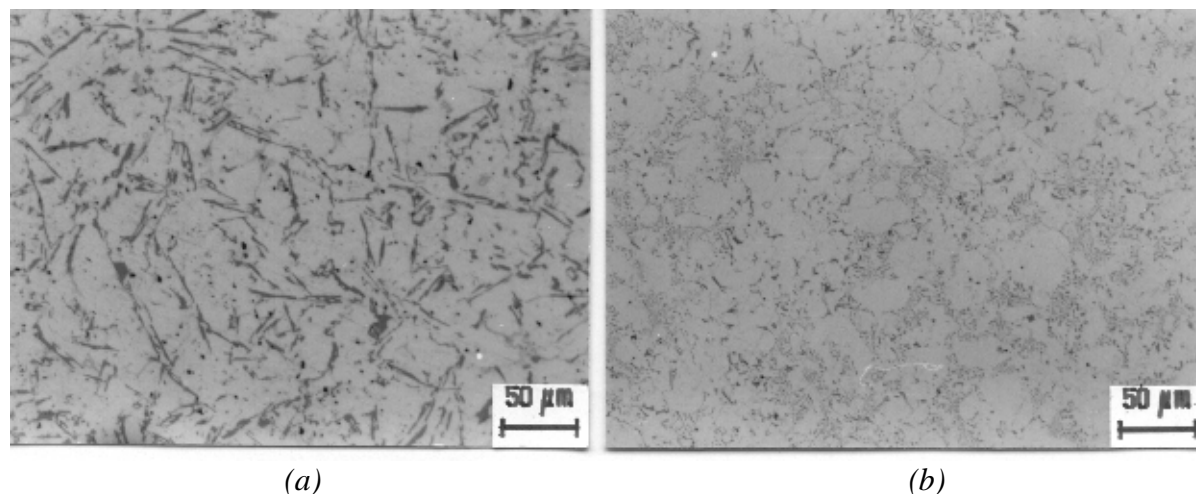


Fig. 1 Microstructures of the squeeze casting (a) A383 and (b) Al/A383 alloys.

Figure 1 shows the microstructures of the squeeze casting A383 and Al/A383 alloys. A large amount of silicon plates precipitated in the A383 Al alloy as shown in Fig. 1a. Several tens micrometers of the silicon plates grew up without any limitations and distributed randomly in the A383 Al alloy. However, in the squeeze cast Al/A383 alloy, as shown in Fig. 1b, the size of the silicon precipitates decreased to a few micrometers and the shape of precipitates in the Al/A383 alloy changed to smaller spheroids. Precipitation of silicon concentrated around different-size and round shape particles, that seems to be the added aluminum powders. It suggests that Al powders did not melt obviously during squeeze casting, but only the surfaces of powders melted and Al powders behaved as a limitation for the growth of the silicon precipitates. Besides, melting of the surfaces of aluminum powders needed to adsorb a lot of heat and would lower the temperature of the A383 alloy melt. This resulted in a rapid solidification rate and refined the size of silicon precipitates.

Figure 2 shows the microstructures of SiCp/Al/A383 composites with (a) 8 vol% 85 μm , (b) 14.5 vol% 85 μm , (c) 21 vol% 85 μm , and (d) 21 vol% 12 μm SiCp. The distributions of SiCp in the matrix are rather uniform and no pore can be found in all composites. These suggest that squeezing a low melting-point alloy (A383) into a mixed preform, composed of pure aluminum powder and SiC particles, is a successful technique to make lower volume fraction (0-25 vol%) composites. Figure 3 shows the microstructures of a squeeze cast SiCp/Al/A383 composite and Al/A383 alloy with higher magnification. It is easier to observe the size and shape of silicon precipitates. Many silicon precipitates nucleated heterogeneously on the SiCp and aluminum powders. Silicon were refined by the addition of SiCp and Al powder due to the growth limitation. However, the size and shape of silicon precipitates in SiCp/Al/A383 composites were not as small and round as that in Al/A383 alloys, as shown in Fig. 3. Adding SiCp, that is decreasing the amount of aluminum powders, reduces the quantity of heat adsorbed by the surface melting of aluminum powders, and results in the less refinement of the silicon precipitates.

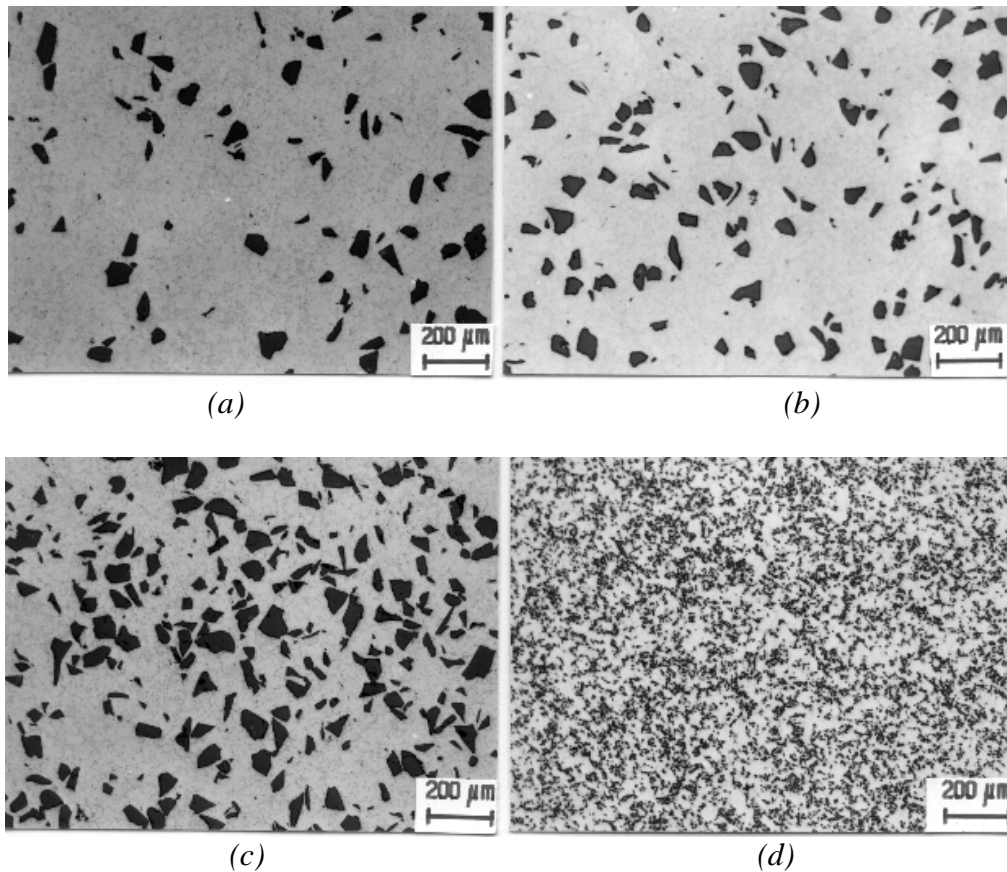


Figure 2 The microstructures of SiCp/Al/A383 composites with (a) 8 vol% 85 μm , (b) 14.5 vol% 85 μm , (c) 21 vol% 85 μm , and (d) 21 vol% μm SiCp.

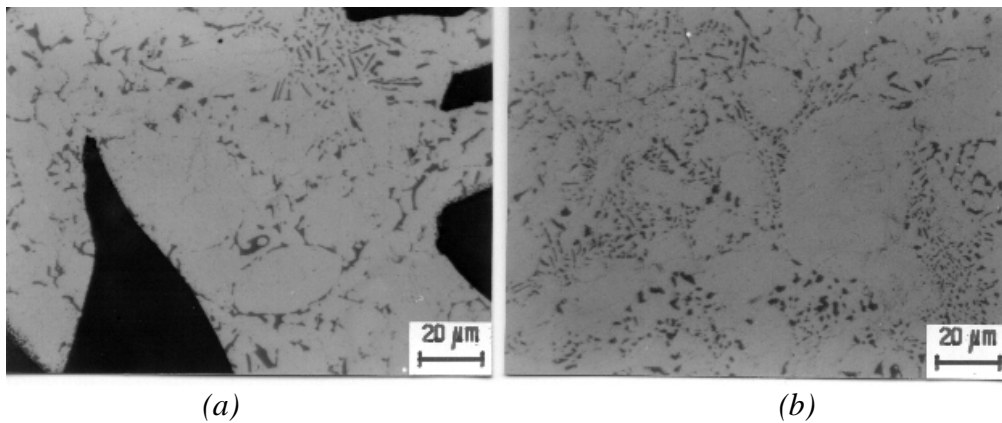


Fig. 3 Microstructures of the squeeze casting (a) 21 vol% 85 μm SiCp/Al/A383 composite and (b) Al/A383 alloy.

Tensile Properties

Table 2 shows the tensile properties of the squeeze cast A383, pure Al/A383 alloys and various SiCp/Al/A383 composites. The tensile strengths of the A383 and Al/A383 alloys are 166 and 188 MPa, respectively. Though the strength of the pure Al is absolutely lower than the A383 alloy, the tensile strength of the Al/A383 alloy is higher than that of the A383 alloy

due to the refinement of the silicon precipitates. By the same reason, the elongation of the Al/A383 alloy increases to 12.2% from 0.65%, elongation of the A383 alloy. However, the yield strength and Young's modulus of Al/A383 alloy are lower than that of A383 alloy because of the existence of pure aluminum in Al/A383 alloy.

Table 2 Tensile properties of various squeeze cast specimens.

Specimens	Tensile Strength MPa	Yield Strength MPa	Young's Modulus GPa	Elongation %
A383	166	142	86	0.7
Al/A383	188	75	76	12.2
8% 85 μm SiCp/Al/A383	180	77	88	7.6
15% 85 μm SiCp/Al/A383	176	85	100	5.3
21% 85 μm SiCp/Al/A383	174	105	112	3.6
25% 85 μm SiCp/Al/A383	174	117	118	2.1
21% 12 μm SiCp/Al/A383	223	121	104	3.0

For the 85 μm SiCp/Al/A383 composites, the tensile strength and elongation decrease from 180 to 174 MPa and 7.6% to 2.1%, respectively, as the SiCp content increases from 8 to 25 vol% because the large stress concentration on SiCp results in the earlier failure of the composites. However, the yield strengths and Young's moduli of the composites arise by the addition of the rigid SiCp. The tensile strength and yield strength of composites can be increased to 223 MPa and 121 MPa, respectively, by changing SiCp size from 85 μm to 12 μm . These must be resulted from the plastic constrain and Si refinement by the fine SiCp.

Comparing the composites and A383 alloy, the tensile properties of composites are better than that of A383 alloy except the yield strength. The major reasons are the refinement of silicon and some low strength pure Al in the composites. As for the Al/A383 alloy, the largest elongation should be resulted from the strongest silicon refinement and lack of SiCp.

Fracture Surfaces

Figures 4 shows the fracture surfaces after tensile tests of the squeeze cast (a) A383, (b) Al/A383, (c) 25 vol% 85 μm SiCp/Al/A383, and (d) 21 vol% 12 μm SiCp/Al/A383 specimens. As shown in Fig. 4a, obvious cleavage of the silicon plates and aluminum matrix without dimples dominates the brittle fracture behavior of the A383 Al alloy. In contrast, little cleavage of the silicon precipitates on the fracture surface of the Al/A383 alloy, shown in Fig. 4b, are associated with a large amount of dimples and explains the better ductility. These fine dimples are resulted from the silicon refinement in the Al/A383 alloy.

From the fracture surfaces of the composites, cleavage and crash of the 85 μm SiCp always happens whether the amount of SiCp was 8 or 25 vol% (Fig. 4c). No decohesion in the interface reveals a good and strong bonding between SiCp and the matrix. Cleavage and crash of SiCp illustrates the large stress concentration on SiCp and results a decrease in tensile strength of composites with higher SiCp content. A larger amount of dimples was found in the composite containing 8 vol% of SiCp. Decreasing amount of dimples as increasing the SiCp content explains the decrease of the elongation. Figure 4d shows the fracture surface of the 21 vol% 12 μm SiCp/Al/A383 composite. Cleavage of the SiCp associating with a large amount of dimples in the matrix is the dominant fracture mode. Some SiCp pull-out was found in the 12 μm SiCp/ Al/A383 composite. Comparing composites with A383 alloy, the

dimple quantity on the fracture surface of composites is much more than that of A383 alloy because of the silicon refinement in composites. This can explain the tensile properties of composites are better than that of A383 alloy, especially for the 21 vol% 12 μm SiC_p/Al/A383 composite.

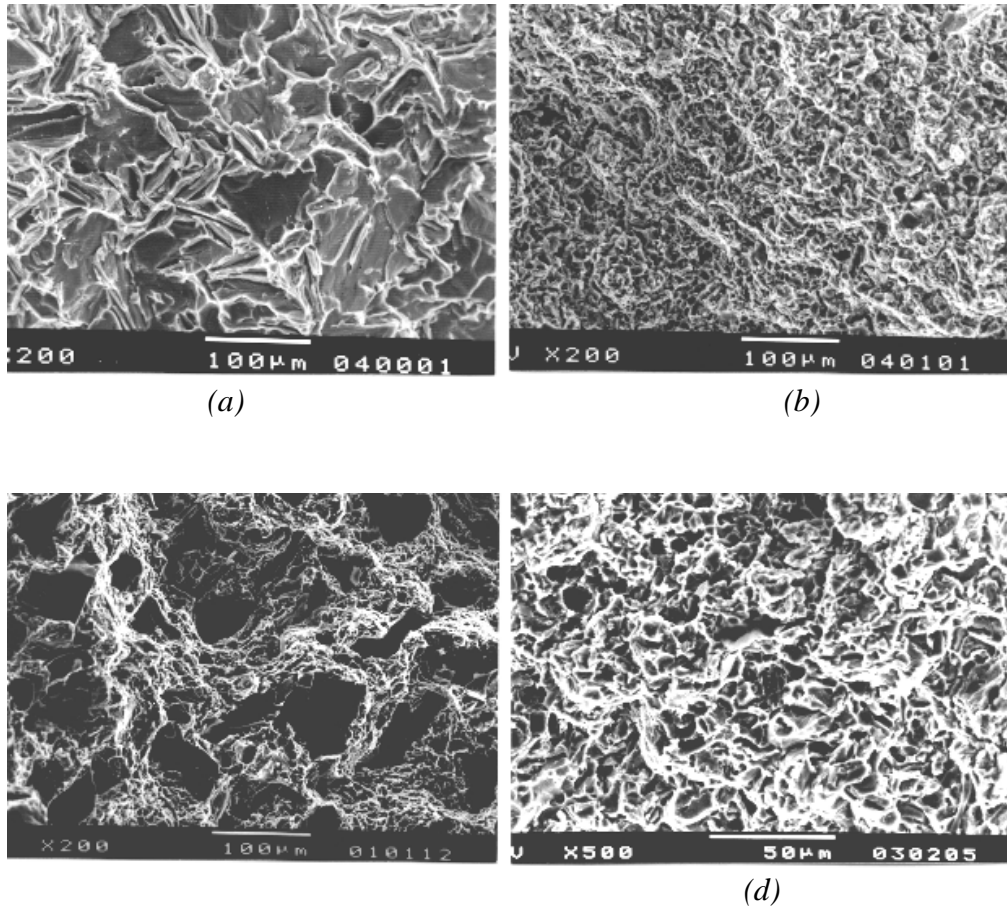


Figure 4 The fracture surfaces of the squeeze cast (a) A383, (b) Al/A383, (c) 25 vol% 85 μm SiC_p/Al/A383, and (d) 21 vol% 12 μm SiC_p/Al/A383 specimens.

CONCLUSIONS

1. A special squeeze infiltration technique, using a lower melting point A383 Al alloy to infiltrate the Al/SiC_p mixed preform, has been developed to fabricate lower SiC_p volume fraction (0-25 vol%) metal matrix composites.
2. The suitable squeeze processing parameters are: 750°C melt temperature, 515°C preform temperature, 75 MPa infiltration pressure, and 4 mm/s ram speed.
3. SiC_p distributed uniformly and no pore was observed for all the composites with various volume fraction or size of particulate reinforcement.
4. The tensile properties of SiC_p/Al/A383 composites (0-25 vol%) are better than that of A383 alloy though pure Al has a low strength, especially for the 12 μm SiC_p composite. This is resulted from the refinement of silicon plates.

ACKNOWLEDGEMENT

The authors are pleased to thank the financial support for this research by the National Science Council of Taiwan, R.O.C. under Grant No. NSC 85-2216-E-007-043.

REFERENCES

1. Fishman, S.G., "Conference Review: Interfaces in Composites", *JOM*, Vol. 38, No. 3, 1986, pp. 26-27.
2. Flom, Y. and Arsenault, R.J., "Interfacial Bond Strength in an Aluminum Alloy 6061-SiC Composites", *Materials Science & Engineering*, Vol. 77, 1986, pp. 191-197.
3. Howes, M.A.H., "Ceramic-Reinforced MMC Fabricated by Squeeze Casting", *JOM*, Vol. 38, No. 3, 1986, pp. 28-29.
4. Mortensen, A., Cornie, J.A. and Flemings, M.C., "Solidification Processing of Metal-Matrix Composites", *JOM*, Vol. 40, No. 2, 1988, pp. 12-19.
5. McCoy, J.W., Jones, C. and Wawner, F.E., "Preparation and Properties of Cast Ceramic/Aluminum Composites", *SAMPLE Quarterly*, Vol. 19, No. 2, 1988, pp. 37-50.
6. Milliere, C. and Suery, M., "Fabrication and Properties of Metal Matrix Composites Based on SiC fiber Reinforced Aluminum Alloys", *Materials Science and Technology*, Vol. 4, Jan., 1988, pp. 41-51.
7. Cappleman, G.R., Watts, J.F. and Clyne, T.W., "The Interface Region in Squeeze-Infiltrated Composites Containing δ -Alumina Fiber in an Aluminum Matrix", *Journal of Materials Science*, Vol. 20, 1985, pp. 2159-2168.
8. Chen, R. and Zhang, G., "Casting Defects and Properties of Cast A356 Aluminum Alloy Reinforced with SiC Particles", *Composites Science and Technology*, Vol. 47, 1993, pp. 51-56.
9. Cook, A.J. and Werner, P.S., "Pressure Infiltration Casting of Metal Matrix Composites" *Materials Science & Engineering A*, Vol. A144, 1991, pp. 189-206.
10. Hwu, B.K., Lin, S.J. and Jahn, M.T., "Effects of Process Parameters on the Properties of Squeeze-Cast SiCp-6061 Al Metal-Matrix Composites.", *Materials Science & Engineering A*, Vol. A207, 1996, pp. 135-141.
11. Hwu, B.K., Lin, S.J. and Jahn, M.T., "The Interfacial Compound and SEM Fractography of Squeeze-Cast SiCp-6061 Al Composites.", *Materials Science & Engineering A*, Vol. A206, 1996, pp. 110-119.
12. Poirier, D.R. and Geiger, G.H., *Transport Phenomena in Materials Processing*, TMS, Pennsylvania, 1994, p. 90.

REACTION SQUEEZE CAST PROCESSING AND INTERMETALLICS DISPERSED ALUMINUM MATRIX COMPOSITES

Hideharu Fukunaga¹, Gen Sasaki², Isao Tsuchitori³, Toshio Fujii⁴
and Nobuyuki Fuyama⁵

^{1,2} Faculty of Engineering, Hiroshima University, 1-4-1, Kagamiyama,
Higashi-Hiroshima, 739 JAPAN,

^{3,4,5} Industrial Research Institute West of Hiroshima Prefecture, 2-10-1,
Aga-minami, Kure, 737 JAPAN

SUMMARY: The new in-situ process, Reaction Squeeze Casting, has been developed by which the intermetallic compounds are dispersed in the aluminum matrix composites to improve the elevated temperature performance. The process conditions were optimized by trial and error. While the conditions to make the sound composites is limited, the short fiber reinforced and intermetallics dispersed aluminum matrix composites have the advantage of strength at elevated temperature by 100°C comparing to the conventional short fiber reinforced composites and have an excellent wear resistivity, which are fabricated by reaction squeeze casting.

KEYWORDS: MMC, reaction, titanium, nickel, squeeze casting, processing, aluminum alloy, intermetallic compounds, mechanical properties

INTRODUCTION

Discontinuous ceramic fiber reinforced aluminum matrix composites decrease extremely in strength at the temperature range exceeding 200°C because of inheriting the matrix strength of aluminum. One of authors reviewed the high temperature performance of SiC and Si₃N₄ whisker reinforced aluminum composites as shown in Fig.1 and 2, respectively[1]. In both figures, there is a steep drop of strength at the temperature exceeding 200°C. This means that it is impossible for us to apply the composites to the structural machine components operating at elevated temperature around 250°C. In order to improve the high temperature strength, the authors have being studied the composites by reaction squeeze casting, whose matrix is strengthened by the dispersed intermetallic compound such as TiAl₃, NiAl₃, FeAl₃. They are produced by reaction between molten aluminum and titanium oxide (TiO₂) and metal powder (Ni,Fe), followed by equation.(1)-(3).



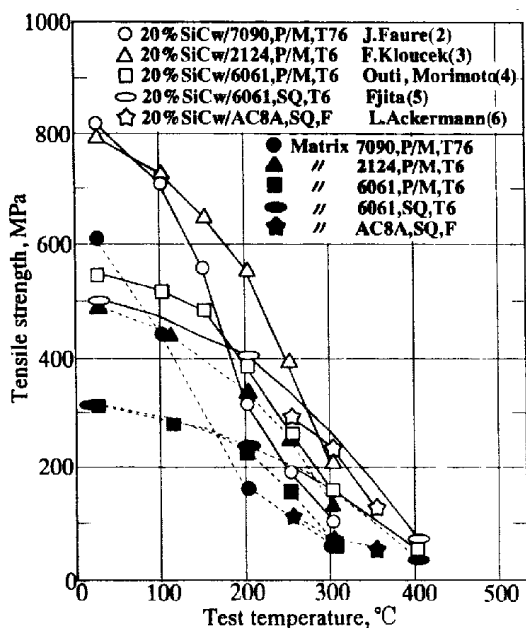


Fig.1 : Effect of matrix alloys, manufacturing process and test temperature on high-temperature tensile strength of SiC whisker reinforced Al alloys. (SQ; Squeeze cast, P/M; Powder metallurgy)

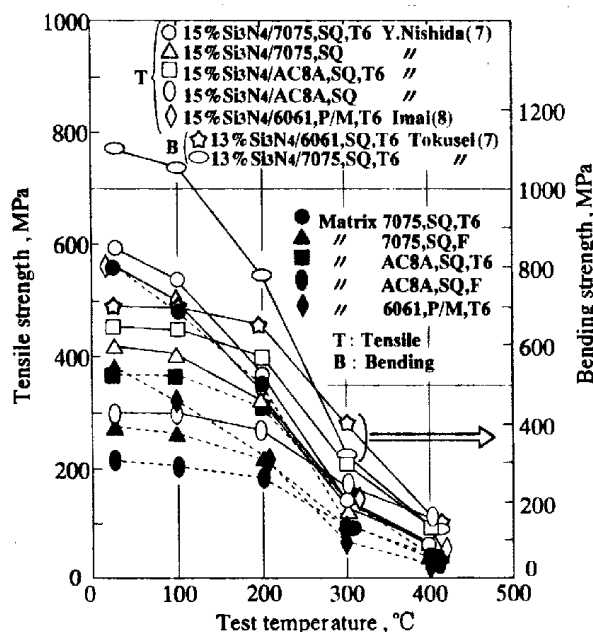


Fig.2 : Effect of matrix alloys, manufacturing process and test temperature on high-temperature tensile strength of Si₃N₄ whisker reinforced Al alloys. (SQ; Squeeze cast, P/M; Powder metallurgy)



Reaction squeeze casting is for the in-situ process to make aluminum matrix strengthened by utilizing the reaction between the oxide or metal powder and molten aluminum, resulting to produce the small intermetallics-dispersed matrix, as well as reinforced by discontinuous ceramic fibers which do not react with the molten aluminum at all. This article offers the processing and properties by summarizing previous papers[10-18].

EXPERIMENTALS

Preparation of preforms

The powder and reinforcement employed in the experiment of reaction squeeze casting are listed in Table 1. The anatase type of TiO₂ powder and whisker, rutile type of TiO₂ powder, Ni and Fe powder were selected as a starting agent, which were reactive with molten aluminum, resulting to intermetallic compounds. Silicon carbide whisker (SiCw) and alumina

Table 1: Properties of powder and reinforcement.

Powder Reinforcement	Diameter μm	Length μm	Density Mg/m ³
TiO ₂ (rutile)	0.2~0.3	-	4.2
TiO ₂ (anatase)	0.3~0.4	-	3.9
TiO ₂ (anatase whisker)	0.5	13	3.9
Ni	3~7	-	8.9
Fe	5~6	-	7.8
SiC whisker	0.2	10~40	3.2
Al ₂ O ₃ fiber	3	150~	3.3

short fiber are also employed as a reinforcement for aluminum matrix, and in some experiments, employed as a reinforcement for powder preforms with small volume fraction of 5 to 15%.

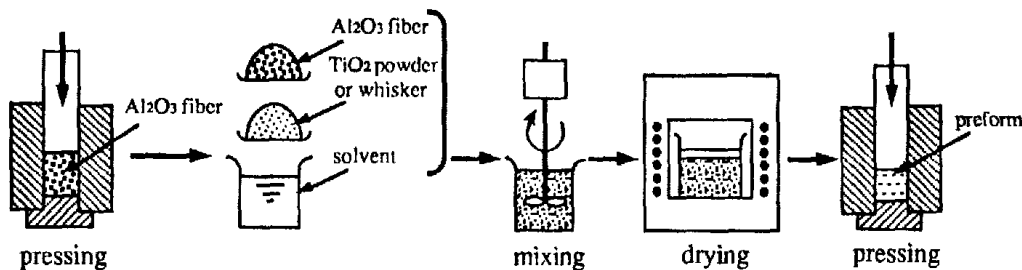


Fig.3 : Preparing process of preform.

Preforms were prepared as shown in Fig.3; adjusting the length of fiber by pressing at 100MPa, mixing them reactive powder in solvent, drying them in electric furnace and finally adjusting their volume fraction to 20-45% by compaction process. Preform size is 44 mm in diameter and 20 mm in height.

Procedure of Reaction Squeeze Casting

The conventional squeeze casting apparatus is outlined in Fig.4. Preform was heated by cylindrical electric furnace to temperature T_p , together with metal die. As soon as molten aluminum at a given temperature, T_m , was poured from the top, punch run down at the speed of 1 cm/s to applied the pressure ranging from 50 to 100 MPa. The pressure were maintained for chill time of 60s. In cases, transient temperature at the center of preform was measured by sheathed thermo-couple of 1.0 mm in sheath diameter as shown in Fig.4 during squeeze casting process.

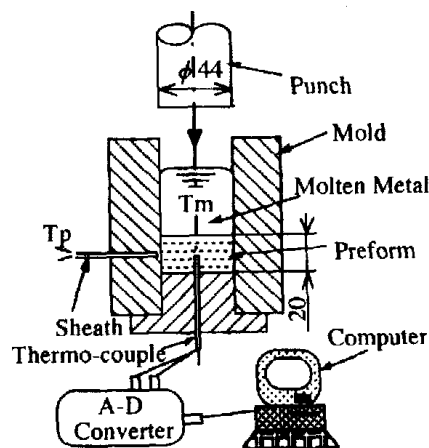


Fig.4 : Outline of direct squeeze casting apparatus.
 T_m : molten aluminum temperature
 T_p : preform temperature

RESULTS AND DISCUSSION

In the beginning of this study, we repeated various kinds of and large numbers of trial and error shots. An example of the results is shown in Table 2 or 3. Those results are summarized as follows from the view points of productivity and reactivity.

- 1) Preforms consisting of monolithic powder and high volume fraction of TiO₂, Fe or Ni does not make the bulkily and uniformly intermetallics-dispersed MMC, because of severe reaction. It is necessary that one or two kinds of powder are mixed with ceramic reinforcement, preventing the infiltration of molten aluminum from choking out by reaction products.
- 2) Infiltrating length of melt into preform and reactivity of preform with molten aluminum are remarkably dependent on not only T_m and T_a, but also volume fraction of powder, however hardly dependent on final squeeze pressure.
- 3) Anatase type of TiO₂ is more easy to react than rutile type.
- 4) It appears that infiltrating process at molten aluminum front is time dependent and enthalpy dependent process accompanying with exothermic reaction and with heat diffusion.

Table2: An example of trial and error results of reaction squeeze casting for TiO₂+SiCw/Al systems.

No.	Preform Vf, %	T _p °C	T _m °C	Infiltrated length, mm
1	15%TiO ₂ (r)+15%SiCw	410	750	0
2	"	340	810	5
3	"	500	750	11
4	"	500	800	13
5	20%TiO ₂ (r)+10%SiCw	340	760	5
6	"	340	780	6
7	15%TiO ₂ (a)+15%SiCw	500	670	0
8	"	500	800	15
9	"	500	830	13

Final squeeze pressure ; $p=100\text{MPa}$, punch speed ;
 $v=1\text{cm/s}$, chill time under final pressure ; $t=60\text{s}$.
 (r) ; rutile type, (a) ; anatase type

Table3: An example of trial and error results of reaction squeeze casting for TiO₂+SiCw+Ni, Fe/Al systems.

No.	Preform Vf, %	T _p °C	T _m °C	Infiltrated length, mm
1	15%TiO ₂ (r)+15%SiCw+5%Fe	500	770	6
2	"	480	820	20
3	20%TiO ₂ (r)+10%SiCw+5%Fe	500	830	6
4	15%TiO ₂ (a)+15%SiCw+5%Ni	500	800	20
5	15%TiO ₂ (r)+15%SiCw+5%Ni	500	800	20
6	5%TiO ₂ (a)+20%SiCw+5%Ni	400	800	20
7	"	450	800	20
8	5%TiO ₂ (r)+20%SiCw+5%Ni	420	740	20
9	"	450	740	20
10	"	475	740	20
11	"	390	770	16

Final squeeze pressure ; $p=100\text{MPa}$, punch speed ;
 $v=1\text{cm/s}$, chill time under final pressure ; $t=60\text{s}$.
 (r) ; rutile type, (a) ; anatase type

Effect of Preform Temperature and Molten Aluminum Temperature

Figure 5 shows the effect of preform temperature (T_p) and molten aluminum temperature (T_m) on infiltration and reactivity when molten pure aluminum forced to infiltrate into the preform with 5% TiO_2 +5% Ni+20%SiCw (volumetric percent) at punch speed 1 cm/s under final squeeze pressure 50 Mpa. The dotted line shows the resultant temperature $T_n = 660^\circ C$ determined by equation (4).

$$T_n = (T_m \cdot V_m \cdot C_{pm} \cdot \rho_m + T_p \cdot V_f \cdot C_{pf} \cdot \rho_f) / (V_m \cdot C_{pm} \cdot \rho_m + V_f \cdot C_{pf} \cdot \rho_f) \quad (4)$$

Where, V_m, V_f : volume fraction of matrix and fiber
 C_{pm}, C_{pf} : specific heat of matrix and fiber
 ρ_m, ρ_f : specific density of matrix and fiber

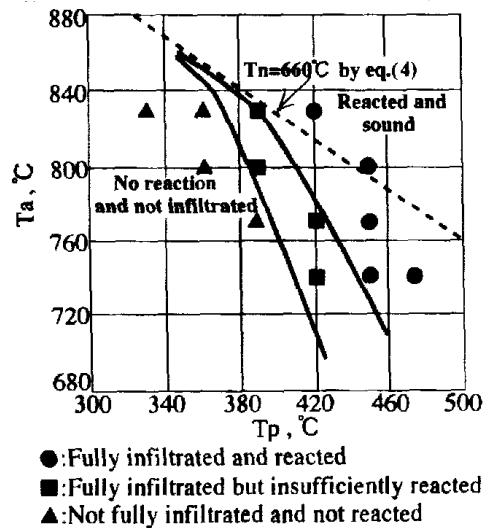


Fig.5 : Effect of molten aluminum and preform temperature on the infiltration and reaction when squeeze-cast to the preform of 20%SiCw+ 5% TiO_2 + 5%Ni.

It is the sufficient condition for full infiltration that T_p and T_m make the resultant temperature higher than melting temperature of aluminum. From the experiment full infiltration and sufficient reaction still achieved enough under the temperature $T_n = 660^\circ C$, when the temperature difference between T_p and T_m becomes small. The reason may explained by small amounts of heat loss and heat generation by exothermic reaction.

Effect of Powder Diameter

The hardness of composites increased when TiO_2 powders in preform react with aluminum, resulting to produce titanium aluminides and Al_2O_3 . Effect of mean diameter of TiO_2 powder on the hardness of composites is shown in Fig.6. The hardness increases with decrease in diameter. The hardness is raised remarkably to Hv850, by employing $0.4\mu m$ in diameter, however there is no hardness raise in the case of $11.8\mu m$ in diameter, at the same volume fraction of TiO_2 . An analysis of X-ray diffraction patterns of the composites employed 0.4 and

11.8 μ m powder are shown in Fig.7. The composites of 0.4 μ m TiO₂ powder consist of Al₂O₃ (Hv=1600-1700), TiAl₃ (Hv=400-700) and Ti₃Al. On the other hand, the composites of 11.8 μ m TiO₂ powder consist of merely Al and TiO₂. That is, the reaction did not finish yet, because the surface area of 11.8 μ m TiO₂ powder is so small comparing to that of 0.4 μ m TiO₂ powder under a certain volume fraction of preform.

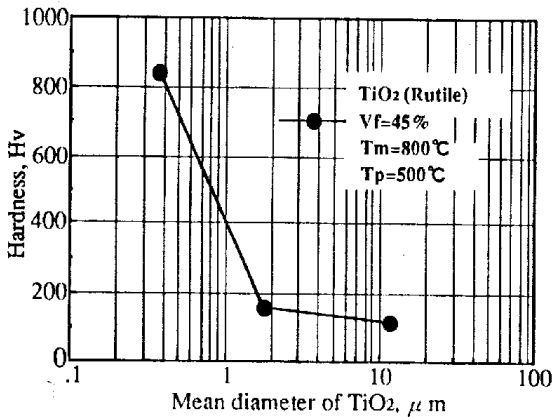


Fig. 6 : Effect of mean diameter of TiO₂ powder on hardness of composites fabricated by reaction squeeze casting with use of molten aluminum under constant volume fraction of preform.

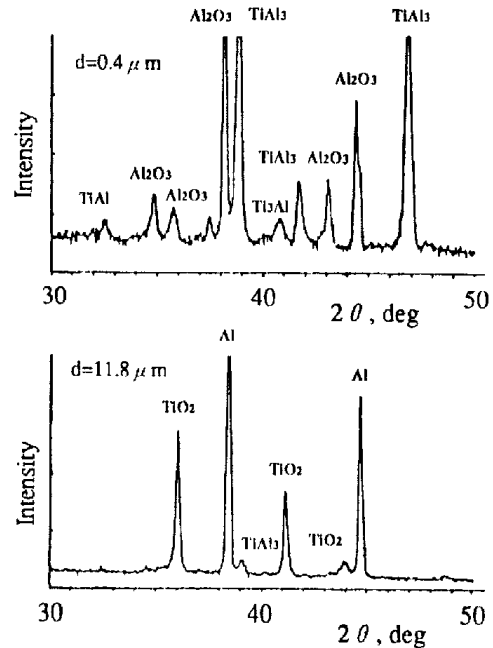


Fig.7 : X-ray diffraction patterns of composites, fabricated by reaction squeeze casting employed molten aluminum and 45% TiO₂ preform. ($T_m=800^\circ\text{C}$, $T_p=450^\circ\text{C}$, $p=50\text{Mpa}$, $v=1\text{cm/s}$)

Effect of Volume Fraction

Figure 8 shows the effect of volume fraction of TiO₂ powder and TiO₂ whisker on the hardness of MMC, fabricated by reaction squeeze casting, which is also reinforced by a certain

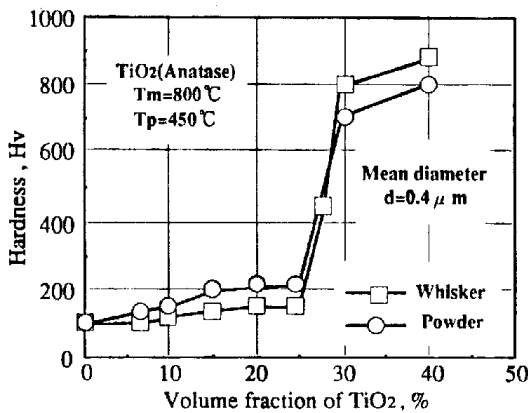


Fig. 8 : Effect of volume fraction of TiO₂ on hardness of composites fabricated by reaction squeeze casting employed molten aluminum, whisker and powder type TiO₂ preform.

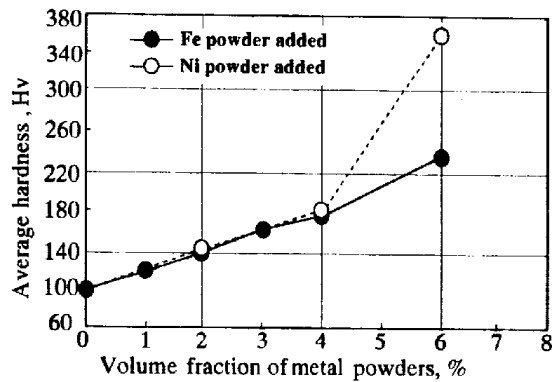


Fig. 10: Effect of volume fraction of Ni and Fe powders on hardness of the Composites with 20% SiCw+Ni or Fe powder. ($T_m=750^\circ\text{C}$, $T_p=350^\circ\text{C}$, $p=100\text{MPa}$, $v=1\text{cm/s}$, $t=60\text{s}$)

volume percent of Al_2O_3 fiber. As the volume fraction of TiO_2 increases, the hardness slightly increased, too. The effect is characterized by that the hardness is raised from Hv200 to Hv750 abruptly when volume fraction reaches to the range from 25% to 30%. There is the critical volume fraction for the synthesis of reaction. The flash temperature determined by heat generation and heat exchange per unit volume may control the synthesis proceed or not. It appears that ignition temperature is. The temperature-time curve at the center of preform are illustrated in Fig.9. There can be seen the great difference in maximum temperature between 20% and 25% of TiO_2 whisker addition.

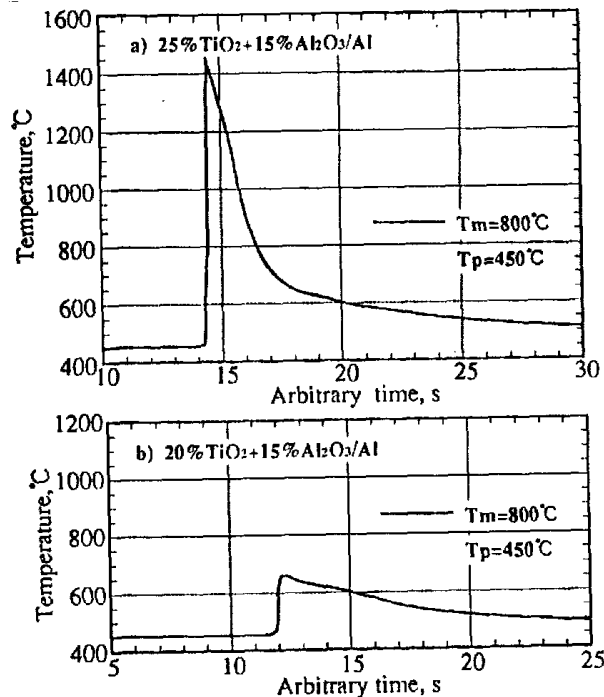


Fig. 9 : Time-Temperature curve of preform with 25% and 20% $\text{TiO}_2 + 15\% \text{Al}_2\text{O}_3$ infiltrated by molten aluminum in reaction squeeze casting process.

Figure 10 shows the micro vickers hardness of MMCs fabricated by reaction squeeze casting in which the preforms consisting of 20% SiC whisker and variable volume fraction of Fe or Ni powder are prepared. The hardness increases with addition of Fe and Ni powder, because they result to become intermetallic compounds by reacting with molten aluminum within about 20 seconds under the pressure 100MPa, before melt is solidified. The microstructures are uniform in the order of the original powder size.

Processing Guide Line

We have induced the processing guide from various kinds of experiments and analysis as follows.

- 1) Reaction squeeze casting is, in the moving boundary process of transient reactive band.
- 2) The best process condition for fabricating the bulky MMC and for producing uniformly intermetallics-dispersed matrix, is as follows: the reaction synthesis proceeds in seconds after molten aluminum finishes to infiltrate to the bottom of preform.
- 3) As for as TiO_2 powder $0.4\mu\text{m}$ in diameter, the hardness of aluminum matrix composites

are controlled up to Hv300 by reaction squeeze casting, however it is difficult to produce the composites more than Hv800 in hardness and 15 mm in thickness.

4) Heat treatment is excellent process to control the hardness of composite, after the insufficiently reacted composites have been fabricated.

MECHANICAL PROPERTIES

The dispersion of reaction products such as Al₂O₃, TiAl₃, NiAl₃ is effective for improving the matrix strength at elevated temperatures and wear resistance of MMC. Figure 11 shows the high temperature strength of the MMC as cast which is fabricated by reaction squeeze casting, employing the preform of 20% SiCw+5%TiO₂+5%Ni and molten aluminum. In the figure, the new composites are compared to the conventional 20%SiCw/Al composites. The new MMC keeps still 320MPa of bending strength at 400°C while the conventional one bears merely against 90 MPa. The advantage of strength offers the application for the structural component of machine operating at elevated temperature 350°C. Figure 12 [17] and Table 4 [18] demonstrate the wear resistivity of MMCs fabricated by reaction squeeze casting. The minute examination into the test pieces shows that the excellent wear resistivity comes from the dispersion of intermetallics in the aluminum matrix.

Table 4 : Built in wear test of piston manufactured by reaction squeeze casting.

Piston materials	Wear, mg
AC8A.Aluminum alloy,T6	4020
Niresist cast iron	460
12%Al ₂ O ₃ short fiber/AC8A,T6	77
5%TiO ₂ whisker+10%Al ₂ O ₃ short fiber/AC8A,T6	30
10%TiO ₂ whisker+10%Al ₂ O ₃ short fiber/AC8A,T6	31
5%TiO ₂ powder+10%Al ₂ O ₃ short fiber/AC8A,T6	51
10%TiO ₂ powder+10%Al ₂ O ₃ short fiber/AC8A,T6	45

Oil temperature; 250 °C, Pulsating load; 6MPa, frequency; 20Hz, 300hrs

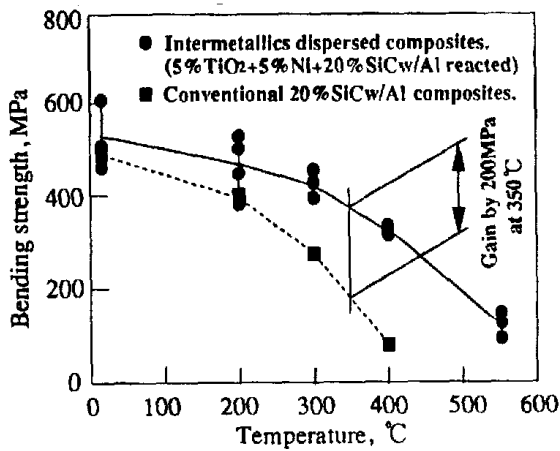


Fig.11: Comparison of bending strength at elevated temperatures between conventional composites and intermetallics dispersed composites fabricated by reaction squeeze casting

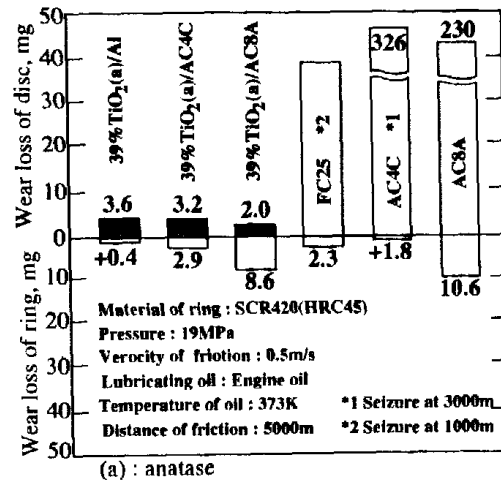


Fig.12 : Comparison of wear resistivity between conventional materials and intermetallics dispersed composites fabricated by reaction squeeze casting.

CONCLUSION

Reaction squeeze casting is a kind of transient process, and a limited condition leads to success to fabricate the bulky and uniform-structured composites. Preparing the preform is another key point, which consists of the discontinuous ceramic fibers, fine oxides and metal powders. It is important that preform and molten aluminum temperature during the process are selected so that the resultant temperature calculated by the rule of energy conservation is nearly liquidus temperature of aluminum.

The intermetallics-dispersed aluminum matrix composites offers an excellent strength at elevated temperatures and wear resistivity subjected to sliding and fretting load.

The process is promising to use practically for wide applications, such as piston, cylinder, cylinder head, vane pump and so on.

REFERENCES

1. Fukunaga, H., "Whisker Reinforced Alloys", *Composite Materials for Extreme severe Environments (in Japanese)*, Morita, M, Ed., Japan Institute for Metals, 1990, pp.25-35.
2. Fanre, J. F. and Ackerman, L., "Dispersion strengthened Aluminum Alloys", Kim, Y. W. Ed., *The Minerals, Metals & Materials Society*, 1988, pp.501-515.
3. Kloucek, F. and Singer, R. F., *Brown Boveri Forshungs Bericht*, KLR-86-81, 1986, pp.1-22.
4. Ouchi, K. et al., *R&D Kobe steel engineering Report (in Japanese)*, Vol. 37, No.3, 1987, pp.31-33.
5. Fujita, T., *Tetsu-to-Hagane (in Japanese)*, Vol. 75, No. 9, 1989, pp.1516-1526.
6. Ackerman, L., et al., *Proceedings of 6th International Conference on Composite Materials*, 1987, Metal Matrix Composites, pp.687-698.
7. Nishida, Y., et al., *Proceedings of 4th US-Japan Conference on Composite Materials*, June 27-29, 1988, Washington D C, pp.429-438.
8. Imai, T., et al., *Proceeding of 4th US-Japan Conference on Composite Materials*, June 27-29, 1988, Washington D C. pp. 109-117.
9. Tokuse, M., et al, *Proceeding the 75th Fall Meeting of Japan Institute of Light Metals (in Japanese)*, 1988, pp. 79-80.
10. Fukunaga, H., Wang, X. and Aramaki, Y., "Preparation of Intermetallic Compound Matrix Composites by Reaction Squeeze Casting", *Mater. Sci. Lett.*, Vol.10, 1991, pp.23-25.

11. Fukunaga, H. and Wang, X., "Preparation and Properties of Intermetallics Distributed Matrix Composites by Reaction Squeeze Casting", *Proceeding of 6th International Conference on Mechanical Behavior of Materials*, Kyoto, Japan, July 28–August 2, 1991, Vol.3, pp. 163-168.
12. Fukunaga, H., and Wang, X., "Process Condition and Structure of Al-Fe or Al-Ni Compounds Distributed Composites by Reaction Squeeze Casting", *Proceeding of 6th International Symposium on Intermetallic Compounds-Structure and Mechanical Properties*, June 17–20, 1991, Sendai, Japan, pp. 1045-1049.
13. Fukunaga, H., "Exploration of New Application of MMCs Manufactured by Squeeze Casting Process ", *Proceeding of 9th International Conference on Composite Materials*, July 12-16, 1993, Madrid, Spain, Miravete, A., Ed., *Metal Matrix Composites*, Vol.1, pp.355-362.
14. Tsuchitori, I. and Fukunaga, H., "Process Control by Reaction Squeeze Casting for Intermetallics-Strengthening of TiO₂/Al Composites", *Proceeding of 9th International Conference on Composite Materials* July 12-16, 1993, Madrid, Spain, Miravete, A., Ed., Vol.2, *Ceramic Matrix Composites and Other Systems*, pp.906-912.
15. Fukunaga, H., Kajikawa, K., Kakehi, T. and Morinaga, N., " Fabrication of Metal Matrix Composites by Reaction Squeeze Casting" *Proceedings of 3rd Japan International SAMPE Symposium*, Kishi, T., Ed., December 7-10, 1993, China, Japan, Vol.1, *Advanced Materials-New Processing and Reliability*, pp.931-936.
16. Tsuchitori, I. and Fukunaga, H., "High Performance Composites by Reaction Hardening of Matrix in TiO₂/Al Alloys system", *Proceeding of Tenth International Conference on Composite Materials*, Whistler, British Columbia, Canada, August 14-18, 1995, Vol.II: *Metal Matrix Composites*, Poursartip, A., Ed., pp.263-270.
17. Tsuchitori, I. and Fukunaga, H., "Reacted Structures and Wear Resistance of Particulate Anatase type TiO₂/Al Alloys Composites", *Journal of Light Metals (in Japanese)*, Vol.46, No.6, 1996, pp.292-297.
18. Fukunaga, H. and Tsuchitori, I., "MMCs Fabricated by Reaction Squeeze Casting and Its Application", *Proceeding of Tenth International Conference on Composite Materials*, Whistler, British Columbia, Canada, August 14-18, 1995, Vol.III: *Processing and Manufacturing*, Poursartip, A., Ed., pp.67-76.

HIGH TEMPERATURE THERMAL EXPLOSIVE SYNTHESIS OF NICKEL/NICKEL ALUMINIDE MULTILAYER COMPOSITES

Huabin Wnag, Jie-Cai Han and Shanyi Du

Center for Composite Materials, Harbin Institute of Technology, Harbin, China

SUMMARY: Full density nickel-nickel aluminide multilayer composites were successfully fabricated by thermal explosive synthesis of metal foil laminations at 620°C for 1h under 1 MPa pressure and post-treatment for 4 hours at 750 °C, 950 °C and 1150 °C under 5 MPa pressure in vacuum, respectively. The ductile nickel layers in composites can significantly improve room temperature toughness by bridging mechanism of multiple cracks. For post treatment at 750 °C and 950 °C, the composites are easy to delaminate at low tensile stress level because of the poor-bonded interface and the existence of Al₂O₃ between Ni₂Al₃ layers, but effects of aluminium oxides is relatively smaller for post-treated at 1150 °C, Ni₃Al layer can deform together with nickel layer like its single crystal by sliding, so it shows significantly strain-hardening and plastic flow as metal. Its mean strain and fracture strength at room temperature are about 13% and 786 MPa respectively.

KEYWORDS: nickel-nickel aluminide multilayer composites, thermal explosive synthesis, post-treatment

INTRODUCTION

Owing to their excellent high-temperature strength, chemical stability and low density, The aluminides of nickel as promising high-temperature structural materials are attracting the attention of many researchers. But their practical application was greatly restricted by their brittleness of room temperature, high sensitivity to composition and hard to shaping, and so on [1]. Recently, combustion synthesis(SHS) method has been applied to manufacture Ni-Al intermetallics [2,3]. However, combustion synthesis is difficult to fabricate full density products. So, J.C. Rawers attempts to produce metal intermetallics composites (MICs) by reaction sintering (hot-press SHS) of metal foils instead of metal powders [4]. The method for producing MICs has many advantages, such as: a) easily formatting full density products, b) conventionally fabricating near net shape composites through pre-deforming before reaction sintering, c) possibly obtaining well-bonded interfaces of metal and intermetallics, d) obtaining MICs of high fracture toughness, high-strength, high elastic modulus and light weight, and so on.

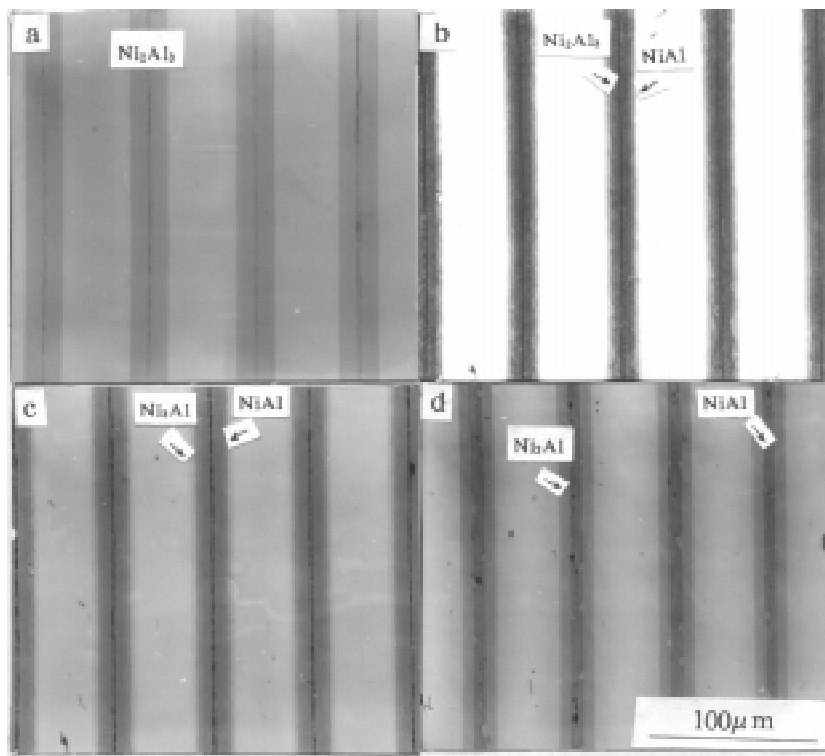
This paper mainly discusses the effects of microstructures, interfaces and aluminium oxide inclusions on tensile properties and behaviors in nickel-nickel aluminide multilayer composites.

EXPERIMENTAL PROCEDURE

Commercially pure Ni and Al foils degreased with acetone were cut into squares (80mm80mm) and stacked into laminations as shown in fig.1 in reference 4. The foil laminations in vacuum was heated to 620 °C for 1 hour under MPa pressure for thermal explosive synthesis, then heated to 750 °C, 950 °C, 1150 °C respectively for 4 hours under 5 MPa pressure for post-treatment. The tensile specimens were electro-discharger machined into flat dog-bone shaped bars. The effective gauge length and width was 20mm 10mm respectively, and the specimen thickness was 1mm. The tensile testing was taken in Instron at a constant crosshead speed of 1mm/min, correspondingly to strain rate of 8.3×10^{-4} /s in the gauge section. The microstructures and cross-sectional view of fractures were evaluated by JEOL probe in backscattered mode. Fracture surface was examined by SEM. Phases in composites were identified by x-ray energy-dispersive spectroscopy (XEDS) in SEM.

RESULTS

Microstructures



*Fig 1. Backscattered electron images of composites
(a) reacted at 620 °C for 1h; (b) post-treated at 750 °C for 4h
(c) post-treated at 950 °C for 4h; (d) post treated at 1150 °C for 4h*

The microstructure of composites by thermal explosive reacting Ni and Al foils at 620 °C for 1 hour under 1MPa pressure in vacuum consists of Ni and Ni₂Al₃ layer as shown in fig. 1 (a). Aluminium oxides coming from Al foil surfaces remain in the middle of Ni₂Al₃ layers.

The phases in composites post-treated at 750 °C, 950 °C and 1150 °C respectively for 4 hours under 5 MPa pressure are shown in fig.1 (b),(c) and (d) correspondingly. By post-treating 4 hours at 750 °C, thin layer of NiAl presents between Ni and Ni₂Al₃ layers. With increasing post-treating temperature to 950 °C, NiAl layer continually grows into Ni₂Al₃ layer and becomes thicker, and simultaneously Ni₃Al layer formats and grows by consuming Ni and NiAl. Aluminium oxides still remain between Ni₂Al₃ layers. After post-treated 4 hours at 1150 °C, Ni₂Al₃ layer was completely consumed, NiAl layer becomes thinner, and Ni₃Al layer grows thicker.

Tensile Properties and Behaviors

Table 1 gives the phases and room-temperature tensile properties of Ni-Ni aluminide multilayer composites post-treated at 750 °C, 950 °C and 1150 °C respectively, after reacted at 620 °C for 1h. The data in table 1 is average value of five specimens.

Table 1: Phases and tensile properties of Ni-Ni aluminide multilayer composites

post-treating temperature	phases	$\sigma_{0.2}$ (MPa)	σ_b (MPa)	δ (%)
750°C	Ni ₂ Al ₃ , NiAl, Ni	204	252	11.3
950°C	Ni ₂ Al ₃ , NiAl, Ni ₃ Al, Ni	83	98	0.51
1150°C	NiAl, Ni ₃ Al, Ni	348	786	12.8

Their typical room temperature tensile stress-strain curves are shown in fig 2.

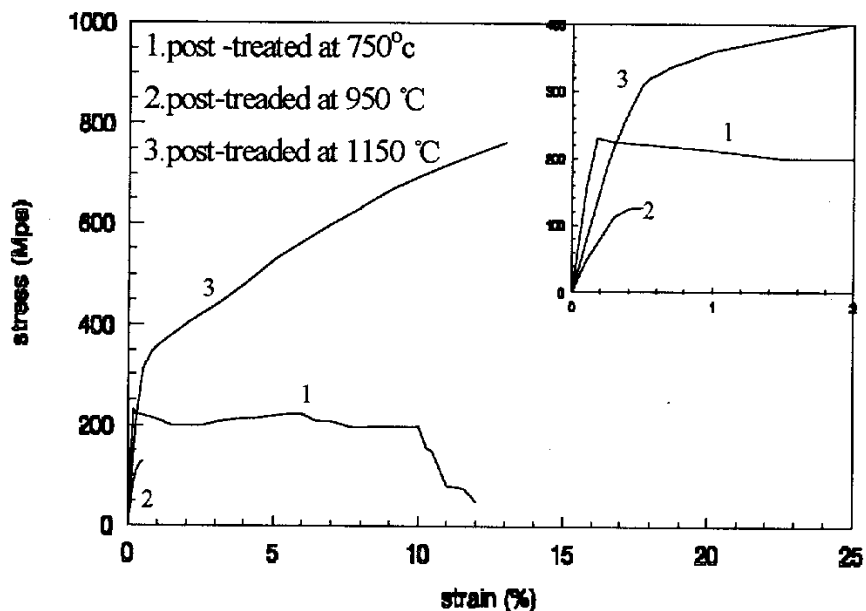
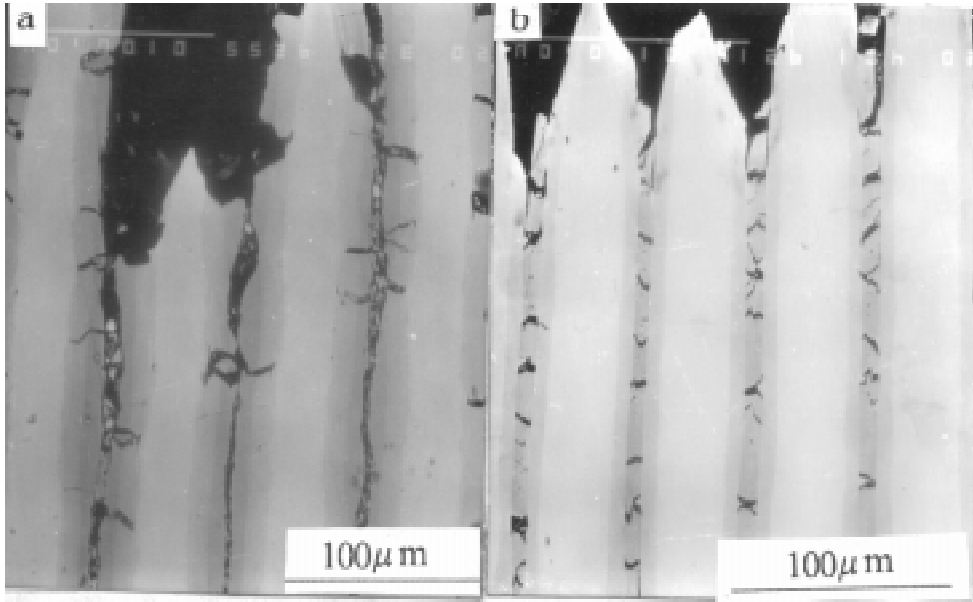


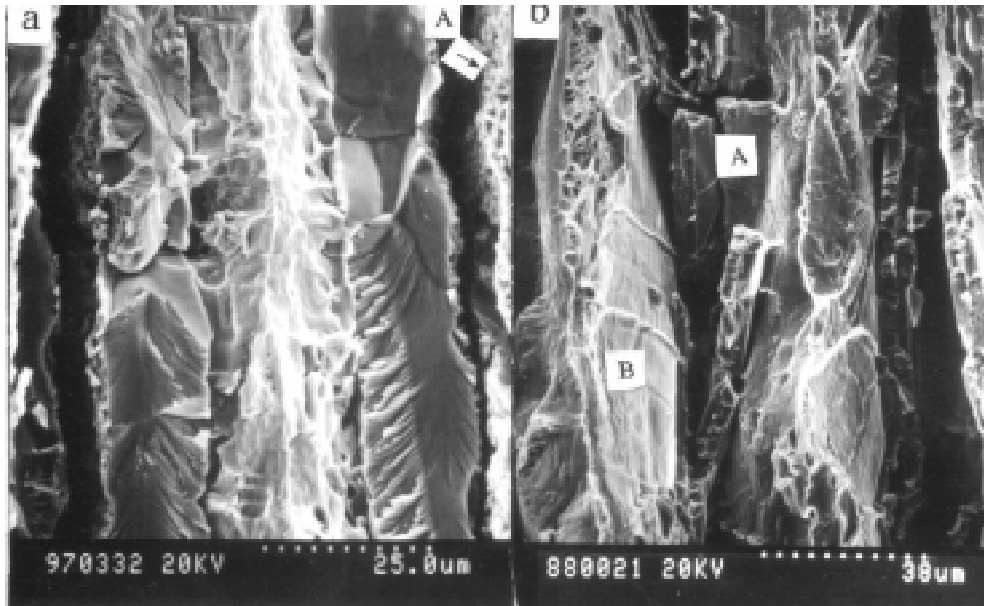
Fig 2. Stress-strain curves of Ni-Ni aluminide multilayer composites.

DISCUSSIONS

Aluminium oxides coming from Al foil surfaces present in the middle of Ni_2Al_3 layers at primarily Al foils position before reacting. It indicates that Ni atoms are hard to diffuse through Al oxide films of Al foils and react with Al atoms, and only Al atoms are easy to diffuse through Al oxide films and format Ni_2Al_3 with Ni atoms.



*Fig 3. cross-sectional view of tensile fracture surface
(a) post-treated at 950°C for 4h; (b) post-treated at 1150°C for 4h*



*Fig 4. fracture surface of tensile specimens
(a) post-treated at 950°C for 1h; (b) post-treated at 1150°C for 4h*

After post-treated at 750°C poor-bonded interfaces between Ni₂Al₃ layers because of existence of Al oxide inclusions rapidly debond in the primary stage of tensile. Composites fail by bridging mechanism of cracks little by little. The sharp turns of curve 1 in fig 2. mean breaking of one or more Ni layers. so curve 1 wind sharply.

In composites post-treated at 950 °C, brittle Ni aluminides is relative thicker, and Ni layer is thinner, the microcracks in NiAl and Ni₂Al₃ layers are longer than others. and Ni₃Al is too thin to inhibit cracks propagating, so it's breaks at low stress level. Aluminium oxides like honeycomb can be viewed at the side of Ni₂Al₃ as shown at point A in fig 4.(a). Fracture surface in ductile Ni layer mainly consists of tearing prism and merely ductile voids. It indicates that cracks rapidly cross thorough Ni layer by tearing without significantly plastic deforming.

For post-treatment at 1150 °C, at the beginning of tension, NiAl layer can coordinately elastic deform with Ni₃Al and Ni layers, stress dispersion in Ni and Ni aluminides abides with combined rule. When stress is higher than the strength of NiAl, NiAl layers begin typically break by transgranular cleavage along its {110} due to intrinsic brittleness of NiAl. Cleavage planes cross mostly with tensile direction at about 45° angle, as shown in fig 3 (b) and at point A in fig 4 (b). Debonded interfaces of between NiAl layer with Al oxide inclusions seldom are viewed in fig 4(b). It suggests that effects of Al oxides is rather smaller at post-treatment at 1150 °C. The length of debonded interface of NiAl and Ni₃Al is very short, it suggests that interface of NiAl and Ni₃Al is strongly-bonded. The density of cleavage cracks in NiAl layers increases with increasing of tensile stress. The modulus of composites decreases little by little, so the slope of tensile curve at about 300 MPa becomes slow. However, cleavage cracks in NiAl layer are difficult to propagate through hard Ni₃Al layers, since merely cracks crossed through Ni layer are shown in fig 3(b). Ni₃Al layers inhibiting crack propagating in NiAl layers can retard the decrease of the effective area of composites, and strength continually increases by work hardening with strain increasing as shown in fig 2. And little debonded interface in the fracture surface shows that interface of Ni₃Al and Ni layer informed by reaction diffusion is strongly bonded too. The single Ni₃Al layer slides mainly in <110> {111} like single crystal and can cooperatively deform with Ni layer, many fine and intensive slipping lines can be clearly viewed in the side of Ni₃Al layer which debonded with NiAl layer as shown at point B in fig 4. Therefore the composites post-treated at 1150°C shows excellent plasticity and good strength. Significantly strain-hardening and plastic flow is presented under the tensile loading.

The slide deformation of Ni₃Al at 45° angle with tensile direction results in stress concentration at the interface of NiAl and Ni₃Al, and their well-bonded interface requires the deformation of NiAl with Ni₃Al layer together, therefore, the cleavage at about 45° angle with tensile direction are induced in NiAl layers.

CONCLUSIONS

- 1) Composites by reaction-synthesis of metal foil laminations and post-treatment at elevated temperature is a conventional and feasible method of producing material.
- 2) The good plasticity and strength can be made by reaction-synthesis at 620 °C for 1h under 1 MPa pressure and post-treated at 1150 °C for 4 hours under 5 MPa pressure in vacuum.

- 3) Ni atoms are hard to diffuse through Al oxide films of Al foils, and only Al atoms are easy to diffuse through Al oxide films and form Ni_2Al_3 with Ni atoms.
- 4) Al oxide inclusions on the aluminium foil surface result in the poor-bonded interface between intermetallics, especially for that post-treated at relative low temperature.
- 5) Generally, Ni_3Al layer is strongly bonded with Ni and NiAl layers.
- 6) The large deformation is attributed to the slide of Ni_3Al layer and cooperatively deformation of Ni_3Al and Ni layer together

REFERENCES

1. H.J.Engell, etc., Advanced structural and functional materials edited by W.G.J.Bunk, 1991.
2. A.S. Rogachov, etc., Inter.J.SHS., Vol. 2, No.1, 1993, P25-38.
3. A.S.Rogachov, etc., Inter. J.SHS., Vol. 3, No.3, 1994, P239-252.
4. J.C.Rawers, etc., Inter. J.SHS. Vol. 2, No.1, 1993, P12-24.

SUPERPLASTIC FORMING OF ALUMINUM MATRIX COMPOSITE SHEETS REINFORCED BY SiC PARTICLES

T.Ninomiya¹, H.Hira¹, N.Kanetake² and T.Choh²

¹*Aerospace Division, Kawasaki Heavy Industries, LTD.,
1.Kawasaki-Cho, Kakamigahara City,Gifu-Pref.504 Japan*

²*Department of Materials Processing Engineering, Nagoya University,
Furo-Cho, Chikusa-Ku, Nagoya,464-01, Japan*

SUMMARY: Superplastic forming of aluminum alloy matrix composites reinforced by SiC particles was studied from their basic deformation properties in a tensile test to the forming applications of various shape parts by gas pressure. The tensile test was performed at elevated temperatures to characterize the optimum strain rate for superplasticity. It is much higher for the aluminum matrix composite sheets than that of a conventional 7475 alloy sheet. One of the forming tests is an axisymmetric conical part, in which the composite sheet is biaxially formed at high strain rate around the suitable rate characterized in the tensile test. It can be successfully formed even in biaxial forming at high strain rate. The others are box shape parts with different geometry, in which the sheet is formed at lower strain rate than that in the conical part forming. The composite sheet can be also successfully formed into box part as well as the conventional 7475 alloy sheet.

KEYWORDS: Metal matrix composite, Superplastic forming, Aluminum alloy, SiC particle, High strain rate, Tensile test, Forming test

INTRODUCTION

Discontinuously reinforced metal matrix composites (MMCs) exhibit a unique combination of high modulus and strength at room temperature and have possibility for secondary forming that is difficult for fiber reinforced composites. The development of forming process is very important to apply the discontinuously reinforced MMC for complex shape products, because the MMC has some difficulties in the conventional manufacturing process including cold forming and machining due to its excellent strength and wear resistance.

Recently superplastic behavior of the discontinuously reinforced aluminum matrix composite was reported in some works[1-3]. Therefore the superplastic forming is one of the useful secondary processes, and it enables precise dimension forming by low applied load. Especially, it is very useful for the MMC because its superplastic behavior appears at higher strain rate than that of conventional aluminum alloys. It means that the forming process enables also high productivity.

In the present work, superplastic deformation behavior in a tensile test and forming applications of various shape parts were investigated for aluminum alloy matrix composites reinforced by SiC particles. The tensile test was performed at elevated temperature to

characterize the optimum strain rate for the superplasticity. One of the forming tests is an axisymmetric conical part, which is selected to examine the possibility of the high strain rate superplasticity in biaxial forming. The others are box shape parts, which are selected as basic shapes aiming the real complex shape parts design.

MATERIAL AND EXPERIMENTAL PROCEDURE

Several aluminum matrix composites reinforced by SiC particles were prepared for the experiment. They are SiCp/2124 and SiCp/8090, and their volume fractions of SiC_p are 17% in both materials. They were both commercially fabricated by P/M method and received as annealed sheets with a nominal thickness of 2mm. Then they were hot rolled into 1.0-1.5mm at 773K to control an initial thickness of the sheet. Conventional superplastic aluminum alloy 7475 was also prepared for comparison of the formability.

Tensile tests at elevated temperatures were performed under various cross-head speeds, and deformation characteristics were evaluated.

An axisymmetrical forming test of a conical part was performed by using the forming equipment shown in Fig.1 with compressed air up to 1 MPa, which enabled to form at high strain rate. The blank disk with 35mm diameter and 1mm thickness is set between a die and a holder, and they are heated in the furnace. The compressed air is inlet from the bottom after reaching the appropriate temperature, and the disk is formed into the conical shape along the die.

Other forming tests of box shape parts with different geometry were performed by using the die set shown in Fig.2 with Ar gas up to 3 MPa. A rectangular blank sheet with 1.5mm thickness is set between the preheated upper and lower dies, and the Ar gas is inlet from the center of the upper die. In this box shape forming, the gas pressure is not constant during the forming process, but it is controlled to the appropriate level which is theoretically predicted on the basis of simple assumptions. The forming tests were carried out in the conditions listed in Table 1. The distributions of the thickness strain of the formed parts were measured and compared among three materials sheets.

EXPERIMENTAL RESULTS AND DISCUSSION

The relationships between the total elongation and the strain rate of 7475 sheets and hot rolled composite sheets are compared in Fig.3. The larger superplastic elongation above 200% can be found in the composite sheets as well as the 7475 alloy. And the maximum elongation of the composites are observed at about 100 times higher strain rate than that in the conventional superplastic aluminum alloy 7475.

Fig.4 shows the appearances of the formed conical parts. They were completely formed in only a few seconds and it means the forming was performed at the rate of around 1×10^{-1} (/sec) which is the suitable rate obtained by the tensile test. From this result, it is confirmed that the superplasticity of the composites at high strain rate which is observed in the uniaxial tensile test is also recognized in the biaxial forming of a conical shape part. The surface of the formed part is smooth in general, but slightly rough surface and a small crack are observed only at the top of the cone. The thickness of the formed part decreases gradually from the flange to the top and the crack is occurred at the top, because the sheet is touched to a die face and its deformation is restricted gradually from the region near the flange during the forming.

The forming tests of box shape parts were performed at the strain rate between 10^{-3} and 10^{-2} /sec that is lower than the suitable rate for the superplasticity of the composites, because of the limit of the gas supply ability of the forming equipment which was fabricated for the conventional superplastic forming (strain rate: 1×10^{-4} to 5×10^{-4} /sec). The results of the forming tests are summarized in Table 1. In the table, “O” and “X” show that the box part was formed with success and unsuccess respectively. All materials were successfully formed in the boxes of type I and II, but a burst of the sheet was occurred in the forming of the type III box at the site shown by an arrow in the figure.

Appearances and sizes of the formed parts are shown in Fig.5. The surfaces of the formed parts were smooth similarly to the conical parts. As above mentioned, the forming rate is very low for the composites, while it is near the suitable one of the 7475 alloy. The m-values of the composites and 7475 sheets at the forming rate are 0.2 and 0.55 respectively. But the composites have the similar formability as the conventional superplastic aluminum even at low strain rate.

Fig.6 shows the longitudinal sections of the formed type II boxes. It can be found that the thickness is also decreased gradually from the flange to the corner along the side wall in all materials. The distributions of thickness reduction of the type II boxes are shown in Fig.7, which are measured from the center of a bottom to the flange along the line shown in the figure. The thickness reductions at the corners of the composite boxes are larger than that of the 7475 alloy.

During the forming process of the type II box, at first the blank sheet is freely bulged in the die, and then touched on the dieface at the side wall and the bottom wall. Finally the box corner is formed and the forming is finished. The forming gas pressure is about 5 to 10 times higher in the forming of the composites than that of the 7475 alloy. The difference of the gas pressure level will lead to the difference of the friction between the die and the sheet. Namely the friction in the case of the composites box is much larger than the 7475 alloy. Therefore, in the box of the composites, the sheet is locally formed in the corner because the sheet slide is restricted in the touched region due to the large friction. Then the thickness at the corner is much more decreased than the 7475 alloy. However the localization of deformation is better for the composite, because the local strain rate around the corner becomes very high and it enables the large elongation without a crack occurrence.

From such a reason, the box shape parts were formed successfully even at lower forming rate than that of the suitable strain rate for the superplasticity of the composite sheets. Therefore, deeper and more complex shape parts can be expected to be formed by the increase of the forming rate.

CONCLUSIONS

Superplastic behaviors of aluminum matrix composite sheets were investigated by the tensile test and the forming tests of conical and box shape parts.

The high strain rate superplasticity of the composite sheets was observed in the tensile tests. And axisymmetric conical part was successfully formed at such a high strain rate. Box shape parts were also successfully formed even at lower forming rate, because the local strain rate around the corner becomes very high and it enables the large elongation without a crack occurrence.

ACKNOWLEDGEMENT

This work was supported by NEDO (New Energy and Industrial Technology Development Organization) and performed as Measures for the Promotion of Regional Technology which are planned by MITI (the Ministry of International Trade and Industry).

REFERENCES

1. Mabuchi, M., Higashi, K. and Okada, Y. "High Strain Rate Superplasticity in Particle Aluminum Composites", *Proceedings of an International Conference on Superplasticity in Advanced Materials*, Osaka, Japan, June 3-6, 1991, Superplasticity in Advanced Materials
2. Imai, T., L'Esperance, G. and Hong, B.D. "High Strain Rate Superplasticity of AlN Particulate Reinforced Aluminum Alloy Composite", *Scripta Metallurgica et Materialia*, Vol.31, No.3, pp.321-326, 1994
3. Hikosaka, T., Imai, T. and Nieh, T.G. and Wadsworth, J. "High Strain Rate Superplasticity of a SiC Particulate Reinforced Aluminum Alloy Composite by a Vortex Method", *Scripta Metallurgica et Materialia*, Vol.31, No.9, pp.1181-1186, 1994

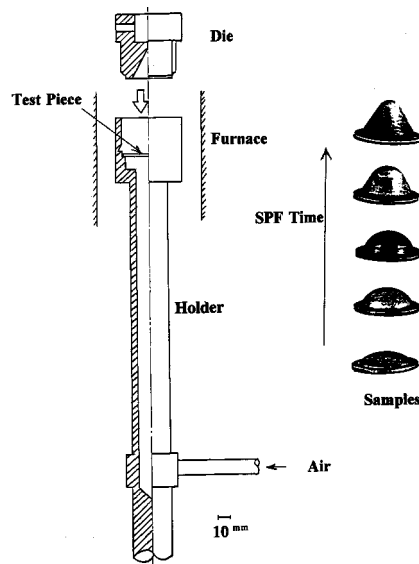


Fig.1 Schematic view of the forming equipment for conical part

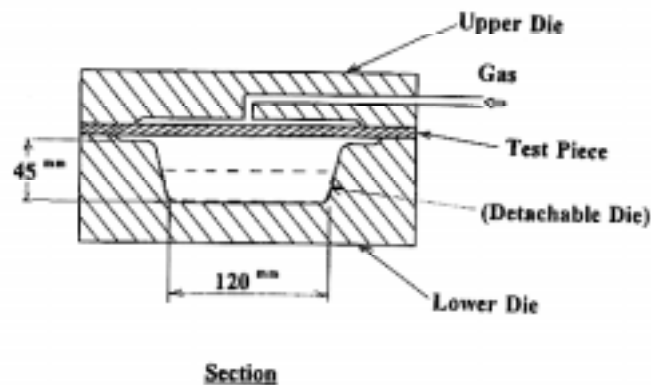


Fig.2 Schematic view of the forming die set for box part

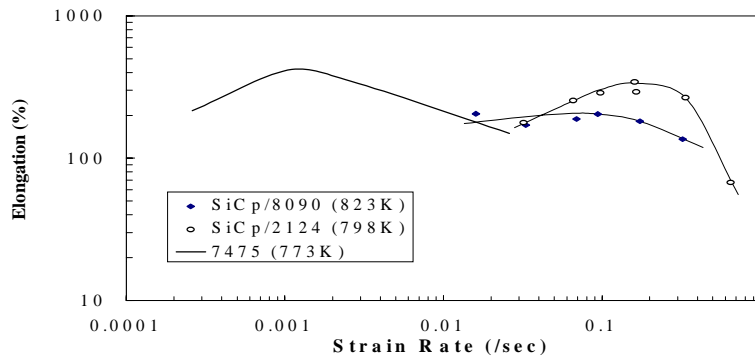


Fig.3 Relationship between elongation and strain rate of 7475 and hot rolled composite sheets






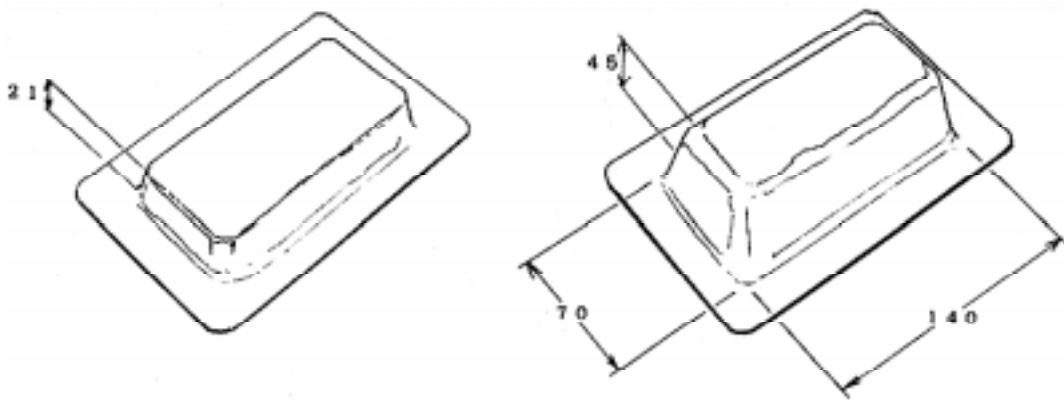
Material	SiC _p /2124 (1.1mm ³)	SiC _p /8090 (1.0mm ³)
Appearance		
Conditions	Temp : 798K Gas Pressure : up to 0.4MPa	Temp : 823K Gas Pressure : up to 0.8MPa

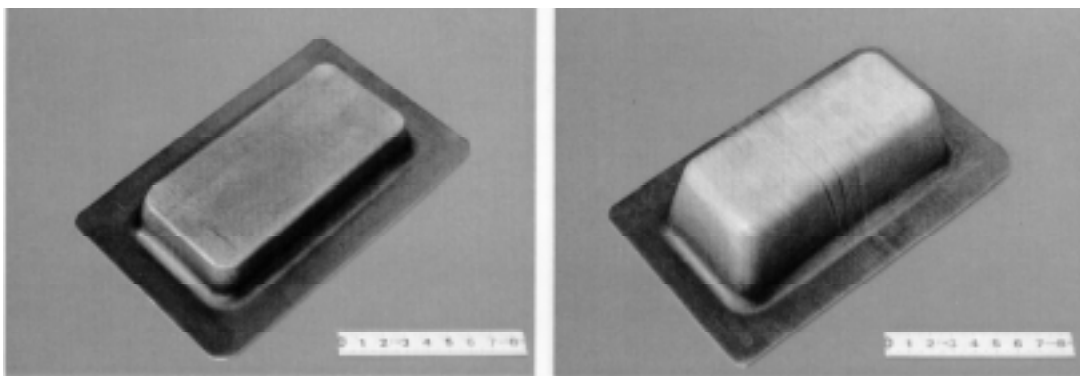
Fig.4 Appearance of the superplastically formed small cone at high strain rate

Table 1. Forming Condition and the Result of Box shape Forming Test

Material	Forming condition		Result of the forming test			type I 
	Forming rate	Temp.	type I	type II	type III	
SiC _p /2124	5x10 ⁻³ (/sec)	773 (K)	○	○	×	type II 
SiC _p /8090		833 (K)	○	○	×	
7475	5x10 ⁻⁴ (/sec)	773 (K)	○	○	×	type III 



(1) box size (unit : mm)



(2) appearance

Fig.5 Appearance and size of superplastically formed box parts

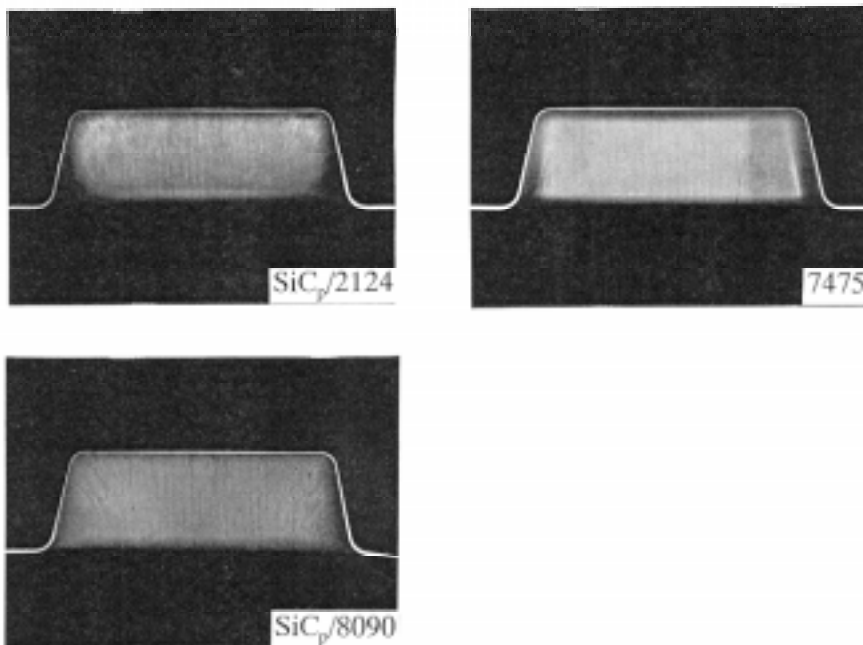


Fig.6 Longitudinal sections of the type II boxes

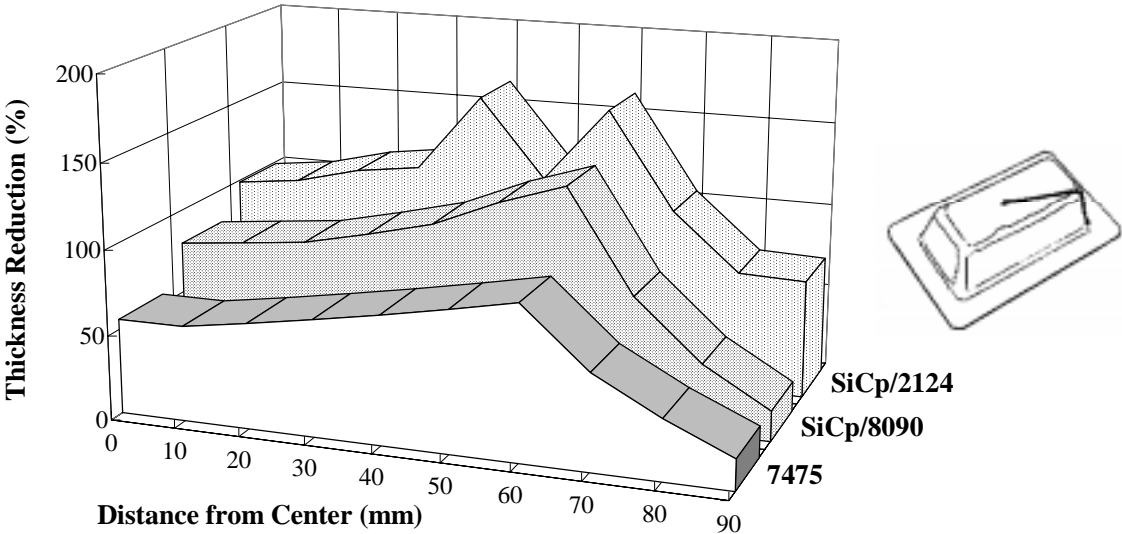


Fig.7 Thickness strain of formed type II boxes

MACHINING OF REINFORCED ALUMINIUM AND MAGNESIUM

K. Weinert, D. Biermann and M. Liedschulte

Institut für Spanende Fertigung, University of Dortmund, 44221 Dortmund, Germany

SUMMARY: Several aluminium and magnesium alloys reinforced with different particles and short fibres have been machined for the investigations. The main problem for the machining of metal matrix composites (MMC) is tool wear, which is caused by the hard and abrasive reinforcements. Therefore it is necessary to find suitable cutting tools for the MMC and the different machining operations. In addition it is required to investigate the cutting conditions considering tool wear, surface quality, accuracy and surface integrity. In this paper the results of investigations concerning turning, milling and drilling of different MMC are presented.

KEYWORDS: metal matrix composites, turning, drilling, milling, wear mechanism, suitable cutting tool materials, diamond coated tools, subsurface zone

IMPORTANT MECHANISMS FOR THE MACHINING OF MMC

The main problem encountered in the conventional machining of MMC is tool wear, which is caused by the hard and abrasive reinforcements. A detailed analysis of the tribological system is necessary to understand the wear mechanism. Figure 1 shows a schematic representation of the elements and parameters of the cutting process. The reason for the extensive tool wear when machining MMC is the direct contact between the particles or fibres and the cutting edge. The dominant wear mechanism is abrasion which is generated by impacts at the cutting edge and relative sliding motion to the rake and clearance face of the cutting tool. These interactions lead to high mechanical and thermal loads. Important are the high dynamic stresses by the direct contact with the reinforcements.

For example: When turning particle reinforced aluminium with a useful reinforcement (volume fraction: 20 vol. %; grain size of the particles: 10 μm) and the listed parameters (cutting speed $v_c = 500$ m/min; feed rate $f = 0.1$ mm/rev; depth of cut $a_p = 1$ mm) about 20 million particles per second are separated with the chip. For the relation of the feed rate 0.1mm per revolution and the grain size about 10 μm it can be assumed, that nearly 2 million particles per second have direct contact with the cutting edge. This calculation shows clearly the high abrasive wear attack particularly at the cutting edge in form of microimpacts. Furthermore the direct sliding contact between reinforcement and rake face as well as clearance face abrade the cutting tool very intensive. Because of the high hardness of the reinforcements it can be similar to a grinding process if cutting tools with an insufficient hardness are used.

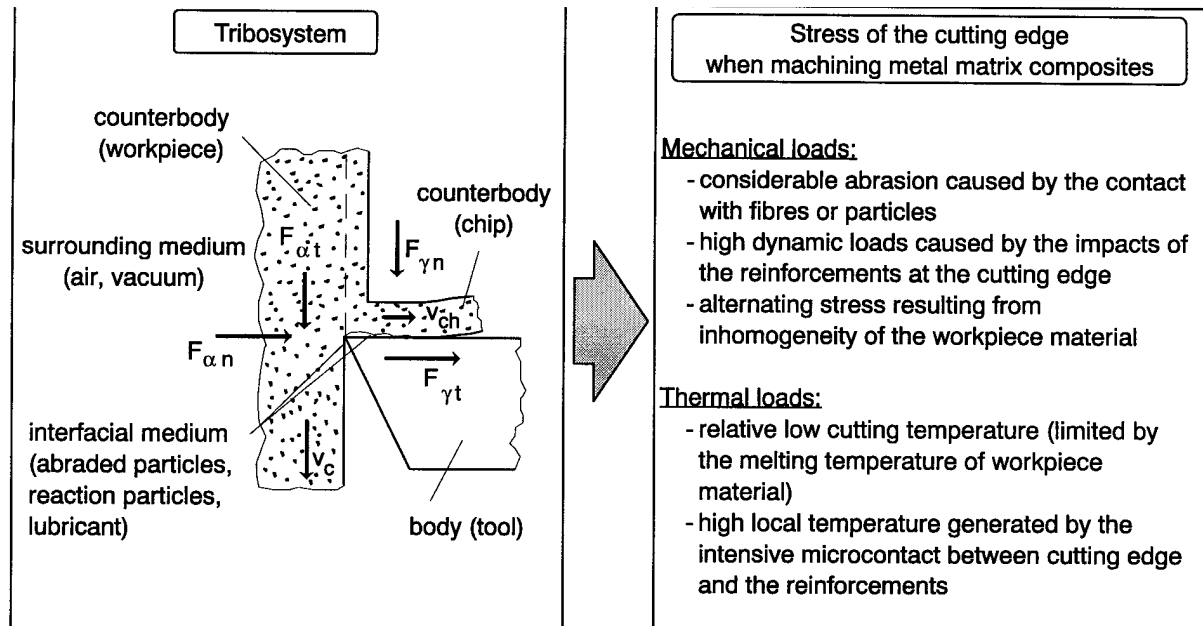


Fig. 1: Mechanical and thermal loads when machining MMC

Concerning the cutting tool materials it is important to consider their microstructural composition. Most of the cutting tool materials which are in common use consist of composite materials. For example: Cemented carbide consists of carbides as hard phase and a Co binder phase. Due to this, decisive factors are the properties of the reinforcement, particularly hardness, dimension and volume fraction but also hardness and grain size of the cutting tool material.

Very important for the comprehension of the cutting process concerning the tool wear are the abrasive wear mechanism: Microploughing, microfatigue, microcutting and microcracking [1]. Depending on the ratio of the properties between the reinforcements and the cutting tool materials the different abrasive wear mechanism are dominant:

Microploughing

Microploughing occurs when hard abrasives interact on the surface of a material which causes high plastic deformations. Several contacts of hard abrasives with microploughing lead to microfatigue. In general this mechanism is not dominant concerning the tool wear when machining MMC because the cutting tool materials have a high hardness and therefore a high resistance against plastic deformation. Nevertheless the high stress produced by the microcontacts between the reinforcement and the cutting tool can cause plastic deformation but the intensity concerning the tool wear is relative low.

Microcutting

The reinforcement removes material from the cutting tool in form of microchips. This mechanism is dominant if the reinforcement is harder than the cutting tool material and the dimension of the reinforcement is higher than the grain size of the hard phases of the cutting tool material.

Microcracking and Fatigue

The wear is produced by high dynamic loads which generates cracks into the cutting tool. These mechanism occur if the hardness and/or the grain size of the cutting tool material is higher compared with the properties of the reinforcements.

Comprehensive tests for the machining of aluminium matrix composites have shown that the suitability of the cutting tool materials mainly depends on the hardness of the reinforcements. But also the relation between the size of the reinforcements and the grain size of the cutting tool materials is important because these factors influence the dominant abrasive wear mechanism [2, 3, 4].

COMPARISON OF THE TOOL WEAR FOR THE MACHINING OF REINFORCED ALUMINIUM ALLOYS AND MAGNESIUM ALLOYS

In order to compare the influence of the matrix material on the machining process some magnesium matrix composites have been investigated. For example the results for milling of two different magnesium matrix composites with a short fibre reinforcement are summarized in Fig. 2. The shape of the cutting edge is described in the table tool geometry in which the main angles (α/α' : normal clearance/side clearance; γ/γ' : normal rake/side rake; κ/κ' : cutting edge angle/minor cutting edge angle) are quantified. The first point is the lower wear rate of polycrystalline diamond (PCD-MG) compared with cemented carbide (CC-MG). This result corresponds to the investigations for the machining of aluminium matrix composites [2]. Another point is the low difference of the wear rate between the different magnesium matrices (AZ 91, QE 22).

The scanning electron microscope (SEM) photographs show the worn cutting edges. The topography of the worn cutting edges are in accordance with the analyzed cutting tools used for the machining of short fibre reinforced aluminium alloys, so that the main wear mechanism can be transferred. Also the results for the machining of particle reinforced materials concerning the tool wear and the tribological mechanism are corresponding for aluminium and magnesium.

When machining δ -Al₂O₃-short fibre reinforced aluminium or magnesium the dominant abrasive wear mechanism is microcracking and fatigue. Because of the low hardness of δ -Al₂O₃-short fibres of approx. 800 HV it is not possible that the short fibre abrade the cemented carbide (approx. 1600 HV) or PCD (approx. 5000 HV) by microcutting. The hard phases of the cutting tools are abraded due to microcracking and fatigue at the cutting edge. The hard phases which are separated can also wear the cutting tool because they slide over the rake and clearance face due to the relative motion to the workpiece and the chips. Hereby the hard phases of cemented carbide (WC) effect like a polishing compound because of their small grain size of approx. 1.5-2 μ m and produce a very smooth topography of the worn surface. In the case of PCD the larger diamond grains (approx. 10 μ m) which are separated as a result of the wear attack by the reinforcements lead to very high local stresses at the cutting edge and can produce a wear out of the PCD insert by a self furrowing effect.

Fig. 3 shows a comparison between the tool wear when milling δ -Al₂O₃-short fibre reinforced magnesium alloys and an aluminium alloy with PCD. The difference between the values of the flank wear are relative low. This corresponds with the fact that also the differences between the strength of the matrix alloys is relative low (AlSi12CuMgNi: R_m = 295 MPa QE 22: R_m = 250 MPa, AZ 91: R_m = 220 MPa) [5, 6].

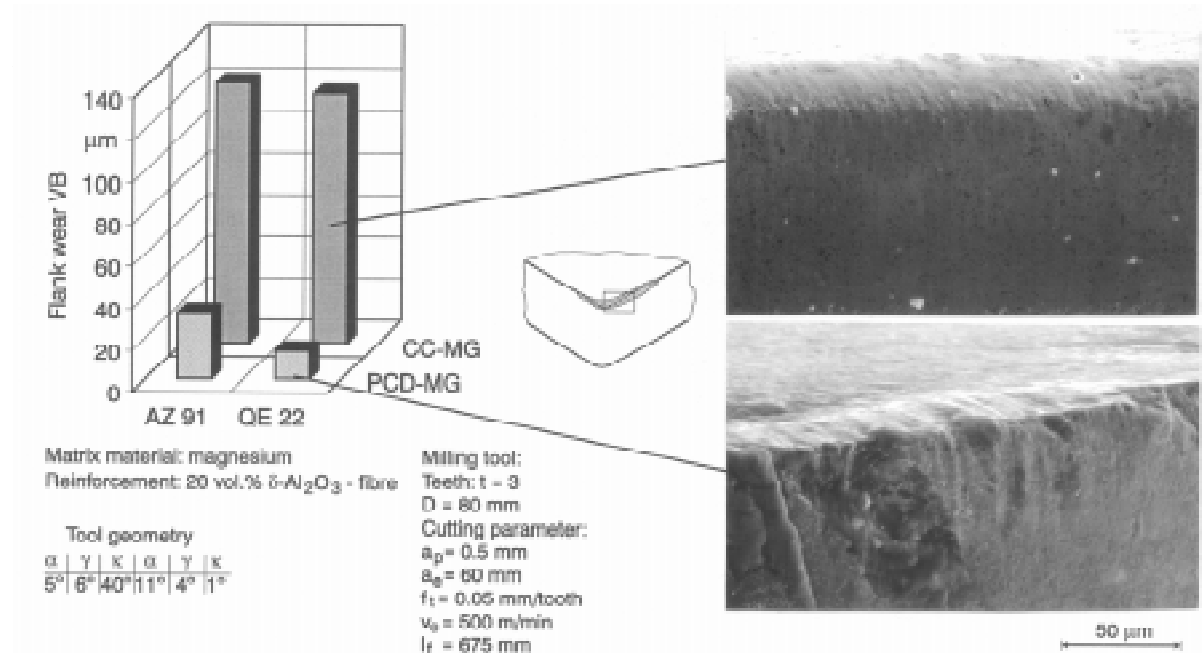


Fig. 2: Tool wear when milling reinforced magnesium with cemented carbide and PCD

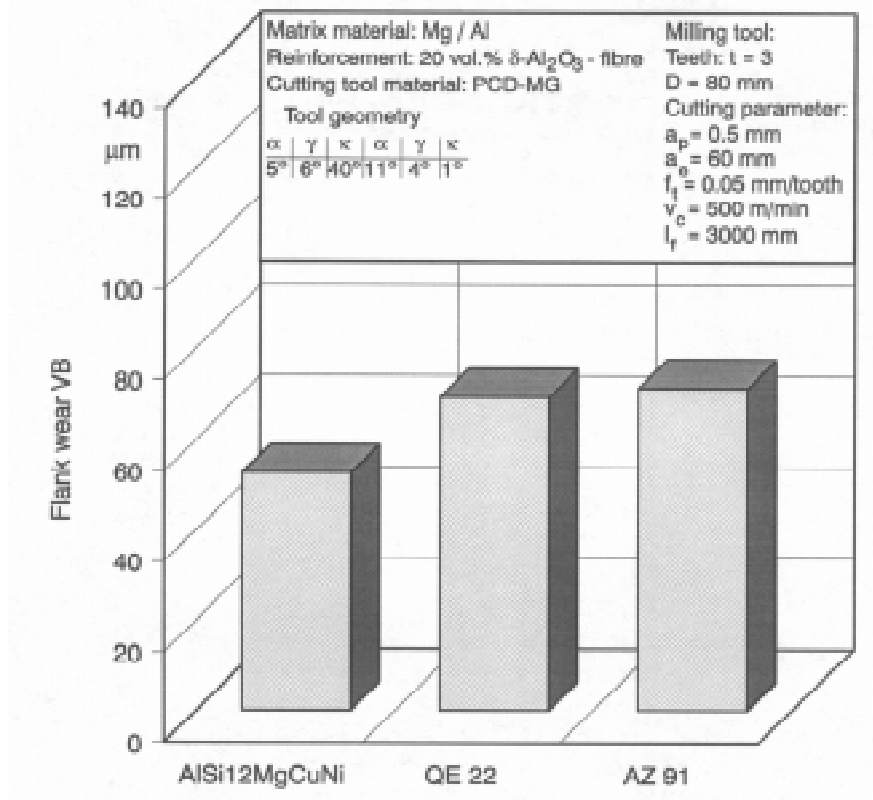


Fig. 3: Tool wear when milling magnesium and aluminium with PCD

As an example for drilling SEM photographs of the tool wear of a cemented carbide drill when machining particle reinforced magnesium are depicted in Fig. 4. The different magnifications present a very regular flank wear. The photograph with the highest magnification (photograph in the middle of the figure) shows the topography of the worn surface which is characterized by grooves. These grooves are mainly parallel orientated to the cutting direction. This is the typical appearance of the wear topography when machining MMC with very hard reinforcements like SiC or B₄C particles. Because the hardness of cemented carbide is lower than the hardness of SiC and B₄C particles, these particles abrade the cemented carbide cutting tool by microcutting which is indicated by the grooves at the worn clearance face. This mechanism leads to a very extensive tool wear. Possibilities to reduce the tool wear are the use of harder cutting tool materials, for example PCD or diamond coatings, or the application of coarse grained cemented carbide [3].

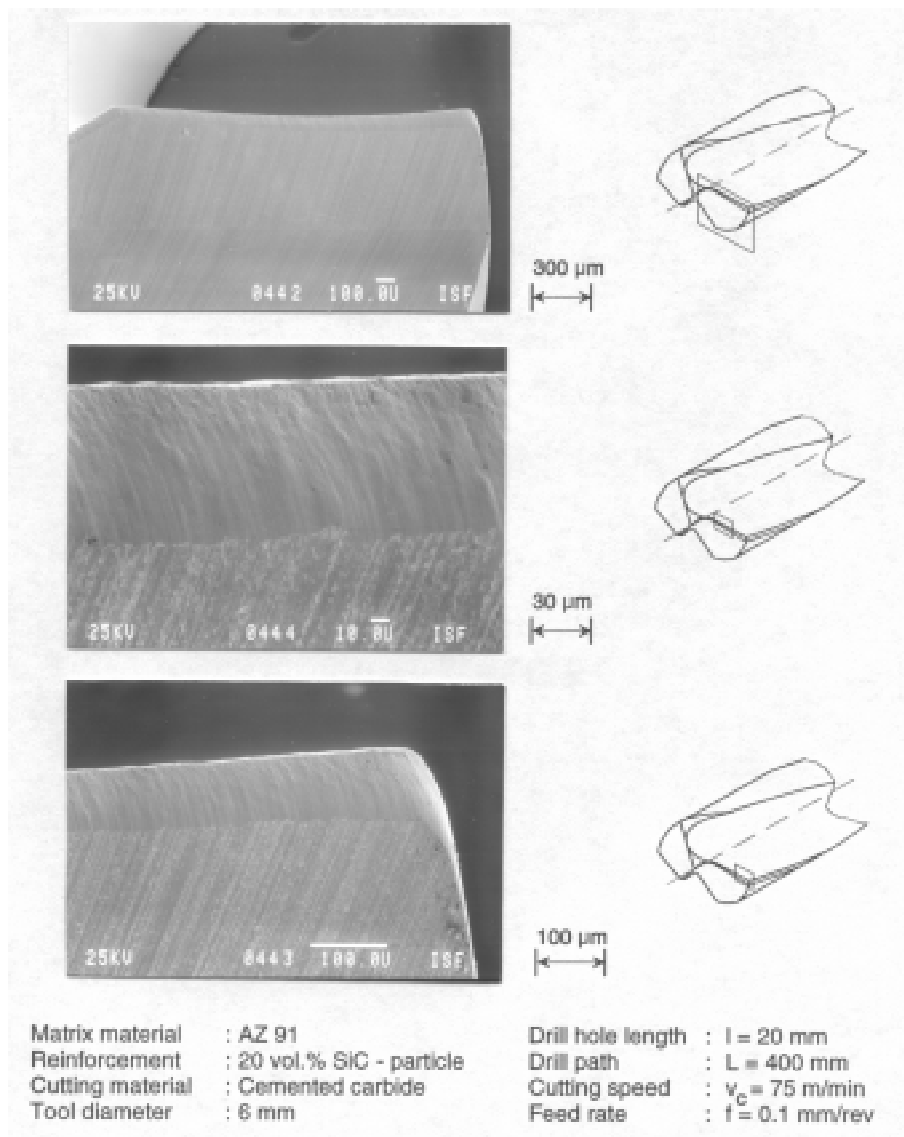


Fig. 4: SEM photographs of the tool wear when drilling particle reinforced magnesium with cemented carbide drill

THE USE OF DIAMOND COATED CEMENTED CARBIDE

Due to the high cost of tools when using PCD, particularly of tools with a complex geometry, such as drills or thread drills, efforts must be made to find suitable coatings in this area. Very important demands are high hardness of the coating and a sufficient bonding between the substrate and the coating to achieve a high resistance against the abrasive wear attack. Former investigations have shown that TiAlN coating on cemented carbide is suitable for turning and drilling of δ -Al₂O₃-short fibre reinforced aluminium. When machining SiC or B₄C reinforced aluminium this coating is early abraded. Because of the very high hardness of SiC or B₄C particles the abrasive wear attack is too strong for this coating. Therefore the coating cannot protect the cutting tool so that there is nearly no advantage reachable compared with the uncoated cemented carbide tool [2, 7].

Diamond coatings are in principle suitable for turning of MMC because of their high hardness. However former investigations about the use of diamond coated cemented carbide tools have resulted that the wear protection is not very efficient. Because of the limited bonding between the coating and the cemented carbide substrate the coating breaks off due to the wear attack of the reinforcements [2].

For the development of suitable diamond coated tools the choice of the substrate material and its preparation is very important to achieve good nucleation of diamond and sufficient bonding between the coating and the substrate. A suitable approach to the problem of sufficient nucleation and adhesion of the diamond film is to use Si₃N₄ ceramic as substrates. In addition Si₃N₄ substrates have a good compatibility with thin diamond films because the deviation of the thermal expansion coefficient is relative low [8]. Therefore some good results have been achieved for the use of diamond coated Si₃N₄ cutting tools for the machining of reinforced aluminium [2]. However, because of lower toughness and higher cost of ceramic compared with cemented carbide particularly for cutting tools with a complex geometry, such as drills or thread drills, diamond coated ceramics are not a fundamental solution.

The use of cemented carbide as substrate is preferred because of the good combination of toughness, wear resistance and resistance to plastic deformation and furthermore the good flexibility to produce tools with a high variety of their shape. However, the binder phase of cemented carbide mainly consists of Co. Co is a good solvent for carbon and a good carbon carrier, it inhibits adhesion of diamond to the carbide substrate and also intensifies the formation of non-diamond material including soot [8]. Therefore an important prerequisite to achieve a suitable diamond coating is to remove the Co binder phase from the surface and the subsurface zone of the cemented carbide substrate. The research in this field leads to a further development of improved diamond coated cemented carbide tools.

Fig. 5 shows SEM photographs of a diamond coated cemented carbide insert. It can be seen that the coating has a very regular grain size and a relative smooth surface topography. The thickness of the coating amounts 10 - 12 μ m.

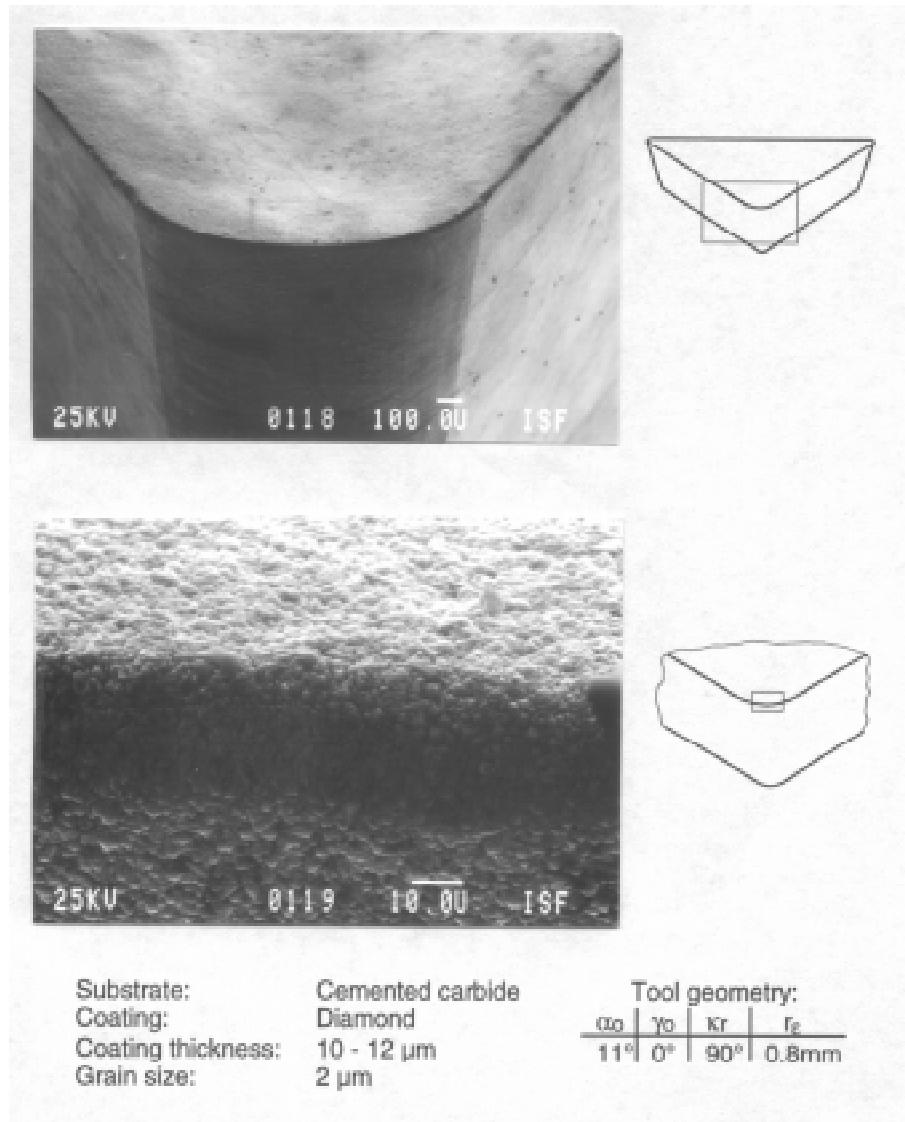


Fig. 5: SEM photographs of a diamond coated insert

Detailed analysis of the tool wear with SEM showed that for the machining of $\delta\text{-Al}_2\text{O}_3$ short fibre reinforced aluminium the diamond coating is in a good condition after a cutting time of $t_c = 7.5$ min (Fig. 7). Only a slight wear in form of abraded diamond grains in the area of the cutting edge can be detected. When turning SiC-particle reinforced aluminium the tool wear is insignificant higher and the diamond coating is removed in places at the cutting edge. But nevertheless the remained coating is sufficient to protect the substrate. Also the wear rates for the diamond coating are in the range of the flank wear when machining with PCD.

The results concerning the tool wear for the use of the diamond coated cemented carbide are depicted in Fig. 6. The diagrams show the development of the flank wear when turning $\delta\text{-Al}_2\text{O}_3$ short fibre (left side) and SiC-particle reinforced aluminium (right side). As reference the flank wear of uncoated cemented carbide tools is marked. In both cases the diamond coating leads to a considerable reduction of the tool wear. The high potential of the diamond coating can be estimated because of the low gradient of flank wear graphs.

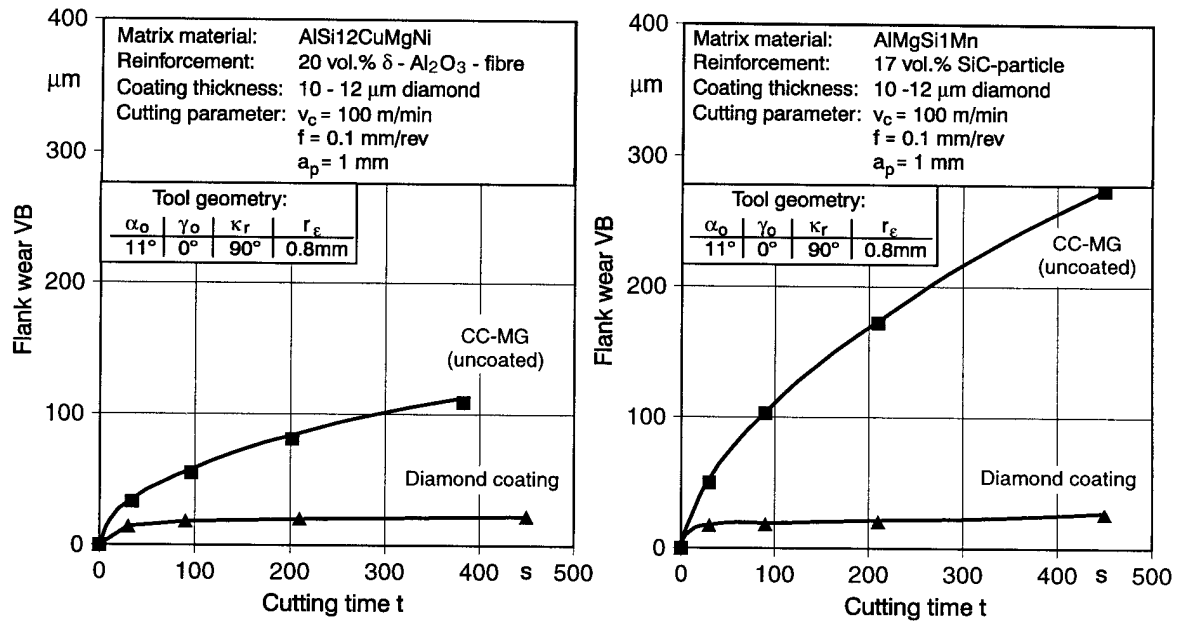


Fig. 6: Tool wear when turning short fibre and particle reinforced aluminium with diamond coated cutting tools.

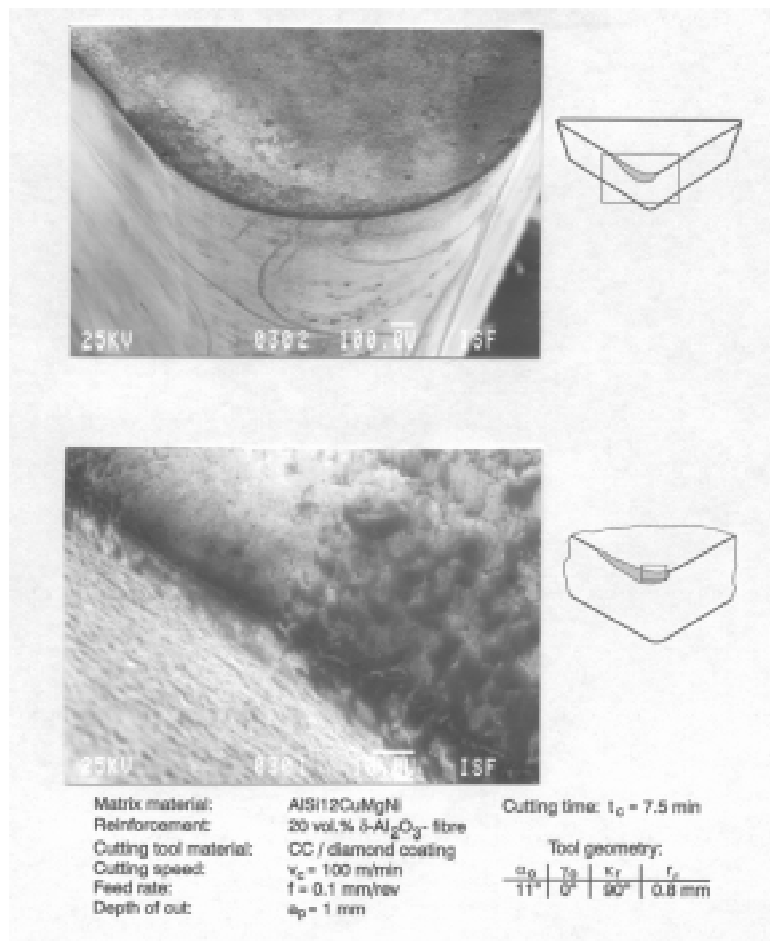


Fig. 7: SEM photographs of the tool wear of diamond coated inserts when turning short fibre reinforced aluminium.

SURFACE TOPOGRAPHY AND SUBSURFACE ZONE

Besides the tool wear another important factor is the surface integrity of MMC. Damage of the reinforcements, caused by the machining process, can lead to a decrease in the properties of the components. The cutting and deformation mechanism affects the surface quality in a multitude of ways. Examples are damages in the form of microcracks, pores, microstructural transformation, plastic deformation, residual stresses and changes in the hardness.

In order to analyze the influence of composite materials on the subsurface zone for turning, milling and drilling, SEM and optical microscope analysis of the machined surfaces and of special cross sections were carried out.

Fig. 8 shows SEM photographs of the surface topography and a cross section of the subsurface zone. PCD was used at a cutting speed of $v_c = 500$ m/min, a feed rate of $f_t = 0.05$ mm per tooth and a depth of cut which amounts to $a_p = 0.5$ mm. The surface exhibits a large number of pores, which primarily develop where individual particles or groups of particles are to be found in the boundary layer of the surface. Particle fragments can be clearly recognized in the area of the pore. The dimension of the fine grooves in the surface corresponds to the dimensions of the particles. Therefore the grooves are attributable to particles torn out in this area. Comparable results could be determined for the machining of short fibre reinforced materials.

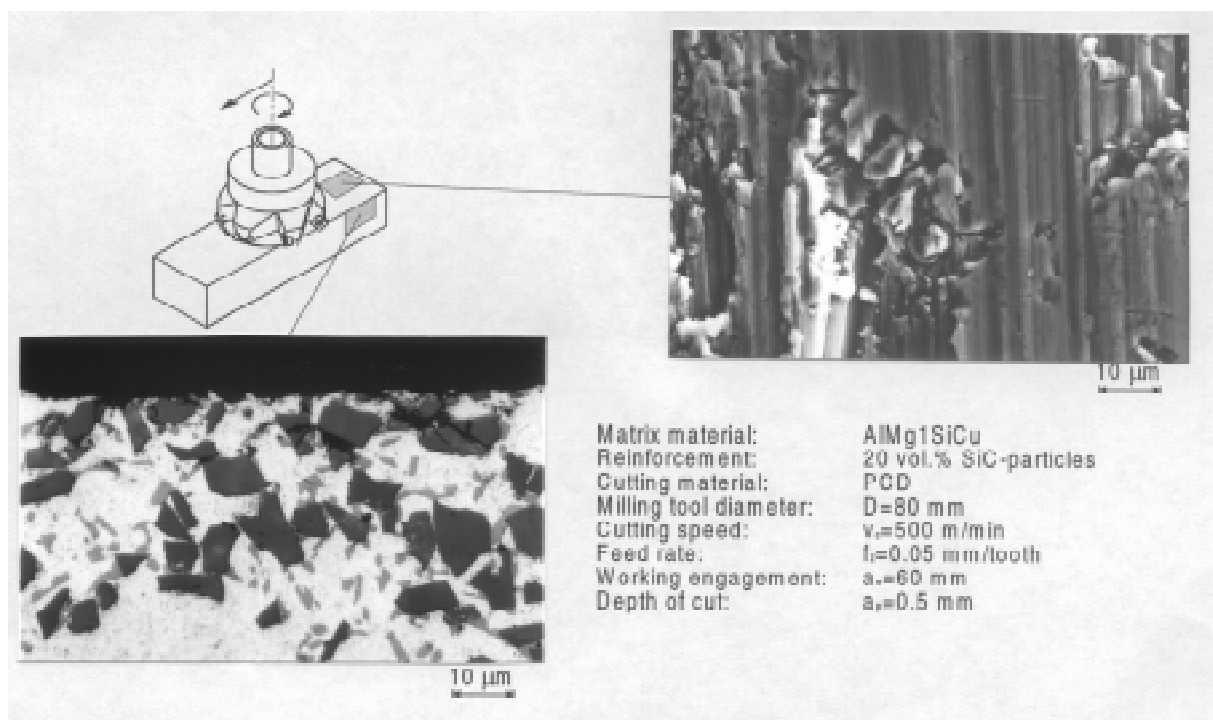


Fig. 8: Surface topography and subsurface zone of a milled reinforced aluminium alloy.

The photograph of the cross section show the condition of the subsurface zone. The particles in the subsurface zone are subjected to enormous stress by the machining process. Particles which lie up to approximately 20 μ m below to the surface are fractured as a result of plastic deformations.

In general it can be summarized that the surfaces of the machined MMC are characterized by pores and grooves attributable to fibres or particles turn out. Damages of the reinforcements, in form of fractures, in the subsurface zone can be caused by the cutting process. The fibre and/or particle fractures are found in a relatively small area of approx. 10 - 30 μm . The damages of the reinforcements increase due to higher specific cutting loads which are caused by the tool wear or the cutting parameters. An important point for milling operations is the ratio between the length of the minor edge chamfer and the feed rate. This influences the number of load cycles because of the contacts between the cutting tool and a defined surface section and therefore it also controls the level of the reinforcement damages.

ACKNOWLEDGEMENTS

The authors would like to thank the DFG (Deutsche Forschungsgemeinschaft) for supporting these investigations.

REFERENCES

1. Zum Gahr, K.-H., "Microstructure and Wear of Materials", Tribology Series 10, Elsevier Amsterdam-Oxford 1987.
2. Biermann, D. "Untersuchungen zum Drehen von Aluminiummatrix-Verbundwerkstoffen", Fortschrittberichte, Reihe 2, Nr. 338, VDI Verlag Düsseldorf 1995.
3. Weinert, K., "A Consideration of Tool wear Mechanism when Machining Metal Matrix Composites (MMC)", Annals of the CIRP, Vol. 42, No. 1, 1993, pp.95-98.
4. Brun, M.K. and Lee, M., "Wear characteristics of Various Hard Materials for Machining SiC Reinforced Aluminium Alloy", The ASME Int. Conf. on Wear of Materials, Vancouver Canada 14.4.-18.4.1988, pp. 539-544.
5. Kainer, K.U., "Herstellung und Eigenschaften von faserverstärkten Magnesium-verbundwerkstoffen", in Metallische Verbundwerkstoffe, Eds.: Kainer, K.U., DGM Informationsgesellschaft Verlag, 1994, pp.219-244.
6. Henning, W. and Neite, G., "Herstellung, Eigenschaften und Anwendung von kurzfaserverstärkten Aluminiumlegierungen", in Metallische Verbundwerkstoffe, Eds.: Kainer, K.U., DGM Informationsgesellschaft Verlag, 1994, pp. 169-191.
7. Weinert, K., Biermann, D. and Meister, D., "Machining of Metal Matrix Composites - Tool Wear and Surface Integrity", Proc. ICCM-10, British Columbia, Canada, Aug. 14-18, 1995, Vol III, Eds.: Pousartip, A., Street, K.N., pp. 589-596.
8. Hintermann, H.E. and Chattopadhyay, A.K., "Low Pressure Synthesis of Diamond Coatings", Annals of the CIRP, Vol. 42, No. 2, 1993, pp. 769-783.

THE EFFECT OF A SLIGHT INTERFACIAL REACTION ON THE MECHANICAL BEHAVIOR OF SQUEEZE-CAST SiCp/6061 AL COMPOSITES

Yan Cui, Lin Geng, Congkai Yao, Xiaoli Li

*P.O. Box 433, School of Materials Science and Engineering
Harbin Institute of Technology, Harbin 150001, P.R. China*

SUMMARY: A slight interfacial reaction was observed in squeeze-cast SiCp/6061Al composites, and this kind of reaction was found to have a particular effect on the mechanical properties of the composites. The results of flexure tests show that this reaction in the composite obviously increases the elastic properties, but it is not beneficial to the fracture strength and ductility. This phenomenon can be interpreted in terms of two different micromechanisms which were analyzed using TEM and HREM observations, acoustic emission (AE) technique and SEM fractography. In addition, a new method of SiC surface modification which can control the interface state was initially presented.

KEYWORDS: SiCp/Al composites, slight interfacial reaction, mechanical behaviour, keying in, crack initiation

INTRODUCTION

The interface between reinforcement and matrix is currently attracting the maximum attention as a result of its nature plays a critical role in influencing the properties and strengthening mechanism of metal matrix composites (MMCs). For SiCp/Al composites, it is believed that a strong interface is necessary for the production of high-dislocation density and effective transfer of load from matrix to the reinforcement, resulting in an increased elastic modulus and strength[1-4]. Since SiC-Al system is out of equilibrium, chemical reactions may occur at interfacial area during the fabrication or service involved high temperatures[5]. Moreover, the interface bond strength is controlled to a large extent by the reactions. Therefore, by understanding the detailed chemical reaction and its effect, it may be possible to control the reaction, which in turn tailor the interfacial properties and overall mechanical behaviour of SiCp/Al composites to meet the specific requirements for various applications[6]. Considerable previous investigations have shown that the formation of a significant amount of brittle compound such as Al_4C_3 or $MgAl_2O_4$ at the Al/SiC interface is detrimental to the stiffness and strength of the composites[7,8]. Compared with the excessive reactions as mentioned above, very few studies have been carried out on a slight interfacial reaction in SiCp/Al composites[4,9], in particular, the effect of this type of reaction has never been reported, which may hinder the design, development and application of the composites.

The aim of this paper is therefore to study the effect of a slight interfacial reaction on the mechanical properties of SiCp/6061Al composites, with particular emphasis on the extent of the reaction and the mechanisms of its effect on mechanical properties.

EXPERIMENTAL

Commercial 6061 aluminium alloy was used as the matrix and angular-shaped SiC particulate with a mean size of about 3.5 μ m was used as the reinforcement. For comparison purposes, some of SiC particulates had been treated in hydrofluoric acid before the fabrication of the composites. Both composites (with the volume fraction of 45% as-received or treated SiC particulates) are fabricated by the squeeze casting method with the same process parameters, namely, the preform without using any binder was preheated with mold in air to 580°C before squeeze casting. Molten Al alloy at 800°C was then poured into the mold, followed by hydraulic compressing under high pressure of 100MPa.

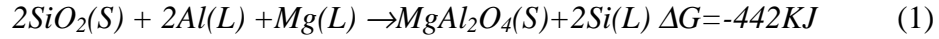
Interface characterization was carried out using TEM and HREM, microscopy samples were observed in detail by Philips CM-12 transmission electron microscope equipped with EDAX system operating at 120kV and JEOL2000EX-II high resolution electron transmission microscope operating at 200kV. Flexure tests were performed on an Instron 1186 universal testing machine at a crosshead speed of 0.5mm/min to determine the mechanical properties of composites. A minimum of 7 specimens was tested for each type of material to eliminate possible segregation effects and to obtain a mean value and standard deviation which would be representative of the materials. All specimens were 3.0 \times 4.0 \times 36.0 mm according to JIS specification. In order to further understand the interfacial effect and its micromechanism, acoustic emissions were monitored during the flexure testing until failure, and then, fractographs were examined using S-570 scanning electron microscope .

RESULTS

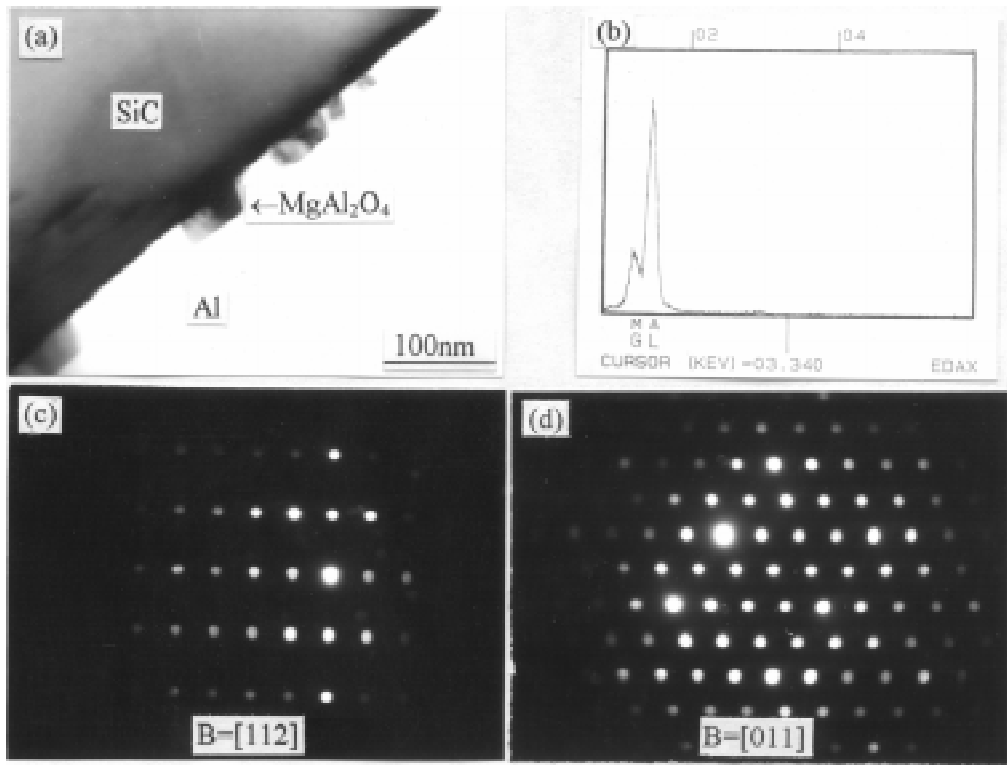
Interface Microstructure

Fig.1(a) is a typical TEM micrograph of the interface in as-cast 6061 Al matrix composites reinforced with the as-received SiC particulates, showing the presence of the isolated reaction product particles with a size of about 50-100nm at SiC-Al interface. These fine particles grow from the SiC surface into the Al matrix, and most of them have angular shapes. These reaction products were clearly identified as spinel MgAl₂O₄ by the EDAX and SADP as shown in Fig.1(b), (c) and (d). In order to further determine the extent of the interfacial reaction, chemical analysis of matrix was carried out using inductively coupled plasma-atomic emission spectrometer. The results showed that the content of Mg in the matrix decreased to 0.69% (from 1.03% in 6061 Al) as a result of the chemical reaction. Based on the amount of the depletion of Mg in the matrix arising from the interfacial reaction and the area of interface/per unit volume (this magnitude was determined by means of the density, volume fraction and specific surface area of SiC particulate), it can be calculated that about 10~20 % of SiC particulate surface was covered by this kind of reaction product, which in turn confirm that the extent of interfacial reaction which had taken place during the fabrication of the composites reinforced with as-received SiC particulates is slight. The formation mechanism of the reaction products is discussed as follows:

Practically, the as-received SiC particulates had always been slightly oxidized before the fabrication of the composites, which had been confirmed using XPS. Thus, the thin native SiO₂ layer around the as-received SiC particulates will firstly react with molten 6061 Al alloy (containing 1.03% Mg element) to form MgAl₂O₄ accords to Eq. (1) during the squeeze casting. Due to the very short time of the contact between SiC and liquid Al alloy (about a few seconds), no further reactions (such as Al₄C₃ formation) occur. In such case, MgAl₂O₄ spinel is the only one type of interfacial compound.



For comparison purpose, the interface of composites with as-treated (acid washed) SiC particulates was examined using TEM and HREM. It can be seen from Fig.2 that the interface is clean as expected, and there is no reaction product or amorphous transition layer. In such cases, the native SiO₂ layer had been removed prior to the composites fabrication as a result of hydrofluoric acid can dissolved the oxide layer easily. In general, the SiC particulates without oxide cover were rejected from the molten Al alloy, but, the composites can be fabricated by squeeze casting technique successfully (without forming the voids at the interfaces, and the SiC is perfectly bonded to the matrix), which is attributed to the high pressure role.



*Fig.1: (a) TEM micrograph showing the interfacial reaction products
 (b) EDAX spectrum for the interfacial reaction product in (a)
 (c), (d) Two zone axes SADP obtained from the interfacial reaction products in (a)*

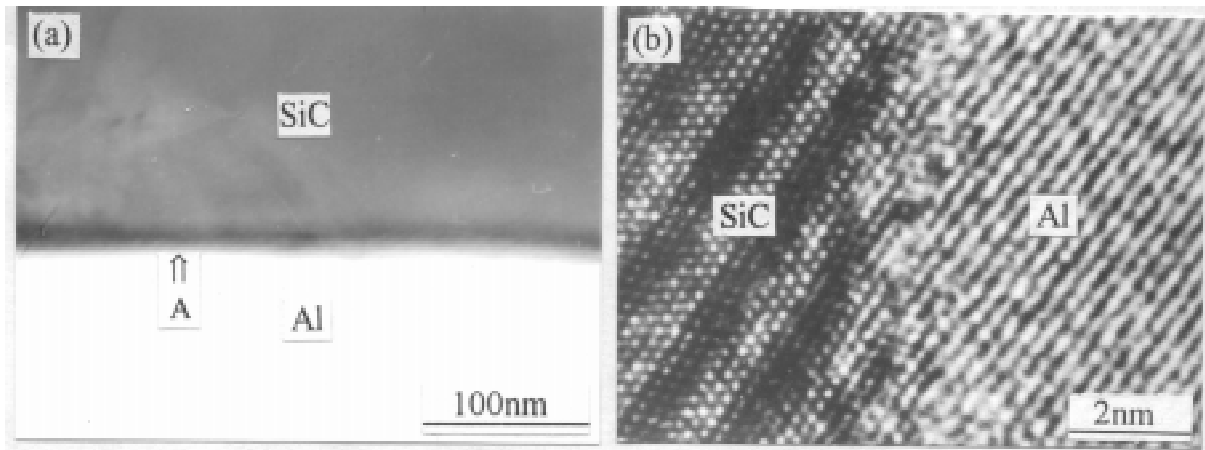


Fig.2: (a) TEM micrograph of the interface in the composite with treated SiC particulates
(b) HREM image of area A in (a)

Flexural Properties

The effect of the thin SiO_2 layer on processing is considered to be beneficial as it appears to improve the wettability of the SiC by liquid aluminum and facilitate the fabrication of SiCp/Al composites, but the effect of the thin layer and the slight interfacial reaction arising from it on mechanical behaviour of the composites still be unknown, which may hinder the development and application of this kind of material. Since perfect SiCp/Al composites with the clean interface have been obtained at the same processing condition except the chemical nature of SiC, it is possible to investigate the law of the above effect. The effect was evaluated using the flexure tests. The results are shown in Table 1. It is evident from Table 1 that the interfacial reaction can have a significant effect on the flexural properties of the composites. As compared to the composites with clean interface, the presence of the fine particulates of MgAl_2O_4 at interface results in 11.4% and 7.3% increase in elastic modulus and elastic limit (0.01 offset) respectively, at the same time, 11.8% decrease in ultimate flexural strength was observed. In addition, the interfacial reaction caused 30.5% decrease in the fracture strain of the composites also.

Table 1: Effect of the slight interfacial reaction on the mechanical properties* of SiCp/6061Al composites

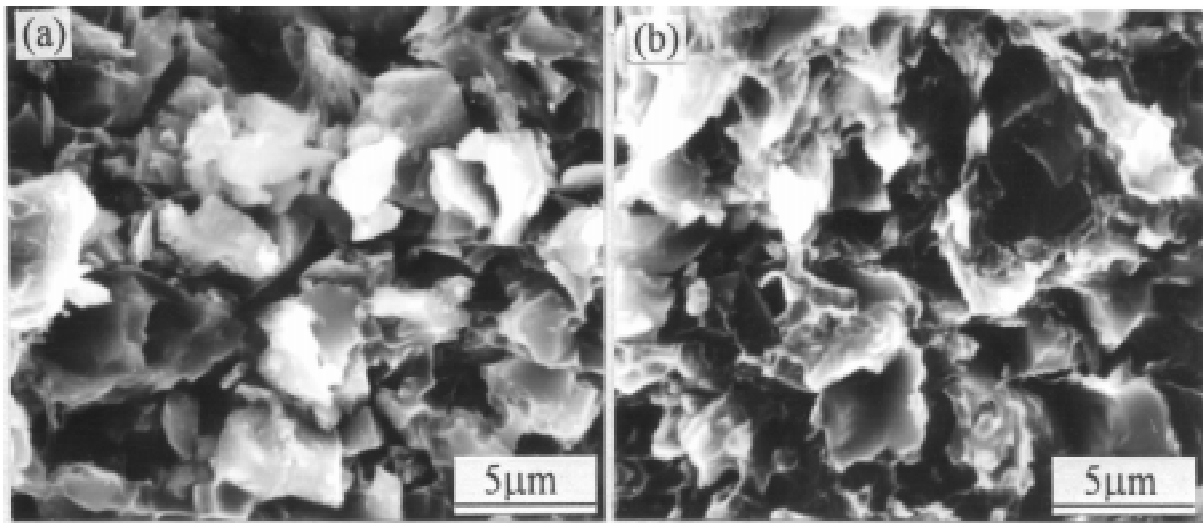
SPECIMEN	E (GPa)	$\sigma_{0.01}$ (MPa)	σ_{fs} (MPa)	ϵ_f (%)
reacted interface	164.9(± 2.1)	156.7(± 6.6)	497.8(± 7.2)	0.73(± 0.03)
clean interface	148.0(± 2.9)	146.0(± 4.5)	564.4(± 13.7)	1.05(± 0.03)

* Shown in parentheses are the standard deviation of samples

DISCUSSION

The micromechanisms of the above particular effect law are now discussed respectively as follows:

Firstly, the discrete particles of compound that are "keyed in" to both phases (as shown in Fig 1) may enhance the bonding of the interface (by the strong chemical bonding and mechanical keying), additionally, they may inhibit the plastic deformation of near-interface matrix when subjected to lower stress level also, thus, improving the load transfer, consequently, enhanced elastic properties were observed.



*Fig.3 SEM fractographs of flexure tested specimens
(a) fracture surface of the composite with the interfacial reaction products
(b) fracture surface of the composite with clean interface*

Secondly, the above "keying in" mechanism might not be responsible for the observed decrease in both fracture strength and ductility. Therefore, the mechanism which can explain the above mentioned degraded properties was investigated using acoustic emission (AE) technique and SEM fractography. The AE signal and stress-strain curve corresponding to it indicated that the decohesion of the interface with reaction products occurs earlier than that of the clean interface, the details of AE response have been described elsewhere [10]. This is due to the brittleness of $MgAl_2O_4$ (its fracture toughness is only one-third of that of SiC). The reaction product is a weak region which is prone to initiate microcrack when subjected to the higher stress level. In addition, the SEM fractographs (as shown in Fig.3) of two kinds of composites after the flexure tests show that the interface debonding without significant deformation of the matrix near the SiC particulate is the major fracture mode of the composites with the reaction products; on the contrary, a large deformation of matrix had occurred around the SiC particulate before interfacial debonding in the composites with clean interface, which suggests that this interface is strong enough to permit the effective transfer of load from matrix to the reinforcement. The SEM observation further confirms the results of AE analysis, namely, the initiation of microcrack in reaction products is accounted for the premature interfacial debonding and some properties degrading.

CONCLUSIONS

1. At lower stress level, the slight interfacial reaction results in the enhanced elastic properties through "keying in" mechanism. Whereas for higher stress level, the reaction degrades the fracture strength and ductility through "crack initiation" mechanism.
2. The suitable acid treatment can modify the interface state and its bond strength, which in turn realize the control and optimization of the overall mechanical properties of SiCp/6061Al composites to maximize its performance in specific application .

REFERENCES

1. Feest, E.A., "Interfacial Phenomena in Metal Matrix Composites", *Composites*. Vol. 25, 1994, pp75-81
2. Ribes, H., Suery, M., Eesperance, G.L. and Legoux, J.G., "Microscopic Emiamination of the Interface Region in 6061- Al SiC Composites Reinforced with As-Received and Oxidized SiC Particles", *Metall.Trans.*, Vol. 21A, 1990, pp 2489
3. Li,S., Arsenault, R.J. and Jena, P., "Quantum Chemical Study of Adhesion at the SiC/Al Interface", *J.Appl.Phys.*, Vol. 64, 1988, pp 6246
4. Wang Ning, Wang Zhirui and George C. Weatherly, "Formation of Magnesium Aluminate (Spinel) in Cast SiC Particulate-Reinforced Al (A356) Metal Matrix Composites", *Metall.Trans.*, Vol. 23A, 1992, pp1423-1430
5. Boq-Kong Hwo, Su-Jien Lin, Min-Ten Jahn, "The Interfacial Compounds and SEM Fractography of Squeeze-Cast SiCp/6061 Al Composites", *Mater.Sci.Eng.*, Vol. A206, 1996, pp110-119
6. Foo, K.S., Banks,W.M., Craven, A.J. and Hendry,A., "Interface Characterization of an SiC Particulate/6061 Aluminium Alloy Composite", *Composites.*, Vol. 25, 1994, pp677-683
7. Ribes, H., Silva, R.Da., Suery, M. and Brtheau,T., "Effect of Interfacial Oxide Layer in Al-SiC Particle Composites on Bond Strength and Mechanical Behaviour", *Mater.Sci.Tech.*, Vol.6, 1990, pp 621-628
8. Vedani,M., Gariboldi, E., Silva, G. and Gregorio,C.Di., "Influence of Interface Properties on Mechanical Behaviour of Particle Reinforced Metal Matrix Composite", *Mater.Sci.Tech.*, Vol.10, 1994, pp132-140
9. Salvo,L., LEsperance,G., Suery, M.and Legoux ,J.G., "Interfacial Reactions and Age Hardening in Al-Mg-Si Metal Matrix Composites Reinforced with SiC Particles", *Mater.Sci.Eng.*, Vol.A177, 1994, pp173-183
10. Cui, Y., Geng, L. and Yao, C.K., "Interfacial Control and Wavelet Analysis of Acoustic Emission Behaviours in SiCp/Al Composites", *Acta Metallurgica Sinica* (in Chinese), to be published

INFLUENCE OF THE INTERFACE ON THE CREEP PROPERTIES OF CARBON FIBRE REINFORCED MAGNESIUM ALLOY AS41

Bernd Sommer¹, Karl Ulrich Kainer¹ and Harry Berek²

¹ *Department of Material Engineering and Technology, Agricolastrasse 6, D-38678 Clausthal-Zellerfeld, Germany*

² *Freiberger NE-Metall GmbH, Lessingstrasse 41, D-09599 Freiberg, Germany*

SUMMARY: This paper deals with the investigation of creep properties of magnesium alloy AS41 reinforced by carbon short fibres. The specimens were produced by direct squeeze-casting. The short fibres showed planar isotropic distribution. The volume content of the fibres is about 16%. The investigation of the microstructure was carried out by optical microscopy and electron microscopy to characterise the interface and identify the precipitates at the interface. The creep tests were performed in a temperature range between 150°C and 300°C for a stress range of 30 MPa to 90 MPa. The results show the possibility of a reduction in the creep rate of the magnesium alloy AS41 by one or two orders of magnitude by introducing a reinforcing phase. The creep exponent determined using Norton-Baily-approach as calculated to lie between 5-7.

KEYWORDS: magnesium matrix composite, creep of MMC, magnesium alloy AS41, carbon fibres, creep exponent, activation energy for creep, interface strength

INTRODUCTION

There is a high demand for light metal matrix composites in automotive and aircraft applications. Light metal matrix composites (MMC) are already used for mass produced components or products e.g. partially reinforced aluminium pistons, crankcases and cylinder heads as well as particle reinforced brake disks [1,2]. A further reduction in weight can be achieved by replacing Al alloy matrix by magnesium alloys or by switching from ceramic fibres or particles to carbon fibres.

Magnesium alloys show poor creep properties due to their low melting point or low melting intermetallic phases. Efforts to improve the creep resistance have led to the development of magnesium alloys with Silver, Yttrium and rare earths (QE and WE series). These alloys are characterised by high melting point rare earth precipitates. Further improvement in the creep resistance is possible by reinforcement of these alloys with fibres.

The magnesium alloy AS41 (4wt% Al, 1wt% Si, 0.3wt% Mn, rem Mg) belongs to a group of magnesium alloys without rare earths as alloying elements, which show nevertheless acceptable creep properties for temperatures up to 150°C [3]. The aim of the reinforcement of this alloy was the extension of the application temperature up to 200°C and to reduce the creep rate in this temperature interval.

Several models have been proposed to explain the creep properties of short fibre reinforced MMC [4-10]. Some are based on continuum mechanics and others on microstructural or micromechanical models. The disadvantage of the micromechanical and microstructural models is its limitation to aligned short fibre MMCs. These models are not applicable to a planar isotropic fibre distribution. The continuum mechanical models enable the random planar distribution of the fibres to be considered but they cannot take into account other microstructural features. In this work these models were used to describe qualitatively the results. A quantitative description is not possible due to the number of parameters involved. Also these parameters cannot be reproduced for each series. The Norton-Baily-law (Eqn 1) was used to determine the creep exponent n and the activation energy Q_c for creep.

$$\dot{\epsilon}_{ss} = \alpha \cdot \sigma^n \cdot e^{\frac{-Q_c}{R \cdot T}} \quad (1)$$

ϵ_{ss} = secondary creep rate

α = constant

σ = applied stress

n = creep exponent

Q_c = activation energy for creep

R = gas constant

T = temperature

EXPERIMENTAL DETAILS

The composite material was produced using direct squeeze casting technique [11]. A porous fibre preform was infiltrated by the molten alloy AS41 under a high pressure. The carbon fibre preforms showing a random planar fibre distribution with a SiO₂-binder were manufactured by Didier Werke AG, Wiesbaden, Germany. The carbon fibres had a diameter of 7 μ m and a mean length of about 150 μ m. The fibre volume fraction of 14-17% was determined by interrupted segment method on metallographic sections of the squeeze cast material. The preform was preheated up to 630°C in CO-atmosphere. The temperature of the melt was 800°C. Specimens were taken from the composite sheets parallel to the planar isotropic distribution of the fibres. Cylindrical creep specimens were produced with a gauge length of 25.4 mm (1"). Constant stress tensions creep tests were carried out in air at temperatures between 150°C and 300°C. Stresses between 30 MPa and 90 MPa were applied. The variation in temperature during the creep tests was ± 1 K. It took an average time of 2-3 hours for heating the specimens to test temperature before loading. Strain was measured using nimonic extensometers rigidly affixed to the specimen holders. The specimen displacement was measured by highly sensitive linear variable displacement transducers with a resolution of $8 \cdot 10^{-6}$ strain. The displacement values and the temperature were recorded simultaneously during creeping.

The electron microscopy investigations were carried out using a Hitachi X650 scanning electron microscope (SEM) and a Philips CM30 transmission electron microscope (TEM) with an acceleration voltage of 300kV. The TEM specimen were prepared by ion milling.

RESULTS AND DISCUSSION

The micrographs in Fig. 2a and b show the difference between a reinforced and an unreinforced material. The unreinforced material shows the typical cast structure with

dendrites. Typical Mg_2Si precipitates (Chinese script) were also observed. This typical cast structure was also observed in the reinforced material. Due to the fibres a more globular structure was formed during the solidification in the squeeze cast process. The distribution of the fibres is not homogenous. Fibre agglomeration and unreinforced areas were observed. An good performed interface without any pore is shown in Fig. 3. Some precipitates in the interface can be observed. Most of them can be identified as Mg_2Si .

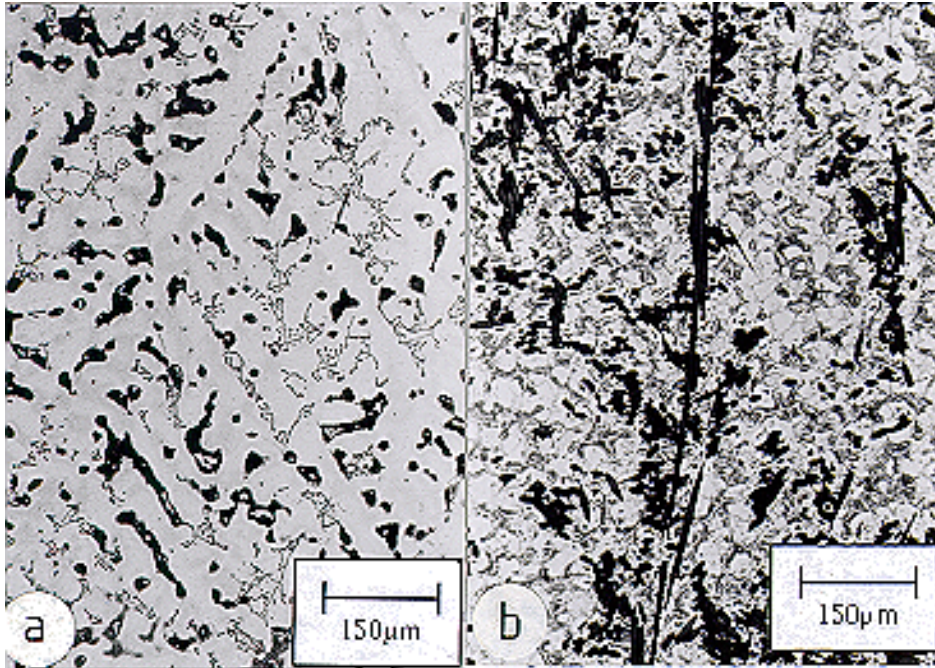


Fig. 2: Microstructure of unreinforced AS41(a) and a carbon fibre reinforced AS41 (b)

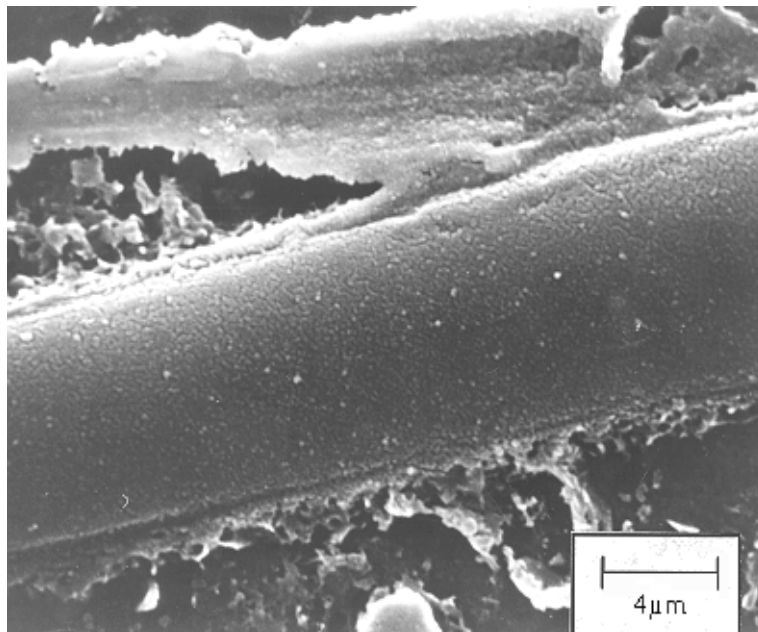


Fig. 3: SEM-micrograph of the interface C-fibre/AS41

One aim of the reinforcement of light metals is the improvement of the creep properties i.e. a general reduction of the creep rate and at the same time increase of the temperatures of application. Fig. 4 shows typical creep curves for two applied stresses for reinforced and unreinforced AS41 at 200°C. The creep curves for the unreinforced as well as for reinforced AS41 show the typical three stages of creep. The MMCs behave differently compared to unreinforced materials. In the primary creep stage the load transfer to the fibres takes place. This leads to an extension of primary creep region which is about 1/3 of the creep time to rupture. This is followed by a shortened steady state creep region where this region takes 1/2 of the creep time.

This phenomenon is typical for short fibre reinforced material because the creep mechanisms in reinforced materials differ from those in monolithic metals [9,10]. Dlouhy et al. have stated that primary creep in short fibre reinforced material is dominated by load transfer from the matrix to the fibres due to a work hardening zone at the interface fibre - matrix [9]. This model was developed for aligned fibres. It is not surprising that the time for primary creep is increased significantly due to the random planar fibre distribution. During creep the fibres are not only carrying the load, they are also obstacles for dislocations. Tertiary creep takes most of the time. It is controlled by recovery processes and by fibre breakage. Only a few fibres in some creep specimen were broken but it has to be determined whether the reason is the creep process.

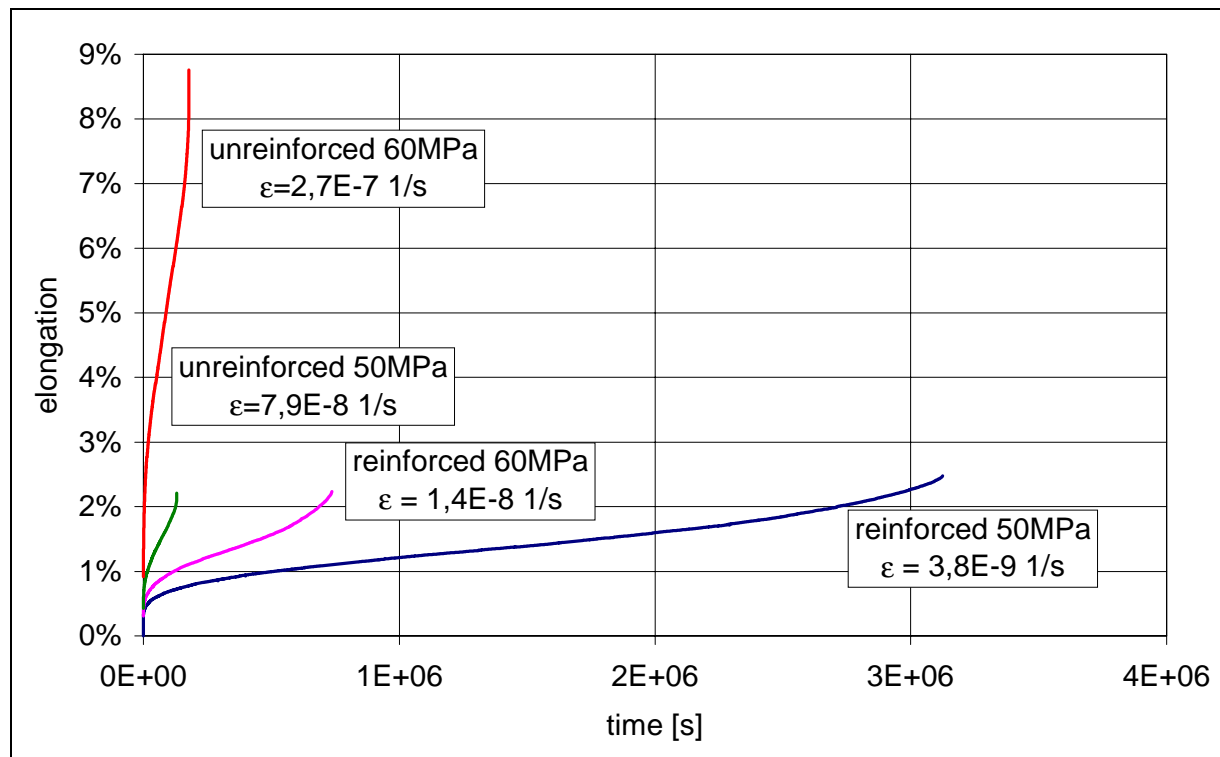


Fig. 4: Comparison of typical creep curves of unreinforced and carbon short fibre reinforced AS41 at 200°C

The behaviour described of the reinforced material is strongly dependent on the testing parameters such as temperature and load. The length of the various creep stages is quite different. For example a creep test at 150°C and 50 MPa shows a primary creep for over 2 months and no secondary or tertiary creep because only work hardening mechanism operates.

In all cases the creep properties of the reinforced metal are much better than the properties of the unreinforced metal. The secondary creep rates of the reinforced materials are more than one order of magnitude lower than those of the unreinforced material. The time to fracture increases also about one order of magnitude.

The values measured of the secondary creep rate for reinforced AS41 are listed in Table 1 and plotted in Fig. 5. The values in Table 1 are mean values of the measured creep rates. The creep exponent n was determined by linear regression. As shown in Fig. 5 only a few measurements to determine the creep exponent n . Nevertheless the points deviate in most cases not very much from the regression line. Hence the experimental results can be qualitatively understood but for a detailed interpretation more work is necessary.

Table 1: Minimal creep rates of carbon short fibres reinforced AS41

	150°C	200°C	225°C	250°C	275°C	300°C	Q
30MPa	-	-	$3.8 \cdot 10^{-9} \text{s}^{-1}$	$8.5 \cdot 10^{-9} \text{s}^{-1}$	-	$1.9 \cdot 10^{-7} \text{s}^{-1}$	144kJ
40MPa	-	$1.3 \cdot 10^{-9} \text{s}^{-1}$	$1.9 \cdot 10^{-8} \text{s}^{-1}$	$1.6 \cdot 10^{-7} \text{s}^{-1}$	$7.7 \cdot 10^{-7} \text{s}^{-1}$	-	178kJ
50MPa	-	$4.1 \cdot 10^{-9} \text{s}^{-1}$	$5.2 \cdot 10^{-8} \text{s}^{-1}$	$3.1 \cdot 10^{-7} \text{s}^{-1}$	-	-	172kJ
60MPa	$5.9 \cdot 10^{-10} \text{s}^{-1}$	$1.8 \cdot 10^{-8} \text{s}^{-1}$	$1.6 \cdot 10^{-7} \text{s}^{-1}$	-	-	-	136kJ
70MPa	$1.2 \cdot 10^{-9} \text{s}^{-1}$	$3.8 \cdot 10^{-8} \text{s}^{-1}$	-	-	-	-	-
80MPa	$2.6 \cdot 10^{-9} \text{s}^{-1}$	-	-	-	-	-	-
90MPa	$1.1 \cdot 10^{-8} \text{s}^{-1}$	-	-	-	-	-	-
n	4.2/13.8	6.4	5.3	6.7	n.d.	n.d.	-

In the temperature range between 200°C and 250°C the values of the creep exponent lie between 5.3 and 6.7. The regression line indicates that the assumption of a power law creep mechanism is correct and also the value of the creep exponent is in the range of the power law creep ($n=3-8$). At 150°C a change in the creep exponent was observed. At stresses between 60MPa and 80MPa the creep exponent is 4.2 and for stresses between 80MPa and 90MPa the creep exponent increases up to 13.8. This may be explained by the high loads (power law breakdown). The tensile yield strength of AS41 is about 90MPa at 150°C. If it is assumed that after load transfer to the fibres the matrix has to bear lower stresses, the stresses in the matrix are less than the yield strength. At high stresses recovery processes are more dominant and this may lead to a breakdown of the interface.

At 200°C the creep exponent of the unreinforced AS41 was 7.7 and is thus greater than that for the reinforced AS41. This behaviour is unusual, but may be explained as follows. A temperature of 200°C is for an unreinforced AS41 a high temperature ($0.7 \cdot T_E$) and several thermally controlled processes are possible. Creep depends strongly on diffusion. As the load in reinforced material is transferred from the matrix to the fibre the matrix carries a lower load and this should have an influence on the creep rate.

The activation energy calculated for creep is given in Table 1. Values between 140kJ/mol and 180kJ/mol were found. These values are higher than the activation energy of self diffusion of magnesium. Thus it can be assumed that the mechanism for creep does not depend on the

creep properties of the matrix. Dlouhy et al. [9] have pointed out that the rate controlled processes for creep in short fibre reinforced metals operate in the workhardening zone (WHZ) surrounding the fibres. Therefore the activation energy depends on the properties of the WHZ.

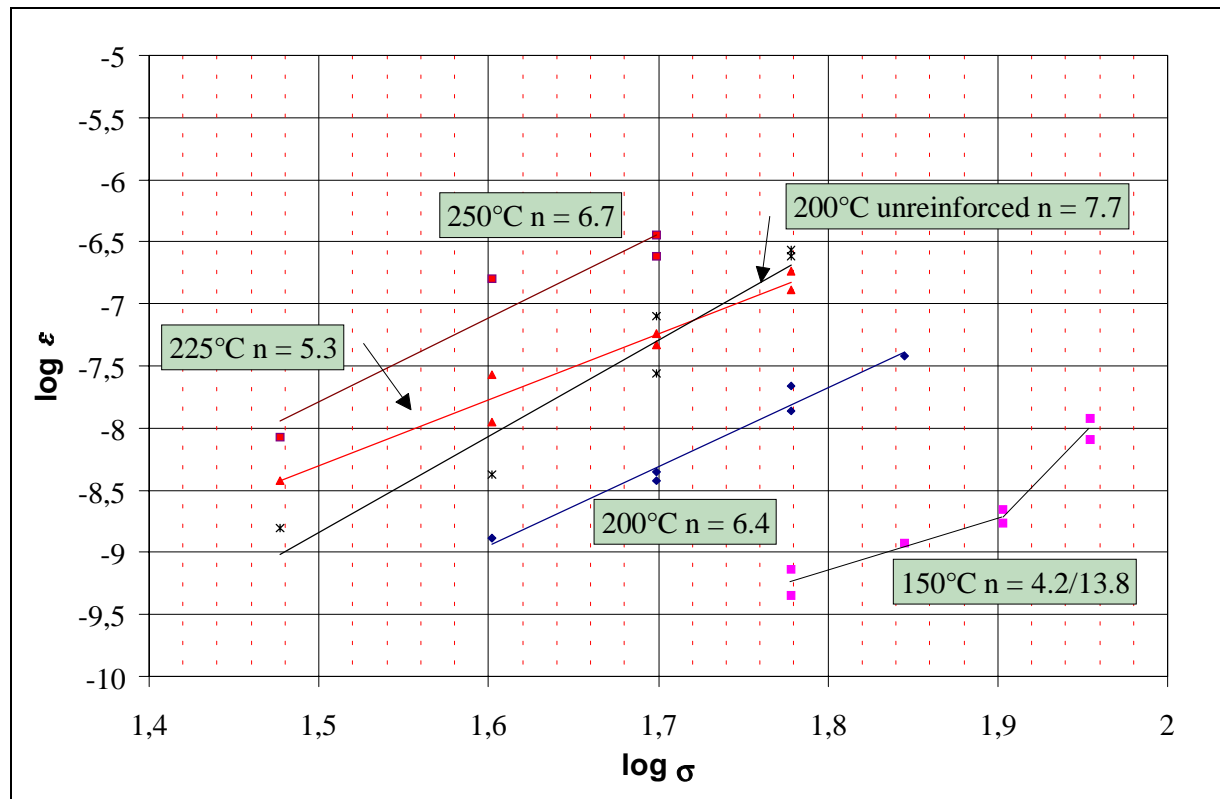


Fig. 5: $\log \varepsilon$ - $\log \sigma$ diagram for reinforced AS41: determination of the creep exponent n

The interface in fibre reinforced metals is very important for the composite properties. Hence the behaviour of the composite depends on the characterisation of the interface. It is well known that wetting of carbon fibres by pure liquid magnesium is very difficult. Nevertheless the high pressure during squeeze casting overcomes this problem. There is only a short time during the casting process for reactions between fibre and matrix to take place. For this reason reaction products such as carbides are not expected. Fig. 3 and Fig. 6 show good bonding between fibre and matrix. The interface is dense and no pores are observed. A small dense layer (0.5 -1.5 μm) of precipitates and some isolated precipitates are visible around the fibres. An analysis of this layer provides the evidence of magnesium, aluminium and silicon. A particular phase could not be identified. The major precipitate which could be identified in the matrix as well as at the interface is the intermetallic phase Mg_2Si . This phase occurs in different forms. In the matrix the typical chinese script form was observed. There are also big blocky precipitates of Mg_2Si (Fig. 8). These precipitates result from a reaction of magnesium and silicon. It is assumed that the silicon comes mainly from the reaction of the SiO_2 -binder of the preform with the liquid or solid magnesium. A reaction between magnesium and SiO_2 leads to Mg_2Si and MgO . The selected area diffraction pattern in Fig. 7 shows rings of weak intensity of a polycrystalline phase. Only very fine distributed particles at the interface matrix precipitates could be the reason for these rings. An analysis of the pattern indicates that these rings could come from MgO , but it is not clear yet. In Fig. 6 other precipitates occur. The EDX-analysis indicated an increased Manganese and Aluminium concentration but an identification of the phase was not possible. Due to these precipitates a high interface strength between the fibres and the matrix can be assumed. Hence it can be considered that the

interface is the reason for the improvement of the creep properties. Further improvement of creep properties can be expected from higher fibre volume fractions.

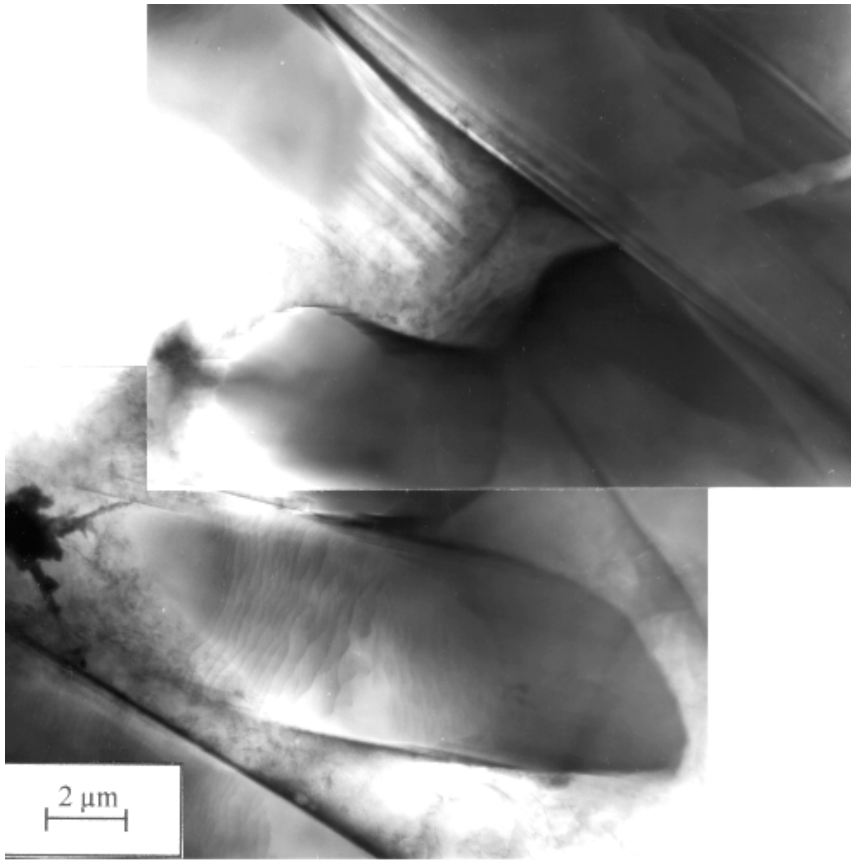


Fig. 6: TEM micrograph of a carbon fibre reinforced AS41 alloy showing a random orientation and some coarse precipitates

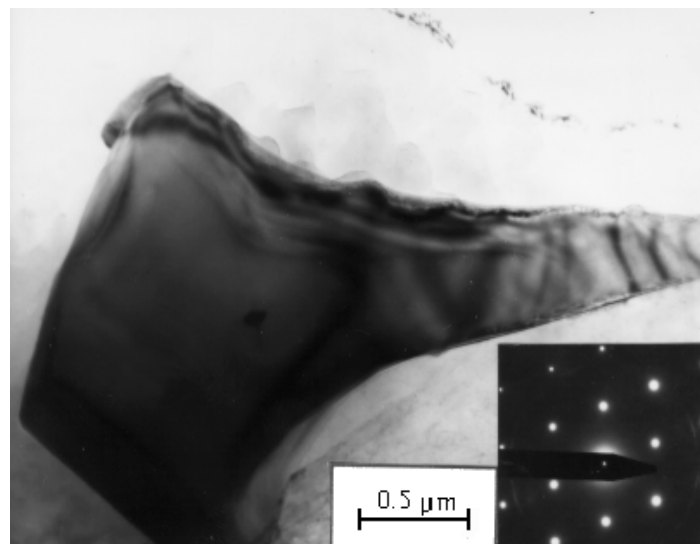


Fig. 7: TEM bright field image of a typical coarse Mg₂Si precipitate

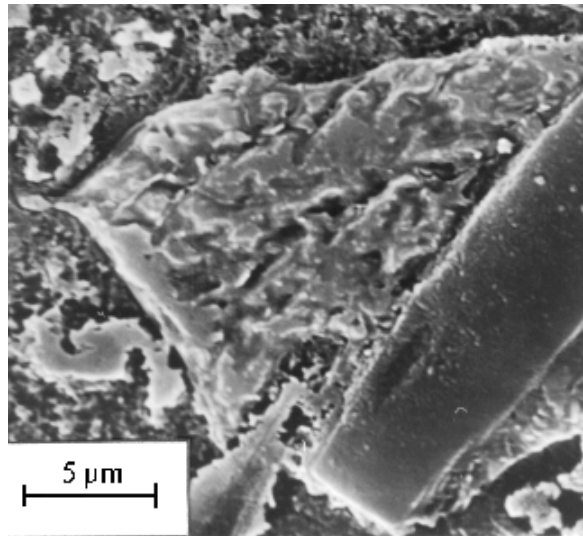


Fig. 8: Mg₂Si situated at a carbon fibre

CONCLUSION

The creep properties of carbon short fibers reinforced magnesium alloy AS41 were investigated. A pronounced improvement of the creep properties for the reinforced alloy in comparison to the unreinforced alloy was observed, although the distribution of the fibres was not homogenous. The analysis of the creep tests using the Norton-Baily approach shows that the creep exponent varies from 5 to 6.5 in the temperature range from 200°C to 250°C. At 150°C a transition of the creep exponent from 4.2 for low stresses to 13.8 for high stresses up to the yield strength was observed. Activation energies were calculated in the range from 140kJ/mol to 180kJ/mol.

ACKNOWLEDGEMENT

The support of this work by the Federal Ministry of Education, Science, Research and Technology (BMBF) is gratefully acknowledged.

REFERENCES

1. Köhler, E. and Henning W.: "Lokal verstärkte Motorteile: MMC's in der Serienproduktion", *Verbundwerkstoffe und Werkstoffverbunde*, G. Ziegler ed., DGM Informationsgesellschaft Oberursel, 1996, pp. 299-302.
2. Clyne, T.W and Withers, P.J., *An Introduction to Metal Matrix Composites*, Cambridge Solid State Sciences Series, Cambridge University Press, Cambridge, 1993
3. Norsk Hydro database, Norsk Hydro, N-Porsgrunn, 1996
4. Kelly, A. and Street, K.N., "Creep of Discontinuous Fibre Composites II. Theory for Steady-state", *Proceeding of the Royal Society*. Vol. 328, 1972, pp. 283-293.283

5. Dragone, T.L. and Nix, W.D., "Geometric Factors Affecting the Internal Stress Distribution and High Temperature Creep of Discontinuous Fibre Reinforced Metals", *Acta metallurgica et materialia*, Vol. 38, No. 10, 1990, pp. 1941-1953
6. Dragone, T.L. and Nix, W.D., "Steady State and Transient Creep Properties of an Aluminium Alloy Reinforced with Alumina Fibres", *Acta metallurgica et materialia*, Vol. 40, No. 10, 1992, pp. 2781-2791
7. McLean, M., "Creep of Metal Matrix Composites Materials and Engineering Design - The Next Decade" The Institute of Metals, Dyson, B.F. and Hzyhurst, D.R., Eds.1989, pp. 287-296
8. Goto, S: and McLean, M., "Role of Interfaces in Creep of Fibre Reinforced Metal-Matrix Composites", *Acta metallurgica et materialia*, Vol. 39, No. 2, 1991, pp. 163-177
9. Dlouhy, A., Eggeler, G. and Merk, N., "A Micromechanical Model for Creep in Short Fibre Reinforced Aluminium Alloys", *Acta metallurgica et materialia*, Vol. 43, No. 2, 1995, pp. 535-550
10. Dlouhy, A., Merk, N. A. and Eggeler, G., "A Microstrutural Study of Creep in Short Fibre Reinforced Aluminium Alloys", *Acta metallurgica et materialia*, Vol. 41, No. 11, 1993, pp. 3245-3256
11. Kainer, K.U., "Cast Magnesium Alloys Reinforced by Short Fibres" Magnesium and their Applications, B.L. Mordike and F. Hehmann eds, DGM Oberursel, 1992, 415-422.

STRAIN ANALYSIS OF INTERFACE OF COMPOSITE FORMED BY PPR METHOD WITH COMPUTER-AIDED TECHNIQUES

Zhang Shuhong, Zhang Daiming, Sun Yong and Shi Qingnan

Kunming University of Science and Technology, Kunming, Yunnan, China, 650093

SUMMARY: The PPR method is a new method to compose metal composites. With this method, different composites such as Cu-steel, Al-steel, Sn-steel, Stainless steel-steel and etc. can be formed. In this paper, the Cu-steel and Stainless steel-steel are taken as the examples formed by the PPR method, the strains both the powder grains and the matrix on the compounding interface are studied by making use of experiment, XRD and the computer-aided techniques. The processing of experimental and analysis are introduced and the mathematics results about the strain distribution, the relationship of strain and rolling force and etc. are given. Some conclusions about the results have been made at the end of the paper.

KEYWORDS: powders plating and rolling method, strain analysis of interface, form a metallic composite, transform moire method

INTRODUCTION

PPR method is the abbreviation of Powders Plating and Rolling method. This is a new method for forming some metallic composites[1]. In this method, a kind of metal powder grains is plated on the other metal band by making use of a special technology first, then both of them are rolling together, a new composite is formed. The thickness of the composite layer formed by this technology could be 0.01mm to 0.20mm. There are some properties about this method that are different from other's of known composing technology. First, it is suitable to be industrialized broad in scope, because the metal as the composing base does not need machining; second, the producing cost is lower relatively than other composing methods; third, the technique is relative simpler than other methods; and the process of producing have almost no pollution. The products formed by this technology could be widely used in architectural decoration, preventing chemical cauterizing and transporting of electrical power and etc..

Since the metal formed the composite-layer is not a sheet but powders before rolled, it has its own special deformation laws and mechanical characteristics. These will also affect the stress and strain distribution and other mechanical properties of the metal base. there surely are many factors to affect the quality and the product cost during the process of rolling and heat treatment after-rolling, such as the state of original composition and rolled composition for the two compositing material, friction coefficients, rolling force, rolling temperature, rolling speed, the time and temperature of heat treatment and etc.. It is very important to study them

in order to bring the technique into real industrialized broad in scope. One of the important aspects is to research the mechanical performance of the composites, because this can provide very useful and essential scientific basis for the process of producing and using the composites. As these factors affect each other, it is difficult to study the mechanical performance and obtain the real magnitude and distribution of the stress and strain by theoretical method. In this paper, the Cu-steel and Stainless steel-steel are taken as the examples formed by the PPR motnod, the strains of the compounding interface are studied by combining experiment, XRD and the Transform Moire method a computer digital-image processing technique[2]. The processing of experimental and analysis are introduced and the patterns of analysis result about the strain distribution, the relationship of strain and rolling force and etc. are provided. Some conclusions about the results are made at the end of the paper.

EXPERIMENTAL PROCESS

Specimen and Experimental Materials

Because this is a metal composite, a metal band must be chosen as the matrix. In this experiment, A3 cold-rolling board is chosen as the matrix. Its size is 250 x 50 x 0.8mm. Two typical metallic powders are chosen as the material of plating layer. One is copper and another is stainless-steel. The copper grain is softer than the matrix and the stainless-steel is harder than the matrix. The diameter of the powder grains is less than 0.08mm.

Main Rolling and Measure Equipment

The rolling machine is type of SG-160 roller. The measure equipment include the type of YD-15/8 dynamic strain equipment, the type of SC 20 ray-displayer and two compress sensor that are stacked the resistance strain sheets on its surfaces, a microscope, XRD and the personal computer are also used for analyzing.

Specimen Treatment Before Rolling

The metal band is dealt with its surface by cleaning and degreases. A special technology is used to cover a kind of metallic powder on the matrix. The layer thickness of the powder grains can be controlled from 0.01mm to 0.20 mm. In order to study the deformation of matrix, the gratings of 20lines/mm had been etched on the part of combining surface by mechanical method before the powder grains were put on it.

Rolling

When both the metallic powders and the matrix are rolled together, the metallic powders on the matrix become a metal-lamella and a composite band is got. Since we want to study the relationship of rolling force and the deformation, the specimens are divided into two groups for every kind of metallic powders that covering on the matrix. Every group specimen is given different compression quantity. It is the main parameter that could be controlled by us. The rolling compressive force correspondingly is measured and recorded.

ANALYSIS AND RESULTS

After rolled, with a microscope the deformed grating can be observed and photographed. Then the Transform Moire method, a method of combining classical Moire experimental technique and analysis theory with computer digital-image processing technique, XRD are used to analyze the strain of the interface of the composite. The relationships of reduction and rolling force, strain and rolling force is studied.

Degree of Compression and Rolling Force

The experiment shows that the relationship between degree of compression and rolling force is very close. If the thickness of the rolled-piece before rolling is H , and the thickness after rolling is h , then the degree of compression is

$$\lambda = \frac{H-h}{H} 100\% \quad (1)$$

The experiment measured rolling forces are calculated by the formula

$$P = aS - b \quad (2)$$

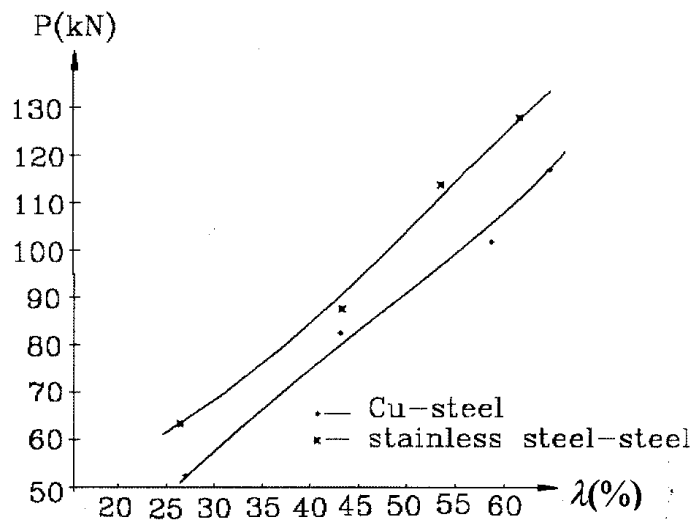


Fig. 1: The relationship of P and λ

Where, S is the shift signal quantity of exported by the ray-displayer that connected with the compress sensor, a and b is material constants. In order to know them, the multiplication of minimal two is used for doing one element linear regression by the computer. Calculated λ and P , their relationships are shown in Fig. 1. Fig. 1 shows that the rolling forces are increase with the degree of compression almost linearly, and the rolling forces are different for different metal composite layers. The rolling force for the stainless steel layer is larger than the rolling force for the copper layer at the same reduction. That is because the powder grain of stainless steel is harder than the copper's. But the slops for these two curves are closely. This means that they increase with the reduction at almost the same proportion.

The Strain Analysis on the Interface of the Matrix

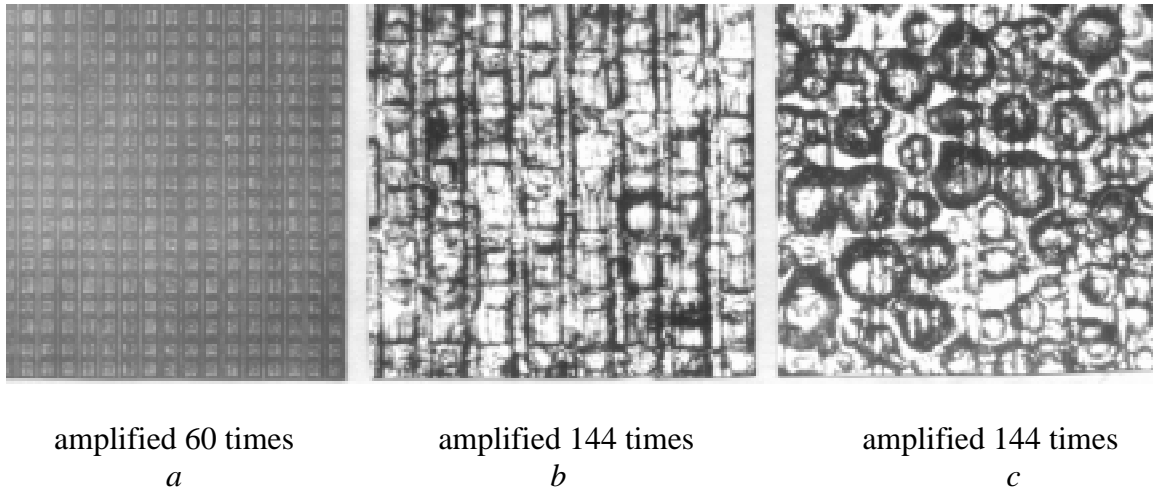


Fig.2: Orthogonal grating on the interface of the composite

After being rolled, the composite lamella was peeled off, and the deformed grating was exposed. With a microscope it can be observed and photographed. The Fig.2a shows the undeformed orthogonal grating and the Fig.2b and Fig.2c show the deformed orthogonal grating. By comparing them, we found that the grating along the rolling direction did not change at all and the pitch of the grating vertically with the rolling direction increased uniformly. It means that there is no spreading in transverse direction and no strain in this direction. The deformation along the rolling direction is uniform and stretch macroscopically. The compression strain exists in microscopical location area nearly interface of the matrix. The harder the powder grain is, the more obvious the phenomenon is. This can be seen from Fig.2c that is covered by stainless steel powder grains.

Although the grating can be seen with the microscope, it will be difficult for treating them with a computer, because parts of them were damaged by the powder grains. A simulated grating was made with the computer for analysing the strain by Transformation Moire Method. The basic principle of this method is the Moiré analysis theory. Since the grating consists of alternate dark and bright stripes, and the grating is vertical with x axis, then the gray levels of the digital grating deformed at any point can be represented approximately by a Fourier series as:

$$f(x) = \sum_{n=-\infty}^{+\infty} C_n \exp\left[j \frac{2n\pi}{p} x\right] = \sum_{n=-\infty}^{+\infty} C_n \exp[j2n\pi\omega x] \quad (3)$$

Where

$$C_n = \frac{\sin(n\pi b / p)}{n\pi}, \quad \omega = \frac{1}{p} \quad (4)$$

j is imaginary unit, n is an integer and shows the time of the harmonic, p is the grating pitch, b is the width of the bright part of the grating, ω is the frequency of the first harmonic, $C_n \exp\left[j \frac{2n\pi}{p} x\right]$ is the n th harmonic component of $f(x)$. Computation of Fourier transformation of the Eqn.1 gives

$$F(\Omega) = F\{f(x)\} = \sum I_n(\Omega - n\omega) \quad (5)$$

Where $F(\Omega)$ is the frequency function of $f(x)$, then $I_n(\Omega - n\omega)$ is the n th harmonic of $f(x)$ correspondingly. The first harmonic $I_1(\Omega - \omega)$ is extracted from the spectra by Fourier band-pass filter. Both real and imaginary parts of the I_1 are shifted by ω' to the direction of the frequency centre, then $I_1(\Omega - \omega + \omega')$ is obtained. Computing the Fourier inverse transform of $I_1(\bar{\Omega} - \bar{\omega} + \bar{\omega}')$, the following is obtained

$$\begin{aligned} i_1(x) &= \int_{-\infty}^{+\infty} I_1(\Omega - \omega + \omega') \exp(j2\pi\Omega x) d\Omega \\ &= C_1 \exp[j2\pi(\omega - \omega')x] \end{aligned} \quad (6)$$

The image of $i_1(x)$ shows a complex Moire pattern. Its real part shows a sinusoidal Moire fringes pattern that is corresponding to the equal displacement Moire pattern produced by the classical and conventional Moire method. If the grating pitch of the reference grating is $p = \frac{1}{\omega}$

The image of $i_1(x)$ shows a complex Moire pattern. Its real part shows a sinusoidal Moire fringes pattern that is corresponding to the equal displacement Moire pattern produced by the classical and conventional Moire method. If the grating pitch of the reference grating is

$$p = \frac{1}{\omega}$$



a: λ=26.1%



b: λ=43.5%



$$c:\lambda=65.2\%$$

Fig.3: The equal displacement Moire pattern for the Cu-steel composite interface

[3], then the grating pitch of the specimen is $p' = \frac{1}{\omega'}$. Fig.3 shows the equal displacement Moire pattern on the Cu-steel composite interface at different reductions. Obviously, the distance f of any two fringes is equal and easy to determine from the gray distribution curve of the patterns. So the average strain can be calculated by the formula

$$\varepsilon = P'/f \tag{7}$$

Table 1: The value of strain and rolling force

	copper - steel				stainless steel - steel			
Rolling force (kN)	51.66	83.96	101.50	118.16	64.93	86.52	114.18	128.95
Strain	0.25	0.57	1.06	1.48	0.25	0.53	0.92	1.21

Fig.4 shows the relationship of strain and rolling force. Because the deformation of the composite during rolling is big plastic deformation, the elastic deformation is omitted. Total strain equal plastic strain. From the curves we can know that relationship between strain and rolling force is not linear. The relationship can also be performed non-linear regression analyses by the computer and expressed by the mathematical formula

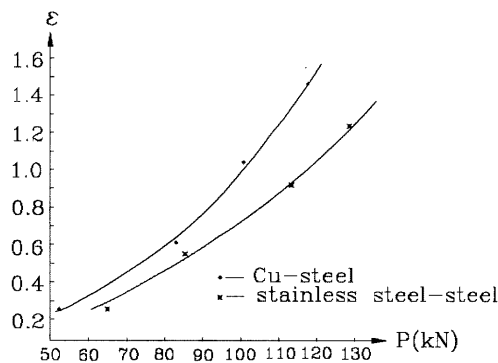


Fig.4: Relationship of strain and rolling force

$$\varepsilon = B_1 \exp(B_2 P) \quad (8)$$

Where ε is strain, P is rolling force, B_1 and B_2 are regression constants. Here $B_1 = 0.0605$, $B_2 = 0.0274$ for copper powder grains, and $B_1 = 0.0576$, $B_2 = 0.0241$ for stainless steel powder grains.

The Strain of the Composite Layer

Unlike other composite, the composite layer is a multitude of metal grains before rolling with PPR method. During the deforming process, the powder grains with bigger diameter first undergo a deformation while the powder grains with smaller diameter slide into the gaps among the grains with bigger diameter. With the pressure increasing, the powder grains gradually flatten out, close to each other, overlap each other and combine into continuous lamella. These metal grains have been cold welded into an even and continuous thin layer covering the interface of the matrix metal. Because the metal powder grains undergo a considerably big deformation in the composite processing with PPR, this affects a strong crushing function on metal grains. The result of XRD examination shows that the crystal's size inside a grain is changed with the pressure increasing. Table 2 presents the value of the crystal'

Table 2: The value of crystal's size and strain in copper grains

rolling force (kN)	0 (not rolling)	83.96	101.50	118.16
crstal's size (A)	1199	241	282	263
crystal's strain (%)	0.02	0.10	0.09	0.08

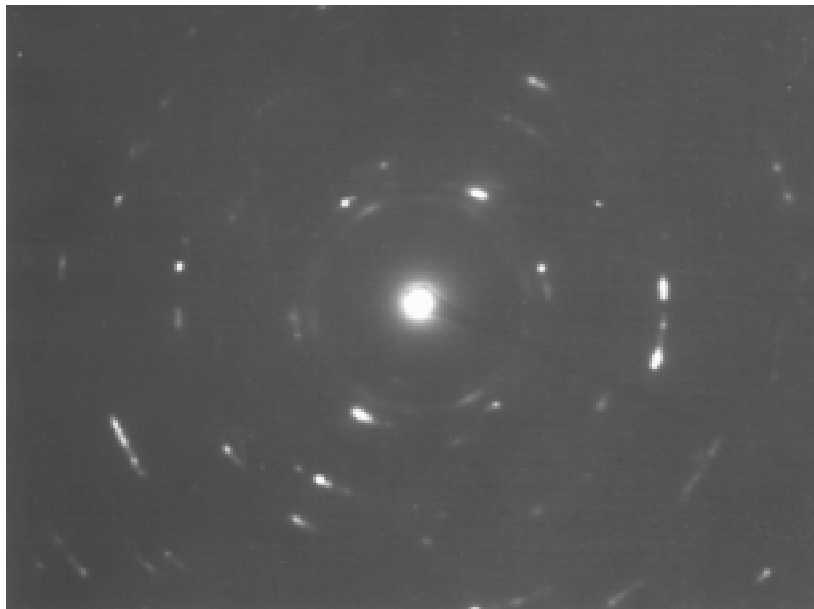


Fig. 5: SADP inside copper powder grains

size and strain examined and analyzed by XRD. The diffraction spots showed in Fig. 5 is the result of SADP. They changed into multiple spots or small arcs and took on a form of a

discontinuous ring distribution. This reveals that the crystals inside the grains are crushed and been super-fineness under the large deformation forces. It is because the crush that made the crystal' size and strain decrease in certain area.

CONCLUSIONS

(1) The rolling forces are different for different metal composite layers at the same quantity of compression with PPR method. But, the rolling force is increased with the degree of compression at almost the same proportion for defferent metal powder grains.

(2) There is no spreading in transverse direction on the interface of the matrix. This means that there is no strain and stress in this direction macroscopically.

(3) The deformation along the rolling direction is uniform on the interface of the matrix macroscopically. So the strain ϵ is also uniform. It increases with the increase of rolling force. It is a stretch strain. The strain along the transverse section and vertically the interface is not uniform, because the velocities of the two surfaces of the composite band are different and the friction forces on the two surfaces are different too. This makes the band to be bent. This problem will be studied in another paper. Since the powder grains were pressed by the rolling force, they press the matrix too. Therefore the compression strain exists in microscopical location area nearly interface of the matrix. The harder the powder grain is, the more obvious the phenomenon is.

(4) The crystal strain inside the grain is not like the strain on the interface of the matix. It does not increase with the increase of the rolling force. If the rolling force is not large enough to crush the crystals inside the grains, the strain will increase with the press force, or else the out film wrapping the metal powder grain is burst, the crystals inside the grains are crushed and the energy is released by the large deformation forces, so the strain inside the grain decreased by contrary.

ACKNOWLEDGMENT

This project is supported by the National Natural Science Foundation of China.

REFERENCES

1. Shi Q.N., Sun Y., Zhang D. M., Zhang S. H., "A Study of Rolling Force in Composite Rolling Process with Metallic Powder and Metallic Sheets", *MSMM'96*, Beijing, 1996.
2. Zhang Shuhong, "Analysis of Local Residue Strain Caused by Thermal-shock by means of Transform Moire Method", *Thermal Stresses'95*, Hamamatsu, Japan, 1995, pp.587-590.
3. Zhang S.H. , "Quantitative Analysis of Digital Fourier Transform Moire Pattern", *Journal of Kunming Institute of Technology*, Vol. 20, No.1, 1995, pp.85-90 (In Chinese).

EFFECTS OF THE INTERFACE ON LOCAL VERSUS GLOBAL LOAD SHARING BEHAVIOR IN METAL MATRIX COMPOSITES UNDER LONGITUDINAL TENSION

B.S. Majumdar¹, T.E. Matikas², D.B. Miracle

USAF Wright Laboratory Materials Directorate, Wright-Patterson AFB, Ohio 45433

¹*UES, Inc., 4401 Dayton-Xenia Road, Dayton, Ohio 45432*

²*University of Dayton Research Institute, Dayton, Ohio 45431*

SUMMARY: The effects of interfaces on load sharing behavior was evaluated by performing single-fiber and multiple-fiber single-ply fragmentation experiments and analysis of SiC/Ti-6Al-4V composites at room temperature. Fiber breaks were monitored by acoustic emission sensors, and the break locations were determined using a novel ultrasonic shear wave back reflection (SBR) technique. Data analysis was performed using Curtin's fragmentation model. High friction stresses were obtained under fragmentation conditions (e.g., 390 MPa for SCS-6 fibers) and were consistent with lack of any significant length of shear crack at the interface. Mechanical data and microstructural observations confirmed local load sharing (LLS) even for "weak" interfaces, and the mechanism is illustrated. The strengths of single-ply composites with different interfaces were predicted extremely well by Zweben and Rosen's LLS model, using a stress concentration factor that was derived based on a simple plasticity model of load transfer.

KEYWORDS : Interface, longitudinal, metal matrix composites, titanium, silicon carbide, Load sharing, fragmentation, single-fiber, local, global, damage, plasticity, slip

INTRODUCTION

The anisotropic nature of fiber reinforced composites necessitates the optimization of interface properties. Thus, the requirement of a strong interface for adequate transverse (90°) strength and creep resistance is at variance to the conventional wisdom of a weak interface for longitudinal strength. A recent review article [1] sheds insight into the issues involved for metal matrix composites. In this paper, the mechanisms by which interface properties influence the longitudinal strength in titanium matrix composites (TMCs), are explored.

In the absence of a matrix crack, the interface becomes important only in the presence of a fiber break. Fairly high shear and compressive radial stresses are generated at the interface next to the break [2-4], and the former can be sufficient to cause interface shear failure and relative fiber-matrix sliding. The sliding resistance at the interface is usually represented by an effective frictional sliding stress, τ . The prevailing understanding is that when τ is high, there is high elastic stress concentration in the adjacent fiber to cause it to fail in a cooperative

or cumulative manner. The ensuing sequence of fiber fractures, implicitly assumed to be coplanar, can lead to failure of the composite. This mechanism is termed local load sharing (LLS). When τ is small, the elastic stress concentration is less due to the longer debond length, and may not induce failure of the adjacent fiber. Consequently, fiber fractures can accumulate at random sites, and this mode of progressive fiber failure is termed global load sharing (GLS). Composite strength models have been developed for both GLS [5,6] and LLS [7,8] modes of fiber fractures. GLS provides higher composite strength and also has the advantage that the strength is not dependent on the volume of the composite, which is important when considering large structures.

The exact role of the interface on load sharing behavior was recently quantified in [9], based on the ratio of the stress concentration in nearest and next nearest neighbors. For a 35 volume percent SiC/Ti-alloy TMC, the model indicates that GLS would occur when τ was less than about 10% of the fiber strength. Using available data on interface friction stress from push-out tests and extracted fiber strength, this implies that GLS would prevail at room temperature for most composites of interest. On the other hand, except for reference [10] where there are concerns regarding the analysis used, available strength data and fiber break density and locations in a number of TMCs [11,12] suggest that LLS is the dominant mechanism. At the load at which the first fiber fails randomly, the stresses in all fibers are quite high, so that even small stress concentrations can set up successive failures of both nearest and next-nearest neighbors. Also, plasticity from a fiber break can produce significant stress concentration and lead to LLS, as will be demonstrated in this paper.

Past experimental efforts for evaluating the influence of the interface on longitudinal properties have typically relied on heat treatments of a composite [13,14], such that the interface is altered by adverse fiber-matrix reactions. Such reactions serve to change (increase) the fiber-matrix bond strength and frictional resistance, which is required for a comparative study, but which have the undesirable consequence of significantly degrading both fiber and the matrix properties. Consequently, strength loss of the composite cannot simply be ascribed to changes in interface conditions and load sharing behavior. This work differs from previous efforts in that attention was focused on the mechanisms of progressive fiber failures at the micro and meso scales, rather than on a macroscopic parameter such as the composite strength. Attention was confined to composites with only limited number of fibers, in single-fiber and multiple-fiber single-ply configurations. In particular, the single-fiber experiments and analysis methodology [15,16] were used to characterize the interface under fragmentation conditions, and to subsequently use that data to evaluate fiber failures in multiple-fiber specimens. The interface was varied by selecting SiC fibers with different coatings, and associated different interface properties. This overall approach using mini/micro-composites is part of our continuing effort at establishing a comprehensive methodology for developing optimized interfaces in TMCs.

EXPERIMENTS

Single-fiber and multi-fiber single-ply specimens were fabricated by hot pressing SiC fibers between two Ti-6Al-4V sheets at 950°C. Tensile specimens with a 25.4 mm gage length x 15.2 mm width x 0.7 mm thickness were prepared by electric discharge machining. Three different fibers were considered: (i) SCS-0 fiber, which is a 140 μm diameter uncoated SiC fibers from Textron Specialty Metals (TSM), (ii) SCS-6 fiber, which is essentially the SCS-0 fiber coated with turbostatic carbon (graphitic) with graded amounts of Si, and (iii) Trimarc

fiber, which is a 125 μm diameter SiC fiber from ARC Amercom, with a "soft-hard-soft" turbostatic carbon coating. These fibers were selected because the interfaces represent a rather wide range of interface tensile (normal) strength [17-19] and frictional push-out stresses (see Table 1), so that the influence of the interface on load sharing behavior can be assessed. Multiple fiber specimens were prepared in two different configurations. One was a 15-fiber specimen with a 0.7 mm fiber spacing, and was used primarily to understand the basic deformation mechanisms. The other multiple-fiber configuration was a 40-fiber specimen with a center-to-center fiber spacing of 200 μm , that is characteristic of typical 30 volume percent TMCs. These 40-fiber samples had smaller specimen dimensions, with a fiber volume percent of approximately 11.6 for the SCS-6 and SCS-0 fibers, and approximately 9 for the Trimarc fibers. Tensile tests were conducted at room temperature (RT), and acoustic emission (AE) sensors were used to detect fiber breaks. The break locations were determined using an ultrasonic shear wave back reflection (SBR) technique [20-22], and those results correlated extremely well with the break locations determined metallographically.

Table 1: Interface and Fiber Strength Data for the SiC/Ti-6Al-4V Systems

Fiber	Extracted Fiber, σ_o , (Lo=25.4 mm) MPa	Extracted Fiber Weibull modulus, m	Push-Out frictional stress, τ , MPa	Normal (Tensile) Interface Strength, MPa	Fragmentation strength, σ_o , Mpa (Lo = 25.4mm)	Fragmentation Weibull modulus, m	Fragmentation friction stress, τ , MPa
SCS-6	4480	14	160-190 ¹	100-120	3300	5	390
Trimarc	3400	20	30 ²	~ 0-20	3050	9	190
SCS-0	1500	6	290-320 ¹	~ 380	1300	6	500

¹ Debond stress, τ_d , corresponding to the maximum load before the load drop, since the load increased rapidly after the load drop. ² Sliding stress in the constant load region following debonding.

DATA ANALYSIS

Past research in single-fiber fragmentation (SFF) testing has relied primarily on the well-known Kelly-Tyson equation [23]: $\tau = (\sigma_f r)/L_c$, where L_c is the critical length of fibers at break saturation, and σ_f is the fiber strength. Since fiber strengths generally follow Weibull statistics, this requires an independent measurement of fiber strengths. Also, the procedure assumes that the insitu strength of the fibers in the composite remain the same as when fibers are tested independently, an assumption that may be violated in TMCs. In addition, the formula does not provide a methodology to assess stress concentration effects and load sharing in multiple fiber samples. After surveying a number of recent models [24,25], the analytical fiber fragmentation model of Curtin [26] was selected for assessing the fragmentation data. We also performed Monte Carlo simulation of the fragmentation experiment, and found excellent correlation with Curtin's model. The three parameters that emerge from the analysis are: the insitu Weibull modulus (m) and Weibull strength (σ_o) of the fiber, and the shear stress, τ , at the interface under fiber-fracture conditions. The details of the application of the model in experiments are described in [15]. Essentially, two plots are obtained from the fragmentation test: (i) the stress plot, which contains the probability ($\text{LnLn}\{1/(1-P_f)\}$) of fiber breaks plotted versus the logarithm of the applied stress, and (ii) cumulative number of breaks plotted versus the fragment length; here P_f is the fiber failure

probability. The analysis involves selection the three parameters that best match the two experimental plots. Among them , m is the simplest to evaluate, since it represents the slope of the stress plot. Also, if $\log(N)$ is plotted versus $\log(\text{stress})$, the curve is linear in the initial stages with a slope close to m (see additional details in [15]); here N is the cumulative number of fiber breaks. Comparison of single and multiple fiber results provide a means of evaluating whether stress concentration effects are operative.

RESULTS

Fig. 1 shows SBR scans for the single fiber specimens. The location of breaks are indicated by the short white line (only a two are marked for the Trimarc fiber). From such scans and the stress-strain-AE data, the stress and fragment length plots were obtained.

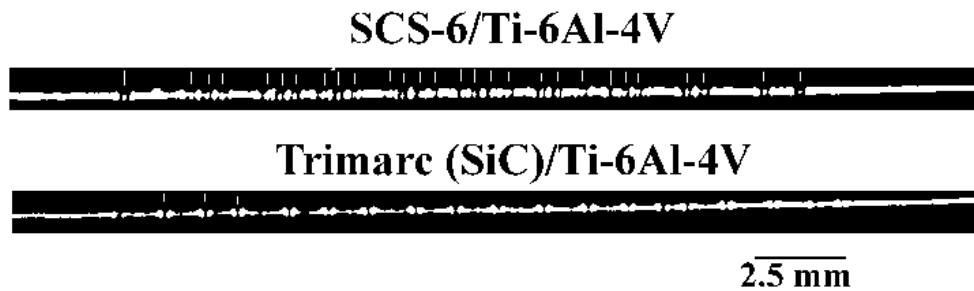


Fig. 1: SBR images for the single fiber specimens: (a) SCS-6 fiber, (b) Trimarc fiber.

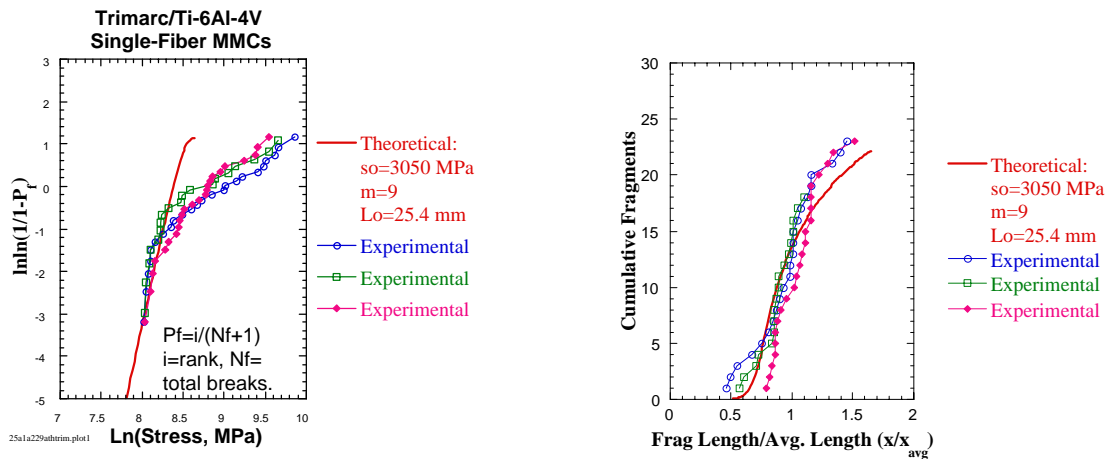


Fig. 2: (a) Weibull stress plot for the single-fiber Trimarc/Ti-6Al-4V sample
(b) Corresponding fragment length distribution plot

Figs. 2a and 2b illustrate the results for the Trimarc/Ti-6Al-4V system. Referring to Fig. 2a, it may be noted that the fiber stress was determined by multiplying the measured strain by the fiber modulus and then subtracting the residual stress in the fiber. This assumes isostrain conditions, which is violated when substantial gaps develop between the ends of the broken fiber. The deviation of the data from the theoretical curve in Fig. 2a is believed to arise from this effect. Hence, only the initial part of the theoretical curve was used to match with the data in Fig. 2a. The second point to note is that the axial compressive residual stress in the fiber was determined by an etching technique to lie between 600 and 900 MPa for both the

single and multiple-fiber specimens. This is well below that based on the assumption of a stress-free fiber at the processing temperature, and is believed to be due to loading of the fiber at the processing temperature (because of the very small amount of fibers).

Using plots such as Fig. 2, the insitu Weibull strength, σ_0 , the Weibull modulus, m , and the frictional sliding stress, τ , were determined. They are listed in the last three columns of Table 1, where σ_0 is determined at the gage length $L_0=25.4$ mm. The table also contains data from tensile tests on extracted fibers, frictional stress from push-out tests, and the tensile (normal) strength measured by using the cruciform specimen geometry [17-19].

A common feature of the data in Table 1 is the significantly higher friction stress obtained from the fragmentation experiment compared with the push-out test. For example, in the case of the Trimarc fiber, the fragmentation frictional stress is nearly six times that obtained from push-out tests. In the case of SCS-6 fibers, the frictional sliding stress determined from the fragmentation experiments is 390 MPa, compared with only 160-190 MPa obtained from push-out tests; the latter is slightly higher than reported values for a 30 volume percent SCS-6/Ti-6Al-4V composite [27]. These high friction stresses under fragmentation conditions suggest that there may be significant clamping of the fiber at the fiber break, which may prevent propagation of the interface crack. If a friction coefficient of 0.5 is assumed for the SCS-6 fiber (based on push-out tests), it implies that in the fragmentation test there is a radial clamping on the fiber of 780 MPa, which is of the order of the yield stress of the matrix, approximately 850 MPa. The analysis in [2,3] suggest that this level of stress can indeed be generated in the proximity of the break. A more recent elastic-plastic analysis [4] indicates that even if a small split was assumed along the interface (representative of a debond crack), the local radial stress at the tip of that crack is negative and singular, suggesting that it would always be very difficult to propagate the interface debond crack under fragmentation conditions.

Fig. 3 illustrates the interface region next to a fiber break in a SCS-6/Ti-6Al-4V specimen.

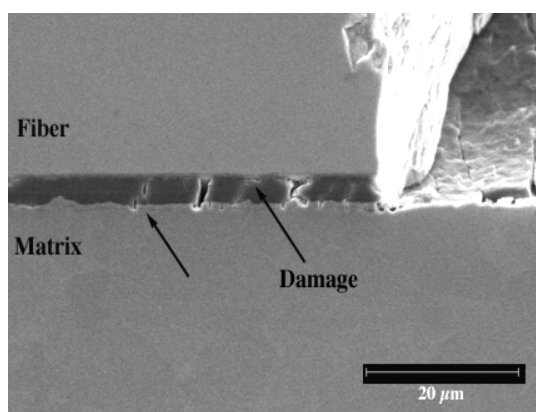


Fig. 3: Micrograph showing coating damage near a fiber break in a SCS-6/Ti-6Al-4V sample.

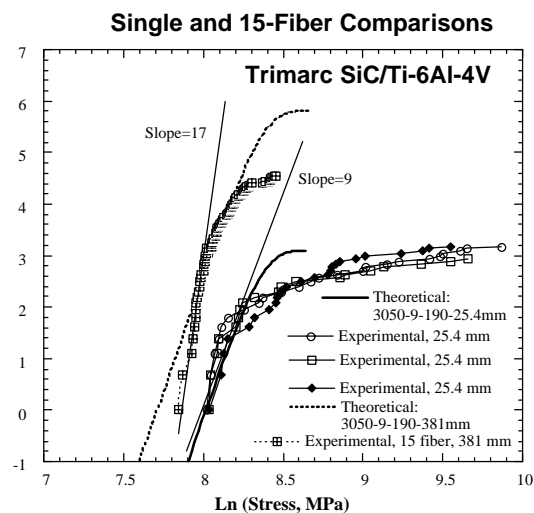


Fig. 4: Cumulative number of breaks versus the stress for the single and 15-fiber Trimarc composite. The predictions for 25.4 mm length and 381 mm length are indicated

Although Fig. 3 illustrates a number of damage features, such as transverse cracks approaching the fiber from the cracked reaction zone, or isolated interface cracks very close to the SiC surface, there is very little evidence of a continuous shear crack along the interface. While it is indeed very difficult to verify shear cracks in such carbonaceous coatings, the observations so far suggest that shear interface failure is extremely limited, which is consistent with the high frictional shear stress evaluated from the mechanical data.

Fig. 4 is a stress plot for a 15-fiber Trimarc/Ti-6Al-4V specimen, where $\ln(N)$ is plotted versus the logarithm of the breaking stress, $\ln(\sigma)$. This method of plotting is necessary because the specimen cannot be taken to fiber fracture saturation. Fig. 4 includes data from the SFF tests, as well as the theoretical curve for a gage length of 25.4 mm, using parameters that were determined earlier, i.e., $\sigma_0=3050$ MPa, $m=9$, and $\tau=190$ MPa; the designation in the plot is 3050-9-190. Also included in Fig. 4 is the theoretical curve for the same set of parameters, but for a total fiber length of 381 mm, which is the total length available for fracture in the 15-fiber/25.4 mm gage-length specimen. The basis for this latter curve is that it represents the failure stress distribution if there was no interaction between the 15 fibers. Thus, any interaction between neighboring fibers would manifest in the form of a lack of agreement with the theoretical 15-fiber curve.

Fig. 4 shows that although the 15-fiber specimen approached the theoretical curve at higher stresses, the experimental data significantly deviated from the 15-fiber theoretical curve at lower values of stresses. During the initial stage, when fiber strain is well represented by the measured strain, the slope for the experimental data is higher than the theoretical slope by about a factor of 2. Since the slope of the curve represents the Weibull modulus, the 15-fiber data suggests a higher apparent Weibull modulus for the fibers. Since there is no reason why the insitu fiber statistics should differ from the SFF samples, the higher apparent Weibull modulus may be interpreted as being due to a stress-concentration effect between neighboring fibers. This is because the occurrence of a break under stress concentration conditions would quickly load up fibers in adjacent locations, thus setting up a succession of breaks with very little increase required in the applied stress/strain. In essence, this would manifest as a higher Weibull modulus.

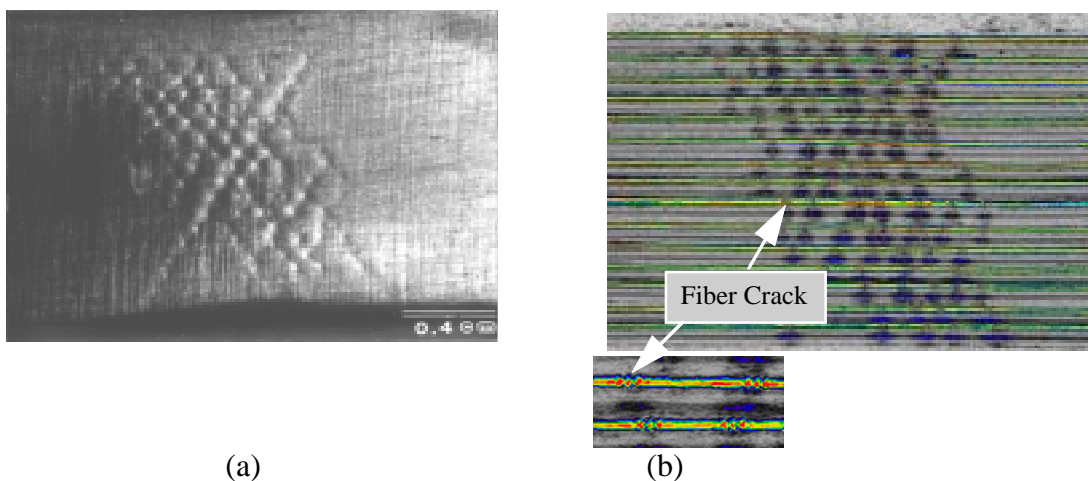


Fig. 5:(a) Face of the 15-fiber Trimarc specimen showing macroscopic slip bands on the specimen face. (b) SBR image, illustrating that the intersection of bands with the fiber correspond to the fiber break locations.

Figs. 5a and 5b correspond to the 15-fiber specimen whose data were plotted in Fig. 4. Fig. 5a is a macroscopic view of the specimen face and shows a criss-cross pattern of slip bands that are concentrated in a relatively small section of the gage length. Figure 5b illustrates the fiber break locations, as imaged by the SBR technique, and shows a one-to-one correspondence between the slip band intersections with the fiber and the fiber break locations. The intense but macroscopic slip bands are not observed in the unreinforced material, nor can they be seen near the specimen edges in Fig. 5a because the fibers are located a small distance away from the edges. Together, Figs. 5a and 5b indicate that fiber fractures have occurred cooperatively, with localized matrix plasticity being responsible for cumulative failure of fibers. This type of LLS behavior is consistent with the higher Weibull modulus for the 15-fiber specimen compared with the single fiber specimen (see Fig. 4).

Interrupted tests, where specimens were periodically unloaded to obtain SBR and plasticity images [15], have confirmed that fiber fractures are strongly influenced by slip bands which propagate from a fiber break and impinge on the neighboring fiber. Note that the LLS behavior that is observed is not inconsistent with the results in [9], since that model predicts that LLS will always occur in single-ply composites. However, the mechanism of stress concentration is different here, and needs to be modeled rigorously.

In order to illustrate how these results translate to higher volume fraction composites, Fig. 6 is presented for the 40-fiber specimens that had a center-to-center fiber distance of 200 μm . The stress-strain curve for the Ti-6Al-4V matrix is also plotted here.

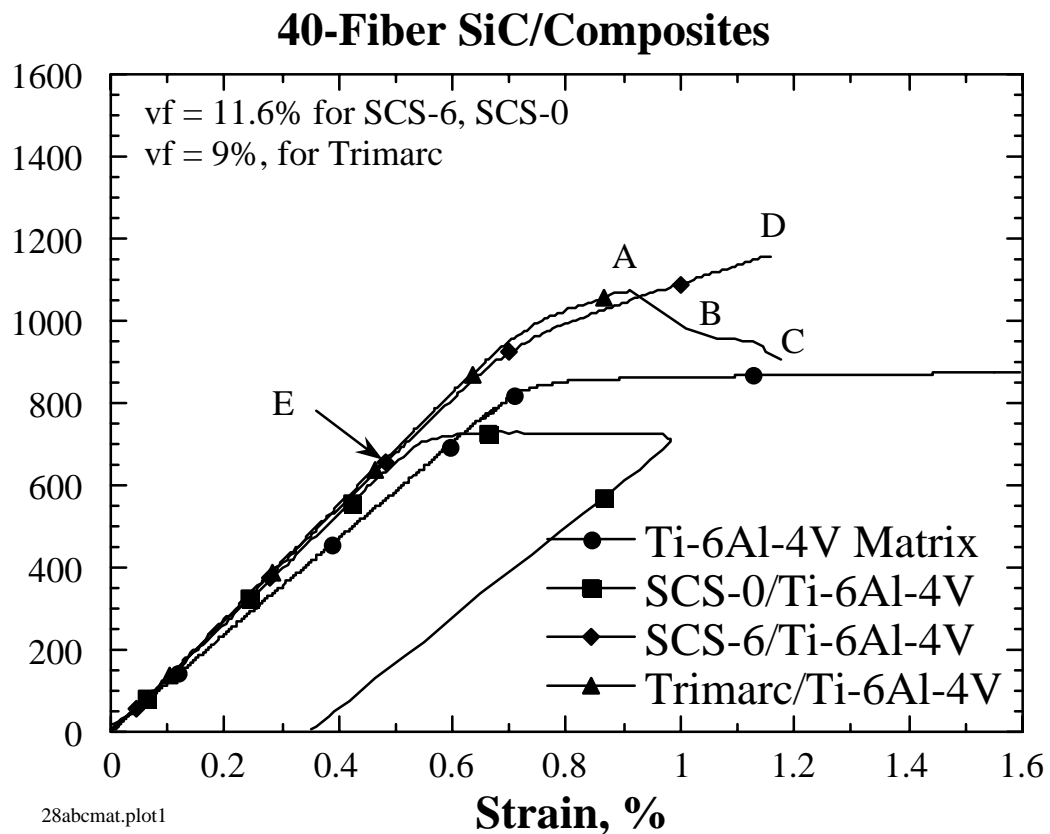


Fig. 6: Stress-strain curves for the 40-fiber single-ply composites and the neat Ti-6Al-4V matrix.

In this figure, point D corresponds to failure of the SCS-6/Ti-6Al-4V specimen, and point A corresponds to an instability point in the Trimarc/Ti-6Al-4V specimen. For the latter specimen, instability ended at point B, and the specimen was subsequently unloaded at point C, by which time the crack in the specimen had almost fully propagated through the specimen width. The SCS-0/Ti-6Al-4V specimen exhibited a constant flow stress well below that of the matrix, and it was unloaded at approximately 1% strain. The stress-strain curve for the SCS-0 case became non-linear at approximately 0.5 % strain, which was substantially lower than the flow stress of the Ti-6Al-4V matrix. Additional important parameters about the data are provided in Table 2.

Table 2: Tensile Data and Predictions for the 40-Fiber Single-Ply Specimens

Type of Fiber	Vol. % Fibers	Yield Strain %	Measured Tensile Strength, MPa	Measured Flow Stress, MPa	Predicted Strength Using Zweben's LLS Model, MPa	Predicted Strength Using Curtin's GLS Model, MPa
SCS-6	11.6	0.66	1160	-	1180	1207
SCS-0	11.6	0.5	-	732	725 ¹	1020
Trimarc	9	0.695	1076		1064	1096

¹ For the SCS-0 fibers, the strain at non-linearity is more relevant than the final flow stress. The non-linearity was observed at approx. 0.5%, and was well predicted by the LLS model.

The most revealing aspect of the above specimens is obtained from optical observation and SBR images. Fig. 7 shows the face of the specimens, wherein it may be observed that an intense slip band has traversed the entire width of the specimen for the SCS-6 and Trimarc fibers, both of which possess relatively weak interfaces. Final fracture took place inside these intense slip zones, and SBR images showed that the fibers were severely fragmented within the zone. No fiber fractures are determined outside the band, consistent with slip not being observed at other locations, as well as lack of any significant AE event prior to specimen fracture. The fiber failure locations confirm LLS in these materials with relatively weak interfaces. The specimen with SCS-0 fibers shows a rather unanticipated behavior, in that the entire gage length is filled with a criss-cross arrangement of localized slip, presumably connecting regions of severely fragmented fibers.

DISCUSSION

The fragmentation experiments and analysis show that useful data can be extracted from the single-fiber fragmentation test, and that the analysis can be used to assess load sharing behavior in multiple-fiber specimens. Thus, local load sharing manifests as a higher insitu Weibull modulus for the multiple fiber specimen compared with the single fiber sample.

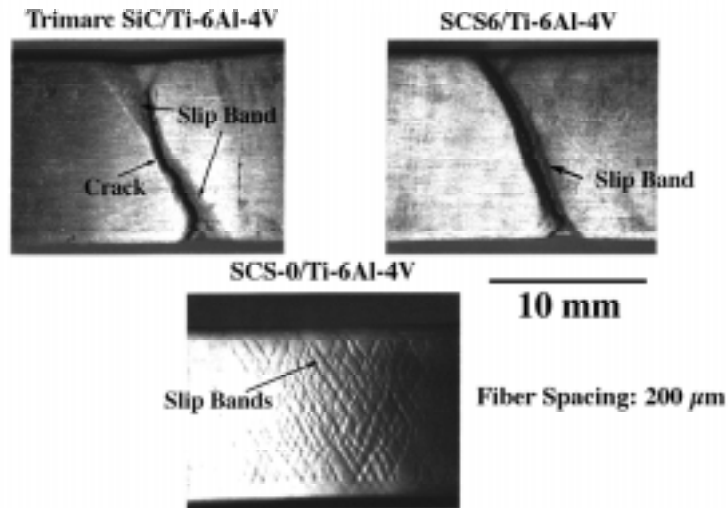


Fig. 7: Macroscopic slip traces on the faces of the 40-fiber specimens. (a) and (b) show that fracture was contained inside the intense slip band that traversed the width of the SCS-6 and Trimarc fiber specimens. Fig. 7(c) shows a criss-cross arrangement of slip bands in the entire gage section of the sample with SCS-0 fibers.

The tests show that the friction stress is much higher under fragmentation conditions than in a push-out test, and this is believed to be due to substantial clamping of the fiber at the location of the break. The microstructures also showed very little evidence of debonding. The high friction stresses are a real effect, and indicate that shear stresses obtained from push-out tests are not applicable when considering fiber failures in longitudinal loaded composites.

A more difficult item to resolve is the discrepancy in the Weibull parameters (see Table 1) obtained from the fragmentation tests versus those obtained by testing extracted fibers, although the difference is modest for the SCS-0 and Trimarc fibers. The worst agreement is for the SCS-6 fibers, and a possible reason is damage to the fibers during testing. This is discussed in more detail in [15] and is based on the SCS-6 coating structure [28]. It may be noted that the SCS-6 fiber has been found to exhibit strength degradation under fatigue crack growth conditions [29-31], whereas Trimarc fibers do not show that behavior [29]. Thus, SCS-6 fibers appear to be more prone to damage than the Trimarc fibers, and explanation may lie in the interlayer next to the SiC surface and the profile of that surface.

As final part of the discussion, we shall attempt to rationalize the strengths obtained from the 40-fiber specimens. In a previous paper [11], we have shown the existence of LLS at RT in a 4-ply SCS-6/Ti-25Al-17V composite. The evidence was based on significant strength over-prediction by Curtin's GLS model [6], and lack of random fiber breaks outside a thin 2 mm band on either side of the fracture surface. It was found [11] that Zweben and Rosen's LLS model [7], based on the occurrence of the second fiber break, provided excellent correlation with the measured strengths. In this model, the critical event is the formation of a doublet, where the second break is due to stress concentration from the first break.

In reference [11], a stress concentration factor of 1.146 was assumed, based on the elastic calculations in [32]. On the other hand, the current observations suggest the scenario shown in Figure 8, where slip bands emanating from the break allow the high modulus fibers to pick up the load at four equivalent locations, making those locations vulnerable to fracture. Since

the load is equally transmitted along the slip bands, at most one fourth of the load in the center fiber is picked up at any one location by the unbroken high modulus fiber. In other words, as a first approximation we obtain a stress concentration factor of 1.25 at the possible fiber fracture location, although this needs to be confirmed by rigorous analysis. The strength prediction follows from the following equation for the fiber stress, σ_f [7,11]:

$$\{\delta \cdot L / L_0^2\} \cdot N_t \cdot C \cdot (\sigma_f / \sigma_0)^{2m} = 1 \quad (1)$$

where δ is the shear lag distance ($= \sigma_f d / 4\tau$), d is the fiber diameter, L_0 is the length on which σ_0 is based, L is the gage length of the sample, N_t is the total number of fibers, and C is a constant, given by $C = 4 \cdot \{k^m - 1\}$, where k is the stress concentration factor, and is assessed to be 1.25 for the single-ply specimens. Substituting in $\sigma_c = v_f \cdot \sigma_f + (1 - v_f) \cdot \sigma_{matrix}$, and noting that σ_{matrix} is the matrix yield stress for the specimens with SCS-6 and Trimarc fibers, the composite strength, σ_c , can be obtained. Here v_f is the volume fraction of fibers. In the predictions, the friction stress was based on the fragmentation tests, and the Weibull parameters corresponded to those of the extracted fibers. The predicted strengths were 1180 MPa and 1064 MPa for the SCS-6 and Trimarc composites, respectively, which show excellent correlation with the corresponding measured values of 1160 MPa and 1076 MPa for these two materials (see Table 2). The corresponding GLS predictions using Curtin's model [6] are 1207 MPa and 1096 MPa, respectively. Although these numbers are also not very far from the measured strengths, the lack of random fiber breaks away from the intense slip zone suggests that the premise of the GLS model is violated in the current samples. In the case of the SCS-0 fibers, the second fiber break model leads to LLS becoming operative at a fiber stress of only 950 MPa (approx. 0.26%, using a fiber modulus of 370 GPa). Adding to this strain the residual strain (approx. 0.24%) in the fiber, the critical condition is predicted at an applied strain of 0.5 % strain, which also correlates extremely well with the experimental data (Fig.6). The constant flow stress for the sample with SCS-0 fibers is not predicted by the model, but the measured value is consistent with that of the yielded matrix modified by 11.6 percent of voided area.

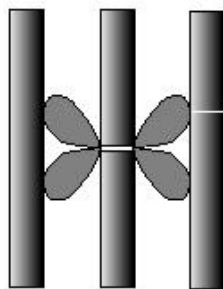


Fig. 8. Sketch illustrating how a fiber break transmits load through local slip zones. The intersection of the lobes with the adjacent fibers are potential fiber failure sites.

CONCLUSIONS

1. A methodology has been established for extracting the interface friction stress and the insitu Weibull parameters from fragmentation tests. The friction stress is much higher under fragmentation conditions than in push-out tests, and the microstructures showed very little evidence of debonding.

2. The methodology is shown to be effective in assessing load sharing behavior in multi-fiber samples with different types of interfaces.
3. The results show that LLS is operative at room temperature even for interfaces that are considered to be relatively weak. Localized plasticity plays a dominant role in enhancing this load sharing mode in preference to GLS.
4. Strengths of composites with closely spaced fibers are very well predicted by a LLS model based on the second fiber break scenario. The model relies on a stress concentration factor of 1.25 for the single-ply material, and was derived based on a simple plasticity mechanism of load transfer.

ACKNOWLEDGMENTS

This research was performed at the USAF Wright Laboratory Materials Directorate, under Contract Nos. F33615-96-C-5258 (BSM) and F-33615-94-C-5213 (TEM). The assistance of T. Campbell in specimen preparation is sincerely acknowledged.

REFERENCES

1. B.S. Majumdar, "Interfaces in Metal Matrix Composites", in Titanium Matrix Composites", Ed. S. Mall and T. Nicholas, Technomic Publications, Lancaster, PA-17604, in press (1997)
2. M.J. Iremonger & W.G. Wood, J. Strain Anal., Vol. 5, pp.212-222 (1970)
3. A.S. Carara and F.J. McGarry, J. Compos. Materials, Vol.2, p.222 (1968)
4. T. Nicholas and J.A. Ahmad, Compos. Sc. and Tech., Vol.52, pp.29-38 (1994)
5. B.W. Rosen, AIAA Journal, Vol.2, No.11, pp.1985-1991 (1964)
6. W.A. Curtin, Composites, Vol.24, No.2, pp.98-102 (1993)
7. Zweben and B.W. Rosen, J. Mech. Phys. Solids, Vol.18, pp.189-206 (1970)
8. S.B. Batdorf and R. Ghaffarian, J. Reinforced Plastics, Vol.1, No.4, pp.165-176 (1982)
9. M.Y. He, A.G. Evans, and W.A. Curtin, Acta Metall., Vol.41, No.3, pp.871-878 (1993)
10. C.H. Weber, X. Chen, S.J. Connell, and F.W. Zok, Acta Met., 42, pp.3443-3450 (1994)
11. C.J.Boehlert, B.S.Majumdar,S.Krishnamurthy, &D.B.Miracle, Met.Trans,in print (1996)
12. D.B. Gundel and F.E. Wawner, Compos. Science and Tech., in press (1996)
13. A.G. Metcalfe and M.J. Klein, Interfaces in Metal Matrix Composites, Ed. A.G. Metcalfe, Academic Press, New York, pp.125-166 (1974)

14. M.G. Watson and T.W. Clyne, *Composites*, Vol.24, No.3, pp.222-228 (1993)
15. B.S. Majumdar, T.E. Matikas, & D.B. Miracle, *J.Composites B:Engg.*, in press (1997)
16. B.S. Majumdar, S.G. Warriar, and D.B. Miracle, *MRS Proc.*, Oct. 1996, in press (1997)
17. D.B. Gundel, B.S. Majumdar & D.B. Miracle, *Scripta Metall.*, 33, p.2057 (1995)
18. D.B. Gundel, B.S. Majumdar & D.B. Miracle, *Proc. ICCM-10*, 2, Ed. A. Poursartip, Woodhead Publishing Ltd. ,U.K., pp. 703-710, (1995)
19. S.G. Warriar, D.B. Gundel, B.S.Majumdar & D.B. Miracle, *Scripta Met.*, 34, 293 (1995)
20. P. Karpur, T. E. Matikas, S. Krishnamurthy, & N. Ashbaugh, *Rev. of Progress in Quant. NDE*, 12B, Ed. by D.O. Thompson & D.E.Chimenti, Plenum Press, New York, pp. 1507-1513 (1993)
21. M.C. Waterbury, P. Karpur, T.E. Matikas, S. Krishnamurthy, and D.B. Miracle, *Composite Science and Technology*, Vol. 52, pp. 261-266 (1994)
22. P. Karpur, T.E. Matikas, S. Krishnamurthy, and D.B. Miracle, *Proc. ICCM-10*, Ed. A. Poursartip and K. Street, Woodhead Publishing Limited, Vol. V, pp. 479-486 (1995)
23. A. Kelly and W.R. Tyson, *J. Mech. Phys. of Solids*, Vol.13, pp.329-350 (1965)
24. L.T. Drzal, M.J. Rich, and P.F. Lloyd, *J. Adhesion*, Vol.16, pp.1-30 (1982)
25. B. Yavin, H.E. Gallis, J. Scherf, A. Eitan, & H.D. Wagner, *Polym. Comp.*, 12, (1991)
26. W.A. Curtin, *J. Mat, Sc.*, Vol.26, pp.5239-5253 (1991)
27. C.J. Yang, S.M. Jeng, and J.M. Yang, *Scripta Metall.*, Vol.24, pp.469-474 (1990)
28. X.J. Ning and P. Pirouz, *J. Mater. Res.*, Vol.6, No. 10, pp.2234-2248 (1991)
29. S.G. Warriar and B.S. Majumdar, submitted to *Mat. Sc. and Engg.* (1997)
30. J.M. Larsen, J.R. Jira, R. John, & N.E. Ashbaugh, *ASTM STP 1253* (1995)
31. P. Kantzos, J.I. Eldridge, D.A. Koss, & L.J. Ghosn, *MRS Proc.*, 273, pp.325-330 (1992)
32. J.M. Hedgepeth & P. Van Dyke: *J. Composite Materials*, vol. 1, p. 294 (1967)

MICROSTRUCTURE AND MECHANICAL PROPERTIES OF AL-4.5WT.%CU/10VOL.%SiC_p METAL MATRIX COMPOSITE FABRICATED VIA MECHANICAL ALLOYING TECHNIQUE

J.K. Kek, L. Lu and M.O. Lai

Department of Mechanical and Production Engineering, National University of Singapore, 10 Kent Ridge Crescent, Singapore 119260.

SUMMARY: Metal matrix composite with composition of Al-4.5wt.%Cu reinforced by 10vol.% SiC particulate has been successfully fabricated via mechanical alloying technique. Ethyl acetate was used as process control agent during mechanical alloying. After alloying, the powder was cold compacted, sintered at 600°C, and extruded at 600°C, with an extrusion ratio of 12.96. The extruded rods were solutionized at 520°C for 4 hours and peak aged at 170°C for 19 hours. Through microstructural observations, different stages of alloying were identified in the process. At the early stage of mechanical alloying, SiC_p were observed to be embedded in the matrix. During the final stage of process, SiC_p were continuously refined. Tensile tests showed that the mechanically alloyed material possessed some superior properties in comparison to that which had not been mechanically alloyed. Increase in both yield stress and elastic modulus had been observed.

KEYWORDS: Mechanical Alloying, Aluminium Metal Matrix Composites, Age Hardening.

INTRODUCTION

The development of metal matrix composites (MMCs) has been one of the major innovations in advanced materials for the past two decades [1]. MMCs combine metallic properties (ductility and toughness) with ceramic properties (high strength and high modulus), leading to higher strength, greater modulus, lower density, and better thermal stability. Discontinuously reinforced MMCs hold the additional advantages of lower fabrication cost, and of more isotropic properties than continuous fibre materials. However the commercialisation of short fibre or whisker reinforced MMCs has been slow due to the relatively high costs associated with currently available reinforcements. More recently, particle reinforced MMCs, with their potential as lower cost, characteristic isotropic, high modulus and strength, high wear resistance, and easily fabricated materials, are becoming more attractive and are reaching commercial production stage [2].

Many processing techniques have been developed to produce particle reinforced MMCs in the attempt to optimise the structure and properties [2-4]. Since most ceramic materials are not well wetted by molten alloys, the cost of improving wettability has limited the commercial application of the conventional molten metal methods. Similarly, there are also other methods such as the infiltration techniques and spray deposition processes. In most cases, however,

high control costs in preventing contamination of liquid metal matrix, as well as prohibitively high melting points have constrained the processes to be less commonly used. As a result, powder metallurgy (P/M) process has become more popular [5,6]. However, one of the major problems in production of MMCs using P/M is either the agglomeration of reinforcement particles due to size difference between powders for the matrix and the particles, or static charge on the particles. To achieve homogeneity of particle distribution, several methods may have to be employed, such as a proper choice of the particle size and the use of polar solvents that neutralise the charge on the surface of the particles [7].

Another alternative method to improve particles distribution is to use mechanical milling (MM) or mechanical alloying (MA) technique [8]. MA is a solid state processing technique allowing production of macroscopically homogeneous composite materials starting from various powder mixtures. It is a ball milling process carried out in a dry ball mill for mixing the mixtures. This process involves repeated welding, fracturing and rewelding of powder particles during the high energy collision between balls and the powder particles. The repeated welding and fracturing finally lead to the formation of alloys and a uniform distribution of very fine powder mixture with a finely controlled microstructure after compaction. In addition to the strengthening caused by uniformly dispersed fine particles, the fine grain size and the high dislocation density of the metal matrix, as a result of work hardening of metal powders, also contributed to the strengthening of the MMCs. One of the advantages of MA is the ease of preparation of alloy powders containing both high and low melting point elements. MA was originally developed in the late 1960s to produce oxide-dispersion strengthened (ODS) nickel-based superalloys [9], it has now been shown capable of producing several stable and metastable crystalline and quasicrystalline intermediate phases, and amorphous phases. The crystalline phases produced usually are of nanometer dimensions. All these effects (very similar to those obtained by other non-equilibrium processing techniques like rapid solidification from the melt, vapour deposition, ion irradiation, etc.) lead to improvements in properties of the alloys. The technique of MA is now applied to all types of materials - metals, ceramics, and polymers, and is being actively pursued by industry, academia, and research laboratories all over the world [10-13].

Aluminium alloys based MMCs are one of the particle reinforced MMCs, under development with MA as a processing route [11]. In an investigation of SiC_p reinforced Al-4.5wt.%Cu composite, well homogeneous distribution of reinforcement in the matrix was achieved by using a planetary ball mill for MA processing [13]. In this paper, composites of Al-4.5wt.%Cu reinforced by 10vol.% SiC_p were fabricated by P/M route, via MA technique as the mixing process for the composite powder at different ball milling durations in a planetary ball mill. Comparison was made with composites that processed via conventional blending method. The microstructure, ageing behaviour, and mechanical properties of the composites were examined in the study.

EXPERIMENTAL PROCEDURES

Elemental Al and Cu powder particles with average particle size of 150 and 50 μm respectively were mechanically alloyed with SiC_p of average particle size of 35 μm in a FRITSCH pulverisette 5 planetary ball mill. 40 hardened steel balls of 16 gram each were used in the ball milling process. The weight ratio of ball to powder was about 16:1. The rotational speed of the turn table was 200 rpm. The corresponding relative speed of the vial was 434 rpm. To prevent excessive cold welding during ball milling, ethyl acetate

(CH₃CO₂C₂H₅) was used as a process control agent (PCA) at various amount for different MA duration. Argon gas was filled into the vial to reduce the oxygen content and therefore minimised the chance of oxidation during ball milling due to temperature rise. After ball milling, the composite powders were cold compacted at about 420 MPa, lubricated with molybdenum disulphide. The green compacts were then sintered at 600°C for 2 hours in an inert environment of forming gas (95%N₂ and 5%H₂). The sintered compacts were hot extruded at 600°C, with an extrusion ratio of 12.96, using dry graphite as lubricant. The morphologies and microstructure of the powder particles after ball milling were examined using scanning electron microscopy (SEM). The extruded rods were machined to standard tensile specimens according to ASTM E 8M. The specimens were solution treated at 520°C for 4 hours, quenched into water at room temperature, and then artificially aged at 170°C for various durations. 15T-scale Rockwell superficial hardness testing was used for determination of the duration of peak ageing. Based on the average values of hardness measurement, the specimens were eventually peak aged at 170°C for 19 hours. Tensile testing was conducted using an Instron testing machine for the peak aged specimens and the fractography study was performed using SEM.

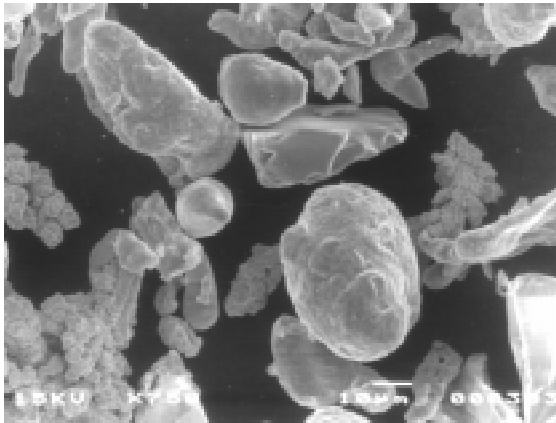
RESULTS AND DISCUSSION

Morphologies of MA Powder Particles

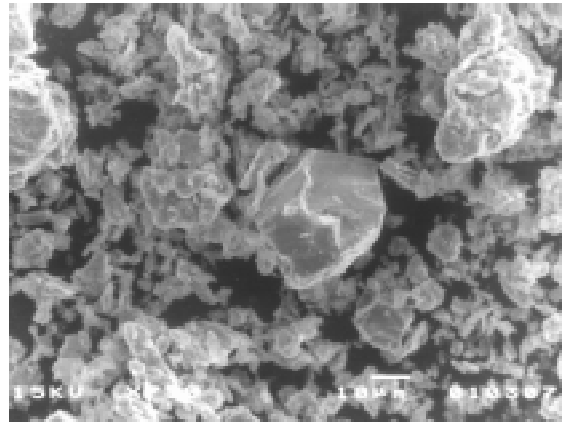
Figs. 1(a) to 1(e) show the typical morphologies of the powder particles after conventional blending (MA 0 hour) and different MA durations (MA of 1, 3, 6 and 12 hours). With MA, the lumpy Cu powder and SiC particles were broken into smaller fragments, and these fragments were more uniformly distributed within the mixture. MA has significantly improved the distribution of SiC_p in the mixture and reduced the extent of segregation in the composite. A reduction in overall particle size can be observed as MA duration increased. The shape of the particles was also changed to be more rounded after MA. Particles with sharp edges were more difficult to be found.

Microstructural Evolution of MA Powder Particles

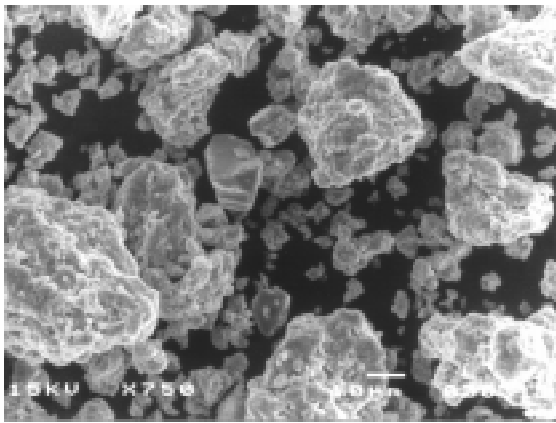
Figs. 2(a) to 2(e) show the microstructures of the powder particles at different MA durations. Cu powder could hardly be found as it finally formed a solid solution in Al. It can be seen that as the MA duration increased, the number of SiC_p embedded into the Al matrix increased and the particle size of SiC_p decreased. The incorporation of SiC_p into the surface of the matrix powders was due essentially to inlaying of SiC_p into the cold welded soft matrix powder under collision force. With the increase in MA duration, soft particles were eventually severely deformed and embrittled by cold deformation. For MA durations of 1 and 3 hours, SiC_p were not well distributed (Figs. 2(b) and 2(c)). In some areas, large clusters of SiC_p could be found while in other areas little could be perceived. For longer MA duration, due to continuing fracturing and rewelding, distribution of SiC_p became more and more homogeneous (Figs. 2(d) and 2(e)). In addition, a change in shape of SiC_p was also observed. At the beginning of MA, SiC_p were seen to be sharp and angular, with non-uniform particle sizes. They were gradually reshaped to a more rounded form and more uniformly refined with increasing MA duration. After 6 hours of MA, better distribution of SiC_p had been achieved. It can be concluded that agglomeration of reinforcement particles due to size and weight differences of powders from the matrix could be improved via MA process. No clustering of SiC_p could be found from Figs. 2(b) to 2(e).



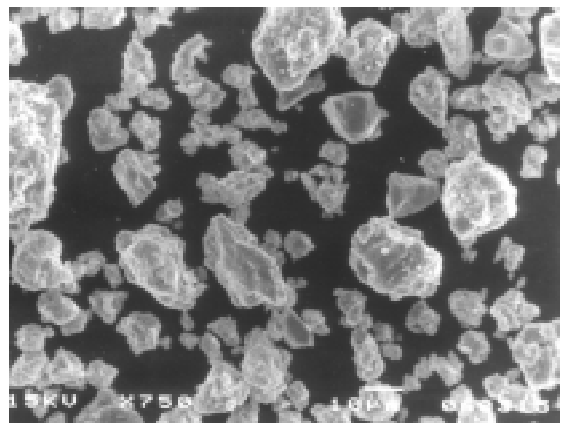
(a) MA 0 hour



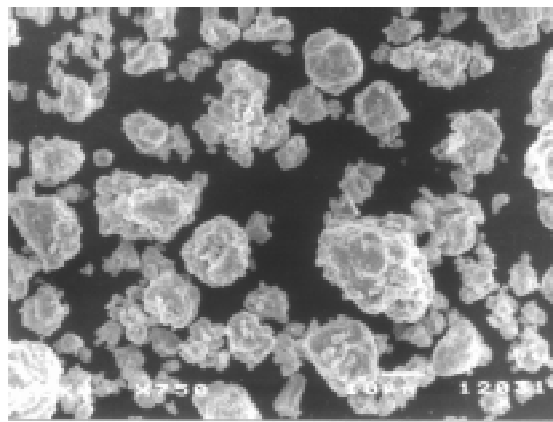
(b) MA 1 hour



(c) MA 3 hours

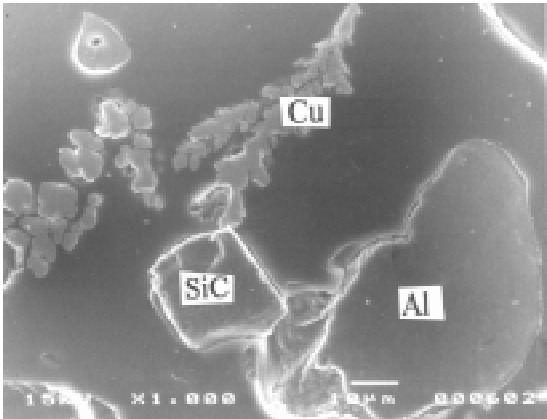


(d) MA 6 hours

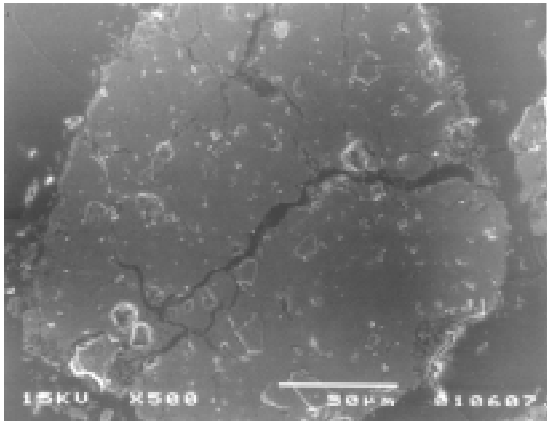


(e) MA 12 hours

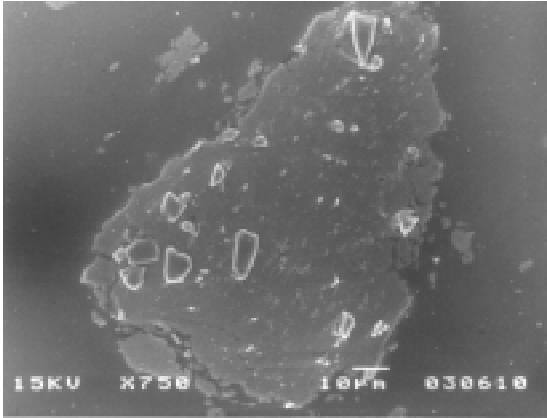
Fig. 1: Morphologies of powder particles at different MA durations.



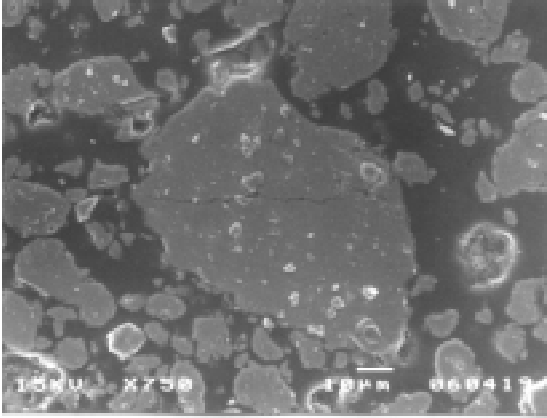
(a) MA 0 hour



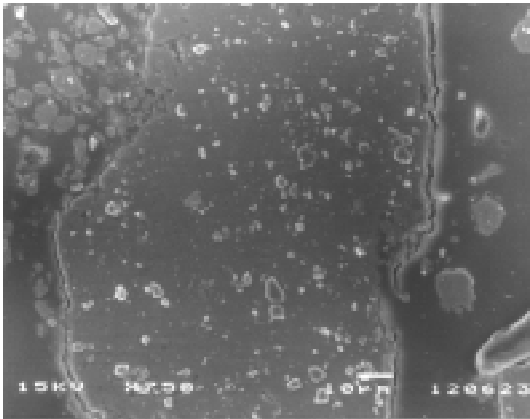
(b) MA 1 hours



(c) MA 3 hours



(d) MA 6 hours



(e) MA 12 hours

Fig. 2: Microstructure of powder particles at different MA durations.

Age Hardening Behaviour

The hot extruded bars were solutionized at 520°C for 4 hours and quenched into water at room temperature. Hardness measurement as a function of artificial ageing time at an ageing temperature of 170°C is given in Fig. 3. For those specimens fabricated by conventional blending method (MA 0 hour), the average hardness readings suggest that the MMC achieved the peak age (T6) condition at about 19 hours of ageing time. However for specimens produced by MA technique, there is no significant trend of reaching peak hardness for the ageing duration from 0 to 23 hours. Since the age hardenability is appreciably reduced by MA process in P/M of Al alloy [12], and hence, superposition of age hardening on dispersion strengthening due to MA has not been attained. This is because the presence of fine grain size after MA significantly contributed to the increase in hardness. The other reason is due to high dislocation density resulted from work hardening of metal powders during ball milling. Consequently, further dispersion strengthening by age hardening will not have much influence once the hardness has already exceeded the peak limit due to the saturation of dislocation density. As a result, the overall hardness values obtained for all MA specimens regardless of MA duration, are found mostly to be higher than the peak hardness value of the non-MA specimen (MA 0 hour). Since the T6 condition for all MA specimens could not be accurately determined, the peak aged duration was taken to be the same as the non-MA specimen, which is 19 hours.

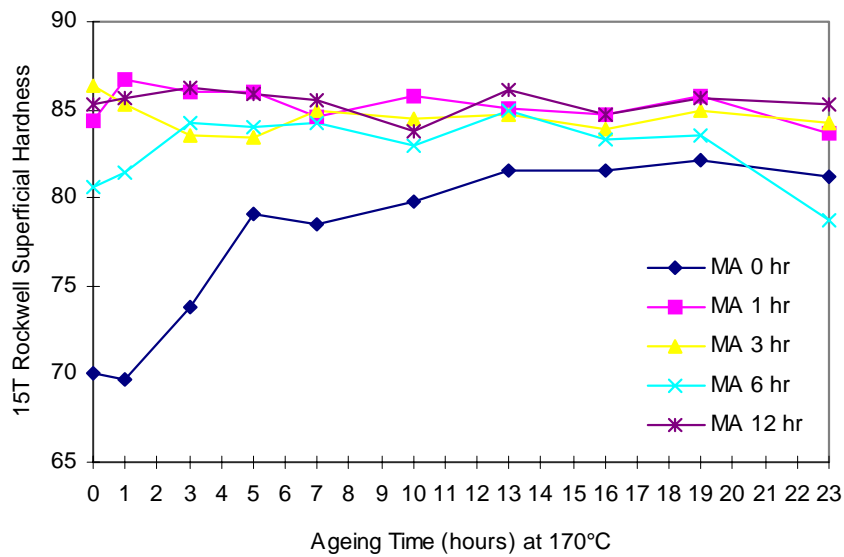


Fig.3: Variation of hardness with ageing time at 170°C for the extruded MA specimens

Mechanical Property

0.2% yield stress and Young’s modulus of the MMC specimens are given in Fig. 4. It can be seen that except for MA duration of 6 hours, 0.2% yield stresses increase after MA. Young’s moduli also increase with MA duration to a maximum value after 6 hours of MA, followed by a decrease. The increase in moduli and yield stresses may be associated with two factors. Firstly, prolonged ball milling led to the homogenisation of SiC_p distribution, an increase in bonding strength between SiC_p and the Al matrix, and to the refinement of SiC_p. Secondly, although the milling vials were protected by Ar atmosphere, existence of oxygen could still be possible due to improper sealing. The residual oxygen would react with Al to form aluminium oxide during milling since new surfaces were formed continuously due to

fracturing of Al particles. Furthermore, the oxygen and carbon that decomposed from the PCA, would also react with Al to form oxide and carbide. These effects could have contributed to the increase in the Young's modulus and yield stress. However, the formation of extra oxide and carbide would decrease the ductility and hence increase the sensibility to produce voids and microcracks. With long MA duration, crystalline size of the particle was refined to nanosize. This refinement of the crystalline size may enhance ductility of the MMC. The Poisson's ratio obtained for the MMC is about 0.3, similar to that of common metallic materials.

MA Duration (hour)	0	1	3	6	12
0.2% Yield Stress (MPa)	219.2	275.8	259.3	217.5	266.5
Elastic Modulus (GPa)	90.0	95.5	99.0	113.0	93.3
Poisson's ratio	0.32	0.3	0.3	0.3	0.3

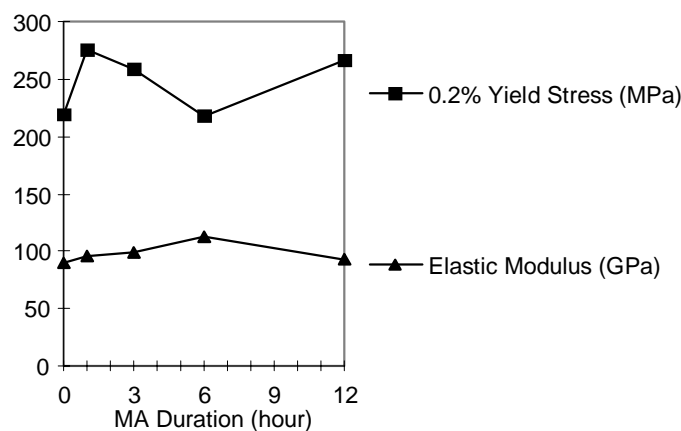
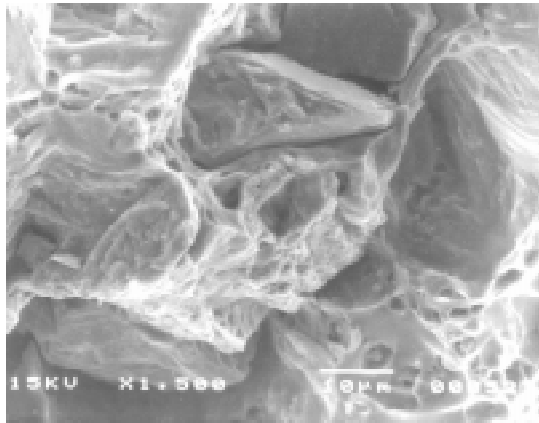


Fig. 4: Mechanical properties of composites at different MA durations

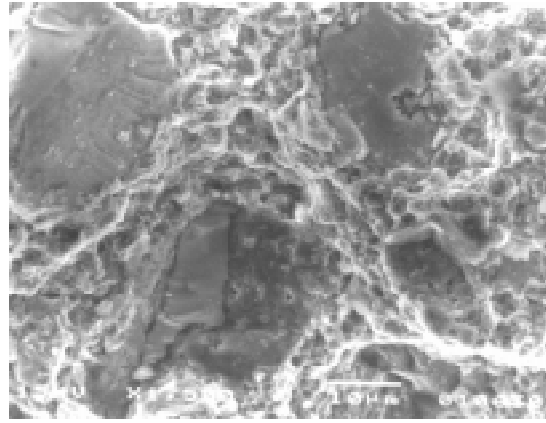
Fractography

Fig. 5 shows the fractographs of the MMC specimens. Generally, fracture is macroscopically brittle, but on a microscopic scale, local ductile fracture of the metal matrix is often observed. Evidence of SiC_p fracture and interfacial failure are also frequently seen. Fig. 5(a) shows the fracture surface of the blended specimen (MA 0 hour). Agglomeration of sharp edged SiC_p in the matrix can easily be observed. These clumps of reinforcement essentially act as large voids in the composite. Large clusters of SiC_p are also more commonly seen on the fracture surfaces of specimens with shorter MA durations. The fractographs suggest that fracture was due mainly to the segregation of SiC_p and/or debonding at the matrix-particle interfaces in conventional blending and at shorter MA duration where a uniform distribution of SiC_p has not been achieved, especially at the locations where weak diffusion bonding between SiC_p took place. Microvoids can also be observed as microvoid coalescence is generally the predominant fracture mode in particulate reinforced MMCs [14]. Almost no agglomeration of SiC_p could be observed after 12 hours of MA. The agglomeration of SiC_p in the matrix and the interfacial bonding strength were improved with increase in MA duration as a result of more SiC_p being well incorporated into and bonded with the matrix materials, leading to the increase in the interfacial strength between Al matrix and SiC_p reinforcement. Hence the fracture mode changes from initial debonding between SiC_p and Al matrix, to inter-particle fracture. For instance, fracture of SiC particles can be seen in Fig. 5(d) (MA 6 hours). This explains partially why the elastic modulus dropped for MA duration of beyond 6 hours. Due to prolong MA, until such time that the particle size of SiC could become excessively refined

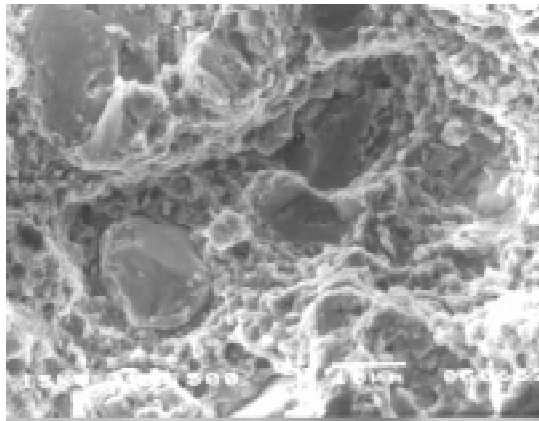
and start losing its effect of high modulus property. Stresses applied to the MMC are transferred through the matrix to the SiC_p. Since the modulus of the SiC is higher than that of Al matrix, once fracture occurred at SiC_p, the load would be absorbed by the Al matrix which caused a decrease in the modulus of the MMC. The yield stress was also increased because the work for the fracture of SiC_p (which is stronger than Al), is greater than the weak debonding force at shorter MA duration.



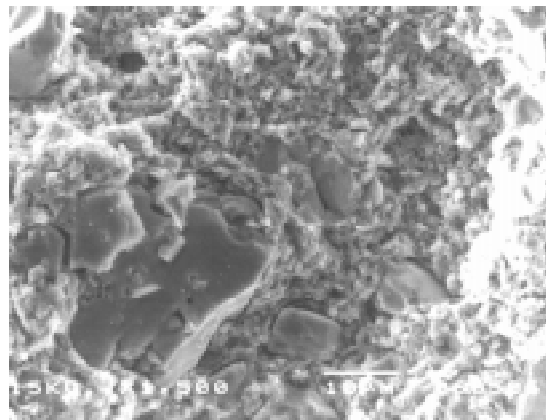
a. MA 0 hour



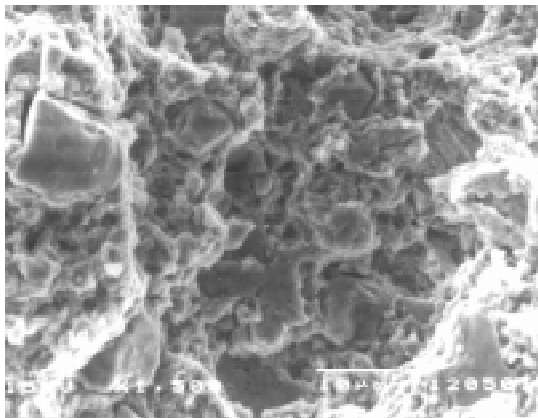
b. MA 1 hour



c. MA 3 hours



d. MA 6 hours



e. MA 12 hours

Fig. 5: Scanning electron micrograph showing the fracture surfaces of the MMC after tensile test at different MA durations.

CONCLUSIONS

Al-4.5wt.%Cu matrix composite reinforced by 10vol.% SiC_p, with uniform distribution of SiC_p leading to superior properties compared with those processed by conventional blending method, has been successfully fabricated via mechanical alloying technique. In addition, MA processing has been observed to significantly reduce the age hardenability of the MMC. The elastic modulus of the MMC was optimised at a MA duration of 6 hours. Further increase in MA duration would only increase its yields stress.

ACKNOWLEDGEMENT

The authors would like to thank Messrs. Lau Pak Kai, Tung Siew Kong, Tay Peng Yeow and Chiam Tow Jong of the same University, for their excellence technical assistance.

REFERENCES

1. Kelly, A., *Compos. Sci. Technol.*, Vol.23, 1985, pp.171-199.
2. Ibrahim, I.A., Mohamed, F.A. and Lavernia, E.J., *J. Mat. Sci.*, Vol.26, 1991, pp.1137-1156.
3. Srivatsan, T.S., Ibrahim, I.A., Mohamed, F.A. and Lavernia, E.J., *J. Mat. Sci.*, Vol.26, 1991, pp.5965-5978.
4. Lloyd, D.J., *Int. Mat. Rev.*, Vol.39, No.1, 1994, pp.1-23.
5. Liu, Y.B., Lim, S.C., Lu, L. and Lai, M.O., *Proc. of ICCM/9*, 1993, Vol.I: Metal Matrix Composites, Miravete, A., Ed., pp.770-778.
6. Liu, Y.B., Lim, S.C., Lu, L. and Lai, M.O., *J. Mat. Sci.*, Vol.29, 1994, pp.1999-2007.
7. Bhanuprasad, V.V., Bhat, R.B.V., Kuruvilla, A.K., Prasad, K.S., Pandey, A.B. and Mahajan, Y.R., *Int. J. Powder Metall.*, Vol.27, 1991, pp.227-235.
8. Benjamin, J.S., *New Materials by Mechanical Alloying Techniques*, Arzt, E. and Schultz, L., Eds, Deutsche Gesellschaft fur Metallkunde e. V., Oberursel, Germany, 1989, pp.3-18.
9. Benjamin, J.S., *Metall. Trans.*, Vol.1, 1970, pp.2943-2951.
10. Koch, C.C., *Ann. Rev. Mater. Sci.*, Vol.19, 1989, pp.121-143.
11. Sundaresan, R. and Froes, F.H., *New Materials by Mechanical Alloying Techniques*, Arzt, E. and Schultz, L., Eds, Deutsche Gesellschaft fur Metallkunde e. V., Oberursel, Germany, 1989, pp.243-262.

12. Tatsuta, M., Kim, D.-G., Kaneko, J. and Sugamata, M., *Science and Engineering of Light Metals*, Hirano, K., Oikawa, H. and Ikeda, K., Eds, Japan Inst. Light Metals, Tokyo, 1991, pp.685-690.
13. Lu, L., Lai, M.O. and Zhang, S., *Key Engineering Materials*, Vol.104-107, 1995, pp.111-124.
14. Crow, C.R., Gray, R.A. and Hasson, D.F., *Proc. 5th International Conference on Composite Materials*, San Diego, California, Harrigan, 1985, W.C., Jr., et al, Eds, pp.843-866.

THE EFFECTS OF INTERFACIAL DEBONDING AND WORK HARDENING ON THE FRACTURE OF METAL-CERAMIC LAMINATES

S.J. Howard^{§,†}, S.K. Pateras[§], and T.W. Clyne[§]

*§Department of Materials Science and Metallurgy, Cambridge University,
Pembroke Street, Cambridge CB2 3QZ UK*

*†Structural Materials Centre, Defence Research Agency, Farnborough,
Hampshire GU14 6ND UK*

SUMMARY: Experiments are described in which laminates made up of alternate layers of aluminium and alumina have been fractured in bending, with the fracture energy being measured. The testing geometry was such as to ensure that failure occurred by propagation of a single, dominant crack. The effect of debonding has been investigated by systematically reducing the interfacial bond strength. In order to study the deformation and fracture of metal ligaments which bridge cracks in neighbouring ceramic layers, sandwich specimens were tested in tension. A model has been developed in which the contribution from metal ligament deformation has been quantified by adaptation of the Bridgman treatment of constrained notch growth. Application of the model to the commercial purity aluminium used in this work necessitated incorporation of the effect of work hardening. Work hardening raises the work of fracture. Fairly good agreement was observed between prediction and experiment for the work done when a single constrained metal layer was tested in tension. Good agreement was also found when the model was applied to fracture of multi-layered laminates. It is expected that interfacial debonding will raise the fracture energy of a laminate during dominant crack propagation and this was observed experimentally. However, in practice multiple cracking may occur in metal-ceramic laminates. This can raise the fracture energy dramatically, but it also makes it more difficult to predict and likely to be sensitive to the specimen dimensions and loading geometry. Interfacial debonding will tend to reduce the incidence of multiple cracking and hence to reduce the fracture energy in cases where it is likely to occur.

KEYWORDS: metal-ceramic laminates, energy absorption, crack bridging, plastic zone, slip line field, interfacial debonding, crack opening displacement, necking, work hardening

INTRODUCTION

There has been extensive interest [1-8] recently in metal/ceramic laminated materials, which offer the potential for attractive combinations of stiffness, creep resistance, wear properties, strength and toughness. This interest follows earlier work on how ceramics can be toughened by the incorporation of dispersed metallic constituents [9-12]. The key issue for the development of such layered materials concerns the retention of acceptable toughness levels when the laminates have sufficiently high loading of ceramic to confer good stiffness, creep resistance and tribological properties.

There have been several studies [1, 6, 7, 13, 14] aimed at prediction of the fracture energy of a laminate composed of alternate layers of brittle and ductile materials. Such modelling is based on the propagation of a single dominant crack (oriented normal to the plane of the layers), although it is recognised that in practice multiple cracking may occur - particularly with relatively high metal contents [8]. Most of the energy absorbed when such crack propagation takes place is expended in plastic deformation of the metal layers while they bridge the cracks between adjacent ceramic layers. A key issue concerns the effect of the constraint imposed by the surrounding ceramic layers. This constraint tends to raise the initial traction needed to generate plastic flow of the metal. However, it will also tend to limit the plastic strain at failure. The net effect is in general to reduce the work of fracture. It has been recognised [9] for some time that one consequence of this is that the fracture energy is expected to fall (approximately linearly) with decreasing metal layer thickness (for a given overall metal volume fraction), although there has been little experimental validation of this.

In the present study, experimental data are presented from specimens with a strong interfacial bond and also from specimens in which this bond has been deliberately weakened. In modelling the fracture process, particular attention is directed towards the effect of the shape of the bridging ligament, which is affected by interfacial debonding.

EXPERIMENTAL PROCEDURES

Material and Specimen Production

Laminates were prepared by diffusion bonding[6] . The process involves stacking alternate layers of alumina and (commercial purity) aluminium in a vacuum hot press. Pressing was carried out at ~650°C and 4 MPa, for about 4 hours. This procedure generates interfaces which are well bonded. Three different metal layer thicknesses were used, with the same ceramic layer thickness (0.5 mm), so that 3 metal volume fractions (from 8% to 61%) were studied. Each specimen contained 7 ceramic layers. Specimens for bend testing were chevron-notched [8] prior to testing, in order to constrain fracture to a single well defined plane and avoid complications due to multiple cracking. Sandwich specimens were also produced, composed of outer ceramic layers (2 mm thick) and a central metal layer (2.6 mm thick). These were tested in tension, after notching of the two ceramic layers, in order to study the deformation and rupture of a bridging ligament. Specimens were also produced with interfaces which had been weakened in a controlled manner. This was done by spraying a discontinuous graphitic layer onto the interface prior to the bonding process. The area coverage with graphitic material (which inhibited interfacial bonding) was about 50%.

Mechanical Testing

All testing was carried out at room temperature, using a servo-hydraulic machine under displacement control. Specimens were loaded in four-point bending with a roller displacement rate of 0.2 mm min⁻¹. The distance between the inner and the outer rollers varied from 12.5 to 20 mm. Roller displacement was measured using an LVDT. Tensile testing was carried out with a range of strain rates. For the sandwich specimens, a clip gauge was used to measure the changing crack opening displacement as straining continued.

MODELLING OF FRACTURE

The principal contribution to the absorption of energy during cracking by a laminate reinforced by ductile layers has been previously identified as deformation of constrained metal ligaments behind the crack tip [13]. This deformation process can be divided into three distinct regimes: (a) small scale yielding, (b) onset of global yielding and (c) necking of the metal ligament until it ruptures. These are considered in detail below. Elastic properties of the metal and ceramic used in the modelling work, taken to represent aluminium and alumina, were values for E of 70 and 350 GPa and for ν of 0.33 and 0.24 respectively. The metal yield stress, σ_Y , was taken as constant.

Small Scale Yielding

The small scale yielding (SSY) behaviour of a metal near the high stress region of a crack tip has been analysed by several researchers[15, 16] . A relationship between the nominal stress, σ_n , and the opening displacement of the crack, u , has been proposed[7, 17, 18] , based on elementary fracture mechanics under plane strain conditions where σ_Y is the uniaxial yield stress of the metal, E is its Young's modulus, h_m is its thickness and Y is a dimensionless constant.

$$\frac{\sigma_n}{\sigma_Y} \approx Y \sqrt{\frac{\pi E}{2\sigma_Y}} \sqrt{\frac{2u}{h_m}} \quad (1)$$

In order to validate this expression and evaluate Y , finite element (FEM) analysis of the constrained notch problem has been performed, using ABAQUS software[7] . A mesh was set up consisting of an elastic - perfectly plastic (metal) layer between two radially notched elastic (ceramic) layers of equal thickness. This was loaded in tension by uniform displacement of the top surface. The results suggest that Y is not a strong function of the ceramic elastic properties or thickness, but is related to the Poisson ratio of the metal layer. For materials with Poisson ratios lower than 0.4, Y was found to be well approximated by the following expression.

$$Y \approx 0.46 / \sqrt{1-2\nu} \quad (2)$$

The FEM results are shown in Fig. 1 for three different ratios of the initial notch opening, u_0 , to the metal layer thickness, h_m . It is clear that the SSY curve for an initial notch opening of zero, ie an infinitely sharp crack, will be similar in form to those predicted for finite initial openings, albeit with a higher maximum constraint expected at the onset of net section plasticity. The good agreement exhibited over the initial sections of the plots indicates that Eqn.(1) gives a reliable indication of the SSY behaviour. The problem of predicting the maximum constraint (peak value of σ_n / σ_Y) is addressed in the next section.

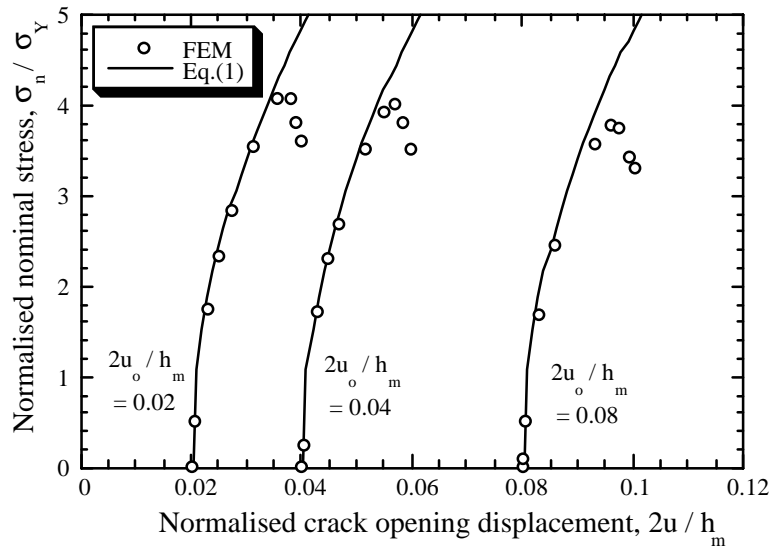


Fig. 1: Plots of normalised nominal stress against normalised crack opening displacement, as obtained by using Eqn. 1) with the value of Y given by Eqn. 2, and by using FEM analysis. These plots refer to the straining of a single metal layer bonded between two ceramic layers, which have missing sections which constitute the initial crack opening displacement.

Onset and Development of Global Yielding

It is well established that the constraint of plastic yielding in an elastic/ductile composite, as indicated by the ratio of the mean axial stress required for net section yielding to the uniaxial (unconstrained) yield stress, can be large. Values between 3 and 8 have been reported in the literature for layered systems, using either experimental[11, 12] or theoretical[13] approaches. In order to predict the stress field ahead of the notch after the onset of global yielding, and therefore the constraint factor, the present work has involved derivation of slip line field solutions for various geometries, following the procedures of Hill[19], Rice and Johnson[20] and Evans and McMeeking[21]. Three different notch shapes, with square, radial or circular geometries (see Fig. 3) were examined in the current study. Predictions from the slip line field analysis of the case of a radial notch were found to be in very good agreement with an expression derived by Bridgman[22], which gives the distribution of axial stress across the section of the neck, σ_{yy} , as a function of the curvature of the free surface, κ_s , ($=1/R$, where R is the radius of curvature) at the section of minimum area. Modifying Bridgman's original expression so that it is applicable to plane strain, rather than the case of axial symmetry which he treated, leads to the following equation.

$$\frac{\sigma_{yy}}{\sigma_Y} = 1 + \int_x^a \kappa dx \quad (3)$$

where a is the semi-thickness of the metal layer at the minimum section, x is the distance from the centre of the metal layer and κ is the radius of curvature of the principal tensile stress trajectory as it passes through the minimum section of the neck (see Fig. 2). It is clear from Fig. 2 that κ is zero at the centre line ($x = 0$) and rises monotonically to a value of κ_s at the free surface ($x = a$), since there can be no stress acting normally to a free surface. Bridgman proposed the following expression for the variation of κ with x :

$$\kappa = \frac{2x}{a^2 + 2aR - x^2} \quad (4)$$

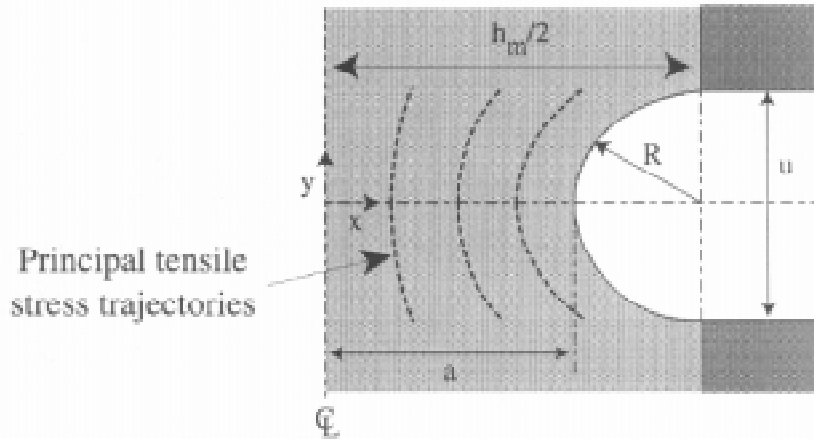


Fig. 2: Schematic depiction of a section through half of the metal layer during necking, showing the dimensions which characterise the radial notch.

Evaluating the integral in Eqn. 3, after substituting from Eqn. 4, gives:

$$\frac{\sigma_{yy}}{\sigma_Y} = 1 + \ln \left(\frac{a^2 + 2aR - x^2}{2aR} \right) \quad (5)$$

The constraint factor, in terms of the nominal stress, is now found by integrating this stress across the section of the narrowest part of the neck and normalising by the original metal layer thickness, h_m , to give

$$\frac{\sigma_n}{\sigma_Y} = \frac{2}{h_m} \left(2\sqrt{a(2R+a)} \tanh^{-1} \left(\sqrt{\frac{a}{2R+a}} \right) - a \right) \quad (6a)$$

It can be seen from Fig. 2 that $a = (h_m - u)/2$ and $R = u/2$, so that this expression can be rewritten:

$$\frac{\sigma_n}{\sigma_Y} = \left(\frac{\chi}{2} - 1 \right) + 2\sqrt{\left(1 - \frac{\chi^2}{4} \right)} \tanh^{-1} \sqrt{\frac{2-\chi}{2+\chi}} \quad (6b)$$

where the parameter χ represents the normalised crack opening displacement ($\chi = 2u / h_m$). The slip line field predictions for a radial type notch are shown in Fig. 3, together with that from the Bridgman model, represented by Eqn. 6. These two curves are in good agreement, which may be taken as confirmation of the accuracy of the Bridgman formula.

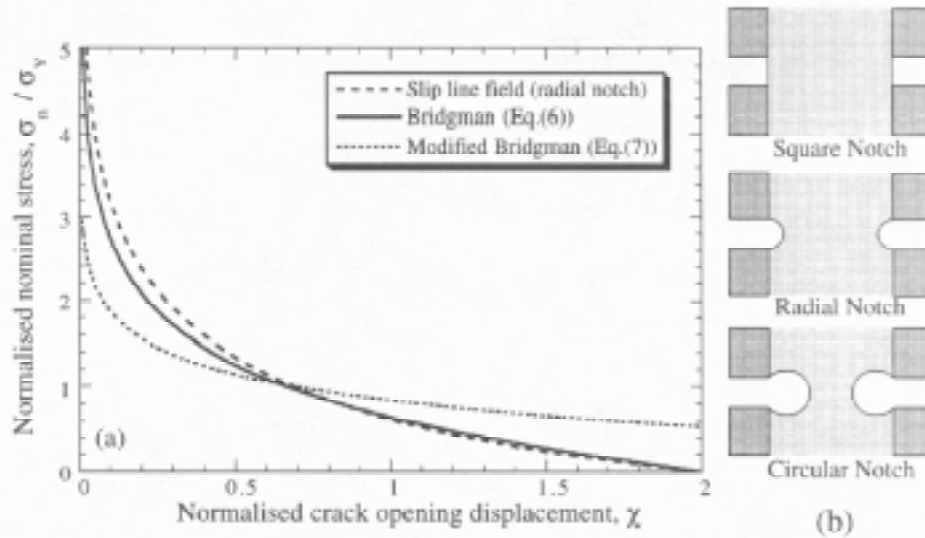


Fig. 3: (a) Predicted plots of the dependence of the nominal stress on the crack opening displacement, obtained from the slip line field treatment and from two versions of the Bridgman equation. (b) Schematic depiction of possible notch geometries

There is, however, a problem with both of these approaches, in that neither takes account of the changes in the shape of the neck which will occur as plastic straining becomes extensive. A basic problem with representing the progression of necking by simply allowing a notch of circular section to progressively increase in radius is that the volume of metal is not conserved during such a process: the simple relationship generated between κ_s and the opening displacement, u , is not physically admissible. A modified form of the Bridgman equation (Eqn. 6) has therefore been developed, based on a conservation of volume approach proposed elsewhere[23] for ductile reinforcements with spherical shape. The resultant modified form of the Bridgman equation is given below.

$$\frac{\sigma_n}{\sigma_Y} = \left(\sqrt{\frac{\chi}{2\pi}} - 1 \right) + \sqrt{\left(4 - \frac{2\chi}{\pi} \right)} \tanh^{-1} \sqrt{\frac{\sqrt{2\pi} - \sqrt{\chi}}{\sqrt{2\pi} + \sqrt{\chi}}} \quad (7)$$

Details of the derivation of this equation are presented elsewhere [24]. The curve predicted using this equation is shown in Fig. 3. It can be seen that the effect of the modification is to reduce the constraint factor immediately after the peak stress, but also to lower the rate at which the nominal stress falls as the crack opening becomes large. This is due to the quadratic relationship found between κ_s and the opening displacement, u , where the notch is initially required to grow very quickly to conserve volume, but after it becomes large it can grow much more slowly.

The Rupture Criterion

Having predicted the behaviour in the initial SSY regime, the maximum constraint factor and the changing load borne by the neck as it thins down, it only remains to identify a criterion for the displacement at which final rupture will occur. This will in practice vary with the fracture characteristics of the metal. In some cases, cavitation and rupture could occur at relatively low displacements, giving a sharp fall in nominal stress as fracture occurs. However, with

highly ductile metals there will be a tendency for the section to progressively neck down to a point, so that after failure the two sections will have included angles of about 90°C . This is certainly the type of behaviour observed with the (commercial purity) aluminium used in the present work. Such necking is expected to lead to a progressive reduction in nominal stress, falling to zero at a normalised displacement ($\chi = 2 u / h_m$) of 2.0 (assuming the initial opening is not larger than the metal layer thickness).

It follows that the modified Bridgman curve in Fig. 3 is actually rather unsatisfactory, since it predicts a normalised displacement at rupture which is considerably above $\chi = 2$. It is difficult to derive an analytical expression which takes account of the complex changes in sectional shape which occur as a bridging ligament necks down. However, it is believed that the modified Bridgman equation is reasonably accurate over the initial part of the displacement range, where the notch is still expected to be approximately radial, and only becomes unreliable at large opening displacements, after the radial notch shape has been substantially deformed.

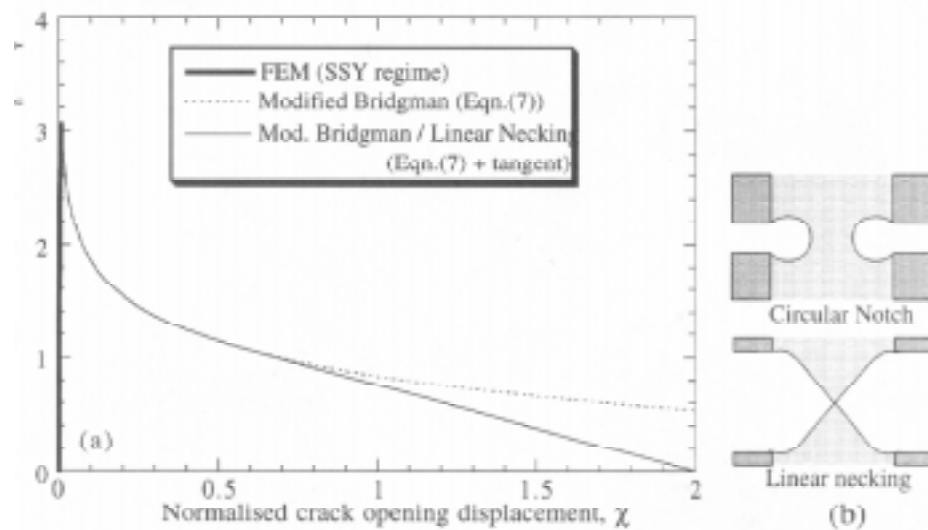


Fig. 4. (a) Predicted plots of the dependence of the nominal stress on the crack opening displacement, showing the effect of the tangent correction (for linear necking) to the modified Bridgman curve. (b) Schematic depiction of initial and final notch geometries .

As a plausible, but arbitrary, attempt to model the very large opening behaviour, a linear dependence of nominal stress on displacement is proposed, by constructing a tangent from the point ($\chi = 2.0, \sigma_n / \sigma_Y = 0$) to the modified Bridgman curve. The full plot is then assumed to follow Eqn. 7 up to this tangent contact point and the tangent itself from there until failure. This is shown graphically in Fig. 4. The initial (SSY) part of the plot is taken as that predicted by FEM; the main point to note about this part of the plot, however, is that the area under the curve (giving the fracture energy) will be very insensitive to the details of the SSY regime, in which an assumption that the stress rises instantly to the maximum constraint factor value would be a perfectly acceptable approximation.

Fracture Energy Prediction

Plots of nominal stress against displacement can be used to obtain the energy absorbed during deformation of the metal ligament, which is given by the area under the curve. The net fracture energy can be obtained from this by adding the contribution from fracture of the

ceramic layers and weighting for the volume fractions of the two constituents. Expressed in terms of normalised displacement and nominal stress, the fracture energy can thus be expressed as

$$G_{tot} = (1 - f_m)G_c + f_m \sigma_Y \frac{h_m}{2} w \quad \text{where } w = \int_0^{\chi_{max}} \frac{\sigma_n}{\sigma_Y} d\chi \quad (8)$$

where χ_{max} is the normalised crack opening displacement when the ligament fractures. The integral, w , can be evaluated once the form of the σ_n/σ_Y against χ plot has been finalised. For example, for the modified Bridgman plot in Fig. 4, with the tangent correction for linear necking, w has a value of 1.61. Providing the values of G_c and σ_Y are known, this would allow the fracture energy to be predicted as a function of the metal volume fraction f_m . It may be noted that, assuming the total energy to be dominated by the contribution from deformation of the metal ligaments (which is normally the case), the fracture energy will increase linearly with h_m , ie with the scale of the layer structure, if the volume fraction of the ductile constituent is held constant. It should, however, be noted that this treatment is based on the assumption that a single crack propagates through the laminate; multiple cracking will raise the value substantially and may occur to different degrees with different scales of layer thickness.

Effect of Work Hardening

Before making a comparison between predicted and measured fracture energies, it should be noted that it has been implicitly assumed hitherto that the yield stress of the metal is a constant and that no work hardening occurs. This assumption needs to be examined carefully, since the plastic strains experienced within the neck region will often become relatively large. Fig. 5 shows an experimental stress-strain plot obtained from tensile testing of a thick sheet of aluminium with a similar composition and microstructure to that of the layers within the laminates. The test was carried out at a strain rate of about $1.4 \times 10^{-4} \text{ s}^{-1}$.

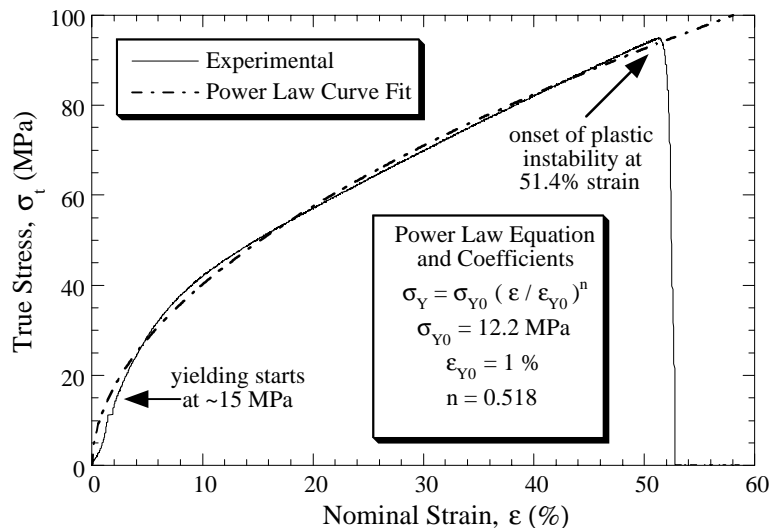


Fig. 5: Stress-strain plots for tensile testing of aluminium with a similar microstructure to that of the layers in the laminates, showing the experimental data and the curve obtained using the equation described in the inset.

It can be seen that the flow stress changes considerably with strain. (This will often be the case with a soft metal, such as unalloyed aluminium which has been annealed.) With such yielding behaviour, it seems likely that significant errors will be introduced by the ascribing of a constant flow stress and it is certainly unclear what single value would be most appropriate in this case. The experimental flow stress is well fitted in the present case by a power law hardening curve having a strain exponent of 0.518 and a yield stress at 1 % strain of 12.2 MPa. The curve was only fitted for stress-strain data above 15 MPa, the point at which yielding started, and before a strain of 51.4 % was attained, when plastic instability occurred. (This is consistent with Considère's construction [25], which predicts the strain at plastic instability to be equal to the strain exponent (=51.8 %).)

The preceding theoretical treatment may be assumed to apply for the case of σ_Y being a function of plastic strain. The predicted area under the plot of normalised nominal stress against normalised displacement will be unaffected. There is, however, a difficulty in attributing a value to the σ_Y term outside the integral in Eqn. 8. If it is assumed that the longitudinal strain across the minimum section is approximately uniform (as Bridgman did), then the most obvious solution is to select a value of σ_Y which represents a weighted average over the range of strain experienced by metal in the ligaments. It should be possible to obtain a reasonable estimate for this in particular cases, perhaps after studying the morphology of failed ligaments.

In order to explore the reliability of using this approach to simulation of the effect of work hardening, tensile tests were conducted on aluminium layers ($h_m = 2.6$ mm) bonded on each side to thick ceramic layers, each being notched through to the metal. The notch width (ie initial crack opening displacement, u_0) was 0.2 mm (so that $\chi_0 = 0.15$). The crack opening displacement during loading was measured with a clip gauge. A typical normalised load-displacement plot is shown in Fig. 6. Normalisation of the load data was carried out using the yield stress / strain dependency from Fig. 5, expressed algebraically in the inset, where the minimum yield stress was taken to be 15 MPa, the value of σ_Y is in MPa and the strain taken to be equal to the increase in notch displacement divided by the original displacement. This relationship between displacement and strain will clearly be unreliable for very small initial displacements, since it effectively assumes that straining is confined to the region within the initial notch, but it should be acceptable for relatively large initial displacements.

The area under the curve in Fig. 6 is about 4.4, which may be compared with the value of w of 1.6 from the modified Bridgman model. Considering the approximations involved in this treatment of work hardening, this represents fair agreement and may be taken as broadly supporting the validity of the modified Bridgman model with the linear necking correction. The major discrepancy between the curves concerns the height of the peak constraint factor. In fact, the magnitude of this peak for the experimental curve is very sensitive to the exact shape of the early part of the flow stress curve and cannot be taken as being reliable. In particular, in this regime the linear relation assumed between strain and notch opening is suspect. In practice, the local strain increased more rapidly with displacement in the early regime than at higher displacements. It follows that the yield stress employed when normalising was too low at small displacements, which has resulted in the normalised nominal stress being too high in this regime. This is an area requiring further investigation.

LAMINATE FRACTURE

Load/displacement plots are shown in Fig. 7 from four-point bending experiments on chevron-notched laminates containing 8%, 35% and 61% of metal by volume. Also shown, for the two higher metal contents, are corresponding plots for laminates with weakened interfaces. The areas under these curves were divided by the corresponding sectional areas to give the fracture energy. Two features are immediately apparent from these plots. Firstly, the fracture energy rises sharply with increasing metal content. This is entirely as expected and it follows from the forms of Eqns. 7 and 8. The second point is that introduction of the weakened interfaces has increased the fracture energy slightly. This is apparently a consequence of an increase in roller displacement at final failure, which presumably arose because interfacial debonding allowed deformation of the metal ligaments to occur over greater lengths. This is consistent with observations made on failed specimens.

The fracture energy data are summarised in Fig. 8, where experimental and predicted values are plotted against the volume fraction of metal. The predicted curves were obtained by substituting the predicted value of the integral w ($= 1.6$) into Eqn. 8 and using three values for the effective yield stress over the strain range, $\bar{\sigma}_Y$: 15, 30 and 60 MPa. These values of the effective yield stress represent the stress at initial yielding of the aluminium, an approximate unweighted average over the strain range observed in Fig. 5 and an intermediate value representing the effect of weighting the effective yield stress towards the lower strain values via the predicted $\sigma_n/\sigma_Y : \chi$ curve (Fig. 4). Clearly, the effect of work hardening in raising the fracture energy is manifest as an increase in the appropriate value of this effective yield stress. The predicted fracture energy is more sensitive to f_m than Eqn. 8 apparently indicates, because it is the ceramic layer thickness, rather than the metal layer thickness, which is being held constant (at a value of 0.5 mm). For this particular case, the curves correspond to the expression:

$$G_{tot} = 20 (1 - f_m) + 402.5 \bar{\sigma}_Y \left(\frac{f_m^2}{1 - f_m} \right) \quad (9)$$

where $\bar{\sigma}_Y$ is the effective yield stress in MPa and the value of 20 J m^{-2} for the fracture energy of alumina has been taken from the literature. In general, the values obtained with the strong interfaces are in quite good agreement with predictions. The experimental values are somewhat higher than those predicted, but this is probably associated with the (limited amount of) local multiple cracking which tends to occur, even with the chevron notch present to constrain the crack plane. (In the absence of the chevron notch, extensive multiple cracking is observed with the higher metal contents [7], which raises the fracture energy substantially.)

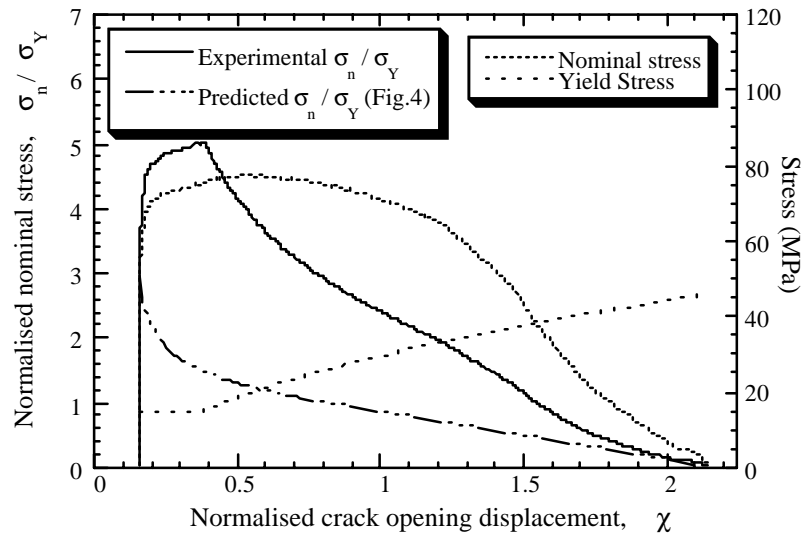


Fig. 6: Experimental data for the nominal stress as a function of crack opening displacement for an aluminium layer sandwiched between two pre-notched alumina layers. The stress values have been normalised by the yield stress, which is also shown as a function of crack opening (derived from Fig. 5). The strain was taken as the increase in displacement divided by the original notch width.

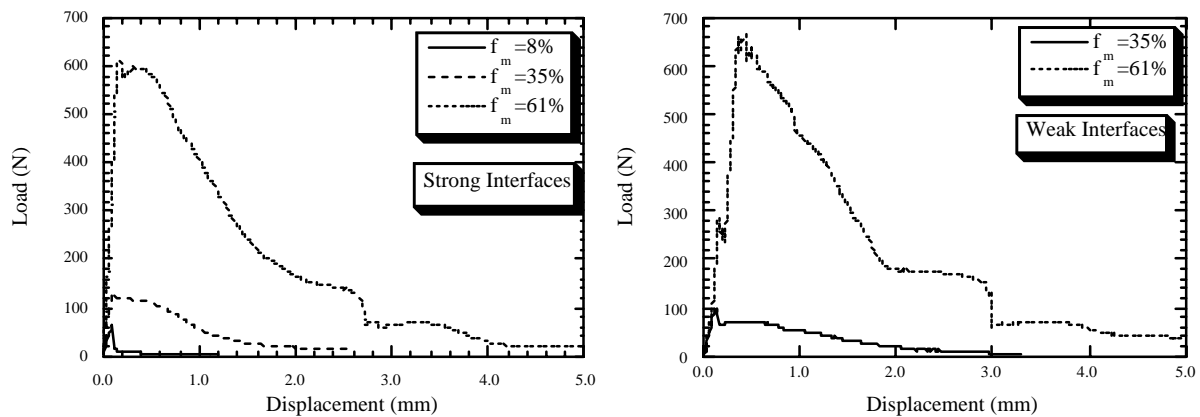


Fig. 7: Load/displacement plots for chevron-notched laminates tested in bending.

For the weakly-bonded laminates, prediction of the fracture energy is difficult, since the extent of debonding is unknown *a priori*. The effect of debonding is to introduce an initial crack opening displacement equal to the total debonded length. This will tend to reduce the magnitude of the peak load (maximum constraint factor), but increase the displacement at ligament rupture. A consequence of the general shape of the load-displacement plot (Figs. 4 and 6) is that the maximum constraint has relatively little influence on the work done, since the load subsequently falls rather sharply with increasing strain. The effect of an increased displacement at failure is therefore expected to be more significant, so that the net effect of weakening the interface is to raise the fracture energy. This is consistent with these observations.

It should, however, be noted that, when multiple cracking is occurring, a weak interface may lead to fewer cracks being generated per unit length of specimen. This means that a reduction

in fracture energy will be effected under many conditions by weakening the interface. It should also be noted that a weak interface may be undesirable for other purposes, such as under conditions where the laminate may fail in shear.

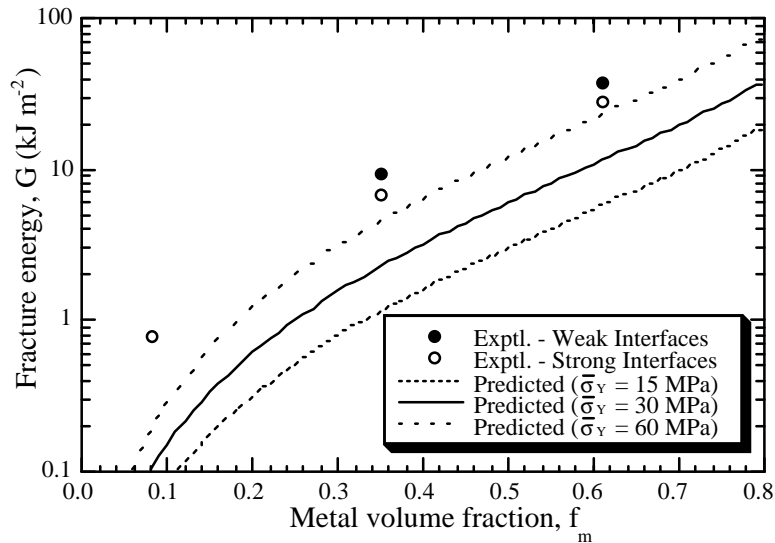


Fig. 8: Comparison between predicted and measured fracture energy of aluminium-alumina laminates. The experimental data were obtained by bending of chevron-notched specimens.

CONCLUSIONS

1. Bending and tensile loading experiments have been carried out on aluminium-alumina laminates in order to measure the fracture energy. This was done on chevron-notched specimens in which fracture took place by propagation of a single dominant crack..
2. Modelling work aimed at predicting the fracture energy of such laminates has been focused on the work done during deformation of metal ligaments which bridge cracks in adjacent ceramic layers. A modified form of the Bridgman equation has been developed to predict the load borne by the bridging ligament as it deforms, necks down and fails.
3. The proposed form of the Bridgman equation is thought to be applicable to metals which undergo extensive plastic deformation and tend to neck down progressively until the load-bearing section falls to zero. Tensile loading experiments on single aluminium layers, constrained by notched ceramic layers bonded on both sides, confirmed that the observed load-displacement behaviour was generally similar to that predicted using this equation. Broad agreement was only observed when account was taken of the work-hardening characteristics of the aluminium. Work hardening tends to raise the total work done by requiring a higher load for deformation to continue, provided it does not lead to premature rupture.
4. Use of the modified form of the Bridgman equation allowed the work done in deforming a single ligament to be evaluated as a function of layer thickness and metal work hardening characteristics. This in turn allowed prediction of the fracture energy of a laminate during single crack propagation, as a function of metal volume fraction, for a given ceramic layer thickness. Comparison between predictions obtained in this way and experimentally measured laminate fracture energies showed good agreement.

5. The characteristic form of the load-displacement curve for constrained single layers shows a fairly sharp peak at low displacement, followed by a rapid fall and then a more shallow gradient as the section necks down. The work done tends to be more sensitive to the factors affecting the displacement at failure than to those which control the magnitude of the initial peak load. Consistent with this were observations that specimens with reduced interfacial bond strengths exhibited slightly higher fracture energies than those with strong interfaces. This is attributed to the effect of debonding in allowing a larger deformation zone in each metal ligament and consequently greater crack opening displacement at failure.

ACKNOWLEDGEMENTS

This work forms part of a project supported financially by the EPSRC. Funding has also been provided for one of us (SKP) by the NSF of the Greek government.

REFERENCES

1. H. C. Cao and A. G. Evans, On Crack Extension in Ductile/Brittle Laminates, *Acta Met. Mater.*, 39(12) (1991), pp. 2997-3005.
2. M. C. Shaw, D. B. Marshall, M. S. Dadkhah and A. G. Evans, Cracking and Damage Mechanisms in Ceramic/Metal Multilayers, *Acta Metall. Mater.*, 41 (1993), pp. 3311-3320.
3. Z. Chen and J. J. Mecholsky, Control of Strength and Toughness of Ceramic/Metal Laminates Using Interface Design, *J. Mat. Res. Soc.*, 8(9) (1993), pp. 2362-2369.
4. T. Ozturk, J. Mirmesdagh and T. Ediz, Strain Partitioning and Plastic Flow in Some Metal/Metal Laminates, *Materials Science and Engineering*, A175 (1994), pp. 125-129.
5. Q. Ma, M. C. Shaw, M. Y. He, B. J. Dalgleish, D. R. Clarke and A. G. Evans, Stress Redistribution in Ceramic/Metal Multilayers Containing Cracks, *Acta Metall. et Mater.*, 43(6) (1995), pp. 2137-2142.
6. S. K. Pateras, M. C. Shaw, W. J. Clegg, A. C. F. Cocks and T. W. Clyne, The Effect of Metal Layer Thickness on Energy Absorption during Fracture of Metal/Ceramic Laminates, in *Proc. 10th Int. Conf. Comp. Mat. (ICCM10)*, A. Poursartip and K. Street (Eds.), Vol. 1, Woodhead, (1995), pp. 731-737.
7. S. K. Pateras, S. J. Howard and T. W. Clyne, The Contribution of Bridging Ligament Rupture to Energy Absorption during Fracture of Metal-Ceramic Laminates, *Key Eng. Mats.*, 127-131 (1996), pp. 1127-1136.
8. M. C. Shaw, T. W. Clyne, A. C. F. Cocks, N. A. Fleck and S. K. Pateras, Cracking Patterns in Ceramic/Metal Laminates, *J. Mech. Phys. Solids.*, 44 (1996), pp. 801-814.
9. P. A. Mataga, Deformation of Crack-Bridging Ductile Reinforcements in Toughened Brittle Materials, *Acta Metall.*, 37(12) (1989), pp. 3349-3359.

10. M. F. Ashby, F. J. Blunt and M. Bannister, Flow Characteristics of Highly Constrained Metal Wires, *Acta Metall.*, 37 (1989), pp. 1847-1857.
11. M. Bannister and M. F. Ashby, The Deformation and Fracture of Constrained Metal Sheets, *Acta Metall. Mater.*, 39 (1991), pp. 2575-2582.
12. M. Bannister, H. R. Shercliffe, G. Bao, F. Zok and M. F. Ashby, Toughening in Brittle Systems by Ductile Bridging Ligaments, *Acta Metall. Mater.*, 40 (1992), pp. 1531-1537.
13. A. G. Evans and R. M. McMeeking, On The Toughening of Ceramics by Strong Reinforcements, *Acta metall.*, 34(12) (1986), pp. 2435-2441.
14. S. Pateras, M. C. Shaw, W. J. Clegg and T. W. Clyne, The Effect of Metal Layer Thickness on the Fracture of Metal/Ceramic Laminates in Bending, in *High Performance Materials in Engine Technology*, P. Vincenzini (Ed.), Techna Srl., (1995), pp. 445-453.
15. N. Levy, Small Scale Yielding near a Crack in Plane Strain: a Finite Element Analysis, *Int. J. Fract. Mechs.*, 7 (1971), pp. 143-156.
16. J. R. Rice, Limitations to the Small Scale Yielding Approximation for Crack Tip Plasticity, *Journal of the Mechanics and Physics of Solids*, 22 (1974), pp. 17-26.
17. M. F. Kanninen and C. H. Popelar, *Advanced Fracture Mechanics*, First edn., Oxford University Press, (1985).
18. H. L. Ewalds and R. J. H. Wanhill, *Fracture Mechanics*, 4 edn., Arnold DUM, London, (1989).
19. R. Hill, *The Mathematical Theory of Plasticity*, Oxford University Press, London, (1950).
20. J. R. Rice and M. A. Johnson, The Role of Large Crack Tip Geometry Changes in Plane Strain Fracture, in *Inelastic Behaviour of Solids*, M. F. Kanninen, W. F. Adler, A. R. Rosenfield and R. I. Jaffee (Eds.), McGraw-Hill, N.Y., (1970), pp. 641-672.
21. A. G. Evans and R. M. Cannon, Toughening of Brittle Solids by Martensitic Transformations, *Acta. Met.*, 34 (1986), pp. 761-800.
22. P. W. Bridgman, *Large Plastic Flow and Fracture*, 1st edn., McGraw-Hill, (1952).
23. L. S. Sigl, P. A. Mataga, B. J. Dalgleish, R. M. McMeeking and A. G. Evans, On the toughness of brittle materials reinforced with a ductile phase, *Acta Met. et Mater.*, 36(4) (1988), pp. 945-953.
24. S. Pateras, *Energy Absorption in Metal/Ceramic Laminates*, University of Cambridge (1997).
25. G. E. Dieter, *Mechanical Metallurgy*, McGraw-Hill, New York, (1986).

EFFECT OF SQUEEZE INFILTRATION SPEED ON INFILTRATION QUALITY AND TENSILE PROPERTIES OF CAST SAFFIL/ALCU4MGAG COMPOSITE

S. Long¹, O. Beffort¹, L. Rohr¹ and H. M. Flower²

¹ *Swiss Federal Laboratories for Material Testing and Research, CH-3602 Thun, Switzerland*

² *Department of Materials, Imperial College, London SW7 2BP, UK*

SUMMARY: In the present work, the effects of squeeze infiltration speed on infiltration pressure gradient, preform saturation, air entrapment and the associated infiltration quality have been theoretically analysed in the light of visualised melt flow behaviour in Saffil chopped fibre preform and the established infiltration hydrodynamics, and empirically investigated by tensile test and microscopy of Saffil/AlCu4MgAg composite infiltrated with systematically varied infiltration speed. It has been found that an increase in infiltration speed gives rise to infiltration pressure gradient and preform saturation. Consequently, the amount of the air entrapped in the preform is decreased and the tensile properties of the fibre casting are improved. It has been concluded that infiltration speed should be maximised within the limit of preform compression strength to achieve quality squeeze infiltration in the atmosphere.

KEYWORDS: metal matrix composite, liquid metal infiltration, Saffil preform, squeeze casting, AlCuMgAg alloy, infiltration processing, tensile properties

INTRODUCTION

To meet the growing requirements for high specific properties of engineering structural materials at room and elevated temperature, intensive research interest has been devoted to incorporate high strength ceramic fibres in light matrix alloys to produce fibrous metal matrix composites (FMMCs). Among the processes developed for fabrication of FMMCs, liquid metal infiltration of fibre preforms aided by external pressure has been attracting a share of research and commercial attention due to the advantages provided by the well-developed casting techniques, such as, cost-effectiveness, potential of net-shape production, processing design versatility and production scale flexibility.

Attainment of satisfactory microstructures and mechanical properties is the ultimate destination of processing research for fabrication of engineering materials. Unfortunately, the wide divergence of processing parameters employed in the infiltration practice, the scattering and, sometimes, discouraging mechanical performance of the cast FMMC materials, and the contradictory interpretations of the observations indicate that the physical nature behind pressurised liquid metal infiltration of fibrous reinforcement preforms for fabrication of cast FMMC engineering structures has not been comprehensively understood and the infiltration

processing design has not been properly related to the formation of microstructure and mechanical properties yet despite that some very good work has been done [1].

According to the nature of pressurised liquid metal infiltration processing, the formation of the microstructure of the fabricated cast FMMC structures is largely co-determined by the physico-chemical interplay between melt flow and the preform consisting of fibres and fibre binder. Achievement of quality infiltration of a chopped fibre preform in the atmosphere relies first on a scientific manipulation of infiltration hydrodynamic parameters, mainly, infiltration speed and pressure, to optimally control the melt flow in the preform and the accompanying air retreat. Based on a quality infiltration, the melt solidification can be regulated to develop desired fibre-matrix bonding, uniform microstructural and phase constitutions.

In the present work, efforts have been contributed to theoretically analyse the effect of squeeze infiltration speed on infiltration quality in terms of infiltration pressure gradient, preform saturation and air entrapment based upon the visualised melt flow behaviour in Saffil preforms and the established infiltration hydrodynamics [2, 3]. Empirically, Saffil preforms have been squeeze infiltrated with AlCu4MgAg melt under systematically varied infiltration speed and optimal thermal parameters. The fabricated material was mechanically and microscopically characterised to visualise the effect of infiltration speed.

Following the procedure of infiltration, melt solidification can take place during and post melt infiltration of the preform. It has been made evident that the melt solidification prior to completion of infiltration, the so-called premature melt solidification, will alter the features of infiltration hydrodynamics and degrade the infiltration quality [4]. Therefore, the theoretical analysis of infiltration hydrodynamics and empirical investigation in the present work are based on the infiltration free of premature melt solidification.

INFILTRATION HYDRODYNAMICS AND INFILTRATION QUALITY

Melt Flow Behaviour in a Chopped Fibre Preform

To correlate the nature of melt flow during infiltration to microstructure formation, it is essential to be aware of the melt flow behaviour in a chopped fibre preform.

Fig. 1 gives the visualised flow behaviour of Al alloy melt in a 28% Saffil preform under squeeze pressurisation. As indicated by its morphology, the melt flow in the fibre preform is dominated by the non-wetting of the melt to the fibres partially coated with SiO₂ binder and the dimensional non-uniformity of the interspaces between the fibres. Under the drive of the external pressure, the melt preferentially penetrates into the interconnected large interspaces at micro scale and, then, penetrates the small ones when the local infiltration pressure increases up to the capillarity of the interspaces in question. Behind the infiltration front, with the increase in infiltration pressure, more and more smaller interspaces are infiltrated, which gives rise to the preform saturation and the associated infiltration quality in terms of non-infiltration interspaces.

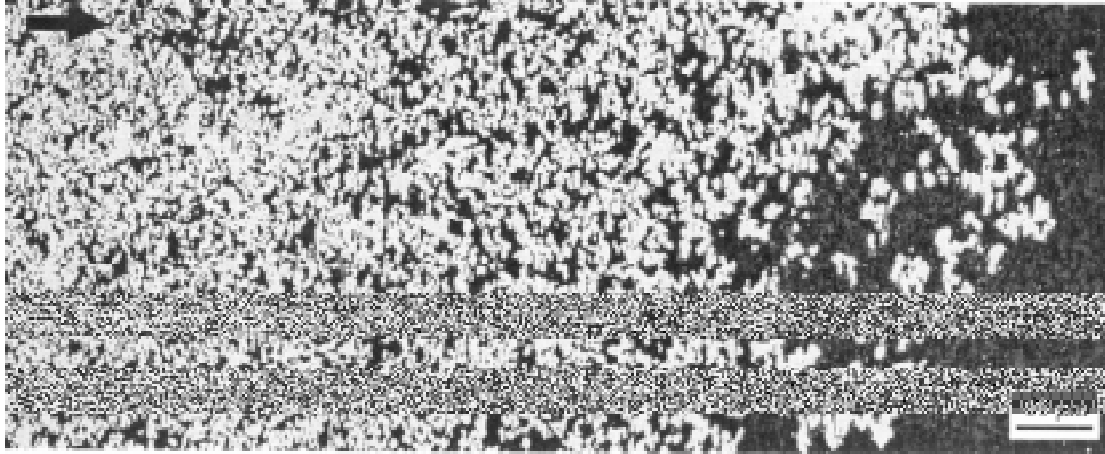


Fig. 1 The morphology of the micro infiltration front formed during unidirectional infiltration of a Saffil preform with Al alloy melt. Note the non-uniformity of fibre distribution in the preform, the non-wetting nature of melt to Saffil fibres, the preferential penetration behaviour of melt into the large interspaces between the chopped fibres, and the variation of the preform saturation by the melt flow in infiltration direction [2]. The arrow indicates the macro infiltration direction.

Infiltration Speed and Infiltration Pressure Gradient

According to the visualised melt flow behaviour and the principles of hydrodynamics, statistic analysis of the effect of the dimension of the infiltrated interspaces, ranging from their maximum value $R_{eq,max}$ to the minimum $R_{eq,P}$, and their orientation D on melt flow in individual interspaces leads to the relationship between infiltration speed in terms of squeeze ram speed V_{ram} , and the local pressure gradient dP/dz in the infiltration direction z as follows

$$\frac{dP}{dz} = \frac{A\mu V_{ram} R_{eq,max}^3}{D(1-V_f)(R_{eq,max}^5 - R_{eq,P}^5)} \quad (1)$$

Where, μ is the dynamic viscosity of the matrix melt, A a constant determined by the infiltration system, and V_f preform fibre volume fraction [3].

This equation shows that under a prescribed infiltration speed, the pressure gradient in the infiltrated preform is inversely proportional to $(R_{eq,max}^5 - R_{eq,P}^5)$, indicating the sensitive nature of infiltration pressure to the change of the dimension of the newly infiltrated interspaces. According to the melt flow behaviour and the $P - R_{eq,P}$ relationship presented in Eq. 1, the infiltration can be described as a three stage process as follows.

- 1). *Initiation of Infiltration:* Infiltration of a preform is initiated when the squeeze pressure is increased up to the minimum capillarity resistance of the largest interspaces between the fibres, corresponding to $R_{eq,P}$ close to $R_{eq,max}$. Due to the limited conducting area of the preferentially penetrated large interspaces but the constant melt flux regulated by squeeze ram speed, the melt flow through the first penetrated interspaces is much higher than the average speed and, correspondingly, the resistance of the preform to melt flow increases dramatically. As a consequence, infiltration pressure increases dramatically to

maintain the constant melt flux regulated by the pre-selected squeeze infiltration speed. The increase in pressure endorses the melt higher penetrating capability, resulting in reduced dimension of infiltrated interspaces and, thereby, decreased melt flow speed. This initial stage of infiltration finishes when the dimension of the newly penetrated interspaces $R_{eq,P}$ decreases down to $0.5R_{eq,max}$ and the infiltration pressure becomes stable and proportional to the further increase in infiltration depth.

- 2). *Stable Infiltration:* After the dimension of the newly infiltrated interspaces becomes smaller than $0.5R_{eq,max}$, the further increase of infiltration depth brings proportional increase of infiltration pressure that is required to overcome the melt viscosity and to maintain the constant melt flux until the infiltration front reaches the base of the preform. However, it must be realised that the unstable P - z features of the initial infiltration stage exists in the infiltration front throughout the stable infiltration stage.
- 3). *Compression of Entrapped Air:* As the infiltration front reaches the base of the preform and seals the venting ducts, the air pre-existing in the un-infiltrated interspaces is entrapped and the infiltration enters its air compression stage. Due to the limited amount of the air entrapped and the constant ram displacement, the stage of the air-compression is characterised by its rapid pressure increase until its value reaches the pre-selected maximum infiltration pressure.

According to the above descriptions, the infiltration pressure--infiltration depth relationship ($P_{inf} - z$) throughout the whole infiltration process can be schematically summarised as shown in Fig. 2.

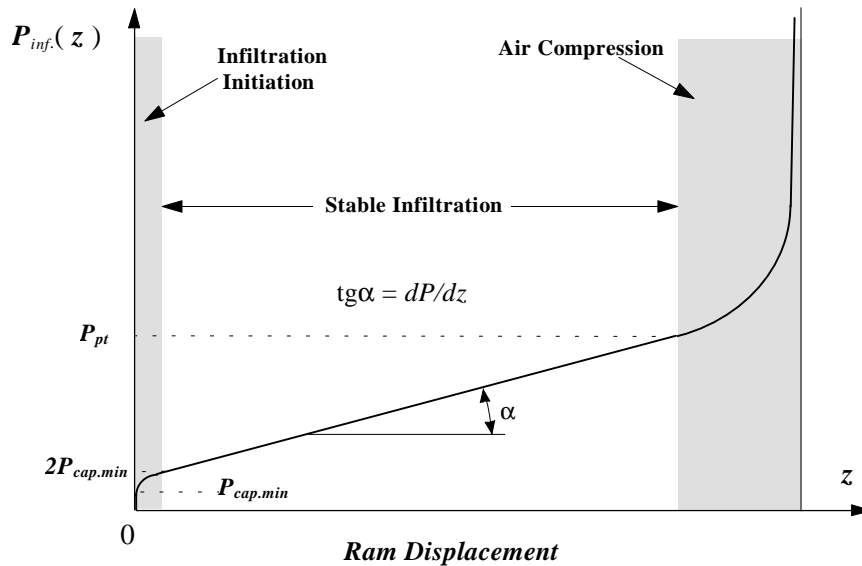


Fig. 2 A schematic showing the variation of infiltration pressure with respect to ram displacement during unidirectional infiltration of a Saffil preform. Where, $P_{cap.min}$ --minimum pressure required for initiating infiltration, P_{pr} --pressure for melt penetrating-through the preform with prescribed processing conditions.

It is important to realise that the infiltration pressure is dominated by the infiltration speed in the conventional squeeze infiltration practice, where the infiltration speed represented by ram,

or plunger speed is pre-selected. The infiltration pressure is a automatic response of the hydraulic system to all the resistance of the preform to the melt penetration at the constant flux regulated by the ram speed. Therefore, for a prescribed melt-preform system, only the infiltration speed can change the P - z relationship.

Infiltration Pressure Gradient and Preform Saturation

As indicated by the above brief description, the squeeze pressurised infiltration in the atmosphere is characterised by the existence of an air entrapment stage that can severely affect the infiltration quality. Therefore, it is important to understand the relationship between the intensity of air entrapment and the infiltration hydrodynamics to co-relate the melt flow behaviour to the geometrical features of the fibre preform and the infiltration speed employed.

Due to the kinetic non-wetting nature of the Al alloy melt to the Saffil fibres, the penetrating ability of the melt into the interspaces between the fibres is regulated by the capillarity laws and the local infiltration pressure applied. If an equivalent radius defined as R_{eq} is proposed as a geometrical measurement of an interspace with geometrical irregularity between fibres in the preform, the infiltration pressure P_{inf} required to penetrate such an individual interspace can be given as follows if the melt-fibre kinetic contact angle is suggested as θ and the surface tension of the melt is σ_{mg} .

$$R_{eq} = \frac{\sigma_{mg} \cos \theta}{P_{inf}} \quad (2)$$

Due to the nature of preferential penetration of the melt flow into large interspaces, the degree of saturation of the preform $S(P_{inf})$ under a local infiltration pressure P_{inf} is equal to the cumulative volume fraction of the penetrated interspaces ranging from the largest interspaces $R_{eq,max}$, to the smallest penetrated ones $R_{eq,P}$. If the fibre over-crossing sites are treated as individual interspaces, the cumulative volume fraction of the infiltrated interspaces, i.e., $S(P_{inf})$ can be approximately given as follows with an assumption of a statistically uniform distribution of all the interspaces in the preform [3]:

$$S(P_{inf}) = \int_{R_{eq,P}}^{R_{eq,max}} V(R_{eq}) dR_{eq} = \frac{(1 - V_f)}{R_{eq,max}^3} [R_{eq,max}^3 - R_{eq,P}^3(P_{inf})] \quad (3)$$

As mentioned, the local infiltration pressure changes in the partially infiltrated preform in the infiltration direction. This pressure change will result in the variation of the degree of preform saturation dS/dz in the infiltration direction as follows [3]

$$\frac{dS}{dz} = \frac{A(1 - V_f)}{\sigma_{mg} \cos \theta R_{eq,max}^3} R_{eq,P}^4 \frac{dP}{dz} \quad (4)$$

According to the pressure distribution expressed in Eq. 1 and the relationship between saturation and local pressure in Eq. 3, the gradient of preform saturation in the infiltration direction dS/dz can be expressed as follows:

$$\frac{dS}{dz} = \frac{A\mu (1 - V_f) V_{Ram}}{D\sigma_{mg} \cos\theta R_{eq,max}} \cdot \frac{(R_{eq,P} / R_{eq,max})^4}{1 - (R_{eq,P} / R_{eq,max})^5} \quad (5)$$

As the above equation indicates, the gradient of preform saturation is a function of $(R_{eq,P} / R_{eq,max})^4 [1 - (R_{eq,P} / R_{eq,max})^5]^{-1}$. Fig. 3 illustrates the variation of the dS/dz with respect to the minimum dimension of the infiltrated interspaces.

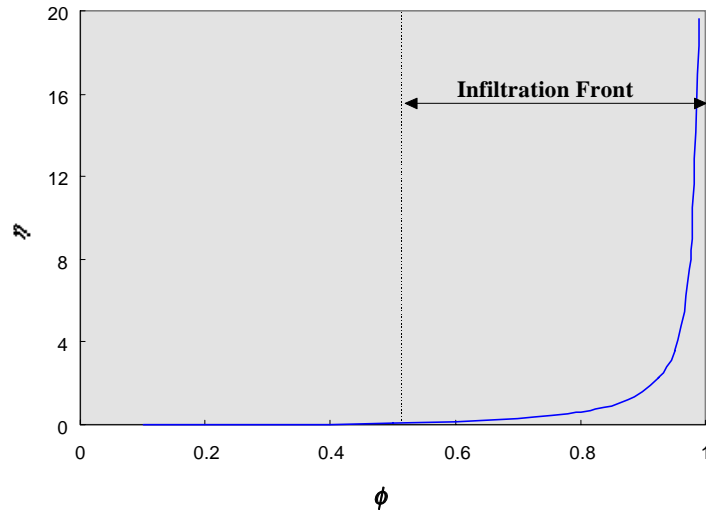


Fig. 3 Effect of ϕ on η . Note the dramatic change of η at the infiltration front. (where, $\phi = (R_{eq,P} / R_{eq,max})$ and $\eta(R_{eq,P}) = (R_{eq,P} / R_{eq,max})^4 [1 - (R_{eq,P} / R_{eq,max})^5]^{-1}$).

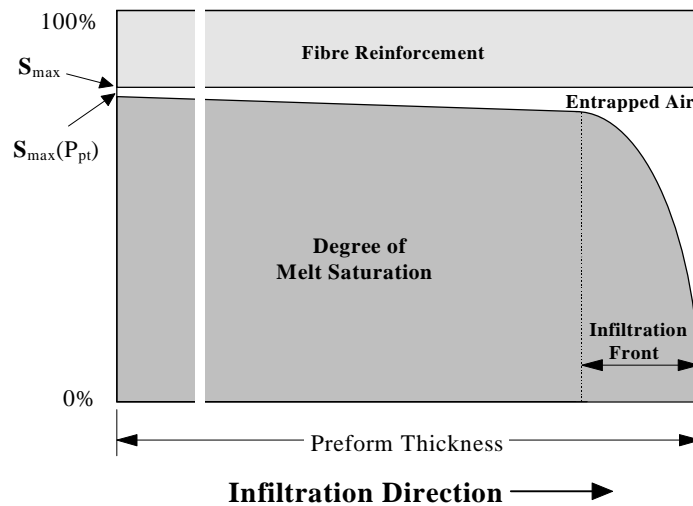


Fig. 4 A schematic showing the volume distribution in a Saffil preform at the moment when the infiltration enters its air-compression stage. Where, S_{max} refers to the maximum saturation achievable, and $S_{max}(P_{pt})$ refers to the maximum saturation achieved under penetrating-through pressure P_{pt} .

As indicated by the figure, the preform saturation is very sensitive to the dimension of the newly infiltrated interspaces. The preform saturation is subjected to a dramatic change at the infiltration front, where $R_{eq.P} > 0.5 R_{eq.max}$, because the newly infiltrated large interspaces contribute significantly to the volume fraction of the infiltrated interspaces. However, after the passing-by of the infiltration front and the infiltration becomes stable, corresponding to the minimum dimension of infiltrated interspaces $R_{eq.P} < 0.5 R_{eq.max}$, the variation of saturation gradient becomes stable.

Before infiltration enters its air-compression stage signalled by the arrival of the infiltration front at the bottom of the preform, the saturation distribution of the preform along the infiltration direction is schematically shown in Fig. 4, which is consistent with the visualised saturation distribution [2].

The figure indicates that at the moment when melt penetrates through the preform, the volume of the un-infiltrated interspaces, occupied by the pre-existing air, mainly concentrates at the infiltration frontier. In the preform behind, where the infiltration pressure linearly increases from $2P_{cap.min}$ to P_{pt} --the penetrating-through pressure at the preform entry, the degree of the preform saturation correspondingly increases from $0.875(1-V_f)$ to $S(P_{pt})$ - the maximum degree of preform saturation achievable at the moment when melt penetrates through the preform under P_{pt} . However, as compared with the conventionally employed maximum squeeze pressure ranging from 50 to 130 MPa, P_{pt} has a very limited value ranging from ~1.0 to ~5.0 MPa for infiltration of 10-30% Saffil preform with speeds of less than 30 mm/s.

The above analysis clearly demonstrates that for infiltration in the atmosphere the air-entrapment is bound to happen on one hand, and indicates the existence of the potential to minimise the air entrapment by optimisation of the infiltration hydrodynamic parameters to reduce the length of infiltration front and to increase in penetrating-through pressure on the other hand.

Infiltration Speed and Air Entrapment

According to Eq. 1, an increase in infiltration speed will not only increase the pressure gradient in the preform and reduce the thickness of the infiltration front, but also gives rise to the value of the penetrating-through pressure. Correspondingly, the saturation of the preform is improved and the amount of the air entrapped and the frequency and dimension of the resultant non-infiltration defects are reduced.

The above analysis has made clear that the full saturation of the preform is not achievable, but the amount of the air entrapped in the preform can be changed by variation of the infiltration speed. Furthermore, as indicated by the above analysis, the maximum pressure conventionally quoted in squeeze pressure infiltration makes no contribution to the control of air-entrapment. Its significance on infiltration quality lies on the control of the size of non-infiltration defects caused by the entrapped air and capillarity, and on the enhancement of melt feeding capability to eliminate solidification shrinkage voids.

EFFECT OF INFILTRATION SPEED ON MICROSTRUCTURE AND TENSILE PROPERTIES

Processing of Saffil/AlCu4MgAg Composite

So far, the effect of infiltration speed on infiltration quality has been theoretically analysed in terms of preform saturation and, thereby, the amount of air entrapped. Obviously, an increase in air entrapment will be manifested as an increase in non-infiltration defects that degrade the soundness of the microstructure and mechanical performance of the material. To visualise this effect, Saffil chopped fibre preforms of 15% fibre volume fractions were squeeze infiltrated with AlCu4MgAg melt with a ram speed varying from 1.5 to 10 mm/s, but a constant maximum pressure of 130 MPa that was maintained until the completion of solidification post infiltration. The thermal processing parameters have been controlled constantly as: melt superheat of 750 °C, preform preheat of 650 °C, and ram and die preheat of 300 °C.

The composite castings produced with different infiltration speeds were subjected to a two step solution heat treatment (480 °C/2h + 500 °C/1.2h), followed by cold water quenching. Subsequently, the castings were aged to T4 (RT/1000h) and T6 (170 °C/4h) temper and machined into A₅ standard round bar dog bone tensile specimens with a gauge section geometry of $\phi 6 \times 36$ mm and tensile tested. Also, the microstructures in as-cast and heat-treated conditions were analysed by light microscopy and the tensile fractures were observed by scanning electron microscopy.

Effect on Tensile Properties

The tensile properties of the material under T4 and T6 conditions are given in Fig. 5a and Fig. 5b, respectively. It is evident that an increase in infiltration speed from 1.5 to 10 mm/s gives rise to the tensile strength from 378 MPa to 436 MPa, and the elongation from 1.6% to 4.6% under T4 condition. Under T6 condition, the tensile strength increases from 478 to 517 MPa, and the elongation from 1.2% to 2.0%, indicating the degradation of the infiltration quality and the resultant tensile properties with the decrease of infiltration speed.

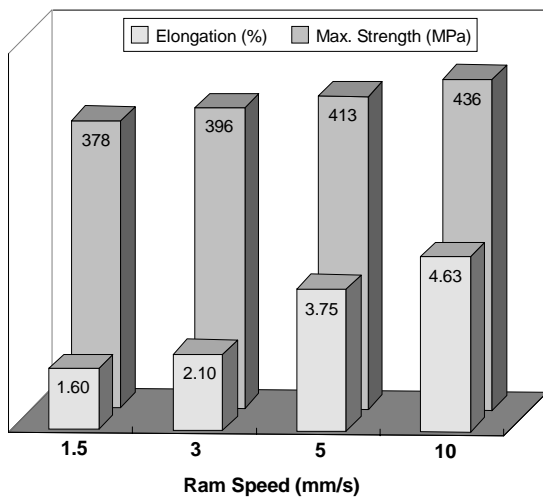


Fig. 5a Effect of infiltration speed on T4 tensile properties of Saffil/AlCu4MgAg.

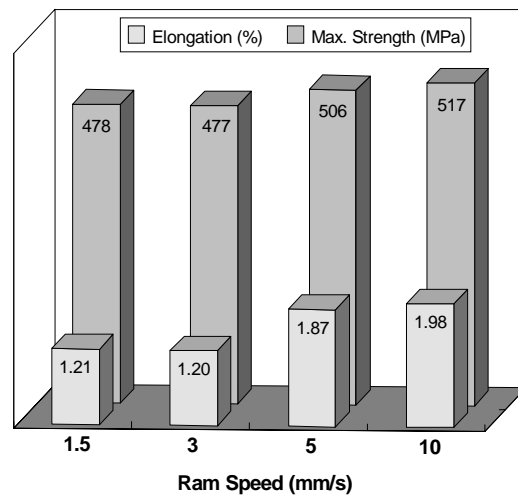


Fig. 5b Effect of infiltration speed on T6 tensile properties of Saffil/AlCu4MgAg.

Effect on Microstructure and Interfacial Bonding

Under high magnification, the existence of non-infiltration defects at fibre contact sites is obvious. However, the microstructures of the composite castings infiltrated with different speeds do not indicated any obvious difference on the dimension and frequency of the defects. The representative microstructures in the as-cast and T6 conditions are given in Fig. 6. Considering the 130 MPa maximum squeeze pressure employed and the existence of 5% porous SiO₂ fibre binder and the large number of fibre contact sites in the preform, it is not surprising that it is hard to note the difference under light microscope.

SEM observation of the tensile fractures, however, reveals the profound effect of the infiltration speed. As indicated by the fracture morphology in Fig. 7a, the material fabricated with high infiltration speed formed a strong fibre-matrix interface and the failure of the material is caused by fibre breakage and matrix shear failure. Consequently, the macro fracture of tensile specimens presents a 45° angle with the tensile direction and no fibre pull-out can be found, indicating a strong fibre-matrix bonding. The reduction of infiltration speed to 3 mm/s not only makes the macro fracture perpendicular to the tensile loading direction, but also characterises the micro fracture morphology by "fibre pull-out" and matrix necking, as shown in Fig. 7b. This fracture feature indicates that, before its final failure, the material was subjected a prevalent interfacial debonding, followed by matrix plastic necking during the tensile event.

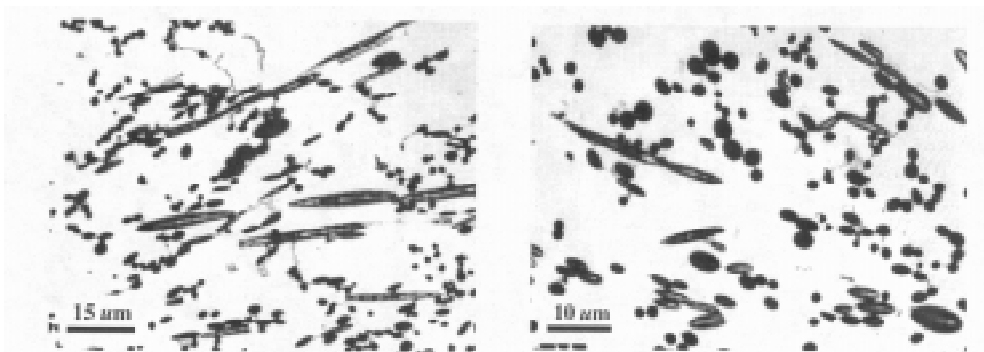


Fig. 6a The representative micrograph of the as-cast 15% Saffil/AlCu4MgAg casting.

Fig. 6b The representative micrograph of the T6 15% Saffil/AlCu4MgAg casting.

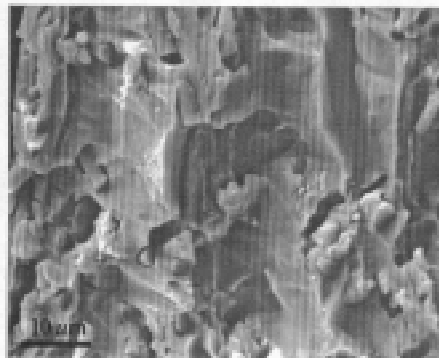


Fig. 7a A fractograph of the T6 15% Saffil/AlCu4MgAg infiltrated with 10 mm/s speed.

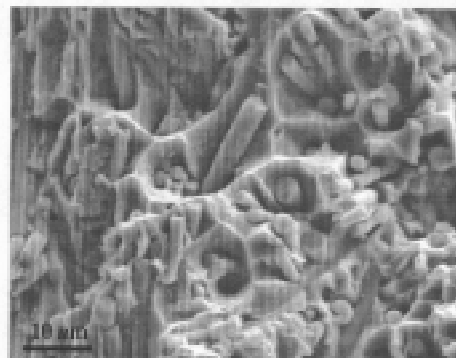


Fig. 7a A fractograph of the T6 15% Saffil/AlCu4MgAg infiltrated with 3 mm/s speed.

Effect of Thermal Parameters

In the present work, effort has been concentrated on visualisation of the effect of the infiltration speed on the infiltration quality and mechanical performance under the thermal conditions that the infiltration is free of premature melt solidification. However, the present authors have experienced in processing instrumentation that the infiltration itself is not conducted under constant thermal conditions because the preform temperature and melt temperature will change dramatically during infiltration on the squeeze casters of industrial scale due to their heat loss prior to infiltration. A time delay during processing is able to induce adverse premature melt solidification that will degrade the infiltration hydrodynamics and impair the development of strong matrix-fibre bonding, resulting in poor mechanical performance [4]. Therefore, there will never be an over-emphasis on strict thermal management to actually control the thermal parameters within the optimal range to ensure infiltration free of premature melt solidification.

CONCLUSIONS

According to the above theoretical analysis and empirical investigation, it is clear that the air entrapment is inevitable in squeeze pressurised infiltration of fibre preforms in the atmosphere. The amount of the air entrapped is determined by the infiltration speed employed, the resultant pressure gradient in the infiltrated preform and the value of the penetrating-through pressure. The maximum pressure employed only functions to compress the entrapped air until it reaches a force balance with back pressure presented by the entrapped air and capillarity.

The entrapped air not only induces non-infiltration defects in the material, but also degrades the fibre-matrix interfacial bonding strength. Consequently, with decreased infiltration speed, the fabricated material will fail at reduced strength and elongation due to the low stress activation of non-infiltration defects and the interfacial debonding. To produce quality cast FMMCs, the infiltration speed should be maximised as far as the ultimate compression strength of the preform allows to minimise the amount of air entrapped.

REFERENCES

1. Kang, C. G. and Seo, Y. H., *J. Mater. Proc. & Tech.*, Vol. 61 (1996), p241-249.
2. Long, S., Zhang, Z. and Flower, H. M., *Acta Metall.*, Vol. 43 (1995), p3489-3498.
3. Long, S., Zhang, Z. and Flower, H. M., *Acta Metall.*, Vol. 43 (1995), p3499-3509.
4. Long, S., Flower, H. M. and Beffort, O., *Effects of Premature Melt Solidification on Pressurised Infiltration Kinetics and Infiltration Quality*, a presentation on *4th Decennial International Conference on Solidification Processing*, 7-10 July, 1997, Sheffield, UK.

THE MECHANICAL PROPERTIES OF PARTICULATE REINFORCED ALUMINUM ALLOY AT ELEVATED TEMPERATURE

J.H. Shyong¹, Y.M. Yeh¹, C.H. Huang² and C. Y. Ma³

¹*Department of Mechanical Engineering, Chung-Cheng Institute of Technology, Tahsi, Taoyuan 335, Taiwan, R. O. C.*

²*Dept. of Ordnance Office, The Army Logistics School, Chung-Li 320, Taiwan, R.O.C.*

³*Material research and Development Center, Chung-Shan Institute of Technology, P.O.Box 90008-8-4, Lungtan, Taoyuan 325, Taiwan, R.O.C.*

SUMMARY: The deformation characteristics at elevated temperature of aluminium alloy 6061 reinforced with particulate SiC have been investigated. The materials investigated contained 10% by volume and 10 μ m by size of SiC particulates. In order to set up a comparative materials data base, the microstructural characteristics of the unreinforced matrix material with identical fabricating and processing history were examined. The results show that at room temperature, the compressive strength of the SiC 10/10/6061Al composite is higher than 6061Al alloy, and there is not so much difference between 200~25°C. But at elevated temperature, the compressive strength of the SiC 10/10/6061Al composite is less than 6061Al alloy.

KEYWORDS: metal matrix composites, particulate reinforced, thermal mechanical property

INTRODUCTION

Metal matrix composites (MMCs) have been developed in the last few years, in order to reduce the weight of components in structural applications and to improve their thermal and mechanical properties. Particulate reinforced MMCs have the advantage of being machinable and workable using conventional processing methods. The particulate-reinforced metal matrix composites have been widely applied to the aerospace industry, because of their desirable properties, including low density, high specific stiffness, and increased wear resistance.

The influence of matrix microstructure and the morphology of the particulate reinforced composite on the compressive strength at elevated temperature is still not clear. In order to reveal the influence of the strengthening mechanism, the compressive tests have been studied on the silicon carbide particulate reinforced aluminum at various temperature. It attempts to characterize their behaviour on experimental observations of the matrix microstructure and reinforcement morphology on uniaxial stress-strain response of the 10/10/6061Al composite. The mechanisms of strengthening and failure in metal matrix composites have been issues of academic research for some time. Many different mechanisms have been proposed. These include: (1) load transfer between the matrix and reinforcement [1,2,3], (2) enhanced

dislocation density in the matrix [4,5], (3) matrix and interfacial precipitation [6,7]. In addition to the wide range of viewpoints on the strengthening of MMCs, there were a variety of failure mechanisms have been reported. These include: (1) cavitation at the interface and within the matrix [8,9,10], (2) ductile failure in the matrix of the composite [11, 12], particle cracking [13], and (4) interfacial decohesion [14]. A recent study has shown aging induced precipitation and microstructure evolution in the matrix of SiC reinforced Al-6061 to be quite different from the unreinforced control alloy which was subjected to identical heat treatment [15]. Such differences in the precipitation kinetics will affect the strength of the composite more than details of strengthening theories such as the rule of mixtures, which assumes the matrix of the composite to be unaffected by the presence of reinforcement.

EXPERIMENTAL DETAILS

The mechanical properties of particulate reinforced MMCs are controlled by a complex interaction between the matrices and reinforcements. The addition of a reinforcing phase of different elastic properties induces strain concentrations. In order to maintain the displacement compatibility across the interface when a far-field strain is applied, dislocations are generated at the composite interface. Also, the difference in thermal expansion coefficients between the two phases necessitates the generation of dislocations to accommodate thermal strain on changing temperature. The interaction of matrix dislocations, with precipitates and with the reinforcing phase determines the mechanical behaviour of the composite. The aim of this study was to study the effect of systematic variations in reinforcement volume fraction, particle size and heat treatment on the mechanical behaviour of SiC reinforced Al-6061. The model materials consisted of a matrix metal (6061Al) and 10% vol. 10 μ m of silicon carbide particulate reinforced composite, as shown in Fig.1. Uniaxial compression test was performed on cylindrical specimens (ϕ :9mm, L:10mm) at various temperature (RT, 100, 150, 200, 250, and 400°C). Before testing, the specimens were isothermal exposure in the testing box 30min at every stage. The results of the 10/10/6061Al composite and pure 6061Al alloy at various temperature are shown in Fig. 2, and Fig. 3. The strength of the 10/10/6061Al composite between RT and 150°C is higher than 6061Al alloy, and no significant difference between 200°C and 250°C, but lower than expected from 250~400°C. The additional reinforcing particles in the composite is the dominant effect on compressive strength at RT~250°C. But at higher temperature the strength afforded by the reinforced particle varied with temperature and matrix temper. The fractographic section of the thermal compressive specimen 10/10/6061Al on SEM is shown in Fig. 4. The composite compressive fracture section on higher temperature exhibit that fewer SiC particles are cracking, and the voids nucleated near by the SiC particles. The voids (2 μ m) most likely nucleate by cracking of the particles.

DISCUSSION AND CONCLUSION

The 10/10/6061Al composite and 6061Al alloy exhibit different thermal mechanical properties. The additional reinforcing particles to the 6061Al matrix metal can increase the compressive stress at room temperature, but decrease at elevated temperature. The main reasons are discussed as follow:

At room temperature:

1. The additional silicon carbide hard particles are presented in softer matrix, they hinder dislocations motion, and enhance the composite strength.
2. The difference in coefficient of thermal expansion

(CTE) between the two phases have been related to a high dislocation density in the matrix. The CTE of aluminum is seven times larger than that of SiC, the thermal mismatch strains occurring at the interface hence high density dislocations and the particles are obstacle to the dislocation movement. This enhances the composite strength as well[16].

At elevated temperature:

1. The thermal mechanical properties of the particulates reinforced composite are controlled by interaction between the matrices and reinforced particles, if the particulate are well bonded to the matrix. However, the SiC particles may be broken, or debonded with the matrix, and left the voids. This induce the displacement discontinuity, and reduce the resistant strength. So that, the matrix deformation play a key role in the thermal compression behavior. At higher temperature, the particles on the matrix, induce an incoherent effect, and disturb the matrix coherent to resist the extra force. So that, the mechanical properties of the composite is less than the pure 6061Al alloy[17].

As stated above, we conclude that at higher temperature ($\geq 250^{\circ}\text{C}$), the matrix metal become soften, then the particles may debond with the matrix, left the voids, and reduce the resistant strength. Because the matrix metal affect significantly the composite characteristics, and determine the mechanical behavior of the composite at higher temperature, in order to increase the compressive strength of composites at elevated temperature, a well control heat treatment process is recommended.

ACKNOWLEDGMENTS

We would like to thank for Material Research and Development Center Chung-Shan Institute of Technology to provide the MMCs. This work was funded by the NSC, ROC (National Science Council, Republic of China) under grant 86-2815-C-014-013-E.

REFERENCES

1. Nardone, V.C. and Prewo, K.M., *Scr. Metall.*, 20, 43.(1986)
2. Nardone, V.C., *Scr. Metall*, 21, 1313. (1987)
3. Cho, K.and Gurland, J., *Met. Trans.*, 19A, 2027.(1988)
4. Arsenault, R.J. and Fisher, R.F., *Scr. Metall.*, 17,67.(1983)
5. Arsenault, R.J., *Mat. Sci. Eng.*, 64, 171.(1984)
6. Christman, T. and Suresh, S., *Acta Metall.*, 6, 1691.(1988)
7. Lewandowski, J.J., Liu, C. and Hunt, W.H. Jr.,*Mat. Sci. Eng.*, A107, 241.(1989)

8. Nutt, S.R. and Duva, J.M., *Scr. Metall.*, 20, 1055.(1986)
9. Nutt, S.R. and Needleman, A., *Scr. Metall.*, 21, 705.(1987)
10. Christman, T., Needleman, A., Nutt, S. and Suresh, S. ,*Mat. Sci. Eng.*, 107A, 49. (1989)
11. McDanel, D.L., *Met. Trans.*, 16A, 1105. (1985)
12. You, C.P., Thompson, A.W. and Bernstein I.M., *Scr. Metall.*,21, 181. (1987)
13. Nair, S.V., Tien, J.K. and Bates, R.C., *Int. Met. Rev.*, 30, 275. (1985)
14. Christman, T. and Suresh S., *Mat. Sci. Eng.*, 102A, 221. (1988)
15. Shyong, J.H., Ruiz, C., Mummery, P.M. and Derby B., *The Relationship Between Microstructure and Mechanical Properties of Particulate Reinforced Metal Matrix Composite, MMC 3rd.*, Inst.of Metals, London. (1991)
16. Shyong, J.H., *The 36th conference on Aeronautics and Astronautics R.O.C.*, Taiwan, 813. (1994)
17. Taya, M. and Arsenault, R.J., *Metal Matrix Composites: Thermo - mechanical Behaviour*, Pergamon Press, Oxford. (1989)

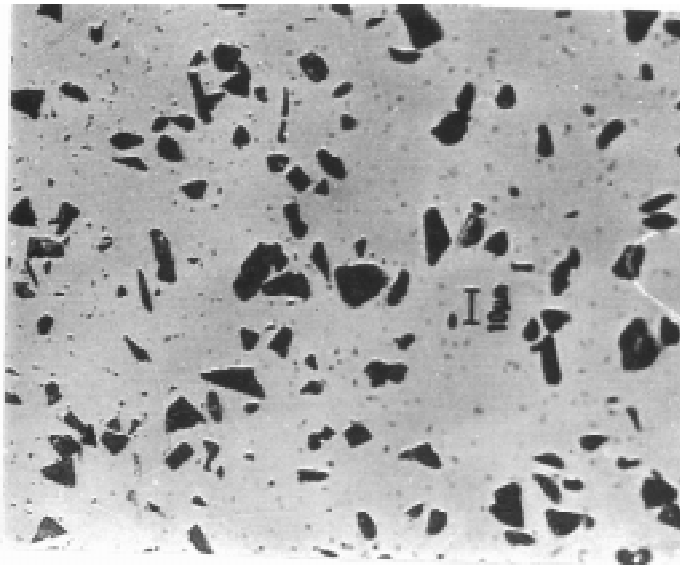


Fig. 1: Transverse micrograph of 10/10/6061

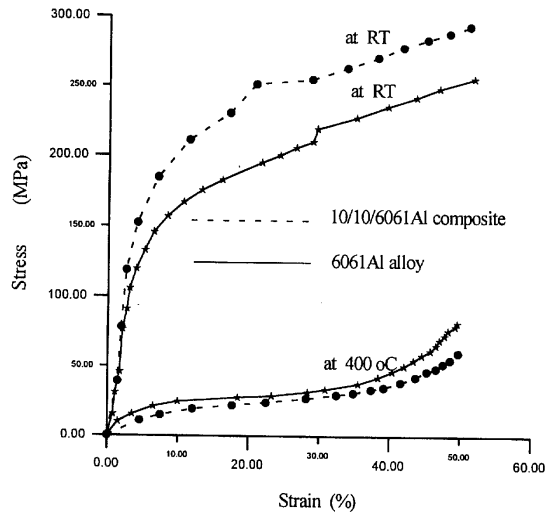


Fig. 2: The compressive true stress-strain curve of 6061Al alloy and 10/10/6061Al composite at RT and 400°C

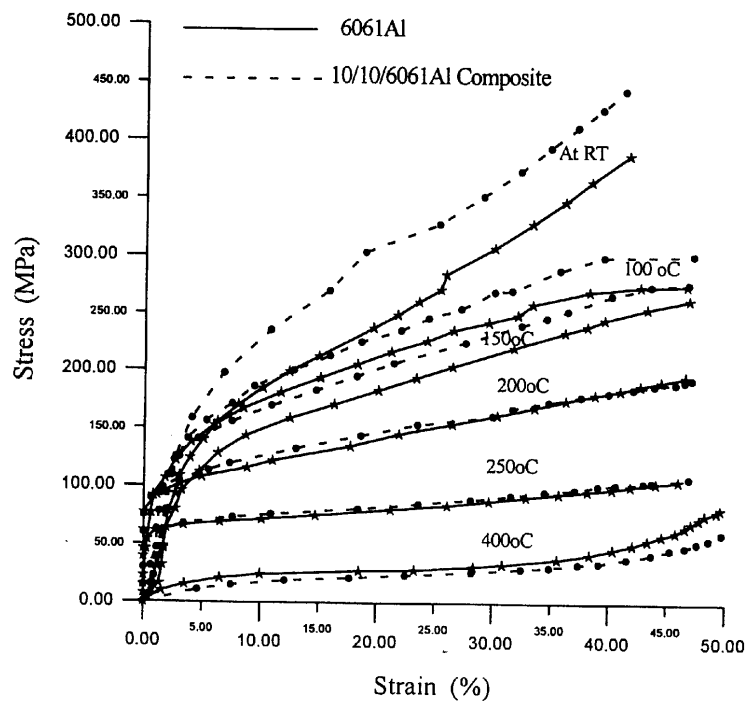


Fig. 3: The compressive true stress of 10/10/6061Al composite and pure 6061Al alloy at various temperature.

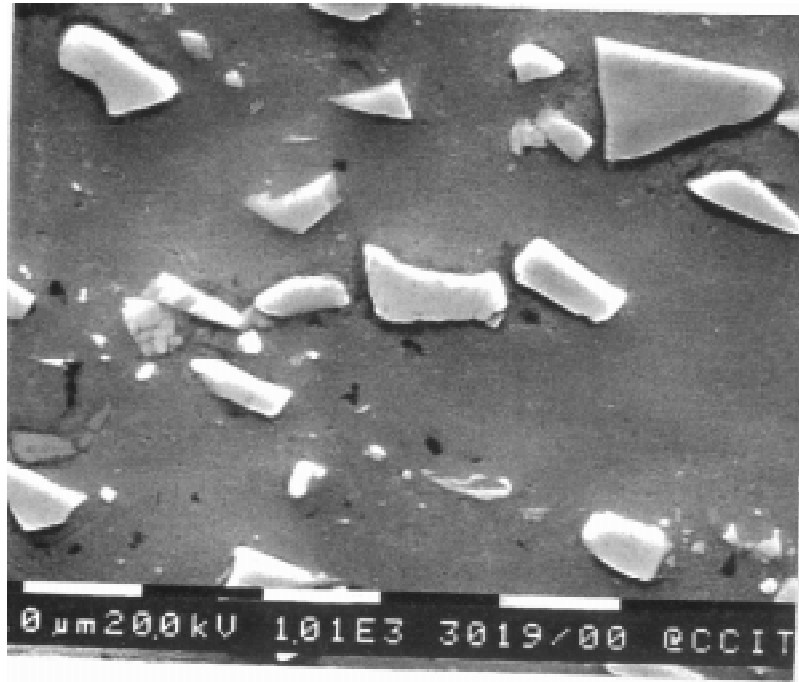


Fig. 4: The microstructure of the compressive fracture surface of SiCp 10/10/6061Al composite at 400°C

PROPERTIES OF DISCONTINUOUSLY REINFORCED COPPER MATRIX COMPOSITES

J.Goñi¹, D.Coupard¹, A.García-Romero¹, M.C.Castro¹, J.Coletto¹, C.Foruria¹ and J.F.Silvain²

¹ INASMET, C. de Portuete 12, Barrio de Igarra s/n, 20009 San Sebastián (Guipúzcoa), Spain

² ICMCB, Institut de chimie de la matière condensée de Bordeaux, Château Brivazac, Avenue du Docteur A.Schweitzer, 33608 Pessac cedex, Bordeaux, France

SUMMARY: Some properties of copper matrix composites based on three typical binary copper alloys (CuSn, CuCr and CuAl) and reinforced with a 13% V_f (volume fraction) of a mixture of both graphite flakes and δ -alumina short fibers have been studied. The hardness of the composites is practically similar to that measured for the unreinforced matrices, although it is higher for the composites manufactured with the highest volume V_f of δ -alumina short fibers (7%). Moreover, the composites have shown a lower coefficient of thermal expansion between the room and 400°C temperatures in comparison with their unreinforced matrices. On the other hand, the bronze based composite has excellent wear resistance and a lower coefficient of friction with respect to its matrix alloy. The tribological properties of this composite are mainly attributed to the thin layer of graphite at the surface of the wear track impeding metal-to-metal contact.

KEYWORDS: Copper matrix composites, graphite, alumina, foundry technique, hardness, coefficient of thermal expansion, coefficient of friction, wear behaviour.

INTRODUCTION

The need for quality in present industrial standards has made Metal Matrix Composites into a relevant and attractive alternative to unreinforced alloys in many components and applications. Copper Matrix Composites (CuMCs) are a new field, recently approached in the USA and Japan, which potentially offers several great advantages and possibilities of application in different industrial fields [1]. Initially, the leading factor for the development of these new materials was weight reduction and the improvement in reliability required by the aerospace industry. However, in recent years it has been clear that many other advantages can also be obtained by reinforcing copper alloys with discontinuous reinforcements such as particles or short fibers. Specifically, hardness, hot strength and above all wear resistance, can be drastically improved by the addition of a hard or a lubricant reinforcing phase (typical V_f : 5-25%) to the copper based alloy [2].

Due to the novelty of CuMCs, many studies are still required to characterize their properties and in use behaviour before their application at industrial scale. Specially interesting is the study of the wear mechanisms and behaviour, due to the large number of components made of bronzes, brasses or other copper alloys where wear is the main operating condition. Although the wear process has been extensively investigated in typical wear resistance materials, and is partially known in the case of aluminium based composites containing solid lubricants and/or hard ceramic particles [3-4], almost no study is available in the open literature on wear or lubricating properties of CuMCs.

Taking into account this situation, the main objective of this work was to determine some properties of discontinuously reinforced CuMCs, manufactured by a typical and widely applied foundry technique and then, compare them with those shown by the same unreinforced copper alloys. The materials selected for this study were composites based on three different binary copper alloys (Cu-Sn, Cu-Al and Cu-Cr), reinforced with a mixture of both graphite flakes and δ -alumina short fibers. The final reinforcement V_f was 13% for all the composites studied.

MATERIALS AND EXPERIMENTAL PROCEDURE

The materials selected for their characterization in the present study are three commercial copper alloys either unreinforced or reinforced with a mixture of both δ -alumina short fibers ($L=200 \mu\text{m}$ and $D=3.2 \mu\text{m}$) and graphite flakes ($160 \mu\text{m}$ average size). The composites were produced by a well-known foundry technique and reinforced with a mixture of both reinforcements whose V_f varied from 6% to 7% and lead to a total V_f of 13% for each composite, depending on the mechanical and tribomechanical properties required. The unreinforced copper alloys were processed by the same foundry technique, under similar working conditions, in order to compare later on the properties obtained with those shown by the corresponding composites.

The different materials manufactured and tested in the present study are summarized in the following Table 1.

Table 1: Materials manufactured and tested

Matrix (% given by weight)	Type of Reinforcement	V_f (%)	Material State
Cu-12%Sn	None	-	As-cast
Cu-12%Sn	δ -Alumina short fibers Graphite Flakes	6-7 7-6	As-cast
Cu-10%Al-5%Ni-5%Fe	None	-	As-cast
Cu-10%Al-5%Ni-5%Fe	δ -Alumina short fibers Graphite Flakes	6-7 7-6	As-cast
Cu-1%Cr-0.2%Zr	None	-	As-cast
Cu-1%Cr-0.2%Zr	δ -Alumina short fibers Graphite Flakes	6 7	As-cast

A representative microstructure of the different CuMCs produced for the present research work is shown in the following Fig.1. The graphite flakes and the δ -alumina short fibers are uniformly distributed inside the copper based matrix and no significant porosity is observed.

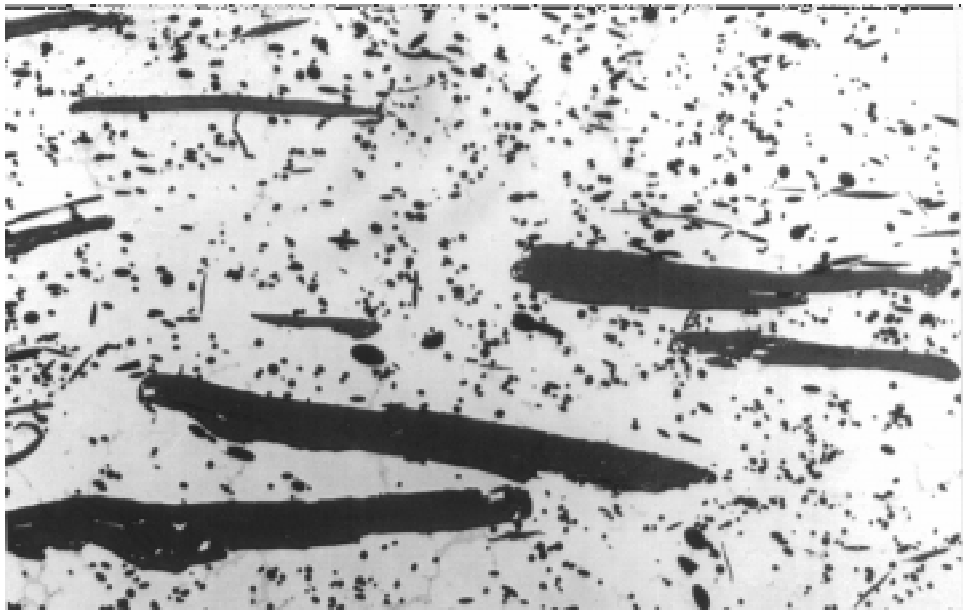


Fig.1: Microstructure of a CuSn/Graphite ($V_f=7\%$) - Alumina ($V_f=6\%$) composite

Both Brinell and Rockwell B were used to estimate the hardness of the composites and the corresponding unreinforced copper alloys, following the standards UNE 7422 and UNE 7424 respectively. The steel ball indenter used for these measurements had a diameter of either 10 mm or 1.5875 mm, for Brinell and Rockwell hardness respectively. In general, the measurement of macrohardness such as Rockwell or Brinell are more suitable than microhardness (e.g., Vickers) because of the typical great dispersion and variation of microhardness in the MMCs due to their usual complex microstructure.

Moreover, the Coefficient of Thermal Expansion (CTE) was measured following the standard ASTM (E228-85) through an Adamel L'Homargy DT 1000 dilatometer. The measurements were carried out with cylindrical test specimens of 2 mm in diameter and 12.5 mm in length, at a heating rate of 2 °C/min between the room and 400 °C temperatures.

Finally, the coefficient of friction and the wear behaviour studies have been performed for the CuSn bronze alloy, and its corresponding manufactured based composite, which is the most usual alloy for mechanical components such as bearings[5]. For that particular application, this alloy requires excellent tribological properties (low coefficient of friction and high wear resistance) under service conditions.

The dry sliding wear and friction tests were carried out in air under unlubricated conditions through a Biceri universal wear test machine. It was used either in the pin-on-reciprocating-plate mode for wear testing or in the pin-on-disk mode for friction tests. For the pin, a bearing ball (10 mm in diameter) made of steel AISI-54100 (UNE F-131) was used. The ball was gripped and the wear samples were cut and machined in squares of 40 mm side. In both cases, the samples were polished using a 3 μm diamond paste and cleaned with alcohol before and after each test. The roughness of the polished bronze, measured with a HOMMEL T 1000 profilometer gave a medium R_a value close to 0.02 μm , while the composite R_a values

suffered a rather great dispersion of between 0.1 μm and 0.6 μm . The samples were weighted accurately before and after each test for further plotting the sample weight loss vs. test conditions. For both the friction and the wear study, each test was repeated three times and the mean value was used for the analysis of the results. The coefficient of friction was calculated using the measurement of change in voltage given by a transducer connected to the wear machine.

The friction tests were carried out at a fixed velocity (V), load (P) and test duration (t) of V=235 mm/s, P=500 g and 200 g, t=30 min., while the wear behaviour was studied by varying the load applied on the sample and the sliding speed. The values tested for both parameters are shown in the Table 2.

Table 2: Wear test conditions

Load (g)	Speed (mm/s)
2.34	67
7.02	100
10.53	133

Optical microscopy was used in order to study the microstructure and detect physical changes in the tribo-deformed surfaces.

RESULTS AND DISCUSSION

Hardness

The following Table 3 summarizes the main results obtained for both the copper matrices and the CuMCs tested.

Table 3: Measured hardness for the different materials tested

Matrix (% given by weight)	V _f Graphite (%)	V _f Alumina (%)	Hardness
Cu-10%Al-5%Ni-5%Fe	-	-	86-88 HRb
	7	6	82-85 HRb
	6	7	88-91 HRb
Cu-12%Sn	-	-	60-67 HRb
	-	-	102 HB5
	7	6	60-67 HRb
	6	7	100-102 HB5
Cu-1%Cr-0.2%Zr	-	-	60-63 HB5
	7	6	69-70 HB5

As can be observed, the hardness of both the composite and the corresponding unreinforced matrix for each copper alloy selected is quite similar, except for the CuCrZr based composite which exhibits approximately a ten percent increase. Moreover, the higher the alumina fiber V_f incorporated inside the matrix, the harder the material, as can be checked for the CuAlNiFe based composite. In this case, the higher alumina fiber content composite is harder than the corresponding unreinforced matrix, when, on contrary, the low alumina fiber content composite is softer than the respective matrix. In general, the hardness of the MMCs reinforced with ceramic particles or fibers is higher than that shown by the unreinforced matrix. However, although in the present work it has not been always the case, it might be attributed to the presence of the soft graphite flakes (hardness of 0.25 GPa) which could be responsible for the relatively low hardness values obtained for the composites in comparison with those initially expected.

Coefficient of Thermal Expansion (CTE)

The high CTE value traditionally shown by copper and its alloys is one of the main physical properties which is required to be notably improved for their application in several potential components such as electronics [6]. In this way, a great improvement of the CTE value can be obtained by means of CuMCs due to the very low thermal expansion reinforcements available in the market for its incorporation inside metallic matrices. For example, the high stiffness long carbon fibers which have a CTE value close to zero in the fiber axis direction and allow the obtention of CuMCs with a very low CTE for a high V_f of carbon fibers, as has been reported in other previous studies [7].

Table 4 shows the CTE values measured for two CuMCs reinforced with a mixture of graphite flakes ($V_f = 7\%$) and δ -alumina short fibers ($V_f = 6\%$) each one, and the corresponding values measured for their unreinforced matrices. A slight reduction of the CTE value, in the range of temperatures studied, has been obtained for both composites in respect to the unreinforced corresponding matrices, due to the reinforcements incorporated which have a considerably lower CTE value.

Table 4: Measured Coefficients of Thermal Expansion

Material	Coefficient of Thermal Expansion α ($\times 10^{-6}$ m/m $^{\circ}$ C)			
	100 $^{\circ}$ C	200 $^{\circ}$ C	300 $^{\circ}$ C	400 $^{\circ}$ C
CuSn alloy	15.65	16	16.36	16.88
CuSn based composite	15.24	15.40	15.65	16.07
CuAlNiFe alloy	15.21	15.45	16.01	17.02
CuAlNiFe based composite	14.22	14.55	15.43	16.32

On the other hand, the variation of the CTE versus the test temperature in the range of temperatures studied is very small for both composites, as in the case of the respective unreinforced matrices. Although the four materials presented a linear behaviour until the 200 $^{\circ}$ C test temperature, the slope for their evolution of the CTE with the test temperature was

continuously increasing after that temperature until 400 °C, as can be checked through the data presented in this Table.

Friction Behaviour

The Fig.2 shows the measured coefficient of sliding friction as a function of the sliding time for both a CuSn bronze alloy and its based composite reinforced with a mixture of graphite flakes ($V_f=7\%$) and δ -alumina short fibers ($V_f=6\%$).

The evolution of the friction coefficient versus time, enables two different states to be distinguished. The transient state develops at the beginning of the friction test, during about the first ten or fifteen minutes, which is characterized by an increase of the friction coefficient (state 1) followed by a decrease until a permanent steady state is reached (state 2).

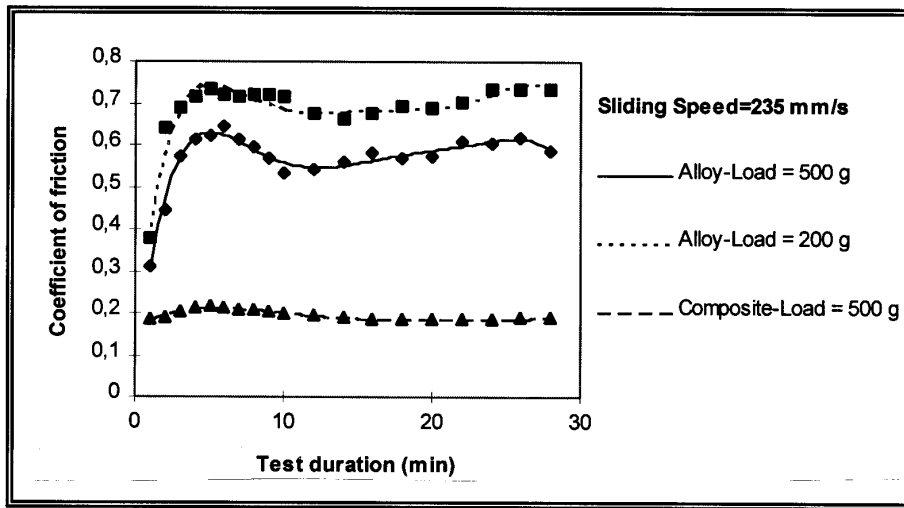


Fig.2: Coefficient of friction vs. test duration

In this steady state and considering a load of 500 g, the coefficient of friction for the composite is close to 0.17 and about one third lower of that of the unreinforced alloy. The highly pronounced wear track in the alloy suggested that the load applied was too great to allow a correct estimation of the coefficient of friction. Thus, a lower applied weight of 200 g was used later on. The coefficient of friction measured in the steady state condition is quite similar but the wear track was still significant.

Wear Behaviour

The wear behaviour was also studied with the same materials used for evaluating the coefficient of friction: a CuSn alloy and a composite based on this alloy and reinforced with a mixture of graphite flakes ($V_f=7\%$) and δ -alumina short fibers ($V_f=6\%$).

Firstly, the plot of the measured CuSn matrix weight loss as a function of the sliding velocity and applied load is presented in the following Fig.3. As is shown, keeping the applied load constant, the sample weight loss increases linearly when increasing the sliding speed from 67 mm/s to 133 mm/s. Moreover, the heavier the load applied on the sample at a constant speed, the higher the weight loss. Considering that the sliding speed is connected to the sliding

distance as a result of a similar wear track length in each test, the wear rate can be defined as the weight loss per unit of sliding distance [8]. Then, the higher the load applied on the sample, the greater the wear rate being otherwise constant for a given load. For example, at a weak load of 2.34 kg, the wear rate is constant around 3.5×10^{-4} g/m, when it is close to 2×10^{-3} g/m for a heavy load of 10.53 kg.

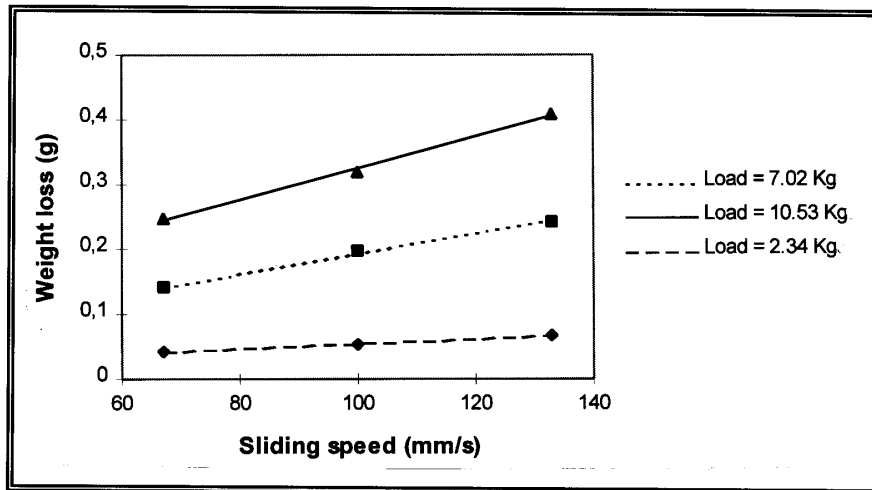


Fig.3: CuSn matrix weight loss vs. the sliding speed

As far as the composite tested is concerned, only one sample of the five studied gave rise to a significant weight loss. Thus, considering both an applied load of 7.02 kg and a sliding speed of 133 mm/s, the composite weight loss was ten times lower than that of the unreinforced matrix. In the same way, the composite weight loss was five hundred times lower under conditions of load and speed such as 2.34 kg and 100 mm/s. For any other combinations of load and applied weight of those shown in the Table 2, the four samples left did suffer very low wear, that is, a wear giving rise to a non-significant sample weight difference before and after the test. Furthermore, by applying more severe wear conditions such as a speed of 166 mm/s and a load of 30 kg, the composite sample did not exhibit measurable weight loss either.

Wear Mechanisms

The Fig.4 shows a micrograph of the wear track after the wear testing carried out for a CuSn copper alloy under a load and speed of 2.34Kg and 67 mm/s respectively.

The wear seems to be controlled by an adhesion mechanism. Adhesive wear occurs when two metallic components slide against each other under a given applied load, and no abrasive is presented [9]. This type of wear is called “adhesive” because of the strong metallic bonds created between surface asperities of both the sample and the counterpart material. Wear results from plastic deformation and shear failure of the weaker of the two metallic surfaces. In theory, when the applied load is low enough, the oxide film present at the surface of the sample can prevent the formation of metallic bonds between the asperities of the sliding surfaces, resulting in low wear rates. This form of wear is called “mild wear”. When the applied load is high, metallic bonds are formed between the surface asperities and the resulting wear rates are high. Thus, it is called “severe wear”. As shown in the Fig.4, the wear mechanism is severe wear. The oxide film at the surface of the bronze is continuously dispersed at the point of contact of each material as a result of the tangential motion at the

interface. Thus, the oxide film can not act as a lubricant which results in a mechanism of severe wear. During the wear test against steel, bronze particles are produced giving rise to a great amount of debris. Also, some of the debris is not ejected from the track but spread again on the surface. By optical examination, a few particles of bronze are seen to have transferred to steel where they remain attached, but most sliding surface of the steel ball remains undisturbed.

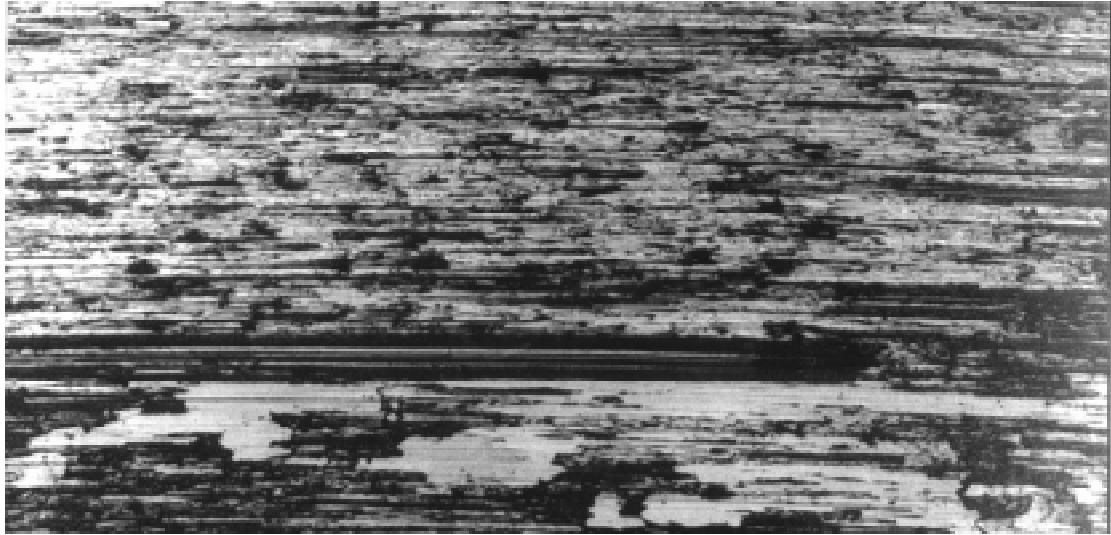


Fig.4: Micrograph of the CuSn bronze alloy wear track

The wear track resulting from the sliding wear of a CuSn based composite against steel under a load and speed of 2.34 Kg and 67 mm/s respectively, is shown in Fig.5 below.

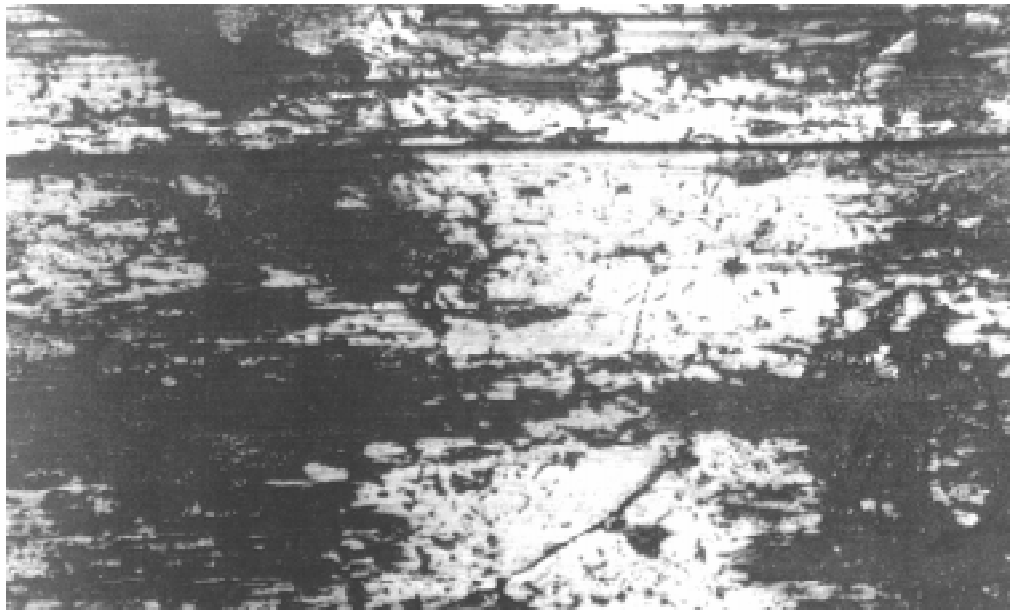


Fig.5: Micrograph of the CuSn/Graphite - Alumina composite wear track

In most samples, whatever the wear conditions, there is nearly neither wear loss, nor grooves and the plastic deformation is low. However, a fine discontinuous graphite layer is dispersed at the surface of the track avoiding metal-to-metal contact. The graphite in the composite is flake graphite and due to its anisotropic crystal structure, it has lubricating properties. During the wear event, the shear stresses lead to a shear process of the graphite flakes. Afterwards, the graphite forms a film on the surface of the wear track and protects the bulk material from adhesion wear. By optical examination, a few grooves can be noticed at the surface of the steel balls with some graphite dispersed at a few points. The wear of the ball may result from a mechanism of abrasive wear induced by the presence of the δ -alumina short fibers inside the matrix. They are also supposed to increase the hardness of the composite giving rise to low plastic deformation around the wear track. Thus, mixing ceramic fibers with lubricant graphite in a metal is a good way of improving the copper tribological properties, reducing both the friction coefficient and the wear tendency of the metallic matrix.

CONCLUSIONS

1. The CuMCs tested have shown a hardness similar to that measured for the corresponding unreinforced matrices, except for the CuCrZr based composite which has presented a ten percent increase. However, the hardness of the composites has been higher in comparison with the matrix for that based on a CuAlNiFe alloy and reinforced with the highest V_f of δ -alumina short fibers used (7%).
2. The coefficient of thermal expansion shown by both CuSn and CuAl copper alloys has been slightly reduced through the incorporation of a 13% final V_f of a mixture of both graphite flakes and δ -alumina short fibers for the range of temperatures tested.
3. The coefficient of friction for the CuSn based composite is around 0.17, being three times lower than that shown by the unreinforced copper alloy.
4. The CuSn based composite shows excellent wear resistance compared to that shown by the unreinforced bronze alloy. For example, the composite weight loss is five hundred times lower under a load of 2.34 kg and a speed of 100 mm/s. Moreover, after a 30 min. wear test under a load and speed of 30 kg and 166 mm/s respectively, the composite did not exhibit higher wear loss than in the former specified conditions.
5. The CuSn bronze alloy weight loss increases linearly when the sliding velocity is increased. Moreover, the heavier the load applied at a constant speed, the higher the weight loss, and the higher the load applied, the greater the wear rate.
6. The tribological properties of the CuSn based composite are mainly attributed to the thin layer of graphite at the surface of the wear track, impeding metal-to-metal contact responsible for the adhesion wear process suffered by the CuSn alloy. The graphite in the composite is flake graphite and due to its anisotropic crystal structure, it has lubricant properties. The δ -alumina short fibers mixed inside the metal are also supposed to play a significant role, giving the composite a higher hardness than the matrix. Consequently, it is not surprising than both the plastic deformation around the wear track and the composite weight loss are low. Thus, mixing ceramic fibers with lubricant graphite in a metal is a good way of improving the composite tribological

properties, reducing both the friction coefficient and the wear tendency of the metallic matrix.

7. Further optimization of the composite processing parameters has to be carried out in order to obtain more homogeneous properties.

REFERENCES

1. A.García and J.Goñi, "Composites de matriz cobre con refuerzo cerámico", *Conference Proceedings, MATCOMP '95*, Sevilla (Spain), 1995, pp.145-151.
2. A.V.Nadkarni, "Copper-based alloys", *Mechanical Properties of Metallic Composites*, Edited by S.Ochiai, Marcel Dekker, Inc., New York, 1994, pp.293-308.
3. I.Shiota and M.Suzuki, "Wear resistance of metal matrix composites", *Mechanical Properties of Metallic Composites*, Edited by S.Ochiai, Marcel Dekker, Inc., New York, 1994, pp.681-704.
4. P.K.Rohatgi, S.Ray and Y.Liu, "Friction and wear in metal-matrix graphite particle composite", *Tribology of Composite Materials*, ASM Int., Conf. Proceedings, Edited by P.K.Rohatgi, P.J.Blau, C.S.Yust and O.Ridge, Tennessee (USA), 1-3 May 1990, pp.1-13.
5. D.T.Peters and K.J.A.Kundig, "Selecting coppers and copper alloys", *Advanced Materials & Processes*, June 1994, pp.20-26.
6. J.K.Weeks and J.L.Sommer, "Copper-graphite composites for thermal management", *40th Int.SAMPE Symposium*, May 8-11, 1995, pp.1708-1717.
7. P.Stefanik and P.Sebo, "Thermal expansion of copper-carbon fiber composites", *Theoretical and Applied Fracture Mechanics 20*, 1994, pp.41-45.
8. A.Arnold, "Wear behaviour of aluminium matrix composites for automotive applications", *Thesis*, INASMET, May 1994.
9. G.R.Kingsbury, "Friction and wear of sliding bearing materials", *ASM Handbook, Vol 18*, 1992, pp.741-757.

EFFECT OF REINFORCEMENT AND PROCESSING ON ISOTHERMAL CREEP PROPERTIES OF DISCONTINUOUSLY REINFORCED ALUMINIUM COMPOSITES

A. F. Whitehouse¹, H. M. A. Winand²

¹*Department of Engineering, Leicester University, University Road, Leicester LE1 7RH, UK*

²*Department of Materials Science and Metallurgy, University of Cambridge, Pembroke Street, Cambridge CB2 3QZ, UK*

SUMMARY: Commercially pure aluminium composites have been prepared containing Al₂O₃ particulates, Saffil or Carbon short fibres, and SiC whiskers with various volume fractions, using powder-blending. Isothermal creep tests have been performed and damage has been characterised using microscopy. The effect of processing has been investigated by comparing short fibre composites produced by powder-blending and infiltration followed in each case by extrusion. It was found that reinforcement distribution and shape were critical in determining creep resistance. Damage initiation was found to dominate composite behaviour, rather than load transfer considerations, for the short fibres and particulates. However, for the finer SiC whisker reinforcement, very good creep properties were observed.

KEYWORDS: damage, creep, cavitation, MMC, failure, reinforcement shape

INTRODUCTION

Previous work [1-3] has suggested that the load transfer effect in discontinuously reinforced composites can result in enhanced creep performance. When a stress is applied to a composite, some portion of the load is transferred to the reinforcement, as a consequence of its higher elastic modulus. As subsequent global plastic flow occurs in the matrix, this introduces a plastic misfit between the two phases, which further increases the load transfer to the reinforcement. This reduces the average stresses in the matrix, and hence reduces the driving force for creep. However, it is not necessarily true that load transfer will be the dominant effect on the composite creep behaviour. A high degree of load transfer also results in a high driving force for stress relaxation, and if this stress relaxation occurs in the form of microstructural damage, the mechanical properties of the composite can be degraded. While considerable work has been done on the creep behaviour of discontinuously reinforced metal matrix composites [1-3] some important questions have not previously been addressed.

It has been established that the fine oxide dispersion present in the matrix of powder-route composites leads to material with good creep resistance [2]. However, there has been little in the way of systematic comparisons to identify the relative importance of reinforcement and oxide dispersion in such systems.

Another important issue is that of damage stability. When damage is initiated in a composite, this will degrade the material by reducing the stiffness. However, if the damage is stable, and acts to reduce local stress concentrations, this may postpone failure, although the creep rate increases. Conversely, if the damage is unstable, this will lead rapidly to failure. It is therefore important to establish how the damage processes influence the overall mechanical response of the composite.

EXPERIMENTAL PROCEDURE

Material Production

Discontinuously reinforced Al composites were prepared using powder blending or squeeze infiltration followed by extrusion [4]. The matrix used was commercially pure (CP) aluminium. The reinforcements used in the powder-route material were spherical and angular alumina particulates (with mean diameter 11 and 13 μm respectively, 20% volume fraction), chopped Saffil alumina fibres and chopped Carbon fibres, both with an average aspect ratio (in the final composite) of 5 and 3 μm diameter (volume fractions of 10 and 20%), and SiC whiskers with aspect ratio 5 and diameter 1 μm (volume fraction 10%). Composite was also prepared using squeeze infiltration followed by extrusion, with volume fractions of 10 and 20%, using Saffil alumina preforms. After extrusion, the average aspect ratio of the Saffil fibres was also 5. In addition, unreinforced CP Al was also prepared using powder blending and squeeze casting followed by extrusion. In the powder-route materials, there was a significant amount of oxide in the matrix, in the form of fine platelets ($\sim 100 \times 30 \text{ nm}$, 0.8 vol%) as demonstrated by Fig. 1. This was derived from the film present on the aluminium powder prior to fabrication, which was broken up and aligned during extrusion. Such a fine oxide dispersion acts as an efficient barrier to dislocation motion, so the powder-route matrices are themselves creep resistant.

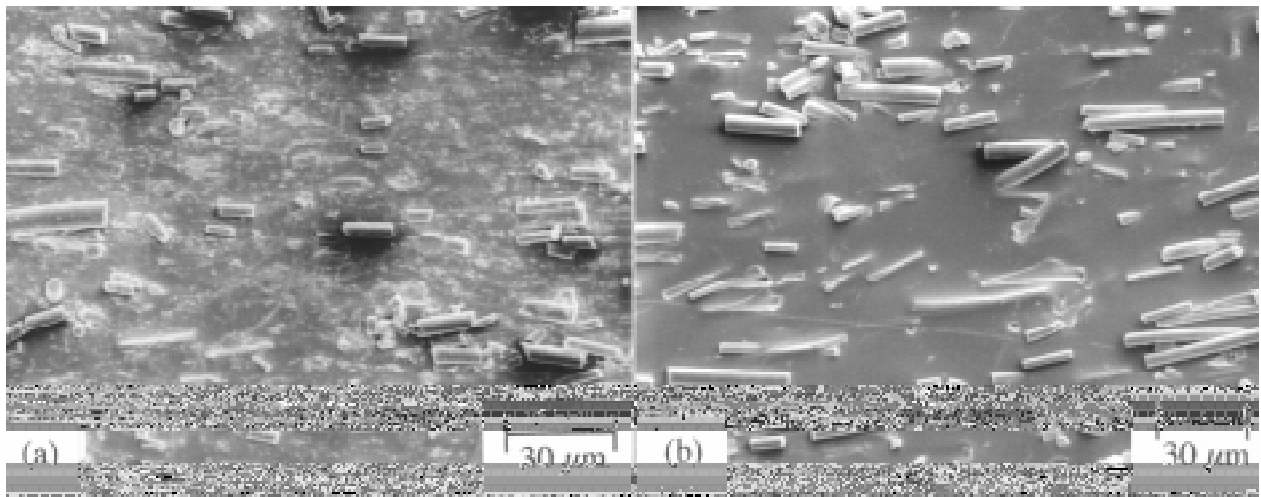


Figure 1: SEM micrographs showing longitudinal sections of CP Al 10 vol% Saffil produced by (a) powder processing and (b) infiltration followed by extrusion.

Creep Testing

Isothermal creep tests were performed at 270 and 300°C with various loads, using a rig which incorporated a twin elliptical infra-red furnace, the load train being placed at the focal line of the furnace. This allowed visual direct access to the specimen during deformation. Both the axial and transverse strains of the specimen were monitored simultaneously during creep using scanning laser extensometry.

Microstructural Characterisation

In order to reveal the damage, specimens were carefully sectioned and electropolished. Details of the preparation procedure are given elsewhere[4]. Microstructural observations revealed that the powder-route composites contained a significant amount of fine oxide in the matrix, which was not present in the infiltrated composites. The grain structure was investigated by anodising the specimens[4]. In all cases the grain structure was elongated in the extrusion direction. Results of initial grain sizes and aspect ratios for selected composites are shown in Table 1.

Table 1: Average grain sizes in as-fabricated composite, with unreinforced material, measured from anodised specimens, processed by powder-route (P) or Infiltration (I)

Material	Average Grain Length (μm)	σ_{n-1} (μm)	Average d (μm)	σ_{n-1} (μm)	Average Grain Aspect Ratio
20% Al ₂ O ₃ ang (P)	22	4	6	1	4
20% Al ₂ O ₃ sph (P)	21	3	5	1	5
20% Saffil (P)	12	3	4	1	3
20% Saffil (I)	32	6	23	6	2
10% SiC _w	60	8	2	1	30
20% C (P)	13	3	4	1	3
CP Al (P)	75	6	7	1	11

RESULTS

The composites did not exhibit significant secondary creep regimes; as has been reported previously with similar composites[5,6]. This is demonstrated by Fig. 2, which shows the proportion of total plastic strain, and proportion of rupture time, spent in each creep regime.

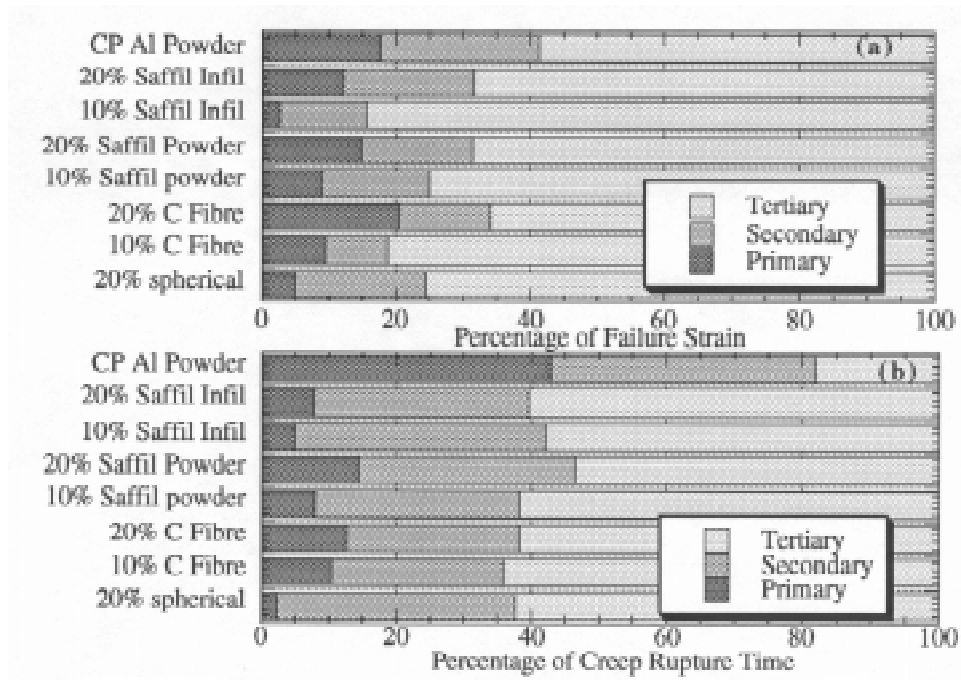


Figure 2: Percentage of (a) strain and (b) time spent in each creep regime for various composites (processed by powder-route or infiltration), and unreinforced powder-route Al tested at 270°C with an initial applied stress of 30 MPa.

Both the primary and secondary regimes are very small, with the tertiary region lasting for the majority of the specimen life in all cases. This suggests that damage is occurring throughout most of the deformation. Conversely, for the unreinforced powder-route material, the majority of the deformation occurs during the secondary creep regime.

Strain to failure data are shown in Fig. 3. Minimum creep rates are shown in Fig. 4. It can be seen that the composites display significantly differing creep responses. The spherical particulate reinforced composite exhibits the lowest creep resistance, with a high strain to failure and a very short rupture time, whereas the unreinforced powder-route material has a much greater creep resistance. It is interesting to note that the unreinforced powder-route aluminium displays better creep resistance than the short fibre and particulate reinforced composites, although not as good as the whisker reinforced material. The powder-route composites have significantly better creep resistance than the infiltrated material. It is also found that the angular particulate reinforcement gives a better creep resistance than the spherical or any of the short fibre reinforced materials. This is perhaps surprising, since from a load transfer argument, the higher aspect ratio fibres should give the best creep resistance. Similarly, it can be seen that the unreinforced powder-route aluminium material exhibits both lower minimum strain rates and higher rupture times than any of the composites, with the exception of the whisker reinforced material.

Fig. 5 shows minimum creep rates for the Saffil composites produced using the two processing routes, together with unreinforced aluminium, also produced by powder and casting methods. It can be seen that the powder-route composite has much better creep resistance than the infiltrated material. What is also interesting to note is that the unreinforced cast aluminium and the infiltrated Saffil composite show very similar values. This suggests that the load is not being effectively carried by the reinforcement in the infiltrated composite.

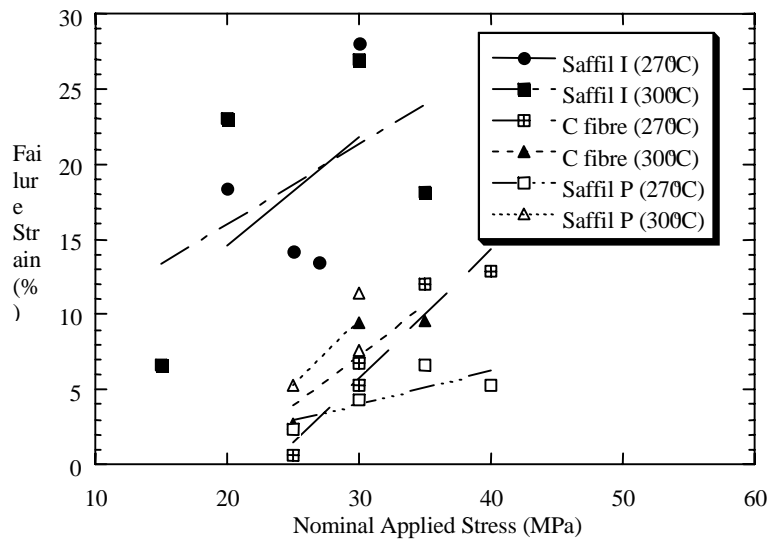


Figure 3: Failure Strain for 10 vol% composites tested at 270°C and 300°C with various applied loads fabricated by powder-route (P) or squeeze infiltration (I).

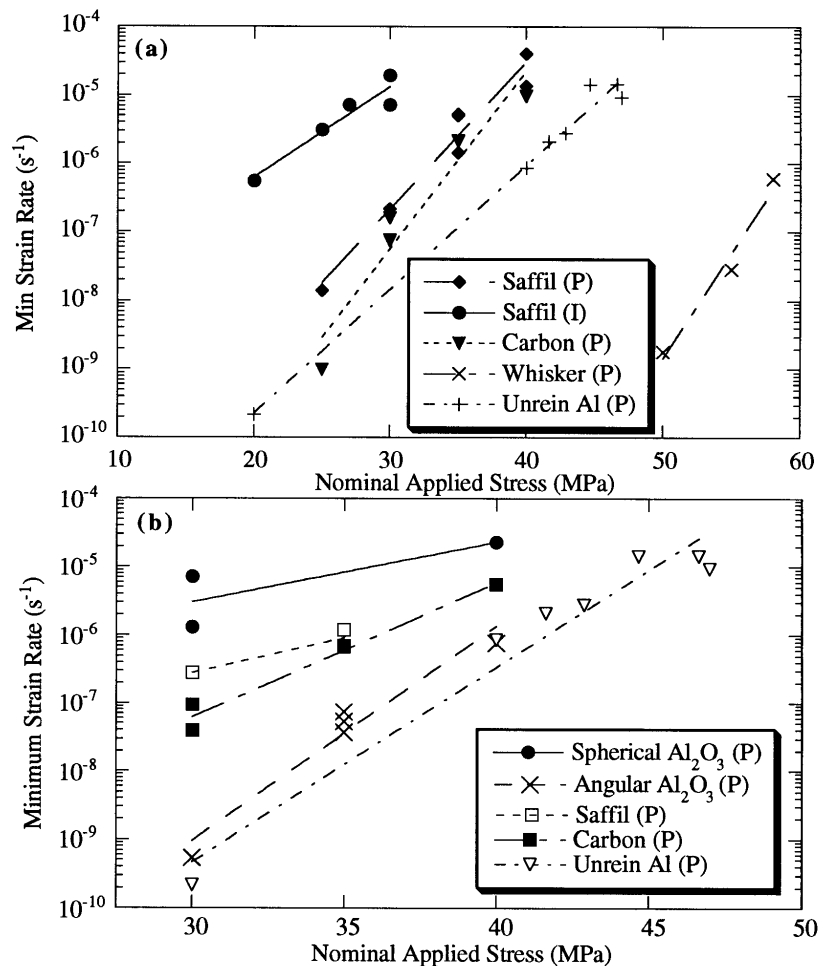


Figure 4: Minimum creep rates for (a) 10 vol% and (b) 20 vol% reinforced composites together with unreinforced powder-route Al tested at 270°C, fabricated by powder-route (P) or infiltration followed by extrusion (I).

DISCUSSION

Effect of Processing Route

Creep Resistance

The initial matrix microstructure was found to be highly dependent on the processing route. The initial grain size was much finer for the powder-route material than for the squeeze infiltrated, and there was a significant extent of fine oxide along the prior particle boundaries of the aluminium. It would therefore be expected that the creep properties of composites prepared using the two methods would be very different. This is confirmed by the creep data. The powder-route composites displayed far better creep resistance than the infiltrated (Figs. 3-5), in terms of failure strain, minimum strain rate and rupture times.

The fine matrix oxide, present in the powder-route composites, has two significant effects. Firstly it results in a fine grain structure by effectively pinning the grain boundaries. Secondly, it provide effective barriers to dislocation motion, thus enhancing the creep resistance of the material.

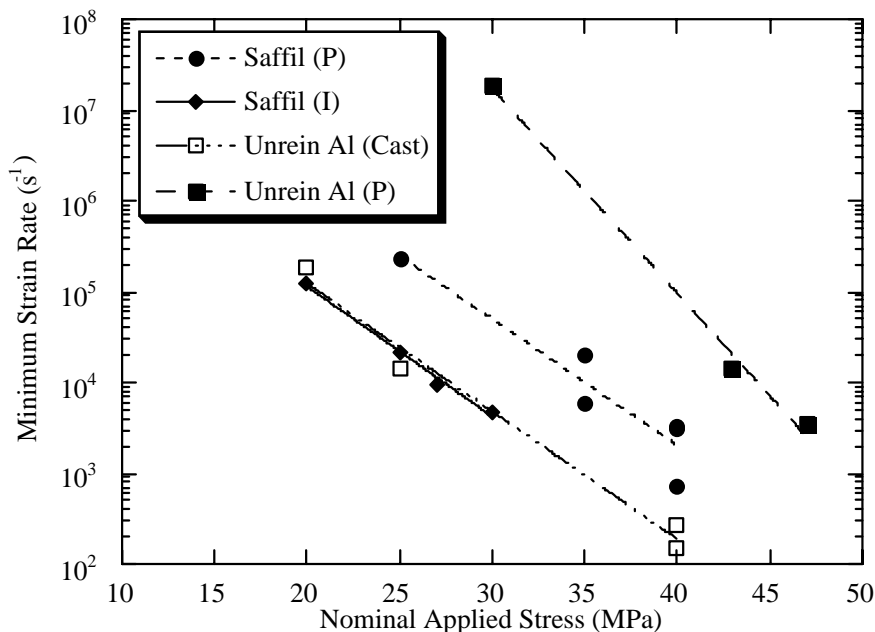


Figure 5: Minimum strain rates for CP Al 10 vol% Saffil reinforced composites, and unreinforced Al produced by powder-route and squeeze infiltration/casting.

Damage Characteristics

The favoured damage sites were found to be different for the two processing routes. This is demonstrated by Fig. 6 which shows electropolished specimens from the two Saffil reinforced composites taken from regions near the fracture surfaces. In the squeeze infiltrated composites damage occurred at the matrix/reinforcement interface of isolated fibres. This damage was distributed fairly homogeneously throughout the specimen, suggesting that it was stable, and could be accommodated without immediately initiating failure. In the powder-route Saffil composites, the reinforcement distribution was found to be poor, with significant

clustering. Large voids tended to open up in these clustered regions, where there is a high degree of triaxial constraint in the matrix. The cavitation was highly localised near the fracture surface, suggesting that it was unstable, and once formed, rapidly lead to the onset of failure.

It is unfortunate that the reinforcement distributions in these composites were not comparable, thus preventing the evaluation of the effect of matrix oxide on the damage processes. However, the powder-route material still displayed significantly better creep resistance than the infiltrated. This therefore suggests that if the distribution of the fibres during the powder-processing could be improved, this would lead to a composite with significantly better creep resistance.

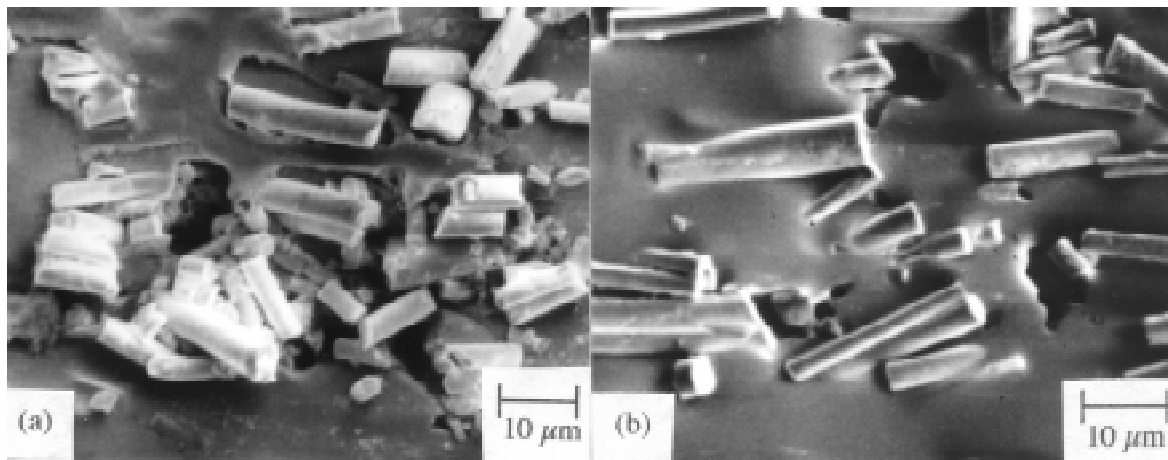


Figure 6: SEM micrographs showing longitudinal sections of CP Al 10vol% Saffil produced by (a) powder processing, and (b) infiltration, taken from regions near the fracture surface.

Effect of Interfacial Bond Strength

It has been established[7] that the interfacial bond in the Al-Al₂O₃ system is strong. This is consistent with the experimental observation[8,9] that debonding occurs when a critical hydrostatic stress is attained at the interface, rather than a critical normal stress. However, in the case of carbon fibre reinforced Al, the interfacial bond strength is much weaker[10]. It is therefore expected that interfacial sliding and decohesion will occur more readily in the Al-C system than in the Al-Al₂O₃ system. This is consistent with microstructural observations taken from failed specimens of the two composites. For example, Fig. 7 shows regions of failed specimen of Al 10 vol% C fibre, with clear evidence of interfacial failure. It was also found that cavitation occurred extensively throughout the specimens, and was not localised near the fracture surface. This confirms that cavitation at individual reinforcement fibres is very easy in the Al-C system, and that the resulting damage, although lowering the composite stiffness, is stable and does not immediately initiate failure. As has already been observed, the Saffil composites exhibited significant fibre clustering, resulting in large cavities and early failure.



Figure 7: Micrographs of 10 vol% (a) C and (b) SiC_w material, taken near fracture surface

Effect of Reinforcement Shape and Aspect Ratio

Failed specimens of angular and spherical particulate reinforced composites are shown in Fig. 8. It can be seen from Fig. 4 that the spherical reinforcement shows much worse creep resistance than the angular. What is interesting is the surprisingly large difference between the two. Since the initial grain size and structure were very similar, the two matrices are expected to have similar strengths. It is also unlikely that the large difference in creep resistance would be due entirely to the small difference in reinforcement aspect ratio between the two reinforcements (~1.5 compared with 1). Also, from Fig. 4 it can be seen that the angular particulate gave better creep resistance than any of the fibre reinforced composites. If load transfer were dominating the creep response, then the higher aspect ratio reinforcements would be expected to have a better creep resistance than the particulate, which is not observed here.

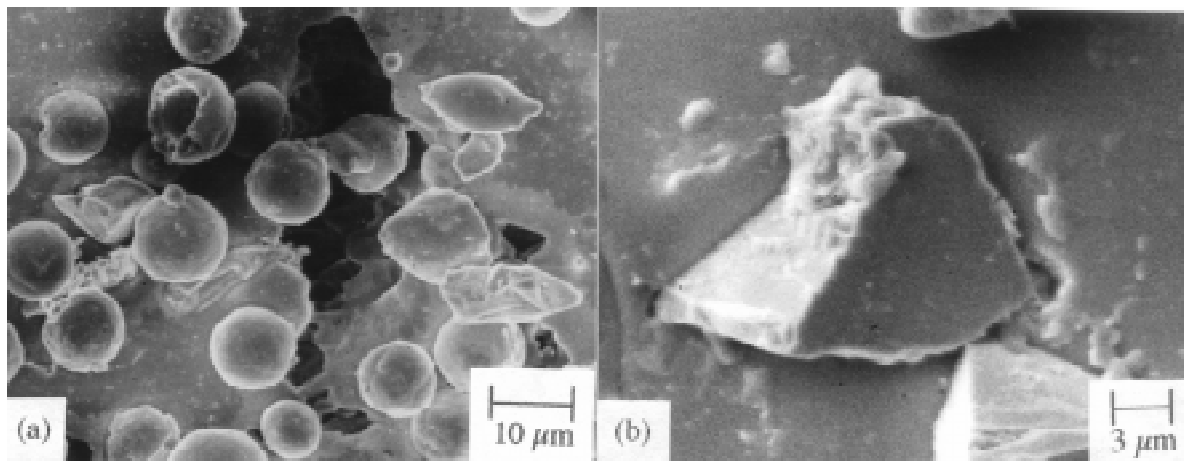


Figure 8: SEM micrographs showing longitudinal sections CP Al reinforced with (a) spherical and (b) angular alumina, taken from regions near the fracture surface.

Both these effects can be explained if the promotion of damage is taken into account. It has been established[8,9] that high local hydrostatic stresses are evolved adjacent to the reinforcement/matrix interface on loading a composite, and that these stresses promote damage. It has also been shown that the higher the reinforcement aspect ratio, the higher the resulting local stress concentration. Therefore, damage will be expected to occur more readily

in the fibre reinforced materials compared with the particulates. If this is the case, and damage does occur more readily in the fibre reinforced materials, this may accelerate the onset of failure giving these composite inferior creep resistance. This also explains why the unreinforced powder-route Al showed significantly better creep resistance than all composites except the whisker reinforced material (Fig.4). If load transfer were dominating the creep response then the composites would give better performance than the unreinforced material. Clearly this is not the case. This suggests that reinforcement of this size range accelerates the onset of failure by promoting internal damage.

In the case of the particulate reinforcements, the distribution of damage is the key factor. From Fig.8, it can be seen that, for the angular reinforcement, cavities tend to form at individual reinforcement particles and that the distribution is fairly homogeneous. Favoured sites were reinforcement angularities [9]. With the spherical reinforcement, cavities did not tend to nucleate at individual reinforcement particles, but instead large cavities opened up in the matrix. This again agrees with finite element predictions [9], that the spherical reinforcement shape does not promote cavitation at elevated temperature. The cavities were also highly localised at the fracture surface, showing that damage was unstable. These microstructural observations show that damage can be accommodated more easily in the angular reinforced material, without leading to failure of the composite. This therefore explains why the angular material showed much better creep resistance than the spherical material.

Effect of Reinforcement Scale

Creep data have shown (Fig. 4) that the whisker reinforcement gave enhanced creep resistance (relative to unreinforced powder-route Al), whereas short fibres were detrimental to the creep resistance. Both reinforcements had an average aspect ratio of 5, so purely on load transfer arguments, their behaviour would be expected to be similar. Clearly this is not the case here.

Experimental observations suggest that the difference in creep properties between the two composites is due to the size of the cavities. It has been shown [4] that when a cavity is nucleated at a reinforcement the size of the cavity is directly related to the size of the reinforcement. Also, since both composites had the same volume fraction of reinforcement (10 vol%), the actual number of whiskers, and hence potential cavitation sites, was much larger than for the short fibre system. For this reason, in the whisker reinforced material, the damage tends to form as a large number of very small cavities (Fig. 7). This observation has also been confirmed by neutron diffraction studies [5]. This contrasts with the short fibre material, where fewer large cavities were observed. Since it is more likely that large cavities will coalesce, this explains why damage was found to limit the creep life of the short fibre reinforced material. In the case of the whisker material, a high level of damage could be accommodated without leading to failure. Therefore, the beneficial effects of load transfer to the reinforcement dominated the composite behaviour. These observations demonstrate that the scale of the reinforcement is important in determining the creep behaviour.

Damage Sites and Distribution

The formation of damage within a composite is not necessarily detrimental to the subsequent creep resistance (or at least, the resistance to creep rupture). The important factor is whether or not that damage is stable. Stable cavitation can act to relax local stress concentrations, and

hence delay the onset of failure. Previous work [4,11] on tensile deformation in these materials has shown that significant damage can be accommodated without accelerating the onset of failure. Whether stable cavities can form in the composite essentially depends on the distribution of that damage in the composite, and the ease with which the cavities can grow and coalesce. Cavitation is favoured by reinforcement angularities and elongation parallel to the applied stress. The shape of the angular particulates and short fibres therefore promoted cavitation at the reinforcement/matrix interface, while that of the spherical particulates did not. This is demonstrated by Figs. 6-8 which show typical regions of failed composite. This agrees with the experimentally favoured cavitation sites observed during tensile deformation at elevated temperature [8]. The distribution of the reinforcement is critical in determining the sites and extent of damage in the composites. Where the reinforcement distribution was homogeneous, then reinforcement shape was the dominant parameter controlling cavitation. However, if there were a significant extent of clustering in the reinforcement, then the resulting high triaxial constraint led to preferential formation of large cavities, rather than small cavities at individual reinforcement fibres or particles. Microstructural observations showed that where the reinforcement distribution was homogeneous, and the shape of the reinforcement promoted cavitation, cavitation was found to occur throughout the specimen, and was not catastrophic. Such damage can be accommodated within the composite without leading rapidly to failure. However, when damage was localised near the point of fracture, this suggests that the onset of cavitation is catastrophic.

CONCLUSIONS

The scale of the reinforcement is important in determining creep resistance. Larger reinforcements (3 μ m diameter, aspect ratio 5 fibres, 10-13 μ m particulates) reduce the creep resistance relative to unreinforced powder-route aluminium. Fine whisker reinforcement (1 μ m diameter, aspect ratio 5) enhances the creep resistance relative to unreinforced powder-route aluminium. Composites produced by powder-processing show significantly better creep resistance than those produced by squeeze infiltration. This is due to the fine oxide dispersion in the powder matrices, which inhibits both dislocations motion and recrystallisation. For the larger reinforcements, the site and distribution of damage is more important than load transfer considerations for determining creep resistance.

Reinforcement distribution is critical in determining damage distribution. Clustered regions of reinforcement are favoured sites for severe cavitation. If damage occurs at isolated reinforcement particles or fibres, it is favoured by reinforcement elongation parallel to the applied stress and by reinforcement angularities. When cavitation occurs at isolated reinforcement particles or fibres, it can be tolerated without immediately leading to failure. Such cavitation can be beneficial in relaxing local stress concentrations. When damage is associated with reinforcement clusters, or occurred within the matrix, the cavities are highly unstable, and rapidly lead to failure of the composite.

ACKNOWLEDGEMENTS

The funding for AFW was provided by the EPSRC. The funding for HMAW was provided by DRA/RAE and the EPSRC.

REFERENCES

1. Nieh, T.G., "Creep Rupture of a Silicon Carbide Reinforced Aluminium Composite", *Met. Trans.*, Vol. 15A, 1984, pp. 139-146.
2. Park, K.T., Lavernia, E.J. and Mohamed, F.A., "High-Temperature Creep Of Silicon-Carbide Particulate Reinforced Aluminum", *Acta Metallurgica Et Materialia*, Vol. 38(11), 1990, pp. 2149-2159.
3. Mohamed, F.A., Park, K.T. and Lavernia, E.J., "Creep-Behavior Of Discontinuous SiC-Al Composites," *Materials Science and Engineering a-Structural Materials Properties Microstructure and Processing*, Vol. 150(1), 1992, pp. 21-35.
4. Whitehouse, A.F., Shahani, R.A. and Clyne, T.W., "Use Of Light and Scanning Electron-Microscope Techniques to Monitor Microstructural Changes In Aluminum-Based Metal-Matrix Composites", *Journal Of Microscopy-Oxford*, Vol. 178(Pt3), 1995, pp. 208-225.
5. Winand, H.M.A. "Damage, Internal Stresses and the High Temperature Behaviour of Metal Matrix Composites," Ph.D. Thesis, University of Cambridge, (1996).
6. Nieh, T.G., Xia, K. and Langdon, T.G., "Mechanical Properties of Discontinuous SiC Reinforced Aluminium Composites at Elevated Temperatures", *J. Eng Mat & Tech*, Vol. 110, 1988, pp. 77-82.
7. Flom, Y. and Arsenault, R.J., "Interfacial Bond Strength in an Al Alloy 6061-SiC Composite", *Mat. Sci. & Eng.*, Vol. A77, 1986, pp. 191-197.
8. Whitehouse, A.F. and Clyne, T.W., "Effect Of Test Conditions On Cavitation and Failure During Tensile Loading Of Discontinuous Metal-Matrix Composites", *Materials Science and Technology*, Vol. 10(6), 1994, pp. 468-474.
9. Whitehouse, A.F. and Clyne, T.W., "Critical Stress Criteria For Interfacial Cavitation In MMCs", *Acta Metallurgica Et Materialia*, Vol. 43(5), 1995, pp. 2107-2114.
10. Mercier, S., Ehrburger, P. and Lahaye, J., "Interfacial Reactivity In Aluminium/Carbon Fiber Composites", *Journal De Physique IV*, Vol. 3(C7 Pt3), 1993, pp. 1723-1726.
11. Whitehouse, A.F. and Clyne, T.W., "Cavity Formation During Tensile Straining Of Particulate and Short-Fibre Metal-Matrix Composites", *Acta Metallurgica Et Materialia*, Vol. 41(6), 1993, pp. 1701-1711.

THE BENDING PROPERTIES AND FRACTURE CHARACTER OF DIRECTIONAL SOLIDIFIED $Al_2O_3/Al-4.5$ CU COMPOSITES

Chu Shuangjie¹, Wu Renjie², Zhao Changzheng²

¹*Cold Rolling Mill Plant, BaoShan Iron & Steel Corporation, Shanghai 200941, P. R. China*

²*Institute of Composite Materials, Shanghai Jiao Tong University, Shanghai 200030, P. R. China*

SUMMARY: In this paper, the directional solidification method was employed and the influence of microstructures of $Al_2O_3/Al-4.5Cu$ metal matrix composites on its mechanical properties at different solidification rates was studied, and found a new method for improving the mechanical properties of metal matrix composites. Experimental results showed that the bending strength and fracture strain of $Al_2O_3/Al-4.5Cu$ composites under the common casting state was the lowest and increased gradually with the increase of directional solidification cooling rate. As the solidified rate was increased to $700 \mu m/s$, its bending strength was 597 MPa; in comparison with that of the common cast state. The bending strength and fracture strain of directional solidified $Al_2O_3/Al-4.5Cu$ composites at $V=700 \mu m/s$ were improved 66% and 135% respectively. The fracture surface of $Al_2O_3/Al-4.5Cu$ composites under common cast state showed the character of brittle fracture, but the fractography of directional solidification $Al_2O_3/Al-4.5Cu$ composites turned to the character of tenacious fracture and the tough nests on the fracture surface became more dense and deep with the increase of directional solidification rate.

KEYWORDS: directional solidification, metal matrix composites, cooling rate, fracture, Mechanical properties

INTRODUCTION

Particulate reinforced metal matrix composite(MMCs) with high specific modules, strength and thermal stability have an extensive attraction for automotive and other structural application at present. For the requirements of low density and reasonably high thermal conductivity, aluminum and magnesium alloys are used as matrices and ceramic particulates such as carbides (e.g., SiC, B_4C), nitrides (e.g., Si_3N_4 , AlN) as well as oxides (e.g., SiO_2 , Al_2O_3) are used as reinforcements [1,2]. In order to improve mechanical properties of metal matrix composites, many studies have been performed [3], but the influence of matrices microstructure on mechanical properties of MMCs is ignored.

Directional solidification technology is an effective method for controlling of solidified microstructure of metal matrix composites [4], when matrix alloy was solidified directionally, it

may improve obviously to the vertical mechanical properties of composites and especially for their high temperature mechanical properties. So that in this paper, the directional solidification method was employed and the influence of microstructures of composites on its mechanical properties at different solidification rates are studied and a new method for improving the mechanical properties of metal matrix composites was found.

EXPERIMENTAL PROCEDURE

The matrix materials selected for this study was Al-4.5(wt.%)Cu casting aluminum alloy and the reinforcement was Al_2O_3 particulate in the average size of $10\mu\text{m}$.

$\text{Al}_2\text{O}_3/\text{Al-4.5Cu}$ composites was fabricated by the melt stirring method under vacuum. In stir casting process, the temperature of molten alloy was about $700\sim 750^\circ\text{C}$, the rotate velocity of the stirring was $1000\sim 1200$ rpm and the fraction of Al_2O_3 particles in the composites was 4vol%. As particles distributed uniformly in the melt by stirring, mixture of particles and the melt was poured into the chill mold which had been preheated at 100°C , the stirring casted $\text{Al}_2\text{O}_3/\text{Al-4.5Cu}$ composites were subsequently cut into specimens with $\Phi 8\times 100\text{mm}$ in dimension.

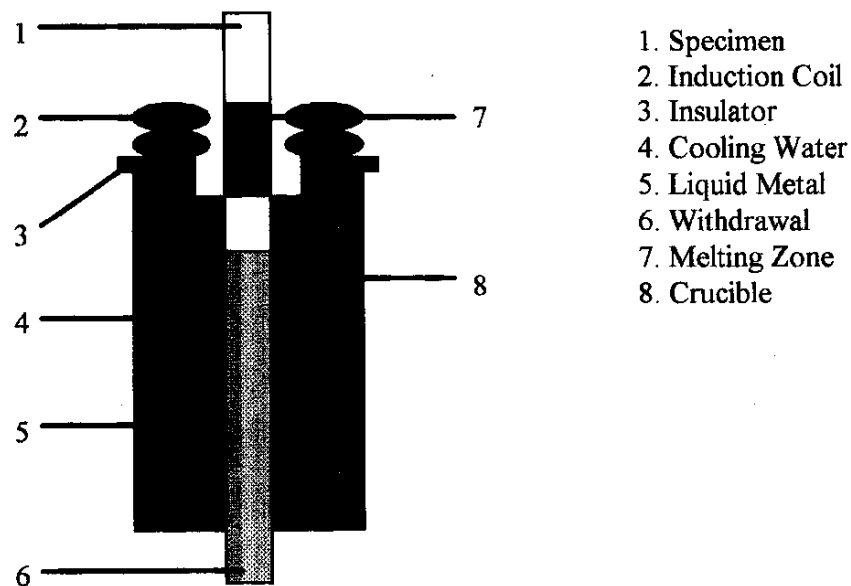


Fig.1 Schematic diagram of apparatus for directional solidification at superhigher rate

Directional solidification of $\text{Al}_2\text{O}_3/\text{Al-4.5Cu}$ composites was carried out by a zone melting and liquid metal cooling (ZMLMC) directional solidification apparatus shown in Fig.1. The temperature gradient ahead of the liquid-solid interface was measured by double platinum-rhodium thermocouples and the solidification rate(V) can be continually adjusted from 0.006 to 10 mm/s. The directionally solidified specimens were cut into sections with the $4\times 5\times 40$ mm in size for the bending strength measurement which was carried out on the New-810 MTS machine with the striped distance of 40 mm and the dropping velocity of the cross head was 0.5 mm/min, then the data was taken by the average bending strength of the five specimens.

The fractography of the sample was observed on the Hitachi-S-520 Scanning Electron Microscope.

RESULTS AND DISCUSSION

The Bending Strength of Directional Solidified Al₂O₃/Al-4.5Cu Composites

The bending strength and fracture strain of Al₂O₃/Al-4.5Cu composites under the condition of directional solidification are shown in Fig.2 and Fig.3. From the figures, it is obviously that with the increase of cooling rate, the bending strength and fracture strain of Al₂O₃/Al-4.5Cu composites are increased and the bending strength of Al₂O₃/Al-4.5Cu composites under the state of the common casting is the lowest. As the solidified rate is increased to 700μm/s, the bending strength is 597 MPa, and in comparison with the common cast state, it has a 66% improvement.

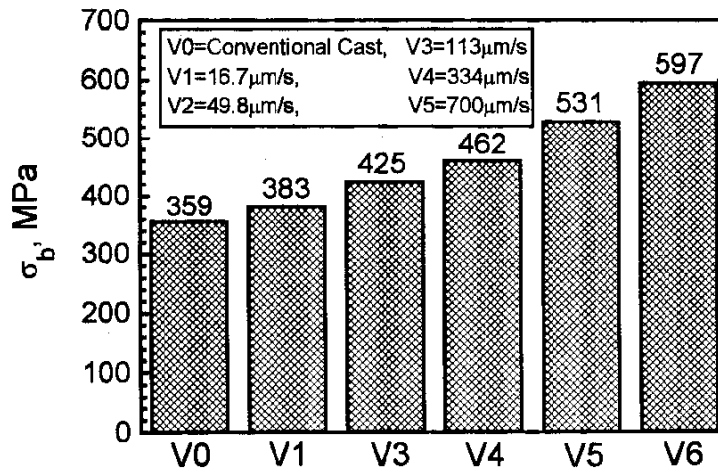


Fig.2 The bending strength of Al₂O₃/Al-4.5Cu composites

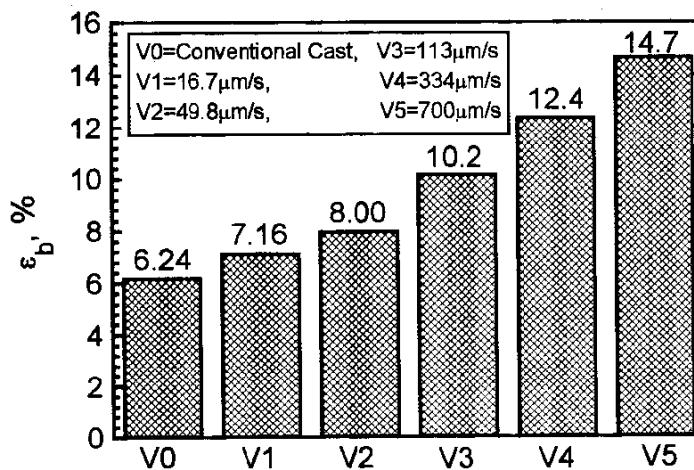


Fig.3 Fracture strain of Al₂O₃/Al-4.5Cu composites

In order to explain this phenomenon, it can be considered that, firstly, with the increase of solidification rate, the primary and secondary dendrite spacing decreased [5], it indicates that even though under directional solidification conditions the fine dendrite structure has better mechanical properties than the coarse dendrite structure [6] and the enduring life can be enhanced with the increase of the number of dendrite-per-unit cross section [6]. Secondly, with the decrease of secondary dendrites length and primary dendrite spacing, it can decrease the perpendicular boundary. Since the boundaries are weak link, so it causes cracks spread easily and the fine dendrite structures decrease the weak linked areas to a certain extent, making the primary dendrite to be lined strictly, thus blocks the spread of cracks, and improving the bending strength of the composites. Finally, with the increase of solidification rate, the distribution of Cu element in the microstructure is more uniform [5], and the dendrite segregation is eliminated, so it hinders the formation of CuAl_2 brittle intermetallic compound, improved surface energy of crack at boundary, and increases obstruction of moving dislocation. On the other hand, directional solidification dendrite are similar to fibers, so the dendrites withstand the load, and block the cracks propagate, and due to the particles are distributed among dendrites, therefore directional solidified $\text{Al}_2\text{O}_3/\text{Al-4.5Cu}$ composites can be looked as hybrid composites and also in-situ composites, these effects would further improve the bending strength of the composites.

Fig.3 showed the fracture strain of directional solidified $\text{Al}_2\text{O}_3/\text{Al-4.5Cu}$ composites at $V=700 \mu\text{m/s}$ was improved 135% in accordance common cast state. Since fracture strain is related to plastic property and the microstructure of the composites play an important role on its plastic property, if the directional solidified dendrite is fine, so the quantity of dendrite in the unit volume is increased at the same deformation, then causes the non-uniform deformation decreased, and also limits cracks due to the stress concentration. In the mean time, the finer dendrites are more flexure in the boundary, it can further block the propagation of cracks, and make the composites to bear the larger deformation before fracture.

It must be pointed out that the microstructure of directional solidified $\text{Al}_2\text{O}_3/\text{Al-4.5Cu}$ composites possess orientation, so its longitudinal properties are better than its transversal properties. This study is only dealt with the longitudinal properties of the composites which paralleling to the directional solidified direction.

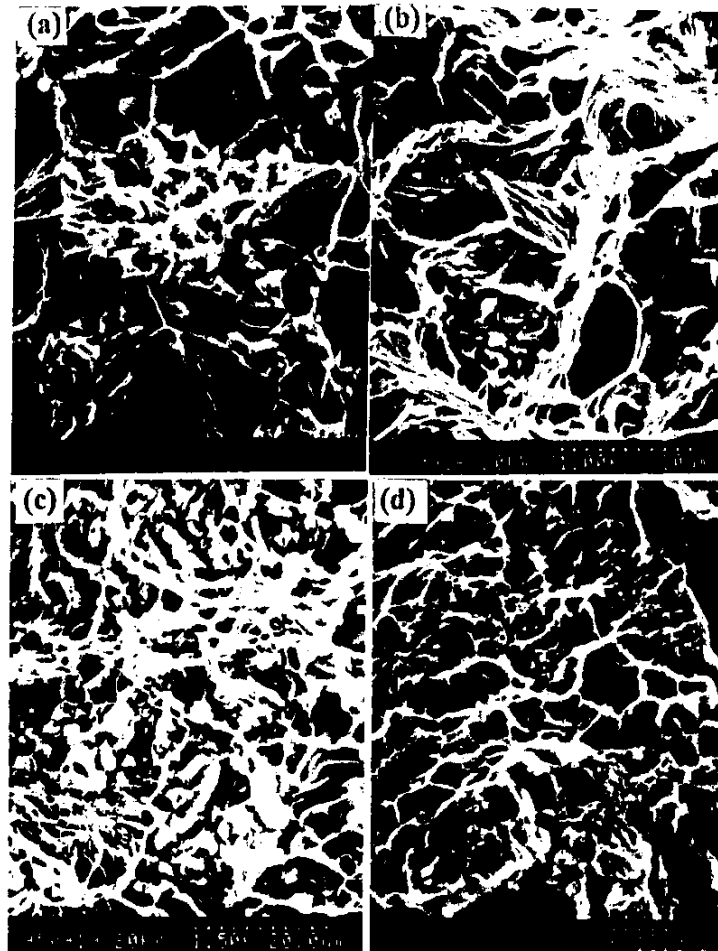
Fracture of directional solidified $\text{Al}_2\text{O}_3/\text{Al-4.5Cu}$ composites

Fig.4 showed the fracture surface of $\text{Al}_2\text{O}_3/\text{Al-4.5Cu}$ composites by Scanning Electron Micrographs. For the conventional casting $\text{Al}_2\text{O}_3/\text{Al-4.5Cu}$ composites, the crystal grains are coarse, it can be seen that the fracture of the common cast-state specimens occurs along the intervals of dendrite, and exists cleavage stages with a few tough nests; but the fractography of directional solidification $\text{Al}_2\text{O}_3/\text{Al-4.5Cu}$ composites shows high tenacity transgranular fracture, and many deep tough nests which glow in quantity with the increase of directional solidification rate. It is related with plastic deformation process and forms mainly microhole-like crystal nucleus, so that it exists small and shallow tough nests on the fracture surface.

Al_2O_3 particles may improve the microhole growth since the edges of Al_2O_3 particles offer the position of microhole growth, and the size and density of Al_2O_3 particles influence on the size of microhole, and with the increase of Al_2O_3 particles density, the size of microhole is decreased. Of course, it is not all Al_2O_3 particles can deliver nucleating positions of tough nests, as shown Fig.4, there are many particles deviating from the center of tough nests.

The work-hardening of the composites also effect on the size of tough nests, if the composites possess very large index number of the work-hardening owing to improve stress increment from yield point to breaking point, it will lead to form more microholes and make the size of tough nests smaller. Besides, strain ratio still effects on the size of tough nests, with the increase of strain ratio, makes tough nests smaller.

Actually, the formation and growth mechanism of tough nests on fracture surface of directional solidified $Al_2O_3/Al-4.5Cu$ composites are the assembly and growth of the microholes. The dislocation link assembled around Al_2O_3 particles, when the load have not exerted on the dislocation links, they are in the equilibrium state, but if the load is exerted on the dislocation links, they will move toward the interface between particles and matrix, and make the interface split into microholes. When the piled dislocations disappear, it makes the dislocation source become active and generate new dislocation links, and then form the microholes, developing to the tough nests.



(a) conventional cast (b) $V=16.7\mu m/s$ (c) $V=49.8\mu m/s$ (d) $V=700\mu m/s$
 Fig.4 Scanning electron micrographs of fracture surface of $Al_2O_3/Al-4.5Cu$ composites

CONCLUSIONS

1. The bending strength and fracture strain of $\text{Al}_2\text{O}_3/\text{Al-4.5Cu}$ composites in the common cast state case are lowest but it was increased with the increase of cooling rate on directional solidified $\text{Al}_2\text{O}_3/\text{Al-4.5Cu}$ composites. When the solidified rate was increased to $700\mu\text{m/s}$, the bending strength and fracture strain of the $\text{Al}_2\text{O}_3/\text{Al-4.5Cu}$ composites were improved 66% and 135% respectively compared with common cast case.
2. The fracture surface of $\text{Al}_2\text{O}_3/\text{Al-4.5Cu}$ composites under common cast state shows the character of brittle fracture, on the fracture surface of the composites, cleavage stages and cracks can be observed, and there were also a few tough nests. The fractography of directional solidified $\text{Al}_2\text{O}_3/\text{Al-4.5Cu}$ composites shows tenacious fracture, with the increase of directional solidification rate and the tough nests on the fracture surface become more dense and deep, since the Al_2O_3 particles played an important role for tough nests nucleation. The formation and growth mechanism of tough nests on the fracture surface are due to assembly and growth of the microholes.

ACKNOWLEDGMENT

This work was supported by the National Natural Science Foundation of China under Grant No. 59471052 and the Foundation of State key Laboratory of Metal Matrix Composites, Shanghai Jiao Tong University.

REFERENCES

1. W. Wang and F. Ajersch, *Mater. Sci. and Eng.*, Vol.187A, 1994, pp.A65-75.
2. D. J. Lloyd, *International Materials Reviews*, Vol.39, No.1, 1994, p1.
3. I. A. Ibrahim, F. A. Mohamed, E. J. Lavernia, *J. of Mater. Sci.*, Vol.26, 1991, pp.1137-1156.
4. W. Kurze, "Directional Solidification eutectic materials", Beijing: Metallurgical industry publishing house, 1989. (in Chinese)
5. S. J. Chu, "Study on the nonequilibrium solidification process of metal matrix composites", Ph.D. thesis, Shanghai, Shanghai Jiaotong University, 1996.
6. D. L. Lin and D. L. Yao, *Acta Metall. Sinica*, Vol.15A, 1978, pp.177-182. (in Chinese)

TRANSVERSE TENSILE CHARACTERIZATION OF SIC/TI-6242 FIBER-REINFORCED MMC'S WITH THE CRUCIFORM SAMPLE GEOMETRY

D.B. Miracle¹, A.F. Kalton², and T.W. Clyne²

¹*Air Force Wright Laboratory, Materials Directorate, 2230 Tenth St Ste 1, Wright-Patterson AFB, OH 45433 USA*

²*Department of Materials Science and Metallurgy, Cambridge University, Pembroke Street, Cambridge CB2 3QZ UK*

SUMMARY: The transverse strength of the interfacial region in many SiC/Ti-alloy metal matrix composites (MMC's) has been studied using single fiber cruciform-shaped samples. This sample geometry avoids the singular stress concentration which exists at the fiber/matrix interface near the free edge. The objective of this research is to extend this approach to MMC's with a high volume fraction of reinforcing fibers. Finite element modeling was used to define the sample geometry. Six-ply uniaxial composites of approximately 0.25 volume fraction of DRA/Sigma 1240 fibers in a Ti-6Al-2Sn-4Zr-2Mo (weight percent, Ti-6242) matrix were subjected to transverse loading from RT to 538°C. It was found that the interface failed as soon as the local radial stress in the interfacial region became tensile for all test temperatures, in agreement with results obtained in single fiber samples. Poisson ratio monitoring at RT showed that the principle mode of damage is the formation of internal cracks, rather than matrix plasticity.

KEYWORDS: Metal matrix composite, interface properties, transverse properties, Cruciform sample, residual stress, Ti-6242

INTRODUCTION

Fiber-reinforced metal matrix composites (MMC's) are being developed for applications in advanced gas turbine engines. While axial properties are generally adequate to meet the design requirements, the off-axis properties are yet deficient. Techniques to quantify off-axis properties typically employ straight-sided samples. Previous studies in single-fiber samples have shown that the stress concentration that exists at the intersection of the fiber/matrix interface and the sample free surface leads to premature failure in straight-sided samples, while interfaces in samples using a cruciform geometry can sustain much higher applied stresses before failure [1-3]. It has therefore been proposed that the properties determined for candidate MMC's using a conventional straight-sided sample geometry may be unnecessarily conservative for compressor ring rotors, which have no free surfaces with intersecting fibers. The objective of this work is to characterize the transverse tensile response of high volume fraction composites in samples which eliminate the influence of the cut fibers at free edges. Results for straight-sided samples and cruciform-shaped samples were compared to assess the influence of the free edge on the tensile properties.

EXPERIMENTAL

Six ply uniaxial composites consisting of a Ti-6Al-2Sn-4Zr-2Mo (weight percent, Ti-6242) plasma-sprayed matrix and DRA/Sigma 1240 SiC monofilaments were used in this study. The 1240 fiber is produced by chemical vapor deposition of SiC on a W core, and has a nominal diameter of 100 μm . The SiC is coated with $\sim 3 \mu\text{m}$ of carbon, followed by $\sim 1 \mu\text{m}$ of a TiB_{1-x} coating. The nominal volume fraction of reinforcements was 0.25. After plasma-spraying the matrix on the fiber, the six plies were consolidated at 954°C/ 103 MPa for 4 hours.

The simple cruciform geometry used for single fiber composites was modified so that the stress in the center of the cruciform was higher than elsewhere along the length of the sample (Figure 1). To achieve this, a sheet of unreinforced Ti-6Al-4V (weight percent) was diffusion-bonded to each side of the composite panel at 850°C/10 MPa for 30 minutes. After machining the profile of the sample with a wire electro-discharge machine (EDM), the Ti-6Al-4V was removed from the cruciform region of the sample, also using wire EDM. Thus, the sample is thinner in the cruciform region ($t \sim 1.5 \text{ mm}$) than elsewhere ($t \sim 3.1 \text{ mm}$). Limited testing of straight-sided samples was conducted to document the influence of the sample geometry on transverse tensile properties. These samples were prepared as above, but the width of the sample was constant at 6 mm between the two end tabs.

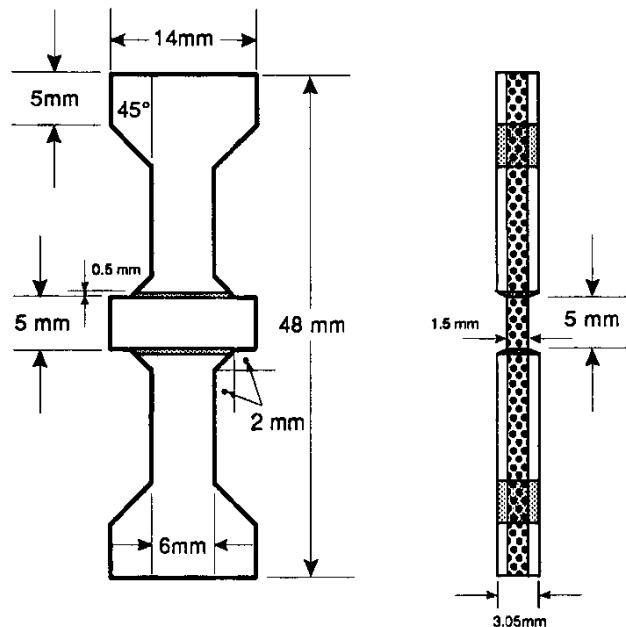


Figure 1. Cruciform sample geometry used.

Finite element modeling using the ABAQUS code was performed to quantify the stresses throughout the sample. Constitutive properties for Ti-6Al-4V were used for the face sheets, and the composite panel was modeled as a homogeneous continuum with the anisotropic properties of the MMC. Details of the modeling can be found in [4,5]. The stresses were sensibly uniform in the reduced-thickness cruciform region, and varied by less than 10% within 1.5 mm on either side of the load axis centerline. The transverse stress in the center of the cruciform was found to be 83% of the applied load divided by the nominal cross-sectional area (the uniform gage width- 6mm- times the thickness of the composite). The applied transverse stress reported elsewhere in this manuscript is determined from the remote load in this fashion. A modest stress concentration was found to exist on the face of the composite

layer just within the cruciform region, along the taper machined in the monolithic face sheet. The stress at this point was about 10% higher than in the center of the cruciform.

Tension tests were performed from RT to 538°C at a nominal strain rate of 10^{-4} /sec. Specimens were heated with a pair of quartz lamps and linear parabolic reflectors. Temperature was maintained to within $\pm 3^\circ\text{C}$ over the short gage length (~ 9 mm) of the sample. At RT, strain was measured with biaxial strain gages, which allowed determination of the strain along the loading axis and also along the fiber axis. The load-axis strain was monitored with a laser extensometer at elevated temperatures. Ti-6Al-4V flags 2 mm wide were spot-welded to the centerline of the sample as reference marks for the scanning laser extensometer. The displacement resolution of the laser extensometer was ± 1 μm . Since the displacement measured by the laser includes a contribution from the region of the sample with tapered thickness, an effective gage length was calculated for each sample tested. Strain was measured for two tests at RT using both a strain gage and laser extensometry. Within experimental error, the strain determined from the laser displacement and the calculated effective gage length matched the strain measured with the strain gage. However, there was a larger point-to-point variability in the data obtained with the laser extensometer.

The modulus and proportional stress were determined for each sample tested. In addition, Poisson's ratio was determined as a function of applied stress for samples tested at RT. This information was used to indicate the mode of deformation that was responsible for the initial nonlinearity in the stress/strain response. The magnitude of the interfacial bond strength was determined from the proportional stress and from a knowledge of the residual stress state in the composite. Limited post-test metallography was used to determine the mode and progression of damage.

RESULTS AND DISCUSSION

Representative microstructures in the as-processed condition are shown in Figure 2. A relatively fine-grained, equiaxed α/β microstructure was obtained. The fibers were not equally-spaced, and had a larger average separation between plies than within the plies. Often, adjacent fibers within a given ply were nearly touching, and this typically resulted in the formation of a matrix crack in response to the large residual hoop stresses (Figure 2(a)). Numerous radial cracks were observed in the reaction zone and the Ti-boride coating (Figure 2(b)). These cracks were typically 3-5 μm long, and did not extend into the matrix, except as noted above. The cracks were deflected at the carbon layer adjacent to the SiC fiber, and were seen to extend for a limited distance along the interface between the carbon layer and the Ti-boride coating (Figure 2(b)).

Representative stress/strain curves for each of the test temperatures are shown in Figure 3. A small amount of bending was observed; up to an axial strain of less than 0.1% at RT, and up to 0.2% at elevated temperatures. This effect was removed in the curves below. A gradual decrease in the slope of the curve occurred following the linear region. Inelastic deformation was over 1% at elevated temperatures, and is less than 0.5% at RT (Figure 3). Most samples showed some evidence of localized inelasticity just before sample failure, and this feature was most pronounced at 538°C. Fracture occurred directly through the strain gage in the sample tested at RT shown in Figure 3, resulting in the large local strain at nearly constant stress just before fracture. In the second sample tested at RT, final fracture did not pass through the strain gage, and the stress was seen to increase at a relatively constant strain value just prior to failure (Figure 4). The modulus decreased with increasing temperature at a higher rate than anticipated from a simple iso-strain rule of mixtures (Figure 5). Significant residual tensile stresses exist in the matrix [6], even at the highest test temperature, and this may contribute

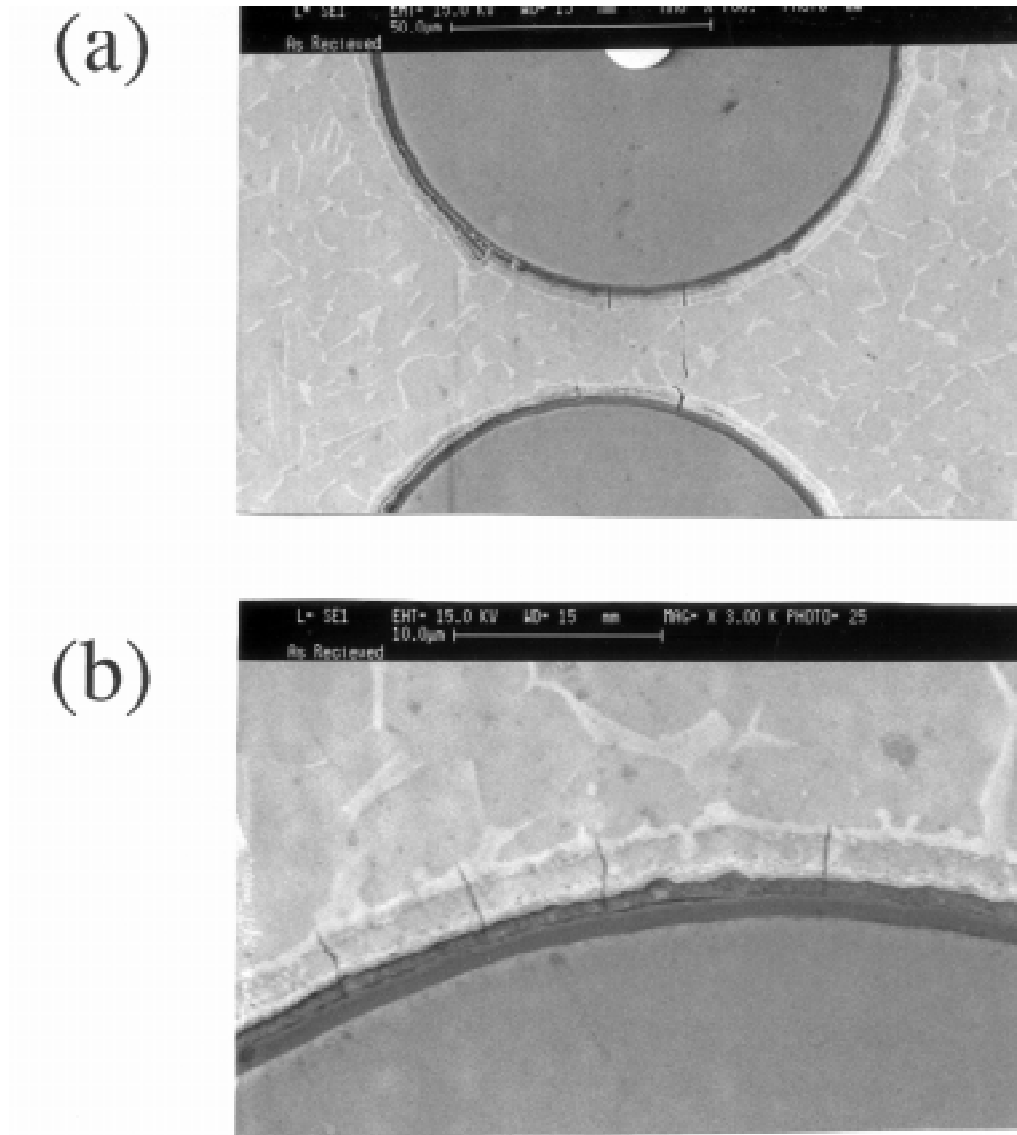


Figure 2 *Microstructures of the as-processed composites. Radial cracks in the reaction zone and the Ti-boride coating are shown in (a), along with load-axis cracks in the matrix between two closely-spaced fibers. A close-up of the radial cracks are shown in (b), the deflection of the radial cracks along the Ti-boride/carbon coating interface can be seen.*

to the higher composite compliance. The damage present in the as-processed condition may contribute to the reduced modulus of the samples. However, it is not clear why a larger reduction is observed at elevated temperature, while the RT modulus is very close to the rule-of-mixtures modulus.

The Poisson ratio for the samples tested at RT show initial values close to 0.5, in agreement with the limited degree of bending observed in the samples. However, a nearly constant value of about 0.36 was observed over most of the elastic range. The Poisson ratio began to decrease significantly just above the proportional stress. This behavior has been correlated

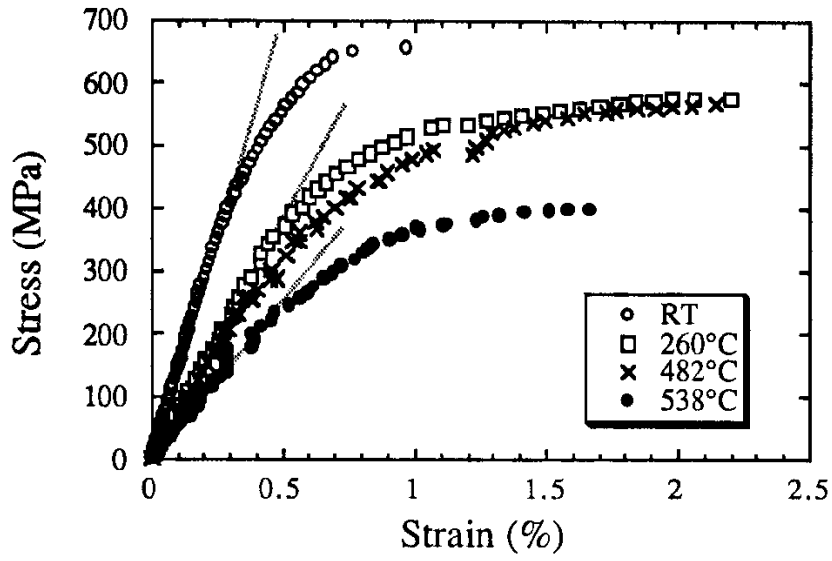


Figure 3 Representative stress/strain curves for cruciform samples tested from RT to 538°C.

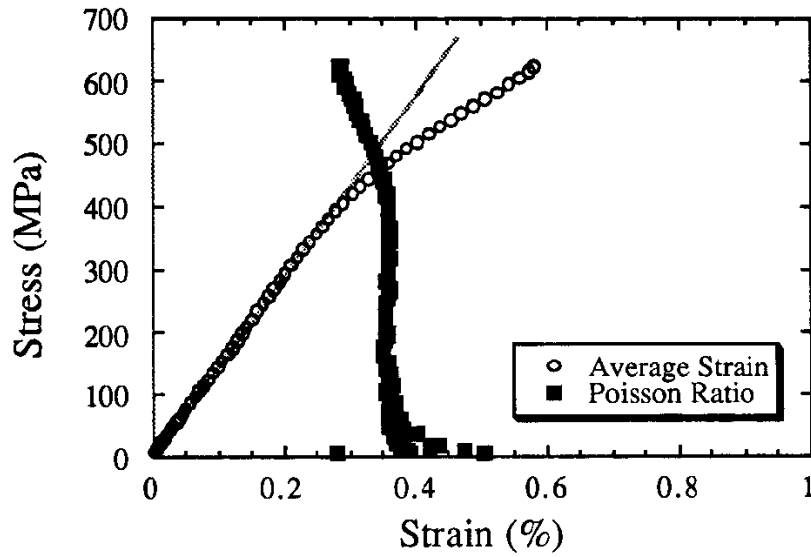


Figure 4 The Poisson ratio of a cruciform sample tested at RT, plotted as a function of the applied stress.

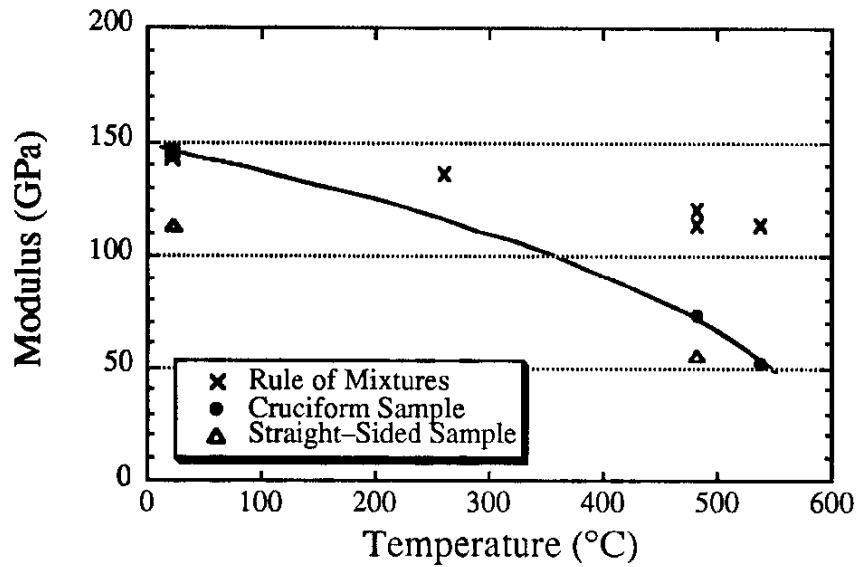


Figure 5 Modulus v. temperature for the samples tested. The data are compared to a simple iso-strain rule of mixtures.

correlated with the formation of cracks as the dominant mechanism of inelasticity [7]. The onset of inelasticity in single-fiber transverse samples has been established to occur as a result of interface debonding [1–3]. Micrographs of samples tested to failure at RT clearly show that the principle mode of inelastic deformation is the extension of cracks at the interface (Figure 6). These cracks extended from radial cracks that presumably existed prior to the application of the mechanical load. In addition, the matrix cracks that formed between closely-spaced fibers became more common. It is important to note that these cracks were always aligned parallel to the loading axis due to the specific orientation of the closely-spaced fibers with respect to the tensile axis. Final fracture occurred by the linking of adjacent debonded fibers (Figure 7). At 482°C, the load-axis cracks became longer and more numerous (Figure 8), consistent with the larger degree of inelastic deformation at this temperature. As at RT, cracks normal to the load axis were very rare, and were generally only seen in the plane of final fracture. This suggests that catastrophic sample failure occurs soon after such a crack links two adjacent debonded fibers. This may be the mechanism of inhomogeneous inelastic deformation that immediately precedes sample failure.

The proportional stress decreased with increasing temperature, as shown in Table 1 and Figure 9. The proportional stress has been taken as the average remote debond stress in the interfacial region. The local stresses in the interfacial region around the fiber periphery are given from the applied stress σ_{appl} by the two equations shown below [3]:

$$\sigma_N = (K_N \sigma_{\text{appl}}) \cos 2\theta + \sigma_{\text{res}} \quad (1)$$

$$\tau_{\text{tan}} = (K_T \sigma_{\text{appl}}) \sin 2\theta \quad (2)$$

where θ is the angle with respect to the load axis, σ_N is the local normal stress at θ , τ_{tan} is the tangential shear stress at θ , and K_N (typically ~ 1.3) and K_T (typically ~ 0.6) are the stress concentration factors for normal and tangential shear stresses, respectively. The magnitude of

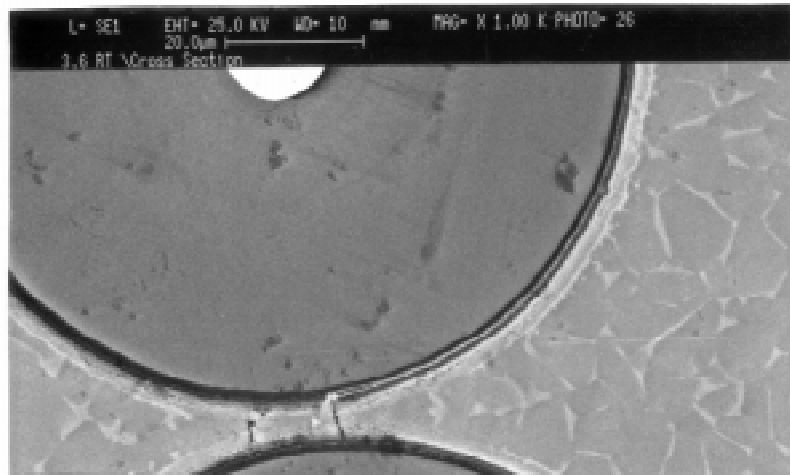


Figure 6 Extension of an interface crack along the Ti-boride/carbon coating interface after testing to failure at RT. The load axis is vertical.

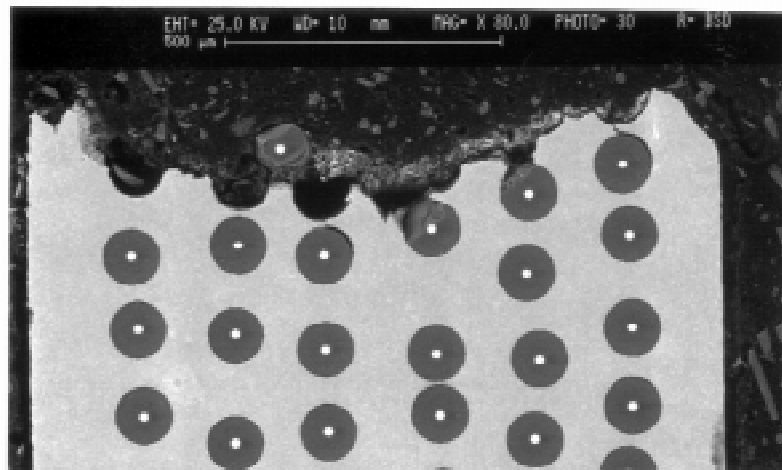


Figure 7 Fracture cross-section of a sample tested to failure at RT. The load axis is vertical.

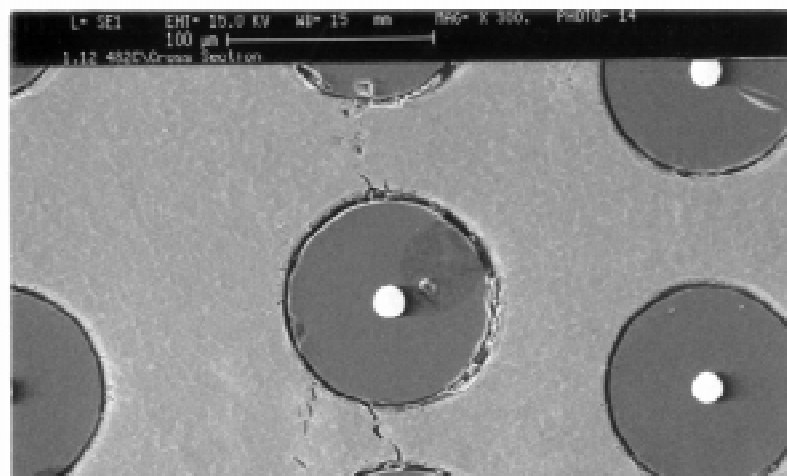


Figure 8 Growth of load-axis cracks in a sample tested at 482°C. The load axis is vertical.

Table 1 Tensile Data for Cruciform and Straight-Sided Samples

Temperature (°C)	Proportional Stress (MPa)	Failure Strain (%)	Modulus (GPa)
RT	298	0.77	146
RT	317	0.58	145
RT (Straight)	138	0.51	113
260	297	2.20	Not Determined
482	213	2.44	72
482	185	2.18	73
482 (Straight)	110	0.61	55
538	162	1.73	51

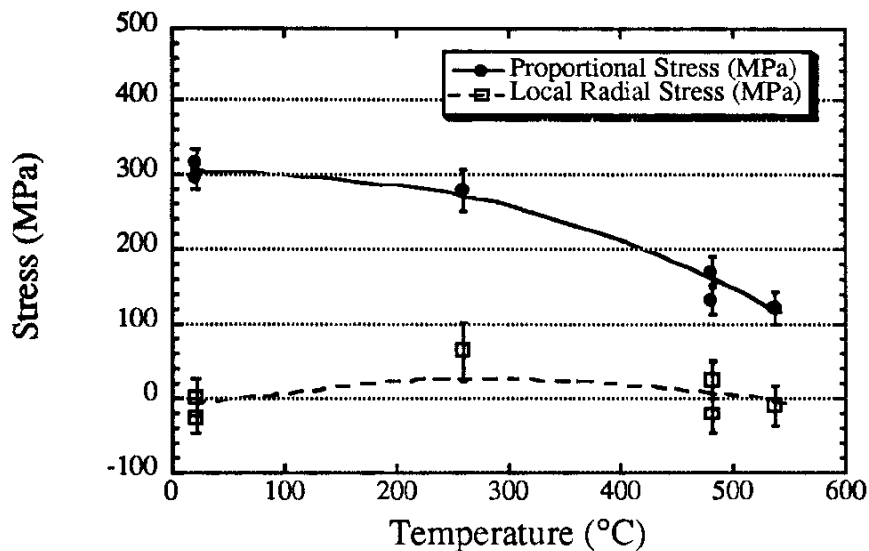


Figure 9 Temperature dependence of the debond stress, and the resulting values of the interfacial bond strength.

the local normal stress depends strongly on the radial residual stress (σ_{res}). These equations are based on extensive finite element analysis of the local stresses around single fibers embedded in a metal matrix [8].

It has been proposed that failure of weak interfacial coatings, such as Trimarc (Amercom Company, USA) and the DRA/Sigma 1240 fibers initiates in response to the tangential shear stresses at $\theta = 45^\circ$ [8,9]. However, the macroscopic displacements associated with this mechanism are very small, and so a macroscopic inelastic response is not anticipated until normal separation of the interface occurs. This failure mode occurs under the influence of the local normal stress, which is maximum at $\theta = 0^\circ$ (Equation 1). The local stress at the interfacial region can therefore be related to the applied stress using Equation 1 above. The applied stress was taken as the proportional stress, and the residual radial stress was calculated from the data provided in [6]. The results are plotted in Figure 9, and clearly show that

interface separation occurs as soon as the local normal stress becomes tensile. The single data point at 260°C falls outside this trend, and requires further verification.

Earlier results obtained for the interfacial strength of the DRA 1240 fiber in a Ti-6Al-4V matrix have shown that the interfacial region has no significant chemical bond [9,10]. The current results show the same general mechanical response as observed in single fiber samples; that is, a gradual decrease in the slope of the stress *v.* strain curve at an applied stress that is just required to overcome the radial residual stress. Thus, the response of the interfacial region is essentially independent of the matrix composition for a given class of alloys (in this case, Ti-based alloys). The principal contribution of the matrix alloy is to establish the magnitude of the residual stress. The residual stresses are higher in the current system than for the Ti-6Al-4V single fiber composite, and so the damage observed in the as-received condition here may not exist in the Ti-6Al-4V composites. Microstructural observations of SiC (1240)/Ti-6Al-4V samples in the as-processed condition are currently underway to address this issue.

Each of the properties determined (proportional stress, modulus, and failure strain) for the straight-sided samples are lower than the values obtained in the cruciform geometry (Table 1, Figure 5). It is proposed that these results occur in response to the stress concentration that exists near the free surface. However, only limited data is available, and so more extensive testing is required to verify this result. It will be important to establish the response of straight-sided samples as a function of sample width. Such studies are proposed for future research.

CONCLUSIONS

The following conclusions are drawn from this study:

1. Significant damage exists at the interfacial region of the SiC (1240)/ Ti-6Al-2Sn-4Zr-2Mo composites in the as-consolidated condition. This damage occurs as radial cracks through the reaction zone and the Ti-boride coating. The cracks are arrested at the matrix, and are deflected along the Ti-boride/carbon interface. Matrix cracks are formed between fiber centers (ie, parallel to the loading axis) when two fibers are close to one another.
2. Macroscopic inelasticity is observed in response to the growth of this pre-existing damage. The principle mode of the damage is the growth of the cracks along the Ti-boride/carbon interface, and the growth of the load axis cracks. This macroscopic inelasticity is not observed until the local normal stress in the interfacial region becomes tensile.
3. The critical failure event is the formation of a crack normal to the loading axis which links two adjacent fibers. This event leads to immediate localization of the damage, resulting in rapid sample failure.
4. Straight-sided samples with an identical process history and microstructure exhibit reduced modulus, proportional stress, and strain to failure. This occurs as a result of the large stress concentration that exists in the interfacial region at the sample free surface.

ACKNOWLEDGEMENTS

The authors would like to acknowledge the following individuals: Dr. A. Wisbey (DRA/Farnborough) for diffusion-bonding the unreinforced face sheets to the composite panels; R. Parkins and B. Whitmore for assistance with the experimental equipment; R. Jenkins for machining the samples; and E. Warwick for assistance with the micrographs.

REFERENCES

1. D.B. Gundel, B.S. Majumdar, and D.B. Miracle; "Evaluation of the Transverse Response of Fiber-Reinforced Composites Using a Cross-Shaped Sample Geometry", *Scripta Metall. Mater.*, **33**, 1995, pp 2057-2065
2. S.G. Warrier, D.B. Gundel, B.S. Majumdar, and D.B. Miracle; "Interface Effects on the Micromechanical Response of a Transversely Loaded Single Fiber SCS-6/Ti-6Al-4V Composite", *Metall. Mater. Trans.*, **27A**, 1996, pp 2035-2043
3. D.B. Gundel, S.G. Warrier, and D.B. Miracle; "The Interface Debond Stress in Single and Multiple SiC Fiber/ Ti-6Al-4V Composites Under Transverse Tension", *Acta Mater.*, In Press
4. A.F. Kalton, D.B. Miracle, and T.W. Clyne; "The Effect of Interfacial Strength on the Response of Ti MMC's to Single Fibre Push-Out and Transverse Tensile Testing", in *Ceramic and Metal Matrix Composites*, (eds. M. Fuentes, J.M. Martinez-Esnaola, and A.M. Daniel) Proceedings 1st Int'l Conf., Trans Tech Pub., Switzerland, 1996, pp 659-669
5. A.F. Kalton, P. Feillard and T.W. Clyne; "The Effect of Interfacial Structure on the Failure of Long Fibre Reinforced Titanium Under Transverse Loading", in *High Performance Materials in Engine Technology*, (ed. P. Vincenzini), Techna Srl., Florence, Italy, 1995, pp 285-292
6. P. Rangaswamy, M.A.M. Bourke, P.K. Wright, N. Jayaraman, E. Kartzmark, and J.A. Roberts; "The Influence of Thermal-Mechanical Processing on Residual Stresses in Titanium Matrix Composites", *Mat. Sci. Eng.*, Accepted for publication
7. B.S. Majumdar and G.M. Newaz; *Phil. Mag. A*, **66**, 1992, pp 187-212
8. S.G. Warrier, B.S. Majumdar, D.B. Gundel and D.B. Miracle, "Implications of Tangential Shear Stress Induced Failure During Transverse Loading of SiC/Ti-6Al-4V Composites," *Acta Materialia*, Submitted for publication
9. D.B. Miracle, D.B. Gundel, and S. Warrier; "Interfacial Structure and Properties for the Design of Fiber-Reinforced Metal Matrix Composites", in *Processing and Design Issues in High Temperature Materials*, (eds. N.S. Stoloff and R.H. Jones), TMS, Warrendale, PA, In Press
10. D.B. Gundel and D.B. Miracle, "The Influence of Interface Structure and Composition on the Response of Single-Fiber SiC/Ti-6Al-4V Composites to Transverse Tension," *Appl. Compos. Mater.*, Submitted for publication

FRACTURE TOUGHNESS EVALUATION OF HYBRID METAL MATRIX COMPOSITES

J. I. Song¹ and K. S. Han²

¹ *Intelligent Machine Research Team, RIST, P.O. Box 135, Pohang, 790-600, Korea*

² *Dept. of Mechanical Engineering, POSTECH, San 31 Hyoja-Dong, Pohang, 790-784, Korea*

SUMMARY: The objective of this study is to evaluate comparison of fracture toughness between static and dynamic behavior in various metal matrix composites(MMCs) fabricated by squeeze infiltration method. A lot of MMCs which comprise various matrix alloy, volume fractions, and types of reinforcements have been tested. Static and dynamic fracture toughness of MMCs remarkably increased due to the addition of ceramic reinforcements. Specifically dynamic fracture toughness was slightly decreased compared with static fracture toughness because of the dynamic loading effect. In this work, major effects which influence toughness could be include the type of reinforcement, volume fraction and combination of reinforcement, and the matrix alloy. And notch fracture toughness which is not produced the pre-crack was discussed.

KEYWORDS: hybrid metal matrix composites, squeeze infiltration method, dynamic fracture, toughness, static fracture toughness, notch fracture toughness

INTRODUCTION

Recently, there has been an effort to use discontinuously reinforced metal matrix composites for engineering structural applications. These composites can offer distinct technological advantages over continuously reinforced MMCs including fabricability using squeeze infiltration method, as well as cost advantages[1-3]. A lot of studies on metal matrix composites(MMCs) have been done but there have been very limited structural applications so far since significant problems remain unresolved, such as complexity of processing, high costs, low fracture toughness and low strain to failure[4, 6, 7].

Many studies have been undertaken concerning the static fracture toughness of aluminum alloys with either SiC particulate or whisker reinforcement. Few studies on comparison between the static and dynamic fracture toughness behavior have been available in the literature. These have been done mainly on the fracture toughness of discontinuous MMCs reinforced by the addition of a single reinforcement, such as Al₂O₃, SiC, and C, etc.[2, 4 - 11]. However, little attention was paid to the effect of hybrid metal matrix composites on fracture toughness behavior. Moreover, reinforcement with a single fiber has been the major subject of research and development, while reinforcement with hybrid fibers which consists of two or more reinforcements has not widely been studied. Evaluation of fracture toughness of short fiber reinforced metal matrix composites becomes important for application as structural materials.

In this study, therefore, the authors conducted the experimental study to investigate the fracture toughness behavior of hybrid MMCs, and also to compare the behavior of static and dynamic fracture toughness. In addition, the plane strain and notch fracture toughness for MMCs were evaluated to find the effect of notch at the crack tip.

EXPERIMENTAL PROCEDURE

Materials and Fabrication

For the fabrication of composite materials, various reinforcements such as alumina, SiC whisker and carbon fiber were used, and Al6061 wrought product and cast Al alloy of AC2B and AC8A were used as a matrix as indicated in Table 1. Typical specifications of reinforcements used are listed in Table 2 [13, 14]. After preparation of preform by vacuum equipment, and then we have fabricated the MMCs by using squeeze infiltration method. Casting ingots for mechanical and fracture toughness tests were given a T6 heat treatment.

Table 1. Specification of various reinforcements used

Material	Chemical composition(w/o)									
	Si	Cu	Mg	Ni	Fe	Mn	Zn	Ti	Pb	Al
AC2B	6.0	3.0	0.4	0.3	0.9	0.4	0.09	0.1	0.15	rem.
AC8A	12.7	1.1	0.9	1.57	0.8	0.1	0.12	0.15	0.04	rem
Al6061	6.0	0.2	1.0	-	0.6	0.1	0.2	0.1	-	rem

Table 2. Specification of various reinforcements used

Material	Density (g/cm ³)	Diameter (mm)	Length (mm)	Aspect ratio(l/d)	T. S (GPa)	E (GPa)
Al ₂ O ₃	3.3	4	150	38	2.0	310
SiC _w	3.2	0.6	15	25	3~14	600
Carbon	1.9	16	144	8.2	1.9	280

Mechanical and Fracture Toughness Tests

Room temperature tensile tests were performed with a universal testing machine. Tensile tests were displacement controlled and the displacement rate was 0.5mm/min. To measure strains, an extensometer with a gage length of 12.5mm was attached in the center of the gage length to round bar specimen. Round tensile specimens with 6.5mm diameter and 65 mm length were machined perpendicular to the direction of the applied pressure.

Static fracture toughness test was carried out at room temperature according to ASTM E399 and 5ton capacity hydraulic testing machine was used. In the case of matrix alloy, we performed the CTS test using the single specimen J-integral test method according to ASTM standard E813. Dynamic fracture toughness test was carried out at room temperature and 300 J capacity instrumented Charpy impact testing machine was used. The fatigue tests for the

induced pre-crack were conducted under constant load amplitude with a R value of 0.1 using a sinusoidal wave form at a frequency of 10 Hz. Crack length measurements were performed using a traveling light microscope (with resolution < 5mm) on the surface of the specimens.

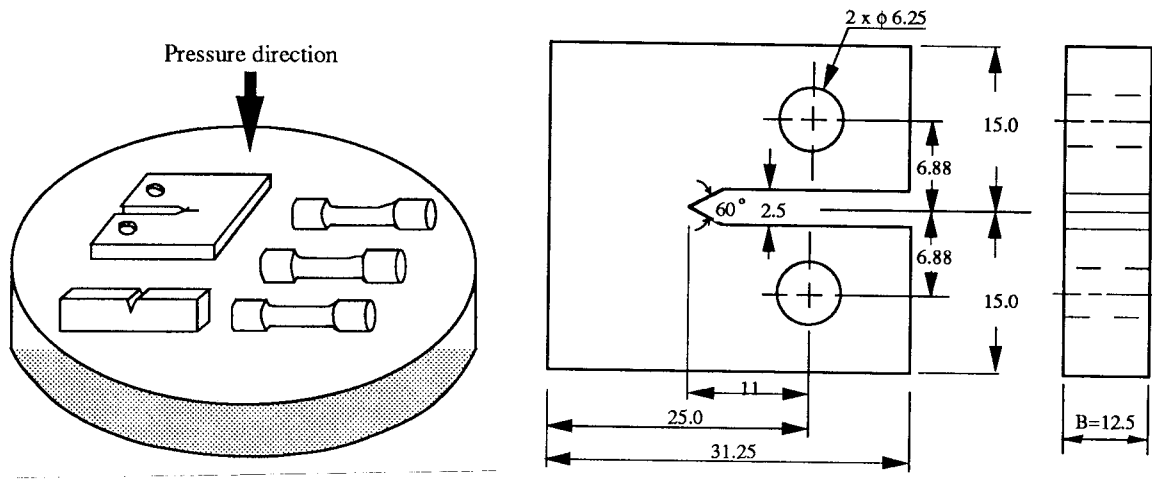
Using P_Q and P_m obtained from experiment, static and dynamic fracture toughness are calculated as followed equation (1) and equation(2), respectively.

$$K_Q = P_Q / B W^{1/2} \cdot Y(a/W) \tag{1}$$

Where, P_Q is 5% offset of maximum load , B and W are thickness and width of specimen, respectively, and Y (a/W) is configuration coefficient of CT specimen.

$$K_{Id} = P_m \cdot S / B W^{3/2} \cdot Y(a/W) \tag{2}$$

Where, P_m is maximum load after impact loading, and S is span of specimen, Y (a/W) is configuration coefficient of 3-point bending specimen.



a) Specimen orientation

b) Static toughness test specimen

Fig. 1 Orientation from cast ingot and dimension of fracture toughness test specimen

Test specimens were machined from cast ingots parallel to the applied pressure direction as shown in Fig.1(a) The static fracture toughness tests were performed on compact tension (CT) type specimens of 25 mm width and 12.5 mm thickness as shown in Fig. 1(b) and the dynamic fracture toughness tests were performed on 3-point bending type specimens of 55 mm width and 10 mm thickness.

RESULTS AND DISCUSSION

Static Fracture Toughness

The various manufacturing methods of composites currently in use dictate that large microstructural variations between different materials are to be expected. This means that fracture toughness behavior of MMCs might be sensitive to actual manufacturing methods, such as the squeeze casting and powder metallurgy route. Fracture toughness behavior of MMCs is associated not only with the matrix, but also affected by some other factors, such as type, size and orientation of reinforcement. Therefore, we have focused on effects of controlling a complexity interaction between the matrix alloy and reinforcement on fracture toughness of short fiber reinforced MMCs.

Table 3 summarizes the results of static and dynamic fracture toughness experimented. We have discussed in three types of metal matrix composites which is used each different matrix alloy as follows. In the case of AC2B based MMCs, firstly, plane strain fracture toughness (K_{1C}) of alumina and hybrid composites was decreased about 50% compared with that of matrix alloy. Comparison of fracture toughness values between Al_2O_3 -15%/Al and Al_2O_3 -12%/C-3%/Al composites were little different as showed 45% and 47%, respectively. We generally understand that mechanical properties of short fiber reinforced metal matrix composite are improved over matrix alloy because of the addition of ceramic reinforcement. Ductility of MMCs, however, decreases remarkably since ceramic reinforcements in composite restrain to deform a matrix alloy. Static fracture toughness of Al_2O_3 /C/Al composite showed greater than that of Al_2O_3 /Al composite. This results seem to be a similar tensile properties, in which elongation of Al_2O_3 /C/Al composite is improved over Al_2O_3 /Al composite. And ductility of alumina composite was decreased with the increase of volume fraction, so that elongation of Al_2O_3 -20%/Al composite was decreased up to 9% compared with that of Al_2O_3 -15%/Al composite. Consequently, reduction of ductility in composites resulted in the deterioration of fracture toughness.

In the case of AC8A based MMCs, static fracture toughness test was performed with notch specimen since AC8A matrix alloy with elongation of 0.3% was very hard to produce the fatigued pre-crack. Therefore, strictly speaking, fracture toughness of AC8A based MMCs must be defined as a fracture toughness (K_C) rather than plane strain fracture toughness (K_{1C}). The static fracture toughness (K_C) of Al_2O_3 -15%/Al and Al_2O_3 -20%/Al composites was decreased up to 27% and 38% respectively compared with that of AC2B matrix alloy. AC8A based MMCs, however, showed less reduction rate than AC2B and Al6061 Al based MMCs. This results are originated in characterization of AC8A Al matrix alloy which has a low strain to failure. It means that AC8A aluminum alloy is not proper to structural materials. Compared amounts of fibers, fracture toughness of Al_2O_3 -20%/Al composites was decreased by 17% over that of Al_2O_3 -15%/Al composites. The increase of volume fraction in MMCs indicates the decrease of fracture toughness due to a low ductility.

Al 6061 based MMCs deals with three effects including hybrid, volume fraction, and notch on their fracture toughness. As mentioned before, static fracture toughness of Al_2O_3 -15%/Al and Al_2O_3 -20%/Al composites was remarkably decreased compared with that of matrix alloy, and was decreased about 20% with the increase of volume fraction. Static fracture toughness of Al_2O_3 /SiC_w/Al hybrid composites showed 14% lower than that of Al_2O_3 -20%/Al composites. Consequently, Al_2O_3 /SiC_w/Al composites appears to be more effective in strength than Al_2O_3 /Al composites[12]. Fracture surfaces of Al_2O_3 /SiC_w/Al composites show a different

type from those of Al₂O₃/Al composites. Overall, the dimple size of fracture surfaces in the hybrid composite appeared much smaller than dimple size of Al₂O₃/Al composites. This fineness of microstructure in Al₂O₃/SiC_w/Al composites is more effective in strengthening than in Al₂O₃/Al composites. FCG rate curves in composites, however, exist over a narrow range of ΔK since the K_{1C} values of MMCs are substantially lower than that of Al matrix alloy. On the other hand, the notch fracture toughness (K_{1C,N}) of Al₂O₃-15%/Al and Al₂O₃/SiC_w/Al composites showed 9% and 13% greater than plane strain fracture toughness (K_{1C}) which is produced the pre-cracked at the crack tip notch. Consequently, notch fracture toughness was increased about up to 10% over plane strain fracture toughness.

Table 3. Results of fracture toughness for various composites

Materials	Fracture Toughness(MPa√m)			
	Static toughness		Dynamic toughness	
	K _{1C}	K _{1C,N}	K _{1d}	K _{1d,N}
AC2B	2	-	1	-
Al/Al ₂ O ₃ -15%	16.7	-	18.8	-
Al/Al ₂ O ₃ -10%/C-5%	1	-	19.5	-
Al/Al ₂ O ₃ -20%	15.3	-	3	-
AC8A	-	4	-	1
Al/Al ₂ O ₃ -15%	-	1	-	16.8
Al/Al ₂ O ₃ -20%	-	1	-	2
Al6061	29.5	-	4	-
Al/Al ₂ O ₃ -15%	17.8	-	26.5	-
Al/Al ₂ O ₃ -15%(N)	-	5	-	27.0
Al/Al ₂ O ₃ /SiC _w (15%)	15.3	-	23.7	-
Al/Al ₂ O ₃ /SiC _w (N)	-	17.6	-	22.6
Al/Al ₂ O ₃ -20%	14.2	-	18.4	-

* N means the notched fracture toughness specimen

In consequence, it can be known that static fracture toughness of MMCs was closely related with the ductility of material itself, as well as volume fraction, types of reinforcements, and matrix alloy. This effect is associated with the more extensive matrix regions surrounding the larger diameter reinforcements which enhance the toughness by producing additional constraint on the fracture event through matrix plastic deformation. Our results are showed similar behavior to Flom and Arsenault[4]. They reported that crack initiation fracture toughness did not depend on SiC particle size and crack growth fracture toughness increases as the size of the SiC particle increase. And notch fracture toughness values show within 10% of the plane strain fracture toughness, K_{1C}. Our results agree with Crowe's results[7] which reported that the apparent fracture toughness fits the relation $K_{1C}(\rho) = K_{1C}(1 + \rho/2c)^{3/2}/(1 + \rho/c)$.

Dynamic Fracture Toughness

The fracture toughness must be evaluated under the dynamic loading condition, when the materials are used for structures such as a pressure vessel that are desired to a higher safety and taken into account of the dynamic loading effect. Dynamic fracture toughness should be needed to an effort to use discontinuously reinforced metal matrix composites for engineering structural applications.

As listed in Table 3, we will discuss the dynamic fracture toughness behavior experimented, as follows. Fig. 2 shows a typical plot of relations between dynamic load vs. time after impact tests, in which the computer aided instrumented Charpy impact testing(CAI) system is used. From P_m of this graph and equation (1), we calculated the dynamic fracture toughness(K_{1d}).

In the case of AC2B based composite systems, dynamic fracture toughness(K_{1d}) of Al_2O_3/Al and $Al_2O_3/C/Al$ composites was decreased about 40% compared with that of matrix alloy. K_{1d} of $Al_2O_3/C/Al$ hybrid composites improves by 5% over that of Al_2O_3/Al composites. This results are well reflected in elongation of carbon hybrid composites, which is more effective in toughening than only alumina composites. The effect of carbon fibers on the fracture toughness characteristics in the $Al_2O_3/C/Al$ composites, however, appears slightly improved.

Fig. 3 shows the SEM photographs of (a) Al_2O_3/Al and (b) $Al_2O_3/C/Al$ composites at near crack tip after impact loading. The fracture surface morphology of Al matrix appears widely dimpled, a so called, ductile fracture. The fracture surface morphology of both Al_2O_3/Al and $Al_2O_3/C/Al$ composites appears to be similar. Specifically, the surface morphologies of

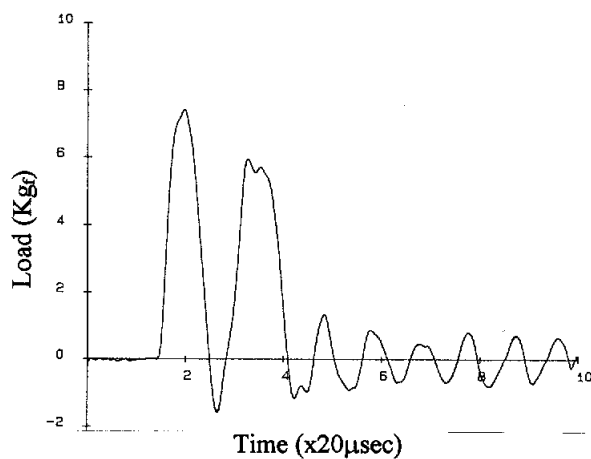


Fig. 2 Typical plot of relations between load vs. time for Al_2O_3/Al composites

$Al_2O_3/C/Al$ composites are far less rough since Al_2O_3/Al composites does not contain carbon fibers. Fracture morphologies of both Al_2O_3/Al and $Al_2O_3/C/Al$ composites appear essentially unchanged. However, the dimple size of matrix clearly increases with increasing fiber size. This dimple pattern could be affected a fracture toughness for each material.

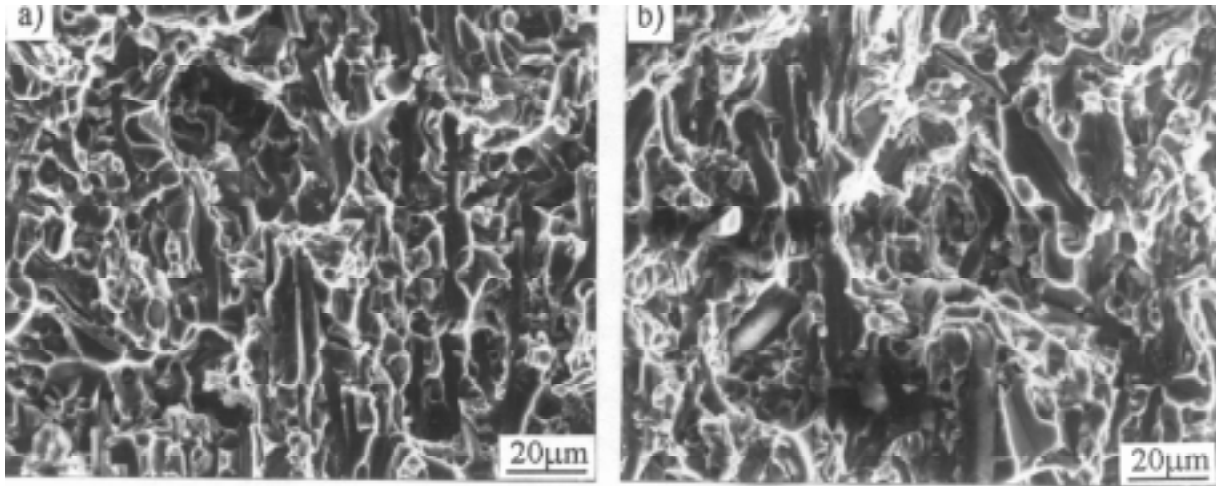


Fig. 3. SEM photographs of (a) $\text{Al}_2\text{O}_3/\text{Al}$ and (b) $\text{Al}_2\text{O}_3/\text{C}/\text{Al}$ composites

In the case of AC8A based MMCs, $K_{1d,N}$ of $\text{Al}_2\text{O}_3/\text{Al}$ composites was decreased about 20 - 30% over matrix alloy. $K_{1d,N}$ of alumina composites was decreased with the increase of volume fraction due to a low ductility. And in the case of A6061 based MMCs, we studied Al6061 based MMCs on the effect of volume fraction, notch and hybrid. Firstly, hybrid effect of $\text{Al}_2\text{O}_3/\text{SiC}_w/\text{Al}$ composites on the dynamic fracture toughness resulted in the decrease of 10% than alumina alone. Pre-cracked dynamic fracture toughness ($K_{1d,N}$) and notch fracture toughness (K_{1d}) of $\text{Al}_2\text{O}_3/\text{Al}$ composites are little different. These are indicated similar behavior to dynamic fracture toughness of $\text{Al}_2\text{O}_3/\text{SiC}_w/\text{Al}$ composites. Consequently, this means that loading speeds may not much affect dynamic fracture toughness behavior.

Fig. 4 shows relationships between static and dynamic fracture toughness for both (a) AC8A and (b) Al6061 based composites. As shown in Fig.4(a), the static fracture toughness of AC8A matrix and composites under quasi static loading rate of $1.23 \text{ MPa}\sqrt{\text{m}}/\text{sec}$ increases about 10% over those of the dynamic fracture toughness under fast loading rate of $5 \times 10^6 \text{ MPa}\sqrt{\text{m}}/\text{sec}$. The results are also consistent with showing a rather large increase in fracture toughness accompanying higher loading rates. On the basis of Duffy's model[9], it can be described that the increase in fracture toughness at the higher rates is due to a combination of an increase in the yield strength and fracture strain at the higher rates. The dynamic fracture toughness of a alumina(Al_2O_3) reinforced aluminum alloy is found to decrease as the volume fraction of alumina increase. The dynamic fracture toughness of a alumina(Al_2O_3) reinforced aluminum alloy is found to decrease as the volume fraction of alumina increase. As shown in Fig.4(b), K_{1C} and K_{1d} values show a large difference as the ductility of matrix alloy increase.

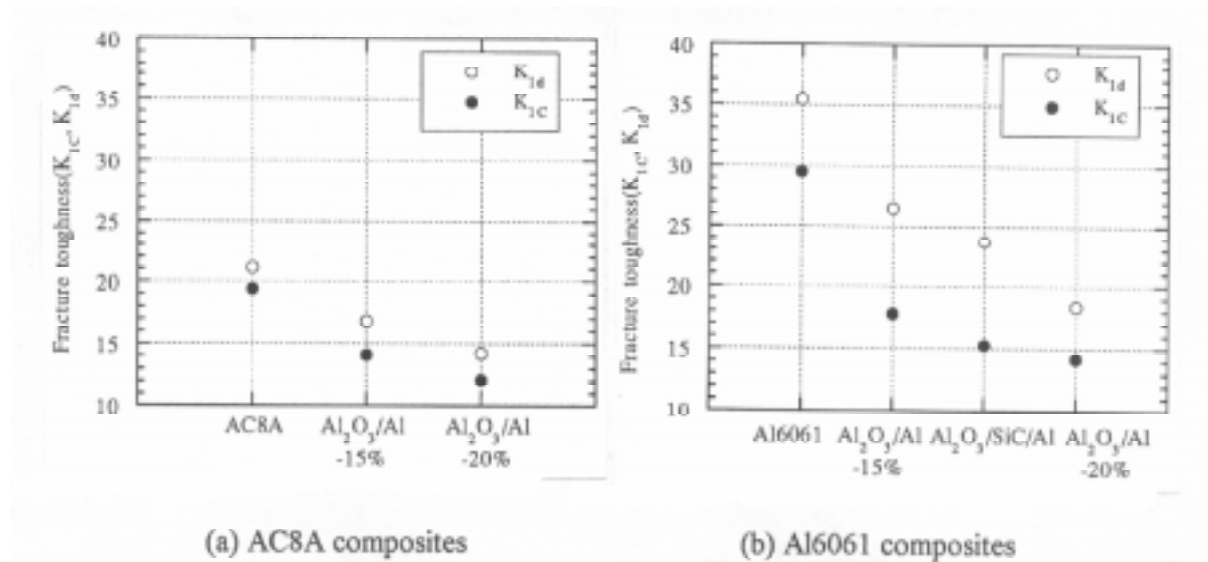


Fig. 4 Relationships between static and dynamic fracture toughness for both AC8A and Al6061 based composites

From these results, fracture toughness (static and dynamic) behavior of MMCs is associated not only with the matrix, but also affected by some other factors, such as type, size and orientation of reinforcement. In addition, the fracture toughness of ceramic reinforced MMCs is controlled by a complexity interaction between the matrix alloy and reinforcement. No single parameter appears to be capable of describing the full toughness response of MMCs.

The poor toughness of MMCs derives from i) a low initiation energy for fracture as a result of their high elastic modulus and low failure strains and (ii) a low propagation energy. Also, it is important to choose fibers of reinforcements for the development of hybrid metal matrix composites whether effects of hybrid reinforcement is always improved all of their engineering properties or not. Moreover, it is possible to improve the fracture toughness of these MMCs by the use of higher failure strain reinforcements and by increasing the propagation energy by the introduction of additional energy absorbing mechanisms such as pull out and reinforcement and matrix debonding.

CONCLUSIONS

In this study, the characterizations of static and dynamic fracture toughness behavior in various metal matrix composites were evaluated. These results can be summarized as follows:

- 1) The static fracture toughness (K_{1d}) of MMCs is found to decrease as the volume fraction of alumina increase. Reduction of ductility in composites resulted in the deterioration of fracture toughness. K_{1d} of $Al_2O_3/C/Al$ hybrid composites slightly improves over that of Al_2O_3/Al composites. Notch fracture toughness ($K_{1c,N}$) of MMCs was increased about up to 10% over that of plane strain fracture toughness (K_{1c}). Major effects which influence toughness could be found the type of reinforcement, volume fraction and combination of reinforcement, and the matrix alloy.
- 2) The dynamic fracture toughness (K_{1d}) of MMCs is found to decrease as the volume fraction of alumina increases. Static and dynamic fracture toughness of MMCs remarkably decreased due to a low strain to failure. K_{1c} and K_{1d} values of MMCs

show a big difference whether the matrix alloy is ductile. The effect of carbon fibers on the fracture toughness characteristics in the $Al_2O_3/C/Al$ composites appears slightly improved. Specifically, dynamic fracture toughness of MMCs was slightly increased compared with that of static fracture toughness because of the dynamic loading effect. Notch dynamic fracture toughness ($K_{I,d,N}$) of MMCs showed insensitive to actual loading speed.

ACKNOWLEDGMENT

This work was supported by Hyundai Motor Co. and Korean Ministry of Science and Technology (KMST) through G-7 PROJECT. The authors wish to thank Hyundai Motor Co. and KMST for financial assistance.

REFERENCES

1. S.F.Moustafa and T.A. El-Bassyouni, " Squeeze casting of a - alumina fiber containing Al - 22% Si composite, APSFS, ,1993,pp. 43 - 46
2. R.J. Arsenault, " Relationship between strengthening mechanisms and fracture toughness of discontinuous SiC/Al composites, J. of Composites Technology & Research, Vol. 10, No. 4, 1988, pp. 140 - 145
3. S. Dionne, S.H.J.Lo and G.J.C.Carpenter, " Mechanical properties of squeeze cast zink - aluminum composites", ICCM 9, Vol.1, 1993, pp. 195 - 199
4. Y.Flom and R.J.Arsenault, "Effect of particle size on fracture toughness of SiC/Al composites material", Acta metall., Vol. 37, No. 9, 1989, pp. 2413 - 2423
5. T.J. Downes and J.E. King, " The effect of microstructure on the fracture toughness of a metal matrix composite, Composites, Vol. 24, No. 3, 1993, pp. 276 - 281
6. M.Manoharan and J.J. Lewandowski, " Crack initiation and growth toughness of an aluminum metal matrix composite, Acta metall., Vol. 38, No. 3, 1990, pp. 489 - 496
7. C.R. Crowe, R.A. Gray and D.F. Hassen, " Microstructure controlled fracture toughness of SiC/Al metal matrix composites ", ICCM 5, 1985, pp. 843 - 866
8. D.L. Davidson, "Fracture Characteristics of Al - 4 Pct Mg Mechanically Alloyed with SiC", Metallurgical Transaction A, Vol.18A, 1987, pp.2115-2126
9. Cho, S .Lee, Y.W. Chang and J. Duffy "Dynamic fracture behavior of SiC whisker reinforced aluminum alloys", Metallurgical Trans. A., Vol. 22A, 1991, pp. 367 - 375
10. K.Surppa and P. Sivakumar, " Fracture toughness evaluation of 2040-Al/ Al_2O_3 particulate composites by instrumented impact ", Composite Science and Technology, Vol. 46, 1993, pp. 287 - 292

11. Giridhar and M.K.Surappa, " Effect of aging on impact fracture behavior of 2040-Al/ Al_2O_{3p} composites made by casting route", ICCM 9, Vol. 2, 1993, pp. 219 - 226
12. J.I.Song and K.S.Han, "Mechanical Properties and Fatigue Crack Propagation Behavior of Hybrid Metal Matrix Composites", SAE Technical Paper Series 960577, 1996, pp.1-12
13. Data Sheet from Japanese Industrial Standards (JIS) : H 5303
14. Data Sheet from ICI Co and Tokaiwhisker Co..

ASSESSMENT OF MICROFRACTURE MECHANISMS IN $Al_2O_3/6061$ AL AND $SiC/6061$ AL DISCONTINUOUS REINFORCED COMPOSITES

J. P. Lucas and J. K. Park

*Department of Materials Science and Mechanics, Michigan State University
A304 Engineering Building, East Lansing, MI 48824*

SUMMARY: Microfracture mechanisms are investigated in artificially aged discontinuously reinforced metal matrix composites (MMCs). Fracture behavior is presented for a 6061 Al alloy reinforced with Al_2O_3 and SiC particulates. Stir-cast processing was used to fabricate both $Al_2O_3/6061$ Al and SiC/6061 Al MMCs. Emphasis is placed on the role played by the particulate/matrix interface in these materials as the interfacial character and integrity influence microfracture mechanisms. Interface and near-interface phase characterization was conducted using electrochemical dissolution, and optical, scanning, and transmission microscopy. Crack initiation and crack propagation behavior was investigated in the under-aged, peak-aged, and over-aged conditions using double notched, 4-pt. bend specimens and half-inch short bar specimens, respectively. The effect of aging, associated microstructure development, and reinforcement type on microcrack initiation and crack propagation mechanisms is discussed.

KEYWORDS: particulate reinforced composites, fracture toughness, microcracking, aging effects, interfacial reaction, spinel, aluminum carbide

INTRODUCTION

Particulate reinforced metal matrix composites (PRMMCs) are steadily emerging as attractive structural materials because of their enhanced properties compared to the unreinforced, monolithic matrix alloy. Improvements in specific strength and specific modulus are common. The coefficient of thermal expansion and wear properties are also improved. Moreover, PRMMCs can be fabricated by conventional thermomechanical metal processing practices [1]. However, PRMMCs tend to exhibit considerably lower elongation, fracture strain, and fracture toughness [2,3] due to premature cracking of the particulates or void formation at the particulate/matrix interface. The lack of fracture toughness still limits the application of particulate reinforced composite materials. Therefore, research continues in efforts to better understand and resolve this issue.

Why there is a lack of fracture toughness in PRMMCs compared to the unreinforced matrix alloy can be related to several factors, for example: (a) the addition of the reinforcement changes the matrix alloying composition, and the matrix microstructure [4], (b) new interfaces are created between the matrix alloy and the reinforcement phases, (c) reaction products and interphase phases develop around the particulates, and (d) the hard, brittle reinforcement

particulates are considerably larger compared to constituent particles; consequently, the particulates are prone to microcracking and/or debonding in the domain of the particulate/matrix interface. Also, clustering of particulates in MMCs occurs. It has been suggested that particulate clusters act as nucleation sites for microcracking and void formation [5]. Accelerated aging also takes place in the PRMMCs due to mismatch of the coefficient of thermal expansion (ΔCTE) between the reinforcement phase and the matrix alloy. Dislocations are punched out in the matrix in the vicinity of the particulates. Matrix precipitates that form on these punched-out dislocations nucleate heterogeneously. Thus, the time is decreased for PRMMCs to reach peak aging [6].

In this study, two types of PRMMCs were investigated. The composites contain the same matrix alloy, 6061 aluminum, reinforced with either SiC or Al_2O_3 particulates. Fracture behavior was determined for the PRMMCs in the underaged (UA), peak aged (PA), and overaged (OA) conditions. The character of the interface and the interfacial microstructure severely influences the fracture mechanisms in the composite materials. The effect of microstructure on microfracture behavior is examined and discussed.

MATERIALS AND EXPERIMENTAL PROCEDURES

$\text{Al}_2\text{O}_3/6061$ and SiC/6061 particulate reinforced metal matrix composites (PRMMCs) were investigated. The materials were fabricated by DuralcanTM by a stir-cast process in which particulates were incorporated into the molten matrix alloy, 6061 aluminum. Incorporation of particulates in the alloy melt tends to promote chemical reactions between the matrix and the reinforcement producing a reaction-product microstructure at the interface. The nominal elemental composition of the matrix alloy is given in Table I. The composite materials examined contained 10 and 20 v/o particulate volume fractions. The average diameters of the SiC and Al_2O_3 reinforcement phases were 14 μm and 18 μm , respectively. Nominal properties of the composite materials are listed in Table II.

Table I. Elemental composition of the matrix alloy of the composite, 6061 Al

Elements	Mg	Si	Cu	Fe	Cr	Mn	Zn	Ti
Content (wt%)	1.12	0.59	0.27	0.11	0.10	0.04	0.02	0.004

Table II. Mechanical Properties of $\text{Al}_2\text{O}_3/6061$ and SiC/6061 Composites.

Materials	Modulus (GPa)	Elongation (%)	UTS (MPa)	YS (MPa)	Particulate Size, (μm)	Hardness* (Hv)
$\text{Al}_2\text{O}_3/6061$ (10 v/o)	81.4	10	296	-----	18	118
$\text{Al}_2\text{O}_3/6061$ (20 v/o)	97.2	4	352	-----	18	121
SiC/6061 (10 v/o)	78.6	7.5	351	321	16	133
SiC/6061 (20 v/o)	97.3	2.8	378	343	16	137
Monolithic 6061	69	15.1	326	305	-----	113

*peak hardness values, T6

All specimens were solution heat treated at 550°C for 90 minutes and quenched in ice brine. Artificial aging was conducted at 180°C, immediately after the solution heat treatment to prevent the natural aging at room temperature. The aging process time ranged from 1 to 3,000 minutes.

After aging, the composite specimens were cast in polymeric metallographic mounts, 3.175 mm in diameter, for polishing to reveal the microstructural features. Initial grinding was accomplished using a 120 grit zirconia/alumina abrasive belt polisher. Plastically mounted specimens were subsequently polished using a lapping wheel using 30 µm, 6 µm and 1µm diamond suspensions. The final polishing step was performed using 0.06 µm colloidal silica suspension on a vibratory polisher (Buehler Vibromet II®) for 2 hours.

Hardness testing was conducted using a Leco, M-400-G microhardness tester equipped with a Vickers diamond pyramid indenter. Hardness indentations were taken exclusively in matrix regions avoiding contact between the indenter and the reinforcement particles using a 10-gram load. A minimum of ten hardness readings were taken for each composite sample.

Fracture toughness tests were conducted on the materials using short bar specimens (width, B = 0.5 in) according to ASTM 1309 test procedures. Fracture toughness testing was conducted on specimens in the under aged (UA), peak aged (PA), and over aged (OA) conditions to ascertain the aging effects. Using the SEM, the fracture morphology was assessed by examining fracture surface of PRMMC specimens. The crack propagation path profile was observed from half-sectioned (transverse to the chevron notch direction) and polished SB specimens using optical and scanning electron microscopy. Particular emphasis was given to the examination of the deformation wake produced by the main crack.

RESULTS AND DISCUSSION

Interfacial Microstructure

The interface regime between the matrix alloy and the particulate is characterized by the reaction products that form during melt casting and subsequent heat treatment. SEM micrographs in Fig. 1 show the matrix/reinforcement interface region for (Al₂O₃)_p/6061 composites. Interfacial reaction product phases are clearly seen in the (Al₂O₃)_p composite. The interfacial reaction product is primarily spinel, MgAl₂O₄ [7]. Typically, the spinel layer is 2 µm thick. The irregular interface structure between (Al₂O₃)_p and the matrix alloy indicates that the Al₂O₃ reinforcement was partially consumed. Spinel forms readily with the reinforcement and promotes strong interfacial bonding between the matrix phase [7-10]. The formation MgAl₂O₄ of is given by the following reaction,



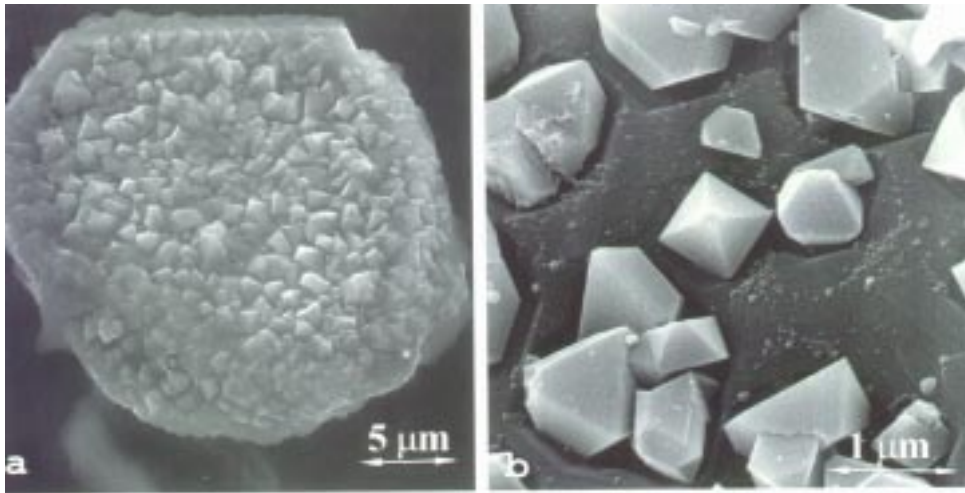
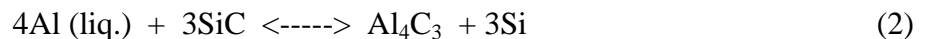


Fig. 1: a) The growth of spine, $MgAl_2O_4$, is shown on an Al_2O_3 particulate.
b) Spinel crystallites are shown.

The interface of $SiC_p/6061$ composites is characterized primarily by the formation of Al_4C_3 as an interfacial reaction product. The morphology of the interfacial reaction product revealed extensive formation of hexagonal-shaped aluminum carbide platelets, Fig. 2. Al_4C_3 platelets are $\sim 0.7 \mu m$ thick and $\sim 3 \mu m$ wide. Interfacial Al_4C_3 forms via following reaction:



This reaction produces elemental Si as a reaction product. The formation of Al_4C_3 can be hindered by increasing the silicon content of the matrix alloy. Si additions to the matrix tend to slow the forward reaction because rejected Si raises the activity beyond its equilibrium content [4,11]. Al_4C_3 is sensitive to moisture; consequently, its presence at the interface may adversely affect the resultant mechanical properties of the composite [12-14] by reducing the interfacial strength, fracture strain, ϵ_f , and/or fracture toughness. The propensity for corrosion increases with Al_4C_3 formation [12,13]. Barrier coatings (SiO_2 and TiO_2) and alternative thermal processing can limit the formation of Al_4C_3 .

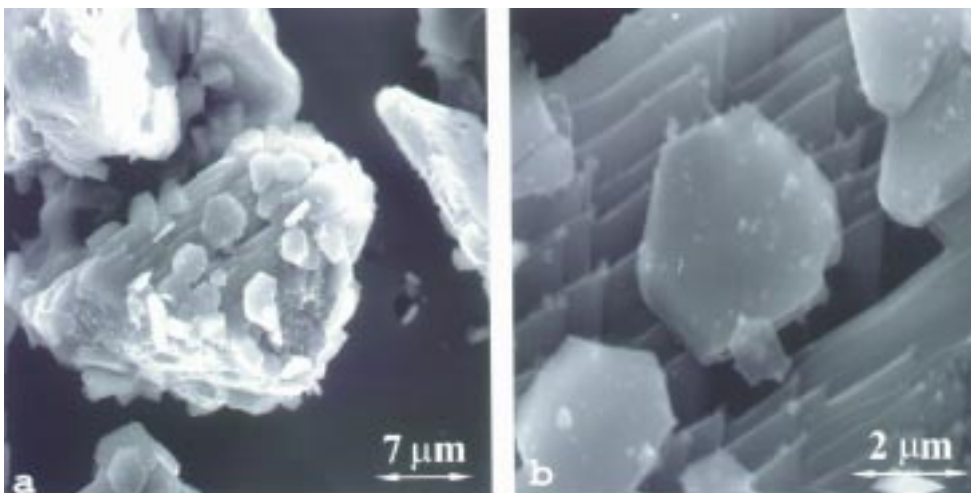


Fig. 2: a) Aluminum carbide, Al_4C_3 , is shown on the interface of a SiC particulate.
b) Isolated Al_4C_3 crystallites are shown.

Aging

Accelerated aging was observed for the composite materials compared to the monolithic matrix alloy. In Fig. 3, the hardness versus aging time data demonstrate accelerated aging as peak hardness occurs sooner for the composite materials. Accelerated aging of particulate reinforced composites is related to the increase in the dislocation density in materials, particularly in the vicinity of the reinforcement, due to mismatch of the coefficients of thermal expansion (ΔCTE) between the matrix alloy and the ceramic reinforcement. The ΔCTE -induced dislocations serve as heterogeneous nucleation sites of aging precipitates [6,15].

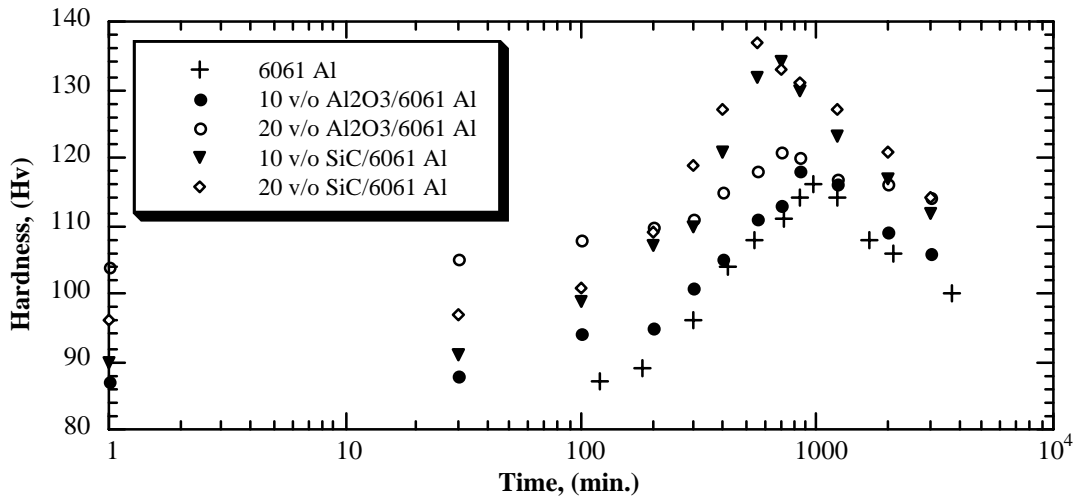


Fig. 3: Microhardness versus aging time. Accelerated aging is demonstrated for the composite materials.

Composites with the higher reinforcement volume percent (v/o) show higher microhardness values both for the solutionized condition and for the as-quenched condition as well. Higher strengths are observed in composites with increasing reinforcement content because of the enhancement in the dislocation density caused by reinforcement/matrix thermal expansion mismatch [15,16].

For the same reinforcement volume fraction, however, SiC_p reinforced MMCs exhibited significantly higher hardness values than do Al_2O_3 reinforced composites in the peak aged condition. The hardness difference can be explained by the changes in matrix composition created by matrix alloying modification and elemental redistribution due to interfacial reactions [4] between the matrix and the Al_2O_3 and SiC particulates. At the Al_2O_3 /6061 Al interface, magnesium is consumed and the pure aluminum is rejected upon the formation of $MgAl_2O_4$ according to the Eqn. 1. The major matrix-strengthening precipitate in 6061 Al-T6 is the β phase (Mg_2Si) [17]. When Mg is consumed by particulate/matrix interfacial reactions, less Mg is available for formation of matrix-strengthening precipitates, Mg_2Si . Mg is copiously consumed during the formation of the spinel phase. In contrast, aluminum is consumed and silicon is rejected by the formation of Al_4C_3 at the SiC/6061 Al interface according to the Eqn. 2. The higher hardness of SiC/6061 Al, presumably, is due to the fact that Mg is not consumed during particulate/matrix interfacial reactions and, consequently, Mg is available to form major matrix-hardening precipitates, Mg_2Si [4,18].

Microfracture

Microcracking and microcrack initiation were examined for both types of composite materials, 20 v/o $\text{Al}_2\text{O}_3/6061$ and 20 v/o $\text{SiC}/6061$, in the UA and OA conditions. Double notched 4-pt. bend specimens were used to capture the nucleation of microcracks in the vicinity of the crack tip. Similar experiments were conducted previously by Lewandowski *et al.* [5] to study crack initiation events. Extensive plastic deformation and microcracking were observed at the notch tip. Of interest here, regarding the composite materials, was the tendency for microcracking and/or void formation at the *particulate/matrix interface* of $\text{SiC}/6061$ composites, whereas microcrack initiation occurred disproportionately by *particulate cracking* in the $\text{Al}_2\text{O}_3/6061$ composite. Microcracking and void formation tendencies for 20 v/o $\text{Al}_2\text{O}_3/6061$ and 20 v/o $\text{SiC}/6061$ composite materials are illustrated schematically in Fig. 4. Regardless of the aging conditions, ~ 67% of the particulates *cracked* during the fracture process for the $\text{Al}_2\text{O}_3/6061$ composites and 33% of the particulates failed by *particulate/matrix debonding*. In stark contrast, ~ 72% of the particulates exhibited *particulate/matrix debonding* for SiC reinforced composites and only 28% of the particulates failed by *particulate cracking*. The differences in microcracking character have implication regarding the fracture resistance of particulate reinforced composite materials. Spinel is known to form a very strong, stable interface with magnesium-containing aluminum alloys [7-9]. Consequently, preferential fracture occurs by transparticulate cracking of the reinforcement phase (Fig. 4a). In contrast, aluminum carbide forms at the interface of SiC/matrix interface. Apparently, the interfacial bond strength of Al_4C_3 is weaker compared to the interfacial bond strength of MgAl_2O_4 . Interface microcracking apparently occurs at lower applied stress in SiC reinforced composites than does transparticulate microcracking which occurs in Al_2O_3 particulate reinforced materials (Fig. 4b). The deformation process zone size was more extensive in $\text{Al}_2\text{O}_3/6061$ composites as noted in Fig. 6. Al_4C_3 is moisture sensitive [19] and may contribute to lower fracture resistance in some composite materials. Due to moisture sensitivity, composites containing interfacial Al_4C_3 exhibit significantly higher fatigue crack propagation rate [20] and show greater susceptibility to sustained-load cracking in moist environments.

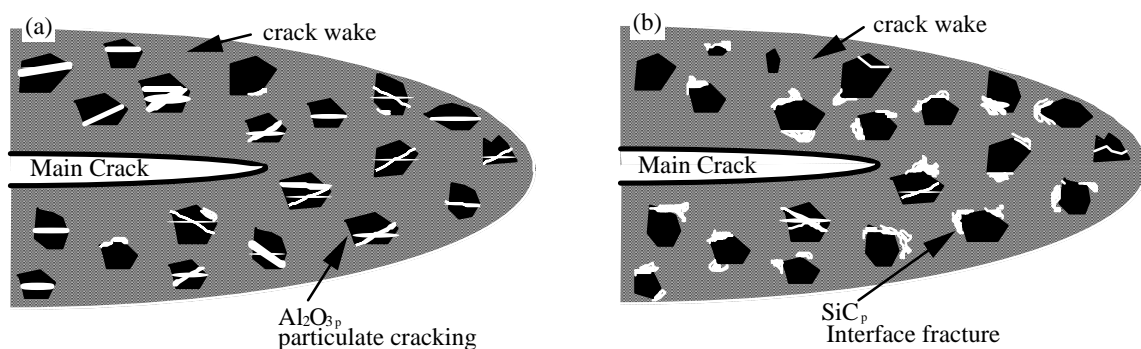


Fig. 4: A schematic representation of microfracture at the crack tip. a) Particulate cracking was the dominant fracture mechanism for $\text{Al}_2\text{O}_3/6061$ composites and b) particulate/matrix debonding was the dominant fracture mechanism for SiC reinforced composite materials.

Fracture Toughness

The fracture toughness was determined for both composite materials in the UA, PA, and OA conditions. Unlike monolithic age-hardenable Al alloys where the fracture toughness and fracture strain recover upon overaging; the fracture toughness and/or fracture strain do not recover for PRMMCs in the overaged condition [5,21-23]. The lack of recovery of the fracture toughness for the PRMMCs investigated in this study is clearly demonstrated in Fig. 5. Klimowicz and Vecchio [23] suggested that the lack of recovery of fracture toughness in overaged 2000-series PRMMCs was due to the strain localization in the matrix ligaments resulting from fracture of the reinforcement particles; and, also due to premature microvoids formation at large second-phase precipitates within the matrix ligaments at the crack tip. The effect of aging time on the fracture toughness of 20v/o $\text{Al}_2\text{O}_3/6061$ and 20 v/o SiC/6061 particulate reinforced metal matrix composites are shown in Fig. 5. Regardless of aging conditions or volume fraction of

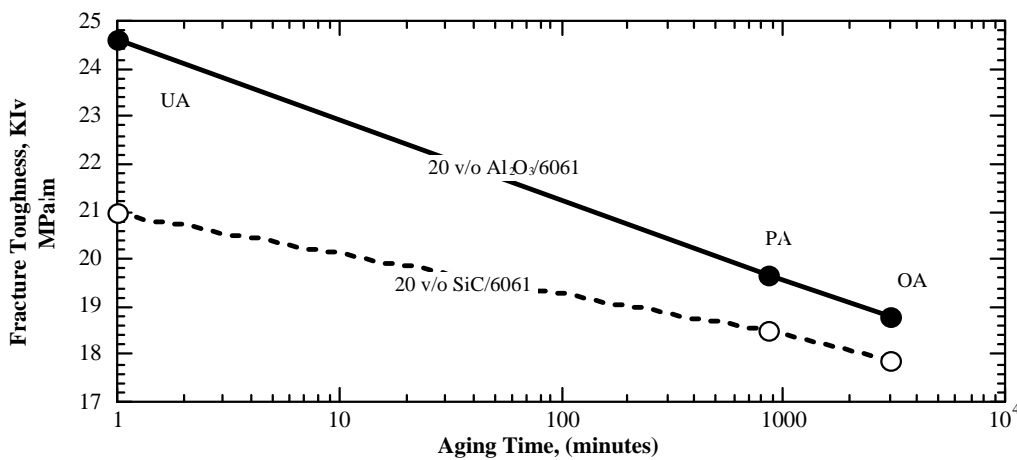


Fig. 5: The fracture toughness versus aging time is shown. The fracture toughness is not recovered with overaging.

reinforcement, Al_2O_3 reinforced composites demonstrated higher fracture toughness. Although neither composite recovered to fracture toughness values approaching the underaged condition, SiC/6061 composites tended to have a lower OA fracture toughness because of (i) premature fracture of the reinforcement/matrix interface which occurred at low nucleation strains, and, (ii) localized strain elevation achieved in the interparticulate ligaments. Also, void nucleation, growth, and coalescence centered around overaged Mg_2Si precipitates in the interparticulate ligaments readily occur. Void formation and growth are impelled by the complex state of stress that exist in the ligaments. Unlike $\text{Al}_2\text{O}_3/6061$ composites which consume Mg during the formation of spinel, Mg is not consumed by the particulate/matrix interface reactions of SiC/6061 composites. Consequently, the density of overaged Mg_2Si precipitates is higher and the interparticle, λ , is smaller for SiC/6061. Smaller λ raises the rate of void nucleation and void link up due to overlap of strain fields around closely-spaced, overaged precipitates in the ligaments. The fracture toughness observed for the composites is consistent with the modified-stress fracture strain model [24,25], which suggests that toughness is controlled by the crack tip process zone size, l^* . The fracture toughness as derived from the modified-stress fracture strain model is given by the following expression,

$$K_{IV} = \alpha \sqrt{\sigma_0 \epsilon_f' E l^*} \quad (3)$$

where E is the elastic modulus of the composite, α is a constant, ϵ_f' is the stress-modified fracture strain, and σ_0 is the composite strength.

Examination of the crack tip wake generated by the crack propagation revealed that the size of the wake (i.e., the plastic deformation enclave) of $Al_2O_3/6061$ composites was consistently larger than the wake of the $SiC/6061$ composites regardless of the aging conditions. The damage zone left by the propagating crack wake is shown in Fig. 6. The crack profiles and the damage enclaves caused by particulate cracking and/or particulate/matrix debonding sketched in Fig. 6 are traces of the actual cracks developed during fracture toughness testing of the composite materials.

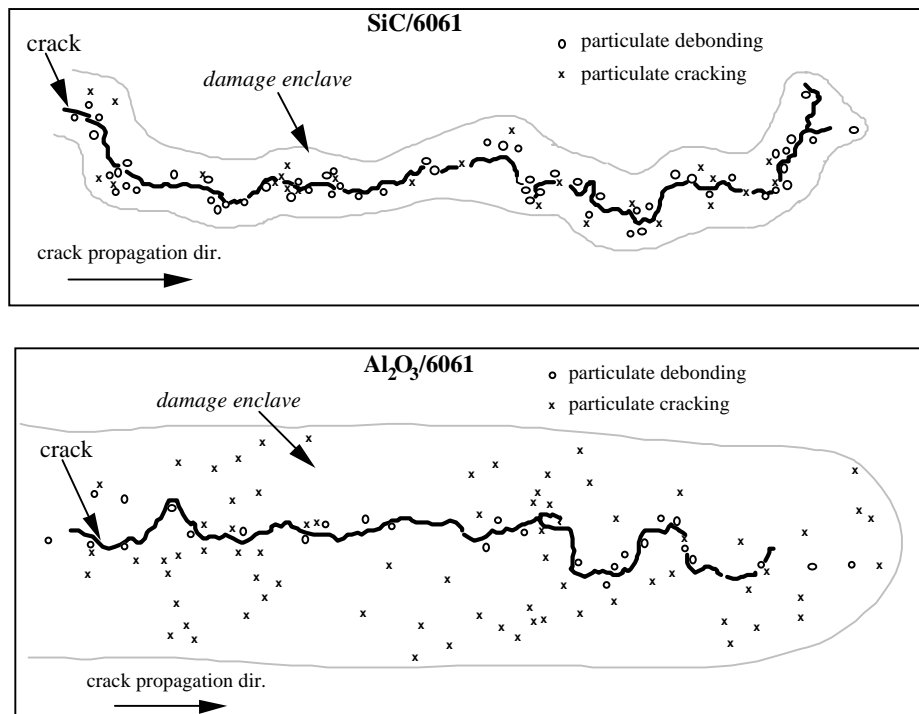


Fig. 6: The damage zone (actual cracks are represented) created by the propagating crack is schematically represented. Particulate cracking was dominant in $Al_2O_3/6061$ composites, whereas particulate/matrix debonding was the dominant in SiC reinforced composite materials. The plastic damage enclave is significantly larger for $Al_2O_3/6061$ composites

Assuming that fracture toughness is controlled by process zone-dominated mechanisms, the results provided in Fig. 6 suggest that $Al_2O_3/6061$ composites should show higher fracture resistance. Indeed, the $Al_2O_3/6061$ composites examined revealed larger crack tip wakes or plastic zone enclaves; thus, they exhibit a higher fracture toughness. In part, the increase in fracture toughness is due to the ability of larger process zone enclaves to dissipate plastic energy associated with crack propagation.

CONCLUSIONS

From this investigation the following conclusions are:

1. The composite materials exhibited accelerated aging compared to the monolithic alloy. Peak aging was attained sooner for materials with higher reinforcement volume fractions. SiC-reinforced MMCs aged faster than Al₂O₃-reinforced MMCs.
2. Spinel, MgAl₂O₄, was the dominate interfacial reaction product between Al₂O₃ and the 6061 matrix alloy. Al₄C₃ formed at the SiC/matrix interface. Aluminum carbide is moisture sensitive and may degrade mechanical properties.
3. The predominant microfracture mechanism in SiC reinforced composites was debonding at the particulate/matrix interface. In contrast, particulate cracking was the dominant microfracture mechanism for Al₂O₃-reinforced MMCs.
4. Fracture toughness was not recovered in the overaged condition for the PRMMCs. Al₂O₃-reinforced MMCs generally exhibited higher fracture toughness compared to SiC-reinforced MMCs. The higher fracture toughness values observed for the Al₂O₃-reinforced composites were directly related to crack tip microfracture mechanisms in which particulate cracking produced a larger size process zone at the crack tip.

ACKNOWLEDGEMENTS

This research was partially supported by the State of Michigan through the Research Excellence Fund, (REF)

REFERENCES

1. M. Hunt, "Aluminum Composites Come of Age," Materials Engineering, Vol. 106 (1989) p. 37.
2. C. P. You, A. W. Thompson and I. M. Bernstein, "Proposed Failure Mechanism in a Discontinuously Reinforced Aluminum Alloy," Scripta Metallurgica., Vol. 21 (1987) p. 181.
3. J. J. Stephens, J. P. Lucas and F. M. Hosking, "Cast Al - 7 Si Composites: Effect of Particle Type and Size on Mechanical Properties," Scripta Metallurgica, Vol. 22 (1988) p.1307.
4. J. P. Lucas, J. J. Stephens and F. A. Greulich, "The Effect of Reinforcement Stability on Composition Redistribution in Cast Aluminum Metal Matrix Composites," Materials Science and Engineering, Vol. A131 (1991) p. 221.
5. J. J. Lewandowski, C. Liu and W. H. Hunt Jr., Powder Metallurgy Composites, Eds. M. Kumar et al., TMS-AIME, Warrendale, PA (1988) p. 117.

6. T. G. Nieh and R. F. Karlak, "Aging Characteristics of B₄C-Reinforced 6061-Aluminum," *Scripta Metallurgica*, Vol. 18 (1984) p.25.
7. A. Munitz, M. Metzger and R. Mehrabian, "The Interface Phase in Al-Mg/ Al₂O₃ Composites," *Metallurgical Transactions A*, Vol. 10A (1979) p. 1491.
8. R. Molins, J. K. Bartout and Y. Bienvenu, "Microstructural and Analytical Characterization of Al₂O₃-(Al-Mg) Composite Interfaces," *Materials Science and Engineering*, Vol. A135 (1991) p. 111.
9. J. C. Lee, K. N. Subramanian and Y. Kim, "The Interface In Al₂O₃ Particulate-Reinforced Aluminum Alloy Composite And Its Role On The Tensile Properties," *Journal of Materials Science*, Vol. 29 (1994) p. 1983.
10. J. C. Lee, G. H. Kim, J. I. Lee and H. I. Lee, "Characterization of Interfacial Reaction in (Al₂O₃)p/6061 Al Composite," *in press*.
11. T. Iseki, T. Kameda and T. Maruyama, "Interfacial Reactions between SiC and Aluminum during Joining," *Journal of Materials Science*, Vol. 19 (1984) p. 1962.
12. D. J. Lloyd, H. Lagace, A. McLeod and P. L. Morris, "Microstructural Aspects of Aluminum-Silicon Carbide Particulate Composites Produced by a Casting Method," *Materials Science and Engineering*, Vol. A107 (1989) p. 73.
13. G. Gonzalez, L. Salvo, M. Suçry and G. L'Esçrance, "Interfacial Reactions In Al-Mg Metal Matrix Composites Reinforced with (Sn/Sb) Oxide Coated SiC Particles," *Scripta Metallurgica.*, Vol. 33 (1995) p. 1969.
14. H. Ribes, M. Suçry, G. L'Esçrance and J. G. Legoux, "Microscopic Examination of the Interface Region in 6061-Al/SiC Composites Reinforced with As-Received and Oxidized SiC Particles," *Metallurgical Transactions A*, Vol. 21A (1990) p. 2489.
15. I. Dutta, S. M. Allen and J. L. Hafley, "Effect of Reinforcement on the Aging Response of Cast 6061 Al- Al₂O₃ Particulate Composite," *Metallurgical Transactions A*, Vol. 22A (1991) p. 2553.
16. M. Vogelsang, R. J. Arsenault and R. M. Fisher, "An In Situ HVEM Study of Dislocation Generation at Al/SiC Interface in Metal Matrix Composites," *Metallurgical Transactions A*, Vol. 17A (1986) p. 379.
17. H. J. Rack and R. W. Krenzer, "Thermomechanical Treatment of High Purity 6061 Aluminum," *Metallurgical Transactions A*, Vol. 8A (1977) p. 335.
18. L. Salvo, M. Suçry, J. G. Legoux and G. L'Esçrance, "Influence of Particle Oxidation on Age-Hardening Behavior of As-Fabricated and Remelted SiC Reinforced Al-1% Mg Alloys," *Materials Science and Engineering*, Vol. A135 (1991) p. 129.
19. J. K. Park and J. P. Lucas, "Moisture Effect on SiC_p/6061 Al MMCs: Dissolution of Interfacial Al₄C₃," *Scripta Materialia*, *in press*.

20. S. S. Yau and G. Mayer, "Fatigue of Metal Matrix Composite Materials," *Materials Science and Engineering*, Vol. 82, (1986) p. 45
21. D. J. Lloyd, "Aspects of Fracture in Particulate Reinforced Metal Matrix Composites," *Acta Metallurgica.*, Vol. 39 (1991) p. 59.
22. M. Manoharan and J. J. Lewandowski, "Crack Initiation and Growth Toughness of an Aluminum Metal-Matrix Composite," *Acta Metallurgica.*, Vol. 38 (1990) p. 489.
23. T. F. Klimowicz and K. S. Vecchio, "The Influence of Aging Condition on the Fracture Toughness of Alumina-Reinforced Aluminum Composites," *Fundamental Relationships Between Microstructure and Mechanical Properties of Metal-Matrix Composites*, Eds. P. K. Liaw and M. N. Gungor, TMS (1990).
24. R.O. Ritchie and A. W. Thompson, "On Macroscopic and Microscopic Analyses for Crack Initiation and Crack Growth Toughness in Ductile Alloys," *Metallurgical Transactions A*, Vol. 16A (1985) p. 233.
25. J. P. Lucas, P. K. Liaw, J. J. Stephens and J. Nunes, "The Effect of Particulate Fracture in Determining Fracture Toughness of Metal Matrix Composites," *Morris E. Fine Symposium*, Eds. P. K. Liaw et al. TMS (1991) p.171.

INFLUENCE OF SiC PARTICLES VOLUME FRACTION ON DUCTILE DAMAGE PROCESS IN AL-SI METAL MATRIX COMPOSITES

N. Bonora¹, F. Iacoviello¹ and G. M. Newaz²

¹ *Industrial Engineering Dept., University of Cassino,
Via G. De Biasio 43, 03043 Cassino (FR), Italy*

² *Mechanical Engineering Dept., Wayne State University, Detroit, 40202 MI, USA*

SUMMARY: It is well known that composites are, in most of the cases, notch insensitive and traditional fracture mechanics concepts, as stress intensity factor, are inadequate to describe material performance. In addition to the complex damage state that takes place in composite materials, metal matrix composites (MMC) present an additional damage process as a result of plastic deformations. One of the basic microstructural process for ductile damage is the formation and growth of cavities in the ductile matrix when irreversible strains take place as a result of the external loading. In particulate composites this process is emphasized by the presence of the brittle particles deep drowned in the matrix where voids are initiated as a result of matrix-particle debonding. In this paper, ductile damage evolution was measured on two Aluminum based MMC characterized by different SiC particles volume fractions. Several experimental tests shown that even if failure strain is very low, plasticity takes place in the material microstructure. Once the ductile matrix is yielded, the included particles debonds acting as microvoids initiators. As result of this process, damage evolution law come out to be very steep.

KEYWORDS: damage, mechanics, microvoids, Al-Li/SiC composites

INTRODUCTION

Linear elastic regime in metal matrix composites (MMC) is characterized by a very low strain range. For instance, Newaz and Majumdar [1] and Brust et alii [2] observed that elastic range in SCS-6/Ti-15-3 MMC is below 0.0035 strain for unidirectional composite and below 0.002 strain for 90° oriented laminate. Non-linearities observed in the stress-strain curve for higher strain levels is the results of two processes: the first, is the plastic deformation that takes place in the ductile matrix; the latter, is the appearance of damage process as a result of the debond between the matrix and the included brittle particles or fibers.

In the present paper the attention is focused on two aluminum-silicium based composites reinforced with 10% and 20% SiC dispersed particles, respectively. Even if the presence of the included SiC particles increases the material stiffness, on the other hand it seems to reduce dramatically the strain to failure.

Experimental observation shows that the bond between the matrix and the included brittle particles is mainly due to the gripping effect of the matrix produced during the cooling down phase of the manufacturing process, (Bonora et alii, [3]). As a consequence of this, SiC particles play the role of microvoids initiators that nucleate under monotonic straining.

Even if, several continuum damage mechanics models that describe the effect of void growth in ductile metals are available (Lemaitre, [4], Chow and Wang, [5], Gurson, [6]), very few of them take into account of the non linear behavior of damage evolution as a function of imposed strain. Recently, Bonora [7],[8] presented a non-linear damage model based on the nucleation, steady growth and coalescence process of microvoids in a ductile matrix.

According to Bonora [7], damage evolution can be given by the following equation,

$$dD = \alpha \cdot \frac{(D_{cr} - D_0)^{\frac{1}{\alpha}}}{\ln(\epsilon_{cr}) - \ln(\epsilon_{th})} \cdot f\left(\frac{\sigma_H}{\sigma_{eq}}\right) \cdot (D_{cr} - D)^{\frac{\alpha-1}{\alpha}} \cdot \frac{dp}{p} \quad (1)$$

where p is the effective plastic strain, D_0 and D_{cr} are the initial and the critical damage; ϵ_{th} and ϵ_{cr} are the threshold strain for which damage processes are initiated and the critical strain to failure; $f(\sigma_H/\sigma_{eq})$ is a function that takes into account of the triaxial state of stress where σ_H is hydrostatic stress and σ_{eq} is the equivalent Mises stress. α is the damage exponent that characterizes the damage evolution law for the material under investigation.

This equation, together with the elastic and plastic equations gives a rational description for the constitutive model of a ductile metal damaged by microvoids growth.

This model comes out also to be able to describe the material response of those ductile metals where the presence of damage, as a result of large included particles, induces brittle fracture. For instance, failure in Al-Li 2091 alloy resulted to be due to the concurrent actions of two-steps process. Initially, plastic deformation takes place in the material in form of narrow slip bands where included particles nucleate microvoids, (Bonora et alii, [3]). Once the plastic deformed region is saturated by nucleated voids, the further increase of the imposed strain induces a sudden linking of the nucleated cavities through cleavage cracks with consequent failure of the material, as shown in Fig.1. This kind of process resulted to be characterized by a well defined damage curve as depicted in Fig.2. Similar damage curve was observed by Chow and Wang [5] on Al 7075 alloy.

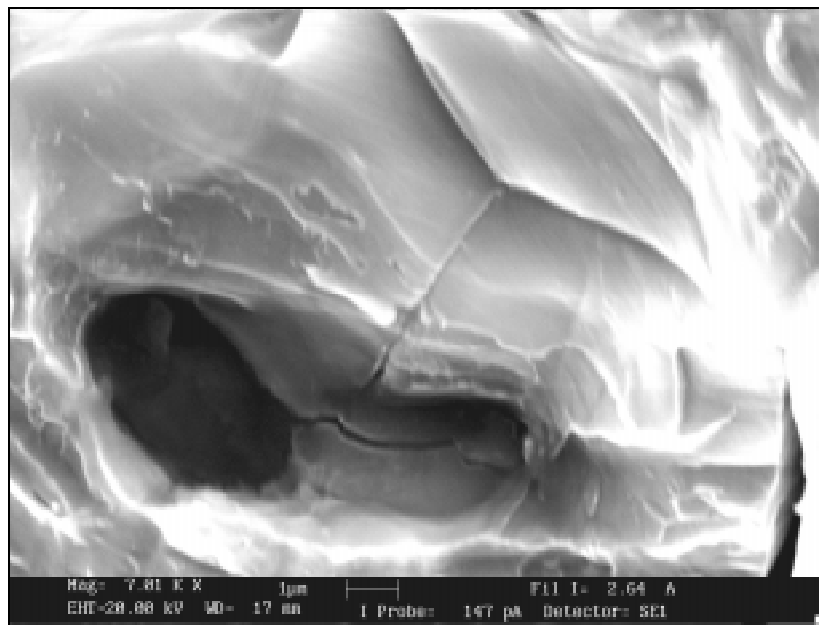


Fig. 1: Cleavage initiating from microvoid in Al-Li, from Bonora et alii, [10]

In both cases, the Bonora's model was able to predict particularly well the experimental data. In this paper, the damage evolution in Al-Si alloy reinforced with SiC particles was studied integrating damage measurements, obtained in form of loss of stiffness, with microstructural observations using electron scanning microscope.

Two were the issues addressed in this work: the understanding of the global material response using a damage description that takes into account of the irreversible deformation process that occurs in the microstructure prior failure and the effect of a different particles content on the damage evolution law.

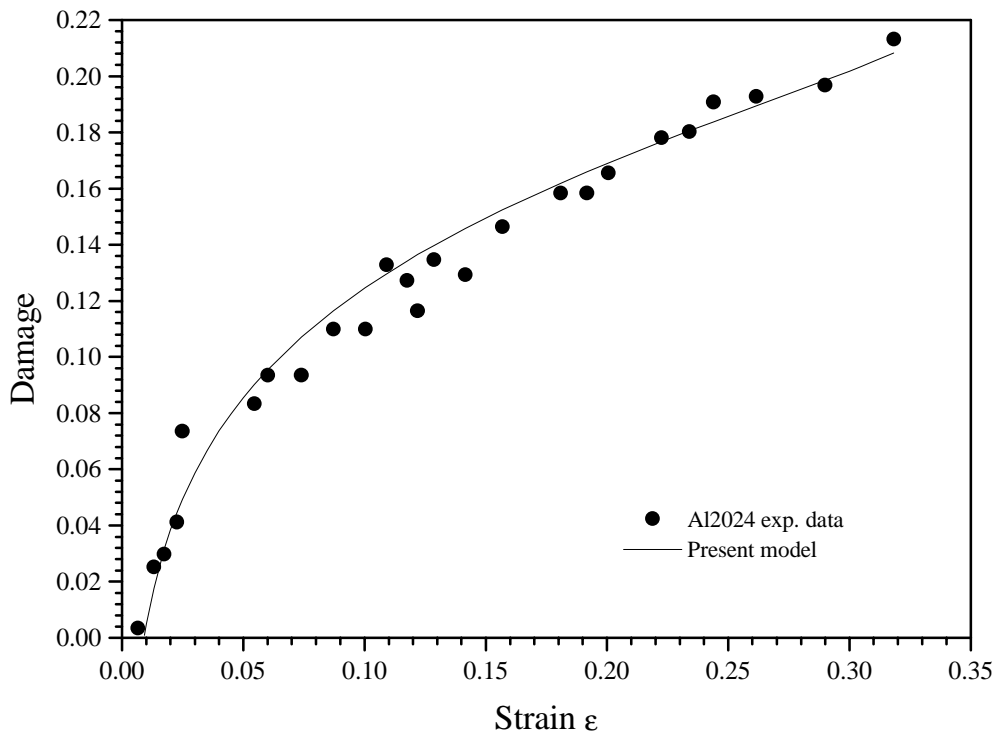


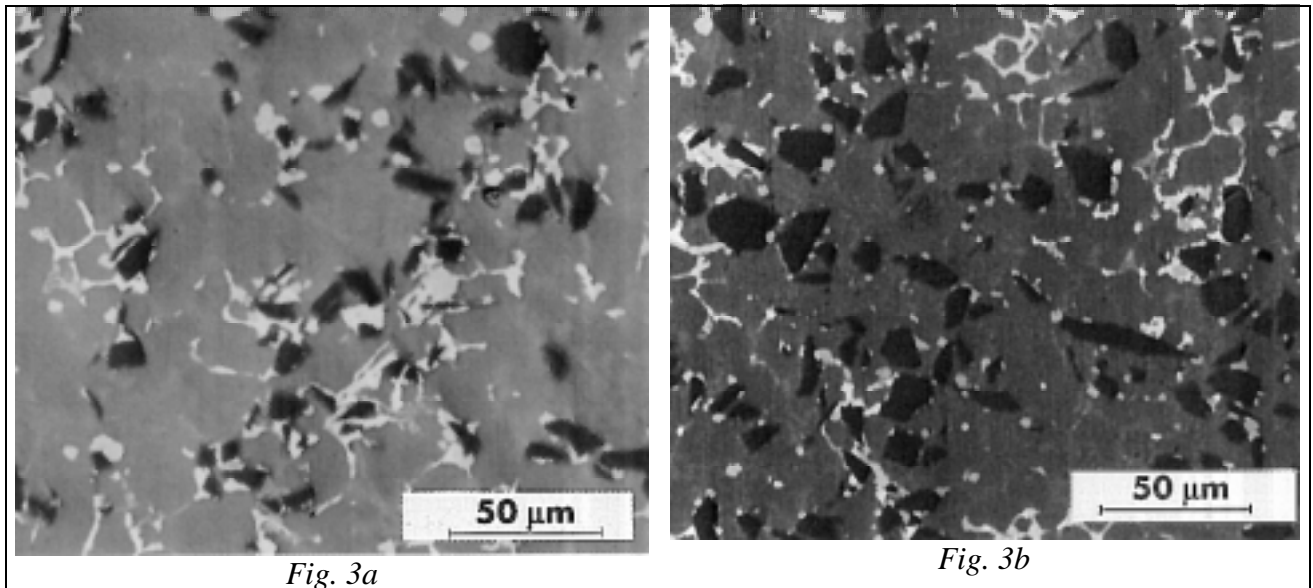
Fig. 2: Damage variable evolution in Al2024.

MATERIAL AND EXPERIMENTAL PROCEDURE

The material under investigation is a Al-Si/SiC composite produced by injection of SiC particles during the pressure die casting process in form of tiles with dimensions: $140 \times 140 \times 12.7$ mm. Zenisek et alii. [9] observed that the mean SiC particle areas $70 \mu\text{m}^2$ for the 10% composites and $100 \mu\text{m}^2$ for the 20%, approximately. A sample of the microstructure is given in Fig. 3a-3b where the back scatter electron image highlights the SiC particles shape and content.

From each tile with 10% and 20% SiC content, at least 10 specimens were obtained and tested. For the specimen geometry, the rectangular strip configuration was chosen. Initially, an hourglass-shape geometry, as proposed by Bonora et alii [10], was used in order to localize the damage process in the pre-defined section instrumented with small strain gauges. Unluckily, this configuration resulted to be not useful as a result of the very low strain at failure of the material that reduced the possibility to control the deformation process and damage acquisition. A more general specimen geometry, as used by Chow and Wang [5], was

used. In this case, no section reduction was performed and damage was monitored, and averaged, on a length of 25 mm. In Fig. 4 the specimen dimensions are given.



Back scatter electron image highlights the SiC particles shape and content in 10 and 20% SiC composites, respectively.

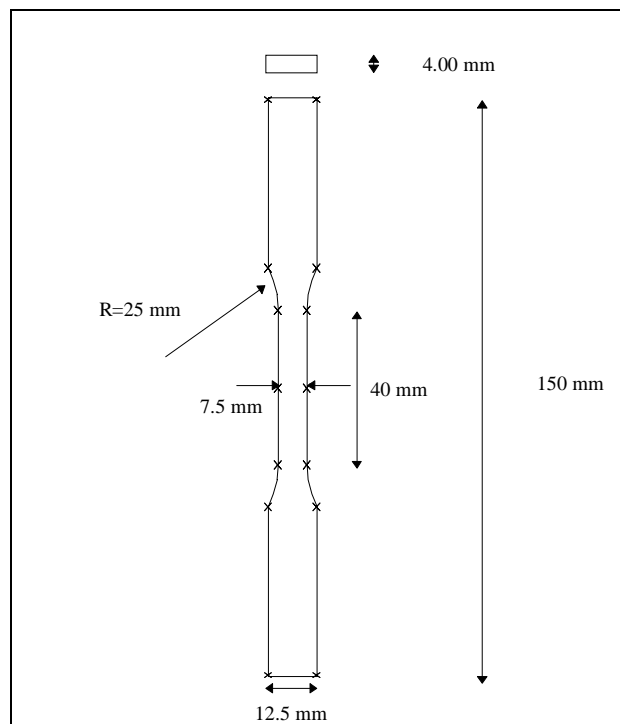


Fig. 4: Specimen geometry and dimensions.

Each specimen was cut with electroerosion machine in order to avoid a too deep material hardening and to obtain a cleaner surface cut. Specimen surfaces were polished to rectify defects caused by the impression or detachment of SiC into or out from the matrix.

For each composites, traction tests were performed both in strain and load control. The results obtained were extremely close indicating a very low scatter in the stress-strain material curve. In Fig. 5, the stress-strain curves obtained with several specimens is plotted for a 20% and 10% SiC particles content.

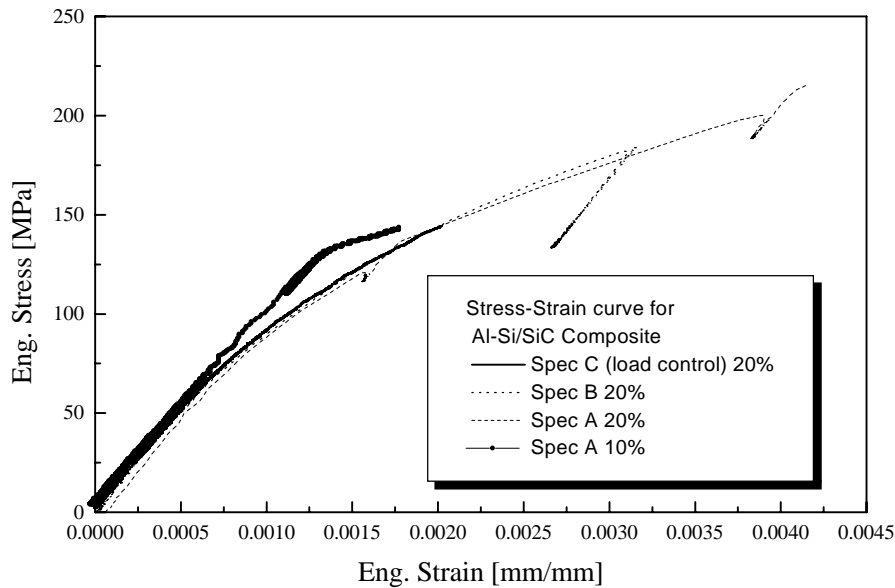


Fig. 5: Stress-strain curves for 10% and 20% Al-Si/SiC composite.

Damage was measured using instant Young's modulus measurements. The instant stiffness is normalized by the reference modulus measured in the very early linear part of the stress-strain curve.

Alternatively, damage measurement using multiple unloading technique has been also performed. Both techniques gave similar damage estimations.

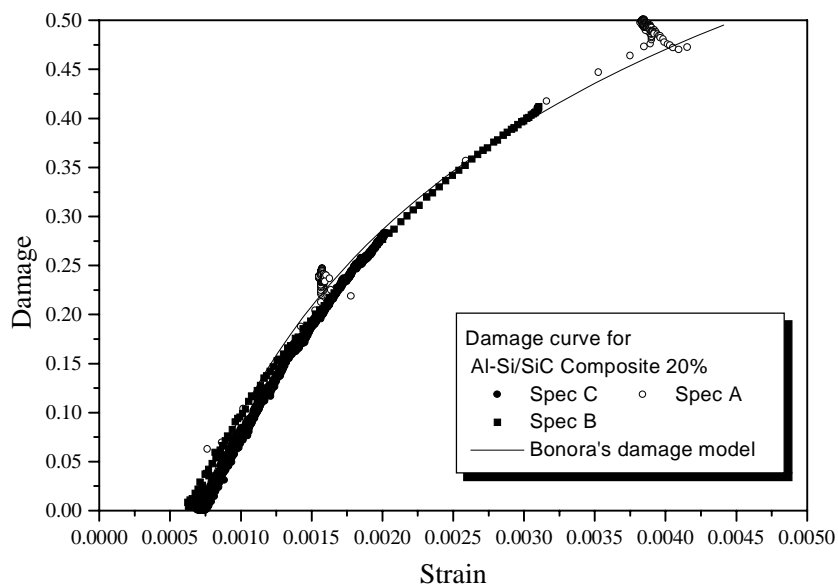


Fig. 6: Damage evolution in 20% Al-Si/SiC composite.

In Fig. 6, the damage curves for the 20% SiC composites are given. Damage cumulates rapidly, almost linearly, with strain. This kind of behavior, for which below a given threshold

strain no damage is produced and as soon as this strain value is exceeded a large amount of damage is generated, is typical of brittle materials. Similarly to Al-Li alloy, here plasticity is localized. In the plastic zone, particles rapidly debond from the matrix reducing the effective net resisting section with a highly localized loss of stiffness that soon induces material failure.

The scanning electron microscope (SEM) analysis revealed that failure process in 10% SiC composite initiates at SiC particle boundary where plastic deformation occurs. If the strain field is strong enough, the particle can be ripped away. When the particle is fully debonded from the matrix, cleavage occurs. In Fig. 7a close up of the fracture surface is given. This picture shows how, after particle debond as a result of plastic deformation, cleavage fracture proceeds through the Aluminum-Si matrix.

In 20% SiC composite failure process maintains the same basic characteristic as illustrated above. However, this multiple sites induced tearing is increased as a result of the higher particles content but cleavage process is arrested by the presence of the neighborhood particles. Thus, failure surfaces results in a completely different morphology, as showed in Fig. 7b, that can explain the higher strain at failure observed macroscopically and the higher value of the critical damage.

CONCLUSIONS

In the present paper, the damage mechanisms in Al-Si composite reinforced with two different SiC particle contents has been investigated.

The presence of the particle reinforcement resulted in a higher material performance in terms of stiffness and strength respect to the base matrix metal. However, this increase of stiffness is accompanied by an highly reduced strain to failure that strongly reduces the material applicability.

The present study highlighted the role of damage mechanisms that takes place in the material under straining. More particularly, the experimental tests performed showed that damage mechanisms are activated as soon as the strain is applied. In this direction, damage measurements indicate that damage process starts for strain higher then 0.0005 mm/mm.

The effect of the particles content strongly affects material failure. In the case of 10% SiC composite, particles performs as a initiation nuclei that trigger cleavage as soon as the particles are debonded by plastic deformation. When the particles content is higher, the same particles has the double action to initiate cleavage and to arrest it. This process results in a higher material damage tolerance, even if strain at failure remains very low.

In order to measure damage using a continuum damage mechanics, the non linear damage model proposed by Bonora has been used and the material damage parameters have been identified. Once again the non linear damage law, as proposed by Bonora, resulted to be able to follows completely the damage evolution in this material.

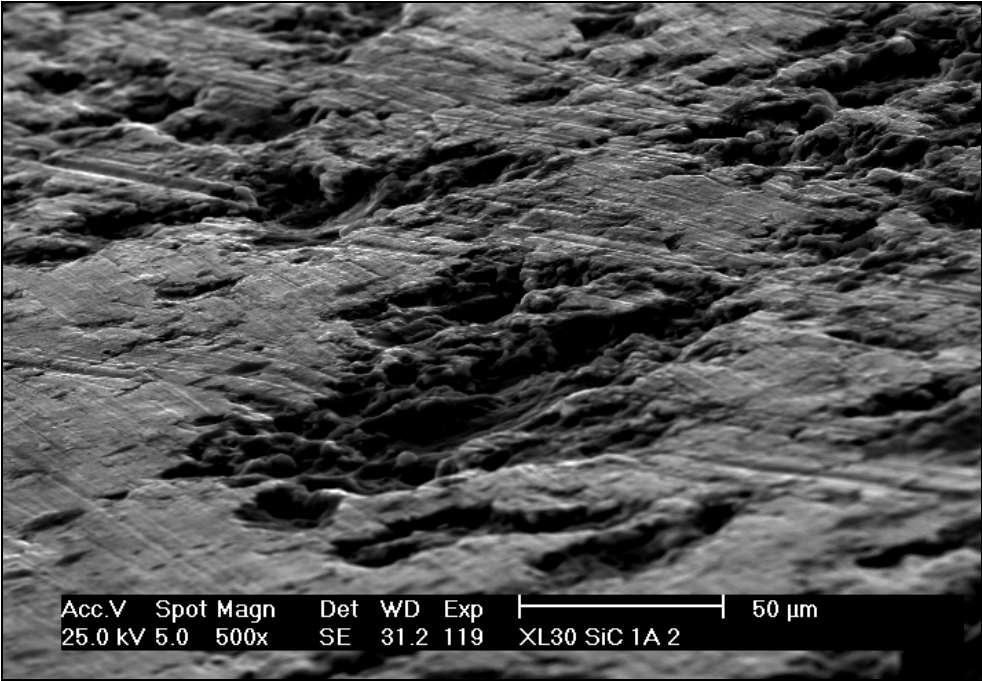


Fig. 7a: Fracture mechanism in 10% Al-Si/SiC composite: close up near a ripped SiC particle surrounded by extended cleavage areas.

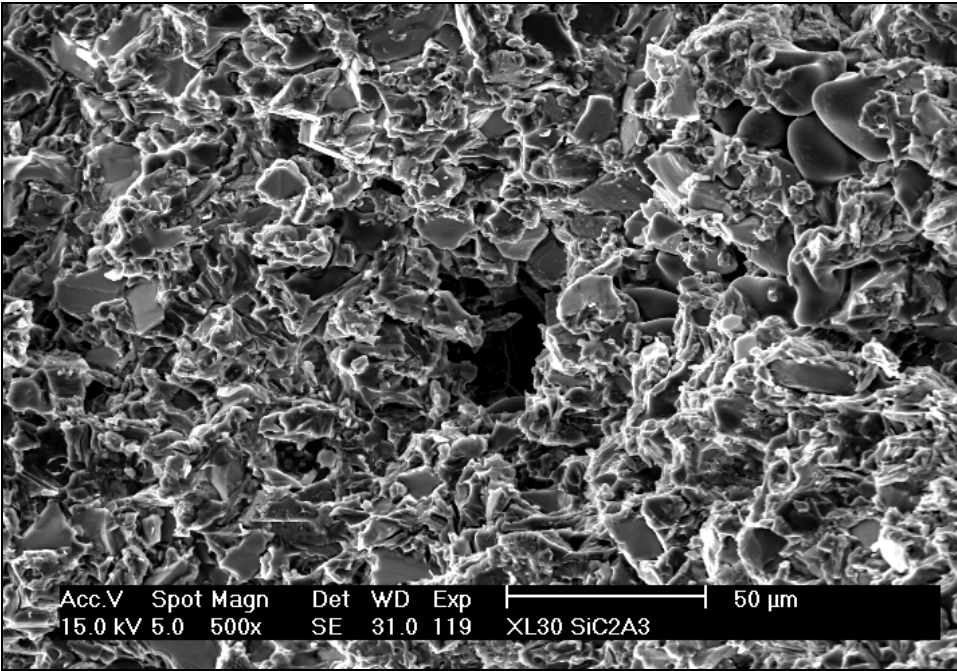


Fig. 7b: Close up of the fracture surface in 20% Al-Si/SiC composite.

ACKNOWLEDGMENT

This work was made possible thanks to the MURST and CNR financial support. The authors gratefully acknowledge.

REFERENCES

1. Newaz G.M. and Majumdar B.S., "Deformation and Failure Mechanisms in MMC", AD-22, ASME Winter Meeting, Atlanta, GA-USA, 1991, pp.55-66.
2. Brust F.W., Majumdar B.S. and Newaz G.M., "Constitutive Response analysis of Metal Matrix Composites Via the Unit Cell Model", Proc. ASTM Symposium on Composite Material, Pittsburgh, PA, USA, 1992,
3. Bonora N., Costanzi M., Newaz G. and Marchetti M., "Microdamage Effects on the Overall Response of long Fibre/Metal Matrix Composites", Composites, Vol. 25, N.7, 1994, pp.575-582.
4. Lemaitre J., "Local Approach to Fracture", Engn. fract. Mech. Vol. 25, No. 5/6, 1986 pp.523-537.
5. Chow C.L. and Wang J., " An Anisotropic Theory of Continuum Damage Mechanics For Ductile Fracture", Engn. Fract. Mech. Vol.27, n° 5, 1987, pp. 547-558.
6. Gurson A.L., " Continuum Theory of Ductile Rupture by Void Nucleation and Growth: Part I- Yield Criteria and Flow Rules for Porous Ductile Media", J. Engn. Mat. Tech., Vol. 99, 1977, pp.2-15.
7. Bonora N., "A Non-Linear CDM Model for Ductile Fracture Based on the Void Nucleation, Growth and Coalescence" submitted for publication on Engn Frac. Mech., 1996.
8. Bonora N., "Effect of Triaxial State of Stress on Ductile Fracture Damage Parameters" submitted for publication on Engn Frac. Mech., 1996.
9. Zenisek P., Lasertova M., Iacoviello F., Cavallini M. and Hyspecka L., " Structure and Mechanical Properties of Al-Si Matrix Composite with additions of SiC Particles", Met. Sci and Tech., Vol. 14, n°1, 1996, pp.37-44
10. Bonora N., Cavallini M., Iacovello F. and Marchetti M., "Crack Initiation in Al-Li Alloy Using Continuum Damage Mechanics", in Localized Damage III Computer-Aided Assessment and Control, Ed. M.H.Aliabadi, A. Carpinteri, S. Kalisky and D.J. Cartwright, Computational Mechanics Publication, Southampton Boston , 1994, pp. 657-665.

AN *IN SITU* STUDY OF FATIGUE CRACK GROWTH IN COMRAL-85 AT AMBIENT AND ELEVATED TEMPERATURES

Greg Heness¹ and Yiu-Wing Mai²

¹ *Department of Materials Science, University of Technology, Sydney, PO Box 123, Broadway
NSW 2007, Australia*

² *Centre for Advanced Materials Technology and Department of Mechanical and
Mechatronic Engineering, University of Sydney, NSW 2006, Australia*

SUMMARY: Direct observation of the interaction of a fatigue crack with the microstructure and reinforcement in Comral-85 metal matrix composite (MMC) at both ambient and elevated temperatures was undertaken. In general particle matrix debonding was the dominant mechanism and is explained in terms of the constraint imposed by the particles on the matrix. Prior to failure the process zone, consisting of debonded particles and microcracked matrix, around and in front of the crack tip increased. There was still little evidence of cracked particles although some became evident. The major growth mechanism was the linkage of debonded particles by the crack growing through the matrix. There was also evidence of the crack seeking particle clusters due to the significant debonding occurring in these regions.

KEYWORDS: metal matrix composite, fatigue, in-situ, crack growth

INTRODUCTION

There has been a considerable amount of investigation into the fatigue behaviour of metal matrix composites (MMCs). Characterisation of the behaviour through S-N curves and crack growth data have been the main areas of research. A number of mechanisms have been observed during fatigue crack propagation. Possible reinforcement-crack tip interactions during fatigue crack growth are particle fracture promoted by coarse particles in high strength matrices; the crack remaining in the matrix promoted by strong interfaces and high modulus particles; crack growth along particle-matrix interfaces promoted by weak interfaces (precipitation, oxidation, reaction).

These crack growth mechanisms have generally been determined from post mortem studies of the fracture surface or thin slices taken perpendicular to the crack plane.. In this study the crack growth mechanisms were observed *in situ*.

Shang and Ritchie have suggested the dominant mechanisms, near threshold, that lead to better fatigue crack growth resistance involve crack deflection around particles and crack trapping by the particles with the composites of coarser particles being the most effective at higher crack growth rates. Shang et al. found that with increasing K levels in the intermediate regime, growth rates become progressively slower in the composites, particularly in the coarse SiCp material compared with the unreinforced alloys. This was the result of a mutual

competition of SiC particle fracture ahead of the crack-tip (enhancing crack growth) and crack bridging from ligaments behind the crack-tip (retarding crack growth).

The effect was more pronounced with the large SiC particles as they are more effective in bridging. As the stress intensities approached K_{IC} the growth rates were found to be higher in both composites compared with the unreinforced alloy due to their much lower fracture toughness. Shang et al. concluded that the fracture crack growth performance of the system studied depends upon the interaction, and in particular the brittle fracture of the SiC particles. The interaction was found to vary with stress intensity level and the size of the carbides.

For many composites the fracture of particles ahead of the crack tip has been given as a reason for enhanced crack growth rates. For very strong or very fine reinforcements this acceleration mechanism is not relevant as little or no particle fracture occurs. Knowles and King have suggested, for these materials, an acceleration mechanism associated with failure at or near the particle-matrix interface.

Factors such as highly faceted crack growth which can lead to crack closure would not be applicable for fine grain size composites. The high dislocation densities associated with the thermal expansion mismatch in MMCs and the closely spaced reinforcements all act to homogenise slip, even in under-aged matrices. As well, the presence of the particles has been shown to accelerate the ageing process in some systems and to cause an increase in precipitate density near the particle reinforcement.

EXPERIMENTAL PROCEDURE

The material used in this study was Comral-85, a spherical ceramic particle (20 vol.%) reinforced 6061 aluminium alloy composite. The composite is produced via the liquid metallurgy route by Comalco Research Centre.

The specimens tested were small compact tension specimens, 20 X 20 mm by 3mm thick and heat treated to the T6 condition. The specimens were polished, ion etched and pre-cracked in a laboratory machine at $6 < \Delta K < 10 \text{ MPa}\sqrt{\text{m}}$. Cracks were grown on a small servo-hydraulic machine outside the SEM. The specimen was then introduced into the microscope chamber in a special loading rig and cycled at rates from 0.3 to 1Hz, at an $R=0.1$ and an initial ΔK of $8.5 \text{ MPa}\sqrt{\text{m}}$. The crack tip region of each specimen was observed and photographed with both video film and still photographs. In order to save wear and tear on the fixture and to allow interactions to be studied at increasing K levels the specimen was removed, at required intervals, from the SEM and cycled outside on the servo-hydraulic and then replaced in the chamber for further observation. A similar loading stage, but with heating facilities, was used for the elevated temperature experiments.

The deformation response of the material in the crack tip zone was first determined by observing stereo pairs of the crack tip in the loaded and unloaded conditions. Some of the displacements visualised in the stereo-viewer were measured using DISMAP, an automated analysis system. From the measured displacements, three elements of the symmetric strain tensor (ϵ_{xx} , ϵ_{yy} , γ_{xy}) were computed at each measurement point, using the large strain definition, and from these values, the principal strains, the maximum shear strain and the mean and effective strains were derived. Thus eight values of strain were obtained at each of the ≈ 40 to 200 points within each field examined.

RESULTS AND DISCUSSION

In all cases studied the major crack growth mechanism was one of particle-matrix debonding ahead of the crack tip followed by linkage to the main crack. Particle cracking ahead of the crack tip that was evident in fast fracture experiments was not observed except at ΔK approaching K_{IC} .

Ambient Temperature Tests

Debonding was not limited to interfaces perpendicular to the applied load and was observed on interfaces parallel to the loading direction. For example, the large particle at centre bottom in Figure 1 is debonded at the top interface. This is particularly clear when viewed stereoscopically. Where debonding occurs on any particle is a function of the relative orientation of the approaching crack tip. For example, the particle at the top of the photograph is debonded on the right hand side a result of the approach of the crack towards that side.

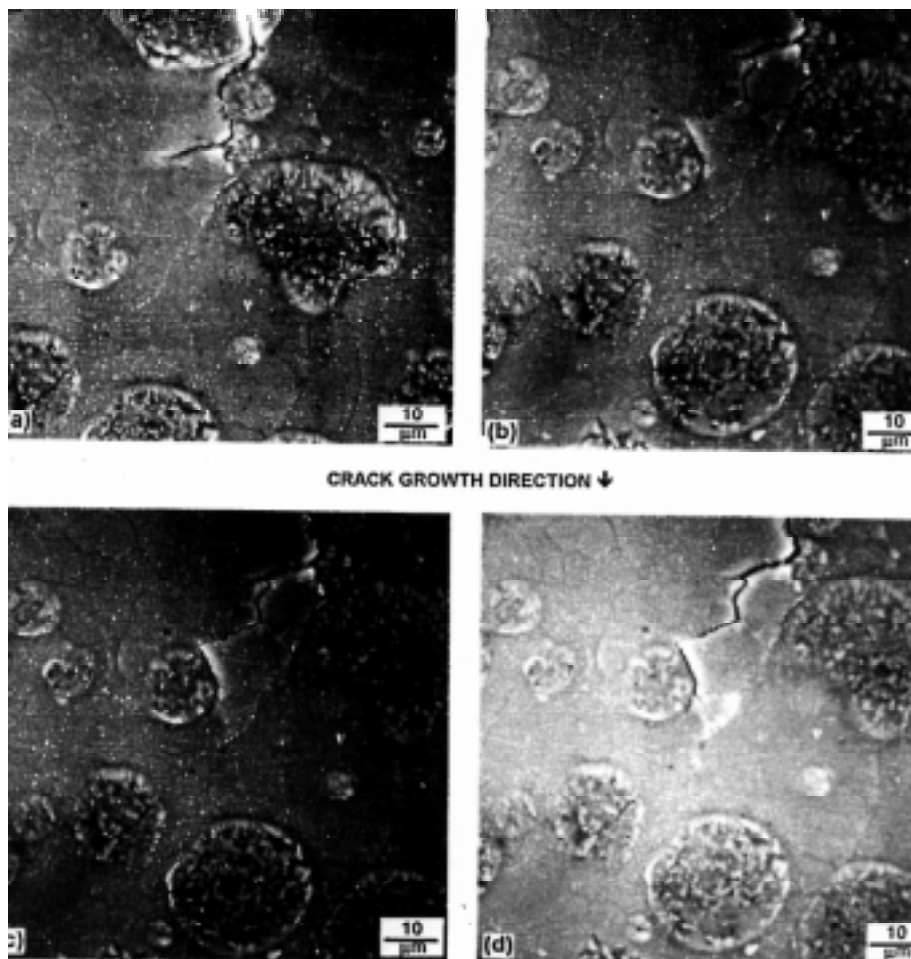


Figure 1. Comral-85 at $\Delta K \approx 10 \text{MPa}\sqrt{\text{m}}$ after (a) 48,000, (b) 53,000, (c) 57,000 and (d) 59,500 cycles.

The rate of crack growth was also found to vary depending on the vicinity of the crack tip to the particles. As the crack negotiated a path around the particles the crack growth rate was seen to decrease. For the case of Figure 1(d) the crack growth rate was seen to reduce as the particle approached the top of the particle. In general it was observed in going around particles

the crack provided crack surfaces at orientations up to 90° to the applied load reducing the effective driving force at the crack tip. Also significant Mode II displacement was observed. The sliding surfaces and the presence of the particles behind the crack tip also provided a wedging action on the crack, the crack opening displacement being observed to be quite large even when the crack tip in front of these disturbances were tightly shut.

The particle on the very left in Figure 1(a) is debonded, visible clearly when viewed stereographically, some 18µm ahead of the effective crack tip. The crack does eventually link up with this particle and can be seen to be “opening up” in Figure 1(b). Evidence of the crack growing parallel to the applied load is seen in Figure 1(c). An estimation of the crack growth rate from the video is approximately 4×10^{-9} m/cycle at a ΔK of 8MPa√m. This corresponds well with values obtained from standard crack growth measurements. Debonding was not limited to one particle near the crack tip.

As the crack grew the incidence of debonding and microcracking in the matrix, along grain boundaries between particles, increased occurring further away from the crack tip as the stress intensity range increased. Growth, then occurs, by a mechanism by which these microcracks and debonds linked up. Crack branching was also observed and seemed to occur at grain boundary intersections. These branches generally only grew a small distance, however, some vied with the main crack for some distance growing at the same rate. In all cases the main crack continued to propagate, the branches slowing down and stopping.

Prior to failure the process zone around the crack tip, consisting of debonded particles and microcracked matrix, increased. The number of particles that started to crack also increased. There was also evidence of the crack seeking particle clusters due to the significant debonding occurring in these regions. Figure 2 shows some of these effects.

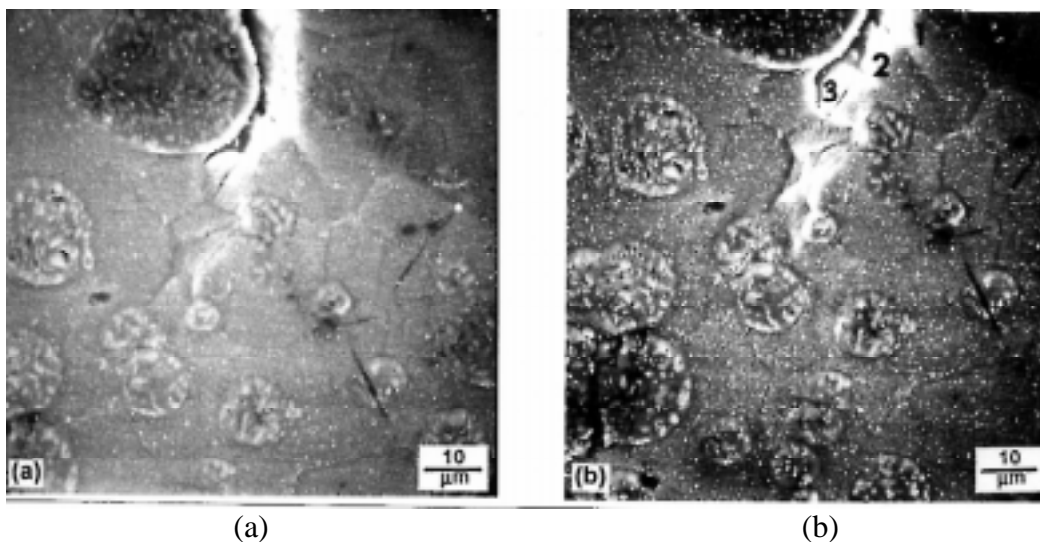


Figure 2. Comral-85 specimen at $\Delta K \approx 12 \text{ MPa}\sqrt{\text{m}}$ after 66,500 cycles outside the SEM and (a) 100 cycles in the SEM and (b) 200 cycles inside the SEM.

Figure 2(a) shows the crack passing along the right side of the particle. Close examination of the video and the photograph via stereoscopic techniques shows that crack branching, along grain boundaries, has occurred. ('1', '2' & '3' in Figure 2b). Large shear deformation was observed. On cycling the microcrack near the bottom of the particle (3 in Figure 2) won out.

Over the next 100 cycles damage accumulation continued between the particle at the top of the figure and the two joined particles in the centre of the photograph. Figure 2(b) shows the crack growing via the linkage of debonds and cracking along grain boundaries.

Over the 100 cycles the crack had now joined the two particles. ΔK was now increased by 2 $\text{MPa}\sqrt{\text{m}}$. At lower magnifications a large degree of debonding was now observed around the crack tip. On reaching the joined particles the crack branched again. Crack opening displacement $2\mu\text{m}$ behind the crack tip was now measured at $10\mu\text{m}$. Microcracking along grain boundaries continued with these microcracks growing in both directions and linking up to form the dominant crack.

With the formation of this deformation zone of debonding and microcracks the crack opening increased dramatically, as shown in Figure 3, and is primarily a result of the large horizontal section of the crack that was the crack branch through the “joint” in the two particles.

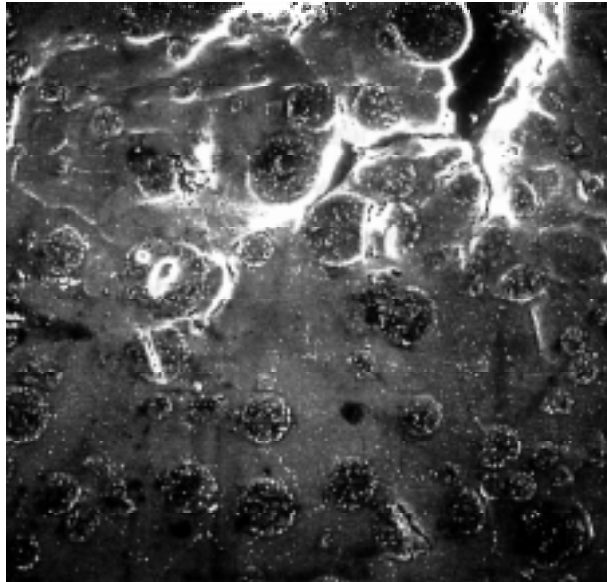


Figure 3. Comral-85 after 66,500 cycles outside the SEM and 400 cycles in the chamber.

Debonding and microcracking can be seen clearly in Figure 3, highlighted by the edge effects or charging in the photograph. The deformation zone is becoming quite large with cracking occurring predominantly at particle agglomerations. Significant debonding occurs at particle agglomerates ahead of the main crack tip. This debonded region then links up with the crack tip resulting in an effective sudden increase in crack length. Of course the effective crack tip in a system like this is very difficult to determine. Significant Mode II displacement is also observed as is large deformation within the matrix and wedging some $100\mu\text{m}$ behind the main crack tip. As failure approaches slip line formation and shear bands are observed as is the classic sharpening/blunting cycle (over approximately 3-4 cycles)

Elevated Temperature Tests

At 180°C similar trends are observed with intergranular crack growth much more pronounced. Grain boundaries parallel to the applied load slide over one another slowing down the local crack growth rate until the deformation in the matrix becomes sufficiently large to cause the crack to proceed again along one or more grain boundaries perpendicular to the applied load assisted by Mode II displacement.

Mode II displacements also accounted for wedging on the crack at the large bend shown in Figure 4 at “B” with the two crack surfaces becoming increasingly misaligned. Figure 4 also shows the growth of the crack through the matrix along the grain boundaries

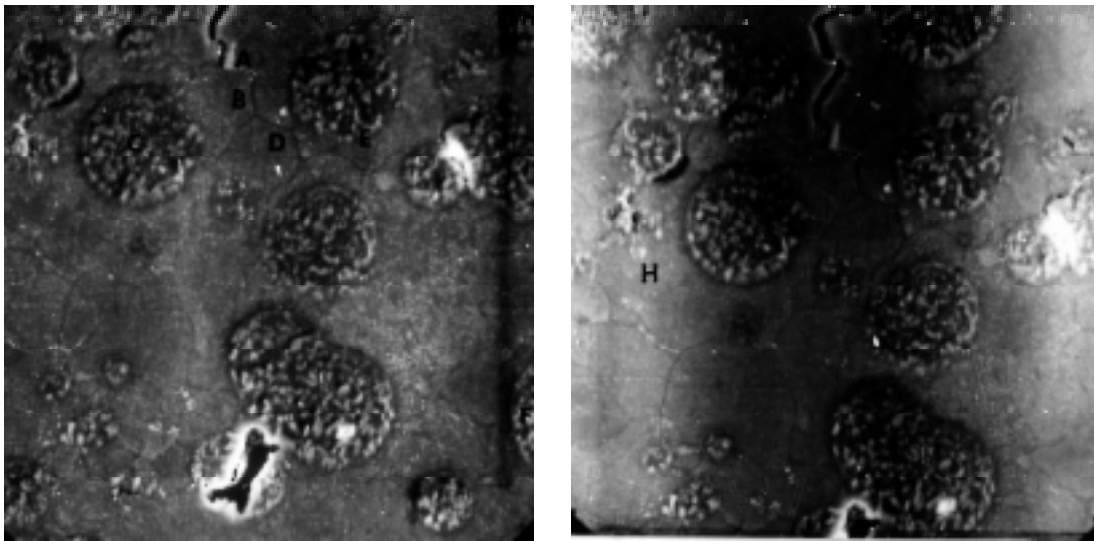


Figure 4. Progress of cracks along grain boundaries through the matrix at elevated temperature for the Comral-85 composite.

Debonding at particle “E” results in the crack deflected to the interface. The joined particles to the right have already debonded and the matrix ligament between them and “E” final tears. the crack eventually follows the grain boundaries down to particle “F”. Thus, although it might appear that the crack would travel straight down between particles “C” and “E” the debonding of particles in the process zone has controlled the crack path.

Indeed debonding can be seen to the left as well along the path from “G” to “H”. Microcracking at “H” eventually leads to crack growth into that region. At this stage there are 3 cracks growing as shown in Figure 5. This also shows the amount of deformation and damage just prior to failure. Microcracking at grain boundaries and particle-matrix interfaces is prevalent along with what appears to be lifting of grains and particles. The level of deformation in the matrix is higher than that of the ambient specimens. The lowering of the yield stress and elastic modulus with increase in temperature could affect this deformation as could any creep mechanisms due to the slow cycle rate.

Grain boundaries were also observed to “open up” ahead of the crack tip and was not evident in the room temperature *in situ* samples. Just prior to failure out-of-plane distortion was observed. Grains and particles were observed to lift up out of the specimen plane. Microcracks ahead of the main crack were seen to grow in both directions as well as cracks at the debonded interfaces. Crack branching along grain boundaries oblique to the main crack

was observed and in some cases where significant crack opening occurred debris was seen to be moving about.

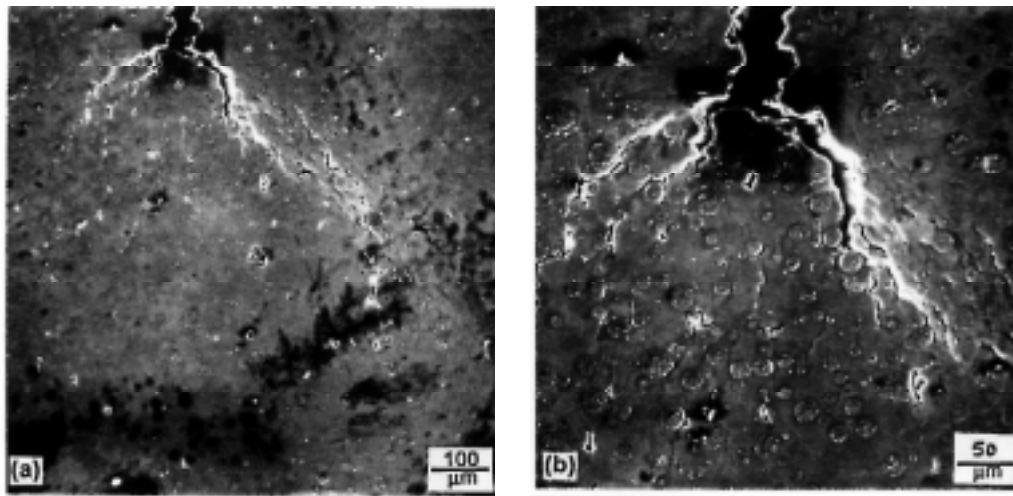


Figure 5. Low magnification photographs of Comral-85 at (a) minimum and (b) maximum loads, fatigued at 180°C.

GENERAL COMMENTS

It appears that the crack tends to grow along grain boundaries, this being particularly evident at the elevated temperatures. Generally intergranular failure suggests some form of creep mechanism or the presence of impurities at the grain boundaries. Creep-fatigue interactions have been documented and usually lead to intergranular cavitation. For aluminium alloys this mechanism has been observed at room and low temperatures. Creep may also be a result of the very low cycle rate in this test and may explain why, although deformation seemed greater at the elevated temperature for the in situ tests, little difference was found in the standard fatigue tests.

Furukawa et al. have investigated creep in the Comral material. Though not complete, their results show that the composite has a higher stress exponent (≈ 8.3 at 200°C) than the corresponding plane alloy. Mishra et al. reanalysed data on SiC reinforced 6061 alloy. They suggest that in these composites dislocations are generated at a grain boundary, travel across the grain and are absorbed by the other grain boundary.

Hadianfard et al. have confirmed the observations made here that the growth of fatigue cracks at the higher levels of ΔK occurs via the linkage of the main crack with microcracks ahead of the crack tip and particle debonding.

Using stereo-opsis the deformation behaviour around the crack tip was observed. A series of photographs were taken as the crack approached the particle and the strain response of the matrix was observed. The strain response represented by Mohr's circles is shown in Figure 6.

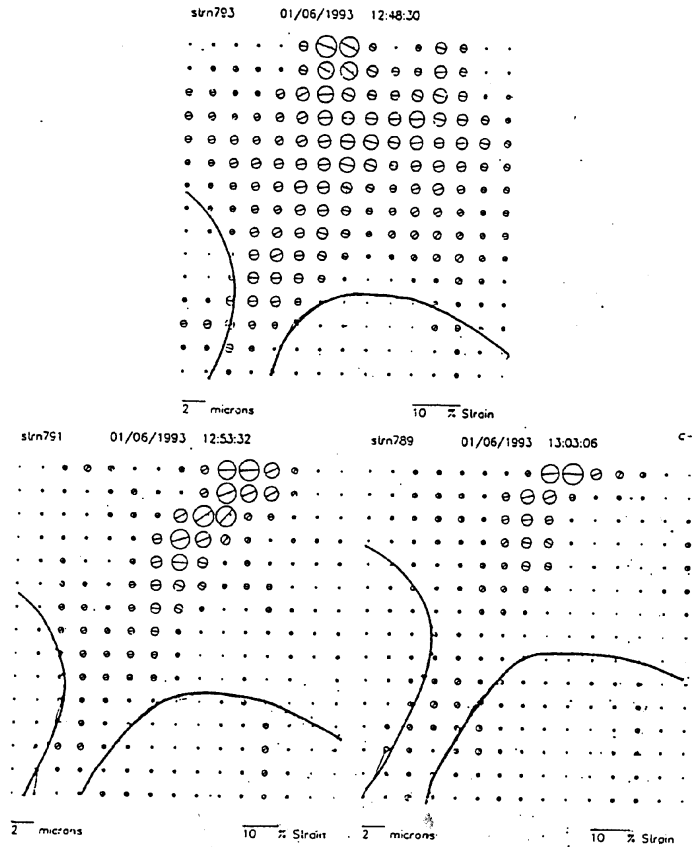


Figure 6. Mohr circles of strain at (a) 57,000 cycles, (b) 58,000 cycles and (c) 59,500 cycles.

As the crack approaches the particle, though growth here is very small, and as damage accumulates two main points can be noted:

1. The shear strain between the crack tip and the particle does not increase significantly but does change orientation, tending to align with the interface;
2. The magnitude of the strain between the crack tip and the particle reduces.

The first point may explain why the observed behaviour of crack growth is to travel toward the side of the particle instead of straight on. Together with the second point of a lower strain at the top of the particle may explain the observed behaviour as shown and discussed in Figure 1(b). The crack eventually curves over to the right and down the matrix-particle interface.

CONCLUSION

Crack growth rates, on a microstructural scale, in this material are a function of the proximity of the crack tip to the particles. Away from the particles the crack grows faster than when it is near a particle. The crack deflection and wedging, caused by the particle, tends to slow the growth rate down. However, as the stress intensity at the crack tip increases, microcrack formation at the particle matrix interface, i.e. debonding, and along grain boundaries, mainly between closely spaced particles and their resultant linkage results in an increased overall growth rate.

The mechanisms observed at elevated temperatures were the same as those at room temperature though more pronounced. There appeared to be much more deformation within the matrix. This is due to the lower yield strength and stiffness at these elevated temperatures as well as the possibility of creep-fatigue interactions. This latter point is the subject of further studies. In both cases, crack growth occurred via particle debonding ahead of the crack tip and is associated with intergranular void formation and coalescence. This suggests that the matrix particle interface is weak and that either creep and/or grain boundary impurities are present.

ACKNOWLEDGEMENTS

The authors would like to thank the Australian Research Council for partial support of this work. Thanks are also due to Dr Malcolm Couper of Comalco Research Centre, Thomastown, Australia, for the supply of Comral-85 for testing and Dr David Davidson of Southwest Research Institute, San Antonio, USA for the use of his testing and SEM facilities.

REFERENCES

- 1 Kumai, S., King, J. and Knott, J., "Short and long fatigue crack growth in a SiC reinforced aluminum alloy", *Fat. Fract. Eng. Mater. Struct.*, 13, 1990, pp. 511-524.
- 2 Kumai, S., King, J. and Knott, "Fatigue in SiC-particulate-reinforced aluminium alloy composites", *J. Mater. Sci. & Eng.*, A146, 1991, pp. 317-326.
- 3 Shang, J., and Ritchie, R., in *Metal Matrix Composites*, Arsenault, R. and Everett, R., Eds., Academic Press, Boston, MA, 1989
- 4 Shang, J., Yu, W. and Ritchie, R., "Role of SiC particles in fatigue crack growth in SiC particulate reinforced aluminium alloy composites", *Mater. Sci. Eng.*, 102, 1988, pp. 181-192.
- 5 Knowles, D. and King, J., "The influence of ageing on fatigue crack growth in SiC-particulate reinforced 8090", *Acta Metall. Mater.*, 39, 1991, pp. 793-806.
- 6 Davidson, D. and Nagy, A., "A low frequency cyclic-loading stage for the SEM", *J. Phys. E. Sci. Instrum.*, 1978, p. 11..
- 7 Heness, G., "Fracture and Fatigue Behaviour of Several Aluminium Matrix-Ceramic Particle Composites", *PhD Thesis*, University of Sydney, 1996
- 8 Rie, K and Schmidt, R., "Lifetime prediction under creep-fatigue conditions", *2nd Int. Conf. on Fatigue*, Munich, 1987, pp. 223-8.
- 9 Glaswin, D., Miller, D., Neate, G. and Priest, R., "Creep, fatigue and creep-fatigue crack growth rates in parent and simulated HAZ type 321 stainless steel", *Fatigue Fract. Engng. Mater. Struct.*, 11, 1988, pp. 355-70.
- 10 Wilson, M., *personal communication*, 1994.
- 11 Furukawa, M., Wang, J., Horita, Z., Nemoto, M., Ma, Y. and Langdon, T., "An investigation of strain hardening and creep in an Al-6061/alumina metal matrix composite", *Metall. & Mater. Trans.*, 26A, 1995, pp. 633-9.
- 12 Mishra, R., Pandey, A., Prasad, K and Mukherjee, A., "Microstructure of a creep tested Al-20 vol% SiC composite", *Scripta Metall. et Mater.*, 33, 1995, pp. 479-84.
- 13 Hadianfard, M. and Mai, Y-W, "In situ SEM studies on the effects of particulate reinforcement on fatigue crack growth mechanism of aluminium-based metal-matrix composite", *J. Mater. Sci.*, 30, 1995, pp. 5335-46.

STRENGTH DEGRADATION IN TITANIUM MATRIX COMPOSITES EXPOSED TO FATIGUE AT ELEVATED TEMPERATURE

David D. Robertson and Shankar Mall

*Department of Aeronautics and Astronautics, Air Force Institute of Technology,
2950 P Street, Wright-Patterson AFB, OH 45433-7765, USA*

SUMMARY: The residual strength of both unidirectional and cross-ply titanium matrix composites are examined after being exposed to isothermal fatigue loading at elevated temperature (427°C). The SCS6/Ti-15-3 composite system was tested with a cyclic fatigue load at 900 MPa maximum stress for the unidirectional layup and at 450 and 300 MPa for the cross-ply layup. Triangular waveforms with a minimum to maximum stress ratio of 0.05 and frequencies of 5 or 10 Hz were used. For the present conditions, the reduction in strength was not significant until after 50% of the expected life. The macroscopic behavior suggests damage accumulation consistent with fiber bridged matrix cracks. Microscopic evaluation of the failed specimens further corroborate this conclusion.

KEYWORDS: residual strength, failure of composites, fatigue, damage, failure mechanisms, fatigue life, titanium matrix composites, metal matrix composites

INTRODUCTION

Various fatigue studies of titanium matrix composites have been accomplished in recent years [1-4]. The long term goal of these and many other such studies have been to develop fatigue life maps for material characterization; thereby providing means for prediction of component design life. However, equally important to the designer is the remaining or residual strength of the material at any given fraction of the fatigue life. The present study examines the residual strength of both unidirectional and cross-ply titanium matrix composites after being exposed to isothermal fatigue loading at elevated temperature.

Damage accumulation during fatigue is expected to have a detrimental effect on the residual strength. This damage consists of the accumulation and distribution of matrix cracks, fiber cracks, and interfacial debonding. Some analytical studies have attempted to characterize the strength of metal matrix composites (MMCs) based on the distribution of constituent damage [5-6]. These investigations have focused on the fiber strength distribution and the interfacial characteristics as the critical parameters controlling the strength of the composite. Such methods have proven reliable for predicting the ultimate strength of virgin material [6]. However, in fatigue damaged specimens, it is possible the main source of damage is matrix cracking. If the fibers bridge these matrix cracks, then any significant reduction in strength may be prevented. However, there is a lack of such information. The present study investigates this important area.

MATERIAL AND EXPERIMENT DESCRIPTION

The material investigated in this study was a titanium matrix composite (TMC) composed of a titanium alloy (Ti-15V-3Cr-3Sn-3Al) continuously reinforced with silicon carbide fibers (SCS-6) at approximately 35 % fiber volume fraction. After consolidation and machining, the specimens were heat treated at 700°C in an argon environment for 24 hours. Both unidirectional, $[0]_8$, and cross-ply, $[0/90]_{2S}$, layups were considered in the present study and fatigued isothermally at 427°C. All specimens possessed a nominal length of 15 cm and width of 0.9 cm. The cross-ply specimens were rectangular coupons while the unidirectional specimens were machined with a dogbone geometry (shoulder radius: 116 cm) to ensure failure within the gauge length.

The experiments consisted of both monotonic and fatigue loading. Some specimens were fatigued to failure while others were stopped at different intervals of their fatigue life and then loaded to failure monotonically to obtain the residual strength. In addition, a few virgin specimens were loaded monotonically to failure (no prior fatigue) to obtain the ultimate strength. The unidirectional specimens were fatigued at a maximum stress of 900 MPa while two maximum stress levels, 300 MPa and 450 MPa, were used with the cross-ply specimens. A 10 Hz frequency triangular waveform with a minimum to maximum load ratio of 0.05 was chosen as the baseline cycle. However, due to extensometer slip at this frequency, the cross-ply tests at 300 MPa maximum stress were performed at 5 Hz. The monotonic tests to failure were loaded at 15 MPa/s. All tests were performed under load-control mode.

The specimen temperature within the gauge length was maintained at 427°C through the use of two 1000 W parabolic strip lamps positioned on either side (front and back) of the specimen face. Three thermocouples were welded onto the specimen within the gauge region (one in the center of the gauge length and two on either side) to monitor the specimen temperature during the test and provide input to the lamp controller. All specimens possessed a 1.27 cm gauge length and the displacement within this was obtained from a quartz rod extensometer positioned on the side of the specimen.

RESULTS AND DISCUSSION

The static, fatigue, and residual strength data is presented in Table 1. In some cases, such as the cross-ply specimen with a 663 MPa residual strength, extensometer slip prevented the strain data from being accurately recorded. Therefore, the strain and modulus data for these cases does not appear in the table. In addition, the static tests to measure ultimate strength and the fatigue tests to obtain the fatigue life are indicated with appropriate footnotes.

Comparison of the residual strength with other parameters listed in the table such as the change in maximum strain and modulus provides some qualitative relations. For instance, an increase in the maximum strain and a decrease in the modulus correlates to a reduction in the residual strength. However, these general trends do not provide a direct quantitative relation for the strength degradation. Also, for a given load level and layup the strength degradation with cycles demonstrates significant scatter, but this is consistent with the fatigue life which displays a factor of two variation in repeated tests as seen with the cross-ply 300 MPa maximum stress experiments.

Table 1. Static, Fatigue, and Residual Strength Test Results for Unidirectional and Cross-Ply Composite Layups of SCS6/Ti-15-3 at 427°C

Layup	σ_{\max} (MPa)	Last Cycle	$\Delta\epsilon_{\max}$ (%)	ΔE (GPa)	σ_{RS} (MPa)
[0] ₈	--	--	--	--	1,386*
[0] ₈	900	7,645	0.002	- 0.2	1,325
[0] ₈	900	15,284	0.014	- 1.6	1,287
[0] ₈	900	20,244	0.109	- 4.0	900**
[0] ₈	900	30,561	--	--	900**
[0/90] _{2S}	--	--	--	--	996*
[0/90] _{2S}	--	--	--	--	844*
[0/90] _{2S}	450	6,598	0.049	- 1.0	768
[0/90] _{2S}	450	8,004	0.021	- 1.0	859
[0/90] _{2S}	450	10,692	--	--	663
[0/90] _{2S}	450	17,023	0.101	- 16.0	450**
[0/90] _{2S}	300	50,010	0.071	- 5.5	767
[0/90] _{2S}	300	80,009	0.081	- 5.0	512
[0/90] _{2S}	300	94,153	--	--	300**
[0/90] _{2S}	300	100,011	0.084	- 13.0	481
[0/90] _{2S}	300	186,003	0.103	- 19.0	300**

* Static Test to Failure

** Fatigue Test to Failure

$\Delta\epsilon_{\max}$: Difference of the maximum strain in the last recorded cycle and the first cycle

ΔE : Difference of the modulus in the last recorded cycle and the first cycle

σ_{RS} : Specimen residual strength

Figures 1 through 3 plot the residual strength versus cycles for the three conditions investigated in this study. Figure 1 presents the unidirectional data while Figures 2 and 3 present the cross ply data. The unidirectional test to 20,244 cycles and the cross-ply 300 MPa maximum stress test to 94,153 cycles each failed in fatigue before they reached their respective target cycle for residual strength determination. These points provide some indication of the scatter in the fatigue life for this material.

The unidirectional data displays a slight drop-off in the strength of approximately ten percent over the first half to two-thirds of the projected fatigue life. The majority of the strength reduction occurs near the end of the life. In fact, it is difficult to capture the residual strength in this region. However, the number of data points is sparse and more testing of the unidirectional material is required before this conclusion can be finalized. In contrast, the cross-ply data at both stress levels displays a reduction in strength with successive cycles that can almost be classified as linear with a scatter band approximately 15% of the virgin material strength. In addition, this characteristic is not affected by the maximum stress level but simply scales according to the fatigue life.

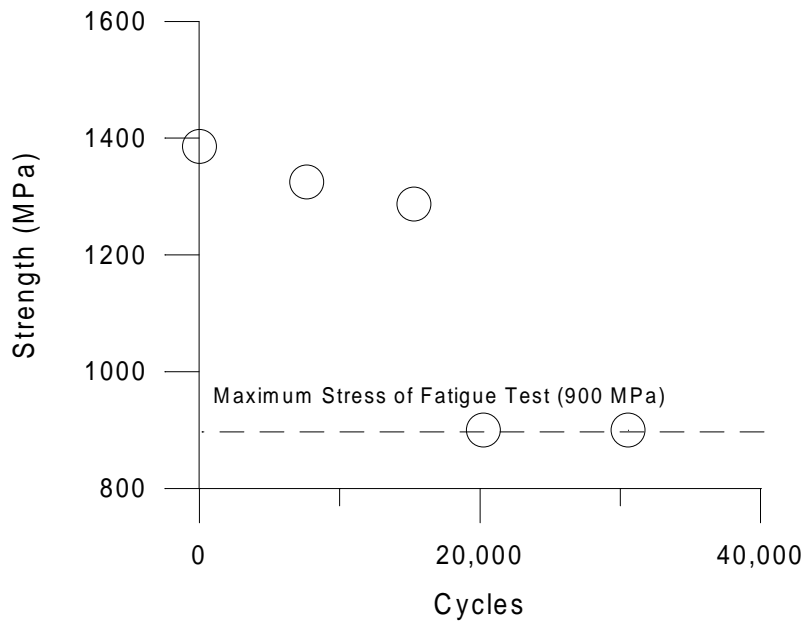


Figure 1. Residual Strength of Unidirectional SCS6/Ti-15-3 at Selected Cycles (900 MPa Maximum Stress)

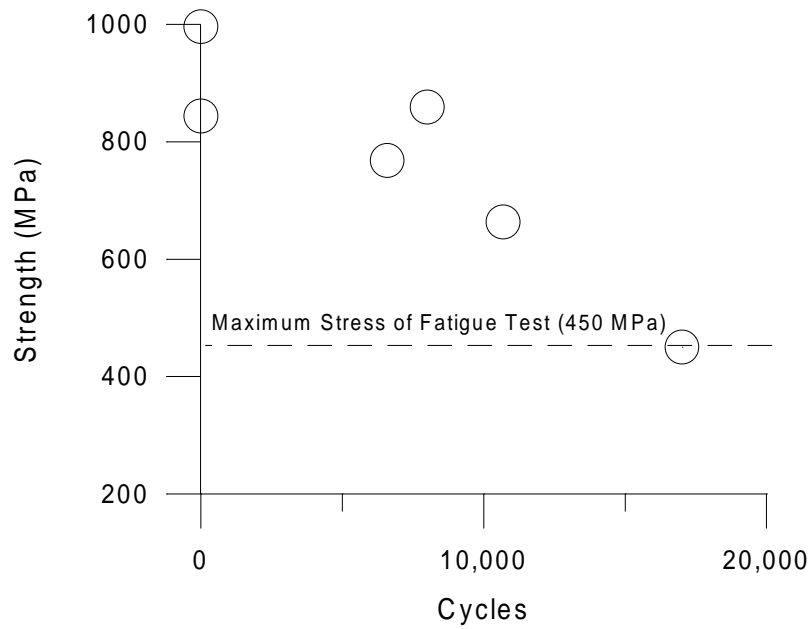


Figure 2. Residual Strength of Cross-Ply SCS6/Ti-15-3 at Selected Cycles (450 MPa Maximum Stress)

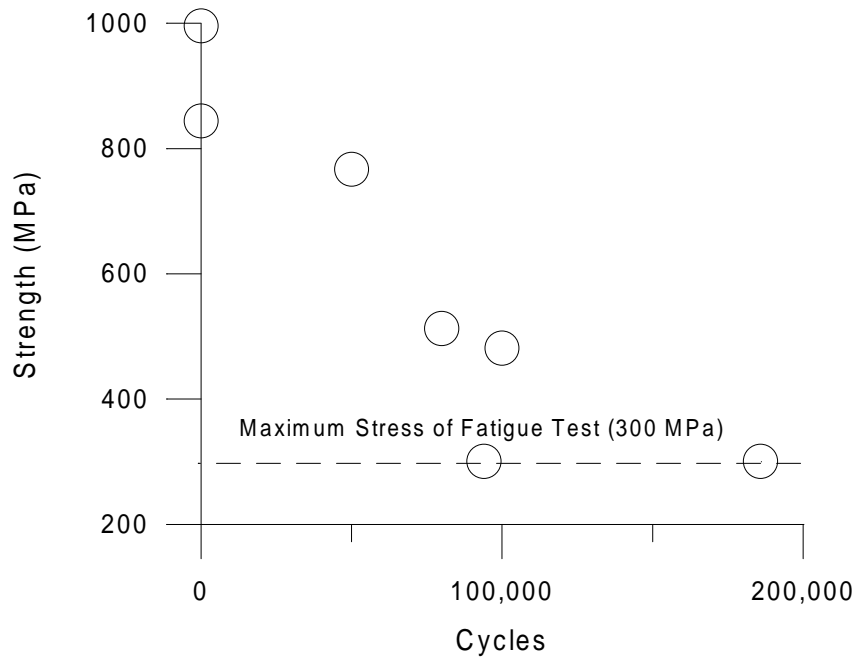


Figure 3. Residual Strength of Cross-Ply SCS6/Ti-15-3 at Selected Cycles (300 MPa Maximum Stress)

Such behavior is reasonable considering the mechanisms involved. The unidirectional specimens experience matrix relaxation within the first few cycles because the microstress in the matrix is above its yield strength of approximately 550 MPa at this temperature (427°C) [7]. A previously developed inelastic micromechanics model was employed for the present study to perform a calculation of the microstress in the matrix [8]. This analysis provided a longitudinal matrix stress of 642 MPa at the peak of the first cycle which is significantly higher than the yield stress. Thus, due to plastic/viscoplastic deformation the matrix will relax with subsequent cycles and its ability to carry load will be reduced. However, because the fibers carry the majority of the load, this will not greatly effect the overall strength of the composite. In addition, if matrix fatigue cracks develop and are bridged by the fibers, then the strength of the composite will still be maintained. It is not until some of the fibers begin to fail near this matrix crack plane that the strength of the unidirectional system will be significantly reduced. Such an effect would not be noticeable until near the end of the fatigue life [9]. The presence of fiber-bridged matrix fatigue cracks is corroborated by microscopic evaluation of a specimen polished down to the first layer of fibers (Figure 4). As this figure shows, there is no evidence of fiber damage even though a matrix fatigue crack extends through several fibers. In fact, little or no fiber cracks were observed in any of the specimens.

On the other hand, the almost linear reduction in strength observed in the cross-ply specimens can be related to the 90° plies providing a predictable mechanism for crack initiation early in the material life. It is well documented that this MMC system possesses a relatively weak fiber/matrix interface which debonds once the clamping effect of the thermal residual stresses in the matrix are overcome [1,10]. This debonding provides a source for crack formation in the 90° plies which then propagate through-the-thickness into the 0° plies [11]. Such a mechanism effectively reduces the crack initiation time to the first few cycles. Thus, strength reduction associated with this is observed early in life. Microscopic evaluation revealed these

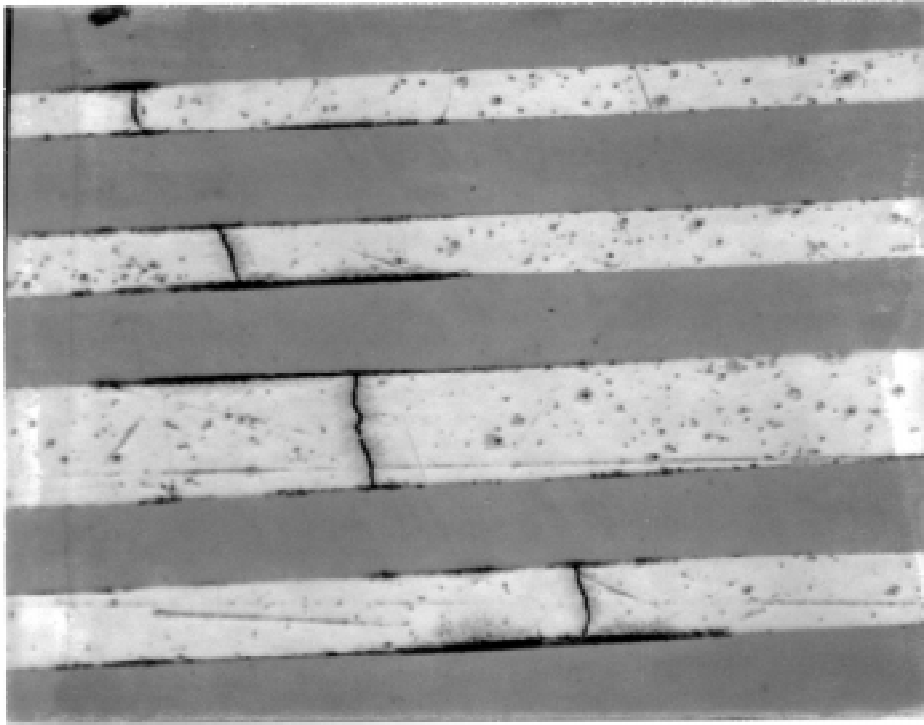


Figure 4. Bridged Matrix Crack in Unidirectional Specimen of SCS6/Ti-15-3

fatigue cracks were bridged by the longitudinal fibers in a similar manner to what is depicted in Figure 4. In addition, multiple site initiation produces a more random distribution of cracks throughout the matrix, and hence, a more gradual reduction in strength is observed as opposed to the unidirectional specimens where a single dominant fatigue crack is the main mechanism. This conclusion is further validated by the observed modulus reduction in the cross-ply specimens. Over a ten percent reduction from the initial modulus was recorded before fatigue failure of the cross-ply while the unidirectional data only shows a drop of about three percent from the initial modulus. Figure 5 plots the modulus reduction for cross-ply specimens that failed in fatigue at both the 450 MPa and 300 MPa maximum stress levels. In the figure, the modulus is normalized with each specimen's initial modulus, and the cycle number is normalized with each specimen's respective fatigue life. At least for the cross-ply, the characteristics of modulus reduction is similar in behavior to the drop in residual strength and offers the best practical method of predicting the residual strength for this layup. However, as previously mentioned, obtaining a direct quantitative relationship is difficult (see Table 1). A more extensive test program is required before any such relationship could be outlined with confidence due to the statistical scatter in the data.

Figure 6 presents all the residual strength data on a single normalized plot. For the normalized cycles, each condition (loading and layup) was normalized with respect to its average fatigue life as measured in this study. The normalization method used for the strength was as follows

$$\text{Normalized Strength} = \frac{\sigma_{RS} - \sigma_{\max}}{\sigma_{\text{ult}} - \sigma_{\max}} \quad (1)$$

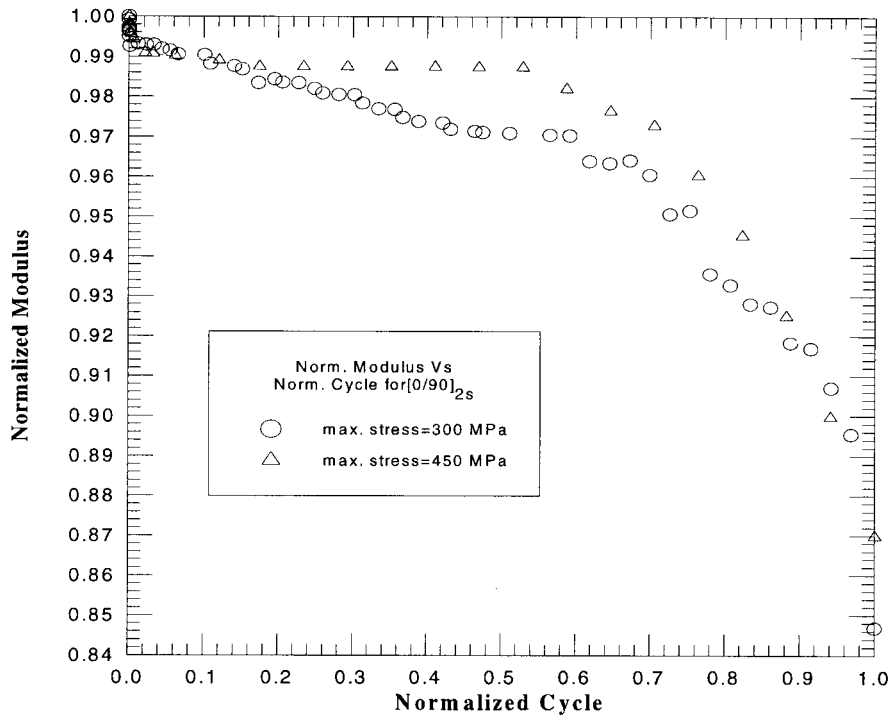


Figure 5. Normalized Modulus Throughout Life for Cross-Ply SCS6/Ti-15-3

where σ_{max} is the maximum stress of the fatigue cycle and σ_{ult} is the average ultimate strength of the virgin material as found in the present study.

A distinct advantage of the above normalization is that all the data from the layups and loading conditions considered in the present work are collapsible to a single scatter band from which a safe operating region may be gleaned. In fact, the scatter associated with this representation is no more than what is observed in the fatigue tests run under identical conditions. Also, it should be noted that the multiple points plotted in Figure 6 for the cross-ply virgin strength are not from additional experiments but due to the different maximum fatigue stress level used in Eq (1). As mentioned in the preceding paragraphs, the damage initiation mechanisms for the unidirectional versus cross-ply material are not the same. However, both systems display similar characteristics of maintaining a significant portion of their strength up to 50% of the expected life.

CONCLUSIONS

The present study examined the SCS6/Ti-15-3 titanium matrix composite for strength reduction due to tension-tension fatigue loading under isothermal conditions (427°). Both unidirectional and cross-ply layups were investigated. The unidirectional specimens exhibited damage mechanisms involving fiber-bridged matrix fatigue cracks which initiated at the surface and/or edge. Although a few small cracks were observed away from the fracture surface, a single dominant matrix crack controlled the progression of damage. Thus, due to crack ini-

tiation time and bridging fibers, the majority of strength reduction occurred near the end of expected life. More tests are required, however, to validate this finding. On the other hand, the

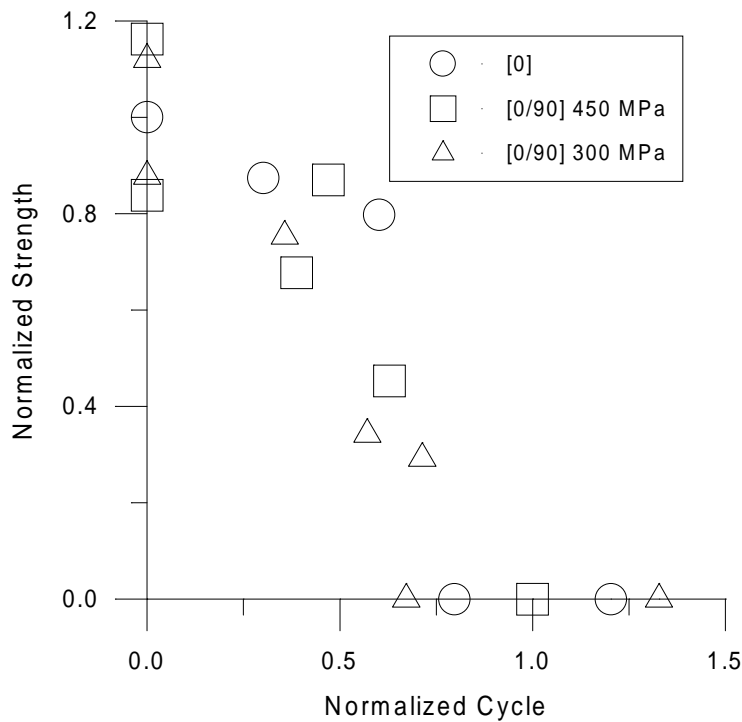


Figure 6. Normalized Residual Strength Versus Life for the SCS6/Ti-15-3 System

cross-ply specimens possessed a predictable crack initiation mechanism in the fiber/matrix interface of the off-axis plies. This reduced the crack initiation time, created a more random distribution of damage, and resulted in a more gradual reduction in strength throughout life than observed in the unidirectional specimens. Nevertheless, both layups maintained significant strength through 50% of the expected life.

Thus, titanium matrix composites subjected to these conditions offer the designer a robust material system. Reduction in the material's strength due to fatigue loading will not be a factor in design as long as conservative component service lives are adopted. However, further characterization with other layups and loading conditions are required before firm conclusions may be drawn.

ACKNOWLEDGEMENTS

This study was supported by the Air Force Office of Scientific Research (Maj Brian Sanders), and the Propulsion Directorate (Ted Fecke) of Wright Laboratory.

REFERENCES

1. Johnson, W.S., Lubowinski, S.J., and Highsmith, A.L., "Mechanical characterization of unnotched SCS6/Ti-15-3 metal matrix composites at room temperature," *Thermal and Mechanical Behavior of Metal Matrix and Ceramic Matrix Composites*, Kennedy, Moeller, and Johnson, eds, ASTM STP 1080 (1990) 193-218
2. Lerch, B.A., Verrilli, M.J., and Halford, G.R., "Fully-reversed fatigue of a Ti-MMC," Proceedings of the American Society for Composites: Eighth Technical Conference, Technomic Pub (1993) 388-396
3. Sanders, B., and Mall, S., "Isothermal fatigue behavior of a titanium matrix composite under a hybrid strain-controlled loading condition," *Materials Science & Engineering A200* (1995) 130-139
4. Boyum, E.A., and Mall, S., "Fatigue behavior of a cross-ply titanium matrix composite under tension-tension and tension-compression cycling," *Materials Science and Engineering, A200* (1995) 1-11
5. Curtin, W.A., "Ultimate strengths of fibre-reinforced ceramics and metals," *Composites*, 24(2) (1993) 98-102
6. Robertson, D.D., and Mall, S., "Incorporating fiber damage in a micromechanical analysis of metal matrix composite laminates," *Journal of Composites Technology & Research*, 18(4) (1996) 265-273
7. Foringer, M.A., Robertson, D.D., and Mall, S., "A micro-mechanistic based approach to fatigue life modeling of titanium matrix composites," *Composites Engineering* (in press)
8. Robertson, D. D., and Mall, S., "A nonlinear micromechanics based analysis of metal matrix composite laminates," *Composites Science and Technology*, 52(3) (1994) 319-331
9. Begley, M.R., and McMeeking, R.M., "Fatigue crack growth with fiber failure in metal-matrix composites," *Composites Science and Technology*, 53 (1995) 365-382
10. Nimmer, R.P., "Fiber-matrix interface effects on the presence of thermally induced residual stresses," *ASTM Journal of Composites Technology & Research*, 12(2) (1990) 65-75
11. Mall, S., and Portner, B., "Characterization of fatigue behavior in cross-ply laminate of SCS6/Ti-15-3 metal matrix composite at elevated temperature," *Journal of Engineering Materials and Technology*, 114, (1992) 409-415

EFFECT OF THE INTERFACE ON THE CRACK DEFLECTION AND FIBER BRIDGING DURING FATIGUE CRACK GROWTH OF SIC/TI-6A1-4V COMPOSITES

S.G. Warrior¹, B.S.Majumdar² and D.B. Miracle

Wright Laboratory Materials Directorate, Wright-Patterson AFB, Ohio-45433, USA.

^{1&2} *UES, Inc., 4401 Dayton-Xenia Rd., Dayton, OH 45432, USA.*

SUMMARY: The effect of the interface on the fatigue crack growth response of titanium matrix composites was examined using four different interfaces. Fiber bridging and fiber failure were observed in all four composite systems at different ranges of stress levels. The fatigue crack growth life of the composites, even for the ones that did not exhibit fiber bridging, was significantly higher than that of the "neat" material. Elastic shielding of the crack tip was observed in all four systems, more significantly for the strongly bonded interface. Normal interface separation and damage ahead of the crack tip was observed in two of the composites with the weaker interface. Finite element analysis suggests that shear stress induced failure precedes normal interface separation and supports the crack growth behavior for the weaker interfaces. A stress based criterion for predicting debonding appeared to explain the crack deflection behavior effectively for the composites.

KEYWORDS: Interface, Fatigue Crack Growth, Crack Deflection, Bridging, Elastic Shielding, Bond Strength, Normal Interface Separation, Shear Failure.

INTRODUCTION

The mechanical characteristics of the fiber-matrix interface significantly influence the fatigue crack growth response of continuous fiber-reinforced composites. It is generally believed from the ceramic matrix composite literature [1] that a "strong" interface prevents interface debonding and facilitates fiber failure, hence negating beneficial effects of fiber bridging on the fatigue crack growth (FCG) and fracture properties of composites. On the other hand, a "weak" interface facilitates interface debonding and crack bridging, which results in a decrease in the crack growth rate. However, there has been only a limited amount of systematic studies of the effect of interface properties (normal bond strength, shear strength, toughness, frictional coefficient etc.) on the fatigue and fracture response of composites, in particular metal matrix composites. The overall objective of the research activity is to develop a thorough understanding of the effect of the interface on the micro-mechanical damage mechanisms and their influence on the fatigue crack growth response of titanium matrix composites. In this study, the FCG response of composites with different coatings, which span a large range of interface bond strengths and fiber strengths, has been investigated.

EXPERIMENTAL

Four sets of fibers with different interfacial characteristics, uncoated SiC fiber (SCS-0, manufactured by Textron Specialty Materials, Lowell, MA), carbon + SiC coated SiC fiber (SCS-6, also manufactured by Textron Specialty Materials), carbon coated SiC fiber (Trimarc 1, manufactured by Amercom, Chatsworth, CA) and yttrium coated SCS-0 fibers were selected for this study. These four systems comprise a wide range of interface properties and fiber strength [2-4] (Table 1). Sample preparation and testing procedures for single-ply composites

Table 1: Interface and Fiber Properties of Composites Tested

Composite System	Normal Bond Strength [2] (MPa)	Debond/Frictional Sliding Stress [3] (MPa)	Virgin Fiber Strengths [4] $\sigma_{mean} \pm S.D.$ (MPa)
SCS-6/Ti-6Al-4V	122 - 145	160	4386 \pm 590
SCS-0/Ti-6Al-4V	> 380	300	1678 \pm 168
Trimarc 1/Ti-6Al-4V	0 - 40	30	3156 \pm 138
Y/SCS-0/Ti-6Al-4V	0 - 20	-	-

used in this study are discussed in detail elsewhere [5]. The position of the first fiber from the outer edge of the specimen was approximately 9 mm (Figure 1). Experiments were performed at different applied stress ranges ($\Delta\sigma_a$) from about 24 MPa to 100 MPa and stress ratios ($R = \text{Minimum stress/Maximum stress}$) of 0.05 to 0.2. In addition to the composite specimens, the unreinforced matrix, "neat" material, was also fabricated and tested in the same manner at $\Delta\sigma_a = 50$ MPa and $R = 0.1$. Following mechanical testing, etched as well as polished samples were prepared using standard metallography techniques. The nature of the damage was assessed by examining the fiber-matrix interface under a scanning electron microscope.

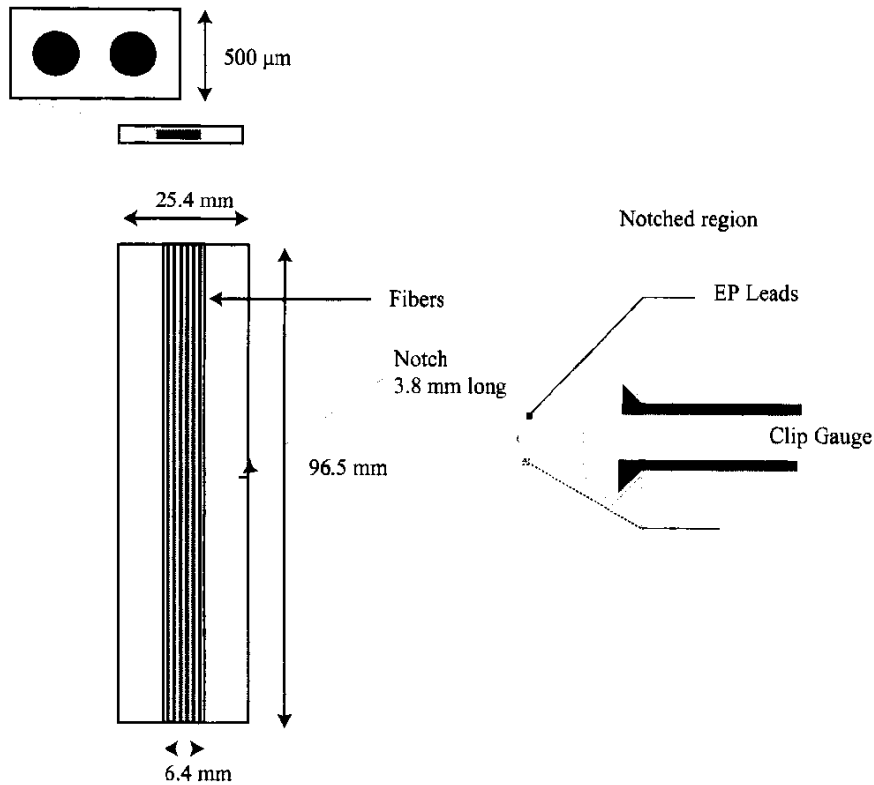


Figure 1: Sketch of the FCG setup

RESULTS

Crack Growth Rates

Figures 2 and 3 show the crack length (a) as a function of the number of cycles (N) and the crack growth rate (da/dN) as a function of the applied stress intensity factor range (ΔK_a), respectively, for the "neat" material and the four composites tested at $\Delta\sigma_a = 50$ MPa and $R = 0.1$. Compared to the neat material, all four composites exhibited enhanced fatigue crack growth life of the specimen starting from an initial fatigue crack length of approximately 6 mm. Different material responses were observed in these composite systems both, as the crack approached the fiber and when the crack was within the fibrous region.

Crack growth in the initial part of the curve ($a < 7$ mm in Figure 2), i.e. in the matrix far away from the fibers, was similar for all the samples. It appears that the presence of the fibers does not noticeably affect the crack growth response when the fibers are reasonably far from the crack tip. As the crack approaches the first fiber ($7 \text{ mm} < a < 9 \text{ mm}$), the crack growth rate (da/dN), decreases for all the composites compared to the "neat" material. As discussed in a later section, this phenomenon is caused by elastic shielding of the crack tip due to the presence of a higher modulus material ahead of the crack tip. The extent to which the deceleration of the crack occurs is more pronounced for the SCS-0/Ti-6Al-4V composite compared to the other three composites.

As the crack grows into the fibrous region ($a > 9$ mm), the growth rate of SCS-6/Ti-6Al-4V and Trimarc 1/Ti-6Al-4V decreases, which is reflected in the a vs N curves flattening out. Eventually, the crack is completely arrested. This phenomenon is caused by the fibers bridging the crack, presented in a later section, and hence reducing the local stress intensity factor at the crack tip. In Y/SCS-0/Ti-6Al-4V, the crack growth rate decreased continuously as the crack crossed the first 10 fibers, following which an increase in the growth rate was observed. This behavior is indicative of the fact that the fibers bridged the crack initially but with continued cycling, fiber failure occurred. In SCS-0/Ti-6Al-4V composites, the crack continued to grow with increasing number of cycles, suggesting that stable crack bridging does not occur in these specimens at these loads.

da/dN versus ΔK_a curves the composites tested at various loads are shown in Figures 4 to 6. SCS-6 composites exhibited fiber bridging characteristics up to $\Delta\sigma_a = 75$ MPa. On continued cycling at $\Delta\sigma_a = 75$ MPa, the bridging behavior ceased and fiber failure was observed. Bridging behavior was observed for Trimarc 1 composites up to $\Delta\sigma_a = 87$ MPa. Increased crack growth rate and fiber failure was observed at $\Delta\sigma_a = 100$ MPa. In SCS-0 composites, bridging behavior was observed at $\Delta\sigma_a = 24$ MPa but not at $\Delta\sigma_a = 34$ MPa and 50 MPa.

Microscopic Analysis

Micrographs of the cracked region in an etched SCS-6/Ti-6Al-4V composite sample tested at $\Delta\sigma_a = 50$ MPa are shown in Figure 7. The crack tip is between the sixth and seventh fiber. The first six fibers are intact and are bridging the crack, although extensive damage to the coating can be observed in the crack plane. An enlarged portion of the crack tip region shows an area in the matrix immediately ahead of the crack tip which has etched preferentially. This region is believed to be the plastic zone based on an estimate of the plastic zone size from fracture mechanics. A scalloped morphology can be noted at the interface ahead of the crack tip with the damage principally located away from the crack plane ($\pm 20 \mu\text{m}$). This latter observation suggests that interface damage due to matrix plasticity occurs before the crack reaches the interface.

Micrographs of polished samples of SCS-6/Ti-6Al-4V composite (Figure 8) confirm damage to the interface ahead of the crack tip indicating the presence of normal stresses at the interface. Damage to the interface ahead of the crack tip was predominantly located inside the

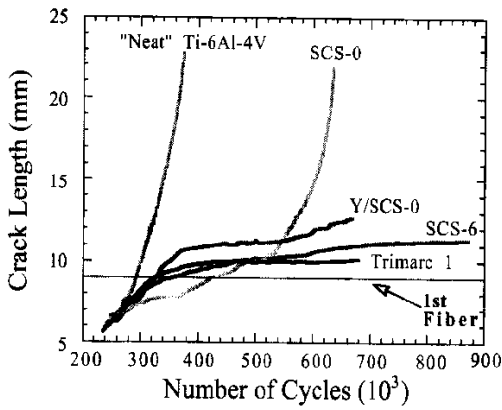


Figure 2: Crack length versus number of cycles at $\Delta\sigma_a = 50$ MPa.

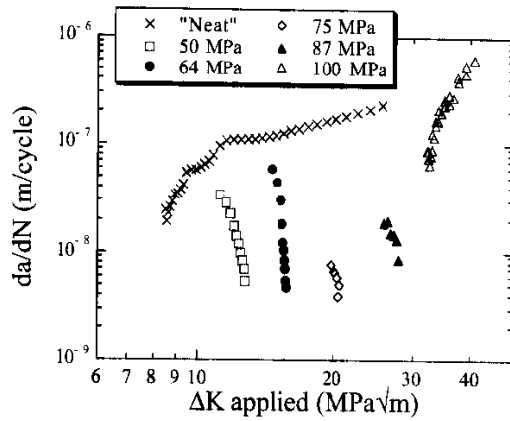


Figure 5: da/dN curves for Trimarc 1/Ti-6Al-4V at different applied stress ranges.

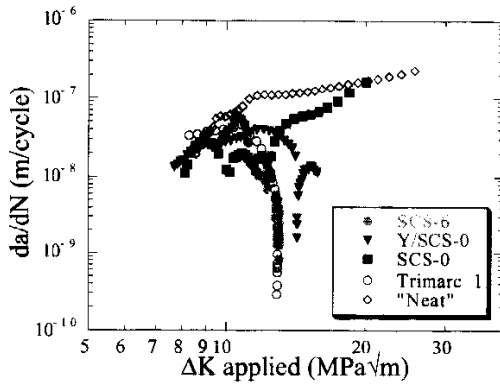


Figure 3: Crack growth rate curves at $\Delta\sigma_a = 50$ MPa.

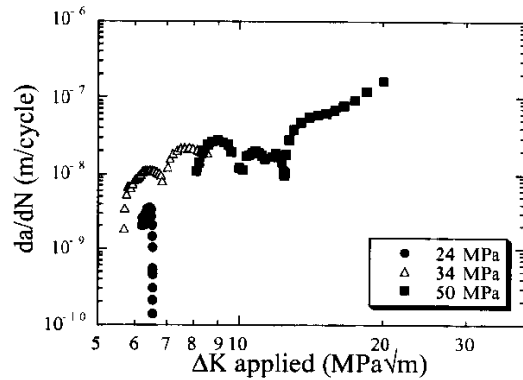


Figure 6: da/dN curves for SCS-0/Ti-6Al-4V at different applied stress ranges.

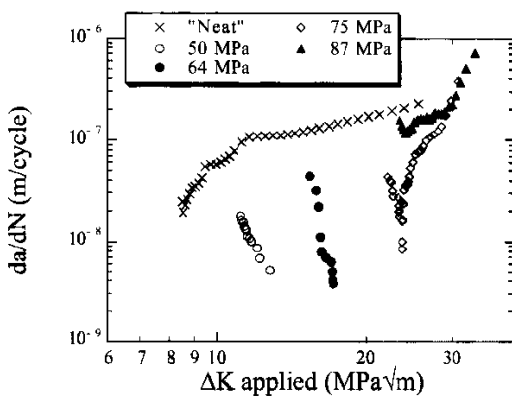


Figure 4: da/dN curves for SCS-6/Ti-6Al-4V at different applied stress ranges.

carbon-rich coating in layer 2, as defined by Ning and Pirouz [6] (Figure 9). Damage to the interface in the crack wake was also observed (Figure 10). This damage was both, in layer 2 and between the reaction product and the coating in the region very close to the crack plane ($< 50 \mu\text{m}$). The damage was exclusively in layer 2 in the region of the interface approximately between 50 and 200 μm . However, at a distance of about 200 μm from the crack plane, the site of interface damage appeared to shift from layer 2 to in between layers 1A and 1B.

Similar to the results for SCS-6 composite, fiber bridging and damage to the coating ahead of the crack tip was observed

in Trimarc 1/Ti-6Al-4V tested at $\Delta\sigma_a = 50$ MPa. Damage to the interface typically occurred within the carbon coating. At higher stress levels ($\Delta\sigma_a = 100$ MPa), fiber failure was observed. Fiber failure was also noted in SCS-0 composites at $\Delta\sigma_a = 34$ MPa and 50 MPa, and Y/SCS-0/Ti-6Al-4V at $\Delta\sigma_a = 50$ MPa after prolonged cycling, in accordance with the growth rate data. At $\Delta\sigma_a = 24$ MPa, fiber bridging was observed in SCS-0 composites, in agreement with the crack growth rates in Figure 6. Damage ahead of the crack tip could not be identified in polished samples of these composites, although interface damage was observed in between the reaction zone and the fibers in the crack wake. For details of microscopic analysis refer to [5].

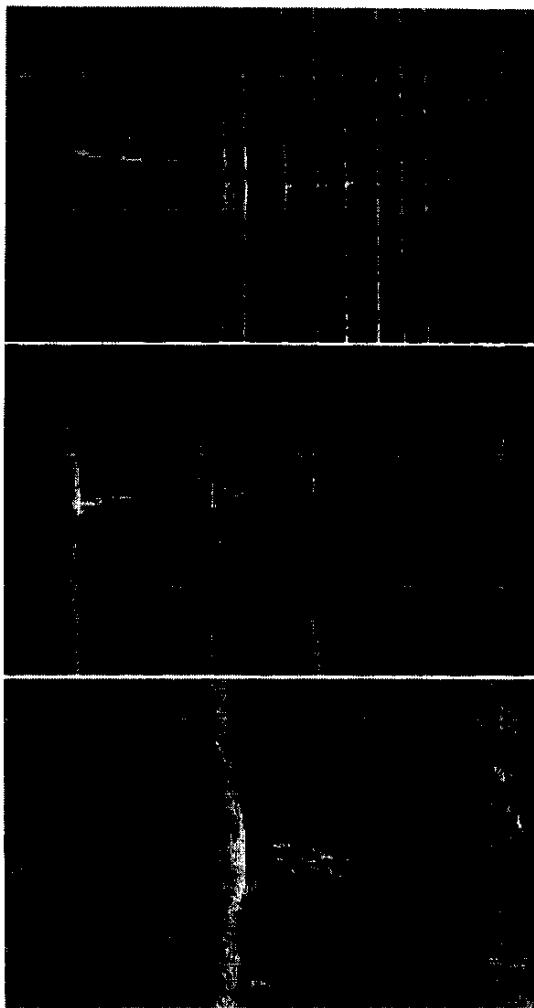


Figure 7 Micrographs of etched SCS-6/Ti-6Al-4V composite.

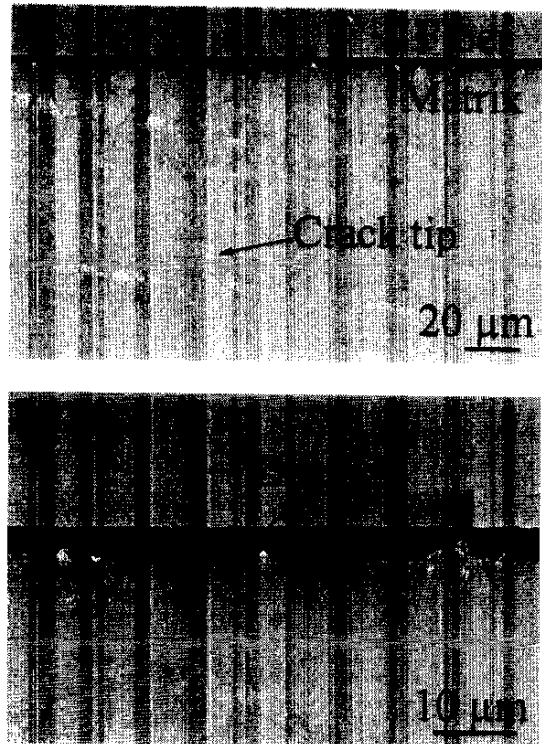


Figure 8 Damage to the interface ahead of the crack tip. a) low magnification and b) high magnification image of the interface directly ahead of the crack tip.

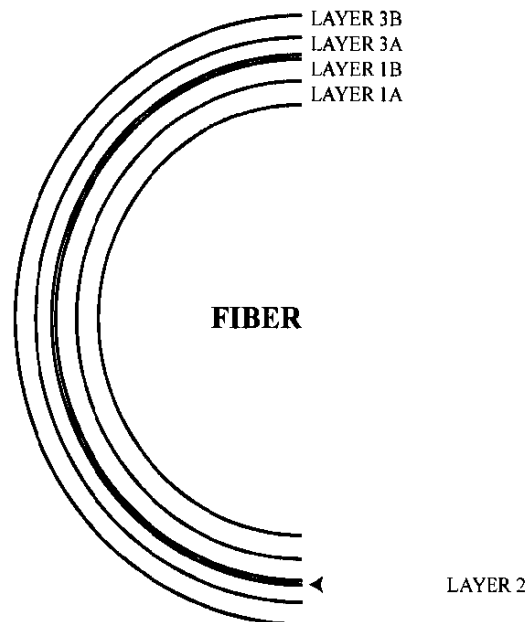


Figure 9 Microstructure of the coating on SCS-6 fibers from reference [6].



Figure 10: Damage to the interface in a fiber bridging the crack. a) at the crack plane and b) at a distance of about 200 μm from the crack plane. **A** denotes damage at the reaction zone/carbon-rich layer, **B** denotes damage in layer 2, and **C** denoted damage in between layers 1A and 1B.

DISCUSSION

Elastic Shielding

Finite element analysis was conducted to determine the local stress intensity factor and the stress distribution at the interface ahead of the crack tip. Results indicate that as the matrix crack approaches a higher modulus material (the fiber in this case), the shielding factor (ξ), defined as the ratio of the local stress intensity factor over the applied stress intensity factor, decreases (Figure 11). ξ is approximately 0.5 when the crack tip is 20 μm from the higher modulus material. Theoretically, $\xi = 0$ when the crack tip reaches the interface. The above analysis assumes that the fiber-matrix interface is strongly bonded. However, if normal interface separation or shear failure and sliding were to occur ahead of the crack tip, load transfer to the higher modulus fibers would be less efficient, resulting in a higher local ΔK at the crack tip. Under such circumstances, an increase in the value of ξ and consequent increase in the crack growth rate is predicted. Thus, fibers that debond ahead of the crack tip are expected to show a reduced rate of crack deceleration compared to fibers that do not debond or possess a higher bond strength. The lower crack growth rate of SCS-0 composite (strong interface) compared to the other three sets of composites (weaker interfaces), as the crack approaches the first fiber, supports this analysis.

Interface Debonding

Interface failure ahead of the crack tip may occur through either shear stress induced failure and frictional sliding or normal stress induced debonding. In order for shear stress induced failure/frictional sliding to occur, the local shear stress at the interface must exceed the shear strength of the interface and the resistance to sliding. For normal stress induced failure, the local radial stress must overcome the normal bond strength plus the compressive radial residual stress. Figures 12 and 13 show the maximum normal and shear stresses at the interface, respectively, as the matrix crack approaches the fiber from finite element analysis. Figure 12 takes into account a compressive residual stress of 300 MPa that exists at the interface [7] due to thermal strains.

The normal bond strengths of the Trimarc 1/Ti-6Al-4V, SCS-6/Ti-6Al-4V, SCS-0/Ti-6Al-4V and Y/SCS-0/Ti-6Al-4V interfaces have been reported to be about 0 MPa, 120 MPa, above 380 MPa and about 0 MPa, respectively [2]. Therefore, normal interface separation ahead of the crack tip is predicted for SCS-6, Trimarc 1 and Y/SCS-0 interfaces when the crack is about 0.1 mm away from the interfaces for the former and about 0.2 mm from the interface for the latter two.

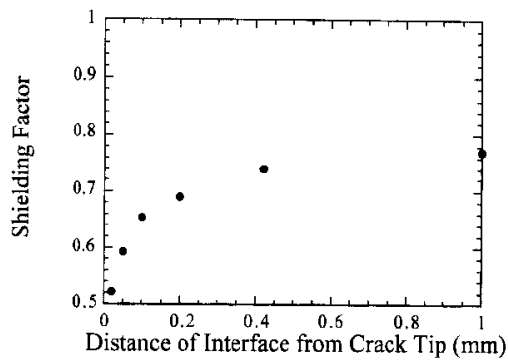


Figure 11: Variation in the shielding factor as the crack approaches the fiber.

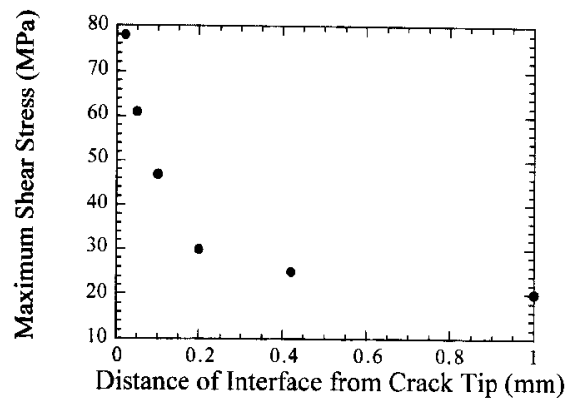


Figure 13: Maximum shear stress at the interface ahead of the crack tip.

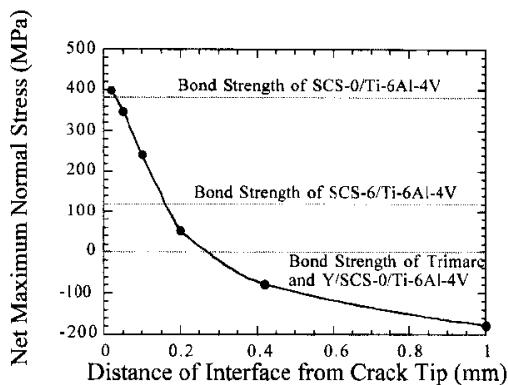


Figure 12: Net maximum normal stress at the interface ahead of the crack. The horizontal lines indicate the crack position when normal interface separation may occur.

On the other hand, the debond/frictional sliding stresses for as-processed Trimarc 1/Ti-6Al-4V, SCS-6/Ti-6Al-4V and SCS-0/Ti-6Al-4V composites are about 30 MPa, 160 MPa and 300 MPa, respectively, based on pushout tests [3]. Since the local normal stress at the location of the maximum shear stress is less compressive than the initial compressive radial stress, Figure 13 alone is not useful in predicting shear failure.

Figure 14 shows the maximum shear stress ($\tau_{xy}(\max)$) and the local normal stress (σ_x) along with a simple condition for shear failure for various positions of the crack. In Trimarc 1 composites, the shear failure criterion is satisfied when the crack is about 1 mm from the fiber, although the normal stress is compressive. Similar results may be deduced for Y/SCS-0 and SCS-6 composite, although the position of the crack when shear failure may initiate is closer to the fiber, about 200 μm , for the SCS-6 composite. In all the three composites with the weaker interface, it appears that shear failure is most likely to precede normal interface separation well before the crack reaches the interface. On the other hand, interface failure cannot occur with SCS-0 fibers until the crack tip is extremely close to the interface. It is, however to be realized that interface damage can be typically identified in metallographic specimens only in the event of normal interface separation. The main effect of shear failure preceding normal interface separation is an increase in the local ΔK and an enhancement of the stress concentration at the site of normal interface separation. Nevertheless, the analysis is in good agreement with the a vs N curve, wherein the SCS-0/Ti-6Al-4V composite shows a marked deceleration compared to the composites with weaker interfaces for crack lengths between $a = 7$ mm and 9 mm.

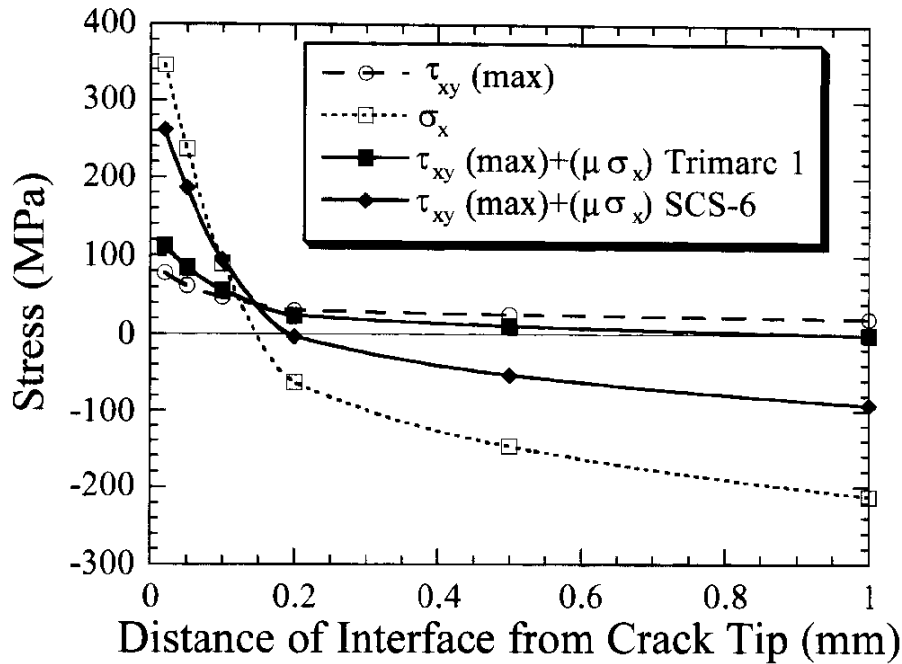


Figure 14: Stress distribution and failure criteria at the interface as a function of the position of the crack. μ is the friction coefficient, 0.1 for Trimarc and 0.53 for SCS-6 [3].

Crack Deflection

Crack deflection and fiber bridging was observed in all four composites, but at different stress ranges. According to a stress based criterion suggested by Cook and Gordon [8] and refined by Gupta, Argon and Suo [9], debonding is predicted if the ratio of the bond strength between the two materials (in the radial direction) to the strength of the uncracked material (in the axial direction) is lower than the ratio of the normal debonding stress at the interface to the stress perpendicular to the crack plane in the material ahead of the crack tip. Figure 15 is taken from the work of Gupta et al. [9], where the independent variable is the Dundurs' parameter, defined as:

$$\alpha = (E_2 - E_1)/(E_2 + E_1) \quad (1)$$

where E denotes the elastic modulus, and subscripts 1 and 2 refer to the material containing the crack and the material ahead of the crack, respectively. Debonding was primarily observed inside the carbon-rich coating in layer 2 for SCS-6 composites, within the carbon coating for Trimarc 1 composite and between the reaction zone and the fiber for SCS-0 composites. These sites of debonding in the composites are in excellent agreement with the stress based criterion.

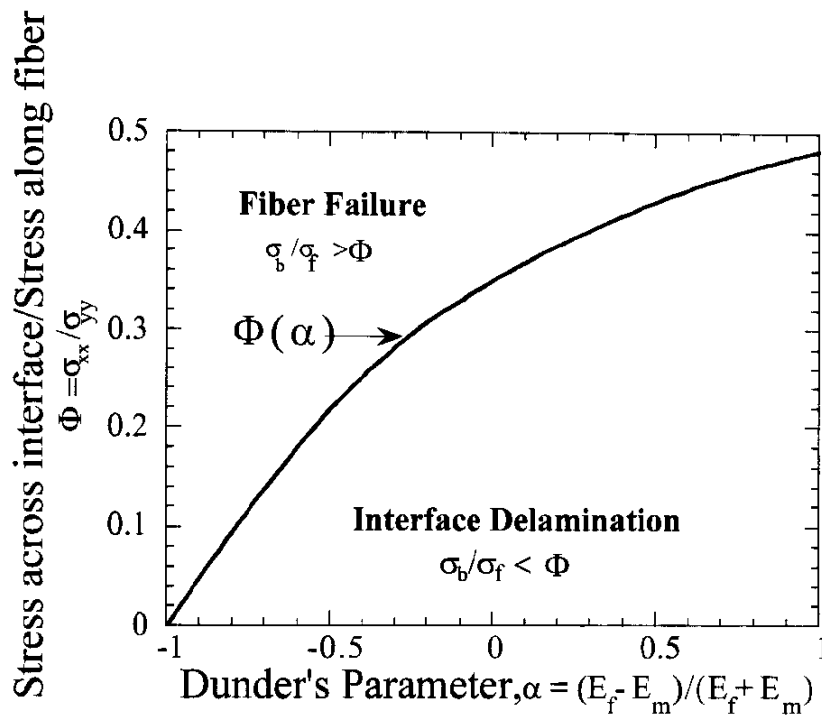


Figure 15: A stress based criterion for predicting the ability of an interface to debond.

The other criterion that has gained attention is the toughness based criterion of He and Hutchinson [10]. Based on this criterion, debonding is predicted if the ratio of the strain energy release rate of the interface to that of the fiber is below 0.5. for the SiC/Ti-alloy system. The strain energy release rate of the SiC fiber has been reported to be about 11 J/m² [11]. For SCS-6/Ti-alloy system, the interface toughness has been measured to be about 5-40 J/m² [12]. Further, for pyrolytic carbon/SiC interface, the toughness has been reported to be in the range of 5-60 J/m² [12]. It therefore appears that the He and Hutchinson's criterion barely predicts debonding in the SCS-6 composite system, where debonding and bridging has been well documented. The applicability of this criterion to other systems cannot be assessed at this time due to the lack of toughness measurements.

CONCLUSIONS

Single-ply multi-fiber composites with different interfaces have been fabricated and tested under fatigue crack growth conditions. Crack arrest associated with bridging fibers occurred at different stress ranges for the four systems. The stress range at which bridging ceased appears to be due to the fibers failing in the crack wake. In all cases, the fatigue crack growth life of the composites, even for the ones that did not exhibit fiber bridging, was significantly higher than that of the "neat" material.

Elastic shielding of the crack tip and associated deceleration of the crack was observed in the presence of the higher modulus material. Similar prediction were made from finite element analysis. This effect appeared to depend on the interfacial properties. The strongly-bonded SCS-0 composite retarded the crack more effectively than the weakly-bonded composites.

Normal interface separation of the interface ahead of the crack tip was clearly observed in SCS-6 composites. Damage to the interface ahead of the crack tip was noted in Trimarcl composites as well. Finite element analysis suggests that shear stress induced failure precedes normal interface separation and supports the crack growth behavior.

A stress based criterion for predicting debonding appeared to explain the crack deflection behavior effectively for the composites. The results, which span a wide range of interface strengths and fiber strengths, suggest that during FCG in the SiC/Ti-alloy system, interface debonding will in general precede fiber breaks and that fiber failure most likely occurs in the crack wake when the fiber stresses exceed the fiber strength.

ACKNOWLEDGMENTS

This study was supported by the Wright Laboratory Materials Directorate under Air Force contract F33615-91-C-5663 to UES, Inc. The authors are grateful to Drs. Jim Larsen, Reji John, Jay Jira, M.L. Gambone, D.B. Gundel and B. Maruyama for several helpful discussions.

REFERENCES

1. Evans, A.G. and Marshall, D.B., "The Mechanical Behavior of Ceramic Matrix Composites", *Acta Mater.*, vol. 37, No. 10, 1989, pp. 2527-2583.
2. Miracle, D.B., Gundel, D.B. and Warriar, S.G., "Interfacial Structure and Properties for the Design of Fiber-Reinforced Metal Matrix Composites", to appear in *Processing and Design Issues in High Temperature Materials*, N.S. Stoloff and R.H. Jones, eds. TMS, Warrendale, PA, 1996.
3. Majumdar, B.S., Warriar, S.G. and Miracle, D.B., "Interface Effects on the Tensile and Fatigue Crack Growth Behavior of Fiber-Reinforced Metal Matrix Composites" to appear in *MRS Proceedings*, MRS, Pittsburgh, PA, 1996.
4. Warriar, S.G. and B.S. Majumdar, "Modeling of Interface Effects on the Fatigue Crack Growth Response of Titanium Matrix Composites", submitted to *Mater. Sci. Engr.*, 1997.
5. Warriar, S.G., Majumdar, B.S. and Miracle, D.B., "Interface Effects on Crack Deflection and Fiber Bridging During Fatigue Crack Growth in Titanium Matrix Composites", submitted to *Acta Mater.*, 1997.
6. Ning, X.J. and Pirouz, P., "The Microstructure of SCS-6 SiC Fiber", *J. Mater. Res.*, vol. 6, No. 10, 1991, pp. 2234-2248.
7. Warriar, S.G., Gundel, D.B., Majumdar, B.S. and Miracle, D.B., "Interface Effects on the Micromechanical Response of a Transversely Loaded Single Fiber SCS-6/Ti-6Al-4V Composite", *Metall. Trans.*, vol. 27A, 1996, pp. 2035-2043.
8. Cook, J. and Gordon, J.E., "A Mechanism for the Control of Crack Propagation in All-Brittle Systems", *Proc. Royal Soc. London*, vol. A 282, 1964, pp. 508-520.
9. Gupta, V., Argon, A.S. and Suo, Z., "Crack Deflection at an Interface Between Two Orthotropic Media", *J. Appl. Mech.*, vol. 59, 1992, pp. S79-S87.
10. He, M.Y. and Hutchinson, J.W., "Crack Deflection at an Interface Between Dissimilar Elastic Materials", *Int. J. Sol. Struct.*, vol. 25, 1989, pp. 1053-1067.
11. Gambone, M.L. and Wawner, F.E., *MRS Proceedings*, vol. 350, pp. 111-116, 1994, MRS, Pittsburgh, PA.
12. Majumdar, B.S., to appear in *Titanium Matrix Composites*, S. Mall and T. Nicholas, eds., Technomic Publications, 1996.

SYNTHESIS OF $\text{YBa}_2\text{Cu}_3\text{O}_{7-x}/\text{Ag}$ COMPOSITE SUPERCONDUCTORS BY A CITRIC ACID SOL-GEL METHOD

A.L. Juwono¹, S. Waluyo², and S. Poertadji¹

¹ *Department of Physics, Faculty of Mathematics and Sciences,
University of Indonesia, Depok, 16424, Indonesia*

² *Present address: PT Iron Hill Mitra Sejati Microelectronic Packaging,
Tangerang, Indonesia*

SUMMARY: $\text{YBa}_2\text{Cu}_3\text{O}_{7-x}$ superconductor and $\text{YBa}_2\text{Cu}_3\text{O}_{7-x}/\text{Ag}$ composite superconductors were synthesized by a citric acid sol-gel method. The weight ratios of silver to $\text{YBa}_2\text{Cu}_3\text{O}_{7-x}$ were varied by 5 %, 10 % and 15 %. Superconducting phenomenon was observed on $\text{YBa}_2\text{Cu}_3\text{O}_{7-x}$ superconductor, and on 5 and 10 weight % Ag composites. X-ray diffraction patterns of $\text{YBa}_2\text{Cu}_3\text{O}_{7-x}$ and $\text{YBa}_2\text{Cu}_3\text{O}_{7-x} / \text{Ag}$ have been analysed by Powder Diffraction Package (PDP) simulation and indicated that all specimens contained $\text{YBa}_2\text{Cu}_3\text{O}_{7-x}$ crystal. Critical current densities (J_c) of $\text{YBa}_2\text{Cu}_3\text{O}_{7-x}$ and $\text{YBa}_2\text{Cu}_3\text{O}_{7-x} / \text{Ag}$ were obtained at 77 K using four-point-probe method (I-V Curve Technique). Silver additions of up to 10 % weight increased the critical current density values and improved the degree of $\text{YBa}_2\text{Cu}_3\text{O}_{7-x}$ crystallization. The presence of large amount of silver degraded the superconducting property and decreased the critical current density.

KEYWORDS: YBCO, YBCO/Ag, citric acid, Powder Diffraction Package, critical current, Meissner effect

INTRODUCTION

Superconductors became important electronic materials after H.K. Onnes in 1911 found a zero resistance of mercury at a critical temperature (T_c) of 4.2 K. After a long period of research, T_c could be raised until 23.2 K for Nb_3Ge superconductors [1]. An interesting invention, that was found by G. Bednorz and K.A. Miller in 1986, was a ceramic oxide based superconductor, $\text{La}_{5-x}\text{Ba}_x\text{Cu}_5\text{O}_{5(3-y)}$ with T_c of 30 K [2]. This material was called a high temperature superconductor. Some modifications have been worked to obtain higher critical temperature materials, such as to substitute La atoms to Y atoms to produce $\text{YBa}_2\text{Cu}_3\text{O}_{7-x}$ (YBCO) system [3]. The highest T_c (220 K) was found by J.T. Chen in 1989 for $\text{Y}_5\text{Ba}_6\text{Cu}_{11}\text{O}_{7-x}$ system [4]. The bulk YBCO superconducting materials have low strength, low modulus and low strain to failure. Other important variables of superconducting phenomenon, beside critical temperature (T_c), are critical magnetic field (H_c) and critical current density (J_c). The main problem is how to produce a material in the superconducting state with T_c , H_c and J_c are as high as possible. To enhance the mechanical properties, T_c , and J_c , some additives, such as silver, silver oxide, zirconia, stainless steel fibres, were added to the material [5].

YBCO system has an orthorhombic perovskite structure as shown in Figure 1 [6]. Difficulty in manufacturing single phase crystal YBCO system has been an interested issue. It has been reported that there are three different techniques in producing superconductors, namely the solid state reaction, the diffusion and the solution reaction. The solution reaction method employs cheaper base materials, processes in lower sintering temperatures and produces more homogeneous system materials in large scale compare to the others two method.

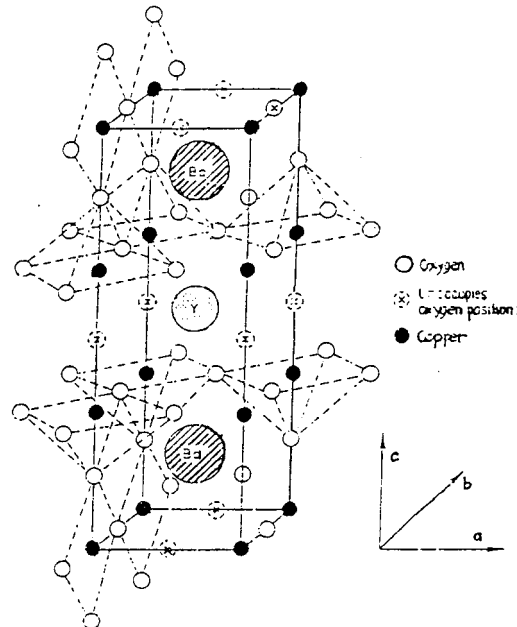


Fig. 1: Orthorhombic perovskite structure of a $YBa_2Cu_3O_{7-x}$ crystal [6]

The aims of this research were examining the synthesis of $YBa_2Cu_3O_{7-x}/Ag$ composite superconductors using a citric acid sol-gel method and observing silver addition to superconducting properties (including T_c , H_c , J_c).

EXPERIMENTAL

Material and Equipment

Both $YBa_2Cu_3O_{7-x}$ superconductor and $YBa_2Cu_3O_{7-x}/Ag$ composite superconductors were produced by the solution reaction, namely a citric acid sol-gel method. The weight ratios of silver to $YBa_2Cu_3O_{7-x}$ were varied by 5 %, 10 % and 15 %. Three samples were prepared for each type of specimen. Basic materials for the synthesis had purity of about 99 %.

The synthesis procedure can be seen in Figure 2. The sol solution was synthesized on a magnetic plate equipped with a magnetic stirrer. While the gel solution was produced in a vacuum evaporation type JEE-4X. Calcination and sintering were proceed in a controlled furnace with temperature range from room up to 1000°C. Pellet shaped specimens were pressed using a hydraulic pressure which had 150 kN maximum power force.

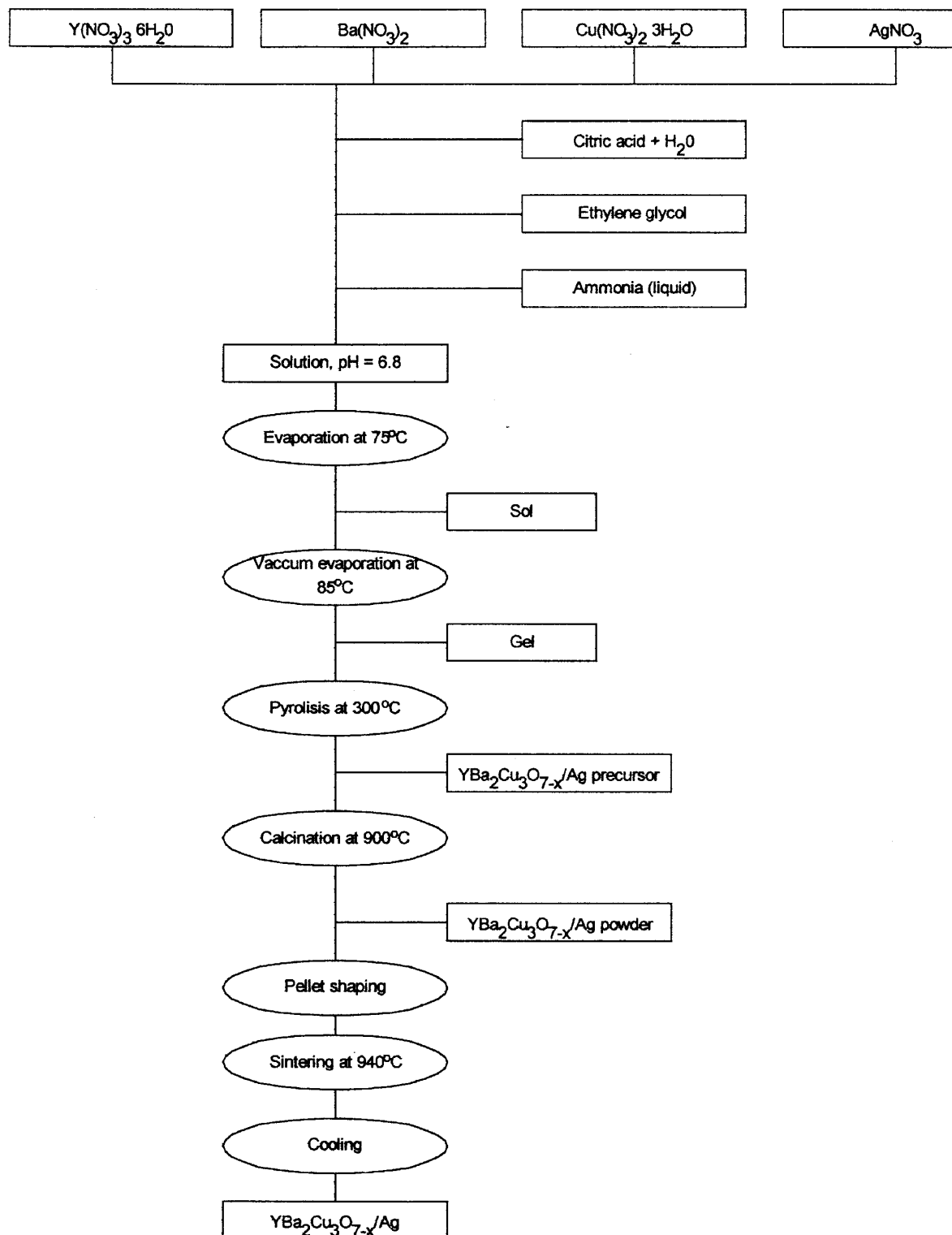


Fig. 2: The synthesis procedure of YBa₂Cu₃O_{7-x}/Ag composite superconductors by a citric acid sol-gel method

Meissner Effect Test

A permanent magnetic of SmCo was used for Meissner effect tests at liquid nitrogen temperature (77 K).

Critical Current Density (J_c) Measurement

A linear four point probe was used for this test. During measurement, the specimens were immersed in liquid nitrogen (77 K). A current-voltage curve was obtained from this work. When the voltage changes from zero to a certain finite value, the current obtained is the critical one.

X-ray Diffraction

A Phillip PW 3710 diffractometer was used to obtain X-ray diffraction patterns. The X-ray source was CoK_α and the diffraction angle was between 20° up to 80° . Powder Diffraction Package (PDP) simulation was applied to analyse the experimental results.

RESULTS AND DISCUSSION

Figures 3 and 4 are X-ray diffraction patterns of $\text{YBa}_2\text{Cu}_3\text{O}_{7-x}$ superconductor and $\text{YBa}_2\text{Cu}_3\text{O}_{7-x}/\text{Ag}$ composite superconductors respectively. Perovskite phase of $\text{YBa}_2\text{Cu}_3\text{O}_{7-x}$ was proved by the highest peak at 38° at both Figures 3a and 4a. Comparing these figures, silver additions increased the intensity of the 38° peak. It means that silver additions improved the degree of crystallinity. These patterns were compared to previous study and gave similar results [7]. There are three other peaks at 45° , 52° and 77° at Figure 4a. These peaks exposed the presence of silver phase in the specimens. This pattern was confirmed by PDP simulation. A detail study showed that as the silver content increased, these three peaks increased accordingly. Thus, simulation showed evidently that the presence of silver phase in the bulk material built a YBCO/Ag system composite superconductor. It was shown that the silver phase did not interfere the perovskite YBCO crystal. Hence, the silver phase filled the void positions between crystal grains and could increase the mass and the current density.

Critical current densities of both $\text{YBa}_2\text{Cu}_3\text{O}_{7-x}$ and $\text{YBa}_2\text{Cu}_3\text{O}_{7-x}/\text{Ag}$ were graphed to weight % Ag as shown in Figure 5. The composite containing 5 and 10 % Ag had higher J_c than the pure YBCO superconductor. In contrast, the J_c value of composite containing 15 % Ag was zero. This deviation was confirmed by Meissner effect test. The superconductor and the composite containing 5 and 10 % Ag exhibited the Meissner effect, while the composite containing 15 % Ag did not demonstrate that one.

Silver additions of up to 10 % weight increased the YBCO grain percentage (this was proved by XRD pattern) and might increase the YBCO grain size [8]. This state resulted decreasing the void fractions. Therefore, the J_c values of the composite superconductors were higher than that of pure superconductor itself. The percentage of YBCO crystal decreased by addition of 15 % weight of Ag and degraded superconducting properties.

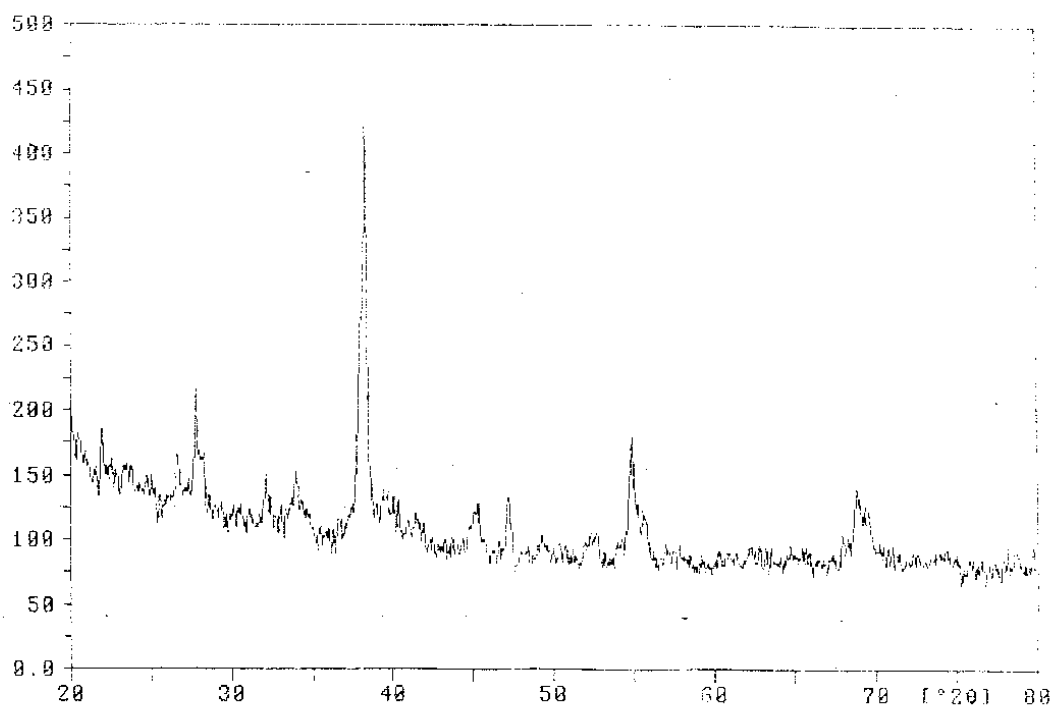


Fig. 3a: X-ray diffraction pattern of $YBa_2Cu_3O_{7-x}$

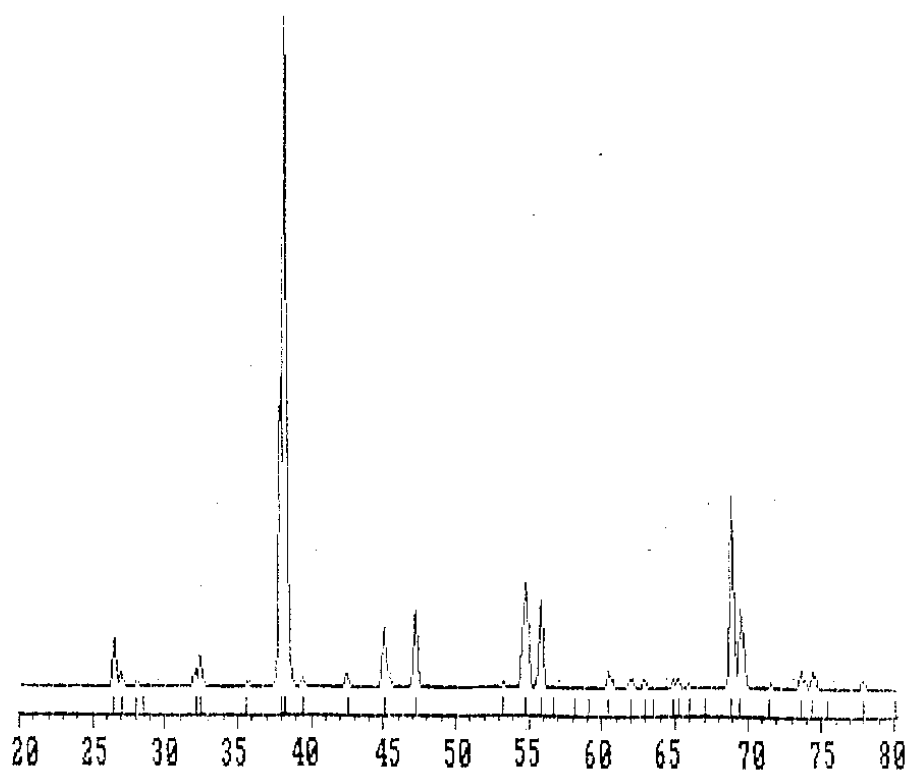


Fig. 3b: PDP simulation of $YBa_2Cu_3O_{7-x}$

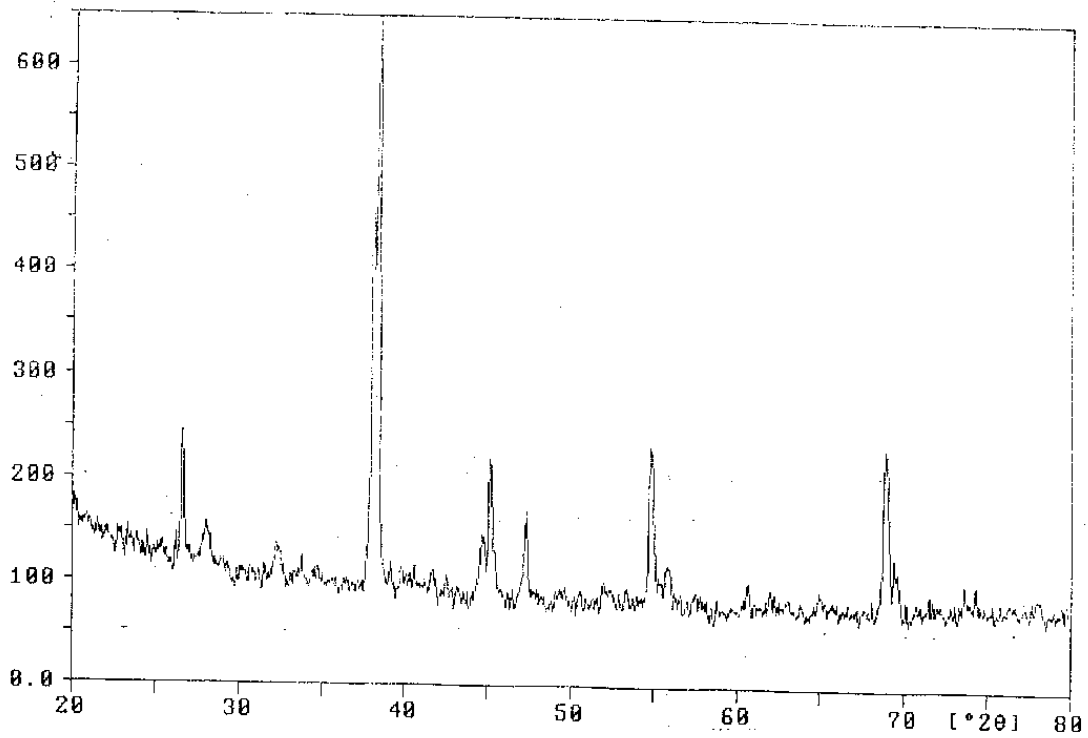


Fig. 4a: X-ray diffraction pattern of $YBa_2Cu_3O_{7.2}/10\% Ag$

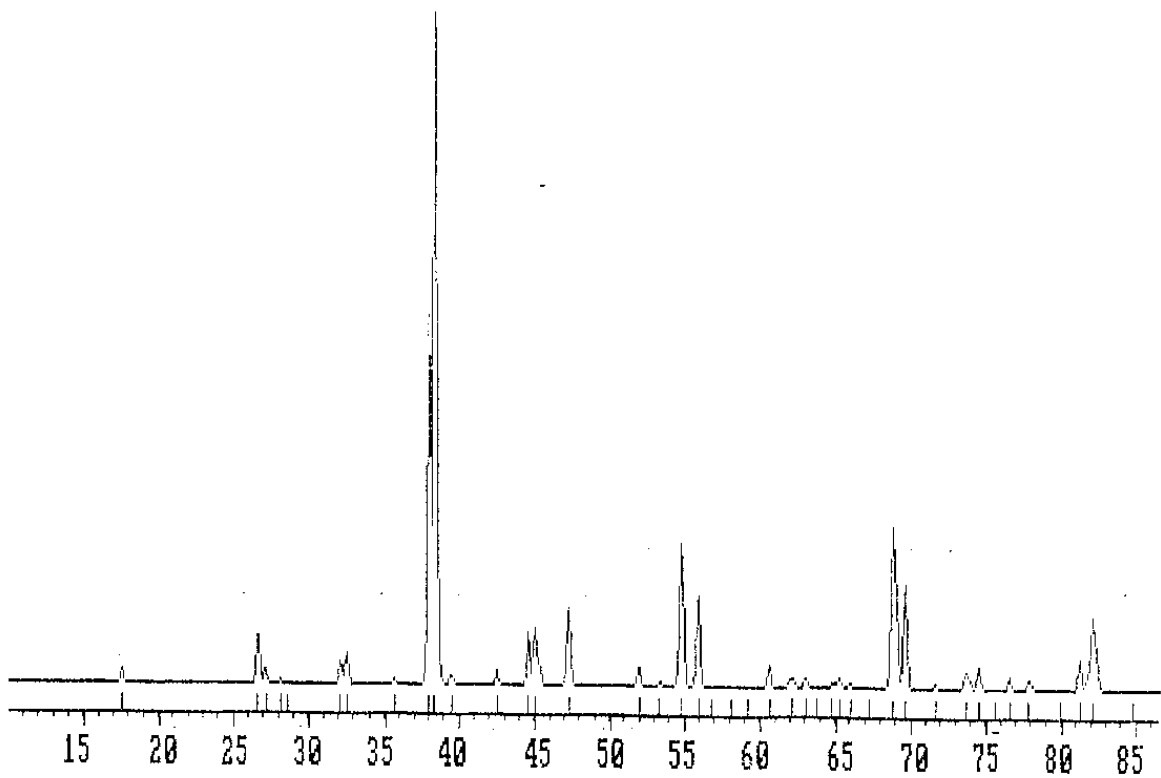


Fig. 4b: PDP simulation of $YBa_2Cu_3O_{7.2}/10\% Ag$

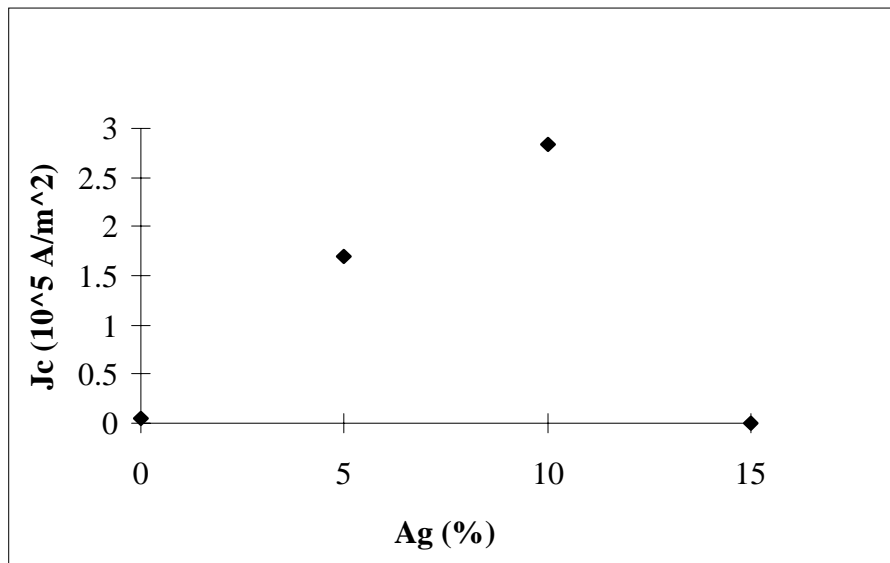


Fig. 5: Graph of critical current densities (J_c) versus weight % Ag of $YBa_2Cu_3O_{7-x}$ and $YBa_2Cu_3O_{7-x}/Ag$

CONCLUSIONS

$YBa_2Cu_3O_{7-x}$ superconductors and $YBa_2Cu_3O_{7-x}/Ag$ composite superconductors have been synthesized by a solution technique, namely a citric acid sol-gel method. The best composition was the $YBa_2Cu_3O_{7-x}/10\%$ Ag which shown the highest J_c . Silver additions of up to 10 % weight increased the critical current density values and improved the degree of $YBa_2Cu_3O_{7-x}$ crystallization. The presence of large amount of silver degraded the superconducting property and decreased the critical current density.

REFERENCES

1. Kittel, C., "Introduction To Solid State Physics", 6th.ed., John Willey & Sons Inc., New York, 1991.
2. Bednorz, J.G. and K.A. Muller, Z. Phys. B 64, 1989, p. 189.
3. Wu, M.K., Ashburn, J.R., Torng, C.J., Hor, P.H., Meng, R.L., Go, L., Huang, Z.J., Wang, Y.O., and Wu, C.W., Physical Review Letters, Vol. 58, 1987, p 908.
4. Chen, J.T., Qian, L.X., Wang, L.Q., Wenger, L.E., and Logothetis, E.M., Modern Physics Letters B3, 1989, pp 1197 - 1206.
5. Vipulandan, C. and S. Salib, Journal of Material Science. Vol. 30, 1995, pp 763 - 769.
6. Grant, P.M., Beyers, R.B., Engler, E.M., Lim, G., Parkin, S.S.P., Ramirez, M.L., Lee, V.Y., Nazzal, A., Vazquez, J.E., and Savoy, R.J., Physical Review B 35, No. 13, 1987, p 7242.
7. Jiaju, D., Jianyi, J, Xiang, W., and Huaqing, Y., Chinese Physics, Vol. 9, No. 4, 1988, pp. 1011 - 1014.
8. Dwir, B., Appl. Phys. Lett. Vol. 55 (4), 1989, p 399.

FABRICATION AND CHARACTERISATION OF CONTINUOUS FIBRE REINFORCED MoSi_2 -BASED COMPOSITES

A.R. Bhatti and R.A. Shatwell

Structural Materials Centre, DRA Farnborough, Hampshire, GU14 6TD, UK.

SUMMARY: High density continuous reinforced MoSi_2 -based composites have been produced by hot-pressing technique. Both SiC and single crystal Al_2O_3 fibre reinforcements were investigated. Modification of MoSi_2 matrix with sialon powder minimises the thermal expansion mismatch with the SiC fibre, thereby suppressing the matrix cracking. No matrix cracking was observed in Al_2O_3 reinforced MoSi_2 composites due to good fibre/matrix thermal expansion match.

Microstructural and EDS studies of interfacial regions in SiC reinforced MoSi_2 /Sialon and single crystal Al_2O_3 reinforced MoSi_2 composites have identified the formation of Mo_5Si_3 and mullite phases respectively. Key issues concerning these reaction phases and their influence on the mechanical properties are presented.

KEYWORDS: MoSi_2 , matrix cracking, continuous fibre reinforcement, thermal expansion, fibre/matrix interface, sialon, mullite, scanning electron microscopy

INTRODUCTION

Molybdenum disilicide (MoSi_2) based composites are very attractive candidates for various high temperature aerospace and industrial applications. MoSi_2 has high melting point of 2030°C , excellent oxidation resistance and good thermal and electrical conductivity [1,2]. Additionally it can be electro-discharge machined which is a significant advantage for the low cost fabrication of components. Mechanically, it exhibits a brittle-to-ductile transition at $\sim 1000^\circ\text{C}$. Creep effects could reduce its high temperature strength.

Several attempts have been made to increase both the low temperature toughness and the high temperature creep resistance of MoSi_2 . Recent work on the addition of SiC powder and whiskers to MoSi_2 [3,4], has shown small improvements both in fracture toughness and high temperature resistance. ZrO_2 additions also improve room temperature fracture toughness [5]. Both strength and creep resistance are improved by alloying MoSi_2 with WSi_2 [6]. Substantial improvements are necessary to achieve the required levels of damage tolerance and strength for high temperature engineering applications. Reinforcing MoSi_2 with continuous fibres could achieve substantial improvements in mechanical properties. The use of refractory metal fibres such as Nb and Ta into MoSi_2 matrix has demonstrated significant improvements in toughness [7,8]. However, this type of fibres react with the matrix at high temperatures which leads to the formation of trisilicides $(\text{Mo,Nb})_5\text{Si}_3$ and $(\text{Mo,Ta})_5\text{Si}_3$ at the interface between MoSi_2 and the refractory metal fibre. Additional reaction barrier coatings are, therefore, necessary in order to minimise reaction effects [9].

In previous study, the use of SiC based, Textron SCS-6 SiC reinforcement to MoSi₂ matrix was investigated [10]. The material showed extensive matrix cracking which occurred during its high temperature processing. This cracking was attributed to the large thermal expansion mismatch between the SCS-6 SiC fibre ($4.6 \times 10^{-6} \text{ }^\circ\text{C}^{-1}$) and the MoSi₂ matrix ($7 \times 10^{-6} \text{ }^\circ\text{C}^{-1}$).

In this paper, the results of an approach, whereby the composition of the matrix is modified by the addition of sialon powder to reduce the thermal expansion mismatch between the SiC fibre and the matrix, are presented. The work was extended to incorporate Saphikon single crystal Al₂O₃ fibre with thermal expansion $\sim 8 \times 10^{-6} \text{ }^\circ\text{C}^{-1}$, a reasonably close match to that of MoSi₂ matrix.

EXPERIMENTAL

Fabrication of Composite Materials

Starting materials were MoSi₂ powder (Starck, Grade C) and Sialon (Vesuvius Zyalons, 101). The fibres used were Textron, SCS-6 and Saphikon single crystal Al₂O₃. The SCS-6 SiC fibre essentially consists of a SiC sheath with an outer diameter of $\sim 140 \text{ } \mu\text{m}$ surrounding a carbon core with a diameter of $\sim 33 \text{ } \mu\text{m}$. The outer surface of the SiC sheath has a carbon rich coating approximately $3 \text{ } \mu\text{m}$ thick. The Saphikon single crystal Al₂O₃ has a diameter $\sim 125 \text{ } \mu\text{m}$.

MoSi₂ and Sialon powders were blended by ball milling. A composite with 10 vol% SCS-6 SiC fibre), reinforcing a matrix, comprising of 60 vol% MoSi₂ and 40 vol% Sialon was prepared via a three stage route. A SiC fibre was wound onto a drum and coated with a slurry, consisting of the blended ceramic powders and dispersants with a polymer binder in an alcohol solvent. The sheet was removed from the drum and dried. Coupons were punched out of the dried sheet and stacked to produce the green composite. This was heated to remove the the binder. The compact was coated with BN and then hot pressed in atmosphere in a graphite die at 1650°C under 18MPa for 1 hour. The pressure was applied using two close fitting graphite plungers in a hydraulic press. The heating was applied by radio frequency induction using a Radyne 150E generator. The composite had density $>99\%$ of theoretical. The hot pressed blocks were rectangular measuring typically $45\text{mm} \times 25\text{mm} \times 8\text{mm}$ in size.

Single crystal Al₂O₃ fibre reinforced MoSi₂ matrix composites were prepared using 100% MoSi₂ powder. The fabrication route was essentially the same as used for SCS-6 SiC reinforced MoSi₂/Sialon composites. A slurry consisting of MoSi₂ and dispersants with a polymer binder in an alcohol solvent was prepared and cast onto the wound up fibres. After drying, sheets were punched out, laid up to produce the green composite compact, pressed and heated to remove the binder. The composite was then hot pressed as before. Two blocks of composites, with 16 and 20 vol% fibre, were produced. Both the composite blocks had density close to theoretical density.

Microstructural examination

The composites were examined by optical metallography, X-ray diffractometry (XRD), Scanning Electron Microscopy (SEM) with Energy Dispersive Spectroscopy (EDS), and Transmission Electron Microscopy (TEM) with EDS system. SEM was performed both in secondary and backscattered electron imaging modes. Samples for TEM observation were pre-coated with Au.

RESULTS AND DISCUSSION

Microstructure of SiC fibre reinforced MoSi₂/Sialon

Figure 1 shows a typical optical micrograph of a cross-section of an MoSi₂-40 vol% Sialon composite reinforced with 10 vol% SCS-6 SiC fibre. The central carbon core and outer carbon coating are evident in this figure. EDS and XRD examination in conjunction with SEM showed that the matrix contained mainly MoSi₂, Mo₅Si₃, and β -Si₃N₄ with a small amount of SiC. Since the sample was not etched, the glassy phase [11] which presumably existed between the β -Si₃N₄ grains could not be detected. Furthermore no SiO₂ was observed in the matrix even though the starting MoSi₂ contained a significant amount of this phase. Some may have reacted with carbon from the binder material or carbon die to give the small amount of SiC picked up in the matrix analysis. The remainder may have been consumed in the formation of the glassy phase.

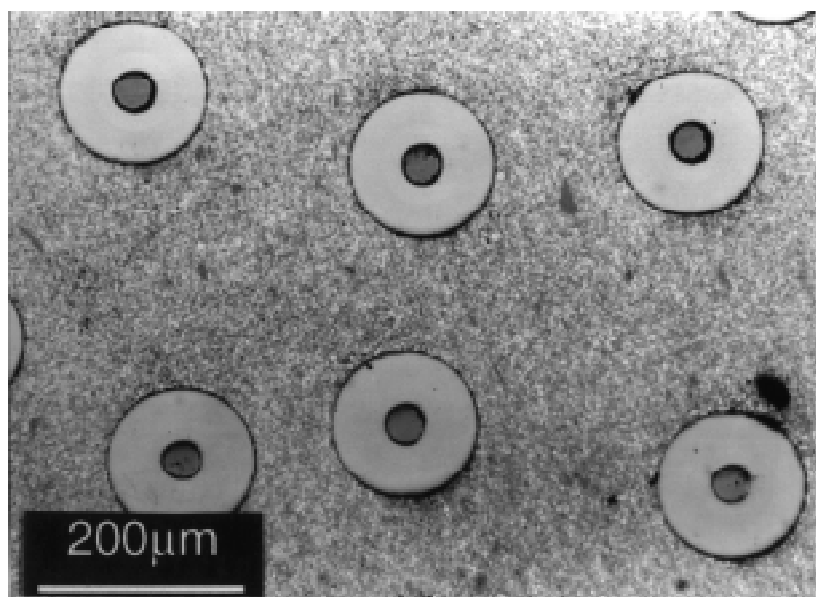


Fig. 1. Optical micrograph of a cross-section of the hot pressed MoSi₂-40 vol% Sialon composite reinforced with 10 vol% SCS-6 SiC fibre.

The addition of low thermal expansion Sialon powder to MoSi₂ was successful in eliminating the formation of cracking in the matrix which was observed in the SCS-6 SiC / MoSi₂ composite investigated previously [10]. This is attributed to the reduction in the coefficient of thermal expansion mismatch between the MoSi₂ matrix and the fibre, resulting from the addition of Sialon powder to MoSi₂.

The C-rich surface coating of the fibre is observed as a ring of black contrast (Fig. 1). This would imply that no severe reaction has occurred between the C-rich surface of the fibre and the matrix during hot pressing cycle. However, closer examination of the interface in cross-section (Fig. 2) reveals penetration of the coating by the bright phase. EDS studies of the bright phase shows that it is Mo₅Si₃. However, removal of the C layer surrounding it suggests that it may have reacted to form Mo₅Si₃C. Since Electron Energy Loss Spectroscopy was not available it was not possible to check for C in the Mo₅Si₃ phase. The formation and penetration of the bright phase at the interface could lead to a strong interfacial bond which may have adverse effects on mechanical properties of the composite.

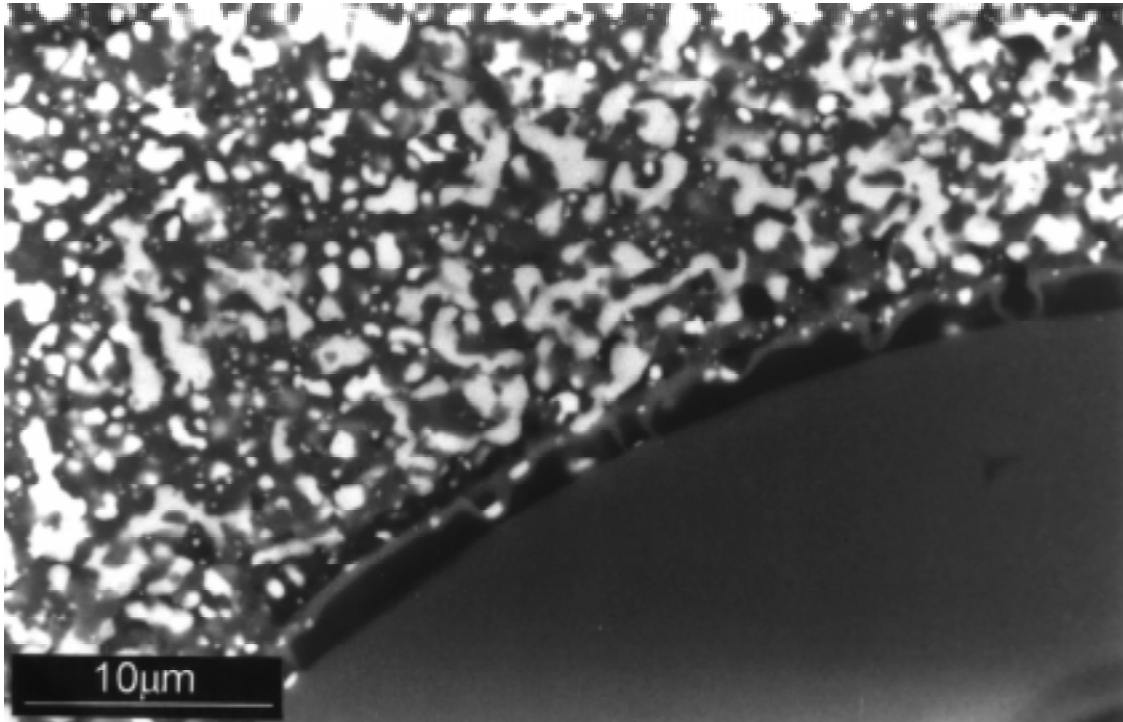


Fig. 2. SEM micrograph showing interfacial region in the hot pressed MoSi_2 -40 vol% Sialon composite reinforced with 10vol% SCS-6 SiC fibre.

Previous work on creep studies in monolithic and SiC whisker reinforced MoSi_2 [12] has demonstrated that SiO_2 has a detrimental effect on the high temperature strength due to grain boundary sliding of MoSi_2 . The absence of SiO_2 in the present composite is therefore likely to have beneficial effect on high temperature mechanical properties. However, the formation and penetration of bright phase at the interface is potentially disadvantageous. Nevertheless, C coating applied to SCS-6 SiC fibre was found to survive hot pressing and should provide at least limited debonding and hence toughening in the matrix.

Microstructure of Al_2O_3 fibre-reinforced MoSi_2

Figure 3 is a typical SEM micrograph showing a cross-section of a hot pressed MoSi_2 matrix composite reinforced with 16 vol% single crystal Al_2O_3 fibres. There is no evidence of any matrix cracking due to high temperature processing of the composite. Figure 4. shows a secondary electron micrograph of the microstructure for the matrix at higher magnification. As seen from Fig. 4 the matrix consisted of three different contrasting phases, light grey, grey, and dark grey. This change in contrast is due to the variation of Mo/Si in these phases. EDS analysis (Table 1) revealed that the light grey and grey phase are Mo_5Si_3 and MoSi_2 respectively whereas the dark phase appears to be glassy SiO_2 with minor fractions of Mo and Al

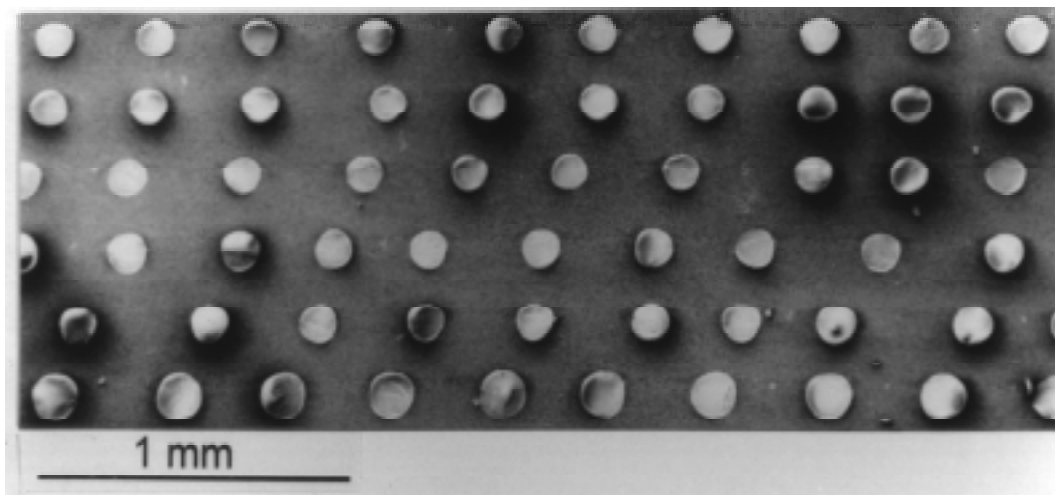


Fig. 3. SEM micrograph of a cross-section of the hot pressed MoSi₂ composite reinforced with 16 vol% single crystal Al₂O₃ fibre.

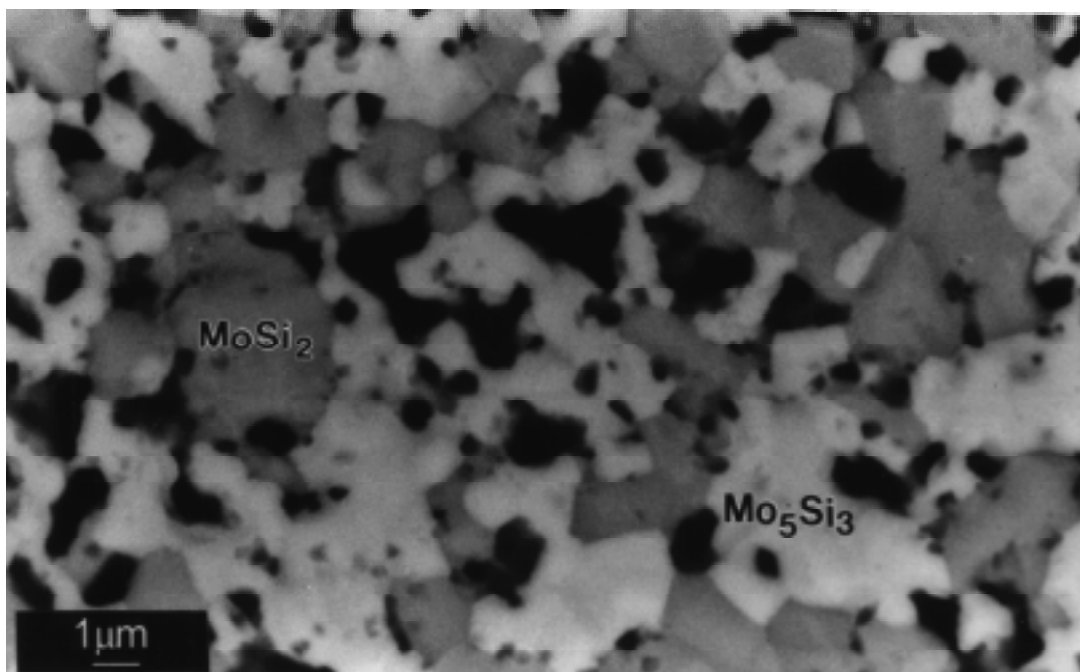


Fig. 4. SEM micrograph of the microstructure of the matrix of the hot pressed MoSi₂ composite reinforced with 16 vol% single crystal Al₂O₃ fibre.

Table 1. SEM and EDS data from matrix phases in Al₂O₃/MoSi₂ Composite

Composition (wt%)	Light Grey	Grey	Dark Grey
Si	15.78	36.60	65-90
Mo	85.22	63.30	Trace
Al			Trace

The microstructure of the fibre/matrix interfacial region along with the compositional profile across the interface, analysed by EDS line scan are shown in Figure 5. There is no indication of any reaction at the interface from these composition profiles. The interface was further

investigated by Transmission Electron Microscopy. This investigation reveals (Fig. 6) that a crystalline phase is present at the interface. The phase was identified to be mullite (marked M in Fig. 6) by EDS and Electron Diffraction (ED) studies [see inset- [113] zone axis for mullite]. The mullite composition was found to be variable and lies in the $3\text{Al}_2\text{O}_3 \cdot 2\text{SiO}_2 - 2\text{Al}_2\text{O}_3 \cdot \text{SiO}_2$ range.

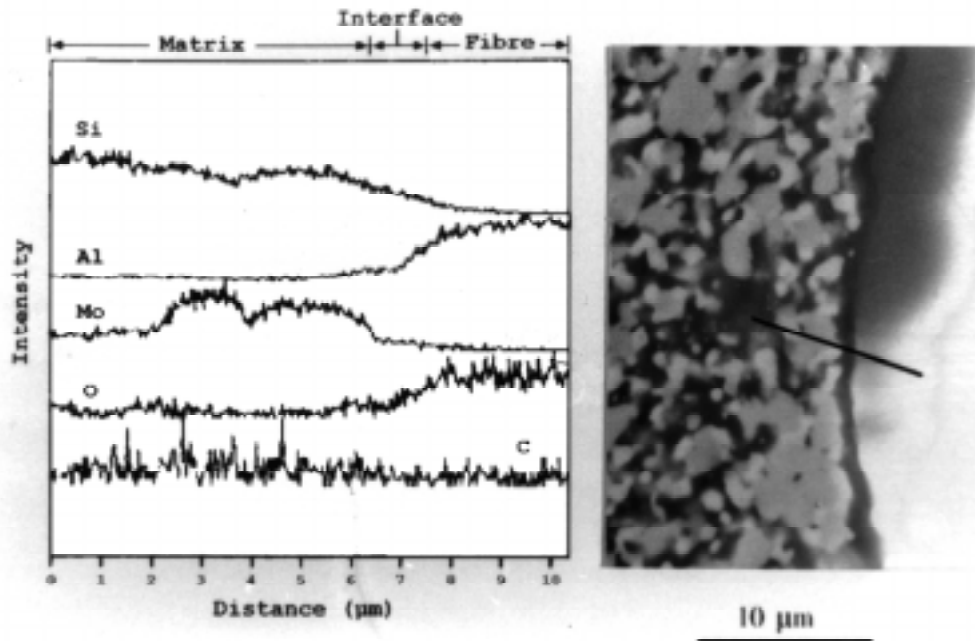


Fig. 5. SEM micrograph showing the interfacial region and the compositional profile across the interface in the hot pressed MoSi_2 composite reinforced with 16 vol% single crystal Al_2O_3 fibre.

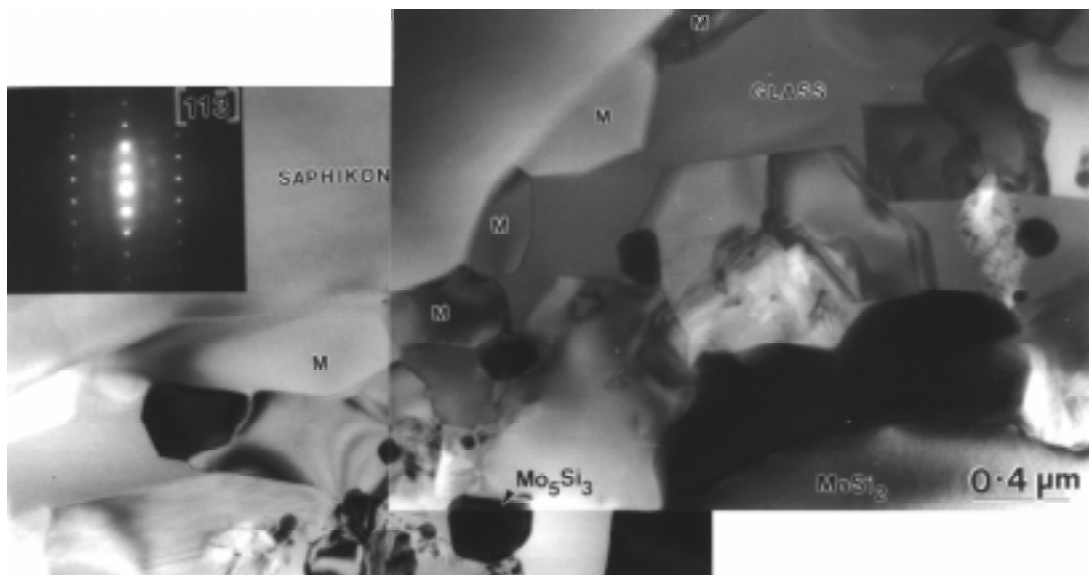


Fig. 6. TEM micrograph of the interfacial region in the hot pressed MoSi_2 composite with 16 vol% single crystal Al_2O_3 fibre. The diffraction pattern (inset) is from the Mullite phase at the interface.

The composite containing 20vol% Al_2O_3 fibre was also examined. It has essentially the same interfacial and microstructure features as the composite containing 16 vol% fibre. As before, the presence of mullite phase was confirmed from TEM and ED observations

The presence of mullite reaction phase at the fibre/matrix interface is likely to influence the mechanical behaviour of the composite. This will, however, depend on the nature of the interfacial bond. The composite will fail in brittle manner if the bond is strong.

Use of various coatings on fibres by different methods has been reported in literature [13] to prevent interfacial reactions and to promote debonding leading to significant enhancement in toughness. The main limitation of this approach is the unavoidable damage suffered by the coating during handling and hot pressing.

Finally it should be noted that thermomechanical stability of a fibre is a major requirement for high temperature structural composites. The SCS-6 SiC and single crystal Al_2O_3 fibres were selected due to their potential for use at high temperatures. The SCS-6 SiC fibres are structurally more stable than Nicalon and Tyranno fibres. However, they suffer from grain growth above 1400°C which reduces their strength. Single crystal Al_2O_3 fibre overcomes this problem of grain growth and retains strength to above 1400°C . The mechanism for the slow strength loss in this fibre may be related to thermal effects on dislocation densities.

CONCLUSIONS

The main conclusions are :

1. This work has demonstrated that the problem of matrix cracking during the processing of SCS-6 SiC/ MoSi_2 may be overcome by the addition of 40 vol% sialon to MoSi_2 , thereby reducing the fibre/matrix overall thermal expansion mismatch. The preservation of C coating (despite local degradation) of the SCS-6 SiC fibre should provide some debonding and pull-out mechanism for enhanced fracture toughness.
2. Single crystal Al_2O_3 fibre-reinforced MoSi_2 composites can be successfully produced without any matrix cracking. This is attributed to good thermal expansion match between the Al_2O_3 fibre and the MoSi_2 matrix.
3. Microstructural and EDS analyses of interfacial regions in SCS-6 SiC reinforced MoSi_2 /Sialon and single crystal Al_2O_3 reinforced MoSi_2 composites have shown the formation of Mo_5Si_3 (or possibly $\text{Mo}_5\text{Si}_3\text{C}$) and mullite phases respectively. Work is underway to identify suitable protective coatings to prevent the formation of such phases at the interface. The objective is to obtain a weak fibre/matrix interface in order to achieve improvements in toughness by fibre debonding and pull-out mechanism.

ACKNOWLEDGEMENTS

The authors would like to acknowledge the technical assistance of Dr.H.S. Ubhi and Dr.P. Korgul in the microscopic and X-ray evaluation.

REFERENCES

1. Meschter, P.J., and Schwartz, D.S., "Silicide-matrix materials for high temperature applications" Journal of Metals, 1989, pp. 52-55.

2. Schlichting, J. "Molybdenum disilicide as a component of modern high temperature composites" (in German), High Temperatures-High Pressures, Vol.10, No.3, 1978, pp. 241-269.
3. Carter, D.H., Petrovic, J.J., Honnell, R.E., and Gibbs, W.S., "SiC-MoSi₂ Composites" Ceramic Engineering & Science Proceedings, Vol. 10, 1989, pp. 1121-1129.
4. Gibbs, W.S., Petrovic, J.J., and Honnell, R.E., "SiC whisker-MoSi₂ matrix composites", Ceramic Engineering & Science Proceedings, Vol. 8, 1987, pp. 645-648.
5. Petrovic, J.J., Honnell, R.E., Mitchell, T.E., Wade, R.K., and McClellan, K.J., "Zirconia - Reinforced MoSi₂ Matrix Composites," Ceramic Engineering & Science Proceedings, Vol. 12, 1991, pp. 1633-1642.
6. Petrovic, J.J., and Honnell, R.E., "SiC Reinforced MoSi₂/WSi₂ Alloy Matrix Composites," Ceramic Engineering & Science Proceedings, Vol. 11, 1990, pp. 734-744.
7. Xiao, L., and Abbaschian, R., "Microstructure and properties of MoSi₂/Nb interfaces with and without alumina coating", Materials Research Society Symposium, Proceedings, Vol. 239, 1992, pp. 567-573.
8. Fitzer, E., and Remmele, W., Proceedings 5th International Conference on Composite Materials, ICCM-5, San Diego, CA, TMS-AIME, Warrendale, PA 1985, pp. 515-530.
9. Deve, H.E., Weber, C.H., and Maloney, M., "On the toughness and creep behaviour of fibre reinforced MoSi₂ intermetallic", Materials Science Engineering , Vol. A153, 1992, pp. 668-675.
10. Bhatti, A.R. "Processing and characterisation of monolithic molybdenum disilicide and silicon carbide fibre-reinforced MoSi₂ matrix composites" Ceramic Engineering & Science Proceedings, Vol. 15, 1994, pp. 1068-1075.
11. Bhatti, A.R., Lewis, M.H., Lumby, R.J., and North, B. "The microstructure of sintered Si-Al-O-N ceramics", Journal of Materials Science, Vol.15, 1980, pp.103-113.
12. Sadananda, K., Jones, K., Feng, J., Petrovic, J.J., and Vasudevan, A.K., "Creep of monolithic and SiC-whisker reinforced MoSi₂", Ceramic Engineering & Science Proceedings, Vol. 12, 1991, pp. 1671-1678.
13. Lu, T.C., Deng, Y.G., Levi, C.G., and Mehrabian, R., "On the strength and stiffness of ductile phase reinforced MoSi₂ Composites for elevated temperatures", Proceedings. Conference, ASM, Cincinnati, OH, 1991.

ON THE ROLE OF CARBON DIFFUSION DURING FIBER/MATRIX REACTION IN SiC FIBER REINFORCED TI-BASED MMCS

S. Krishnamurthy * and D.B.Miracle

*Materials Directorate, Wright Laboratory,
WL/MLLM, Wright-Patterson AFB, OH 45433-7817, USA
UES, Inc, 4401 Dayton-Xenia Rd., Dayton, OH 45432-1894, USA

SUMMARY: There are numerous reports dealing with the reaction of Ti alloy matrices with the carbon-rich protective coating of the reinforcing SiC fibers. The focus of most of these past studies was on the reaction zone products. However, simple calculations based on available diffusivity data indicate that the diffusion of carbon from SiC fiber coating into Ti alloy matrix is not limited to the near-fiber region, but can occur over a long range relative to the fiber diameter. In this paper, experimental work involving appropriate heat treatments of a variety of Ti-based composites is reported and microstructural evidence for long range diffusion of carbon is presented in the form of carbide precipitation in the Ti matrix. It is also shown that the increased carbon content of the titanium alloy matrix leads to significant microstructural changes and markedly different heat treatment response of SiC /Ti composites as compared to fiberless Ti alloy matrix.

KEYWORDS: titanium matrix MMC, SiC fiber, fiber/matrix reaction, carbon diffusion, heat treatment, carbide precipitation

INTRODUCTION

Fiber reinforced titanium matrix composites are candidate materials for advanced aerospace applications due to their significantly higher specific stiffness and strength compared to monolithic alloys. Several titanium-based compositions have been previously investigated for use as matrix alloys with SiC fiber reinforcement [1, 2]. These matrices have ranged from the conventional near- α , ($\alpha+\beta$), and metastable β alloys to the Ti aluminide alloys with ($\alpha_2+\beta_0$) or ($\alpha_2+\beta_0+O$) microstructure. The SCS-6 SiC fiber from Textron has been used extensively as reinforcement for several titanium-based matrices. This fiber has a 3 μm thick carbon-rich outer coating containing SiC particles which enables retention of a high strength level in the fiber and protects the fiber from adverse reaction with matrix alloy at high temperatures [3].

The present work is concerned with the role of the SiC fiber's C-rich outer coating in the fiber/matrix reaction occurring during composite processing. There are several studies dealing with fiber/matrix reactions in titanium matrix composites (TMCs) [4-9]. The nature of the reaction zone in these composites is dependent on matrix alloy composition and can consist of different layers of silicide and carbide phases. In addition to the reaction zone, the matrix region immediately adjacent to the fiber/matrix interface has been studied in certain cases such as the Ti-24Al-11Nb/SCS-6 TMC [7]. In this alpha-2 titanium aluminide based composite, a beta-depleted matrix region was formed around the reaction zone. Different possible explanations for the formation of the beta-depleted layer were proposed including Al enrichment, Nb depletion, carbon diffusion, and oxygen diffusion [2, 7]. However, the previous studies were unable to validate any of these possible explanations for the formation of the beta-depleted layer in the Ti-24Al-11Nb/SCS-6 composite.

It should be noted that much of the previous work was focused on the reaction zone products and the region immediately adjacent to the reaction zone, with a couple of exceptions. In a recent study of Ti-6Al-4V/SCS-6 and Ti-24Al-11Nb/SCS-6 composites involving microhardness testing, matrix hardening was observed at distances up to 50 μm from the fiber [10]. This was attributed to chemical strengthening of the Ti alloy matrix due to interstitial carbon migration [10]. Another recent study on Ti-6Al-4V matrix composite reinforced with the Sigma SM1140+ type of SiC fiber, having a 4.5 μm thick carbon coating, reported that the beta transus of the composite matrix was displaced to higher temperature by $>45^\circ\text{C}$ [11]. It was suggested that this shift in transus arises from carbon diffusion into the matrix [11]. The main objective of the present study was to provide experimental evidence for the extent of carbon diffusion from the SiC fiber coating into titanium alloy matrices. Other objectives of this work were to investigate the effect of matrix composition and microstructure on carbon diffusion and to quantify the effects of fiber/matrix reaction on the heat treatment response of the MMC matrix in terms of the resulting microstructures.

Thermodynamic Considerations

The Ti-rich side of the titanium-carbon binary phase diagram has been redrawn from published data [12] as shown in Fig. 1. An important feature of this phase diagram is the peritectoid transformation $\beta + \text{TiC} \rightarrow \alpha$, which occurs at 920°C and ~ 1.4 at.% C. It is observed that the solubility of carbon in the α phase is higher than in the β phase over a large temperature range below the peritectoid temperature. The implications of these aspects of phase equilibria in the binary system to the studies of SiC fiber reinforced Ti alloy matrix composites will be discussed later.

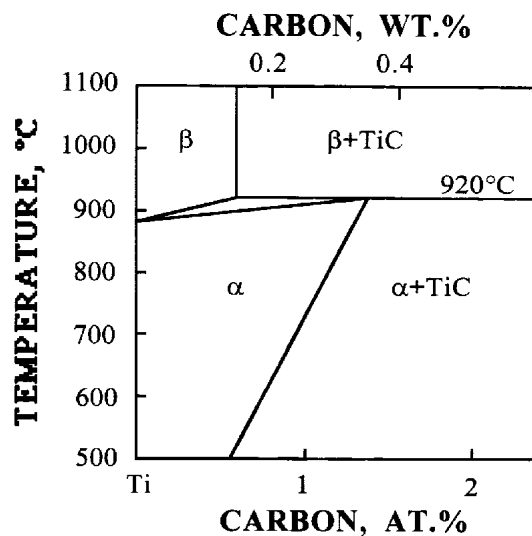


Fig. 1: Titanium side of the Titanium-Carbon phase diagram

Diffusion Calculations

The data for the diffusion of carbon in the α and β phases of titanium are available in the literature [13]. The respective diffusion coefficients are reported to be:

$$D_c^\alpha = 5.06 \exp(-43500 \text{ cal. mol}^{-1}/RT) \text{ cm}^2 \text{ s}^{-1} \quad (1)$$

$$\text{and } D_c^\beta = 108 \exp(-48400 \text{ cal. mol}^{-1}/RT) \text{ cm}^2 \text{ s}^{-1}. \quad (2)$$

Typically, the titanium-based MMCs are consolidated in the temperature range 925°C - 1000°C, which corresponds to the sub-transus region for most of the titanium alloys except the metastable beta alloys. Within this temperature interval, D_c^β is ~3 times higher than D_c^α . In this sub-transus processing region, the alloy may have ($\alpha+\beta$) or ($\alpha_2+\beta_0$) microstructure depending on the composition, usually with the β or β_0 phase providing a continuous path for interstitial diffusion. If one ignores the effects of alloy chemistry, phase ordering, and fiber/matrix reaction product layers, the distance over which the diffusion of C from SiC fiber coating into Ti alloy matrix occurs can be estimated. The simple expression

$$x = \sqrt{D t} \quad (3)$$

provides an estimate of the maximum distance for one dimensional mass transfer. Calculations performed on this basis using the D_c^β values given by the Equation (2) indicate that the diffusion distance of carbon in Ti matrix at the MMC processing temperatures is quite large. For example, processing for 5 min. at 1000°C is estimated to result in a carbon diffusion distance of 134 μm .

EXPERIMENTAL

This study used 6 different titanium-based matrix alloys with a variety of microstructures, as listed in Table 1. Three different compositions forming the ($\alpha_2+\beta_0+O$) microstructure were included in this work in order to understand the effects of variation in the relative amounts of phases in this important class of alloys. Table 1 also shows the β -transus temperature for each alloy.

Table 1. Matrix alloy compositions, microstructures, transus and heat treatment temperatures used in this work

Matrix Alloy	As-Consolidated Matrix Microstructure	β -Transus, °C	Supra-Transus Heat Treatment Temperature, °C
Ti-6Al-4V *	$\alpha + \beta$	995	1050
Ti-25Al-10Nb-3V-1Mo (Super Alpha-2)	$\alpha_2 + \beta$	1075	1150
Ti-24Al-17Nb	$\alpha_2 + \beta_0 + O$	1130	1150
Ti-24Al-17Nb-1Mo	$\alpha_2 + \beta_0 + O$	1110	1150
Ti-22Al-23Nb	$\alpha_2 + \beta_0 + O$	1100	1125, 1150
Ti-15Mo-2.7Nb-3Al-0.2Si * (TIMETAL 21S™)	β	815	900

* These two compositions are given in wt.%. The remaining compositions are in at.%.

Uniaxially reinforced composite panels comprised of each of these titanium alloy matrices with SCS-6 SiC fiber reinforcement were fabricated by diffusion bonding using the foil-fiber-foil method. The MMC consolidation was performed in the sub-transus temperature range for all the panels except the one based on TIMETAL 21S™. All composite panels contained 4-ply, with a nominal fiber volume fraction of 35%. Some of the matrix alloy foils were also

consolidated into "fiberless" panels using identical consolidation conditions, in order to obtain baseline data from the matrix alloy without the reinforcing fibers.

Two types of heat treatments were performed on these materials: (1) Supra-transus heat treatments were conducted on small coupon samples which were wrapped in Ta foil and encapsulated in evacuated vycor tubing. The samples were rapidly heated to a temperature above the beta-transus of the matrix alloy, isothermally heat treated for different periods and water-quenched, and (2) Isochronal heat treatments for 2 hr at several sub-transus and supra-transus temperatures, controlled cooling at the rate of 28°C/min. to 815°C, and aging at 815°C for 8 hr, followed by furnace cooling. The supra-transus heat treatment temperatures used are listed in Table 1. The heat treated specimens were characterized by optical microscopy, SEM, electron microprobe analysis with x-ray energy dispersive spectroscopy (EDS) as well as wavelength dispersive spectroscopy (WDS). The matrix microstructures were also quantified by using an NIH image analysis program.

RESULTS AND DISCUSSION

The typical fiber distribution in the 4-ply composite panels which were fabricated by the foil-fiber-foil approach is shown in Fig. 2. The as-consolidated microstructures of the composites studied are presented in Fig. 3. The phases observed in these matrix microstructures are listed in Table 1. As Fig. 3 shows, the phases present in these microstructures are generally equiaxed and are distributed on a fine scale.

The effect of supra-transus heat treatments on these composite matrices is shown in Fig. 4. These micrographs clearly indicate extensive precipitation within each of the titanium alloy matrices. The scale and extent of precipitation appears to vary with the matrix alloy composition. One common feature is that the volume fraction of precipitates is highest in the region close to the fiber and it decreases with increasing distance from the fiber. In fact, little or no precipitation was observed in the matrix regions which were close to the surface of the composite panel and more than a fiber diameter away from any of the fibers. The heat treated composites based on Ti-24Al-17Nb and Ti-24Al-17Nb-1Mo matrices showed precipitation of two different phases (Fig. 4c and 4d).

A more detailed characterization using x-ray energy dispersive spectroscopy (EDS) and wavelength dispersive spectroscopy (WDS) was conducted on the heat treated Ti-22Al-23Nb/SCS-6 samples. The precipitate microstructure was allowed to coarsen by heat treating it at 1125°C/2 hr/WQ. The resulting microstructure (Fig. 5) was suitable for performing a qualitative compositional analysis. The EDS analysis of the precipitate in this material yielded major peaks of Ti and a minor peak of Nb. There was no detectable Al peak. The WDS analysis of the precipitate particles indicated a distinct carbon peak, as depicted in Fig. 6. In contrast, WDS analysis of the matrix showed no observable carbon peak (Fig. 6). Further x-ray and transmission electron microscopy characterization of these precipitate phases is currently underway. However, based on the observed heat treatment response including the sites of precipitation and the results of WDS analysis, it is reasonable to suggest that these precipitates are carbides.

The precipitation observed in the Ti-24Al-17Nb and Ti-24Al-17Nb-1Mo composite matrices requires additional explanation. These alloys contain lower levels of the beta-stabilizing additions and exhibit high beta-transus temperatures (Table 1). It appears that the supra-transus heat treatment temperature which was used for these two compositions was not adequate to obtain a fully beta microstructure, and the carbide precipitation is associated with the remnant alpha-2 phase.

The influence of interstitials on the microstructure and properties of titanium and titanium alloys is well known. The diffusion of carbon from the SiC fiber coating into the titanium-based composite matrix is expected to stabilize the alpha-2 phase relative to the beta phase. This is borne out by the results shown in Figs. 7 and 8. Figure 7 shows the microstructures of

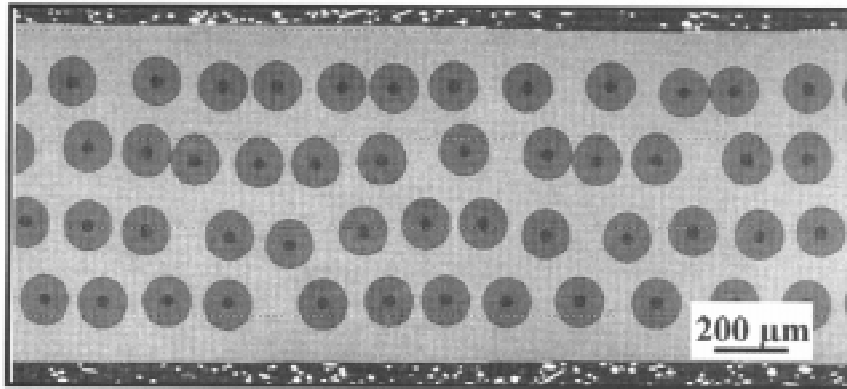


Fig. 2 - SEM micrograph of a transverse section of a Ti-24Al-17Nb-1Mo [0], composite panel

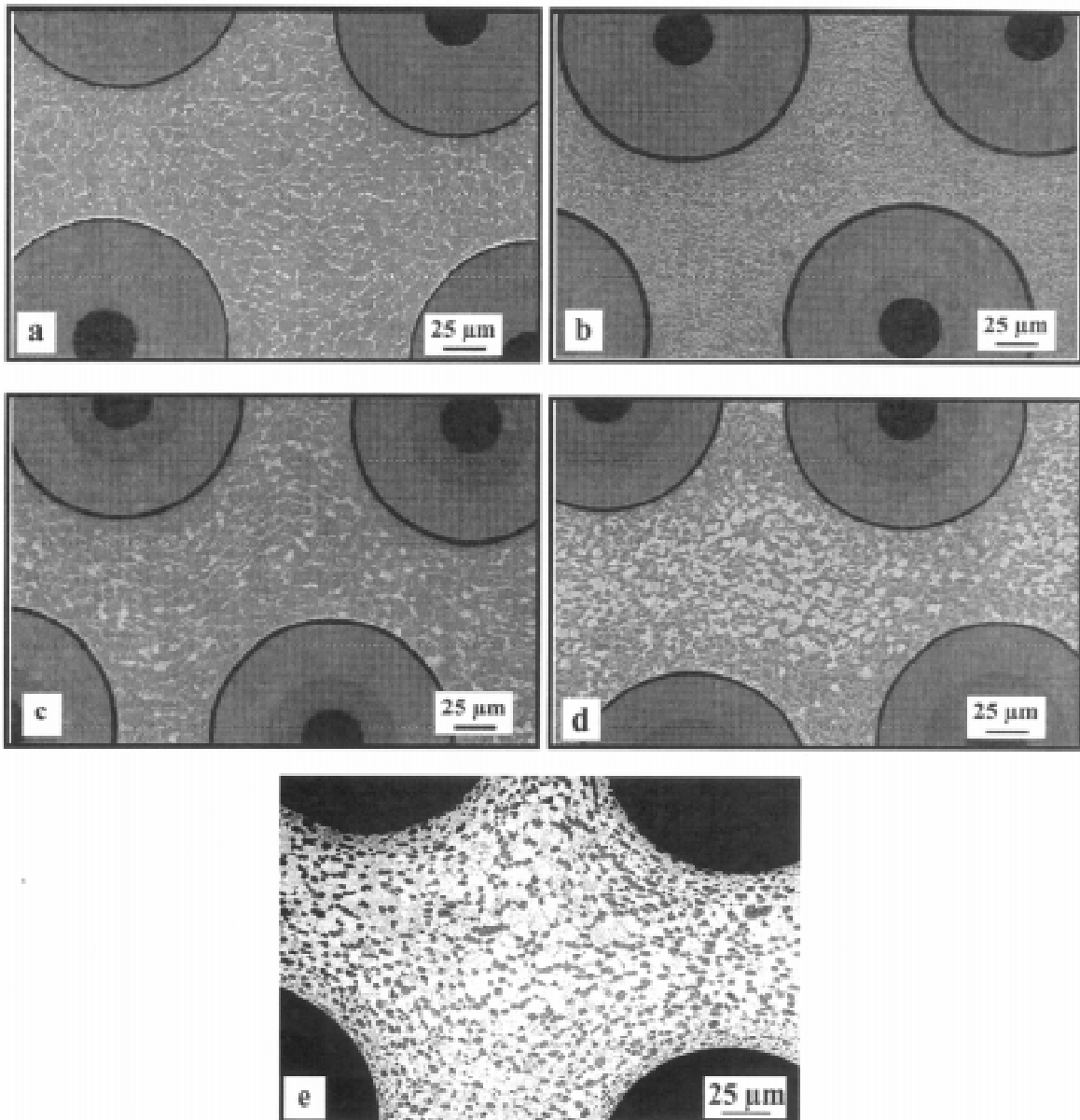


Fig. 3 - SEM micrographs showing transverse sections of as-consolidated composites from different matrices: (a) Ti-6Al-4V, (b) Ti-25Al-10Nb-3V-1Mo, (c) Ti-24Al-17Nb, (d) Ti-24Al-17Nb-1Mo, and (e) Ti-22Al-23Nb

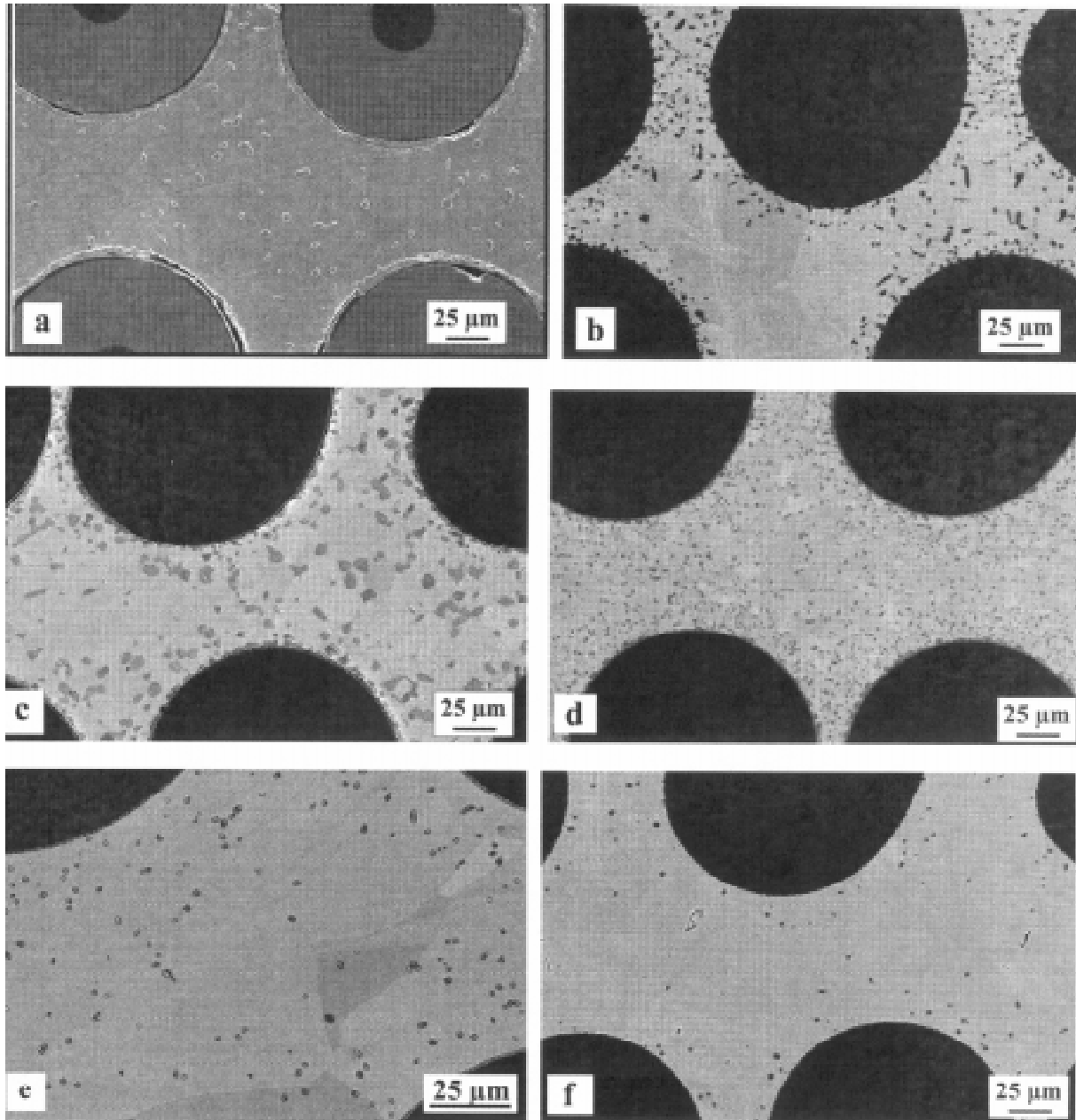


Fig. 4 - (a) Secondary electron image, and (b)-(f) back-scattered electron images of transverse sections of the composites following supra-transus heat treatments: (a) Ti-6Al-4V, (b) Ti-25Al-10Nb-3V-1Mo, (c) Ti-24Al-17Nb, (d) Ti-24Al-17Nb-1Mo, and (e) Ti-22Al-23Nb, and (f) Ti-15Mo-2.7Nb-3Al-0.2Si

fiberless Ti-22Al-23Nb matrix and Ti-22Al-23Nb/SCS-6 composite matrix, following identical heat treatments in the sub-transus range. These micrographs show significantly different amounts of the alpha-2 phase (dark phase seen in these micrographs). The results of quantitative analysis of the alpha-2 content in heat treated composite matrix and fiberless matrix samples are plotted in Fig. 8. These results illustrate that the heat treatment response of composite matrix and fiberless matrix can be markedly different over a wide range of heat treatment temperatures. The pronounced increase in the alpha-2 content of the composite matrix is also consistent with the expected effect of interstitial carbon.

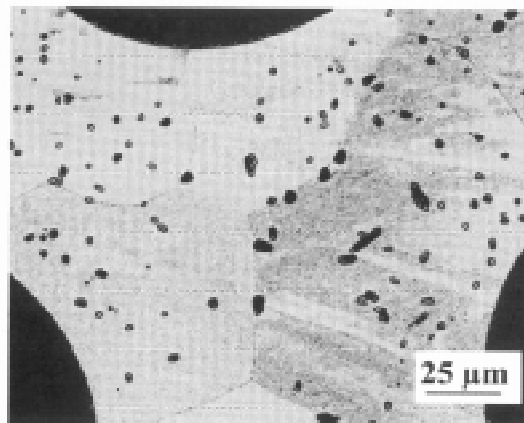


Fig. 5 - SEM back-scattered electron micrograph of Ti-22Al-23Nb/SCS-6 composite following heat treatment at 1125°C/2hr/WQ

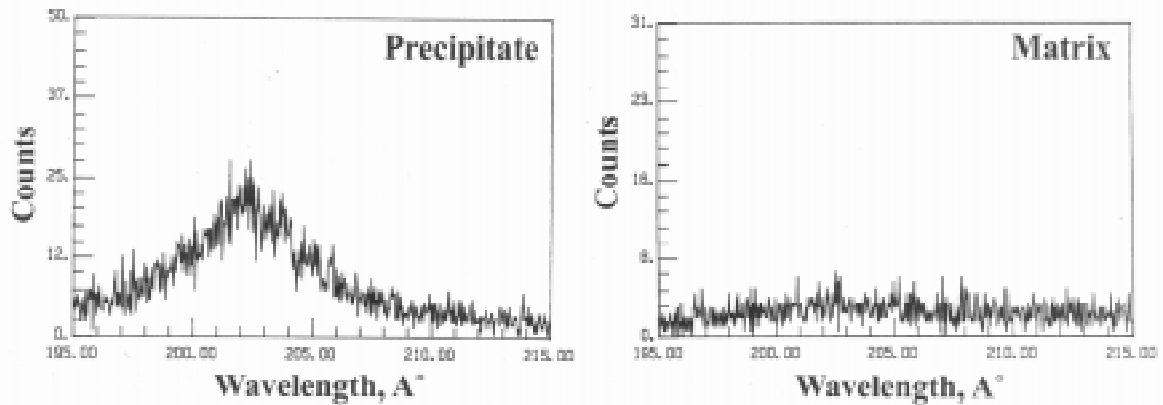


Fig. 6 - X-ray wavelength dispersive spectroscopy analysis of the precipitate and matrix phases depicted in Fig. 5

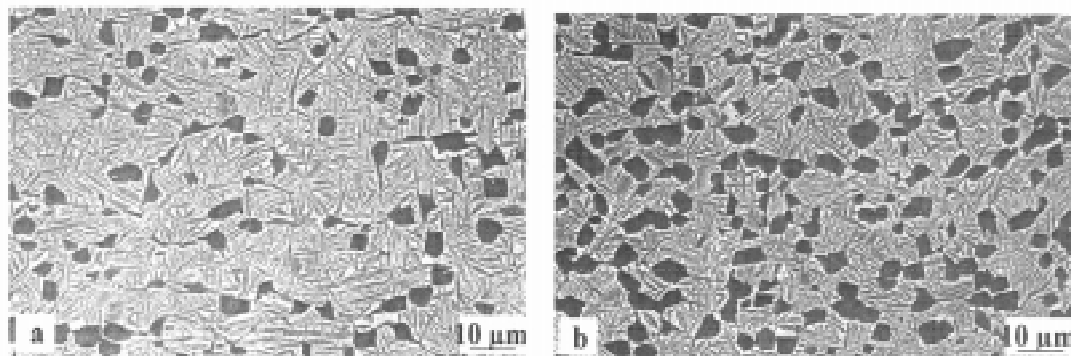


Fig. 7 - SEM micrographs showing the effect of heat treatment at 1050°C/2hr, cooling at 28°C/min to 815°C, and aging at 815°C/8hr/FC on (a) Fiberless Ti-22Al-23Nb matrix and (b) Ti-22Al-23Nb/SCS-6 Composite matrix

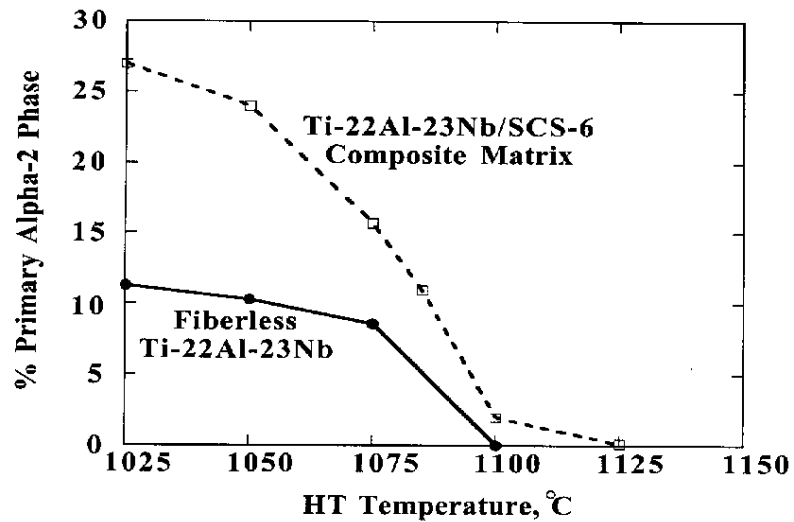


Fig. 8 - A comparison of the effect of heat treatment on the microstructure of Ti-22Al-23Nb fiberless matrix and SiC reinforced Ti-22Al-23Nb matrix composite

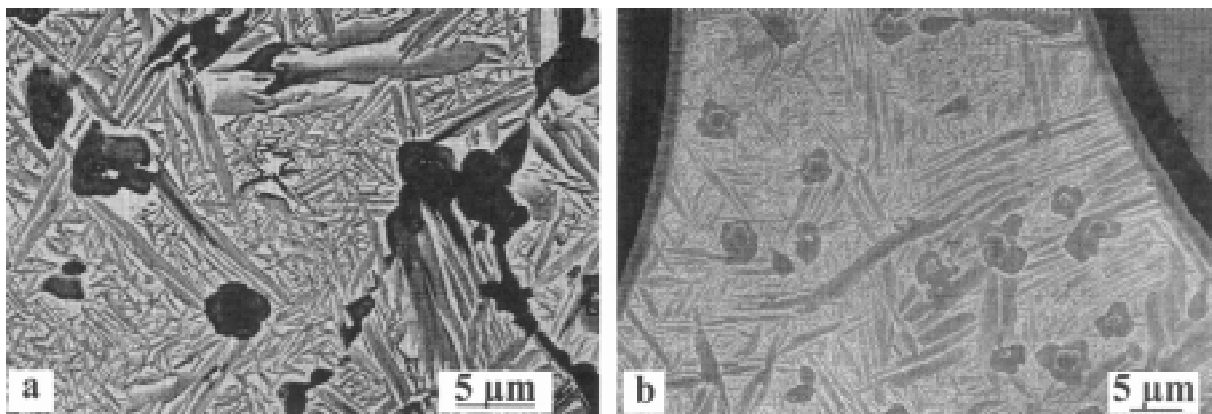


Fig. 9 - SEM micrographs depicting the precipitation of carbide particles in Ti-22Al-23Nb/SCS-6 composite which was heat treated at a sub-transus temperature

Previous work has shown that the titanium-based composites may require post-consolidation heat treatments in order to achieve an optimum balance of properties [14]. The present results indicate that the solubility of carbon in the matrix plays a major role in determining the microstructure resulting from consolidation and post-consolidation heat treatments. Significant levels of carbon can dissolve in the composite matrices, under the normally used processing conditions. It is also important to note that the higher solubility of carbon in the alpha or alpha-2 phase can lead to the precipitation of carbide even in sub-transus heat treatment conditions, as shown in Fig. 9.

CONCLUSIONS

The following conclusions are drawn based on the results of this work:

1. The consolidation processing of SiC fiber reinforced Ti alloy matrix composites is accompanied by the formation of a reaction zone as well as the diffusion of carbon from the protective coating of the fiber into the matrix. The carbon diffusion from fiber coating into Ti alloy matrix is not limited to the near-fiber region, but occurs over a long range, relative to the fiber diameter.
2. The diffusion of carbon into the composite matrix stabilizes the alpha phase (or alpha-2 phase, depending on the alloy composition). This leads to markedly different heat treatment response of the composite matrix as compared to the "fiberless" matrix, and shows that microstructural data obtained from heat treatments of "fiberless" material cannot be directly applied to perform heat treatments of the composite.
3. Precipitation of carbide phase can occur under supra-transus as well as sub-transus heat treatment cycles.
4. The microstructure of the Ti alloy matrix which is controlled by the alloy composition and heat treatment has a significant effect on the solubility and diffusion of carbon in the matrix.

ACKNOWLEDGMENTS

This research was performed at the Air Force Wright Laboratory, Materials Directorate, under AF Contracts F33615-91-C-5663 and F33615-96-C-5258. The authors would like to acknowledge the technical assistance of Mr. W.A. Houston and Dr. J. Woodhouse of UES Inc., in metallographic specimen preparation and microprobe analysis, respectively.

REFERENCES

1. Smith, P.R. and Froes, F.H., "Developments in Titanium Metal Matrix Composites," *Journal of Metals*, March 1984, pp. 19-26.
2. Miracle, D.B., Smith, P.R. and Graves, J.A., "A Review of the Status and Developmental Issues for Continuously-reinforced Ti-Aluminide Composites for Structural Applications," in *Intermetallic Matrix Composites III*, MRS Symposium Proceedings, Vol. 350, Graves, J.A., Bowman, R.R. and Lowandowski J.J., Eds., MRS, Pittsburgh, PA, 1994, pp. 133-142.
3. DiCarlo, J.A., "Fibers for Structurally Reliable Metal and Ceramic Composites," *Journal of Metals*, June 1985, pp. 44-49.
4. Martineau, P., Pailler, R., Lahaye, M. and Naslain, R., "SiC Filament/Titanium Matrix Composites Regarded as Model Composites - Part 2: Fiber/Matrix Chemical Interactions at High Temperatures," *J. Mater. Sci.*, Vol. 19, 1984, pp. 2749-2770.
5. Rhodes, C.G. and Spurling, R.A., "Fiber-Matrix Reaction Zone Growth Kinetics in SiC-Reinforced Ti-6Al-4V as Studied by Transmission Electron Microscopy," in *Recent Advances in Composites in the United States and Japan*, ASTM STP 864, Vinson J.R. and Taya M., Eds., ASTM, Philadelphia, 1985, pp. 585-599.
6. Das, G., "A Study of the Reaction Zone in an SiC Fiber-Reinforced Titanium Alloy Composite," *Metall. Trans. A*, Vol. 21A, June 1990, pp. 1571-1578.
7. Baumann, S.F., Brindley, P.K. and Smith, S.D., "Reaction Zone Microstructure in a Ti₃Al + Nb/SiC Composite," *Metall. Trans. A*, Vol. 21A, June 1990, pp. 1559-1569.

8. Gundel, D.B. and Wawner, F.E., "Interfacial Reaction Kinetics of Coated SiC Fibers with Various Titanium Alloys," *Scripta Metall.*, Vol. 25, 1991, pp. 437-441.
9. Hall, I.W., Lirn, J.-L., LePetitcorps, Y. and Bilba, K., "Microstructural Analysis of Isothermally Exposed Ti/SiC Metal Matrix Composites," *J. Mater. Sci.*, Vol. 27, 1992, pp. 3835-3842.
10. Pickard, S.M. and Miracle, D.B., "An Experimental Study of Residual Stresses in SiC Fiber-Reinforced Ti-Based Composites," *Mater. Sci. and Engrg.*, Vol. 203, No. 1/2, Nov. 1995, p. 59.
11. Sweby, S., Dowson, A. and Bowen, P., "Effects of Matrix Microstructure on the Fatigue Crack Growth Resistance of Titanium Metal Matrix Composites," *Proceedings Tenth International Conference on Composite Materials*, Whistler, British Columbia, Canada, August 14-18, 1995, Vol. II: Metal Matrix Composites, Poursartip, A. and Street, K., Eds., Woodhead Publishing Limited, pp. 513-520.
12. Cadoff, I. and Nielson, J.P., "Titanium-Carbon System," *Trans. ASM*, Vol. 45, 1953, pp. 972-991.
13. Wagner, F.C., Bucur, E.J. and Steinberg, M.A., "The Rate of Diffusion of Carbon in Alpha and Beta Titanium," *Trans. ASM*, Vol. 48, 1956, pp. 742-761.
14. Smith, P.R., Khobaib, M. and Graves, J.A., "Creep Behavior of an Alpha-2 and an Orthorhombic Ti-Based Matrix," *Scripta Metall.*, Vol. 29, 1993, pp. 1313-1318.

DAMAGE ACCUMULATION AND FRACTURE IN METAL MATRIX COMPOSITES

J. D. Boyd, R. D. Evans, G. de Kleine and S. Tao

*Department of Materials and Metallurgical Engineering,
Queen's University, Kingston, Ontario, Canada, K7L 3N6*

SUMMARY: This paper describes the effects of particle size and distribution on damage behaviour in particle reinforced metal matrix composites (PRMMCs) under different loading conditions. Two types of PRMMCs were studied: 1) molten metal processed and squeeze cast aluminum A356 + 15 μm diameter SiC, and 2) solid state powder processed and extruded commercial purity Al + 0.8, 3, or 12 μm SiC.

Three types of damage behaviour were observed: 1) Tensile loading - large, clustered particles. Damage is a combination of particle cracking and interface decohesion, and is concentrated in particle clusters. 2) Tensile loading - small, uniformly distributed particles. Particle cracking is suppressed, and fracture occurs by growth and coalescence of voids originating at particle interfaces. 3) Compression - large, uniformly distributed particles. Interface decohesion occurs due to tensile stresses which result from non-homogeneous flow of the matrix around the particles.

KEYWORDS: particle-reinforced MMCs, particle cracking, decohesion, damage, fracture

INTRODUCTION

The micromechanism of fracture in particulate reinforced metal matrix composites (PRMMCs) is a "locally ductile" process whereby the ductile fracture mechanism of void nucleation and growth occurs over a small fraction of the stressed volume and the macroscopic ductility is low.

Hence, ductile fracture models which were developed for materials containing low volume fractions ($< 1\%$) of uniformly dispersed particles [1,2] do not accurately predict the observed effects of particle volume fraction on fracture ductility or fracture toughness in PRMMCs [3]. In PRMMCs, the fracture process is a continuous nucleation and growth of voids (damage) with increasing strain until a critical damage condition for fracture is reached. The critical level of accumulated damage is 2 - 5 %, whether measured by an averaged property (eg., elastic modulus [4]) or by a microscopic measurement (eg., % damaged particles [5]). Most studies of the fracture behaviour of PRMMCs have been for particle sizes of 10 μm or larger, where particle cracking is the dominant damage mechanism [6,7]. In molten metal processed PRMMCs, the particle distribution is non-uniform (clustered), and damage is concentrated in the particle clusters [4,5]. The current models for void nucleation and growth and the prediction of fracture ductility in PRMMCs have been recently reviewed [8].

The objective of the present study was to determine the effects of particle size and distribution on damage behaviour in PRMMCs under different loading conditions. In particular, damage mechanisms were determined for material containing uniformly distributed particles $< 1 \mu\text{m}$ diameter, and compared with previous results for clustered distributions of larger particles.

EXPERIMENTAL

Materials

Two types of PRMMCs were studied. The first type was molten metal processed and squeeze cast aluminum A356 matrix alloy (Al-7Si-0.35Mg) reinforced with $15 \mu\text{m}$ diameter SiC particulate. Processing details are given elsewhere [5]. The second type of PRMMC studied was solid state powder processed commercial purity aluminum matrix (Al-0.26 Fe-0.18 Si) reinforced with 10 vol.% of SiC particulate, either $0.8 \mu\text{m}$, $3 \mu\text{m}$ or $12 \mu\text{m}$ diameter. $6.3 \mu\text{m}$ Al powder was mixed with the SiC, compacted and hot extruded at 500°C to 6.3 mm diameter rod with an extrusion ratio of $\sim 15:1$. This material was supplied by Risø National Laboratory, Denmark.

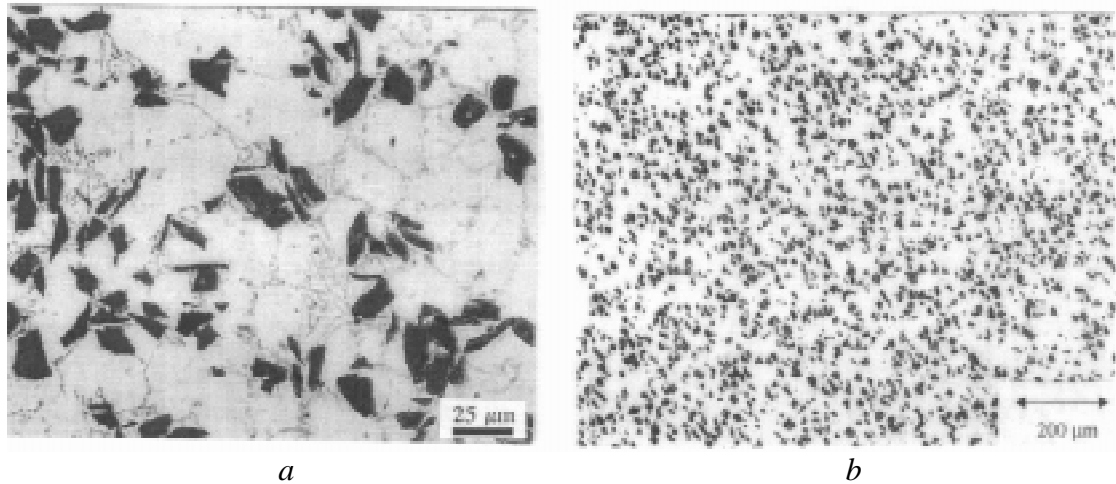
Particle distributions were characterized by optical metallography and image analysis. The mean values of volume fraction (V_f) and particle diameter (d) are given in Table 1. It was obvious from optical metallography (Fig. 1) that the particle distribution was non-uniform ('clustered') in the molten metal processed/squeeze cast material, and much more uniform in the powder processed/extruded material, especially for the smaller particle sizes.

Table 1: Characterization of MMC Materials

Material	V_f (%)	d (μm)	σ_y (MPa)	ϵ_f (%)
molten metal processed/squeeze cast A356-SiC	14.1 ± 1.9	15.0 ± 5.5	198	3.3
powder processed/extruded Al-SiC ($12 \mu\text{m}$)	11.2	10.1 ± 5.0	141	29
powder processed/extruded Al-SiC ($0.8 \mu\text{m}$)	10.7	0.8 ± 1.1	166	23

V_f = volume fraction of particulate
 σ_y = tensile yield stress

d = mean particle diameter
 ϵ_f = true fracture stress



*Fig. 1: Particle Distributions a) Molten Metal Processed/Squeeze Cast (15 μm)
b) Powder Processed/Extruded (0.8 μm)*

Fracture Tests and Characterization of Damage

Tensile tests were carried out on all materials at a crosshead speed of 0.005 mm/s, and fracture surfaces were examined by SEM. The sample dimensions were 4 mm diameter x 14 mm gauge length. Tensile yield stresses and fracture strains are reported in Table 1.

Four-point bend tests of double-notch samples were also carried out on the molten-metal processed/squeeze cast materials. This allowed the nature and extent of pre-fracture damage to be determined from examination of the microstructure at the uncracked notch. A complete description of this technique is given elsewhere [5].

Direct observations of damage initiation in the 3 μm powder-processed/extruded material were made by performing notched tensile tests *in-situ* in an environmental scanning electron microscope (ESEM). The sample dimensions were 5.4 mm² cross-section, 25 mm length, with a 3.5 mm notch in the centre of the gauge length. The microscope was focussed to observe initiation and development of damage at the notch tip.

Machining Tests and Characterization of Damage

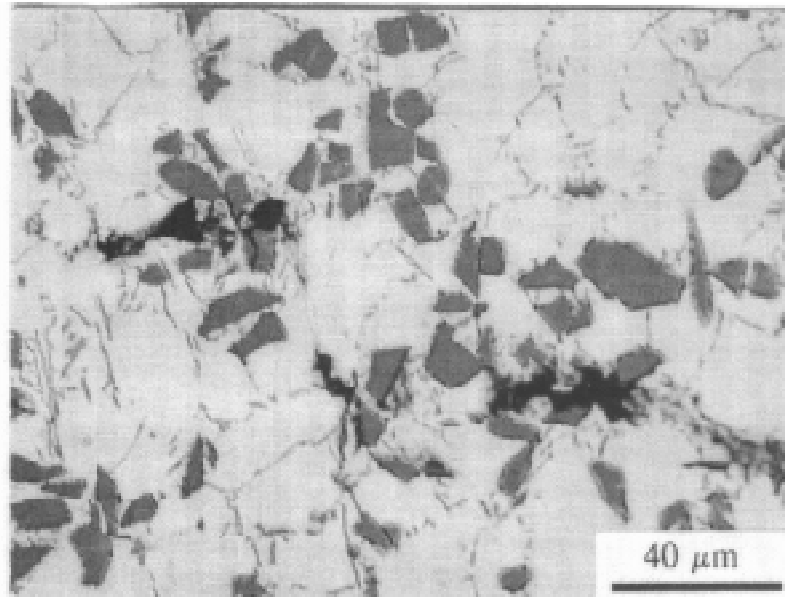
Machining tests were carried out by orthogonal cutting the ends of cylinders of the MMC samples. The cylinders were 5.0 mm diameter x 1.25 mm wall thickness. The cutting tool was a polycrystalline diamond (PCD) tool bit having a rake face angle of 7° and a tool nose radius of 0.8 mm. In orthogonal cutting, both the (single) cutting edge and the feed direction are perpendicular to the direction of workpiece (rotational) velocity. The depth of cut was held constant at 1.25 mm, feed rate was either 0.05 or 0.20 mm/rotation, and the rotational speed was either 500 rpm or 1500 rpm.

Machined chips were collected and mounted to examine either the chip surface or cross section by optical metallography and SEM. “Quick-stop” samples were obtained by stopping the lathe suddenly, which captured the chip on the workpiece. Material was cut from the workpiece with the chip attached so that the complete deformation zone could be studied. The flow pattern of the material in the deformation zone was enhanced by etching the mounted and polished samples in 0.5 % HF for approximately 30 s.

RESULTS

Damage in Molten Metal Processed MMCs Containing 15 μm Particles

The development of damage prior to fracture was studied by examining the region near the tip of the uncracked notch in the double-notched 4-point bend samples. Fig. 2 shows that damage was not uniformly distributed, rather it developed preferentially at clusters of particles. The damage was a combination of particle cracking and interface decohesion, and approximately 5 % of particles were damaged at the point of fracture initiation. Examination of the region near the cracked notch indicated that the crack path linked damage clusters. SEM of fracture surfaces revealed evidence of particle cracking, interface decohesion, small dimples associated with Si needles and localized areas of matrix rupture. Measurements of area fraction of SiC particles (cracked and decohered) on the fracture surface gave values of 22-30% for all samples, again indicating that fracture propagated through the high V_f regions of the particle clusters.



*Fig. 2: Damage at Uncracked Notch in 4-Pt. Bend Test
(Molten Metal Processed/Squeeze Cast (15 μm))*

Damage in Powder Processed MMCs Containing 0.8 μm , 3 μm and 12 μm Particles

In comparison with the squeeze-cast A356-SiC material, the extruded Al-SiC had lower yield strength and much higher fracture strain (Table 1). *In-situ* ESEM tests of material containing 3 μm particles showed that the damage initiation was in the form of particle-matrix decohesion, with minimal particle cracking. After void nucleation at interfaces, damage progressed by void growth and coalescence in the matrix (Fig. 3). The damage and fracture characteristics were strongly dependent on particle size. For the 12 μm particles, the dominant damage mechanism was particle cracking. Fracture surfaces of this material revealed a combination of cracked particles and ductile failure in the matrix with ~ 1 μm dimples (Fig. 4a). There was no particle cracking in the MMCs containing 0.8 μm particles and the only damage associated with the particles was interface decohesion. Fracture surfaces

of this material showed completely ductile failure with $\sim 1 \mu\text{m}$ dimples (Fig. 4b). A few of the dimples contained visible particles. There were also some secondary dimples $\sim 0.1 \mu\text{m}$ in diameter (Fig. 4b @ arrow).

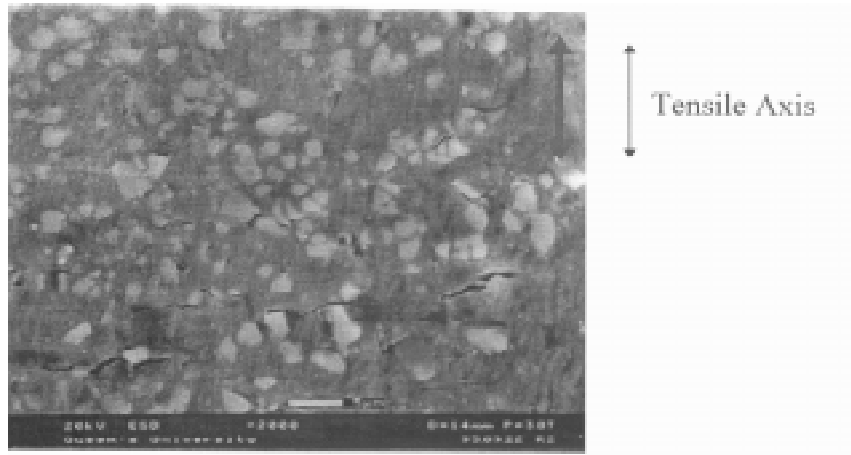
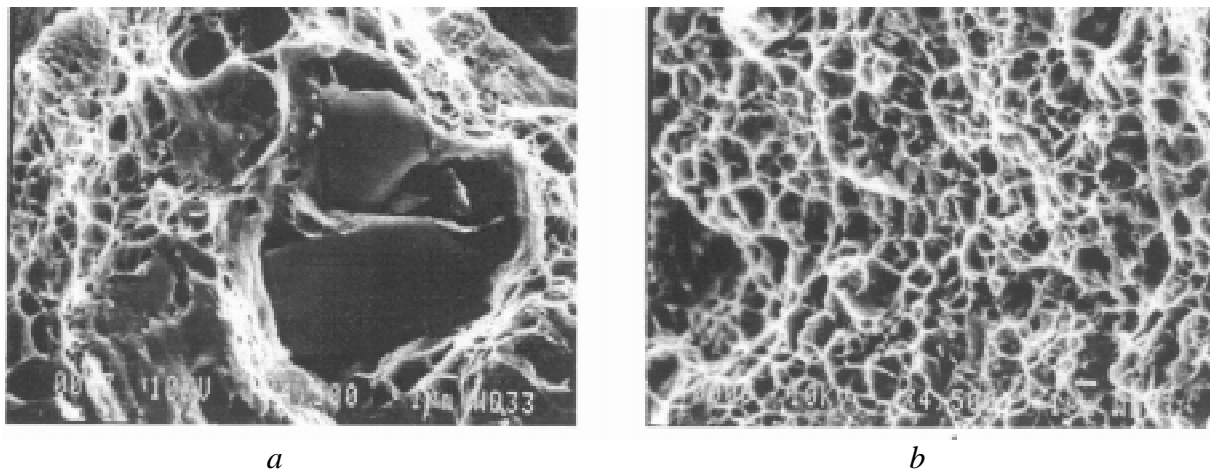


Fig. 3: Damage Observed During In-Situ ESEM Test (Powder Processed/Extruded ($3 \mu\text{m}$))

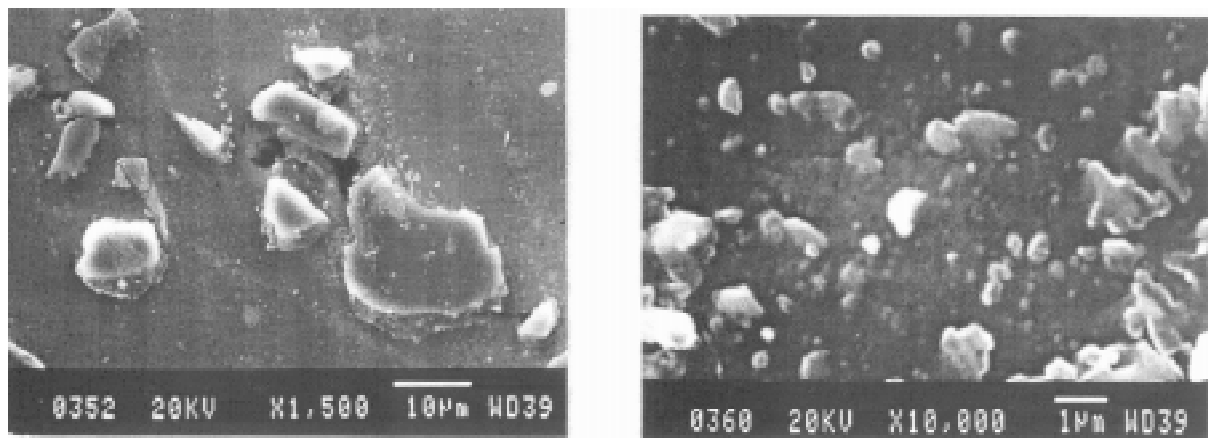


*Fig. 4: Fracture Surfaces in Tensile Tests (Powder Processed/Extruded)
a) $12 \mu\text{m}$ b) $0.8 \mu\text{m}$*

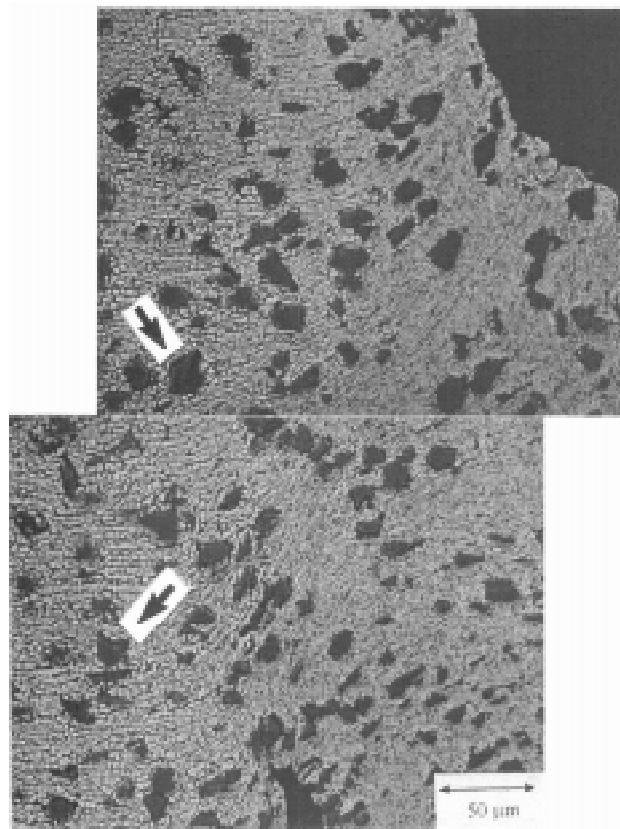
Damage During Machining of Powder Processed MMCs

In all cases, the chips produced were quasi-continuous and had a serrated edge, indicating segmented chip formation [9]. Again, there was a distinct effect of particle size on damage mechanism. For the samples containing $12 \mu\text{m}$ particles, there was clear evidence of interface decohesion and void growth in the machined chips (Fig. 5a). Increasing the rotational speed increased the strain rate and resulted in a corresponding increase in damage. In contrast, there was no evidence of damage in the machined chips of the $0.8 \mu\text{m}$ MMC (Fig. 5b). A quick-stop section of the $12 \mu\text{m}$ material revealing the flow pattern in the deformation zone is shown in Fig. 5c. The non-homogeneous flow of the matrix around the particles is evident and voids which have formed at particle interfaces are indicated by arrows. Quick-stop sections of the $0.8 \mu\text{m}$ MMCs showed no evidence of non-homogeneous flow around particles and no void formation in the deformation zone. The distinctly different damage behaviour for the 2

particle sizes was reflected in the ease of chip fracture. The 0.8 μm MMC produced long chips, whereas the 12 μm MMC fractured more frequently and produced shorter chips.



(b)



(c)

Fig. 5: Damage During Orthogonal Machining (Powder Processed/Extruded)
a) Chip Cross-Section (12 μm) b) Chip Cross-Section (0.8 μm)
c) Quick-Stop Sample Showing Deformation Zone (12 μm)

DISCUSSION

The results demonstrate the effects of particle size and distribution on the pre-fracture damage mechanisms. The degree of damage is also a function of stress state, and differs widely for the predominantly tensile stress state in bend- and tensile tests, in contrast with machining where there is a combination of compression and shear stresses. Three different combinations of loading condition and particle distribution are considered, and damage models are described for each: i) tensile loading - large, clustered particles, ii) tensile loading - small, uniformly distributed particles, iii) compression - large, uniformly distributed particles. Schematic diagrams for each case are shown in Fig. 6.

Tensile Loading - Large, Clustered Particles

The damage is concentrated in particle clusters (Figs. 2 and 6a). Cracking and interface decohesion of individual particles as well as matrix failure are observed in the damage clusters. The voids which develop in the particle clusters do not grow extensively in the tensile direction. This is consistent with constraint of plastic flow in the matrix leading to triaxial stress intensification. The maximum tensile stress can be estimated by considering the deformation of a volume of matrix between particles to be equivalent to uniaxial deformation between elastic platens with sticking friction at the interface [4]. In a typical particle cluster, the dimensions of the constrained matrix are approximately $1\text{-}2\ \mu\text{m} \times 15\ \mu\text{m}$, which gives $\sigma_{\text{max}} = 1600 - 3000\ \text{MPa}$ [5]. Thus, high tensile stresses in the particle clusters lead to damage by particle cracking, as well as interface decohesion.

The critical condition for fracture would be determined by the size and spacing of the damage clusters. It has been shown that the fracture toughness (K_{IC}) depends strongly on the degree of particle clustering [5].

Tensile Loading - Small, Uniformly Distributed Particles

For particle diameters $3\ \mu\text{m}$ or less, there is no particle cracking and the sole damage mechanism is particle-matrix interface decohesion (Figs. 3 and 6b). There are 2 reasons why the particle fracture stress is not reached. With uniformly distributed particles, there is no stress intensification by plastic constraint. Secondly, the fracture stress of SiC increases with decreasing particle diameter, because the probable length of an intrinsic flaw is proportional to particle diameter [7]. Although the damage is relatively uniformly distributed, Fig. 3 indicates that the voids which form at particle interfaces grow primarily in the lateral direction perpendicular to the tensile axis.

The fracture condition is that for void coalescence, and the resulting fracture surfaces show dimples predominantly $1\ \mu\text{m}$ in diameter, which is comparable to the particle spacing. The $0.1\ \mu\text{m}$ secondary dimples could form at small Al_2O_3 particles which originate with the powder processing. Thus, it is expected that the fracture strain will vary with mean particle spacing, as shown by the data in Table 1.

Compression - Large, Uniformly Distributed Particles

Ideally, orthogonal cutting occurs by a pure shear deformation at the plane which separates the workpiece from the chip. In reality, deformation occurs over a significant volume of the workpiece material, under a combination of compressive and shear stresses. Deformation

begins well ahead of the tool bit, as seen in Fig.5c. The workpiece material is initially compressed in the direction perpendicular to the tool rake face, then deformed by shear into the chip. The observations on damage in the deformation zone can be explained by considering simple compressive loading (Fig. 6c). With large particles (Fig. 5a), tensile stresses develop in the matrix normal to the compression axis due to non-homogeneous flow of the matrix, leading to interface decohesion. There is no particle cracking because the particles are in compression. The degree of non-homogeneous flow, and the magnitude of the tensile stresses decrease with decreasing particle diameter [10]. This explains the absence of damage in the MMCs containing $0.8\ \mu\text{m}$ particles (Fig.5b)

Fracture of chips takes place when a critical damage level is reached and void coalescence occurs. Since the damage rate is higher at the larger particle size, fracture is frequent and the mean chip length is small. Conversely, the damage rate is low for small particle size and the chips are much longer.

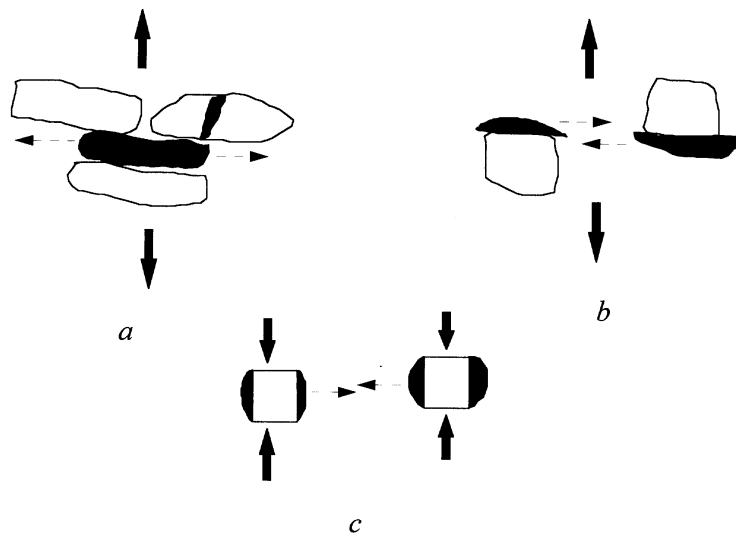


Fig. 6: Damage Models for Different Particle Distributions and Load Geometries
 a) Tensile - Clustered, Large Particles b) Tensile - Small Particles
 c) Machining - Large Particles
 (dashed arrows indicate direction of void growth)

CONCLUSIONS

The following characteristics of damage accumulation and fracture in PRMMCs have been described:

1. In MMCs containing large ($> 10\ \mu\text{m}$), clustered particles (such as produced by molten metal processing), local tensile stresses in the particle clusters are high leading to preferential damage initiation in those regions. Under these conditions, damage is a combination of particle cracking and interface decohesion. Fracture toughness varies inversely with the degree of particle clustering.
2. Particle cracking is suppressed in MMCs containing small ($< 3\ \mu\text{m}$), uniformly distributed particles (such as produced by powder processing). Fracture occurs by growth and coalescence of voids originating at particle interfaces, and fracture ductility varies inversely with mean particle spacing.

3. When deformed in compression (e.g., machining), interface decohesion occurs due to tensile stresses in the matrix which result from non-homogeneous flow of the matrix around the particles. With decreasing particle diameter, the damage rate decreases and chip formation becomes more difficult.

ACKNOWLEDGEMENTS

This research was supported by an industrial consortium (Alcan, Inco, Sherritt Technology, Ontario Hydro, Comdev) and the Natural Sciences and Engineering Research Council of Canada. The authors are grateful to Dr. Yi-Lin Liu of Risø National Laboratory, Denmark for providing the powder processed/extruded material for this study.

REFERENCES

1. Brown, L.M. and Embury, J.D., “ The Initiation and Growth of Voids at Second Phase Particles”, *Proceedings of the 3rd International Conference on the Strength of Metals and Alloys*, Institute of Metals, London, 1973, pp. 164-168.
2. Hahn, G.T. and Rosenfield, A.R., “ Metallurgical Factors Affecting Fracture Toughness of Al Alloys”, *Metall. Trans.*, Vol. 6A, 1975, pp. 653-670.
3. Clyne, T.W., and Withers, P.J., *An Introduction to Metal Matrix Composites*, Cambridge University Press, Cambridge, 1993, pp. 230-251.
4. Lloyd, D.J., “Aspects of Particle Fracture in Particulate Reinforced MMCs”, *Acta Metall. Mater.*, Vol. 39, 1991, pp. 59-72.
5. Tao, S. and Boyd, J.D., “Mechanisms of Damage Accumulation and Fracture in Particulate Reinforced Metal-Matrix Composites”, *Mechanisms and Mechanics of Composites Fracture*, Eds., Bhagat, R.B., Fishman, S.G. and Arsenault, R.J., ASM, Materials Park, 1993, pp. 29-40.
6. Mummery, P. and Derby, B., “The Influence of Microstructure on the Fracture Behaviour of Particulate Metal Matrix Composites”, *Mater. Sci. Eng*, Vol. A135, 1991, pp. 221-224.
7. Lewis, C.A. and Withers, P.J., “Weibull Modelling of Particle Cracking in Metal Matrix Composites”, *Acta Metall. Mater.*, Vol. 43, 1995, pp. 3685-3699.
8. Whitehouse, A.F. and Clyne, T.W., “Cavity Formation During Tensile Straining of Particulate and Short Fibre Metal Matrix Composites”, *Acta Metall. Mater.*, Vol. 41, 1993, pp. 1701-1711.
9. Jawahir, I.S. and Van Luttervelt, C.A., “Recent Developments in Chip Control Research and Applications”, *CIRP ANNALS Manufacturing Technology*, Vol. 42, 1993, pp. 659-693.
10. Humphreys, F.J. and Hatherley, M., *Recrystallization and Related Phenomena*, Galliard, London, 1995, pp. 256-264.

RUPTURE OF 7075/AL₂O₃ COMPOSITES AT HIGH TEMPERATURE

H. J. McQueen, E. V. Konopleva and G. Avramovic Cingara*

Mechanical Engineering, Concordia University, Montreal H3G 1M8, Canada

**Ontario Hydro Technologies, Toronto, M8Z 5S4, Canada*

SUMMARY: Aluminum alloy matrix composites 7075 with 10 and 15% Al₂O₃ particles have been deformed by torsion in the range 250-540°C at strain rate $\dot{\epsilon} = 0.1-4 \text{ s}^{-1}$. The strength decreased gradually as test temperature rose and $\dot{\epsilon}$ declined; but maximum ductility was found at 400°C. Optical and scanning electron microscopic examination showed that particles became aligned at an angle near 45° to the torsion axis and did not break up. Cracked particles were sometimes observed in the shoulder and more often in the gage. All specimens tested at 300-500°C had the cracks on the surface; these were rows of short cracks propagated in the plane of maximum shear stress. At 400°C in both composites with 10 and 15% Al₂O₃, samples contained many cracks on the surface and a few big cracks inside the gage; particles were the sites for formation of fine cracks. At 500°C, polarized optical microscopy revealed mainly elongated grains with internal substructure and also some areas of fine equiaxed crystallites. The drop in ductility at 500°C has been related to the formation of large precipitate particles at that temperature.

KEYWORDS: particulate, aluminum matrix, hot workability, rupture, cracking, TEM, SEM, optical microscopy, subgrains, grain boundary precipitates

INTRODUCTION

Particulate Al matrix composites (AMC) synthesized by liquid metal mixing have great potential because of their improved mechanical properties, low density and reasonable cost. Components may be finally produced by casting directly to shape or to billets for subsequent mechanical shaping, such as extrusion [1-6]. While this last type of processing has the possibility of rapid, large volume production, it requires that the AMC have adequate workability which is always reduced relative to the matrix alloy by the reinforcing particles.

The aluminum matrix composites derive their mechanical properties from the high dislocation density and the residual stresses induced by the difference in coefficient of thermal expansion (ΔCTE) [2,6-9]. The strengthening can be increased by fine substructures or grain sizes developed by TMP which are also designed to produce the required shape. The induced dislocation densities increase with rising strain and strain rate and falling temperature to an even greater extent than in the matrix alloy as the particle volume fraction increases because of the preexisting ΔCTE dislocations and the enhancement of inhomogeneous plastic flow by the rigid particles [5,6-29]. The properties developed depend strongly on the alloy in which the solutes, dispersoids and precipitates also influence the TMP results [22,26-32]. Finally the strength of the matrix may be augmented in some alloys by precipitation hardening which is frequently altered compared to the bulk alloys by the presence of the high dislocation

densities and residual stresses. Matrix alloys are generally strengthened by the precipitates to a greater degree in the order 6000 series (Mg_2Si), 2000 series ($CuAl_2$) and 7000 series ($Zn-Cu-Mg$) [27-31,33-39].

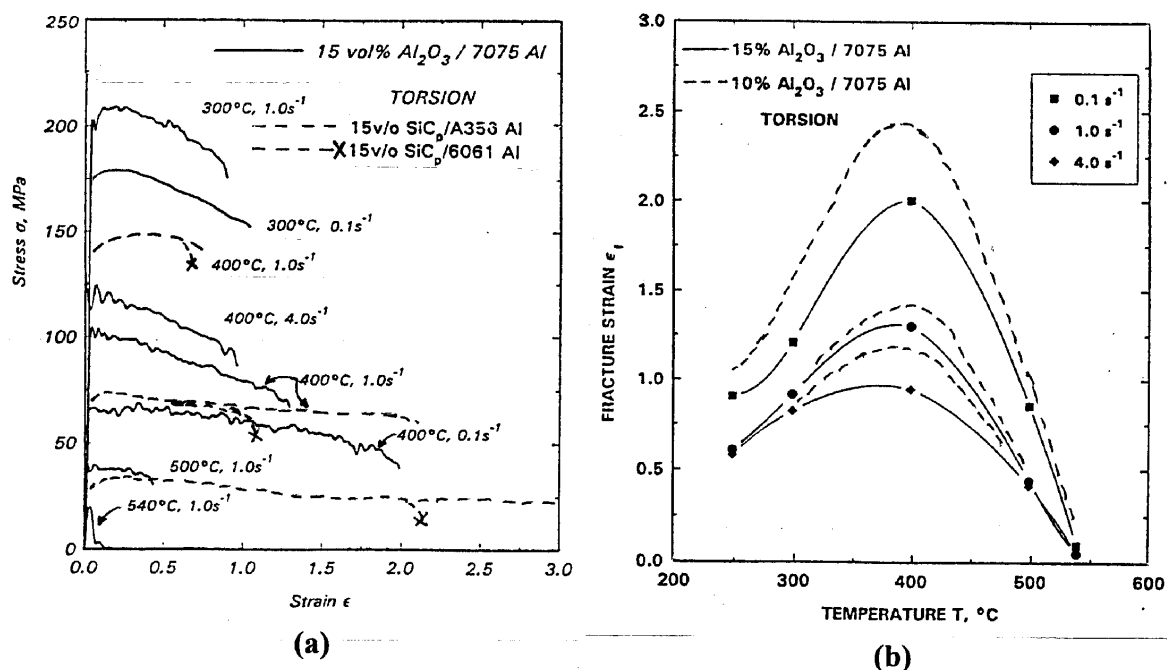


Figure 1. Schematic torsion flow curves of 7075/15%Al₂O₃ (a) showing the development a long steady state plateau at 400°C. The 6061 and A356 composites with 15%SiC exhibit much lower flow stresses and extensive plateaus at 500°C, 1 s⁻¹. (b) The ductility of 7075/15%Al₂O₃ increases as strain rate decreases most noticeably near the temperature of the maximum. The ductility of 7075/10%Al₂O₃ is higher near the maximum due to the lower particle content but is not different at 500 and 540°C.

The workability at high temperatures of the composites depends strongly on the presence of the reinforcing particles. The matrix up to about 30% by volume contains subgrains produced by dynamic recovery DRV; however, these are always smaller, less polygonized and more misoriented than in the alloy alone under the same conditions [14-22,26-31,38,39]. In another 30%, there are dense dislocation tangles with limited cellularity, either close to the particles or in shear bands defined by groups of particles. In the remaining regions, there are cellular structures with high misorientation walls (possibly derived from the second regions as a result of DRV or dynamic recrystallization DRX) [13,15-22,26-31]. The microstructure tends to move towards the second type from an increase in particle volume fraction or a decrease in temperature, whereas the partial DRX regions are favored by increase in both these factors. Neither the high density of dislocations nor the DRX structures are found in the matrix alloys during hot working [33,34,40]. Moreover, the DRX regions are quite different from classical DRX [40,41] in that growth of the grains associated with mobile high angle boundaries does not occur so that there is no spread of recrystallization throughout the matrix [27-29].

The workability depends greatly on the matrix since the more highly alloyed (increasing in order 6000, 2000 and 7000 series) are generally stronger due to solute or particles which have various sizes and distributions dependent in previous history [26-28,33-37]. In general higher matrix strength reduces the ductility because of higher stress concentrations which cause particle matrix decohesion much more frequently than particle fracture as at ambient temperature [1,11,13,23-25]. In consequence, the ductility increases as the temperature rises

reaching true fracture strains of ϵ_f about 2 at 400°C, 1 s⁻¹ in torsion, which is indicative of reasonable workability for extrusion or rolling [8-11,16,25]. The ductility also depends on specific features of the matrix for example in A356 (7% Si) alloy or matrix the size and distribution of the 6.5% Si eutectic particles has a deleterious effect unless greatly refined by strontium modification as described previously [25,26]. While composites with alloys A356, 6061 and 2618 increase in ductility as T rises above 400°C [9,10,22,25,26], the ductility of 7075 composites decreases markedly between 400 and 500°C [30-32]. The objective is to examine the failures in 7075/10%Al₂O₃ and 7075/15%Al₂O₃ in order to clarify the causes.

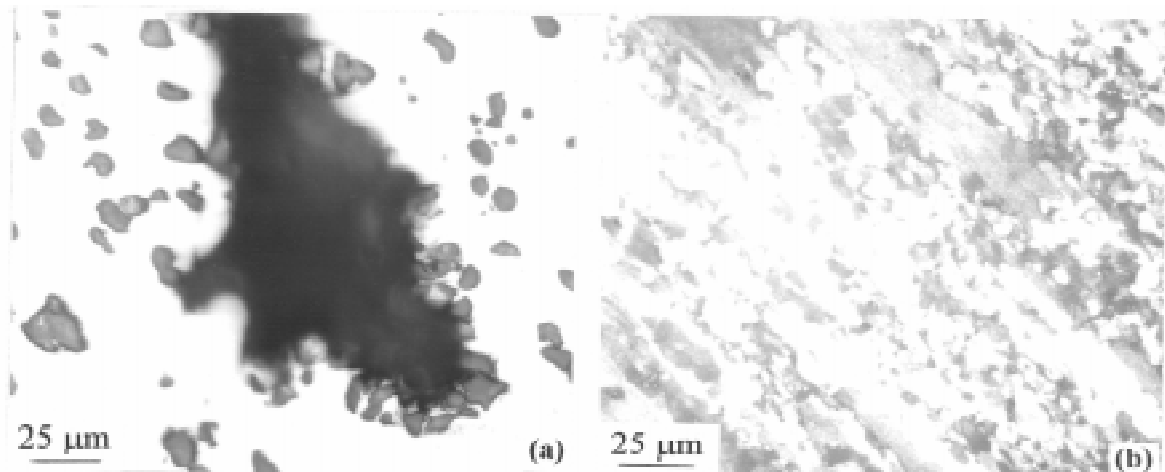


Figure 2. Optical micrographs exhibiting: (a) at 250°C, 1 s⁻¹ (unpolished), cellular particle distribution and large crack possibly at a shrinkage defect; (b) 500°C, 1 s⁻¹ (anodized, polarized light) elongated grains and small crystallites difficult to distinguish from particles.

TECHNIQUES

The torsion tests are conducted at constant temperature T (200-540°C) and surface strain rate $\dot{\epsilon}$ (0.01-4 s⁻¹), to determine the surface stress σ (von Mises uniaxial equivalent) according to techniques and principles explained frequently before [9,10,32,41]. The flow curves strain harden to a peak stress σ_p and then decline rapidly to failure at 200 or 300° but at 400 and 500°C decline very gradually to a fracture strain ϵ_f , which may be the result of deformation heating, microstructural evolution or gradual formation of voids. Constitutive equations of the sinh-Arrhenius type relating σ_{max} to T and $\dot{\epsilon}$ have been derived for use in finite element modeling of extrusion [9,10,32,42]. After fracture, the non-rotating end is extracted by longitudinally displacing the load cell mount to permit rapid quenching in less than 3 s.

The specimens are examined on a tangential flat (normal to radius just below the gage surface) by either optical microscopy (OM) of unetched surfaces or of anodized surfaces with polarization (POM) [28]. The same tangential section was used for SEM examination. For TEM, slices were cut normal to a radius and near the surface; they were thinned by mechanical dimpling and ion milling on a GATAN ion mill [17-20,30].

In torsion, initially equiaxed grains near the specimen surface are elongated and twisted into helicoids (like spiral springs) about the torsion axis to a degree dependent on the total strain [41]. The specimen surface becomes rumpled in association with these spirals and the uniformity of deformation can be assessed by macroscopic examination. The tangential

section exhibits the elongated and thinned grains at an angle to the torsion axis which increases as strain rises; a second phase becomes strung out along the grain boundaries. The tangential flat is usually produced in unison with a chord section in the attached shoulder so it is possible to observe the original structure and the increase in strain across the transition file. In contrast to optical microscopy, SEM permits observation of both the polished section and the adjacent surface at high magnification as a result of the great depth of focus. With an ability to peer into them, shallow surface cracks may be tracked from the curved surface into the flat tangential section where they terminate because they have been polished away. The depth of cracks entering from the surface was clearly confirmed on longitudinal diametral sections.

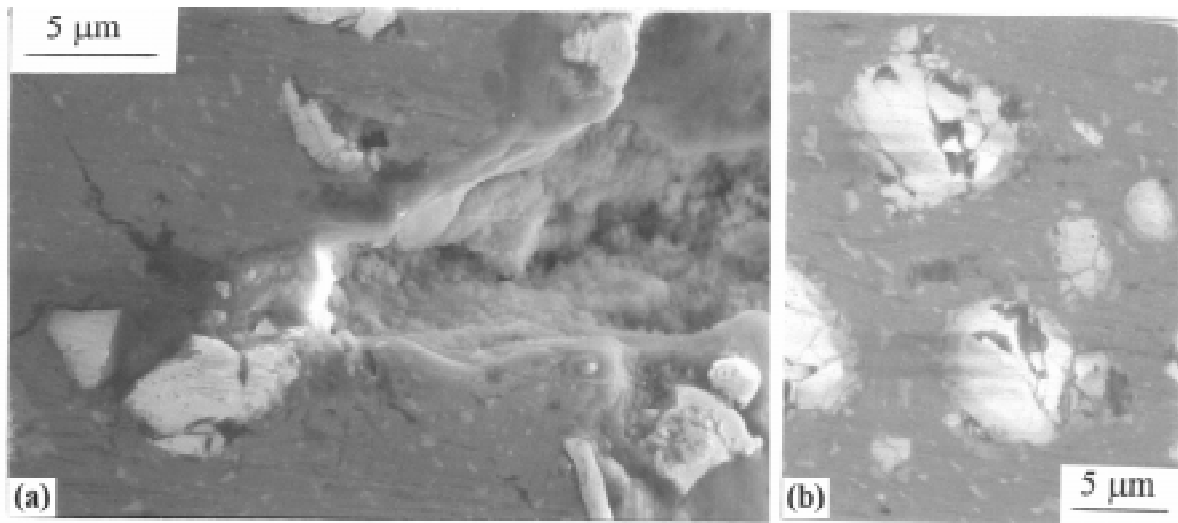


Figure 3. SEM micrographs of tangential section of 7075/10%Al₂O₃ at 300°C, 0.1 s⁻¹: (a) one of the few large cracks away from the rupture zone very close to the surface. Particles are associated with it but there is evidence of the matrix tearing. Note the bifurcation where the crack meets a large particle and the decohesion ahead of it; (b) some cracked Al₂O₃ particles with almost no evidence of decohesion.

RESULTS

Some schematic flow curves with representative flow stresses are shown for 7075/15%Al₂O₃ and 7075/10%Al₂O₃ along with 6061/15%SiC and A356/15% SiC for comparison (Fig. 1) [9,10,21,25,26,32]. The flow stress is clearly reduced by increase in T and decrease in $\dot{\epsilon}$. The 7075 composites are stronger than the others notably at low T and the strength is raised by the higher volume fraction of reinforcements. All the curves exhibit long slightly drooping plateaus at 400°C compared to limited ductility at 300°C. On raising T to 500°C, the plateaus are much curtailed for 7075 composites but extended for 6061 and A356 ones. In Fig. 2, the fracture strains ϵ_f , rise rapidly with rising T near 250-350°C and passes through a maximum at 400°C for 7075 whereas it continues to increase at a slower rate for the other two matrices [9,10,22,25-28,32].

The optical micrographs of unpolished sections exhibit the reinforcing particles in a fairly uniform array, however, they are sometimes in cells and occasionally agglomerated as a result of their exclusion by the fast growing primary dendrites (Fig. 2a) [1,2,6,16-21,31]. In some specimens with high strains, the particles are lined up parallel to the spiral grain boundaries.

In longitudinal sections showing their depth, the cracks run irregularly through the matrix, including many particles as though they had connected voids at interfaces. There are occasions when the cracks are quite wide and in contact with clusters of particles indicative of shrinkage voids from solidification (Fig 2a).

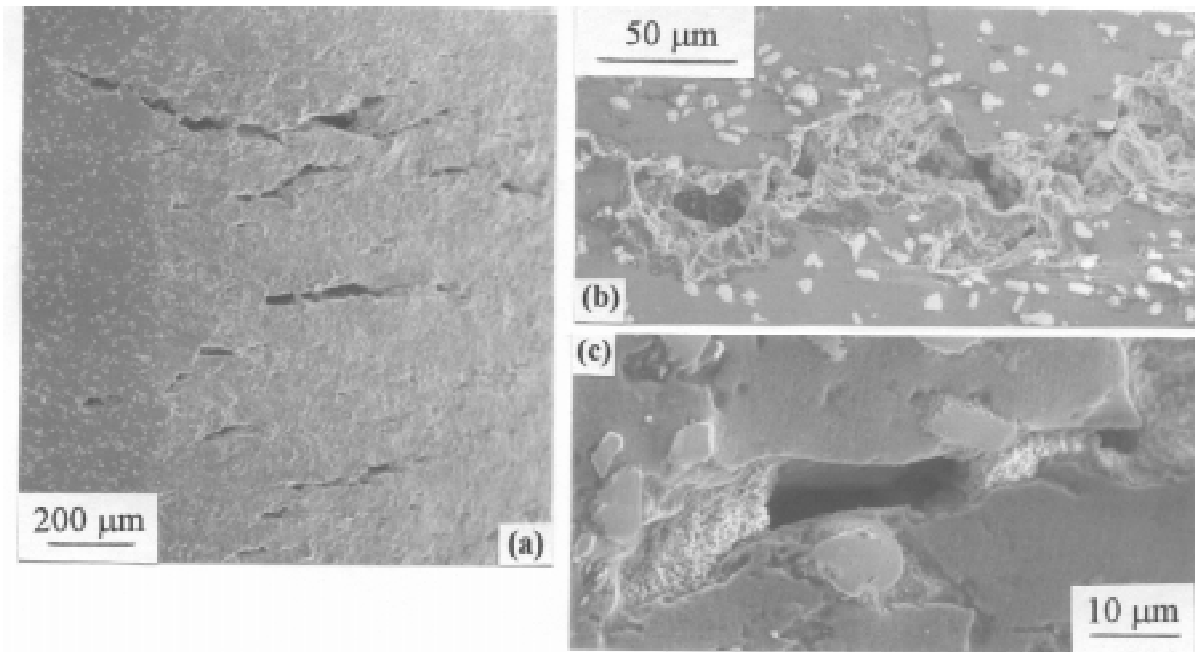


Figure 4. SEM micrographs of tangent section, surface of 7075/10%Al₂O₃ at 400°C, 0.1 s⁻¹: (a) many medium sized surface cracks with some extending into the section; (b) deepest end of the largest crack showing interaction with closely spaced particles; and (c) at higher strain rate 4 s⁻¹, a deep narrow crack associated with several particles, none are broken.

The SEM examination of the 7075/10%Al₂O₃ composite on the tangential section (after repeated polishings to improve the quality) revealed cracking variation with T and $\dot{\epsilon}$. At 300°C 0.1 s⁻¹ ($\epsilon_f = 1.80$) in regions away from the principal one, many short narrow cracks were barely visible. In the areas scanned (Fig. 3), one large crack was noted at the boundary of the polished tangent and the surface; it was comparatively wide and was associated with some particles. Sharper secondary cracks emanated from the tip (near a particle) and one of these ran along a reinforcement interface. Many particles appeared to be cracked, although the pieces had not been separated by plastic strain; however, some particles in the shoulder chord section nearby were also cracked. Secondary cracks and fissures between more closely spaced particles were observed near the principal fracture.

At 400°C 0.1 s⁻¹ ($\epsilon_f = 2.3$, the maximum), many cracks were apparent along the gage surface, all lying roughly parallel to the plane of maximum shear stress; however they did contain sharp kinks and bifurcations associated with particles (Fig. 4). There were a few cracks in the tangential section mostly at the edge where it meets the surface. One such crack which obviously had penetrated downwards from the surface is quite wide in the axial direction and is very irregular possibly indicating a solidification defect. Near the fracture surface there were many auxiliary cracks in which one could see protruding particles as well as tears at many particles. The matrix fracture appears dimpled, that is ductile; this would be consistent with observations of 25°C fractures [23,24]. At 400°C, 4 s⁻¹ ($\epsilon_f = 1.1$), the behaviour was similar to the previous specimen; however the surface cracks were shorter and not so open. The cracking directions seemed to be primarily defined by the deformation geometry and to

touch randomly on particles where were not broken. However 40-50% of the particles were broken at 4 s^{-1} compared to only a few at 0.1 s^{-1} (some broken in the shoulder).

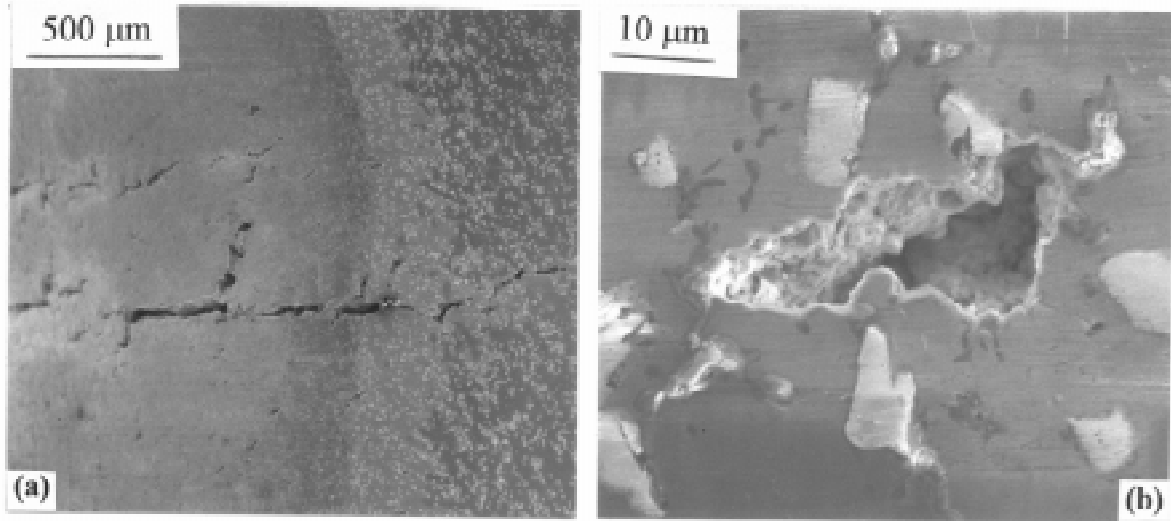


Figure 5. SEM micrographs of 7075/10%Al₂O₃ near tangent-surface intersection for 500°C, 0.1 s⁻¹: (a) several very large deep cracks; (b) away from the cracks mainly in the matrix, particles exhibit neither fracture nor decohesion.

At 500°C, 1 s⁻¹ ($\epsilon_f = 0.4$), there were many fewer cracks than at 400; 0.1 s⁻¹ but they were much larger, more opened up and penetrating more deeply into the tangential section (Fig. 5). While much of the crack was in the matrix, the end was associated with decohesion in a cluster of particles. Very few particles were broken; although some of the larger ones in the shoulder were cracked. In the 7075/15%Al₂O₃ composite under the same conditions ($\epsilon_f = 0.45$), few cracks were observed away from the main crack and the particles were not broken. There appeared to be voids at some particles preferentially at clusters, but most interfaces appeared perfect.

The examination of the tangential sections by POM (Fig. 2b) was partially successful only at the highest temperature because at lower T the cells were not well developed [31]. Moreover, the particles gave varying contrast due to their optical characteristics in contrast to their uniform dark appearance against the bright unetched matrix. In the specimens at 500°C (0.1 or 1 s⁻¹), some elongated grains showed uniform contrast due to the subgrains being at a similar angle to the extinction condition (Fig. 2b). Other grains close to polarizing extinction exhibited cells with a range of contrasts; however, the misorientations cannot be determined by this method. There appeared to be equiaxed recrystallized grains separating the long grains but more careful analysis revealed that most of these were particles [31]. In a specimen at 400°C, 0.1 s⁻¹, the TEM examinations revealed substructures of variable density, degree of polygonization and misorientation: subgrains away from Al₂O₃ particles and either fine cells or DRX grains near to them. (Fig. 6) [30]. In addition the precipitates occurring at different temperatures were identified and their association with subboundaries or grain boundaries noted (Fig. 7).

DISCUSSION

The ductility of the 7075 composites up to 400°C varies with T and $\dot{\epsilon}$ in a similar way to that of other AMC which were all much less than their respective matrices [9,10,25-28]; this indicates that the fracture is controlled by the matrix particle interactions. The drop in

ductility of 7075 composites in similarity to the matrix alloy and dissimilarity to other AMC indicates that this is likely a matrix feature. The matrix character has been shown to significantly affect ϵ_f in the case of A356 where fine Si eutectic particles in the composite give rise to a ductility equaling that of unmodified A356 alloy in which the Si particles look like $12\ \mu\text{m}$ long needles but are actually interconnected flakes [25,26]. The decrease in ductility of 7075 with such rise in T is well known and has been associated to large precipitates, when one might expect them to be dissolving [35-37].

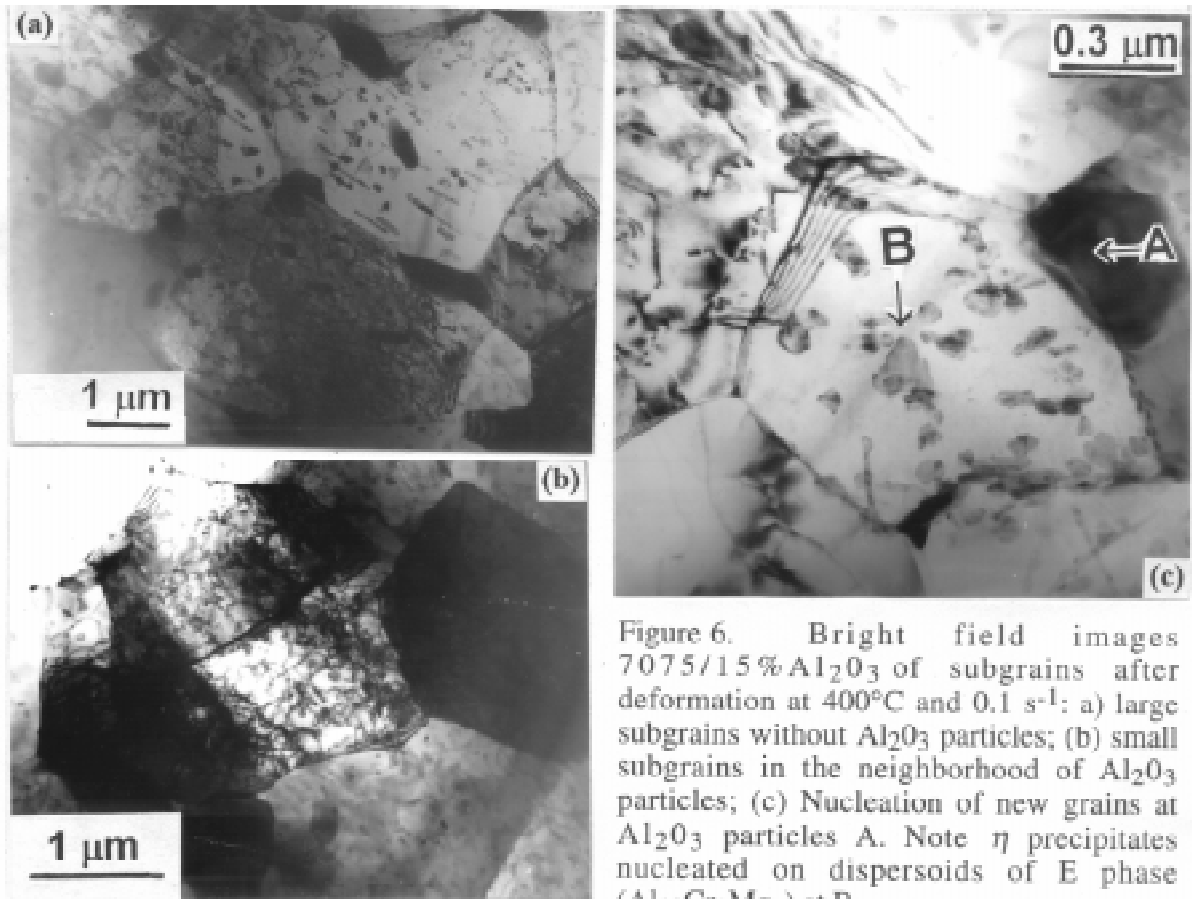


Figure 6. Bright field images 7075/15% Al_2O_3 of subgrains after deformation at 400°C and $0.1\ \text{s}^{-1}$: (a) large subgrains without Al_2O_3 particles; (b) small subgrains in the neighborhood of Al_2O_3 particles; (c) Nucleation of new grains at Al_2O_3 particles A. Note η precipitates nucleated on dispersoids of E phase ($\text{Al}_{18}\text{Cr}_2\text{Mg}_3$) at B.

The POM and TEM observations (Figs. 2b,6) provide evidence of substructures which are equivalent to those in other AMC [6,11,12,14,16-23]. The occurrence of subgrains agrees with other observations of 7075/ Al_2O_3 composites [38]. The increase in scale and cellularity of the substructure as T rises is consistent with the decline in flow stress which has been greater in 7075 composites than those of other matrices thus resulting in more closely similar high T values. The decrease in ductility is thus not due to especially high dislocation densities and associated stress concentrations.

The SEM observations show an alteration in the cracking behavior. At 300°C (Fig. 3), where the stress is high there is evidence of cracked particles, decohesion and a few random cracks because ϵ_f is rather low due to rapid fracture at the principal crack which appears related to linking up of voids at particle matrix interfaces. At 400°C (Fig. 4), the flow stress is decreased so there is reduced particle damage but there are many more minor cracks which have had opportunity to develop because of the much greater fracture strain. At 500° , (Fig. 5) there are no broken particles, much less decohesion and almost no minor cracks because of the low fracture strain indicative of matrix microstructural instabilities which enhance crack

propagation. Foils from different deformation temperatures show alteration of particle morphologies in TEM examination [37]. At 500°C, large precipitates are found mainly in grain boundaries (Fig. 7); diffraction shows that these are a phase which is absent at lower T because other metastable particles had formed with much smaller size and more uniform distribution.

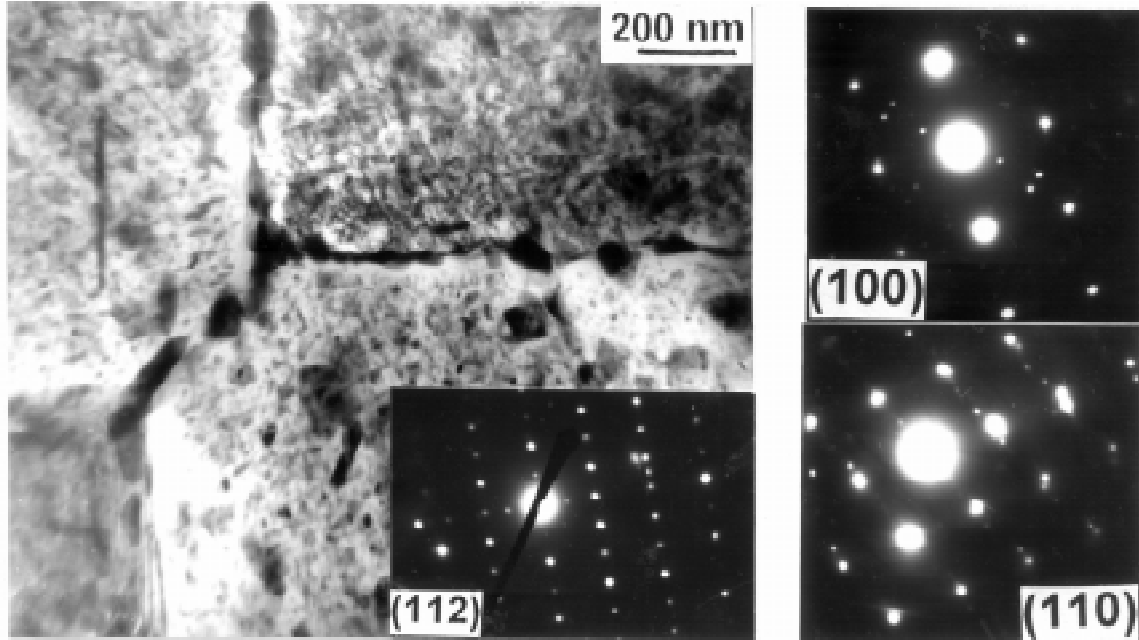


Figure 7. Nonuniform precipitation of T phase inside of subgrains in grain boundaries and at triple junctions after deformation at 500°C and 1 s^{-1} . SAD patterns taken from individual T phase particles, $(\text{AlZn})_{49}\text{Mg}_{32}$ in (100), (112) and (110) matrix orientations.

The low ductilities of the 7075 composites above 450°C (Fig. 1), are thus seen to be a peculiarity of the matrix alloy in developing new stable precipitates mainly at grain boundaries [37]. The ductility could be improved by delaying the formation of this phase until the forming process is completed. Starting with material in the solution treated condition has the disadvantage that the high solute level and dynamic precipitation of fine particles at initiation of straining may cause very high stress peaks which would require extreme break-out pressures in extrusion [5,34,43,44]. The alternative is to lock the alloying elements in fairly large particles stabilized at a lower temperature so that it would require a prolonged time to redissolve them at the high temperature. This procedure would also lead to lower extrusion pressures. The presence of the deleterious T phase particles leads to poor surface quality in 7000 series extrusions thus conferring on these alloys reputation for very poor extrudability.

CONCLUSIONS

For the 7075 composites with 10 or 20% Al_2O_3 the flow stress declines from 200 to 540°C and the level of DRV with formation of subgrains rises in a manner similar to composites of 6061 and A356 alloys. The 7075 composite ductility rises like the others up to 400°C but in contrast decreases severely at 500 and 540°C in similarity to the bulk alloy behavior. Up to 400°C, cracks initiate at matrix-particle interfaces and propagate by linking up through the

matrix. At 500°C there is limited void formation but matrix failure at a low strain. The cause appears to be invigorated precipitation of a T phase as large particles on the grain boundaries

REFERENCES

1. D.J. Lloyd, "Composite Science and Technology", 35, (1989), 159-1791.
2. D.J. Lloyd, "Advanced Structural Materials", D.S. Wilkenson, ed., (Pergamon Press, Oxford 1989), pp. 1-21.
3. A.R. Kjar, J.L. Miihelich, T. Srithavan and C.J. Heathcock, "Light Weight Alloys for Aerospace Applications", E.W. Lee et al. eds., (TMS-AIME, Warrendale PA 1989), pp. 273-288.
4. H.J. McQueen and P. Sakaris, "Composite Structures and Materials", S. Hoa and R. Gauvin, eds., (Elsevier Applied Science, London, 1992), pp. 297-306.
5. H.J. McQueen and O. Celliers, "Can Metal. Quart", 34, 1995, 265-273.
6. H.J. McQueen and X. Xia, (Joint Canada-Japan Workshop on Composites, Kyoto, August 1996). J. Sci. Eng. Comp. Mat. 1997 (in press).
7. R.J. Arsenault, L. Wang and C.R. Feng, Acta Metal. 39, (1991), 47-57.
8. R.J. Arsenault, "Strength of Metals and Alloys", (ICSMA9, Tel-Aviv), D.G. Brandon et al., eds., Freund Pub. Co. Ltd., London, U.K., 1990, vol. 2, pp. 31-46.
9. P. Sakaris and H.J. McQueen, "Aluminum Alloys: Their Physical and Mechanical Properties - Proceedings ICAA3", L. Arnberg, E. Nes, O. Lohne, N. Ryum, eds., (NTH-Sinteff, Trondheim, Norway, 1992), Vol. 1, pp. 554-559.
10. P. Sakaris and H.J. McQueen, "Advances in Production and Fabrication of Light Metals", (Edmonton), M.M. Avedesian et al., eds., CIM Montreal, 1992, pp. 605-617.
11. J.R. Pickens, T.J. Langan, R.O. England and M. Liebson, "Metal. Trans.", 18A, (1987), 303-312.
12. C. Demetry, J.T. Beale and F.R. Tuler, "Advanced Structural Materials", D.S. Wilkenson, ed., Pergamon Press, Oxford, 1989, pp. 33-39.
13. K.N. Subramanian, T.R. Bieler and J.P. Lucas, "Key Engineering Materials", G.M. Newa Z et al., eds, Trans. Tech. Pub. Ltd., 1995, 104-107, part 1, pp. 175-213.
14. F.J. Humphreys, W.S. Miller and M.R. Djazeb, "Met. Sci. Tech.", 6, 1990, 1157-1166.
15. T.R. Bieler, "Hot Workability of Steels and Light Alloys-Composites", H.J. McQueen, E.V. Konopleva and N.D. Rayan (eds.), Met. Soc. CIM, Montreal, 1996, pp. 124-154.
16. X. Xia, P. Sakaris and H.J. McQueen, "Proc. Ninth Intl. Conf. on Composite Materials", (ICCM/9, Madrid), 1993, pp. 157-162.

17. X. Xia, H.J. McQueen and P. Sakaris, "Developments and Applications of New Ceramics and Metal Alloys", R.A.L. Drew and H. Mostaghad, eds., Met. Soc. CIM, Montreal, 1993, pp. 135-142.
18. X. Xia and H.J. McQueen, "Microstructural Science, (Intl. Met. Soc. Conf., Montreal", 1994, 22, (1995), 297-314.
19. X. Xia, P. Sakaris and H.J. McQueen, "Recent Developments in Light Metals", Met. Soc. CIMM, Montreal, 1994, pp. 123-134.
20. X. Xia, P. Sakaris and H.J. McQueen, "*Mat. Sci. Tech.*", 10 (1994), pp. 487-494.
21. X. Xia, H.J. McQueen and P. Sakaris, "*Scripta. Metal. Mat.*", 32, (1995), 1185-1190.
22. X. Xia, J. Zhao and H.J. McQueen, (Joint Canada-Japan Workshop on Composites, Kyoto, August 1996). *J. Sci. Eng. Comp. Mat.* 1997 (in press).
23. X. Xia and H.J. McQueen, "Proc. Tenth International Conf. on Composite Materials", ICCM-10, (Whistler, B.C.) A. Poursartip and D. Street, eds., Woodhead Pub., Abington, UK, Vol. II, 1995. pp. 233-240.
24. X. Xia and H.J. McQueen, "Failure Analysis and Prevention (ICFAP '95, Beijing)", C.Q. Chen and M.D. Chaturvedi, eds. Intl Academic Pub., Beijing, 1995, pp. 242-247.
25. H.J. McQueen, P. Sakaris and J. Bowles, "Advance Composites 93", (Australia), T. Chandra, A.K. Dhingra, eds., (TMS-AIME, Warrendale, PA, 1993), pp. 1193-1198.
26. H.J. McQueen, E.V. Konopleva and M. Myshlyaev, "Strength of Materials (ICSMA/10, Sendai)", H. Oikawa et al., eds., (Japan Inst. Metals, 1994) pp. 773-776.
27. H.J. McQueen, X. Xia, E.V. Konopleva, "Al Alloys, Physical and Mechanical Properties" (ICAA4), T. Sanders and E.A. Starke, Georgia Inst. Tech. Atlanta, 1994, vol.2, pp. 645-652.
28. H.J. McQueen, E.V. Konopleva, M. Myshlyaev and Q. Qin, "Proc. Tenth International Conf. on Composite Materials, ICCM-10", (Whistler, B.C.) A. Poursartip and D. Street, eds., Woodhead Pub., Abington, UK, Vol. II, 1995. pp. 519-530.
29. H.J. McQueen and X. Xia, "Recrystallization 96 and Related Topics" (Proc. 3rd Intl. Conf., Monterey, Oct. '96). T.R. McNelley, (ed.), TMS-AIME, Warrendale, PA (in press).
30. G. Avramovic Cingara, H.J. McQueen and Q. Qin, "Hot Workability of Steels and Light Alloys-Composites", H.J. McQueen, E.V. Konopleva and N.D. Ryan (eds.), Met. Soc. CIM, Montreal, 1996, pp. 143-150.
31. E.V. Konopleva, H.J. McQueen, J. Zhao, Q. Qin and J. Sarruf, "Recent Metallurgical Advances in Light Metals Industries", S. MacEwen and J.P. Gilardeau, eds., Met. Soc. CIM, Montreal, 1995, pp. 519-530.

32. Q. Qin, H.J. McQueen, and J.J. Jonas, "Recent Developments in Light Metals", Met. Soc. CIMM, Montreal, 1994, pp. 213-222.
33. H.J. McQueen, "Hot Deformation of Aluminum Alloys", T.G. Langdon and H.D. Merchant, eds., TMS-AIME, Warrendale, PA, 1991, pp. 31-54.
34. H.J. McQueen, *ibid* [30], pp. 105-120.
35. E. Evangelista, E. DiRusso, H.J. McQueen, "Homogenization and Annealing of Al and Cu Alloys", H.D. Merchant et al. eds, TMS-Aime, Warrendale, PA, 1988, pp. 91-104.
36. H.J. McQueen, E. Evangelista, A. Forcellese, "Modeling the Deformation of Crystalline Solids", T. Lowe and T. Rollett eds., TMS-AIME Warrendale PA, 1991, pp. 31-54.
37. E. Cerri, E. Evangelista, A. Forcellese, H.J. McQueen, "*Mat. Sci. Eng.*", 1995, A197, pp. 181-198.
38. D. Yu and T. Chandra, "Advanced Composites '93", (Wollongong), T. Chandra et al., eds, TMS-Aime, Warrendale, PA., 1993, pp. 1073-1077.
39. A. Razaghian, D. Yu and T. Chandra, *ibid* [37], pp. 1067-1071.
40. H.J. McQueen, E. Evangelista, and M.E. Kassner, *Z. Metallkunde*, 82, 1991, 336-345.
41. E. Evangelista, N.D. Ryan and H.J. McQueen, "*Metal. Sci. Tech.*", 9, 1991, 75-92.
42. H.J. McQueen, E. Evangelista and N.D. Ryan, "Recrystallization '90, (Intl. Conf. Recrystallization in Metallic Materials)", T. Chandra, ed., TMS-AIME, Warrendale, PA., 1990, pp. 89-100.
43. H.J. McQueen and O.C. Celliers, *Can. Metal. Quart.* 1997 (in press).
44. H.J. McQueen, J. Charlton and E. Herba, *Materials World 1997* presented at European Conf. Composite Materials 7, London, May 1996.

RELATIONS OF THE MESOSCOPIC DAMAGE MECHANISMS WITH THE MACROSCOPIC PROPERTIES OF METAL MATRIX COMPOSITES

Chen Haoran¹ and Su Xiaofeng²

^{1,2} *State Key Laboratory of Structural Analysis of Industrial Equipments, Dalian University of Technology, Dalian, 116023, P. R. China.*

SUMMARY: Generalized self-consistent finite element iterative averaging method is united with the Gurson model for the parametric investigation of the damage mechanisms and their relations with the macroscopic tensile properties of the SiC reinforced Al₅₄₅₆. The mesoscopic damage mechanisms studied here contain two types: interphase debonding between the reinforcement and matrix and the nucleation, growth, and coalescence of the voids in the matrix. The interphase debonding could promote the nucleation and growth of the voids in matrix, which increases the ductility of the metal matrix composite, while the strengthening effects of the brittle reinforcements decrease unfavorably.

KEYWORDS: mesoscopic damage mechanisms, macroscopic properties, interphase debonding, void nucleation and growth, strengthening, ductility, parametric investigation, generalized self-consistent finite element iterative averaging method

INTRODUCTION

The damage and failure mechanisms of the metal matrix composites contain three types, namely, reinforcement fracture[1, 2], matrix-reinforcement interfacial debonding[3, 4], and ductile failure in matrix by the nucleation, growth, and coalescence of the voids from the cracking of the intermetallic inclusions and dispersoids in the matrix[5, 6]. The damage and failure mechanisms are often investigated by experimental methods, starting from metallographic observations of the strained composites. However, the numerical study by the mesomechanics of the effects of damage mechanisms on the macroscopic deformation and ductility of metal matrix composites which could not quantitatively investigated by experiments alone is also needed[7-9].

The authors, in the previous works[10, 11], developed a generalized self-consistent finite element iterative averaging method to study the strengthening mechanisms and macroscopic elastoplastic properties of metal-matrix composites, which was proved to be an effective method. In this paper, the method is united with the Gurson model for the parametric investigation of the damage mechanisms mentioned above and their relations with the macroscopic tensile properties of the SiC reinforced Al₅₄₅₆, as part of attempts for the derivation of the whole picture of damage mechanisms of metal matrix composites.

FUNDAMENTAL THEORIES OF THE CONSTITUENT DAMAGE AND THE MACROSCOPIC TENSILE PROPERTIES OF METAL MATRIX COMPOSITES

Nucleation, Growth, and Coalescence of the Voids in Ductile Metal—the Damage and Failure of the Matrix

The yield condition for porous plastic solids in terms of a internal variable f , the void volume fraction, proposed by Gurson[12], and developed by Tvergaard[13] is of the form

$$\phi(\sigma_e, \sigma_m, \bar{\sigma}, f) = (\sigma_e/\bar{\sigma})^2 + 2fq_1 \cosh(q_2\sigma_m/2\bar{\sigma}) - 1 - q_3f^2 = 0 \quad (1)$$

where σ_e and σ_m are, respectively, macroscopic Von-Mises effective stress and hydrostatic stress acting on the voided material, while $\bar{\sigma}$ is the tensile flow strength of the matrix material. The parameters q_1 , q_2 and q_3 introduced by Tvergaard[13] are

$$q_1 = 1.5, \quad q_2 = 1, \quad q_3 = q_1^2 = 2.25 \quad (2)$$

In general, the evolution of the void volume fraction arises from the growth of existing voids and the nucleation of new voids

$$\dot{f} = (\dot{f})_{growth} + (\dot{f})_{nucleation} \quad (3)$$

Since the matrix material is plastically incompressible

$$(\dot{f})_{growth} = (1-f)G^{ij}\dot{\eta}_{ij}^p \quad (4)$$

Where $\dot{\eta}_{ij}^p$ is the plastic strain rates of the porous plastic solid, and G^{ij} is the inverse of metric tensor G_{ij} . Following Gurson[12], the rate of void nucleation controlled by plastic strain could be expressed by

$$(\dot{f})_{nucleation} = A\dot{\bar{\sigma}} \quad (5)$$

As suggested by Chu and Needleman[14], parameter A is chosen so that void nucleation follows a normal distribution. Thus, with a volume fraction of void nucleating inclusions f_N , a mean strain for nucleation ϵ_N and a standard deviation s_N

$$A = \left(\frac{1}{E_t} - \frac{1}{E} \right) \frac{f_N}{s_N \sqrt{2\pi}} \exp \left[-\frac{1}{2} \left(\frac{\epsilon^p - \epsilon_N}{s_N} \right)^2 \right] \quad (6)$$

Here, E is Young's modulus, while E_t is the current tangent modulus.

Considering the coalescence effects of two neighbouring voids when the void volume fraction exceeds a critical value f_c , Tvergaard and Needleman[15] proposed

$$f^* = \begin{cases} f & f \leq f_c \\ f_c + \frac{f_u^* - f_c}{f_F - f_c} (f - f_c) & f > f_c \end{cases} \quad (7)$$

where $f_c=0.15$, and $f_F=0.25$. f_u^* given by $1/q_1$ is the ultimate value at which the macroscopic stress carrying capacity vanishes.

The plastic strain rates of the porous plastic solid taken in a direction normal to the flow potential satisfy

$$\dot{\eta}_{ij}^p = \lambda \frac{\partial \phi}{\partial \sigma^{ij}} \quad (8)$$

By setting the plastic work rates equal to the matrix dissipation

$$(1-f)\bar{\sigma}\dot{\epsilon}^p = \sigma^{ij}\dot{\eta}_{ij}^p \quad (9)$$

the scalar multiplier, λ , in terms of the Jaumann derivative of Cauchy stress, $\hat{\sigma}^{ij}$, is determined to be

$$\lambda = \frac{1}{h} p_{ij}\hat{\sigma}^{ij} \quad (10)$$

where

$$h = - \left[(1-f) \frac{\partial \phi}{\partial f} G^{ij} \frac{\partial \phi}{\partial \sigma^{ij}} + \frac{E_t E}{(E - E_t)(1-f)\bar{\sigma}} \left(A \frac{\partial \phi}{\partial f} + \frac{\partial \phi}{\partial \bar{\sigma}} \right) \sigma^{ij} \frac{\partial \phi}{\partial \sigma^{ij}} \right] \quad (11)$$

and

$$p_{ij} = \frac{\partial \phi}{\partial \sigma^{ij}} \quad (12)$$

Then, the relation between the Jaumann derivative of Cauchy stress and the Lagrangian strain increment is given in the form

$$\hat{\sigma}^{ij} = C^{ijkl} \dot{\eta}_{kl} \quad (13)$$

where

$$C^{ijkl} = L_e^{ijkl} - \frac{L_e^{ijmn} p_{mn} p_{rs} L_e^{rskl}}{h + p_{rs} L_e^{rsmn} p_{mn}} \quad (14)$$

with the elastic moduli represented by L_e^{ijkl} . In the numerical computation of finite element scheme, Eqn (13) is generally transformed into the incremental constitutive relation in terms of convected rate of Kirchhoff stress and Lagrangian strain rate [16], which is omitted here.

Fracture of Brittle Solids—the Damage and Failure of Interphase

The crack criterion for the brittle solid takes the form of maximum principal stress criterion. If σ_1 , σ_2 and σ_3 are used to represent the three principal stress, crack happens when

$$\text{Max}(\sigma_1, \sigma_2, \sigma_3) \geq \sigma_0 \quad (15)$$

Here, σ_0 is the tensile strength of brittle solid.

Tensile Properties of Metal Matrix Composites Based on the Constituent Damage Initiation and Propagation

The generalized self-consistent finite element iterative averaging method is used in this paper to investigate the tensile properties and damage mechanisms of metal matrix composites. The detailed description of GSCFEIAM is given in [11] and will not be repeated here. The composite tensile properties with constituent damages are of the form

$$\begin{aligned} 1/E_c^{ep} = & 1/\bar{E}_m^{ep} + V_f(1/E_f - 1/\bar{E}_m^{ep})\bar{a}_f \\ & + (V_i - V_{di})(1/E_i - 1/\bar{E}_m^{ep})\bar{a}_i + V_{di}(1/E_d - 1/\bar{E}_m^{ep})\bar{a}_d \end{aligned} \quad (16)$$

Here, E_c^{ep} is the composite incremental tensile modulus, while \bar{E}_m^{ep} represents incremental tensile modulus of the porous matrix. E_f and E_i are Young's moduli of reinforcements and interphase, respectively. For the numerical stability in computation, the cracked parts in the interphase are regarded as a new phase with rather weak modulus E_d which is 1/10000 of E_f . V_f and V_i are, respectively, the volume fractions of reinforcements and initial interphase when no damage occurs, while V_{di} represent the volume fraction of the cracked parts in interphase evolving with the external loading. The average stress concentration factors for reinforcements and residual interphase are \bar{a}_f and \bar{a}_i , respectively, and \bar{a}_d is the average stress concentration factor of cracked parts. The incremental tensile modulus of the matrix \bar{E}_m^{ep} could be written as

$$\bar{E}_m^{ep} = \frac{1}{\frac{1}{E_m} + \frac{d\bar{\epsilon}_m^p}{d\bar{\sigma}_m}} \quad (17)$$

where E_m is the Young's modulus of the matrix; while $d\bar{\sigma}_m$ and $d\bar{\epsilon}_m^p$ are, respectively; the average incremental Von-Mises effective stress and plastic strain of the matrix.

NUMERICAL RESULTS

The tensile properties and mesoscopic distributions of constituent damages for SiC-Al₅₄₅₆ with interphase strength equal to 500MPa, in various loading stages, are studied within a plane strain framework. The aspect ratio and volume fraction of reinforcement are 4 and 20%, respectively. The interphase thickness adopted here is 1% of reinforcement radius. The constituent properties are: Aluminium matrix(5456): $E = 73$ GPa, $\nu = 0.33$, $\sigma_{pl} = 241$ MPa (proportional limit), $\sigma_{0.2} = 259$ MPa (0.2% offset yield), and $n = 0.01$ (work hardening exponent); SiC_w: $E = 485$ GPa, $\nu = 0.2$; Interphase: $E = 300$ GPa, $\nu = 0.25$. The void in matrix will nucleate according to the plastic strain nucleation criterion with $f_N = 0.05$, $s_N = 0.01$ and $\varepsilon_N = 0.05$.

Stress Strain Curve of the Composite with Interphase Strength Equal to 500MPa

The composite stress-strain curve for the composite with interphase strength equal to 500MPa is shown in Fig. 1 with the curve of the circumstance without any damages in the composite as a reference. It is can be seen that the moduli of two curves are the same, because in the elastic deformation stages there is no damages in composites. While in the elastoplastic deformation stages, the composite initial work hardening rate of interphase strength 500MPa begins to decrease sharply, and the succeeding work hardening rate of this composite decreases continuously to the end of the loading stages.

The Propagation of Mesoscopic Damages of the Composite

The contours of the situations of interphase debonding and void distribution in matrix for the composite with interphase strength equal to 500MPa are shown in Fig. 2, when the external load is in the stage of 350MPa, 500MPa and 650MPa, respectively. The zones encircled by black lines represent the interphase debonding. From these contours, because of the weak interphase strength and stress concentration, the interphase debonding and voids in matrix initiate during the early loading stage, especially around the corner of reinforcement. In the mid-term loading stage, the interphase debonds completely ahead of the end of reinforcement and over half of the side wall of reinforcement. The nucleation and growth of voids develop progressively, spreading fast from the corner of reinforcement to the whole matrix. While in the latter loading stage, except the region around the corner of reinforcement a little higher and the region ahead of the reinforcement end a little lower, the distribution of void volume fractions in matrix is roughly homogeneous.

DISCUSSIONS

The interphase debonding is a rapid process, which results in the sharp decrease of the composite macroscopic work hardening rate. The interphase debonding in the region of reinforcement end will decrease the void nucleation and growth in the matrix ahead of the end of reinforcement because of the stress relaxation, while the interphase debonding in the region of reinforcement side wall will promote the void nucleation and growth in the matrix between the side wall of reinforcements, because the shear lag transfer of load will be hindered by the interphase debonding, which causes more load carried by the matrix in this region, and interphase debonding speed is nearly identical to that of the propagation of void nucleation. The void propagation and distribution in the matrix tend to be homogeneous, which are stable

well before final failure [6]. The damage is carried by the whole metal matrix. Thus, excellent composite ductility could be derived. However, the strengthening effect for the composite degrades unfavorably.

Several authors have argued that characterization of the stress-strain response for metal matrix composites in terms of 0.2% offset yield $\sigma_{0.2}$ is incomplete [11, 17, 18]. As the results show in this paper, to characterize the composite stress-strain curves in terms of $\sigma_{0.2}$, we will run risk of losing the insight of both the initial work hardening rate and succeeding ones. The characterization of composite stress-strain response should contain several parameters, for example, proportional limit, initial work hardening rate and succeeding work hardening rates which should be taken further examinations.

CONCLUSIONS

1. The situation of the interphase debonding dominates the propagation and distribution of void nucleation and growth in matrix.
2. The interphase debonding increases the composite ductility, while results in the strengthening effects of the brittle reinforcements decreasing unfavorably.
3. Characterizing the composite stress-strain curves in terms of $\sigma_{0.2}$, we will run risk of losing the insight of both the initial work hardening rate and succeeding ones.

ACKNOWLEDGMENTS

The work was supported by the Key Project of National Natural Science Foundation of China

REFERENCES

1. Lloyed, D.J., "Aspects of fracture in particulate reinforced metal matrix composites", *Acta Metall. Mater.*, Vol. 39, 1991, pp. 59-71.
2. Llorca, J., Martin, A., Ruiz, J. and Elices, M., "Particulate fracture during deformation of a spray formed metal-matrix composite", *Metall. Trans.*, Vol. 24A, 1993, pp. 1575-1588.
3. Nutt, S.R. and Duva, J.M., "A failure mechanism in Al-SiC composites", *Scripta Metall.*, Vol. 20, 1986 pp. 1055-1058.
4. Mummery, P.M., Derby, B. and Scruby, C.B., "Acoustic emission from particulate reinforced metal matrix composites", *Acta Metall. Mater.*, Vol. 41, 1993, pp. 1431-1445.
5. Kamat, S.V., Hirth, J.P. and Mehrabian, R., "Mechanical properties of particulate-reinforced Aluminum-matrix composites", *Acta Metall.*, Vol. 37, 1989, pp. 2395-2402.

6. Whitehouse, A.F. and Clyne, T.W., "Cavity formation during tensile straining of particulate and short fibre metal matrix composites", *Acta Metall. Mater.*, Vol. 41, 1993, pp. 1701-1711.
7. Tvergaard, V., "Model studies of fibre breakage and debonding in a metal reinforced by short fibres", *J. Mech. Phys. Solids*, Vol. 41, 1993, pp. 1309-1326.
8. Llorca, J., Needleman, A. and Suresh, S., "An analysis of the effects of matrix void growth on deformation and ductility in metal-ceramic composites", *Acta Metall. Mater.*, Vol. 39, 1991, pp. 2317-2335.
9. Nutt, S.R., "Void nucleation at fibre ends in Al-SiC composites", *Scripta Metall.*, Vol. 21, 1987, pp. 705-710.
10. Chen, H.R., Su, X.F. and Williams, F.W., "The effect of imperfect interphase on overall average mechanical properties and local stress fields of multi-phase composite materials", *Composites*, Vol. 26, 1995, pp. 347-353.
11. Chen, H.R., Su, X.F. and Zheng, C.L., "Elastoplastic Behaviour of short fiber reinforced metal matrix composites", *Proceedings Tenth International Conference on Composite Materials*, Whistler, British Columbia, Canada, August 14-18, 1995, Vol. II: Metal Matrix Composites, Poursartip, A. and Street, K.N., Eds, pp1184-1190,
12. Gurson, A.L., "Continuum theory of ductile rupture by void nucleation and growth: part I-yield criteria and flow rules for porous ductile media", *J. Engng. Mater. Tech.*, Vol. 99, 1977, pp. 2-15.
13. Tvergaard, T., "Influence of voids on shear band instabilities under plane strain conditions", *Int. J. Fract.*, Vol. 17, 1981, pp. 389-407.
14. Chu, C.C. and Needleman, A., "Void nucleation effects in biaxially stretched sheets", *J. Engng. Mater. Tech.*, Vol. 102, 1980, pp. 249-256.
15. Tvergaard, T. and Needleman, A., "Analysis of the cup-cone fracture in a round tensile bar", *Acta Metall. Mater.*, Vol. 32, 1984, pp. 157-169.
16. Saje, M., Pan, J. and Needleman, A., "Void nucleation effects on shear localization in porous plastic solids", *Int. J. Fract.*, Vol. 19, 1982, pp. 163-182.
17. Christman, T., Needleman, A. and Suresh, S., "An experimental and numerical study of deformation in metal-ceramic composites", *Acta Metall.*, Vol. 37, 1989, pp. 3029-3050.
18. Levy, A. and Papazian, J.M., "Tensile properties of short fiber-reinforced SiC/Al composites: Part II. finite-element analysis", *Metall. Trans.*, Vol. 21A, 1990, pp. 411-420.

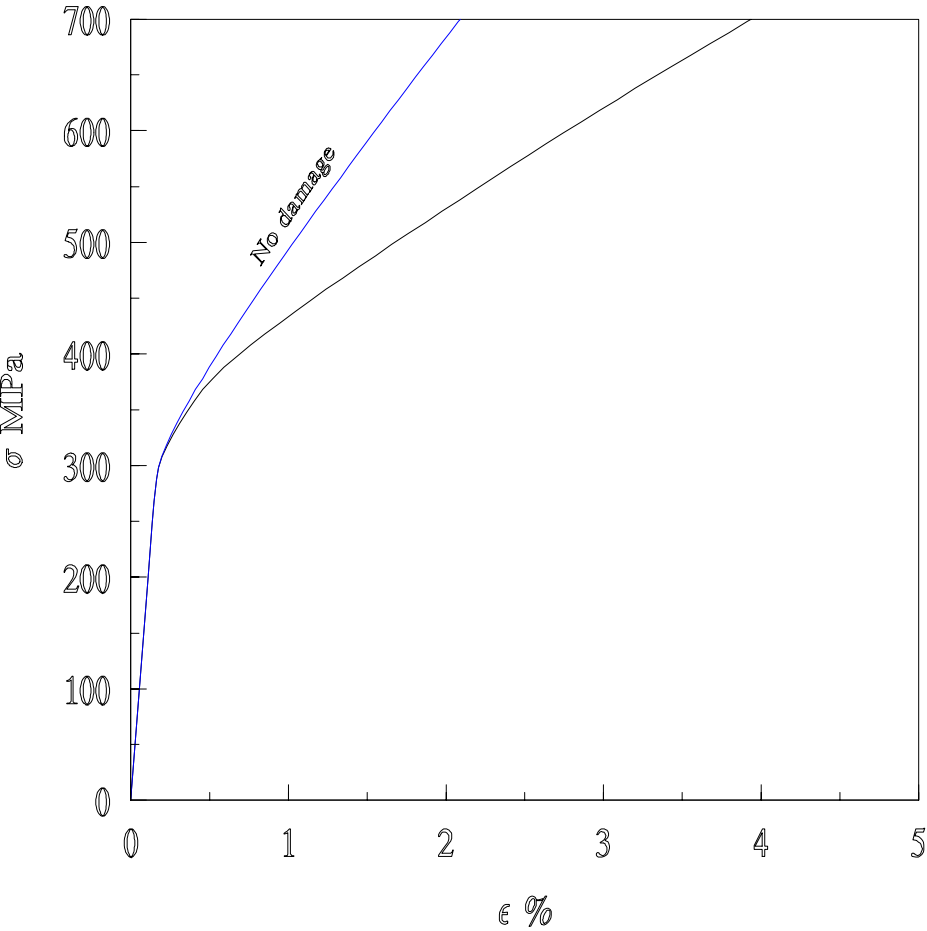
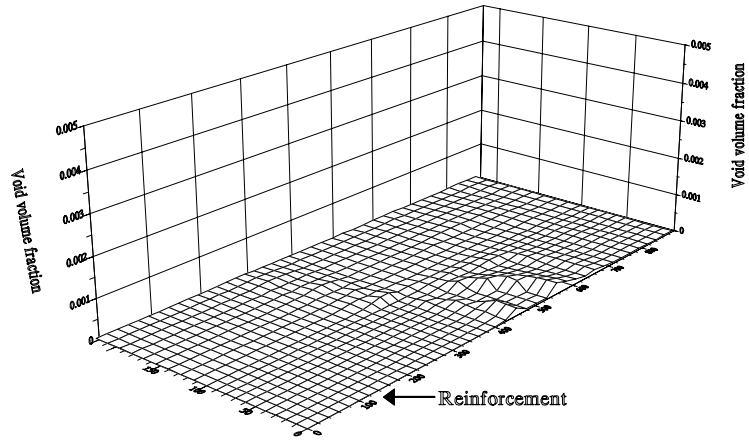
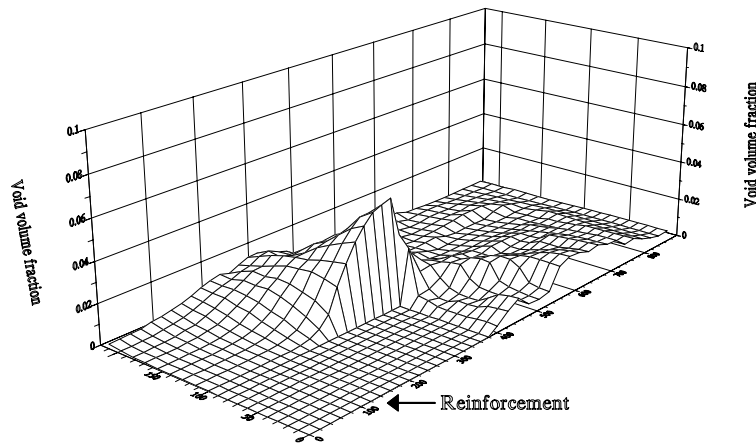


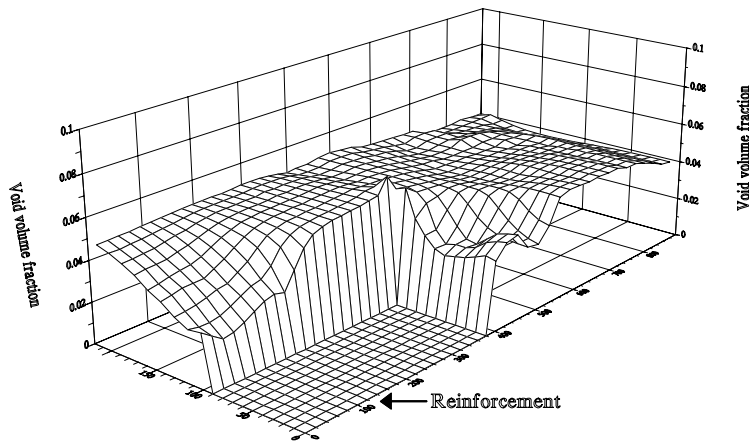
Fig. 1: The composite stress-strain curve of interphase strength, 500MPa. The circumstance without any damage in the composite is also shown as a reference.



2. (a) External load, 350MPa



2. (b) External load, 500Mpa



2. (c) External load, 650mpa

Fig. 2: Contours of interphase debonding and void distribution in the matrix, with external load in the stages of 350MPa, 500MPa and 650MPa. The zones encircled by black lines represent the interphase debonding.

SYNTHESIS AND COMPRESSION BEHAVIOUR OF AL₂O₃-AL₃Ti IN SITU INTERMETALLIC MATRIX COMPOSITE

Huaxin Peng, Ceng Liu, Dezun Wang

Harbin Institute of Technology, P.O.Box 433, Harbin, 150001, P.R.China

SUMMARY: Fully dense Al₂O₃-Al₃Ti intermetallic matrix composite containing 30vol.% Al₂O₃ particles was in situ processed by combining squeeze casting technique with combustion synthesis utilizing the reaction between TiO₂ powder and pure Al. Using XRD, DTA, SEM and TEM techniques, the reaction process and microstructure of the in-situ composite were examined. Compressive behaviour of the composite have been investigated at 25-600°C and compared with that of cast Al₃Ti alloy.

The in situ formed spherical α -Al₂O₃ particles with a size of 0.2-1 μ m are uniformly distributed in the Al₃Ti matrix. The grain size of the Al₃Ti matrix with a little amount of Al₂Ti precipitates is about 2-10 μ m. The in situ composite possess high compressive strength at room temperature up-to 600°C and is about six to nine times greater than that of cast Al₃Ti alloy. The high compressive strength of the composite is mainly attributed to the dispersion strengthening of Al₂O₃ particles through grain boundary strengthening and the increase of cleavage strength of Al₃Ti.

KEYWORDS: combustion synthesis, Al₂O₃-Al₃Ti, squeeze casting, compressive strength, strengthening mechanisms

INTRODUCTION

In recent years, much attention has been paid to the development and application of composites, such as metal matrix composite (MMC) and intermetallic matrix composite (IMC). Hundreds kinds of composites were manufactured and many fabrication processes were developed. Traditionally, composites have been produced by such processing techniques as powder metallurgy (PM), preform infiltration, spray deposition and various casting technologies, e. g. squeeze casting. In all the above techniques the reinforcement e.g. SiC whisker and particulate is combined with the matrix material. In this case the scale of the reinforcing phase is limited by the starting powder size, which is typically of the order of microns to tens of microns and rarely below 1 μ m.

In the last decade new in situ processing technologies for fabricating metal and ceramic composites have emerged. In situ techniques involve chemical reactions resulting in the formation of the reinforcement. Some of these technologies include SHS (Self-propagating High Temperature Synthesis), DIMOXTM, XDTM, VLS and MA (Mechanical Alloying) [1-6]. Due to the very fine and thermodynamically stable reinforcing phase, it is expected that the in

situ formed composites may reveal not only excellent dispersion of fine reinforcing particles, nascent interface, but also high thermodynamically stability and high temperature performance.

Al_3Ti has a lower density and probably better oxidation resistance than other Al-Ti intermetallic compounds. Such attractive characteristics also make Al_3Ti a potential candidate for low-density high-temperature structural material. But due to its low cleavage strength, the application is far limited. One way to improve the strength is to introduce reinforcements into Al_3Ti matrix. Unfortunately, few report was found.

Fukunaga [7] fabricated in situ composite by reaction squeeze casting between TiO_2 whisker and molten Al, but the microstructure of the composite is ununiform with the hardness ranging from Hv30 to Hv1050. Wang [8] et al prepared the TiO_2/Al bulks by squeeze cast and sintered them at 810°C and 910°C to produced $\text{Al}_2\text{O}_3/\text{Ti}_x\text{Al}_y$ in situ composite. These techniques related to high temperature synthesis, for instance, self-propagating high temperature synthesis (SHS), and the fatal weakness of this process is porous of the products. Therefore, many consolidation techniques were employed to make the product density. Such as SHS+HIP, SHS+Hot-extrusion[9]. Most of these techniques can provide high density, e.g., 99 pct of theoretical density, but also incur an economic penalty.

The relatively high porosity in the products are thought to be due mainly to (1) the low density of the reactant mixture resulting in outgasing during reaction (2) intrinsic volume changes between reactants and products in the combustion synthesis reaction. If the density of the reactant is increased, the density of the products is expected to be improved. But for the powder-SHS process, it is impossible to achieve full-density reactant, and high green density will result in high ignition temperature.

In this paper, the fully dense $\text{Al}_2\text{O}_3\text{-Al}_3\text{Ti}$ in situ composite was synthesized by reaction between TiO_2 powder and molten Al via squeeze casting route. The method combines the synthesis and the densification steps into a one-step process.

EXPERIMENTAL DETAILS

The anatase TiO_2 powder with the average diameter of $0.6\mu\text{m}$ and pure Al (99.7%) were employed as the raw materials. TiO_2/Al bulks with 35% volume fraction of TiO_2 (determined according to the reaction formula) were prepared by squeeze casting method[7]. Subsequently, the squeeze-cast TiO_2/Al bulks were heat treated to form final $\text{Al}_2\text{O}_3\text{-Al}_3\text{Ti}$ composite in a special medium.

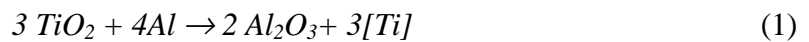
Using DTA, XRD, SEM and TEM techniques, the reaction process and the microstructure of the composites were investigated in details. The TEM foils were prepared by conventional procedure which involved cutting discs with diameter of 3.0 mm, mechanical polishing them to $50\mu\text{m}$, and dimpling to $20\mu\text{m}$ and finally ion milling. SEM and TEM observations were carried out on S-570 and EM420, respectively. Compression test at strain rate $4.2 \times 10^{-4} \text{s}^{-1}$ were conducted in Gleeble1500 test machine to failure in most cases. The specimens ($\phi 9 \times 20 \text{ mm}$) were prepared by electro-discharge machining and grinding. The composites density were determined by water immersion technique.

RESULTS AND DISCUSSION

Synthesis Process

Thermodynamic Background

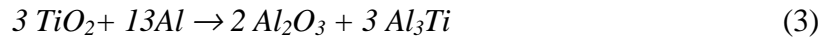
The free energy of formation (ΔG_T) of TiO_2 , and Al_2O_3 were calculated according to the function of free enthalpy of substance[10]. The results indicated that the reaction between TiO_2 and Al to form Al_2O_3 was possible. The reaction heat (ΔH_T) under different temperature were also calculated and the results show that the reaction between TiO_2 and Al is an exothermic reaction. The reaction formula used for thermodynamic calculation are as follows:



and



in general:



In case of $T=1200K$, the theoretical adiabatic temperature of Eqn 1 (T_{ad}) is about 2300K. This temperature is slightly lower than the melt point of Al_2O_3 , but higher than that of Al and Ti.

Squeeze Casting Process and DTA Analysis

During the squeeze casting process for TiO_2/Al , the TiO_2 powder was directly pressed to fabricate preform with a determined volume fraction ($V_f=35\%$). The infiltration and compound were achieved between TiO_2 and Al. The processing parameters were shown in Table 1. No reaction occurred through the squeeze casting process. According to the reaction dynamics, the reaction can be achieved by farther increasing the temperature, but this is limited in squeeze casting technique. Subsequently, the heat characteristic of the reaction between TiO_2 and Al was shown by the differential thermal analysis (DTA) curve in Fig.1. The results indicated that an exothermic reaction occurred in the range $750^\circ C-820^\circ C$ after Al in the cast block had molten in the range $660^\circ C-670^\circ C$.

Table 1: The processing parameters for TiO_2/Al bulk materials

Tm ($^\circ C$)*	Td ($^\circ C$)	Tp ($^\circ C$)	P (MPa)	τ (s)
800-820	500-550	500-550	30-31	20-25

* Tm, Td, Tp- the temperature of molten Al, die and preform, respectively.
P- applied pressure, τ - dwell time of pressure

Reaction Process Achieved by Heat Treatment

According to the results of DTA, the reaction between TiO_2 and Al was achieved by heat treatment. The squeeze cast TiO_2/Al blocks were heated in a special medium in furnace and the process were examined through the observation window. When the temperature reached to $800^\circ C$ indicated by the thermometer, the exothermic reaction usually began simultaneously.

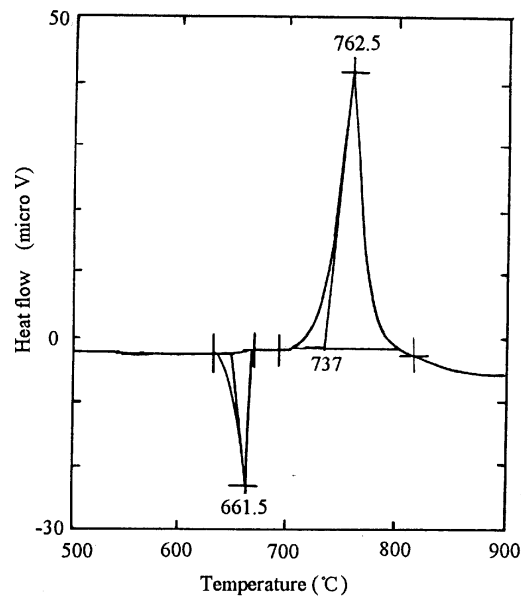


Fig.1: DTA curve showing an exothermic reaction of TiO_2/Al block

High exothermicity result in high brightness of the blocks. Occasionally, the reaction began locally at one point or side and propagated to the whole blocks in a short time. This is the same as the propagation of the combustion wave in SHS. A typical combustion wave propagating process recorded by an auto camera with a rate of 2.5 pictures per second was shown in Fig. 2.

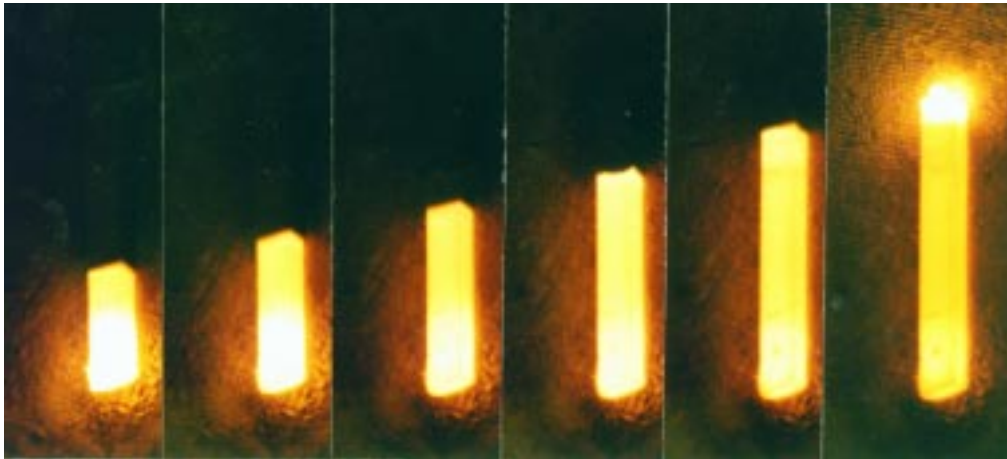


Fig.2: The true SHS process of TiO_2/Al to produce in situ composite

In order to characterize the changes of the microstructure, the microhardness of SHS sample with unreacted part were determined from unreacted area to reacted area by a microsclerometer with a load of 5Kg and a dwell time of 10s, the result was shown in Fig.3. The size of the transition region was about 1 mm, the hardness changed significantly with a microhardness increment of more than 600. This indicated that the material was strengthened remarkably after the reaction.

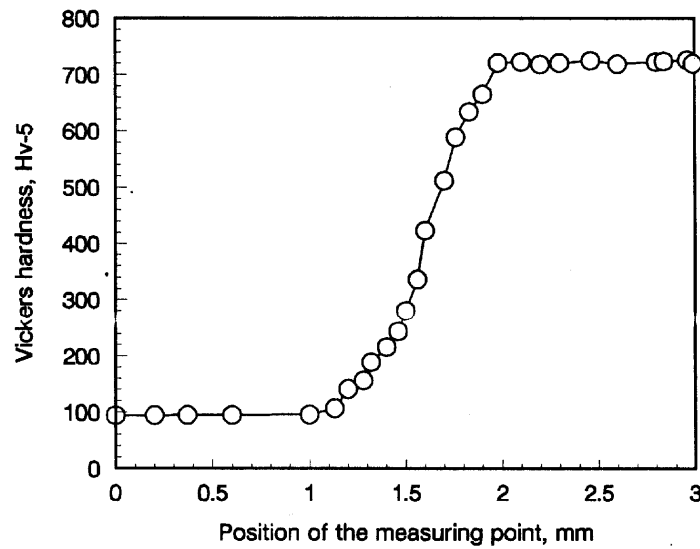


Fig.3: Microhardness changes from unreacted area to reacted area of the SHS sample

Microstructure and its Formation Mechanisms

No reaction occurs during the squeeze casting process for TiO_2/Al bulk materials (Fig.4a). There are only $\alpha\text{-Al}_2\text{O}_3$ and Al_3Ti peaks in the X-ray diffractograph (XRD) of the products produced from TiO_2/Al (Fig.4b), i.e., the product were composed of Al_2O_3 and Al_3Ti . This indicated that the reaction between TiO_2 and Al had taken place to form Al_3Ti and Al_2O_3 . According to Eqn 3, the formation of 1 volume of Al_2O_3 will be followed by 2.26 volume of Al_3Ti . So the product is Al_2O_3 reinforced Al_3Ti matrix composite.

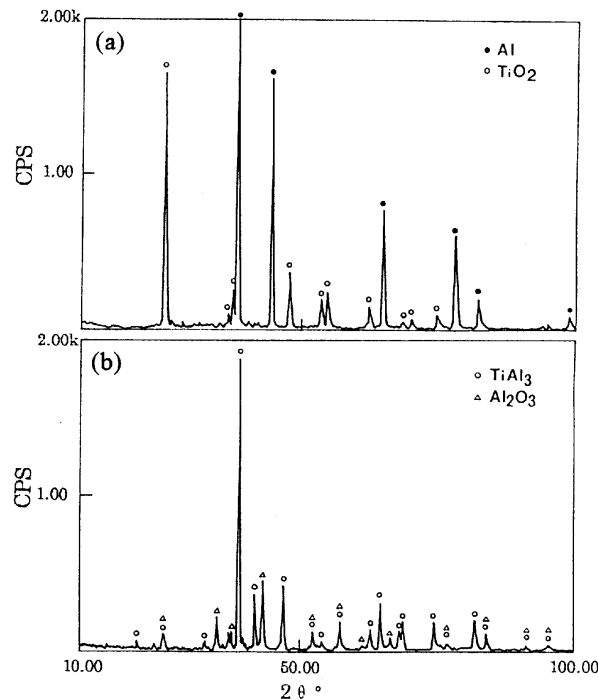


Fig.4: X-ray diffraction pattern of as-cast TiO_2/Al bulk(a) and reaction product(b)

A typical scanning electron micrograph of the composites were shown in Fig.5 which indicated that the densities of the composites are more than 98 pct of the theoretical density (the density of the composites is 3.56g/cm^3 and the theoretical density of Al, Al_2O_3 and Al_3Ti used in calculation is 2.7g/cm^3 , 3.99g/cm^3 and 3.37g/cm^3 , respectively). The reinforcement produced by reaction are very fine, uniform distribution and in particulate-shape in the matrix. The dimension of the particles is less than $1\mu\text{m}$. The dark zone was Al_3Ti matrix. If the volume fraction of TiO_2 in the TiO_2/Al blocks is further lowered, we can get the Al_2O_3 and Al_3Ti mixing reinforced aluminium matrix composite (MMC).

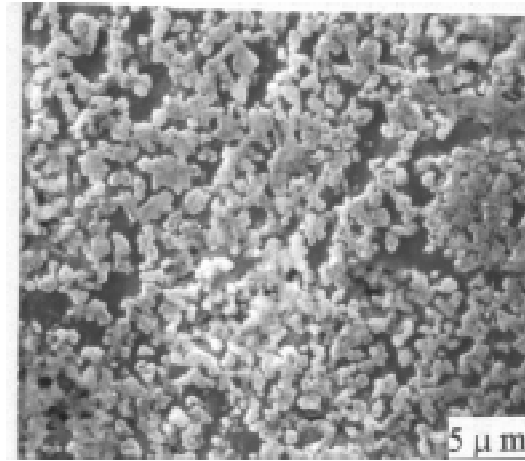


Fig.5: Typical SEM micrograph of in situ composite

TEM observations gave more information of the microstructure as shown in Fig.6. Block-like and particle-shape Al_3Ti phase with a relative large dimension ($2\text{-}10\mu\text{m}$) formed in the composite (Fig.6a), but this size is much smaller than the grain size of cast Al_3Ti alloy (about 1 mm) [11]. Fine grain may be beneficial to the strength of materials. Many Al_2O_3 particles were dispersed around or within Al_3Ti phases (Fig.6b,c). Helix dislocations were also observed in Al_3Ti phases as shown in Fig.6c. Besides these, a strip-like precipitates were found in the Al_3Ti matrix (Fig.6d). These phase were determined to be Al_2Ti precipitates.

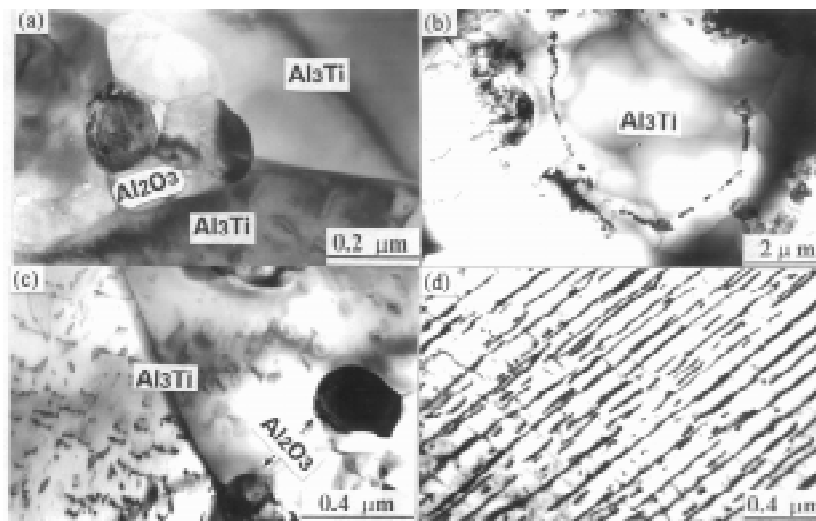


Fig.6: TEM images of the microstructure of the composite

Based on the results presented above and thermodynamic calculation, the following is believed to be the mechanisms for the reaction synthesis:

First, the reaction between TiO_2 and Al to produce Al_2O_3 particles and [Ti]. Subsequently, a solidification process between remained Al and Ti displaced from the reaction to form nascent Al_3Ti matrix and Al_2Ti precipitates. According to the aluminium-titanium equilibrium diagram, these results can be well understood[12]. During this process, the distribution of Al_2O_3 particles produced by the first reaction process would be influenced.

Compressive Behaviour and Strengthening Mechanisms

Load versus displacement curves of the in situ composite compressed under different temperature is shown in Fig.7. The curve of TiO_2/Al bulk materials is also presented for comparison. The obtained values of yield stress are plotted as a function of temperature in Fig.8. In the tested temperature range, the curves have a common feature: after yielding, load begin to decrease and soon the curves are terminated by fracture, fracture often precedes yielding except that of TiO_2/Al as seen in Fig.7. Such a small fracture strain relatively mean that the composite does not exhibit any ductility in this temperature range. This is because of the native brittleness of Al_3Ti with DO_{22} -type structure and presence of large amount of Al_2O_3 particles.

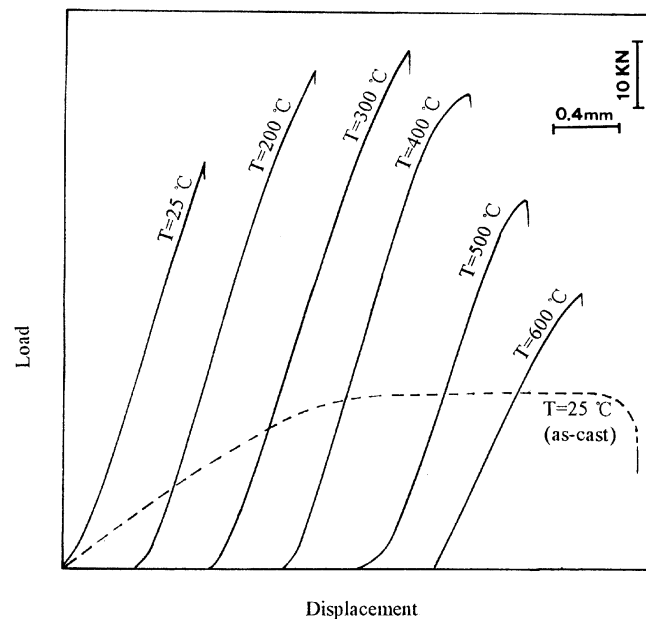


Fig.7: Load versus displacement curves of the composite compressed under different temperatures

The yield stress increase gradually from 1200 MPa to 1566 MPa with increasing temperature up to about 300°C and then decrease rapidly until about 600°C. But the compressive strength also maintained at 645 MPa at 600°C. The strength of $\text{Al}_2\text{O}_3\text{-Al}_3\text{Ti}$ composite is about six to nine times greater than that of unreinforced cast Al_3Ti alloy in the tested temperature range as shown in Fig.8.

Based on these results and microstructural examination, the following is believed to be the strengthening mechanisms for the composite:

The dominant mechanism is dispersion strengthening performed through grain boundary strengthening and increase of cleavage strength of Al_3Ti matrix, i.e., the presence of fine Al_2O_3 particles impeded propagation of the cleavage cracks in the matrix. Besides, the dislocations and fine grain strengthening are also beneficial to the strength of the composite.

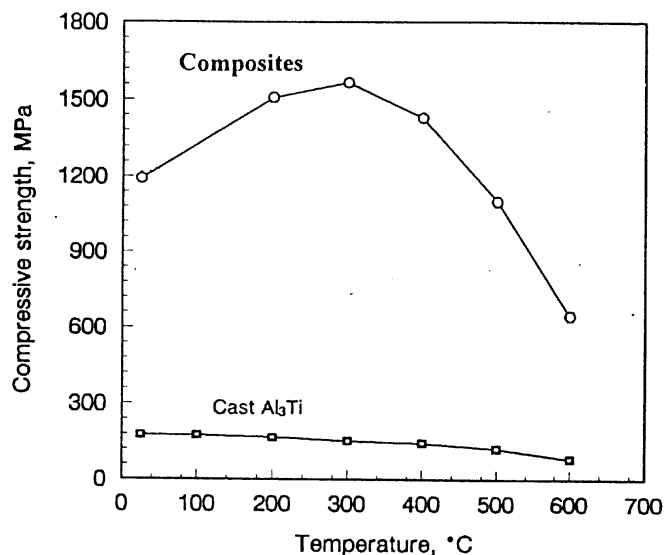


Fig.8: Compressive strength of the composite as a function of temperature. The compressive yield strength of cast Al_3Ti alloy is also shown for comparison

CONCLUSIONS

The differential thermal analysis (DTA) of squeeze-cast TiO_2/Al bulk indicated that an exothermic reaction occurred after the temperature reached to 750°C . The reaction between TiO_2 and Al is a high exothermicity reaction. A high temperature combustion synthesis of fully dense $\text{Al}_2\text{O}_3 - \text{Al}_3\text{Ti}$ in situ composite were successfully achieved for squeeze-cast TiO_2/Al blocks by heating the blocks in a special medium.

Very fine-scale and excellent dispersion of reinforcing phase (Al_2O_3 particles) ranging from 0.2 to $1.0\mu\text{m}$ were obtained in the Al_3Ti matrix. The discussion on the reaction mechanisms concluded that the in situ process include a reaction process and a solidification process.

The in situ composite possess high compressive strength at room temperature up to 600°C and is about six to nine times greater than that of cast Al_3Ti alloy. The dominant strengthening mechanism is dispersion strengthening performed through grain boundary strengthening and increase of cleavage strength of Al_3Ti matrix.

ACKNOWLEDGMENT

This work is supported by the National Nature Science Foundation of China (No. 59271009).

REFERENCES

1. Subhash, K. and Michael K., Formation of TiC in In Situ Processed Composites via Solid-Gas, Solid-Liquid and Liquid-Gas Reaction in Molten Al-Ti, *Material Science and Engineering*, Vol. A162, 1993, pp. 153-162
2. Rice R. W., Microstructural Aspects of Fabricating Bodies by Self-Propagating Synthesis, *Journal of Materials Science*, Vol. 26, 1991, pp. 6533-6541.
3. Stanislav, A. and Nagelberg, A. S., Formation of Al₂O₃/Metal Composites by the Directed Oxidation of Molten Aluminium-Magnesium-Silicon Alloys: Part I, Microstructural Development, *Journal of American Ceramic Society*, Vol.75, No.2, 1992, pp.447-454.
4. Kuruvilla, A. K., Prasad, K. S. and Mahajan, Y. R., Microstructure-Property Correlation in Al/TiB₂ (XD) Composites, *Scripta Metallurgica et Materialia*, Vol.24, 1990, pp.873-878.
5. Gotman, I. and Koczak, M.J., Fabrication of Al Matrix in situ Composites via Self-Propagating Synthesis, *Material Science and Engineering*, Vol.A187, 1994, pp.189-199.
6. Lee, K.M., and Moon, I. H., High Temperature Performance of Dispersion Strengthened Al -Ti Alloys Prepared by Mechanical Alloying, *Material Science and Engineering*, Vol. A 185, 1994, pp.165-170.
7. Fukunaga, H. and Wang, X.G., Preparation of Intermetallic Compound Matrix Composites by Reaction Squeeze Casting, *Journal of Material Science Letters*, Vol.10, 1991. pp.23-25.
8. Wang, D.Z., Liu, Z.R., Yao, C.K., and Yao, M., A Novel Technique for Fabricating in situ Al₂O₃/Ti_xAl_y Composites, *Journal of Material Science Letters*, Vol.12, 1993. pp.1420-1421.
9. Munir, Z. A. and Tamburini, U.A., Self-Propagating Exothermic Reactions: The Synthesis of High-Temperature Materials by Combustion, *Materials Science Reports*, Vol. 3, No. 7-8, 1989, pp. 277-365.
10. Barin, I. and Knacke, O., *Thermochemical Properties of Inorganic Substance*, Springer-Verlag, New York, 1977.
11. Yamaguchi, M., Umakoshi, Y., and Yamane, T., Plastic Deformation of the Intermetallic Compound Al₃Ti, *Philosophical Magazine*, Vol. 55, No. 3, 1987, pp. 301-315.
12. Peng, H.X., Wang, D.Z., Geng, L. and Yao, C.K., Formation Mechanisms of the Microstructure of Al₃Ti-Al₂O₃-Al in situ Composite, Proceedings of the International Conference on Advanced Materials, Beijing, China, August 12-15, 1996, Wang, T. C. and Chou, T.W., Eds, pp. 268-272.

EFFECT OF INTERFACIAL DAMAGE ON RESIDUAL TENSILE STRENGTH FOR SCS-6/TI-15-3 METAL MATRIX COMPOSITE

Chitoshi Masuda ,Yoshihisa Tanaka and Yu-Fu-Liu

National Research Institute for Metals, 1-2-1, Sengen, Tsukuba, Ibaraki, Japan

SUMMARY: Effect of thermal cycling is discussed on the performance of a metal matrix composite with special emphasis on the interfacial degradation between fiber and matrix. Material used in this study was Ti-15V-3Cr-3Al-3Sn alloy matrix reinforced by SiC fiber (SCS-6/Ti-15-3 MMC) fabricated by HIP method at 880°C. The thermal cycling test was performed at the temperature range from 380°C to 880°C under 2 holding times. After thermal cycling the residual tensile strength was determined and the fracture surface was examined by a SEM.

The interfacial reaction layer thickness increased with increasing the total holding time for both aging at 880°C and thermal cycling test. The residual tensile strength for thermal cycling test drastically decreased with increasing the cycling number up to about 100 cycles and the strength tended to be saturate over 100 cycles. The shear strength estimated by multiple fracture theory on the basis of the interval of fractured fiber also decreased with increasing cycling number. The residual tensile strength estimated by the modified rule of mixture on the basis of the average fiber strength was equal to the experimental data for as received material and thermal cycling of 24 cycles under the holding time of 60 minutes, while for 240 cycles the estimated value from the minimum strength of the fiber was the same as the experimental one. It is suggested that for the shorter cycling range the multiple fracture would occur during the tensile test, while for the longer cycling range the weakest fiber breakage would lead to catastrophic failure of composite.

KEYWORDS: Metal matrix composites (MMC), Titanium alloy based MMC, Interfacial reaction layer, Interfacial shear stress, Thermal cycling, Residual tensile strength

INTRODUCTION

Titanium matrix alloy composites are one of the most promising materials for high temperature structural applications such as gas turbine components. However, the use of these materials for turbine engine applications often depends on their ability to withstand both cyclic loading and thermal cycling, especially the thermal cycling damages induced from the mismatch of the thermal expansion coefficients between fiber and matrix. On the other hand, the load cycling damages are induced by the starting or stopping of turbine engine. Actually the machines are affected with both thermal cycling and load cycling. There are a few reports concerning the fatigue strength, the fatigue crack propagation properties tested at room temperature and thermo-mechanical properties, while there are very few reports about the degradation of the SCS-6/Ti metal matrix composite (MMC) under thermo-mechanical conditions. According to Johnson et al., the thermo-mechanical damage was not so predominant up to 2000 cycles tested from 93°C to 650°C under in-phase and out-of-phase for SCS-6/Ti-15-3 MMC[1]. As far as we know, there has been no report to discuss the effect of thermal cycling damage on the mechanical properties for SCS-6/Ti-15-3 MMC.

Therefore we referred to another MMC system as follows. The post tensile strength decreased with increasing thermal cycling after 153°C to 815°C thermal cycling test for SCS-6/Ti-24-11 MMC[2]. The effects of the thermal cycling or load cycling at high temperature on the degradation of those composites were not yet clearly shown.

To discuss the effect of the thermal cycling on the interfacial degradation, the SCS-6/Ti-15-3 MMC was tested under the temperature range from 380°C to 880°C in vacuum in this paper. After the thermal cycling test the residual tensile strength was determined and the interfacial reaction thickness, the interval of fractured fiber in composite were also examined. The interfacial shear stress, the residual tensile strength of composite were estimated.

EXPERIMENTAL PROCEDURES

The material studied here was Ti-15V-3Cr-3Al-3Sn alloy matrix with the continuous SiC fiber reinforcement at an average volume fraction of 0.3 (SCS-6/Ti-15-3 MMC). The composite was processed using the foil/fiber/foil consolidation process and the materials was supplied from Mitsubishi Heavy Industries, Japan. The SiC fiber was composed of b-SiC deposited on a 40 mm carbon monofilament substrate with a double pass carbon-rich coating applied to the fiber surface for chemical compatibility consolidations. The Ti-15V-3Cr-3Al-3Sn alloy, as processed in foil form, consists of the b-phase. The composite was fabricated by HIP method at 880°C under 100 MPa for 1.5 hour. The solution treatment and aging treatment were performed at 780°C for 30 min and 482°C for 1000 min, respectively, to stabilize microstructures of the Matrix. Photograph 1 shows the optical micrographs of the polished section of the composite perpendicular to fiber axis. The micrograph indicates that the SiC fiber is hexagonal aligned in the matrix without touching other fibers.

As received composites were in a form of plates, with a thickness of 2.5mm. From those plates (130 mm x 200 mm) specimens were machined to a width of 9 mm and a length of 55

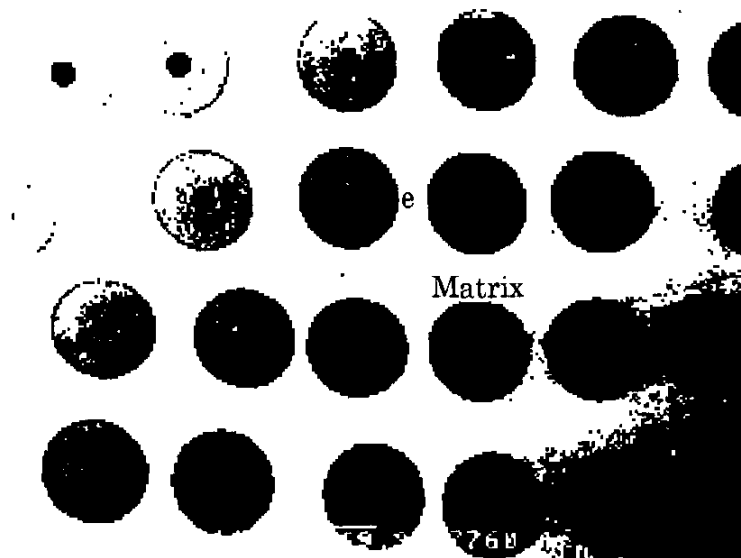


Photo. 1 Cross sectional micrograph of SCS-6/Ti-15-3 MMC.

mm. The fiber axis was located in the longitudinal direction of the specimen. The central part of the specimen was machined to reduce the thickness to 1.2 mm and 10mm length. Shape and dimension of the specimen are shown in Fig. 1. Thermal cycling test was

performed using the image heating furnace at the temperature range from 380°C and 880°C in vacuum under 2 holding times of 6 min and 60 min. The heating and cooling rates were 500°C/min. Fig. 2 shows a schematic drawing of heat cycles used in this experiment. After thermal cycling test, the tensile strength was evaluated at room temperature. The tensile test was performed using an Instron type testing machine with a crosshead speed of 0.5mm/min. After the test, The fracture surface and side surface near fracture plane were observed using a scanning electron microscope (SEM). The thickness of interfacial reaction layer was measured on the transverse cross sectional surfaces before and after thermal cycling tests. Moreover the push-out test was performed on the cross sectional thin plate cut from the thermal cycling specimen after test and the strength of the dissolved fiber from the composite was also examined after thermal cycling test.

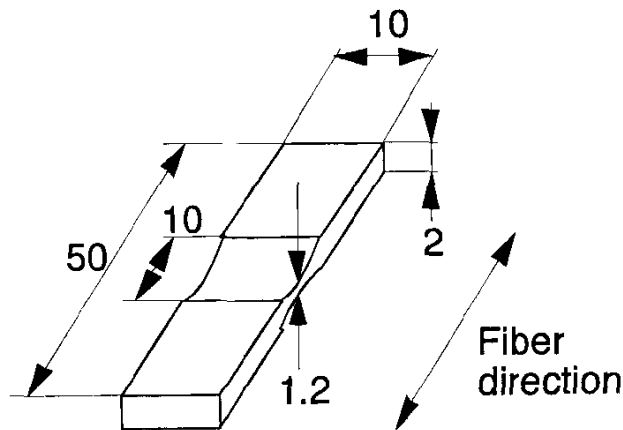


Fig. 1 Specimen figure

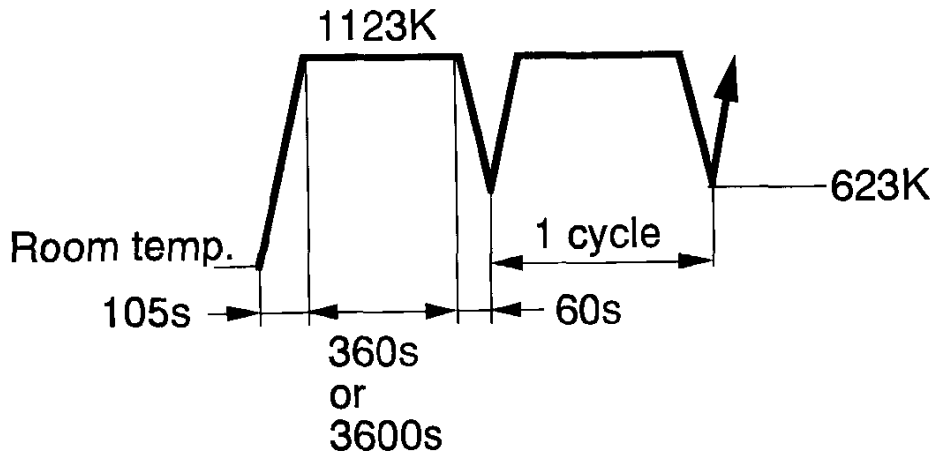


Fig. 2 Thermal cycling conditions

RESULTS AND DISCUSSIONS

Reaction layer thickness

Photograph 2 shows the typical example of the cross sectional optical micrographs of

the composite for as received and thermal cycled. The gray part shows the SiC mantle and its outer circumferential black ring shows the carbon coating layer. The white area shows the matrix. On the Photo. 2(a) the black circular area shows the carbon core filament. The SiC fiber, outer carbon coating layer were clearly found on the photographs. A dark weak line was seen out side of the carbon coating layer. A zone between carbon coating layer and the dark line is reaction layer. The thickness of reaction layer increased with increasing total holding time at 880°C.

Figure 3 shows the variation of reaction layer thickness to the total holding time at 880°C. In the figure the data after aging at 880°C were also included. The composite material was HIPed at 880°C for 1.5 hour. In this condition the reaction layer thickness was 0.8 mm. The reaction layer thickness linearly increased with increasing holding time as shown in Fig. 3. Moreover, the reaction layer thickness after thermal cycling test was nearly the same as that after aging. It is suggested that the reaction between fiber and matrix would be controlled by diffusion of element included in both materials.

The reaction layer thickness was examined at 930°C and 980°C and the activation energy was estimated to about 243kJ/mol. This value was very high in comparison to the previous data[3]

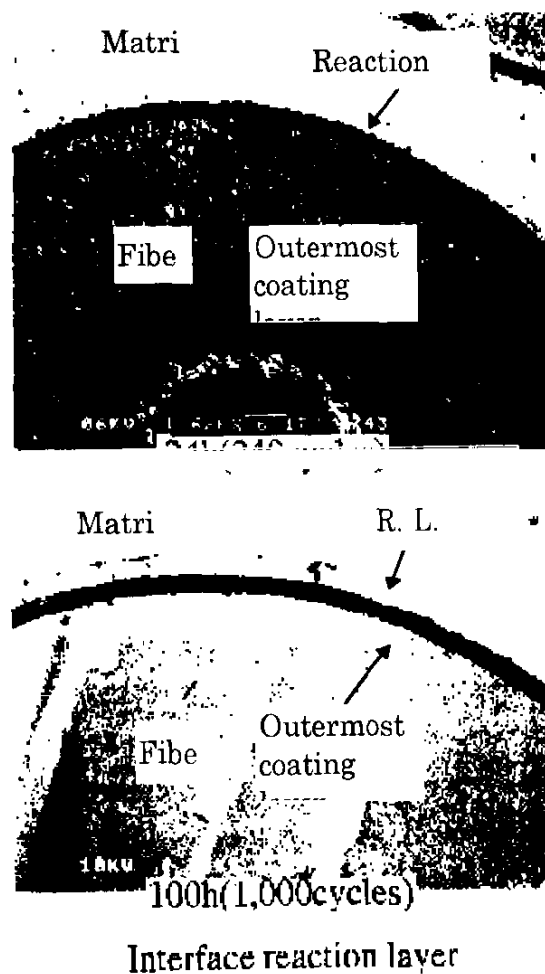


Photo. 2 Micrographs of reaction layer for SCS-6/Ti-15-3 MMC.

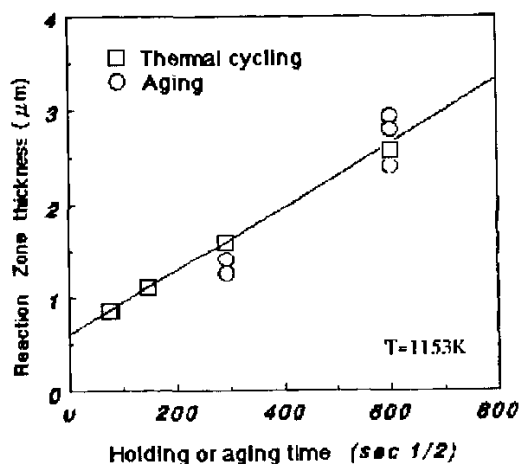


Fig. 3 Variation of reaction layer thickness to total holding time for SCS-6/Ti-15-3 MMC

Residual tensile strength

After thermal cycling the residual tensile strength was examined and the results are shown in Fig. 4. In Fig. 4 (b) for total holding time of 100 hours the strength of virgin material was about 1.8 GPa and the elongation was about 1.1%. After thermal cycling of 1000 cycles the strength decreased to about 1.2 GPa in comparison for virgin material. But the results after 100 and 1000 cycles were not so different. In Fig. 4(a) shown the results for total holding time of 24 hours the strengths for after 24 and 240 cycles were about 1.6 and 1.2 GPa, respectively, while the elongation of 240 cycles was much shorter than that of 24 cycles. It is suggested that the tensile strength and elongation would be influenced by the thermal cycling number.

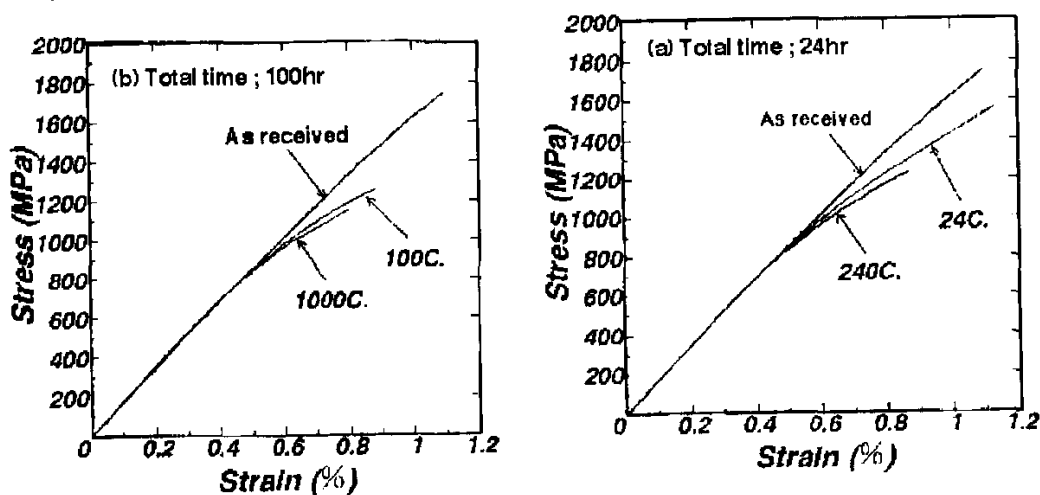


Fig. 4 Residual tensile stress to strain of SCS-6/Ti-15-3 MMC for (a) 100 hrs and (b) 24 hrs.

Figure 5 shows the relationship between the residual tensile strength and thermal cycling. In this figure, the data for holding time of 6 and 60 minutes are plotted with different symbols and datum for as received materials is also plotted. The residual tensile strength

was drastically decreased with increasing thermal cycling number and the strength saturated to be about 1.2 GPa over 100 cycles. For SCS-6/Ti-24Al-11Nb composite[2] the residual tensile strength after thermal cycling also drastically decreased with increasing cycle up to about 500 cycles and saturated to nearly zero over 500 cycles. In this case the alternate temperature range was 665°C from 150°C to 815°C and tested in air which are different with this study. Many transverse cracks were observed on the specimen surface after 500 thermal cycles, while in our study none were observed.

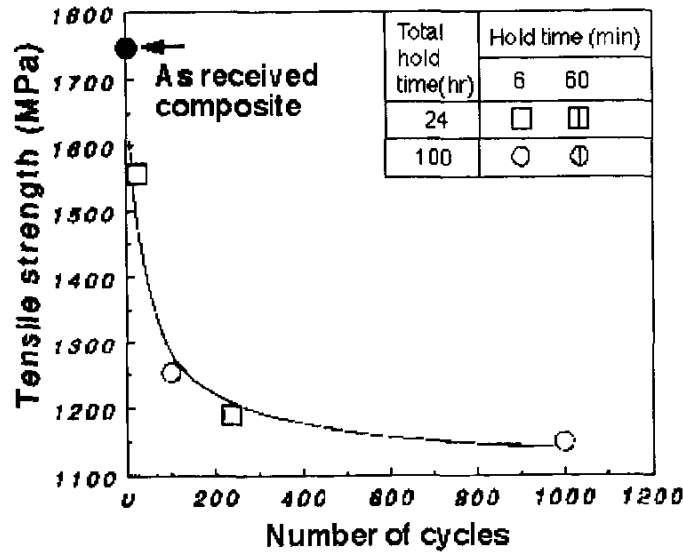


Fig.5 Relationship between residual tensile strength and thermal cycling number for SCS-6/Ti-15-3 MMC

Figure 6 shows the residual tensile strength after aging and thermal cycling for SCS-6/Ti-15-

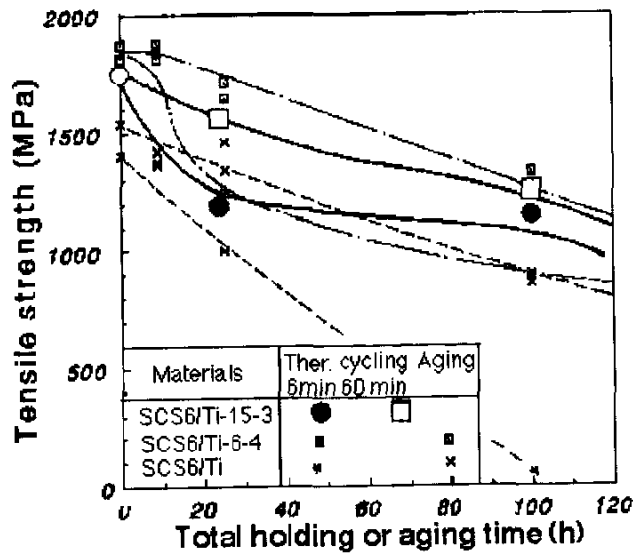


Fig. 6 Variation of residual tensile strength to thermal cycling for SCS-6/Ti and Ti alloy MMC

3MMC are compared with reported data for SCS-6/Ti-6-4 MMC, SCS-6/Ti MMC[4]. SCS-6/Ti-6-4 MMC and SCS-6/Ti MMC were tested in the temperature range from 350°C to 850°C for thermal cycling and aging test was performed at 850°C. These testing conditions were different from our study, but the alternated temperature range for thermal cycling was the same for both. Therefore those data were plotted on the same figure to be compared with our data. For aging condition the strengths of SCS-6/Ti-6-4 and SCS-6/Ti MMC's linearly decrease with increasing time. But after thermal cycling the strength for SCS-6/Ti-6-4 MMC drastically decreases over 6 hours and saturates after it. For SCS-6/Ti MMC the strength linearly decreased with increasing time up to about zero MPa. For our results the strength for the holding time of 60 min was higher than that for 6 min, but for the holding time of 100 hours the strength was nearly the same for both holding times. It is suggested that the resistance of thermal cycling is higher for SCS-6/Ti-15-3 MMC than those for SCS-6/Ti-6-4 MMC and SCS-6/Ti MMC in spite of lower maximum holding temperature.

Intervals of fractured fibers

Photograph 3 shows the micrographs of the side surface of the specimen. The white areas were the matrix and gray bar or acicular was silicon carbide fiber. In the upper side of the micrographs is fracture surface where some pull out fibers were found. The transverse cracks on the fiber were also seen. The interval of the fractured fiber was examined on the micrographs except for near final fracture surface.

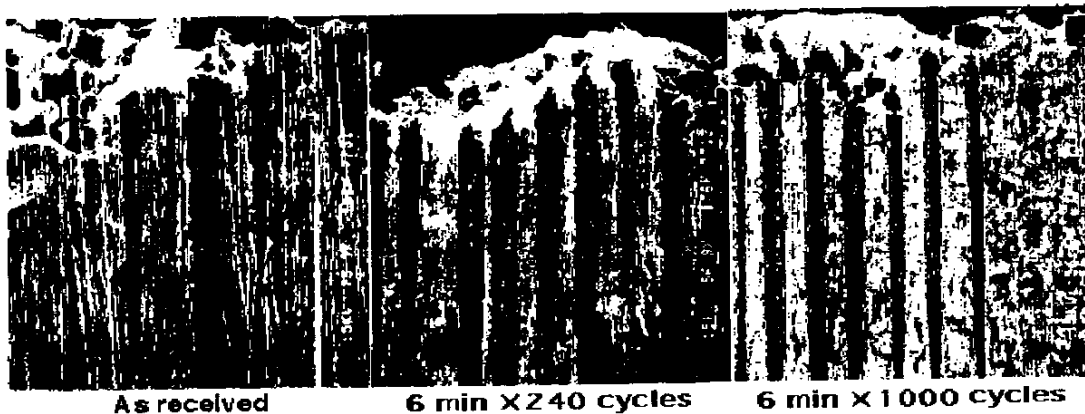


Photo. 3 Micrographs of fractured fiber after thermal cycling observed on the side surface of the specimen for SCS-6/Ti-15-3 MMC.

Figure 7 shows the relationship between the probability and interval of the fractured fiber. The data was plotted on the log-normal probability paper. The dispersion of data for virgin materials was less than those for 240 and 1000 cycles. The average intervals increased with increasing cycles.

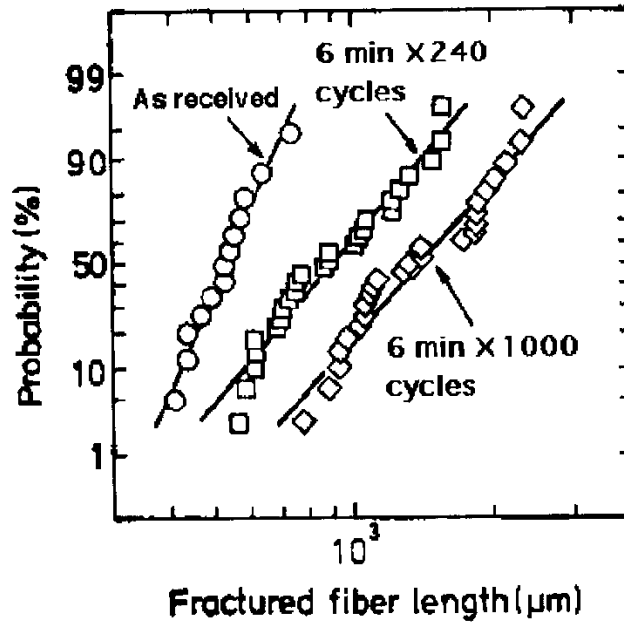


Fig. 7 Probability of interval of the fractured fiber in SCS-6/Ti-15-3 MMC.

Interfacial shear stress

The interfacial shear stress was estimated by the multiple fracture theory based on the following equation[5].

$$x = (V_m/V_f)(\sigma_{m,u}R_f/2\tau) \tag{1}$$

where V_m and V_f are the volume fractions of matrix and fiber, respectively and $\sigma_{m,u}$ and τ are ultimate strength of matrix and shear stress, respectively. R_f is the radius of the fiber.

Figure 8 shows the variation of shear stress to thermal cycles for SCS-6/Ti-15-3 MMC. The

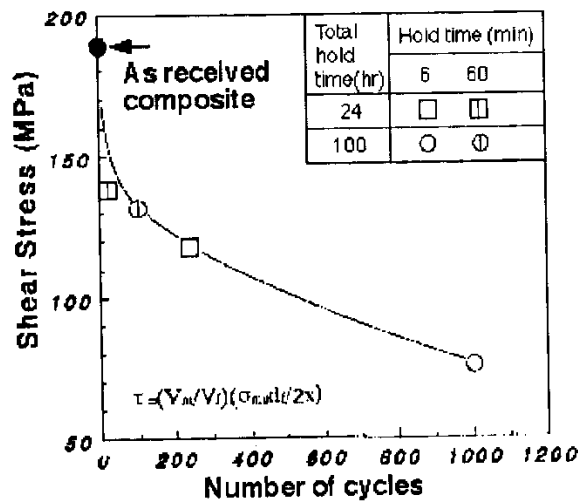


Fig. 8 Estimated shear stress after thermal cycling for SCS-6/Ti-15-3 MMC.

shear stress also drastically decreased with increasing cycles. The trend of the shear stress is nearly same as the residual tensile strength shown in Fig. 5.

Estimation of residual tensile strength of SCS-6/Ti-15-3 MMC

The modified mixed rule of composites was proposed by Kagawa et al.[6] and could be written.

$$\sigma_c = \sigma_f [1 - (R_f \sigma_f / (2 \tau L_g))] V_f + \sigma_m (1 - V_f) \quad (2)$$

where σ_c , σ_f , and σ_m are the strength of composite, fiber and the strength of matrix at fracture of composite, respectively. σ_f is the average strength of fiber. L_g is the gauge length.

In this case the fiber strength was not obtained. In order to estimate the strength of composite after thermal cycling test the fiber strength after aging was used. The average fiber strengths for virgin material and after 24 hours aging were about 4.76 GPa and 3.68 GPa. Moreover the maximum and minimum fiber strengths were also used.

The estimated values and bands of strength were also designated in Fig.9. For as received materials and 24 cycles tested at the holding time of 60 min the estimated values from average fiber strength are nearly equal to the experimental ones. On the other hand, for 240 cycles tested at the holding time of 6 min the estimated value from the minimum fiber strength was nearly the same as the experimental one. It is suggested that the residual strength of composite for short cycling number could be estimated by the average fiber strength, but for longer cycling number the residual strength of composite would be controlled by the weakest fiber, when the weakest fiber included in composite would be broken at first, suddenly the whole fracture of composite would be induced.

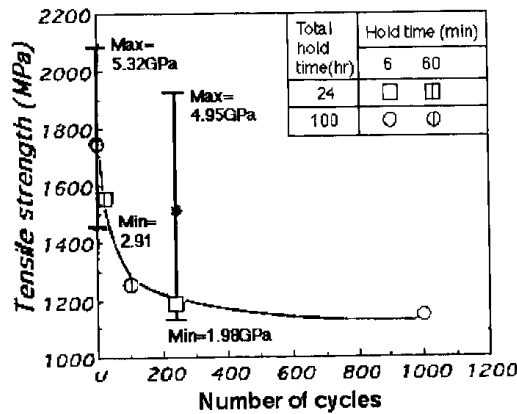


Fig. 9 Estimated residual tensile strength after thermal cycling for SCS-6/Ti-15-3 MMC.

CONCLUSIONS

- 1) The reaction layer thickness of the composite linearly increases with increasing the time for both of aging or thermal cycling conditions. It is suggested that the interfacial reaction would be controlled by diffusion of elements included in composite. The activation energy was also estimated to 240 kJ/mol.
- 2) The residual tensile strength after thermal cycling test drastically decreased with increasing

cycle number up to about 100 cycles. After that the strength tended to be saturated up to about 1,000 cycles. The effect of holding time on the residual strength was not so significant. It is suggested that the thermal cycling effect is very significant to residual strength of composite.

3) The interval of fractured fiber was examined on the side surface near tensile fracture surfaces. The intervals increased with increasing thermal cycling number.

The shear stress after thermal cycling was estimated by the multiple fracture theory on the basis of the interval of the fractured fiber. The shear stress also drastically decreased with increasing the thermal cycling number.

4) The residual tensile strength of composite was estimated by the modified rule of mixture on the basis of the average, maximum and minimum fiber strength extracted from the composite after aging test. For shorter cycle range the best estimation of composite strength was obtained using the average fiber strengths, while for the longer cycling range the minimum fiber strength leads to a better agreement with experimental data. It is suggested that for the shorter cycling range the multiple fracture process would occur, while for longer cycling range the weakest fiber would be broken at first, the catastrophic fracture of composite would be induced.

REFERENCES

1. M., W.S. Johnson, Y.A. Bahei-El-Din, and M.G. Castelli, "Analysis of thermo-mechanical fatigue of unidirectional titanium metal matrix composites", NASA Technical Memorandum, 104105, July(1991).
2. S.M.Russ, "Thermal fatigue of SCS-6/Ti-24Al-11Nb ", *Met. Trans.*, 21A(1990) 1595-1602.
3. D.B. Gundel and F.E. Wawner, "Interfacial reaction kinetics of coated SiC fiber with various titanium alloys", *Scripta Metall. Mater.*, 25(1991)437.
4. I. Shiota, Y. Imai and Y. Shinohara, "Relationship between interfacial reaction and tensile strength of SiC filament reinforced Ti alloy composites", to be printed on NRIM Report(in Japanese).
5. Y.Kagawa and H. Hatta, "Tailoring Ceramic Composites", *Agune Shoufusha*,(1990)286.
6. Y. Kagawa, T. Fujita and A. Okura, "Temperature dependence of tensile mechanical properties in SiC fiber reinforced Ti matrix composite", *Acta Metall. Mater.*, 42(1994)3019.

FULLY-COUPLED THERMOMECHANICAL ANALYSIS OF VISCOPLASTIC COMPOSITES UNDER QUASISTATIC AND DYNAMIC ENVIRONMENTS

Eui-Sup Shin, Seung-Jo Kim and Yong-Hyup Kim

*Department of Aerospace Engineering
Seoul National University, Kwanak-ku, Seoul, 151-742, Republic of Korea*

SUMMARY: The thermo-elasto-viscoplastic responses of composite materials are predicted on the basis of fully-coupled thermomechanics. An unmixing-mixing scheme is utilized to describe the thermo-elasto-viscoplastic behavior of orthotropic composites. The equation of motion and the energy conservation equation are formulated with the constitutive arrangement by the unmixing-mixing concept. In computational aspects, the governing equations are reformulated with the finite element method, and then the time marching techniques fit for the full discretization are applied. As a numerical study, a series of quasistatic and dynamic analyses are performed. The progress of viscoplastic deformation, the stress-strain relation, and the temperature change owing to the coupling effect are examined when composite laminates are subjected to repeated cyclic loading.

KEYWORDS: thermo-elasto-viscoplasticity, unmixing-mixing scheme, composite material, thermomechanical coupling, finite element method

INTRODUCTION

Advanced composite materials have widely been used in severe mechanical and/or thermal environment for various applications. For example, metal matrix composites may exhibit viscoplastic deformation at high temperatures [1]. Up to date, many kinds of constitutive theories have been suggested to simulate the viscoplastic response of the anisotropic materials. Most of the theories were extended from the classical plasticity models or the unified viscoplastic models for isotropic materials by introducing macroscopic composite mechanics [2-4]. On the other hand, there have been several efforts made, based on micromechanics which predicts the overall behavior of composite from the individual properties of constituent materials [5-7].

To solve the complex thermomechanical problems, in principle, all the governing equations in continuum mechanics must be solved simultaneously because the mechanical fields and the thermodynamic fields are coupled interactively. As summarized in Table 1, there are three types of mathematical formulation that depend on the treatment of thermomechanical variables. The coupling between mechanics and thermodynamics has a weak effect on the behavior of elastic materials. But the

coupling effect is not always negligible for viscoplastic materials, especially when the materials are repeatedly used under cyclic loads. With the development of the viscoplastic deformation, a certain portion of mechanical energy is converted to heat, thus resulting in an irreversible rise in temperature. Up till now, numerical analyses for the isotropic materials with the fully-coupled formulation have been performed by several researchers [8-10]. Therefore, the quantitative prediction of thermomechanical coupling effect in the viscoplastic composites is also necessary to accurately analyze the behavior of composite structures operated under intense surrounding conditions.

In this paper, a series of numerical analyses are performed with a focus on the coupling effect. The development of viscoplastic deformation, the stress-strain relation, and the temperature change are carefully examined when composite laminates are cyclically subjected to static and dynamic mechanical loads.

Table 1: Three types of thermomechanical formulation

Coupling Type (interrelation)	
Mechanical Fields	Thermodynamic Fields
stress, strain, viscoplastic strain, displacement, etc.	temperature, heat flux, energy, entropy, etc.

GOVERNING EQUATIONS AND FINITE ELEMENT METHOD

Governing Equations

Thin composite laminates which infinitesimally deform in a plane are considered, and the governing equations are briefly summarized in the following [7,10]. The detailed information on unknowns and equations is listed in Table 2.

- Equation of motion

$$\nabla \cdot \sigma + f = \rho \ddot{\mathbf{u}} \quad (1)$$

- Energy conservation equation

$$\rho c_v \dot{\theta}_+ = -\theta \boldsymbol{\alpha} : \mathbf{A}^{-1} : (\dot{\boldsymbol{\varepsilon}} - \dot{\boldsymbol{\varepsilon}}^p) + \xi \boldsymbol{\sigma} : \dot{\boldsymbol{\varepsilon}}^p + \nabla \cdot (\boldsymbol{\chi} \cdot \nabla \theta) \quad (2)$$

By applying the principles of thermodynamics (energy conservation and entropy production), Eqn 2 is derived for a class of viscoplastic composites. The terms in the right-hand side are the contribution to thermal energy by thermoelastic and viscoplastic deformation, and heat conduction, respectively.

- Strain-displacement relation

$$\boldsymbol{\varepsilon} = \frac{1}{2} [\nabla \cdot \mathbf{u} + (\nabla \cdot \mathbf{u})^T] \quad (3)$$

- Constitutive equation ; unmixing-mixing scheme

$$\dot{\boldsymbol{\varepsilon}} = \mathbf{A} \dot{\boldsymbol{\sigma}} + \boldsymbol{\alpha} \dot{\theta}_+ + \dot{\boldsymbol{\varepsilon}}^p \quad (4)$$

$$\dot{\boldsymbol{\varepsilon}}^p = \sum_{k=1}^N \mathbf{B}_{[m_k]} \dot{\boldsymbol{\varepsilon}}_{[m_k]}^p \quad (5)$$

$$\dot{\boldsymbol{\sigma}}_{[f]} = \mathbf{C}_{[f]} \dot{\boldsymbol{\sigma}} + \boldsymbol{\beta}_{[f]} \dot{\theta}_+ + \sum_{k=1}^N \mathbf{D}_{[f_k]} \dot{\boldsymbol{\varepsilon}}_{[m_k]}^p \quad (6)$$

$$\dot{\boldsymbol{\sigma}}_{[m_i]} = \mathbf{C}_{[m_i]} \dot{\boldsymbol{\sigma}} + \boldsymbol{\beta}_{[m_i]} \dot{\theta}_+ + \sum_{k=1}^N \mathbf{D}_{[m_{ik}]} \dot{\boldsymbol{\varepsilon}}_{[m_k]}^p \quad (7)$$

The deformed state in the matrix is represented with a set of variables for the

N -parts of the matrix. Here, tensor B relates the viscoplastic deformation of matrix to the overall viscoplastic response of composite. Three terms in the right-hand side of Eqn 6 or 7 stand for the microstress contributed from overall loading, thermal expansion, and matrix viscoplasticity, respectively.

○ Constitutive equation ; Bodner-Partom theory

$$\dot{\epsilon}_{[m,i]}^p = \frac{D_o}{\sqrt{J_{[m,i]}^2}} \exp\left[-\frac{1}{2}\left(\frac{Z_{[m,i]}^2}{3J_{[m,i]}^2}\right)^n\right] S_{[m,i]} \quad (8)$$

$$S_{[m,i]} = \sigma_{[m,i]} - \frac{1}{3} \text{tr}(\sigma_{[m,i]}) \mathbf{1} \quad (9)$$

$$J_{[m,i]}^2 = \frac{1}{2} S_{[m,i]} : S_{[m,i]} \quad (10)$$

$$\dot{Z}_{[m,i]} = m_1 (Z_1 - Z_{[m,i]}) \sigma_{[m,i]} : \dot{\epsilon}_{[m,i]}^p - A_1 Z_1 \left(\frac{Z_{[m,i]} - Z_2}{Z_1}\right)^{r_1} \quad (11)$$

where D_o , Z_1 , Z_2 , m_1 , A_1 , r_1 , and n are the viscoplastic constants of the matrix.

Table 2: List of unknowns and equations

Unknowns		Equations	
		Eqn of Motion ; (1)	2
Macro-Level Variable		Energy Conservation Eqn ; (2)	1
Stress Tensor	3	Strain-Displacement Relation ; (3)	3
Strain Tensor	3	Constitutive Eqn	
Displacement Vector	2	(Unmixing-Mixing Scheme)	
Temperature	1	Strain Rate Eqn ; (4)	3
Viscoplastic Strain Tensor	3	Viscoplastic Flow Law ; (5)	3
		Fiber Stress Eqn ; (6)	3
Micro-Level Variable		Matrix Stress Eqn ; (7)	$N \times 3$
Fiber Stress Tensor	3	Constitutive Eqn	
Matrix Stress Tensor	$N \times 3$	(Bodner-Partom Theory)	
Matrix Deviatoric Stress Tensor	$N \times 4$	Flow Law and Kinetic Eqn ; (8)	$N \times 3$
Matrix Viscoplastic Strain Tensor	$N \times 3$	Deviatoric Stress Definition ; (9)	$N \times 4$
Matrix Deviatoric Stress Invariant	N	Stress Invariant Definition ; (10)	N
Matrix Internal State Variable	N	Evolution Eqn ; (11)	N
Total →	$15 + N \times 12$	Total →	$15 + N \times 12$

Finite Element Method

Variational formulation starting from the governing differential equations is performed in order to solve the fully-coupled problems. The displacement and the temperature are spatially interpolated with the isoparametric finite elements.

$$\begin{Bmatrix} u(x,y;t) \\ v(x,y;t) \end{Bmatrix} = [H_U(x,y)] \{U(t)\}, \quad \begin{Bmatrix} \epsilon_x(x,y;t) \\ \epsilon_y(x,y;t) \\ \gamma_{xy}(x,y;t) \end{Bmatrix} = [B_U(x,y)] \{U(t)\} \quad (12)$$

$$\theta_-(x,y;t) = [H_\theta(x,y)] \{\Theta(t)\}, \quad \begin{Bmatrix} \partial\theta_+/\partial x(x,y;t) \\ \partial\theta_-/\partial y(x,y;t) \end{Bmatrix} = [B_\theta(x,y)] \{\Theta(t)\} \quad (13)$$

The principle of virtual work is applied to the equilibrium state. By using the divergence theorem, the semi-discretized form of the equation of motion can be derived, and then the Newmark integration method is applied to obtain a fully-discretized approximation.

$$\begin{aligned} \left([K_U] + \frac{4}{\Delta t^2} [M_U] \right) \{\Delta U\} &= \{ {}^{t+\Delta t}R_U \} - \{ {}^tF_U \} + [A_\theta] \{\Delta \theta\} + \{\Delta P_U\} \\ &+ [M_U] \left(-\frac{4}{\Delta t} \{ {}^t\dot{U} \} + \{ {}^{t+\Delta t}\dot{U} \} \right) \end{aligned} \quad (14)$$

where

$$[K_U] = \int_{\Omega} [B_U]^T [A]^{-1} [B_U] d\Omega \quad (15)$$

$$[M_U] = \int_{\Omega} \rho [H_U]^T [H_U] d\Omega \quad (16)$$

$$\{R_U\} = \int_{\Omega} [H_U]^T \{\bar{f}\} d\Omega + \int_{\Gamma_F} [H_U]^T \{\bar{t}\} d\Gamma_F \quad (17)$$

$$\{F_U\} = \int_{\Omega} [B_U]^T \{\sigma\} d\Omega \quad (18)$$

$$[A_\theta] = \int_{\Omega} [B_U]^T [A]^{-1} \{\alpha\} [H_\theta] d\Omega \quad (19)$$

$$\{\Delta P_U\} = \int_{\Omega} [B_U]^T [A]^{-1} \{\Delta \varepsilon^p\} d\Omega \quad (20)$$

Next, the Galerkin method is used for the restatement of the energy conservation equation. Through the procedure of finite element discretization with the Crank-Nicolson technique in a time domain, the following is obtained.

$$\left([M_\theta] + \frac{\Delta t}{2} [K_\theta] \right) \{\Delta \theta\} = \{\Delta E_\theta\} + \{\Delta P_\theta\} - \Delta t [K_\theta] \{ {}^t\theta \} \quad (21)$$

where

$$[M_\theta] = \int_{\Omega} \rho c_t [H_\theta]^T [H_\theta] d\Omega \quad (22)$$

$$[K_\theta] = \int_{\Omega} [B_\theta]^T [\chi] [B_\theta] d\Omega \quad (23)$$

$$\{\Delta E_\theta\} = - \int_{\Omega} [H_\theta]^T \{\alpha\}^T [A]^{-1} \{\Delta \tilde{\varepsilon}\} d\Omega \quad (24)$$

$$\{\Delta P_\theta\} = \int_{\Omega} \xi [H_\theta]^T \{\Delta w^p\} d\Omega \quad (25)$$

Computational Algorithm

The resulting equations are nonlinear with fully-coupled terms, therefore, the incremental solutions are obtained iteratively. Because of the numerical stiffness of viscoplastic rate equations, a subincrementing technique is adopted at Gauss integration points. The algorithm for the developed finite element code is as follows :

- (1) Initialize all the variables at $t=0$, and determine Δt .
- (2) Apply the load increment, and start the iteration stage with $i=0$.
- (3) Assemble the matrices in Eqn 14, and solve it.
- (4) Calculate the nonlinear terms in the energy conservation equation.

$$\{ {}^{(i)}\Delta \tilde{\varepsilon} \} = \int_t^{t+\Delta t} \{ {}^{(i)}\theta \} \left(\{ {}^{(i)}\dot{\varepsilon} \} - \{ {}^{(i)}\dot{\varepsilon}^p \} \right) d\tau \quad (26)$$

$$\{ {}^{(i)}\Delta w^p \} = \int_t^{t+\Delta t} \{ {}^{(i)}\sigma \}^T \{ {}^{(i)}\dot{\varepsilon}^p \} d\tau \quad (27)$$

- (5) Assemble the matrices in Eqn 21, and solve it.
- (6) Calculate the nonlinear term in the equation of motion.

$$\{ {}^{(i)}\Delta \varepsilon^p \} = \int_t^{t+\Delta t} \{ {}^{(i)}\dot{\varepsilon}^p \} d\tau \quad (28)$$

- (7) Check the convergence criteria with the relative errors.
- (8) If it converges, update all the variables to the current values. Return to C2.
- (9) If it diverges, increase the iteration index i by one. Return to C3.

NUMERICAL RESULTS AND DISCUSSION

Metal Matrix Composite

The metal matrix composite, SCS-6/Ti-15-3 (silicon-carbide fiber, titanium alloy matrix), is selected as the standard material system in numerical analyses. The material properties are chosen at a high temperature, 815°C [10]. The fiber volume fraction is 0.6, and the unmixing-mixing model has one part of fiber and two parts of matrix. The typical stress-strain curves are shown in Fig.1

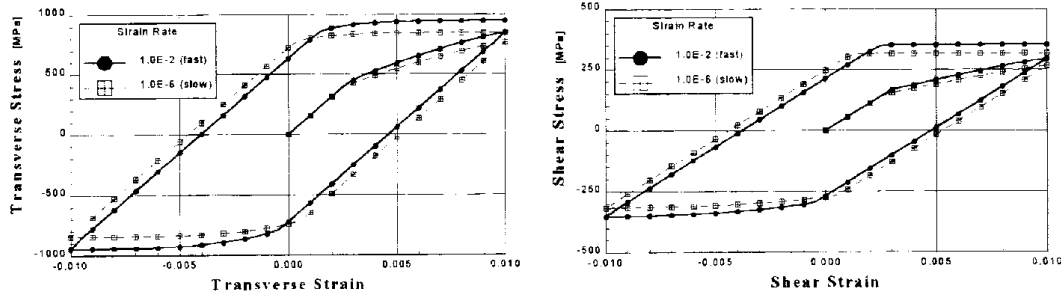


Fig.1: $\sigma_2-\epsilon_2$ and $\tau_{12}-\gamma_{12}$ curves for SCS-6/Ti-15-3

Quasistatic Problems

The initial-boundary value problems are examined for the square laminate in Fig.2. The stacking sequence of the composite laminate is $[0/\pm 45/90]_s$, and the traction load σ is along x -axis. Considering the symmetry, a quarter of the laminate is discretized by triangular elements. The applied traction force is tension, unloading, compression, and unloading (T,U,C,U) during t_c for one cycle, as shown in Fig.3. The traction is successively loaded up to the twentieth cycle. A total of five examples are tested to compare fully-coupled quasistatic solutions, as listed in Table 3.

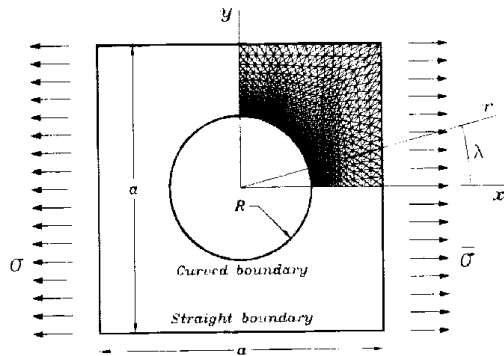


Fig.2: Composite laminate with a hole

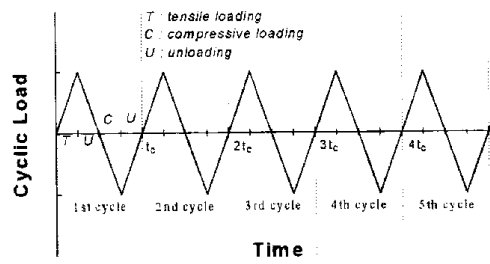


Fig.3: Time history of cyclic loading

Fig.4 is the contours for the developed viscoplastic work during 0~1s in the first cycle of STAT1. The maximum value is predicted at the upper boundary of the hole in the 90° ply. The dissipated viscoplastic work is one measure of the heating effect owing to thermomechanical coupling. Therefore, the coupling effect may become apparent around the upper boundary of the hole.

Table 3: Numerical tests for quasistatic loading

	t_c [s]	σ_{max} [MPa]	a [m]	R [m]
STAT1	4.00	=225	4.00	1.00
STAT2	40.0	=225	4.00	1.00
STAT3	400.	=225	4.00	1.00
STAT4	4.00	=225	0.40	0.10
STAT5	4.00	=225	0.04	0.01

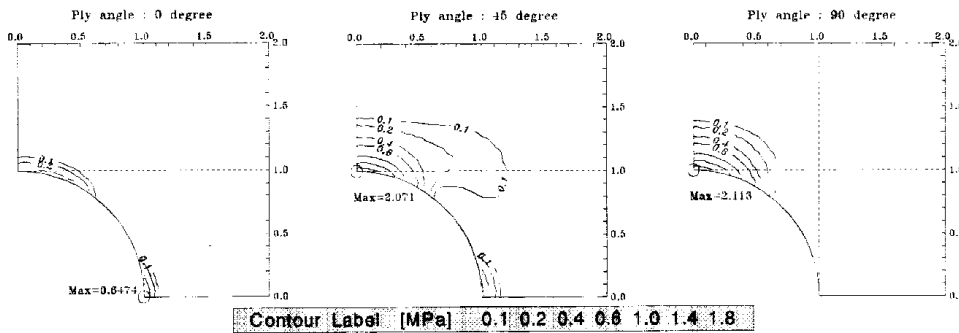


Fig.4: Developed viscoplastic work during 0~1s (1st cycle) - STAT1

To examine the coupling effect, the temperature changes from the base temperature θ_0 are predicted at a boundary point. In Fig.5, the cycle number is a dimensionless parameter of the current time t with reference to t_c . Because the laminates deform viscoplastically around the point, the upper bounds of temperature values increase gradually, except in STAT5.

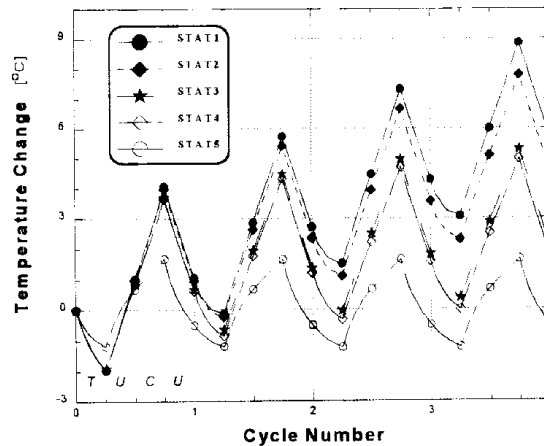


Fig.5: Temperature change vs. cycle number up to the 4th cycle at $(r, \lambda) = (R, 90^\circ)$

Fig.6 shows the distribution of the temperature change along hole boundary. The distribution patterns are obviously different for each problem. They depend mainly on the heat conduction term in the energy equation. If the load is applied at a higher rate, viscoplastic work will be accumulated on a local area with less heat conduction. Therefore, the local heating effect lasts as in STAT1 or STAT2. When the number

of repeated cycles is increased, heating effect will be considerable. In contrast, heating is relatively weak in STAT3 because of slower loading. By drawing a comparison between STAT1, STAT4, and STAT5, it can be seen that the laminate size also plays an important role. For a small laminate, because the thermal energy easily spreads to the surrounding, the coupling effect is almost negligible.

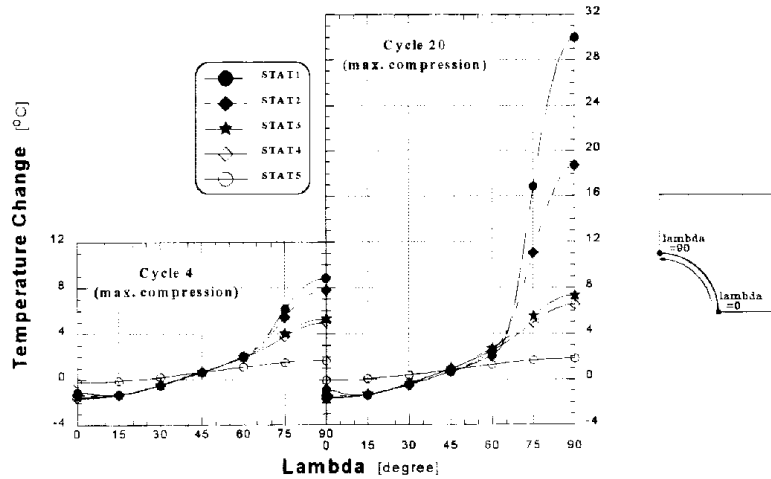


Fig.6: Distribution of temperature change at $t/t_c = 3.75$ and 19.75 .

Dynamic Problems

When t_c has the same order as the fundamental period t_n for the initial elastic state of the laminate, dynamic analyses must be performed including an inertia term. As shown in Fig.7, consider a laminate supported by rigid walls. The thickness is 0.01m and the stacking sequence is $[0/\pm 45/90]_s$. The point force is cyclically applied with the range of $\pm P_{max}$, as shown in Fig.2. The t_n is determined by solving the generalized eigenvalue problem of the free vibration for the elastic deformation. The natural mode shapes for the lowest four modes are shown in Fig.8 with their periods $2\pi/\omega$. The fundamental period is equal to 1.566ms. Two examples in Table 4 are tested. In DYNA1, the load cycle t_c is 7.831ms, five times of t_n .

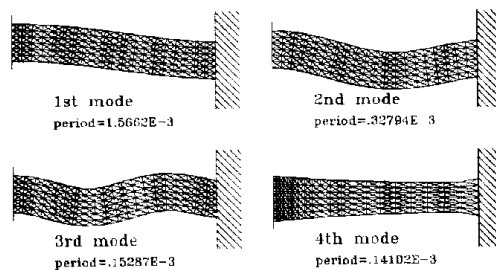
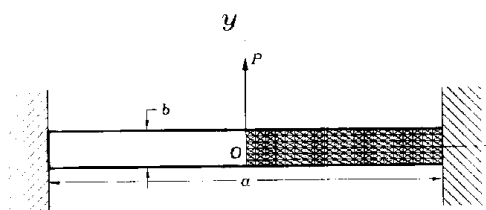


Fig.7: Laminate supported by rigid walls Fig.8: Natural mode shapes and periods

Table 4: Numerical tests for dynamic loading

	t_c [ms]	P_{max} [kN]	a [m]	b [m]
DYNA1	7.831	± 195.8	1.00	0.09
DYNA2	1.566	± 35.24	1.00	0.09

In Fig.9, deflection at the center of the laminate is plotted with the cycle number. In the legend of the figure, T.E. designates thermo-elasticity, and T.E.VP. thermo-elasto-viscoplasticity. The curve of quasistatic(Q) T.E.VP. is also drawn to observe the characteristics of dynamic(D) T.E.VP. The deflection curve of Q.T.E.VP. linearly increases or decreases with constant amplitude, which implies that no viscoplastic deformation occurs. The result of D.T.E. means that the deflection steadily grows owing to the component of the first natural mode. But the curve of D.T.E.VP. is a contrast to these curves. Though the difference between them is not obvious at the initial stage, the difference becomes outstanding after the third cycle as the viscoplastic deformation develops. Note that viscoplastic deformation provides the source of damping in the thermomechanical system, so the range of deflection is confined within about 0.01m.

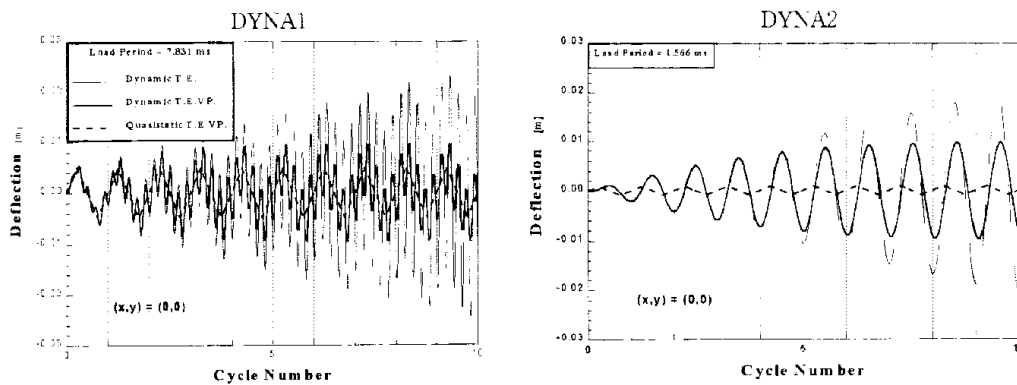


Fig.9: Deflection vs. cycle number up to the 10th cycle

Next the progress of viscoplastic deformation is visualized in Fig.10 and Fig.11. The contour maps are for the viscoplastic work per unit volume. A considerable amount of the irreversible work is developed in the upper and the lower area of the center and the right boundaries, because the normal stress σ_x is large in those regions. The other parts of the laminate deform elastically. The viscoplastic deformation dissipates mechanical energy into thermal energy, so the dynamic motion of the laminate does not diverge.

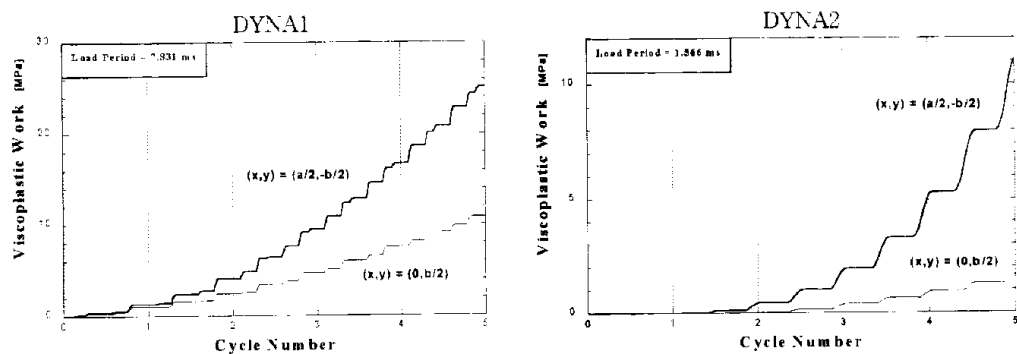


Fig.10: Viscoplastic work vs. cycle number up to the 5th cycle

The response of temperature change due to the coupling effect is shown in Fig.12. The result of D.T.E. shows that the phases of heating and cooling are repeated

proportionally to the deflection without any viscoplastic effect. The heating effect is serious in the D.T.E.VP. case. The maximum temperature change is about 30°C in the tenth cycle. This confirms the fact that, to constrain a divergent motion, viscoplastic work is transformed to thermal energy which is accumulated in the insulated system.

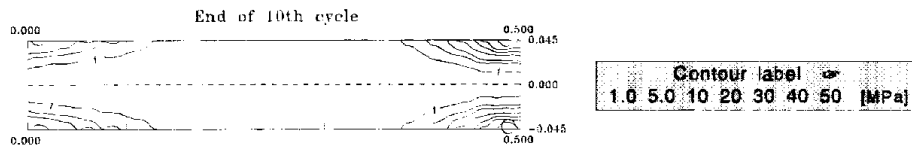


Fig.11: Developed viscoplastic work at $t/t_0 = 10.0$ - DYN A1

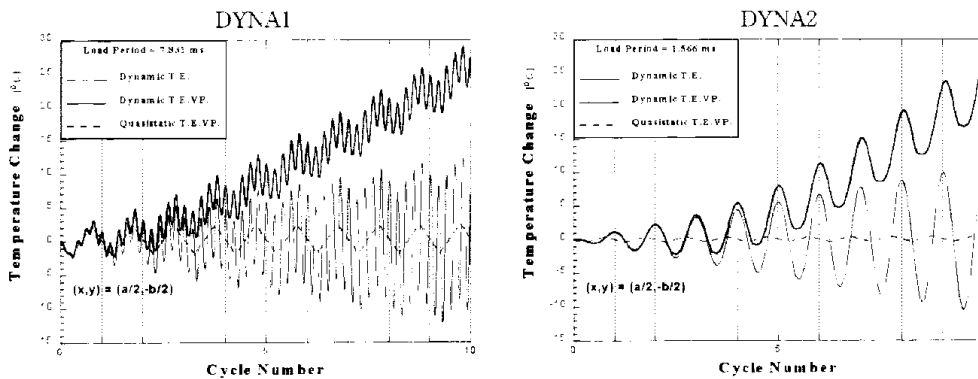


Fig.12: Temperature change vs. cycle number up to the 10th cycle

CONCLUSIONS

Finite element analyses are performed to show the thermo-elasto-viscoplastic behavior of composite materials under fully-coupled thermomechanical situations. As a result, it is concluded that heating effect due to the irreversible viscoplastic work may be significant depending on the repeated cycles, the applied load levels, etc. In quasistatic problems, especially, the thermal conduction in the energy equation can relieve the cyclic heating effect. In dynamic environment, the viscoplastic work dissipates mechanical energy into thermal energy, which plays the role of a damping mechanism. The numerical studies will give guidelines for an analyst whether or not the fully-coupled formulation should be adopted to adequately simulate the behavior of composite materials in a given thermomechanical environment.

REFERENCE

1. *Thermal Structures and Materials for High-Speed Flight*, edited by E. A. Thornton, Vol. 140, Progress in Astronautics and Aeronautics, AIAA, Washington, DC, 1992.
2. Robinson, D. N., and Duffy, S. F., "Continuum Deformation Theory for High-Temperature Metallic Composites," *Journal of Engineering Mechanics*, Vol. 116, No. 4, 1990, pp. 832-844.
3. Gates, T. S., and Sun, C. T., "Elastic/Viscoplastic Constitutive Model for Fiber

- Reinforced Thermoplastic Composites," *AIAA Journal*, Vol. 29, No. 3, 1991, pp. 457-463.
4. Ha, S. K., Wang, Q., and Chang, F. K., "Modeling the Viscoplastic Behavior of Fiber-Reinforced Thermoplastic Matrix Composites at Elevated Temperatures," *Journal of Composite Materials*, Vol. 25, 1991, pp. 334-374.
 5. Dvorak, G. J., and Bahei-El-Din, Y. A., "Plasticity Analysis of Fibrous Composites," *Journal of Applied Mechanics*, Vol. 49, 1982, pp. 327-335.
 6. Aboudi, J., "Micromechanical Analysis of Composites by the Method of Cells," *Applied Mechanics Reviews*, Vol. 42, No. 7, 1989, pp. 193-221.
 7. Kim, S. J., and Shin, E. S., "A Thermoviscoplastic Theory for Composite Materials by Using a Matrix-Partitioned Unmixing-Mixing Scheme," *Journal of Composite Materials*, Vol 30, No. 15, 1996, pp. 1647-1669.
 8. Allen, D. H., "Thermomechanical Coupling in Inelastic Solids," *Applied Mechanics Reviews*, Vol. 44, No. 8, 1991, pp. 361-373.
 9. Odabas, O. R., and Sarigul-Klijn, N., "Thermomechanical Coupling Effects at High Flight Speeds," *AIAA Journal*, Vol. 32, No. 2, 1994, pp. 425-430.
 10. Shin, E. S., Yoon, K. J., and Kim, S. J., "Elasto-Viscoplastic Analysis of Composite Materials Considering Thermomechanical Coupling Effects," AIAA Paper 96-1578, April 1996.

THE FAILURE MECHANISM IN MONOFILAMENT-REINFORCED TITANIUM UNDER AXIAL COMPRESSION

J. E. Spowart and T. W. Clyne

*Department of Materials Science and Metallurgy
Cambridge University, Pembroke Street, Cambridge CB2 3QZ UK*

SUMMARY: Experiments have been carried out in which titanium reinforced with SiC monofilaments has been subjected to compressive loading parallel to the fibre axis. Apparent strengths of about 3 GPa have been obtained. It has been established that extensive matrix plasticity precedes failure during these tests. Calculations and strain gauge measurements suggest that failure may have been precipitated in these tests by inelastic long range buckling of the specimen. This is troublesome in view of the limited availability of material which is sufficiently thick to avoid the problem. Tests were therefore carried out to measure the *in situ* compressive strength of monofilaments located near the compression surface of a beam subjected to bending. Preliminary work has given an upper bound on this strength of about 8-9 GPa. Such stresses would be generated in a typical composite under an applied axial compressive stress of less than 4 GPa. This is much less than predicted strengths obtained using the concept commonly applied to polymer composites that failure occurs by shear yielding of the matrix on planes parallel to the fibre axis. It is therefore proposed that compressive failure of the fibres will often limit the strength of this class of material.

KEYWORDS: MMC, titanium matrix, compressive loading, kinking, buckling

INTRODUCTION

Most models for compressive failure of long-fibre composites focus on shear yielding of the matrix parallel to the fibre axis, which occurs more readily when there is significant misalignment between this direction and the loading axis. Argon[1] proposed that the axial compressive strength of the composite, σ_{c*} , can be expressed as

$$\sigma_{c*} = \frac{k}{\phi} \quad (1)$$

where k is the matrix shear yield stress and ϕ is the angle between the loading axis and the (local) fibre axis. For perfectly aligned fibres ($\phi=0^\circ$), Rosen[2] proposed that the strength should be given by

$$\sigma_{c*} = \frac{G_m}{(1-f)} \quad (2)$$

where G_m is the matrix shear modulus and f is the fibre volume fraction. In effect, these two models were combined by Budiansky and Fleck[3], who proposed that

$$\sigma_{c^*} = \frac{k}{(\gamma_Y (1-f) + \phi)} \quad (3)$$

where $\gamma_Y = k / G_m$. This gives predictions tending to those of Rosen and Argon in the limits of low and high misalignments respectively.

Both the Argon and Budiansky and Fleck models centre on a failure mechanism in which a localised band of rotated fibres forms across the entire specimen width as the surrounding matrix yields in shear, i.e. the formation of a "kink-band". This failure stress will subsequently be referred to as the kinking stress. In contrast, the Rosen limit to compressive strength refers not to localised failure, but to global instability of the entire matrix and fibre assembly, as an alternative to kinking. It should be noted that for any given material, the Rosen limit is usually at least an order of magnitude larger than the kinking stress, unless the misalignment is taken to be extremely small.

EXPERIMENTAL PROCEDURES

Material And Specimen Preparation

The composite material, consisting of 36 vol% SiC monofilament (SM1240) in a matrix of Ti-6Al-4V, was prepared by DRA, using the foil-fibre-foil hot pressing technique[4]. The work described here was carried out using material supplied in the form of 12-ply plate, having a thickness of 2.0 mm. In addition to this composite material, mechanical testing was also carried out on unreinforced material in the form of 2 mm thick rolled sheet. Specimens for metallographic examination and mechanical testing were cut from this plate using electro-discharge machining, followed where appropriate by mechanical polishing.

Characterisation of Fibre Alignment

As reported in a previous publication[5], maximum fibre misalignment values were obtained experimentally using the method of Yurgartis[6]. Briefly, this involves taking accurate metallographic sections at low angles to the specimen loading axis and measuring the aspect ratios of the individual fibre profiles produced. These values were then transformed into angular misalignments with respect to the loading axis. Plotting the individual results on a histogram revealed that there was a spread of misalignments (around zero) of $\Delta\phi = \pm 2.0^\circ$.

Mechanical Testing

Compression testing was carried out on specimens with dimensions of $75 \times 10.0 \times 2.0$ mm and $75 \times 5.0 \times 2.0$ mm. These were cut with the long axis parallel to the edge of the original plate and hence to the nominal axis of fibre alignment. Strain gauge rosettes were attached to the centres of both the large faces, in order to monitor compressive strain, Poisson ratio and specimen bending. The specimens were held in two pairs of hydraulic grips, with a closing force of 30 kN. The grips were machined from low alloy steel, which was then hardened. One of the mating surfaces of each pair had a rectangular recess with dimensions of either

31.5 × 10 × 1.8 mm, or 30.0 × 5 × 1.8 mm, within which the specimen was located, and the other had a flat surface. Thus, the gauge lengths of the 5.0 mm specimens were about 13 mm, and those of the 10.0 mm specimens were about 11.5 mm. These are sufficiently short to avoid full-column elastic Euler buckling. The surfaces of the grips to be in contact with the specimen were all grit blasted to improve the transfer of shear load. Testing was carried out under displacement control, at a strain rate of 3 × 10⁻⁴ s⁻¹.

RESULTS AND DISCUSSION

Elastic and Plastic Deformation

A typical stress-strain plot is shown in Fig.1(a). Data are presented for the axial strain on both sides of the specimen. These coincide closely up until about 7 millistrain, when they slowly bifurcate prior to final failure. Also shown, in Fig.1(b), is a plot of the Poisson ratio against axial strain, for one of the two sides. (The 1, 2 and 3 directions correspond to the fibre axis, the in-plane transverse direction and the through-thickness transverse direction, normal to the plane of the titanium foils.) It can be seen in Fig.1(a) that the specimen experiences macroscopic plastic deformation at compressive strains above about 12 millistrain (1.2%). This is confirmed by the Poisson plot (Fig.1(b)), which shows a noticeable rise, associated with global matrix plasticity, at strains about 10 millistrain (1.0%). Clearly, a significant amount of plastic flow occurs before final failure.

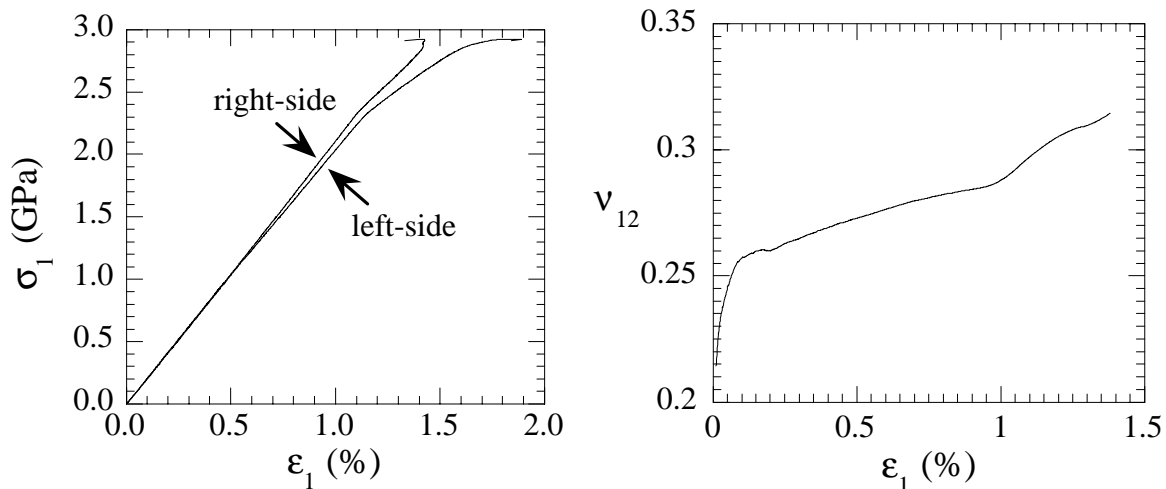


Fig.1: Data from a typical mechanical test. (a) Stress-strain plots, obtained using outputs from the load cell and from the two axial strain gauges on either side of the specimen, and (b) a Poisson plot, using outputs from the axial and transverse strain gauges on one side of the specimen.

Table 1: Measured and calculated elastic constants and yielding / failure data for the composite.

Source	Property	Material		
		Ti-6-4	SiC monofilament	Ti-6-4 / 36% SiC
Measured (av. of 3 tests)	E_1 (GPa)	-	-	211
	ν_{31}	-	-	0.30
	σ_{1AY} (GPa)	0.90	-	2.10
	σ_{1A^*} (GPa)	-	-	2.90
Estimated	ΔT (K)	-	-	-500 [†]
Handbook Data or Calculated (After Li[7])	E_1 (GPa)	115	409	225
	ν_{31}	0.36	0.20	0.30
	G_{21}	42.3	-	63.4
	α_1 (K ⁻¹)	9.0×10^{-6}	4.0×10^{-6}	5.82×10^{-6}
	$\sigma_{1m\Delta T}$ (GPa)	-	-	0.243
	$\sigma_{3m\Delta T}$ (GPa)	-	-	0.083
	$\sigma_{1f\Delta T}$ (GPa)	-	-	-0.430
	σ_{1AY} (GPa)	0.9	-	2.06
	E_T (GPa)	-	-	97.3
	E_T (GPa)	-	-	~130

[†] The actual temperature drop during processing is significantly greater than this, but some creep and plastic flow might be expected during cooling, so that the effective ΔT value represented by the residual stresses is reduced.

Some simple calculations can be made concerning both elastic and plastic regimes. For example, the Eshelby method[8] can be used to calculate the elastic constants and also to treat the onset of plastic flow. This can be done by evaluating the volume-averaged matrix stresses under a given applied stress, taking account of residual thermal stresses, and applying a suitable yield criterion. In the present case, the von Mises criterion was used.

The Eshelby method can also be used to predict the maximum work-hardening rate expected on the basis of load transfer to the fibres after yielding occurs, assuming that the matrix itself does not work-harden, (a reasonable assumption for Ti-6Al-4V). Results from these operations are presented in Table 1. It can be seen that there is good agreement between measured and calculated values for both the elastic constants and for the applied compressive stress at the onset of yielding.

Failure

As previously reported[5], some specimens failed by the formation of a type of kink band, as is consistent with the modelling approach of Argon. However, when the Argon formula for prediction of the failure stress is applied, the agreement with experiment is very poor. This remains true when developments of the approach, such as that of Budiansky & Fleck, are applied. This is illustrated by Fig.2, which shows a plot of failure stress (normalised by the matrix shear yield stress, $k = 0.450$ GPa) as a function of fibre misalignment angle, ϕ . On this plot, various data are shown from previous work on polymer composites, together with results from the current work. It can be seen that, while agreement between theory and experiment

appears good for many polymer composites, the observed strengths are well below those predicted for these MMCs. Indeed, if the Argon predictions were to be fulfilled for this material, even assuming the value of ϕ could be as high as 2° , then the kinking stress would be about 12.9 GPa; it would be very surprising if such high strengths could be achieved. Conversely, the measured compressive strength of about 2.9 GPa corresponds to a ϕ value of about 10° , which is quite inconsistent with microstructural observations.

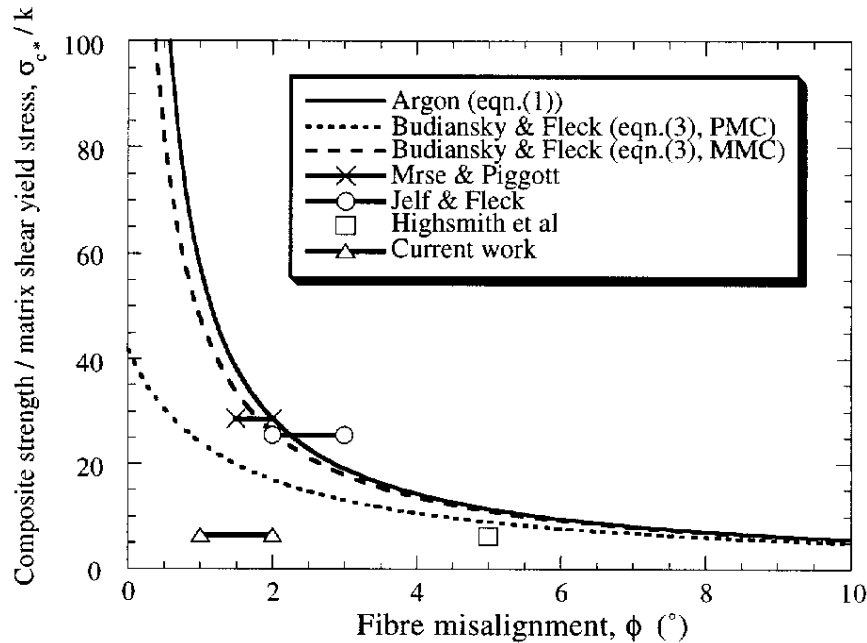


Fig.2: Experimental strength data, as a function of fibre misalignment, from the current work and from previous studies on polymer-based composites[9-11], together with predictions from the Argon[1] (eqn.(1)) and Budiansky & Fleck[3] (eqn.(3)) models. The latter is shown for values of f and $\gamma\gamma$ typical of polymer- and metal-based long fibre composites.

For monofilament-reinforced metals, the high matrix shear yield stress and/or the good fibre alignment elevate the kinking stress above the level at which alternative failure mechanisms are likely to occur. (Note that the Rosen limit for our MMC material is 66.1 GPa, which is quite impossible).

Mechanical tests were also performed on unreinforced (matrix-only) specimens having the same dimensions as the composite. It was found that a form of inelastic buckling failure occurred in all cases. After yielding at around 0.9 GPa, limiting loads of ~ 1.0 GPa were approached, as the specimen became increasingly deformed. Fig.3 shows the longitudinal profile of a matrix-only specimen after loading. (The figure has been foreshortened by a factor of 2.5 in the axial direction in order to accentuate the curvature.) It is evident that considerable plastic deformation has occurred upon buckling.

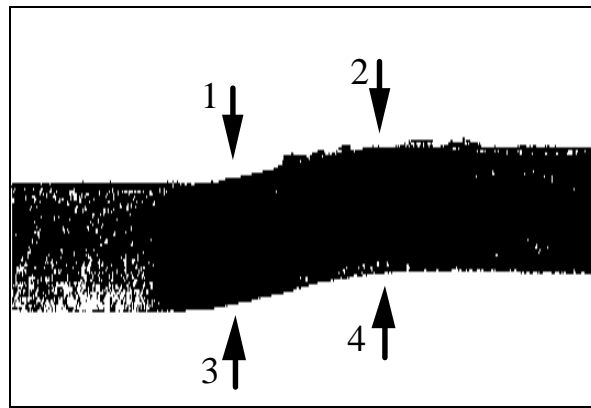


Fig.3: Profile of matrix-only specimen after compressive loading. (Note that this image has been artificially compressed in the loading direction to accentuate the specimen curvature which has occurred.) The numbered arrows refer to the positions of the strain gauges in Fig.4.

In view of this result, it was decided to repeat some of the tests on reinforced specimens, in order to ascertain whether or not they too adopt similarly buckled shapes prior to failure. As the suspected buckling mode would not be detected via gauges placed in the middle of the gauge length, axial strain gauges were placed at the quarter-length points on both sides. Fig.4 shows the axial strains measured at these four points during compressive loading. These strains are indeed consistent with the buckled configuration seen in the unreinforced specimens. It is worth noting that the lateral deflections of the specimen producing these strains would be undetectable by eye.

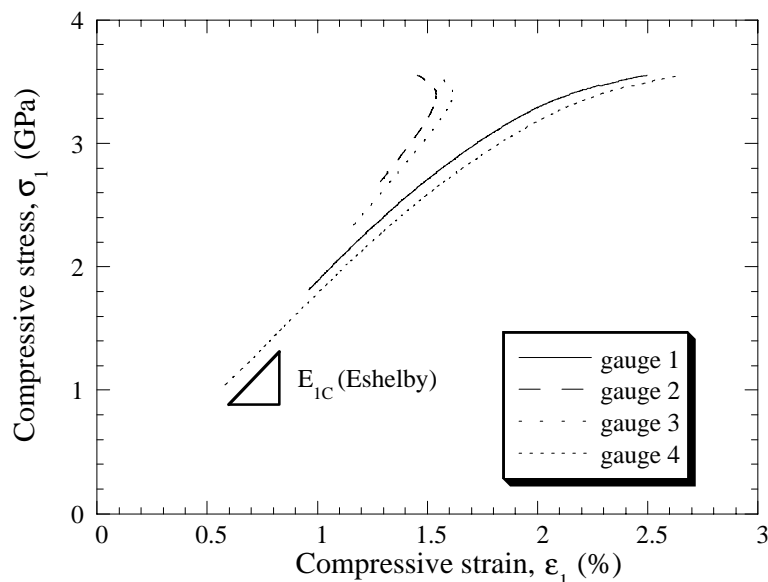


Fig.4: Compressive stress vs. axial strains for 5.0 mm wide specimen, with strain gauges placed at the quarter-length points, on both sides of the specimen. Note that the curvatures at the ends of the gauge length are approximately equal and are in opposite senses.

PREDICTION OF MACROSCOPIC BUCKLING LOADS

Elastic Case

The simplest approach to predicting a macroscopic buckling instability in an axially compressed column is due to Euler[12]. In the fully elastic regime, the buckling load P_c can be related to the gauge length of the sample, the moment of inertia in the plane of buckling (I) and the axial modulus (E).

$$P_c = \frac{C\pi^2 EI}{L^2} \quad (4)$$

where, for a rectangular column, $I = bh^3/12$ and C is a constant related to the degree of clamping provided by the loading fixture. The value of C ranges from 1 (when the clamping is such that the tangents to the curves at the ends of the column are constrained to remain parallel with the loading axis, but the ends themselves may translate sideways during loading) to 4 (where the ends are neither allowed to rotate or translate relative to the loading axis). The buckled profiles of the matrix-only specimens are consistent with the condition corresponding to $C = 1$, as are the strain data for the reinforced specimen.

The elastic buckling stress σ_c^{el} is therefore given by

$$\sigma_c^{el} = \frac{P}{A} = \frac{C\pi^2 EI}{(L/r)^2} = \frac{C\pi^2 E}{s^2} \quad (5)$$

where the radius of gyration is given by $r = \sqrt{I/A}$ and the slenderness ratio by $s = L/r$. The critical slenderness ratio s_c is the value of s below which the fully elastic (Euler) treatment becomes inappropriate, i.e. for $s < s_c$ then $\sigma_Y < \sigma_c^{el}$.

From Eqn.(5), the value of s_c is therefore given by

$$s_c = \sqrt{\frac{\pi^2 C E}{\sigma_Y}} \quad (6)$$

For the present case, using the elastic constants from Table 1, along with the measured composite yield stress (σ_{Yc}) of 2.1 GPa and the most likely clamping condition ($C = 1$), gives $s_c = 30$. These specimens had slenderness ratios varying from 20.0 to 22.5, so it would be expected that inelastic (i.e. plastic) buckling would occur well before elastic buckling. (It follows that reducing the gauge length sufficiently to prevent Euler buckling was inadequate to prevent plastic buckling in this case).

Inelastic Case

A suitable approach to predicting the lowest stress at which an inelastic material will buckle is given by Shanley[13]. In his analysis, the inelastic buckling criterion is very similar to the Euler equation (Eqn.(4)), but with the elastic modulus E replaced by the instantaneous tangent modulus E_T , where E_T is given by $\partial\sigma/\partial\varepsilon$ evaluated at the buckling load. The Shanley formula therefore gives the inelastic buckling stress (σ_c^{in}) as

$$\sigma_c^{\text{in}} = \frac{C\pi^2 ET}{s^2} \quad (7)$$

Values for E_T taken from the literature[7] (data from tensile tests on the same material - see Table 1) were used to calculate σ_c^{in} for various slenderness ratios. These are plotted, along with the elastic (Euler) predictions, in Fig.5.

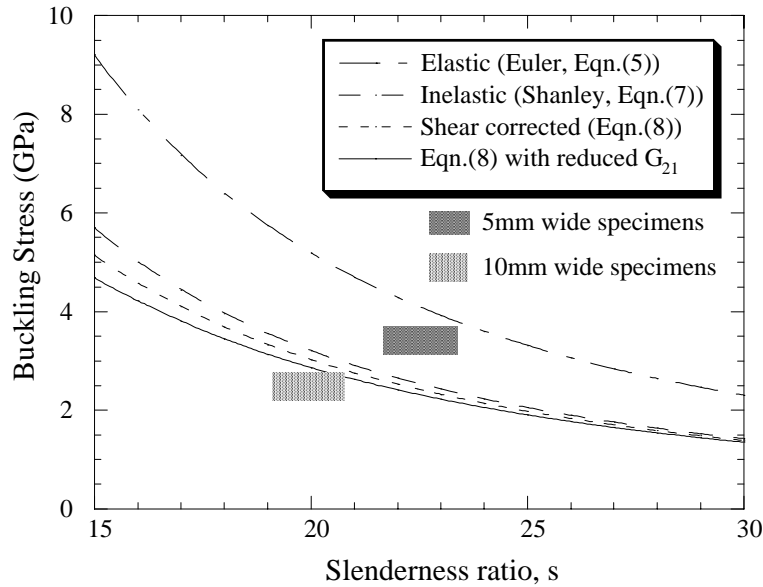


Fig.5: Experimental strength data as a function of slenderness ratio, s with the predictions based on macroscopic specimen buckling, either elastic or inelastic (Eqns.(5), (7) and (8)).

Also plotted on the figure are inelastic buckling predictions that have been corrected for shear deformation, according to Eqn.(8), below[14], where G_{21} has been evaluated using the Eshelby method (see Table 1).

$$\sigma_c^{\text{in,corr}} = \frac{\sigma_c^{\text{in}}}{1 + \frac{1.2 \sigma_c^{\text{in}}}{G_{21}}} \quad (8)$$

Although this is generally a small correction, it becomes significant at low slenderness ratios (i.e. short, stubby beams) and is therefore included for completeness. It may also be argued that, since the axial modulus of the composite approaches E_T with increasing plastic strain, the shear modulus should be reduced (making the correction more significant) so Eqn.(8) is also plotted using a 50% reduced shear modulus as an attempt to incorporate this effect.

Several points can be made regarding this figure.

- (a) Experimental failure strengths are of the same magnitude as predicted inelastic buckling stresses, and are much closer than those predicted on the basis of a fibre kinking mechanism.

- (b) Experimental failure strengths are 36% larger for 5 mm wide specimens, even though they are slightly more slender than 10 mm wide specimens. This may be due to the grips providing less effective clamping at the higher loads attained with wider specimens (i.e. $C < 1$, allowing the specimen ends to rotate).
- (c) Inelastic buckling may be much more important in MMCs than in PMCs due to their more pronounced inelastic behaviour prior to compressive failure. Also, PMC specimens can be produced of sufficiently low slenderness ratios to preclude even inelastic buckling effects.
- (d) Much squatter specimens are required to avoid inelastic buckling in these MMC compression specimens, either through production of thicker section material (which may be prohibitively expensive or technically difficult) or via hotpress diffusion bonding of several as-consolidated panels (which will impose a further heat-treatment on the material).

ALTERNATIVE SPECIMEN GEOMETRY FOR COMPRESSION TESTING

A specimen geometry allowing large axial compressive loads to be imposed on a single layer of reinforcing fibres, without encountering difficulties due to global specimen instability, is one in which the fibres are located on the compression side of a beam. This has been suggested previously for this type of testing[15]. A single fibre layer was consolidated between matrix foils to produce a reinforced "monosheet". This monosheet was then diffusion bonded to a stack of Ti-6Al-4V plates, in order to form a deep beam. This beam was then loaded in 4-point flexure. During the test, axial strains at the surface of the beam were measured by using a strain gauge, as shown in Fig.6. According to the plastic theory of deep beams, it is relatively easy to show[16] that the strains actually experienced by the sub-surface fibres are similar to the measured surface strains, to within a few %. Bending of the fibres is minimised by using a deep beam, with the fibres well away from the neutral axis. In fact, the minimum bend radius to which these fibres were exposed during this test was about 150 mm, which may be compared with a reported value necessary to cause failure of about 10 mm.

The main objective of this testing was to establish the compressive strength of the reinforcing fibres themselves, when they undergo brittle fracture within the plastically deforming matrix. Preliminary tests have been aimed at establishing an upper bound to this strength by extracting fibres from the matrix before and after subjecting the monosheet to a specified compressive strain. Fibres were extracted by using a strong etch of 25 % HF acid in water to dissolve the surrounding matrix. Fig.7 shows such extracted fibres, the loaded specimen in this case having been subjected to a strain of 2%. It is clear that this strain was sufficient to cause extensive compressive failure. The absence of significant damage to the fibres from the unloaded specimen confirms that damage did not arise during material preparation or matrix dissolution.

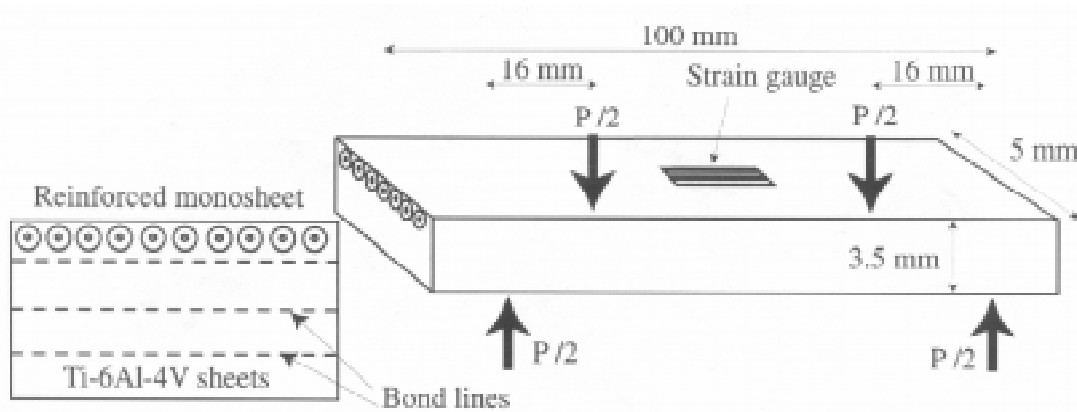


Fig.6: Specimen construction and dimensions for compression testing by flexure.

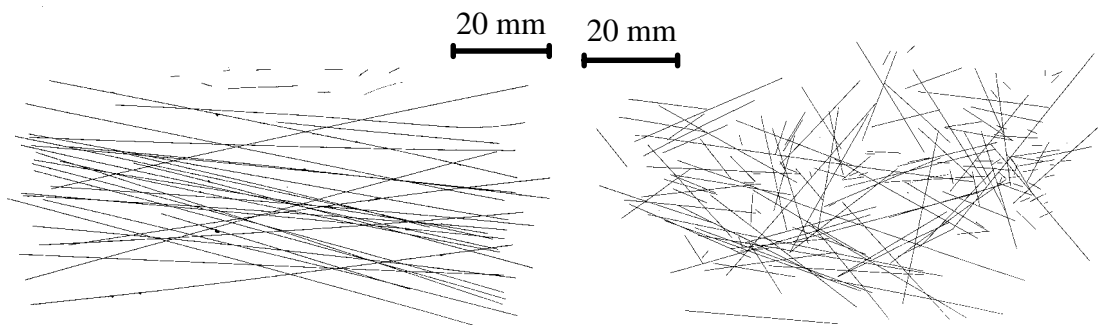


Fig.7: Photographs of extracted fibres from specimens subjected to (a) no loading and (b) bending so that the compressive surface was subjected to a strain of 2.0%.

By completing a series of tests, at different compressive strains, it was found that a strain of 1.6 % was sufficient to promote significant fibre fracture. This corresponds to an applied axial compressive stress of 6.5 GPa. The total axial stress on the fibres is higher than this due to the presence of thermal residual stresses. The axial thermal residual stress was calculated as -1.75 GPa, using $\Delta T = -900$ K from the diffusion bonding temperature and an overall fibre volume fraction of 1.5 %, so that the total axial compressive stress in the fibres was ~ 8.3 GPa. This represents an upper bound on the fibre compressive strength. This figure may be compared with typical *in situ* tensile strengths exhibited by these fibres of about 3-4 GPa.

FIBRE COMPRESSIVE STRENGTH AND FAILURE

Although the fibre compressive strength measured via beam-bending is an upper limit, it is still well below the compressive stress expected in the fibres at the onset of kinking, according to either the Argon or Budiansky and Fleck models. Reading directly from the graph of Fig.2, the kinking stress predicted for the MMC material being studied here is 12.9 GPa. At these stress levels, even assuming elastic load sharing between matrix and fibres, the axial compressive stress in the fibres would be about 23.4 GPa; taking plasticity into account would substantially increase this figure. It therefore seems paradoxical that some of the specimens clearly failed in a manner similar to kinking. However, it seems likely that such features arose after instabilities had been produced by fibre fracture, which allowed gross local plastic deformation of the type seen during kinking.

From a knowledge of the compressive strength of the fibres, is possible to predict the compressive strength of the composite based on a fibre failure criterion. Assuming a fibre compressive failure strain of 1.6 %, the matrix will already be fully plastic at this stage, so a simple equal strain condition can be invoked to predict the failure stress.

$$\sigma_{c*} = f\sigma_{f*} + (1-f)\sigma_{Ym} \quad (9)$$

When appropriate values are inserted into this equation, $\sigma_{c*} \approx 3.6$ GPa is obtained as an upper limit on the composite compressive strength. This is only slightly greater than observed failure values obtained hitherto of about 2.9 GPa., which suggests that the true strength might be measurable by conventional compressive testing of composite material, providing minor steps can be taken to reduce further the danger of inelastic buckling. Further work of this type is required before it can be confirmed that a completely different failure criterion is appropriate for prediction of the compressive strength of such MMCs than has been used hitherto for polymer composites.

CONCLUSIONS

1. MMC material composed of Ti-6Al-4V reinforced with SiC monofilaments has been tested in compression. Apparent failure stresses of about 3 GPa have been obtained.
2. Such strength levels are substantially below those predicted on the basis of established theories of compressive strength, based on failure occurring when the matrix undergoes shear yielding on planes parallel to the fibre axis. Such predictions give rise to extremely high values (>10 GPa) for these materials, as a consequence of the excellent fibre alignment they exhibit and the high matrix yield stress.
3. It has been established that, although the specimen dimensions employed were such as to ensure that elastic (Euler) buckling could not occur, it is probable that failure was initiated by inelastic long range buckling. This is consistent with measurements made during loading which confirmed that matrix plasticity was well developed by the time that failure occurred.
4. While the measured strength values are thus invalid, it is suspected that these composites will not in fact sustain appreciably higher stresses. This postulate is based on preliminary measurements of the compressive failure strength of the monofilaments, undertaken by incorporating them into the compressive face of a beam loaded in bending. These experiments have tentatively established an upper bound on the compressive strength of these monofilaments, when located within this matrix, of about 8.6 GPa. It follows that the composites would fail, by compressive failure of the fibres, at applied stresses of the order of 3.7 GPa.

ACKNOWLEDGEMENTS

Financial support has been provided by the EPSRC, via a CASE award with DRA Farnborough. The authors have benefited from a number of fruitful discussions with and technical assistance from researchers at DRA Farnborough and DRA Sigma, particularly Prof.C.M.Ward-Close, Dr.R.A.Shatwell, Mr.J.Robertson and Mr.A.Wisby. Miss E.Ciechan, of Cambridge University, has provided technical assistance with certain aspects of the work.

REFERENCES

1. A. S. Argon, "Fracture of Composites", Vol. 1, Academic Press, New York, (1972).
2. B. W. Rosen, "Strength of Uniaxial Fibrous Composites", in "Mechanics of Composite Materials", F. W. Wendt, H. Liebowitz and N. Perrone (Eds.), Pergamon Press, Oxford, (1970), pp. 621-651.
3. B. Budiansky and N. A. Fleck, "Compressive Failure of Fibre Composites", *J. Mech. Phys. Sol.*, 41 (1993), pp. 183-211.
4. P. D. Nicolaou, H. R. Piehler and M. A. Kuhni, "Fabrication of Ti-6Al-4V Matrix, SCS-6 Fiber Composites by Hot Pressing Using the Foil-Fibre-Foil Technique", in "Developments in Ceramic and Metal-Matrix Composites", K. Upadhyaya (Ed.), TMS, Warrendale, (1991), pp. 37-47.
5. J. E. Spowart and T. W. Clyne, "Deformation and Failure of Monofilament-Reinforced Titanium under Axial Compressive Loading", *Key Eng. Mats.*, 127-131 (1996), pp. 833-842.
6. S. W. Yurgartis, "Measurement of Small Angle Fiber Misalignments in Continuous Fiber Composites", *Comp. Sci. Tech.*, 30 (1987), pp. 279-293.
7. D. S. Li and M. R. Wisnom, "Unidirectional Tensile Stress-Strain Response of BP-SiC Fiber Reinforced Ti-6Al-4V", *J. Composites Tech. and Res.*, 16(3) (1994), pp. 225-233.
8. T. W. Clyne and P. J. Withers, "An Introduction to Metal Matrix Composites", Cambridge University Press, Cambridge, (1993).
9. P. M. Jelf and N. A. Fleck, "Compression Failure Mechanisms in Unidirectional Composites", *J. Comp. Mats.*, 26 (1992), pp. 2706-2726.
10. A. L. Highsmith, J. J. Davis and K. L. E. Helms, "The Influence of Fiber Waviness on the Compressive Behavior of Unidirectional Continuous Fiber Composites", in "Composite Materials, Testing and Design, ASTM STP 1120", G. C. Grimes (Ed.), ASTM, Philadelphia, (1992), pp. 20-36.
11. A. M. Mrse and M. R. Piggott, "Compressive Properties of Unidirectional Carbon Fibre Laminates: II. The Effects of Unintentional and Intentional Fibre Misalignments", *Comp. Sci. Tech.*, 46 (1993), pp. 219-227.
12. Timoshenko, "History of Strength of Materials", McGraw-Hill, New York, (1953).
13. F. R. Shanley, "Inelastic Column Theory", *J. Aeronaut. Sci.*, 14(5) (1947), pp. 261.
14. S. P. Timoshenko and J. M. Gere, "Theory of Elastic Stability", McGraw-Hill Book Company, New York, (1961), pp. 46.
15. S. J. Deteresa, S. R. Allen, R. J. Farris and R. S. Porter, "Compressive and Torsional Behaviour of Kevlar 49 Fibre", *J. Mat. Sci.*, 19 (1984), pp. 57-72.
16. S. P. Timoshenko and J. M. Gere, "Mechanics of Materials", D. Van Nostrand Company, New York, (1972).

SUPERPLASTIC DEFORMATION MECHANISMS OF SIC WHISKER AND PARTICULATE REINFORCED ALUMINIUM COMPOSITES

K. C. Chan and B. Q. Han

*Department of Manufacturing Engineering
The Hong Kong Polytechnic University, Hung Hom, Kowloon, Hong Kong*

SUMMARY: Although in the past decades there have been many investigations on high-strain-rate superplasticity of discontinuous metal matrix composites, their deformation mechanisms have not yet been fully understood clearly. In the present paper, high-strain-rate superplastic behavior of 6061/SiC_w and 8090/SiC_p aluminum composites was investigated and compared. It was found that a maximum elongation of 440 % was obtained for the 6061/SiC_w aluminium composite at $1.7 \times 10^{-1} \text{ s}^{-1}$ and at 873 K which is just slightly above its solidus temperature. A maximum elongation of 300 % was obtained for the 8090/SiC_p aluminum composite at $1.83 \times 10^{-1} \text{ s}^{-1}$ and at 848 K which is just slightly above its solidus temperature. It was considered that dislocation climb/glide was the major accommodation mechanism for the 6061/SiC_w aluminum composites. However, grain boundary sliding and interfacial sliding accommodated by dislocation movement were the major deformation mechanisms for the 8090/SiC_p aluminum composite. The predictions resulting from the simple theoretical models were shown to be in consistence with the experimental results.

KEYWORDS: superplasticity, metal matrix composites, deformation mechanisms

INTRODUCTION

In the last decade, discontinuously reinforced aluminium based metal matrix composites (MMCs) have been successfully manufactured through powder metallurgy technology. These high performance MMCs are attractive for many structural applications because of their high specific strength and modulus of elasticity. These composites, however, have lower ductility when compared with their monolithic alloys. In recent years, some aluminium-based MMCs of fine equiaxed grained structure were found to be able to behave superplasticity under the conditions of high strain rates and high testing temperatures [1-7]. These findings are important since one of the major drawbacks of conventional superplastic forming technology is that the forming rate is too low. The discovery of superplastic behaviour of some aluminium-based MMCs at high-strain-rates, thus makes these materials to be even more attractive to industry.

There are two common types of commercially available discontinuous reinforced MMCs, i.e. whisker and particulate reinforced composites. Both of them have been observed to behave superplastically. Although there are many investigations on high-strain-rate superplasticity of MMCs, their deformation mechanisms have not yet been fully understood clearly.

EXPERIMENTAL INVESTIGATIONS

A 20vol. % SiC whisker reinforced 6061 aluminium composite and a 17 vol.% SiC particulate reinforced 8090 aluminium composite were examined and compared in this paper. The composites were manufactured by powder metallurgy, and the material were supplied in sheet form having a thickness of 2mm. For the 6061/SiC_w aluminium composite, the size of the reinforcement was 0.45 ~ 0.65 μm in diameter and 5 ~ 80 μm in length, and its solidus temperature was found to be 857K. Whereas, the average particle size and the solidus temperature of the 8090/SiC_p aluminium composite was about 3 μm and 833K respectively.

The relationship between the total elongation-to-failure and the initial strain rate of the composite at different test temperatures for 6061/SiC_w was shown in Fig.1. A maximum elongation of 440 % was obtained at the strain rate of $1.7 \times 10^{-1} \text{ s}^{-1}$ and at 873 K which is just slightly above the solidus temperature of 6061/SiC_w. Similarly, the relationship between the elongation and the initial strain rate of 8090/SiC_p aluminum composite at different test temperatures was shown in Fig.2. A maximum elongation of 300 % was obtained at the strain rate of $1.8 \times 10^{-1} \text{ s}^{-1}$ and at 848 K which is just slightly above the solidus temperature of 8090/SiC_p.

The change of flow stress at true strain of 0.2 with strain rate of the 6061/SiC_w aluminum composite was shown in Fig. 3. The m value in the range of 10^{-2} to 10^0 s^{-1} was about 0.34. The change of flow stress at true strain of 0.2 with strain rate of 8090/SiC_p aluminum composite was shown in Fig. 4. The m value in the range of 10^{-2} to 10^0 s^{-1} was about 0.37 - 0.53.

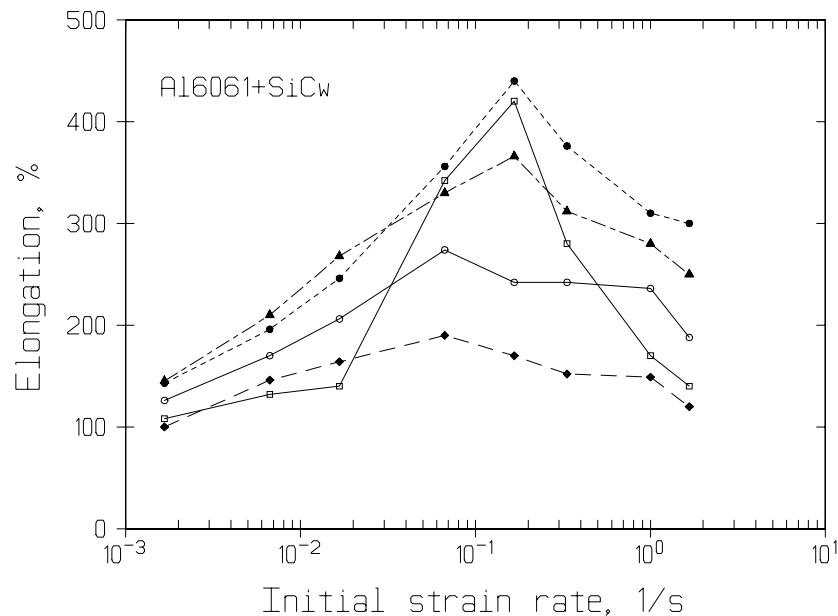


Figure 1. Change of elongation with strain rate at different temperatures for 6061/SiC_p aluminum composite. ●873 K; □883 K;▲ 853 K; ○ 833 K; ◆ 813 K.

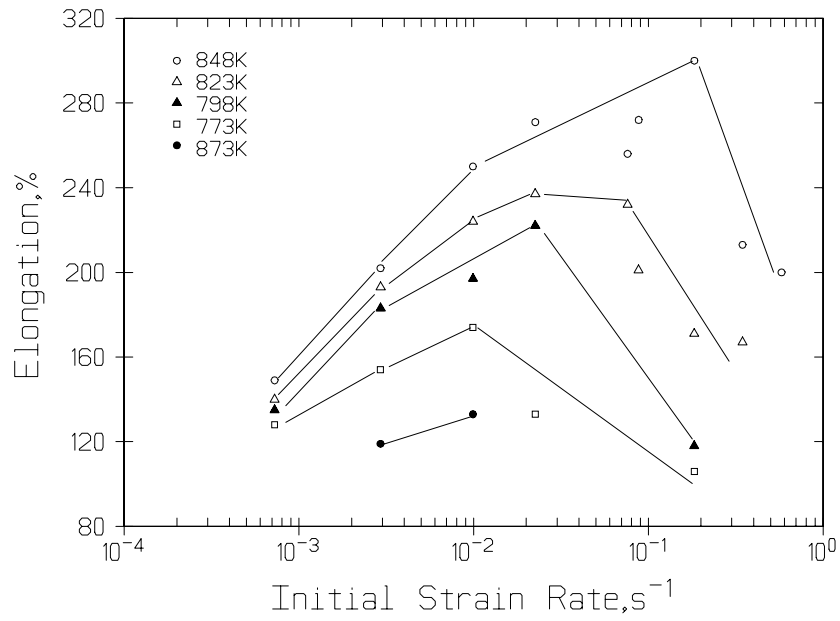


Figure 2. Change of elongation with strain rate at different temperatures for 8090/SiC_p aluminum composites.

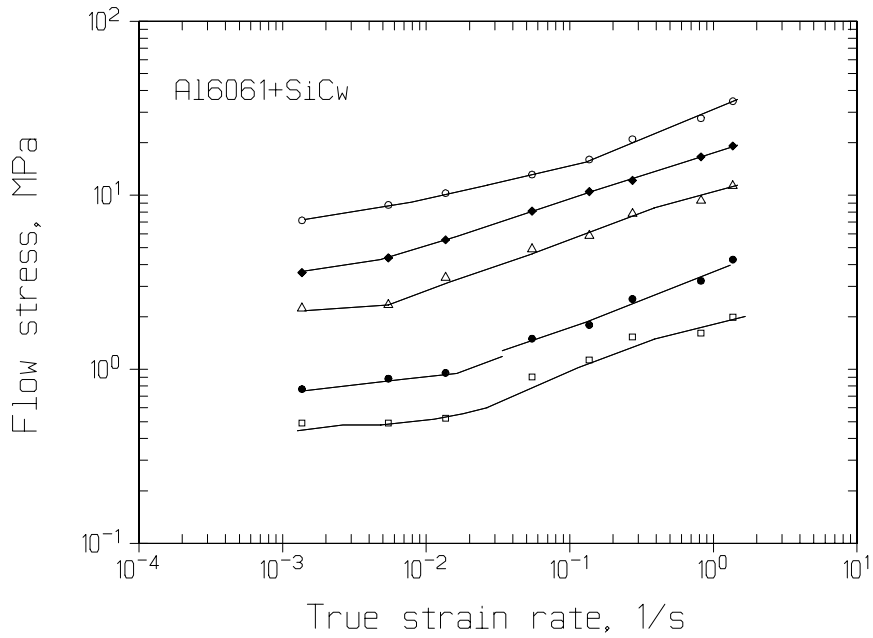


Figure 3. Change of flow stress with strain rate at different temperatures and at true strain = 0.2 for 6061/SiC_p aluminum composite. ○ 813 K; ◆ 833 K; △ 853 K; ● 873 K; □ 883 K.

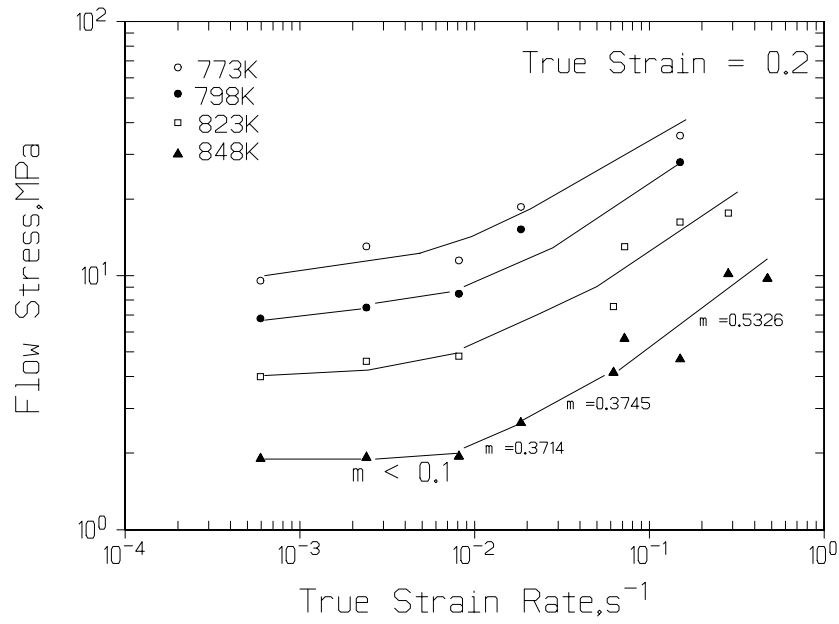


Figure 4. Change of flow stress with strain rate at different temperatures for 8090/SiC_p aluminum composite.

SUPERPLASTIC DEFORMATION MECHANISMS

The strain rate sensitivity, m , was an important indicator of superplastic deformation mechanism. It was argued that when $m = 0.5$, grain boundary sliding and interfacial sliding accommodated by dislocation movement along the grain boundaries would be the major deformation mechanisms for some fine-grained superplastic aluminum composites [8-11]. On the other hand, solute-drag controlled dislocation climb/glide mechanism was considered to be superplastic deformation mechanism for aluminum composites [12] when m is well below 0.5.

In the present study, dislocation climb/glide was assumed to be the major accommodation mechanism for the 6061/SiC_w aluminum composite as m is only 0.34. The constitutive equation [13] for creep under the dislocation climb/glide mechanism could be expressed as:

$$\dot{\epsilon} \approx \beta \gamma^2 (D/b^2)(Gb^3/kT)(\sigma/G)^3 \quad (1)$$

where β was a dimensionless constant, γ was a constant, D was the diffusivity, G is shear modulus, T is absolute temperature, b is Burgers vector, k is Boltzmann's constant.

In order to apply this equation to the high-strain-rate superplastic deformation, the glide velocity v_g , should be expressed as $\beta/(D/h^2)(\sigma b^3/kT)$, where h was the climb distance of dislocation. Moreover, the presence of threshold stress, σ_0 , in the high-strain-rate superplastic deformation of aluminum composites should be considered and the equation (1) could be modified as:

$$\dot{\epsilon} = \alpha \frac{Gb^3}{kTh^2} \exp\left(-\frac{Q}{RT}\right) \left(\frac{\sigma - \sigma_o}{G}\right)^3 \quad (2)$$

where α was a constant whose value depended on microstructural factors and Q was the activation energy of superplastic deformation. The experimental result for the temperature of 853 K which was slightly below the solidus temperature was used to determine the constant α . At this temperature, the threshold stress was 1.2 MPa and the true strain rate was $1.4 \times 10^{-1} \text{ s}^{-1}$ at the flow stress of 5.85 MPa. If h was assumed to be $12b$ [14], α was calculated to be about 6.8462×10^3 . In order to compare the predicted strain rate with the experimental results, the strain rate at the optimum temperature of 873 K which was slightly higher than the solidus temperature was predicted using the equation (2). At this temperature, the threshold stress was 0.22 MPa. If h was assumed to be $5b$ [15], the constitutive relationships relating strain rate and flow stress for the 6061 aluminium composite at the optimum temperature of 873 K is hence given as follows.

$$\dot{\epsilon} = 1.3762 \times 10^{-2} (\sigma - 0.22)^3. \quad (3)$$

For the 8090 aluminium composite, since a relatively high m value of 0.37~0.53 was found in the high-strain-rate range, grain boundary sliding and interfacial sliding accommodated by dislocation movement along the grain boundaries would be the major deformation mechanisms. Recently, the authors have developed a model to predict the high-strain-rate superplastic deformation of aluminium composites based on the deformation mechanisms of grain boundary sliding and interfacial sliding [10]. According to their model, the constitutive equation which describing the stress-strain relationship of superplastic particulate reinforced composite deformed at temperatures slightly above its solidus temperature is expressed as:

$$\dot{\epsilon}_t = \frac{1}{75\sqrt{3}} \left[\left(1 - \frac{1}{p}\right) b D_I + \frac{1}{f} (2p - 1) b D_{GB} \right] \frac{(\sigma - \sigma_o)^2}{kTG} \quad (4)$$

where D_I is interfacial diffusivity, D_{GB} is grain boundary diffusivity, p is the ratio of the matrix grain size to the particle size of the reinforcement and $f = [\pi / (3\sqrt{2} v_r)]^{1/3}$ where v_r is the volume fraction of reinforcement. At the optimum temperature of 848K, the constitutive equation is obtained as follows.

$$\dot{\epsilon} = 3.292 \times 10^{-3} (\sigma - 0.5)^2. \quad (5)$$

Figure 5 shows the comparison between the theoretical prediction and the experimental findings for the composites. The predictions are in consistence with the experimental findings. However, it should be pointed out that the constitutive equation for the 6061 aluminium doesn't take the shape and size of the grain and whiskers into consideration. Moreover the assumed climb distance used in this equation is not so accurate. A more precise model for superplastic whisker reinforced aluminum composites should be worthwhile to develop.

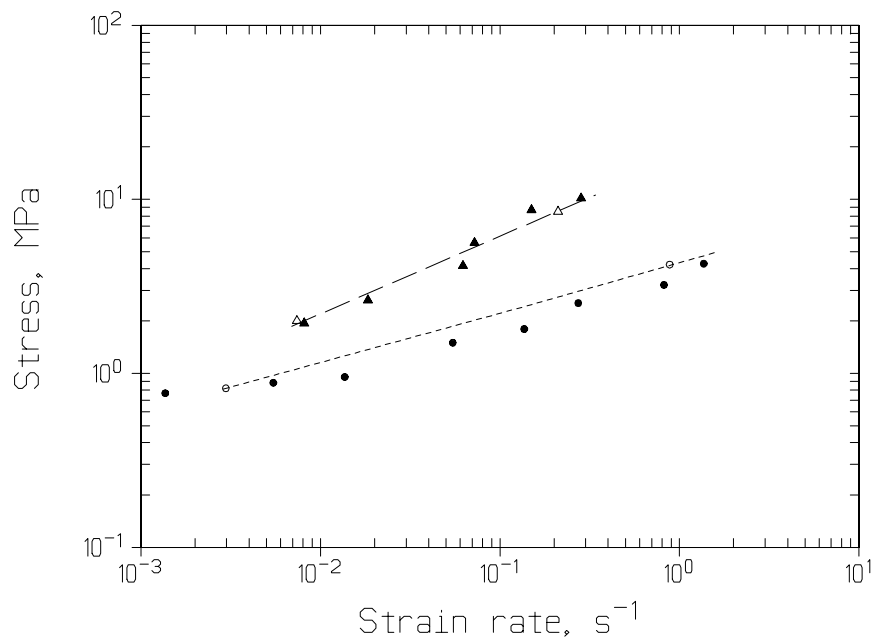


Figure 5. Comparison of the theoretical predictions (\circ 6061/SiC_w; Δ 8090/SiC_p) with experimental findings (\bullet 6061/SiC_w; \blacktriangle 8090/SiC_p).

CONCLUSIONS

High-strain-rate superplasticity of 6061/SiC_w and 8090/SiC_p aluminum composite was investigated and compared. A maximum elongation of 440 % was obtained for the 6061/SiC_w aluminum composite and a maximum elongation of 300 % was obtained for the 8090/SiC_p aluminum composite. The strain rate sensitivity, m , was found to be about 0.34 for 6061/SiC_w and about 0.5 for 8090/SiC_p aluminum composite. Dislocation climb/glide was considered to be the major accommodation mechanism for the 6061/SiC_w aluminum composites and grain boundary sliding and interfacial sliding accommodated by dislocation movement was the major deformation mechanisms for the 8090/SiC_p aluminum composite. The predictions resulting from the simple theoretical models were shown to be in reasonable agreements with the experimental results. However, a more precise model for superplastic whisker reinforced aluminum composites with consideration of whisker size and shape is particularly worthwhile to develop.

REFERENCES

1. T.G.Nieh, C.A.Henshall and J.Wadsworth, *Scri. Metall.* 18, 1405 (1984).
2. T.Imai, M.Mabuchi, Y.Tozawa and M.Yamada, *J. Mater. Sci. Lett.* 9, 255 (1990).
3. M.Mabuchi and T.Imai, *J. Mater. Sci. Lett.* 9, 761 (1990).
4. H.Xiaoxu, L.Qing, C.K.Yao and Y.Mei, *J. Mater. Sci. Lett.* 10, 964 (1991).
5. M.Mabuchi, K.Higashi, K.Inoue, S.Tanimura, T.Imai and K.Kubo, *Mater. Sci. Eng.*, A156, L9 (1992).

6. Chia-Chaw Perny, Jiun-Ren Hwang and Ji-Liang Doong, *Mater. Sci. Eng.*, A171, 213 (1993).
7. H.Iwasaki, M.Takeuchi, T.Mori, M.Mabuchi and K.Higashi, *Scri. Metall. Mater.*, vol.31, No.3, 255 (1994).
8. T.G. Nieh, J. Wadsworth, *Mater. Sci. Eng.*, A147, 129 (1991).
9. R.S. Mishra, T.R. Bieler and A.K. Mukherjee, *Acta Metall. Mater.*, 43(3), 877 (1995).
10. B.Q. Han, K.C. Chan, T.M. Yue and W.S. Lau, *Scr. Metall. Mater.*, 33(6), 925(1995).
11. K.C. Chan, B.Q. Han and T.M. Yue, *Acta Metall. Mater.*, 44(6), 2515 (1996).
12. Sherby, T.G. Nieh and J. Wadsworth, *Mater. Sci. Forum*, 170-172, 13 (1994).
13. J. Weertman and J.R. Weertman, *Constitutive Relations and Their Physical Basis*, 191, edited by S.I.Anderson, J.B.Bilde-Sorensen, N.Hansen, T. Leffers, H. Lilholt, O.B. Perterson, Roskilde, Riso National Laboratory (1987).
14. J. Friedel, *Dislocation*, 104, Pergamon Press (1964).
15. F.R.N. Nabarro, *Theory of Crystal Dislocations*, 683, Dover Publications, INC. (1987).

SUPERPLASTICITY OF CERAMIC PARTICULATE REINFORCED MAGNESIUM ALLOY COMPOSITES FABRICATED BY A MELT STIRRING METHOD

Suk-Won Lim ¹, T. Imai ², Y. Nishida ² and D. Jiang ³

¹ Yeong Dong College, 11 GeumSan-Ri, KangNung-City, KangWon-Do, 210-840, Korea

² National Industrial Research Institute of Nagoya, 1 Hirate-cho, Kita-ku, Nagoya 462, Japan

³ Harbin Institute of Technology, Harbin, 150001, China

SUMMARY: The superplasticity at high strain rate was investigated for the TiC_p/Mg-5wt.%Zn and the AlN_p/Mg-5%Al composites, fabricated by a melt stirring method, extrusion and hot rolling. For the TiC_p/Mg-5wt.%Zn composites with $V_f = 0.20$, a strain rate sensitivity of 0.3 and the total elongation of 300 % were exhibited in a strain rate of $6.7 \times 10^{-2} \text{s}^{-1}$ at 743K. The m value of the AlN_p/Mg-5wt.%Al composites was 0.4 and the maximum total elongation was about 200% in strain rate of 0.5s^{-1} at 673~698K. The fracture surfaces of these composites showed fibrous features, indicating the presence of a kind of glass phase, which was resulted from tensile testing temperature below the solidus temperature of the composites. The presence of a glass phase can apparently enhance the HSRS phenomenon in Mg matrix composites.

KEYWORDS: magnesium matrix composite, high strain rate superplasticity, melt-stirring method, titanium carbide, aluminum nitride

INTRODUCTION

A magnesium matrix composites has a great potential to apply to automobile, aerospace industries since the density of magnesium is low as compared with other metal alloys and the composite is expected to achieve excellent mechanical, physical and thermal properties [1~3]. High Strain Rate Superplasticity (HSRS) is expected to offer the efficiently near-net shape forming method for aluminum matrix composites, since HSRS materials usually exhibit an elongation of 250~600% at a high strain rate of about $0.1 \sim 10 \text{s}^{-1}$ [4~12]. However, superplastic magnesium alloys and magnesium matrix composites developed up to date were Mg-8.5wt.%Li-1wt.%Y, ZK60 and AZ61 which indicate the total elongation of 460~700 % at a lower strain rate of $3 \sim 4 \times 10^{-3} \text{s}^{-1}$ and at a temperature of 453~623K because of their relatively larger grain size of about $35 \mu\text{m}$ [13~17] and Mg-9wt.%Li-5wt.%B₄C with a fine-grain of $2 \mu\text{m}$ prepared by a foil metallurgy can produce superplastic behavior at 423~473K [14]. These Mg alloys and the composite are conventional superplastic materials.

It was found that a SiC_p/ZK60 composite made by PM methods shows an m value of 0.5 and the total elongation of 350% at very high strain rate of about 1.0s^{-1} [16] and that a TiC_p/Mg-5wt.%Zn composite fabricated by a melt stirring method can produce an m value of about 0.3

and the total elongation of 300% at the strain rate of $0.1s^{-1}$ [17]. The results show that it is important to investigate systematically an effect of component of composites such as size and volume fraction of reinforcement, matrix alloys and interfaces between reinforcement and matrix on superplastic characteristics of magnesium matrix composites.

The purpose of this study is to reveal the HSRS in ceramic particulate reinforced Mg alloy composite fabricated by a melt stirring method. In addition, the superplastic deformation mechanism of the Mg matrix composite will be discussed.

EXPERIMENTAL PROCEDURES

TiC (average particle size of 2-5 μ m) and AlN (that of 0.72 μ m) particles were used as reinforcement. Molten magnesium alloy heated at 973K was stirred with pre-heated TiC and AlN particles in a magnesia crucible under argon atmosphere by using a melt stirring method. The volume fraction (V_f) of TiC particle was 0.10 and 0.20. In the case of $V_f=0.10$, the stirring was performed for about 350 seconds and in the case of $V_f=0.20$, the stirring time was about 450 seconds. The stirring time was about 420 seconds and the V_f was 0.15 for AlN particle. The as-cast composite was further solidified in permanent mould. Table 1 and 2 show chemical composition of magnesium alloy matrix and ceramic particles.

Table 1 Chemical compositions of magnesium, aluminum and zinc (wt.%)

	Mg	Al	Cu	Mn	Pb	Zn	Fe	Si
Mg	99.96	0.003	0.001	0.006	----	----	0.006	0.003
Al	----	99.99	0.001	----	----	----	0.002	----
Zn	----	tr.	----	----	0.002	99.99	tr.	----

Table 2 Chemical compositions of AlN and TiC particles

	Fe	Si	Cu	Mn	Mg	Zn	Ni	Cr	O	N	Na	TiC
AlN	ppm 22	ppm 26	ppm 7	ppm 3	ppm 2	ppm 2	ppm 2	ppm 2	wt.% 0.99	wt.% 33.4		
TiC	wt.% 0.1							wt.% 0.03		wt.% 0.008		wt.% 99.46

Hot extrusion and hot rolling were used to produce the HSRS composite. The hot extrusion was performed at an extrusion ratio of 44 at a temperature of 673K. Subsequent hot rolling was carried out at 698K. Thickness reduction per each pass was less than 0.1 and the reheating time between each rolling pass was about 5 minutes. The final thickness of the hot-rolled composite was less than 0.75mm. Tensile specimens with a 4mm gage width and a 5.5mm gage length were made. Specimens were deformed at 673, 698, 723 and 743K in strain

rates ranging from 1×10^{-4} to 2 s^{-1} . Microstructure and fracture surface of the samples were examined by SEM and TEM.

EXPERIMENTAL RESULTS AND DISCUSSION

Figures 1 show the SEM microstructures of TiC_p/Mg alloy composites fabricated by (a) melt stirring, (b) melt stirring and extruding and (c) melt stirring and extruding, further hot-rolling (denoted by hot-rolled, hereafter), respectively. Although reinforcement-free magnesium layer and TiC particulate agglomerate are present in as-cast composite(a) and in the even as-extruded(b), TiC particles were noted to be dispersed homogeneously in the hot-rolled composite(c) and defects were removed.

HSRS of TiC_p/Mg -5wt.%Zn composite

The flow stress, σ , relates to true strain rate, $\dot{\epsilon}$, via the equation $\sigma = k \dot{\epsilon}^m$. In the equation, the strain rate sensitivity exponent, m , is the slope of the curve $(\text{dln } \sigma / \text{dln } \dot{\epsilon})$, where k is a constant incorporating structure and temperature dependencies. Normally, the m value must be larger than 0.3 in order to observe superplasticity in a material. A high m value material can suppress the development of necking and leads to a high total elongation.

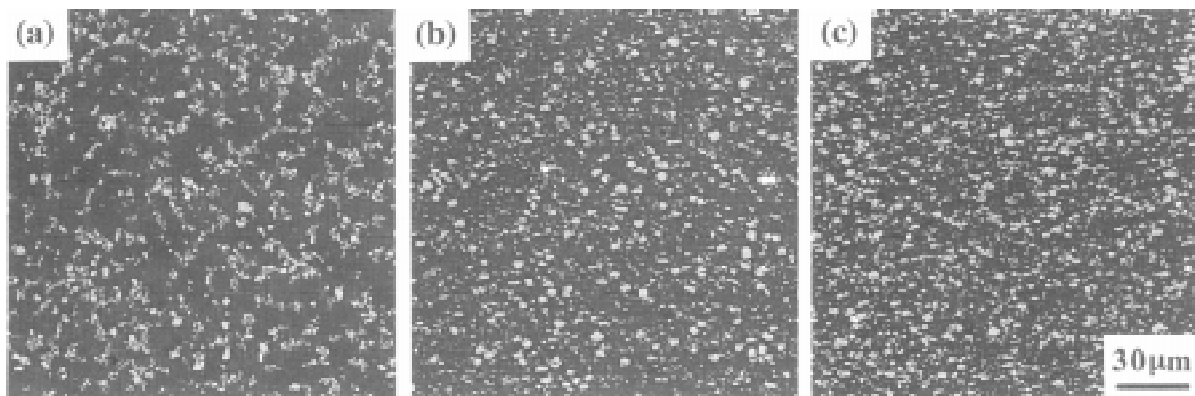


Fig.1 SEM microstructures of TiC_p/Mg -5wt.%Zn composite fabricated by (a) melt stirring, (b) melt stirring and extruding and (c) hot-rolling and extruding after melt stirring.

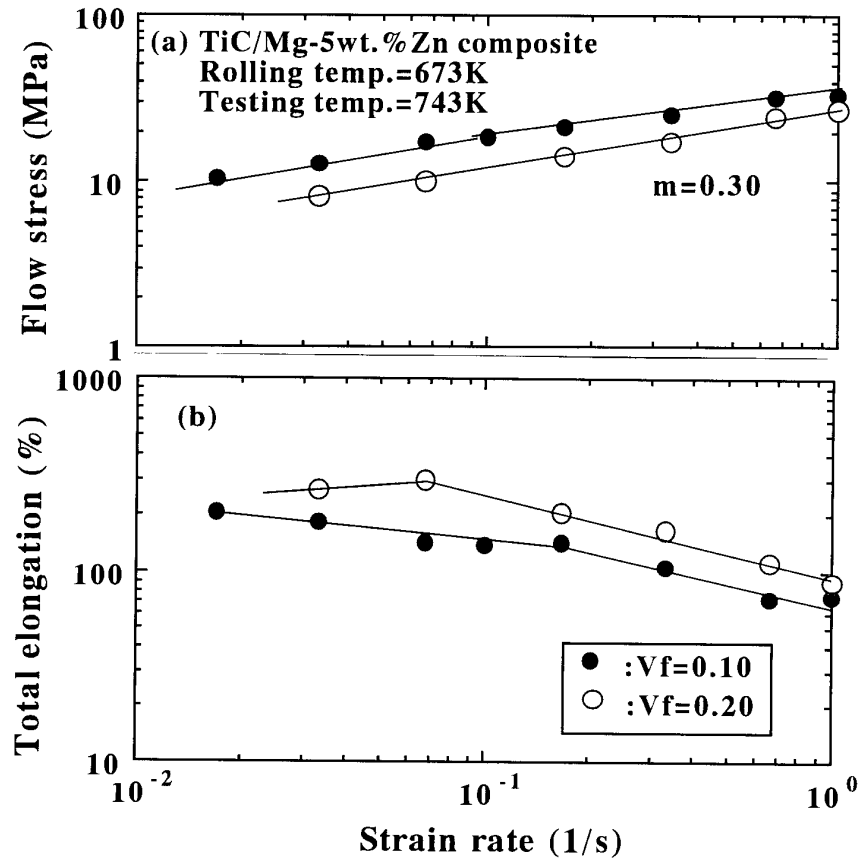


Fig. 2 . Relationships (a) between the flow stress and the strain rate and (b) between the total elongation and the strain rate of $TiC_p/Mg-5wt.\%Zn$ composite melt stirred, extruded and hot-rolled.

The relationship between the flow stress and the strain rate of the hot-rolled $TiC_p/Mg-5wt.\%Zn$ composites with volume fractions of $V_f=0.10$ and 0.20 is shown in Fig.2(a). The flow stress of the both composites increases linearly with increasing strain rate. The strain rate sensitivity value of the composite with $V_f=0.20$, m , is about 0.43 at $743K$ and in strain rate range from 0.067 up to $0.33s^{-1}$, but the m value of the composite with $V_f=0.10$ is about 0.33 in strain rate range from 0.017 up to $0.167s^{-1}$. This result is in agreement with the HSRS observations in ceramic whisker or particulate reinforced aluminum alloy composites [4~7].

Total elongation of the $TiC_p/Mg-5wt.\%Zn$ composite as a function of strain rate is shown in Fig.2(b). A maximum total elongation of about 300% was obtained at the strain rates of $0.067s^{-1}$. At strain rates greater than $0.17s^{-1}$, the elongation value begin to decrease, despite the fact that the m value remains high (see Fig. 2(a)). It is attributed to excessive cavitation in test samples deformed under extremely-high strain rate.

Generally, a total elongation of over 100% can be obtained in a wide strain rate region from $0.01s^{-1}$ up to $0.7s^{-1}$. The results suggest that casting defects in the $TiC_p/Mg-5wt.\%Zn$ composite fabricated by melt stirring method can be removed by extrusion and hot rolling. In particular, these thermomechanical processes are very effectively in dispersing TiC particle and to produce homogeneous microstructure. The reason that the maximum elongation value does not coincide with the maximum m value.

Superplastic Characteristics of Mg-5wt.%Al Alloy

The relationship between the flow stress and the strain rate of the hot-rolled Mg-5wt.%Al alloy is shown in Fig.3(a) as a function of temperature. The logarithmic flow stress of the Mg-5wt.%Al alloy increases approximately with increasing logarithmic strain rate and decreasing temperature. The strain rate sensitivity value of the Mg-5wt.%Al alloy is about 0.25 at 673~723K in strain rates range from 2.0×10^{-4} to 0.6 s^{-1} . And the Mg-5wt.%Al alloy does not have threshold stress in strain rate range from 2.0×10^{-4} to 1.5 s^{-1} .

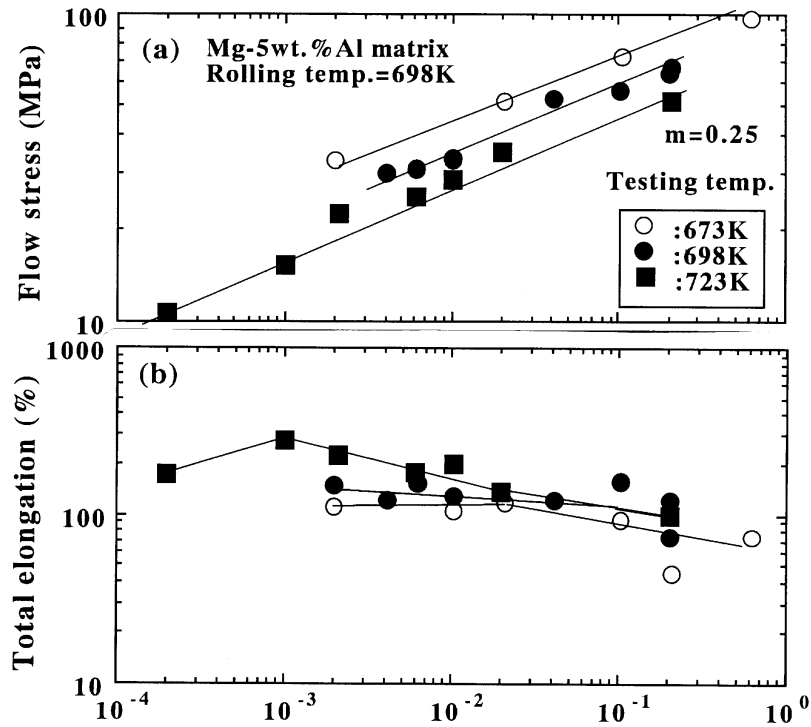


Fig.3 Superplastic characteristics of Mg-5wt.%Al alloy fabricated by a melt stirring method before extruding and hot-rolling.

Total elongation of the Mg-5wt.%Al alloy is shown in Fig.3(b) as a function of temperature. The total elongation at 673K and 698K becomes less than 150% in the strain rate range from 2.0×10^{-3} to $2.0 \times 10^{-1} \text{ s}^{-1}$, but the elongation at 723K increases more than 150% in the strain rate range from 2×10^{-4} to $2 \times 10^{-1} \text{ s}^{-1}$. Maximum total elongation of about 300% in the Mg-5wt.%Al alloy is obtained in the strain rate of $1 \times 10^{-3} \text{ s}^{-1}$ at 723K. Therefore, the results indicate that the Mg-5wt.%Al alloy alone is a conventional superplastic alloy.

HSRS of AlN_p/Mg-5wt.%Al Composite

The relationship between the flow stress and the strain rate of AlN_p/Mg-5wt.%Al composite hot-rolled after extrusion is shown in Fig.4(a). The flow stress of the composite increases with increasing strain rate and decreasing temperature. The *m* value of the composite becomes less than 0.1 in strain rate range less than 0.1 s^{-1} , which means that the composite has a threshold stress in the relatively lower strain rate range. However, the *m* value of the composite increases to 0.39~0.43 in the strain rate from about 0.1 s^{-1} to 1.5 s^{-1} at 673~698K. These high *m* values reveal that the AlN_p/Mg-5wt.%Al composite can produce the HSRS in the higher strain rate

range, but the m value of the composite deformed at 723K decreases to 0.18 in the same strain rate range.

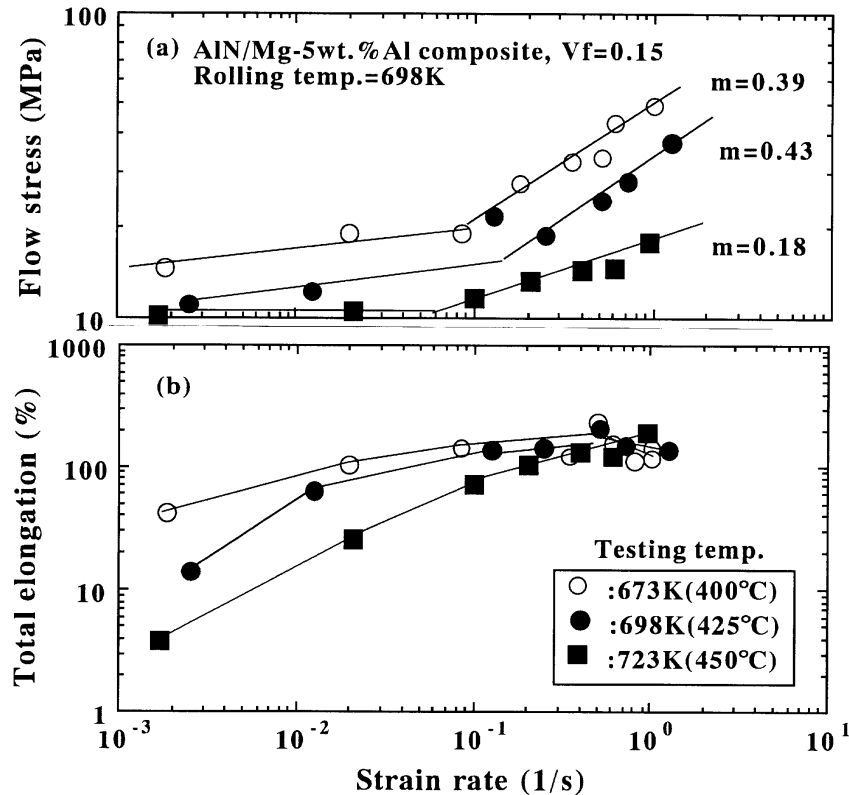


Fig. 4 Superplastic characteristics of the AlN_p/Mg-5wt.%Al composite fabricated by a melt stirring method before extruding and hot-rolling.

The maximum total elongation of more than 200% is obtained in the composite in a high strain rate of about 0.5s^{-1} at 673~698K as shown in Fig.4(b). By comparison, the composite deformed at 723K shows the maximum total elongation of about 200% at a higher strain rate of 1.2s^{-1} . At relatively lower strain rates less than 0.1s^{-1} , the total elongation begins to decrease in temperature range of 673~723K, which is coincident with the fact that the m value is very low. The decrease of elongation in the relatively lower strain rate range might be attributed to excessive cavitation during high strain rate deformation[13]. Nonetheless, a total elongation of over 100% can generally be obtained in a wide strain rate range (0.02s^{-1} to 1.2s^{-1}). The results suggest that hot rolling after extrusion can effectively produce homogeneous microstructure in the AlN_p/Mg-5wt.%Al composite and leads to HSRS, and it is noted that the optimum strain rate of about $0.5\sim 1.0\text{s}^{-1}$ for the AlN_p/Mg-5wt.%Al composite is higher by 10 times than that in the TiC_p/Mg-5wt.%Zn composite and it is thought that the result is caused by fine AlN particle size of $0.72\mu\text{m}$.

Microstructure

The TEM microstructures of the AlN_p/Mg-5wt.%Al composite hot-rolled is shown in Fig.5. The grain size of the composite before test and after superplastic deformation is less than about $2\mu\text{m}$ and fine AlN particle is dispersed homogeneously along grain boundaries so as to retain grain growth during hot rolling, heating and superplastic deformation. Therefore, it is

thought that primary deformation mechanism of the HSRS for the AlN_p/Mg-5wt.%Al composite is grain boundary sliding.

Fig.6 shows relationship between total elongation and strain rate for the TiC_p/Mg-5wt.%Zn with TiC volume fraction of 0.10, 0.20[17] and the AlN_p/Mg-5wt.%Al composites and the Mg-5wt.%Al matrix made by a melt stirring method and for the SiC_p/ZK60 PM composite[16]. Arrows with the numbers of (1)~(5) in Fig.6 indicates optimum strain rate of the superplastic materials at which maximum total elongation is obtained. The TiC_p/Mg-5wt.%Zn composite with $V_f=0.20$ has the grain size of about 2 μm [17] and matrix of the SiC_p/ZK60 PM composite consists of grains with 0.5 μm [16] and the AlN_p/Mg-5wt.%Al composite includes the grain size of less than 2 μm but the grain size of the Mg-5wt.%Al alone becomes more than 20 μm . The optimum strain rate in Fig.6 is arranged in order of SiC_p/ZK60 > AlN_p/Mg-5%Al > TiC_p/Mg-5%Zn ($V_f=0.20$) > TiC_p/Mg-5%Zn ($V_f=0.10$) > Mg-5%Al alone. Therefore, the results reveal that optimum strain rate at which maximum total elongation is obtained in magnesium matrix composites is associated with grain size.

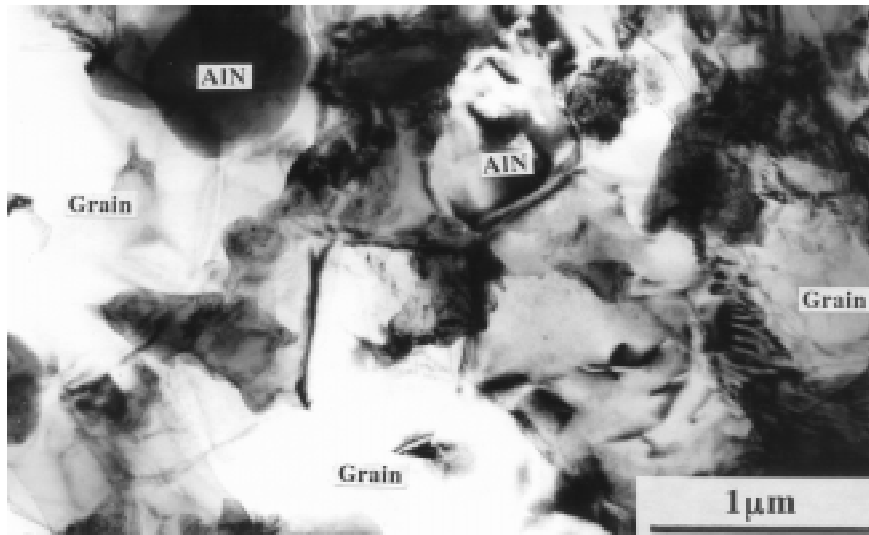


Fig.5 TEM microstructures of AlN_p/Mg-5wt.%Al composite hot-rolled.

CONCLUSIONS

The superplastic characteristics of Mg-5wt.%Al matrix, TiC_p/Mg-5wt.%Zn and AlN_p/Mg-5wt.%Al composites, fabricated by a melt stirring method, extrusion and hot-rolling were investigated. The following results were obtained

- (1) Mg-5wt.%Al alloy indicates a m value of about 0.25 and the total elongation of about 300% was obtained in low strain rate of 10^{-3}s^{-1} at 723K.
- (2) The composite had a threshold stress in strain rate range lower than 0.1s^{-1} , although the flow stress of Mg-5wt.%Al alloy decreased simply with decreasing strain rate.
- (3) The strain rate sensitivity (m value) of the AlN_p/Mg-5wt.%Al composites is about 0.40 in strain rate range higher than 0.1s^{-1} and the composite hot-rolled after extrusion exhibited a total elongation of about 200% in strain rate of 0.5s^{-1} at 673~698K.
- (4) The m value of the TiC_p/Mg-5wt.%Zn composites with $V_f=0.20$ is about 0.33 and the total elongation of about 300% was obtained in strain rate of 0.067s^{-1} at 743K.

- (5) The composites have a fine grain size of about $2\mu\text{m}$ since TiC and AlN particles were dispersed homogeneously along grain boundaries so as to avoid grain growth during superplastic deformation.
- (6) The fracture surface of the composites showed fibrous features and a presence of glass phase which is resulted from excessive sliding in TiC particle-Mg and AlN particle-Mg matrix alloy interfaces.

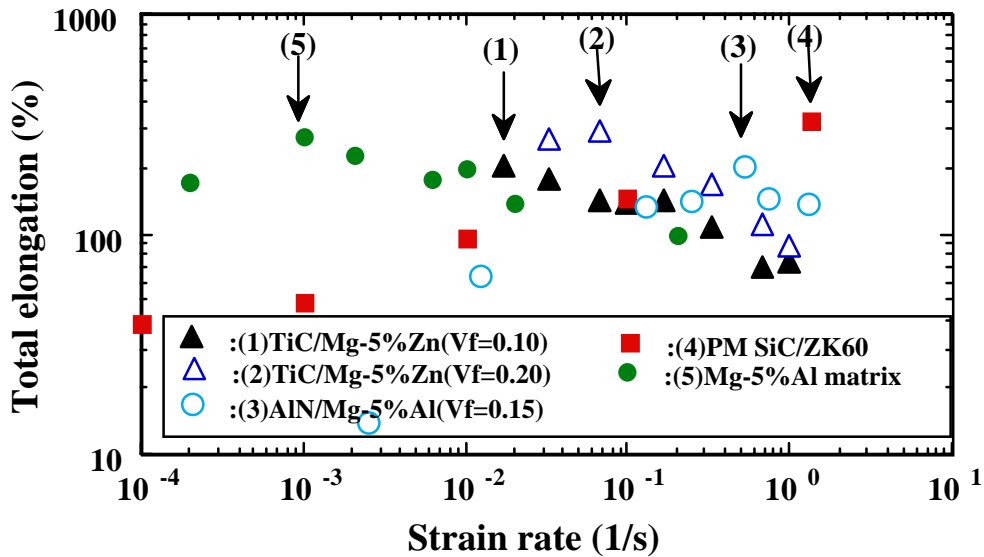


Fig. 6 Relationships between the total elongation and the strain rate of TiC_p/Mg-5wt.%Zn((1), (2)), AlN_p/Mg-5wt.%Al(3), PM SiC_p/ZK60(4) composites and Mg-5wt.%Al matrix(5).

REFERENCES

1. B.A.Mikucki, "Heat Treatment of Magnesium-Zinc Alloy Reinforced with Silicon Carbide Particulate", *Fundamental Relationships Between Microstructure & Mechanical Properties of Metal-Matrix Composites*, Edited by P.K.Liaw and M.N.Gungor, 1990, pp.715-726.
2. B.A.Mikucki, W.E.Mercer 2 and W.G.Green, "Extruded Magnesium Alloys Reinforced with Ceramic Particles", *SAE Technical Paper 900533*, International Congress and Exposition, Detroit, Michigan, February 26-March 2, 1990, pp.1-9.
3. V.Laurent, P.Jarry, G.Regazzoni and D.Apelian, "Processing-Microstructure Relationships in Compocast Magnesium/SiC", *J.Mater.Sci.*, Vol.27, No.16, 1992, pp.4447-4459.
4. T.Imai, M.Mabuchi, Y.Tozawa and M.Yamada, "Superplasticity in β -Silicon Nitride Whisker Reinforced 2124 Aluminum Composite", *J.Mater.Sci.Lett.*, Vol.9, No.9, 1990, pp.255-257.
5. M.Mabuchi, T.Imai, K.Kubo, H.Higashi, Y.Okada and S.Tanimura, "Superplasticity in As-Extruded Si₃N_{4w}/6061 Aluminum Composites Processed at a Ratio of 100:1", *Mater.Lett.*, Vol.11, No.10,11,12, 1991, pp.339-342.

6. T.Imai, G.L'Esperance and B.D.Hong, "High Strain Rate Superplasticity of AlN Particulate Reinforced Aluminum Alloy Composites", *Scripta Metall. Mater.*, Vol.31, No.3, 1994, pp.321-326.
7. T.Imai, G.L'Esperance, B.D.Hong and J.Kusui, "High Strain Rate Superplasticity of AlN and TiC Particulate Reinforced Aluminum Alloys", *Proceedings Sixth International Conference on Composite Materials*, Edited by A.R.Bunsell, A.K.Kelly & A.Massianh, Woodhead Publishing Limited, 1993, pp.533-538.
8. T.G.Nieh, T.Imai, J.Wadsworth and S.Kojima, "High Strain Rate Superplasticity of a Powder Metallurgy SiC Particulate Reinforced 6061 Al Composite", *Scripta Metall. Mater.*, Vol.31, No.12, 1994, pp.1685-1690.
9. T.Imai, G.L'Esperance, B.D.Hong and S.Kojima, "High Strain Rate Superplasticity of AlN Particulate Reinforced IN90 Pure Aluminum Composite", *Scripta Metall. Mater.*, Vol.31, No.8, 1995, pp.1333-1338.
10. H.Xiaoxu, L.Qing, C.K.Yao and Y.Mei, "Superplasticity in a SiC_w-6061 Al Composite", *J. Mater. Sci. Lett.*, Vol.10, No.16, 1991, pp.964-966.
11. M.Kon, J.Kaneko and M.Sugamata, "Superplastic Deformation of SiC Whisker Reinforced Aluminum Alloy Composites", *J. Japan STP*, Vol.35, No.402, 1994, pp.823-828.
12. T.Hikosaka, T.Imai, T.G.Nieh and J.Wadsworth, "High Strain Rate Superplasticity of a SiC Particulate Reinforced Aluminum Alloy Composite by a Vortex Method", *Scripta Metall. Mater.*, Vol.31, No.9, 1994, pp.1181-1186.
13. M.M.Tilman, R.L.Crosby and L.A.Neumeier, "Superplasticity in Selected Magnesium-Base Alloys", *Bureau of Mines Report of Investigations* 8382, 1979.
14. J.Wolfenstine, G.Gonzalez-Doncel and O.D.Sherby, "Tension versus Compression Superplastic Behavior of a Mg-9wt%Li-5wt%B₄C Composite", *Mater. Lett.*, Vol.15, No.4, 1992, pp.305-308.
15. P.Metenier, G.Gonzalez-Doncel, O.A.Ruano, J.Wolfenstine and O.D.Sherby, "Superplastic Behavior of a Fine-Grained Two-Phase Mg-9wt.%Li Alloy", *Mater. Sci. Eng.*, Vol.A125, 1990, pp.195-202.
16. T.G.Nieh, A.J.Schwartz and J.Wadsworth, "Superplasticity in a 17vol.% SiC Particulate Reinforced ZK60A Magnesium Composite", *Mater. Sci. Eng.*, Vol.A208, 1996, pp.30-36.
17. S.W.Lim, T.Imai, Y.Nishida and T.Choh, "High Strain Rate Superplasticity of TiC Particulate Reinforced Magnesium Alloy Composite by Vortex Method", *Scripta Metall. Mater.*, Vol.32, No.11, 1995, pp.1713-1717.

ELECTROCHEMICAL PLATING OF COMPOSITE COATINGS

Steinhäuser, S.; Wielage, B.

*Institute for Composite Materials
Technical University Chemnitz-Zwickau
D-09107 Chemnitz, Germany*

SUMMARY: The surface properties of structural units extremely influence their behaviour. In many cases the structural units are stressed in the surface region by a combination of mechanical, tribological, corrosive and thermal influences. Under these circumstances, deposition with composite coatings is an effective surface protection. These deposits can be coated on steel, light metals, ceramics, plastics and other materials. The composite coatings consist of a metal matrix with, in general, non-metal solid particles or short fibres. One of the most important coating process is the electrochemical plating. Following a survey on the manufacture, some properties, applications of composite coatings and new developments are presented. Especially fine particles of diameters less than 100 nm are available and are investigated in connection with electroplating experiments.

KEYWORDS: electrochemical plating, electrochemical composite deposition, nickel electrolytic, matrix materials, dispersal materials, solid particles, nano-particles, structure of coatings, microhardness of coatings, wear behaviour of coatings, nickel composite coatings

INTRODUCTION

Survey of Composite Coatings

The composition, structure and surface determine the properties of materials. The stress of materials causes a degradation of properties or even damages. The coating of materials can reduce these effects of stress in many cases. Especially the composite coatings are suitable. A great variety of coatings and as well as additional treatment processes are known (Fig. 1). Dispersal of solid phases combination of matrix (base material) and dispersal phases, determine the properties - therefore careful selection is very important. Mainly non-metal components in the form of particles or - in small amounts - of short fibres, are used. These second phases are incorporated during growth of the coating (e. g. electroplating from suspensions, thermal spraying) or later created inside the coatings (e. g. thermal treatment of electroless nickel coatings with phosphorus or boron causes precipitation hardening). Dispersed phases can also be incorporated into cavities within the coatings (e. g. infiltration of MoS₂ or polymers, production of phosphates or nitrides, incorporation of dispersed phases in pores or microcracks of chromium deposits [2]). Molten metal (e. g. steel) in a process called compound casting can contain dispersed carbides (e. g. VC, WC, MoC) [3] and will

Possibilities of Manufacture			
Electrochemical Plating		Thermal Spraying	
Electroless Plating	Electrophoresis	Plasma Welding	Deposit Welding
Melting		Melting on	
Multilayer	Nanolayer-sequences	Gradient Coatings	
Combination of different processes			
Additional Treatment			
Heat Treatment	Thermochemical Treatment	Laser-, Electron-, Plasma-Beam-Treatment	
Infiltration		Incorporation	

Fig. 1: Possibilities of manufacture and additional treatment of composite coatings

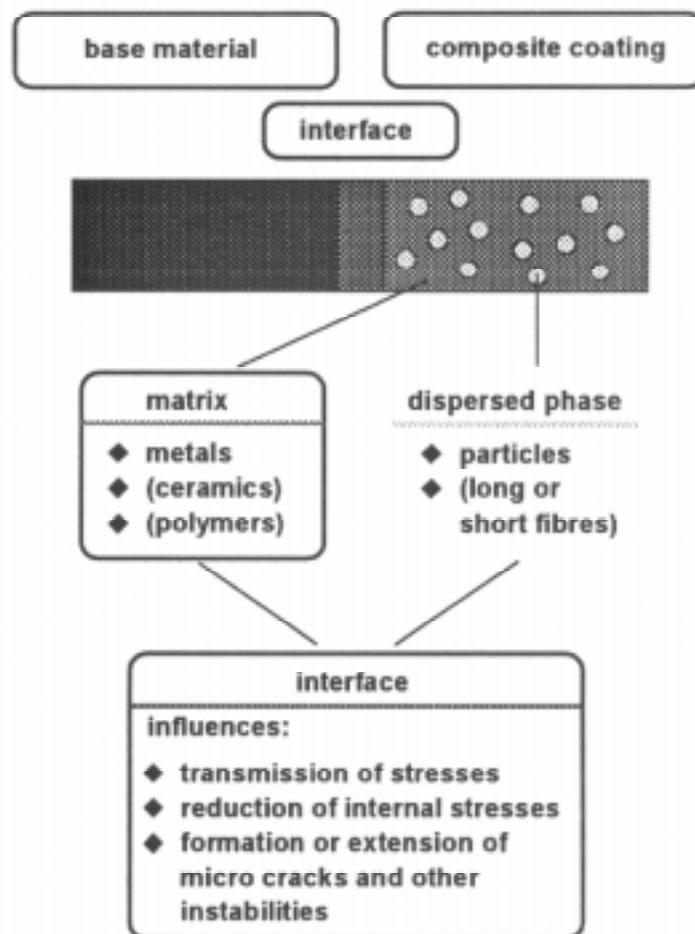


Fig. 2: Schematic depiction of a composite coating

be cast on the surface of highly stressed tools (e. g. drop forging die). By similar methods, laser or electron beams (remelting), plasma (plasma welding) or deposit welding can be used. In this way hard alloys on basis iron, nickel or cobalt with carbides, borides and others have been produced. Multilayer and nano-coatings are also kinds of composite coatings. Such systems are useful as deposits on tools (particularly CVD). Similar layers are produced with PVD. Gradient coatings can be produced e. g. by thermal spraying. Also combinations among diverse coating processes are possible, e. g. a combination of electrochemical with PVD or thermochemical processes. From the large number of methods incorporating solid particles into coatings, most already frequently contain the dispersal phase within the coating materials or coating medium.

Electrochemical plating of composite coatings and the thermal spraying of composite coatings presently are one of the most important techniques for fabrication of composite coatings. Some examples are the electroplating of Ni-, Fe - and Al - dispersion coatings. Important applications are found in motor production (especially small motors for tools, such as power saws but also for motor cycles and cars) and to prevent or reduce wear of tools. Ni- and CBN- dispersal coatings are used for abrasive tools. Electrochemical composite deposits find applications in textile industry (e. g. to rough up fibres) and for improvement of unclosed pair elements. The thermal sprayed composite coatings will be applied at high tribological and corrosive loads, e. g. for energy generation (e. g. gas turbines), steel manufacture and metal forming. [4] - [6]

Structure - Properties - Relations of Electrochemical Composite Coatings

The composite coatings depending on application consist of a matrix and various dispersal phases (see Fig. 2). Material and structural interactions of different constituent phases induce modified composite properties. The dispersal phases can change the coatings structure and the coatings properties as well as the surface properties and the materials bond.

Composite coatings are used for the primary coating and for repair coating. They induce

- raising of strength and support effect (high strong phases in an unhardened, tough matrix)
- formation of zones sensitive to absorb or scatter energy, relax stress and divert, catch or bridge cracks
- improvement of tribological properties (wear reduction, friction modification)
- improvement of corrosion resistance and of decorative effect
- improvement of thermal resistance
- raising of porosity and roughness
- raising of catalysing effects
- production of barrier effects (e. g. thermal insulation).

Examples for matrix and dispersal materials are:

matrix materials

- metals (e. g. Ni; Cu; Fe; Cr; Co; Ag; Au; Zn; Sn; Cd; Pb; Pd; Al)
- metal alloys (e. g. NiCr; NiAg; CuNi; CuAg; NiCrBSi; steel alloys)

dispersal materials

- carbides (e. g. SiC; TiC; Cr₃C₂; WC; B₄C; ZrC; HfC)
- oxides (e. g. Al₂O₃; SiO₂; TiO₂; Cr₂O₃; ZrO₂; UO₂; BeO)
- borides, nitrides (e.g. Cr₃B₂; TiB₂; ZrB₂; HfB₂; BN; B₄N; TiN; AlN)
- diamond
- graphite; MoS₂
- others (e.g. glass; CaF₂; BaSO₄)

The incorporated particles modify coating properties in various ways (Fig. 3):

- they influence the material structure of coating during the coating growth
- modification of coating properties by their pure existence of the particles in the coating.

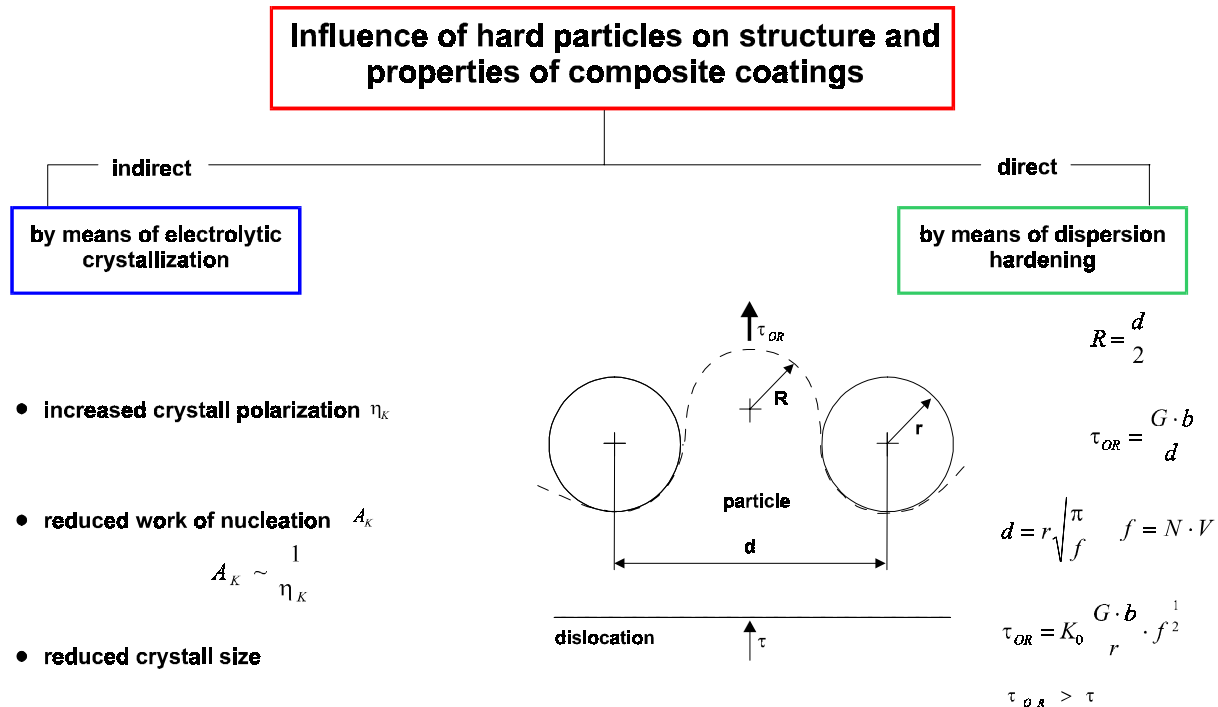


Fig. 3: Influence of hard particles on structure and properties (G shear modulus, b BURGERS vector, N particle number, V particle volumen, τ shear stress, τ_{OR} OROWAN stress)

The existence of particles in the electrolyte, especially in the region of phase boundary, influence the electrochemical system and therefore the material structure of coatings materials. The electrical-insulating particles partly blocking the specimen surface, whereby the cathode-side current density and the cathode-polarization increases. This leads finally to a reduction of the matrix-crystallite. The mechanically properties can be improved. Fig. 3 points out, that incoherent build in particles effect a dispersion hardening (orowan-mechanism).

In particular the strengths raising is based on the interactions between the particles and the dislocations. A cutting of the particles by the dislocation lines is dominant in case of coherent particles. If the coherence decreases, the particles are surrounded with a coherence field which hinders the motion of dislocations. Biggest work hardening effect will occur if the particles are incorporated incoherently and are harder than the matrix. Then the particles cannot be cut and must be encircled by forming dislocation rings. The Orowan-mechanism is valid in the range of micro elongation; the obstacles are encircled at higher elongation's by cross slide [7].

It can be seen from the theory of dispersion hardening that realising maximum hardness small and hard particles of uniform shape have to be finely dispersed in the coating. The most favourable particle size (the critical diameter) should be between 10 and 20 nm. Optimal work hardening will be realised if on the one hand the particle diameter is near the critical diameter for

a high strength and on the other hand somewhat over the critical diameter for a sufficient toughness. The interaction components between particles and dislocations will decrease and therefore the dispersion hardening effect as well, if the diameter of particles is higher than the critical diameter. For thermodynamically stable particles their spatial distribution will be preserved at higher temperatures as well. In this case the particles prevent recrystallization and grain growth and raise the high temperature strength. The existence of particles in the coating results in matrix work hardening, reduces the internal tensile stresses and improves the tribological surface properties (e. g. decrease of adhesion and friction).

Properties of metal matrix and of particles frequently complement each other synergetically. The content, distribution, shape, size and the hardness of hard particles and properties of matrix cause the strength and wear behaviour of coatings.

The application of the very fine nano-particles yields two particular advantages:
a genuine dispersion-hardening effect,
the reduction of the layer - thickness.

Until recently sufficiently fine particles, necessary for the dispersion hardening, so far have not been available. But since a few years some companies and institutes are offering powders with diameters of less than 100 nm. Our institute was one of the first to carry out experimental investigations for applications of nano-particles.

EXPERIMENTAL

It is well-known that the technological realisation is based on two basic principles:

- Small particles can be dispersed in the electrolyte. They get to the phase boundary between electrolyte and cathode-surface as a result of external, forced convection and - probably - of small electrophoresis effects. As a consequence of migration and of electrostatic effects the particles move to the region of deposit and are inserted. Where they have to be fixed until they are buried by the electro-crystallising matrix.
- Bigger particles are forced to sink to the cathode surface by suitable technical methods or they are already in a "fixed bed" and then incorporated into the growing layer.

The choice of fabrication method depends on particle size. The dispersal method can be applied up to particle diameters of approximately 10 μm . Examples of coatings with fine, but also with coarse particles are shown in Fig. 4 and 5.

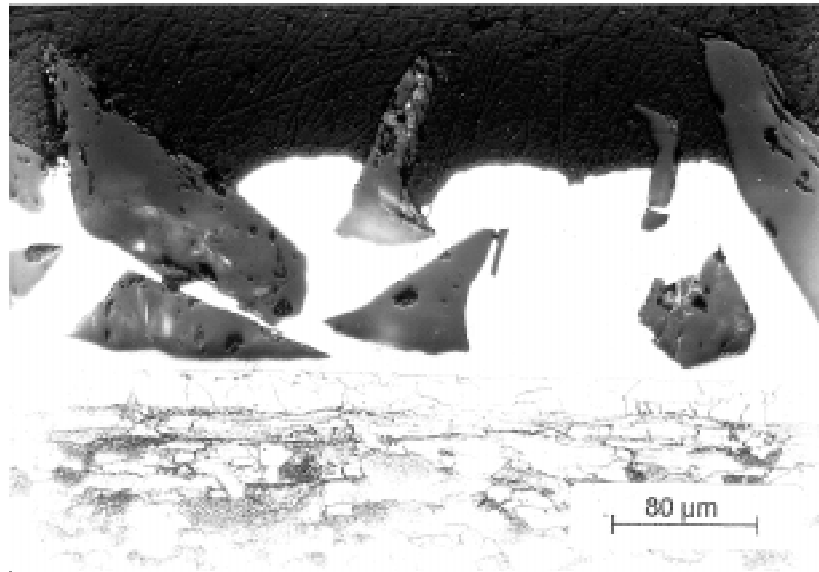


Fig. 4: Micrograph showing a Ni-SiC-composite coating for grinding

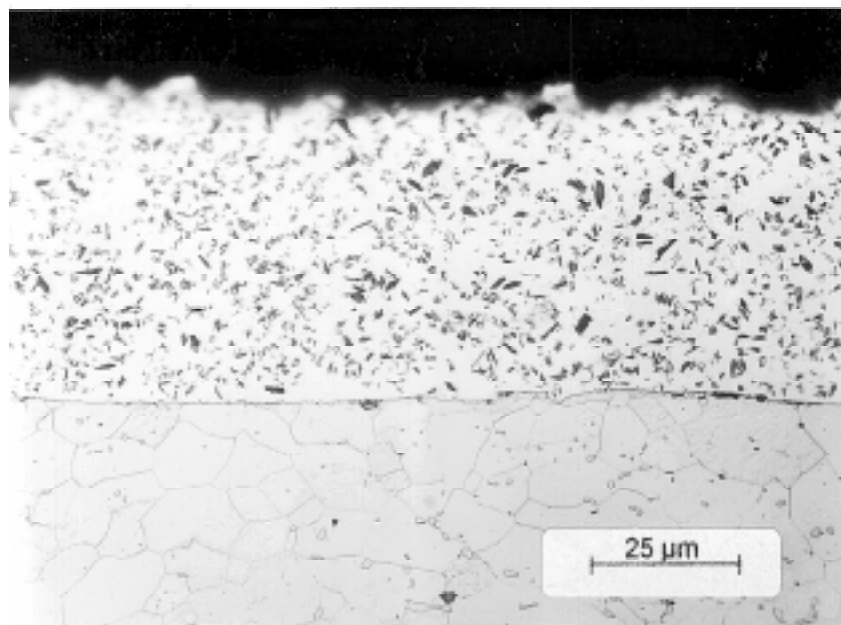


Fig. 5: Micrograph showing a conventional Ni-SiC-composite coating

Our investigations are carried out applying a special electrolyte bath based on nickel sulphate with SiO₂- nano-particles of fixed diameters of both 100 or 500 nm (Monospher ®, Fa. Merck, Darmstadt, Germany). Later on investigations will be carried out with smaller particles (up to ca. 10 nm diameter). The particles were dispersed in the electrolyte-fluid by mechanical stirring. At the samples surface particles were placed in the increasing nickel deposition by electro-crystallization (see Fig. 6).

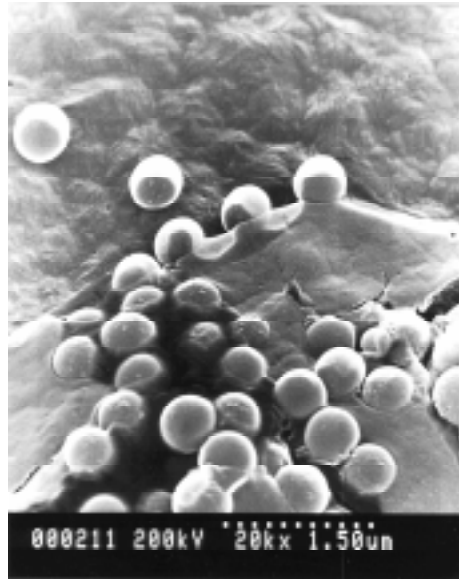


Fig. 6: SEM micrographs of surface electroplated Ni-SiO₂ - coatings

To render the placement of the small particles, different problems have to be solved:

The dispersion of the particles in the electrolyte fluid. That means that the particles are wettable and do not reaggregate in the electrolyte bath.

The creation of a stable suspension fluid.

A homogenous distribution of the installed particles in the cathodic deposition.

The particles have to possess a sufficient hardness.

Regarding to electroplating, several problems must be solved in future. The field of research "nano-particles" for the manufacture of dispersal coatings is still developing. For instance, investigations are necessary for the creation of stable suspension or for the moving of nano-particles to the cathode. The agglomeration of powder-particles in the electrolytic bath must be prevented. Also particle properties as e. g. hardness need improvement.

RESULTS AND DISCUSSIONS

It was achieved to install nano-particles in a electrolytic deposited nickel-layer (see Fig. 6, 7). The incorporation of solid particles in the coating was evaluated just qualitatively by image analysis. But it was obviously clear that the solid content of the coating increases with the content in the electrolytic bath.

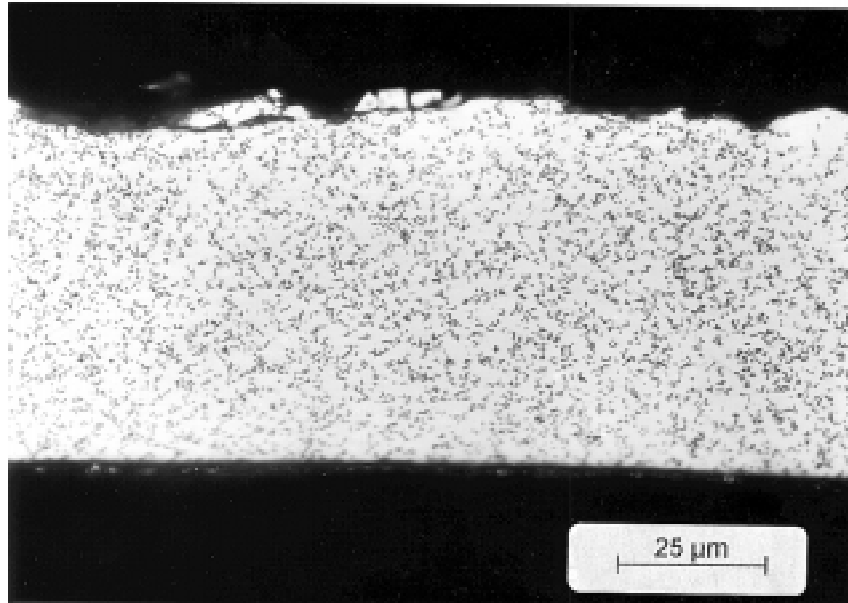


Fig. 7: Micrograph showing a Ni-SiO₂ (Monospher ®) - composite coating

A comparison with Al₂O₃- and SiC-particles of diameters 5 to 10 µm was performed by separate experiments. These results were published in former papers and are verified by other authors.

It is approved to increase the hardness within the incorporation of solid particles into the layer (Fig. 8).

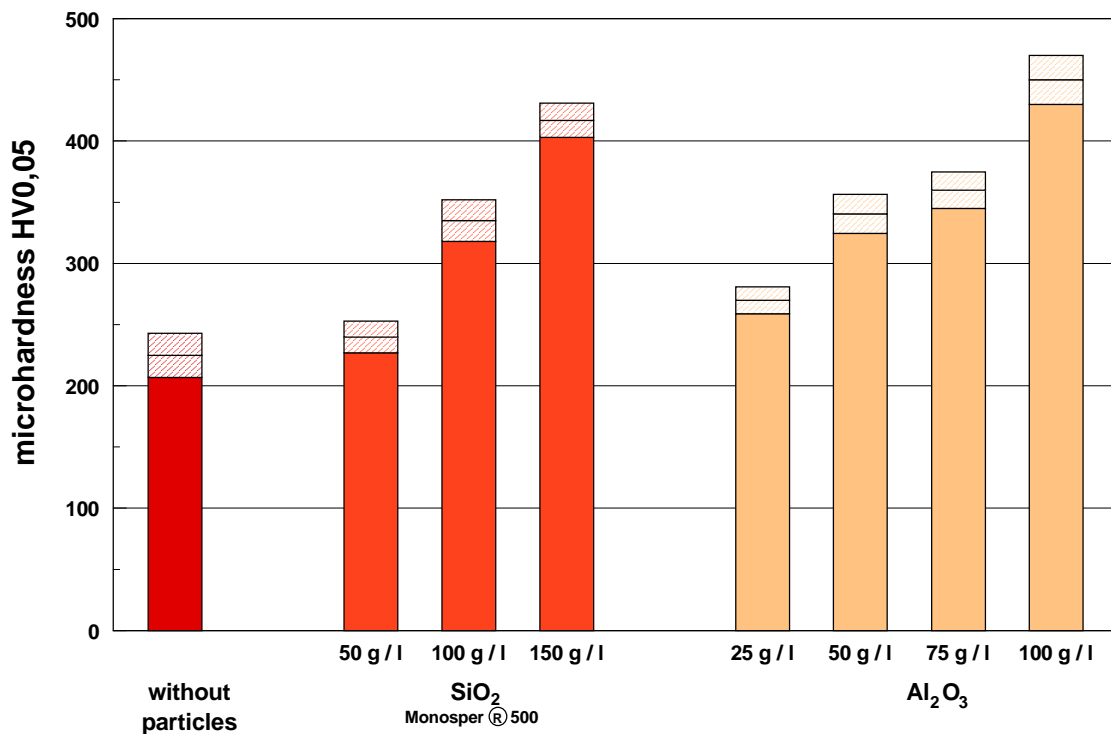


Fig. 8: Microhardness of nickel composite coatings as function of the particle size and content in the electrolytic bath

The increase of the wear resistance of these layers was pointed out by the oscillation-wear test (see Fig. 9).

The test under oscillation load creates a wear trace, a calotte in the specimen. The specimen moves oscillation under the counter-body. The counter-body is a ball (ceramic or steel) and has a diameter of 5 mm [8]. Parameter of the test are: Load $F_N = 10$ N, the frequency $f = 20$ Hz, testing time $t = 20$ min. The oscillation wear is determined $J_h^* = d_s^2 (8 R)^{-1} (R - \text{counter-body radius, } d_s \text{ calotte width})$.

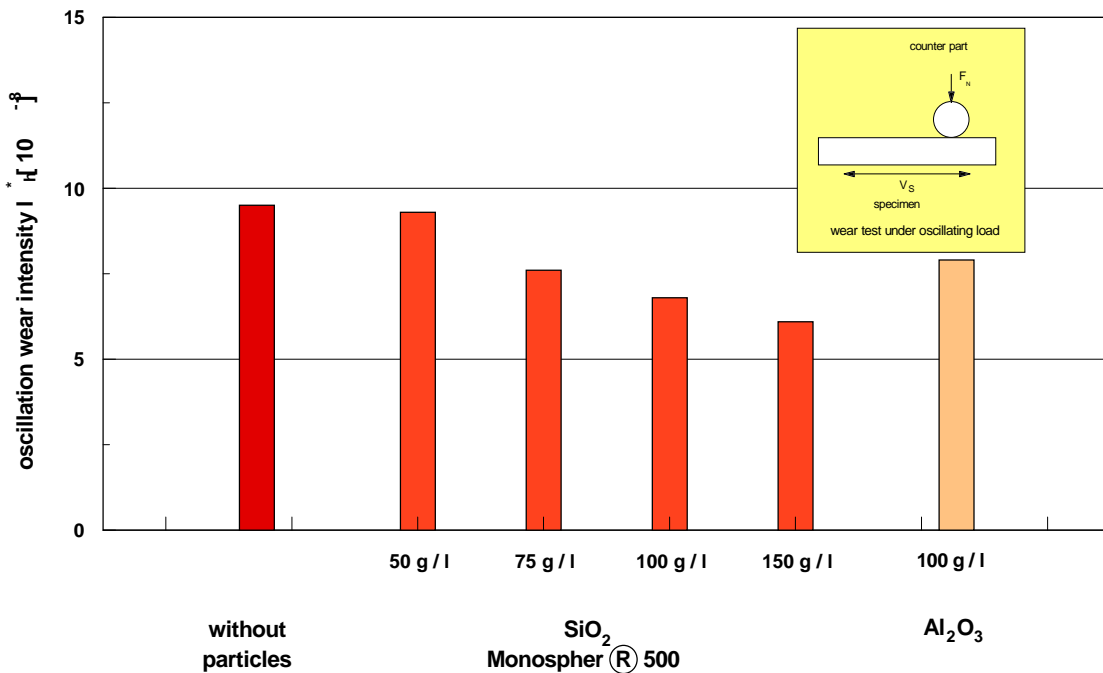


Fig. 9: Oscillation wear behaviour of nickel composite coatings (hard particles content in the electrolytic bath)

The results of oscillation wear are interesting because coatings containing monospheres are better because they show less wear than those with alumina. It is most likely that the reason is particle form. Monospheres are of spherical shape whereas alumina particles have a sharp-edged form and therefore promote the abrasive wear. It was shown that the placement of nano-particles also effects an improvement of the deposition. It can be proved that the spherical nano-particles are capable to open new and favourable options for electrochemical plating of dispersal coatings.

CONCLUSIONS

It can be established, that

- * it is possible to install extreme high grade particles (nano particles with diameters from 1 μm to 10 nm) into electrolytic deposited layers.
- * within the deposition of the high grade particles the hardness and the wear-resistance was improved.
- * with these nano particles it is possible to produce dispersion hardening layers.

It can be proved that the spherical nano-particles are capable of opening new and favourable options for electrochemical plating of dispersal coatings.

It can be stated that composite coatings, especially the electrochemical deposition offer favourable options for the improvement of the tribological properties of materials and thus make broad applications in significant scale possible.

ACKNOWLEDGEMENTS

The authors would like to acknowledge the employees of the Institute of Composite Materials, especially Dr. Podlesak. Furthermore they would like to thank Dr. Broszeit (TH Darmstadt, Germany) and the Merck-company (Darmstadt, Germany) for their help with the manufacture of electrochemical composite coatings.

REFERENCES

1. S. STEINHÄUSER: 'Disperse nichtmetallische Phasen in Oberflächenschichten (Compositschichten),' *Tagungsband 'Nichtmetalle in Metallen 94'*, 11 - 22, Hirschfeld, D. 'ed.,' DGM Informationsgesellschaft mbH, Oberursel Germany 1995.
And: *Materialwissenschaft und Werkstofftechnik* **26** (1995) 608 - 614
2. U. BURAN: 'Herstellung und Eigenschaften von Hartchromschichten mit Feststoffeinlagerung,' *Tagungsband 'Verbundwerkstoffe und Werkstoffverbunde,'* 741-748, 'ed.,' G. Leonhardt, et. al., DGM Informationsgesellschaft mbH, Oberursel Germany 1993.
3. U. DRAUGELATES; B. BOUAIFI; TH. PLEGGGE: 'Verbesserung der tribologischen, korrosiven und thermischen Eigenschaften von Schutzschichten durch Einlagerung von WSC und NbC,' *Tagungsband 'Verbundwerkstoffe und Werkstoffverbunde,'* 329-344., 'ed.,' G. Leonhardt, et. al., DGM Informationsgesellschaft mbH, Oberursel Germany 1993.
4. S. STEINHÄUSER; A. HENKER; et. al.: 'Galvanisch abgeschiedene Compositeschichten unter besonderer Berücksichtigung grober Feststoffteilchen,' *Tagungsband 'Verbundwerkstoffe und Werkstoffverbunde,'* 353-360, 'ed.,' G. Leonhardt, et. al., DGM Informationsgesellschaft mbH, Oberursel Germany 1993.
5. K. MAIER: 'Ni-SiC-Dispersionsschichten im Motorenbau,' *Tagungsband 'Verbundwerkstoffe und Werkstoffverbunde,'* 283-690, 'ed.,' G. Leonhardt; et. al., DGM Informationsgesellschaft mbH, Oberursel Germany 1993.
6. J. LUKSCHANDEL: 'Nickel-Diamant-Schichten für komplexe Beanspruchungen,' *Tagungsband 'Verbundwerkstoffe und Werkstoffverbunde,'* 691-697, 'ed.,' G. Leonhardt, et. al., DGM Informationsgesellschaft mbH, Oberursel Germany 1993.
7. W. SCHATT: 'Einführung in die Werkstoffwissenschaft', Deutscher Verlag für Grundstoffindustrie Leipzig, Germany 1984, 346-347 und 391.
8. G. SCHMIDT; S. STEINHÄUSER: 'Characterization of wear protective coatings,' *Tribology International* **29**(1996)3, 207 - 213.

SIC_P-AL COMPOSITES FABRICATED WITH A MODIFIED EXTRUSION METHOD

S. Kohara

*Department of Materials Science and Technology, The Science University of Tokyo, Noda,
Chiba 278, Japan*

SUMMARY: In the present study, an attempt was made to realize the low cost metal matrix composites. SiC powder as a reinforcement, extrusion as a fabrication method and unsealed three-piece can as a container for powder were adopted in this study. The three-piece can composed of a cylinder and two lids was formed by assembling the three pieces to make a can without sealing. Mixtures of SiC and atomized aluminum powders with the compositions of 10-20 vol.% SiC were put into the cans and extruded at high temperatures. The effects of die shape and extrusion temperature were investigated to determine the optimum extrusion conditions. The hardness, the tensile strength and the wear resistance of fabricated composites were tested. The SiC_P-Al composites fabricated with this method can be used as the wear resisting material.

KEYWORDS: metal matrix composites, SiC powder, aluminum, particulate dispersion strengthening, wear resisting material, extrusion, unsealed can

INTRODUCTION

For the industrial applications of fiber or whisker reinforced metal matrix composites, the high cost of the composites is a problem. Both fiber and whisker are good reinforcements for metals, however, their costs are too high for the industrial uses. Inexpensive fabrication methods as well as inexpensive reinforcement materials are required for the development of the industrial metal matrix composites. Compared to fibers or whiskers, ceramic powders are inexpensive, but can be used as the reinforcement for metals. The particulate shape of ceramic powders may have less strengthening effects on the metal matrix than that of fibers or whiskers. In general, the hardness of ceramics is higher than that of metals. Therefore,

the properties other than strength, such as hardness or wear resistance, should be considered for the use of the ceramic powder reinforced metal matrix composites.

Silicon carbide powder is one of candidates as the reinforcement for metal matrix. Powder of silicon carbide is manufactured on a industrial scale at present and the cost of powder is not so high as that of fiber or whisker. In general, silicon carbide particulate reinforced aluminum has been fabricated with the liquid phase processing, such as pressure infiltration or squeeze casting [1] . However, the liquid phase processing is rather energy consuming compared to the solid phase processing.

Extrusion is an efficient manufacturing process using the plastic deformation of material and has been used for the fabrication of particulate materials in the field of powder metallurgy [2] [3] [4] [5] . Extrusion as a solid phase processing can be applied for the fabrication of metal matrix composites with particulate raw materials. In the extrusion of metal powder, powder is usually packed in a thin metal can and sealed after degassing or evacuation and then extruded. However, this is time consuming treatment. Unsealed can instead of evacuated and sealed can is possibly used for reducing cost and saving time.

In the present study, a new method for fabricating the low cost SiCp-Al composites by extrusion with unsealed can has been investigated and the properties of the fabricated composites have been assessed.

EXPERIMENTAL

Silicon carbide (β -SiC) powder and atomized aluminum powder were used as the raw materials in the present study. The powders were blended using a powder mixer with the compositions of 10, 12.5, 15, 17.5 and 20 vol.% SiC and packed into aluminum cans. The dimensions and the shape of the can used in this study are shown in Fig.1. The can is composed of three pieces, a cylinder and two lids, and assembled to form a can. The lids were made from a commercial aluminum rod and the cylinders, from a commercial aluminum pipe by machining. A lid was tightly fitted one end of the cylinder and the blended powder was poured into the can and then, another lid with a small hole to let escape gas was fitted the other end of the cylinder as shown in Fig.1.

The can including blended powders was set in a extruding machine and extruded with the ram speed of 0.6 mm/s. The extrusion temperatures were 450-635 °C. The aluminum layer was removed by machining after extrusion. Three types of dies with different semidie angles shown in Fig.2 were adopted in this study to determine the optimum die shape for the extrusion of composites.

The tensile strength of the extruded composites was measured with the specimens cut from the extruded bars. The hardness was measured at the cross-sections of the extruded bars and the average values were determined. The wear resistance of the composites was tested with a pin on disc type wear tester.

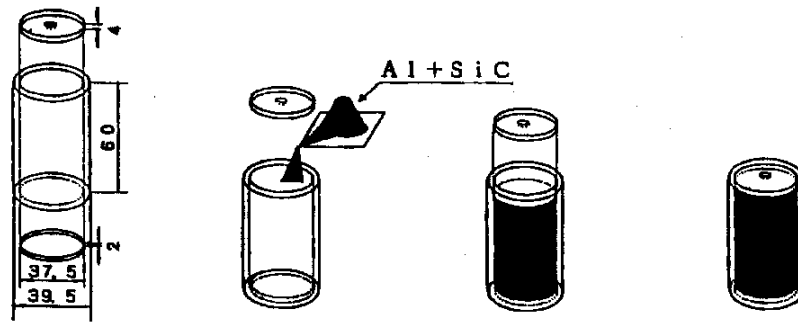


Fig. 1 Powder billet for extrusion, dimensions and the preparing process.

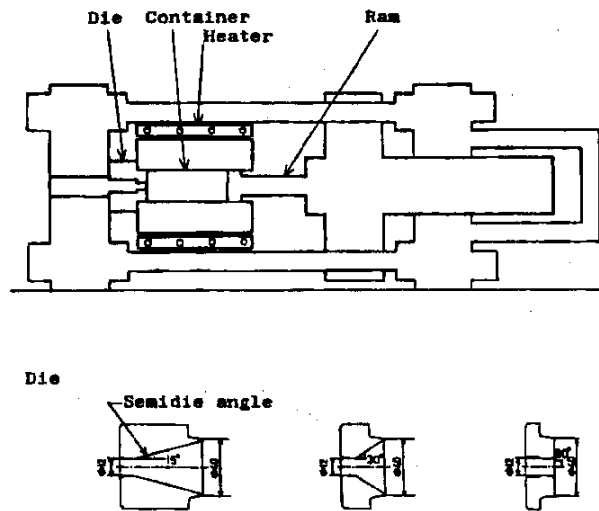


Fig. 2 Extruding machine and dies used in the present study.

RESULTS

The results of the extrusion experiments with three types of dies and extrusion temperatures from 450 to 600 °C are summarized in Table 1. The extruded bars were evaluated by the appearance as the three grades; good, not good and bad. The surface of the good extruded bar was smooth, but cracks were observed on the surface aluminum layer of the badly extruded bar. The experimental results show that the lower the SiC content, the smaller the semidie angle and the higher the extrusion temperature, the better the extruded products. From the results of the above mentioned experiments, the next extrusion experiments were carried out using only a die with semidie angle of 15 ° and at temperatures from 450 to 635 °C. The experimental results are summarized in Table 2. With these conditions, good extruded products were obtained in most cases except at low (450 °C) or high (635 °C) temperatures. With the extrusion temperatures from 550 to 625 °C, good extruded products with 10 to 20 SiC vol.% were obtained. The hardness of the extruded composites

Table 1 Results of extrusion experiments (1).

Semidie angle	15 °	30 °	90 °
SiC %			
20	▲ ▲ ○ ○	▲ ▲ ▲ ▲	▲ ▲ ▲ ▲
15	▲ ○ ○ ○	▲ ▲ ▲ ○	▲ ▲ ▲ ○
10	○ ○ ○ ○	▲ ▲ ○ ○	▲ ▲ ▲ ○
	450 500 550 600	450 500 550 600	450 500 550 600 °C

Table 2 Results of extrusion experiments (2).

Semidie angle	15 °
SiC %	
20	▲ ▲ ○ ○ ○ ▲
17.5	▲ ▲ ○ ○ ○ ▲
15	▲ ○ ○ ○ ○ ▲
12.5	▲ ○ ○ ○ ○ ▲
10	○ ○ ○ ○ ○ ▲
	450 500 550 600 625 635 °C

○ : Good ▲ : Not good ▲ : Bad

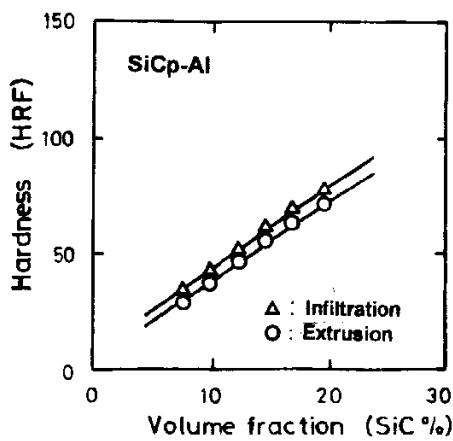


Fig. 3 Change in hardness with SiC volume fraction.

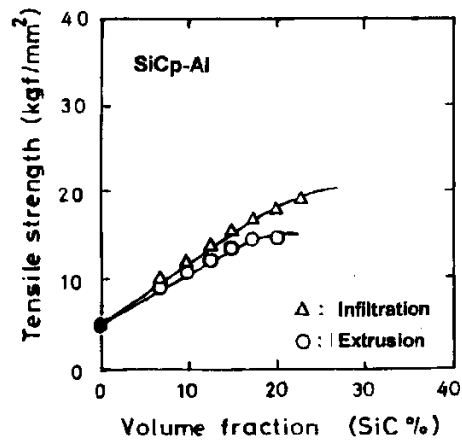


Fig. 4 Change in tensile strength with SiC volume fraction.

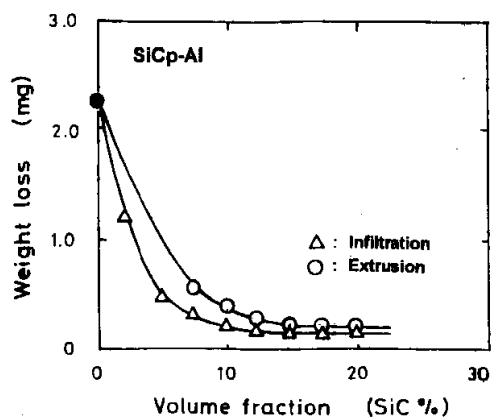


Fig. 5 Change in weight loss in wear test with SiC volume fraction.

is plotted against the SiC content in Fig.3. The average hardness of the composites increased with SiC content up to 20%. The tensile strength of the composites was measured with the specimens machined from the extruded bars. The change in tensile strength with SiC content is shown in Fig.4. The tensile strength of the extruded composites increased with SiC content up to 15%, but did not increase at 20%. The changes in the stress-strain curves of the extruded composites were checked. The tensile strength varied little, but the elongation at fracture decreased very much by making the composite.

The results of the wear test is shown in Fig.5 and compared with the composites made by other method. The weight loss in the wear test of the composites decreased with increasing the SiC content. Though the wear resistance of the extruded SiCp-Al composites is a little inferior to the SiCp-Al composites made by the infiltration method, the difference between the two types of composites is not so large.

DISCUSSION

In the industrial application of the fiber or whisker reinforced metal matrix composites, the high cost of the composites is a big problem. If fiber or whisker is not used, the cost of the composites will be lowered, but the properties of the composites will also fall behind. Ceramic powders instead of fibers or whiskers can be used as the reinforcement for the metal matrix, however, the strengthening effects of the ceramic powder on the metal matrix will not be good as fibers or whiskers because of the particulate shape of particles. Therefore, the properties other than strength should be considered for the application of the composites. Although the tensile strength of the SiC powder reinforced aluminum is not high enough, the special features of the ceramic powder reinforced aluminum should be hardness or wear resistance.

Usually particles of aluminum powder are covered by a thin aluminum oxide film and the

adhesion between the film and matrix is so strong that the oxide film can not be removed easily. Even if the can packed with aluminum powder is evacuated, the oxide film will still remain on the surface of particles. It is better to break the surface layer by the severe plastic deformation in extrusion and create the new surface for the consolidation of metal powder. The lid and cylinder are welded by the severe plastic deformation during extrusion and form a closed can. Thus, unsealed cans can be used as the container for fabricating aluminum matrix composites

The strength of the SiCp-Al composites made by the infiltration method was higher than that of the SiCp-Al composites made by this method. It may be due to the difference in the bonding between SiC particles and aluminum matrix. The infiltration method is a liquid phase processing, but extrusion is a solid phase processing. The interfacial bonding in the liquid phase processing is stronger than that in the solid phase processing.

The tensile strength of this composites rather falls with increasing the SiC content in the range higher than 20 vol.% SiC. This fact may suggest the limit of this method, that is, that of particulate particle dispersion strengthening by the solid phase processing. However, the SiCp-Al composites is useful as a wear resisting material when the cost is taken into consideration.

CONCLUSIONS

The fabrication method and the properties of SiC particulate reinforced aluminum as the low cost metal matrix composite were investigated and the followings were concluded.

- (1) The new modified extrusion method with unsealed three-piece can is applicable for fabricating the SiCp-Al composites.
- (2) The tensile strength of the fabricated composites increases with the SiC content up to about 15 vol.% SiC, but increases little for the higher SiC content.
- (3) The wear resistance of the SiCp-Al composites fabricated with this method is high enough and comparable with that of the composites made by the infiltration method.

REFERENCES

1. S.Kohara; *Materials and Manufacturing Processes*, **5**, 1990, p.51.
2. S.Krishnamurthy, I.Weiss and F.H.Froes; *Proceedings of Powder Metallurgy and Related High Temperature Materials*, 1987, p.135.
3. A.Murase and G. Abe; *Proceedings of Powder Metallurgy World Congress Part 2*, 1993, p.859.
4. Y.Ohashi, T.Fukuda, M.Nishiguchi, and J.Kikuchi; *Proceedings of Powder Metallurgy World Congress Part 2*, 1993, p.863.
5. H.Hoshino and S.Kohara ; *Advances in Powder Metallurgy and Particulate Materials Vol.6*, 1994, p.31.

PROPERTIES OF PARTICLE REINFORCED MAGNESIUM ALLOYS IN CORRELATION WITH DIFFERENT PARTICLE SHAPES

F. Moll, K.U. Kainer

*Institut für Werkstoffkunde und Werkstofftechnik, Technische Universität Clausthal,
Agricolastrasse 6, D-38678 Clausthal-Zellerfeld, Germany*

SUMMARY: The magnesium alloy QE22 (2.5% Ag, 2.0% RE, 0.6% Zr) was used as matrix material for particle reinforced magnesium base composites. The alloy was reinforced by Al₂O₃ platelets applying the squeeze casting technique to fabricate the composite whereas QE22/SiC_p composites were produced by powder metallurgical methods. To determine the influence of a particle reinforcement unreinforced materials were obtained for comparison using both production routes. Investigations have been carried out into mechanical properties and the microstructure of both composites and unreinforced materials in the as prepared and T6-heat treated condition. Particle reinforcement leads to a distinct improvement in Young's moduli of the magnesium alloy. The improvement is highest for plate-like particles and lowest when rounded particles are used. Using the Tsai-Halpin model to calculate the Young's moduli results in an overestimation of stiffnesses of almost all the composites. Reinforcement reduces elongations to fracture but increases the strength properties of the alloy.

KEYWORDS: Magnesium base composites, particle reinforcement, Tsai-Halpin model, microstructure, mechanical properties

INTRODUCTION

The increasing demand for new and lightweight materials has forced the importance of magnesium as a constructional material in recent years. The use of magnesium on the other hand is limited by the low stiffness, the low strength at elevated temperatures, low wear resistance and the high coefficient of thermal expansion. Up to a certain degree these properties may be improved by conventional alloying techniques. A more extensive enhancement of critical properties is realisable by means of a reinforcing phase like particles, short fibres or long fibres. Reinforcement of magnesium materials by particles has proved to be advantageous as the production processes enable isotropic composites to be produced economically. The reinforcing effect is less than in the case of a fibre reinforcement but it is possible to achieve a whole range on properties that can be varied by varying the parameters such as matrix alloy, particle shape, size as well as particle volume fraction. Powder metallurgical as well as casting methods can be used to produce particle reinforced magnesium alloys. Both processes enable the manufacturing of near net shaped parts. In the powder metallurgical route gas atomised powder is mixed with the particles and subsequently

consolidated by extrusion, powder forging, etc. to fully dense materials. In the case of casting methods squeeze casting has proved to be very effective. The reinforcing phase which has to be shaped into porous preforms is infiltrated by the magnesium base alloy under pressure. The volume fraction of the reinforcement is limited by the produceability and uninfiltrability of the preforms.

EXPERIMENTAL DETAILS

Fabrication of Composites and Material Testing

To reinforce the alloy QE22 by alumina platelets preforms containing 20 vol.% Al_2O_3 platelets were infiltrated by the alloy applying the direct squeeze casting process. A sketch of the tool for the 500 t- squeeze casting press used for composite fabrication is given in figure 1.

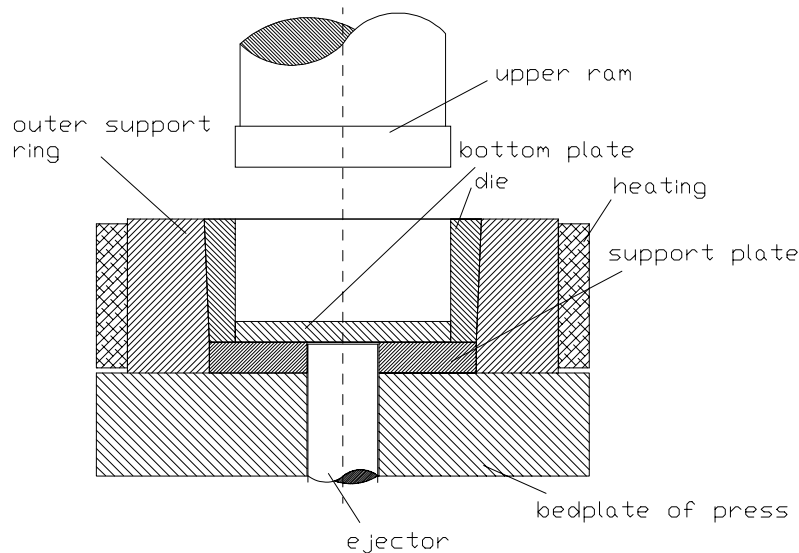


Fig. 1: Direct squeeze casting press [1]

Starting the squeeze cast process the particle preform is put onto the bottom plate of the mould and the molten alloy is poured over the preform. Then the upper ram is vertically moved downwards to close the mould and to squeeze the melt into the preform. The applied pressure is exerted in two stages of 50 MPa for 15 sec and 130 MPa for 90 sec to prevent the melt from spraying out of the gap between ram and die and to ensure a complete infiltration of the preform. Following the infiltration the melt solidificates rapidly due to the difference of temperature between the melt and the tool. A premature solidification is avoided by preheating the preform up to 1000°C and overheating the melt up to 800°C [1]. Figure 2 shows a SEM micrograph of the alumina particles. The particles are in mono-crystalline condition and hexagonal shaped with a diameter of 15 μm and a thickness of around 1 μm . Further details of physical and mechanical properties of the particles can be taken from table 1 and the nominal composition of alloy QE22 is given in table 2 [3].

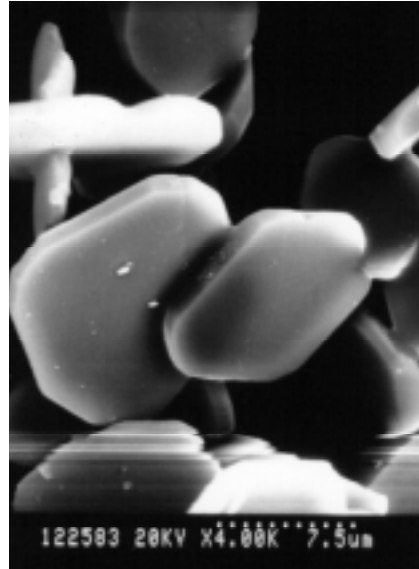


Fig. 2: Al₂O₃ platelets

Table 1: Physical and mechanical properties of α-Al₂O₃ platelets

	Young's modulus [GPa]	aspect ratio (l/d)	density [g/cm ³]
α-Al ₂ O ₃	450	15:1	3,96

Table 2: Chemical composition of magnesium alloy QE22 (wt%)

	Ag	Cu	Fe	Mg	Mn	RE	Si	Zr
QE22	2,5	0,01	0,003	rem.	0,03	2,0	0,01	0,6

The production of P/M QE22/SiC_p composites was carried out by hot extrusion after mixing and milling of matrix powder and particles. The matrix powder was obtained from gas atomisation and showed an average size of d₅₀ = 39µm [4].

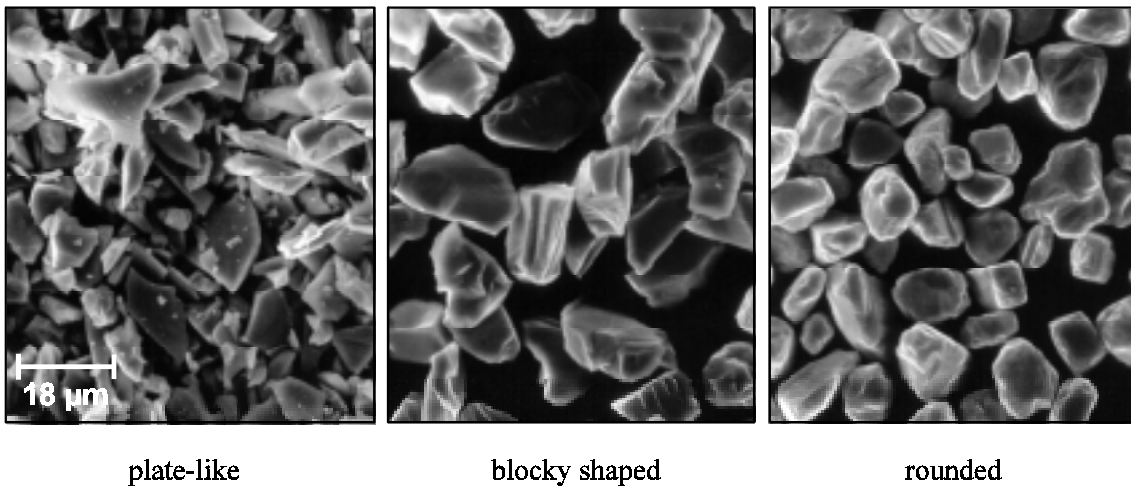


Fig. 3: SiC particles

Table 3: Physical and mechanical properties of SiC particles

	Young`s modulus [GPa]	aspect ratio (l/d)	density [g/cm ³]
SiC	400	plate-like: 3:1, blocky: 2:1, rounded: 1:1	3,21

To maintain a powder/particle size ratio of about 5:1 as proposed by Schröder [2] SiC particles possessing a mean diameter of $d_{50} = 9\mu\text{m}$ were incorporated as reinforcements in a volume fraction of 20%. The shapes of the particles were different: plate-like, blocky shaped and rounded particles (fig. 3). The properties of SiC particles are given in table 3 [3]. The powder/particle blends received from mixing and milling were precompacted and encapsulated to make extrusion possible. These capsules were heated for 30 min. at a temperature of 400°C before extrusion, which was executed by a 400t extrusion press. The degree of deformation ϕ [$\phi = \ln(A_0/A)$] was selected between 2,8 and 3,0.

Materials produced by squeeze casting and extrusion were machined into specimen for tensile testing with a diameter of 5mm and a gauge length of 25mm and samples for metallographic investigations. Tensile tests were carried out using an INSTRON 1095 testing machine with a cross head speed of 0.5 mm/min. The force was recorded by tension control using an extensometer to evaluate exactly the Young`s modulus. Light microscope and SEM were applied for microstructural analysis.

RESULTS AND DISCUSSION

Microstructure of composites

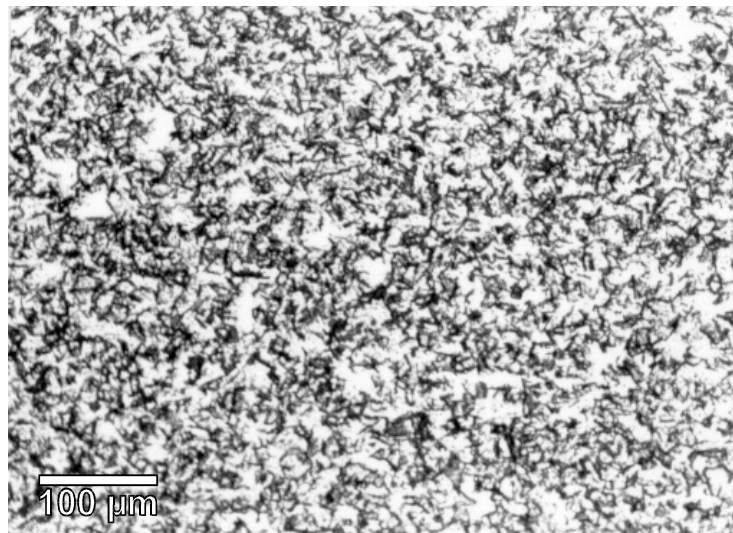


Fig. 4: Micrograph of QE22/Al₂O₃ platelet composite

As can be seen from figure 4 the QE22/Al₂O₃ composite shows a homogenous distribution of the platelets after squeeze casting. In some cases the preforms cracked due to high stresses and deformation of the preforms and small unreinforced areas were generated in the composite materials. This may be attributed to destruction and delamination of particles.

A T6 heat treatment (525°C/6h solution heating, oil quenching, 205°C/8h ageing) resulted in a formation of different precipitations like $Mg_{12}(Nd_2Ag)$ and $(Mg, Ag)_{12}Nd$ in the matrix.

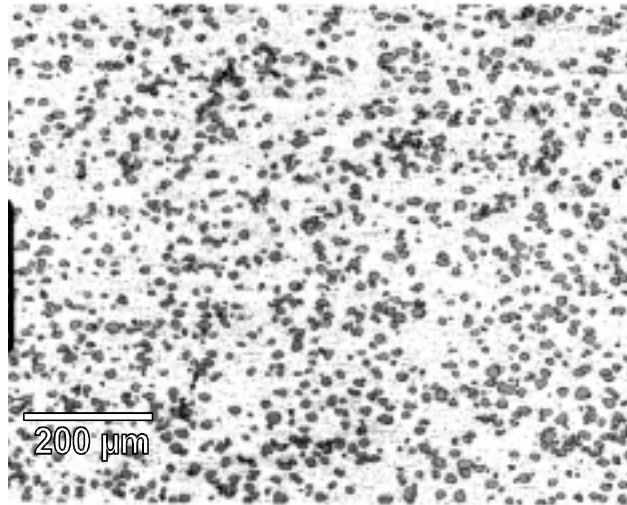


Fig. 5: Microstructure of a P/M QE22/SiCp (20 vol.%, rounded), extrusion direction

Regarding the QE22/SiC_p composites produced by powder metallurgy a uniform distribution was found for the blocky shaped and rounded particles whereas the plate-like particles have a tendency to agglomerate. The particles became aligned in lines parallel to the direction of extrusion (fig. 5).

Mechanical properties of composites

A particle reinforcement of magnesium alloys appears to be most suitable, if an improvement of the elastic modulus is required. However, to estimate the degree of improvement using the linear or inverse rule of mixture is insufficient in the case of a particle reinforcement. A further development of these models, applicable to short fibres and particles, is the Tsai-Halpin model [5], which takes the geometry of the reinforcement into account (eqns. 1, 2):

$$E_C = \frac{E_M(1 + 2SqV_P)}{1 - qV_P} \quad (1)$$

when

$$q = \frac{(E_P / E_M) - 1}{(E_P / E_M) + 2S} \quad (2)$$

E_C, E_M, E_P = Young`s moduli of the composite, matrix and particles
 V_P = Volume fraction of particles
 S = particle aspect ratio (l/d)

It is evident from figure 6 and 7 that the enhancement of stiffness is overestimated by applying the Tsai-Halpin model except the QE22/SiC_{p (rounded)} composite in the heat treated condition, which elastic modulus is slightly underestimated. The discrepancy between the measured and calculated moduli becomes smaller with decreasing aspect ratio. Delamination and damage of particles as well as pores unavoidably remaining in the extruded material are responsible for these differences. A T6 heat treatment increases the Young`s modulus of squeeze casted QE22 in the unreinforced and reinforced condition. An alteration of stiffness

of alloy QE22 (P/M) is dependent on the shape of SiC particles used as reinforcements. The Young's modulus is increased most by plate-like particles from 46 GPa for the unreinforced alloy up to 77 GPa. The smallest increase is obtained from rounded particles. The heat treatment lowers the Young's modulus of unreinforced QE22 and equalises the moduli of all the P/M composite materials.

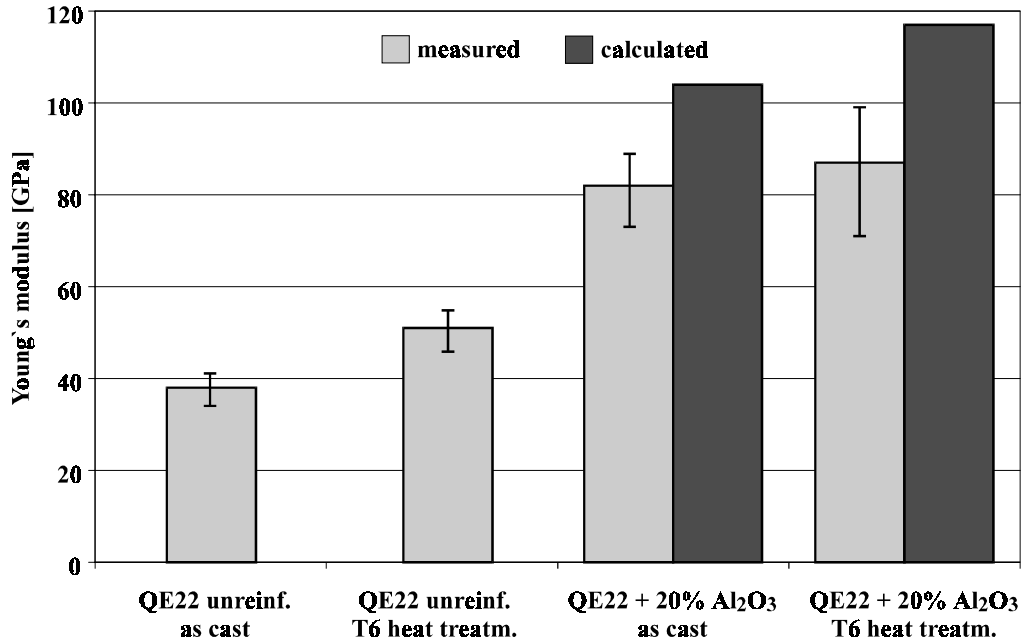


Fig. 6: Young's modulus of squeeze casted QE22 and QE22/20 vol.% Al₂O₃(platelet) composite

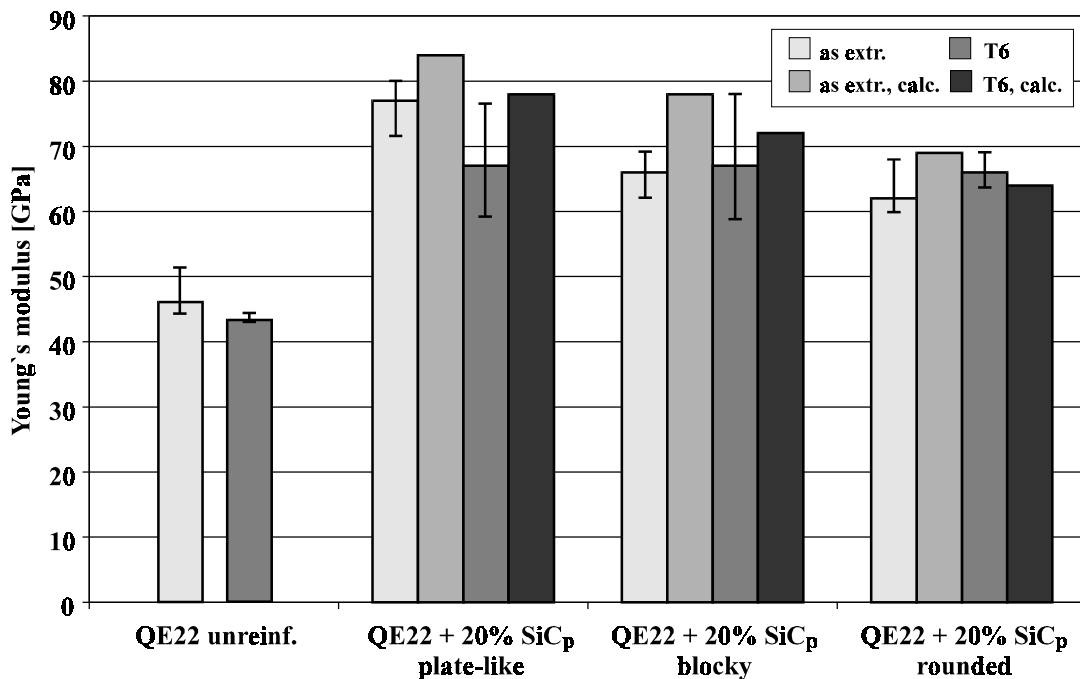


Fig. 7: Young's modulus of P/M produced QE22 and QE22/20 vol.% SiC_p composites

Regarding the tensile properties of the squeeze casted materials investigated the strongest increase of the ultimate tensile strength was obtained from the unreinforced alloy after heat treatment (fig. 8). However, the strengths of the composites are just below that value;

therefore a positive influence of the particle reinforcement on the tensile strength of squeeze casted QE22 is obvious. A more distinct improvement of tensile properties was achieved in the case of the powder metallurgically produced composites, as given in figure 9. Since the shape of blocky and rounded SiC particles is nearly globular they enhance the tensile strength more than plate-like particles do. A heat treatment hardly changes the different tensile strengths.

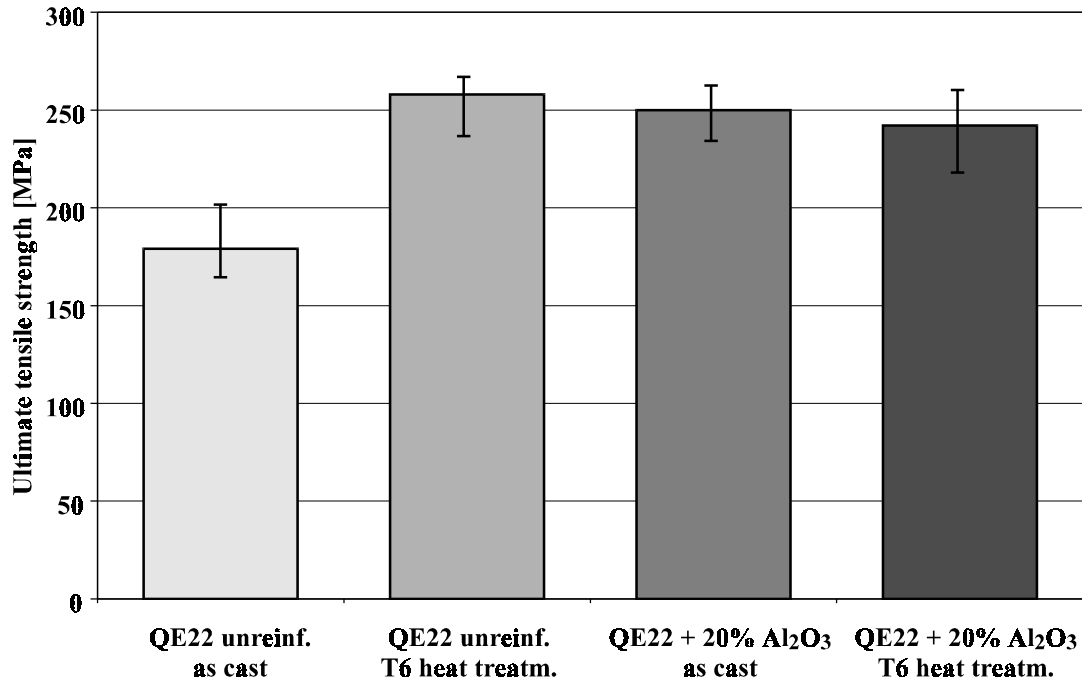


Fig. 8: Ultimate tensile strength of squeeze casted QE22 and QE22/Al₂O_{3(platelet)} composite

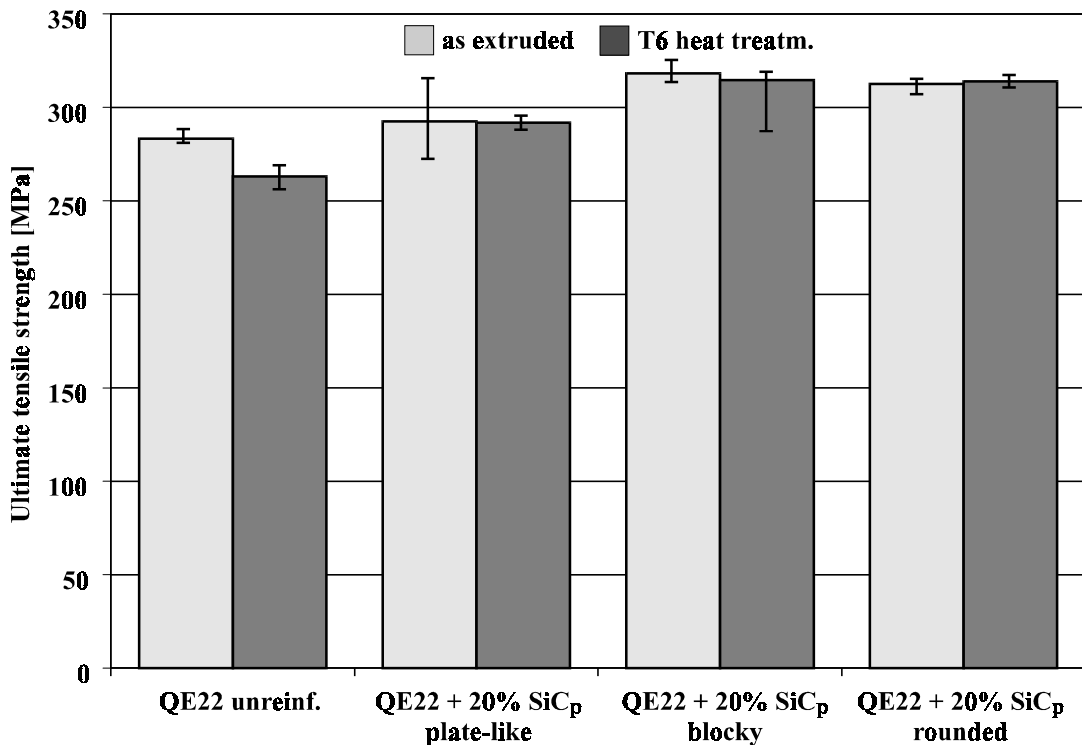


Fig. 9: Ultimate tensile strength of P/M produced QE22 and QE22/SiC_p composites

The particle reinforcement generally leads to a marked loss of ductility, which is seen from fig. 10 and 11. The elongation to fracture of the squeeze casted alloy decreases of about 90% due to the alumina platelets in the as cast and heat treated condition. The reduction of ductility of the P/M material depends as strength properties on the shape of SiC particles incorporated into the alloy. The composite reinforced by plate-like particles shows the lowest elongation to fracture of around 5%. With decreasing aspect ratio of the particles the ductility increases up to about 8% in the case of the rounded particles. The heat treatment reduces all the ductilities of the unreinforced alloy and composites.

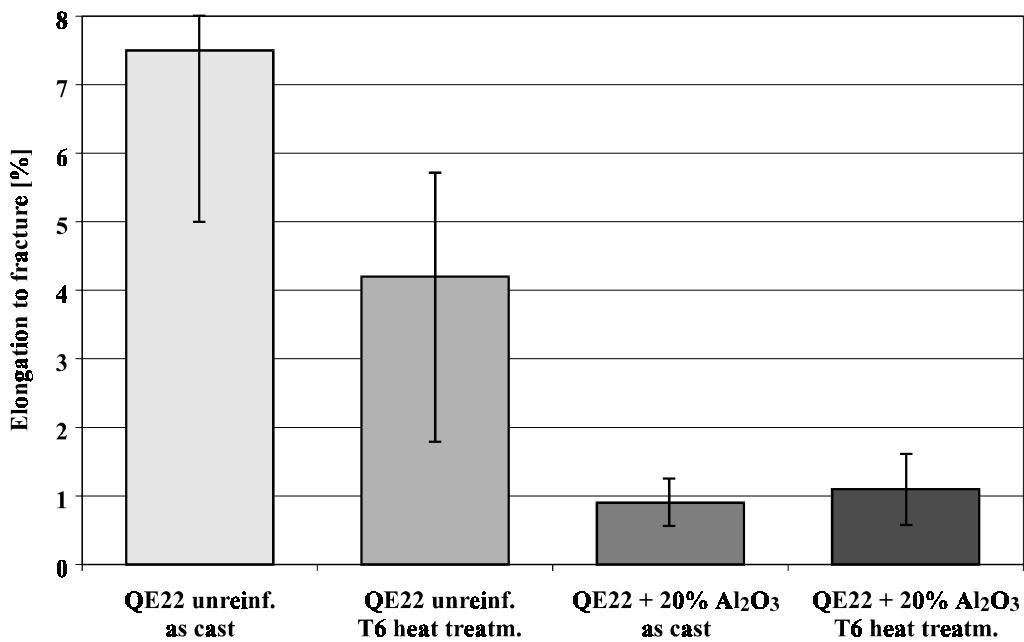


Fig. 10: Elongation to fracture of squeeze casted QE22 and QE22/Al₂O₃(platelet) composite

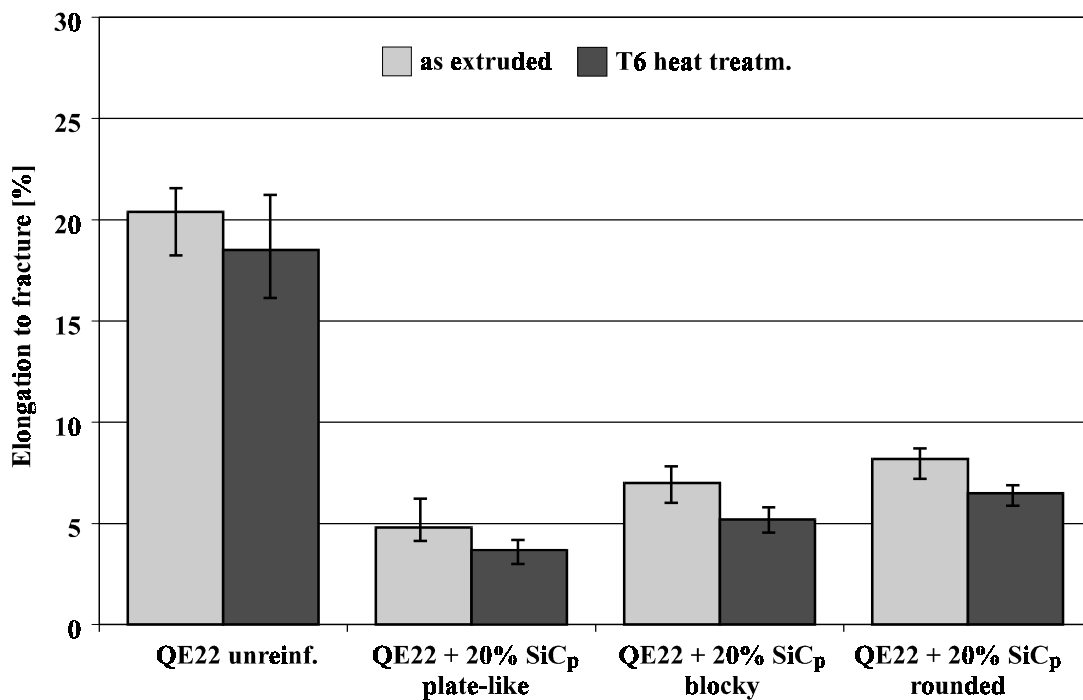


Fig. 11: Elongation to fracture of P/M produced QE22 and QE22/SiC_p composites

CONCLUSIONS

Particle reinforced magnesium matrix composites can be produced using powder metallurgical methods as well as the squeeze casting technique. Various matrix alloys and particles of different shapes, sizes and volume fractions enable a manufacture of composites providing certain properties. The alloy investigated showed a distinct improvement of stiffness as a result of the particle reinforcement, which is independent of the production method applied. Using the Tsai-Halpin model to estimate elastic moduli of particle reinforced magnesium base composites seems to be suitable only for a small particle aspect ratio and composites free of microstructural defects. The tensile strength of alloy QE22 was increased by the alumina platelets incorporated by squeeze casting and the differently shaped SiC particles used for P/M techniques. In contrast to elastic moduli the strongest increase in strength was obtained by rounded particles. A condition for obtaining this improvement is a homogenous distribution of the particles throughout the matrix. Concerning the powder metallurgy this was achieved by maintaining a size ratio of matrix powder to particle of 5:1. However, all the composite materials showed a much lower elongation to fracture than the unreinforced alloys and this reduction of ductility varies with the shapes of particles. Reinforcements with globular particles appear to be appropriate for applications requiring high strengths combined with a sufficient ductility. Particles with a high aspect ratio such as plate-like particles should be used if a high stiffness is demanded.

REFERENCES

1. Kainer, K.U. and Böhm, E., "Pressgießen (Squeeze Casting) von Magnesium-legierungen", *VDI-Bericht No. 1235*, 1995, pp. 117-125
2. Schröder, J., "Untersuchungen zum Aufbau und den mechanischen Eigenschaften von partikelverstärkten Magnesium-SiC-Verbundwerkstoffen", *PhD-Thesis*, Technische Universität Clausthal, 1991
3. Moll, F. and Kainer, K.U., "Microstructure and properties of Magnesium-SiC_p-composites influenced by production techniques and particle shapes", *Proc. 29th Int. Symposium on Automotive Technology & Automation (ISATA)*, Florence, Italy, June 3-6, 1996, Vol. 1, Roller, D. (ed.), Automotive Automation Ltd., UK, pp. 363-369
4. Knoop, F.M. and Kainer, K.U., "Erzeugung und Konsolidierung gasversduster Magnesiumpulver", *Metall*, No. 6, 1994, pp. 461-465
5. Halpin, J.C., "Primer on composite materials: Analysis", *Technomic Pub.*, rev. edn., 1984, Lancaster, PA, U.S.A., p. 130

FRACTURE BEHAVIOR OF CAST SiC_p-AL COMPOSITES UNDER ELEVATED TEMPERATURE

Daifeng Wang¹, Fengying Wu¹, Pengxing Li², Renjie Wu², Jingkun Guo¹

¹ Shanghai Institute of Ceramics, Chinese Academy of Science,
1295 Dingxi Road, Shanghai 200050, P. R. China

² State Key Lab of Metal Matrix Composites, Shanghai Jiaotong University,
1954 Huashan Road, Shanghai 200030, P. R. China

SUMMARY: Several kinds of aluminum alloy matrix reinforced with silicon carbide particles had been prepared by casting route and tested at various temperatures and strain rates. By observation of composites' fracture microstructure, two fracture mode had been determined, namely cavity-coalescing type and interface-debonding type. In the testing range of present paper, main factor influencing fracture mode is strain rate. At lower strain rate, cavity could be well developed to be operating damage process, in which isolated cavity nucleated in the initial stage of deformation and preferentially grew along matrix grain boundaries to form microcracks; while interfacing debonding significantly occurred at higher strain rate, and interlinkage of adjacent debonded SiC-Al interface turned to be the predominant damage mechanism. The influence of temperature on transition of fracture mode might be indirect and needs further study.

KEYWORDS: metal matrix composite, mechanical behavior at high temperature, fracture process, microstructure

INTRODUCTION

During the last decade, silicon carbide reinforced aluminum alloy matrix(SiC-Al) composite had demonstrated some favorable characteristics, including low raw material cost, easier control of the preparation process and less damage of reinforcement, property isotropy and machinability by conventional means. To examine the potential of such kind of materials to be applied under high temperature and to improve their workability, numerous research works had been done on the high temperature mechanical behavior of SiC-Al composites, especially on creep and superplasticity[1-3]. Meanwhile, SiC-Al composites could be manufactured at lower cost by employing casting route, however, research on cast SiC-Al composites' properties and microstructure under elevated temperature is in lack.

In the present paper, several kinds of SiC-Al composite prepared by compo-casting process had been tested under various temperature and strain rate, and the fracture microstructure was checked to determine the fracture characteristics of SiC-Al composite under elevated temperature and to reveal the role of SiC-Al interface.

EXPERIMENTAL

Composites employed in the present work were prepared by compo-casting route, in which SiC particles were added into solid-liquid state matrix alloy, followed by mechanical stirring and solidification. Ingots were then hot-pressed or extruded to reduce casting porosity, and machined to tensile specimens. Prior to testing, some specimen were heat treated to maintain microstructural stability during deformation, excepting the ones used for superplasticity testing ,where dynamic recrystallization was desired, and the 5083Al matrix material samples, which can not be strengthened by heat treatment. Testing and material parameters were summarized in Table 1.

Table 1: Material and testing parameters

Testing Type	Temperature (°C)	Strain Rate (s ⁻¹)	Material	Heat Treatment
Creep	300, 350	10 ⁻⁹ ~10 ⁻⁶	15 vol% SiC-2024Al	500°C, 1hr solution 190°C, 8hr aging
Superplasticity	~500	10 ⁻⁵ ~10 ⁻¹	10 vol% SiC-2024Al	none
Tension	200~400	~10 ⁻³	15 vol% SiC-5083Al 15 vol% SiC-5083Al-2Li	500°C, 1hr solution 150°C, 5hr aging (Li-containing ones only)

The microstructure of tested materials were examined using Hitachi S-520 SEM and Philips SEM515 SEM. In addition to fracture surface observation, more emphasis were put on sectioned microstructure analysis, in which specimens were sectioned along the longitudinal direction, then diamond polished and then slightly etched with a mixture of 0.5% HF, 1.5% HCl and 2.5% HNO₃.

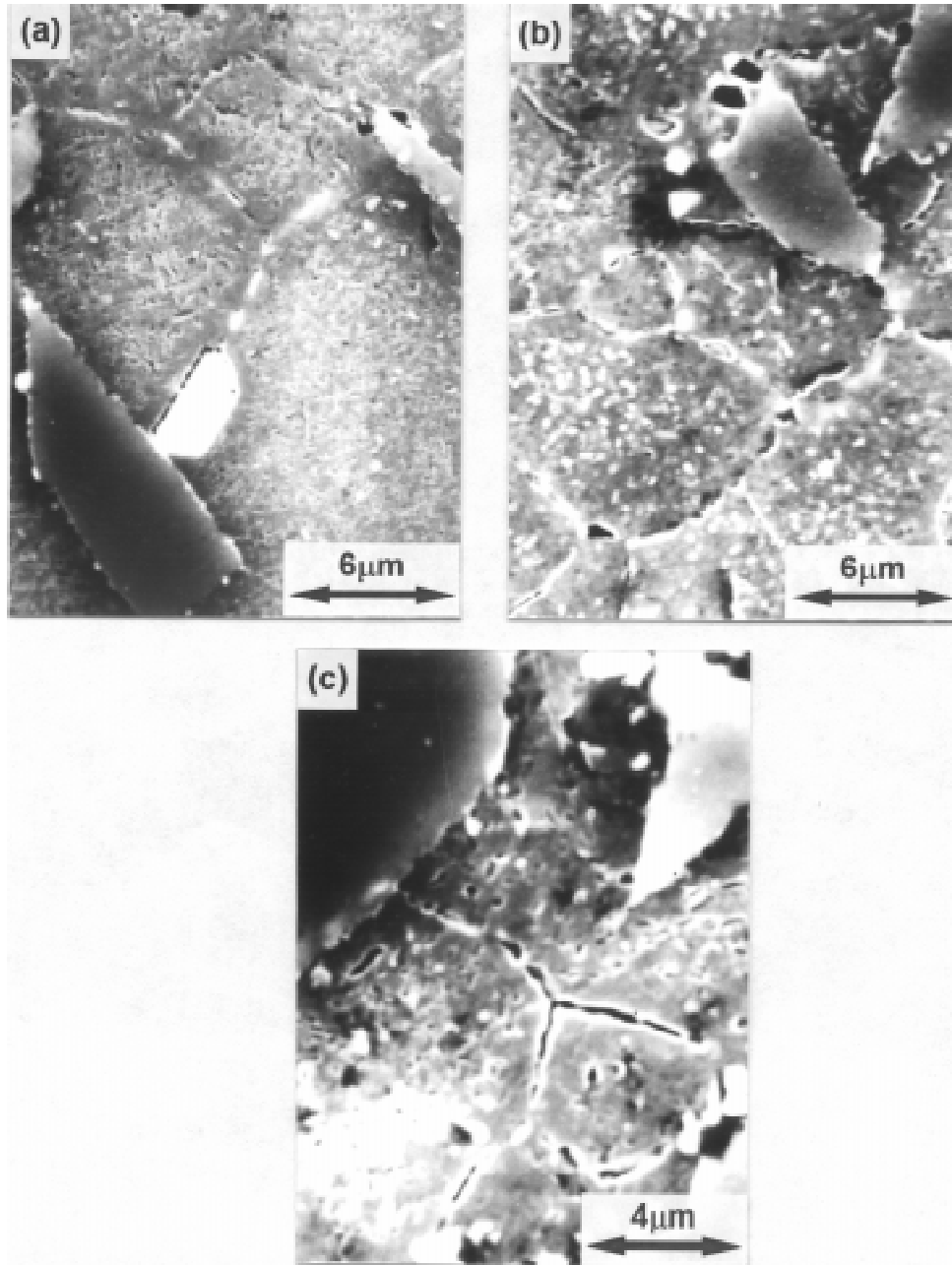
RESULTS AND DISCUSSION

Fracture Microstructure of Creep Tested Specimen

The typical microstructure of creep tested composite is shown in Fig. 1. At a very low strain level, voids were found to appear at the grain boundaries perpendicular to the stress direction, which might be related to the directional diffusion of vacancies from the interior of grain to grain boundary[4]. As the strain increases, however, nucleating cavities were observed at the grain boundary triple points and about the interfacial coarse precipitates (Fig. 1(a)).

With creep time and macro strain further increasing, cavities began to grow, as shown in Fig. 1(b). It could be seen that the shape of cavities on the grain boundary and the coarse precipitate-matrix interface was elongated along the interface to form discontinuous microcracks, and that some new cavities nucleated within matrix. In a detailed quantitative work on creep cavitation, it was determined that the matrix cavities growth was controlled by diffusional mechanism during steady state creep of the SiC-Al composite[5]. It is interesting to note that the cavities on the SiC-Al interface still remained the original quasi-equiaxed shape.

Fig. 1(c) shows the prior-to-failure microstructure in the composite. In the case of the operation of a diffusion controlled growth mechanism, the grain boundary cavities eventually inter-linked to form microcracks along grain boundary, leading to final failure. Consequently, the SiC-Al interface was found to delay the propagation of grain boundary microcracks (Fig. 1(c)), indicating a high bonding strength between SiC particles and matrix.



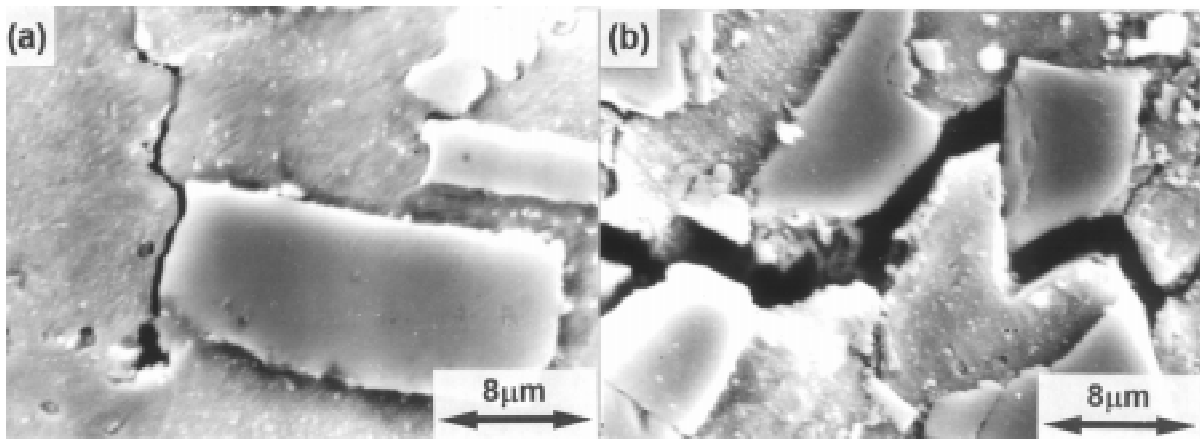
*Fig.1: Fracture microstructure of 15vol% SiC-2024Al creep tested at 300°C and 29.4MPa
(a) Cavity nucleation; (b) Cavity growth; (c) Formation of microcrack*

Fracture Microstructure of Superplastically Tested Specimens

Fig. 2 shows the fracture microstructure of SiC-2024Al composite deformed at 495°C and $2 \times 10^{-4} \text{ s}^{-1}$ to an elongation of about 150%, in which debonding of SiC-Al interface was found

to be the main feature. In Fig.2(a), it could be seen that a microcrack initialized in interfacial region was propagating to adjacent interface, indicating that the interface turned to be the preferential site of microcrack formation. Furthermore, microcracks were observed to propagate along SiC-Al interfaces and no evidence of matrix deformation in the area was found (Fig.2(b)), which hints significantly weakening of interface occurred during superplastic deformation. Compared to creep testing, the superplastic deformation temperature was much higher and near to that of matrix solidus point (502°C). Some researchers had reported interfacial solution element segregation and liquid phase was observed in superplastic composites [6, 7]. Therefore, it might be some kind of interfacial liquid phase that leading to interfacial weakening.

By the meantime, some cavities were also observed in regions of low SiC particle fraction, however, their size were smaller than that of those in creep tested specimens. Considering higher temperature and lower stress level compared to creep testing, it was reasonable to conclude during superplastic deformation the cavities still grew in diffusional mechanism, and hence the cavity growth rate was rather low to have significant impact on composite fracture process.



*Fig.2: Fracture microstructure of 10vol% SiC-2024Al composite superplastically deformed at 495°C and $2 \times 10^{-4} \text{ s}^{-1}$.
(a) Microcrack initialized in interfacial region; (b) Microcrack propagation*

Fracture Microstructure of Tension Tested Specimen

Fig.3 shows fracture microstructure of SiC-5083Al composites tensioned at 300°C and about 10^{-3} s^{-1} . In SiC-5083-2Li composite, where lithium was added to improve wetting between SiC particles and melted matrix alloy, reinforcement distributed uniformly. However, debonding of SiC-Al interface was observed, and adjacent debonded interfaces were found to linkup and form microcracks (Fig.3(a)).

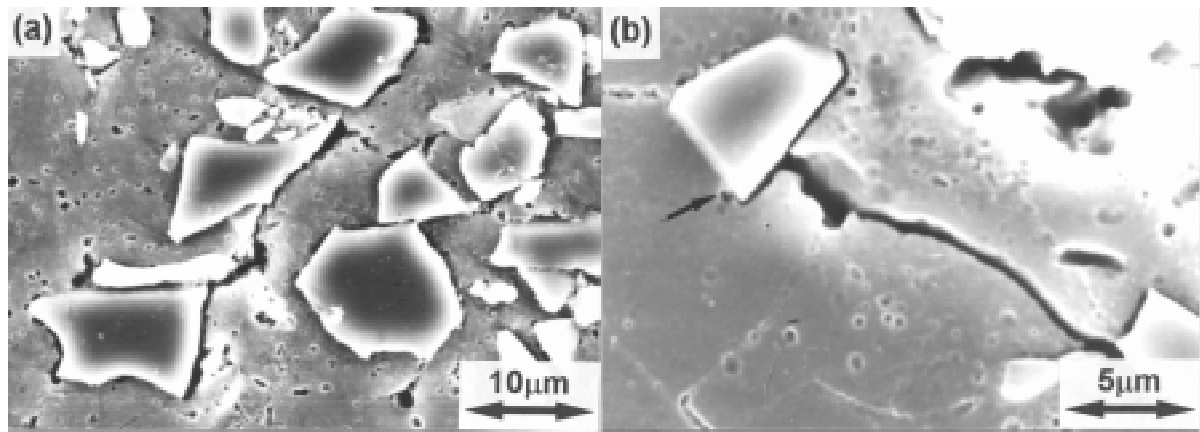


Fig.3: Fracture microstructure of SiC-5083Al composite tensioned at 300°C and $\sim 10^{-3} s^{-1}$
 (a) SiC-5083Al-2Li; (b) SiC-5083Al

In 5083Al matrix material, SiC phases were severely segregated due to poor wetting and particle clusters were found to be the origin of crack formation. It is worth noting that microcrack propagated along matrix grain boundary was found to be stopped in front of isolated particle (Fig.3(b)).

For both materials, matrix cavities were observed. Compared with those found in crept specimens, their shape maintained equiaxial. The high deformation rate obviously hindered intensive development of matrix cavitation.

High Temperature Fracture Mode of Cast SiC-Al Composites

Based on above observation and analysis, fracture characteristics of cast SiC-Al composites under elevated temperature were summarized in Table 2. From these information, two fundamental fracture mode were determined. Under low strain rate (*e.g.* creep testing), cavitation intensively occurred, and the composite failed in cavity coalescence mode. While increasing strain rate (tension) or simultaneously increasing temperature (superplasticity), influence of matrix cavitation became minor and interface debonding turned to be dominating factor of composite failure. The two failure mode are illustrated in Fig. 4.

It could be found from Fig.4 that in the testing range of the present work, strain rate determined the fracture mode. Under elevated temperature, diffusion process is remarkable, and deformation difference between various material component at low strain rate could be accommodated by diffusion related process, for example, diffusion-controlled cavity growth under creep condition. While increasing strain rate, deformation difference between matrix and SiC reinforcement can not be accommodated by diffusional process and the composite failed by interface debonding. The role of deformation temperature in failure mode transition is not clear, might in an indirect way including variation of interfacial strength and matrix phase composition, and needs further study.

Table 2: Summary of fracture characteristics of cast SiC-Al composites under various high temperature deformation

Characteristics	Creep	Superplasticity	Tension
Fracture surface morphology	Ductile dimples with size near that of SiC particles, and tearing on SiC-Al interfaces	Cavities with size much larger than SiC particle radius	Ductile dimples with size near that of SiC particles, and tearing on some of SiC-Al interfaces
Damage mechanism	Cavitation occurred at matrix grain boundary, SiC-Al interface associated with coarse precipitates	Debonding of SiC-Al interface and cavitation on matrix grain boundary	Debonding of SiC-Al interface
Formation of microcracks	Linkup of cavities grew in diffusional mechanisms	Interlinkage of debonded interfaces	Interlinkage of debonded interfaces in SiC particle-aggregated area
Microcracks propagation path	Along matrix grain boundaries and matrix-precipitate interfaces, and well bonded SiC-Al interface resisted the propagation	Preferentially along SiC-Al interfaces	Along matrix grain boundaries and SiC-Al interfaces, and the interface resisted crack propagation under certain condition

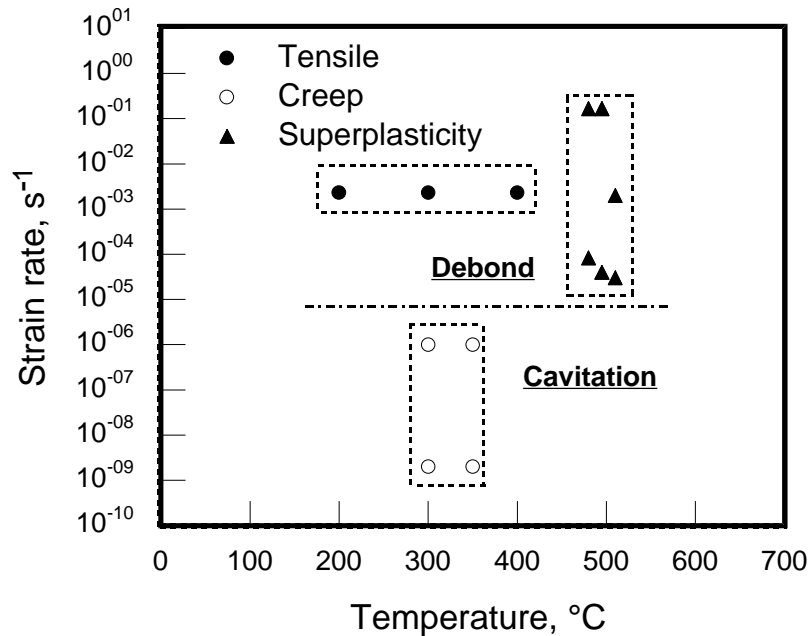


Fig.4: Fracture mode determined in cast SiC-Al composites by present work

CONCLUSIONS

By observing fracture microstructure of several cast SiC-Al composites under elevated temperature, two fundamental fracture mode had been determined as cavity coalescence mode and interface debonding mode. Following conclusions were obtained:

1. In the testing range in present work, strain rate determined the fracture mode. Cavity coalescence mode occurred in the case of low strain rate, where main damage mechanism was cavitation within matrix, and cavities aggregated and interlinked to form microcracks leading to final failure. Interface debonding mode took place at higher strain rate, in which reinforcement-matrix interface debonded due to strain discrepancy or weakening of interface strength and hence linkuped to form microcracks.
2. Cavitation occurred during high temperature deformation of SiC-Al composites. Cavity nucleation was related to matrix precipitates, and the most preferential nucleating site were including triple points of matrix grain boundary, interjection of grain boundary and SiC-Al interface.
3. Influence of testing temperature on high temperature fracture process of SiC-Al composite might be indirect and needs further study.

ACKNOWLEDGMENT

Financial supports from China National Science Foundation under grant No. 9590015-02 and No. 9392300-4-5 are greatly appreciated.

REFERENCES

1. T. G. Nieh, K. Xia and T. G. Langdon, "Mechanical properties of discontinuous SiC reinforced aluminum composites at elevated temperatures", *J. Engng. Mater. Tech.*, 110(1988), 77–82
2. K. T. Park, E. J. Lavernia and F. A. Mohamed, "High temperature creep of silicon carbide particulate reinforced aluminum", *Acta Metall. Mater.*, 38(1990), 2149–2159
3. J. Wadsworth and T. G. Nieh, "Superplasticity in ceramic and metal matrix composites and the role of grain size, segregation, interfaces, and second phase morphology", *Mater. Sci. Engng.*, A166(1993), 97–108
4. H. G. Edward and M. F. Ashby, "Intergranular fracture during power-law creep", *Acta Metall.*, 27(1979), 1505–1518
5. Daifeng Wang , Pengxing Li, Randy Grishaber, Qiang Li and A. K. Mukherjee, "Cavitation and its influence on the creep facture process of cast SiC particle reinforced aluminum alloy composites", submitted to *J. Mater. Sci.*
6. M. Strangwood, C. A. Hipsley and J. J. Lewandowski, "Segregation to SiC/Al interfaces in Al based metal matrix composites", *Scrip. Metall. Mater.*, 24(1990), 1483–1487
7. K. Koike, M. Mabuchi and K. Higashi, "*In situ* observation of partial melting in superplastic aluminum alloy composites at high temperatures", *Acta Metall. Mater.*, 43(1995), 199–206

SQUEEZE CASTING AND CHARACTERIZATION OF AL₂O_{3p}/ZL102 COMPOSITE

X.L. Guo¹, B.Y. Wu², J. Tao¹ and S.L. Li¹

¹ Composite Institute, Department of Materials Science and Engineering,
Nanjing University of Aeronautics & Astronautics, Nanjing 210016, P.R. China

² Department of Mechanical Engineering, Southeast University,
Nanjing 210018, P.R. China.

SUMMARY: In this research, the Al₂O_{3p} / ZL102 composite is used for the squeeze casting and metal module casting respectively. Its microstructure is characterized by optical microscope and scanning electron microscope (SEM). Its tensile strength, elongation and wear resistance are tested. The optimum pressure parameters of squeeze casting are achieved based on the above characterization. The results show that by use of the technique of squeeze casting, the microstructure become dense and the pore defects which usually appeared in metal module casting are completely eliminated, the binding force between the Al₂O₃ particles and metal matrixes is increased. The surface of the specimen become smooth and bright. The tensile strength, elongation and wear resistance are improved compared with that of metal module casting.

KEYWORDS: squeeze casting, metal module casting, Al₂O₃ particles, ZL102, tensile strength, elongation, wear resistance

INTRODUCTION

During the past 30 years, the metal matrix composites (MMCs) have been paid more attention for its advanced properties. This kind of material is developed rapidly in the advanced techniques area, esp. in the area of military, aeronautics and astronautics [1, 2]. Up to date, a series techniques are used to prepare MMCs, which can be divided into three types according to the state of metal matrix during synthesis: (1) liquid synthesis, (2) solid synthesis, (3) two-phase-area synthesis. However, the application of MMCs is still limited because of some problems, e.g. the interface reaction, high oxygen content, gas content and cinder content, complicated technology and high cost etc. [3, 4].

Recently, the squeeze casting techniques are used in the production of fiber reinforced metal matrix, and shows some obvious advantages than the common technology [5]. In this paper, we report our research on the production of Al₂O_{3p} / ZL102 composite by the squeezes casting technique.

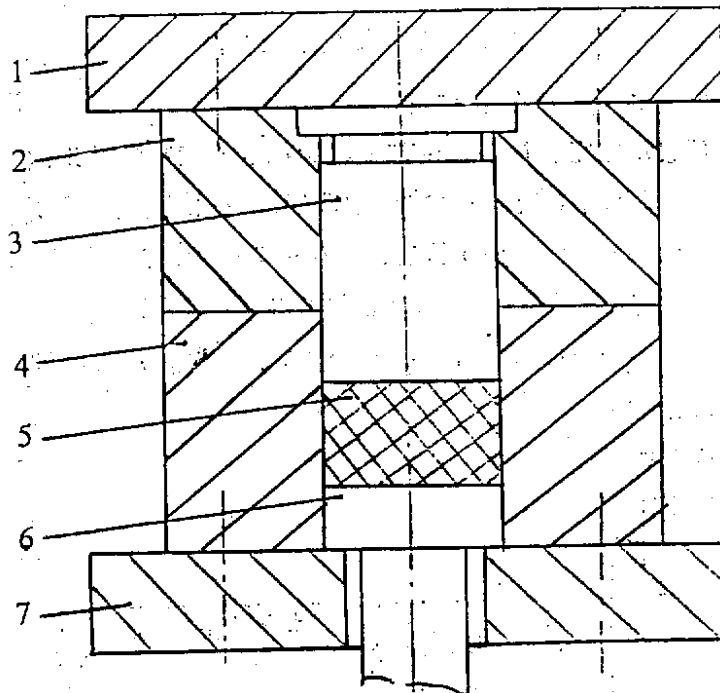
EXPERIMENTAL PROCEDURE

The average diameter of Al_2O_3 particles used in this experiment is in the range of $0.3\mu\text{m}\sim 1\mu\text{m}$. The ZL102 alloy is chosen as the metal matrix. The chemical composition of ZL102 alloy is shown in table 1.

Table 1: Chemical composition of ZL102(wt%)

Si	Cu	Fe	Al
12.5	0.01	0.05	87.4

The $\text{Al}_2\text{O}_3/\text{ZL102}$ composite is prepared by adding the pre-heated 6% Al_2O_3 particles at the temperature of 200°C into the ZL102 alloy at the state of semi-solidification by a method of mechanical stirring. Afterwards, the semi-solidified alloy is heated to the temperature of $710\sim 730^\circ\text{C}$ for squeeze casting. The squeeze casting module is schematically drawn in figure 1. It was pre-heated to $250\sim 300^\circ\text{C}$ before pouring.



*Fig.1: Schematically drawn of squeeze casting module
1-roof of upper module, 2-upper module, 3-squeeze head,
4-lower module, 5-casting, 6-push pole, 7- roof of lower module*

The technological parameters of squeeze casting are shown in table 2.

Table 2: Squeeze casting parameters

pouring temperature ($^\circ\text{C}$)	module temperature ($^\circ\text{C}$)	pressure (MPa)	holding time (s)
710~730	250~300	0~115	60

The microstructures of Al_2O_3 / ZL102 Composites are analyzed by optical microscope and scanning electron microscope (SEM). According to the ASTM standard, the tensile specimen is prepared for the testing of tensile strength and elongation. The wear resistance of Al_2O_3 / ZL102 composite is tested.

RESULTS AND DISCUSSION

Under the observation of optical microscope, the Al_2O_3 particles distribute uniformly in the matrix of ZL102 (see Fig.2).

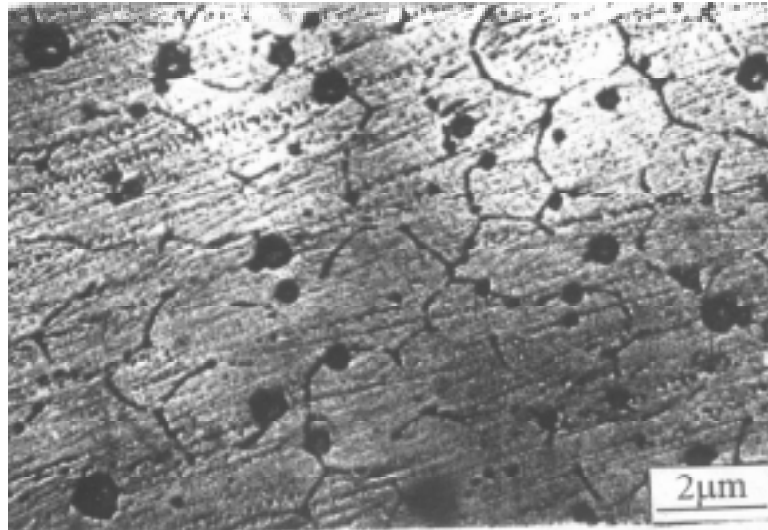


Fig.2: Distribution of Al_2O_3 particles in the matrix of ZL102 (pressure: 85MPa).

Fig.2 also shows that most of the Al_2O_3 particles usually distribute in the grain boundary, which is related to the solidification process. It can be sure that the Al_2O_3 particles uniformly distributed in the grain boundary will be able to effectively resist the deformation of matrix and reinforce the ZL102 alloy. By use of SEM, the microstructure of the Al_2O_3 / ZL102 composite is observed at high magnification. The results indicated that pore defects which often appeared in the metal module castings are completely eliminated and the microstructure become dense. Compared with that of metal castings, the surface brightness is improved. This is attributed to the reason that the filling ability of liquid Al_2O_3 / ZL102 composite is improved by the squeezing force.

The tensile strength and elongation of squeeze castings versus the pressure are shown in figure 3. It reveals that tensile strength and elongation of squeeze castings are higher than that of metal module castings (pressure=0) and are increased with the increase of pressure. However, when the pressure is over 85MPa, the tensile strength is increased slowly with the increase of pressure. Whereas the elongation get its optimum values at the pressure of 85MPa. This is due to the reason that with the increase of pressure, the pores in the matrix is eliminated and the binding force between the matrix and the particle is increased, which made the tensile strength and elongation increased. But if the pressure is too high, the resistance of Al_2O_3 particles to the deformation of matrix is greatly increased and the elongation is decreased. Therefore, the brittleness is increased.

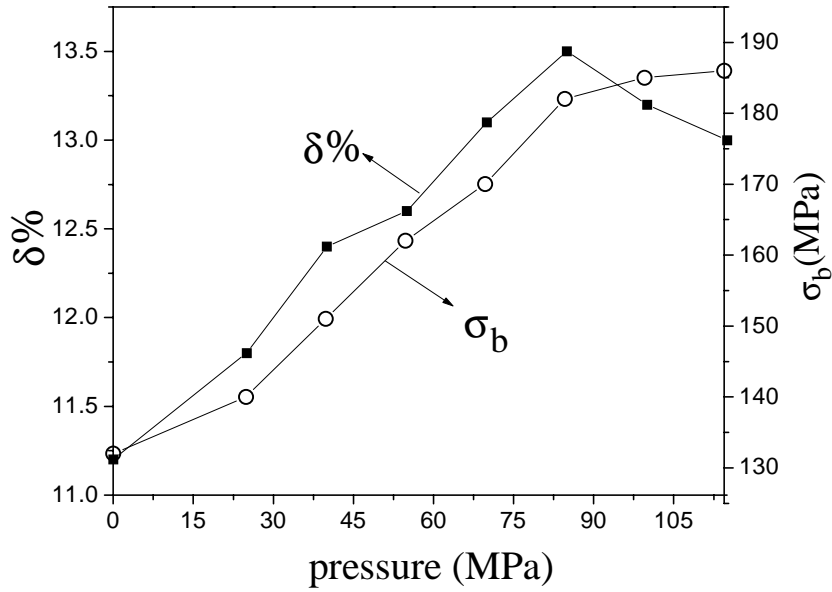


Fig.3: The tensile strength and elongation of $Al_2O_{3p}/ZL102$ Composite versus the pressure.

Fig.4 represents the wear resistance of $Al_2O_{3p}/ZL102$ composite versus the pressure.

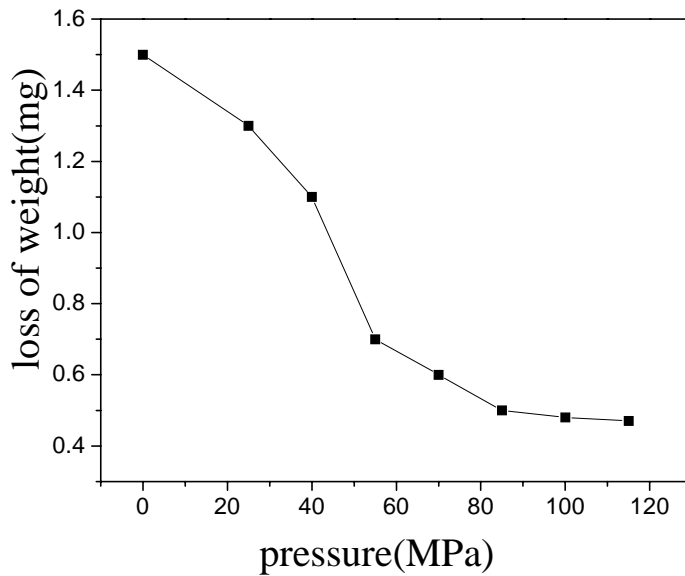


Fig.4: Wear resistance of $Al_2O_{3p}/ZL102$ composite versus the pressure.

The wear resistance of $Al_2O_{3p} / ZL102$ is mainly determined by its tensile strength. Fig.4 indicated that the wear resistance also increases with the increase of pressure, but it is increased slowly as the pressure is over 85MPa. Based on the results of Fig.3 and Fig.4, the optimum pressure value in this experiment is determined as 85MPa.

CONCLUSIONS

1. By use of the technique of squeeze casting, the pore defects in MMCs can be completely eliminated, the tensile strength, elongation and wear resistance can be greatly improved.
2. The optimum pressure can be determined according to the variation of mechanical properties versus pressure. In this research, the optimum pressure is determined as 85MPa.
3. The improvement of squeeze casting to the quality of $Al_2O_{3p} / ZL102$ composite is attributed to the fact that the binding force between the Al_2O_3 particles and ZL102 matrix is increased and the pore defects is eliminated under the squeeze force.

ACKNOWLEDGEMENT

The authors would like to express their thanks for financial support from the foundation of Aeronautics Institute of China.

REFERENCES

1. Wang huijie, He jianwei, QinShuyi and Lei yanquan, "Review to the Aeronautics Composite Techniques in China", Proceedings of China Conference on Composites, Beijing, Aug.14-18, 1996, pp1-6.
2. Yu qiao, Zhu daitong, Mao huamin, "Introduction and Review of Composite Materials in the Application of Aeronautics industry", Proceedings of China Conference on Composites, Beijing, Aug.14-18, 1996, pp8-15.
3. Liu kaiwen, Zhang jishan and Chen guoliang, "Fabrication of Particle Reinforced Metal Matrix and Intermetallics Matrix Composite by the unequilibrium Method", Proceedings of China Conference on Composites, Beijing, Aug.14-18, 1996, pp14-18.
4. Zhang jishang, Zheng yu, Chui hua, Duan xianjin and Chen guoliang, "New Formation technique of MMCs-Spray Forming", Proceedings of China Conference on Composites, Beijing, Aug.14-18, 1996, pp214-219.
5. Yang chuang, Liu shikai, Zhang jixi, Qin shuyi and Lei yanquan, "Strench and Fracture Process of $Al_2O_{3f}/Al-5\%Cu$ Composites and Effects of directional arrangement", Proceedings of China Conference on Composites, Beijing, Aug.14-18, 1996, pp247-251.

COLD ROLLING OF PARTICLE REINFORCED ALUMINUM MATRIX COMPOSITE AND MECHANICAL PROPERTIES

N. Kanetake, T. Kaneko and T. Choh

*Department of Materials Processing Engineering, School of Engineering
Nagoya University, Furo-cho 1, Chikusa-ku, Nagoya 464-01, JAPAN*

SUMMARY: Cold rolling and subsequent annealing processes are investigated to fabricate SiC particle reinforced pure aluminum composite sheets. Bar type of the composite with rectangular section was prepared by a powder extrusion. They were cold rolled in various reduction and subsequently annealed at various temperatures. A limit cold rolling reduction is measured for the composites with various SiC volume fractions. The effects of cold rolling reduction and annealing temperature on tensile properties of the composite sheets are evaluated and compared with those of unreinforced pure aluminum sheets. The composite sheet with lower SiC volume fraction than 10% can be successfully cold rolled in higher reduction than 90 %. The proof stress and tensile strength of the composite sheets rolled in higher reduction than 60 % are independent on the rolling reduction, while those of unreinforced pure aluminum sheets are increased with the reduction. Those properties of rolled pure aluminum sheets are rapidly decreased by subsequent annealing at around 548 - 573K, but those of composite sheets are only gradually decreased with annealing temperature.

KEYWORDS: metal matrix composite, pure aluminum, cold roll, anneal, mechanical property, SiC particle, powder extrusion

INTRODUCTION

Metal matrix composites (MMCs) which are reinforced with ceramic particles or short fibers are very useful to realize lightweight structural parts, because they have high specific stiffness and strength and good wear resistance. However the MMCs have not been much put to practical use in the automobile or machine industries, though many trial products have been made in various fields. Recently only a few products of MMCs can be found in those industries, for example a piston, a cylinder block and an intake valve for automobile engine. Most of them are bulk type products and they are produced directly into the final parts by liquid processing routes like a squeeze casting or a pressure infiltration. Simple shape billets of aluminum matrix composites can be now easily fabricated by either liquid phase routes like melt stirring, rheocasting, compocasting and spray deposition methods or solid phase routes like powder extrusion, hot press and HIP processes. However economical secondary processes to produce complex shape parts from those billets have not yet been established to apply them much more into the mass-products.

As the MMCs can be deformed like conventional metals even at room temperature as well as elevated temperature, a deformation processing is an alternative secondary process for complex shaped components of MMCs. The authors are now focusing on the deformation processing of particle reinforced aluminum matrix composites [1 - 6].

On the other hand, sheet type products of MMCs are far behind in developing and applying in industrial fields compared with bulk type ones. It may be impossible to produce directly final parts of sheet type MMCs. They should, in the first place, be rolled from MMC billets fabricated by liquid or solid routes, then the rolled sheets should be formed into final complex shaped parts like conventional metal sheets. In general aluminum alloy sheets are hot and cold rolled and subsequently heat treated under various process conditions to arrange their optimum microstructure and mechanical properties. As the MMC consists of ductile matrix metal, hard particles and their interfaces, it will be subjected to more complicated internal stress state and microstructural behavior than conventional metals during deformation and heat treatment processing.

In the present work cold rolling and subsequent annealing processes are investigated for SiC particle reinforced pure aluminum composite sheets. At first a limit cold rolling reduction, that is the maximum rolling reduction at which the cold rolling can be successfully performed without crack initiation, is measured for the composites with various SiC volume fractions. The effects of rolling reduction and subsequent annealing temperature on mechanical properties of the composite sheets are evaluated and compared with those of unreinforced pure aluminum sheets.

EXPERIMENTAL PROCEDURE

Materials

A SiC particle reinforced pure aluminum matrix composite was used in the present work. It was prepared by the powder extrusion method to perform a good dispersion of particles and to prevent some complicated chemical reactions between the matrix aluminum and particles. The matrix is an air atomized A1050 pure aluminum powder with mean diameter of around 40 μ m and the reinforcement is SiC particulate with mean diameter of 4.3 μ m.

The matrix aluminum powder and SiC particles whose volume fractions are 5, 10, 15 and 20 % were mixed using a V-type mixer for 10 hours. The mixed powder was directly consolidated by extrusion at 773K into the bar type specimen with a rectangular section to be used for subsequent rolling. The thicknesses of the bars are 3.0, 6.0 and 10.0 mm and their widths are all 10.0 mm. An A1050 pure aluminum ingot material which was also processed by extrusion and rolling in the same way was used as a reference material.

Rolling and tensile test

When the composite was rolled in higher reduction than its rolling limit, a large crack in the center of width at the top or many small cracks at the sides were observed in the rolled sheet. The limit rolling reduction (reduction in height) of the composite, that is the maximum rolling reduction at which no cracks are initiated in the rolled sheet, was investigated using the specimen with thickness of 3.0mm. The specimen was rolled at room temperature by a method of multi pass rolling as shown in Fig. 1. Initially it was rolled in reduction of 10, 20 or 30 % per pass (this stage is called a rough rolling), and the limit reduction in the rough rolling (R_p) was decided as the maximum total reduction at which no cracks are observed in the rolled sheet. The specimen

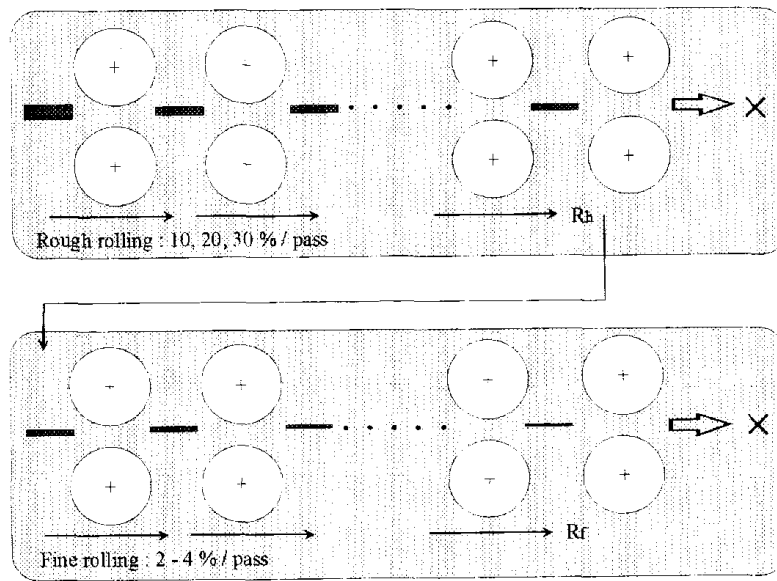


Fig. 1: Rolling process to estimate limit rolling reduction (R_r , R_f) in rough and fine rolling.

rolled until R_h was subsequently rolled in around 3 % per pass (it is called a fine rolling), and the limit reduction in fine rolling (R_f) was also decided in the same manner. The effect of rolling reduction per pass in the rough rolling on the limit rolling reductions R_h and R_f was investigated for the composites with various SiC volume fractions.

Mechanical properties of the rolled composites were measured by a tensile test. In order to make uniform in 0.5 mm final thicknesses of sheets which were rolled in various reductions, extruded composite bars were pre-rolled in respective fitting reductions and subsequently annealed at 623K for 1 hour. So processed initial specimens were further rolled in reductions of 60, 70 (75 for the pure aluminum), 90 and 95 % at room temperature. The cold rolled specimens were subsequently annealed at various temperatures for 1 hour. The tensile tests were performed for not only as-rolled specimens but also annealed ones to investigate the effects of rolling reduction and annealing temperature on the mechanical properties of composite sheets.

RESULTS AND DISCUSSION

Limit rolling reduction

Fig. 2 shows the result of rolling test which was performed by 10 % pass reduction in the rough rolling for the composites with various SiC volume fractions. An open circle means successful rolling without crack initiation in the rough rolling and a broken line shows the limit reduction (R_h). A closed circle means similarly successful rolling in the fine rolling and a solid line shows the final limit reduction (R_f). A cross mark means initiation of some cracks in the fine rolling. On the other hand, an arrow means that the limit reduction (R_f) is much higher, but the further rolling is impossible to perform because of a mechanical limit of the used rolling mill.

The limit rolling reductions (R_h , R_f) of the composites which depend on the SiC volume fractions

can be seen in Fig. 3. The limit reduction in the rough rolling (R_h) depends on the pass reduction and it increases with decreasing pass reduction. But the final limit reduction (R_f) after the fine rolling is independent on the pass reduction in the rough rolling. Therefore it can be found that the rolling limit of the SiC particle reinforced pure aluminum composite does not depend on the reduction per pass but only the total reduction. The composites with SiC volume fractions below 10% can be cold rolled in higher reduction than 90% without initiation of any cracks. Even the composite with 20% volume fraction can be successfully cold rolled in around 70% rolling reduction.

Mechanical properties

Proof stress, tensile strength and uniform elongation of the composites with the 10% SiC volume fraction which were rolled in various reductions are shown in Fig. 4 in comparison with those of

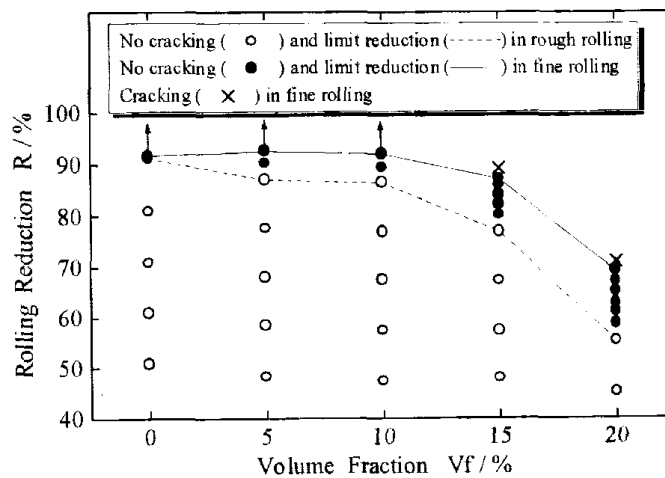


Fig. 2: Rolling situation in rough rolling with 10% pass reduction and fine rolling.

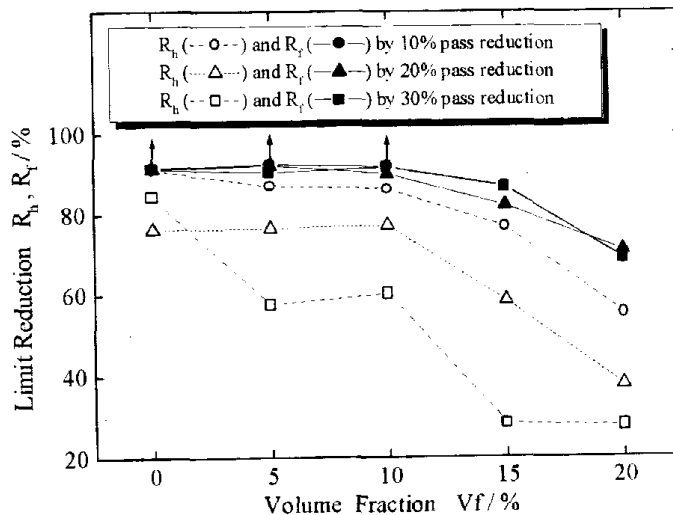


Fig. 3: Effect of pass reduction in rough rolling on limit total reduction.

pure aluminum specimens. The proof stress and tensile strength of the pure aluminum are increased with the rolling reduction, while those of the composite are hardly varied or slightly decreased. When hard particles are dispersed in metal matrix, strain hardening of the matrix metal is accelerated, because much dislocation can be easily generated and accumulated in the matrix due to the dispersed particles. Therefore the strain hardening of the composite is larger and saturated at smaller deformation than the unreinforced metal. As a result the reinforcement effect of the dispersed particles in the rolled composite sheet is reduced with increasing rolling reduction.

The composite with 10% SiC volume fraction and pure aluminum which were rolled in different reductions were annealed at various temperatures for 1 hour and their proof stress, tensile strength and uniform elongation were measured. Figs. 5, 6 and 7 show the effects of the annealing temperature on the mechanical properties of the sheets. Their changes by annealing are very remarkable in the pure aluminum. The proof stress and tensile strength are slowly decreased at lower temperature than 548K and rapidly decreased at 573K, then they are not changed at higher temperatures than 573K. The elongation is rapidly increased by annealing at 573K, it means that the rolled sheet is almost completely annealed at that temperature. On the other hand, the tensile properties of the rolled composite sheets are not rapidly change at any temperatures but only slowly changed from 498K to 723K. From the result it is predictable that the recrystallization of the matrix aluminum by annealing is gradually progressed with increasing temperature but not completed in the composite, while it is rapidly progressed and completed at around 548-573K in the pure aluminum. Such tendency of change in mechanical property is independent on the rolling reduction of sheets. Therefore the reinforcement effect of SiC particles, namely the difference of the property between the composite and pure aluminum is the largest in the sheet annealed at around 573K.

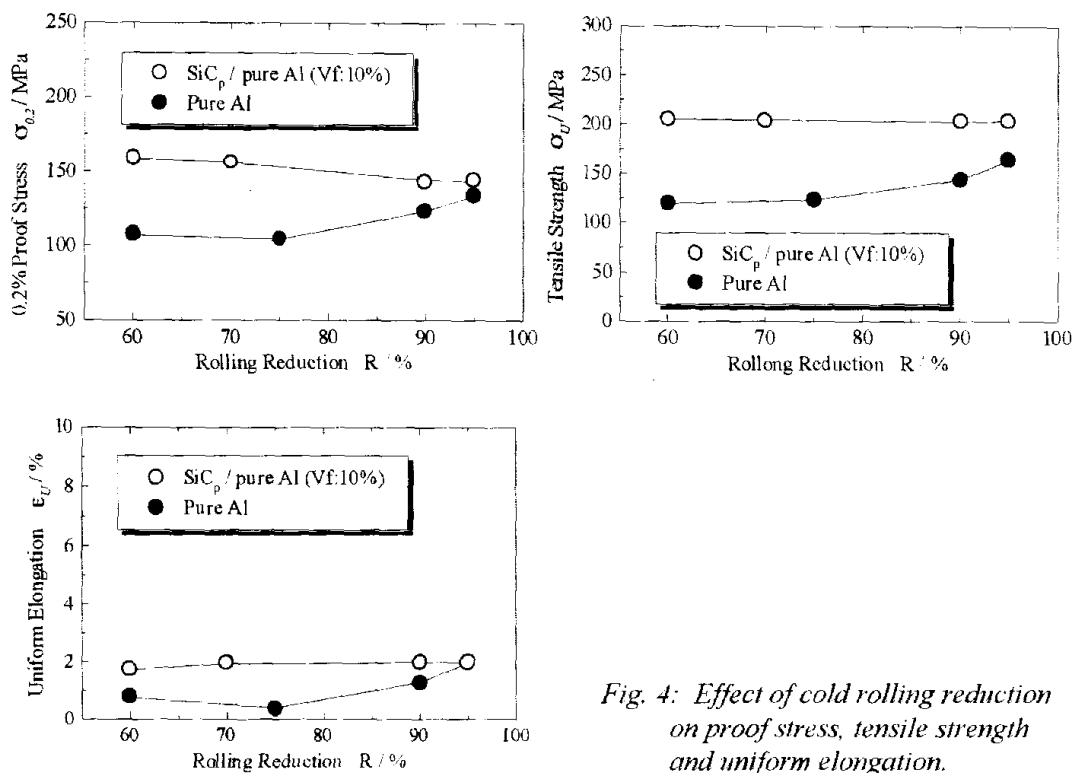


Fig. 4: Effect of cold rolling reduction on proof stress, tensile strength and uniform elongation.

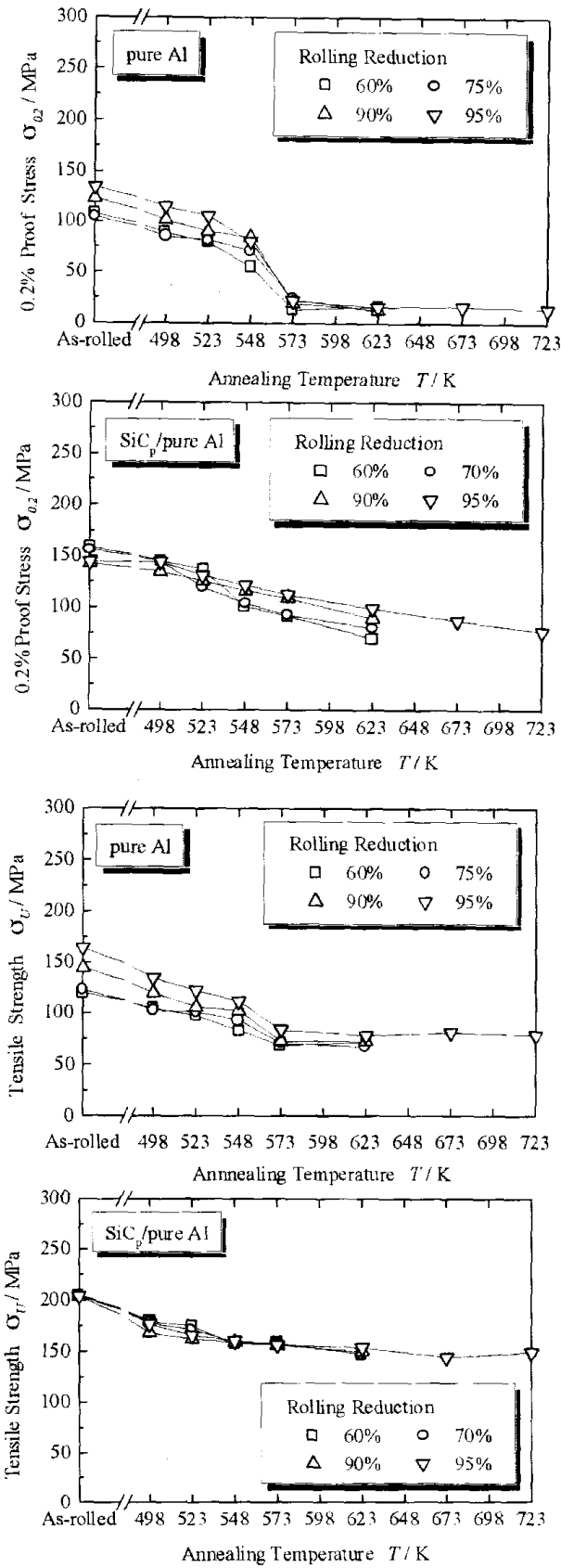


Fig. 5: Effect of annealing temperature on proof stress of cold rolled sheets.

Fig. 6: Effect of annealing temperature on tensile strength of cold rolled sheets.

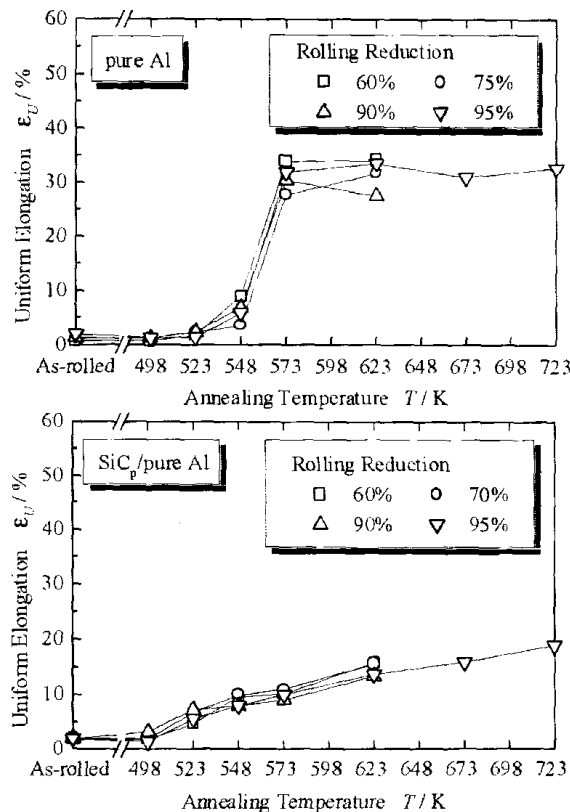


Fig. 7: Effect of annealing temperature on uniform elongation of cold rolled sheets.

CONCLUSION

The cold rolling limit of the SiC particle reinforced pure aluminum composite does not depend on the reduction per pass but only the total reduction. The composites with lower SiC volume fractions than 10 % can be cold rolled in higher reduction than 90 % without initiation of any cracks. Even the composite with 20 % volume fraction can be successfully cold rolled in around 70 % rolling reduction. The proof stress and tensile strength of the composite sheets rolled in higher reduction than 60 % are hardly varied or slightly decreased with the rolling reduction, while those of unreinforced pure aluminum sheets are increased. Those properties of rolled pure aluminum sheets are rapidly decreased by subsequent annealing at temperature of 548 - 573K, but those of composite sheets are only gradually decreased with annealing temperature.

REFERENCES

1. N. Kanetake and H. Ohira, *J. Mater. Proces. Tech.*, **24** (1990),281-289.
2. N. Kanetake and T. Choh, *Proc. 3rd Int. SAMPE Metals Conf.*, M414, (1992).
3. N. Kanetake and T. Choh, *Proc. 9th Int. Conf. Composite Materials*, (1993), 634-641.
4. N. Kanetake, M. Ozaki and T. Choh, *Mater. Sci. Tech.*, **11-4**(1995),357-362.
5. N. Kanetake, M. Nomura and T. Choh, *Mater. Sci. Tech.*, **11-12**(1995),1246-1252.
6. N. Kanetake, H. Saiki and T. Choh, *Proc. 10th Int. Conf. Composite Materials*, (1995),107-114.

AN IN-SITU STUDY OF THE FRACTURE MECHANISMS OF SiCw/AZ91 MAGNESIUM MATRIX COMPOSITES

Mingyi Zheng, Kun Wu, Wencong Zhang, Min Zhao

P.O.Box 433, School of Materials Science and Engineering, Harbin Institute of Technology, Harbin 150001, P.R.China

SUMMARY: In this paper, the fracture processes of squeeze cast SiCw/AZ91 magnesium matrix composites were studied with in-situ scanning electron microscope (SEM) and transmission electron microscope (TEM) tensile techniques. When the composite was loaded, plastic deformation took place in local stress concentration regions, then developed into microcrack. A large number of microcracks initiated in the matrix and these cracks linked abruptly, resulting in catastrophic fracture of the composite. The results indicated that the poor ductility of the composites was attributed to the local stress concentration because of the addition of the whiskers and the low inherent ductility of the matrix magnesium alloy. The fracture processes of the composites was matrix-controlled.

KEYWORDS: Magnesium alloy, SiC whisker, metal matrix composites, squeeze cast, in-situ SEM, In-situ TEM, tensile, microcrack, fracture.

INTRODUCTION

Magnesium alloys are becoming increased favored for structural application. This is not only due to their relatively low density, which can reduce weight and save energy substantially, but also due to their good damping capacity, castability and mechinability. However, the disadvantages of relatively low strength at room and elevated temperature, low elastic modulus and wear resistance, and poor corrosion resistance, restrict their use in applications where stringent requirements must be met. Magnesium alloys reinforced with discontinuous phases, such as short fibers [1-2], particles [3-6], or whiskers [7-8] can eliminate all the disadvantages except for poor corrosion resistance, showing that magnesium matrix composites have increasing potential in automotive, high performance defense and aerospace applications.

However, the poor ductility and fracture toughness limited their use in many structural applications. The strain to failure was often around 1% in these composites. In order to widen their application areas, low ductility of the composites has to be improved.

Compared with Al-MMCs, only a few studies [5-6, 9-11] have been reported on the fracture mechanisms of discontinuously reinforced Mg-MMCs, the fracture mechanisms of the composites are poorly understood.

As for SiCw/Al composites, much effort has been focused on their fracture mechanisms, the mechanical properties of the matrix, whisker, interface between whisker and matrix, and coarse intermetallic particles play important roles in the fracture behavior of the composites.

Several techniques have been used to study the fracture behavior of metal matrix composites. SEM fractography analysis, SEM and TEM examination of the crack path in controlled fracture test specimens which were stopped and unloaded just prior to unstable crack growth [11], are based on observation of damaged microstructure of postmortem samples, providing no further information on the critical events in fracture process. In-situ SEM and TEM tensile techniques can provide dynamic observation of the crack initiation and propagation. In-situ SEM tensile technique can only be used to observe the changes of surface microstructure, while in-situ TEM straining technique can give more information, such as the emission and motion of dislocations in the process of deformation, site of crack initiation, propagation path, as well as the effect of interface and precipitates on the crack initiation and propagation.

Because of the HCP crystal structure of Mg alloys, the fracture mechanism of Mg-MMCs is different from that of Al-MMCs. To elucidate the relationship between fracture micromechanisms and microstructure of the composites, dynamic observation of fracture processes in squeeze cast SiCw/AZ91 magnesium matrix composites was performed with in-situ SEM and TEM tensile techniques.

EXPERIMENTAL

The materials used in this study were SiCw/AZ91 magnesium matrix composites fabricated by squeeze casting method. Commercial heat treatable AZ91 magnesium alloy (8.5-9.5% Al, 0.45-0.90% Zn, 0.15-0.30% Mn, 0.20% Si, 0.01% Ni, balance Mg) was used as matrix, TWS-100 β -SiC whisker was used as reinforcement whose volume fraction in preform is 20% without binder. Squeeze casting was carried out by pouring molten AZ91 overheated to 800°C into the SiC whisker preform, which was preheated to 800°C and placed in the squeeze cast mold preheated to 300°C, and then by infiltrating the melt into the preform under the pressure of 100 MPa. The processes of melting and pouring were performed under CO₂/SF₆ atmosphere.

The specimens used for in-situ SEM tensile were machined from the above squeeze casting ingot into thin plates, the dimensions of which were shown in previous work [12]. A sharp notch (0.2 mm in depth, 0.1mm in width) was made in the center of the specimens by electric discharge machining (EDM). For clear observation, the observation surfaces of the specimens were metallographically polished. In-situ SEM tensile processes were performed with a HITACHI S-570 SEM equipped with a tensile stage, the strain rate was about $2 \times 10^{-4} \text{ S}^{-1}$.

The in-situ TEM tensile specimens with dimension of $3 \times 5 \text{ mm}^2$ were also prepared from squeeze casting composites, and mechanically ground into 0.3 mm thick thin foils, then dimpled with Gatan dimpler, finally were ion milled to perforation using a liquid nitrogen cold stage to prevent heating during the ion milling process. In-situ TEM tensile processes were performed in a H-800 TEM equipped with a strain stage operating at 175 KV.

RESULTS AND DISCUSSION

The fracture behavior of discontinuously reinforced MMCs is very sensitive to the reinforcement, the interface and the matrix, although it is difficult to identify clearly the dominant mechanism and contributions by each mechanism. Dynamic observation with in-situ tensile techniques make it possible to suggest the dominant mechanism and its contributions.

From in-situ SEM dynamic observation, it is found that when load was applied, microcracks started to be initiated at the ends of whisker and damaged whiskers, as shown in Fig.1. Some microcracks in the matrix can also be observed. When applied load increased, major crack formed at the center of the precrack and some microcracks formed around the crack tip, see Fig.2. When high load was applied, major crack grew to some extent, but more microcracks formed in the matrix and some microcracks linked together. After applying more load, microcracks linked together abruptly, leading to the catastrophic failure of the composites along a direction perpendicular to the applied stress axis.

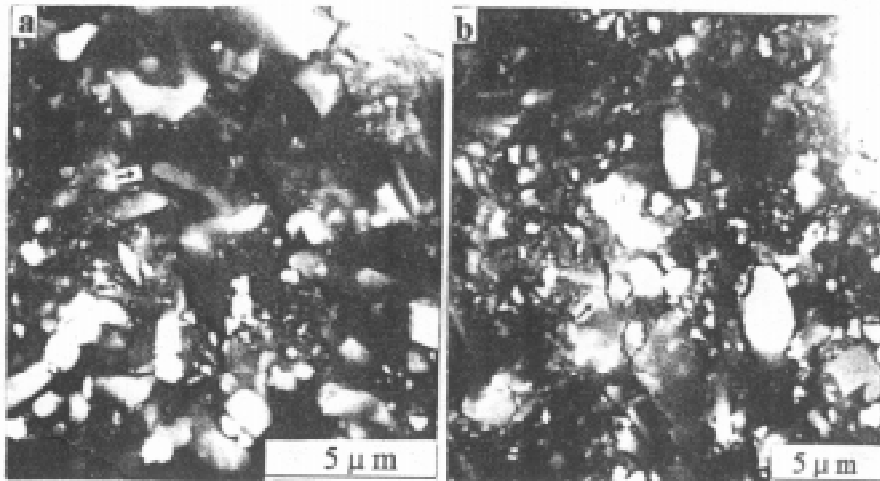


Fig.1: Microcracks initiated at (a) whisker ends, (b) damaged whiskers.

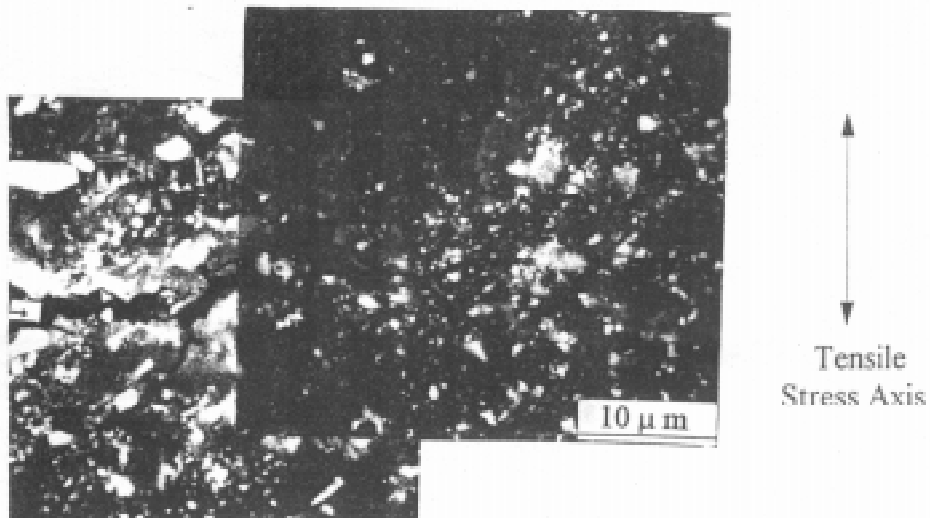


Fig.2: Major crack formed in the composites.

In order to further observe the microstructural changes in the composites in the case of deformation and fracture, in-situ TEM tensile was performed, which can give more information, such as the emission of dislocations in the process of deformation, as well as the influence of interface and precipitates on the crack initiation and propagation. Although the stress conditions between the TEM foil specimen and bulk material are different, the former is under plane stress condition, the latter is under plane strain condition, dynamic observation can provide insight into the poor ductility of the composites[13].

As the thin foil was loaded, crack initiated at the edge of the perforation perpendicular to the tensile direction, accompanied by the emission of dislocations which went ahead quickly to form dislocation free zone(DFZ) at the crack tip, as shown in Fig.3. It also can be seen that the motion direction of the dislocations was changed because of the pile up of dislocations at the interface. At the same time, the original dislocations existing in the matrix also went ahead.

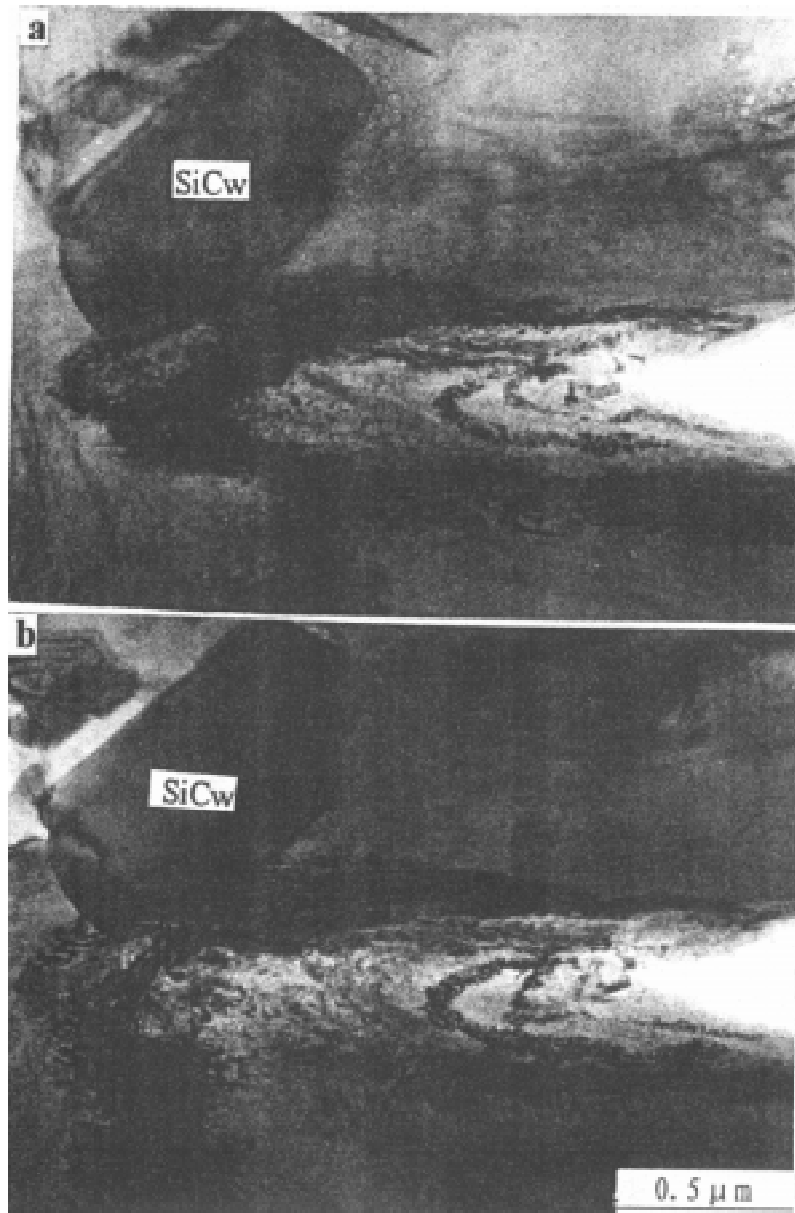


Fig.3: Interaction between dislocations and SiC whiskers, (a) pile up of dislocations at interface, (b) motion of dislocations after further straining.

After further loading, a large number of microcracks formed in the magnesium matrix, and local thinning appeared to occur during the microcrack formation. Most of local thinning and microcracks were adjacent to the SiC whiskers, as shown in Fig.4. Dislocations stacked in local thinning regions.

With increase in the applied load, some microcracks propagated, and some local thinning developed to microcracks. Upon further straining, these microcracks quickly linked together, leading to catastrophic fracture of the composites, along a direction perpendicular to the tensile axis of the specimen.

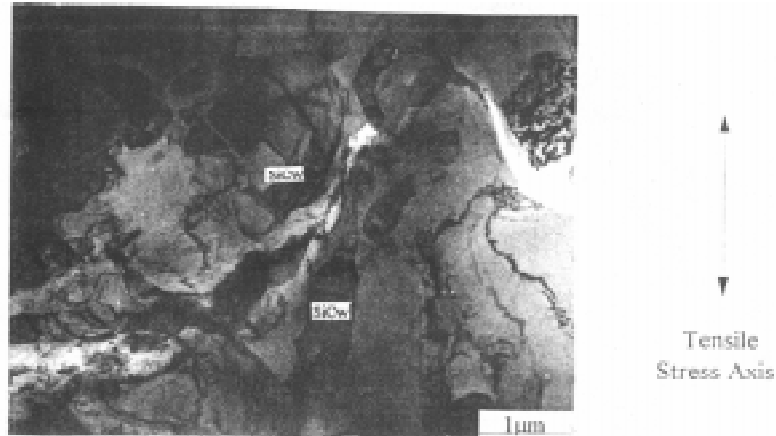


Fig.4: Local thinning and microcracks formed in the composites.

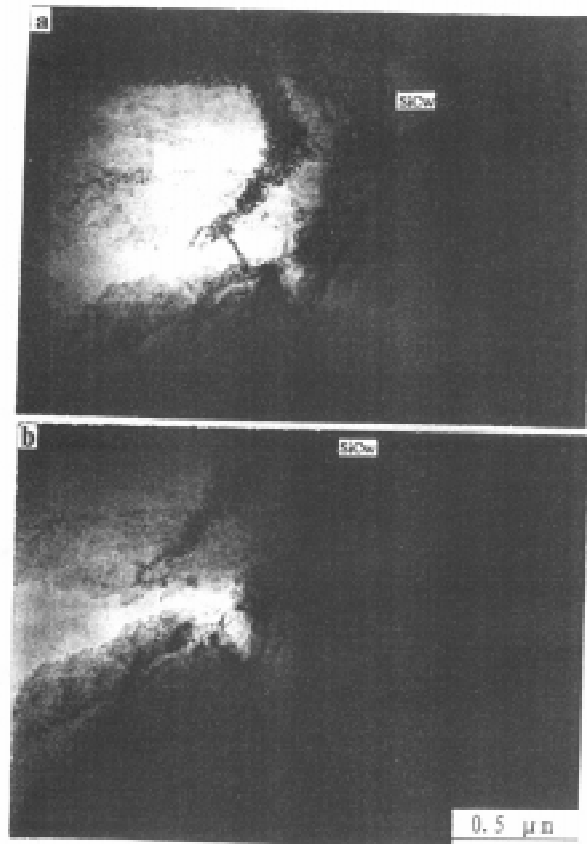


Fig.5: Interaction between propagating crack and SiC whisker, (a) crack blunted at a whisker, (b) crack bypassed the whisker after further straining.

Because the regions in the vicinity of the whisker are stress concentration sites, local thinning and microcracks initiated in these regions, the interface between the matrix and whisker accelerated the crack growth. On the other hand, the interface prohibited the crack propagation, the dislocations piling up at the interface forced the crack to change its propagation direction and bypass whisker, as shown in Fig.5. The former effect was more evident.

Fig.6 shows the crack propagation path in the composite, there is less evidence of whisker cracking and interface debonding, the bond of the interface between the matrix and the whisker was relatively strong. And cracks propagated mainly through the matrix, indicating a matrix-controlled fracture mechanism.

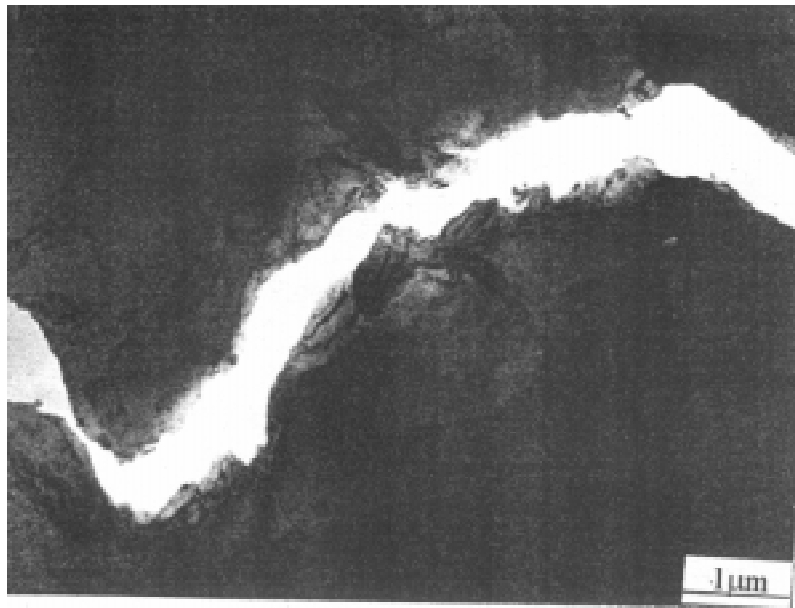


Fig.6: The path of crack propagation in the composites.

The in-situ TEM fracture process was almost as same as the results obtained by in-situ SEM tensile technique. The whole composite fracture process is as follows: local thinning and microcracks initiated, microcracks linked with each other leading to catastrophic fracture of the composites, there was no single major crack forming in the in-situ TEM fracture process.

Due to the large difference in CTE between Mg and SiC whisker, severe stress concentration arised in the Mg matrix adjacent to the Mg-SiCw interface. Because of the limited number of active slip systems available for plastic deformation in the magnesium alloys (h.c.p.Crystal structure), their ability of deformation is poor. During the process of deformation, because the local stress concentration can not be easily relaxed by plastic deformation of the matrix, many microcracks formed in the matrix nearby the matrix - whisker interface at the very low stress. Fast weakest linkage of these microcracks resulted in the catastrophic failure of the composites. The fracture process was matrix-controlled.

CONCLUSIONS

1. A large number of local thinning and microcracks formed at very low stress, fast weakest linkage of these microcracks resulted in the catastrophic failure of the SiCw/AZ91 magnesium matrix composites. No single major crack formed in the in-situ TEM fracture process.

2. Inhomogeneous distribution of stress and exhaustion of local plasticity was responsible for the poor ductility of the SiCw/AZ91 composites. The fracture mechanism was matrix-controlled.

REFERENCES

1. Kainer, K.U. and Mordike, B.L., Production and Properties of Fiber Reinforced Magnesium Alloys, *Metall.*, Vol. 44, 1990, pp. 438-443 (in Germany).
2. Kainer, K.U., Cast Magnesium Alloys Reinforced by Short Fibers, *Proceedings Magnesium Alloys and Their Applications*, Oberursel, Germany, 1993, DGM Informationsgesellschaft, Mordike, B.L. and Hehmann, F., Eds, pp. 415-422.
3. Mikucki, B.A., Mercer, W.E. and Green, W.G., Extruded Magnesium Alloys Reinforced With Ceramic Particles, *Light Metal Age*, Vol. 6, 1990, pp. 12-16.
4. Wilks, T.E., Cost- Effective Magnesium MMCs, *Adv. Mater. Processes*, Vol. 8, 1992, pp. 27-29.
5. Matin, A. and Llorca, J., Mechanical Behaviour and Failure Mechanisms of a Binary Mg-6%Zn Alloys Reinforced with SiC Particulates, *Mater. Sci. Eng.*, Vol. A201, 1995, pp. 77-87.
6. Luo, A., Processing, Microstructure, and Mechanical Behaviour of Cast Magnesium Metal Matrix Composites, *Metall. Mater. Trans.A*, Vol. 26A, 1994, pp. 2445-2455.
7. Kim, J.S., Sugamata, M. and Kaneko, J., Effect of Hot Extrusion on The Mechanical Properties of SiC Whisker/AZ91 Magnesium Alloy Composites, *J. Japan Inst. Metals*, Vol. 55, No. 5, 1991, pp. 521-528.
8. Kim, J.S., Kaneko, J. and Sugamata, M., High Temperature Deformation of SiC Whisker/AZ91 Magnesium Alloy and SiC Whisker/2324 Aluminum Alloy Composite, *J. Japan Inst. Metals*, Vol. 56, No.7, 1992, pp. 819-827.
9. Purazrang, K., Schroeder, J. and Kainer, K.U., Tensile and Fracture Toughness Behaviour of Reinforced Magnesium Composites, *Proceedings of ECCM4*, Stuttgart, F.R.G., September, 1990, pp. 301-306.
10. Hino, H., Komatsu, M., Hirasawa, Y. and Sasaki, M., Effects of Reaction Products on Mechanical Properties of Alumina Short Fiber Reinforced Magnesium Alloy, *Proceedings of 5th Annual ASM/ESD Advanced Composites*, Michigan, September, 1989, pp. 201-208.
11. Purazrang, K., Abachi, P. and Kainer, K.U., Mechanical Behavior of Magnesium Alloy MMCs Produced by Squeeze Casting and Powder Metallurgical Techniques, *Composites Eng.*, Vol. 3, No. 6, 1993, pp. 489-505.
12. Cao, L., Jiang, C.P., Yao, C.K. and Lei T.C., Study of the Whiskers Rotation in Metal Matrix Composites, *Composites*, Vol. 22, No. 2, 1990, pp. 127-131.
13. Dong, S.H., Lee, T.C., Robertson, I.M. and Birnbaum, H.K., Dynamic Studies of the Crack Initiation and Growth Mechanisms in Al/SiCp Composites, *Scr. Metall.* Vol. 23, 1989, pp. 1413-1418.

STUDY ON FABRICATION TECHNIQUE OF AL₂O₃/STEEL COMPOSITE PIPE BY CENTRIFUGAL SHS PROCESS

Wei Cancun¹, Zhou Xiang¹ and Tao Jie²
¹Jiangsu Gaoxin Ceramic-Metal Composite

Pipe Company Ltd., Yang Zhong city, P.R. China

²*Dept. Of Materials Science and Engineering, Nanjing University of Aeronautics & Astronautics, Nanjing 210016, P.R. China*

SUMMARY: Al₂O₃/steel composite pipe is produced by centrifugal SHS (Self-propagating High-temperature Synthesis) process. The density of the ceramic layer can be improved by centrifugal force, additives and preheat treatment of steel pipe and raw material mixture. Meanwhile, controlling these technology parameters is also advantageous to avoid the cracks in the Al₂O₃ layer and gain a good distribution of residual stress, so that the Al₂O₃/steel composite pipe possesses high strength, high resistance against abrasion thermal and mechanical shock.

KEYWORDS: centrifugal shs process, Al₂O₃ steel composite pipe, centrifugal force

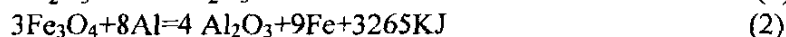
INTRODUCTION

A centrifugal SHS process was developed to produce ceramic-metal composites pipes. Merzhanov initiated the fundamental investigation of the process in 1975[1]. Odawa obtained a number of original results and produced large-sized pipes[2]. This kind of Al₂O₃/steel composite pipe has high strength and high resistance against corrosion and abrasion, which was recently used for the transportation of molten aluminum and high-temperature slag.

In this work, the effects of centrifugal force, preheat treatment and additives on the properties of the Al₂O₃/steel composite pipe are investigated and discussed.

TECHNOLOGICAL PRINCIPAL AND CONDITION

The exothermic reaction in the system above is formulated as follows.



In formula (1) and (2) the reaction temperature is 3753K and 3509K respectively, both exceed the boiling point (2723K) of pure aluminum, which results in the evaporation of a large amount of aluminum during the SHS reaction, so that a lot of gasholes are produced in the molten ceramic layer. Therefore, the reaction temperature of SHS should be maintained below the

boiling point of aluminum through the use of some additives, which is also beneficial to the densification of the ceramic layer.

In order to improve the properties of the ceramic layer, the following problems must be considered:

- (1) appropriately increasing the centrifugal force contributes to the exculsion of gases.
- (2) strictly control the reaction temperature and keep it below the boiling point of aluminum.
- (3) the stoving of the raw material mixture is effective in reducing the gashole percent.
- (4) taking measure to decrease the viscosity of the molten ceramic so as to densify the ceramic layer.

In order to make a composite pipe containing an inner ceramic layer of high quality, the weight ratio of Fe_2O_3 powder to Al powder should be 2.70~2.95, and 8~12% SiO_2 and some additives should be applied into the thermit mixture.

Fe_2O_3 powder (-200 mesh) and aluminum powder (-100 mesh) are blended to meet the need of the reaction mentioned above by using ball-milling. Some additives such as SiO_2 , Al_2O_3 and Si are added to the thermit mixture. A carbon steel pipe is used as outer pipe. After the steel pipe is filled with the thermit mixture and set in the centrifugal machine, start the machine and ignite the mixture at one end of the pipe by tungsten filament, when the centrifugal acceleration reaches 200 m/s^2 . The combustion velocity is controlled between 0.1~0.2m/s, and the pipe rotates for 2~3 min at high speed after the end of the combustion. Then decrease gradually the rotating speed of the pipe and stop the machine when the temperature of the pipe cools down 600~700°C. A diagram of the manufacturing process is shown in figure 1.

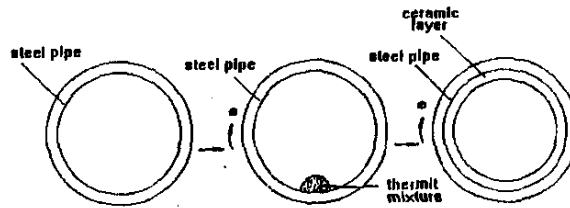


Fig. 1: A diagram of the manufacturing process

RESULTS AND DISCUSSION

The Al_2O_3 /steel composite pipes with 80mm to 600mm in inner diameter and 4000 mm in maximum length can be produced by the technological process described above. The main properties of the composite pipes are in the following:

hardness value: Hv 1200~1450, collapse strength under pressure: 300~400MPa, wear resistance: 30~50 times better than steel pipes.

Being influenced by centrifugal force during the fabrication of the composite pipes, the molten Fe and ceramic produced from the thermit reaction are separated into stratified layers due to the difference in density. The ceramic layer is formed on the inner surface and the iron layer is formed in the intermediate region between the outer steel pipe and the ceramic layer.

During the combustion reaction, gaseous products are formed at elevated temperature which hinder the densification of ceramic layer. The centrifugal force intensifies the combustion heat exchange and increases combustion rate. It also accelerates the separation of gaseous products and molten products, leading to the exclusion of gases and the densification of the ceramic layer. However, that is not to say that the greater the centrifugal force, the better the properties of the composite pipes. Our experimental results show that good bonding between the ceramic layer and the outer steel pipe can be gained when the centrifugal force is 250 to 300g while the

layer and the outer steel pipe can be gained when the centrifugal force is 250 to 300g while the weight ratio of the reaction mixture to the steel pipe is 0.25 to 0.45. No cracks could be found in the ceramic layer with smooth surface.

The additives such as SiO_2 , Si and mineral feldspar composed of Al_2O_3 , SiO_2 and alkali metal oxide can improve the density of the ceramic layer owing to the formation of eutectic mixture which has low melting point and good fluidity[3]. The ceramic layer consists of α - Al_2O_3 , FeAl_2O_4 , and a eutectic mixture formed from SiO_2 , K_2O , Na_2O and Al_2O_3 . The SEM observation shows that the amount of eutectic mixture is much more in the inner ceramic layer than in the outer layer. This is because the density of eutectic mixture is lower than that of the Al_2O_3 and the FeAl_2O_4 , and the centrifugal force causes the separation of different density phases. The formation procedure of the ceramic products is that the Al_2O_3 (melting point 2030°C) first nucleates at the inner surface of the steel pipe and grows into a dendritic structure along the radial direction of the pipe because of the effect of the temperature gradient. With the further decreasing of the temperature, the FeAl_2O_4 (melting point 1780°C) solidifies within the space of the dendritic Al_2O_3 structure. Finally, the eutectic mixture solidifies in the FeAl_2O_4 grain boundary. The centrifugal force plays an important role in the formation and distribution of these phases. When it surpasses a certain value, it will result in the descending of the density of the ceramic layer due to the lack of the low-melting-point phase in the inner layer. Generally, the centrifugal force should not be above 250g when 10~15% additives are mixed into the thermit. Moreover, the degree of phase separation is also related to the thickness of the ceramic layer. When the composite pipe with a thin inner layer is produced, the centrifugal force could be raised, and even surpassed 300g. The mullite structure formed from SiO_2 and Al_2O_3 may separate from the matrix as long as the centrifugal force is great enough, which is unfavorable to the densification of the ceramic layer. Therefore, the rotative velocity of the steel pipe is dominated by the pipe size (inner diameter), the density and thickness of the ceramic layer and the viscosity of the melting reaction products. It tends to decrease with the increasing inner diameter of the pipe, the thickness of the ceramic layer and the amount of the low melting-point phases.

The preheat treatment of the thermit mixture has a good effect on the properties of the ceramic layer. This is because the gases and moisture absorbed in the powder mixture can be disposed of in the preheat treatment. The preheat process increases the combustion temperature and duration above the melting point of the ceramic, leading to the exclusion of gases and the densification of the ceramic layer. The density and hardness of the layer increase with the increase of the preheat temperature.

CONCLUSIONS

1. During the fabrication of the Al_2O_3 /steel composite pipe by centrifugal SHS process, good bonding can be gained when the centrifugal force is 250g to 300g while the weight ratio of the reaction mixture to the steel pipe is 0.25 to 0.45.
2. The additives such as SiO_2 , Si and feldspar improve the density of the ceramic layer.
3. The optimum rotation velocity of the steel pipe is influenced by the inner diameter of the pipe, the density and thickness of the ceramic layer and the composition of the thermit mixture. With the increase of the pipe size, the thickness of the ceramic layer and the amount of the low-melting-pointing phases, the optimum velocity decreases.

REFERENCES

- [1] Merzhanov A.G., Yuxhvid U.I. Self-propagating high-Temperature Synthesis, in: Proc. The first US-Japanese Workshop on Combustion Synthesis, 1990, 1-22.

- [2] Odawa O. Long ceramic-lined pipes produced by a centrifugal-thermite process. *J. Am. Ceram. Soc.*, 1990, 73(3), 629-633
- [3] Yin S., Liu Mo, Guo Z.M. Additives in ceramic composite pipes made by a centrifugal-SHS process, *International Journal of SHS*, 1993, 2(1): 69-74 .

HIGH TEMPERATURE COMPRESSIVE DEFORMATION BEHAVIOR OF SiC_w/6061Al COMPOSITE AT LIQUID-SOLID DUAL PHASE ZONE

L. Geng, J. Q. Hu and B. Liu

*P.O. Box 433, Department of Materials Science, Harbin Institute of Technology,
Harbin 150001, P.R. China.*

SUMMARY: The SiC_w/6061Al composite was fabricated by squeeze casting technique, and the compressive plastic deformation behavior of the composites was investigated at the liquid-solid dual phase temperature zone (560°C ~ 640°C). There are three stages in the true stress-strain curves of the composites. The first stage is a elastic stage; the second stage is a soften stage, and at lower temperature (such as 560°C) a peak appears in the stress-strain curve, which is due to the rotation and broken of the whiskers; the third stage is a strengthening stage which is coincident with the work hardening of the matrix alloy. With increasing strain rate, the second stage is enhanced, and a obvious peak is formed in the stress-strain curve when the strain rate reach 1.0s⁻¹. SEM results show that most of the SiC whiskers rotates to the direction perpendicular to the applied load direction, and some whiskers were broken during the plastic deformation.

KEYWORDS: silicon carbide, whisker, aluminum, high temperature, plastic deformation

INTRODUCTION

High temperature plastic deformation forming is one of the most important technique for the application of the SiC_w/Al composite. Recently, it was found that the SiC_w/Al composites exhibit a very high plastic deformation ability at the liquid-solid dual phase zone temperatures of the matrix aluminum alloy [1,2]. Many works have been done about the tensile deformation behavior at the dual phase temperatures of the SiC_w/Al composites [1-6]. However, in order to provide a basis for the applications of the high temperature plastic deformation forming, it seems more important to study the compressive deformation behavior at the dual phase temperatures of the SiC_w/Al composites.

Optimum superplasticity is often attained in practice at very low strain rates, of the order of 10⁻³s⁻¹. However, it was demonstrated by Nieh et al. [1] that it is possible to achieve superplastic-like flow and tensile elongation of up to 300% in a 20vol.% SiC_w/2124Al composite at a 525°C using a strain rate of 3.3×10⁻¹s⁻¹. High strain rate superplasticity provides a practical route for the plastic forming of the SiC_w/Al composite, and at the liquid-solid dual phase zone temperatures, the high strain rate superplasticity becomes easy to be realized.

So far, most of researches about high strain rate superplasticity are on the composites fabricated by powder metallurgy. Recently more and more works have been carried out on the

composites fabricated by squeeze casting route which has industrial advantages in many respects [2,3,5]. However, all the works are done using tensile tests, and there is no report using compressive tests. In fact, compressive test is more similar to the practical processes of the plastic forming of the composites. The objective of this paper is to investigate the compressive plastic deformation behavior of the squeeze casting SiCw/6061Al composites at the liquid-solid dual phase zone temperatures ($560^{\circ}\text{C} \sim 640^{\circ}\text{C}$) using high strain rates ($0.12 \sim 1.00\text{s}^{-1}$).

MATERIALS AND EXPERIMENTAL PROCEDURES

The SiCw/6061Al composite used here was fabricated by using β -SiC whisker (TWS-100) as the reinforcing element and the commercial 6061 alloy as the base metal. Squeeze casting technique was used for fabricating the composite. Mold and whisker preform temperature, pouring temperature and applied pressure were 450°C , 750°C and 60MPa , respectively. The whisker volume fraction (V_f) is 20%.

The solidus temperature of the matrix alloy in the composite, around which the test temperatures were chosen, was measured to be 580°C by DSC technique. The compressive deformation tests were conducted in air over the temperature range of 560 to 640°C with 20°C interval using the strain rate of 0.12s^{-1} . More high strain rates, such as 0.37 , 0.56 and 1.00s^{-1} , were also adopted with a fixed deformation temperature to study the effect of strain rate on the compressive deformation behavior of the SiCw/Al composites. The microstructure of the deformed composites was observed by SEM.

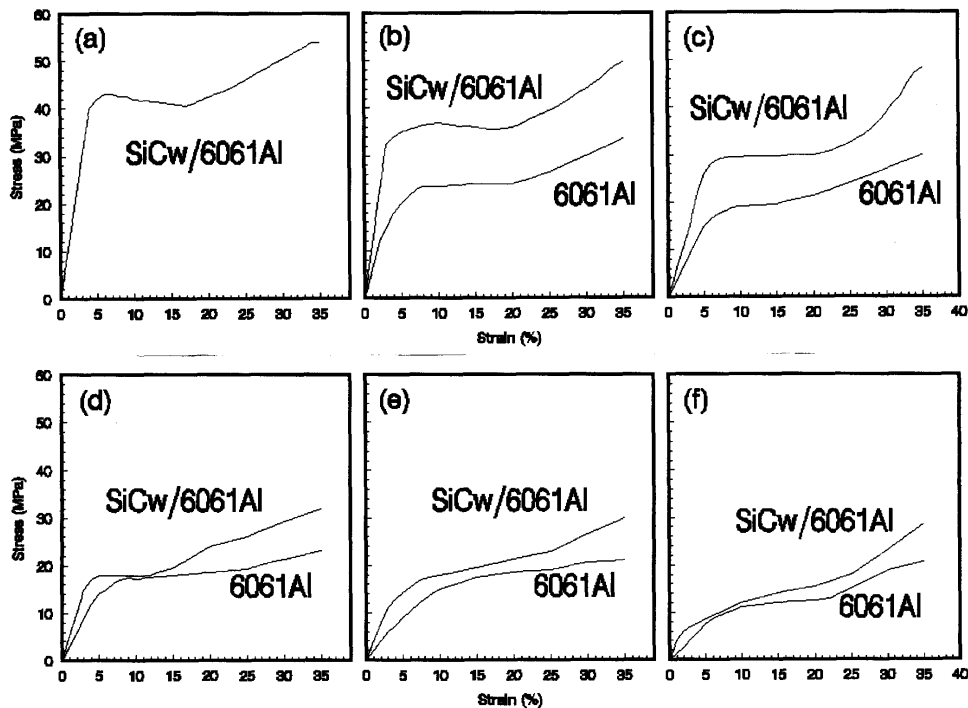


Fig.1: True stress-strain curves of the SiCw/6061Al composites and 6061Al with a strain rate of 0.12s^{-1} at different temperatures, (a) 540°C , (b) 560°C , (c) 580°C , (d) 600°C , (e) 620°C , (f) 640°C .

RESULTS AND DISCUSSION

The true stress-strain curves of the SiCw/6061Al composite and 6061Al obtained in the compressive condition at different temperatures with a strain rate of 0.12s^{-1} are shown in Fig.1. It can be seen that there are three stages in the curves. The first stage is elastic stage, in which the stress increases linearly with increasing strain. It can also be seen that the maximum stress in the first stage decreases with increasing temperature, and when the temperature is higher than 600°C , the first stage becomes not clear.

Fig.1 also shows that there is not distinguish three stages in the true stress-stain curves of the 6061Al, and in the low strain stage, the 6061Al has a lower resistance to the compressive deformation. This indicates that the high deformation resistance of the SiCw/Al composite in the first stage comes mainly from the SiC whiskers. Interface plays a very important role to ensure an effective function of the SiC whiskers. The load transfer ability of the SiC-Al interface decreases with increasing temperature because of the soften of the matrix. When the temperature is higher than 600°C , more and more liquid phase appears in the matrix, and the liquid phase prefer appears near the SiC-Al interfaces. With increasing temperature, more and more whiskers are surrounded by liquid phase, resulting in the losing of the load bearing ability of the whiskers. Therefore, the first stage gradually disappear when the temperature is higher than 600°C as shown in Fig.1.

The second stage is a soften stage, which can be seen clearly in the true stress-strain cures of the SiCw/Al composite deformed at the temperature lower than 600°C . From the true stress-strain curves of the 6061Al, it can be seen that there is also a soften stage in the same strain range, which is resulted from the dynamic recovery. Therefore, dynamic recovery of the matrix alloy is one of the reasons resulting in the soften of the SiCw/Al composite in the second stage.

Whisker rotation and broken is also one of the reasons leading to the soften of the SiCw/Al composite [7]. At lower temperature, the matrix alloy has a higher strength to limit the whisker rotation, so it needs a higher stress to made the whisker rotation. When the stress is high enough, more and more whiskers began to rotate to the direction perpendicular to the compressive load direction, resulting in a decrease of the flow stress of the composite, so a peak is formed in the true stress-strain curve in this case, as shown in Fig.1(a). With increasing temperature, the strength of the matrix alloy decreases, and more and more whiskers can rotate under a lower stress, so the peak in the stress-strain curve of the SiCw/Al composite gradually disappears.

Fig.2 is SEM photos showing the whisker distribution in the SiCw/Al composites deformed at different temperatures. All the photos were taken in the direction perpendicular to the compressive direction. It can be seen that almost all the SiC whiskers rotate to the direction perpendicular to the compressive direction. Some broken SiC whisker can also be found, especially in the composite deformed at lower temperature. The whisker broken can also leads to the soften of the composite and therefore contributes to the peak in the stress-strain curves.

The third stage is a strengthening stage. In this stage the matrix alloy is strengthened by work hardening, which leading to the increase of the flow stress of all the SiCw/Al composite in the third stage.

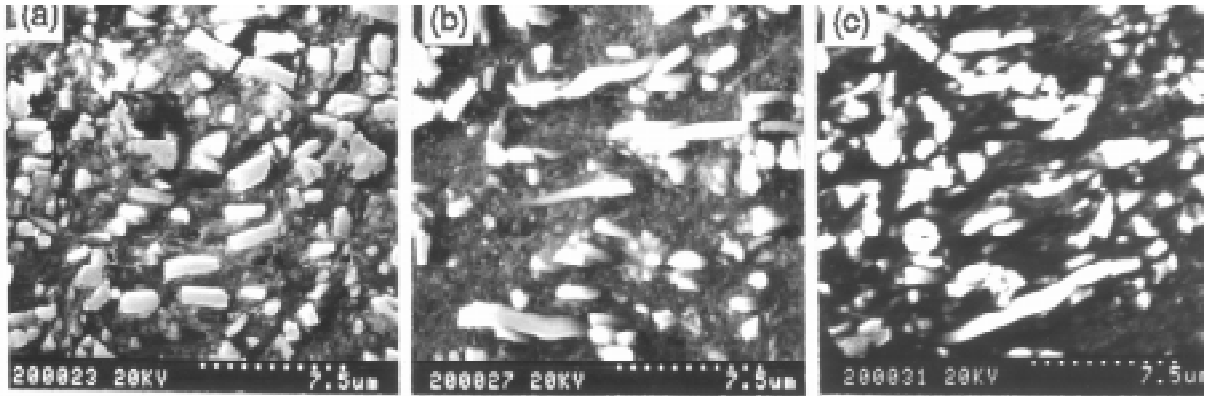


Fig.2: SEM photos showing the whisker distribution in the SiCw/Al composites deformed at different temperatures, (a) 540°C, (b)580°C, (c)620°C

The effect of deformation temperature on the flow stress at the strain of 0.35 is shown in Fig.3. It can be seen that the flow stress decreases with increasing temperature, and at 600°C there is a sharp decrease, especially for the SiCw/Al composite. Fig.3 indicates that the flow stress is much lower if the deformation is carried out at the liquid-solid dual phase temperatures.

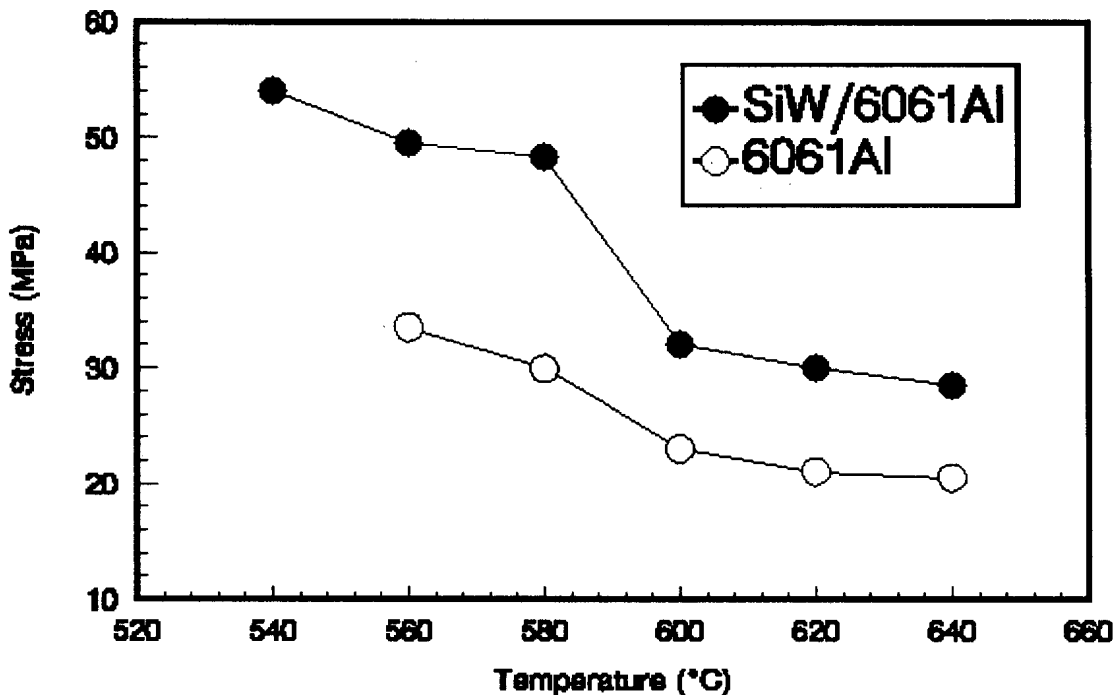


Fig.3: Effect of deformation temperature on the flow stress of the SiCw/6061Al composite at the strain of 0.35

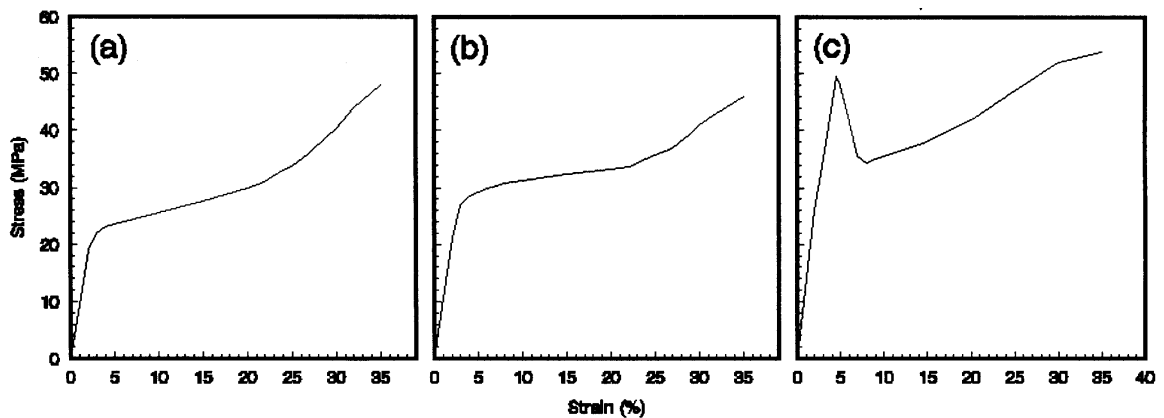


Fig.4: True stress-strain curves of the SiCw/6061Al composites deformed at 600°C with strain rate of 0.37(a), 0.56(b) and 1.0s⁻¹(c)

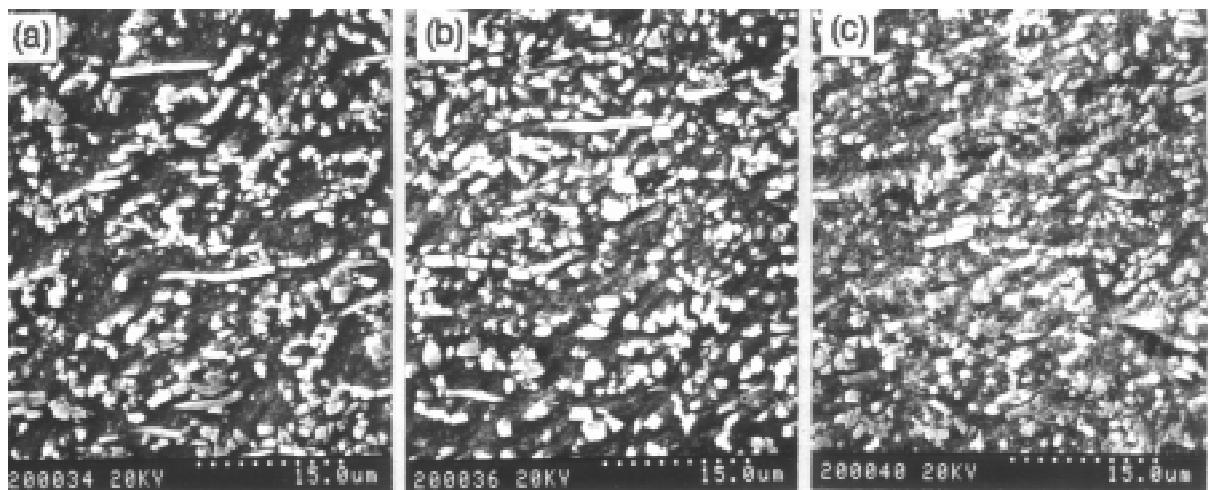


Fig.5: SEM photos showing the whisker distribution in the SiCw/Al composites deformed at 600°C with strain rate of 0.37(a), 0.56(b) and 1.0s⁻¹(c)

In order to study the effect of strain rate on the deformation behavior of the SiCw/Al composite, the compressive tests were also carried out for the composite at 600°C with strain rate of 0.37, 0.56 and 1.0s⁻¹. The true stress-strain curves of the composite in these conditions are shown in Fig.4. It can be seen that in the strain rate range of 0.12 to 0.56s⁻¹, the strain rate does not affect the deformation behavior of the composites. However, when the strain rate reaches 1.0s⁻¹, a peak appears in the true stress-strain curve. The sharp decrease of the flow stress means a high speed rotation of the whisker and a great amount of broken of whisker (as shown in Fig.5). Therefore, although the SiCw/Al composite can be plastic deformed in the liquid-solid dual phase temperatures without any cracks with a strain rate of 1.0s⁻¹, it is also not suitable to deform the composite with a strain rate higher than (or equal to) 1.0s⁻¹, because the whisker broken may lead to the decrease of the properties of the SiCw/Al composites.

CONCLUSIONS

1. The SiC/6061Al composite fabricated by squeeze casting route can be hot-compressed in the liquid-solid dual phase temperatures with a high strain rate from 0.12 to 1.00s⁻¹ without any cracks.
2. There are three stages in the true stress-strain curves of the SiCw/Al composites. The first stage is elastic stage, in which stress increases linearly with increasing strain; the second stage is a soften stage, which is resulted from the dynamic recovery of matrix alloy and whisker rotation and broken; the third stage is strengthening stage, which is because of the work hardening of the matrix alloy.
3. All the SiC whiskers rotate to the direction perpendicular to the compressive direction during the compressive deformation, and some broken whiskers are also found by SEM.
4. strain rate has no effect on the deformation behavior of the SiCw/Al composite within 0.12 to 0.56s⁻¹. When the strain rate reaches 1.0s⁻¹, a peak appears in the stress-strain curve, which means a high speed rotation and a great amount of broken of the whiskers.

REFERENCES

1. Nieh, T.G., Henshall, C.A. and Wadsworth, J., "Superplasticity at high strain rate in a SiC-2124 Al composite", *Scripta Metall.*, Vol.18, 1984, pp. 1405.
2. Kim, Jae-hong, Lee, Dong-nyung and Oh, Kyu-hwan, "High Temperature Deformation Behavior in a 2124Al/15Vol%SiCw Composite", *Scripta Metall. Mater.*, Vol.29, 1993, pp. 377.
3. Lim, Suk-wan and Nishida, Yoshinori, "Superplasticity of Whisker Reinforced 2024 Aluminum Alloy Composites Fabricated by Squeeze Casting", *Scripta Metall. Mater.*, Vol.32, No.12, 1995, pp.1911.
4. Mabuchi, M., Higashi, K. and Langdon, T.G., "An Investigation of the Role of a Liquid Phase in Al-Cu-Mg Metal Matrix Composites Exhibiting High Strain Rate Superplasticity" *Acta Metall. Mater.*, Vol.12, No.5, 1994, pp.1739.
5. Imai, Tsunemichi, Tochigi, Isao, Ai, Kyosuke, Gille L'Esperance and Hong, Bande, "High strain Rate Superplasticity of a β -SiC₃N₄ Whisker Reinforced Pure Aluminium Composite Made by Squeeze Casting", *Scripta Mater.*, Vol.34, No.10, 1996, pp.1627.
6. Nieh, T.G. and Wadsworth, J., "High-strain-rate superplasticity in aluminum matrix composite", *Mater. Sci. Eng.*, A147, 1991, pp.129.
7. Xiong, Z., Geng, L. and Yao, C.K., "Investigation of high-temperature deformation behavior of a SiC whisker reinforced 6061 aluminium composite", *Compos. Sci. Technol.*, Vol.39, No.2, 1990, pp.117.

SiC PARTICLES VOLUME FRACTION INFLUENCE ON FATIGUE CRACK PROPAGATION IN Al-Si METAL MATRIX COMPOSITES

F. Iacoviello¹, N. Bonora¹, L. Jaresová¹, Z. Jonsta², L. Hyspeckà²

¹ *Università di Cassino, Industrial Engineering Dept.,
via G. De Biasio 43, 03043 Cassino (FR) Italy.*

² *VSB Technical University, 708 00 Ostrava, Czech Republic.*

SUMMARY: Metal matrix composites mechanical properties are strongly dependent on the microstructure and on the characteristics and the properties of the dispersed particles. The base materials, the manufacturing modalities, the heat treatment influence the final microstructure. In this work, the SiC particles volume fraction influence on fatigue crack propagation has been investigated considering an Al-Si based alloy. Different microstructures corresponding to the different SiC volume fractions have been also investigated by means of both optical and scanning electron microscope, using secondary electron emission and the electron back scattering.

KEYWORDS: fatigue crack propagation, SiC particles volume fraction, fatigue fracture surface

INTRODUCTION

Metal matrix composites have been developed with the aim to obtain lighter materials with high specific strength and stiffness. These properties are particularly interesting in the aerospace industry. Aluminium based MMCs reinforced using particles or whiskers can be considered when not extreme properties are required, thanks to their relatively low cost. Their advantages are usually connected to their isotropy in mechanical properties and the use of conventional metallurgical processes for the allowing fabrication. SiC particles are commonly used as reinforcing material thanks to its good thermal conductivity and chemical compatibility with aluminium [1].

In this paper a 10 or 20 volume percent of added SiC particles eutectic Al-Si based MMC have been investigated, both analysing the microstructure and investigating the influence of SiC volume fraction on fatigue crack propagation.

EXPERIMENTAL MATERIALS AND TECHNIQUES

Chemical composition of the metal matrix and mechanical properties of investigated MMC both with 10 and with 20 volume % are shown in Table 1.

Table 1: Matrix chemical composition (wt.%; the Al is rest) [2] and mechanical properties for MMCs with 10 and 20 vol.% SiC particles.

	Si	Fe	Cu	Mn	Mg	Ni	Ti	Zn	Others
Min.	9.5	0.8	3.0	0.5	0.3	1.0	0.0	0.00	0.03
Max.	10.5	1.2	3.5	0.8	0.5	1.5	0.2	0.03	0.10
		σ_y [MPa]			σ_{UTS} [MPa]			A%	
F3D.10S		152			241			1.2	
F3D.20S		186			303			0.8	

SiC particles have been injected during the pressure die casting process with a nominal volume fraction of 10 and 20. MMC has been cast in plates measuring about 12.7x140x140 mm. Specimens machining has been difficult: very hard SiC particles quickly blunted the saws. A water jet with a slow jet feed rate of 17 mm/min has been used to cut specimens followed by milling, hand grinding and polishing. Similar difficulties have been encountered in the preparation of sections for microstructural studies and WDX phase analyses: diamond grinding paste had to be used.

MMCs fatigue crack propagation has been investigated according to ASTM E647 standard, using a computer controlled INSTRON 8501 servohydraulic machine in constant load amplitude conditions. Tests have been done in laboratory conditions, at a frequency of 20 Hz, with a sinusoidal waveform, considering a stress ratio of 0.5 (i.e. R). Crack lengths have been measured using both a compliance method with a double cantilever crack mouth gauge and an optical method with a x40 magnification. CT (Compact Type) specimens have been utilised, with the notch obtained via electroerosion.

In order to control the results repeatability, fatigue tests have been repeated three times with the same test conditions.

Fracture surface have been observed using a scanning electron microscopy (SEM) with EDX analysis.

MICROSTRUCTURE

Microstructure reveals a strongly non-uniform SiC distribution at and close to the surface of both the considered composites [3]. In the middles of the specimens the SiC distribution uniformity is higher.

Secondary electron emission and electron back scattering techniques allowed to characterise the MMC microstructure.

Matrix microstructure is very fine grained, with a matrix grain size of about 15.7 μm and 13.6 μm respectively for the 10 and the 20 SiC percent. During solidification, SiC particles are preferential nucleation sites [4], so the high quantity of SiC particles implies a little matrix

grain size. Moreover, microstructure shows particles resembling Chinese script [5], large rounded particles, a grey background composed only by aluminium (the dendrites of the matrix), and other phases that are too fine to be exactly analysed by the methods employed in this work. For example, some attempts to analyse particles smaller than 3 μm diameter suggest a composition like $\text{Al}_7\text{Cu}_4\text{Ni}$. Table 2 shows the chemical composition of the main microstructures observed in the considered MMC.

Table 2: Results of WDX analysis for Al based MMC with 10 and 20 % SiC particle volume fraction.

Morph.	Likely Phases	Al	Si	Mg	Fe	Mn	Ti	Ni	Cu
Chinese script	Al_3NiCu	61.8± 0.7	1.03± 0.83	0.04± 0.01	0.85± 0.08	0.04± 0.01	0.01± 0.005	19.4± 0.2	16.8± 0.24
Large rounded	$(\text{Al,Cu,Ni})_{15}$ $(\text{Fe,Mn})_3\text{Si}_2$	71.4± 0.54	11.3± 0.37	0.02± 0.007	8.7± 0.064	6.84± 0.26	0.05± 0.066	0.08± 0.148	0.92± 0.226
Dendrites	Al + (Si)	97.7± 0.4	1.47± 0.09	0.16± 0.035	0.02± 0.013	0.03± 0.007	0.01± 0.013	0.06± 0.055	0.52± 0.234
Matrix		66.5± 0.17	30.1± 0.17	0.02± 0.01	0.51± 0.04	0.30± 0.03	0.14± 0.02	0.70± 0.04	1.78± 0.07
SiC particles	SiC	0.30± 0.074	67.8± 0.71	0.01± 0.01	0.04± 0.013	0.02± 0.019	0.00± 0.007	0.06± 0.026	0.14± 0.08

RESULTS

Fatigue crack propagation is strongly affected by the SiC volume fraction, by the SiC particles non-uniform distribution and by the MMC microstructure. Figures 1 and 2 show the fatigue crack propagation in 10% and 20% volume fraction MMC in the $\text{da/dN}-\Delta K$ diagram (i.e. fatigue crack propagation rate-applied stress intensity factor amplitude).

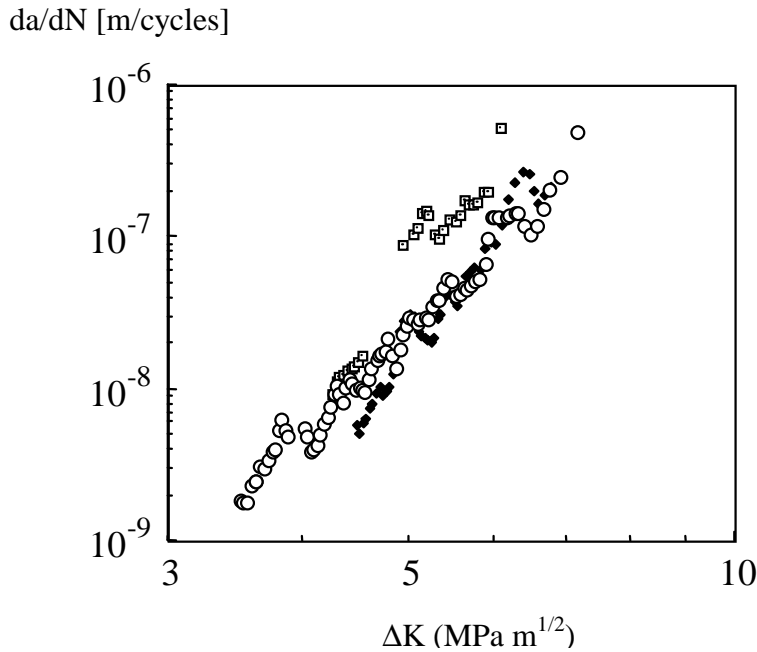


Fig. 1: da/dN - ΔK diagram (10% SiC particles volume fraction, $R=0.5$, 20Hz).

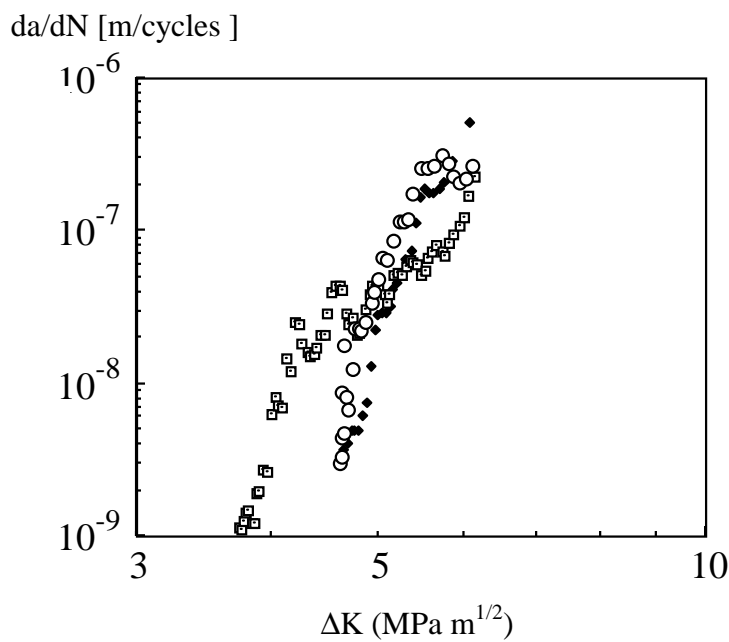


Fig. 2: da/dN - ΔK diagram (20% SiC particles volume fraction, $R=0.5$, 20Hz).

Fatigue crack propagation is characterised by an high dispersion of results in the da/dN - ΔK diagram [6], both for the 10% and the 20% SiC particles volume fractions. Considering the same value of the applied stress intensity factor value, the corresponding fatigue crack propagation rate can change for a factor of one according to the different specimens. This result is probably connected to the non-uniformity in the SiC distribution.

Fatigue crack propagation in da/dN - ΔK diagram is characterised by an evident fluctuation of the experimental points. This fluctuation is connected with the variations in the fatigue crack

direction. This direction can change from the orthogonality to the loading direction to an angle of about $\pm 30^\circ$. This result has been obtained using SEM observations of the lateral crack path after nickeling of the crack surface. Corresponding to each variation in crack propagation direction, fatigue crack propagation rate increase or decrease with a high rate, that can be higher than the rate obtained interpolating the experimental results using the Paris-Erdogan relationship [7].

$$\frac{da}{dN} = C \cdot \Delta K^m \quad (1)$$

where C and m are interpolation coefficients obtained by applying the least square method to the experimental results in the stage II of III.

The phase II of III of fatigue crack propagation, where experimental results have usually a linear behaviour in the log-log diagram $da/dN-\Delta K$, shows a continuous slope variation and the Paris-Erdogan relationship can be used only considering that it could be related with not too high correlation coefficients. Fig. 3 shows the interpolation coefficients "C" and "m" for the fatigue crack propagation in the two considered MMCs.

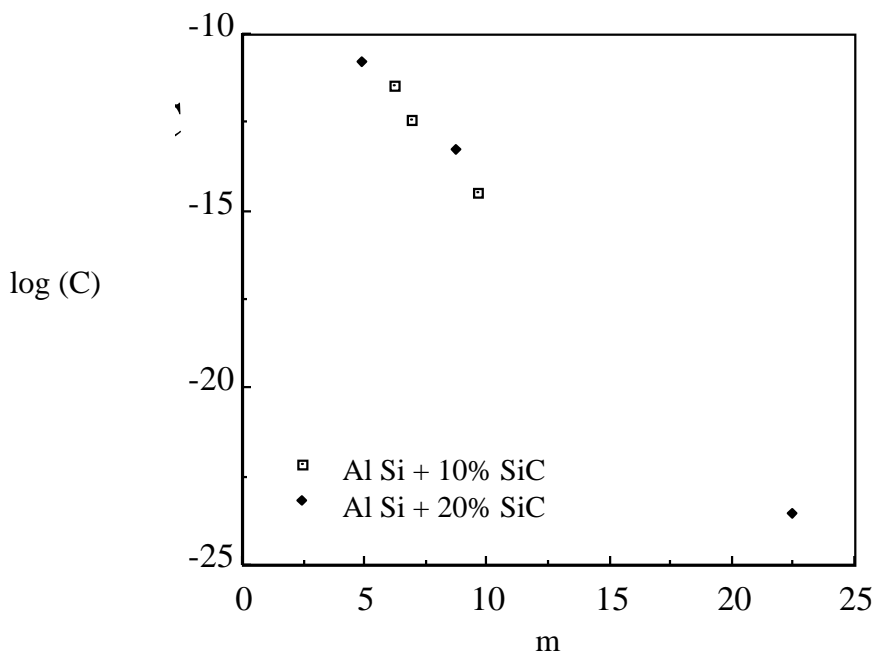


Fig. 3: Paris-Erdogan relationship interpolation coefficients in the logC-m diagram.

Using a logC-m diagram, considering the same experimental conditions, C-m values have usually a linear behaviour [8-10], and this linear behaviour could be related to the fatigue crack propagation micromechanisms, i.e. striation formation. According to our results, considering the low correlation coefficients of relationship (1), it is not evident that the linear behaviour of logC-m values is correlated with the fatigue crack propagation mechanisms. More results are necessary to obviate the influence of SiC distribution on the stage II of fatigue crack propagation with its peculiar oscillations.

Investigated MMCs show a strongly brittle behaviour, and fatigue crack propagation is affected by the SiC particles presence and distribution. Figures 4 and 5 show two different fracture morphologies, with dendrites inside the fracture (Fig. 4) or secondary cracks (Fig. 5).

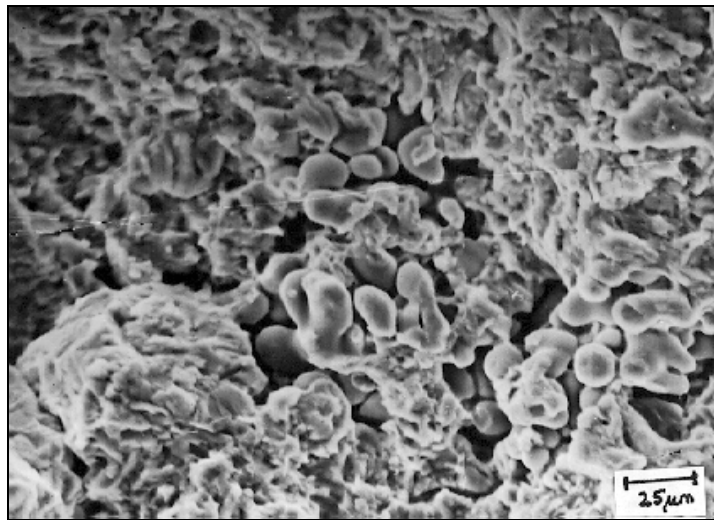


Fig. 4: SEM micrograph of the fatigue crack surface: dendrite inside a crack (10% SiC particles volume fraction).

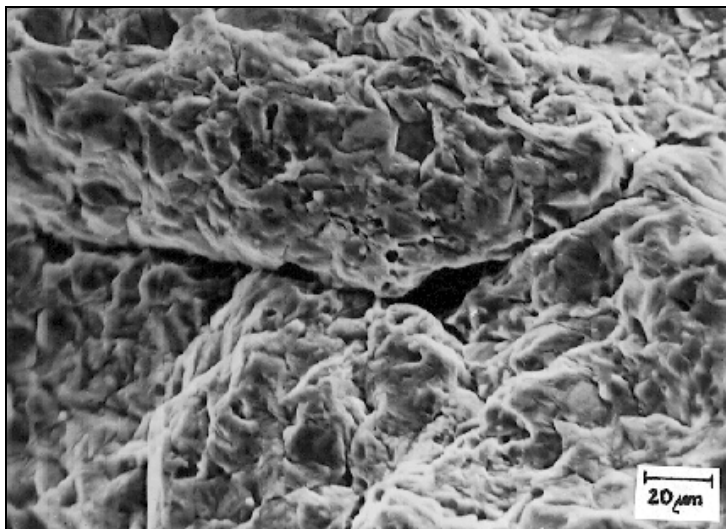


Fig. 5: SEM micrograph of the fatigue crack surface: secondary crack (10% SiC particles volume fraction).

Differences between 10% SiC and 20% SiC are not so evident and surely included in the high statistical dispersion of the results. This is evident in the stage I of III (threshold stage), where a little increasing of ΔK_{th} value with the increasing of SiC volume fraction can be only supposed. Differences in ΔK_{th} values and in the slope m values are probably due to the different influence of crack closure effect [11,12]. This effect can be crack tip plasticity induced, oxide-induced or roughness-induced. Considering that the oxide formation is not SiC particles volume fraction dependent, crack tip plasticity-induced and roughness-induced crack closure effect connected with the formation of significant mode II displacements. The first effect can provide an higher contribution at higher ΔK , the second effect can provide an

important contribution to the role of microstructure in influencing near-threshold crack growth.

SiC volume fraction influence is more evident in the stages II and III. In fact, higher SiC particles volume fractions correspond to higher slope m values. The higher slope m values are also connected to ΔK_{\max} values ($= (1-R)K_{IC}$) that decrease with the increasing of the SiC particles volume fraction. ΔK_{\max} values change from about $6.5 \text{ MPa}\cdot\text{m}^{1/2}$, corresponding to 20% SiC particles volume fraction, to about $7.5 \text{ MPa}\cdot\text{m}^{1/2}$, corresponding to 10% SiC particle volume fraction. The higher SiC particles volume fraction corresponds to a more brittle behaviour and to lower values of the toughness K_{IC} .

SiC particles influence on fatigue crack propagation has been investigated using optical observations of the crack surface after nickeling and a partial polishing. Figures 6 and 7 show the result of these observations respectively for the 20 % and the 10% SiC particles volume fraction MMC.

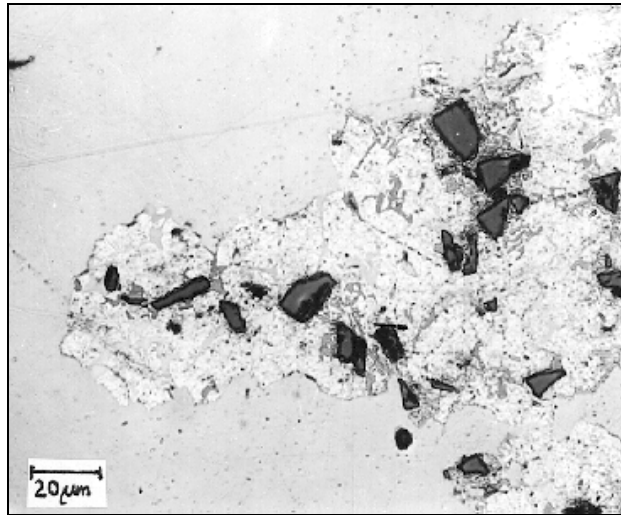


Fig. 6: Optical micrograph of the fatigue crack surface after nickeling and partial polishing (20% SiC particles volume fraction).

It is evident that interfaces metal matrix - SiC particles do not act as preferential path for the fatigue crack propagation that propagates in the metal matrix.

It is possible to calculate the reverse plastic zone r_{rpz} using the following relationship [13]:

$$r_{rpz} = 0.04 \left[\frac{\Delta K}{\sigma_y} \right]^2 \quad (2)$$

Considering the ranges of applied ΔK for the two MMC, r_{rpz} is between about 20 and 100 μm for the 10% of SiC particles and between about 14 and 50 μm for the 20% of SiC particles.

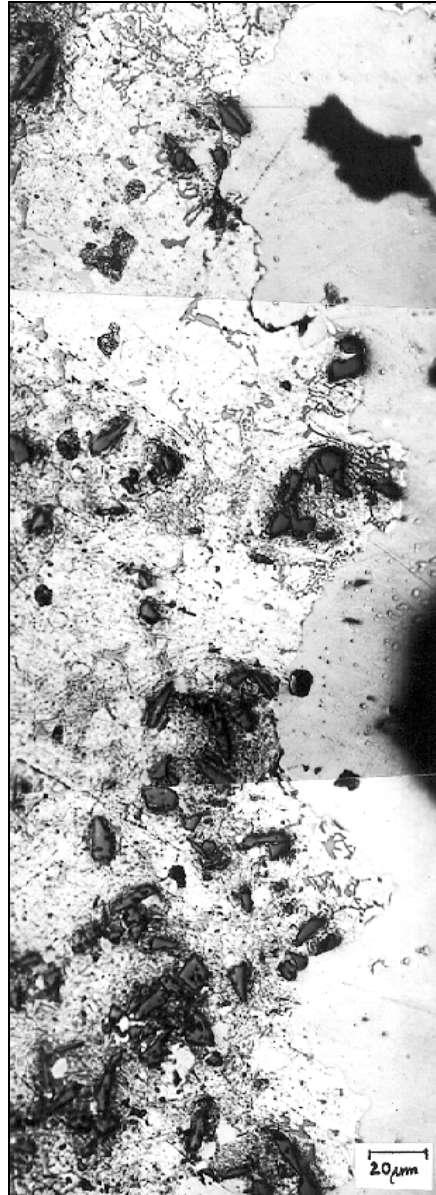


Fig. 7: Optical micrograph of the fatigue crack surface after nickeling and partial polishing (10% SiC particles volume fraction).

These values are comparable with the grain sizes and also with SiC particles dimensions, lesser than 10 μm . However they are lower than the average spacing between SiC particles that can act in the same way as dispersoids, preventing the development of long planar slip bands.

SiC particles can act to deviate crack path, especially considering that the non-uniformity of SiC particles distribution can facilitate this process. The crack path deviation modifies the stress intensity factor situation at crack tip where it could be effective a mixed mode I+II stress intensity factor, and a strong decreasing of fatigue crack propagation is evident. Sudden increasing of the fatigue crack growth rate are connected with an increasing of the component I of the effective stress intensity factor that act at the crack tip. Moreover, the non-uniform SiC particles distribution imply the presence of SiC particles free zones with dimensions that are comparables or higher than the reverse plastic zone. When crack tip meets one or more of

these SiC particles free zones, fatigue crack propagation proceeds via ductile striation forming and a lower fatigue crack growth rate is obtained.

CONCLUSIONS

Al-based MMC with 10% and 20% SiC particles volume fraction microstructure has been investigated. Metal matrix grain size, secondary phase presence and SiC particle distribution have been analysed.

Fatigue crack propagation has been also investigated using CT specimens, considering a stress ratio equals to 0.5 and three fatigue tests for each considered test conditions.

Fatigue crack propagation results are characterised by a high dispersion. Fatigue crack does not propagate at the metal matrix-SiC particles interfaces, but SiC particles non-uniform distribution can participate to deviate the crack path. These deviations are connected with evident oscillations in the results in $da/dN-\Delta K$ diagram and a Paris -Erdogan relationship that can interpolate the experimental results in the stage II only with low correlation coefficients. The influence of SiC volume fraction on fatigue crack propagation is difficult to distinguish to the statistical dispersion. However, more evident differences are shown in stage II and III and they are essentially due to the roughness-induced crack closure effect and to the decreasing of the toughness with the increasing of the SiC particles volume fraction.

REFERENCES

1. Knowles D.M., King J.E., *Acta metall.mater.*, vol.39, n.5, p.793, 1991.
2. ALCAN Handbook: Duralcan Composites F3D.10S and F3D.20S.
3. Zenisek P., Losertova M., Iacoviello F., Cavallini M., Hyspeckà L., *Metallurgical Science and Technology*, vol.14, n.1, 1996.
4. Lloyd J.D. *Inter. Mater. Reviews*, vol. 39, n.1, p.1, 1994.
5. Bäckerud L., Chai G., Tamminen J. *Solidification Characteristics of Aluminium Alloys*, vol.2, Foundry alloys, University of Stockholm, AFS/Skanaluminium.
6. Cavallini M., Iacoviello F. *Int. J. of Fatigue*, vol.17, n.2, p.135, 1995.
7. Paris D.C., Erdogan F. *ASME Publication*, n. 62-WA 234.
8. Iost A., Lesage J. *J. Eng. Fract. Mech.*, vol.36, p.585, 1990.
9. Sinclair G.B., Pieri R.V. *Int. J. of Fatigue*, vol.12, p.57, 1990.
10. Iost A. *Int. J. of Fatigue*, vol.13, p.25, 1991.
11. W. Elber, *ASTM STP 486*, p.280, 1971.
12. R.O.Ritchie, S.Suresh *Metallurgical Transactions A*, vol.13A, p.937, 1982.
13. Levy N., Marcal P.V., Ostergren W.J., Rice J.R., *Int. J. Fract. Mech.* vol.7, p.143, 1971.

MODELLING AND EXPERIMENTAL CHARACTERISATION OF PHASE STRAIN EVOLUTION IN 10 VOL% AL/SiC_w COMPOSITE DURING THERMO MECHANICAL LOADING

T. Lorentzen and Y. L. Liu

Materials Department, Risø National Laboratory, P.O. Box 49, Roskilde, Denmark

SUMMARY: This paper addresses the experimental characterisation of the phase strain response to thermo mechanical loading using neutron diffraction, with the aim to evaluate numerical predictions of phase strain evolution. By the use of neutron diffraction we characterise the initial residual phase strains in the two phases of a 10vol% Al/SiC_w composite. When compared to numerical simulations by the Finite Element Method (FEM), it is apparent, that such predictions over estimates the thermal residual phase strains. FEM-simulations of subsequent room temperature loading shows some discrepancies as compared to neutron diffraction experiments, though the phase strain evolution is qualitatively in agreement with the experimental evidence. It is evident that the cell-model idealisation of real composites does not accurately reflect the real state of internal stress development in the two constituent phases.

KEYWORDS: neutron diffraction, residual stresses, thermal stresses, internal stresses, finite element method, phase strains, Al/SiC, in-situ

INTRODUCTION

Metal matrix composites are born with an inherent mis-match in both coefficients of thermal expansions and elastic/plastic deformation characteristics. It is well known that this leads to a state of initial residual strains and stresses in the composites during the production phase. Subsequent loading will first of all be affected by these residual strains, but further more this will also develop internal mis-match strains and stresses due to the incompatibility in deformation characteristics.

The generation of phase strains and stresses are typically modelled by the FEM cell-model approach [1-3] which, however, is an idealisation of the real composite consisting of many inclusions. Despite that such FEM-simulations may render realistic results judged on the macroscopic deformation of the composite, the individual phase strain evolution, and the microstructural reasoning for the qualitatively correct macroscopic properties is still uncertain. In order to evaluate the quality of these popular FEM cell-models on a microstructural level this calls for experimental techniques capable of monitoring the stress/strain evolution on the scale of the detailed information presented by the numerical predictions.

Experimental techniques based on high energy synchrotron X-ray diffraction are being perfected [4] to the state where the spatial resolution approaches the scale of typical inclusions, but further development is still needed. Hence, the detailed contour results of FEM-simulations are not at present readily evaluated experimentally. However, volume average stresses and strains over many inclusions can today be characterised by neutron diffraction [5,6]. It is the aim of the present work to quantify experimentally the extent to which volume average phase strains as determined by FEM cell-modelling are in agreement with experimentally observable quantities.

MATERIAL CHARACTERISATION

The material considered is a pure aluminium based composite containing 10vol% SiC whiskers and fabricated by a powder metallurgical route described in [7]. The SiC-whiskers supplied by Mandoval Ltd., UK, have a mean diameter of 1 μ m and following extrusion the average aspect ratio was found to be approximately 7. A neutron diffraction texture analysis verified that more than 70vol% of the whiskers are aligned with their <111> texture component within 7 degrees to the extrusion axis. The matrix texture of the extruded composite was also characterised by neutron diffraction and showed a strong <111> fibre texture with more than 35vol% of the grains oriented with their <111> lattice direction parallel to the extrusion axis.

In the idealised cell-model considered here the local strains around the inclusion grows very large during thermo mechanical loading, and hence an appropriate constitutive behaviour of the matrix material must be characterised to equally large strain levels. This is accomplished by elevated temperature compression tests performed on \varnothing 6mm cylindrical specimens of 6mm height. The materials characterisation is performed to strains of approximately 1., and at temperatures of 20, 100, 200, 300, 400 and 500°C. The experimental results described by a modified voce type equation are shown in Fig.1 displaying the materials input to the numerical simulations.

NEUTRON DIFFRACTION

Neutron diffraction is an attractive tool for probing bulk residual/internal strains in crystalline materials and has matured tremendously during the last decade [8,9]. It is based on traditional Bragg scattering experiments, whereby a selected lattice plane spacing, d_{hkl} , is used as an internal strain gauge. By the diffraction nature of the technique it provides the ability to monitor the individual phase strains in the two phases of the composite.

The initial thermal strains are characterised by comparing lattice parameters measured in the composite with those obtained from samples of the pure aluminium matrix material as well as a sample of “free” SiC whiskers contained within a sealed quartz tube. The in-situ straining of the composite samples while monitoring the evolution of phases strains, is accomplished using a loading rig developed for the neutron spectrometer [10].

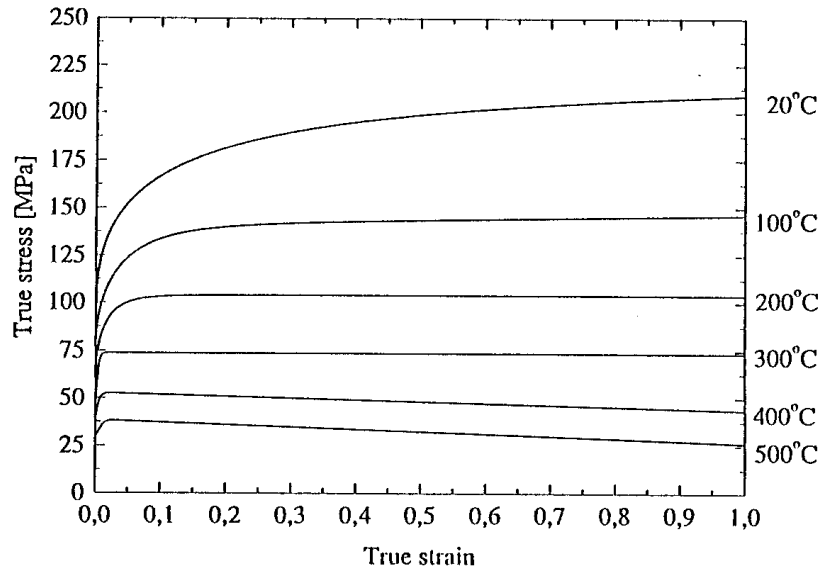


Fig. 1: Thermo mechanical behaviour of the matrix material as determined by elevated temperature compression tests.

In the investigation we focus only on the lattice strains along the extrusion/loading axis. The inclusion lattice strain response is characterised by measuring on the SiC_{111} reflection of the cubic SiC whiskers, which is the orientation predominantly aligned along the extrusion axis. For the matrix lattice strain response we use the Al_{111} reflection which has also proven to be the dominating texture component for the matrix material after extrusion. The sample of the 10vol% composite is loaded in uniaxial tension to a total deformation of 10%.

FEM CELL-MODELLING

The numerical simulations are based on a 2D axisymmetric mesh with a single embedded inclusion. It may be argued that 3D simulations are more appropriate, however, the less cpu-intensive 2D-simulations do, render a guidance to how well these idealised numerical simulation procedures do render results in agreement with experimental evidence.

The FEM cell-model is shown in Fig.2 giving the relative dimensions of the model, which is constraint to maintain straight surfaces along the free outer surface ($x=0.2$) as well as along the free top surface ($y=1.0$). The constitutive behaviour of the matrix alloy has been described above and is readily included as a elastic, isotropic hardening plastic material with temperature dependent Young's moduli and hardening characteristics, whereas the inclusion is assumed to behave purely elastic with no temperature dependent properties.

The initial phase of the numerical simulation is an incremental cooling and subsequently the model is incrementally strained towards a total deformation of 10% at room temperature. Lack of convergence typically prevents us from reaching 10% total strain, as the local strain grows very large, and in-fact may exceed the extent to which the materials behaviour has been characterised.

The simulations are done using the implicit ABAQUS code using 760 8-node biquadratic elements and is run as a sequential executing job on the Silicon Graphics Power Challenge computer at Risø National Laboratory.

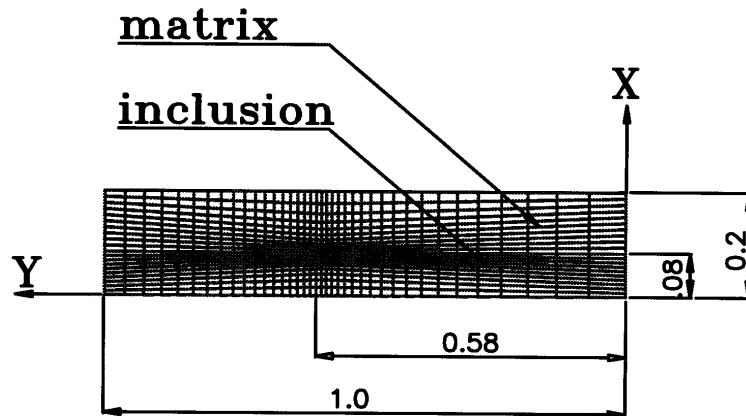


Fig. 2: FEM cell-model showing the idealised axisymmetric mesh and its relative dimensions.

DISCUSSION

The initial phase of the numerical simulation is a step wise free thermal contraction of the composite from a selected temperature. In the present investigation we have simulated this cooling process from temperatures ranging from 500°C to 100°C, with 500°C being the highest temperature at which the materials data are available, and which is close to the actual extrusion temperature. The results in terms of volume average elastic strains in the extrusion direction are presented in Fig.3.

In contrast to the linear behaviour expected from purely elastic materials properties [11], we note the effect of both plasticity and temperature dependency giving rise to gradient variations with temperature. The results of neutron diffraction investigations show a residual thermal strain in the matrix of 618×10^{-6} while the inclusion thermal strain was measured to be -1395×10^{-6} . These results are incorporated in Fig.3 as horizontal dotted lines showing that whereas the inclusion results point towards a “stress-free” temperature of 470°C, then the matrix residual strain level indicates a much lower temperature near 175°C. Among the two phases of the composite the purely elastic inclusions are the simplest internal strain gauge of the two; one which is not prone to any relaxation phenomena related to creep or diffusion though it is expected that the numerical simulations would render an upper bound on realistic observable thermal strains of the inclusions, as the simulations are done on an idealised perfectly aligned system. This points towards the fact that the realistic “stress-free” temperature is in fact close to the extrusion temperature near 500°C. On the other hand when looking at the matrix response experiments indicate a much lower thermal residual strain level than would arise by cooling from 500°C. It may be argued that the matrix response is merely a measure on a specific hkl-reflection of the polycrystalline aggregate and that single crystal anisotropy and choice of hkl-reflection affects the observable strain levels. However; aluminium is not a very anisotropic metal with the stiff $\langle 111 \rangle$ -orientation being only 9% stiffer than the typical macroscopic moduli. It is evident that the idealised numerical

predictions to a strong extent over estimates the matrix residual strain level as compared to the volume average matrix strain measured by neutron diffraction over a volume containing a large number of inclusions. The relative low level of matrix residual strains may point towards the lack of adequate relaxation phenomena in the materials description, however, the matrix strain level is to be balanced by the inclusion strains where we observe good correlation using a “stress-free” temperature of 500°C. This is hence indicating that the idealised FEM cell-model, at least based on volume average values of elastic strains, does not perform very well in terms of predicting the matrix deformation, while there is good correlation between experiments and simulations when it comes to the simple elastically deforming inclusions.

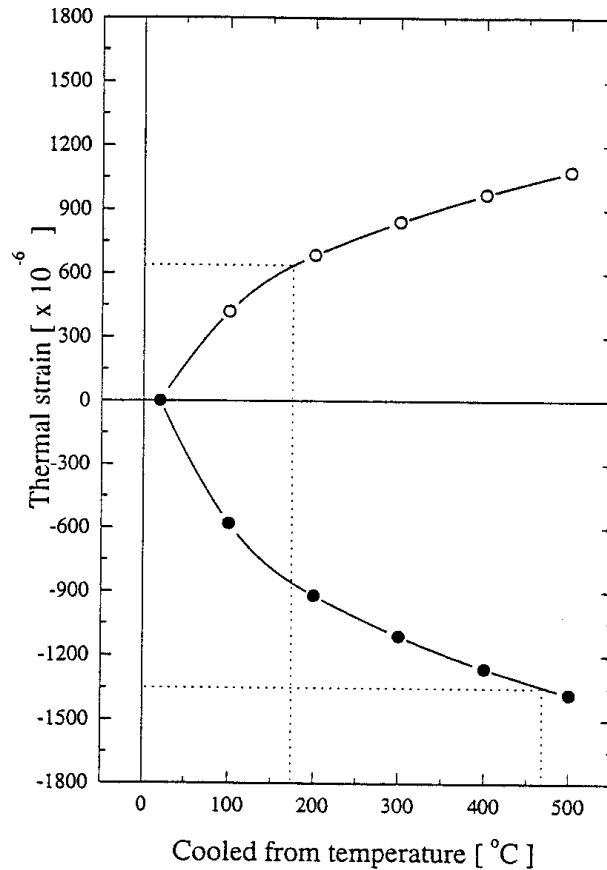


Fig. 3: Thermal residual strains in the two phases of the composite. Here shown as a function of the temperature from which the numerical simulation of the cooling sequence was initiated. Dotted lines indicate residual strain levels as measured by neutron diffraction.

Following the simulation of the generation of thermal mis-match strain during cooling we proceed to room temperature loading in uniaxial tension. These simulations are based on the cooling sequence from 500-20°C as predicted above, and hence originates from a situation where the initial volume average inclusion strain nicely resembles the level observed experimentally, while the volume average matrix strain is about 75% higher than observed experimentally. The numerical results shown in Fig.4 and are to be compared with the experimental results from the neutron diffraction experiments in Fig.5. The numerical results are qualitatively in agreement with the experimental observations, however, some discrepancies are observed on the numerical levels.

It is evident that the evolution of elastic phase strains in the inclusion is much stronger from the cell model predictions than can be observed experimentally, even in this situation where the initial residual strain level is accurately estimated. An obvious reason for part of the discrepancies is that the inclusions of the real composite are not as perfectly aligned as assumed by the model. For the matrix response we also observe that the numerical simulations over estimates the evolution of elastic phase strains. It is, however, noticed that the discrepancies throughout the total strain range appears to be attributed entirely to the lack of correspondence in the initial thermally induced residual strain level at the outset of the loading sequence.

The overall correspondence between numerical predictions and experimental characterisation of the phase strain evolution would have been improved had we selected a lower “stress-free” temperature, however, at present it would be pure speculation as to specifying a more proper “stress-free” temperature than the 500°C at which the matrix material does still retain some measurable strength.

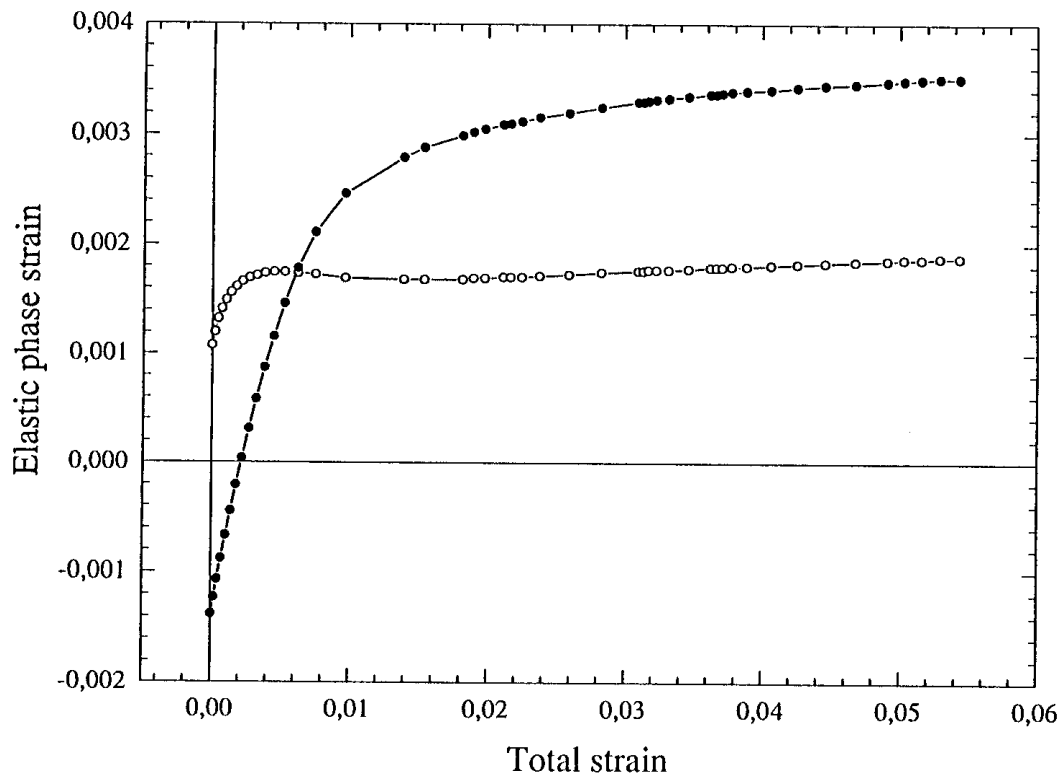


Fig. 4: Numerical predictions of the volume average elastic strain $\langle \epsilon_Y \rangle$ in matrix (O) and in the inclusion (●) along the loading direction.

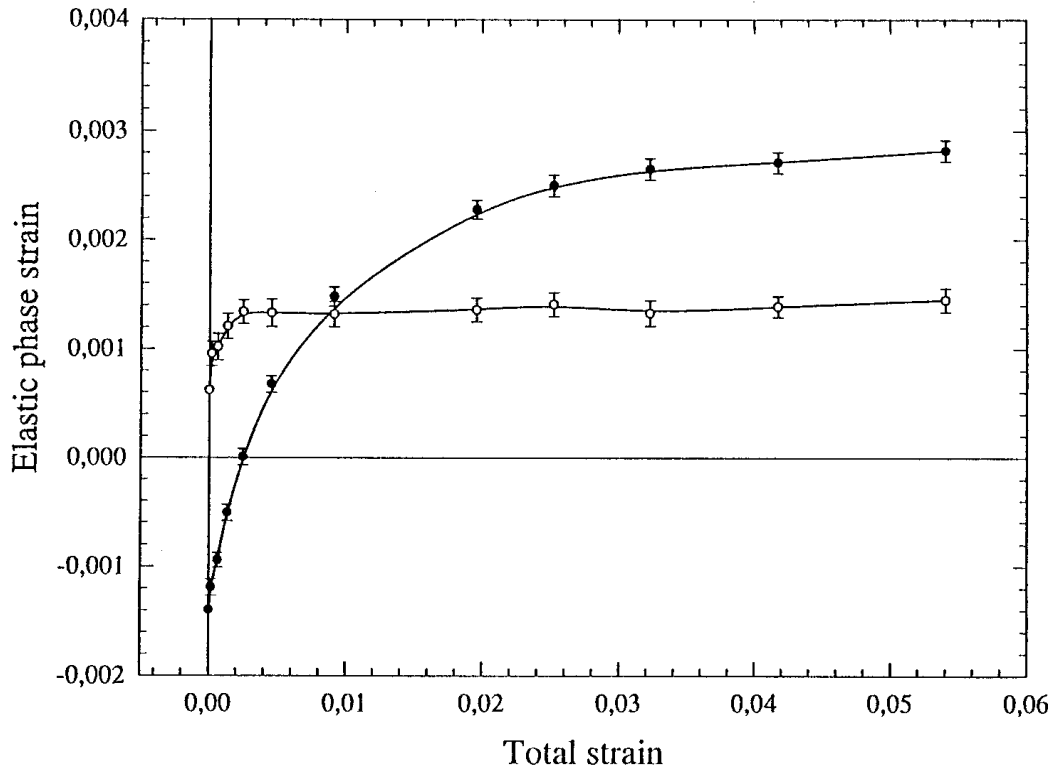


Fig. 5: Experimental characterisation of the volume average elastic strain $\langle \varepsilon_Y \rangle$ in matrix (O) and in the inclusions (●) along the loading direction.

CONCLUSION

The present investigation has highlighted the applicability of the neutron diffraction technique in the evaluation of an FEM cell-model approach of the thermo mechanical behaviour of composites. The investigation has highlighted how the utilisation of this novel experimental technique provides a step towards an evaluation of the micro mechanical value of FEM cell-models at a level of detail not achievable with other techniques at present. Such models have until recently mostly been evaluated by their capability to predict macroscopic deformation characteristics. The diffraction experiments has shown that the numerical predictions of phase strains are in qualitative agreement with observations, though there are some discrepancies in the quantitative estimates. We have pointed out that one of the reasons for the discrepancies is the idealised alignment of the inclusion in the model, however, the experimental results also point towards problems in realistic predictions of the relative strain levels between matrix and inclusions as it is not possible to define a single “stress-free” temperature in the simulations which render realistic thermal residual strains in both phases of the composite. It may be added that possibly problems do also remain in verifying a proper description of the thermo mechanical behaviour of the matrix material when being part of a composite as compared to the behaviour when being a “free” monolithic material.

ACKNOWLEDGEMENTS

The present investigation was conducted as part of the centre activities within the “Engineering Science Centre for Characterisation and Modelling of Materials” at Risø.

REFERENCES

1. Christman, T., Needleman, A. and Suresh, S., "An Experimental and Numerical Study of Deformation in Metal-Ceramic Composites", *Acta Metall.*, 37, 1989, pp. 3029-3050.
2. Levy, A. and Papazian, J. M., "Tensile Properties of Short Fibre Reinforced SiC/Al Composites, Part II", *Metallurgical Transactions A*, 21, pp. 411-420.
3. Tvergaard, V., "Analysis of Tensile Properties for a Whisker Reinforced Metal", *Materials Science and Engineering*, 125, 1990, pp. 203-213.
4. Lorentzen, T., Clarke, A. P., Poulsen, H. F., Garbe, S. and Graafsma, H., "Local Strain Contours around Inclusion in Wire Drawn Cu/W Composite", *Composites Part A*, 1997, in press.
5. Povirk, G. L., Stout, M. G., Bourke, M., Goldstone, J. A., Lawson, A. C., Lovato, M., MacEwen, S. R., Nutt, S. R. and Needleman, A., "Thermally and Mechanically Induced Residual Strains in Al-SiC Composites", *Acta Metall. Mater.*, vol. 40, No. 9, 1992, pp. 2391-2412.
6. Lorentzen, T., Sørensen, N. J. and Liu, Y. L., "A Comparison of Numerical Predictions and In-situ Neutron Diffraction Measurements of MMC Phase Response", Numerical predictions of deformation processes and the behaviour of real materials. Proceedings of the 15th Risø International Symposium on Materials Science, Risø (DK), September 5-9th 1994, edited by S. I. Andersen, J. B. Bilde-Sørensen, T. Lorentzen, O. B. Pedersen and N. J. Sørensen, Risø National Laboratory, Roskilde, Denmark, 1994, pp. 405-412.
7. Liu, Y. L., Hansen, N., Juul Jensen, D., Lilholt, H., Nielsen, P. and Fei, N. J., "Microstructure, Texture and Mechanical Properties of Al-SiCw Composites Manufactured by Powder Blending", *Advances in Powder Metallurgy*, edited by J. G. Gasbarre and W. F. Jandeska, Metal Powder Industries Federation, Princeton, vol. 3, 1989, pp. 461-474.
8. Allen, A. J., Hutchings, M. T., Windsor, C. G. and Adreani, C., "Neutron Diffraction Methods for the Study of Residual Stress Fields", *Advances in Physics*, vol. 34, No. 4, 1985, pp. 445-473.
9. Hutchings, M. T. and Krawitz, A. D., "Measurement of Residual and Applied Stress using Neutron Diffraction, Proceedings of the NATO advanced research workshop ARW-900367, Oxford, UK, Kluwer Academic Publishers, London, 1992.
10. Lorentzen, T. and Sørensen, N., "A New Device for In-situ Loading of Samples During Neutron Diffraction Strain Measurements", *Metal Matrix Composites - Processing, Microstructure and Properties*, Proceedings of the 12th Risø International Symposium on Materials Science, Risø, edited by N. Hansen, D. Juul Jensen, T. Leffers, H. Lilholt, T. Lorentzen, O. B. Pedersen, and B. Ralph, Risø National Laboratory, Roskilde, Denmark, 1991, pp. 489-496.
11. Lorentzen, T., Lin, Y. L. and Lilholt, H., "Relaxation of Thermal Induced Internal Stresses in Metal Matrix Composites", Proceedings of the 9th International Conference on Composite Materials (ICCM-9), edited by A. Miravete, University of Zaragoza, Woodhead Publishing Limited, Spain, vol. 1, 1993, pp. 371-378.

SYNTHESIS AND CHARACTERIZATION OF SI-N=C=N CONTAINING PRECERAMIC POLYMERS

Hai-Feng Hu, Zhao-Hui Chen, Chun-Xiang Feng, Chang-Rui Zhang,
Yong-Cai Song, Jia-Yu Xiao, Zheng-Fang Xie, Wen-Wei Zheng, Zheng-Xiang Fan

*Department of Material Engineering and Applied Chemistry, Changsha Institute of
Technology, Changsha 410073, P.R.China*

SUMMARY: In the paper, a kind of novel precursors with Si-N=C=N in the main chains were synthesized and characterized. The mediocre ceramic yields were obtained after heattreatment for $[\text{MeHSiNCN}]_n$ and crosslinking treatment for $[\text{MeViSiNCN}]_n$.

KEYWORDS: precursor, Si-N=C=N unit, pyrolysis, ceramic yield

INTRODUCTION

Since the successful applications of organosilicon precursors in manufacturing ceramic fibres (e.g., Nicalon fibre) [1] and ultrafine powders [2], and the potential advantages in manufacturing complex, continuous fibre reinforced ceramic composites [3], much effort has been focused on devising novel precursors with high ceramic yields and good processability. The precursors ever studied usually bear the main chains with Si-C, Si-C-C, Si-N, Si-Si-N, Si-N-N, etc., leading to Si-C, Si-N, Si-C-N ceramics upon pyrolysis [4-8]. Here we reported a kind of novel precursors containing Si-N=C=N units as the main chains.

EXPERIMENTAL PROCEDURE

Agents and Synthesis

Silver cyanamide (Ag_2NCN) was synthesized according to literature [9]. Dichlorosilanes and toluene were fresh distilled and all manipulations were conducted in an inert atmosphere.

In a 500ml three neck round bottom flask equipped with a stirrer, a condenser, and a dropping funnel, 12.8g silver cyanamide and 300ml toluene were added. The temperature of the oil bath was raised to reflux toluene for 30 minutes, then dichlorosilanes (typically 7.0ml dichlorodimethylsilane mixed with 50ml toluene) were added dropwise into the flask in 30 minutes. The reaction was sustained for another 2 hours to assure the completion of the reaction, then gravity filtration was applied to remove the precipitate (AgCl) and reduced-pressure distillation (353K/2mmHg) to remove toluene.

Measurement and Instrumentation

Infrared analysis was conducted by using Hitachi 270-30 infrared spectrophotometer (KBr disc). Number average molecular weights (M_n) of samples were measured with a corona 114 molecular weight apparatus by vapor phase osmometry (VPO) in a toluene solution. The molecular weight distributions were measured using a Waters-244 liquid chromatograph with Ultrastaygel as the gel-permeation chromatograph (GPC) column in toluene solution. ^1H nuclear magnetic resonance ($^1\text{H NMR}$) spectra were obtained on an AC-80 high resolution NMR spectrometer at 80 MHz with deuterated chloroform as a solvent and tetramethylsilane as an external reference. Elemental analysis of carbon, hydrogen, and nitrogen were performed on a PE2400 CHN elemental analyzer. Thermogravimetric analysis curves were obtained by a Rigaku TGA thermal analyser in $40\text{cm}^3\text{min}^{-1}$ nitrogen flow up to 1273 K at a heating rate of 10Kmin^{-1} .

RESULTS AND DISCUSSION

Structural Elucidation

The reaction, according to the formula, should follow the process:



Me_2SiCl_2 , Ph_2SiCl_2 , MeViSiCl_2 (Vi: $-\text{CH}=\text{CH}_2$), and MeHSiCl_2 were chosen as dichlorosilanes. The properties of synthetic products were listed in Table 1.

Table 1: The properties of synthetic products

Product	Appearance	M_n	n
$[\text{Me}_2\text{SiNCN}]_n$	oil	860	8.8
$[\text{Ph}_2\text{SiNCN}]_n$	gum	1780	8.0
$[\text{MeViSiNCN}]_n$	oil	1440	13.1
$[\text{MeHSiNCN}]$	waxy solid	—	—

$[\text{Me}_2\text{SiNCN}]_n$, $[\text{Ph}_2\text{SiNCN}]_n$, $[\text{MeViSiNCN}]_n$ dissolved well in benzene, toluene, and xylene. The average number of units in the chains was approximately 10, indicating the products were oligomers or low molecules. The dispersive indexes were around 1.5, showing no cyclic products present.

But $[\text{MeHSiNCN}]_n$ dissolved poorly in aromatic solvents, hinting that crosslinking had occurred and branched structure had formed.

Elemental analysis (Table 2) agreed well with theoretical values in the case of $[\text{Me}_2\text{SiNCN}]_n$, $[\text{Ph}_2\text{SiNCN}]_n$, and $[\text{MeViSiNCN}]_n$, indicating the supposed structures were reasonable. But for $[\text{MeHSiNCN}]_n$ the hydrogen content deviated lower from that of the theoretical value, indicating the existence of the branched structures at the site of the Si atoms due to the loss of hydrogen, which was in accordance with the poor dissolution in aromatic solvents.

Table 2: Elemental analysis results (%wt)

Product	C		H		N		Si	
	exp.	theo.	exp.	theo.	exp.	theo.	exp.	theo.
[Me ₂ SiNCN] _n	37.1	36.7	6.2	6.1	27.9	28.6	28.8	28.6
[Ph ₂ SiNCN] _n	68.4	70.3	4.6	4.5	11.2	12.6	15.8	12.6
[MeViSiNCN] _n	44.7	43.6	5.9	5.4	25.1	25.4	24.3	25.4
[MeHSiNCN] _n	29.0	28.6	2.6	4.8	32.4	33.3	36.0	33.3

The assumed structures were again confirmed by IR patterns (Table 3) and ¹HNMR spectra. For [Me₂SiNCN]_n, characteristic peaks were 2960cm⁻¹(γ_{as}CH₃), 2900cm⁻¹(γ_sCH₃), 2160cm⁻¹(γN=C=N), 1410cm⁻¹(single δ_{as}CH₃), 1260cm⁻¹(δ_sSi-CH₃), and 950cm⁻¹(γSi-N). For [Ph₂SiNCN]_n, peaks at 1630cm⁻¹ and around 1800cm⁻¹ were ascribed to the stretching vibrations of the rings. For [MeViSiNCN]_n vibrations of unsaturated groups were 1600cm⁻¹(γ_sC=C) and 3100cm⁻¹(γ_{as}=CH). For [MeHSiNCN]_n peaks at 2160cm⁻¹ ascribed to Si-H vibration couldn't be distinguished from N=C=N stretching vibration.

For cyanamide, there usually existed two isomers: N=C=N ↔ N-C≡N, which was characterized by double peaks at 2160cm⁻¹. In our experiment, there was only one single peak at 2160cm⁻¹, indicating there was no end groups of N=C=N in the main chains (actually dichlorosilanes were a little excess).

Table 3: The ascription of vibrations in IR patterns

Wave Number(cm ⁻¹)	Ascription
3100m	γ _{as} =CH
2960m	γ _{as} CH ₃
2900m	γ _s CH ₃
2160s	γ _{as} N=C=N and γ _{as} Si-H
1800w	aromatic rings(C-H)
1630w	aromatic rings(C=C)
1610w	γ _{as} C=C
1410s	δ _{as} CH ₃
1260s	δ _s Si-CH ₃
950m	γSi-N

In ¹HNMR there were only simple peaks for [Me₂SiNCN]_n at 0.3ppm(single, broad, strong), for [Ph₂SiNCN]_n at 7.2ppm(single, mediocre strong), for [MeViSiNCN]_n at 0.8ppm(strong, single), 5.8-6.1ppm(double, mediocre strong), and for [MeHSiNCN]_n at 0.8ppm(single, strong), 4.7ppm(single, broad, mediocre strong).

Ceramic Yields Upon Pyrolysis

Ceramic yield is one of the most important index to evaluate the usefulness of the precursor. Generally high ceramic yield is helpful.

The four synthetic polymers were applied to TG to determine the ceramic yield, and the results were listed in Table 4.

As shown above, ceramic yield in $[\text{MeHSiNCN}]_n$ was as high as 56%, while in $[\text{Me}_2\text{SiNCN}]_n$ was nearly none. Two reasons might contribute to the rather low yields: the linear structures caused segment-after-segment breakage of the main chains and crosslinking for $[\text{MeHSiNCN}]_n$ and $[\text{MeViSiNCN}]_n$ was not enough. Thus $[\text{MeViSiNCN}]_n$ was crosslinked in N_2 in the presence of 0.5% wt dicumyl peroxide(DCP), then it changed from oil to waxy solid, followed by pyrolysis to obtain 55%wt ceramic. $[\text{MeHSiNCN}]_n$ was heattreatment at 453K for 6 hours, then was pyrolyzed to obtain 64% ceramic. In Fig. 1 there showed the TG curves for the treated polymers. Large weight loss occurred during 450-1000K, and the crosslinked polymer were rather stable before 450K. The mechanism involved during the pyrolysis is being under study.

Table 4: Char yields upon pyrolysis

Product	Char Yield (wt%)
$[\text{Me}_2\text{SiNCN}]_n$	3.6
$[\text{Ph}_2\text{SiNCN}]_n$	27.8
$[\text{MeViSiNCN}]_n$	41.2
$[\text{MeHSiNCN}]_n$	56.0

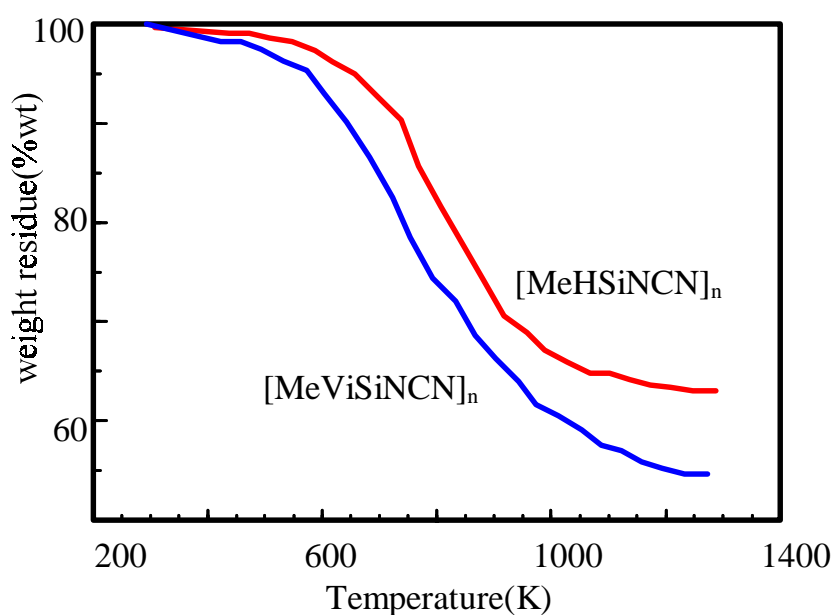


Fig. 1: TG curves for samples after treatment (ramping rate 10K/min, N_2)

CONCLUSION

By reacting silver cyanamide and chlorosilanes (dimethyldichlorosilane, methylvinyl-dichlorosilane, diphenyldichlorosilane, methyldichlorosilane) in refluxing toluene, the synthetic products which were characterized by IR, ¹HNMR, GPC, and elemental analysis to bear the linear and light branched structure $-(SiRR'N=C=N)-_n$ were obtained. Upon pyrolysis ceramic yields ranged from nearly zero to 56%(wt). Heat treatment of $[MeHSiNCN]_n$ and crosslinking treatment of $[MeViSiNCN]_n$ gave ceramic yields(upon pyrolysis) of 64% and 55%, respectively.

REFERENCES

1. Yajima,S., "Special Heat-Resisting Materials from Organometallic Polymers", *American Ceramic Society Bulletin*, vol.**62**, No.8, 1983, pp.893-898.
2. Suzuki, M., Maniette, Y., Nakata, Y., and Okatani, T., "Synthesis of Silicon Carbide-Silicon Nitride Composite Ultrafine Particles Using a Carbon Dioxide Laser", *Journal of the American Ceramic Society*, vol. **76**, No.5, 1993, pp.1195-200.
3. Nakano, K., Kamiya, A., Nishino, Y., Imura, T., and Tsu-Wei, Chou., " Fabrication and Characterization of Three Dimensional Carbon Fiber Reinforced Silicon Carbide and Silicon Nitride Composites", *Journal of the American Ceramic Society*, vol.**78**, No.10, 1995, pp.2811-14.
4. Yajima, S., Hesagawa, Y., Okamura, K., Matsuzawa, T., "Development of High-Tensile-Strength Silicon Carbide Fibre Using an Organosilicon Polymer Precursor", *Nature(London)*, vol.**273**, 1978, pp.525-526.
5. Boury,B., Corriu, R.J.P., Leclercq, D., Mutin, H., Planex, J.P., and Vioux, A., "A Catalytic Preparation of a New Pre ceramic Polymers: Transformation into SiC." **IN: Inorganic and Organometallic Polymers with Special Properties**, Laine, R.M., Ed., Academic Publishers, Netherlands, pp.255-266.
6. Gary, T.B., Timothy, P., Angelotti, L. F., Grish, C., John, A.M., " Alkyl- and Aryl-silylsesquizes: Effects of the R Group on Polymer Degradation and Ceramic Char Composition", *Journal of Material Science*, vol.22, 1987, pp.2609-2614.
7. Mocaer,D., Pailler, R., Naslain, R. et al., "Si-C-N Ceramics with a High Microstructural Stability Elaboration from the Pyrolysis of New Polycarbosilazane Precursors. Part I. The Organic/Inorganic Transition", *Journal of Material Science*,vol. **28** ,1993, pp.2615-2631.
8. Coloumbier, C., and Cuer, J.P., "Preparation of Polysilazanes for Use in Ceramic Production", Fr.Demande FR2633301, 1989.
9. Parshall, G.W.(Editor-in-Chief), *Inorganic Syntheses*, vol.**15**, pp.165, McGraw-Hill Book Company, Inc., London, 1974.

ELASTIC DEFORMATION BEHAVIORS OF PARTICULATE REINFORCED COMPOSITES

Quan Gaofeng, Chai Donglang & Song Yujiu

*State Key Laboratory for Mechanical Behavior of Materials,
Xi'an Jiaotong University, Xi'an, 710049 P.R.China*

SUMMARY: The elastic deformation of particulate reinforced aluminum and magnesium alloy matrix composites are both experimentally and analytically studied. The materials are made by P/M method. It is found that there are great differences in elastic deformation performances between composite materials and controlled alloys. The composites have much higher elastic moduli than controlled alloys, and the higher the content of the ceramic particles is, the higher the modulus is. Moreover, most composites in this work have much higher elastic limits than those of the controlled materials. The analytical studies, with simple quasi-tri-dimensional models for the both, also clarify these rises, and can give out some better quantitative estimations.

KEY WORDS: Al and Mg alloy matrix composites, elastic deformation, modulus, elastic limits, particle content, quantitative analysis, mechanical property estimation

INTRODUCTION

Metal matrix composites have achieved great attention both in materials science and engineering application fields due to their superiority in mechanical property and performance, especially reinforced with short fibers and/or particles. Even though a number of studies are focused on their fabricating method, fracture performance, interfacial characterizations, etc., there is no denying the fact that almost any component and/or structure is working during service within elastic deformation stage. Up till now there is not much analytical work on the behavior of elastic or small deformation of the composites, and a lot of digital computation work is taken with various models on stress-strain behavior of the composites with regular meso-structures [1,2]. Previous work of the present author has clarified that the particulate reinforced metal matrix composites have excellent strength properties which can be analyzed quantitatively with a mechanical model by some fuzzy theoretical treatments [3,4]. The elastic modulus (Young's modulus) is the most important both mechanics and physics parameter for a specific structural composite, which has been modeled by many researchers [5]. But most of the models have not included the interactions of stress fields of the neighboring particles, which may be a unavoidable factor of discrepancy in calculated results and the practical measured ones. In this work the elastic moduli of some aluminum and magnesium alloy matrix composites contained various contents of SiCp (silicon carbide particles) are measured and analyzed with a consideration of interactions of neighboring particles. Also the engineering elastic limits of them are determined and interpreted with a previous proposed model.

EXPERIMENTAL PROCEDURE

SiC_p reinforced aluminum (SAE2024) and magnesium alloy matrix composites are fabricated by P/M method (The former is called aluminum composite, the latter called magnesium composite for short). The normal sizes of the particles are 5μm, 10μm, and 20μm, and the metal or alloy powder's size are ranged from 5μm to 54μm. The compositions of the matrix are given in Table 1. The volume fractions of SiC_p are from 0.05 to 0.40. The mixtures of the ceramic and metal powders are cold-pressed in a mold, hot-pressed and followed by hot-extrusion (extrusion ratio 1:16) and heat-treatment (T6, solutioned and aged to about peak hardness). The round tension samples are machined to measure the stress-strain curve (see Fig. 4), on which the elastic limit (engineering proportional limit), proof stress, ultimate strength and ductility are determined on an INSTRON1195 testing machine. The elastic moduli are determined from both microstrain and a linear regression method on the straight length of the curves.

Table 1: The Compositions of The Matrix Alloys

Alloy / Chemistry	Al	Mg	Si	Cu	Zn	Mn	Zr	Fe
Aluminum(2024)	Bal.	1.6	<0.20	4.55	<0.10	0.10		<0.10
Magnesium(MB15*)		Bal.			5.00		0.60	

* MB15 is a Chinese Brand of Mg-Zn-Zr alloy

RESULTS AND ANALYSIS OF ELASTIC MODULUS

Measured Modulus of Aluminum Composites

The practical measured elastic moduli of the aluminum composites are showed in Fig. 1, in which the increasing tendency in elastic modulus with the ceramic particle volume fraction is very outstanding. The increase in elastic modulus is one of the most interesting features of these materials, and less affected by the fabricating routine but the constituents and their distributions. In this work the superior orientation of the long axis of ellipsoid-like particles to the extrusion direction is found and the expectation of the specific ratio are analyzed. The superior orientation may cause the axial elastic modulus to increase more. In the extreme situation in this work, the maximum elastic modulus of the composite containing a SiC_p fraction of 0.40 is as high as 168.7 GPa, which is 2.41 times of the matrix alloys.

Elastic Modulus Results of Magnesium Composites

Table 2 shows the measured results of elastic modulus in magnesium composites, companied with the specific modulus and strength data, and as a comparison the aluminum composites' data enclosed. It is also seen that the moduli of the composites increase greatly. It can be noticed that in the same table the absolute property value of magnesium composites may not be superior to those of aluminum composites, but the specific value of the formers have some advantages in air and space applications.

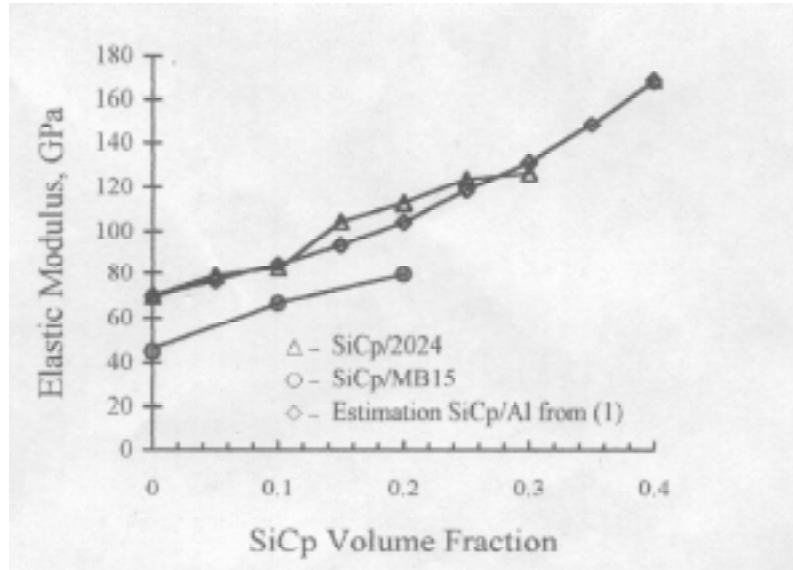


Fig. 1: Elastic moduli of aluminum and magnesium composites vs volume fraction of SiCp

Table 2: Property data of Magnesium composites vs those of aluminum composites

Material	E , GPa	σ_p , MPa	ρ , g/cm ³	E/ρ , 10 ⁶ m	σ_p/ρ , 10 ³ m
Magnesium(MB15)	45	180	1.76	2.609	10.436
0.10SiC _p /MB15	67.0	266.0	1.904	3.591	14.250
0.20SiC _p /MB15	79.5	274.3	2.05	3.957	15.900
0.20SiC _p /2024	112	318.0	2.89	3.954	11.228

Analysis of The Modulus for Particles Reinforcing Composites

According to a multi-particle model, in which a consideration of interactions of neighboring stress fields of the particles is introduced with superposition at the spherical shell surface of a radius of R , which is defined as the half-distance of neighboring particles. Let E_0 be the modulus of the composite, ν_0 the Poisson ratio, K_0 the volume modulus, and G_0 the shear modulus, and $\eta = a/R$ the spacing ratio of the particles (suppose all particles spacially homogeneous distribution, a is the normal radius of the particles). So we obtain such an expression [8]:

$$\frac{2E_0}{3(1-\nu_0)} = \sum_{i=1}^n \frac{V_i}{\frac{1}{4G_0} - \frac{\eta^3}{3K_0} + \frac{1+\eta^3}{3K_i}} \quad (1)$$

where V_i represents the volume fraction of the constituents, the whole composite can be treated as two constituents: the matrix and reinforcement, so $V_1=1-V_p$, $V_2 =V_p$. And K_i represents the volume modulus of the constituents. As soon as the distribution pattern is certain, the relation between V_p and η is solely certain. For instance, the relation of the two parameters for a simply body-centered cubic distribution can be written as:

$$\eta^3 = 1.4702 V_p \quad (2)$$

This equation also is a limitation of the application of Equ.1, i.e., $(V_p)_{\max} 0.68$. The v_0 can be determined by other method, i.e., ROM method [6]:

$$v_0 = \sum_{i=1}^m V_i v_i \tag{3}$$

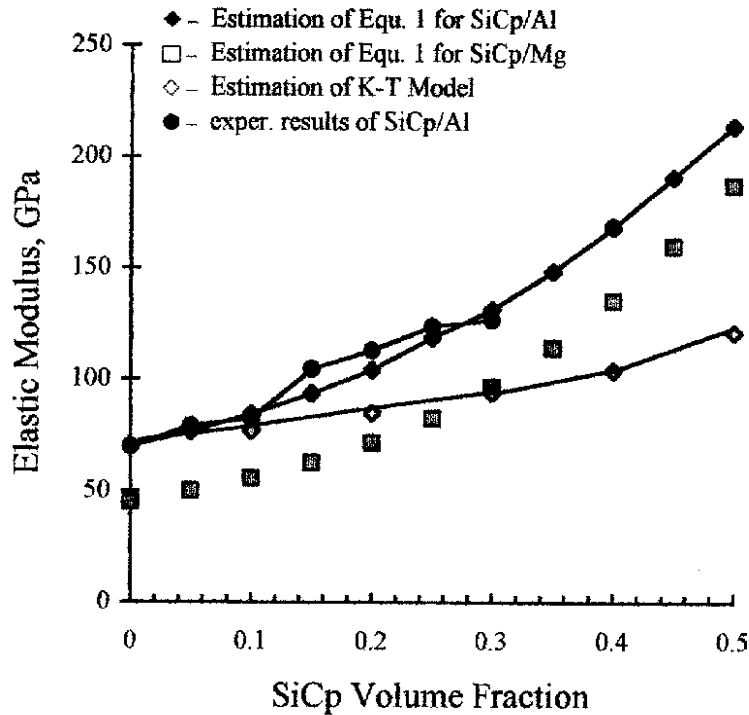


Fig. 2: Comparisons of Present model with Kuster & Toksoz’s Model and Experimental data

Fig. 2 show the estimations of moduli from Equ. 1 for the aluminum (diamond mark) and magnesium (square mark) composites, also the practically measured data. It is obviously seen that the present model would more accurate than Kuster and Toksoz’s model (triangle mark)[7]. The higher points at 0.150.20 of volume fraction than the estimations is caused by longer oriented silicon carbide particles (the average axial specific ratio equals 2.17), which were produced by different factories.

RESISTANCE TO ELASTIC DEFORMATION BEHAVIORS

Elastic Deformation Patterns of Composites with Various Contents of Particles

Elastic deformation resistance has most important significance in both material and structure design, also in working life of machines. Almost all practical mechanisms are required not to be deformed elastically over a given amount. In more exact meaning, the elastic limit σ_e is used as a design parameter, but in most application situations the engineering proportional limits, σ_p is adopted as both design parameter and criterion of material qualification. In this work they are measured by the way that the intersection of the tension curve and the straight line with a 50% slope of straight length of the tension curve is taken as σ_p point. The results are showed in Fig. 3.

These results illustrate that the σ_p is increasing with the volume fraction of SiC_p, and this is merely found in published work. Also, σ_p of magnesium composites are much higher than the controlled alloy. This is more profitable to all mechanical applications, especially in aerospace structures. The increase in proportional limits of the composites has also confirmed the appropriateness of the fabricating techniques. Fig. 4 is the copies of the local tensile curves of some typical materials, which show a direct evidence of the increases in elastic limits and elastic moduli.

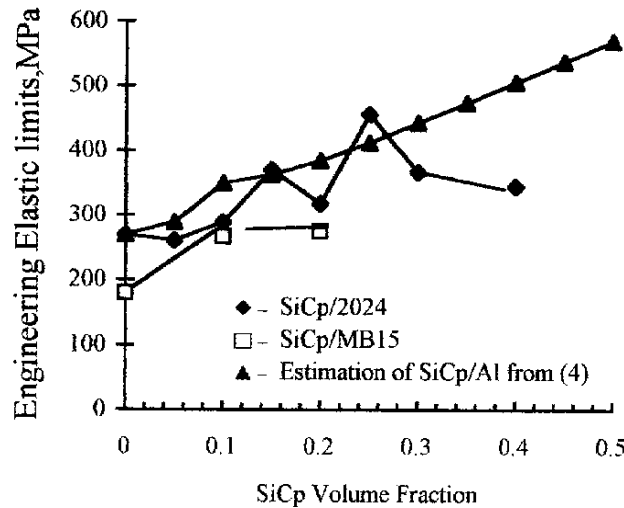


Fig. 3 Engineering proportional limits of the composites

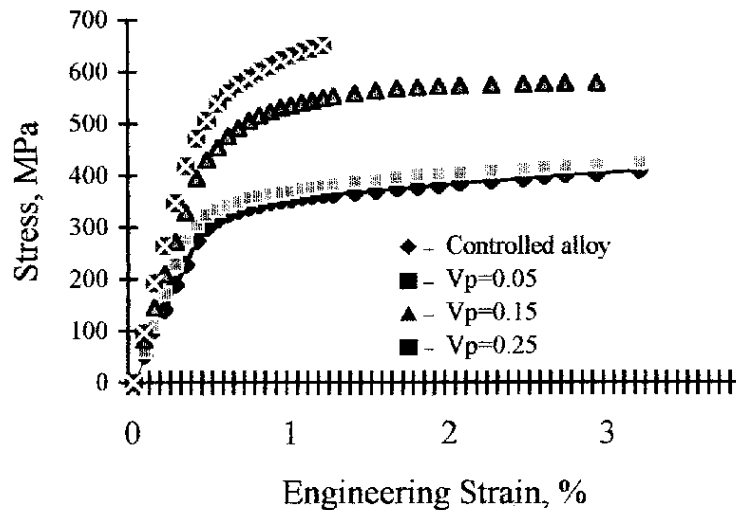


Fig. 4 Recorded stress-strain curves of aluminum composites

Analysis and Verification for Elastic Limits of DRMMCs

According to a previous model proposed by the present authors [3], in which the meso-structure distribution in the composites can be seen as a body-centered cubic pattern, the lower and upper elastic limits are written as:

$$\sigma_{cp}^l = \begin{cases} [1 + A_2(k_c^L E_2 / E_1 - 1)]\sigma_{mp}, & \sigma_z / \tilde{\sigma}_1 \geq 1 \\ \frac{1 + A_2(k_c^L E_2 / E_1 - 1)}{\omega_1 + \omega_2 k_c^L E_2 / E_1} \sigma_{mp}, & \sigma_z / \tilde{\sigma}_1 < 1 \end{cases} \quad (4)$$

$$\sigma_{cp}^u = \begin{cases} \frac{1 + A_2(k_c^L E_2 / E_1 - 1)}{\omega_1 + \omega_2 k_c^L E_2 / E_1} \sigma_{mp}, & \sigma_z / \tilde{\sigma}_1 \geq 1 \\ [1 + A_2(k_c^L E_2 / E_1 - 1)]\sigma_{mp}, & \sigma_z / \tilde{\sigma}_1 < 1 \end{cases} \quad (5)$$

where $k_c^L = \frac{2\eta^2}{1+\eta^2} \frac{\lambda}{1+\lambda}$ is defined as “striain constraint factor”, and ω_1 and ω_2 are the structural parameters determined by a , R , l and V_p , E_1 and E_2 are the elastic moduli of the matrix and reinforcement, respectively, A_2 is the area fraction of the reinforcement on an arbitrary cross section. σ_z and $\tilde{\sigma}_1$ are the equivalent stress at the top of the particle and the effective axial stress in the matrix by the particle. Some attention must be paid that the real elastic limit of a specific composite is inevitably fallen between σ_{cp}^l and σ_{cp}^u .

From the two estimate formula one can be sure to determine the range of elastic limit of a particular composite whose meso-structural parameters are known. Fig. 5 shows the estimated results. It is necessary to question that the residual micro- and meso-stresses between the constituents must have some effect on the elastic limit, especially in the matrix with lower elastic limit.

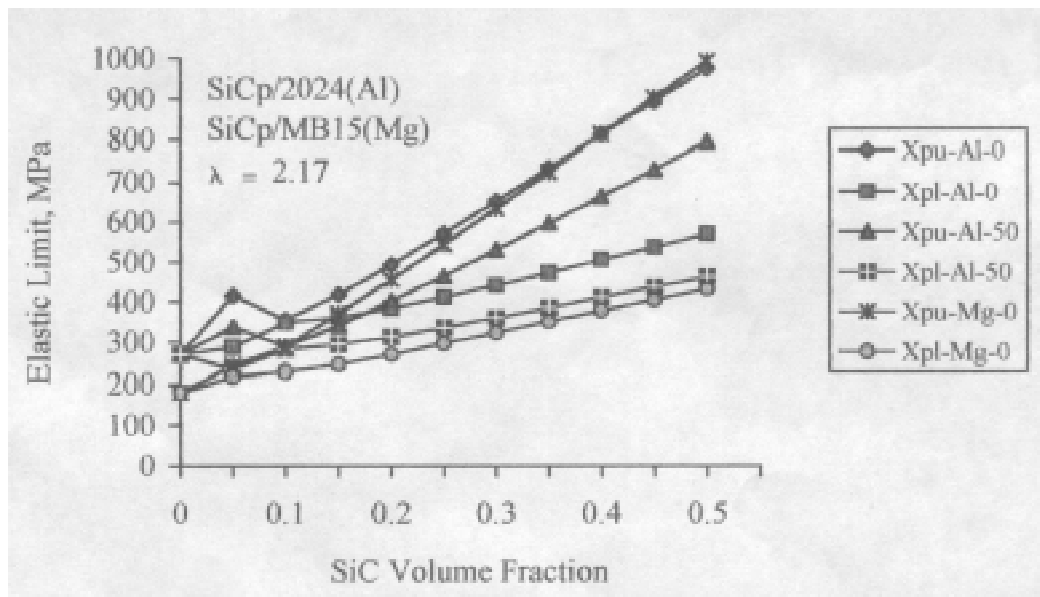


Fig. 5: Estimate results from Eqs. (4, 5) and comparison with experimental data (Xpu-Al-0 means the upper elastic limit and the both residual stresses are zero for aluminum composites, and Xpl-Al-50 denotes the lower elastic limit and the interfacial residual stresses are equal to 50MPa, and so forth).

As a rational deduction the superposition method further can be introduced to deal with the problem. If the effective radial residual stress near the interface between a particle and the matrix is $\langle \sigma_r^R \rangle$ and the tangential stress is $\langle \sigma_\psi^R \rangle$ [5], then the real elastic limits (lower and

upper) can be determined by σ_{mp} with $\sigma_{mp} - \langle \sigma_r^R \rangle$ in the first formula of Equ. 5, and σ_{mp} with $\sigma_{mp} - \langle \sigma_\psi^R \rangle$ in the second one. Fig. 5 also gives the estimations which include the interfacial residual stresses. In the light of the situation with presumed regular residual stress consideration, the elastic limits vary very much. Actually the residual stresses are not constant in different position and near different particles, and that needs more complicated model to deal with.

CONCLUSIONS

1. The composite materials made by P/M method have much higher resistance to elastic deformation, illustrated by both higher elastic modulus E and higher elastic limit σ_{cp} .
2. A model to evaluate the modulus of composites including interactions of neibeghring particles is proposed and a better agreement with the experimental data has been achieved.
3. An analytical model for estimation of elastic limits of discontinuously reinforced metal matrix composites is applied to interpret the increase in elastic limits of the composites, in which the difference in stress at different position of the matrix causes the estimation to drop in the range of lower and upper elastic limits. Experimental results seem to support the model.

REFERENCES

1. H. Fukuda and A. Wada, "Monte Carlo simulation for the strength of unidirectional composites", *Proceedings of the International Conference on Advanced Materials*, August 12-15, 1996, Wang Tzuchiang, Tsu-Wei Chu Eds, pp499-504
2. Schaeffer B., "Numerical modeling of the mechanical behaviour of composite materials", *Proceedings of the International Conference on Advanced Materials*, August 12-15, 1996, Wang Tzuchiang, Tsu-Wei Chu Eds, pp593-598
3. G. F. Quan, D. L. Chai, "A quantitative evaluation and experimental study on the elastic limits for DRMMCs", *Scripta Metall. Et Mater.*, Vol.33, No.12, 1995, pp 1987-1991
4. G. F. Quan, D. L. Chai, Y. J. Song, "Studies on strengthening mechanisms of DRMMCs", *Proceedings Tenth International Conference on Composite Materials*, Whittler, British Columbia, Canada, August 14-18, 1995, Vol.II: Metal and Ceramics Matrix Composites, A and Street, K. N., Eds, pp521-525
5. G. F. Quan, *Doctorate thesis of Xi'an Jiaotong University*, June 1994.
6. L. Zhou, F. Q. Fan, *Composite mechanics*, Advanced Education Press, Beijing, 1989, pp327-332.
7. G. Berryman, "Long-wave propagation in composite elastic media, I and II", *J. Acoust. Soc. Am.*, Vol.68, No.6, 1980, pp1809-1830.

DETECTION OF DISLOCATIONS IN SHORT FIBRE REINFORCED MAGNESIUM ALLOYS BY NON-DESTRUCTIVE METHODS

J. Kiehn¹, K.U. Kainer¹, Z. Trojanová², F. Chmelík² and P. Lukáč²

¹ *Department of Materials Engineering and Technology, Technical University of Clausthal, Agricolastr. 6, D-38678 Clausthal-Zellerfeld, Germany.*

² *Department of Metal Physics, Faculty of Mathematics and Physics, Charles University, Ke Karlovu 5, CZ-12116 Prague 2, Czech Republic.*

SUMMARY: Alumina short fibre preforms showing planar isotropic fibre distribution were infiltrated by commercially pure magnesium applying a direct squeeze cast process. Bending beams for internal friction measurements and rods for dilatometer and acoustic emission experiments were machined from the solution treated samples. During thermal cycling temperature, elongation and acoustic emission of the sample rods were recorded simultaneously. Thermal cycling causes internal stresses due to the difference in the coefficients of thermal expansion of the composite components. These stresses lead to permanent deformation of the specimen by creep and plastic flow. The total acoustic emission and the burst emission activity are correlated with plastic deformation mechanisms of the material. Damping and reversible stress relaxation experiments performed after thermal cycling show a strong dependence of the critical strain amplitude on the top cycle temperature and indicate an increase in the dislocation density with the top temperature.

KEYWORDS: acoustic emission, stress relaxation, damping, dilatation, thermal cycling, magnesium, alumina short fibre, thermal stresses

INTRODUCTION

During the last decade metal matrix composites (MMCs) based on magnesium have been developed and manufactured by various techniques to achieve low density composites with a high specific strength, stiffness and creep resistance even at elevated temperatures [1]. Additional advantages of Mg composites in comparison to unreinforced Mg alloys are e.g. improvements in the fatigue and wear resistance and a significant reduction of the thermal expansion. For economic reasons the development of Mg MMCs is focused on short fibre or particle reinforced MMCs rather than continuous fibre reinforced. A volume fraction of at least 15-20% reinforcement is preferential for an effective increase of strength and stiffness in particle or short fibre reinforced Mg MMCs [2,3]. For applications that require tensile creep strength a short fibre reinforcement of advanced creep resistant Mg alloys is recommended. Squeeze casting is considered as an economic method for producing short fibre reinforced Mg MMCs [2,4]. The load transfer from matrix to fibre is maintained by the interface that is strongly influenced by reaction products. Silica stabilised δ -Al₂O₃ fibres can be preheated in air up to temperatures higher than the liquidus temperature of Mg alloys without any damage and show almost no degradation during solidification of the Mg melt in the squeeze cast process or during subsequent heat treatment of the MMC [5]. For many Mg alloys reaction

product formation at the interface can be controlled by a proper heat treatment and therefore δ -Al₂O₃ short fibre reinforced Mg MMCs show a sufficient interface strength and a good thermal stability of the mechanical properties [6]. Mg melt infiltration of δ -Al₂O₃ short fibre preforms by squeeze casting is a promising way to improve the mechanical properties of Mg alloys at room and elevated temperatures beyond the limits of alloy development at a reasonable cost/benefit ratio.

Thermal stresses are generated in MMCs due to the difference in the coefficients of thermal expansion (Δ CTE) between the reinforcement and the matrix during the production process or any further temperature change. These thermal stresses can lead to the generation of new dislocations as it was proposed by Arsenault and Fisher [7] and shown by the etch-pit technique for Cu-W composites [8]. The dislocation generation owing to CTE mismatch is considered as one important strengthening mechanism [9]. Because of the induced thermal stresses thermal cycling is one of the most severe thermal environments and assumed to be more dangerous for MMCs than for monolithic alloys [10]. In-situ transmission electron microscopy observations have proven the increase in the dislocation density in Al-SiC composites during thermal cycling [11,12]. Large acoustic emission activity during the first three cooling intervals of thermally cycled SiC-particle reinforced Mg alloy QE22 was explained by the generation of fresh dislocations and displacement of the dislocations under the increasing thermal stresses during cooling [13]. The effect of thermal cycling on the microstructure, mechanical properties and stress state of MMCs is very well summarised in the standard text books on MMCs [10,14-16]. Such dimensional changes are a result of the thermal stresses introduced by thermal cycling and the relaxation mechanisms influenced by a lot of parameters (i.e. applied temperature-time profile, mechanical properties and their temperature dependencies, creep conditions, additional external load). The deformation of MMCs during thermal cycling holds the potential for a MMC forming process [17,18].

The effect of thermal cycling on the properties of squeeze cast δ -alumina short fibre reinforced Mg alloys has been investigated recently. Low load hardness measurements of δ -alumina short fibre reinforced magnesium alloy AZ91 after thermal cycling between 40°C and 300°C indicate a work hardening effect for the matrix [19]. Dilatometer investigations show that the dimensional stability during thermal cycling strongly depends on the top temperature of the thermal cycle (henceforth top cycle temperature - T_{top}), the thermal history of the specimens and the mechanical properties of the matrix alloy [20,21]. It has been shown that for higher top cycle temperatures compressive stresses along the main axis prevail during the thermal cycle and result in shortening of the specimens. Reversible stress relaxation measurements were carried out in order to investigate the thermal stability of thermally cycled AZ91 and QE22 MMCs and good correlation was found between precipitation effects and the stress relaxation [22,23]. For large numbers of cycles an interface damage was indicated by a sharp increase of the stress relaxation [23]. Damping measurements, that have been evaluated in the framework of the Granato-Lücke theory, have shown a strong dependence of the amplitude dependent damping on T_{top} but not on the number of cycles up to 100 cycles between RT and 300°C [24]. Internal friction values are strongly influenced by ageing [25,26].

Measurements of elongation, acoustic emission (AE) and internal friction are well suited non-destructive methods to investigate the dislocation generation in δ -Al₂O₃ short fibre reinforced Mg alloys during thermal cycling. In-situ measurements of acoustic emission and elongation in combination with internal friction measurements after thermal cycling will help to differentiate the matrix deformation mechanisms during thermal cycling.

EXPERIMENTAL DETAILS

The commercially pure magnesium (cp-Mg with Al and Si as main impurities) was reinforced with SiO₂ stabilised δ -Al₂O₃ short fibres (Saffil[®] from ICI) using squeeze casting [1,2,4]. The preforms consisting of the short fibres (mean diameter and length 3 μ m and 87 μ m, respectively, after squeeze casting) and a binder (containing Al₂O₃ and starch) were preheated to a temperature higher than the temperature of the magnesium melt (preform 1000°C, melt 800°C) and then inserted into a preheated die (290 to 360°C). The pressure for forcing the melt into the die with the preform was applied in two stages (50MPa for 30s and 130MPa for 90s). The second step closes pores and shrinkage cavities. The short time of contact between the liquid metal and the fibres leads to only slight reactions between the fibres and the matrix. Mg₂Si and Mg₁₇Al₁₂ are formed at the matrix-fibre interfaces due to reactions of the melt with the Saffil[®] fibres and/or the binder. Diffractometer phase analysis provided some evidence for the presence of MgO. The fibres do not act as centres for heterogeneous nucleation due to high temperature of the preform [2]. The materials prepared were exposed to a solution annealing 520°C/5.5h finished by hot water quenching.

Specimens for the damping and the reversible stress relaxation measurements were machined as bending beams (88mm long with thickness of 3mm) with the reinforcement plane parallel to the main specimen plane. The damping measurements were carried out in vacuum (about 50mPa). The specimens fixed at one end were excited into resonance (the frequency ranged from 150 to 160Hz) by a permanent magnet and the sinusoidal alternating current in the exciting coil. Damping was measured as the logarithmic decrement δ of the free decay of the vibrating beam. The signal amplitude is proportional to the strain amplitude ϵ . Experimental details are described by Buchhagen et al. [27]. The reversible stress relaxation measurements were performed with an electronic balance that enables a defined strain to be applied to the bending beam by lifting or lowering the balance arm. The time dependent change of the stress in the beam is proportional to the change of the weight read out by computer. A more detailed description of the experiment including some correcting and averaging mathematical operations is given in [28]. The bending beams were heated in a resistance furnace for 15mins at various top temperatures and quenched in water. The damping measurements were performed at RT and afterwards the reversible stress relaxation at 31°C.

Specimens for the measurements of dilatation were machined as rods (50mm long and 5mm in diameter) with the reinforcement plane parallel to the main specimen axis. The specimen and a quartz piece of the same dimensions as the specimen were mounted into the specimen holder of the dilatometer. The thermal expansion of both was transmitted by quartz rods to the inductive displacement transducers outside the radiant furnace used for controlled heating and the elongation of the quartz rods eliminated by the differential measurement. A spring applies a force of 2N on the quartz rods to ensure good contact between the quartz rods and the specimens. The temperature was determined by the means of a PtRh10-Pt thermocouple mounted near to the MMC sample. Cooling of the specimens was realised by compressed air. A sawtooth time-temperature profile was applied with 15min intervals for heating and cooling respectively (Fig. 1). One quartz rod was used as a waveguide and the AE transducer was mounted on its surface by silicon grease. The computer controlled DAKEL AE facility consisting of a DAKEL-LMS-16 AE analyser and a high sensitive LB10A PZT transducer (85dB ref. 1V/ms⁻¹) with a flat response over a frequency range from 100 to 500dB and with built-in preamplifier 30dB was used to detect AE. This system operated with a two-threshold levels detection recommended by an ASTM standard [29]. The AE signal was filtered, amplified and then evaluated independently at two different threshold levels to get two AE

counts, N_{C1} and N_{C2} . The difference between the threshold levels was set at 20dB (corresponding total gains 105dB, 85dB, respectively) to discriminate high amplitude AE. Thus, the count N_{C1} corresponds to the lower threshold level and involves all AE counts detected (total AE count) whereas the count N_{C2} involves AE counts with higher amplitude only (burst AE count). No acoustic emission was observed during a check test with an unreinforced specimen. At all tests, another AE LB10A transducer placed on a steel piece close to the dilatometer equipment and a second, identically set up channel unit were used to monitor external disturbances, as net shoots, electromagnetic noise, external vibrations etc. Only very few such signals have been detected by this channel. The signals detected correspondingly in the measuring channel, if any, have not been taken into account.

RESULTS AND DISCUSSION

Fig. 9 shows the increase of AE counts with increasing fibre volume fraction V_f . Note also the increasing AE burst count indicating more frequent rapid release of large stress concentrations. Increasing matrix twinning as it was observed for thermally cycled cp-Mg in [6] may be proposed to explain this behaviour.

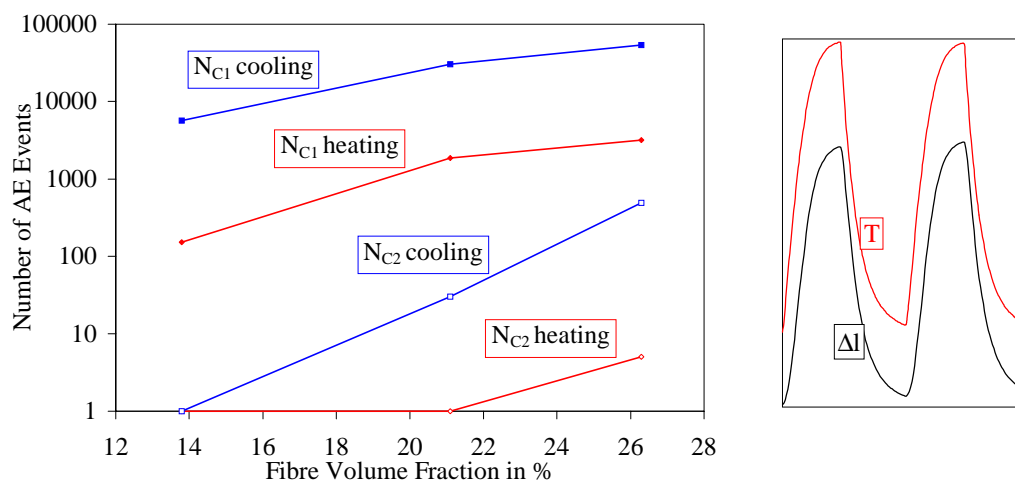


Fig. 9: Acoustic emission activity of thermally cycled δ - Al_2O_3 short fibre reinforced cp-Mg vs fibre volume fraction. AE counts were evaluated for the whole heating and cooling periods of the 2nd cycle between 35 and 300°C. The box on the right side shows the sawtooth profile of temperature and elongation

In the following the response of the δ - Al_2O_3 short fibre reinforced cp-Mg MMC on thermal cycling with step by step increased top cycle (20K/15min) temperature will be discussed. Thermal cycling with step by step increased T_{top} leads to increasing plastic deformation as shown in Fig. 4. Thus, a change in the structure and density of dislocations can be assumed and is reflected in the internal friction measurements (Fig. 2 and Fig. 3.). Fig. 2 shows the strain dependence of the logarithmic decrement δ measured at room temperature for cp-Mg composite thermally cycled with step by step increased T_{top} . It is seen that the strain dependencies of δ for all the top cycle temperatures investigated exhibit two regions. In the first region of lower strain amplitudes the logarithmic decrement is only weakly dependent on the maximum strain amplitude whereas in the second region of higher strains it depends

strongly on the strain amplitude. The critical strain at the transition from region one to two is shifted to lower values with increasing T_{top} . The value of the critical strain for Mg-26.2 vol.% Saffil[®] composites is higher than that for Mg-20vol.% Saffil[®] studied by Trojanová et al. [30]. The differences in the damping behaviour between specimens thermally cycled to various temperatures can be attributed to the interaction between dislocations and point defects including small clusters of foreign atoms and to changes in the dislocation density. The strong strain amplitude dependence of the logarithmic decrement (Fig. 2) suggests dislocations unpinning processes that can be explained using the Granato-Lücke theory [31]. According to this theory the dislocation segments are pinned by weak and strong pinning points and the strain amplitude dependent logarithmic decrement δ_H can be expressed by Eq. 1.

$$\delta_H = \frac{C_1}{\varepsilon} \exp(-C_2 \varepsilon) \quad \text{with} \quad C_1 = \frac{\rho L^3 F_B}{6 b l^2 M} \quad \text{and} \quad C_2 = \frac{F_B}{b l M} \quad (1)$$

where ρ is the dislocation density, L and l is the mean distance between strong and weak pinning points, respectively, b is the magnitude of the Burgers vector of dislocation, F_B is the binding force between weak pinning points and a dislocation and M is the unrelaxed modulus. The values of C_1 and C_2 are presented in Tab. 1. The value of C_2 is decreasing with increasing T_{top} . The decrease in C_2 for the top temperatures below about 160°C is stronger than that above 160°C. The values of C_1 exhibit no monotonic variation with temperature.

Table 1: Amplitude independent damping δ_0 and the Granato-Lücke constants C_1 and C_2 calculated for the curves presented in Fig. 2.

$T_{top}/^{\circ}\text{C}$	20	60	100	120	160	200	240	280
$\delta_0 \cdot 10^3$	2.57	2.24	2.45	2.88	3.09	2.95	4.45	4.69
$C_1 \cdot 10^4$	3.98	1.57	1.73	3.25	1.26	1.96	1.43	1.62
$C_2 \cdot 10^3$	1.93	1.41	1.10	1.19	0.72	0.74	0.55	0.49

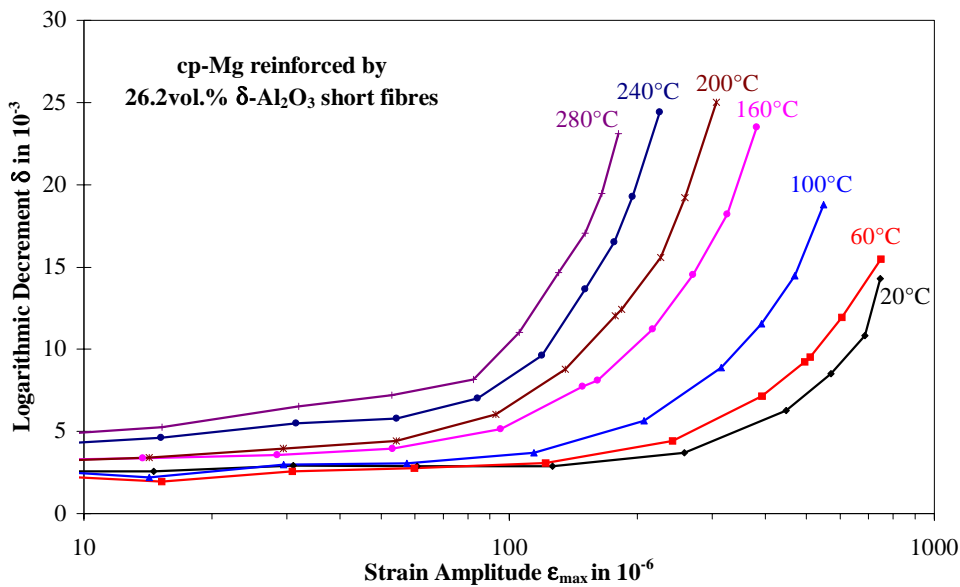


Fig. 2: Logarithmic decrement vs strain amplitude of thermally cycled $\delta\text{-Al}_2\text{O}_3$ short fibre reinforced cp-Mg with step by step increased top cycle temperature (20K/15min). Damping measurements were performed at RT after thermal cycling up to T_{top} as noted at the curves.

The stress relaxation measurements for the monolithic cp-Mg and the composite show a monotonic increase of the reversible stress relaxation ($\Delta\sigma/\sigma = \Delta E/E = \text{modulus defect}$) with time indicating a dislocation mechanism. Fig. 3 shows the modulus defect after 3600s versus T_{top} for reinforced and unreinforced cp-Mg. The values of the modulus defect for the cp-Mg samples are much higher than those for alloys measured by Kiehn et al. [22] indicating the strong influence of foreign atoms in solid solution on the modulus defect. The curve for the monolithic cp-Mg in Fig. 3 may be explained by fluctuations in the concentration of foreign atoms in solid solution. The curve for the cp-Mg MMC is more even because of the strong influence of the dislocation generation due to ΔCTE . The decrease from 160°C with its minimum at 200°C may refer to changes in the deformation mechanism of the composite during thermal cycling as also indicated by the variation of N_{C2} with T_{top} .

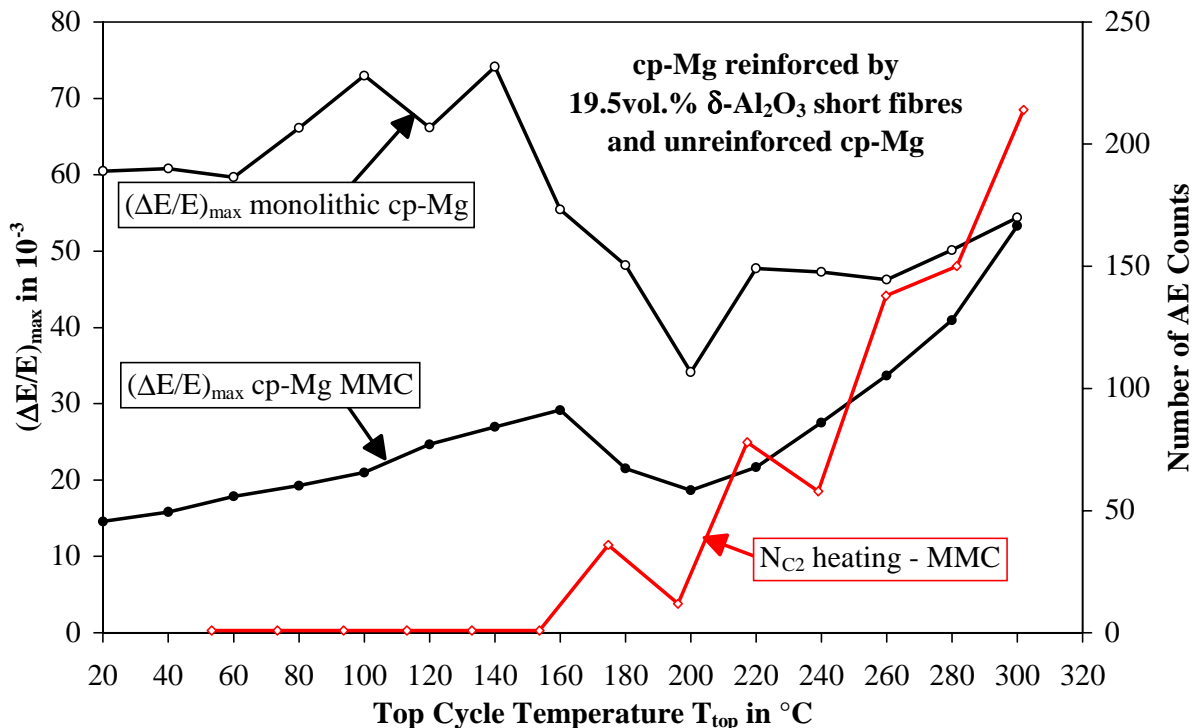


Fig. 3: Reversible stress relaxation $\Delta E/E$ after 3600s of reinforced and unreinforced cp-Mg vs top cycle temperature of thermal cycling (one cycle each T_{top}). The modulus defect of the cycled specimens was measured directly after the damping experiments (Fig. 2). For comparison the burst count of the thermally cycled composite from Fig. 4 is presented.

The dimensional changes during thermal cycling and the acoustic emission activity are compared in Fig. 4. The total number of AE counts (N_{C1}) increases with increasing T_{top} as well as the residual elongation. For top cycle temperatures higher than 160°C a significant number of high amplitude AE counts (N_{C2}) is registered. This coincides with the change of the Granato-Lücke constant C_2 (Tab. 1) and the modulus defect of the composite (Fig. 3) with T_{top} at about 160-170°C and might be attributed to deformation by twinning. It is worthwhile to note that the count values measured during heating and cooling period of one cycle do not differ very much up to $T_{\text{top}} = 200^\circ\text{C}$. For higher temperatures the number of AE counts during cooling is higher. Diffusional deformation processes and dislocation annihilation may take

place in the high temperature stage of the heating interval while during the cooling interval dislocation glide may dominate.

The effect of thermal cycling with T_{top} varied from 200°C to 400°C (5 cycles at each temperature) on the dimensional stability and acoustic emission is shown in Fig. 5. A comparison with Fig. 4 shows that the AE activity may be dependent on the starting top cycle temperature or the crystallographic orientation of the grains in respect to the fibres which was not checked. The total number of the AE counts and even more the number of burst emissions are reduced by starting the experiment at $T_{top}=200^\circ\text{C}$. As mentioned above the AE effects are more pronounced for the cooling interval of a cycle at higher top cycle temperatures. The figure can be subdivided in three characteristic temperature regions. The first region up to $T_{top}=280^\circ\text{C}$ is characterised by a monotonic growth of the residual expansion and a slight increase of the AE activity. The residual expansion shows an intermediate behaviour up to $T_{top}=340^\circ\text{C}$. A shortening of the specimen in the first cycle of a temperature step is followed by specimen growth along the main specimen axis in the following cycles. In this second region the AE activity is increased about two orders of magnitude in comparison to the first region and remains approximately constant. Thermal cycling with $T_{top}\geq 340^\circ\text{C}$ results in shortening of the specimens due to dominating compressive internal stresses. This effect was also observed in reinforced Mg alloys. Specimens with the reinforcement plane perpendicular to the main specimen axis show the complementary behaviour: shortening in the first region and elongation in the third region [21]. The AE activity grows with ongoing shortening of the specimen. Almost no AE bursts have been observed during the whole experiment.

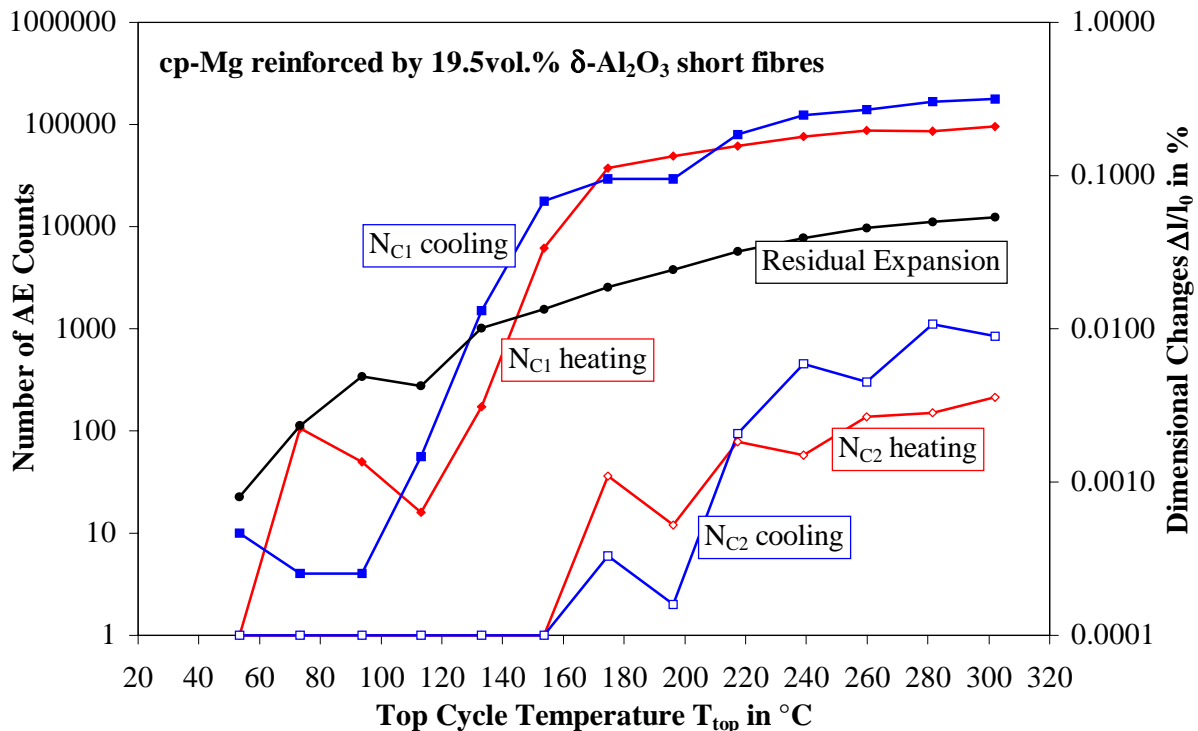


Fig. 4: Comparison of acoustic emission activity and dimensional changes vs top cycle temperature during thermal cycling. AE counts were evaluated for the whole heating and cooling periods of the cycles between 33°C and T_{top} .

The most important feature of thermal cycling is the generation of dislocations and the stress relaxation by dislocation motion. Their movement is determined by the required stress in dependence of the temperature, the distribution of pinning points (i.e. l and L), the internal

stresses and the crystallographic orientation of the grains in respect to the fibres. According to Arsenault and Shi [11] the dislocation density ρ may be calculated as

$$\rho = \frac{B\Delta CTE\Delta T V_f}{bt(1 - V_f)} \quad (2)$$

where B is a geometric constant (between 4 and 12 depending on the reinforcement shape), ΔT is the temperature difference of the cycle and t is the smallest dimension of the reinforcement. The analysis of the damping measurements (Tab. 1) shows that the dislocation density ρ and the distance between the weak pinning points l increases up to $T_{top}=280^\circ\text{C}$. This agrees well with damping measurements [24] with T_{top} varied between 100°C and 450°C that indicate a minimum value for the Granato-Lücke constant C_2 between $T_{top}=300^\circ\text{C}$ and 400°C . Electrical resistivity measurements revealed only slight changes in the distribution of foreign atoms during thermal cycling up to $T_{top}=300^\circ\text{C}$ [32]. The approximately constant concentration of weak pinning points and the increase in dislocation density leads to an increase in l which means that the dislocations can break away from pinning points under lower stresses and the critical strain decreases (Fig. 2). The yield stress of the matrix decreases with increasing temperature, too. The stress necessary for the dislocation breakaway decreases with increasing temperature and, hence, thermal cycling may make easy the breakaway of dislocations. Thus, the dislocations can move and internal plastic flow occurs accompanied by AE (Fig. 4 and 5).

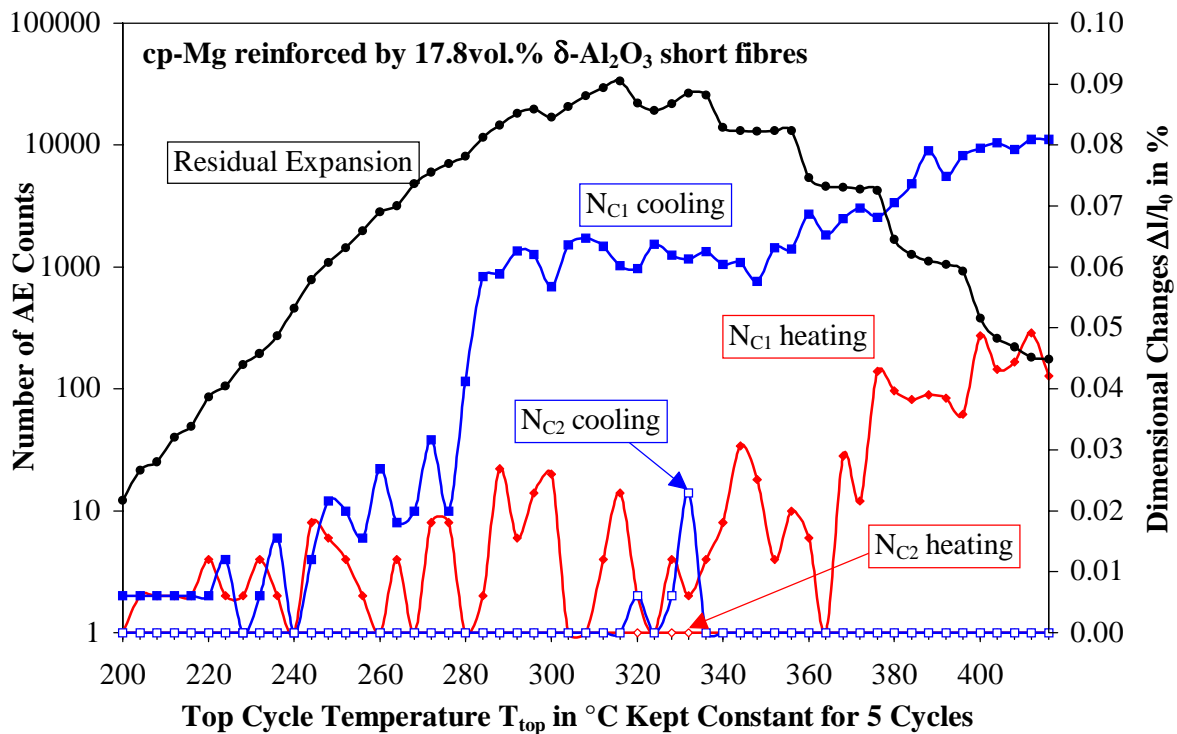


Fig. 5: Comparison of acoustic emission activity and dimensional changes vs top cycle temperature during thermal cycling. AE counts were evaluated for the whole heating and cooling periods of the cycles between 37°C and T_{top} .

The increase of AE activity with the fibre volume fraction V_f (Fig. 1) can be explained as a result of the dislocation generation during thermal cycling (Eq. 2). The variation of AE total count with increasing T_{top} can be explained if we consider that the thermal stresses and the dislocation density grow with increasing T_{top} assuming that Eq. 2 is valid up to $T_{top}=300^\circ\text{C}$. To explain the thermal cycling behaviour between $T_{top}=280^\circ\text{C}$ and 340°C (Fig. 5) a dynamic equilibrium of dislocation generation and annihilation may be proposed, leading to a constant value of ρ and significant AE. The change in the sign of the internal stresses from tension to compression in the main specimen axis for $T_{top}\geq 340^\circ\text{C}$ (Fig. 5) as well as the increased top cycle temperatures itself may lead to accelerated dislocation annihilation resulting in a decrease of the dislocation density and thereby more effective AE generation at lower temperatures. Additionally the change in the stress state could make twinning more favourable.

CONCLUSIONS

The influence of thermal cycling on the microstructure, especially on the dislocation generation and movement, can be characterised by non-destructive methods such as measurements of the internal friction, acoustic emission activity and residual elongation. The AE activity is proportional to the fibre volume fraction. Up to $T_{top}=300^\circ\text{C}$ the damping increases with increasing T_{top} and the critical strain decreases. Thermal cycling experiments with step by step increased top cycle temperature reveal several threshold values where the dislocation related behaviour changes.

ACKNOWLEDGEMENT

This work was supported by the Deutsche Forschungsgemeinschaft. The authors acknowledge also support of this work by the Grant Agency of the Czech Republic under grant 106/96/0208, the Grant Agency of the Academy of Sciences under grant A2041607 and the Grant Agency of the Charles University under grant GAUK147/96. The experiments were carried out at the Department of Materials Engineering and Technology of the Technical University of Clausthal. One of the authors (PL) is most grateful to Alexander von Humboldt Foundation for financial support during his stay in Clausthal.

REFERENCES

1. Oakley, R., Cochrane, R.F. and Stevens, R., "Recent Developments in Magnesium Matrix Composites", *Key Eng. Mater.*, Vols 104-107, 1995, pp. 387-416.
2. Kainer, K.U., "Cast Magnesium Alloys Reinforced by Short Fibres", *Magnesium Alloys and Their Applications* ed. by Mordike, B.L. and Hehmann, F., DGM Informationsgesellschaft, Oberursel, 1992, pp. 415-422.
3. Roos, U., Kainer, K.U. and Mordike, B.L., "Influence of Particle Shape on the Mechanical Properties of P/M produced QE22/SiCp-Composites with Various Particle Volume Fraction", *Proc. of the Powder Metallurgy World Congress PM'94*, Société Française de Métallurgie et de Matériaux, Paris, France, Vol. 3, 1994, pp. 2249-2252.

4. Kainer, K.U. and Böhm, E., "Optimizing of Properties of Magnesium Alloys by Squeeze Casting", *Proc. of 29th Int. Symp. on Automotive Technology and Automation*, Automotive Automation Ltd., Croydon, GB, 1996, Roller, D., Ed., pp. 653-660.
5. Kainer, K.U., "Influence of Heat Treatment on the Properties of Short-Fibre-Reinforced Magnesium Composites", *Mater. Sci. Eng.*, Vol. A135, 1991, pp. 243-246.
6. Köhler, C. and Kainer, K.U., "Thermal Stability of Mg-Alumina Composites", *Proc. of Advanced Composites'93*, ed. by Chandra, T. and Dhingra, A.K., The Minerals, Metals & Materials Society, Warrendale, 1993, pp. 1243-1249.
7. Arsenault, R.J. and Fisher, R.M., "Microstructure of Fibre and Particulate SiC in 6061 Al Composites", *Scripta Metall.*, Vol. 17, 1983, pp. 67-71.
8. Chawla, K.K. and Metzger, M., "Initial Dislocations Distributions in Tungsten Fibre-Copper Composites", *J. Mater. Sci.*, Vol. 7, 1972, pp. 34-39.
9. Arsenault, R.J., in *Metal Matrix Composites: Mechanisms and Properties* ed. by Everett, R.K. and Arsenault, R.J., Academic Press, San Diego, 1991, p. 79.
10. Taya, M. and Arsenault, R.J., *Metal Matrix Composites*. Pergamon Press, Oxford, 1989.
11. Arsenault, R.J. and Shi, N., "Dislocation Generation due to Differences Between the Coefficients of Thermal Expansion", *Mater. Sci. Eng.*, Vol. A81, 1986, pp. 175-187.
12. Vogelsang, M., Arsenault, R.J. and Fisher, R.M., "An In Situ HVEM Study of Dislocation Generation at Al/SiC Interfaces in Metal Matrix Composites", *Met. Trans.*, Vol. 17A, 1986, pp. 379-389.
13. Lukác, P., Chmelík, F., Roos, U., Kainer, K.U. and Mordike, B.L., "Acoustic Emission During Thermal Cycling of a Mg based Metal Matrix Composite", *Proc. of 2nd Int. Symp. of Advanced Materials and Technologies - Innovation'95*, December 5-7, 1995, Prague, Czech Republic, pp. 280-282.
14. Suresh, S., Mortensen, A. and Needleman, A., *Fundamentals of Metal-Matrix Composites*. Butterworth-Heinemann, Stoneham, 1993.
15. Clyne, T.W. and Withers, P., *An Introduction to Metal Matrix Composites*. Cambridge University Press, Cambridge, 1993.
16. Ochiai, S., *Mechanical Properties of Metallic Composites*. Marcel Dekker, New York, 1994.
17. Chen, Y.-C., Daehn, G.S. and Wagoner, R.H., "The Potential for Forming MMC Components via Thermal Cycling", *Scripta metall. mater.*, Vol. 24, 1990, pp. 2157-2162.
18. Pickard, S.M. and Derby, B., "The Deformation of Particle Reinforced Metal Matrix Composites During Temperature Cycling", *Acta metall. mater.*, Vol. 38, 1990, pp. 2537-2552.

19. Köhler, C., "Thermische Beständigkeit von Kurzfaserverstärkten Magnesium-Al₂O₃-Verbundwerkstoffen", PhD Thesis, Technical University of Clausthal, Clausthal-Zellerfeld, Germany, 1994.
20. Köhler, C., Kiehn, J. and Kainer, K.U., "Structure and Stability of Cast Short Fibre Reinforced Mg Alloys", *Proc. of Cast Composites'95*, Polish Foundrymen's Technical Associations, 1995, pp. 13-16.
21. Kiehn, J., Eilers, M., Kainer, K.U., "Formänderung von kurzfaserverstärkten Magnesiummatrix-Verbundwerkstoffen infolge thermischer Wechselbelastung", *Proc. of Werkstoffwoche'96*, Stuttgart, Germany, May 28-31, 1996, Vol. 6, Deutsche Keramische Gesellschaft, Köln, in press.
22. Kiehn, J., Köhler, C. and Kainer, K.U., "Stress Relaxation Behaviour of Thermally Cycled Short Fibre Reinforced Mg Alloys", *Proc. Tenth Int. Conf. on Composite Materials ICCM-10*, Whistler, British Columbia, Canada, August 14-18, 1995, Vol. II: Metal Matrix Composites, Poursartip, A. and Street, K.N., Eds, pp. 661-668.
23. Kiehn, J., Riehemann, W. and Kainer, K.U., "Stress Relaxation of Short Fiber Reinforced Mg Metal Matrix Composites after Thermal Cycling", *Mater. Sci. Forum*, Vols 210-213, 1996, pp. 503-510.
24. Kiehn, J., Trojanová, Z., Lukác, P. and Kainer, K.U., "Effect of Thermal Cycling on the Damping Behaviour of Mg Matrix Composites", *Key Eng. Mater.*, Vols 127-131, 1997, pp. 993-1000.
25. Riehemann, W., "Detection of Internal Stresses in Metal Matrix Composites by Stress Relaxation Measurements", *Mater. Sci. Forum*, Vols 210-213, 1996, pp. 511-518.
26. Trojanová, Z., Pahutová, M., Kiehn, J., Lukác, P. and Kainer, K.U., "Dislocation Generation in Mg Matrix Composites due to Thermal Cycling", *Key Eng. Mater.*, Vols 127-131, 1997, pp. 1001-1008.
27. Buchhagen, P., Riehemann, W. and Mordike, B.L., "Reversible Stress Relaxation of Saffil Fibre Reinforced AZ91", *Magnesium Alloys and Their Applications* ed. by Mordike, B.L. and Heilmann, F., DGM Informationsgesellschaft, Oberursel, 1992, pp. 455-460.
28. Riehemann, W., Fleischer, P. and Martens, V. "Measurement of Stress Relaxation Strength in Engineering Materials for High Precision Applications", *J. Alloys and Compounds*, Vols 211/212, 1994, pp.596-599.
29. ASTM Standard Practice for Acoustic Emission Examination of Fiberglass Reinforced Plastic Resin (FRP) Tank/Vessels, May 31 1985.
30. Trojanová, Z., Lukác, P., Riehemann, W. and Mordike, B.L., "Damping in Magnesium Matrix Composites", *Mater. Sci. Forum*, Vols 210-213, 1996, pp. 519-626.
31. Granato, A. and Lücker, K., "Theory of Mechanical Damping Due to Dislocations", *J. Appl. Phys.*, Vol. 27, 1956, pp. 583-593.

32. Vostrý, P, Stulíková, I., Kiehn, J., Samatová, M., Kainer, K.U. and Knoop, F.M., "Electrical Resistometry of Mg-Based Microcrystalline Alloys and Mg-Based Composites", *Mater. Sci. Forum*, Vols 210-213, 1996, pp. 635-642.

PROCESS AND TRIBOLOGICAL BEHAVIOR OF 6061 AL/GR._(P) COMPOSITES

R. J. Chang and C. B. Lin

*Department of Mechanical Engineering, Tamkang University, Taipei,
Taiwan 25137, R. O. C*

SUMMARY: The present study, the composite of 6061 Al alloy castings which contained graphite particles which are $6\mu\text{m}$ of an average particle size with 2,4,6 wt% has been produced successfully by ourselves. The wettability between the graphite particles and the 6061 Al alloy matrix is improved by coated copper on the graphite particles. The composites which have cast with the smaller graphite particles are so superior than the composites which have cast with the larger graphite particles in tensile property. The fractograph of 6061 Al alloy is a shear cleavage style, the fractograph of composites becomes the cup and cone without obvious necking. The weight loss decreases with the increasing of graphite particle contents and wear speed. The worn surfaces coarse grooves morphology, however, the number of coarse grooves of 6061 Al alloy is more than 6061 Al alloy-graphite particles composites after wear test. Moreover, the bands between the coarse grooves have been found. The band width of 6061 Al alloy-graphite particles composite is wider than 6061 Al alloy.

KEYWORDS: composites, yield stress, tensile stress, hardness, graphite particles, tribology, coated copper, cementation process fractograph, wear rate, seizure,

INTRODUCTION

About 40 % of the power loss in engine system is attributed to the adverse effects of friction in reciprocating engine components[1]. In order to improve the efficient of engine and enable fuel economics to be gained in transport engineering application, the fabrication of the engine system will be through weight and wear rate reduction and lubricating condition addition between the contact objects[2,3]. Aluminium alloys provide designers and engineers with a group of materials with valuable properties which include: excellent corrosion resistance; high specific strength; high electrical and thermal conductivities[2,4], however, it also has a weakness in wear resistance[2]. During the past 15 years, the researchers who were Rohatgi et al.[2,5,6] had worked on the development in aluminium alloy-graphite particles composites. Under optimum conditions, the aluminium-graphite composite becomes self-lubricating because of the transfer of the graphite particles embedded into the tribosurfaces and its formation into a thin film which prevents direct contact between the worn surfaces. The coefficient of friction; contact temperature rise and wear rate could be reduced .

According to the investigative reports[5-17] of tribology in aluminium alloy-graphite particles composites by Rohatgi et al., the tribological behaviors would be affected by some parameters

which include: the shape and containing of graphite particles, the bonding strength between the graphite particles and aluminium alloy, the processes of fabrication and the sliding wear conditions. According to Gibson et al.[2,5], a reduction in efficient of friction, wear rate and contact temperature rise, due to add the graphite particles at low addition levels about 2wt%. However, at high addition levels as 8wt%, the mechanical properties have been reduced significantly. The coefficient of friction in composites containing granular graphite is lower than composites which contain flake graphite as reported by Liu et al.[16]. Prasad et al. have studied that if the bonding between particle and matrix is poor, the interface as equivalent to preexisting cracks. According to Rohatgi et al.[18,19], graphite particles can be coated Cu or Ni which increased the wettability and decreased the porosity between the graphite and matrix in composites. Prasad et al[7]. has reported that composites have been manufactured by powder metallurgy process, however, it has reverse effect in tribological properties. This anomalous behavior was attributed to increased porosity in the composites. Gibson et al. has manufactured the composites which were added suitable amounts of graphite particles by compocasting process[2], due to the dry sliding wear test, found to possess superior dry wear properties over the matrix alloy. The cluster of graphite particles was investing by Prasad[7] who concluded that crack nucleation due to cluster by graphite particles, such that could be reveal tribological behavior. The applied pressure could be increased without seizure when the 6061 Al alloy added graphite particles as reported by Prasad et al.[6]. As the sliding velocity increases, the wear rate was decreased by Rohatgi et al.[20] The wear rate was increased as increasing sliding distances as reported by Gibson et al.[2] In fully or partially lubricated conditions of 6061 Al alloy matrix with SAE30 oil on a pin-on-disc wear test apparatus, the wear speed and the applied pressure range could be increased without seizure. However, the P-V limits of the aluminium-graphite particles composites are higher than the aluminium alloy matrix by Das et al.[6]

In this paper, the process of 6061 Al alloy castings contain graphite particles which are $6\ \mu\text{m}$ of an average particle size with 2,4,6 wt% have been investigated. Moreover, we also explore the effect of 6061Al alloy add $6\ \mu\text{m}$ graphite particles in tensile stress, hardness and tribological properties.

EXPERIMENTAL DETAILS

Materials Preparation

The chemical composites of the 6061 aluminium alloy are 0.532%Si-0.833%Mg-0.035%Mn-0.207%Cu-0.149%Fe-0.0165%Ti-0.103%Cr. The lubricant phases used in this work are a graphite particle with a mean size of $6\ \mu\text{m}$. Composites containing up to 6wt% graphite particles were prepared by a prior technique, which involved the steps of mixing and degassing, where the graphite particles were coated copper by cementation process prior to add 6061 molten alloy, the coated copper procedure shows as Fig.1 and has been reported elsewhere[19] . Specimens for the hardness, tensile and wear tests were cut and machinery from these composites and T6 treatment ($532\ ^\circ\text{C}$ 2hr, $160\ ^\circ\text{C}$ 18hr).

Mechanical Test

The hardness tests were performed by using B-Scale Rocker's hardness apparatus (load time fully plastic deformation is 47 sec); tensile tests were performed by using Instron tensile apparatus with 5mm/min cross head speed.

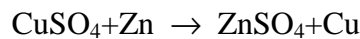
Wear Test

The wear test, which were of the pin-on-disc type. Before the wear tests, each specimen was ground up to grade 1200 abrasive paper, making sure that the wear surface completely contacted the surface of the disc (HRC 62 ± 2). Wear tests were carried out under dry conditions by sliding the specimen under applied constant load up to 29.4N and constant sliding velocity up to 0.8m/sec. The weight losses were calculated from the difference in weight of the specimens measured before and after the test to the nearest 0.1mg using an analytical balance. For all tests were performed at room temperature (27°C, relative humidity 75%), for each test data, at least six runs were performed. Microstructural observations were carried out using an optical microscope (OM) on the graphite particles distributed in the 6061 Al matrix.

RESULT AND DISCUSSION

Coated Copper by Cementation Process

Fig.1 shows the flow chart of graphite particles be coated copper. According to the paper [19,21], copper can be displaced from the copperbearing salts by Zn by the following cementation process.



The displaced copper from CuSO_4 in the nascent form has a positive charge for a period and the surface of suspended graphite particles in the solution is likely to have a negative charge as reported by [22]. Fig.2 shows the coated copper on the surface of graphite particles. According to Fig.2(b) and (c) of EDS and Mapping analysis respectively, the copper elements have been detected on the surface of graphite particles uniformly. According to the Fig.2, the surface of graphite particles was covered with uniform copper.

Dispersion of Copper Coated Graphite Particles in 6061 Al Alloy

Fig.3 shows the microstructures of the 6061 Al alloy and the composites with 2,4,6 wt% graphite particles. Fig.4 shows the magnification from Fig.3(d) by SEM. According to the Fig.4, 6 μm graphite particles have been added in the aluminium alloy. Moreover, the graphite particles have been dispersed in the aluminium alloy uniformly as shown in Fig.3. Consequently, according to the Fig.3 and 4, we have produced the composites of 6061 Al alloy-6 μm graphite particles composites successfully by our processing equipment and casting condition which were designed by ourselves in this experiment. However, we can't produce the composites which add 6 μm graphite particles without any coated copper in our processing route and the same casting condition. This is attributed to the graphite particles can't be wet with the aluminium molten and the density of graphite particle is less than the

aluminium molten, so that the graphite particles were floating up to the molten and can't uniform mixture with the aluminium molten.

Tensile Properties

The variations in mechanical properties with 6061 Al alloy and 6061Al/2,4,6 wt% graphite particles composites are shown in Table 1. The ultimate tensile stress and yield stress decreases with the increases in graphite particles contents were expected. For example, the ultimate tensile stress of the 6061 Al alloy is 26.3 kg/mm^2 and the composite which contains $6 \mu\text{m}$ and 2 wt% graphite particles is 22.4 kg/mm^2 . There is a 14.8% reduction in ultimate tensile stress. According to the paper[23], the Al-12wt%Si with $40 \mu\text{m}$ and 2wt% graphite particles composites, the tensile stress reduces from 207 MPa in the matrix to 164 MPa. There is a 20.7% reduction in tensile stress. This is attributed to the cracks of the larger graphite particles have been nucleated and created the stress concentration that could be reduced the fracture toughness easier than the smaller graphite particles. Moreover, the graphite particles are soft structure. Consequently, the composites which have cast with the smaller graphite particles are so superior than the composites which have cast with the larger graphite particles in tensile property. Moreover, the elongation and hardness of the composites have no obvious decrease with increase the graphite particles as shown in Table 1. Otherwise, the fractograph of tensile test specimens, the shear cleavage of the matrix alloy, the fractograph of composites were become cup and cone style but has no obvious necking with increased the graphite particles. This is attributed to the crack nucleation, propagation and linking up between the interface of graphite particles and Al alloy.

Tribological Behavior

Fig.5 shows that the weight loss versus graphite particles contents of 6061 Al alloy- $6 \mu\text{m}$ graphite particles composites. The weight loss has obvious decrease with increasing the graphite particle contents. This is attributed to the high level addition of graphite particles can form the lubricating film to prevent the direct contact wear in the short time compared with the low addition in the same wear condition. Fig.6 shows that microstructures of worn surface. Fig.6(a) and (b) show the worn surface morphology of 6061 Al alloy and 6061 Al alloy-6wt% graphite particles composites before wear test respectively. According to the Fig.6(a) and (b), the surfaces are rough and with fine grooves. This is attributed to the each specimen who has been polished by grade 1200 abrasive paper, making sure that the wear surface completely contacted the surface of the disc. Fig.6(c) and (d) show the worn surface morphology of 6061 Al alloy and 6061 Al alloy-6wt% graphite particles composites after wear test. According to Fig.6(c) and (d), the surfaces reveal coarse grooves, however, the number of coarse grooves of 6061 Al alloy is more than 6061 Al alloy-6wt% graphite particles composites after wear test. Moreover, the bands between the coarse grooves have been found. The band width of 6061 Al alloy-6wt% graphite particles composite is wider than 6061 Al alloy matrix as shown in Fig.6(c) and (d). This is attributed to the mating surface of 6061 Al alloy has no lubricants, so that the seizure was happened seriously on the mating surface as shown in Fig.6(c). Moreover, the 6061 Al alloy-graphite particles composites becomes self-lubricating because of the transfer of the graphite particles embedded in its matrix to the tribosurfaces and its formation into a thin film which prevents direct contact and seizure between the mating surface. Fig.7 shows that wear weight loss versus wear speed. It shows that the weight loss decreases with increasing the wear speed and graphite particle content, especially in wear speed of 0.8m/s and graphite content of 6wt %, the wear loss

amounts of composites were less than others. Moreover, in the same graphite particle content and wear condition, the weight loss decreases with increasing the wear speed.

CONCLUSION

In this paper, the composite of 6061 Al alloy castings which contained graphite particles which are $6\ \mu\text{m}$ of an average particle size with 2,4,6 wt% has been produced successfully by ourselves. The wettability between the graphite particles and the 6061 Al alloy matrix is improved by coated copper by cementation process on the surface of graphite particles. Moreover, the graphite particles dispersed in the 6061 Al alloy matrix uniformly from the observation of the microstructure. In this paper, we also explore the effect of 6061 Al alloy add $6\ \mu\text{m}$ graphite particles in tensile stress, hardness and tribological properties as detailed below:

1. The elongation and hardness have no obvious reduction with increasing graphite particle contents.
2. The composites which have cast with the smaller graphite particles are so superior than the composites which have cast with the larger graphite particles in tensile property.
3. The fractograph of 6061 Al alloy is a shear cleavage style, when 6061 Al alloy adding the graphite particles the fractograph become the cup and cone with no obvious necking.
4. The weight loss decreases with increasing of graphite particles contents and wear speed.
5. The worn surfaces reveal coarse grooves morphology, the number of coarse grooves of 6061 Al alloy are more than 6061 Al alloy-graphite particles composites after wear test. Moreover, the bands between the coarse grooves have been found. The band width of 6061 Al alloy-graphite particles composite is wider than 6061 Al alloy.

REFERENCE

1. K. Funatani and K. Kurosawa, *Advanced Materials and Processes*, Vol.146, No.6 (1994) pp.27-29
2. P. R. Gibson, A.J. Clegg and A. A. Das, *Materials Science and Technology*, Vol.1 (1985) pp.559-567
3. M. Fujine, T. Kaneko and J. Okijima, *Advanced Materials and Processes*, Vol.143 No.3 (1993) pp.20
4. D. Huda, M. A. EI Bradie and M. S. J. Hashmi, *Journal of Materials Processing Technology*, Vol.37 (1993) pp.529-541
5. P. R. Gibson, A. J. Clegg and A. A. Das, *Wear*, Vol.95 (1984) pp.193-198.
6. S. Das, S. V. Prasad and T. R. Ramachandran, *Wear*, Vol.133 (1989) pp.173-187
7. A.K. Jha, S. V. Prasad and G. S. Upadhyaya, *Wear*, Vol.133 (1989) pp.163-172
8. S. K. Biswas and B. N. Pramila Bai, *Wear*, Vol.68 (1981) pp.347-358

9. B. P. Krishnan, N. Raman, K. Narayanaswamy and P. K. Rohatgi, *Wear*, Vol.60 (1980) pp.205-215
10. B. P. Krishnan, N. Raman, K. Narayanaswamy and P. K. Rohatgi, *Tribology International*, Vol.16, No.5 (1983) pp.239-244
11. P. K. Rohatgi and B. C. Pai, *Transactions of the ASME*, Vol.101 (1979) pp.376-380
12. P. K. Rohatgi and B. C. Pai, *Wear*, Vol.59 (1980) pp.323-332
13. S. Biswas and P. K. Rohatgi, *Tribology International*, Vol.16No.2 (1983) pp.89-102
14. P. K. Rohatgi, Y. Liu, M. Yin and T. L. Barr, *Materials Science and Engineering*, Vol.A123 (1990) pp.213-218
15. P. K. Rohatgi, Y. Liu and T. L. Barry, *Metallurgical Transactions A*, Vol.22A (1991) pp.1435-1441
16. Y. Liu, P. K. Rohatgi and S. Ray, *Metallurgical Transactions A*, Vol.24A (1993)pp.151159
17. P. K. Rohatgi and S. V. Prasad, *Journal of Metals*, Nov. (1987) pp.22-26
18. M. Suwa, K. Komuro and S. Iijima, *Casting*, Vol.61, No.3 (1989) pp.139-147
19. B. C. Pai and P. K. Rohatgi, *Materials Science and Engineering*, Vol.21 (1975) pp.161-167
20. P. K. Rohatgi, S. Ray and Y. Lin, *Internation Materials Reviews*, Vol.37, No.3 (1992) pp.129-149
21. P. H. Strickland and F. Lawson, *Proc. Australasian Inst. Mining Met.*, 237(1971) pp.71
22. F. I. Clauss, *Solid Lubricants and Self Lubricating Solids*, Academic Proess; New York, 1972, p67
23. B. P. Krishnan, M. K. Surappa and P. K. Rohatgi, *Journal of Materials Science*, Vol.16 (1981) pp.1209-1216

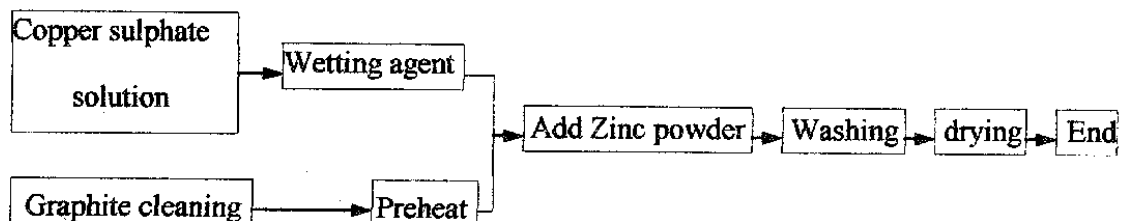
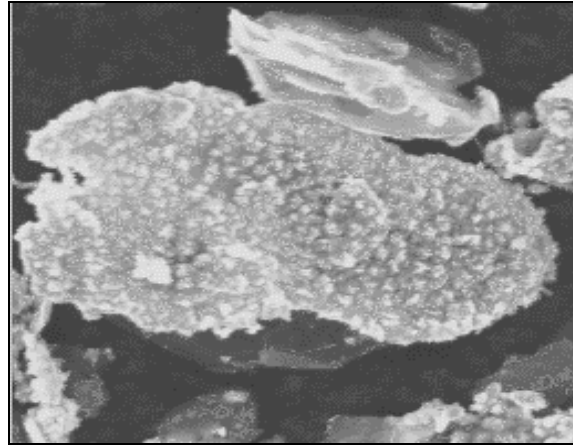
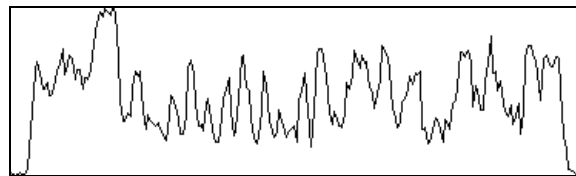


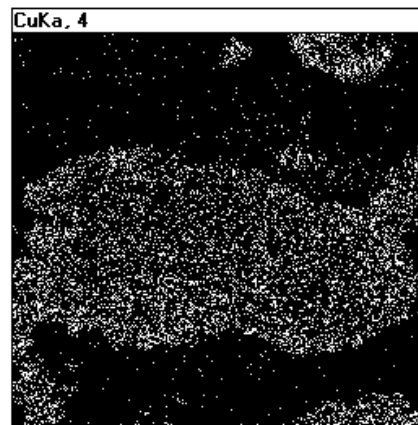
Fig.1: The flow chart of coated copper by cementation process on graphite particles



(a)



(b)



(c)

Fig.2: (a)Scanning electron micrographs (b)DES (c)Mapping analysis of coated copper on graphite particle surface

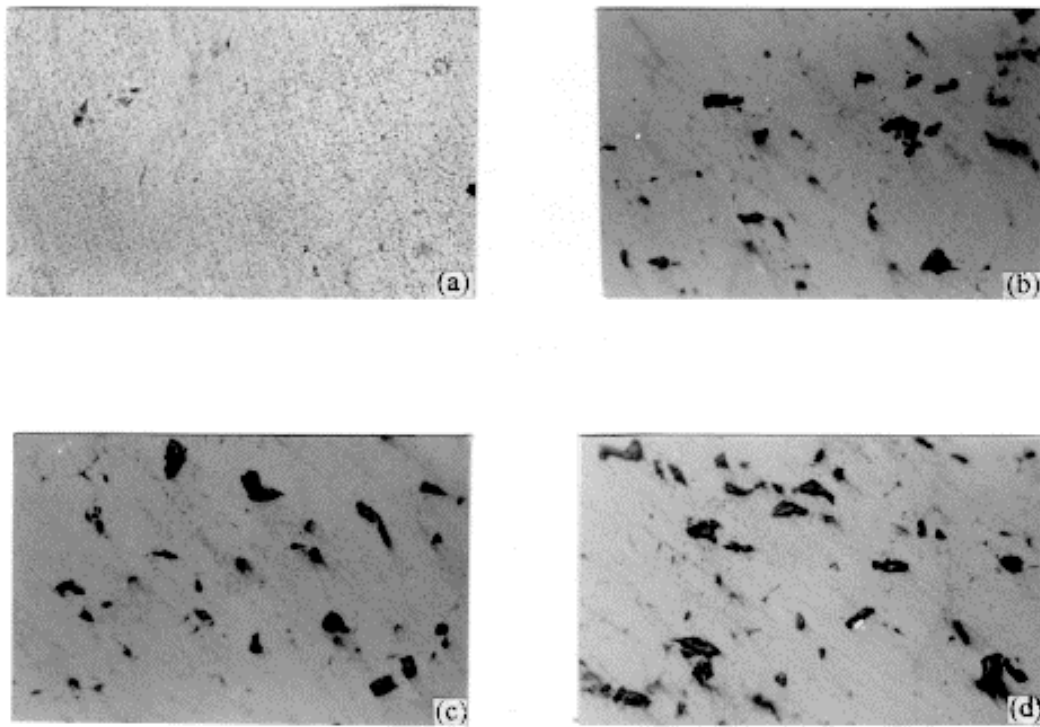


Fig.3: Optical micrographs of 6 μ m graphite particles dispersed in 6061 Al alloy matrix (a)0wt%(b)2wt%(c)4wt%(d)6wt% (Magnification, 500X)

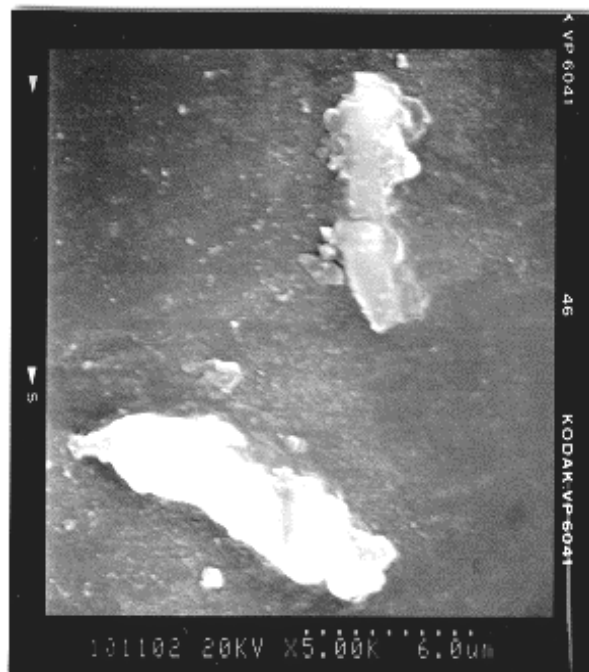


Fig. 4: Scanning electron micrograph of 6 μ m graphite particles dispersed in 6061 Al alloy (Magnification 5000X)

Table 1 Mechanical properties of 6061 Al alloy containing different percentage of 6 μ m graphite particles

property Gr. _(p) %	Yield stress (kg/mm ²)	Ultimate tensile stress (kg/mm ²)	Elongation %	Hardness HRB
0wt%	20.4	26.3	9.46	60
2wt%	22.3	22.4	4.62	62
4wt%	18.9	18.9	2.98	58
6wt%	13.0	13.0	3.33	52

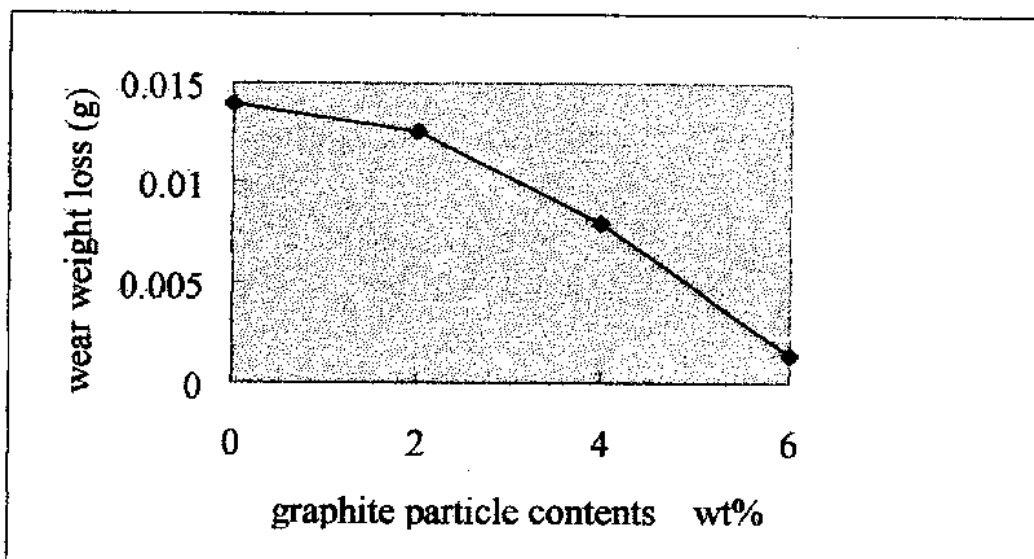


Fig.5: Wear weight loss of 6061 Al alloy- graphite particle composites as a function on graphite particle contents: sliding speed, 0.6m/s; sliding distance, 144m; applied pressure 0.69 MPa

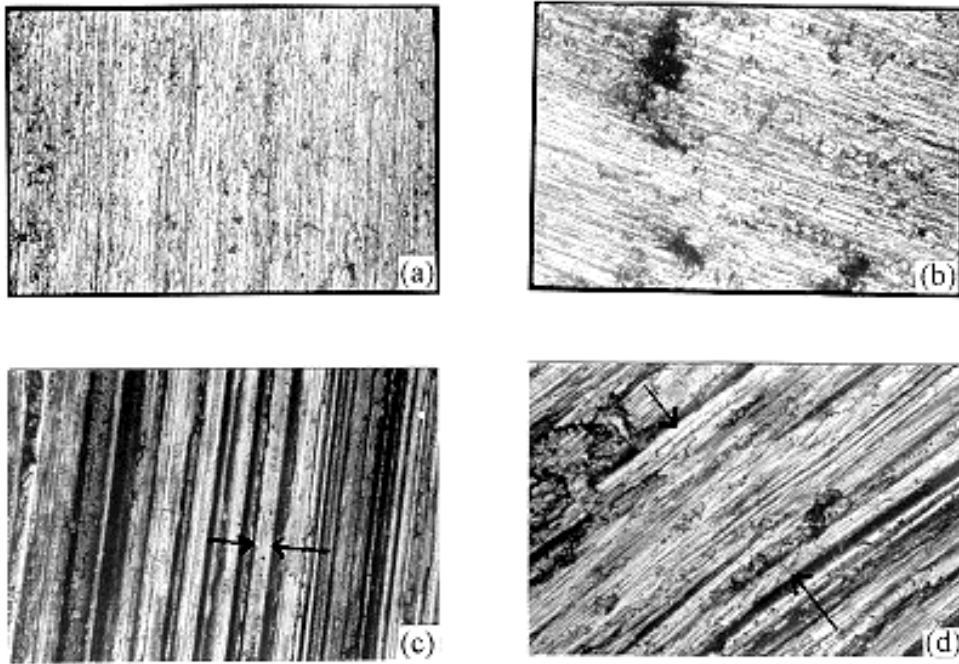


Fig.6: Optical micrographs of worn surface of (a)matrix alloy and (b)6 wt% composite before wear test, (c)matrix alloy and (d)6 wt% composite after wear test: sliding speed 0.6m/s; sliding distance 144m; applied pressure 0.69 MPa (Magnification, 200X)

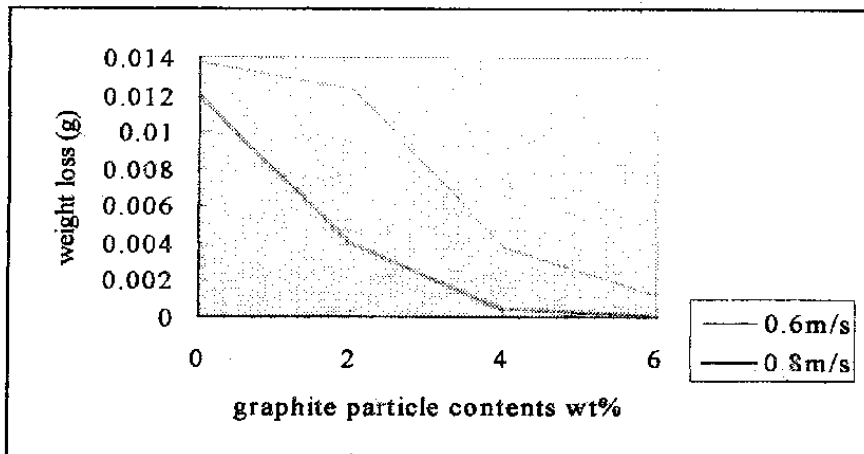


Fig.7: Wear weight loss of 6061 Al alloy-graphite composites as a function on wear speed: sliding distance, 144m; applied pressure 0.69 MPa

HARDNESS PROPERTY AND WEAR RESISTANCE OF ZN-AL/ Al_2O_3 _p OR SiC_p PARTICULATE COMPOSITE

Tao Jie, Cui Yihua and Li Shunlin

*Department of Material Science and Engineering, NUAU
29 Yudao Street, Nanjing 210016, P.R. China*

SUMMARY: The hardness value and the wear resistance of Al_2O_3 _p or SiC_p /Zn-Al composite, prepared by means of rheological casting technology, are investigated separately in this work. The results show that the addition of Al_2O_3 _p or SiC_p increases the hardness values of the matrix at both room and high temperature and improves the wear resistance of the material. The hardness values and the wear resistance of the composite rise with the increase of the particle volume fraction or the decrease of the particle size. The raising of test temperature results in a rapid descending of its hardness values. However, the addition of Al_2O_3 _p or SiC_p improves the property of high temperature resistance of Zn-Al alloys significantly. Moreover, the effect of quenching, tempering or cycling heat treatment on the hardness values of the composite is also studied.

KEYWORDS: Zn-Al composite, Al_2O_3 _p, SiC_p , hardness, value, wear resistance

INTRODUCTION

In order to improve the properties of Zn-Al alloys and broaden their application ranges, Zn-Al composite reinforced by carbon fiber, SiC_w , Al_2O_3 short fiber, SiC_p or Al_2O_3 _p have been prepared and investigated [1-5]. The results [4] of the research of Al_2O_3 _p or SiC_p Zn-Al composite indicate that the composite possesses better properties such as flexural strength, compressive strength and thermal expansion coefficient than the alloy, except impact toughness values. In this work, the hardness property and the wear resistance of Al_2O_3 _p or SiC_p /Zn-Al composite are emphatically investigated. Considering the requirement of practical application of the composite, we have studied the effect of temperature and heat treatment such as quenching, tempering or thermal cycling on the properties of Al_2O_3 _p or SiC_p /Zn-Al composite. In addition, the relation between the hardness values and the wear resistance of the composite and the particle size or the particle volume fraction is also discussed.

1 SAMPLE FABRICATION AND EXPERIMENTAL PROCEDURE

The matrix is ZA4-3 die alloy (4.04 wt% Al, 3.02 wt% Cu, 0.046 wt% Mg, the rest Zn), and ZA27 alloy (26.66 wt% Al, 2.31 wt% Cu, 0.016 wt% Mg, the rest Zn). The adopted reinforcement is Al_2O_3 _p and SiC_p with diameters of 14 μm , 28 μm and 50 μm . The Al_2O_3 _p or SiC_p /Zn-Al composite blanks with the particle volume fractions of 5%, 10% and 15% are prepared by means of the rheological casting method. The specimens are cut from the composite

blanks, and machined into the size of 10mm×10mm×30mm and 6mm×10mm×30mm for the hardness property and the wear resistance experiment respectively.

The hardness values of the composite at room temperature are tested on HD8-187.5 Universe Hardness Gauge. The variation of its hardness with the increase of temperature is measured in the device, with the heating medium of α -methyl silicone oil. Moreover, the hardness values of the samples quenched into the water from 300 °C and tempered in α -methyl silicone oil at 100°C for 1h are individually determined.

The composite specimens for the wear resistance are run against T8(0.8 wt% C, the rest Fe) at 0.84 ms⁻¹ sliding speed at room temperature in air without lubricant. Before testing, all specimens must be thoroughly cleaned with acetone.

2 EXPERIMENTAL RESULTS

The hardness values of the materials increase significantly with the incorporation of the particles, rise with the increase of the particle volume fraction or the reduction of the particle size.

The hardness values of the composite in the process of isothermal treatment at certain temperature soon tends to reach a stable value. The variation of hardness values of the composite in the process at 100°C is shown in Table 1.

Table 1 Hardness values of SiC_p/ZA27 composite in the process of isothermal treatment at 100°C

Materials	Vp%	0min.	30min.	90min.	240min.	300min.	360min.
ZA27	0	68	40	41	42	42	42
SiC _p /ZA27	5	78	62	61	60	59	59
SiC _p /ZA27	10	82	65	64	65	64	64
SiC _p /ZA27	15	90	69	69	70	70	71

The stable hardness values at each investigated temperature are listed in Table 2. It is obvious that the hardness values of both the matrices and the composites reduce rapidly with the increase of the test temperature.

Table 2 Variation of hardness values of Al₂O_{3p} or SiC_p/Zn-Al composite with temperature

Materials	20°C	100°C	120°C	150°C
ZA4-3	66	42	30	10
ZA27	68	45	34	17
10%14 μ mAl ₂ O _{3p} /ZA4-3	84	64	48	26
10%14 μ mSiC _p /ZA4-3	83	60	45	25
15%14 μ mSiC _p /ZA27	89	67	52	30

The variation of hardness values at room temperature after three times isothermal treatment at 100°C is shown in Table 3, in which it is obviously observed that the treatment has only a slight influence on the hardness feature of the composites and the matrix alloys. However, after treated at 150°C, the matrix alloys possess a attenuation value(Δ HB)14~16 of the hardness, while the composites only 4~6 of that.

Table 3 Relation of hardness values of Al_2O_3 or SiC_p /Zn-Al composite with cycling number at 100°C

Materials	cycling number			
	0	1	2	3
ZA4-3	66	64	64	63
10%28 μ m Al_2O_3 _p /ZA4-3	72	71	71	70
15%28 μ m Al_2O_3 _p /ZA4-3	79	76	71	70
5%28 μ m SiC_p /ZA4-3	82	80	79	79
15%28 μ m SiC_p /ZA4-3	86	85	85	85

Table 4 shows the variation of hardness values of Al_2O_3 or SiC_p /Zn-Al composite specimens quenched from 300°C or tempered at 100°C.

Table 4 Hardness values of Al_2O_3 or SiC_p /Zn-Al composite after quenching or tempering

Materials	Vp	original	After quenching	After tempering
ZA4-3	0	66	66	65
ZA27	0	68	67	64
14 μ m Al_2O_3 _p /ZA4-3	5	77	79	77
	10	84	83	82
14 μ m SiC_p /ZA4-3	5	79	76	77
	10	83	81	79
	15	85	86	83
14 μ m SiC_p /ZA27	5	82	76	75
	10	85	85	81
	15	89	90	90

It was found that during the wear experiment the wear rates of both the matrix alloy and the composite increase with increasing the applied load. With a larger increasing degree, however, the property of the matrix alloy is noticeably greater than that of its composite (see Table 5).

Table 5 Variation of the wear rate with applied load at a time of 30min.

Materials	Vp	$W_L \times 10^{-6} \text{ mm}^3/\text{mm}$		
		9.8N	49N	147N
ZA4-3	0	2.72	3.07	9.92
14 μ m Al_2O_3 _p /ZA4-3	15%	1.75	1.82	2.04
14 μ m SiC_p /ZA4-3	15%	1.56	1.74	1.98
50 μ m Al_2O_3 _p /ZA4-3	10%	2.16	2.85	3.84

3 DISCUSSIONS

The hardness property of metal matrix composites (MMCs) composed of reinforcement and a matrix alloy is certainly influenced by that of each component, the effect of which corresponds to "role of mixture" in the composites. The increase of the particle volume fraction of

reinforcement with high strength and hardness makes the hardness values of the composites increase. Apart from this regularity, the hardness of the composite is also sensitive to the microstructure. Therefore, the hardness property of Al_2O_3 or SiC_p /Zn-Al composite is not only dominated by the mechanical properties of Al_2O_3 or SiC_p , but also by its size, shape and distribution. It was found in the experiment that the hardness values of the composite decrease with the increase of the particle size. The addition of Al_2O_3 or SiC_p changes the solidification process of the zinc alloy and makes its microstructure fine, leading to a lot of interfaces between Al_2O_3 or SiC_p particles and the matrix alloy. These interfaces impede the dislocation motion in the material, resulting in the dislocations pile-up, so as to force the going-on deformation load to increase. This is why the composite possesses greater hardness values than the matrix alloy. The larger the Al_2O_3 or SiC_p volume fraction, the more the square of interfaces between the particle and the alloy, and the stronger the impediment to the dislocation motion, hence, the hardness values of the composite rise. The increase of Al_2O_3 or SiC_p size causes the reduction of the interface square and the microstructure uniformity, and the decrease of anti-deformation ability, as a result, bringing about the descent of the hardness values of the composite. It is obviously seen that the properties of the particle/alloy interface (i.e. interface square, bonding strength) have an important effect on the hardness feature of the composite.

The zinc alloys, with low melting point temperature, have weak heat-resistance. Therefore, the testing temperature influences outstandingly the hardness values of the alloy and their composites. Comparing the variation of the hardness values of the alloys with those of the composites, it is found that both of them have similar descending degree, and that the hardness values of the composites at 100°C are nearly equal to those of the alloys at room temperature. Thus, it can be said that Al_2O_3 or SiC_p still plays a strong role in reinforcing the materials even if the temperature is higher than 100°C . Generally speaking, the addition of reinforcement like particle or fiber or whisker into a metallic matrix improves its heat-resistance properties significantly. As to the zinc alloy with low melting point temperature, the addition of stiff ceramic particles is an effective way to increase its hardness values at high temperature.

It can be seen in Table 3 that the cycling heat treatment at 100°C results in a slight descending of hardness property of both the matrix alloy and its composite ($\Delta\text{HRB}=3\sim 4$). However, after 150°C cycling treatment, the attenuation value of the hardness of the composite ($\Delta\text{HRB}=4\sim 6$) is lower than that of the alloy ($\Delta\text{HRB}=14\sim 16$). It is indicated that there is no or a little damage in the interfaces between the particles and the alloy. More importantly, it also shows that Al_2O_3 or SiC_p still possesses a marked reinforcing effect. This result is similar to the conclusion which is drawn from the studies on the strength of Al_2O_3 /ZA12 zinc alloy composite at high temperature[5].

The microstructure of the matrix alloys and their composites has not significant changes after they are quenched from 300°C , thus, there is no large difference in the hardness values of the alloy and their composites before and after the treatment. On the other hand, since there is large difference of thermal expansion coefficient between Al_2O_3 or SiC_p particles and the alloy, thermal residual stress arises at the interface of the particles and the matrices during the manufacturing or quenching process of the composite. The residual stress at the interface aggravates the impediment to the dislocation motion in the material. Moreover, it causes the local stress concentration at the sharp edges of multiangular particles, leading to the local debonding at the interface. The former is advantageous to the hardness values of the materials, while the latter is harmful. As a comprehensive result, the quenching treatment has a little influence on the hardness property of both the matrix alloys and their composites. Nevertheless the hardness values of the quenched specimens, tempered at 100°C , go down slowly, because some of piled-up dislocations are enabled to move again.

The zinc alloy due to its lower melting point has low recrystallizing temperature. Therefore the heat produced during wearing process makes the alloy soften and the adhesion occur easily. The addition of Al_2O_{3p} or SiC_p stiffer ceramic particles into the softer zinc alloy constitutes a superior soft-stiff coordination, reducing the possibility of the adhesion to occur. Thus, Al_2O_{3p} or SiC_p /Zn-Al composite exhibits better wear resistance than the alloy. The increase of applied load results in the raising of the temperature on the sliding surface so that severe softening and melting of the matrix degenerate the wear behavior of the composite.

4 CONCLUSIONS

- (1) The addition of Al_2O_{3p} or SiC_p into the zinc alloys improves their hardness values both at room and high temperature significantly. The hardness property of Al_2O_{3p} or SiC_p /Zn-Al composite is mainly influenced by the factors like Al_2O_{3p} or SiC_p particle volume fraction, Al_2O_{3p} or SiC_p size and the testing temperature. The larger percentage of particles and the smaller particle size brings about the better hardness property of the composite. The higher the testing temperature, the lower the hardness values of the composite.
- (2) The hardness values of the composite after the cycling heat treatment below (including) $150^\circ C$ have a slight descending degree, and seem to reach stable values through the treating once or twice.
- (3) The quenching treatment from $300^\circ C$ or less has an effect to a small extent on the hardness property of the composite, while tempering at $100^\circ C$ causes its hardness values to lower.
- (4) The wear resistance of the composite rises with the increase of the particle volume fraction or the decrease of the particle size. The effect of applied load and the sliding time on the wear resistance of the composite is the same as reported in Ref.[6].

REFERENCES

- 1 Dahotre N B, McCay T D, McCay M H. Laser surface modification of zinc-base composites. JOM, 1990, 42(6):44
- 2 Murphy S, Arikan R.A. Metallographic study of wear in planar-random fiber-reinforced composites with an aluminum-zinc-copper alloy matrix. Wear, 1992, 155:105
- 3 Tao J, Lu X H, Wang Y L. Fabrication and properties of C/Zn composite. Journal of Nanjing Aeronautical Institute, 1989, 21(3):33-44
- 4 Tao Jie, Xiao Jun, Cui Yihua et al. Investigation on mechanical properties of Zn-Al/SiC particulate composites. Transactions of NUAA, 1995, 12(1):23
- 5 Zhu H X, Liu S K. Properties of SiCw reinforced Zn12Al composite. Materials Science Progress, 1992, 6(1):88-91
- 6 Pearsall K J, Eliezer Z, et al. The effect of sliding time and speed on the wear of composite materials. Wear, 1980, 63:121-130

A STUDY ON THE MICROSTRUCTURE OF ALUMINA BORATE WHISKER REINFORCED ALUMINUM COMPOSITE

W. D. Fei, L. J. Yao, and C. K. Yao

*School of Materials Science and Engineering, Harbin Institute of Technology,
Harbin 150001, P. R. China*

SUMMARY: The squeeze casting method was used to fabricate alumina borate whisker reinforced aluminum composite with the whisker volume fraction of 25%, the matrix alloy is Al-Si-Mg alloy (AC8A alloy). The microstructure of the composite was studied Using TEM observation. The results indicated that the feature of the microstructure of the composite can be described as follows: the first one is that the interfacial reaction exists between the whisker and Al-Si-Mg alloy; the second one is that twins and dislocations were found in the whisker; the third one is that higher densified dislocation exists in the matrix of the composite. The twin and dislocation in the whisker were considered as the results of relaxation of residual stress due to the thermal mismatch between the whisker and aluminum alloy.

KEYWORDS: alumina borate whisker, aluminum matrix composite, microstructure, twin, dislocation, thermal mismatch, residual stress, stress relaxation

INTRODUCTION

Because of higher properties and formability, aluminum matrix composites reinforced by whisker were widely studied, it is very important to reduce the cost for large scale application of this kind of materials. Sukanuma et al [1] and the Hu et al [2] showed that the properties of alumina borate whisker ($\text{Al}_{18}\text{B}_4\text{O}_{33}$) reinforced aluminum composite exhibits excellent properties and low cost, so the composite was received more interesting.

Although many studies were about the microstructure and properties of alumina borate whisker reinforced aluminum composite[1-4], few studies were concerning the evolution mechanism of the microstructure of composite, especially the defect in the whisker. As well known, the microstructure plays a key role on the properties of composites, it is very important to understand and control the microstructure for the optimization of composite properties. In the present research, the microstructures both in the matrix and whisker was investigated by TEM observation, and the formation mechanism of the microstructure in the composite was discussed in detail.

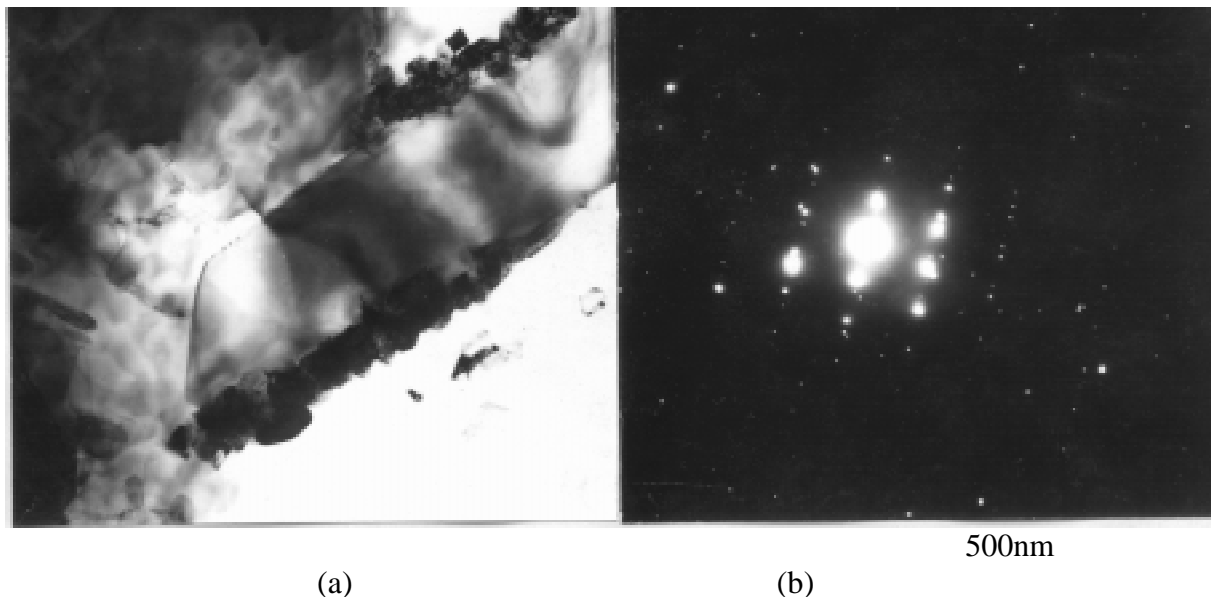
EXPERIMENTS

The $\text{Al}_{18}\text{B}_4\text{O}_{33}$ whisker reinforced AC8A alumni alloy composite was fabricated by squeeze casting method, and the volume fraction of the whisker is 25%, the composition of AC8A alloy is Si: 11.0mass%, Mg: 1.0mass%, Cu: 0.8mass%, Ni: 1.0mass%, 87.2mass%. The casting temperature is 800°C , and the temperature of the mold is about 450°C .

The specimens for TEM observation is prepared by ion milling manhood. The TEM observation was carried out in a CM-12 type transmission electron microscope with the operation voltage of 120kV.

RESULTS AND DISCUSSION

The TEM micrograph of the interface $\text{Al}_{18}\text{B}_4\text{O}_{33}$ /AC8A composite was shown in Fig.1, it is clear that an obvious interfacial reaction exists between the whisker and the AC8A alloy, we had identified that the interfacial reaction product is MgAl_2O_4 with spinal structure and shown that the interfacial reaction can affect the composite properties greatly[2-4].



*Fig.1: TEM photos of the interface of $\text{Al}_{18}\text{B}_4\text{O}_{33}$ /AC8A composite
(a) micrograph, (b) SADP*

Fig. 2 is the TEM micrograph of $\text{Al}_{18}\text{B}_4\text{O}_{33}$ /AC8A composite, dislocation and pile-up of dislocation can be found in the whisker and the dislocations are not straight, which means that the dislocations are movable in the whisker. The presence of movable dislocation suggested that the whisker can be deformed by dislocation motion. The stress which lead to the dislocation motion in the whisker may be the relaxation of thermal residual stress in the composite.

As the great difference of the coefficient of thermal expansion (CTE) between the whisker and matrix alloy, the residual stress must be induced into the composite when the composite was cooled down from fabrication temperature. The thermal residual stress may be so high that the dislocation in the whisker can be moved by it.

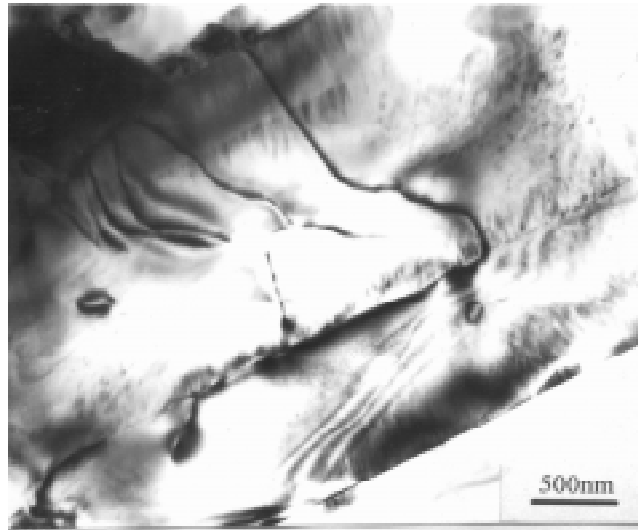


Fig.2: Dislocation in $Al_{18}B_4O_{33}$ whisker in $Al_{18}B_4O_{33}/AC8A$ composite

Fig. 3 is the twin in the $Al_{18}B_4O_{33}$ whisker, from Fig. 3, it can be seen that the twin plan is parallel to the longitudinal direction of whisker. Because the main growth direction of the whisker is the longitudinal direction, the twin shown in Fig. 3 is deformation twin, not growth twin. The formation of deformation twin in the whisker is due to the relaxation of thermal residual stress in the whisker as discussed above.

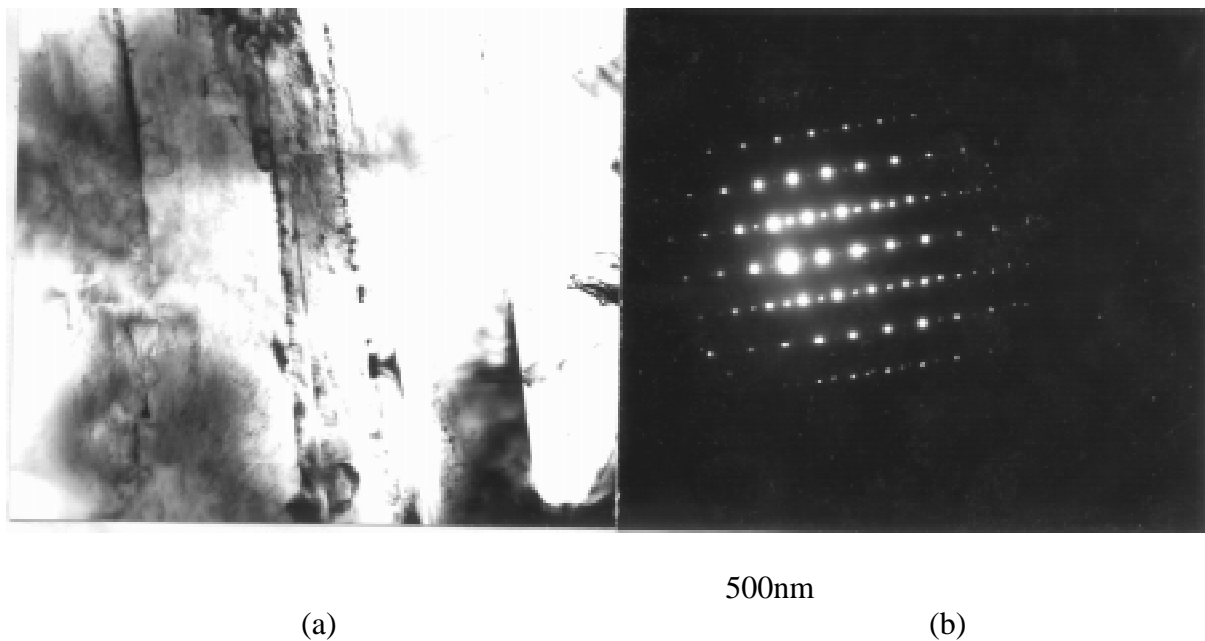


Fig. 3: Twin in $Al_{18}B_4O_{33}$ whisker in $Al_{18}B_4O_{33}/AC8A$ composite

TEM observation (see Fig. 2 and Fig. 3) show that $Al_{18}B_4O_{33}$ whisker can be deformed by dislocation motion and deformation twin. The results is very interesting, the residual stress in the composite can be relaxed by whisker deformation, on the other hand the dislocation motion and deformation twin formation may affect the deformation mechanism of the composite, which need to be studied further.

Because of Si content of Si in AC8A alloy is higher, the phases in the matrix of the composite are aluminum and silicon. TEM micrographs of matrix in $Al_{18}B_4O_{33}/Al$ composite are shown in Fig. 4. In Fig. 4(a), the high density of dislocation can be seen in aluminum phase of the matrix; and the deformation twin in silicon phase of the matrix can be found. High density of defects in the matrix suggests that the matrix was deformed greatly. It is clear that the driving force for the matrix deformation is the same for the deformation of whisker, i.e. the residual stress in the composite is very high, which can be higher than the yield strength of the composite. Comparing the density of defects in the matrix with that in the whisker, it can be found that the density in the matrix is much higher than that in the whisker, which is due to the yield strength of the matrix is much lower than that of the whisker, plastic deformation must be higher in the matrix than that in the whisker at same residual stress.

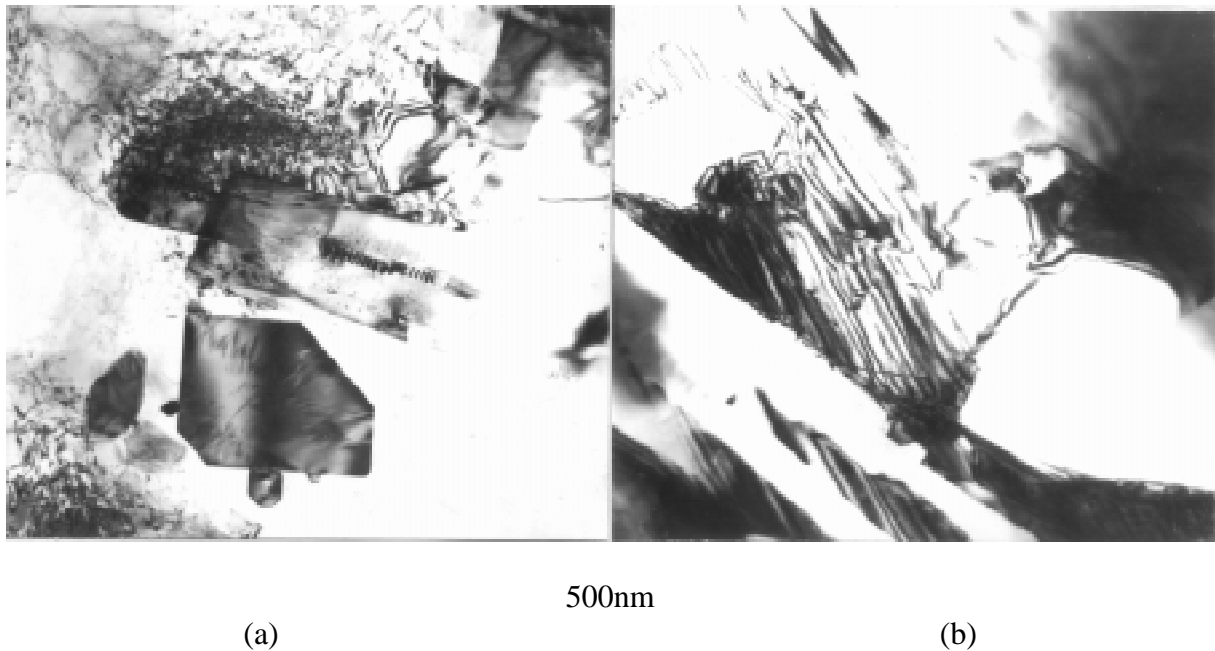


Fig. 4: TEM micrographs of the matrix in $Al_{18}B_4O_{33}/Al$ composite
(a) Al phase, (b) Si phase

The residual stress in metal matrix composite is almost avoided, which can influence many properties of the composite. From the present study, one can find that the residual stress can be relaxed by two ways: one is plastic deformation of the whisker, another is plastic deformation of the matrix. Because the difference of CTE between the whisker and aluminum alloy is quite high, when the composite was cooled down from fabrication temperature, the residual stress must be induced into the composite, and the residual stress is higher than the yield strength of the composite, so the plastic deformation takes place.

The plastic deformation of the whisker and matrix may take place at various temperatures during the cooling process of the composite, because of the residual stress in the composite may be very high, the deformation of the composite due to relaxation of the residual stress may be a continuous process. The high density of dislocations in the matrix can enhance the strength of the matrix or the composite. The residual stress can be relaxed both in the matrix and whisker, which can reduce the residual stress level in the composite, which may be beneficial to the shape stability of the composite parts, in the point of view, to study this effect is important for some applications of the composite.

CONCLUSIONS

Interfacial reaction exists between the $\text{Al}_{18}\text{B}_4\text{O}_{33}$ whisker and AC8A alloy.

Dislocation and deformation twin were observed in $\text{Al}_{18}\text{B}_4\text{O}_{33}$ whisker in $\text{Al}_{18}\text{B}_4\text{O}_{33}/\text{AC8A}$ composite, the formation of the defects is due to the relaxation of residual stress in the composite.

High densified dislocation exists in Al phase and deformation twin in Si phase in $\text{Al}_{18}\text{B}_4\text{O}_{33}/\text{AC8A}$ composite, which also results from the relaxation of residual stress in the composite

REFERENCES

1. Suganuma K., Fujita T., Suzuki N., and Niihara K., "Alumina Borate whisker Reinforced Aluminum Composite" J. Mater. Sci. Letter, vol. 9, pp. 633-635
2. Hu J., Fei W.D., Jiang X.D., Li C and Yao C.K., "A Study on Alumina Borate Whisker Reinforced Aluminum Composite" J. Mater. Sci. Tech. 1993, No. 1, 1-3 (in Chinese)
3. Fei W.D., Jiang X.D. Li C. and Yao C.K., "Effect of Interfacial Reaction on the Young's Modulus of Alumina Borate Whisker Reinforced Aluminum Composite" J.Mater.Sci Letter, 1996, Vol. 15, 1495-1497
4. Hu J., Fei W.D., Li C. and Yao C.K., "Aging Behavior of Alumina Borate Whisker Reinforced AC8A-Al Composite" 1st Inter. Con. on Composite Eng., New Orleans, 1994

CASTING WELDING OF ALUMINIUM ALLOY REINFORCED WITH ALUMINA MATERIAL

C. K. Mu and C. B. Lin

Department of Mechanical Engineering, Tamkang University, Taipei, Taiwan 25137, R. O. C

SUMMARY:

The metal matrix composites which is extruded in shape directly its particles have orientation arrangement along the longitude direction of the extruded shape. 700°C A356 molten aluminum alloy and 600°C 7005Al/Al₂O_{3(p)} composites seamless pipe we can find pores in the joint interface, therefore it's not joined completely. 700°C A356 molten Al alloy and 620°C 7005Al/Al₂O_{3(p)} composites seamless pipe, we can find no pores in the joint interface and the no particles drop. it can join completely. 700°C A356 molten Al alloy and 640°C 7005Al/Al₂O_{3(p)} composites seamless pipe, we can find no pores in the joint interface and the particles drop. It can join completely. 700°C A356 molten Al alloy and 660°C 7005Al/Al₂O_{3(p)} composites rod the casting welding strength is 4.58kgf/mm² and the fracture is in the A356 Al alloy zone. From metallurgical examination we can find the particles are drop and push, finally there are less Al₂O₃ particles in the free surface and more particles in the central

KEYWORDS: seamless pipe, metal matrix composites, extrusion particulate, graphite, casting welding.

Introduction

Metal Matrix composites (MMCs) alloy can be reinforced by ceramics particulates, continuous fiber, chopped fiber or whisker. Most attention is currently paid to particulate reinforced aluminum alloy, titanium, magnesium and copper alloys. Al₂O₃ is the preferred particulate reinforcement, although other materials such as SiC, B₄C and TiC have also been used in Al alloys[1]. MMCs are now widely used for structural applications due to properties such as high specific strength, high specific stiffness, high hardness, high damping capacity and high wear resistance compared to most monolithic metals. Selecting the kind and quantity of second phase can tailor coefficient of thermal expansion and thermal conductivity. Existing and potential applications for metal matrix composites including: cylinder liners, aircraft stabilizer, heat exchanger material for hypersonic aircrafts, electrodes for power semiconductor devices, automotive drive shaft tubes, and packaging structures in integrated circuits[2].

In many of these applications it is also desirable to fabricate the MMCs into complex shapes via joining processes. Joining procedures for composites without any major reductions in strength is a important conduction for application of metal matrix composites[3]. This document presents a review of the present situation for joining of Al-

base MMCs and A356 Al alloy.

According to J. R. Kennedy et al. [6] which indicate that. For a given temperature, the viscosity of molten MMCs is higher than that of molten matrix alloy. The high viscosity and lesser wetness of this molten region prevents manipulation of the pool.

In the gas metal arc welding process, coalescence is produced by heat from an arc between a metal electrode and the work shielded by an atmosphere of argon, helium, CO₂, or a mixture of gases. According to M. B. D. Ellis et al. [1] which indicate that. The filler will increase the wetness, decrease the viscosity and avoiding the second phase combine directly with each other to increase joint strength.

It appears from published literature of T. N. Baker [10] that welding techniques such as Electron Beam Welding and Laser Beam Welding, which employ a rapid thermal cycle and heat affected zone is narrow. But it is difficult to control energy. The heat was conducted across the interface to the matrix, and the local temperature at the Metal Matrix Composites interface was high enough to cause dissolution of the reinforcement. If the input energy is not enough to produce chemical bonding between second and matrix material.

From published literature [5] the characteristics of the associated joints of MMCs includes: the difference in microstructure between the matrix and the hydrogen solubility of aluminum increases as the temperature increases; the high viscosity of this molten region prevents manipulation of the pool [3]; the second phase damage and dispersion [2]; at the heat affected zone the compounds formed at the interface [5]; joint properties of wetness, pressure and time [7]; the cooling rate; the quantity of heat input [11]; and surface treatment, i.e. aluminum is easily reactive with oxide. This tenacious oxide layer made welding of aluminum rare. The melting temperature of aluminum oxide which is more than three times the melting temperature of aluminum. Hydrogen absorbed during its molten state, enhance strength of the joint, it becomes the challenge in joint process. At the jointing processes there is a possibility that the aluminum alloy will react with second phase, and brittle compounds would be produced, such as: $4Al + 3SiC \rightarrow Al_4C_3 + 3Si$, which increase viscosity of the pool. The pores in the joint interface are hard to be excluded, and become the stress concentrators. The joint strength would be decreased. As welding energy input and pressure were increased, second phase dissolution and the volume fraction became greater. The volume fraction and type of reinforcement which influence the wettability of matrix and filler. In the meantime, the separation uniformity of second phase would affect the joint strength. In proceeding the joint of MMCs, it would produce different ductile compounds between second phase and metal matrix according to different energies in heat affected zone.

The objective of this project is to joint 7005Al/Al₂O_{3(p)} composites seamless pipe and A356 aluminum alloy, the found a new joining technique and their jointing parameter, including: jointing temperature, pressure, and microstructure etc. they will be tested for their joint properties, which includes: jointing strength, and discuss the influences on interface microstructure and jointing strength in different temperatures to ensure the feasibility of this method.

Experiment Process

Material Producing Process

The material system of this research adopts 7005Al/10Vt% Al₂O_{3(p)} Composites seamless pipe and A356 Al alloy (7% Si-0.5% Mg). The fabrication of 7005 Al/10 Vt%

$\text{Al}_2\text{O}_{3(p)}$ composites billet adopts C. B. Lin, U.S.A. Invent Patent No:5401338[13]. The 7005 Al composition (0.35% Si-0.40% Fe-2.0% Cu-0.2% Mn-3% Mg-0.3% Cr-7% Zn-0.2% T), the shapes of Al_2O_3 particles are irregular, α -phase, the average particle size is $13\mu\text{m}$. 7005 Al/ $\text{Al}_2\text{O}_{3(p)}$ composites seamless pipe (OD=19mm, ID=15mm) is made by the process of direct extrusion.

Cast Welding

The production process of casting welding 7005 Al/ $\text{Al}_2\text{O}_{3(p)}$ composites seamless pipe with A356 Al alloy is to directly pour the 700°C A356 Al molten composites alloy into the metal mold; and cast welding with the 7005 Al/ $\text{Al}_2\text{O}_{3(p)}$ composites seamless pipe which warmed up in 500°C , 600°C , 620°C , 640°C furnace ($\pm 3^\circ\text{C}$). After one minute, take the compound casting out of the furnace to air cooling. The most important thing is that the entire casting welding process should be under the production of the Argon to prevent the oxidation on the surface of the seamless pipe and affect the joint strength. Proceeding the cast welding under the conditions above, there are many pores in the joint interface when the temperature of the seamless pipe is 500°C . When the temperature of the seamless pipe is 620°C ~ 640°C , there are no pores in the joint interface but the seamless pipe is severely distorted even collapsed (show as Fig.1) Based on the problem, this research is trying to offer a new cast welding process to the problem above.

The cast welding process in this research shows as Fig.2. First, mix the graphite particles with acetone in proper concentration to slurry state; pour it between the seamless pipe and the arbor. Then remove the acetone from the slurry by baking it. Take out arbor, formed a 2mm thin graphite layer showed as Fig.2(a). The reason why using the graphite is that the graphite would not cause the reaction with the 640°C warm-up seamless pipe. then fill the NaCl particles in the seamless pipe and cool-press the NaCl particles to attach the pipe which could increase the density of the green compact as Fig.2(b) shows. The reason why removing the steam from the NaCl is to prevent the steam dismosed to the inner layer of the seamless pipe in the cast welding which might cause the reaction and affect the surface of the inner layer. Clamp the done pipe with the Gr layer and NaCl green compact into the mold surrounded by Argon in the furnace. After separately warm up the pipe 30 minutes in 500°C , 600°C , 620°C , and 640°C to reach the equilibrium temperature. Then pour the 700°C A356 molten Al alloy into the furnace. Cast welding with the pipe one minute, then take out the compound casting and cool it in room temperature. Finally, wash out the graphite and NaCl by water. NaCl is easy to dissolve in water, so the filler is easy to wash out, which is the excellence of this method.

Besides, to further understand the joint strength under the conditions of the casting welding above; we cut a 40mm L \times 15mm D 7005 Al/10Vf% $\text{Al}_2\text{O}_{3(p)}$ composite extrusion rod and put in the metal mold of the furnace. Under the protection of Argon, warm up in the 660°C work temperature. After 30 minute warm-up, pour the 700°C A356 molten Al alloy into the metal mold and casting welding with the rod one minute; then take out the compound casting from the furnace to air cool it.

Metallographic Analysis

From the longitude direction of 7005 Al/ $\text{Al}_2\text{O}_{3(p)}$ composite billet and the seamless pipe, and the joint interface of the done cast welding compound casting; cut the metallographic samples. Polish them with #200~#1200 grid carbimet papers, followed by final polishing with 1 and 0.05 μm alumina slurries. The microstructure was observed using a Nikon

optical microscope.

Tensile strength

We cut the tensile test specimen that shown in Fig.3. Let the specimen relax stress using annealing treatment. Final pull the specimen use the instron tensile machine under room temperature and 2 mm/min cross head speed.

Result and discussion

The vertical distribution of Al_2O_3 particles in the billet of Al alloy and seamless pipe is illustrated as in Fig. 4. Through this diagram, we can find 13 μm Al_2O_3 particles uniform all distribute in matrix of the billet, and the seamless pipe which is extruded in shape directly its particles have orientation arrangement along the vertical of the extruded shape. The cast welding 700 $^\circ\text{C}$ of 7005Al/ $\text{Al}_2\text{O}_{3(\text{p})}$ composites seamless pipe and 640 $^\circ\text{C}$ A356 molten Al alloy is illustrated as in Fig. 5. besides, the comparison of Fig. 1 and Fig. 5 can prove that we can use new cast welding method of this research to prevent the molten Al alloy from melting its thin seamless pipe in the process of cast welding, and reach the purpose of joining. Fig. 6 is the observation of joint of 700 $^\circ\text{C}$ A356 molten Al alloy and 600 $^\circ\text{C}$ 7005Al/ $\text{Al}_2\text{O}_{3(\text{p})}$ composites seamless pipe. We can find holes exit in the joint plane, therefore it is not joined completely, the joint has boundary which is not jointing yet. This is because the heat transfer of the 700 $^\circ\text{C}$ molten Al alloy is not sufficient to make the 7005Al/ $\text{Al}_2\text{O}_{3(\text{p})}$ composites seamless pipe to reach melting phenomenon. Now, rise the temperature of the seamless pipe of 7005Al/ $\text{Al}_2\text{O}_{3(\text{p})}$ composites to 620 $^\circ\text{C}$ and make it conduct microstructure of joint of cast welding with 700 $^\circ\text{C}$ molten Al alloy as illustrated in Fig. 7. In this figure, we can find no holes in the joint plane, at this time 700 $^\circ\text{C}$ molten Al alloy transmit heat to 620 $^\circ\text{C}$ seamless pipe, because it reaches the melting temperature, so it makes the surface of seamless pipe melt and reach the completely jointed condition, in addition, we can know it by observing Fig. 7. In this figure, the joint of 7005Al/ $\text{Al}_2\text{O}_{3(\text{p})}$ composites seamless pipe is not straight any more, this is because the surface is melted. Besides, now the molting of seamless pipe is in a kind of slurry condition representing it doesn't become liquid completely, in certain viscosity it won't make the denser particles of Al_2O_3 have the sinking phenomenon. Now, if we rise the temperature of the seamless pipe of 7005Al/ $\text{Al}_2\text{O}_{3(\text{p})}$ composites to 640 $^\circ\text{C}$ to conduct the condition of joint of cast welding with 700 $^\circ\text{C}$ molten Al alloy as illustrated in Fig. 8. In this diagram we can find the joint plane has no holes, but now 7005Al/ $\text{Al}_2\text{O}_{3(\text{p})}$ composites seamless pipe becomes liquid, it makes the denser particles of Al_2O_3 sink to the bottom and A356 at that time is also liquid making the sinking particles flowing to A356 molten Al alloy, and the temperature of the molten is very high, the solidifying speed is slower making dendrite have enough time to produce, making Al_2O_3 particles be jostled to dendrite arm, and making the particle not well-distributed as illustrated in Fig. 9. According to the above phenomena, we can make a conclusion that previously heat the 7005Al/ $\text{Al}_2\text{O}_{3(\text{p})}$ composites seamless pipe to 620 $^\circ\text{C}$ can make it join with 700 $^\circ\text{C}$ molten Al alloy well. This fine combination represents the joint has no holes, and the particles won't have sinking phenomenon. This conclusion implies when Al alloy and particulate metal matrix composites conduct cast welding, especially when the particles are denser, we should control the temperature to avoid the particles sinking and having the phenomenon of not well-distributed.

Except the observation on the joint interface of cast welding we discussed above, this

research discusses also the joint strength. Now the tensile test on the 700°C A356 molten aluminum alloy jointed with 660°C extrusion bar, it would be found that the average of joint strength is 4.58 kgf/mm² and the fracture is occurred on the region of A356 aluminum alloy. From observing on the joint interface of composites casting(Fig.10), the particles deposited and pushed were found. The particles deposited occurred in liquid phase of both A356 aluminum alloy and 7005Al/Al₂O_{3(p)} composites rod. The pushing occurred in the process of cooling and the particles were depositing faster especially in the joint interface. But in the process of cooling, the 7005Al/Al₂O_{3(p)} composites bar will turn from slurry phase into solid phase. Yet the Al₂O₃ particles would not deposit in the slurry phase, then the particles would gradually be pushed to the center of the casting bar and the final cooling area would be formed as Fig.11 shows that the distribution of the Al₂O₃ particles formed as an apparent slope density distribution from the free surface. Based on the result, the fracture of this composite casting locates in the A356 aluminum alloy zone. In the end, we conclude that when the high temperature aluminum alloy being casting welding with the particulate metal matrix composites, the consideration on the deposition and push of the particles has an apparent influence on the joint strength.

Conclusion

In this research, the 7005 Al/10 Vf% Al₂O_{3(p)} composites billet has been casted ,and been directly extruded to the seamless pipe(ID=15mm OD=19mm) and the diameter 29mm extruded rod. This research is also trying to offer a new research on joining 700°C molten Al alloy with 500°C ~ 700°C 7005 Al/10 Vf% Al₂O_{3(p)} composites seamless pipe and 660 °C 7005 Al/ Al₂O_{3(p)} composites rod, and offer a new method on cast welding. This new method is to lay a graphite inside the seamless pipe, fill in the dry NaCl powder, and well press the NaCl powder to a green compact. In this method, it would prevent the seamless pipe being melted by the high temperature molten Al alloy and get a well casted compound casting. The conclusions are as followed:

- (1)The metal matrix composites which is extruded in shape directly its particles have orientation arrangement along the longitude direction of the extruded shape.
- (2)700°C A356 molten aluminum alloy and 600°C 7005Al/Al₂O_{3(p)} composites seamless pipe we can find pores in the joint interface, therefore it's not joined completely.
- (3)700°C A356 molten Al alloy and 620°C 7005Al/Al₂O_{3(p)} composites seamless pipe, we can find no pores in the joint interface and the no particles drop. it can join completely.
- (4)700°C A356 molten Al alloy and 640°C 7005Al/Al₂O_{3(p)} composites seamless pipe , we can find no pores in the joint interface and the particles drop. It can join completely.
- (5)700°C A356 molten Al alloy and 660°C 7005Al/Al₂O_{3(p)} composites rod the casting welding strength is 4.58kgf/mm² and the fracture is in the A356 Al alloy zone. From metallurgical examination we can find the particles are drop and push , finally there are less Al₂O₃ particles in the free surface and more particles in the central.

Acknowledgement

This work was supported by the National Science Council, Taiwan, Republic of China.

REFERENCE

1. M. B. D. Ellis, "Joining of Al- Based Metal Matrix Composites- A Review", *Materials and Manufacturing Processes*, Vol. 11, No. 1, 1996, pp 45-66.
2. Narendra B. Dahotre, T. Dwayne McCay, and Mary Helen McCay, "Laser Induced Liquid Phase Reaction Synthesis Assisted Joining of Metal Composites", *Materials and Manufacturing Processes*, Vol. 9, No.3, 1996, pp.447-466.
3. Bob Irving, "What's Being Done to Weld Metal-Matrix Composites?", *Welding Journal*, June 65-67, 1991.
4. B. P. Krishnan, N. Raman, K. Narayanaswamy and P. K. Rohatgi, "Performance of an-Si-Graphite Particle Composite Piston in a Diesel Engine", *Wear*, 60, pp.205-215, 1980.
5. M. Naka, J. C. Feng, and J. C. Schuster, "Phase Formation in SiC/ Metal Joints at High Temperatures", *Materials Transaction, JIM*, Vol. 37, No. 3, 1996, pp.394 to 398.
6. J. R. Kennedy, "Microstructural Observations of Arc Welded Boron- Aluminum Composites", *Welding Research Supplement*, March 120- 124, 1973.
7. P. G. Partridge, D.V. Dunford, "The role interlayers in diffusion bonded joints in metal matrix composites", *Journal of Materials Science* 26, 1991, pp. 2255-2258.
8. S. Fukumoto, A. Kasahara, A. Hirose, and K. F. Kobayashi, "Transient liquid phase diffusion bonding of continuous SiC fiber reinforced Ti- 6Al - 4V composite to Ti- 6Al- 4V alloy", *Materials Science and Technology*, September 807- 812, 1994, Vol. 10.
9. T. Wagner, R. Kirchheim and M. Ruhle, "Chemical Reactions at Metal / Ceramic Interfaces during Diffusion Bonding", *Acta metall. mater*, Vol. 43, No. 3, 1995, pp. 1053-1063.
10. C. Hu, H Xin, and T. N. Baker, "Formation of Continuous Surface Al- SiCp metal matrix composite by overlapping laser tracks on Al6061 alloy", *Materials Science and Technology*, March 227- 232, 1996, Vol. 12.
11. T. J. Lienert, E. D. Brandon, and J. C. Lippold, "Laser and Electron Beam Welding of SiCp Reinforced Aluminum A-356 Metal Matrix Composite", *Welding of composite*, Vol. 28, No. 11, 1993, pp.1341-1346.

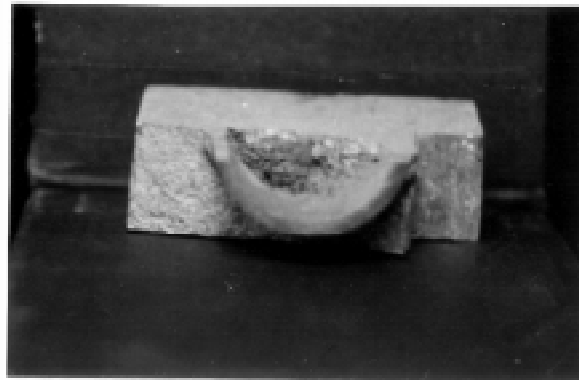


Fig1. The cast welding molten 700 °C A356 Al alloy and 600 °C 7005 Al/Al₂O_{3(0p)} composites seamless pipe, OM photo.

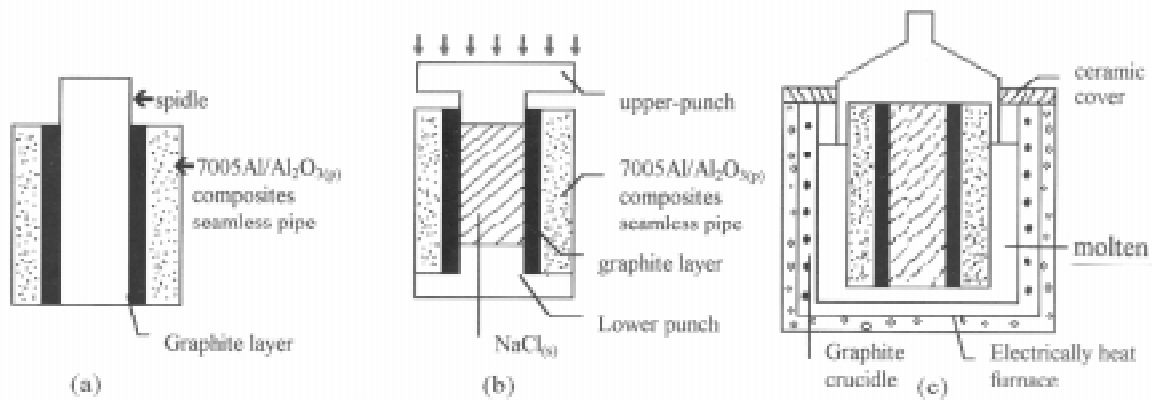


Fig2. The figure of the graphite layer and NaCl_(s) in 7005 Al/Al₂O_{3(0p)} composites seamless pipe.

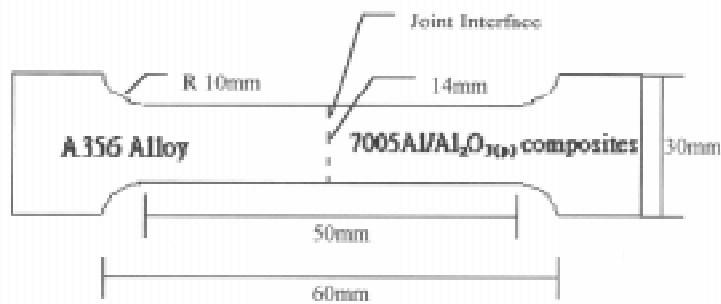


Fig3. The tensile specimen of the compound casting.

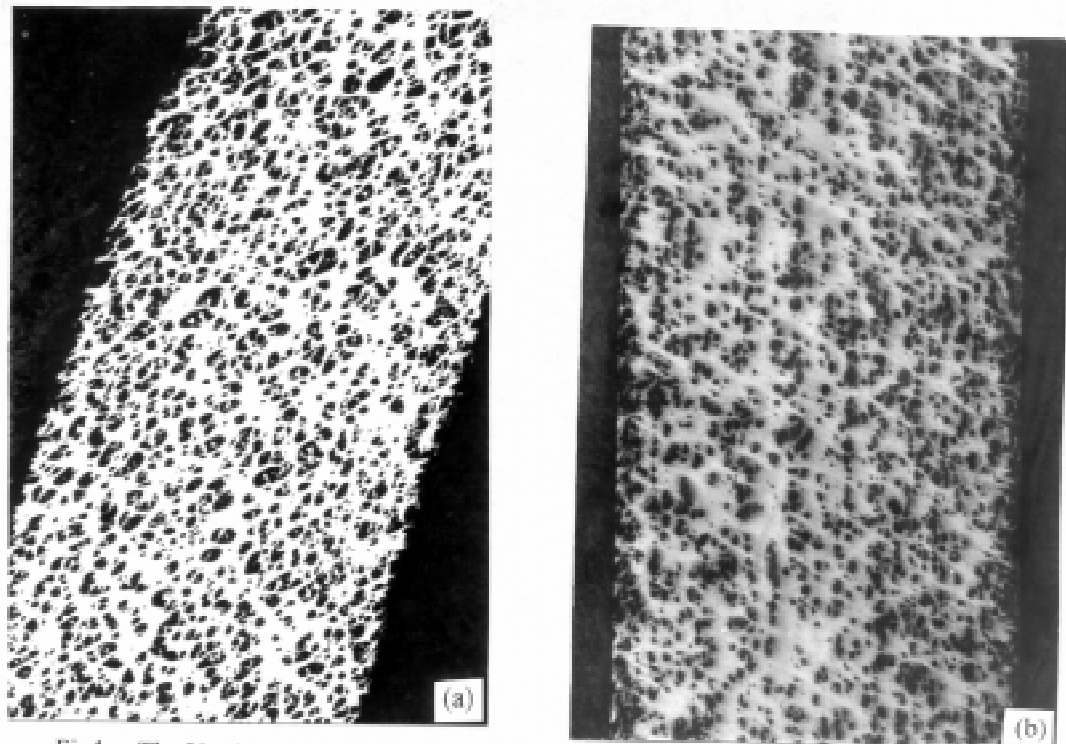


Fig4. The Vertical distribution of Al₂O₃ particle in the billet of Al alloy(a) and seamless pipe(b), OM. 100X

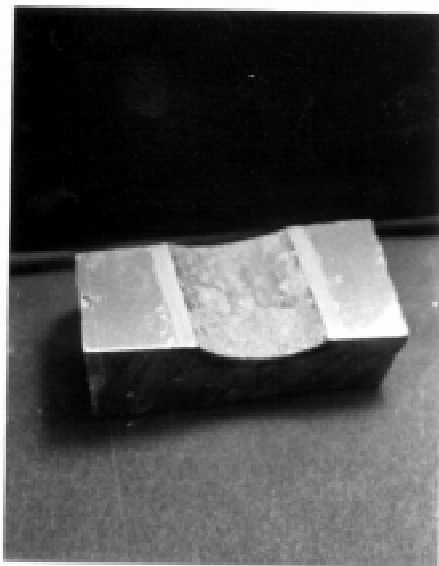


Fig5. The Cast welding 700 °C of 7005Al/Al₂O_{3(p)} composites seamless pipe and 700 °C A356 molten Al alloy, OM. 100X

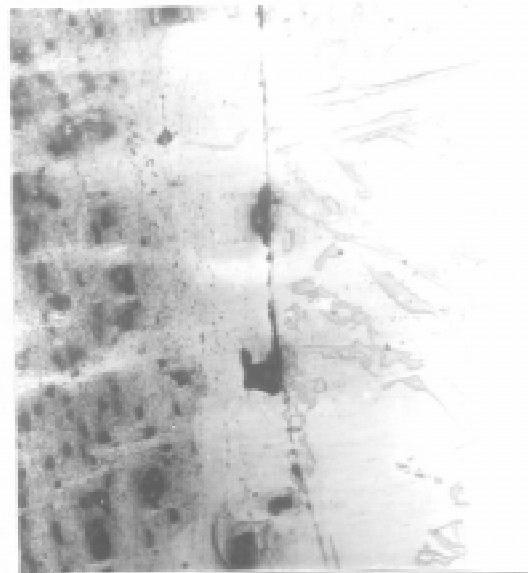
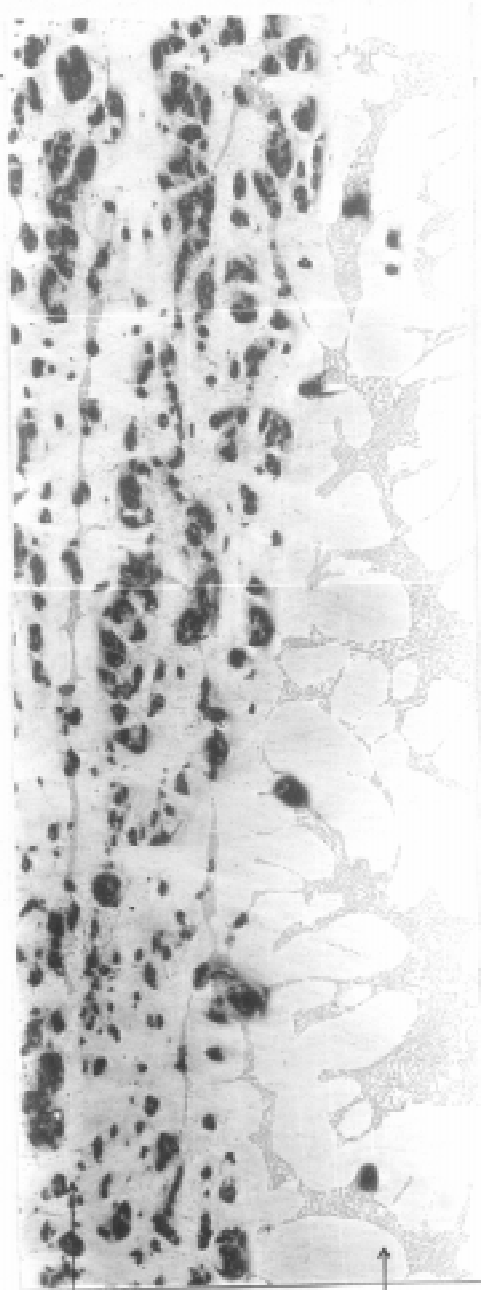
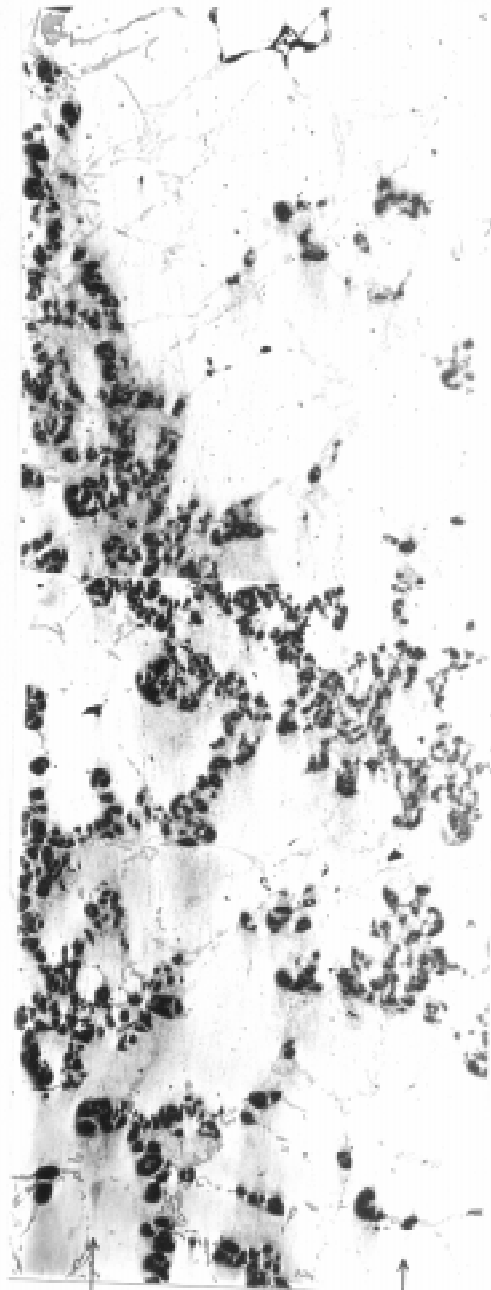


Fig6. The observation of joint 700 °C A356 molten Al alloy and 600 °C 7005Al/Al₂O_{3(p)} composites seamless pipes, OM.



7005Al/Al₂O₃(PI) composites
seamless pipe A356

Fig7. The observation of joint of 700 °C A356 molten Al alloy and 620 °C 7005Al/Al₂O₃(PI) composites seamless pipe, OM, 100X



7005Al/Al₂O₃(PI) composites
seamless pipe A356

Fig8. The observation of joint of 640 °C 7005Al/Al₂O₃(PI) composites seamless pipe and 700 °C A356 molten Al alloy, OM, 100X

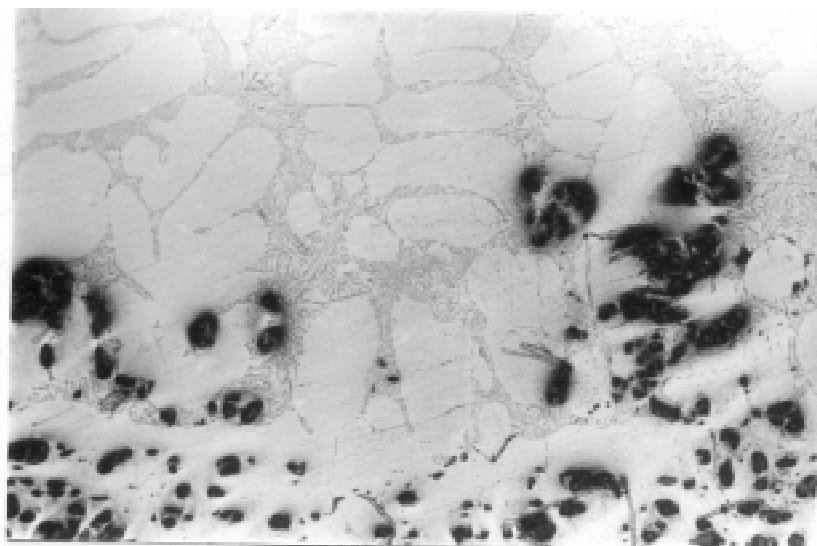


Fig9. Al₂O₃ particles be jostled to dendrite arm, OM.

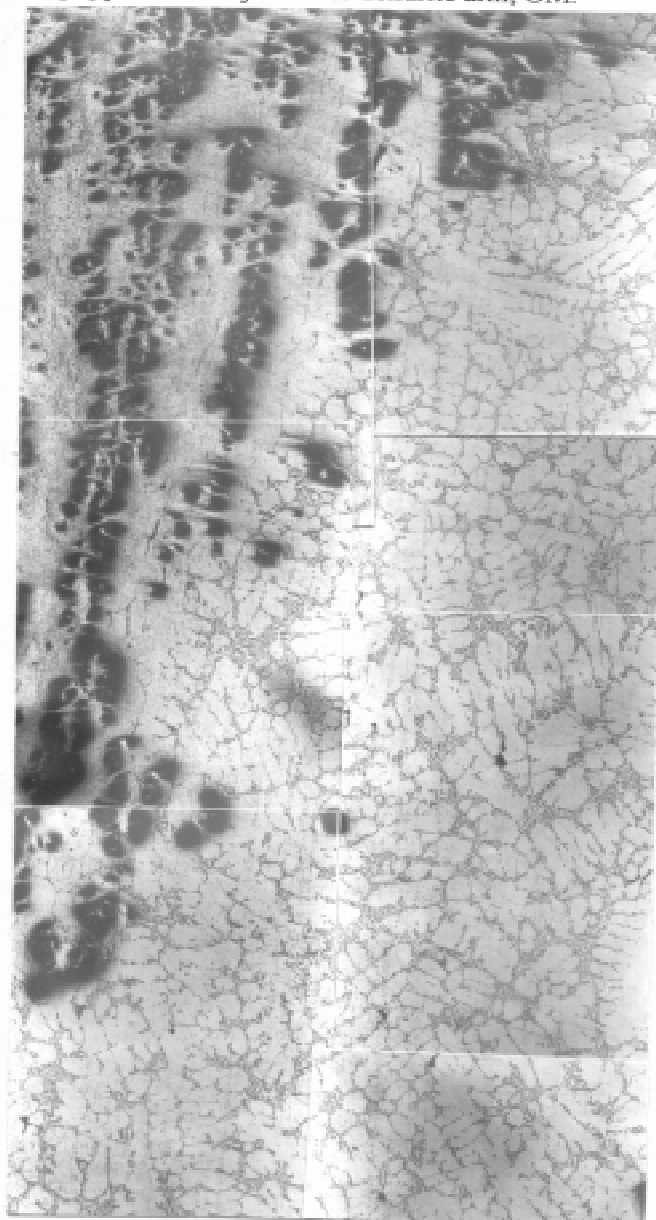


Fig10. The observation of joint of 700 °C A356 molten Al alloy and 660 °C 7005Al/Al₂O_{3(p)} composites rod, OM. 100X

THE EFFECT OF SQUEEZE CASTING AND HOT EXTRUSION PROCESS ON THE MECHANICAL PROPERTIES OF SIC_p/AL COMPOSITES

C. G. Kang¹, Y. H. Seo²

¹*Engineering Research Center for Net Shape and Die Manufacturing, Pusan National University, San-30, Jang Jeon-Dong, Kum Jung-Ku, Pusan 609-735, South Korea*

²*Department of Mechanical and Precision Engineering, Pusan National University*

SUMMARY: The silicon carbide particulate reinforced metal matrix composites were fabricated by melt-stirring method. The volume fractions of reinforcements were 5vol% to 20vol% and the mean size 13 to 22. Then MMC billets were extruded at 500 under the constant extrusion velocity of 2mm/min. Extrusion force, particle rearrangement, microstructure and mechanical properties of both primary billets and extruded bars have been investigated. The properties that were most useful in extruded composite products were the increased modulus of elasticity and strength. Through extrusion process, the particles could be more homogeneously distributed along the extrusion direction. Experimental values of Young's modulus and 0.2% offset yield strength for extruded composites were compared with theoretical values calculated by the Eshelby model.

KEYWORD: metal matrix composites, melt-stirring method, squeeze casting, homogeneous distribution, hot extrusion, optimal die

INTRODUCTION

In fabrication process of light parts, considerable attention has been given to the fabrication and property characterization of metal matrix composites. These composite systems have exhibited improvements in not only mechanical properties at room and elevated temperatures but also wear behavior. And high directional properties can be obtained by the secondary processing, such as extrusion, rolling, and forging etc.[1-4] Among the fabrication methods the mechanical agitation method which is to stir the liquid metal with solid ceramic particles have the problems as follows ; the uniform distribution of the reinforcements is disturbed due to the low wettability and the density difference between the molten metal and the reinforcements. Mechanical properties of extruded composites depend on many factors, e.g. degassing condition before extrusion and the extrusion conditions. If these parameters are chosen correctly, considerable improvements in tensile strength compared with the unreinforced alloy can be achieved. In this study, the particulate reinforced composites were manufactured with the distribution method improved on the convenient experimental equipment[5]. After tensile testing of primary specimens, fracture surfaces were examined in the SEM and microhardness measurements were carried out on polished specimens. To improve the mechanical properties, the primary billets were hot extruded with curved die. Tensile properties of the primary and secondary specimens were examined with the calculated results by Eshelby's theory[6].

EXPERIMENTAL

Al6061 alloy (Al-Si-Mg) was employed in this study [7]. The green silicon carbide particles (Norton 39 Crystolon grain) used in the experiments were supplied by Norton Company [8]. Manufacturing methods of primary billets were as follows. When the temperature of molten metal reached 670, particle addition was started. The impeller speed was controlled as 750 rpm and the preheating temperature of particles was 650. The temperature of the mold was 200. Applied pressure was 100 MPa. The speed of injection plunger was 16 mm/sec and the pressure time was 30 sec. The fabricated billets were of 44 mm diameter and of 70~80 mm height [4].

The extrusion experiment was carried out with the curved die of constant strain rate. Die profile as a function of die length Z was described by [9]

$$R(Z) = \sqrt{\frac{1}{\pi} \frac{F_0}{(\lambda - 1)Z/L + 1}} \quad (1)$$

- R : die profile
 F_0 : initial cross section area in billet (mm^2)
 λ : extrusion ratio (D_1^2/D_2^2)
 Z : extrusion direction
 L : die length (mm)

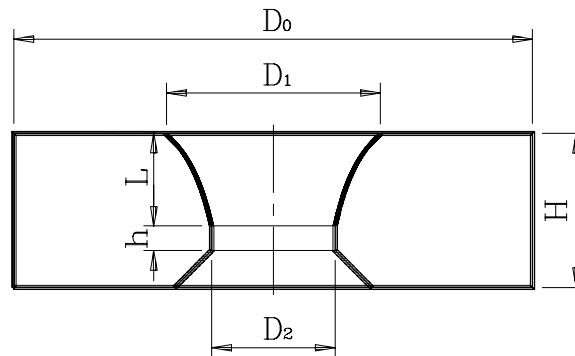


Fig.1: Curved shape die used for hot extrusion.

Table 1. Die dimensions used for hot extrusion

$D_0(\text{mm})$	$D_1(\text{mm})$	$D_2(\text{mm})$	L	h	H	λ
84	35	12	15	4	25	8.51

Fig.1 shows the curved shape die used for hot extrusion. The equipments for hot extrusion were composed of 25 ton universal testing machine, heating furnace, extrusion punch, upper/lower container, extrusion die and dummy block [9]. Table 1 shows die dimensions and extrusion ratio (λ) used for hot extrusion. The primary billets manufactured by melt stirring and squeeze casting were fabricated for extrusion billets by machine. The billets were fabricated to diameters of 35 mm and lengths of 60 mm. The billets, extrusion die and dummy block were put in upper container and were kept constant at the experimental temperature by furnace. The experimental temperature was set to 500. It was observed through a preliminary

experiments that the surface appearance of MMCs extruded by the conventional extrusion method was smooth at the ram speed 2mm/sec.

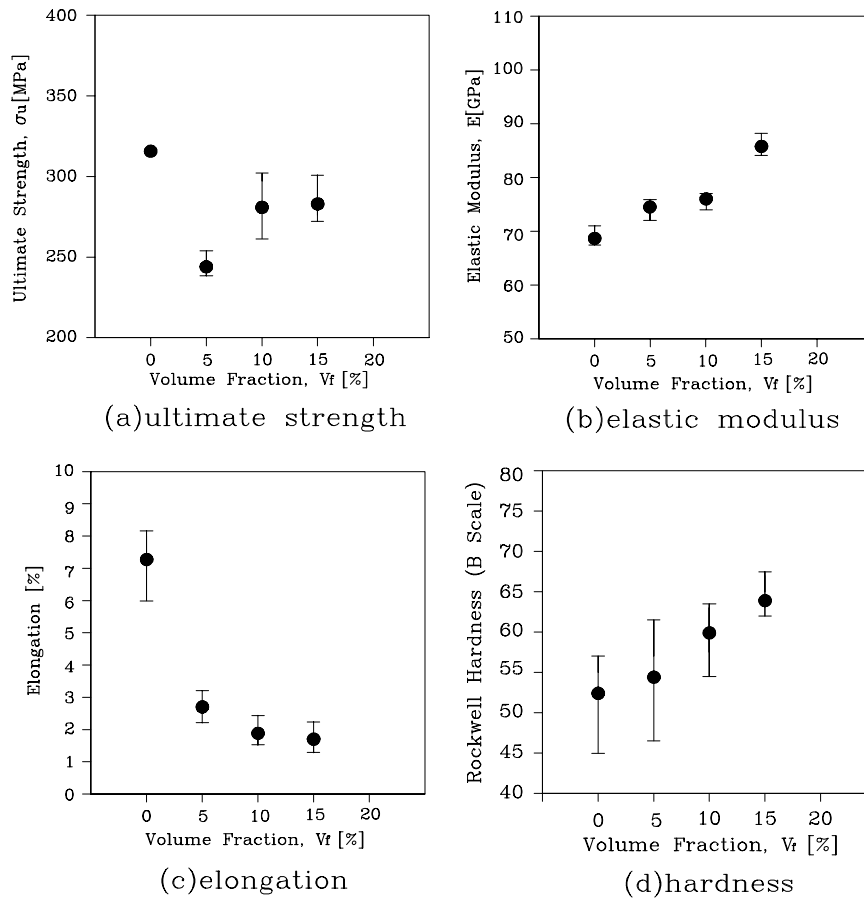


Fig.2(a)-(d): Effects of the volume fraction of reinforcement on mechanical properties of SiC_p(13)/Al6061.

RESULTS AND DISCUSSION

The specimens were heat-treated by a T6 thermal treatment and tested, at room temperature, on an MTS at a cross head velocity of 1/min.

Fig.2(a)(d) shows the effects of the volume fraction of reinforcement on mechanical properties of SiC_p(13)/Al6061. Fig.2(a) shows the tensile strength according to the variation of volume fraction of reinforcements. Tensile strength of the unreinforced Al6061 was rather higher than that of the reinforced materials. In SiC_p(13)/Al6061 composites manufactured by the melt-stirring and squeeze casting, when the volume fraction of reinforcements was above 5vol%, ultimate strength could be improved.

Fig.2(b) shows the variation of elastic modulus with the volume fraction of reinforcement. The elastic modulus was proportional to the volume fraction of reinforcement. Fig.2(c) shows the relationship between the elongation and the volume fraction. Elongations were decreased

with increasing volume fraction. Hardness tests were performed on a Rockwell Hardness Machine (B scale). In Fig.2(d), the increase of hardness was proportional to volume fraction.

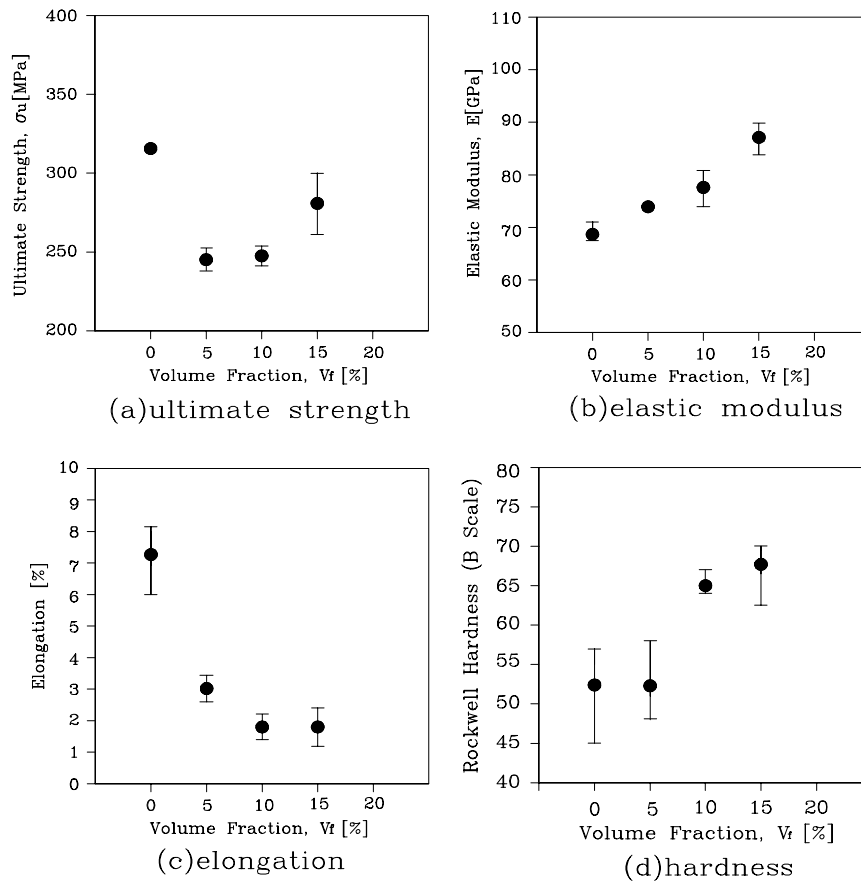


Fig.3(a)-(d): Effects of reinforcement content on mechanical properties of $\text{SiC}_p(22)/\text{Al6061}$.

Fig.3(a)(d) shows the effects of the volume fraction of reinforcement on mechanical properties of $\text{SiC}_p(22)/\text{Al6061}$.

In Fig.4(a)(c), SEM examinations were conducted on the tensile fracture surfaces. Some specimens failed during tensile testing, achieving lower than ultimate strength and elongation of the wrought Al6061. In all of these cases macroscopic features were observed on the fracture surfaces that could be correlated to the occurrence in the microstructure of large defects from the fabrication and processing of the material. In Fig.4(a) and Fig.4(b) for 5vol% and 10vol%, respectively, the large dimples were associated with SiC particulates. The smaller dimples were not associated with ductile fibrous failure of the aluminum matrix. This is consistent with the low ductility of these materials. In Fig.4(c) fracture surfaces of composite with the reinforcement of 15vol% were similar. Fracture surfaces consisted of cracked SiC particulates embedded in larger dimples and surrounded by finely dimpled aluminum matrix. As the interface bonding force between the matrix and the reinforcements was stronger, the ductile fracture regions Fig.4(c) were larger than those of Fig.4(a) and Fig.4(b). The improvement of strengthening effectiveness could be expected above 10vol% in $\text{SiC}_p(22)/\text{Al6061}$ composites manufactured by only melt-stirring and squeeze casting process.

SiC_p/Al6061 composites fabricated by the melt-stirring and squeeze casting couldn't exhibit improved mechanical properties as compared to the unreinforced Al6061.

Fig.5(a)(d) shows mechanical properties of 13 SiC_p/Al6061 extruded as function of volume fraction. In Fig.5(a), ultimate strengths for the volume fraction of 5, 10, 15 and 20vol% were 335, 339, 351 and 361MPa, respectively. After hot extrusion process, the ultimate strength was increased higher, about 25% to 35%, than that of the specimens fabricated by only melt-stirring and squeeze casting. From this results, it was improved linearly with increasing the volume fraction of the reinforcements.

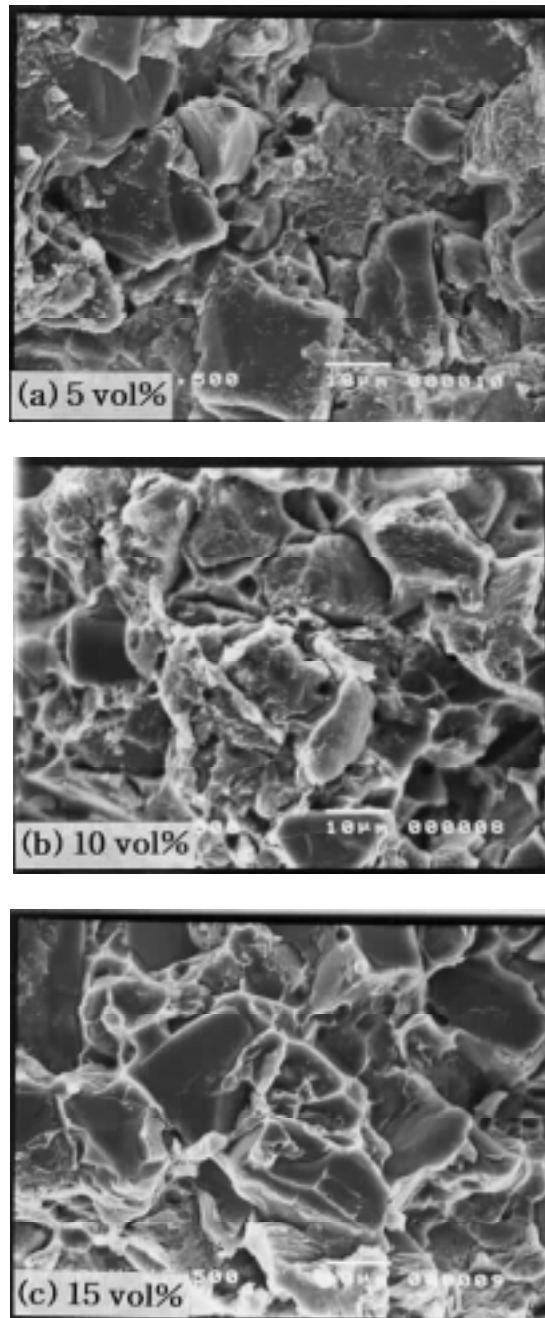


Fig.4: SEM fractograph of Al6061/SiC_p tensile specimen (average size of SiC_p=22).

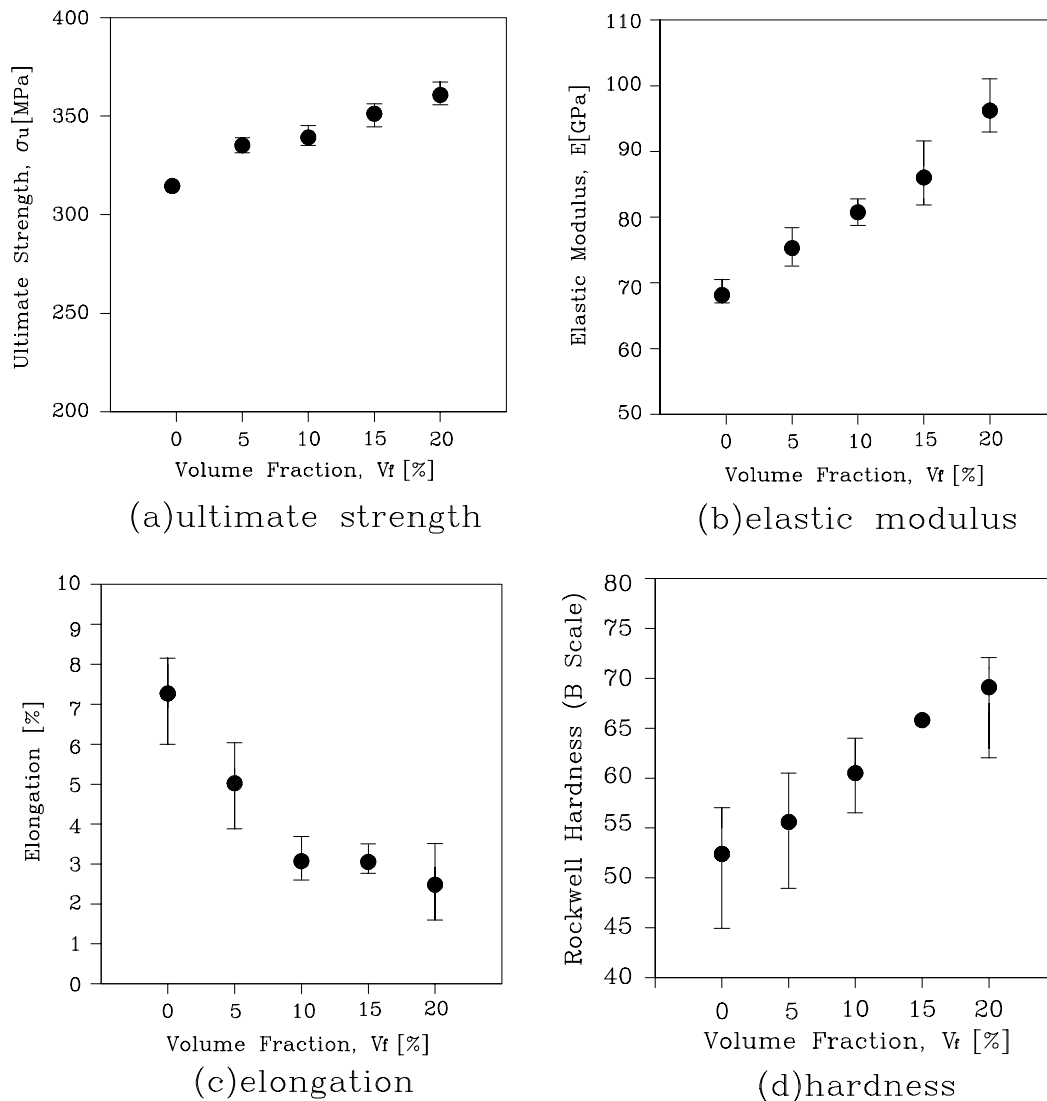


Fig.5(a)-(d): Mechanical properties of $SiC_p(13)/Al6061$ extruded as function of volume fraction.

Elastic modulus was proportioned to the increase of volume fraction in Fig.5(b). Elongation for the volume fraction 5, 10, 15 and 20vol% were 5.02, 3.08, 3.05 and 2.48%, respectively, in Fig.5(c). With the increase of the volume fraction, the stiffness was increased, however, the elongation was decreased. Fig.5(d) shows Rockwell hardness. Hardness for the volume fraction 5, 10, 15 and 20vol% were 55, 58.4, 67 and 70.7HR, respectively. Elastic modulus and hardness for the MMC specimens were improved linearly with increasing the volume fraction of the particles regardless of hot extrusion. Through extrusion process, however, the particles could be more homogeneously distributed along the extrusion direction.

Fig.6(a)(c) shows the microstructure for composites. The mean size of SiC_p is 13 and the volume fraction of SiC_p is 10vol%. The particulate reinforcements within the composite billet were conglomerated in the entry of extrusion container and were aligned in the middle of the container. The distribution state of the particulate reinforcements was improved in the exit of it[11].



Fig.6: Microstructure of particle arrangement during hot extrusion process with 13size, $V_f=10\text{vol}\%$ (a)Die entry (b)Die middle (c)Die exit (\rightarrow : extrusion direction).

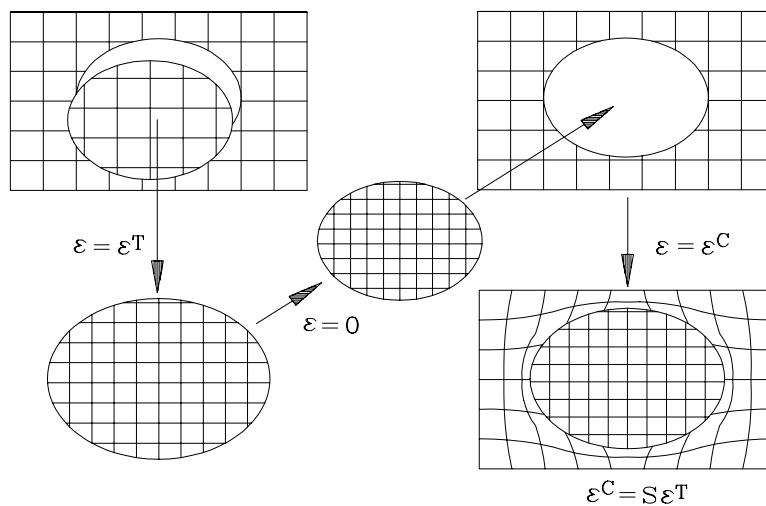


Fig.7: Eshelby's cutting and welding model.

THEORETICAL MODEL AND RESULTS

Eshelby's cutting and welding model is shown in Fig.7. The region of the reinforcement is cut from the unstressed elastically homogeneous material and the shape change is imagined to undergo a size change as a uniform ellipsoid. Then the strain is defined as the transformation strain ϵ^T . Surface tractions to make $\epsilon=0$ are applied in order to return to its initial shape before removal. There is no sliding along the interface between the matrix region and the reinforcement region, and the surface tractions are then removed. When equilibrium is reached, strain is defined as a constrained strain ϵ^C . The stress within the reinforcement can be calculated in terms of the strain ($\epsilon^C - \epsilon^T$) and the stiffness tensor of the material C_M [12].

$$\sigma_I = C_M(\epsilon^C - \epsilon^T) \quad (2)$$

ϵ^C can be obtained from ϵ^T by means of Eshelby ' S_{ij} ' tensor.

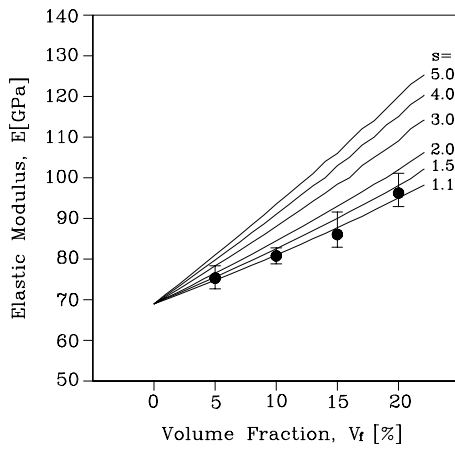


Fig.8: Comparison between the extrusion and Eshelby theory (13 SiC_p)

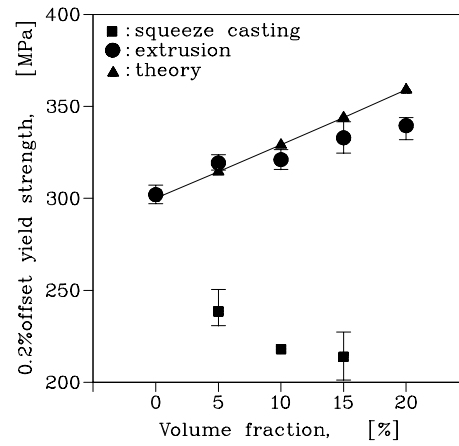


Fig.9: Comparison of 0.2% offset yield strength between the experimental results (22 SiC_p) and the theoretical analysis ($s=1.5$)

$$\epsilon^C = S_{ij} \epsilon^T \quad (3)$$

Mixture rule is used to include the volume fraction f of all the inclusions.

$$(1-f) \langle \sigma \rangle_M + f \langle \sigma \rangle_I = 0 \rightarrow \langle \sigma \rangle_M = -\frac{f}{1-f} \langle \sigma \rangle_I \quad (4)$$

The mean stresses are given as follows ;

$$\langle \sigma \rangle_M = -f C_M (S_{ij} - I) \epsilon^T, \quad \langle \sigma \rangle_I = (1-f) C_M (S_{ij} - I) \epsilon^T \quad (5)$$

Leading to the equation for the composite stiffness tensor C_C

$$C_C = [C_M^{-1} - f \{ (C_M - C_I) [S - f(S - I)] - C_M \}^{-1} \times (C_M - C_I) C_M^{-1} \Gamma^{-1} \quad (6)$$

The relation between the stress σ^A and the strain ε^A by the applied load can be written with the composite stiffness tensor.

$$\sigma^A = C_c (\varepsilon^A + \bar{\varepsilon}^A) \rightarrow \varepsilon_3^A + \bar{\varepsilon}_3^A = C_{3c}^{-1} \sigma^A = \frac{\sigma^A}{E_{3c}} \quad (7)$$

(E_{3c} : axial Young's modulus)

Fig.8 represents the comparison between experimental datas and theoretical analyses of the Eshelby model for SiC_p(13)/Al6061 composites. The mean values of experimental datas were within the limits of aspect ratios 1.1 to 2.0. It was difficult to obtain the uniform distribution of reinforcements through the conventional manufacturing, resulting in particle clustering and low work of adhesion. Experimental datas can be predicted with Eshelby approaches in the elastic region.

Tresca yield criterion is written as

$$\sigma_{YM} = \bar{\sigma}_{3M} - \bar{\sigma}_{1M} (= \Delta\sigma) \quad (8)$$

Flow occurs at an applied stress σ^A equal to

$$\sigma^A = \sigma_{YM} - (\langle \sigma_3 \rangle_M^A - \langle \sigma_1 \rangle_M^A) \quad (9)$$

The deviatric stress $\Delta\sigma$ to occur the yield stress in the matrix region may be written as

$$\Delta\sigma = (\bar{\sigma}_{3M} - \bar{\sigma}_{1M}) = \sigma^A + (\langle \sigma_3 \rangle_M^A - \langle \sigma_1 \rangle_M^A) \quad (10)$$

In Fig.9, when the volume fractions of reinforcements were 5vol%, 10vol%, 15vol% and 20vol%, after extrusion, 0.2% offset yield stresses for SiC_p(22)/Al6061 composites were 319MPa, 321MPa, 333MPa and 340MPa, respectively. The theoretical values were about - 1.5%, 2.4%, 3.3%, 5.7% higher than the experimental values, resulting from various reinforcement size high particle aspect ratio and local stress concentration in the vicinity of the reinforcements. Due to a factor of the inner defects this phenomenon appear in the initial deformation of the composites. It is very difficult to predict exactly mechanical properties of particulate reinforced metal matrix composites.

CONCLUSIONS

Mechanical properties of primary billets manufactured by melt-stirring and squeeze casting method were compared with both the strengths of extrusion specimen and the predicted values of Eshelby model for SiC_p/Al6061 composites, respectively. The following results were obtained by theoretical and experimental datas.

- (1) SiC_p/Al6061 composites fabricated by the melt-stirring and squeeze casting couldn't exhibit improved mechanical properties as compared to the unreinforced Al6061.
- (2) After hot extrusion process, the ultimate strength was increased about 25% to 35%, which is higher than that of the specimens fabricated by only melt-stirring and squeeze

- casting. From this results, it was improved linearly with increasing the volume fraction of the reinforcements.
- (3) Elastic modulus and hardness for the MMC specimens were improved linearly with increasing the volume fraction of the particles regardless of hot extrusion. Through extrusion process, however, the particles could be more homogeneously distributed along the extrusion direction.
 - (4) The experimental results obtained through an extrusion process of SiC_p/Al6061 composite were in a good agreement with the theoretical datas.

REFERENCES

1. H. Morimoto, H. Iwamura, K. Ohuchi, Y. Ashida, "Fabrication of thin wall tubes of SiC whisker reinforced 6061 aluminum alloy composite by extrusion and their mechanical properties", J. of Jap. Inst. Light Metal, Vol.45, No.2, 1995, pp.8287
2. S. Watanabe, K. Saitoh, S. Okaniwa, "Extrudability of discontinuous aluminum alloy composite billets", J. of Jap. Inst. Light Metal, Vol.40, No.4, 1990, pp.278284
3. T. Hikosaka, "Effect of Thermal Cycling on the Properties of Aluminum Alloy-Alumina Short Fiber Composites Hot Extruded", J. of Jap. Inst. of Casting, Vol.66, No.6, 1994, pp.424429
4. D. F. Hasson, S. M. Hoover & C. R. Crowe, "Effect of thermal treatment on the mechanical and toughness properties of extruded SiC_w/aluminium 6061 metal matrix composite", J. of Mat. Sci. 20, 1985, pp.4147~4154
5. Young-Ho Seo, Chung-Gill Kang, "Particle Behavior Characteristics and Mechanical Properties of SiC_p/Al Composites with Squeeze Casting Process", Journal of the Korean Foundrymen's Society, Vol.15, No.1, 1995, pp.2534
6. Y. D. Eshelby, "The determination of the elastic field of an ellipsoidal inclusion, and related problems", 1957, pp.376396
7. Metal Handbook, Vol.2, ASM, 1990, pp.102-103
8. Norton Co., Advanced ceramics engineered materials, pp.2935
9. C. G. Kang, Y. H. Seo, "Extrusion Die Design for Orientation Control of Short Fiber Reinforced Aluminum Metal Matrix Composites", Second International Conference Composites Engineering, New Orleans, Aug, 1995, pp.2124
10. Y. H. Seo, C. G. Kang, "Deformation Behaviour Characteristics of Reinforcement in Hot Deformation of Metal Matrix Composites", Proceedings of the KSME Fall Annual Meeting(), 1994, pp.179184
11. Y. Lu, P. K. Liaw, "Effects of Particle Orientation in Silicon Carbide Particulate Reinforced Aluminum Matrix Composite Extrusions on Ultrasonic Velocity Measurement", J. of Comp. Mat., Vol. 29, No. 8, 1995, pp.10961115
12. D. Huda, M. A. El Baradie, M. S. J. Hashmi, "Analytical study for the stress analysis of metal matrix composites", J. Mater. Process. Tech. 45, 1994, pp.429~434

MICROSTRUCTURE OF $\text{LaB}_6\text{-ZrB}_2$ IN SITU COMPOSITE PREPARED BY ELECTRON BEAM HEATED MELTING METHODS

Chang-Ming Chen, W. C. Zhou, L. T. Zhang, L. F. Cheng and Y. D. Xu

National Laboratory of Solidification Processing, Northwestern Polytechnic University, Xi'an 710072, P.R. China

SUMMARY: Directional solidification of $\text{LaB}_6\text{-ZrB}_2$, by use of an electron beam heating technique, yielded orientated ZrB_2 fibers in a LaB_6 matrix. The average diameter of the ZrB_2 fibers was about 0.2-1.2 μm , with fiber lengths up to 100 μm . Primary plate-like LaB_6 dendrites formed upon the solidification of an ingot with a composition of $\text{LaB}_6\text{-18 wt\% ZrB}_2$. LaB_6 was the first phase to nucleate when eutectic growth occurred, and ZrB_2 showed a non-faceted growth. For the ingot solidified with planar growth the orientation relation of the phases was:

Growth direction : $[001]_{\text{LaB}_6} // [00.1]_{\text{ZrB}_2}$
Interfacial plane: $(\bar{1}10)_{\text{LaB}_6} // (01.0)_{\text{ZrB}_2}$

KEYWORDS: lanthanum hexaboride, zirconium diboride, eutectic microstructure, in situ composite, electron beam

INTRODUCTION

In situ composites prepared by directional solidification have received considerable attention because of their enhanced interphase bonding and microstructure stability. In the past decades, a great effort has been directed towards developing oxide-oxide [1] and metal-metal [2] eutectic in situ composites, and a few types of carbide-diboride eutectic systems [3] have also been studied. However, little work has been done on boride-boride eutectics which usually possess higher melting points. Recently, the d- and f- transition metal-boride eutectics have been studied by Paderno [4] and revealed unusual thermionic and mechanical properties. The $\text{LaB}_6\text{-ZrB}_2$ system was reported to have the best fracture toughness (up to 20.3 - 27.8 $\text{MPa}\cdot\text{m}^{1/2}$) and the highest bend strength (up to 1200 MPa). It appears that the boride in situ composites are potentially a new type of structural materials with unusual mechanical properties. Although good mechanical properties of these composites have been reported, the morphology and crystallography of the $\text{LaB}_6\text{-ZrB}_2$ eutectic are not clear. The aim of this work was to investigate the microstructure and crystallography of directionally solidified $\text{LaB}_6\text{-ZrB}_2$ eutectic by using a floating zone melting furnace with electron beam heating.

EXPERIMENT

The LaB_6 and ZrB_2 powders used in the experiment were produced in Institute of Materials Problem in Ukraine. The purity of LaB_6 was >99.4%, with major impurities of 0.3% Fe and 0.1% O, and with Si and Mg as minor impurities. The purity of ZrB_2 was >98.2%, with major impurities of 0.3% Fe, 0.3% Mg and 0.15% O, and minor impurities of 0.03% Ca and 0.04% Al. The impurity concentrations were reported by the supplier.

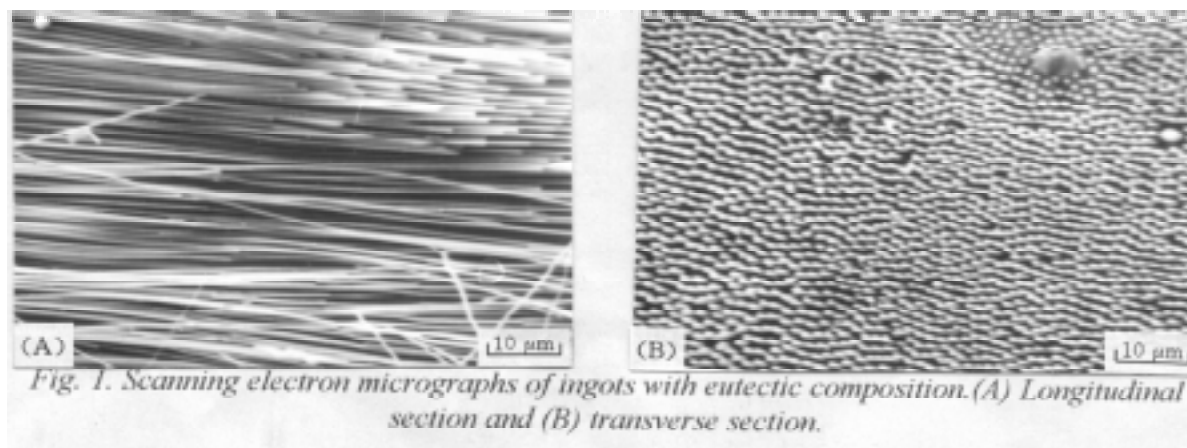
Ordan'yan [5] reported an eutectic composition of 80 wt % LaB_6 and 20 wt % ZrB_2 , with a liquidus temperature of 2470°C, and Paderno [4] reported 79 wt % LaB_6 and 21 wt % ZrB_2 at the same temperature. As the constituents evaporate in high vacuum at high temperatures, the variation of composition may cause an irregular structure, so samples with different starting compositions were prepared to obtain the regular structure. Our experiments showed that the sample with a composition of 80 wt % LaB_6 and 20 wt % ZrB_2 had no primary phase, and this composition was preferred for our studies.

The weighed powders were blended in an ethanol slurry for 1 hr, then dry pressed and melted by electric arc to form rods. The rods are about 6 mm in diameter and 120 mm in length. Directional solidification was accomplished by a floating zone melting furnace with electron beam heating, with 10 kW of power and a vacuum of 5×10^{-5} Torr.

The final specimens were cut by electric discharging along and across the axes of the rods to get longitudinal and transverse sections. After polished with diamond paste and etched with nitric acid, the specimens were examined by ARMA Model 1000B scanning electron microscope (SEM). Line-intercept method was used to measure the interfiber spacing. Thin foils were prepared by ion beam thinning and examined by JEM-200CX transmission electron microscope (TEM) to determine the crystallography of the eutectic phases.

RESULTS AND DISCUSSION

All the samples by zone melting had a gray surface layer, probably because of higher evaporation rate of LaB_6 than ZrB_2 at high temperature, as higher concentration of LaB_6 was determined in the substance collected from the furnace inwall than that in the ingot and almost single ZrB_2 phase was formed on the surface of the samples. The slower the growth rate, the thicker the surface layer formed on the sample, and cracks usually occurred on the layer, probably because of evaporation of boride at a solid state. Fig. 1 shows the scanning electron



micrographs of an ingot at eutectic composition solidified at a rate of 2.5 mm/min. The structure consists of very fine orientated ZrB_2 fibers (light phase) uniformly distributed in the matrix of lanthanum hexaboride. The average diameter of ZrB_2 fibers was about 0.2-1.2 μm , with fiber lengths up to 100 μm . The fibers were generally parallel to the rod axis, as the growth direction follows the thermal gradient. Considerable off-axis growth was observed at the periphery of rods, especially at higher growth rates. Disrupted structure was observed in the eutectic samples, as shown in Fig. 2(A). The disrupted structure was seen in the early stage of growth in metal eutectics [6] before establishment of a preferred orientation, so the growth direction may not be the preferred orientation in LaB_6 - ZrB_2 system when observing the disrupted structure. Another reason for the formation of the disrupted structure may be a power fluctuation. As boride evaporated and trapped gas run out when the primary rod began melting, the electron beam emission may be blocked because of bad vacuum and the power may fluctuate abruptly. This may cause nucleation in front of the liquid/solid interface before a preferred growth occurred along the thermal gradient. In this case, the nucleated phase appears to be LaB_6 , and ZrB_2 fiber branching was observed in the eutectic grain formed afterwards.

In certain growth condition, the non-planar front was obtained. Fig. 2(B) is an example of longitudinal section showing a cellular growth, and “colony” structure was formed at a growth rate of 8 mm/min. As growth direction is normal to the solid-liquid interface, the planar interface must be maintained to obtain well orientated eutectic structure.

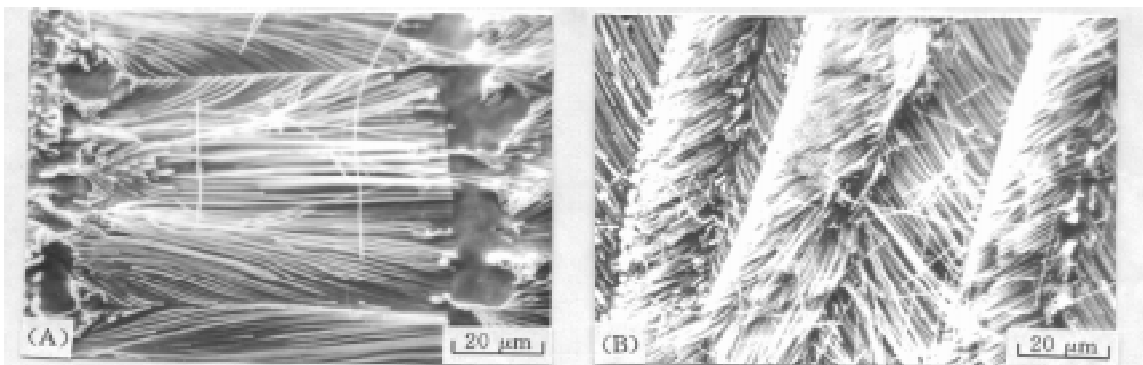


Fig. 2. SEM micrography of eutectic ingot along the longitudinal section showing (A) disrupted structure and (B) colony structure.

The rods with off-eutectic compositions were also directionally solidified at a growth rate of 1.5 mm/min. Fig. 3 shows a SEM micrograph of a sample with a hypoeutectic composition of

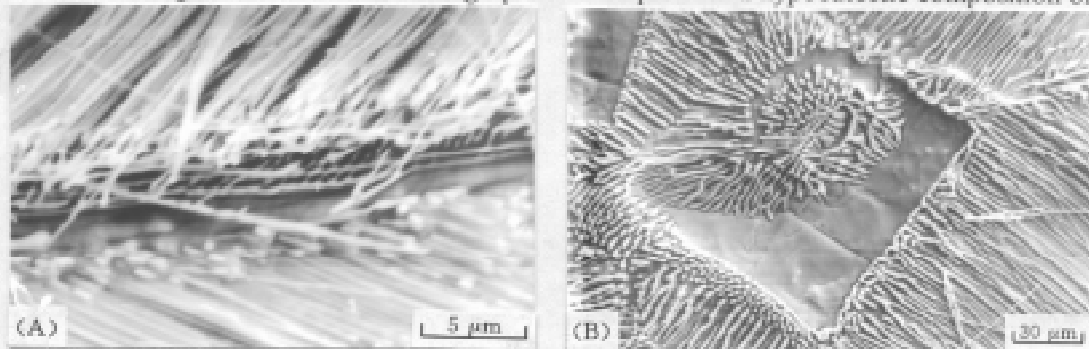


Fig. 3. SEM micrographs of hypoeutectic ingots. (A) Longitudinal section and (B) transverse section

The rods with off-eutectic compositions were also directionally solidified at a growth rate of 1.5 mm/min. Fig. 3 shows a SEM micrograph of a sample with a hypoeutectic composition of

$\text{LaB}_6\text{-ZrB}_2$. Primary plate-like LaB_6 appears, and obviously different width of LaB_6 plates is observed along the growth direction. In a transverse section of the sample, some rectangular LaB_6 phase are observed and the spiral growth appears parallel to $[001]_{\text{LaB}_6}$ direction. Such orientation assumption would agree with tetragonal symmetry of lanthanum hexaboride and the observed circular growth morphology of spirals. The similar behavior has been observed where growth morphology and crystallographic orientations are very closely coupled [7,8]. The eutectic appears to grow directly from the primary lanthanum hexaboride. In Fig. 4, a transverse section of a hypereutectic ingot, primary ZrB_2 clearly grows in a dendritic manner and has a layer of LaB_6 surrounding it before any eutectic appears.

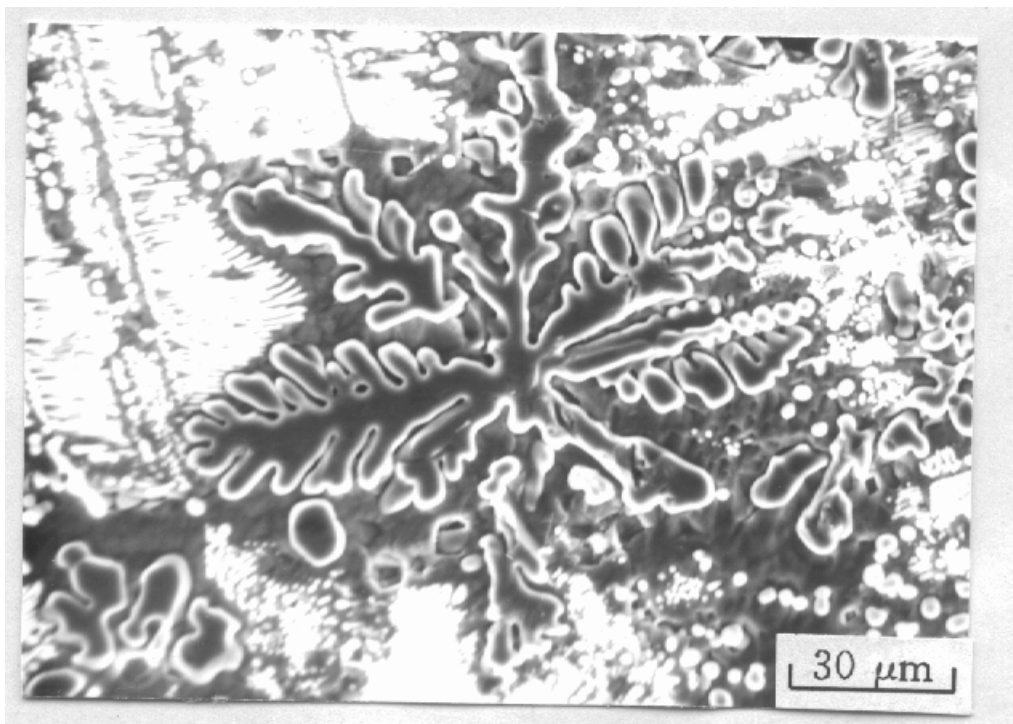


Fig. 4. SEM micrographs of hypereutectic ingots along the transverse section showing the morphology of primary ZrB_2 phase.

Fig. 5 shows a transmission electron micrograph and an electron diffraction pattern taken from a longitudinal section of an eutectic ingot at a growth rate of 2.5 mm/min. The fibers were well orientated along the growth direction and the interfacial plains were smooth. This suggests that low energy interface be formed in this system. The growth direction of the LaB_6 matrix and the ZrB_2 fibers were $[001]_{\text{LaB}_6}$ and $[00.1]_{\text{ZrB}_2}$ direction respectively, which were perpendicular to $(001)_{\text{LaB}_6}$ plane. The crystallographic relation between the matrix and the fiber deduced from Fig. 5(B) was:

$$\begin{aligned} \text{Growth direction : } & [001]_{\text{LaB}_6} // [00.1]_{\text{ZrB}_2} \\ \text{Interfacial plane : } & (\bar{1}10)_{\text{LaB}_6} // (01.0)_{\text{ZrB}_2} \end{aligned}$$

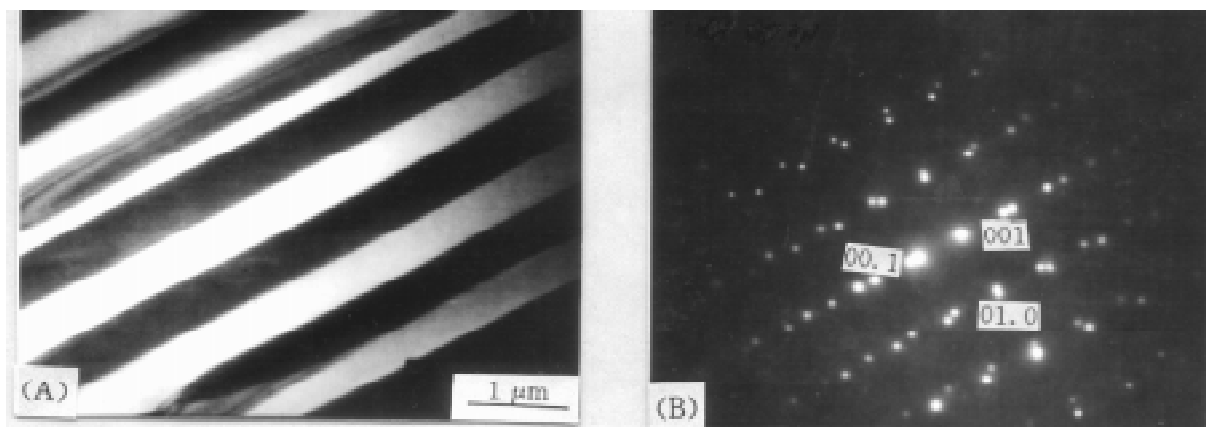


Fig. 5. (A) Transmission electron micrograph and (B) selected area electron diffraction for the longitudinal direction of $\text{LaB}_6\text{-ZrB}_2$ eutectic.

Fig. 6 shows the structural relation between LaB_6 and ZrB_2 phases. It is known that lanthanum hexaboride has a cubic CaB_6 -type structure with a single cubic arrangement of metal atoms centered by boron atom octahedron. The zirconium diboride has hexagonal AlB_2 type structure with alternate crystallographic plane along the hexagonal c axis, having flat hexagonal nets of metal or boron atoms. The intraoctahedral B-B distance in lanthanum hexaboride and B-B distance in zirconium diboride in the flat hexagonal net are 0.1765 nm and 0.1829 nm respectively. The lattice mismatch between the matrix and the fiber is only 3.16%, well below the critical value of 16% for a semicoherent interface[1].

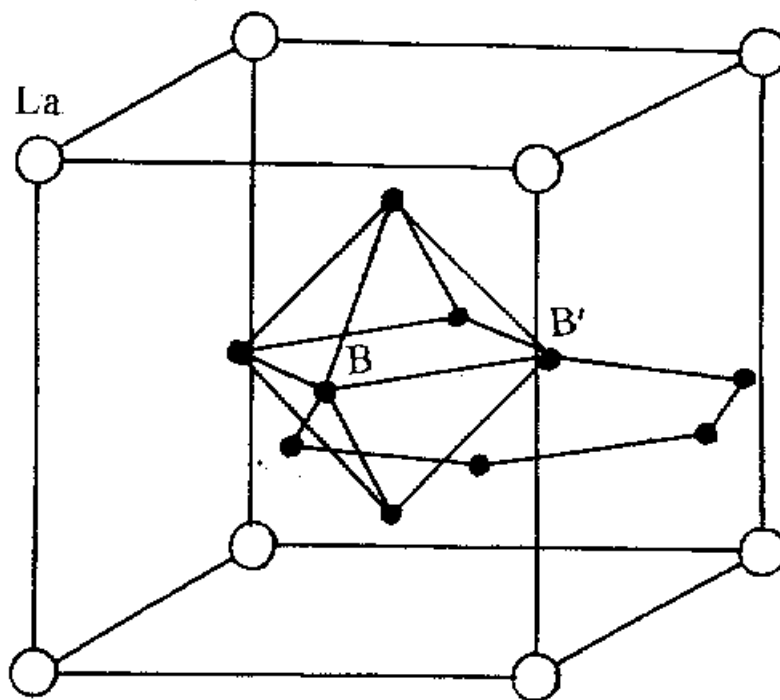


Fig. 6. Structural relation between LaB_6 and ZrB_2 phases during cocrystallization. $\text{B-B}'$ is a common boron pair shared by both phases.

CONCLUSIONS

Orientated microstructures of $\text{LaB}_6\text{-ZrB}_2$ system have been produced by use of a electron beam heated floating zone melting method. For the ingots with planar growth, both phases grow in the [001] directions with orientation: $(\bar{1}10)_{\text{LaB}_6} // (01.0)_{\text{ZrB}_2}$. The misfit between the two phases was calculated to be below the critical value of 16% for a semicoherent interface.

REFERENCES

1. Minford, W. J., Bradt, R. C., and Stubican, V. S., "Crystallography and Microstructure of Directionally Solidified Oxide Eutectics", J. Am. Ceram. Soc., Vol.62, No.3-4, 1979, PP.154-157.
2. Hertzberg, W., And Kraft, K. W., "Fracture Mechanism in Controlled Cu-Cr Eutectic Alloy", Trans. Met. Soc. AIME, Vol.227, 1963, PP.580-85.
3. Sorrell, C., Beratan, H. R., Bradt, R. C., and Stubican, V. S., "Directional Solidification of (Ti,Zr) Carbide-(Ti,Zr) Diboride Eutectics", J. Am. Ceram. Soc., Vol.67, No.3, 1984, PP.190-194.
4. Paderno, Yu. B., Paderno, V. N. And Filippov, V. B., "Some Peculiarities of Structure Formation in Eutectic d- and f- transition Metals Boride Alloys", AIP Conf. Proc., Vol.231, 1990, AIP, New York, 1991, PP.561-569.
5. Ordan'yan, S., Paderno, Yu. B., and Horoshilova, I. K., "Interaction in the system $\text{LaB}_6\text{-ZrB}_2$ ", Powder Metallurgy USSR, No.11, 1983, PP.87-89 (in Russian).
6. Hogan, M., Kradt, R. W., and Lemkey, F. D., "Eutectic Grains", Adv. Mater. Res., Ed. by Herbert Herman, New York, 1971, PP.83-216.
7. Frank, C. and Ives, M. B., "Orientation-Dependent Distribution of Germanium", J. Appl. Phys. Vol.31, 1960, PP.1996-2002.
8. Gupta, P., Wang, F. Y, and Li, C. H., "Growth in the Eutectic System $\text{BaNb}_2\text{O}_6\text{-SrNb}_2\text{O}_6$ ", J. Crystal Growth, Vol.29, No.2, 1975, PP.203-208.

NANO-STRUCTURES OF PITCH-BASED CARBON FIBERS AND THE COMPATIBILITY WITH ALUMINUM MATRIX COMPOSITES

Takakazu Suzuki

*National Institute of Materials and Chemical Research
1-1, Higashi, Tsukuba, Ibaraki 305, Japan*

SUMMARY: The degradation of pitch-based carbon fibers at the interface of aluminum and fibers which have wide range of Young's moduli and variety of structures has been studied. The tensile strengths of the composites before and after heating at 773-873K for 2h in Ar, have been examined. The X-ray structure parameters: $L_c(002)$ and d_{002} , and the nano-structures: radial-, random-, and onion-structure have been evaluated. The interfacial interaction of the fibers and aluminum has been discussed with the results of TEM and EDX. The tensile strength changes drastically with nano-structural difference. The onion structured fibers where the basal planes of graphitic sheets are oriented in the direction of parallel to the surface, show less reactivity with aluminum than the other structured fibers. It follows from this that structurally controlled pitch-based carbon fibers are effective to enhance the properties of the carbon fiber reinforced aluminum.

KEYWORDS: pitch-based carbon fibers, $L_c(002)$, d_{002} , random-, radial-, onion- structure, compatibility, aluminum .

INTRODUCTION

Recently pitch-based carbon fibers of various types of structure and wide variety of Young's moduli (E), derived from a coal or a petroleum pitch, have been developed. Although a large number of researches have been carried out into carbon fiber/aluminum composite system [1-9], little is known about the compatibility of those various pitch-based carbon fibers with aluminum.

It has been known that more graphitized pitch-based carbon fibers are less reactive with aluminum than PAN based carbon fibers [4]. The fact suggests that pitch-based carbon fibers have advantage in the reinforcement for aluminum matrix composites. Kohara and Muto reported that the different structure of aluminum carbide crystal caused different kinds of the fracture at the interface of PAN based-carbon fibers and aluminum [7].

The purpose of this paper is to investigate the compatibility with pitch-based carbon fibers and aluminum for the development of aluminum matrix composites. The changes in tensile strength of pitch-based carbon fibers/aluminum before and after heat treatment have been investigated.

The X-ray structure parameters and the nano-structures of the pitch-based carbon fibers have been examined. The interface interaction of the fibers and aluminum have been discussed with TEM and EDX analysis.

EXPERIMENTAL

Preparation of Pitch-based Carbon Fibers/Aluminum Composites

MOCVD from tri-isobutyl aluminum was applied for preparations of pitch-based carbon fibers/aluminum composites. Aluminum of 1 μ m thick was formed on carbon fibers uniformly without degradation by CVD process at 533K in deposition temperature, 3990Pa in Ar, whose throwing power for the multifilament was excellent. The pitch-based carbon fibers used and PAN-based carbon fibers for comparison are listed in Table 1. The fibers represented by NS - were supplied from Nippon steel Co., XN-, JIS- were from Nippon Petrochemicals Co., Ltd., P- was from The Union Carbide Co. currently renamed as Amoco Performance Products Co., and T300 and M40 were from Torey Co.

The pitch-based carbon fibers/ aluminum composites were heated at 773- 873K for 7.2ks in Ar of 96 kPa. Some composites after the heat treatment were immersed into a 5 mass% HF aqueous solution at room temperatures in a few minutes until dissolving out aluminum.

Table 1: Properties of the carbon fibers

fiber	tensile strength	E	$L_c(002)$	d_{002}	nano-structure	remark
NS-20	2068MPa	189GPa	2.56 nm	0.3456 nm	random	1
XN-30	3230MPa	294GPa	6.97 nm	0.3458 nm	radial	2
NS-30	2538MPa	309GPa	-	-	random	1
P-55	2069MPa	379GPa	14.0 nm	0.3439 nm	radial	2
NS-40	2597MPa	404GPa	8.85 nm	0.3430 nm	random	2
XN-50	3230MPa	490GPa	15.8 nm	0.3428 nm	radial	1
JIS-50	3880MPa	505GPa	14.1 nm	0.3445 nm	onion	2
XN-60	3230MPa	588GPa	-	-	radial	2
NS-60	2734MPa	597GPa	20.3 nm	0.3442 nm	random	1
XN-70	3293MPa	666GPa	19.9 nm	0.3412 nm	radial	2
JIS-70	3961MPa	704GPa	16.4 nm	0.3433 nm	onion	2
T300	3100MPa	250GPa	1.6 nm	0.3613 nm	particle	PAN
M40	4410MPa	392GPa	3.0 nm	0.3560 nm	particle	PAN

1:coal-pitch, 2:petroleum-pitch

Tensile Strength of the Pitch-based Carbon Fibers/Aluminum

The ultimate tensile strengths of the composites and fibers were quantified by a tensile machine (Minebea TCM-50). The tensile speed was 8m/s. More than 20 specimens in every series were applied for testing. All the data were evaluated with the Weibull analysis to compare the mean value, the variation coefficient and the Weibull parameter for each series.

Analysis by SEM, XRD, TEM and EDX The interlayer spacing between graphitic planes: d_{002} of the pitch-based carbon fibers and the thickness of graphitic crystallite: $L_c(002)$, were determined from the (002) profile obtained. The peak position and the width at half maximum intensity of the corrected profiles supplied the values of d_{002} and $L_c(002)$.

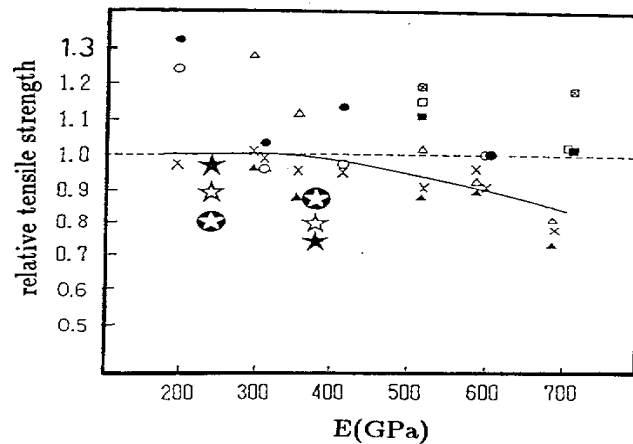
To confirm and quantify the aluminum carbide formation of heat treated P-55/aluminum composite at 773-873K for 7.2ks, gas chromatogram (Simadu GC 9A) and 40kV XRD (Rigaku GFX-RAD3C) were used.

The interfaces of pitch-based carbon fibers/ aluminum after the heat treatment were analyzed with TEM and EDX. The TEM studies were carried out on 300kV TEM instrument (Hitachi H-9000HR). The EDX studies were carried out on FESTEM instrument (VG HB501) and 100kV XMA instrument (KEVEX DELTA) whose probe was 1nm ϕ .

RESULTS AND DISCUSSION

Tensile Strength of the Pitch-based Carbon Fibers/Aluminum Composites

The relative tensile strength of the pitch-based carbon fibers/aluminum composite based on Weibull analysis are shown in Fig. 1. Here, the relative strength means the value divided the second tensile strength after some treatments by the original tensile strength of pitch-based carbon fibers. With the increase of the Young's modulus of the fibers (E), the relative tensile strength divided the strength of the aluminum coated fibers by the tensile strength of the no-coated fibers before heat treatment, decreases. The relative strengths of coal pitch-based carbon fibers/aluminum are slightly higher than 1. On the other hand, the relative strength of petroleum pitch-based carbon fiber/aluminum with heat treatment is slightly less than 1, in spite of the same fabrication condition and the same heat treatment are applied. The pitch-based carbon fiber recovers its original strength, if there is no degradation in the fibers. In other words, the decrease of the strength of fibers removed from aluminum is interpreted as fiber degradation itself. The tensile strength of pitch-based carbon fibers removed from aluminum without heat treatment tend to recover its original strength. The relative strength removed from aluminum after heat treatment, however, decreased gradually as a function of the Young's modulus.



symbols	radial	random	onion	PAN	Al removal
before heating	△	○	□	☆	
after heating	▲	●	■	★	X □ ☆

Figure 1. Changes in the relative tensile strengths of carbon fibers/aluminum composites and aluminum removal fibers

Fiber Strength after Removal of Aluminum

Here, as shown in Fig. 1, the relative tensile strengths of the fibers are examined after the aluminum is dissolved in a 5 mass% aqueous solution of HF. Generally after the aluminum is removed the fiber should exhibit its original properties, unless fiber degradation has occurred due to the aluminum coating. Heat treatment at 773-873K should promote stress relaxation even if any change in relative fracture strength has occurred due to internal stress. Examination of Fig. 1 from this angle leads to the judgment that the strength degradation in a fiber with a Young's modulus of 200-300 GPa is due to a decrease in the cross-sectional area of the fiber accounted for by the reaction products.

Fibers with a Young's modulus of more than 500 GPa (except those with an onion structure) tended to degrade, indicating a relative fracture strength of 1 or less for the fibers after aluminum removed. However, the carbide concentration (as calculated from the thickness of the black band by TEM observation) tended to decrease for fibers with a higher Young's modulus. In the XN-70/Al composite, the black-band part became discontinuous, indicating that the concentration was even lower.

There are two conceivable mechanisms for the degradation in strength of aluminum reinforced with carbon fibers.

- (1) Fiber's section reduction mechanism [1]
- (2) Notching stress concentration mechanism [2]

Owing to the variety of fibers and their structures, it can be easily be supposed that these mechanisms have varying degrees of involvement. Kohara and Muto reported that the pattern of carbide development differed depending on the type of PAN-based carbon fiber. They showed that in the case of PAN-based carbon fiber with high modulus, degradation of strength occurs due to the notch effect, since carbide also develops on the inside of the fiber [7].

The similarity between the strength degradation of pitch-based carbon fiber and that of PAN-based carbon fiber gives rise to the possibility that the same type of carbide development will occur also in pitch-based carbon fibers.

X-ray Structural Parameters of the Pitch-based Carbon Fibers and SEM Images

Lc(002) and d_{002} of the carbon fibers determined are shown in Table 1. The images of a scanning electron microscopy of the fractured surface of the pitch based carbon fibers show that the NX- fibers and P-55 fiber have a radial structure, and the NS- fibers have a random structure. JIS- fibers have an onion structure. The different structure of carbon fibers will exert influence on the physical and chemical interaction with aluminum. In other words, it will induce different residual stresses and different reactivity.

Analysis for the Interface Interaction by TEM and EDX

To compare various pitch-based carbon fibers in terms of interface interaction such as carbide formation, TEM observation was performed on the interfaces of fiber-aluminum composites. The fibers tested were NS-20, P-55, NS-60, XN-70, and JIS-70 heat-treated at 773K for 7.2ks.

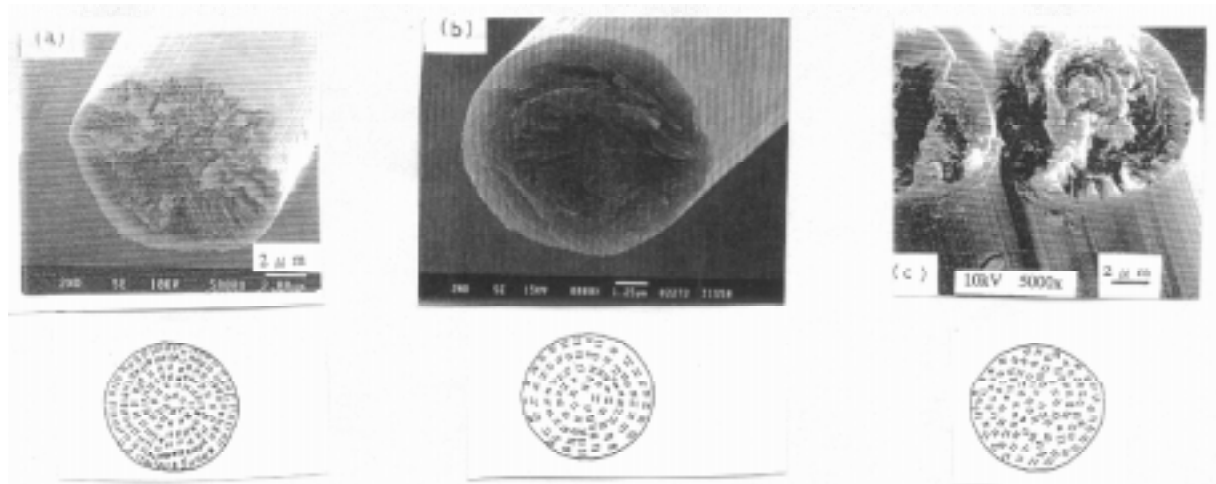


Fig. 2 nano-structures of pitch-based carbon fibers left: radial structure, middle: onion structure, right: random structure

The results show that a contrasting black-band layer of reaction products formed in the neighborhood of the interface, except in the JIS-70/Al composite of an onion structure. In the NS-20/Al composite, a layer approximately 10 nm thick formed along the outer circumference of the fiber, as shown in Fig. 4. Assuming that there is a uniform layer of reaction products approximately 10nm thick, 5ppm of reaction products will form per unit volume of coated aluminum. However, the said presumed amount of reaction products is extremely low in comparison with the 200ppm of formed carbide obtained by gas chromatography [10].

The point analysis by EDX showed that the black-band layer contained 21 mass% oxygen, and 3 mass% carbon. In contrast, the inner part of the fiber consisted of 100 mass% carbon and the non-black-band layer contained 98 mass% aluminum or more. With line analysis,

gentle concentration gradients were obtained for both carbon and aluminum, while the profile for oxygen had a peak on the interface, suggesting that a concentration of oxygen exists at the interface.

As shown in Fig. 4, similar results were obtained with the P-55/Al composite. The black band had a thickness of approximately 10nm, which was nearly equal to that of the NS20/Al composite.

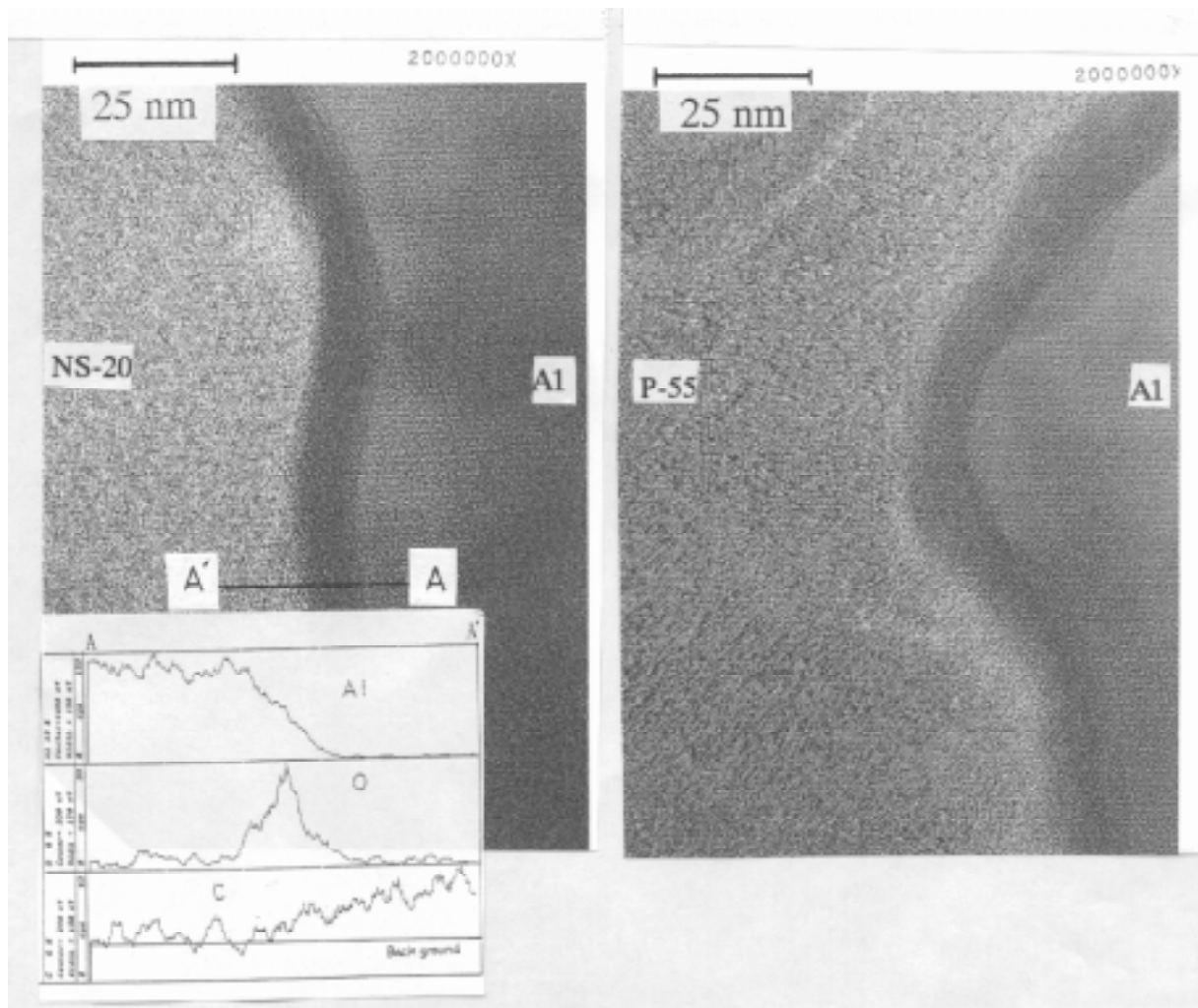


Figure 3. TEM and EDX of NS-20/Al(773K,2h), Figure 4. TEM of P-55/Al(773K,2h)

Furthermore, as seen in the upper and lower right parts of Fig. 4, the black-band part shows a number of protuberances as if indicating a process of tissue proliferation; carbon appears to have diffused into the aluminum. Fig. 6 shows a TEM image of the NS-60/Al composite. Here, the average thickness of the black-band layer decreased to approximately 5nm. Since a clear lattice pattern was observed in some areas, the spacing of lattice planes was found by magnifying the lattice. On the assumption that a lattice that would provide aluminum with the maximum strength would be caused by the Al (111) plane, since $d=2.33 \text{ \AA}$ the spacing of lattice planes in the part derived from the reaction products would be about 4 \AA . This is very close to the $d=4.22 \text{ \AA}$ at $I/O=100$ for the (111) plane of oxycarbide ($\text{Al}_4\text{O}_4\text{C}$). When this is taken into consideration along with the presence of a great deal of oxygen and little

carbon, the possibility arises that oxycarbide is present as a reaction product. When the result of XRD shown in Fig. 6 was assigned with JCPDS in the light of this possibility, the minute peaks could be identified more precisely and were found to be identical with the JCPDS standard peaks for Al_2OC , and $\text{Al}_4\text{O}_4\text{C}$, thus confirming their presence.

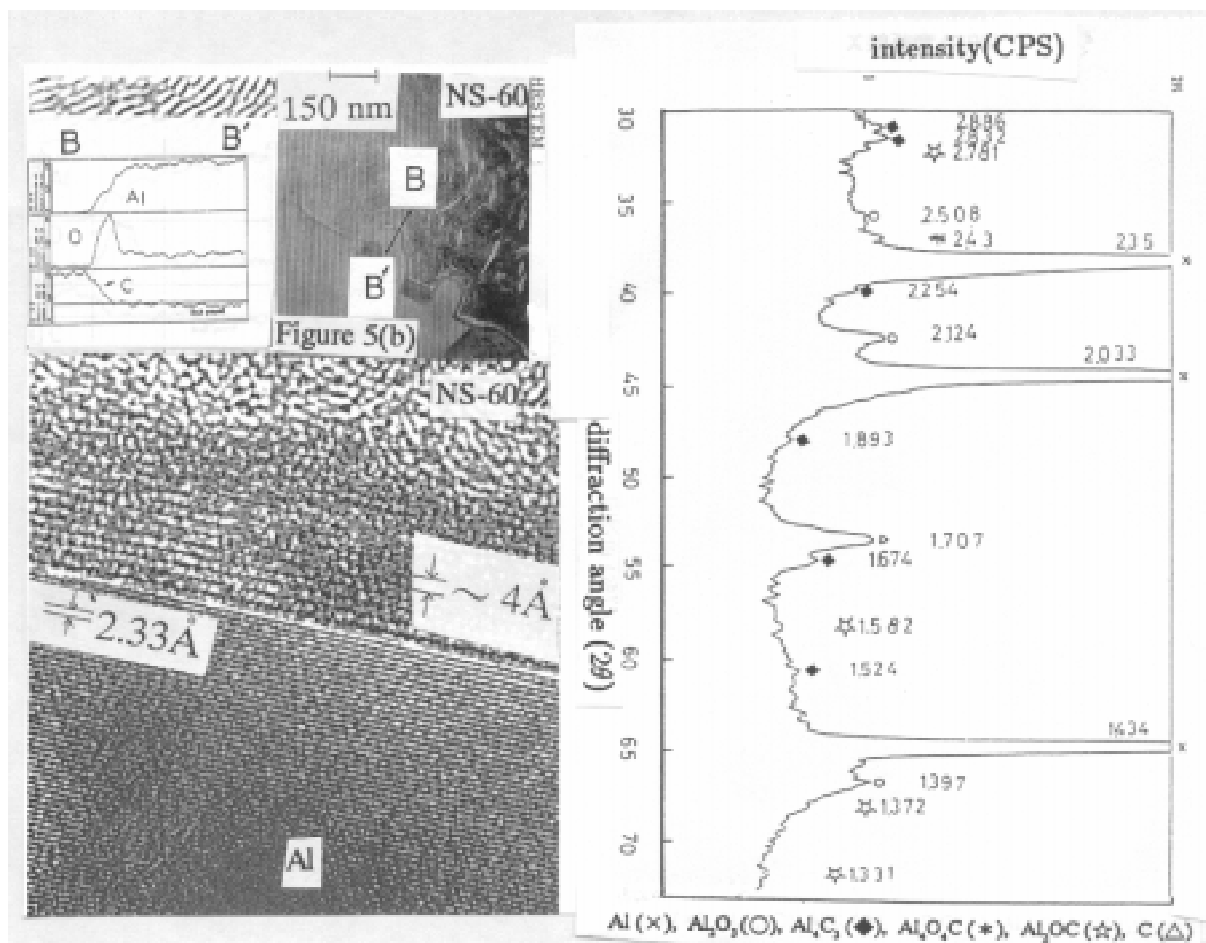
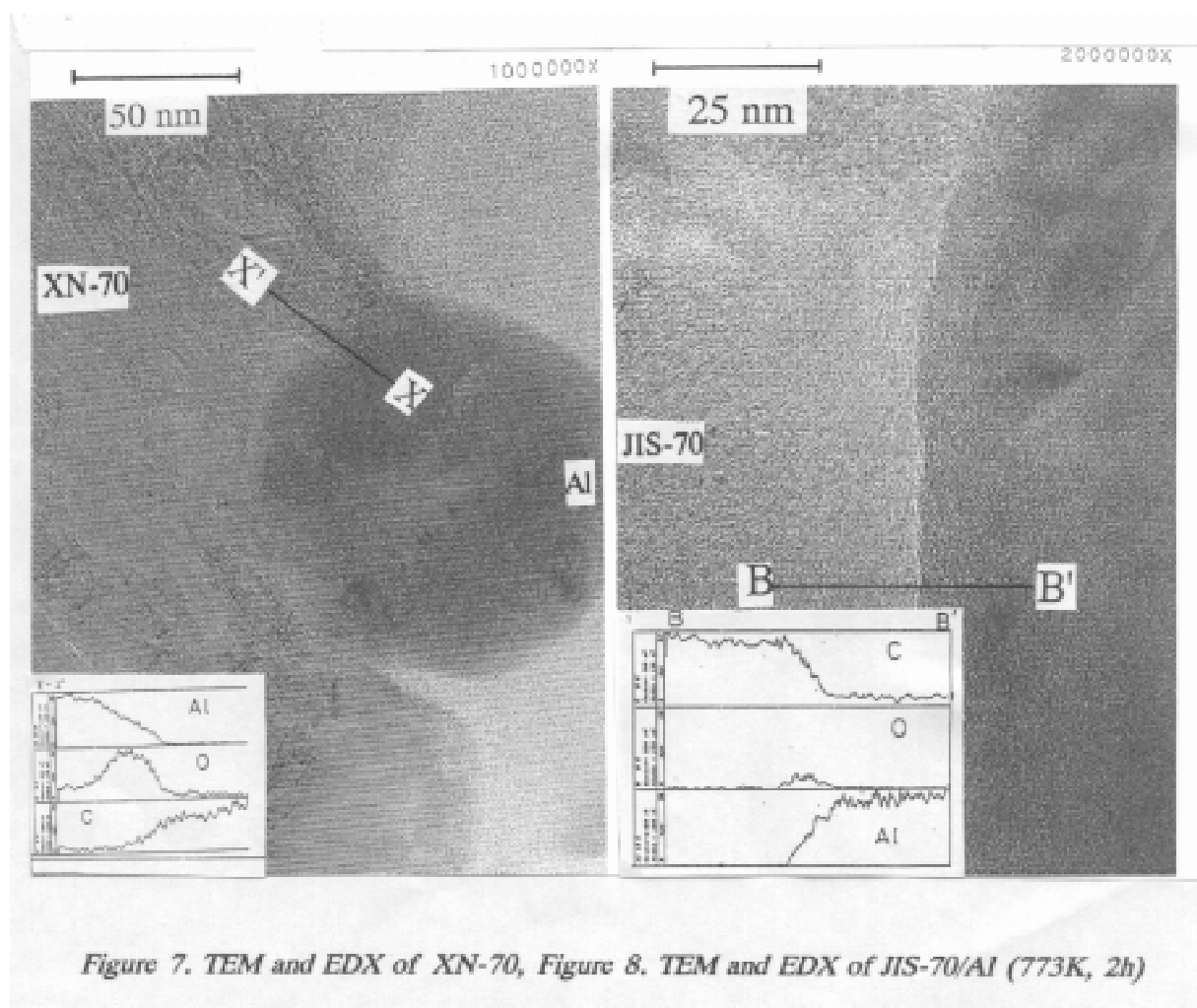


Figure 5. TEM and EDX of NS-60/Al (773K, 2h), Figure 6. XRD of P-55/Al (773K, 2h)

Furthermore, a notch never before observed in any other fiber was discovered on the circumferential surface of the fiber of the NS-60/Al composite. The observational results for this are shown in Fig. 5(b).

In addition, the observational results for the XN-70/Al composite are shown in Fig. 7. Unlike the previous observation, there are some parts where aluminum in particle form seems to have obtruded into the fiber surface. These may be parts where the fiber surface has high reactivity. A black-band was detected here as well, with analytical results similar to those previously obtained. However, the oxygen and carbon contents were relatively high, 36 mass% and 19 mass%, respectively. On the other hand, in the SEM picture shown in Fig. 8, no black band was observed in the JIS-70/Al complex with an onion structure. However, an oxygen concentration remarkably lower than in previous composites and a comparatively steep gradient of aluminum or carbon concentration were found in the line profiles by EDX. In previously mentioned series, oxygen was clearly detected in the black-band part, but this oxygen had been derived from oxygen and water absorbed on the fiber surface. Here, the

amount absorbed should depend on the nano-structure of the fiber. Hennig [11], who studied the oxidative reaction of single crystal graphite below 1073 K, reported that molecular oxygen reacted preferentially with carbon on the edge plane of graphite crystal, while it reacting little with carbon on the basal plane. Reasoning based on the report, it is anticipated that the oxygen absorption properties will vary with the nano-structure of the fiber. That is, it is presumed that water will be most easily absorbed on the surface of a fiber of radial structure, and least easily on the surface of an onion structure. Murayama and Ohuchi have reported that oxygen absorbed on the surface accelerated the formation of carbide [12]. Considering all these factors, it can safely be said that a fiber which allows more oxide and/or absorbed oxygen to exist on its surface will form carbide more easily. Water and oxygen will not easily absorb into an onion structure, since the surface consists of basal planes. Hence there will be only a small amount of oxide on the surface. These expectations accord with the fact that a distinct black band did not appear in the TEM image.



Reactivity of Pitch-based Carbon Fiber with Aluminum

The reactivity of pitch-based carbon fiber with aluminum may be considered as follows. As shown in Fig. 9, fiber with a low Young's modulus has high reactivity with aluminum and reaction proceeds uniformly over the entire fiber surface. In contrast, fiber with a high Young's modulus has low reactivity due to its highly developed graphite crystalline. Therefore, it is expected that strength will decrease greatly in the latter fiber due to

the notch effect, if any locally weak parts, e.g., parts that are highly reactive due to minute defects, initiate reactions.

It is clear that in an onion structure the carbide layer is very thin and that the fiber degradation is comparatively minor. This means that the fiber of an onion structure itself has some sort of diffusion barrier layer, thereby suggesting the possibility that it may be usable without any special coating.

On the other hand, the oxidation velocity of carbon fiber reached a minimum at the diameter of the graphite crystals around $d_{002} = 0.342\text{nm}$ [13]. The reason for this has been discussed as follows. The oxidation tends to proceed during the underdeveloped stage of the graphite crystalline, while defects develop as the graphite crystalline develops, thereby allowing oxygen to diffuse. These defects promote oxidation until the oxidation velocity reaches a minimum at a certain point. It is not clear whether the same would be applicable to reactivity between aluminum and graphite, but as described earlier, it is clear that oxygen has a significant effect at least on the formation of carbide, so from this point of view it is possible that a similar process may occur. When Fig. 1 is reviewed in terms of the degradation of the carbon fiber after the aluminum is removed, carbon fiber with a Young's modulus of approximately 400GPa may be interpreted as being comparatively good compatibility with aluminum. However, another view is that there will be problems associated with its properties and reactivity from the aspect of the size of the graphite crystalline [14].

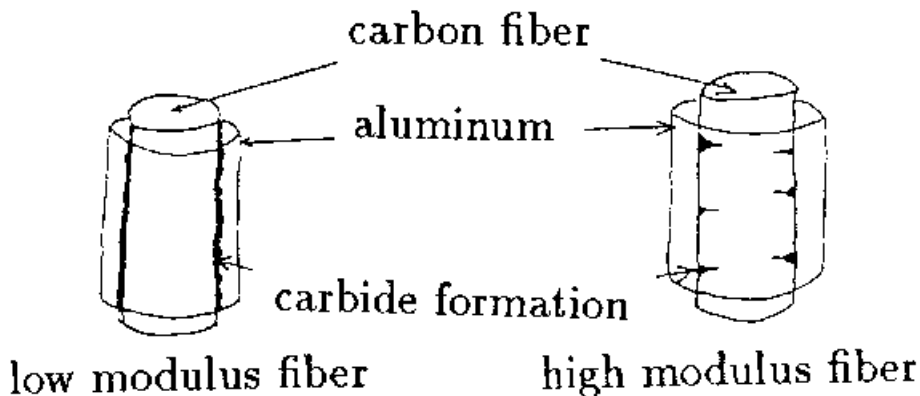


Fig. 9. The morphology of aluminum carbide formation and the relationship with the Young's moduli.

CONCLUSIONS

Based on the results and considerations described above, as a design guideline for compound materials with enhanced performance it is recommended that when aluminum is reinforced with some kind of pitch-based carbon fiber, pitch-based carbon fiber with an onion structure where the basal planes are oriented in the direction of parallel to the fiber circumferential surface should be used as filament reinforcements. On the other hand, when any kind of pitch-based carbon fiber with a high modulus of elasticity is used, special precautions should be taken against possible fiber degradation.

REFERENCES

1. Blankenbures, G., Effect of Carbide Formation on the Mechanical Behavior of Carbide-Aluminum Composites, Journal of Australian Institute of Metals, Vol.14, 1969, p.p. 236-241.
2. Jackson, P.W., Some Studies of the Compatibility of Graphite and Other Fibers with Metal Matrixes, Metals Engineering Quarterly, Vol. 9, 1969, p.p. 22-30.
3. Baker, A.A., Shipman, C., Cripwell, P.A., Jackson, P.W., "Oxidation of Aluminum-Coated Carbon Fibres and Carbon-Aluminum Composites", Fibre Science Technology, Vol. 5, 1972, p.p. 285-302.
4. Amateau, M.F., "Progress in the Development of Graphite-aluminum Composites using Liquid Infiltration Technology, Journal Composite Materials, Vol.10, 1976, p.p. 279-296.
5. Khan, I.H., "The Effect of Thermal Exposure on the Mechanical Properties of Aluminum-Graphite Composites, Metallurgical Transactions A, Vol. 7A 1976, p.p. 1281-1289.
6. S.J. Baker, W. Bonfield, "Fracture of Aluminum-Coated Carbon Fibres", Journal Materials Science, Vol.13, 1978, p.p. 1329-1334.
7. Kohara, S. and Muto, N., "Degradation behavior of Carbon Fibers by Molten Aluminum, Journal of Japan Institute of Metals, Vol. 52, 1988, p.p.1063-1069.
8. Suzuki, T., Umehara, R., Watanabe, S., "Mechanical Properties and Metallography of Aluminum Matrix Composites reinforced with Cu-, or Ni-plating Carbon Fibers", Journal Materials Research, Vol.8, 1993, p.p. 2492-2498.
9. Friler, J.B., Argon, A.S., Cornie, J.A., Strength and Toughness of Carbon Fiber Reinforced Aluminum Matrix Composites, Materials Science Engineering, Vol. A162, 1993, p.p.143-152.
10. Suzuki, T, "Compatibility of Pitch-based Carbon Fibers with Aluminum for the Improvement of Aluminum-matrix Composites", Composites Science and Technology, Vol.56, 1996, pp.147-153.
11. Hennig, G.R., "Electron Microscopy of Reactivity Changes near Lattice Defects in Graphite" Chemistry and Physics of carbon, ed. by Walker, P.L.Jr., Marcel Dekker, New York, Vol. 2, 1966, 1-49
12. Murayama, B. and Ohuchi, F.S., "H₂O Catalysis of Aluminum Carbide Formation in the Aluminum-silicon System, Journal Materials Research, 1991, p.p. 1131-1134.
13. Arai, Y and Sato, K., (private communication)
14. Hirai, T., (private communication)

PREPARATION AND THE PROPERTIES OF SiC/MoSi₂ COMPOSITES

J. Pan ^{1,2}, B. W. Liu ¹, D. M. Yang ¹, M. K. Surappa ² and Y. Zhuo ¹

¹ Department of Materials Engineering and Applied Chemistry,
Changsha Institute of Technology, Changsha 410073, China.

² Department of Metallurgy, Indian Institute of Science, Bangalore-560012, India.

SUMMARY: Hot press sintering and hot press reaction sintering techniques have been used to prepare SiC particle reinforced MoSi₂ composites. Microstructure of hot pressed SiCp(20vol%)/MoSi₂ composite showed uniform distribution of 1~3μm sized SiC particles in MoSi₂ matrix. *In situ* SiC/MoSi₂ composite had a 97.5% relative density. SiC particle had a size less than 1μm and a volume fraction of 15%. Composites prepared by both the routes have been found to possess higher flexural strength, indentation fracture toughness and hardness compared to monolithic MoSi₂. Compressive tests done at 1200°C and 1400°C showed that 0.2% compressive proof strength of both composites was increased obviously. Vickers hardness values of composites at 800°C have been found to be improved compared to MoSi₂.

KEYWORDS: molybdenum disilicide silicon carbide composites, hot press, reaction sintering, flexural strength, indentation fracture toughness, compressive strength, hot hardness

INTRODUCTION

Intermetallic matrix composites (IMCs) are currently being investigated for high temperature structural applications. Molybdenum-disilicide (MoSi₂) intermetallic is a promising candidate for the applications in oxidizing atmospheres. Its melting point (2030°C) is higher than Fe-Al, Ni-Al and Ti-Al intermetallic compounds and it has excellent oxidizing and thermal corrosion resistances. Its outstanding oxidation resistance is a result of the formation of a glassy silica (SiO₂), which is a very protective, adherent and coherent layer [1]. However, in most of intermetallics, the major problems include extreme brittleness and poor impact strength at a lower temperature, and an insufficient strength and creep resistance at elevated temperatures. Therefore, it is necessary to improve the room-temperature fracture toughness, elevated-temperature strength and creep resistance, if MoSi₂ is to be used as structural material. Previous studies show that an improved strengthening/toughening is possible through the incorporation of second phase reinforcements, that is, reinforcing MoSi₂ matrix with ceramic particle, whisker or continuous fiber. MoSi₂ is stable in contact with a large number of carbide, nitride, oxide and boride ceramic reinforcements, such as SiC, TiC, Si₃N₄, ZrO₂, Al₂O₃, Y₂O₃, TiB₂ and ZrB₂ at elevated temperature. In recent years, much attention has been paid to the preparation of MoSi₂ based intermetallic matrix composites [1~7]. Amongst the reinforcements used, SiC is considered to be more desired. The results of Gac *et al* [8] have shown that room-temperature flexural strength and fracture toughness of SiC

whisker/MoSi₂ composite were 310 MPa and 8.2MPam^{1/2}, respectively, and they were higher by 100% and 54%, compared to the matrix. Ghosh *et al* [3] reported that the hot hardness of SiC particle/MoSi₂ composite was higher than the monolithic MoSi₂ at temperatures below 1400°C .

The purpose of the present work is to enhance the room-temperature toughness and the high temperature strength, by incorporating SiC particle in MoSi₂ matrix. For this, hot press sintering and *in situ* reaction sintering process have been employed to fabricate SiC particle reinforced MoSi₂ composites.

EXPERIMENTAL

98.5% pure SiC (-150 mesh), 99.5% pure Mo₂C (-300 mesh), 99% pure Si(-200 mesh), 99.9% pure MoSi₂ (-120 mesh), were used in the present study. The powder mixture containing about 20 vol% of SiC and 80 vol% of MoSi₂, the mixture of Mo₂C and Si in a molar ratio of 1:5 were wet mixed in ethyl alcohol and milled for 48h, in different ball grinding cans of a planetary ball miller. The resulting powder mixtures were then cold formed in a graphite die and sintered in a vacuum furnace. After evacuating the furnace, it was filled with argon and the mixture containing the die was heated. The mixture of SiC and MoSi₂ was hot pressed at 1600°C at 24.5MPa for 45min. This yielded SiCp/MoSi₂ composite. Similar conditions were employed to prepare monolithic MoSi₂. The mixture of Mo₂C and Si was hot pressed at 1350°C for 2h and then at 1700°C for 1h under 27.5 MPa pressure. During hot pressing the following chemical reaction is expected to take place: Mo₂C + 5Si → SiC + 2MoSi₂, SiC would form *in situ* in the matrix of MoSi₂ resulting in SiC/MoSi₂ composite.

The optical and SEM observations were carried out for understanding the microstructure, reinforcing phase distribution and fractograph of all the three materials. Phase identification was done by a GEIGER-FLEX X-ray diffractometer. A Thermoflex TG-DTA was used to know the endothermic and exothermic reaction during composite fabrication using mixture of Mo₂C and Si powder.

Flexural strength was determined from 3-point bend test, using a cross head speed of 0.05 mm/min and a span length of 20 mm. 3×4×30mm size specimen were cut by electro-discharge machining. Vickers hardness indentations were used to estimate the room-temperature fracture toughness(K_{IC}). For this the average length of indentation crack was measured using an Interactive Image Analysis System(IBAS-2), and K_{IC} was calculated by the following equation [9] :

$$K_{IC} = 0.0752P(1/C)^{3/2} \quad (1)$$

where P is the load (98N and 196N were used), C is the crack half-length. Meanwhile, Vickers hardness (Hv) was also calculated. In addition 3-point bend test was also used to measure K_{IC}. For this 16mm span length specimen was used. A chevron-notch specimen with a size of 2×4×20mm and a chevron-notched precrack of 2mm depth was used. K_{IC} was given by [10] :

$$K_{IC} = \frac{P_C S}{B W^{3/2}} f(C/W) \quad (2)$$

where, P_C is the load at fracture. S is the span length. B , W are the specimen width and height. C is the precrack depth. $f(C/W)$ is a function of C/W , calculated by $2.9(C/W)^{1/2} - 4.6(C/W)^{3/2} + 21.8(C/W)^{5/2} - 37.6(C/W)^{7/2} + 38.7(C/W)^{9/2}$.

0.2% compressive proof strength at 1200°C and 1400°C were measured using an *Instron* model 1195 at a crosshead speed of 0.5mm/min. The specimen with a size of 8mm ϕ ×12mm was heated in air, at a rate of 20°C/min and specimen was kept at set temperature for 10min before testing. Vickers hardness at 800°C was measured on 15mm ϕ ×5mm size specimen, using a indentation load of 49N.

RESULTS AND DISCUSSION

Microstructural Features

Typical micrographs of unreinforced MoSi₂, hot pressed SiCp /MoSi₂ and *in situ* SiC/MoSi₂ composites are shown in Fig.1. In the polished section of MoSi₂ (Fig.1a), a dark phase was found distributed along the grain boundaries of the light matrix. Its volume fraction, measured by IBAS-2, was approximately 14.2%. X-ray diffraction results indicate that there exist a small amount of Mo₅Si₃ phase in monolithic MoSi₂, which corresponded with the light gray phase (A phase shown in Fig.1a). In hot pressed SiCp/MoSi₂ composite, the phases present include MoSi₂, α -SiC and Mo₅Si₃. SiC particle was easily seen in optical micrograph (the gray phase in Fig.1b). Its size was in the order of 1 to 3 μ m. As a result of addition of SiC particle, change in the grain size of MoSi₂ matrix was observed. In the monolithic MoSi₂ grain were equiaxed and had a size of 9 μ m. In the composite the matrix had a grain size of 3 μ m (Table 1). In the *in situ* SiC/MoSi₂ composite microstructure MoSi₂,

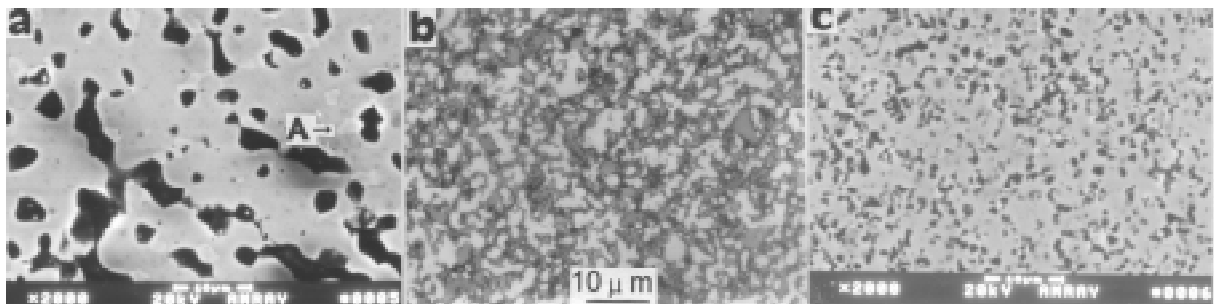


Fig.1: Micrographs showing the morphology of MoSi₂ and two SiC reinforced MoSi₂ composites: (a) MoSi₂ (b) hot pressed SiCp /MoSi₂ (c) *in situ* SiC/MoSi₂.

β -SiC and a few Mo₅Si₃ phases were identified by XRD. In the present work composite processed by the *in situ* reaction was better compared to the one processed by hot pressing in term of microstructure and properties. It also had the theoretical density. Small SiC particles (<1 μ m) were dispersed in MoSi₂ (Fig1.c). The glassy phase and cavity were almost absent.

The DTA result showed that there was a large exothermic peak in the temperature range of 1200~1375°C, hence the reaction $\text{Mo}_2\text{C} + 5\text{Si} \rightarrow \text{SiC} + 2\text{MoSi}_2$ could be completed under

Table 1: Microstructural features of three kinds of materials

Materials	Density (gcm^{-3})	Relative density	MoSi ₂ grain size (μm)	SiC size (μm)	Other phases
MoSi ₂	5.72	91.0	9	—	Mo ₅ Si ₃
Hot pressed SiCp/MoSi ₂	5.00	88.8	3	1~3	α -SiC, Mo ₅ Si ₃
<i>in situ</i> SiC/MoSi ₂	5.48	97.5	6	<1	β -SiC, Mo ₅ Si ₃

the present processing condition. In XRD phase analysis, it was found that the major phases were MoSi₂ and β -SiC, consequently the reaction should be completed. Grain size of MoSi₂ matrix observed in polarized light was about 6 μm , smaller than monolithic MoSi₂ prepared by hot pressing.

Mechanical Properties at Room Temperature

The room temperature mechanical properties of MoSi₂ and two kinds of SiC reinforced MoSi₂ composite are given in Table 2. It could be noted that Vickers hardness (Hv) had little

Table 2: Mechanical properties of three kinds of materials

Materials	Hv(GPa)		K _{IC} (MPam ^{1/2}) *		K _{IC} † (MPam ^{1/2})	σ_{FS} (MPa)
	98N	196N	98N	196N		
MoSi ₂	7.88	7.98	2.46	2.01	4.31	414
Hot pressed SiCp/MoSi ₂	10.38	10.59	4.54	4.92	5.95	539
<i>in situ</i> SiC/MoSi ₂	11.05	10.99	3.15	2.57	4.94	534

Note: * — K_{IC} measured by the indentation method

† — K_{IC} measured by the 3-point bend test method

σ_{FS} — Flexural strength

change with increasing indentation load. Hv of unreinforced MoSi₂ was lower than 9GPa, which is that of a single crystal MoSi₂ [1]. This could be due to presence of many cavities in MoSi₂. Pronounced improvement in hardness and flexural strength were obtained by incorporating SiC particle into MoSi₂. This could be attributed to the dispersion strengthening effect of SiC and the fine grain size of the matrix. From the results of the 3-point bend test for the chevron-notched specimens, it was seen that fracture toughness of hot pressed SiCp/MoSi₂ was 5.95MPam^{1/2} (about 38% up) and that of *in situ* SiC/MoSi₂ was 4.94 MPam^{1/2} (about 15% up), respectively. In addition, indentation test is a method to measure K_{IC} of a brittle material. The calculation values given by equation(1) were lower than that measured by the bend test. And ones calculated with using two levels of load also had a small

difference (see Table 2). This needs to be studied. Relatively significant improvement in toughness was seen in both the composites. The average indentation K_{IC} of SiCp/MoSi₂ and *in situ* SiC/MoSi₂ was increased by 112% and 28% comparing to that of the monolithic MoSi₂. Consequently, SiC particle reinforced MoSi₂ composite not only had an enhanced strength but also had improved fracture toughness.

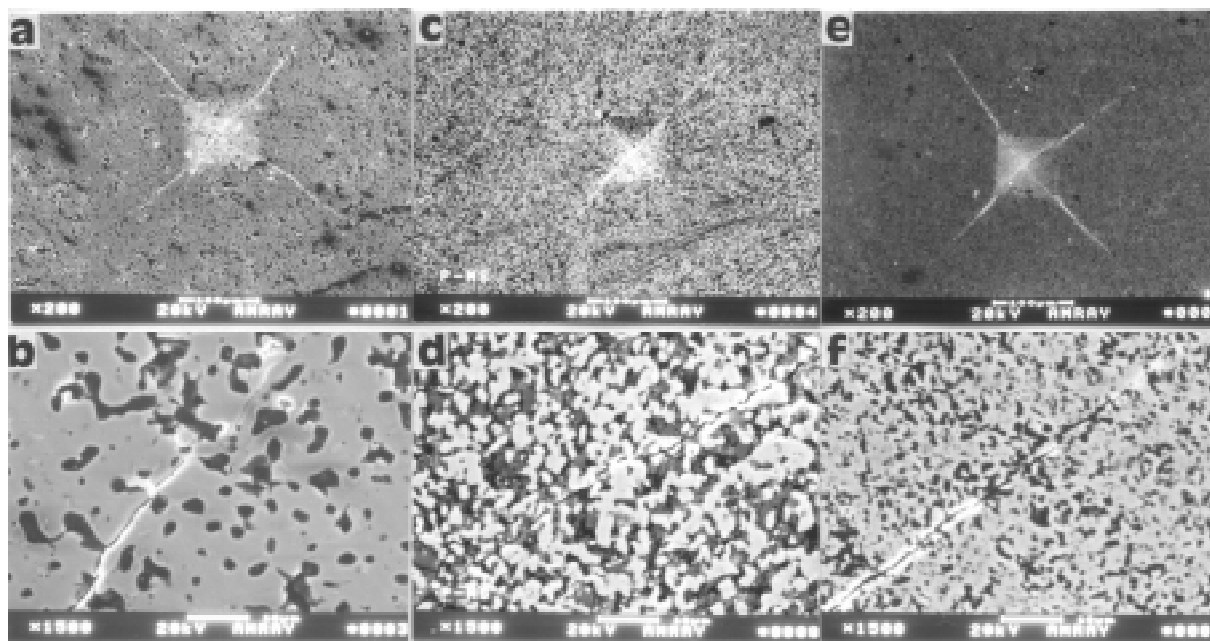


Fig.2: SEM photographs of the indents and cracks for different materials (indentation load: 98N): (a,b) MoSi₂ (c,d) hot pressed SiCp/MoSi₂ (e,f) *in situ* SiC/MoSi₂

Fig.2 shows the indentation and the cracks along its corner in all the three materials. It is widely known that, in brittle material, the fracture toughness can be enhanced by interrupting the crack propagation through lowering the stress field at an advanced crack tip. For particle or whisker reinforced composite, this may be achieved by the crack deflection, crack bridging or whisker pull-out. In monolithic MoSi₂, an indentation crack traveled primarily in MoSi₂ phase but not in the dark phase (Fig.2b) which indicates that this phase may not be deleterious to fracture toughness of MoSi₂. In hot pressed SiCp/MoSi₂ composite, the crack was likely to pass the SiC particle (Fig.2d) and hence was deflected slightly during propagation. It may be a main mechanism that increased the fracture toughness. In the *in situ* SiC/MoSi₂ composite, the indentation crack was shorter (Fig.2e) and passed not only through MoSi₂ but also through the dark reinforced phase (Fig.2f). It was suggested that this reinforced phase had a stronger energy-absorptivity in the process of crack propagation, so K_{IC} of this material was also higher than that of MoSi₂.

Mechanical Properties at Elevated Temperature

MoSi₂ shows a ductile characteristic at a higher temperature, for instance at 1200°C, thereby the sample could not be fractured during bending test (shown in Fig.3). In the case of SiC particle reinforced MoSi₂ composite, the specimen also had a bent shape but the temperature was much higher compared to monolithic MoSi₂, which means composite can maintain its stiffness until a higher temperature than monolithic MoSi₂. It was still

difficult to know the flexural strength of monolithic MoSi_2 and its composite at a temperature higher than 1200°C . In the present work, a compressive test was used to evaluate their high-temperature strength. Above 1200°C , the specimen would be compressed to a drum shape finally as shown in Fig.4, but a compressive yield stress could be read from the stress-strain curve. Fig.5 gives the comparisons of those three materials tested at 1200°C and 1400°C . At 1200°C , hot pressed $\text{SiCp}/\text{MoSi}_2$ had a 37% and *in situ* SiC/MoSi_2 had a 58% increase in strength compared to the monolithic MoSi_2 . At 1400°C , there is an obvious degradation in the strength of all these three materials, i.e, 76% for MoSi_2 , 77% for hot pressed $\text{SiCp}/\text{MoSi}_2$ and 71% for *in situ* SiC/MoSi_2 . But the absolute values show improvement in strength due to SiC particle incorporation. Another evaluation test for MoSi_2 matrix composites was to measure their Vickers hot hardness at 800°C . The result was $6.47\text{GPa}(\text{MoSi}_2)$, $6.76\text{GPa}(\text{SiCp}/\text{MoSi}_2)$ and $7.84\text{GPa}(\text{in situ SiC}/\text{MoSi}_2)$, which also showed the strengthening effect of SiC particle at elevated temperature.

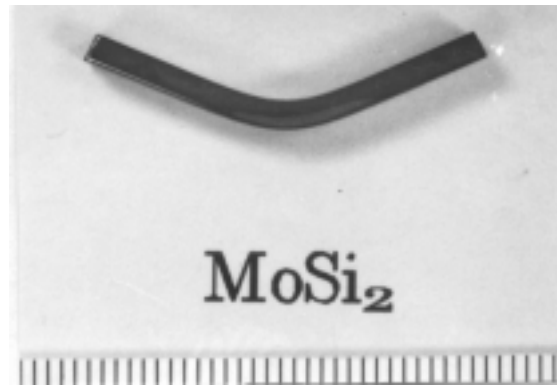


Fig.3: The bending test specimen of MoSi_2 after experiment at 1200°C

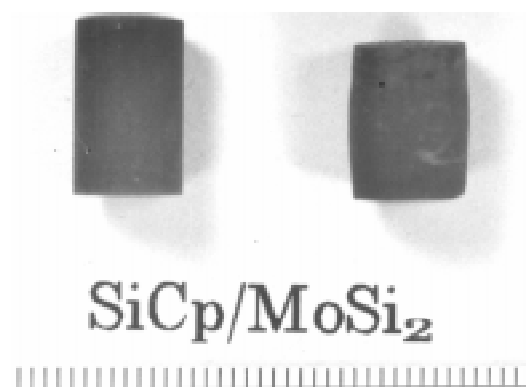


Fig.4: Compressive test specimen of $\text{SiCp}/\text{MoSi}_2$ before(left) and after(right) test at 1400°C

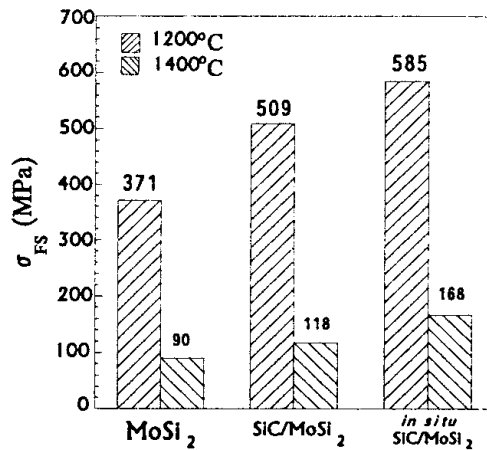


Fig.5: Compressive yield strength comparisons at 1200 °C and 1400 °C of three kinds of materials.

CONCLUSION

- 1) SiC particle reinforced MoSi₂ composite was prepared by the hot press process successfully. SiC particle with a size of 1~3μm was dispersed homogeneously in MoSi₂ matrix. SiCp/MoSi₂ composite had a smaller grain size, higher Vickers hardness, fracture toughness and flexural strength than that of the monolithic MoSi₂.
- 2) By utilizing the reaction between Mo₂C and Si powder, an *in situ* grown SiC/MoSi₂ composite was synthesized. It had 97.5% of the theoretical density. SiC had a size smaller than 1μm and was dispersed in matrix homogeneously. The *in situ* SiC/MoSi₂ composite also had improved hardness, fracture toughness and flexural strength.
- 3) MoSi₂ matrix composites prepared by both routes had improved high temperature strength and hot hardness.
- 4) Addition SiC particle into MoSi₂ matrix reflected in improvement in toughness at room temperature and strength at high temperature.

ACKNOWLEDGEMENTS

The authors would like to thank Mr. A.C. Zhou for helping to prepare material samples. They are also grateful to Mr. G.Yang for helping with the SEM observation, to Prof. S.Z Liu for doing the XRD experiment and to Mr. G.Q.Zhu for performing the compressive test at elevated temperature.

REFERENCES

1. Petrovic, J.J. and Vasudevan, A. K., *Intermetallic Matrix Composites II*, MRS, Pittsburgh, Pennsylvania, 1992, pp. 229-239.
2. Chang, H., Kung, H. and Gibala, R., *ibid*, pp. 253-258.
3. Ghosh, A. K., Basu, A. and Kung, H., *ibid*, pp. 259-266.
4. Wiedemeier, H. and Singh, M., *Journal of Materials Science*, Vol.27, 1992, pp. 2974-2978.
5. Kakitsuji, A. and Miyamoto, H., *Journal Japan Society of Powder and Powder Metallurgy*, Vol. 39, No.10, 1992, pp. 819-822.
6. Alman, D. E., Shaw, K. G., Stoloff, N. S. and Rajan, K., *Materials Science & Engineering*, A155, 1992, pp. 85-93.
7. Cook, J., Khan, A., Lee, E. and Mahapatra, R., *ibid*, pp. 183-198.
8. Gac, F. D. and Petrovic, J. J., *Journal of American Ceramic Society*, Vol. 68, No. 8, 1985, pp. C200-C201.
9. Zhang, Q. C., *Mechanical Properties of Ceramic Materials*, Science Press, 1987 (in Chinese).
10. Guan, Z.D., *Physical Properties of Inorganic Materials*, Qinghua University Press, 1992 (in Chinese).

MODELS OF ANODIC DIFFUSION WHEN JOINING PSZ TO NICKEL

Yu Wang and Robert G. Bathgate

*School of Engineering and Technology,
Deakin University, Geelong, Victoria 3217, Australia.*

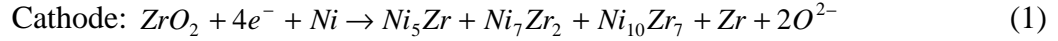
SUMMARY: The anodic process during current enhancement joining of partially stabilised zirconia to nickel was modelled. The model indicated that the current functioned to dissociate ZrO_2 and to promote interphase formation. NiO formation at the anodic junction was categorised into three stages related to the current density applied, oxygen diffusion, reaction control and mixed control by both the reaction and nickel diffusion. In the first stage, no interphase formed but oxygen diffused into the Ni anode; in the second, the thickness of the NiO was proportional to the current density; whereas, in the mixed control stage, the NiO thickness was restricted by an upper limit. The NiO thicknesses predicted by the models agreed with those observed by SEM. The model also provided useful guidance for process control.

KEYWORDS: Current enhancement joining, Interface modelling, Interface diffusion, Interface reaction, Ceramic/metal joining, Joining mechanism

INTRODUCTION

Composites of dissimilar materials rely on good interfacial bonding between the constituents. The general approach is to set up a reaction circumstance by elevating the temperature or making active additions to the junction. Pomerantz proposed a method which introduced electrical current to enhance the bond of glass and metal [1]. Subsequently this method was used to join zirconia and nickel [2]. The basis of the ZrO_2 and nickel joint is shown in Fig 1. The ZrO_2 and nickel to be joined were assembled as a symmetrical electrolyte cell ($Ni|ZrO_2|Ni$) with an extra piece of nickel as the second electrode. The two electrodes were connected to an external DC power supply and a current was passed through the cell from the left side to the right. The left-hand electrode is an anode and the right-hand is a cathode, with respect to junctions I and II. In practice, this cell was heated up to 1241 K, maintained at this temperature for 30 minutes before the external potential was applied. The current ran for 60 minutes and then it was switched off, whilst, the cell was cooled. A strong joint was found at the cathodic junction, which had about 3.5 times higher strength than only diffusion bonding of the same materials [3]. In contrast, no bonding was normally found at the anode if the current density was applied higher than 20 mA/cm^2 . By SEM inspection, a single layer of NiO was found at the anodic junction; whilst, a complex multi-layer structure (Zr-Ni intermetallics) was formed at the cathodic junction [2]. The effects produced by the current and how they enhanced the joint strength are of great interest. Basically the joining process can be described as an electrochemical event. Since ZrO_2 is an ionic conductor, oxygen anions (O^{2-}) are the principal charge carriers in the ZrO_2 and the zirconium cations (Zr^{4+}),

electrons (e^-) and charged holes (H^+) take secondary roles. When the cell is subjected to external potential, charges carried by electrons pour into the junction II where they can exchange their carriers from electrons to oxygen anions in order to enter the ZrO_2 . At the junction I, they swap back to flow away. Electrode reactions occur at both the cathodic and anodic junctions to sustain steady current flow. They are:



Eqn. 1 represents the ZrO_2 dissociated to arrest electrons and to generate O^{2-} ions. (2) is the opposite process. Since the anodic reaction is relatively simple, it could be simulated accurately. The present study is focused on modelling the process at the anodic junction. Specifically, it addresses the dependence of interlayer formation on the process parameters and material constants. This is thought to be a key element in the joining mechanism. In fact, the modelling not only determined the interaction at this junction, but also demonstrated the basic routine for cathodic junction study. Furthermore, the results provided useful advice for control of the joining process.

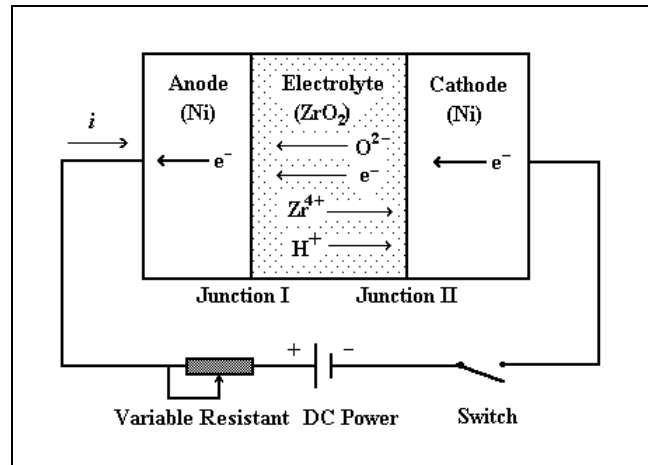


Fig. 1: Schematic of Electrolyte Cell

STATIC REACTION MODEL

Current enhancement can primarily be understood by first examining its static structure, the so called static reaction model. Suppose that electrochemical reaction is the sole process in the cell, then the relationship between the interphase formation and process parameters could be established by Faraday's law [4]. The law states that the amount of chemical change occurring at an electrode is proportional to the quantity of electricity passing through the cell. For the specific case of Eqn. 2, the law was expressed as:

$$\Delta N_{mole}^O = \frac{t_{O^{2-}} Q}{n F} \quad (mole) \quad (3)$$

where ΔN_{mole}^O is the amount of oxygen anions; n is the number of charges involved per molecule and F is Faraday's constant; Q is the amount of passed electricity and, because only

O^{2-} ions appears in the reaction (2), its transport number ($t_{O^{2-}}$) must be involved. Since current (I) is a derivative of Q with respect to the process time (t), $I = \frac{dQ}{dt}$, a more usefully alternative representation can be derived as:

$$\frac{d N_{mole}^O}{d t} = \frac{t_{O^{2-}} I}{n F} \quad (\text{mole / sec}) \quad (4)$$

This directly represents the dependence of oxygen production on the current applied.

In the junction I, supposing that the cross sectional area was stipulated as A_I and there was a NiO layer formed with a thickness $d X_I^{NiO}$, the molar amount of oxygen anions, required by the NiO formation, is represented as:

$$\Delta N_{mole}^O = C_O^{NiO} A_I d X_I^{NiO} \quad (\text{mole}) \quad (5)$$

where C_O^{NiO} expresses the mean volume concentration of oxygen in NiO. So then, the changing rate of the NiO thickness is derived as:

$$\frac{d X_I^{NiO}}{d t} = \frac{1}{A_I C_O^{NiO}} \frac{d N_{mole}^O}{d t} \quad (6)$$

Substituting (4) into (6), we obtain the relationship between the NiO thickness and process parameters as

$$\frac{d X_I^{NiO}}{d t} = \frac{\left(\frac{t_{O^{2-}}}{n F} \right) \left(\frac{I}{A_I} \right)}{C_O^{NiO}} \quad (7)$$

where $\left(\frac{I}{A_I} \right)$ is the current density, denoted by i_I and an electrochemical coefficient is defined as $h_O = \frac{t_{O^{2-}}}{n F}$. Therefore, (7) can be simplified to:

$$\frac{d X_I^{NiO}}{d t} = \frac{h_O}{C_O^{NiO}} i_I \quad (8)$$

Since i_I was kept constant during the joining process, (8) can be integrated over a time t with the initial condition $t = 0$, $X_I^{NiO} = 0$. The final solution is

$$X_I^{NiO} = \frac{h}{C_O^{NiO}} (i_I \times t) \quad (9)$$

(9) is the final expression for the NiO thickness. It indicates that the NiO thickness is proportional to a multiple of the current density and process time. The ratio depends on material constants and oxygen concentration. The influence of joining temperature on the thickness was embedded in the transfer numbers ($t_{O^{2-}}$).

ANODIC NICKEL DIFFUSION MODEL

The static reaction model has given a fundamental description of the joining process. However, (9) shows the thickness would increase without limit when the current density tended to be large. This is unacceptable. Hence the process couldn't be reaction alone and the model was modified by introducing a diffusion mechanism. An anodic nickel diffusion model was proposed which stated that both reaction and mass diffusion would occur concurrently in the process. The reaction would start and, once it had dissociated an amount of ZrO_2 , the diffusion would begin instantaneously and continue concurrently with the reaction. As the first step of study, the modelling considered only kinetic aspects, that is limited to the isothermal part of the process. The goal was to determine the thickness function for the NiO formation.

Anodic Simplified Nickel-Diffusion Models

Fig 2 represents a basic scheme of kinetic nickel-diffusion, where the left side is the anode and the right is the ZrO_2 . The vertical axis expresses nickel concentration and the horizontal is distance. Nickel is the diffusing species because its diffusivity is far larger than that of oxygen in NiO [5]. The simplest case is to assume the nickel diffuses only in the NiO layer, which is called the anodic simplified nickel-diffusion model.

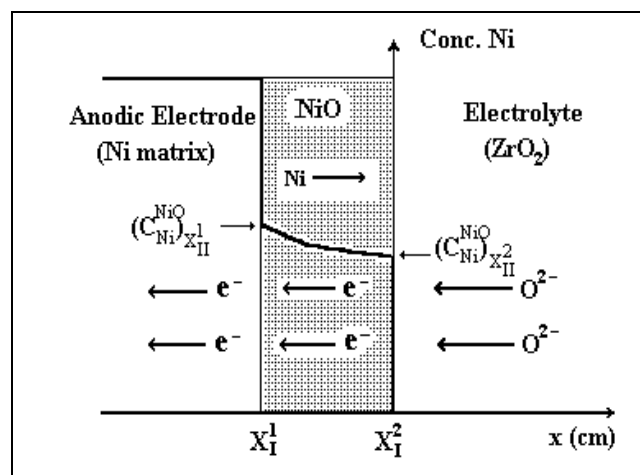


Fig. 2: Nickel Diffusion Profile at Anodic Junction

In the simplified model, junction X_1^1 was immobile. Nickel atoms in the anode diffused through the NiO layer to junction X_1^2 , where they met and reacted with the oxygen anions to form NiO. The possibility of Ni diffusing into ZrO_2 had been denied. It notes that the NiO layer actually became a part of the anode. After a given time, the Ni concentration profile would be like the bold line shown in Fig 2, where $(C_{Ni}^{NiO})_{X_1^1}$ and $(C_{Ni}^{NiO})_{X_1^2}$ are boundary concentrations determined by the Ni-O phase diagram. If $C_{Ni}^{NiO}(x, t)$ expresses the nickel concentration function in the NiO layer and \tilde{D}_{Ni}^{NiO} is the chemical diffusion coefficient, the nickel flux, toward the junction X_1^2 , can be expressed as:

$$J_{Ni}^{X_I^2} = -A_I \tilde{D}_{Ni}^{NiO} \left(\frac{\partial C_{Ni}^{NiO}}{\partial x} \right)_{X_I^2} \quad (\text{mole / sec}) \quad (10)$$

At junction X_I^2 , the amount of nickel, postulated by the NiO formation, is the same as (5) but the boundary concentration should be used. Then:

$$\frac{d N_{Ni}^{NiO}}{dt} = (C_{Ni}^{NiO})_{X_I^2} A_I \frac{d X_I^2}{dt} \quad (11)$$

Suppose that the anodic reaction is faster than the diffusion process, the NiO formation would be controlled by the supply of nickel atoms, or by the Ni diffusing through the NiO. Therefore, at junction X_I^2 the mass conservation can be satisfied by balance between (10) and (11) as:

$$-A_I \tilde{D}_{Ni}^{NiO} \left(\frac{\partial C_{Ni}^{NiO}}{\partial x} \right)_{X_I^2} + (C_{Ni}^{NiO})_{X_I^2} A_I \frac{d X_I^2}{dt} = 0 \quad (12)$$

Re-arranging (12) to give the boundary moving velocity, we have

$$\frac{d X_I^2}{dt} = -\frac{1}{(C_{Ni}^{NiO})_{X_I^2}} \tilde{D}_{Ni}^{NiO} \left(\frac{\partial C_{Ni}^{NiO}}{\partial x} \right)_{X_I^2} \quad (13)$$

Since the ordinary derivative of C_{Ni}^{NiO} can be expressed as [6]:

$$\left(\frac{\partial C_{Ni}^{NiO}}{\partial x} \right)_{X_I^2} = -\frac{E_0}{\sqrt{t}} \quad (14)$$

where E_0 is a constant independent of the process time. Substituting (14) into (13) with a coefficient m defined as

$$m = \frac{2 E_0 \tilde{D}_{Ni}^{NiO}}{(C_{Ni}^{NiO})_{X_I^2}}, \quad (15)$$

the boundary moving rate is obtained:

$$\frac{d X_I^2}{dt} = \frac{m dt}{2\sqrt{t}} \quad (16)$$

Integrating (16) over t , with initial condition $t = 0$, $X_I^2 = X_I^1$, we have the thickness function of the NiO layer as:

$$X_I^{NiO} = X_I^2 - X_I^1 = m\sqrt{t} \quad (17)$$

(17) is the final thickness function for the NiO corresponding to the reaction model (9). It implies that the thickness of NiO would be proportional to \sqrt{t} , where the coefficient m is a constant related to the concentration gradient, boundary concentration and diffusivity of nickel in NiO layer. This function differs from (9) since it is independent of the applied current density.

Anodic Full Nickel-Diffusion Model

The simplified nickel diffusion model obviously comes into conflict with the reaction model. The disappearance of the current factor from the function indicates some important event has been omitted. Therefore the simplified model could not be used to explain the whole anodic

process. This culpable negligence may be caused by the model's original specification. A full nickel diffusion model is proposed to reconcile this problem by releasing the restrictions and eventually establishing a comprehensive thickness representation. Major restrictions in the simplified model are (a) the nickel diffuses only in the NiO layer and (b) the electrochemical reaction must be faster than the diffusion at the junction X_I^2 . These problems are designated as two moving boundaries and interaction transition respectively.

Two Moving Boundaries

When the nickel diffusion in the nickel matrix (anode) is taken into account, the predicament becomes nickel diffusing across two junctions (X_I^1 and X_I^2). Starting the discussion with diffusion mass conservation at the X_I^1 , the flux of nickel input from the left is

$$J_{X_I^1}^{in} = -A_I \tilde{D}_{Ni}^{Ni} \left(\frac{\partial C_{Ni}^{Ni}}{\partial x} \right)_{X_I^1} \quad (18)$$

where C_{Ni}^{Ni} is the concentration function of Ni in the anode and \tilde{D}_{Ni}^{Ni} is the diffusion coefficient of nickel. At the NiO side of X_I^1 , the flux of nickel output would be

$$J_{X_I^1}^{out} = -A_I \tilde{D}_{Ni}^{NiO} \left(\frac{\partial C_{Ni}^{NiO}}{\partial x} \right)_{X_I^1} \quad (19)$$

At the X_I^1 , the nickel accumulation rate, which is the NiO formation, can be expressed as:

$$\left(\frac{d N_{Ni}^{NiO}}{d t} \right)_{X_I^1} = \left[(C_{Ni}^{Ni})_{X_I^1} - (C_{Ni}^{NiO})_{X_I^1} \right] A_I \frac{d X_I^1}{d t} \quad (20)$$

According to the mass conservation law, the accumulation part would be equal to the difference between the input flux and the output flux. It is expressed as

$$\left[(C_{Ni}^{Ni})_{X_I^1} - (C_{Ni}^{NiO})_{X_I^1} \right] \frac{d X_I^1}{d t} = \left[\tilde{D}_{Ni}^{NiO} \left(\frac{\partial C_{Ni}^{NiO}}{\partial x} \right)_{X_I^1} - \tilde{D}_{Ni}^{Ni} \left(\frac{\partial C_{Ni}^{Ni}}{\partial x} \right)_{X_I^1} \right] \quad (21)$$

Therefore,

$$\frac{d X_I^1}{d t} = \frac{\tilde{D}_{Ni}^{Ni} \left(\frac{\partial C_{Ni}^{Ni}}{\partial x} \right)_{X_I^1}}{\left[(C_{Ni}^{Ni})_{X_I^1} - (C_{Ni}^{NiO})_{X_I^1} \right]} \left[\frac{\tilde{D}_{Ni}^{NiO} \left(\frac{\partial C_{Ni}^{NiO}}{\partial x} \right)_{X_I^1}}{\tilde{D}_{Ni}^{Ni} \left(\frac{\partial C_{Ni}^{Ni}}{\partial x} \right)_{X_I^1}} - 1 \right] \quad (22)$$

It is found that the sign of the X_I^1 velocity would vary depending on the ratio of the nickel output flux over the nickel input flux.

Assuming $J_{X_I^1}^{in} \gg J_{X_I^1}^{out}$, which means the self diffusion of nickel is larger than substitutional diffusion, we simplified (22) to:

$$\frac{d X_I^1}{d t} = \frac{-\tilde{D}_{Ni}^{Ni} \left(\frac{\partial C_{Ni}^{Ni}}{\partial x} \right)_{X_I^1}}{\left[(C_{Ni}^{Ni})_{X_I^1} - (C_{Ni}^{NiO})_{X_I^1} \right]} \quad (23)$$

Following the principle of (14), the concentration gradient is expressed as:

$$\left(\frac{\partial C_{Ni}^{Ni}}{\partial x} \right)_{X_I^1} = -\frac{B_0}{\sqrt{t}} \quad (24)$$

with a coefficient:

$$k = \frac{2 B_0 \tilde{D}_{Ni}^{Ni}}{\left[(C_{Ni}^{Ni})_{X_I^1} - (C_{Ni}^{NiO})_{X_I^1} \right]} \quad (25)$$

Then the boundary moving rate is:

$$\frac{d X_I^1}{d t} = \frac{k}{2 \sqrt{t}} \quad (26)$$

At the junction X_I^2 , the moving rate of the junction would be the same as (16) deduced by the simplified model. The total thickness increase rate of the NiO layer would be the difference between the moving rates of its two boundaries.

$$\frac{d X_I^{NiO}}{d t} = \frac{d X_I^2}{d t} - \frac{d X_I^1}{d t} = \frac{m}{2 \sqrt{t}} - \frac{k}{2 \sqrt{t}} \quad (27)$$

Integrating the X_I over a time t , the thickness of the NiO layer is obtained:

$$X_I^{NiO} = (m - k) \sqrt{t} \quad (28)$$

where m and k are constants at the given temperature. Eventually the thickness predicted by the two moving boundaries will still be independent of the current density and just smaller than that predicted by the simplified model.

Interaction Transition

Now considering the problem of interaction transition. The mathematical representation that the reaction is quicker than the diffusion of nickel is $\frac{d N_{mole}^O}{d t} > \frac{d N_{Ni}^{NiO}}{d t}$. Substituting (4), (11) and (16) sequentially into this equation, the limiting condition for the simplified model is obtained:

$$i_I \geq (C_{Ni}^{NiO})_{X_I^2} \frac{m}{2 h_O \sqrt{t}} \quad (29)$$

This means the model can only be used in cases of a large current density.

In the reverse case, when nickel diffusion is faster than the electrochemical reaction,

$$i_I < (C_{Ni}^{NiO})_{X_I^2} \frac{m}{2 h_O \sqrt{t}} \quad (30)$$

the motion of boundary X_I^2 would be governed by the reaction. It means that mass conservation at X_I^2 would be satisfied between (4) and (11). The result would be similar to (8) but the boundary concentration should be used. However, the X_I^1 moving rate, given by (26), is not changed. Hence the thickness growing rate of NiO is:

$$\frac{d X_I^{NiO}}{d t} = \frac{h_o}{\left(C_{Ni}^{NiO}\right)_{X_I^2}} i_I - \frac{k}{2\sqrt{t}} \quad (31)$$

and the thickness function is derived as

$$X_I^{NiO} = \frac{h_o}{\left(C_{Ni}^{NiO}\right)_{X_I^2}} (i_I \times t) - k\sqrt{t} \quad (32)$$

Note that $X_I^{NiO} < 0$ would be physical meaningless. Consequently, (32) must have a minimum current density at $X_I^{NiO} = 0$. It is:

$$i_I^{\min} = \left(C_{Ni}^{NiO}\right)_{X_I^2} \frac{k}{h_o \sqrt{t}} \quad (33)$$

It implies that no NiO layer forms when the current density is less than i_I^{\min} . The physical scenario is that the oxygen produced by ZrO_2 dissociation is not enough to form NiO, but diffuses into the nickel matrix.

Hence it is seen that the whole anodic process could be divided into three stages by two critical current densities:

$$X_I^{NiO} = 0 \quad \left(i_I \leq \left(C_{Ni}^{NiO}\right)_{X_I^2} \frac{k}{h_o \sqrt{t}} \right) \text{ oxygen diffusing; } (34)$$

$$X_I^{NiO} = \frac{h_o}{\left(C_{Ni}^{NiO}\right)_{X_I^2}} (i_I \times t) - k\sqrt{t} \quad \left(\left(C_{Ni}^{NiO}\right)_{X_I^2} \frac{k}{h_o \sqrt{t}} < i_I < \left(C_{Ni}^{NiO}\right)_{X_I^2} \frac{m}{2h_o \sqrt{t}} \right) \text{ reaction control; } (35)$$

$$X_I^{NiO} = m\sqrt{t} - k\sqrt{t} \quad \left(i_I > \left(C_{Ni}^{NiO}\right)_{X_I^2} \frac{m}{2h_o \sqrt{t}} \right) \text{ diffusion control; } (36)$$

Eqn. 34 and 35, at the limiting case when $i_I = i_I^{\min}$, produce the same result $X_I^{NiO} = 0$, demonstrating continuity. However, the similar comparison for Eqn. 35 and 36, when $i_I = i_I^{up} = \left(C_{Ni}^{NiO}\right)_{X_I^2} \frac{m}{2h_o \sqrt{t}}$, i.e. the upper limit for (35), does not yield the same result. When i_I^{up} is substituted into (35), it becomes

$$X_I^{NiO} = \frac{m}{2} \sqrt{t} - k\sqrt{t} \quad (37)$$

This is smaller than (36) by $\frac{m}{2} \sqrt{t}$. Therefore, a transition between complete reaction and diffusion control modes has to be considered and is thought to be a mixed control stage. In this stage the reaction and diffusion controls would work successively in the incompatible time domain. To judge their contribution individually, we define a critical time t_c . In the time range from 0 to t_c , the process is controlled by the reaction; from t_c to t , it is controlled by the diffusion. Based on t as the whole process time, t_c would be the termination of reaction control.

In the mixed control stage the function of the layer's thickness would be expressed as two parts:

$$X_I^{0-t_c} = \frac{h_o}{\left(C_{Ni}^{NiO}\right)_{X_I^2}} i_I t_c - k\sqrt{t_c} \quad \text{reaction control} \quad (38)$$

$$X_I^{t_c-t} = (m-k) \left[\sqrt{t} - \sqrt{t_c} \right] \quad \text{diffusion control} \quad (39)$$

In the sequence of the time, the total thickness of NiO would be a linear sum of these two parts, $X_I^{NiO} = X_I^{0-t_c} + X_I^{t_c-t}$. So then,

$$X_I^{NiO} = \frac{h_o}{(C_{Ni}^{NiO})_{X_I^2}} i_I t_c + m \left[\sqrt{t} - \sqrt{t_c} \right] - k \sqrt{t} \quad (40)$$

where t_c can be worked out from the applied current density as:

$$\sqrt{t_c} = (C_{Ni}^{NiO})_{X_I^2} \frac{m}{2 h_o i_I} \quad (41)$$

It is quite clear that when $t_c \rightarrow 0$, (40) shrinks back to the diffusion control function (36). While the $t_c \rightarrow t$, the function shrinks to the reaction control function (35). Consequently, (40) does express the transition between the two control modes. Since t_c is not a real identified process parameter, it is better to express the relationship in terms of current density (i_I). Substituting (41) into (40) instead of t_c , we obtain

$$X_I^{NiO} = (m-k) \sqrt{t} - \frac{m^2 (C_{Ni}^{NiO})_{X_I^2}}{4 h_o i_I} \quad \left(i_I \geq (C_{Ni}^{NiO})_{X_I^2} \frac{m}{2 h_o \sqrt{t}} \right) \quad (42)$$

(42) is the thickness function in the transition segment. It can still be a function of process parameters and material constants. It links with (35) at the current density of i_{II}^{up} and with (36) when $i_{II} \rightarrow \infty$. It proposes that complete diffusion control (36) would not happen in a real situation and there is an upper limit of NiO thickness. Summarising the deduction, the thickness of the NiO by the full nickel-diffusion model is represented as a system of the segmental functions, that is a combination of (34), (35) and (42):

$$\left\{ \begin{array}{l} X_I^{NiO} = 0 \quad \left(i_I \leq (C_{Ni}^{NiO})_{X_I^2} \frac{k}{h_o \sqrt{t}} \right) \\ X_I^{NiO} = \frac{h_o}{(C_{Ni}^{NiO})_{X_I^2}} (i_I \times t) - k \sqrt{t} \quad \left((C_{Ni}^{NiO})_{X_I^2} \frac{k}{h_o \sqrt{t}} < i_I < (C_{Ni}^{NiO})_{X_I^2} \frac{m}{2 h_o \sqrt{t}} \right) \\ X_I^{NiO} = (m-k) \sqrt{t} - \frac{m^2 (C_{Ni}^{NiO})_{X_I^2}}{4 h_o i_I} \quad \left(i_I \geq (C_{Ni}^{NiO})_{X_I^2} \frac{m}{2 h_o \sqrt{t}} \right) \end{array} \right. \quad (43)$$

VERIFICATION AND SIGNIFICATION

With diffusion data of $\tilde{D}_O^{Ni} = 7.37 \times 10^{-9}$ [7] and $\tilde{D}_{Ni}^{NiO} = 2.03 \times 10^{-9} \text{ cm}^2 / \text{sec}$ [8], phase diagram and transport number of $t_{O^{2-}} = 0.35$, (43) has been numerically solved using Mathematica software. Comparison of the mathematical solution with experimental results is shown in Fig 3, where the solid line shows the predicted thickness of NiO layer by the full nickel diffusion model and the stars are the real thicknesses measured using scanning electron microscopy. The model coincided with the experimental results. Especially, no NiO was found when current density of 0.2 mA/cm^2 was applied and there was a thin NiO layer when the current was 0.95 mA/cm^2 , as compared with the calculated $i_H^{\text{min}} = 0.35 \text{ mA/cm}^2$. The threshold for the mixed control was $i_I^{\text{up}} = 6.8 \text{ mA/cm}^2$.

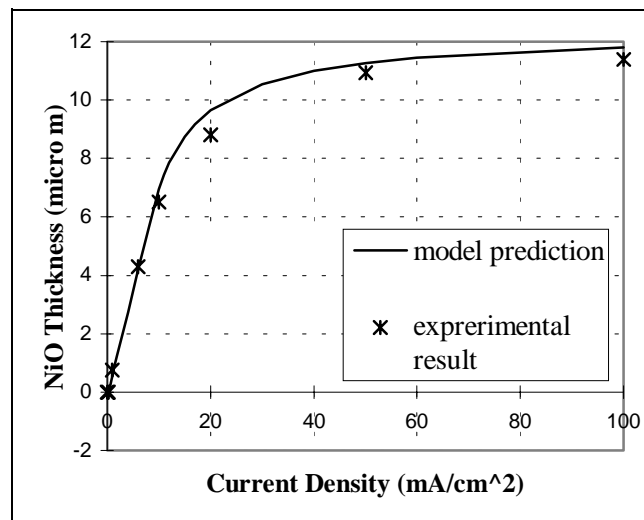


Fig. 3: Comparison of Prediction and Experiment

Considering anodic joining, a significant application of model is its prediction of the phenomenon of anodic junction separation. In Eqn. (43), when the current is more than the critical density (i_I^{up}), the process goes into the mixed control mode. There is a time segment of diffusion controlled NiO formation, then the reaction proceeds faster than nickel diffusion. In sequence, the oxygen produced by the reaction would be more than requirement by NiO layer formation. It would require another sink to absorb those excessive oxygen anions. The considerable event is oxygen combination reaction:



If we recognise that joining was performed at high temperature, the resultant O_2 in (44) would be in gas form and tend to evaporate from the junction to atmosphere. Consequently the O_2 evaporation could function to reduce the cohesion of the two materials. It is not surprising the anodic junction may be separated on those occasions when the applied current density was too high. Only when the current density is controlled, so that the process remains in the reaction control mode, can the anodic junction realise good bonding. Experiments have been carried out to prove this prediction. Table 1 lists the joined strengths at the anodic junction with shear tests [3]. It clearly illustrates anodic junction separation at between 3 and 15 mA/cm^2 which compares with the theoretical value of 6.8 mA/cm^2

Table 1 Joined Shear Strengths at Anodic Junction

<i>Sample</i>	<i>Temp. (K)</i>	<i>Time (min.)</i>	<i>Current density</i>	<i>Shear strength</i>
01	1241	60	0 mA/cm ²	60.8 MPa
02	1241	60	0.05 mA/cm ²	61.5 MPa
03	1241	60	2 mA/cm ²	46.4 MPa
04	1241	60	3 mA/cm ²	42.1 MPa
05	1241	60	15 mA/cm ²	0 MPa
06	1241	60	20 mA/cm ²	0 MPa

CONCLUSION

(1). Electrical current enhancement is a process combining electrochemical reaction with diffusion. In the process, current functions to dissociate the ZrO₂ and provide oxygen at the anode for nickel oxide formation.

(2). The formation of an anodic interlayer (NiO) is governed by the applied current density, process time and material constants. Anodic full nickel diffusion model is a comprehensive description of the NiO formation. In sequence, two critical current densities divide the formation into three stages, no NiO interlayer, reaction controlled growth of the NiO layer and growth by mixed reaction and diffusion control. In the first stage, no NiO formed but oxygen diffused into anode; in the second stage, the NiO thickness is proportional to current density and in mixed control stage, the thickness reaches an upper limit.

(3). Anodic junction joining is directly dependent on the magnitude of current density. Only when the current was adjusted, to keep the process in reaction control, could bonding occur. Larger current led to junction separation because oxygen gas was formed.

REFERENCES

1. Pomerrantz, D. I., "Anodic Bonding", U.S. Pat. 3,397-278, Aug.13, 1968.
2. Wagner, T., Kirchheim, R. and Ruhle, M., "Electrochemically-induced Reaction at Ni/ZrO₂ Interface", *Acta metall.mater.*, Vol. 40, Suppl. pp S85-93 (1992).
3. Wang, Y., Janardhana, M. N. and Bathgate, R. G., "Joining of PSZ Ceramic and Nickel with Electrical Current Enhancement", *The Proceeding of the 10th Int. Conf. on Composite Materials*, Whisler, B. C. Canada, Vol. 4, pp 641-648 (1995).
4. Laidler, K. J. and Meiser, J. H., "Physical Chemistry", *The Benjamin/Cummings Publishing Company Inc.*, 1982 pp 253.
5. Cahn, R. W., Haasen, P. and Kramer, E. J., "Materials Science and Technology -A Comprehensive Treatment", *VCH Verlagsgesellschaft mbH. Weinheim*, Vol 11, pp 317-319 (1994).
6. Crank, J., "The Mathematics of Diffusion" *2nd Edition*, *Oxford Univ. Press*, pp 32 (1975).
7. "Smithells Metals Reference Book" Edited by Brandes, E. A., (*7 Edition*) pp 13-92.
8. Kaur, I., "Handbook of grain and Interphase Boundary Diffusion Data", *Ziegler Press*, pp 1130.

THE INFLUENCE OF SOLIDIFICATION ON THE INTERFACE OF CF/Al-4.5Cu COMPOSITES

Chu Shuangjie and Wu Renjie

*Institute of Composite Materials, Shanghai Jiao Tong University,
Shanghai 200030, P.R.China*

SUMMARY: In this paper, CF/Al-4.5Cu composites was fabricated by using of squeeze cast method, and then the microstructures in the interface of CF/Al-4.5Cu composites were observed and analysed by means of SEM and TEM. As results, when the solidification cooling rate decreased, crystallize quantity of θ -CuAl₂ phase in the interface region decreased and microsegregation of Cu element around carbon fiber surface also decreased, but the size of θ -CuAl₂ phase increased. As the solidification cooling rate increased, crystallize quantity of reaction product Al₄C₃ in the interface of CF/Al-4.5Cu composites was increased, but the size of Al₄C₃ phase decreased.

KEYWORDS: CF/Al-4.5Cu composites, interface, solidification, cooling rate

INTRODUCTION

Since carbon fiber (CF) reinforced metal matrix composites have a high specific strength, high specific modules and excellent high temperature characteristics, so a lot of works were dealt with it [1]. But the strength of CF/Al composites fabricated by liquid infiltration method almost can not reach the calculation value by theory (ROM value), it is suggested that the interfacial reactions of CF/Al composites have a serious effect on the strength of the composites [2].

The interface is an important component of CF/Al composites, the interface of metal matrix composites is related to a lot of factors, such as the microstructure of the interface, adhesion and chemical reaction between reinforcement and matrix, as well as diffusion of alloy elements between two phases, therefore the interface is a very complicated problem. Previously there are not quite understand for forming process on the microstructure of interface and influence of the interface on mechanical properties of composites, but recently a lot of research works are engaged on the interface [3,4], such as: interface chemical reaction, the interface microstructure, the effect of the interface on mechanical properties of composites, the influence of thermal treatment on the interface reaction and microstructure, the relation of interface microstructure with failure and damage of composites, et al. But, due to the interface microstructure and its forming process are very complicated, they are effected by the manufacturing of technologies, processing parameters, applied condition, and environment, so that there are only few works relate to interface theory.

In this paper, CF/Al-4.5Cu composites will be selected as investigation object, to study the relationship of reaction products in the interface with solidification process and recognize sufficiently on the interface of CF/Al composites.

EXPERIMENTAL PROCEDURE

Composites Preparation

CF/Al-4.5Cu composites was fabricated by squeeze cast method, the schematic diagram of squeeze cast apparatus was shown in Fig.1. The processing parameters were divided into two groups:

(A) pouring temperature of Al-4.5Cu alloy was 800°C, the preheating temperature of carbon fibers (CF) preforms T_f was 500°C, the preheating temperature of the mould was 300°C;

(B) pouring temperature of Al-4.5Cu alloy was 820°C, the preheating temperature of carbon fibers (CF) preforms T_f was 600°C and the preheating temperature of the mould was 400°C.

Two groups of samples were produced by squeeze casting process under the pressure of 100 MPa, the loading time of constant pressure was 3 minutes, and the volume fraction of fibers V_f in composites are about 45%.

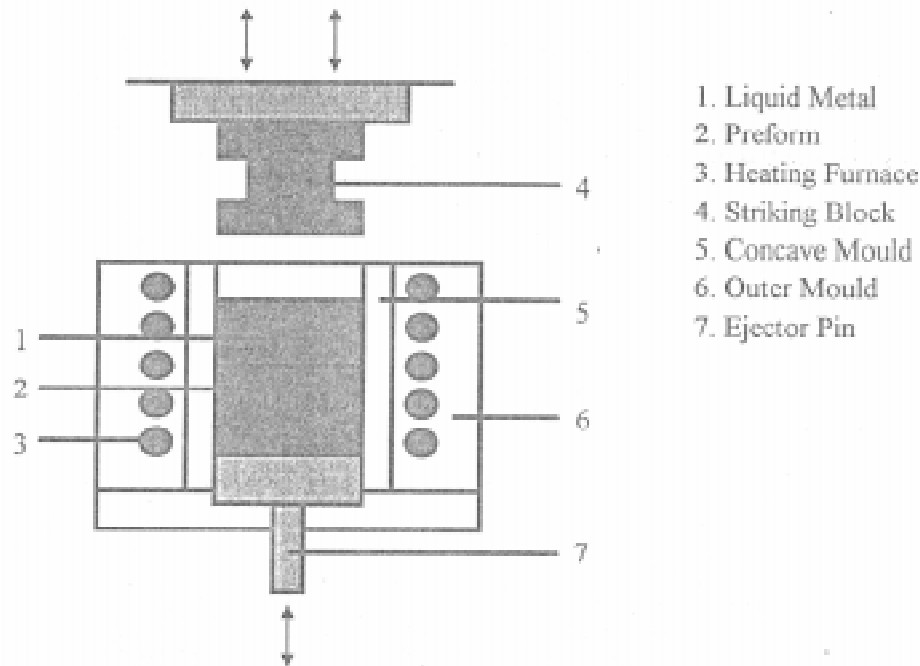


Fig.1: Schematic diagram of a apparatus for squeeze cast MMCs.

Interface Microstructure Analyses

Specimens were first cut into pieces by the linear cutting machine, with a thickness of 0.5 mm, and mechanically polished to a thickness about 100 μ m, then mechanically thinned on a Gatan 656/3 polished machine and reduce the thickness to approximately 15 μ m, final thinning was carried out by using of argonion plasma bombardment by Gatan model 600-TMP machine. All thinned specimens were stored in a freezer to prevent possible natural aging when not in use. The interface microstructure was observed in the TEM 420 with EDAX at 300 KV of operating voltage.

EXPERIMENTAL RESULTS AND DISCUSSION

The Relationship of CuAl_2 Phase Precipitated in the Interface with Solidification Process

Fig.2 shows the interface microstructures of different samples of CF/Al-4.5Cu composites fabricated by squeeze cast. By comparing the interface microstructure in cross-section of sample A with B, it is obviously that eutectic $\theta\text{-CuAl}_2$ phase formed on the surface of carbon fiber and with increase of preheating temperature of CF, crystallize quantity of $\theta\text{-CuAl}_2$ phase decrease and the shape of $\theta\text{-CuAl}_2$ phase is changed from block-like to particle-like or worm-like. The reason is that, according to the phase diagram of Al-4.5Cu alloy [5], an eutectic reaction will occur under nonequilibrium solidification condition, quantity of precipitated $\theta\text{-CuAl}_2$ phase depends mainly on the degree of the solidus moved leftward and according to the lever rule and the quantity of precipitated $\theta\text{-CuAl}_2$ phase increased with the increase of degree of the solidus moved leftward. From A to B, the solidification cooling rate decreased with increase of preheating temperature of reforms, and in the meantime, the degree of solidus moved leftward decreased, which can be accounted by the decrease of the quantity of $\theta\text{-CuAl}_2$ phase.

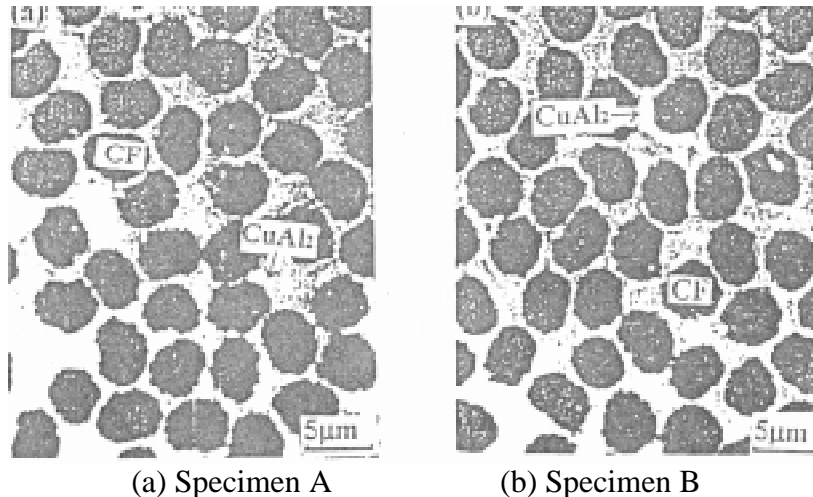


Fig.2: Distribution of CuAl_2 phase in the interface of CF/Al-4.5Cu composites

Comparing the interface microstructures of specimen A with B, the size of eutectic $\theta\text{-CuAl}_2$ phase of B is larger than that of A, it is due to the cooling rate between them was different, in which the preheating temperature of B was higher than that of A, so that cooling rate of B is lower than A. According to solidification theory, if the cooling rate is lower, solidification process needs long time in the local area and the precipitated phase is bigger at the same time. For this reason, the eutectic phase of specimen B is bigger than that of A.

The Relationship of Al_4C_3 Phase Precipitated with Solidification Process

The interface microstructures are further examined by a transmission electron microscopy (TEM), it is shown that the interface microstructures has evidently effected by manufacture technology parameters. During processing of CF/Al-4.5Cu composites, the important technology parameter is a solidification cooling rate, because at higher temperature, the time of CF contacting with liquid or solid aluminum alloy will greatly influence on the forming kinetics of the carbon-aluminum reaction compound [6].

Fig.3 shows the distribution of Al_4C_3 in the interface of CF/Al-4.5Cu composites fabricated by squeeze cast under the condition of different technology parameters such as A and B. These results suggest that the quantity of precipitated Al_4C_3 phase in A specimen is obviously more than that in B, but the dimension of precipitated Al_4C_3 phase in A is smaller than that in B.

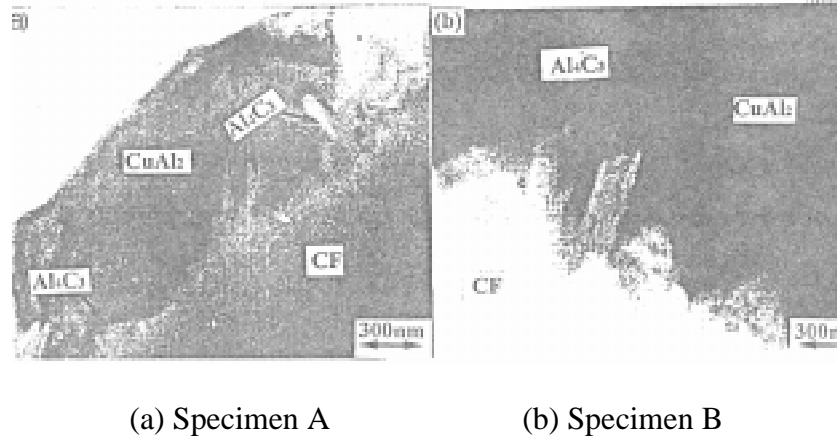


Fig.3 Distribution of Al_4C_3 phase in the interface of CF/Al-4.5 Cu composites

During processing of metal matrix composites, the solidification cooling rate does influence on shape, size and distribution of precipitated phases. In the case of squeezing cast CF/Al-4.5Cu composites, the factors of the influence on solidification cooling rate are pouring temperature of liquid metal, preheating temperature of preform and mould temperature, et al. So that, the cooling rate of specimen A is lower than B.

Fig.4 shows the SAD pattern of the Al_4C_3 phase and $CuAl_2$ phase in B specimen, it identifies that Al_4C_3 and $CuAl_2$ phase precipitated in the interface of CF/Al-4.5Cu composites.

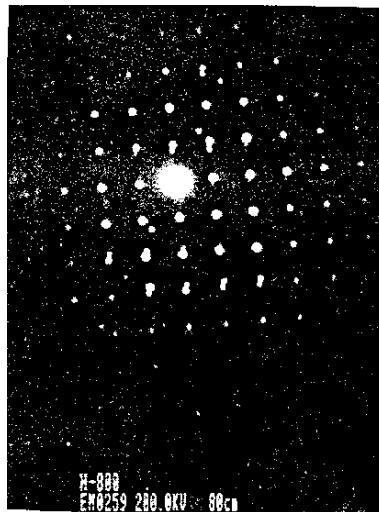
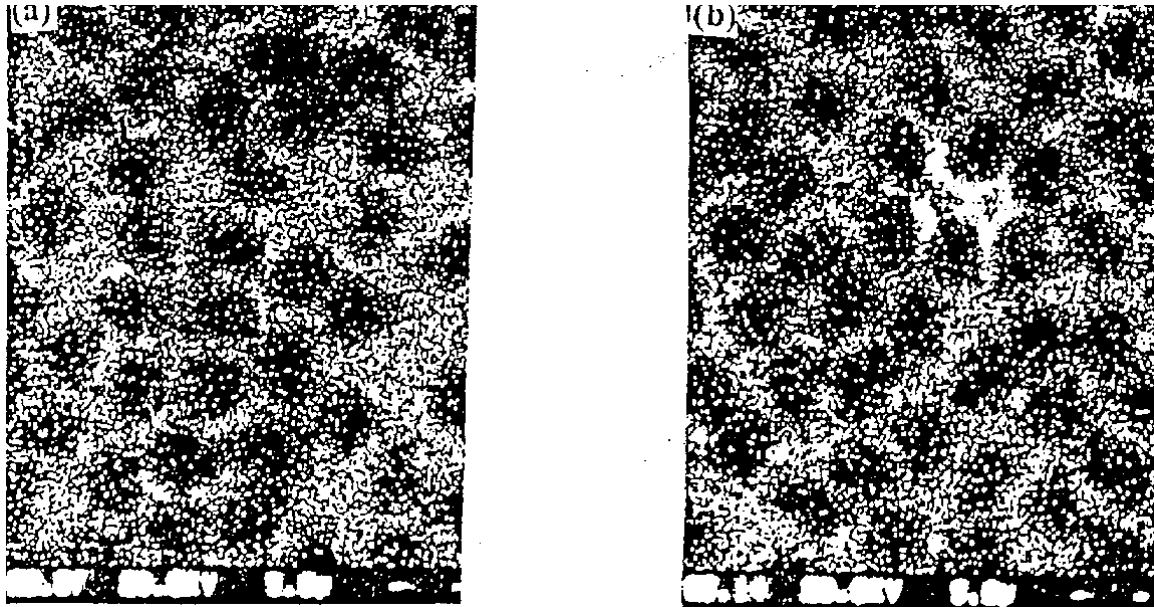


Fig. 4 The SAD pattern of $CuAl_2$ and Al_4C_3 phase in the interface of CF/Al-4.5Cu composites

Previously some works [7,8] have showed that Cu element accumulate easily in the interface of composites, it is because that probably reducing the interface energy according to Gibbs' interface absorption theory. For specimen A and B, Fig.5 shows Cu element segregation surrounding CF and the extent of Cu element segregation in specimen A is larger than B.

According to forming mechanism of the segregation suggested by literature [9] that before forming Al_4C_3 , Cu atoms have accumulated on the surface of CF first and during the growth of Al_4C_3 by interface reaction, Cu atoms are necessary as an initiator. When the segregation extent of Cu element is more large, the rendered Al atoms are turn to small. So since the segregation extent of Cu element in specimen A is larger than B, under the same condition of the interface reaction, the amount of Al atoms rendered by specimen A is lower than B.



(a) Specimen A

(b) Specimen B

Fig.5: Distribution of Cu element around carbon fiber surface.

In the meanwhile, with the decreasing of solidification cooling rate, the touching time between carbon fiber and liquid Al will increase, it means the interface reaction time is also prolonged by comparing A with B. Due to the touching time and temperature between carbon fiber and liquid Al alloy will greatly effect on the forming kinetics of carbon-aluminum reaction compound, so that with increase of the touching time and temperature, the forming condition for carbon-aluminum reaction compound is easier, therefore, it would lead that the size of precipitated Al_4C_3 in B case is larger than that in A, and with the increase of Cu element segregation, the diffusion hinder effect for Al atoms increased, i.e. the diffusion of Al atom becomes difficult and restricts the growth of Al_4C_3 .

Besides, when the CuAl_2 forming, it will restrict the growth of Al_4C_3 and trend to precipitate $\theta\text{-CuAl}_2$ phase intensively, so that the dimension of Al_4C_3 phase in case A is smaller than B. Normally, the quantity of precipitated Al_4C_3 phase in specimen B should be large than A, but actually it is inverse since the nucleation rate of Al_4C_3 phase in specimen A is higher than B.

CONCLUSIONS

1. In the interface of CF/Al-4.5Cu composite fabricated by squeeze cast, with decrease of solidification cooling rate, the extent of Cu element segregation on the surface is decreased and the quantity of precipitated $\theta\text{-CuAl}_2$ phase is also decreased, but the size of $\theta\text{-CuAl}_2$ phase is increased.

2. TEM analysis showed that in the interface of CF/Al-4.5Cu composites fabricated by squeeze cast, the quantity of precipitated Al_4C_3 is increased with increase of solidification cooling rate, but the size of Al_4C_3 phase is decreased.

ACKNOWLEDGMENTS

The authors acknowledge gratefully to the financial support by the National Natural Science Foundation of China, the Doctorate foundation of the State Education Commission of China, and the State Key Laboratory of Metal Matrix Composites of China.

REFERENCES

1. Thomas F. Klimowicz, "The Large-Scale Commercialization of Aluminum-Matrix Composites", *J. Minerals Met. Mater.*, Vol.46, No.11, 1994, pp.49-53.
2. R. Henriksen and T. E. Johnsen, "Influence of microstructure of fibre/matrix interface mechanical properties of Al/Si composites", *J. Materials Science and Technology*, Vol.6, No.9, 1990, pp.857-861.
3. N. Patankar, V. Gopinathan and P. Ramakrishnan, "Chemical Interactions at the carbon fiber aluminum interface", *Scripta Metallurgica et Materiala*, Vol.24, 1990, pp.2197-2203.
4. Tsai hongwei, Zhang Guoding, Wu Renjie, "Interface reaction kinetics study of SiC/Al composites", *Acta Aeronautica et astronautica sinica*, Vol.13, No.5, 1992, pp.A349-342.
5. Li Leiqing, "The collection of illustrative plates of casting aluminum alloy", Changsha, Central south university of technology, 1987. (in Chinese)
6. Zhang Guoding, Feng Shaoren, J. A. Cornie, "Control of interface reactions between P-55 fibers and aluminum alloy matrices during pressure infiltration processing", Vol.12B, No.12, 1991, pp.570-575.
7. Li ming, Gu mingyuan and Zhang Guoding, "Effects of alloying element Cu on the interfacial microstructure of C/Al-Cu composite", *J. Materials Engineering*. No.1, 1994, pp.1-3. (in Chinese)
8. Shojiro Ochiai, Tadao Arai, Kenji Tokinori, et al, "Tensile strength of unidirectional γ - Al_2O_3 fibre/Al-5 mass% Cu matrix composite at room and high temperatures", *J. Mater. Sci.*, Vol.27, 1992, pp.4667-4677.

Chu Shuangjie, "Study on the nonequilibrium solidification process of metal matrix composites", Ph.D. thesis of Shanghai Jiao Tong University, 1996. (in Chinese)

THE SLIDING WEAR RESISTANCE BEHAVIOR OF NiAl AND SiC PARTICLES REINFORCED ALUMINUM MATRIX COMPOSITES

Rong Chen¹, Akira Iwabuchi², Tomoharu Shimizu²,
Hyung Seop Shin³ and Hidenobu Mifune²

¹ *Institute of Composite Materials, Shanghai Jiao Tong University, Shanghai 200030, China.*

² *Department of Mechanical Engineering, Faculty of Engineering, Iwate University,
Morioka 020, Japan.*

³ *Department of Mechanical Engineering, Andong National University, Andong,
Kyungbuk 760-600, Korea*

SUMMARY: The sliding wear resistance behavior of NiAl and SiC particles reinforced aluminum alloy matrix composites against S45C steel was studied. Experiments were performed within a load range of 3.5 N to 82.7 N. At low loads, the wear resistance of the SiCp/Al and NiAlp/Al composites was superior to that of unreinforced aluminum alloy. With increasing the applied load, the wear rates of the composites increased to levels comparable to those of unreinforced matrix alloys. The wear rates of NiAlp/Al and SiCp/Al composites above 13.5 N were much lower than those of aluminum alloy. The wear rates of steel against a aluminum alloy were lower than those against the SiCp/Al composites. The NiAlp/Al composites worn the steel at the maximum wear rate at lower loads near 5 N. As load increased, the wear rates of steel against NiAlp/Al became smaller and were almost the same as those worn against aluminum.

KEYWORDS: particle reinforced metal matrix composites, SiCp/Al composites, NiAlp/Al composites, wear resistance behavior, wear, friction

INTRODUCTION

Particle reinforced metal matrix composites are recognized to have better wear resistance for the presence of hard particle. These materials can be used as a reinforced parts in piston, brake disk and in several wear resistance applications. The tribological behavior of MMCs depends on the type of MMCs, counterface materials and the contact situation.

An increase in the sliding wear resistance of particle or whisker reinforced aluminum alloys has been measured by many researchers in recent years [1-10]. Pramila Bai et al [6] found the fact that SiC particle reinforced A356 aluminum composites improved the wear resistance was attributed to the presence of SiC particles which reduced the propensity for materials flow at the surface, and the formation of iron-rich layers on the surfaces of composite during sliding. However, results of sliding wear conducted by various researchers do not show a consistent trends, Bhansali and Mehrabian [7] found that there was an absence of any significant improvement in wear resistance under abrasive wear conditions for the 20 wt% SiCp/2024Al composite worn against steel. It was attributed to the presence of brittle Al₄C₃ at the interface between particle and matrix. Alpas and Embury [8] showed that under the

conditions where SiC particles promoted subsurface cracking and materials removed by delamination, SiC reinforcement did not contribute to the wear resistance of aluminum alloys.

Recent studies [8-10] revealed that wear resistance was largely affected by the strength of interface between particle and matrix as well as the mechanical properties of the materials. Alpas et al [11-12] found that when particles lose their ability to support the applied load due to particle fracture, interface debonding and pull-out, particle reinforcement may cause no improvement or even a deterioration in the wear properties.

The NiAl particle reinforced aluminum alloy (Al-Ni-Mg-Mn series alloy) composite was considered to have a better interface bonding between particle and matrix and better wear resistance compared with unreinforced aluminum alloy [13]. Besides, since the hardness of NiAl particle is lower than that of SiC particle, it is predicted that the NiAl particle reinforced aluminum composites give the counterface small wear damage. However, the research on the sliding wear resistance of the NiAlp/Al composites worn against the steel was less reported in the existed literature. The purpose of this paper is to understand the sliding wear resistance of the SiCp/Al and NiAlp/Al composites with different volume fraction (5 vol% and 10 vol%) worn against S45C steel, and to study the effects of the applied load and different types of particles on the sliding wear mechanisms.

EXPERIMENTAL METHODS

The experimental apparatus used was a pin-on-disk type tribometer, which was modified in the previous works [14]. A moving lower specimen (disk) and a fixed upper specimen (pin) were mounted at the ends of a driven shaft and a fixed shaft respectively. Normal load was applied to the specimens by a dead weight at the upper end of the fixed shaft supported by two sliding ball bearings. The rotating motion of the fixed shaft induced by frictional torque was restricted by a plate spring on which strain gauges were attached for measuring the frictional torque. The relative distance between the specimens was measured by a dial gauge type displacement transducer placed on a fixed upper specimen. The frictional force and the relative distance were recorded continuously by a recorder. The dry sliding wear tests were carried out at a constant sliding velocity of 0.15 m/s within the applied normal load range of 3.5 N to 82.7 N. The sliding distance was all up to 1000 m.

The disk specimens were made of an aluminum alloy (Al 91.4 %, Ni 3.0 %, Mg 4.8 %, Mn 0.8 %) with or without reinforced particles of NiAl and SiC at volume fraction of 5 vol% and 10 vol% respectively. These alloy and composites were produced by the Ryobe Company in Tokyo, Japan, by means of liquid aluminum alloy stirring method. The dimensions of the disk specimen were a diameter of 19.5 mm and a height of 8 mm which was machined from the rods fabricated by directly die-casting. The average NiAl and SiC particle sizes are 50 and 10 μm respectively, the Vickers hardness of NiAl particle was about 270 Hv. The counterface material used as a fixed pin was 0.45%C steel, S45C, with the Vickers hardness of 225 Hv. The diameter and the length were 4 mm and 8 mm respectively. The mean contacting diameter was 13 mm on the disk specimen. The wear surfaces of the disk and pin specimens were polished by the SiC abrasive papers up to 1000 grits. The polished surfaces were then cleaned ultrasonically in acetone for 15 minute. The center line average surface roughness Ra was 0.2 μm for aluminum alloy, 0.4 μm for NiAlp/Al composite, 0.6 μm for SiCp/Al composite and 0.3 μm for S45C steel respectively.

The weight losses of specimens were measured with an accuracy of 0.1 mg using an electronic analytical balance. The specific wear rates were calculated as the volume loss divided by the sliding distance and the applied load. The results were taken as the average from at least three tests. Microstructural investigations and semi-quantitative chemical analyses on the worn surfaces were performed by SEM and EDXA(energy dispersive X-ray analysis).

RESULTS

The Specific Wear Rates of Aluminum Alloy and Composites

The specific wear rates of the aluminum alloy, the NiAlp/Al and SiCp/Al composites at applied loads from 3.5 N to 82.7 N within the sliding distance of 1000 m are shown in Fig. 1. The specific wear rate of aluminum alloy is decreased with increasing the applied load between 3.5 N to 9.4 N. However, it is increased at the load from 9.4 N to 13.5 N. Severe wear appears above 13.5 N. Large aluminum debris particles were formed at the initial stage of sliding and severe surface damage happened to occur.

At the lowest load of 3.5 N, the wear rate of aluminum alloy is about an order of magnitude larger than those of the SiC and the 10 pct NiAl particle reinforced composites. It reveals that at small loads, aluminum alloy shows lower wear resistance than particle reinforced composites. The wear rate of the 5 pct NiAl particle reinforced composite is in the moderate, about 5 times of those of other composites. The specific wear rate of composites is increased with the load, and at 9.4 N, the specific wear rates of composites are almost close to that of

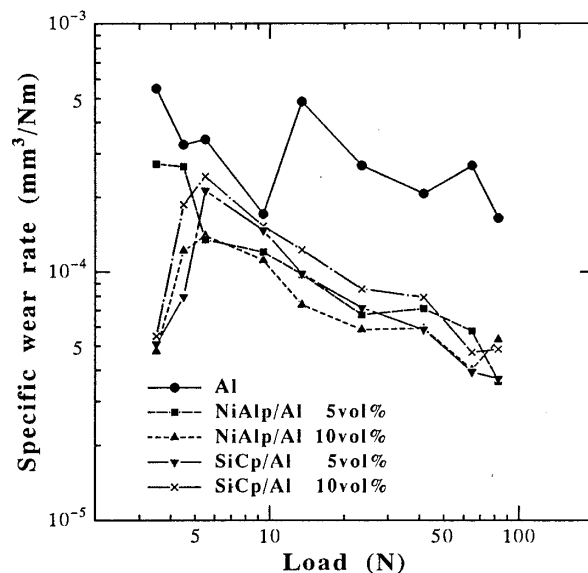


Fig. 1: The specific wear rate of aluminum alloy, 5 vol% and 10 vol% NiAlp/Al and SiCp/Al composites versus the applied load.

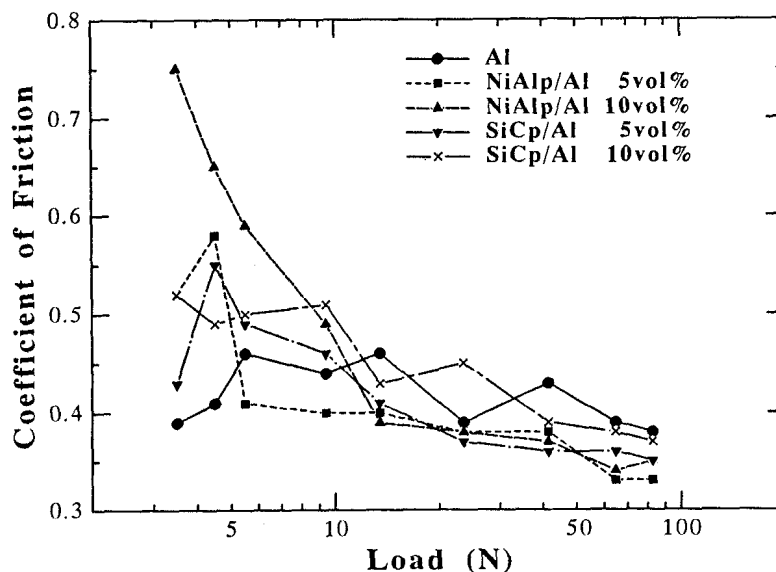


Fig. 2: The coefficient of friction versus the applied load.

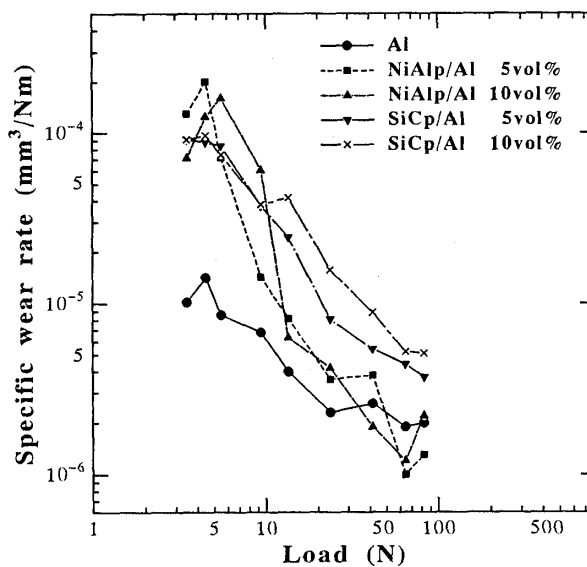


Fig. 3: The specific wear rate of S45C steel worn against aluminum alloy and composites versus the applied load after the sliding distance of 1000 m.

unreinforced aluminum alloy, and then, no improvement of wear resistance of composites at this load level. However, above 9.4 N, the specific wear rate of composites decreases with increasing the applied load, even when the applied load is increased to 82.7 N. It reveals that particle reinforced composites have the ability to increase wear resistance at higher loads.

Fig. 1 shows that the NiAlp/Al composites seem to have a litter better wear resistance than the SiCp/Al composites within load range from 5.5 N to 82.7 N, even at the fact that the hardness of NiAl particle is smaller than that of SiC particle. However, at the low load range below 4.5 N, the wear rate of 5 pct NiAlp/Al composite is higher than other composites. Increasing the

volume fraction of particle decreases the wear rate of NiAlp/Al composites. On the contrary, the wear rate of SiCp/Al composites is increased by increasing the volume fraction of particle over the load applied.

The coefficients of friction of aluminum alloy and composites are shown as in Fig. 2. It is obvious that the coefficient of friction between S45C steel and 10 pct NiAlp/Al composite is the largest at the lowest load of 3.5 N, it was above 0.75 and decreased with increasing the load, and then, the coefficient of friction became the same with those of other materials between 0.4 and 0.5 at loads above 9.4 N. Meanwhile, the 5 pct NiAlp/Al composite had the largest coefficient of friction at 4.5 N, however, it drop quickly with increasing the load.

The Specific Wear Rate of the Counterface Materials, S45C Steel

In practical use, it is important to know the total wear of the entire tribological system. The wear rates of the counterface materials S45C steel worn against aluminum alloy, NiAlp/Al and SiCp/Al composites are shown in Fig. 3. The specific wear rate of the steel against aluminum alloy is smaller compared with those against SiCp/Al composites at entire loads and NiAlp/Al composites at load range below 9.4 N. The SiCp/Al composites worn the steel at higher wear rate, especially when the applied loads are above 9.4 N. The wear rates of the steel against SiCp/Al composites are about an order of magnitude larger than those of against NiAlp/Al composites and aluminum alloy at 13.5 N. The wear rates of the steel are increased by the increase of volume fraction of SiC particle.

The specific wear rates of steel against NiAlp/Al composites are affected seriously by change of applied loads. Under the applied loads below 13.5 N, the NiAlp/Al composites worn the steel at a large wear rate. The wear rate of steel reached the maximum at 4.5 N for 5 pct composite and at 5.5 N for 10 pct composite. The maximum wear rate at relatively low loads is about 10-15 times of those at high loads. When the load is above 4.5 N for 5 pct composite and 5.5 N for 10 pct composite, the wear rates begun to drop and finally became the same with those of against aluminum alloy.

DISCUSSION

Wear Resistance at Low Loads

At the lowest applied load, the high wear resistance of SiCp/Al materials is attributed to the presence of SiC particle in the matrix. The particle protrusions are found as high as 6 μm . These protruded particles act as load supporting elements and are useful to prevent the softer aluminum matrix becoming directly involved in the wear process at low loads. The presence of SiC particle is also useful to prevent the matrix aluminum alloy from early fracture at low loads. Fig. 4 shows the coefficient of friction and the relative distance between the surfaces of a pin and a disk for the aluminum alloy (a) and SiCp/Al composite (b) versus the sliding distance at 3.5 N. For aluminum alloy, the coefficient of friction jumps to about two times of the usual value at several sliding distance, meanwhile, the relative distance is also changed abruptly as shown in point A and B in Fig. 4 (a). The increasing of coefficient of friction and the abrupt change in distance may be attributed to the formation of wear particles between surfaces due to the aluminum damaged at the contact surface. However, at the same load for SiCp/Al composite, no such phenomenon could be found as shown in Fig. 4 (b).

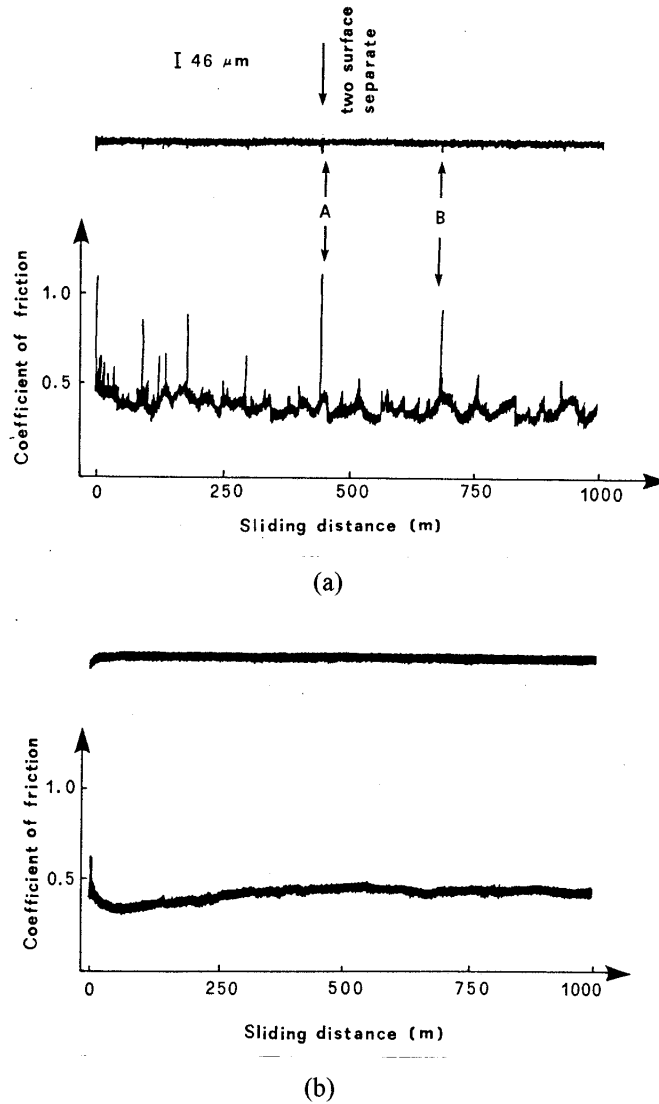


Fig. 4: The coefficient of friction and distance change between the contact surface at 3.5 N (a) Aluminum alloy (b) 5 vol% SiCp/Al composite.

The chemical composition of worn surface of the disk is also changed by the presence of SiC particle. Energy dispersive X-ray analyses were performed to determine the relative atomic percentages of metallic elements (Al, Si, and Fe) on the worn surfaces of the SiCp/Al composites at low load. Two typical areas which are full with and without SiC particles were selected. The results reveal that the relative content of Fe element at the surface with SiC particle is larger than that of the surface without SiC particle at 3.5 N. It implies that transfer of Fe element from steel to the surface of the composites is increased by the abrasive action of the presence of SiC particle in the matrix.

The NiAl particle does not stand proud of the surface. It is not able to prevent the softer matrix aluminum alloy directly involved in wear process. As a result, the wear rate of 5 pct NiAlp/Al composite at 3.5 N is about five times of that of the SiCp/Al composites. However, it is still lower than that of unreinforced aluminum alloy because the hardness of NiAl particle is larger than that of aluminum alloy and the particle is not fracture at low loads.

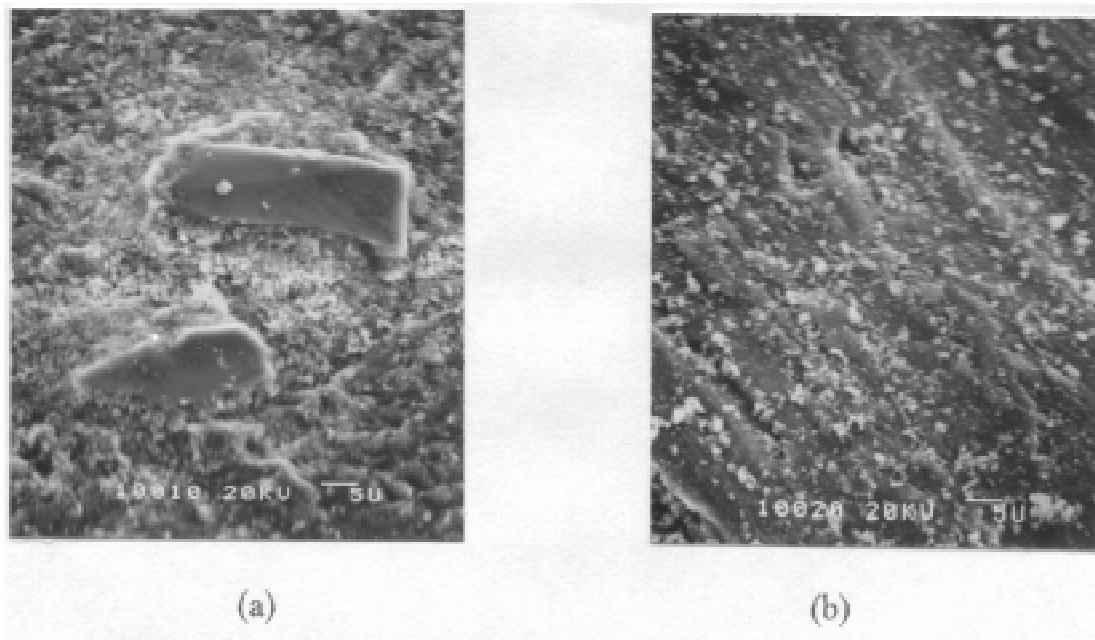


Fig. 5: The worn surface of 10 vol% SiCp/Al composite (a) at 3.5 N showing the SiC particle in structural integrity (b) at 9.4 N.

Wear Resistance at Middle and High Loads

When the load is increased to reach the fracture strength of the particle, the particles begin to fracture and lose their ability to support the load. Fig. 5 (a) shows the SiC particles in structural integrity on the wear surface of the SiCp/Al composite at 3.5 N, it reveals that the particles do not fracture at low loads. However, at the loads higher than 9.4 N, it is very difficult to discover these particles in structural integrity as shown in Fig. 5 (b). The particle near the contact surface may induce the nucleation of crack due to the interface debonding between particle and matrix than monolithic aluminum alloy. In sliding wear process, these cracks may propagate and connect to form the subsurface cracks, the subsurface damage process is increased by the presence of particle. The subsurface crack is also found for the 10 pct SiCp/Al composite as shown in Fig. 6. As a result, when the load increased up to 9.4 N, the wear rates of composites increased to levels comparable to that of the unreinforced aluminum alloy.

When the load is increased above 13.5 N, the wear process of the aluminum alloy may be a deformation and damage accumulation process. The depth of the deformed layers of the aluminum alloy below the worn surfaces is more deeper than that of the composites since the yield strength of the composites is larger. Besides, the surface temperature increased with the applied load and sliding distance. Aluminum alloy is easily to occur thermal softening and recrystallization at high temperature compared with the composites because the strength of the composites at high temperature is greater. As a result, the wear rate of the aluminum alloy is increased drastically at the load higher than 13.5 N. No this transition to severe wear can be found for the composites. However, the deformation and damage of the worn surface is also very obvious. Some of the deformed layer is broken, and several broken particles become fragmented and accumulated as shown in Fig. 7.

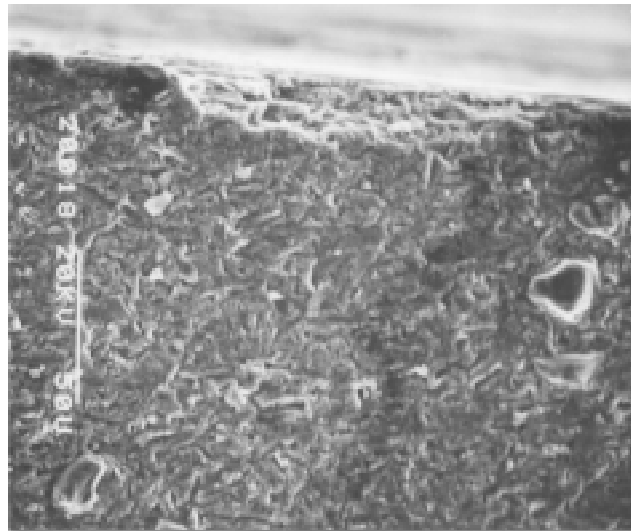


Fig. 6: The cross section perpendicular to worn surface of 10 vol% SiCp/Al composite at 40 N showing the subsurface crack is occurred.

The Wear Rate of the Counterface Material at Different Loads

The wear rate of the steel against the SiCp/Al composites is larger than that of against unreinforced aluminum alloy over the load applied for the presence of high hardness of SiC particle in the matrix. It is interesting that even if the hardness of NiAl particle is smaller than that of SiC particle, the wear rate of steel against the NiAlp/Al composite is about twice higher than that against the SiCp/Al composite at low loads near 5 N as shown in Fig. 3. The

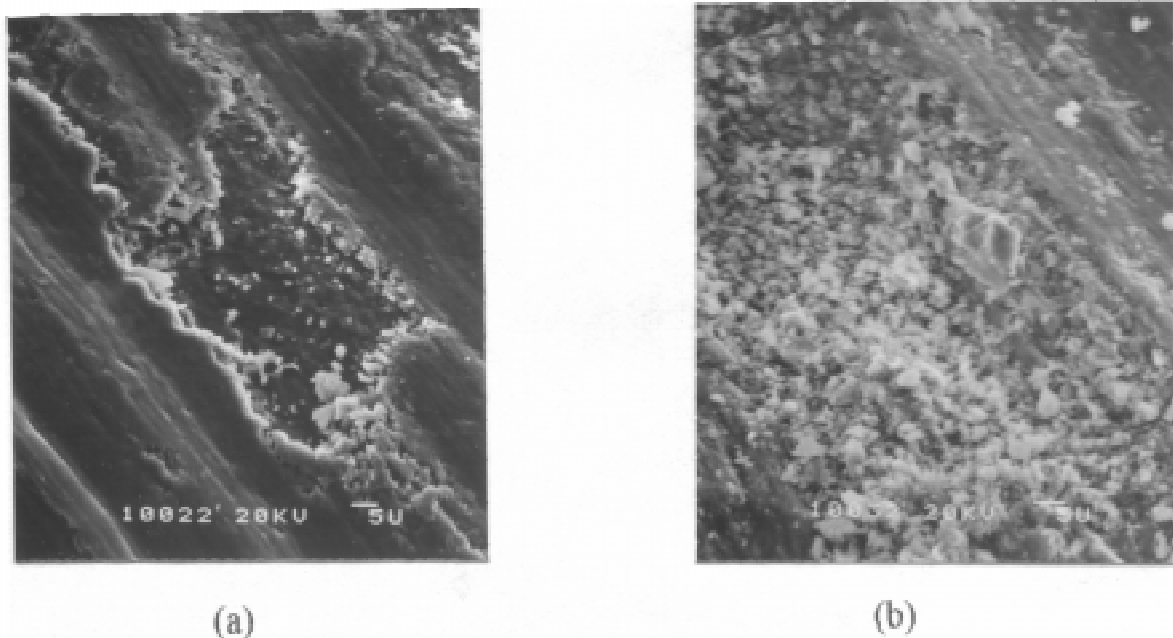


Fig. 7: The worn surface of 10 vol% SiCp/Al composite at 64 N (a) showing the tribolayer fractured (b) showing the broken particle fragmented and accumulated.

coefficient of friction versus sliding distance of a NiAlp/Al composite at 3.5 N shows that within the sliding distance of 250 m, the coefficient of friction is only 0.4, then, the coefficient of friction is increased with the sliding distance and reached twice of the initial value. The wear mechanism was changed after the sliding distance of 250 m. The NiAl particle is not stand proud of the contact surface, however, at several meter sliding wear, the soften aluminum alloy was fractured, as a result, the contact surface became the steel and the NiAl particle, the harder NiAl particle could abrade the S45C steel surface, and the NiAl particle wear the steel at very high wear rate. As a result, the coefficient of friction and the weight loss of steel is increased. At low load, the higher intensity of Fe means that the transfer of steel to surface of a NiAlp/Al composite is higher, meanwhile, and the transfer of aluminum to the surface of steel (pin) is lower. At the applied load above 9.4 N, the NiAl particles are easy to fracture and become fragment, it can be seen that the coefficient of friction between steel and 10 pct NiAlp/Al composite is decreased with the applied load as shown in Fig. 2. the broken NiAl particles could not abrade steel at high wear rate. The transfer of Fe to the surface of NiAlp/Al composite is lower. As a result, the wear rate of steel at high loads become smaller.

CONCLUSIONS

At low loads, the wear resistance of SiCp/Al and 10 pct NiAlp/Al composites are about an order of magnitude better than that of unreinforced aluminum alloy, which is attributed by the fact that the particles support the applied load, prevent the soften aluminum matrix to wear directly with steel.

The wear rates of the SiCp/Al and NiAlp/Al composites increased to a levels comparable to that of unreinforced aluminum alloy at medium loads of 4.5 N to 9.4 N because of particle fracture and damage of subsurface crack layers.

The transition to severe wear takes place for unreinforced aluminum alloy at 13.5 N. However, no transition could be found for the SiCp/Al and NiAlp/Al composites due to their better yield strength at high temperature.

The SiCp/Al composite wore steel at the wear rate of 5-10 times of unreinforced aluminum alloy over the load applied because of the presence of hard particle. High volume fraction of SiC particle worn against steel at high wear rate.

At low applied loads, the NiAlp/Al composite worn against steel at higher wear rate than SiCp/Al composite. The wear rates of steel against the NiAlp/Al composite become the similar with that against the aluminum alloy when the NiAl particle is fractured at high loads above 13.5 N.

ACKNOWLEDGMENTS

The authors would like to thank the Ryobe Company in Tokyo for supply of the materials, and useful discussion with Professor K. Katagiri at Iwate University is greatly appreciated.

REFERENCES

1. F.M. Hosking, F. Folgar Portillo, R. Wunderlin and R. Mehrabian, "Composites of aluminum alloys: fabrication and wear behavior", *Journal of Materials Science*, Vol. 17, 1982, pp. 477-498.
2. M.K. Surappa, S.V. Prasad and P.K. Rohatgi, "Wear and abrasion of cast Al-alumina particle composites", *Journal of Wear*, Vol. 77, 1982, pp. 295-302.
3. A. G. Wang and I.M. Hutchings, "Wear of alumina fiber-aluminum metal matrix composites by two body abrasion", *Journal of Materials Science and Technology*, Vol. 5, 1989, pp. 71-76.
4. K. C. Ludema, "A review of scuffing and running in of lubricated surfaces with asperities and oxides in perspective", *Journal of Wear*, Vol. 100, 1984, pp. 315-331.
5. A. T. Alpas and J. Zhang, "Effect of SiC particulate reinforcement on the dry sliding wear of aluminum-silicon alloys (A356)", *Journal of wear*, Vol. 155, 1992, pp. 83-104.
6. B.N. Pramila Bai, B.S. Ramasesh, and M.K. Surappa, "Dry sliding wear of A356-Al-SiCp composites", *Journal of wear*, Vol. 157, 1992, pp. 295-304.
7. K.J. Bhansali and R. Mehrabian, "Abrasive wear of alumina-matrix composites", *Journal of Metal*, Vol. 34, 1982, pp. 30-34.
8. A.T. Alpas and J.D. Embury, "Sliding and abrasive wear resistance of an aluminum-SiC particle reinforced composite", *Scripta Metall. Mater.*, Vol. 24, 1990, pp. 931-935.
9. S.J. Lin and K.S. Liu, "Effect of aging on abrasion rate in an Al-Zn-Mg-SiC composite", *Journal of Wear*, Vol. 121, 1988, pp. 1-14.
10. J. Yang and D.D.L. Chung, "Wear of bauxite particle reinforced aluminum alloys", *Journal of wear*, Vol. 135, 1989, pp. 53-65.
11. A.T. Alpas and J. Zhang, "Effect of microstructure (particulate size and volume fraction) and counterface materials on the sliding wear resistance of particulate-reinforced aluminum matrix composites", *Metallurgical and Materials Transactions A*, Vol. 25, 1994, pp. 969-983.
12. W. Ames and A.T. Alpas, "Wear mechanisms in hybrid composites of graphite-20 pct SiC in A356 aluminum alloy (Al-7 pct Si-0.3 pct Mg)", *Metallurgical and Materials Transactions A*, Vol. 26, 1995, pp. 85-98.
13. H. S. Shin, K. Katagiri, T. Sato, Y. Shoji, H. Kanemaru and H. Oumra, "The mechanical properties of SiC and NiAl particles reinforced aluminum alloy composite manufactured by dia-cast", *Transactions of JSME*, in the press
14. A. Iwabuchi, K. Hori and H. Kubosawa, "The effect of oxide particles supplied at the interface before sliding on the severe-mild wear transition", *Journal of Wear*, Vol. 128, 1988, pp. 123-137.

FABRICATION OF SiC-REINFORCED AZ91D MAGNESIUM-BASED COMPOSITES

Jason S.H. Lo and Graham J.C. Carpenter

*Materials Technology Laboratory,
Canada Centre for Mineral and Energy Technology (CANMET),
Department of Natural Resources Canada
568 Booth Street, Ottawa, Ontario K1A 0G1, Canada*

SUMMARY: The very low density of magnesium makes it an attractive metal for reinforcement with hard particulates to form a metal matrix composite. However, the high chemical reactivity of magnesium creates difficulties in producing composites in an economic manner. Squeeze casting provides a promising route with potential for making near-net shape castings or composites with selective reinforcement. Here, we report developments in a program to develop a composite composed of SiC particulates embedded in a matrix of magnesium alloy AZ91D using squeeze casting.

The process involves the fabrication of a SiC particulate preform followed by the subsequent squeezing of the molten magnesium alloy into the preform under pressure. Preforms with a volume fraction of 40 vol % of particulate were used. The procedures employed in the fabrication of these composites are presented. In addition, results are included showing the characterization of the composites using scanning and transmission electron microscopy to reveal the phases formed and the interfacial characteristics. Special attention is given to the reaction products in the bulk alloy and at the interfaces between SiC particles and the AZ91D matrix alloy when different binders were employed.

KEYWORDS: squeeze casting, magnesium-based metal matrix composites, particulates, perform, interfacial reactions

INTRODUCTION

The very low density of Mg makes it an attractive candidate for reinforcement with strong particles or fibres to form a metal-matrix composite (MMC). However, the high chemical reactivity of Mg creates difficulties in manufacturing commercial composites in an economic manner (1-3). Squeeze casting is a promising route for making Mg MMC's, with advantages for producing near-net shaped castings or composites with selective reinforcement.

In principle, reinforcing a magnesium alloy with particulates such as SiC should provide an improvement in strength and modulus of the composite over the unreinforced counterpart. However, many factors resulting from the fabrication process can cause degradation rather than improvements to the mechanical properties of composites (4-7). This is especially true in the case of squeeze cast magnesium-based composites, where the process conditions and materials used will determine the state of stress and the interfacial reactions between the particles, binder and the matrix alloy.

In this study, the squeeze-casting technique was used to fabricate particulate SiC-reinforced AZ91D magnesium alloy composites. The process consisted of two stages; the preform fabrication and the infiltration under pressure of molten AZ91D into the preform. Both the SiC particulate preforms and SiC/AZ91D composites were fabricated at MTL/CANMET.

It has been found that the amount and content of both the binder and its reaction products can have a significant effect on the composite. In the case of a magnesium-based composite, the high reactivity of the magnesium leads one to expect that the formation of reaction products will be more problematic than in the case of aluminum or zinc-aluminum based composites. Therefore, it is crucial both that a suitable binder be selected and that appropriate processing routes are developed for making magnesium composites. For this purpose, the microstructures of the composites in the as-cast condition are being examined using optical microscopy, scanning electron microscopy (SEM) and transmission (TEM)/scanning transmission (STEM) electron microscopy. Special attention was paid to the reaction products formed both in the matrix and at the particle/matrix interfaces.

EXPERIMENTAL PROCEDURES

Table 1 shows the chemical composition of the AZ91D alloy selected for this investigation. The SiC reinforcement particulates were supplied by Northern Co. The average particle size of the SiC was reported to be 17 μm .

Table 1. Chemical composition (wt %) of the AZ91D alloy.

Mg	Al	Zn	Mn	Si	Cu	Ni	Fe
bal.	8.5-9.5	0.5-0.9	>0.15	<0.02	<0.015	<0.001	<0.005

In the preform fabrication stage, the SiC particulates were held together by either an alumina (Al_2O_3) or a proprietary non-oxide binder to form a rigid three-dimensional network of inter-connecting particulates. The volume fraction of SiC particulate in a preform was 40 vol.%. The infiltration stage began by placing a preform in a die preheated to ($\sim 600^\circ\text{C}$) and the superheated AZ91D alloy ($\sim 100^\circ\text{C}$ above its melting temperature) was introduced into the die. A punch was then lowered into the die at a speed of 1 mm/s, forcing the molten metal to infiltrate the preform. The pressure exerted by the punch on the molten metal was steadily maintained until the molten metal had completely solidified, which normally took about 1 minute. On completion of the pressure infiltration operation, the punch was retracted from the die and the composite product was removed.

To evaluate the particulate microstructures using SEM, the specimens were coated with a thin layer of gold. TEM specimens were cut in the form of sections $\sim 200\ \mu\text{m}$ thick with a diamond wheel. Discs, 3 mm in diameter, were then ground mechanically to a thickness of $\sim 80\ \mu\text{m}$ and dimpled on one side using a Gatan Dimple Grinder, until the central region was $\sim 10\ \mu\text{m}$ thick. Final thinning to perforation was carried out in a Gatan Precision Ion Polishing System (PIPS) by argon-ion beam sputtering at 4keV at an incident angle of 4° . Finally, the specimens were ion-wiped on each side for 10 min. at 1.5 keV, before examination at 200 kV in a Philips CM20FEG TEM/STEM fitted with an Oxford Instruments atmospheric thin-window energy dispersive X-ray (EDX) detector with an eXL analyzing system, as well as a Gatan 666 parallel electron energy loss spectrometer (PEELS). Recent replacement of the PEELS with a Gatan Imaging Filter (GIF) has permitted preliminary experiments using energy-filtered imaging.

3. RESULTS AND DISCUSSION

Examination in the TEM at low magnifications showed that the SiC particulates were well dispersed in the AZ91D alloy matrix (e.g. Figure 1) using both types of binders; this is desirable, because it has been shown that clustering of the particulate can lead to embrittlement (4, 5). The SiC particles were readily distinguished from the matrix Mg alloy by the presence of faults or microtwins and few dislocations. In contrast, the Mg matrix contained a high density of dislocations, possibly caused by differential contraction of the two phases during cooling after melt infiltration, resulting in the build-up of residual stresses in the matrix surrounding the particulates.

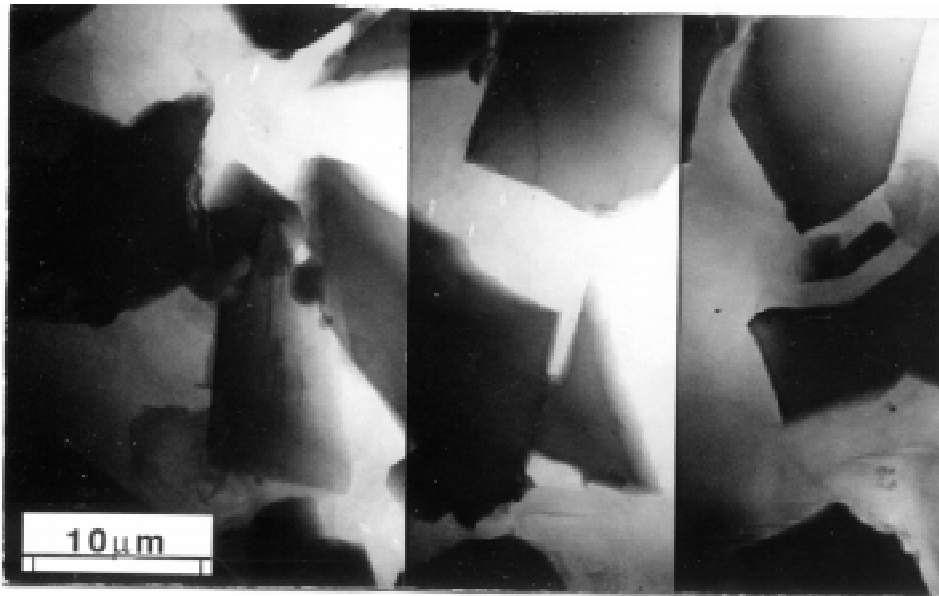


Fig. 1 Low magnification TEM micrograph illustrating SiC particulates in the matrix of AZ91D Mg alloy.

In earlier work [2, 3], we have shown that the SiC particles are frequently separated from the matrix by an interfacial film composed of nanocrystalline oxide particles (10~70 nm diameter), to a depth that depends upon the fabrication conditions. An example that shows the continuous nature of the oxide film in a sample made using the Al₂O₃ binder is shown in Figure 2 produced by energy-filtered imaging using the O K edge. These films can be up to ~500 nm in thickness; larger clumps of oxide within the AZ91D matrix have also been observed. Selected-area electron diffraction (SAD), EDX and PEELS analysis were used to show that this phase was composed of magnesium oxide, MgO, which promoted embrittlement by means of interparticle fracture.

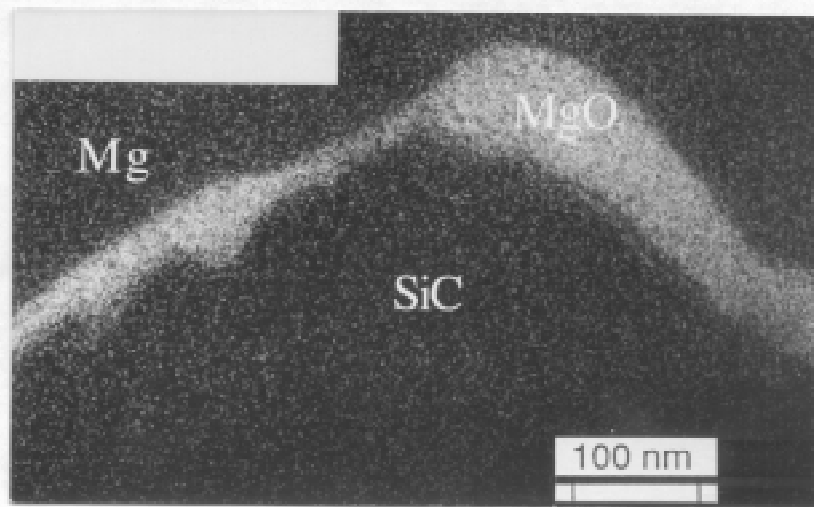


Fig. 2 Oxygen map produced by energy-filtered imaging, showing the presence of a continuous layer of MgO between a SiC particle and the AZ91D matrix.

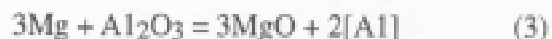
Recent work indicated that the MgO may arise from: (a) possible oxide formation on the surface of the SiC as a result of heating during the binding operation, according to the reaction:



followed by reduction of the silica:



or (b) where an oxide binder is used, the reduction of that oxide by the molten Mg may occur, e.g.:



Indirect evidence for the presence of oxide on the surfaces of the SiC particulate has been observed in SEM images of a preform fired in air, as shown in Figure 3, where it is clear that the surfaces have been substantially modified in comparison to the as-received powder (Figure 3). Further cross-sectional TEM work is being carried out in an effort to confirm that this change in surface appearance is caused by oxide formation during heating.

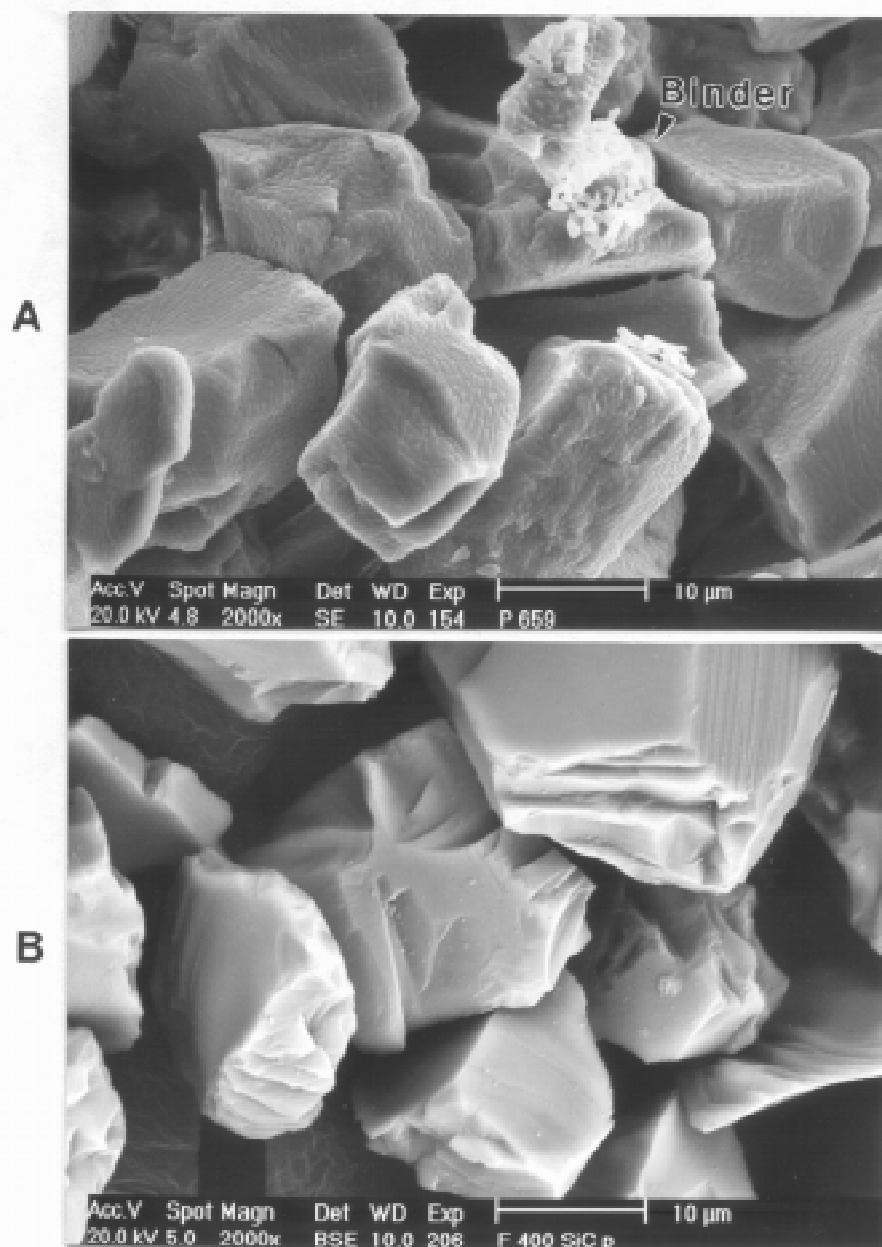


Fig. 3 Secondary electron SEM images of SiC particulates: a) from the preform following firing; b) virgin material, prior to fabrication.

In addition to the oxide films, second-phase particles, principally Mg_2Si and $Al_{12}Mg_{17}$ (γ -phase), have been observed in the alloy matrices for all samples examined. The Mg_2Si , in the form of roughly rectangular particles that were occasionally as large as $\sim 25 \mu m$ in length, appears to originate from the reaction between the SiO_2 and the Mg matrix as in equation (2) above.

The Al/Mg γ -phase is quite commonly found in unreinforced samples of the AZ91D alloy as a result of the high Al content. In the composite, it tends to be present as large particles ($\sim 1 \mu m$ in diameter) at the particulate/matrix interfaces. Two mechanisms are thought to be involved in the formation of the γ -phase in the magnesium composites: (a) the solubility of the Al contained in the solidified matrix alloy falls with decreasing temperature, causing the excess aluminum to be rejected during cooling, and (b) where an Al_2O_3 binder is used, the Al concentration in the matrix is elevated above that in the AZ91D alloy, as a result of the reaction between magnesium and the Al_2O_3 binder, equation (3) above.

The precipitation from solid solution of the γ -phase in the form of fine platelets ($\sim 100 \text{ nm}$ diameter) within the grains of the matrix alloy has also been noted and is believed to be dependent upon the cooling rate following solidification. Occasionally, evidence for the presence of small quantities of the residual binder material has been observed in TEM specimens of the solidified composite.

Once the phase constituents had been analysed using a combination of EDX, PEELS and electron diffraction [1, 2], X-ray mapping has proved to be invaluable for surveying the microstructures of newly fabricated composite samples. An example is shown in Figure 4, where several phases were present in a sample for which the preform was fabricated in air and an Al_2O_3 binder was used. The X-ray maps of Figure 4, clearly show that the phases labelled "A" in Figure 4 contained both Mg and Si, and thus were composed of Mg_2Si . In a similar manner, it can be seen that the precipitate marked "B" comprised the γ -phase. The oxygen map also reveals the continuous layer of oxide between the SiC particles and the matrix. The Mg_2Si particles were often associated with oxide in this sample, as expected from the reactions given in equations (1) and (2).

The oxygen map of Figure 4 can be compared to that from a more recent sample, Figure 5, where it is clear that improved fabrication procedures using a non-oxide proprietary binder and an inert atmosphere for processing the preform have reduced the oxide level to the presence of a relatively few discrete oxide particles at the SiC interfaces, together with occasional small clumps within the AZ91D matrix. This processing route also appears to lead to a reduction in the formation of Mg_2Si , in parallel with the lower propensity for MgO formation gas expected from equation [2].

It is clear that the new processing route leads to definite improvements in microstructure. There is evidence that the presence of MgO at the particle/matrix interfaces leads to interparticle failure in tensile tests (2). Similarly, the presence of Mg_2Si , which readily fails by cleavage, may result in embrittlement (1). The improved microstructures resulting from the new processing procedures are therefore expected to translate into significantly improved mechanical properties for SiC/AZ91D composites.

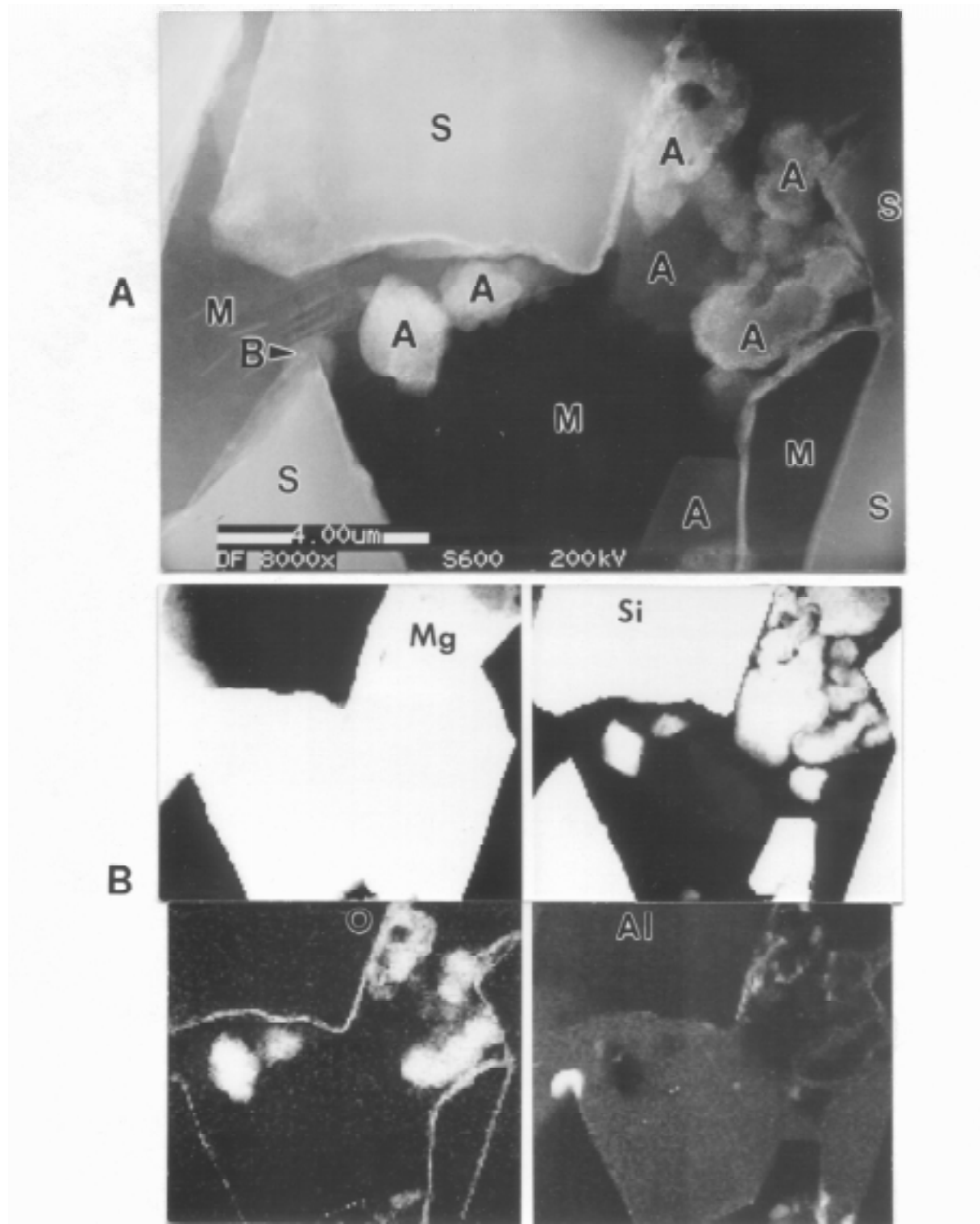


Fig. 4 X-ray mapping using a sample from a batch of material prepared using an Al₂O₃ binder and fired in air, leading to continuous oxide films at the SiC/matrix interfaces: (a) dark-field STEM image (S = SiC, M = AZ91D Mg alloy matrix, A = Mg₂Si, B = Al₁₂Mg₁₇); (b) X-ray maps using K peaks from the EDX spectrum.

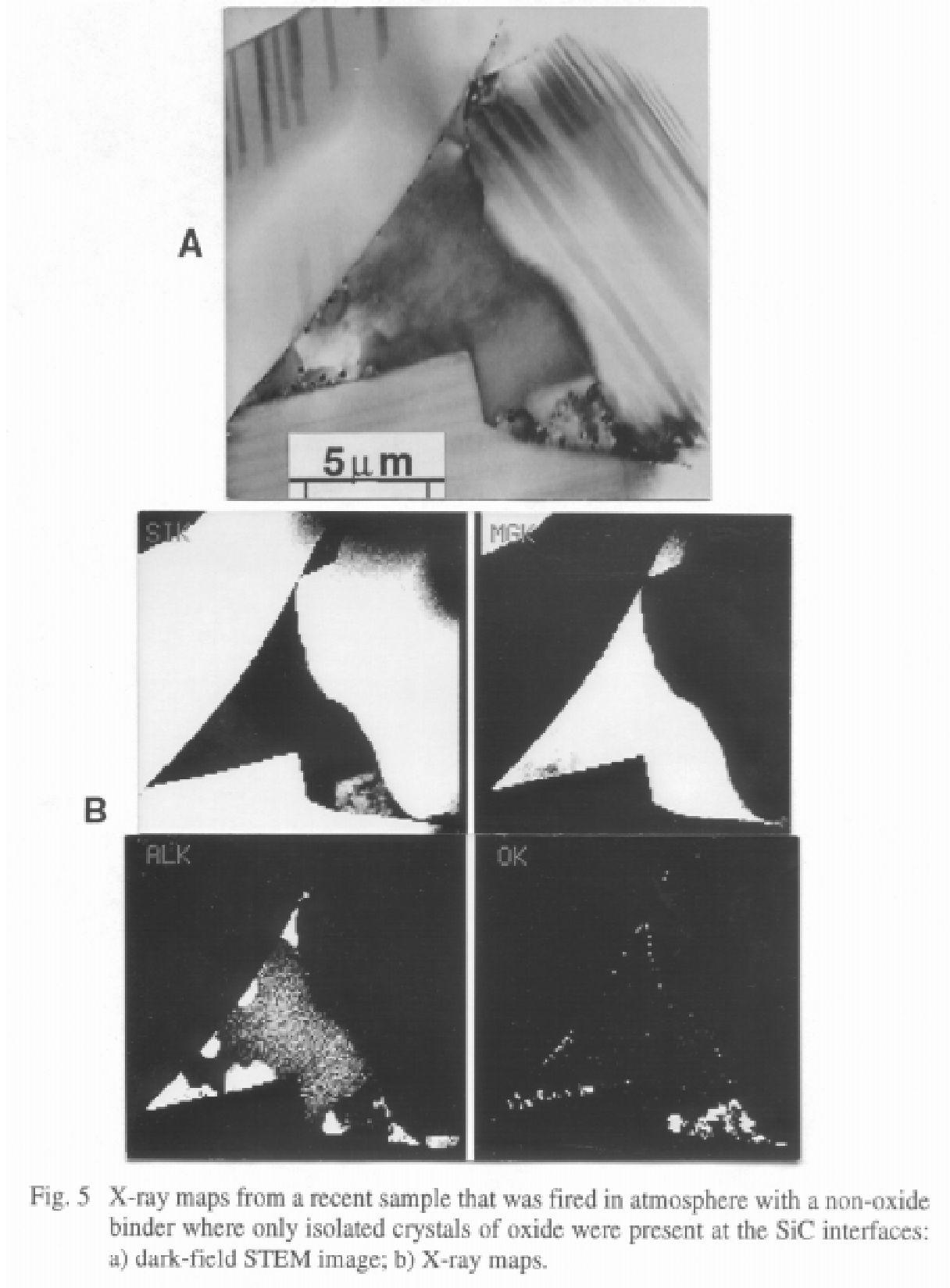


Fig. 5 X-ray maps from a recent sample that was fired in atmosphere with a non-oxide binder where only isolated crystals of oxide were present at the SiC interfaces: a) dark-field STEM image; b) X-ray maps.

4. CONCLUSIONS

Based on the observations of the squeeze-cast composites of SiC in a matrix of AZ91D Mg alloy, using optical, scanning and transmission electron microscopy, the following conclusions are drawn:

1. Squeeze casting leads to uniform dispersion of SiC particulates in the Mg alloy matrix;
2. The large difference between the coefficient of thermal expansion of the matrix and the particulates generates sufficient stress to form a high density of dislocations in the matrix;
3. A nanocrystalline MgO film is often formed at the particle/matrix interfaces and clumps of oxide may also be present within the AZ91D matrix;
4. It appears that the presence of an oxide film on the SiC particulate, created during processing of the preform in air before squeeze casting, may be a significant source of the oxygen that results in the formation of MgO;
5. An oxide binder such as Al_2O_3 may also be reduced by the molten Mg, leading to MgO formation;
6. Oxide formation may be minimized through the use of an inert atmosphere during the firing operation used in making the SiC preform and by employing a non-oxide binder; these processing changes result in a significant improvement in the microstructures of the SiC/AZ91D composites;
7. The formation of Mg_2Si is often observed and is expected to cause embrittlement; its presence may be related to the reactions that give rise to the MgO phase, so that the new processing procedures may also lead to a reduction in Mg_2Si formation.

5. ACKNOWLEDGMENT

The authors would like to thank the following colleagues at MTL/CANMET for their support during this project: R. dos Santos for the preparation of the squeeze-cast composite, M. Charest for the preparation of the TEM specimens and B.R. Casault for support with the SEM examination.

6. REFERENCES

- [1] K. Hicks, G. Love, V.D. Scott and R.L. Trumper, "Degradation of Nicalon Fibers in Magnesium-Based Composite", *Processing of the 9th International Conference on Composite Materials*, edited by Antonio Miravete (University of Zaragoza, Woodhead Publishing Ltd., 1993), Vol 1, p. 325.
- [2] J. Lo, M. Shehata, G. Carpenter, A. Luo and M. Pegguleryuz, "Microstructural and Interfacial Characteristics of SiC Reinforced AZ91D Magnesium Based Composite", *Processing International Metallographic Society Conference*, Montreal (1994), in *Microstructural Science* (1995), Vol. 22, p. 237.
- [3] J. Lo, G.J.C. Carpenter and M. Charest, "International Characteristics of Squeeze Cast SiC Reinforced AZ91D Magnesium Based Composites", in *Design Fundamentals of Composites Intermetallics/Metal/Ceramic Systems*, edited by R.Y. Lin, Y.A. Chang, R.G. Reddy and C.T. Liu, published by TMS, USA, 1996, p. 29.

- [4] W.H. Hunt, O. Richmond and R.D. Young, "Fracture Initiation in particle hardened materials with high volume fraction", *Proceedings of the Sixth International Conference on Composite Materials, Second European Conference on Composite Materials, London, July 1987*, edited by F.L. Matthews, N.C.R. Buskell, J.M. Hodgkinson and J. Morton (Elsevier, Amsterdam, 1987), Vol. 2, p. 209.
- [5] D.J. Lloyd, "Aspects of Fracture in Particulate Reinforced Metal Matrix Composites", *Acta Metall.*, Vol. 39(1) (1991), p. 59.
- [6] B. Inem and G. Pollard, "Interface Structure and Fractography of a Magnesium-Alloy, Metal Matrix Composite Reinforced with SiC Particles", *Journal of Materials Science*, 28 (1993), 4427.
- [7] G. Elssner and T. Suga, "Determination of the Fracture Energy and the Fracture Resistance of Interfaces", *J. Phys. (Orsay)*, 1985, C4, p. 657.

EFFECT OF MICROSTRUCTURE, INTERFACE AND ON THE AGING BEHAVIOUR OF A356 AL/SiC_p COMPOSITES

J. J. Yeh, L. D. Chen, C. B. Lin

Department of Mechanical Engineering, Tamkang University, Taipei, Taiwan 25137, R.O.C.

SUMMARY: This research we used dilution method directly to pour the melting high concentration A356 / 40wt%SiC_(p) composite material into the molten of Al alloy, and prepared A356/0wt%, 10wt%, 20wt%SiC_(p) composite material, and finally pour into the permanent mold which is 300-500 °C to become the casting. Then we do age hardening treatment to these composites material. We have also studied the influence of both the Al₃C₄ growth amount at interface and the non-uniform of SiC particulate distributed in the matrix to the aging behavior. For the A356/10wt% SiC_(p) composites, the hardness increase as both interface layer produce and growth increase, but decrease with non-uniformity of SiC particulate distribute in the matrix. For the A356/20wt% SiC_(p) composites, the age hardening would not be influenced by the non-uniform and the interface reaction layer.

KEYWORDS: silicone carbide, metal matrix composites diltion, interface, non-uniformity, accelerated aging

Introduction

PMMCs is a kind of material having special function and structure, that is formed by spreading of Al₂O₃, SiC, Si₃N₄, B₄C strengthening phase grains or Gr, MoS₂ lubricant phase grains among Al, Mg, Ti alloy base. PMMCs has the following advantages: cheaper cost of the grain type second phase, isotropic properties, better specific strength, stiffness, hardness and wear resistance. In addition, the thermal conductivity and thermal expansion coefficients are freely adjustable, and it can be made by traditional manufacturing methods like casting, rolling, forging and extrusion. Therefore, PMMCs has been applied to automotive industry, such as cylinder liners [1], brake roto disc [2]; wear resistant materials, such as cemented carbides [3], electrical contact supports [4], electronic packaging [5]; recreational and sporting equipment such as bicycle frame, golf head, chain wheels [6], having highly develop value for industry.

There are several developed manufacturing methods for PMMCs, like vortex method under vacuum [6], compocasting [7], infiltration process [8], spray process [9]; powder metallurgy [10]; Lanxide's process [11]; XDTM process [12]. These methods have their

own advantages and shortages, and can be adopted by different product characteristics. For example, using powder metallurgy process for getting high particle concentration, and using vortex method under vacuum process for mass production of ingot and billet to save cost. Duralcan USA use this patented process can produce 6305 kg per over and lower the PMMCs price dramatically.

Due to the thermodynamics unstability and the long melting period, some strengthening phase in high temperature Aluminum alloy molten will lead to a interface chemical reaction. Such as SiC particle in high temperature Aluminum alloy molten would have the reaction.



Si will be melted in Aluminum molten, and Al_3C_4 will be formed in the interface of SiC particulate and Aluminum molten[13]. Formation of Al_3C_4 can increase the viscosity of Aluminum molten, lower the fluidity[14] and decrease the mechanical properties of Al/SiC [15]. In order to prevent the interface reaction of Al and SiC, we can use squeeze casting and spray casting[16], or prevent the SiC particulate between 100 °C to 1200 °C to form a thin SiO_2 layer on SiC particulate surface.

Using the mentioned vacuum vortex method for mass production, we require a fine vacuum system and larger supply equipment. In addition, the whole equipment need a good insulation system to prevent heat loss from the stirring system and use for separating of SiC particulate. For the shortages mentioned, the first part of the study propose a “dilute method”, using small oven with vacuum vortex method to make high concentration A356/40wt%SiC(p) composite molten, then pour it into degassed A356 Aluminum molten directly, and stir it without vortex, and let SiC particulate distribute among the whole large molten uniformly.

Particulated metal matrix type composite can improve properties by aging, such as raising its ductility[17], ultimate tensile strength[18], fracture resistance[19] and wear resistance[20]. These changes mainly is due to that a lot of dislocation will be occurred in the interface because of the great difference of thermal expansion coefficient between the strengthening phase and metal matrix after the that treatment of the composite material[21]. In Arsenault and Shi's theory [22] model of dislocation Strength, dislocation density increase as strengthen phase amount increase, and decrease with particulate size, while in the same material and aging condition. An important assumption of the theory is that the strengthening phase particulate are spread uniform among the matrix, but, in reality, particulate type metal matrix composite will be affected by Van Der weal's force, gravity segregation, cooling rate and the dendrite pushing to form the particulate in the matrix non-uniformly[23]. XLE Guohong et.al [24] proposed a pushing sensitive coefficient(ϵ) for the quantity comparison of the particulate pushing strength. and $\epsilon = \text{non-uniformity} / \text{particulate average size}$.

$$\text{non-uniformity} = \sqrt{\frac{1}{20} \sum (A_i/A - 1)^2}$$

Where A is average value, A_i is the area points of 20 grains

Under the same aging condition, metal matrix composite material spend less aging time than parent metal to reach the maximum hardness[25]. Janowski Pletkas reported[26] that while in aging treatment of 201Al/SiC_(p) composite material, 24 μm SiC particulate strengthen metal composite has the more accerlation aging than 63 μm and 142 μm and it can accerlate the aging as increase the second phase particulates amount[27].For Al- 7% Si- 0.3% Mg / SiC_(p) composite material, if a 50nm SiO_2 layer is

formed on SiC particulates surface, the spinnell will be formed in the interface, and lower the amount of Mg in base, lead to a decrease of aging hardness[28].

Some references[29] found that in particulate type metal matrix composite material the standard variation of its aging hardening hardness is larger. This is due to the non-uniformity of the particulate macro distribution among the matrix. Therefore, the second part of this paper will study the relationship of the casting mold temperature, melting temperature, and the non-uniformity of the SiC particulate amounts, and explore the effect if the non-uniformity to the aging hardening curve.

Experiment Detail

The Material prepared

This research adopts A356/SiC_(p) composite material to be its material system and melting casting by prior technique [30]; in which the components of A356 Al alloy is 7%Si-0.3% Mg. The SiC particulate is irregular, α -phase, and the size of particulate average is 80 μ m. First, we used dilution method directly to pour the melting high concentration A356 / 40wt%SiC_(p) composite material into the molten of Al alloy ,and prepared A356/0wt%, 10wt%,20wt%SiC_(p) composite material ,and finally pour into the permanent mold to become the casting. Following we put the ingot in the air furnace of 320 °C to do homgenizing heat treatment for 4 hours. In order to research the influence that melting temperature affect SiC particulate and the reaction of Al alloy matrix, we adopt these melting temperature that 700 °C, 750 °C,800 °C and 850 °C. After we mix and dilution the high temperature composite material and the melting temperature of A356 Al alloy above well, and then put it into the high temperature melting furnace to keep the temperature for 2 hours, and finally we pour it into permanent mold. Besides, in order to research the influence that the temperature permanent mold affect the SiC particulate distributing in matrix, we set up the temperature of permanent mold to 300 °C, 400 °C and 500 °C.

Observation of microscopic structure

We cut A356/40wt%SiC_(p) composite material, the melting temperature of 700 °C-850 °C, and the 300 °C-500 °C of permanent mold temperature to form A356/0-20wt%SiC_(p) composite material sample. Samples were grinded by #100 to #1200 SiC carbmet papers, and polished in 1 μ m and 0.05 μ m Al₂O₃ particulate suspension liquid. The observation of microscopic structure uses Nikon optical microscope (OM) to observe the distributing which SiC Particulate in A356 Al alloy matrix. In addition, we use Image Analysis(IA) to measure the non-uniformity of SiC particulate distributing in matrix.

Age hardening heat treatment

We put A356/SiC_(p) composite material samples which have the different quantity of SiC particulate, melting temperature, and permanent mold temperature into the air furnace of 540 \pm 3 °C for 8 hours, and later, we quench them quickly into 15 °C water. Then, we put samples into age hardening heat treatment in which temperature is 155 \pm 3 °C. During aging processing, we get samples from isothermal furnace every 2 hours. And measuring their hardness by B-Scale Rockwell's hardness. We calculate the average in 10 points hardness from every sample, and finally we get age hardening curve from all kind of terms.

Result and Discussion

The condition that SiC particulate distributes in A356 Al alloy matrix.

The condition that 40wt% and 80 μ m SiC particulate distributes in A356 Al alloy matrix is in Fig. 1. From Fig. 1, we can see that high concentration SiC particulate distributes in Al alloy matrix well. From Fig. 2, we can see the condition that SiC particulate distribute in Al Alloy matrix, which 300 °C mold temperature and 700 °C-850 °C melting temperature of A356 / 10wt% SiC(p) composite ingot. From reference [13], we know that SiC particulate in high temperature melt is thermodynamic unstable. And from Figure 2 (e) of high time microscope structure, we also know that SiC particulate and Al alloy will become Al_3C_4 in their interface reaction layer, and Si crystals would form near SiC particulate. As a result of the forming of Si crystals and interface Al_3C_4 , it makes SiC particulate look darker in our observation by OM. Therefore, from figure 2, we can see the interface reaction layer of 750-850 °C is thicker than that of 700 °C melting temperature. But the interface reaction layer of 750-850 °C would not change obviously. Moreover, from table 1, we know the non-uniformity of the different melting would change less. From Figure 3 (a) to (c), we can know that when A356/ 10wt% Al Alloy melting temperature and 300 °C, 400 °C, 500 °C mold temperature, SiC particulate in A356 Al Alloy matrix would distribute differently. We can see the distribution of SiC particulate would cluster by following the raising of mold temperature. And its non-uniformity is increasing with the mold temperature arising. This is because that the raising of mold temperature and the heat transfer of melting temperature can result in the slow of cooling rate. Therefore, it would have enough time for dendrite to grow, and which can make SiC particulate to be pushed more easily to dendrite arm, and then cluster together. From Figure 4, we can see the distribution of 0-20wt% SiC particulates in the matrix which are in 700 °C melting, 300 °C mold temperature, its non-uniformity is shown table 1. From Figure 4 and table 1, we know the degree of SiC particulate which were pushed would decrease with the quantity of SiC particulate arising. This is because that the increasing of the quantity of SiC particulate will prevent the growth of dendrite. Therefore, SiC particulate would be not so easy to be pushed to dendrite arm.

The influence that the non-uniformity of SiC particulate to age hardening treatment.

From Figure 5, we can see the age hardening curve of A356/10wt% SiC(p) composites which in 700-850 °C melting temperature, and 300-350 °C mold temperature. We can find the peak aging is between 5-9 hours under the mold temperature of 300-500 °C. We can also find the hardness of 300 °C mold temperature under 700-750 °C melting temperature is bigger than that of 400 °C and 500 °C. However, the hardness of 300-500 °C mold temperature is not changing obviously under the 800-850 °C melting temperature. This is because that the non-uniformity increases with the arising of mold temperature.

From reference [21], we know that the age hardening of particulate Al Alloy composite material is because that interface thermal stress of particulate and Al Alloy produce dislocation. Then, when SiC particulate cluster together, it would make the dislocation density of matrix decreasing, and then decrease its aging hardness. However, when the heat of melting temperature transfer to permanent mold, it would make mold temperature arising, and make the mold temperature of 300 °C arising, which means decreasing its solidifying rate to make the clustering degree of SiC particulate increase. In this way, as high melting temperature, the non-uniform of the SiC particulate and hardness in 300-500 °C mold temperature are approximate.

In Figure 6, the age hardening curve of A356 /20wt% SiC composites under 700-850 °C melting temperature and 300-500 °C mold temperature, we can find the peak aging of 300-500 °C mold temperature divides into two parts. 6 hours is the first peak aging which value is 55 HRB, and 14 hours is the second peak aging which value is 80 HRB. From Figure 5 and 6, we find that it cannot accelerate the age hardening that increasing the quantity of SiC particulate.

Besides, for the same melting and mold temperature, the hardness of 20wt% SiC particulate. This is because that the increasing of quantity in SiC particulate will hinder dislocation motion. The age hardening curve is the same in 300-500 °C mold temperature, because the mold temperature will not effect their non-uniform of 20wt% SiC particulate quantity.

The influence that interface reaction layer to age hardening treatment

Figure 7, the age hardening curve of A356/10wt% SiC(p) composites under 300-500 °C mold temperature and 700-850 °C melting temperature. We can find the hardness of 700 °C melting temperature is lower than that of 750-850 °C. The result is that SiC particulate is more stable in 700 °C. That means SiC particulate and Al Alloy produce more interface reaction layer, figure 2. The forming of Al_3C_4 reaction layer leads to the decreasing of residual stress in the interface between SiC particulate and Al Alloy matrix, in the mean while, the dislocation density is reducing, too. On the contrary, the increasing of driving energy in Al Alloy matrix will produce more dislocation and arise its hardness. Otherwise, the interface reaction layer is less in 700 °C melt, and driving energy decreases dislocation density in Al alloy matrix. The result will decrease these hardness. From Figure 8, we can see the age hardening curve of A356/20wt% SiC(p) composites material under 700-850 °C melting temperature and 300-350 °C mold temperature. These aging hardness could not change with the melting temperature arising, in other words, they would not change with the interface reaction layer. It is because that while SiC particulate is increasing, the Al Alloy matrix amount is decreasing. Through the interface reaction layer can decrease the dislocation, the matrix is too less to enhance matrix density. Therefore, when the quantity of SiC particulate is 20wt%, the melting temperature will not effect its hardness.

Conclusion

This research uses further designing technique of PMMCs to produce A356/40wt% SiC(p) Composites material. Besides, we used dilution method directly to pour the melting high concentration A356 / 40wt%SiC_(p) composite material into the molten of Al alloy ,and prepared A356/0wt%, 10wt%,20wt%SiC_(p) composite material ,and finally pour into the permanent mold which is 300-500 °C to become the casting. Then we do age hardening treatment to these composites material, and we get several conclusions:

- 1.This interface reaction layer between SiC particulate and Al Alloy is arising with the melting temperature enhance, and there are Si crystals near SiC particulate.
- 2.The non-uniformity of the distribution of SiC particulate in Al Alloy matrix is increasing when the permanent mold temperature is arising.
- 3.In A356/10wt% SiC(p) composites material matrix, its hardness is lowering with the non-uniform increasing.
- 4.for the A356/20wt% SiC_(p) composites, the age hardening would not be influenced by the non-uniformity and the interface reaction layer.
- 5.For the same melting temperature and the mold temperature, the age hardening of the

quantity of 20 wt % SiC particulate composites increase more than that of 10wt%. However, the increasing of the quantity of SiC particulate would not produce the behavior of increasing accelerated aging.

Acknowledgement

This work was supported by the National Science Council, Taiwan, Republic of China.

Reference

1. Honda Motor Co., 1991, Brochure. Tokyo, Japan.
2. Alcan, 1991, Product Brochure San Diego, C.A.
3. R.W. Stevenson, ASM Metals Handbook, 7, 773 (1984)
4. K. Kubozono and T. Mori, 1989, in: Proceedings of 1st Japan International Conference, P.387. CN. Igata et al., eds. Chiba, Japan.
5. C. Zweben, J. Metals, 44, 15 (1992).
6. M.D. Skibo and D.M. Schuster, 1988, U.S. patent No. 4759995, July, 26.
7. P.K. Balasubramanian, P.S. Rao and B.C. Pai, Composites Sci. and Techn. 39, 241-245 (1990)
8. G.R. Cappleman and P.A. Hubert, J. Mater. Sci. 10, 85-96 (1985)
9. M. Gupta, I.A. Ibrahim, F.A. Mohame and E.J. Laverniak, J. Mater. Sci. 26, 6673. (1991)
10. P.K. Brindley, Mat. Res. Soc. Symp. Proc. 81, 419 (1987)
11. P. Xiao and B. Perby, 1991, in: Surface and Interfaces, British Ceramics Proceedings (R. Morrell and G. Partridge, eds.) 153-159, Stoke-on-Trent, U.K.: The Institute of Ceramics.
12. L. Christodoulou, D.C. Nagle and T.M. Brubacher, 1986, International Patent No. WO86/06366, November, P.6.
13. D.J. Lloyd, H.P. Lagace and A.D. McLead, The Third International Conference on Composite Interfaces (Cleveland, Ohio: Elsevier Publishing Company, 1990), pp. 359-376.
14. M. Mortensen, 1989, In: Solidification of Metal Matrix Composites edited by P.K. Rohatgi (The Minerals, Metals & Materials Society) pp 1-21.
15. A. Mortensen, Proc. 9th Riso International Symposium on Metallurgy and Materials Science, ed. S. Andersen, H. Lilholt and O. Pedersen, 144-155 (1988).
16. K. Phillips, A.J. Perry, G.E. Hollox and E. DeLaMotle J. Mater. Sci., 6, 270-273 (1971)
17. J. Lorca, A. Needleman and S. Suresh, Acta Metall. Mater. 39, 2317 (1991)
18. E.J. Mahon, J.H. Howe and A.K. Vasudevan, Acta, Metall. Mater. 38, 38 (1990)
19. J.J. Lewandowski, C. Liu and W. Hunt, Mater. Sci. Eng. A107, 241 (1989)
20. Y.M. Pam, M.E. Fine and H.S. Cheng, Scripta Metall. Mater. 24, 1342 (1990)
21. T. Christman and S. Suresh, Mater. Sci. Eng. A102, 211 (1986)
22. R.J. Arsenault and N. Shi, Mater. Sci. Eng. 81, 175 (1986)
23. P.K. Rohatgi, F.M. Yarandi, Y. Liu and R. Asthana, Mater. Sci. Eng. A147, 11 (1991)
24. XIE. Guohong, L. Songchun, W. Wuxian and W. Runie, Acta, Metallurgica, 31, NO6, 275 (1995)
25. M. Vogelsang, R.J. Arsenault and R.M. Fisher, Metall. Trans. 17A, 379 (1988)
26. G.H. Janowski and B.J. Pletka, Materials Transactions Metallurgical, 26A, 3027 (1995)
27. I. Dutta, D.C. Bourell and D. Latimor, J. Comp. Mater. 122, 829 (1988)
28. H. Ribes and M. Suery, Scripta Metallurgica, 23, 705 (1988)
29. S. Suresh, T. Christman and Y. Sugimura, Scripta Metall. Mater, 123, 1599 (1988)
30. C.B. Lin, U.S.A. Invent Patent NO: 5401338, Mar (1995)

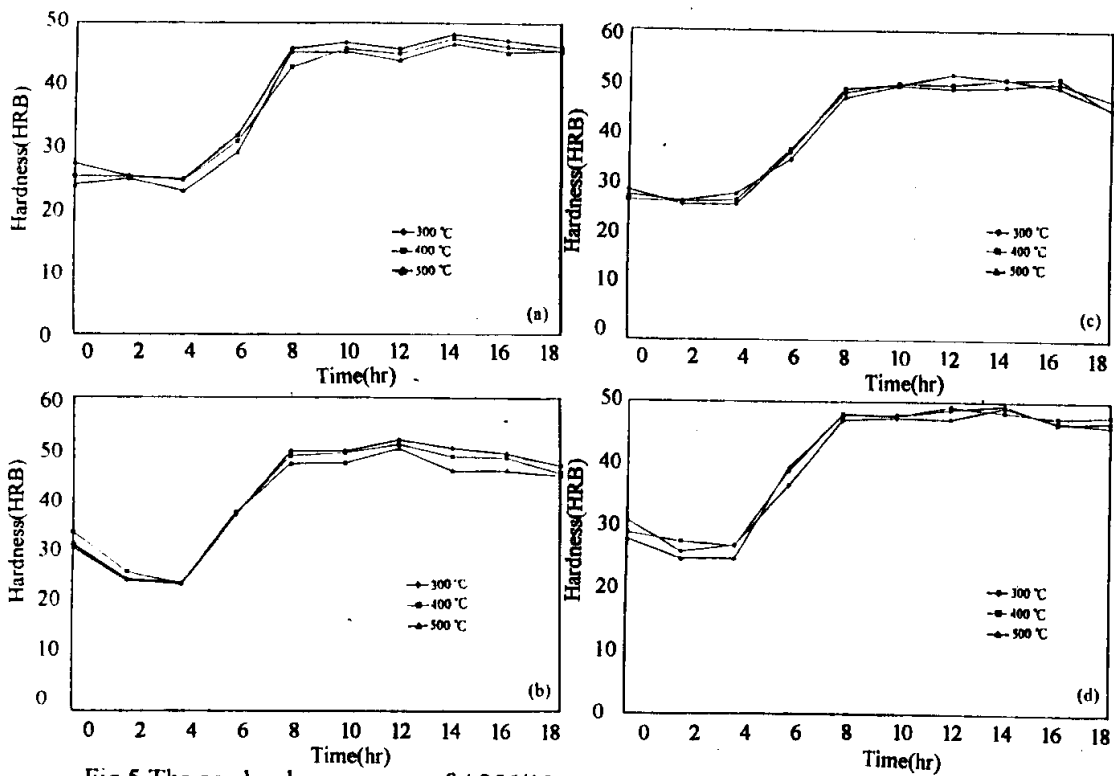


Fig.5 The age hardening curve of A356/10wt% SiC_p composite at 700 °C-850 °C molten temperature and 300 °C-500 °C mold temperature (a)700 °C; (b)750 °C; (c)800 °C; (d)850 °C.

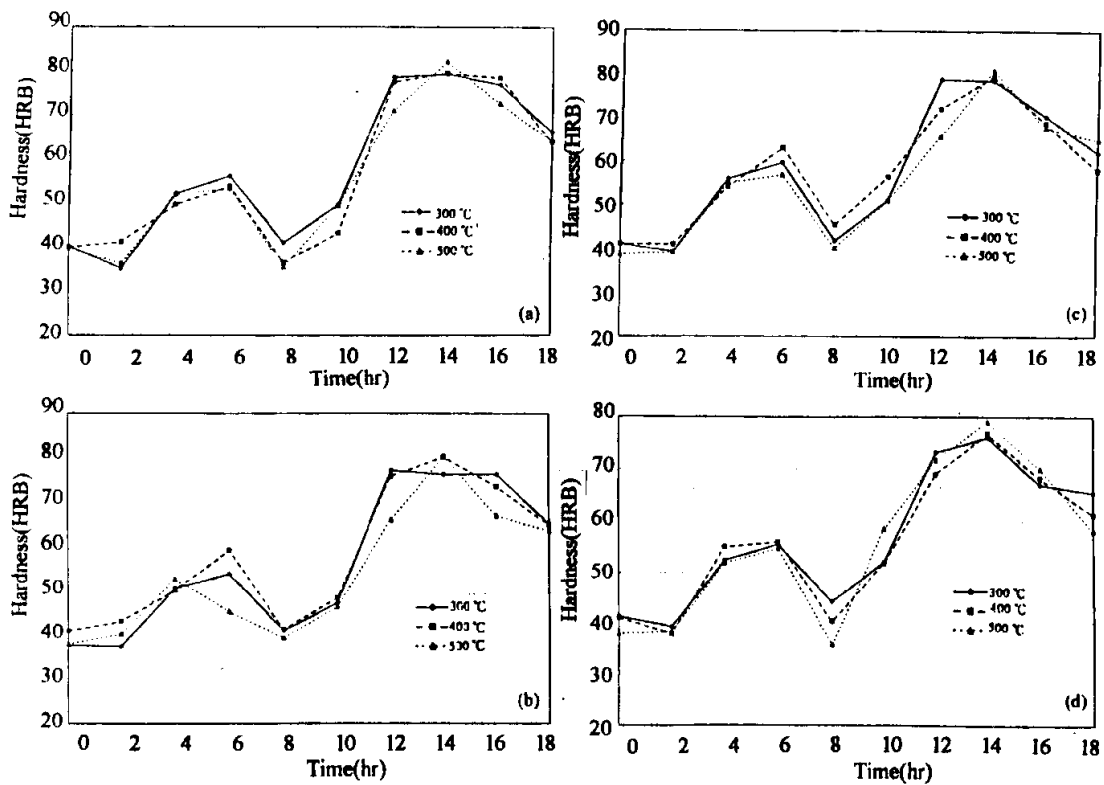


Fig.6 The age hardening curve of A356/20wt% SiC_p composite at 700 °C-850 °C molten temperature and 300 °C-500 °C mold temperature (a)700 °C; (b)750 °C; (c)800 °C; (d)850 °C.

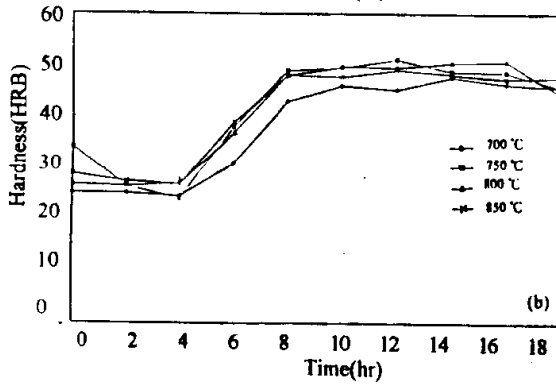
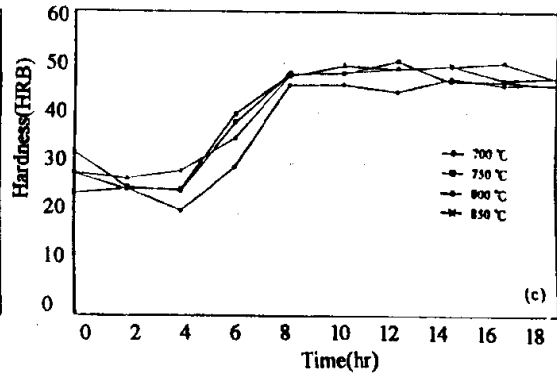
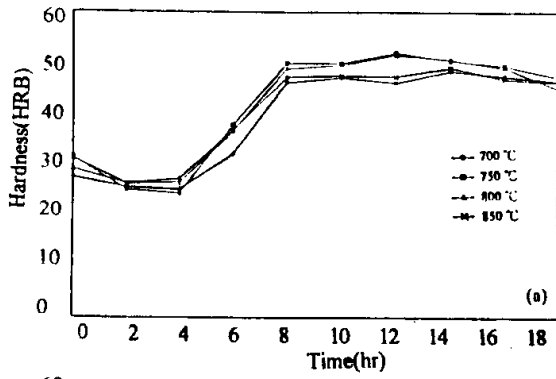


Fig.7 The age hardening curve of A356/10%wt SiC_(p) composite at 700°C-850°C molten temperature and 300°C-500°C mold temperature (a)300°C; (b)400°C; (c)500°C.

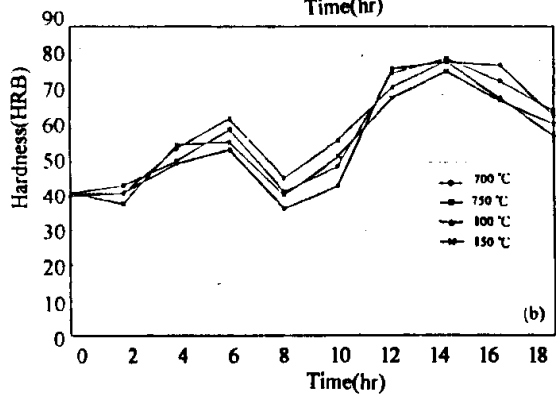
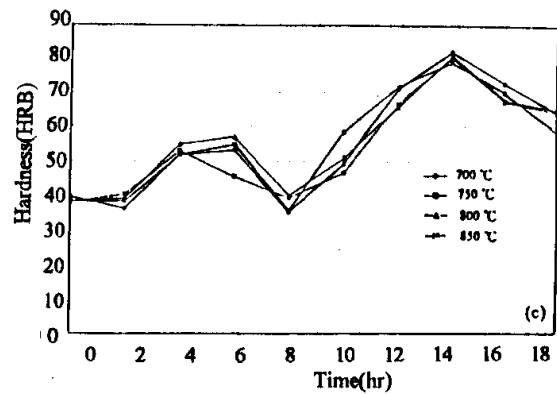
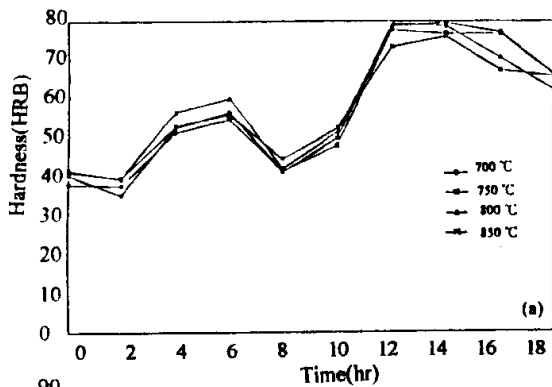


Fig.8 The age hardening curve of A356/20%wt SiC_(p) composite at 700°C-850°C molten temperature and 300°C-500°C mold temperature (a)300°C; (b)400°C; (c)500°C.

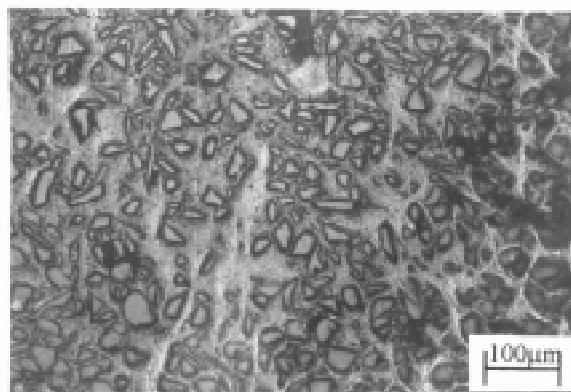


Fig.1 The observation of 40wt%,80µm SiC particulates in A356 Al alloy matrix

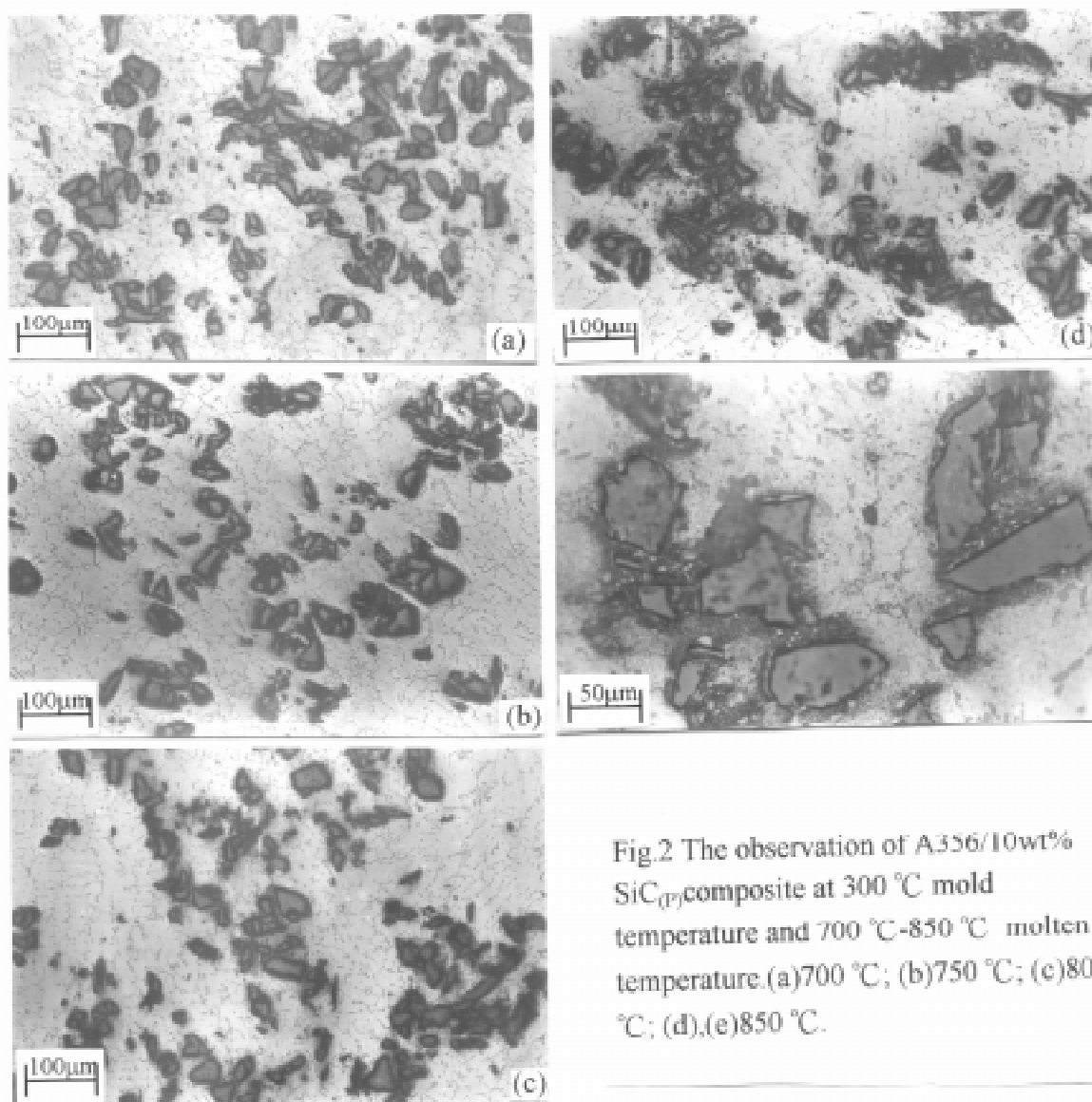


Fig.2 The observation of A356/10wt% SiC(p) composite at 300 °C mold temperature and 700 °C-850 °C molten temperature.(a)700 °C; (b)750 °C; (c)800 °C; (d),(e)850 °C.

Table.1-The non-uniformity of A356/10wt%,20wt% SiC_(p) at 700 °C-850 °C molten temperature and 300 °C-500 °C mold temperature.

mold temperaure (°C)	melting temp(°C) non- uniform	700 °C		750 °C		800 °C		850 °C	
		10 wt %	20 wt %	10 wt %	20 wt %	10 wt %	20 wt %	10 wt %	20 wt %
300 °C		0.90	0.86	0.92	0.86	0.95	0.88	0.99	0.87
400 °C		0.95	0.88	0.97	0.90	0.97	0.89	0.97	0.90
500 °C		0.99	0.90	0.99	0.91	0.98	0.89	0.99	0.92

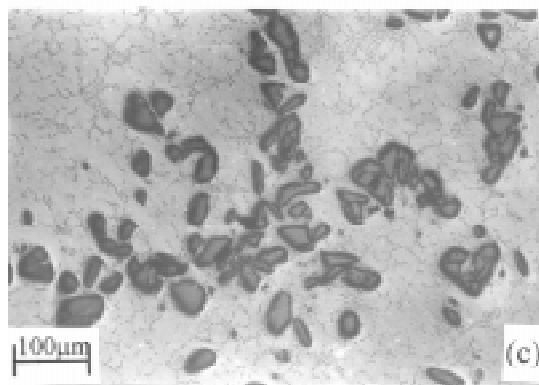
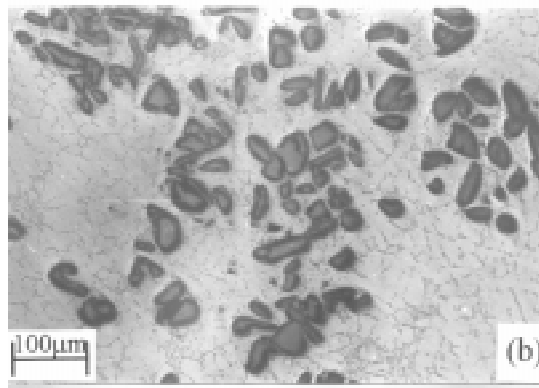
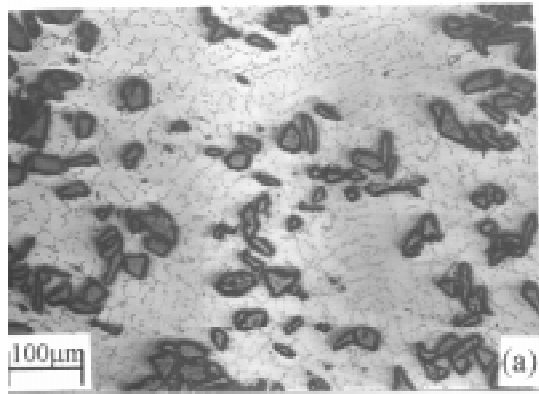


Fig.3 The observation of A356/10wt% SiC_(p) composite in Al alloy matrix at 700 °C molten temperature and 300 °C -500 °C mold temperature (a) 300 °C; (b) 400 °C; (c) 500 °C.

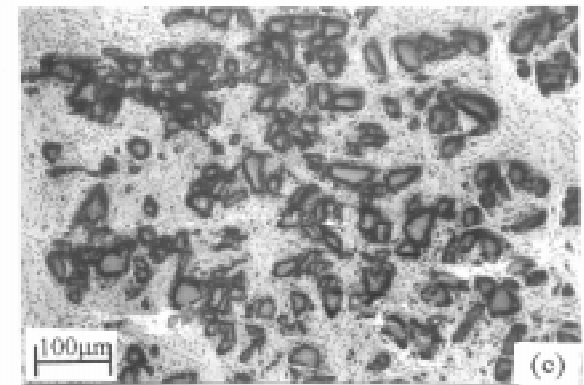
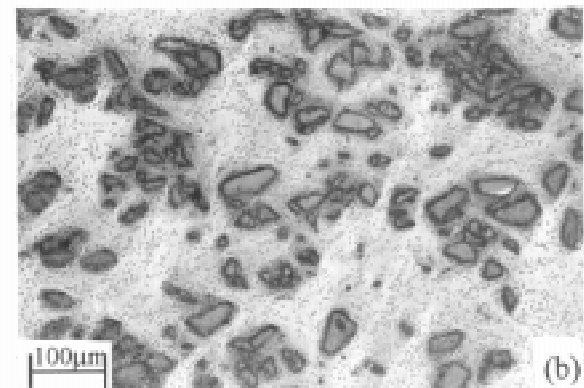
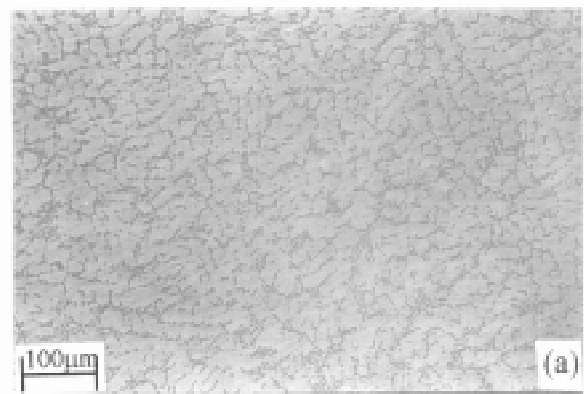


Fig.4 The observation of A356/SiC_(r) composite at 300 °C mold temperature and 700 °C molten temperature. (a) 0wt%; (b) 10wt%; (c) 20wt%.

THE INFLUENCE OF HEAT-TREATMENT ON THE DRY SLIDING WEAR BEHAVIOUR OF SAFFIL-REINFORCED AA6061 COMPOSITES

H.C. How and T.N. Baker

*Metallurgy and Engineering Materials Group,
Department of Mechanical Engineering,
University of Strathclyde, Glasgow G1 1XN, UK*

SUMMARY: The steady-state wear of elemental aluminium alloy AA6061 and AA6061 based Saffil fibre-reinforced composites, manufactured by a PM route, was investigated with a pin-on-disc configuration under dry sliding conditions. For both the monolithic alloy and the MMC, a better dry sliding wear resistance was found in the peak-aged condition than after over-ageing, except for the lowest load, where the alloy shows an insignificant difference. Scanning electron microscopy suggested that the controlling wear mechanism for all the specimens was load dependent. With the improvement in the flow stress of the alloy matrix, the wear resistance of the MMC was found to be better in the peak-aged than the over-aged condition, as the tendency for the fracture of Saffil fibres was reduced and resulted in a decrease in the delamination rate.

KEYWORDS: dry sliding wear, heat-treatment, Saffil fibre, aluminium alloy, metal-matrix composites, pin-on-disc.

INTRODUCTION

Aluminium alloy based metal matrix composites have been commercialised by Toyota Motor Company in making the ring land of diesel engine pistons [1]. Following this application, many studies reported an improvement in the lubricated sliding wear resistance by incorporating the ceramic reinforcement into the aluminium alloys, regardless of the test methods used [2]. However, in a dry sliding condition, the wear resistance of the composite was complicated. Although several studies reported that the enhancement of wear resistance was achieved by the incorporation of ceramics [3-4], others suggested that this phenomenon was not always the case, as the benefit of the ceramic reinforcement was found to be load dependent [2,5]. For example, while the composite showed a substantial improvement in wear performance at low loads, a comparable or even inferior wear resistance was shown by the composite, compared to the monolithic alloy, as the applied load was sufficiently high to cause the fracture of the reinforcements.

In view of the many applications which require a heat-treatment to optimise the mechanical properties, the influence of the heat-treatment on the wear resistance has also received attention. The literature contains several references to lubricated sliding and abrasive wear resistance of 2000 series aluminium-SiC metal-matrix composites (MMCs) which showed improved wear resistance when tested in the over-aged compared to the peak-aged condition. The improvement was found to be due to the ageing effects on the interface bonding between

the reinforcement and the matrix [6-8]. For example, Pan and Cheng [6] found that the over-aged 20 vol% SiC reinforced 2124 Al based composite had a better lubricated sliding wear resistance than that in peak-aged condition, which was considered to be due to the change of the fracture path associated with the precipitation of intermetallics. This in turn reduced the extent of pull-out of the SiC particles and caused less damage to both the pin and the disc by third body wear processes. Wang and Rack [7], and Lin and Liu [8] also reported a similar improvement in abrasive wear performance in an over-aged condition.

While AA2014-SiC and AA6061-SiC MMCs have been studied extensively, far less attention has been given to AA6061- Al_2O_3 fibre (Saffil) MMCs. Previous work showed that the enhancement of the wear performance of the composites was load dependent. In the present study, three different loads were used to investigate the influence of heat-treatment on the steady-state dry sliding wear resistance of an AA6061 elemental alloy and a Saffil-reinforced AA6061 composite.

EXPERIMENTAL DETAILS

Materials

The materials used in this research were an AA6061 elemental alloy (1.1%Mg, 0.76%Si, 0.30%Cu, 0.20%Cr, 0.32%Fe, 0.02%Zn) and 20vol.% δ -alumina(Al_2O_3) fibres (also known as Saffil) reinforced AA6061 elemental alloy based composite, which were produced by a powder metallurgy route from the elemental powders. The as-extruded elemental alloys and composites were machined into a pin of length 20mm with a flat surface of 6mm in diameter at both ends, in the direction parallel to the extrusion axis, so that the Saffil fibres were normal to the flat surface. Before testing, the samples were given a T6 heat-treatment, of $530 \pm 5^\circ\text{C}$ for 2 hours, iced water quenched and then artificially aged at 160°C for a period of time before quenching in ice water. Ageing periods of 16 hours and 10 hours were given to the monolithic alloy and the composites respectively, to achieve the peak-aged (PA) condition [9]. To produce the over-aged (OA) condition, the materials were aged at 260°C for 24 hours following the same solution treatment and quenching as above. The Vickers hardness of the as-extruded (AEx) and heat-treated specimens is given in Table 1. Each value is an average of 6 indentations made with a load of 20kg.

Table 1: Vickers hardness and the density of the materials

Volume Fraction, %	Hardness, HV20			Calculated Density, g/cm^3
	As-extruded	Peak-aged	Over-aged	
0	47	122	56	2.70
20	60	118	63	2.82

EN24 discs (1.40%Ni, 1.17%Cr, 0.63%Mn, 0.38%C, 0.29%Si, 0.25%Mo, bal. Fe) were used as the counterfaces. They were heat-treated to the hardness of 560HV30, in a manner similar to that used by Gurcan and Baker [10].

Experimental Procedure

The pin-on-disc configuration was used for the unlubricated sliding wear testing at room temperature in air under dry conditions, with the pin mounted vertically on the tester arm at one end and the other pin surface held against the rotating EN24 disc. The AA6061 alloys and composites were used as the pin, and the EN24 disc was used as the counterface. All the tests were performed under a constant sliding velocity of 0.19m/s at loads of 1.1N, 9.8N and 48.3N. The friction force was recorded during the tests via a load cell, which consisted of four strain gauges (full-bridge).

Prior to the test, the flat surface of the pin was lightly finished by sliding against 600 grit SiC paper which was adhered to the disc specimen, while the pin was mounted on the tester arm. The EN24 disc specimens were ground to a constant roughness of about $0.70\mu\text{m}$ Ra, and measured using a Talysurf 5-120 surface profilometer.

The wear of the pins was recorded by measuring the weight loss of the pins using a micro balance of accuracy 10^{-5} g. Except for the load of 1.1N, where the process was interrupted every 300m, to enable a measurable weight loss to be recorded, each measurement was made by interrupting the test every 100m of sliding distance. The weight loss recorded was converted to a volume loss by dividing by the calculated density of the material [11]. All the specimens followed a single track of 50mm in diameter and the EN24 disc was changed for each surface of the pin tested. Before each measurement, the pin was cleaned ultrasonically while immersed in methanol and then blown dry in air. The disc was cleaned by the same method as the pin although no measurement of weight change was made. Two readings were made for each weighing of the pin and the mean taken.

The microscopic examination of the monolithic alloy and the composites was undertaken by scanning electron microscopy (SEM). An EDAX facility, which was incorporated into the SEM, was used to provide chemical compositions from the worn surfaces.

RESULTS

Under dry sliding conditions, it is found by experiment that a running-in period is sometimes observed before a steady-state wear rate was achieved [12]. In the present study, although the steady-state wear behaviour is the main interest, it is worth noting that as the applied load increased to 48.3N, the metallic debris generated during the first few meters of running-in accumulated at the leading edge of the pin due to the repeated sliding along the same track. A greater extent of accumulation was consistently found on the monolithic alloy than the composite, regardless of the conditions of heat-treatment. As the accumulated debris were weakly attached at the leading edge of the pin specimen and might suddenly detach as sliding action proceeded, the debris was removed by a light pressure, after the first 100m of sliding distance was completed. Fig. 1 shows the accumulated debris which was removed from the leading edge of the pin. As a result of this removal, the wear rate of the monolithic alloy for the first 100m of sliding distance was found to be up to eight times greater than that of the composite. If the accumulated debris is not removed and its weight is taken into account when the pin is weighed, then less wear may be recorded for the monolithic alloy than the composite. Therefore, if the wear results produced within a short sliding distance are taken as normal, without having distinguished the running-in period from the steady-state wear process, the benefit of Saffil reinforcement in improving the wear resistance of the aluminium

alloy would have been misleading. In the present experiments, some evidence of extruded material at the trailing edge [2] was found in both the monolithic alloy and the composite and the extent increased with the applied load.

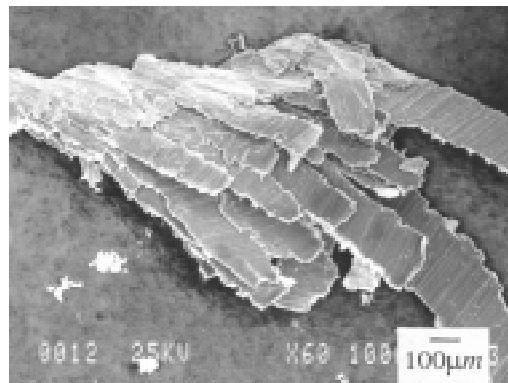


Fig. 1: SEM micrograph shows the accumulated debris which was removed from the leading edge of the monolithic alloy.

By plotting the volume loss versus sliding distance, the running-in period was identified and the relationship between the steady-state wear and the sliding distance was then plotted by normalising with the running-in wear rate, as in Fig. 2. For all cases, the running-in period was completed by a sliding distance of less than 700m, except for the load of 1.1N, where the running-in period of the composite was found to be prolonged to 1200m. Fig. 2 shows that the steady-state wear rate for both the monolithic alloy and the composite increased linearly with sliding distance. Using the principle of least squares, the wear rate, together with the standard error, was computed. The maximum standard error which resulted from the regular interruptions of the test was found to be $\pm 6\%$. This confirms the linear relationship between the steady-state wear rate and the sliding distance.

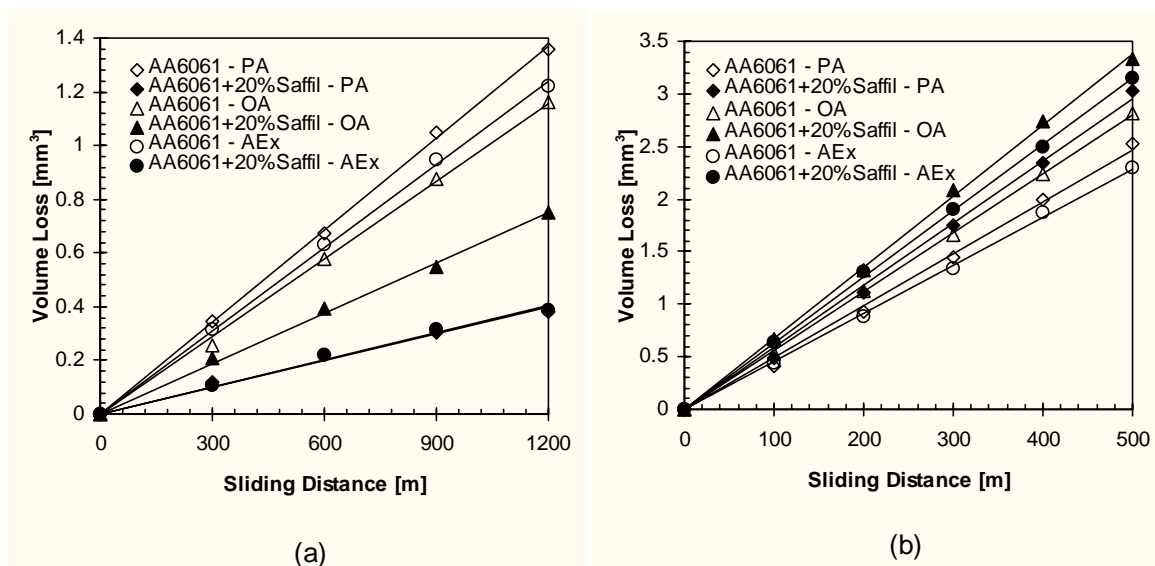


Fig. 2: Relationship between the steady-state volume loss and the sliding distance at two extreme loads, (a) 1.1N and (b) 48.3N.

Fig. 3 demonstrates the wear rate for both the monolithic alloy and the composite at three applied loads, as well as after different heat-treatments. The error bar indicates the variations from the mean value due to two duplicated tests. While the monolithic alloy and the

composite showed a marginal difference in wear rate at a load of 9.8N, wear rates for the monolithic alloy and the composite tested at the two extreme loads were clearly distinctive, regardless of the heat-treatment conditions. At the lowest load, the composite consistently showed a better wear performance than the monolithic alloy, whereas the opposite trend was found using the highest load. Compared with specimens in the as-extruded and the over-aged conditions, the peak-aged composite showed a marginal improvement in wear resistance at lower loads. Such a marginal improvement was not evident as the applied load increased to 48.3N. For the monolithic alloy, wear rates for the as-extruded and both the aged specimens were almost identical at loads of 1.1N and 9.8N. As the load increased to 48.3N, the as-extruded alloy showed the lowest wear rate followed by the peak-aged alloy, while the over-aged alloy demonstrated the highest wear rate.

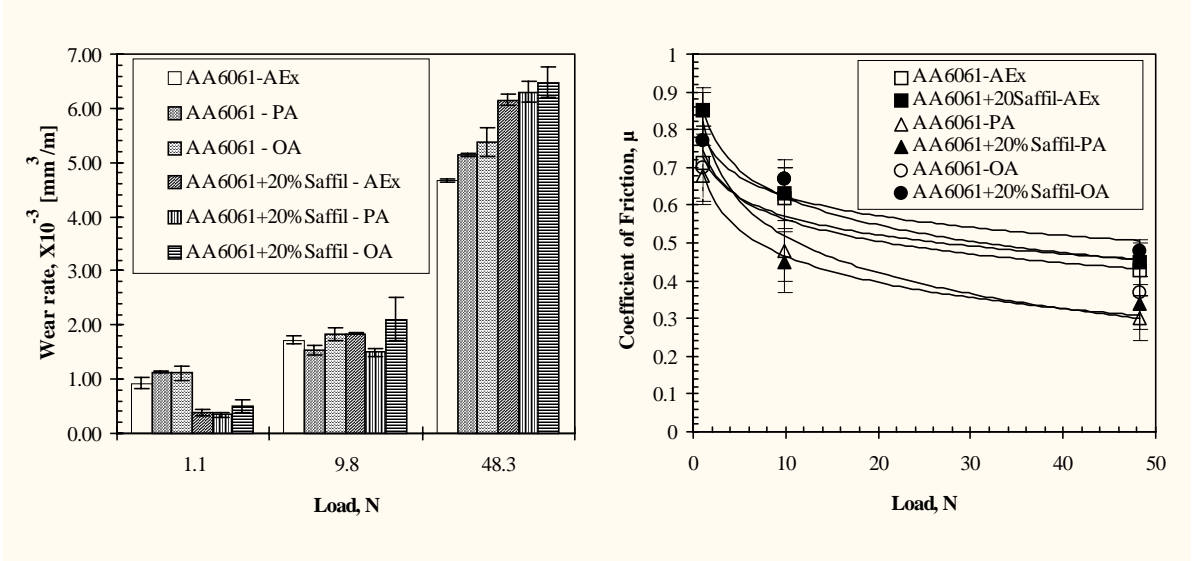


Fig. 3: The influence of heat-treatment on the wear rate

Fig. 4: The friction behaviour of both the monolithic alloy and the composite

The coefficient of friction was calculated by dividing the recorded friction force by the normal applied load and was plotted against load, as in Fig. 4. Regardless of the heat-treatment conditions, the coefficient of friction generally decreased logarithmically with the load. At a load of 1.1N, the coefficient of friction of the composite was consistently higher than that of the monolithic alloy. However, no such trend was observed as the load increased to 9.8N and 48.3N.

DISCUSSION

SEM observations showed that the worn surface morphology of all the tested specimens shared the similar features, except for the composite when tested at a load of 1.1N. Fig. 5 shows the typical worn surface morphology of the composites tested at the two extreme loads. As reported in our earlier work [13], in which the influence of the applied load on the peak-aged materials was considered, the wear mechanism for the composites was found to be load dependent. At a load of 1.1N, the presence of the reinforcing Saffil limited the extent of direct contact between the matrix and the hard asperities of the mating disc surface, which in turn, prevented plastic deformation on the pin specimen extending from the contact surface to a greater depth. As a result, strain-hardened shear ripples associated with brittle cracks, were formed on the worn surface. Cyclic loading due to repeated sliding caused propagation of these brittle cracks and eventually the ripple delaminated giving loose debris. Fig. 5a and 5b

show a typical example of this mechanism, in which a small fraction of the shear ripples, indicated as 'R' in Fig. 5b, was about to delaminate to become flake-like debris, as it was surrounded by extensive cracks. When the load increased to 48.3N, the presence of the reinforcing Saffil becomes detrimental as the applied load was high enough to cause an increase in the area fraction of direct contact between the alloy matrix and disc asperities, Fig. 5c. Consequently, a greater depth of plastic deformation was induced, which further, caused fracture of the Saffil fibres beneath the worn surface, Fig. 5d. Such a fracture nucleated a void, as indicated at 'V', which inevitably favoured the delamination process.

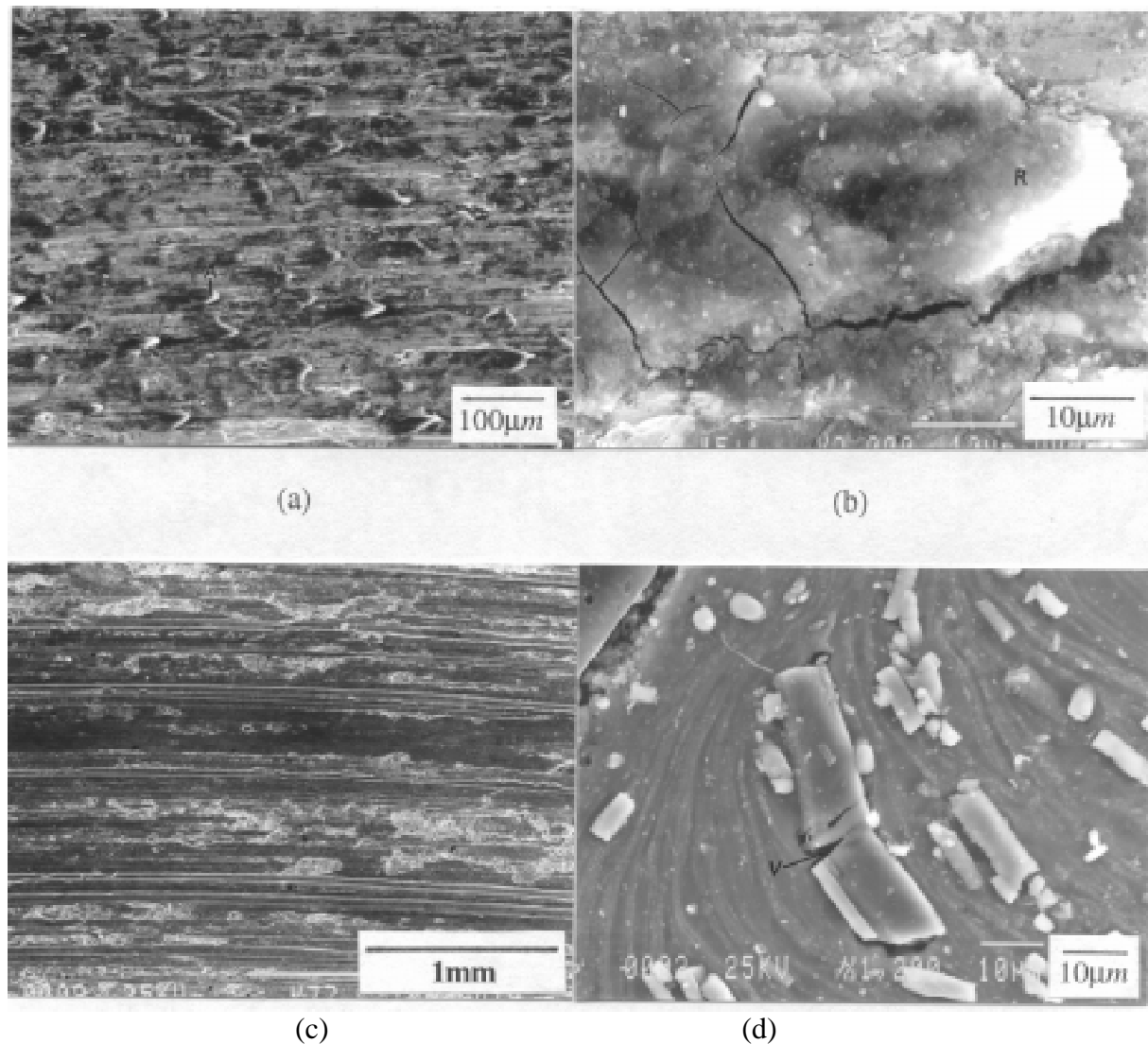


Fig. 5: SEM micrographs of the composite tested at two extreme loads, (a) formation of shear ripples associated with brittle cracks on the worn surface, 1.1N, (b) high magnification of region 'A' in (a), (c) typical morphology of the worn surface, 48.3N, (d) subsurface deformation with fracture of the fibre, 48.3N

Despite of the higher hardness, the difference in the wear rate of the peak-aged monolithic alloy tested at loads of 1.1N and 9.8N, was found to be insignificant, compared with the as-extruded and the over-aged specimens. As the load increased to 48.3N, the as-extruded alloy, which has the lowest hardness, surprisingly showed the best wear resistance. These results obviously contradicted the Archard prediction [14], in which wear rate is found to be

inversely proportional to the hardness. As shown in our earlier study [13], a layer of compacted debris, which consisted mainly of Al and Fe, was formed on the contact surface of the pin specimen. In an Al-Si based MMC, a similar layer was also found by Venkataraman and Sundararajan [15], and the microhardness of this particular layer was reported to be higher than the bulk hardness by a factor of six. Based on this observation, the use of Archard's equation in predicting the dry sliding wear behaviour became complicated. However, neither bulk hardness nor surface layer hardness was suggested here, but rather, to point out that the use of Archard's equation in predicting wear behaviour was not appropriate in the wear system for which delamination was a dominant mechanism. For example, Saka, Pamies-Teixeira and Suh [16] found that although the increased hardness decreased the deformation rate, the loss of coherency at the matrix-particle interface with increasing hardness favoured crack nucleation, which eventually increased the rate of the delamination process. Although the presence of the fine precipitates in this case possibly limits the degree of plastic deformation, at the same time, at a load of 48.3N, they result in severe localised cracking due to extensive plastic strain. Therefore, this suggests that the absence of the fine precipitates formed during the ageing treatment, may be the reason for the best wear resistance which was found in the as-extruded alloy tested at a load of 48.3N.

By incorporating the Saffil fibres into the alloy matrix, the influence of the incoherent precipitates was over taken by the presence of the Saffil fibres. As mentioned earlier, when tested at a load of 48.3N, an extensive plastic deformation of the matrix caused fracture of the Saffil fibres at a depth of approximately 50 μ m beneath the worn surface. The fractured fibre nucleated a void, as indicated at 'V' in Fig. 5d, which has the potential to propagate and may link-up with the neighbouring voids to favour a delamination process, as the crack approaches the worn surface. By increasing flow stress of the alloy matrix, it was possible to reduce the extent of plastic deformation, which in turn, prevented or minimised fracture of the fibres. According to Alpas, Hu and Zhang [17], the flow stress is proportional to the hardness of the material. Thus, it is considered that the improvement in flow stress may lead to a better wear resistance in the peak-aged composite, when tested at higher loads, compared to the as-extruded and the over-aged composites. However, such an improvement was not capable of reducing the tendency for the fracture of Saffil as the applied load increased to 48.3N. This in turn lead to an insignificant difference in the wear performance of the composites at all heat-treatment conditions.

It was surprising to note that when tested at a load of 1.1N, the wear rate of the over-aged composite was higher than that of the as-extruded composite, which in turn showed a similar wear rate to that of the peak-aged composite, despite the fact that both the as-extruded and the over-aged composites have almost the same hardness. Several studies have revealed that a greater extent of ceramic pull-out was observed for the peak-aged specimen compared to the over-aged specimen [6-8]. For example, Pan and Cheng [6] attributed this observation to the change of the fracture path from the matrix/SiC interface in the peak-aged specimen to the alloy grain boundary in the case of the over-aged. By contrast, embrittlement of the reinforcement-matrix interface through increased S'/S precipitation in the vicinity of the reinforcement, decreased the wear resistance of 2009-SiCp composite as observed by Sannino and Rack [18]. By examining the over-aged specimen foil using transmission electron microscope (TEM), tilted to various angles, no evidence of second phase precipitates or a reaction layer was observed at the Saffil/matrix interface, Fig. 6. This suggests that a good bond between the Saffil fibres and the matrix was established, and difference in the extent of Saffil pull-out due to different heat-treatment conditions was unlikely in this study. Furthermore, in the present study, it was only in specimens tested at a load of 1.1N that some

broken Saffil fibres ($\sim 5\mu\text{m}$ in length), indicated as 'S' in Fig. 7, were revealed on the worn surface. For the case of higher loads, no evidence of Saffil fibres was observed on the worn surface and it is believed that the broken fibres were crushed and mixed together with the compacted debris and formed the mixed surface layer [13]. Even though the broken fibres were observed on the composites tested at a load of 1.1N, the number of broken fibres was too small for the dominant wear mechanism to be considered as fibre pull-out, compared to the observed greater extent of shear ripples associated with cracks. Compared to the as-extruded and the peak-aged composites, fewer shear ripples were observed on the worn surface of the over-aged composite. Based on the previous study [13], the formation of shear ripples was found to be increased in proportion to the volume fraction of Saffil fibres, while the wear rate showed the opposite trend. Although the mechanism of formation of shear ripples is not clearly understood at this stage, the presence of fewer of these features in the 10vol.% Saffil reinforced-composite, which was found in the previous study, resulted in an increase in the wear rate by more than twice that of the 20vol.% Saffil-reinforced composite. This suggests that the wear rate for the composite was sensitively dependent on the volume fraction of the reinforcement. Thus, the inferiority of the wear resistance of the over-aged composite, in this case, may be due to an inhomogeneous distribution of the Saffil fibres, which lead to variations in the volume fraction of Saffil at the contact surface. However, it was not possible to quantify the volume fraction (or area fraction) of the Saffil on the worn surface by using SEM, as most of the Saffil was smeared by the alloy matrix which had been plastically deformed.

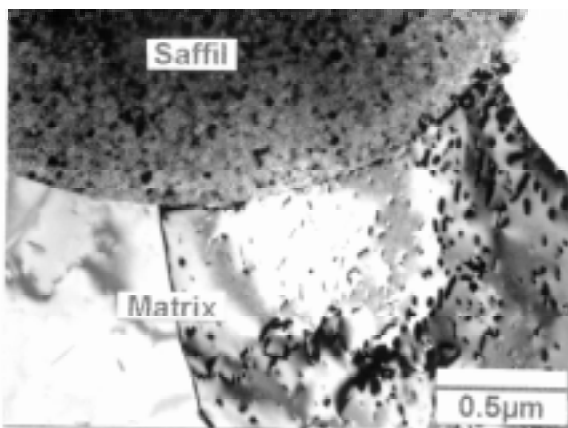


Fig. 6: Transmission electron microscopy of the over-aged composite.



Fig. 7: SEM micrograph of broken Saffil fibres on the worn surface of the as-extruded composite, 1.1N.

CONCLUSIONS

The influence of heat-treatment on the dry sliding wear behaviour of a PM route elemental alloy AA6061 and a 20 vol.% Saffil-reinforced composite was investigated, under three different applied loads. On the basis of this study, the following conclusions were reached:

1. The steady-state wear rate for both the alloy and the composite was found to be linearly proportional to the sliding distance, regardless of the heat-treatment conditions.
2. At loads of 1.1N and 9.8N, similar wear rates were found for the monolithic alloy, but as the load increased to 48.3N, the as-extruded alloy showed the best wear resistance.
3. While the composite consistently showed a better wear resistance than the monolithic alloy at a load of 1.1N, the opposite trend was found at a load of 48.3N.

4. Compared to the as-extruded and the over-aged conditions, the increased in flow stress of the peak-aged composite lead to a better wear resistance at a load of 9.8N, where the tendency for the fracture of Saffil was considered to be reduced.
5. Little evidence for pull-out of Saffil fibres was observed in this work, regardless of the heat treatment conditions. Transmission electron microscopy revealed a clean Saffil/matrix interface with no evidence of a reaction layer.
6. The coefficient of friction generally decreased logarithmically with load, and was higher in the composite than the monolithic alloy, when tested under a load of 1.1N.

ACKNOWLEDGEMENTS

One of the authors, H.C. How thanks the Malaysian Government and the Standards and Industrial Research Institute of Malaysia (SIRIM) for the provision of a research scholarship.

REFERENCES

1. J. Dinwoodie, E. Moore, C.A.J. Langman, W.R. Symes, "The Properties and Applications of Short Staple Alumina Fibre Reinforced Aluminium Alloys", 5th Inter. Conf. on Composite Materials, San Diego, 1985, Metallurgical Soc. Inc, Warrendale, USA, 671-685
2. C. Perrin and W.M. Rainforth, "The effect of alumina fibre reinforcement on the wear of an Al-4.3%Cu alloy", *Wear* 181-183 (1995), 312-324
3. L. Cao, Y. Wang and C.K. Yao, "The wear properties of an SiC-whisker-reinforced aluminium composite", *Wear* 140 (1990), 273-277
4. B.K. Prasad, O.P. Modi and A.K. Jha, "The effects of alumina fibres on the sliding wear of a cast aluminium alloy", *Tribology International*, 27 (1994), 153-158
5. J. Zhang and A.T. Alpas, "Wear regimes and transitions in Al₂O₃ particulate-reinforced aluminum alloys", *Materials Science and Engineering*, A161 (1993), 273-284
6. Y.M. Pan and H.S. Cheng, "Effects of particle size and heat treatment on wear of SiC/Al composites", Morris E. Fine Symposium, Peter K. Liaw, J.R. Weertman, Harris L. Marcus and Joseph S. Santner (eds.), 1991, The Minerals, Metals & Materials Society, 143-151
7. A. Wang and H.J. Rack, "The effect of aging on the abrasion behavior of SiC_w/2124 metal matrix composites", *Metal and Ceramic Matrix Composites: Processing, Modelling and Mechanical Behaviour*, R.B. Bhagat, A.H. Clauer, P. Kumar and A.M. Ritter (eds.), 1990, The Minerals, Metals and Materials Society, Warrendale, PA, 487-498
8. S.J. Lin and K.S. Liu, "Effect of aging on abrasion rate in Al-Zn-Mg-SiC composite", *Wear* 121 (1988), 1-14
9. Y. Song and T.N. Baker, "Accelerated aging processes in ceramic reinforced AA6061 composites", *Materials Science and Technology*, 10 (1994), 406-413

10. A.B. Gurcan and T.N. Baker, "Wear behaviour of AA6061 aluminium alloy and its composites", *Wear* 188 (1995), 185-191
11. H.C. How and T.N. Baker, "The influence of sliding velocity on the dry sliding wear behaviour of a Saffil-reinforced AA6061 composite", *Proc. of the 5th European Conf. on Adv. Mat. and Processes and Applications*, L.A.J.L. Sarton and H.B. Zeedijk (eds.), 1997, Vol.1, Neth. Soc. for Mat. Sci., 41-44
12. I.M. Hutchings, *Tribology : Friction and Wear of Engineering Materials*, E. Arnold, Great Britain, 1992, 84
13. H.C. How and T.N. Baker, "Dry sliding wear behaviour of Saffil-reinforced AA6061 composites", accepted by *Wear*
14. J.F. Archard, "Contact and Rubbing of Flat Surface", *J. Appl. Phys.*, 24 (1953), 981-988
15. B. Venkataraman and G. Sundararajan, "The sliding wear behaviour of Al-SiC particulate composites-II, The characterization of subsurface deformation and correlation with wear behaviour", *Acta Mater.*, 44 (1996), 461-473
16. N. Saka, J.J. Pamies-Teixeira and N.P. Suh, "Wear of two-phase metals", *Wear*, 44 (1977), 77-86
17. Alpas, H. Hu and J. Zhang, "Plastic deformation and damage accumulation below the worn surfaces", *Wear*, 162-164 (1993), 188-195
18. A.P. Sannino and H.J. Rack, Dry sliding wear of discontinuously reinforced aluminum composites : review and discussion, *Wear* 189(1995)1-19

MOISTURE ABSORPTION IN VOIDED POLYMER COMPOSITES

L.M.P.Fellows and A.R.Chambers

*Department of Engineering Materials, University of Southampton,
Highfield, Southampton SO17 1BJ, UK.*

SUMMARY: The objective of this research was to investigate the relationship between void content and moisture uptake in a carbon fibre/epoxy resin system. Void contents in the range 0.5-2.5% were produced by varying the cure cycle and the effect on moisture uptake established by a controlled weighing programme. It was found that whereas there was a determinable link between moisture uptake and void content, anomalies occurred. These were attributed to the location of voids within the composite. C-scan, which takes account of both surface and bulk effects gave a better correlation with moisture uptake than void content as measured by image analysis.

KEYWORDS: carbon/epoxy, moisture absorption, voids, void measurement, c-scan, image analysis

INTRODUCTION

A major factor which limits the performance of composite materials is the presence of defects which are produced during manufacture; the most common being voids or porosity. The presence of such defects has a marked effect on the mechanical properties and the effect is proportional to void content [1].

Voids and defects also affect moisture absorption, saturation levels, diffusivity and mass gain [2,3]. The latter is especially important with sandwich panels which will not readily release moisture which has been absorbed. Considering that mass is so important to the aerospace industry, it is surprising that comparatively little research has been undertaken to establish the relationship between void content and moisture uptake.

The objective of this work was to investigate this relationship for a typical carbon fibre/epoxy aerospace composite system. The cure cycle was altered to give voidage in the range 0% - 2.5%.

EXPERIMENTAL

Panels

Nine, eight ply, panels were produced using woven carbon cloth and an epoxy resin system containing 30% thermoplastic (ICI-977-2). The normal cure cycle to produce a low voidage product involves heating at 2°C/min to the cure temperature of 185°C. The variation in the void

levels was achieved by altering the times at which the pressure was applied during the cure cycle. By keeping cure temperatures and times constant it was ensured that the other important variables such as degree of cure, dimensions and fibre volume fractions would be unaffected and hence not influence the objectives of this research. The only possible exception was panel A which included an additional dwell at 145°C. A brief summary of the cure cycles amendments is given in Table 1.

Table 1: Cure cycle amendments

PANEL	CURE CYCLE AMENDMENTS
G	Control Panel (as manufacturer's spec.)
I	No compaction pressure
C	No vacuum
D	Pressure applied at t=40 min
F	Pressure applied at t=70 min
E	Pressure applied at t=80 min
H	Pressure applied at t=110 min
B	Vacuum maintained to t=70 min
A	Extra dwell period at t=65 min

Assessment of Panel Quality and Voidage

Accurate measurement of void content at levels below 2% is difficult. Image analysis is destructive and time consuming, but with increased operator skill can give an accurate assessment of bulk voidage and void distributions. Hence, although not ideal from a practical standpoint, image analysis was used in order to establish void levels. Coupons (four from each panel) were cut and carefully prepared and polished to a 1µm finish prior to assessment using Vista Image Analysis.

From an industry standpoint, assessment by non-destructive methods such as ultrasonics is a more attractive option. Hence, the panels were C-scanned in order to establish an overall picture of panel quality. Thus it was also possible to establish whether a relationship between attenuation and absorption exists.

Absorption Tests

Three coupons from each panel (50mm x 50mm) were taken from regions adjacent to those from which the image analysis samples were cut. They were immersed in a bath at 353K and weighed periodically over a four month period in order to produce a plot of weight gain as a function of root time. Prior to weighing each sample was towel dried. The results presented are the average of three weighing made on a Mettler balance accurate to .00005g.

In addition, plaques of cured neat resin were immersed in order to establish the saturation levels of the neat resin.

This value was used in a rule of mixtures relationship to predict the saturation levels for each panel. This analysis assumed no absorption by the fibres.

RESULTS

C-scan

The results of the T/T C-scan investigation are shown in Fig. 1. The light areas are more attenuated which implies more interaction with defects. It should be noted that the C-scans are a plan view which gives a summation of all the points through the thickness at each location. They do not give the spatial location of defects within the through thickness section.

It can be seen from Fig. 1 that the variations in the cure cycle had been successful in producing panels of different quality. Panel A is especially good whereas panel I is poor. Variations of the signal within the panels indicates inhomogeneity. This was taken into account in selecting the samples for image analysis and absorption tests. The average attenuation was recorded for each panel and is shown in Table 2.

Image Analysis

The percentage of voids for the nine panels are given in Table 2. It can be seen that void levels in the range 0% and 2.5 % have been achieved. In all comparative graphs, the results for panel I (2.5% voids) have been omitted as this is the extreme case, and its inclusion would make it difficult to separate the other results.

At present the standard method of quoting void contents is to give an average percentage void content over the entire panel. However, this gives little idea of the variation in levels across the sample. Fig. 2 shows typical void distribution in the mid-section of the panel. One more important factor which is overlooked in quoting void contents is the surface porosity. Figures 3 & 4 show micrographs of the edges (ie the surfaces) of samples with very different surface qualities. The former has a layer of resin at the surface whilst the latter is almost entirely resin starved. This extra 'surface voidage' is not detected under image analysis as the exposed fibres do not register as voids. However, under ultrasonic investigation, these surface irregularities will have an effect on the attenuation of the signal - and hence it is possible that a sample showing low void content under image analysis may show high attenuation (see panel F).

Table 2: Moisture, C-scan and image analysis results

PANEL	A	B	C	D	E	F	G	H	I
%m/%m	0.53	0.53	0.81	0.84	0.80	0.91	0.98	1.27	4.0
%Vv	0.10	0.09	0.57	1.34	1.06	0.09	0.92	1.54	2.3
Signal Ampl (αV)	2932	2486	1968	1729	1928	1469	1827	376	27
Initial Slope	0.97	1.17	1.68	1.59	1.71	1.84	1.73	4.15	7.2

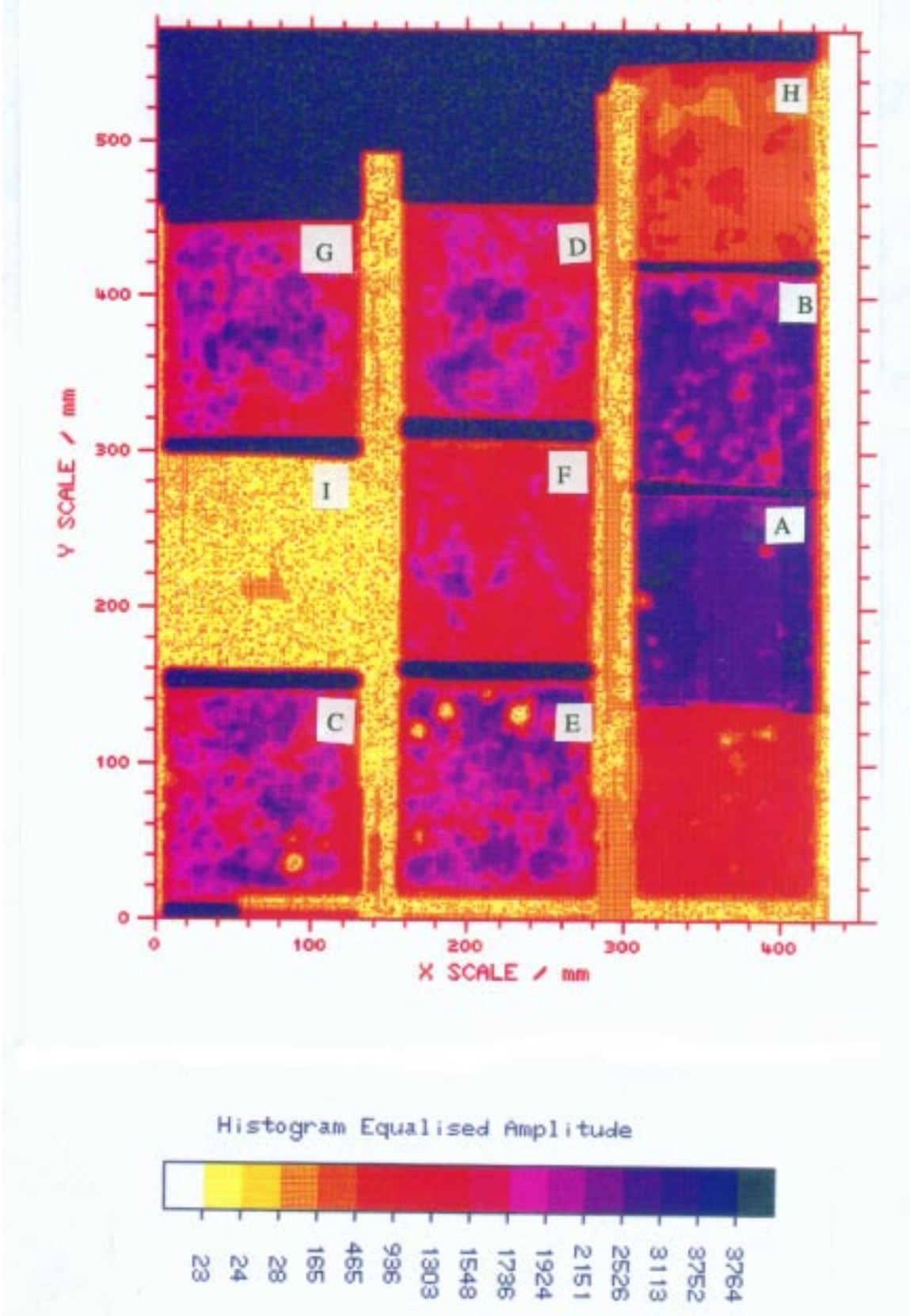


Fig. 1: C-scan results, 5MHz probe

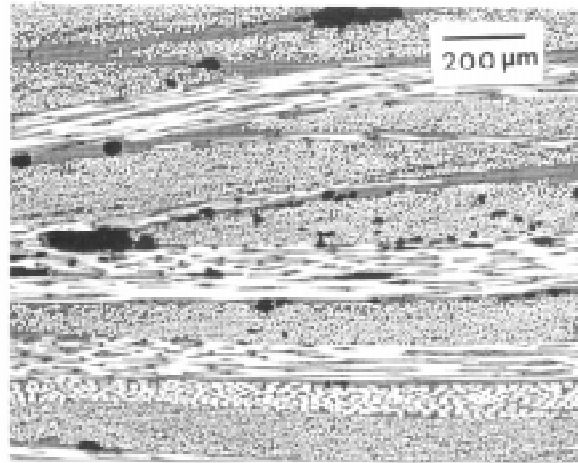


Fig. 2: Voids in centre of Panel H

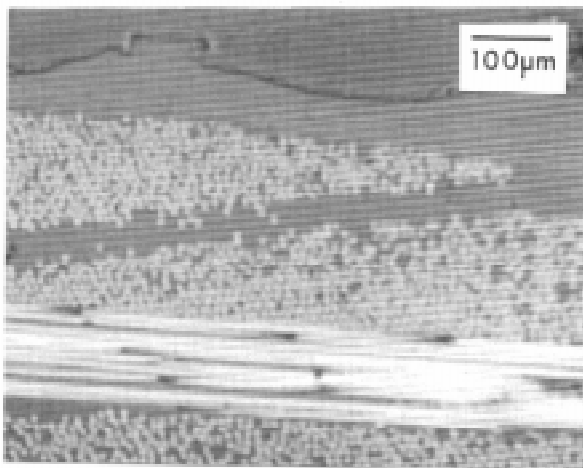


Fig. 3: Resin rich surface (Panel D)

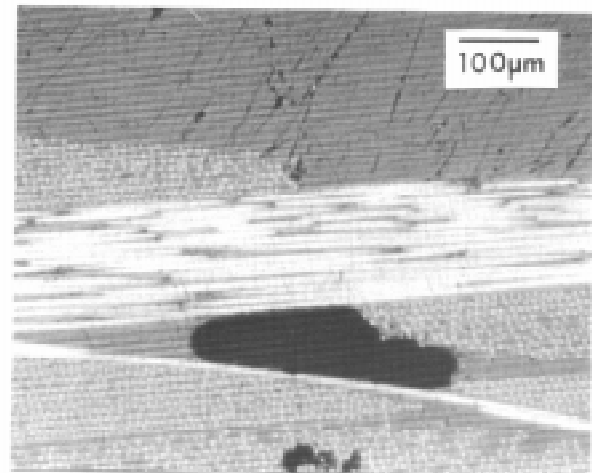


Fig. 4: Resin starved surface (Panel F)

Moisture Absorption

With the exception of panels H and I, the normalised ratio of %m/%m predicted was less than 1. It is clear that these panels had not achieved full saturation during the time of immersion. However, by looking at the absorption curves it is also obvious that panels A and B are unlikely to achieve unity. This implies that the presence of fibres within the system in some way impedes the ingress of water, and that all free volume space occupied in the neat resin system is not occupied in the woven composite. Panels H and I absorbed more water than predicted. This suggests that void filling may be taking place.

Table 2 also shows significant variations in the initial slope of the absorption curve. Panels H and I had the greatest rate of initial uptake which is consistent with their higher normalised weight gains. Given that voidage is the major variable, the results suggest that the effect of voidage is significant.

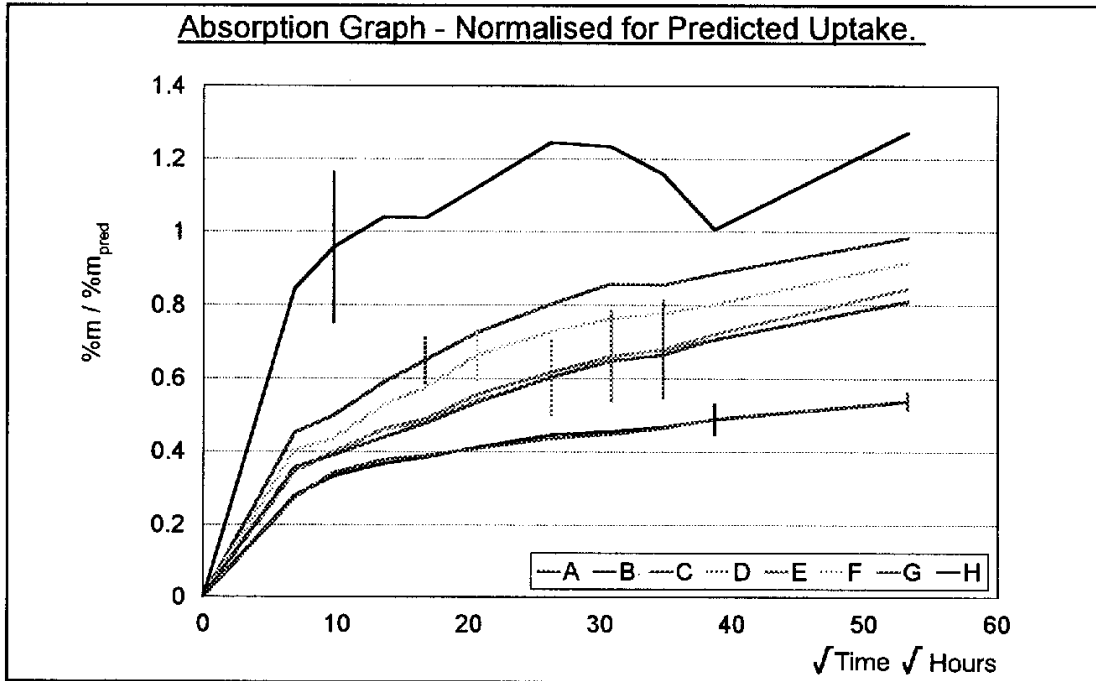


Fig. 5: Moisture absorption curves

Relationship between Attenuation and Moisture Uptake

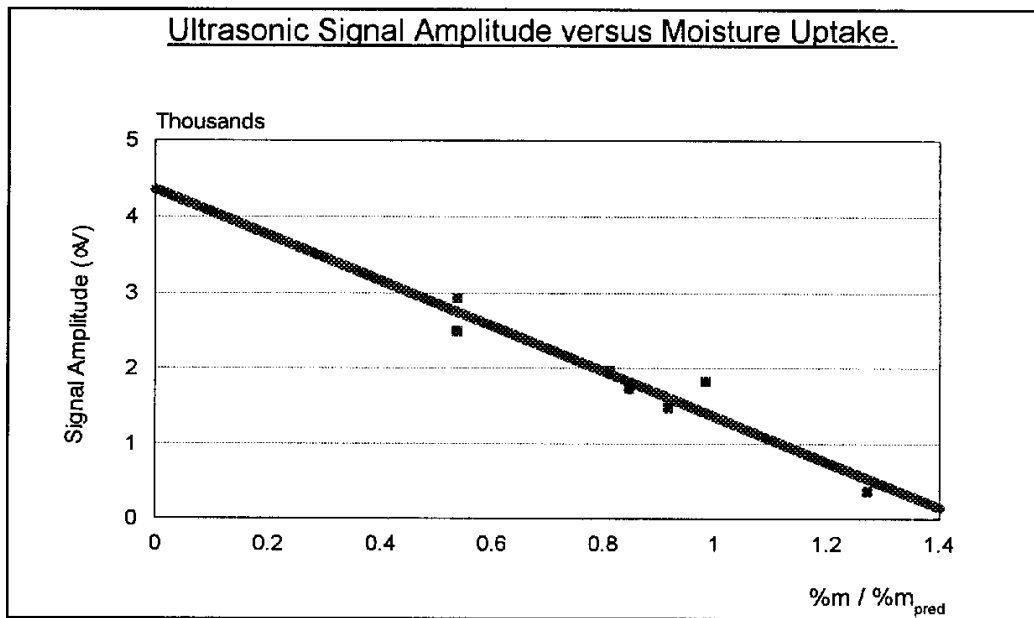


Fig. 6: Relationship between C-scan and moisture uptake

Fig. 6 indicates that there is a relationship between attenuation and uptake. From a practical standpoint, this is encouraging as it suggests that it may well be possible to use C-scans to identify panels which will saturate quickly.

Relationship between void content and moisture uptake

The general trend is for moisture absorption to increase as void volume fraction increases (Fig 7).

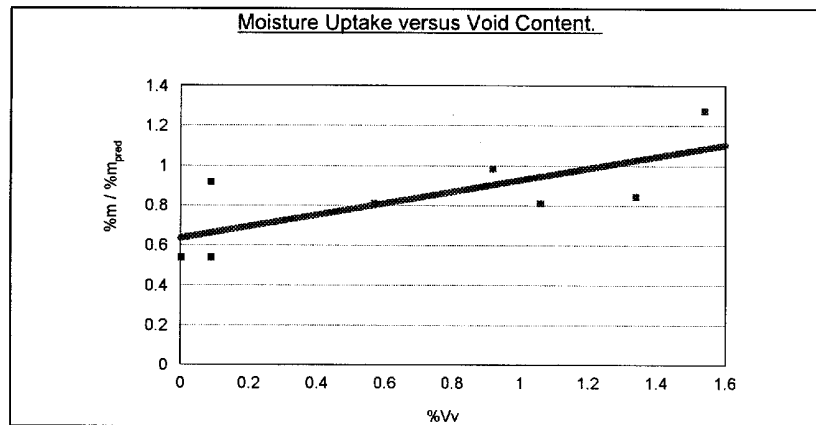


Fig. 7: Void content and moisture uptake

However there are some deviations; most significantly panels F and H show higher absorptions than predicted, whereas panels D and E show lower absorptions. The results suggest either errors in the image analysis results (image analysis specimens not being representative of the panel) or that factors other than internal voids influence the absorption process. Reassessment of the image analysis results confirmed the original results and hence the influence of other factors is indicated.

DISCUSSION

Water is absorbed by [1] :

- : bulk diffusion
- : capillary action
- : diffusion into defects

Bulk diffusion is an important factor which is determined by the resin system and the degree of cure. With the possible exception of panel A which had the extra dwell in the cure cycle, the degree of cure would be expected to be the same for all the panels. Hence bulk diffusion factors are not believed to be responsible for the observed results.

Ingress due to capillary action should also be the similar for all panels since they are essentially the same in terms of volume fraction and lay-up. However, uptake due to capillary action will also depend upon the presence, location and shape of voids. Voids running parallel to fibres will facilitate capillary action whereas voids entrapped in resin rich areas will not. Although inhomogeneity in the distribution of voids was observed with some panels (D & E show local

areas of voidage), there was no strong evidence to support capillary action as being the major influence on the results.

Diffusion of moisture into voids could account for the results. However, there was no clear correlation between up-take and voidage. For example panels F & G were close to saturation whereas panels D & E which had higher void contents were not. It is interesting to compare the results of B & F which both had 0.09% voids. Panel F had a significantly higher initial slope and up-take. Clearly, factors other than void content are involved.

Panels F and H (both saturated) had high surface voidage whereas the remaining samples had lower surface voidage and/or thicker resin surface layers. The presence of voids or exposed fibres at the surface would facilitate up-take by effectively increasing the length of the diffusion front. Voids in the centre of the panels would have no effect at all until reached by the diffusion front. In the case of the panels which did not saturate, this clearly did not happen. Thus it is believed that surface quality has an important effect on moisture absorption of composites because it defines the diffusion front.

The surface quality factor also explains why the correlation between C-scan (which takes account of surface effects) and moisture absorption was better than image analysis and moisture absorption. Detailed image analysis in the surface region is required if a better correlation with moisture absorption is to be obtained.

CONCLUSIONS

This paper has shown that there is a determinable link between void content and moisture uptake - although anomalies have been observed. A much more extensive investigation of the link between void size, shape and location and the absorption of moisture is required. For industry's purposes it is worth noting that a good correlation between ultrasonic scanning and absorption levels can already be obtained, although it is first necessary obviously to account for the effects of different void free resin systems.

REFERENCES

1. Judd, N.C.W. and Wright, W.W., "Voids and Their Effects on the Mechanical Properties of Composites - an Appraisal", *SAMPE Journal Jan/Feb 1978*; pp. 10-14.
2. Harper, B.D., Staab, G.H. and Chen, R.S., "A Note on the Effects of Voids Upon the Hygral and Mechanical Properties of AS4/3502 Graphite/Epoxy", *Journal of Composite Materials*, Vol. 21, 1987; pp. 280-289.
3. Judd, N.C.W. "Absorption of Water into Carbon Fibre Composites", *The British Polymer Journal*, March 1977.
4. Shirrell, C.D. and Halpin J., "Moisture Absorption and Desorption in Epoxy Composite Laminates", *Composite Materials: Testing and Design (Fourth Volume)*, ASTM STP 617, 1977, pp. 514-528.

SHIELDING EFFECTS OF DIFFERENT ASPECT RATIO OF ALUMINUM FLAKES IN CONDUCTIVE PLASTICS FOR INJECTION MOLDING PROCESSES

Huang-Lung Hung¹, Chao-Chang A. Chen², C. B. Lin², C.H. Liu¹, Tung-Han Chuang³

¹*Graduate Institute of Mechanical Engineering, TamKang University, Taipei, Taiwan, R.O.C.*

²*Department of Mechanical Engineering, TamKang University, Taipei, Taiwan, R.O.C.*

³*Institute of Material Engineering, National Taiwan University, Taipei, Taiwan, R.O.C.*

SUMMARY: This paper presents a study of comparing three aspect-ratio conductive plastic composite materials based on acrylonitrile-butadiene-styrene (ABS) compounded with aluminum flakes for the shielding effectiveness of injection molding products against electromagnetic interference (EMI). Aspect ratio (AR) of these conductive plastics is 6, 156 and 695 as well as content is ABS/AL 37wt%, ABS/AL 10.4wt%, and ABS/AL 36wt%, respectively. The EMI values were obtained between 45 dB and 28 dB for AR695 conductive plastics. The relationship of EMI value regarding aspect ratio, conductive network, critical concentration, and gate system of injection mold are also discussed.

KEYWORDS: electromagnetic interference (EMI), aluminum flakes, conductive plastics composite, injection molding

INTRODUCTION

Recent widespread use of electronic devices has increased electromagnetic interference (EMI) problems due to the generation of electromagnetic energy. Electromagnetic wave interference will become an invisible public hazard in the twenty-one century [1,2]. Electromagnetic wave covers wide range of frequencies including radio frequency, TV signal, radar and X-ray [2]. Besides the possible harmfulness to humans, some precise machines including aircraft guidance systems, and medical equipment such as electrocardiograph, pacemakers and related computer systems may be interfered to malfunction [2].

Currently, most of the cabinets of electronic and computer products are manufactured by injection molding processes using engineering plastics, such as ABS and PPO. Since surface resistivity of plastics is $10^{16}\sim 10^{17}$ Ω/Sq , plastics are usually categorized as insulation materials to EMI shielding effectiveness [3]. Plastic materials need to be upgraded its electromagnetic interference shielding effectiveness for satisfying the regulations around the world. In general, metal shielding is the traditional way to be adopted because of its good shielding effectiveness. However, the weight of metal shielding is too heavy for making complex shapes and the equipment of treatment of corrosive protection on the surface is expensive to keep products competitive. Thus metallizing plastic cabinets are popular for

meliorating the above imperfection [4]. Generally, conductive plastics are made by adding conductive fibers or flakes in the base resin. The most common fillers are carbon fibers, nickel coated graphite (NCG) fibers, stainless steel fibers, and aluminum fibers or flakes. The amount of fillers in the resin is usually among 7-20 % of the total volume depending upon the level of shielding required [5]. In this research, aluminum flakes are adopted as metallic fillers to be directly combined into polymer to produce conductive plastics composite resin. Some challenges for use of conductive plastic composite materials are listed as follows:

1. Dimensional aspect ratio (AR) of aluminum flakes must be high enough to form conductive network.
2. Volume of aluminum flakes needs to be sufficiently high to form overlap or conductive network.
3. Gating system of injection molding has to be modified for improving distribution of aluminum flakes in ABS polymer.
4. Cluster and distortion of aluminum flake flow in mold interior need to be solved during injection molding.

Different aspect ratio and its filler of weight percent are known to affect EMI shielding effectiveness [6]. The higher aspect ratio of aluminum flakes is in the resin matrix, the easier for aluminum flakes to form overlap or conductive network that provides a continuous conductive path throughout other flakes in plastic [7]. From the viewpoint of cost and shielding effectiveness, injection molding process was used in this research to fabricate products of three aspect-ratio conductive plastic composite materials based on acrylonitrile-butadiene-styrene (ABS) compounded with aluminum flakes. Aspect ratio of these conductive plastics is 6, 156, and 695 as well as content is ABS/AL 37wt%, ABS/AL 10.4wt%, and ABS/AL 36wt%, respectively. Relationships between EMI shielding effectiveness and aspect ratio, weight percent, and gate system of injection molding are also investigated for improving the EMI values to meet the industrial demands.

LITERATURE REVIEW

M.T. Kortschot and R.T. Woodhams [6] proposed the characteristics of a conductive filler in terms of efficiency and critical concentration. The concentration of the conductive particles is the overriding factor to determining the composite conductivity, shielding effectiveness, and cost. At the critical concentration, the percolation threshold is reached as network formation commences and then the resistivity decreases greatly. A few weight percentage beyond the critical concentration will invariably produce a composite that has useful conductivity. An “efficient” EMI additive may be defined as one which has a very small critical concentration [8]. Few studies have examined the relationship between critical concentration and parameters such as particle size and shape, or filler dispersion. Davenport [6] compared the critical concentration of conductive fibers of various aspect ratios with their dry packing fractions. A correlation between packing fraction and critical concentration was found and a critical concentration was reported that exceeded the packing fraction for fibers with aspect ratios greater than 100.

Therefore, the most important characteristic of any filler, in terms of both packing density and EMI efficiency, is its geometry or aspect ratio. The aspect ratio of a particle is defined usually as the ratio of the longest dimension to the shortest dimension: for short fibers is the length over diameter (L/D), and for flakes is the mean diameter over thickness (D/T) [6].

Davenport [6] concluded that electromagnetic effectiveness becomes higher when aspect ratio increases. It is the higher aspect ratio to form the network of conductive easily. But the mechanical property of products will decrease as the content of filler increases. Carmona, Barreau, Delhaes, and Canet [6] proposed a geometric scaling law with which the fitted data obtained a dispersion of carbon fibers in an epoxy matrix. They concluded that for sufficiently large aspect ratio, critical concentration (ϕ^*) is inversely proportional to the square of aspect ratio (AR)

$$\phi^* \propto (1/AR)^2 \quad (1)$$

Thus the larger aspect ratio number is, the smaller critical concentration of aluminum flakes reaches the same level of conductivity.

J. Martinsson and J.L. White [7] provided an ABS (Acrylonitrile-Butadiene-Styrene) polymer filling with aluminum flakes by injection molding, the aluminum flake was generally orientated with its major axis in the direction of flow. The electrical anisotropy of electromagnetic interference composite is caused by the orientation of flake during molding. The neighborhood of the gate was found to possess unusually high particulate conditions. The abnormally high concentrations of aluminum flakes near gate are consistent with the mechanism of the observed pressure fluctuation. This phenomena conduces to the segregation of aluminum flakes when injection molding. B. Terselius, Y. Sjonell, and J. Jansson [9] reported that a large orientation of fiber was found at mold gate region. It was probably created when the melt flows through the narrow gate.

From above literature review, higher aspect ratio of aluminum flakes can increase conductive effectiveness, but the orientation, fracture, and segregation phenomena of aluminum flakes during injection molding need to be solved to improve its mechanical properties while maintaining the EMI shielding effectiveness. Three aspect ratio value of aluminum flakes (AR6, AR156, and AR695) were used in the experimental for comparing the EMI effectiveness of injection molding products.

EXPERIMENTAL

Three kind of conductive plastics composite material were used in this paper for comparing the EMI effectiveness. The first conductive plastics material is AR6 and content is ABS/AL 37wt% that was produced by a local company, Alotex Polymer Alloy Company in Taiwan. The other two conductive plastics materials are AR156 and AR695 that were produced in the laboratory at the National Taiwan University (NTU), each content is ABS/AL 10.4wt% and ABS/AL 36wt%, respectively.

The model MPL2000 injection molding machine made by the Outstanding Company in Taiwan was used in this research. A steel mold was fabricated with a set of specimen mold cavities of tensile, impact, and electromagnetic shielding effectiveness test specimens as specified in the ASTM standards: ASTM D638, ASTM D256, and ASTM D4935-89. Fig. 1 shows the EMI shielding effectiveness test disk according the ASTM standard. After injection molding process, these electromagnetic interference shielding effectiveness specimens were tested at the Industry Technology Research Institute of Measurement Center, tensile and impact specimens were measured at the National Taiwan University.

The electromagnetic shielding effectiveness method adopted in this paper is the ASTM D4935-89 coaxial transmission test that uses a two-piece calibration sample and a corresponding solid test disk. These two samples as shown in Fig. 1 must be of equal thickness and maintained at a high degrees of flatness. This technique is valid over the range of 0.03GHz to 1.5GHz. The test, shown schematically in Fig. 2, requires the reference sample at the right hand side first be evaluated and the received power be recorded as baseline value. This was accomplished by clamping the reference sample between the two halves of the sample holder, attaching the coaxial cables and supplying a sinusoidal signal to one side of sample holder, while measuring the received power at the other side of the holder. This through transmission approach can be modified using the same apparatus to give an indication of the component of the total shield attenuation that can be attributed to each of reflection and absorption. By attaching the receiving side of the coaxial cable to a second connector on the same side of the specimen holder as the input coaxial cable, a measure of the reflected power can be obtained.

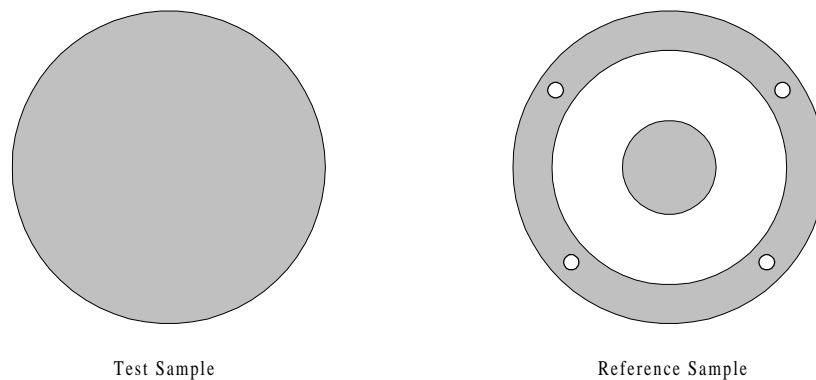


Fig. 1: Electromagnetic shielding effectiveness test disk

Table 1: Impact data of ABS plastic of unfilled aluminum flakes

Impact specimens	ΔE (J)	$\Delta E / L$ (J / m)
I 10101	Failed	Failed
I 10102	1.882	148.20
I 10203	2.061	162.30
I 10104	2.181	171.90
I 10105	1.862	146.61
I 10106	2.072	163.17

Table 2: Impact data of ABS plastic of filled aluminum flakes

Impact specimens	ΔE (J)	$\Delta E / L$ (J / m)
I 20101	0.335	26.40
I 20102	0.323	25.44
I 20103	0.321	25.28
I 20104	0.358	28.17
I 20105	0.331	26.08

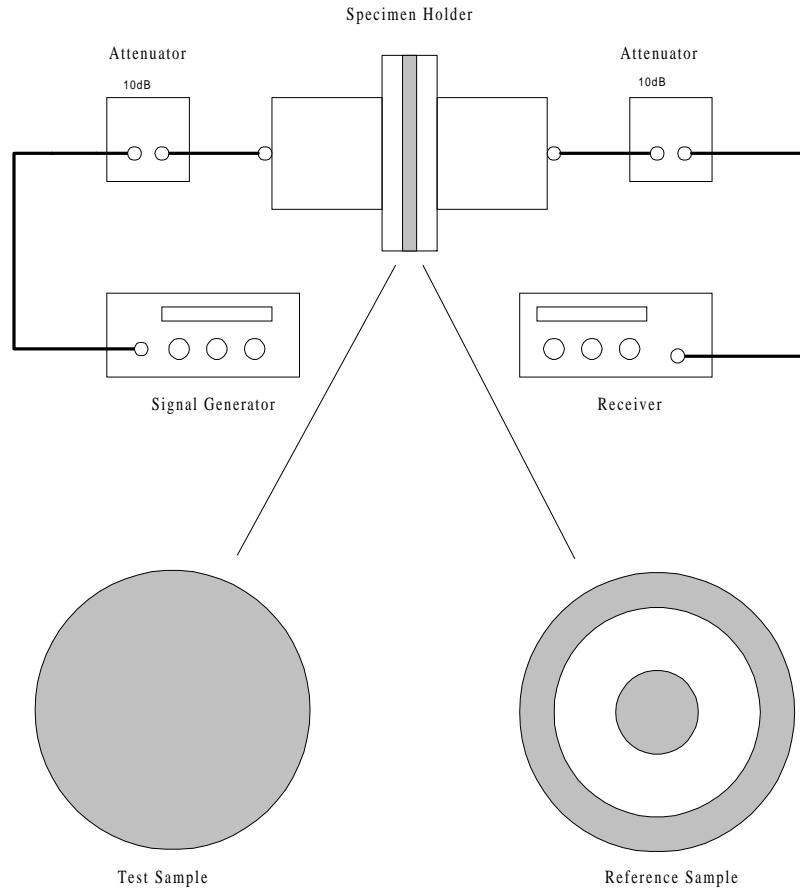


Fig. 2: ASTM D4935-89 coaxial transmission test for EMI value.

RESULTS AND DISCUSSION

Experimental tests were made for tensile, impact, electromagnetic interference shielding effectiveness. The first test material is AR6 conductive plastics composite material with ABS/AL 37wt%. Because of low aluminum flake aspect ratio, the value of electromagnetic shielding effectiveness is too low for industrial applications. As shown in Fig. 3, the aluminum flakes were cut to chip formation by screw when compounding. Consequently, the low aspect ratio made its length not enough to form the network of conductivity. The tensile strength is about 70% ABS plastic of unfilled aluminum flakes, and the impact strength is about 20% ABS plastic of unfilled aluminum flakes as shown Tables 1-2. The interface between aluminum flakes and ABS polymer form crack effect in interior. The low tensile and impact strength for the ABS filled with aluminum flakes were obtained in the experiment due to the molecular chain strength and cluster were destroyed at some region to make strength lower than the unfilled ABS plastic. Orientation flow and undispersive problem of the filled aluminum flakes may affect the mechanical property too.

The other two conductive plastics composite materials, AR156 and AR695 that were produced at NTU, each with content as ABS/AL 10.4wt% and ABS/AL 36wt%. The EMI shielding effectiveness values for AR156 material is too low for industrial applications as shown in Fig. 4. The aspect ratio of AR156 should be enough to form a network of conductivity. But the volume critical concentration of aluminum flakes cannot reach packing

fraction that is needed to form network of conductivity. The flow of aluminum flakes was dragged by molten ABS polymer to generate orientation phenomena that decrease aluminum flakes of overlap or conductivity network of formation percent. EMI shielding effectiveness was also affected by mold geometry that easily cause distortion or entanglement of aluminum flakes.

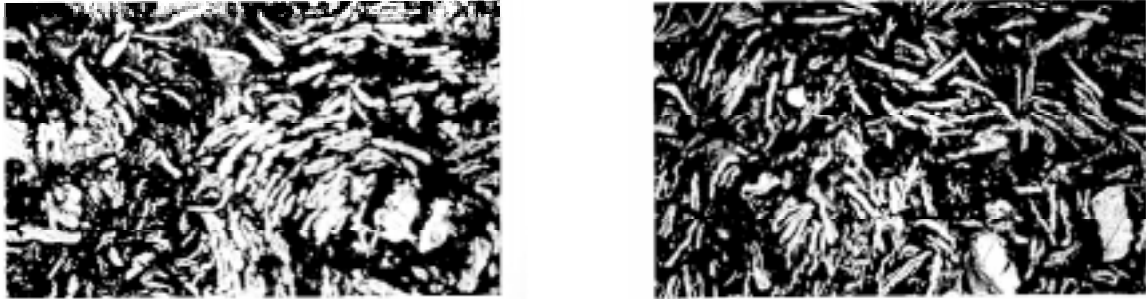


Fig. 3: Microstructure photos of distorted and undispersive aluminum flakes in ploymer after injection process of AR6 conductive plastics (mag.: 200 ×)

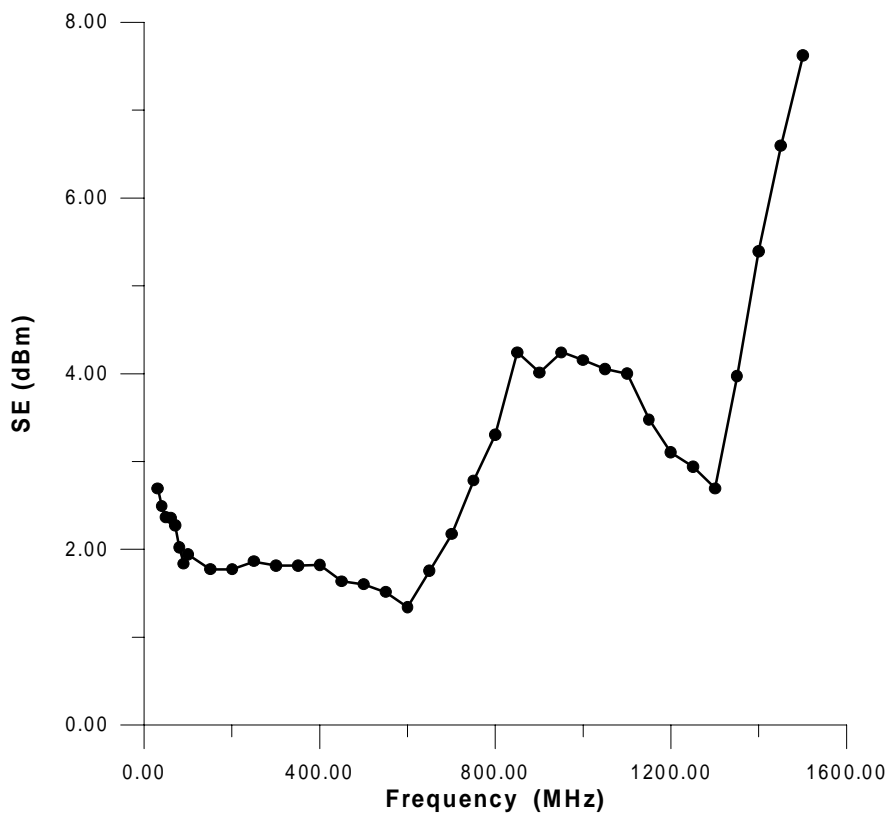


Fig. 4: Electromagnetic shielding effectiveness cover of filled aluminum flakes of conductive polymer (AR156)

The final test material is AR695 with content of ABS/AL 36wt%. The aluminum flake is 12.5 mm length, 2 mm width, and 18 μm thickness. Fig. 5 shows the EMI shielding effectiveness values locating between 45 dB and 28 dB for injection molding specimen of AR695 material. The high aspect ratio and enough volume of aluminum flakes in polymer successfully form a network of conductivity as shown in Fig. 6. However, as shown in Fig. 6, the dispersive problem still needs to be improved by considering the injection mold of gate system, runner system, and mold cavity shape in the next step of this project. If aluminum flakes can be dispersive in ABS polymer, the conductive network will be formed in internal of electronic device cases. The electromagnetic interference function is then obtained.

At the current stage, conductive plastic with high aspect ratio of aluminum flakes, such as AR695 material was produced at NTU and its EMI shielding effectiveness values were obtained close to the industrial demands. By the above modified methods of mold and injection process, electromagnetic interference shielding effectiveness is expected to meet the industrial needs in the near future.

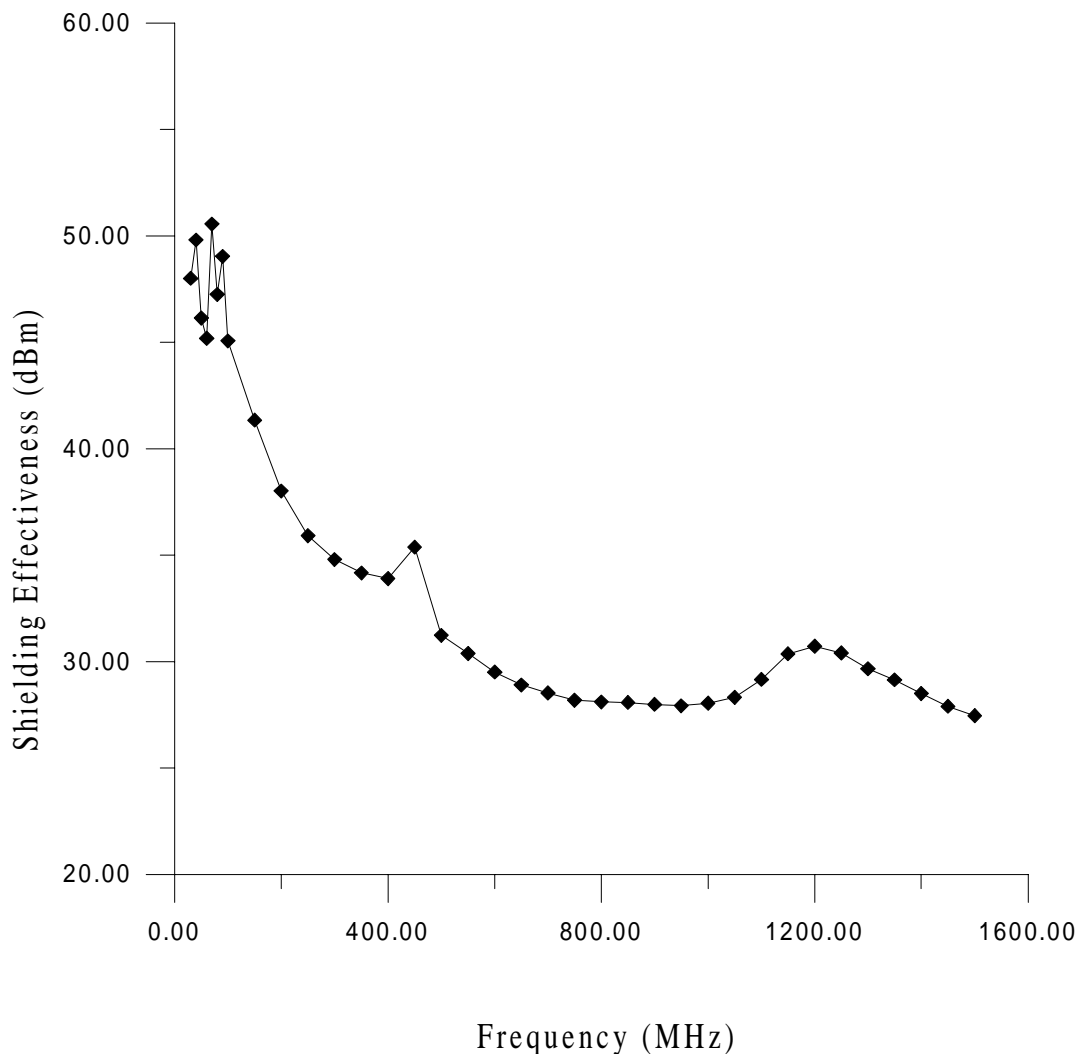


Fig. 5: Electromagnetic shielding effectiveness cover of filled aluminum flakes of conductive polymer (AR695)

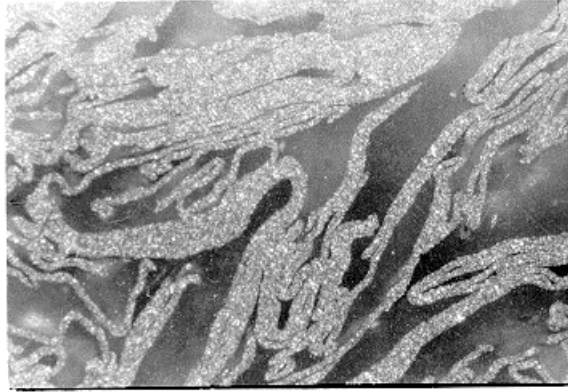


Fig. 6: Microstructure photo of connected network by aluminum flakes in polymer after injection process of AR695 conductive plastics (mag. : 50 ×)

CONCLUSION

This paper is to compare three aspect-ratio conductive plastic composite materials based on ABS compounded with aluminum flakes for the shielding effectiveness of injection molding products against EMI. The EMI values were obtained between 45 dB and 28 dB for AR695 conductive plastics. Some conclusions can be drawn as follows:

1. The effects of aspect ratio of aluminum flakes in polymer is obviously important to form an internal network of conductivity for injection molding products against electromagnetic interference shielding effectiveness.
2. The volume critical concentration of aluminum flakes is an imperative factor to form a conductive network for electromagnetic interference shielding effectiveness.
3. EMI shielding effectiveness was also affected by mold geometry that easily cause distortion or entanglement of aluminum flakes.

ACKNOWLEDGEMENT

The authors wish to thank National Science Council (NSC) in Taiwan, Republic of China under grant number NSC 85-2622-E-002-015 for the financial support and also Mr. Kuo-Yen Hsia and Mr. Chung-Ming Lu for their valuable assistance.

REFERENCES

1. Donald W. Radford and Boyle C. Cheng, "Ultra-Lightweight Composite Materials for EMI Shielding", *SAMPE*, Quarterly, 1993,P54~61.
2. *EMI/RFI Shielding Guide*, General Electrical Company.
3. James M. Margolis , *Conductive Polymers and Plastics* , Chapman and Hall , 1989 .
4. D. K. Chen, C. M. Ma, and Andrew T. Hu, "The processing and Characterization of EMI Shielding PP Composites", *36 Th. International SAMPE Symposium*, April, 1991, P15~18.

5. C.C. Wu, The Investigation of EMI Shielding of PC/ABS Conductive Composites, *Master Thesis of Graduate Institute of Material Engineering*, Tatung Institute of Technology, 1994.
6. M.T. Kortschot and R.T. Woodhams, "Electromagnetic Interference Shielding with Nickel-Coated Mica Composites". *Polymer Composites*, October, 1985, Vol.6, No.4, P296~303.
7. J. Martinsson and J.L. White, " Characteristics of Thermoplastics Containing Electrically Conducting Asymmetric Pasticles : Anisotropic Electrical Conductivity of Injection Molded Parts and Extrusion Behavior ", *Polymer Composites* , October , 1986, Vol.7 , No.5 , P.302~314.
8. A. Crossman , "Conductive Composites Past,Present,and Furture" , *Polymer Engineering and Science*, Mid-June, 1985, Vol.25, No8, P507~513.
9. Ylva Sjonell , Bjorn Terselius , and Jan-Fredrik Jansson , " Injection Molding of Polypropylene Discs. I : Effect of Holding Pressure on Orientation Distribution " , *Polymer Engineering and Science* , Mid-June 1995 , Vol.35 , No.11 , P950~956.

NEUTRON DIFFRACTION STUDY OF THE CO-DEFORMATION BEHAVIOUR OF A BERYLLIUM-ALUMINIUM COMPOSITE

David H Carter and Mark A.M. Bourke

*Materials Science and Technology Division, Los Alamos National Laboratory Los Alamos
NM 87545, USA*

SUMMARY: Neutron diffraction measurements of the mean phase elastic strains during compressive loading were performed on a beryllium-aluminum composite with a composition of Be-47.5Al-2.5Ag. The material was produced from hot isostatically pressed powder fabricated by rapid solidification using a centrifugal atomization process. Under rapid solidification, BeAl undergoes liquid phase separation, resulting in a three-dimensional interpenetrating morphology, where each phase is continuous. Strain measurements were taken at the Los Alamos Neutron Scattering Center (LANSCE) using a pulsed neutron source, which provided time-of-flight diffraction data. Elastic strains in the individual phases were measured as a function of compressive load and used to quantify the deformation behavior. The Al phase is highly constrained by the Be phase due to the morphology of BeAl. This constraint, as well as the high stiffness and low Poisson's ratio of Be causes unexpected deformation behavior. Notably, the Al phase develops compressive strains in the direction perpendicular to the compressive loading axis.

KEYWORDS: beryllium alloys, neutron diffraction, beryllium, aluminium

INTRODUCTION

The possibilities of combining beryllium with aluminum to take advantage of the high specific strength and modulus of Be and the ductility of Al, have been recognized for many years. The Be-Al phase diagram has a eutectic reaction with no compounds, and there is little solid solubility of Be in Al, or of Al in Be. The microstructural length scale of the phases, their morphology, and their distribution depends on the solidification rate and processing history.

A sub-liquidus metastable liquid miscibility gap has been identified in the Be-Al system, [1-3] depicted on Fig. 1. Using a thermodynamic approach, Murray and Kahan [3] calculated the critical point of this miscibility gap as 1100 °C at 68 at% Be.

Sufficiently rapid rates of solidification can result in melt undercooling below the spinodal, leading to the possibility of liquid phase separation. Within the range of spinodal decomposition, there is no nucleation barrier to the separation of phases, and both of the resulting phases are continuous. Upon complete solidification, two intimately interpenetrating phases exist. The resulting microstructure, depicted in Fig. 1, can be described as a three-dimensional interpenetrating composite.

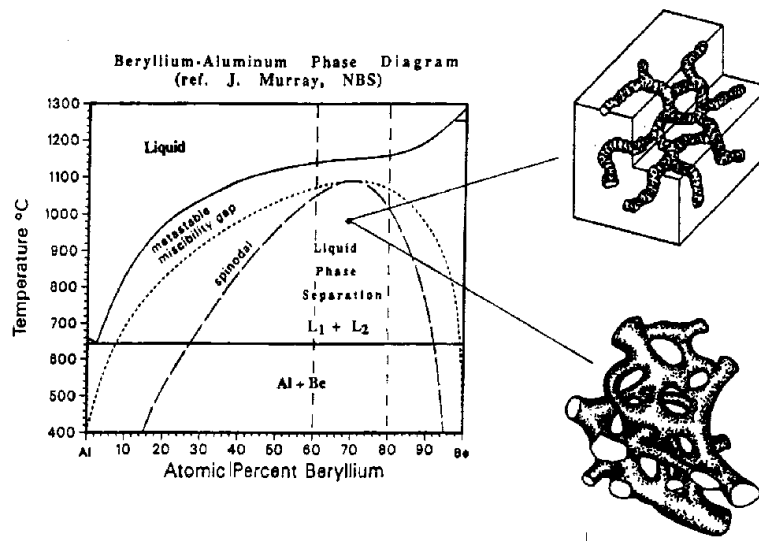


Fig. 1: Suggested Be-Al phase diagram from [1, 3] and depiction of a three-dimensional interpenetrating composite morphology

Through recent advances in rapidly solidified powder processing techniques, fine-grained BeAl has been produced with a morphology indicative of liquid phase separation, and has been shown to have excellent strength and ductility. Commercially available Be is brittle and exhibits poor tensile elongation. The tensile elongation of rapidly solidified BeAl, however, is in the range of ten percent or more while maintaining a yield strength of 350–400 MPa.

The goal of this research was to examine the deformation behavior of the individual phases in BeAl in order to better understand its ductility. Neutron diffraction is an ideal method for studying co-deformation of two phase composites because it provides a measure of strain in each crystallographic orientation in each phase individually. Unlike x-rays which are limited to surface measurements, neutrons provide a volumetric or bulk average strain.

BACKGROUND

The use of neutron diffraction for strain measurement is described in the literature [4–6]. At the Manuel Lujan Jr. Neutron Scattering Center, Los Alamos National Laboratory (LANSCE), neutrons are produced in pulses by spallation interactions of 800 MeV protons with a tungsten target. At a pulsed neutron source, the entire diffraction pattern can in principle be acquired from a single pulse of polychromatic neutrons, although many pulses are usually needed to build up adequate statistics. Each detector is at a fixed angle and records the entire diffraction pattern based on the “time of flight” of the diffracted neutrons. Bragg’s law can be related to time of flight by rewriting it as

$$\lambda = \frac{ht}{mL} = 2d_{hkl} \sin \theta \quad (1)$$

where λ is the neutron wavelength, h is Planck’s constant, t is the time taken for a diffracted neutron to travel the total flight path L , and m is the mass of the neutron. Bragg reflections for a select number of hkl planes in each phase can be fitted to obtain

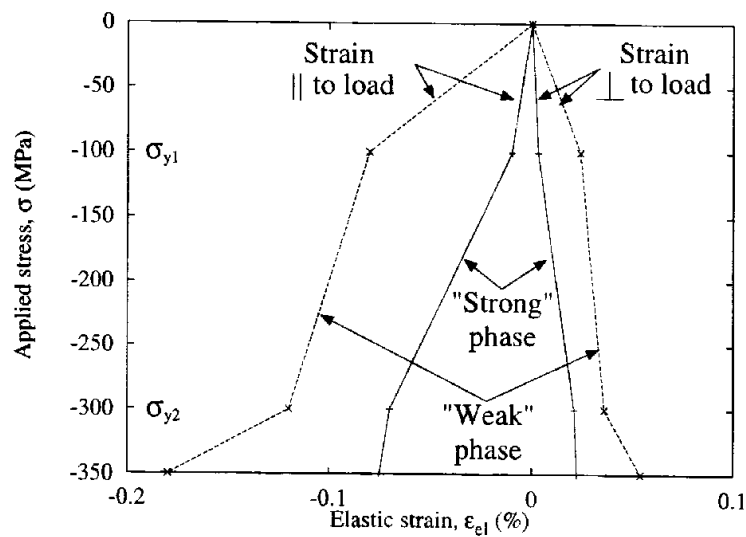


Fig. 2: Hypothetical results from a neutron diffraction experiment on a composite showing strains both parallel and perpendicular to the compression axis.

individual interplanar spacings. Elastic strains for individual reflections are calculated using

$$\varepsilon_{hkl} = \frac{\Delta d_{hkl}}{d_{hkl}} = \frac{\Delta \lambda_{hkl}}{\lambda_{hkl}} = \frac{\Delta t_{hkl}}{t_{hkl}} \quad (2)$$

In addition to calculating strains for individual hkl lattice planes, a Rietveld profile refinement [7] yields lattice parameters. All of the lattice reflections contribute to the determination of the lattice parameter. The intensities and positions of all Bragg peaks are predicted from an assumed crystal structure using the Los Alamos Generalized Structure Analysis System program (GSAS) [8]. The strain is then calculated by replacing values of interplanar spacings in Eqn 2 by the values of the lattice parameters (a_c , for Al, a_c and c_c for Bè).

Neutron diffraction has previously been used to study the co-deformation of a number of composites [9–14]. Fig. 2 shows the stress-strain data expected from a compression test in a hypothetical two phase composite, in which one phase can be considered the weaker or softer material, and the other, the stronger or harder material. Strain measured parallel to the loading direction is negative, and perpendicular to the loading direction is positive. The stresses are not those within each individual phase, but rather the applied values. Also, neutron diffraction measures only the elastic strain, not the total strain. However, from these data, information can be derived regarding the transfer of load from one phase to the other, and inferences can be made about the effects of plasticity and the overall co-deformation.

Both phases are elastic up to a certain load, when the weaker phase begins to yield. Parallel to the loading direction (Fig. 2) yielding of the weaker phase at σ_{y1} causes the rate of elastic straining, $d\varepsilon_{el}/d\sigma$, to diminish, because the weaker phase accommodates less elastic strain, and thus carries a smaller proportion of the load. The stronger phase must accommodate more of the load, and therefore the curve deflects in the opposite direction. The stronger phase eventually reaches its yield strength. At this point, σ_{y2} , the load begins to shift from the stronger phase back to the weaker phase, and therefore the curves deflect in the opposite direction. If both phases become perfectly plastic the

rate of elastic straining would be constant, $d\varepsilon_{el}/d\sigma = 0$.

Perpendicular to the loading direction (Fig. 2) the strains would be positive, for a compression test, and the ratio with the strains parallel to the loading direction is related to the Poisson's ratio (ν) for each phase. As before, the inflection points in the curves indicate load transfer due to yielding.

EXPERIMENTAL

Materials

The material has a composition of Be-47.5Al-2.5Ag, fabricated at the Los Alamos National Laboratory. Silver was added to this alloy to study age hardening [15]. Rapidly solidified powder was produced using a centrifugal atomization process. Each individual powder particle is a mixture of Be and Al with the morphology shown in Fig. 1. The powder was screened to a mesh size of -325 which, when hot isostatically pressed, produced a very fine microstructure with grain sizes on the order of 5 μm . The sample was examined in the as-HIPped condition, with the Ag in a super-saturated solid solution with the Al. Processing details and mechanical properties of this series of alloys are presented elsewhere [16, 17].

Neutron diffraction

Diffraction data are acquired as counts/ μsec versus time of flight in msec. The individual peaks are sharp, well defined and well separated for times greater than about 10 msec. In Fig. 3, the data between 12 and 30 msec are plotted as a function of interplanar spacing (Eqn 1). The general shape of the background intensity in the acquired data reflects the Maxwellian distribution of neutron energies in the incident beam. In this figure, the intensities are normalized by the incident spectrum to give a flat background, and individual Bragg peaks for Be and Al are indexed. The tick marks below the diffraction spectrum indicate predicted reflections for Be (lower marks) and Al (upper marks). The solid line through the data is the result of a Rietveld refinement, and the lower line is the difference curve associated with this refinement, showing that the fit is quite accurate. Aluminum does not scatter neutrons as readily as Be, therefore longer count times are required to obtain reasonable fits to the Al reflections.

Compression tests

A cylindrical compression sample was machined with a diameter of 7.96 mm and a height of 24 mm. Prior to the compression test, a diffraction spectrum was acquired with no applied load to compare with the diffraction spectra from two different powders. The first was the starting Be-47.5Al-2.5Ag powder from which the compression sample was fabricated. The second was nominally pure Be, also produced by centrifugal gas atomization, with a particle size of 5 microns. Each powder was sealed in a cylindrical can with approximately the same dimensions as the compression sample. These measurements were performed to determine the residual stress developed during composite processing.

Measurements were performed at LANSCE in the stress rig shown in Fig. 4, described in [14]. This apparatus fit into a 0.74 meter diameter cylindrical chamber in the beam. It was also necessary to ensure that the loading remained axial and that the incident and diffracted beams were unimpeded.

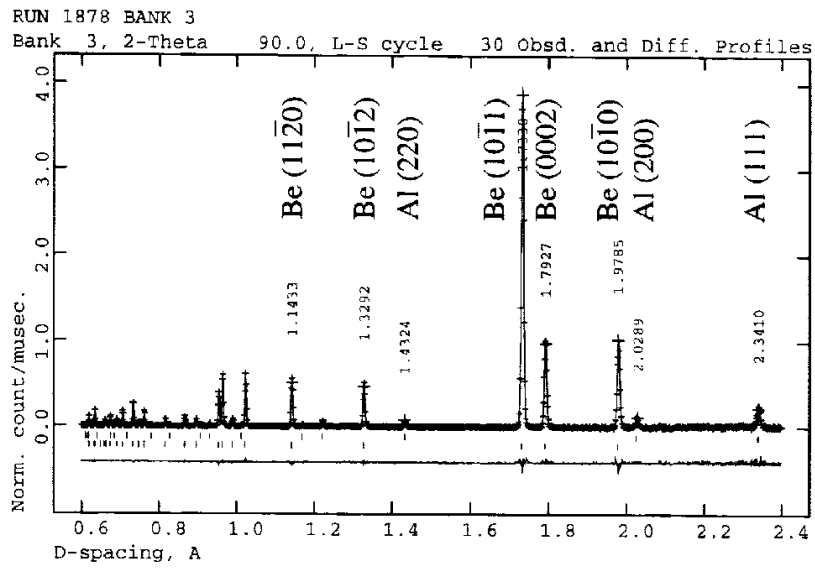


Fig. 3: Typical neutron diffraction spectrum for BeAl

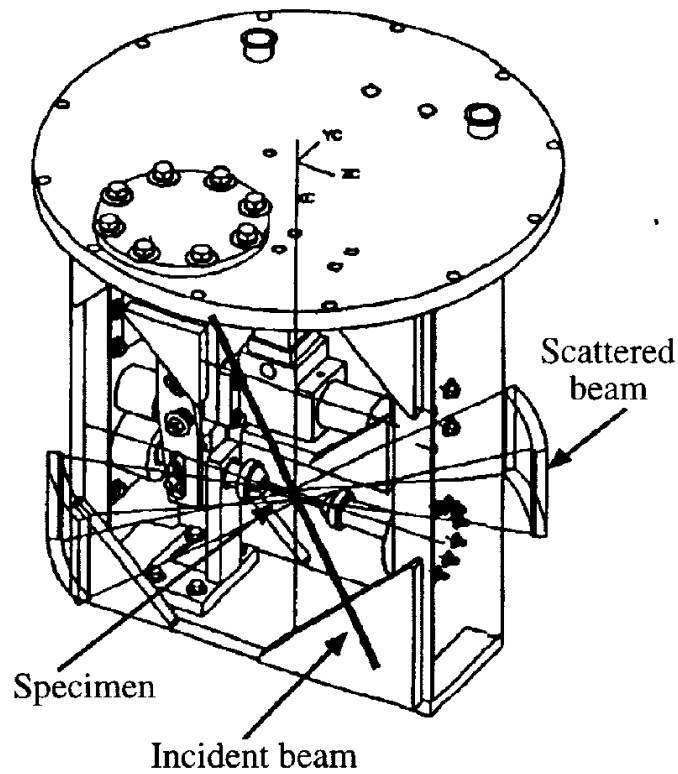


Fig. 4: Stress rig used for compression test in the neutron beam, from [14]

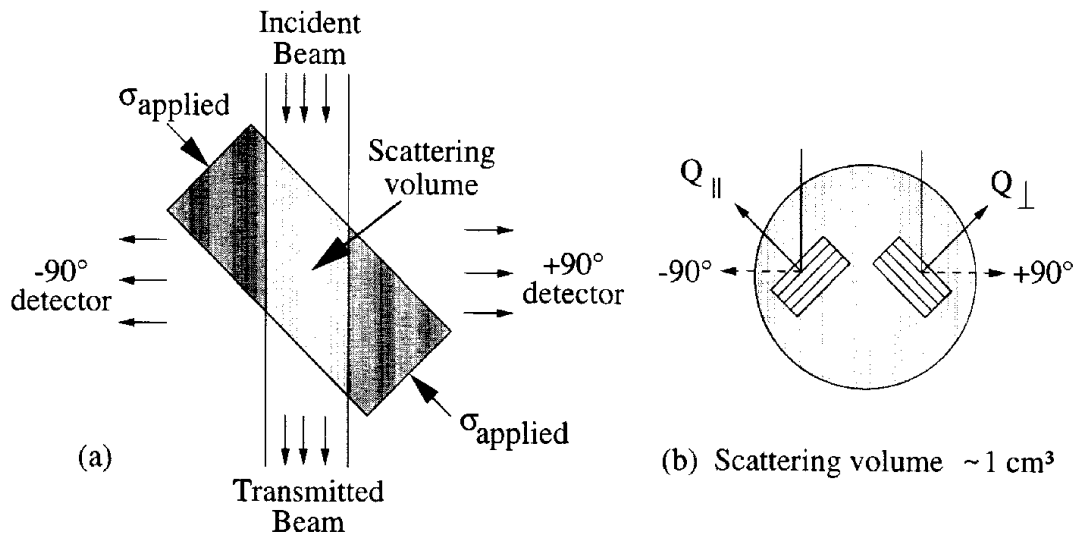


Fig. 5: Scattering geometry: (a) Axial and transverse strains are measured simultaneously in $+90^{\circ}$ and -90° detector banks, respectively. (b) Diffraction from planes perpendicular to applied stress measures strain parallel to applied stress (Q_{\parallel}), diffraction from planes parallel to applied stress measures strain perpendicular to applied stress (Q_{\perp}).

The orientation of the compression sample relative to the neutron beam is shown on Fig. 5. By placing the specimen loading axis at an angle of 45° to the incident beam, strains parallel and perpendicular to the loading axis were measured simultaneously by detectors forming angles with respect to the incident beam of -90° (Q parallel to the load) and $+90^{\circ}$ (Q perpendicular to the load) where Q indicates the diffraction direction.

Prior to the compression experiment, a diffraction pattern was acquired at a nominal load of -5 MPa to be used as the stress-free reference. The sample was loaded at a strain rate of $2 \times 10^{-4} \text{ sec}^{-1}$ in increments of applied stresses of 10–50 MPa up to a maximum applied stress of ~ 323 MPa. The sample was held for 2–4 hours at each applied stress, while diffraction data were acquired.

The overall strain was measured using an extensometer. The measured strain includes both elastic and plastic components. At higher loads, the sample exhibited a slight stress relaxation but this is not considered to affect the measurements, since no significant broadening of the diffraction peaks was observed. Beryllium is an excellent reflector of neutrons, substantially reducing the time required to obtain an accurate diffraction pattern. The longer count times were required to obtain sharp peaks for the Al phase.

RESULTS AND DISCUSSION

During processing, residual stresses may be imparted due to the difference in thermal expansion coefficients between Be ($11.6 \mu\text{m}/\text{m}\cdot\text{K}$) and Al ($23.6 \mu\text{m}/\text{m}\cdot\text{K}$). That is, after cooling from the pressing temperature (590°C) the Be phase will initially be in compression, and the Al in tension. But, such strains are unlikely to significantly effect the ductility, since the plastic strain imparted into the composite upon loading is substantially greater. Consequently, the stress-strain curve should converge with that of the composite having no residual stress.

Table 1 shows the residual strains with respect to both the starting Be-47.5Al-2.5Ag

Table 1: Initial residual strains

Phase and basis for ε_T	ε_T in a_o	ε_T in c_o
Be with respect to Be powder	-1.62×10^{-4}	-2.76×10^{-4}
Be with respect to Be-47.5Al-2.5Ag powder	-1.53×10^{-4}	-3.54×10^{-4}
Al with respect to Be-47.5Al-2.5Ag powder	$+3.26 \times 10^{-4}$	

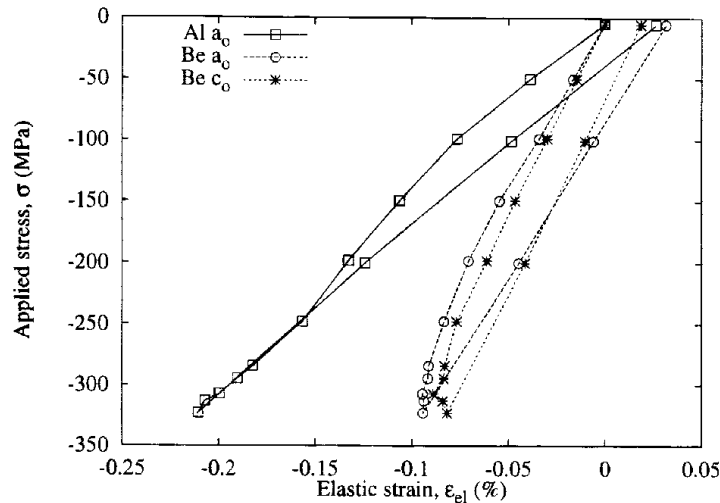


Fig. 6: Strains parallel to the loading direction

powder and Be powder. As expected, Be is in compression with respect to both the starting powder and nominally pure Be powder. Al is in tension with respect to the starting powder. The difference in the lattice parameter of Be between the starting powder and the Be powder is slight, indicating that there is no residual stress in the starting powder.

A wealth of information from individual peak fit data was obtained, and will be the subject of further work. Individual planes in Al and Be begin to yield at different applied stresses. For example, Be grains oriented such that the compression axis is perpendicular to the pyramidal plane ($10\bar{1}1$) behave substantially different from those in the basal plane (0002) or the prismatic plane ($10\bar{1}0$) orientations. However, this discussion will focus on strains calculated from the Rietveld refinements which are volume average strains.

Shown in Fig. 6 are strains parallel to the loading direction. Strains in these and subsequent plots are calculated relative to the initial stress state (-5 MPa) and assumed zero initial strain, therefore they do not account for the probable initial residual strains.

Strains parallel to the compression axis follow the expected behavior from Fig. 2. Each phase in Fig. 6 goes through two inflections. Both phases remain elastic until approximately -100 MPa, where the Al phase begins to yield. That is, for each additional increment in applied stress, the Al phase accommodates less elastic strain. The Be phase bears a higher proportion of the load, which results in slightly more elastic strain. Therefore the Al curve deflects downwards, and the Be curves deflect in the opposite manner. Because Be has a much higher elastic modulus than Al (300 GPa for Be and 70 GPa for Al), the inflections in the stress-strain curves for Be are not as obvious as those for Al. At a stress level close to -250 MPa, a second inflection occurs in both curves, where the

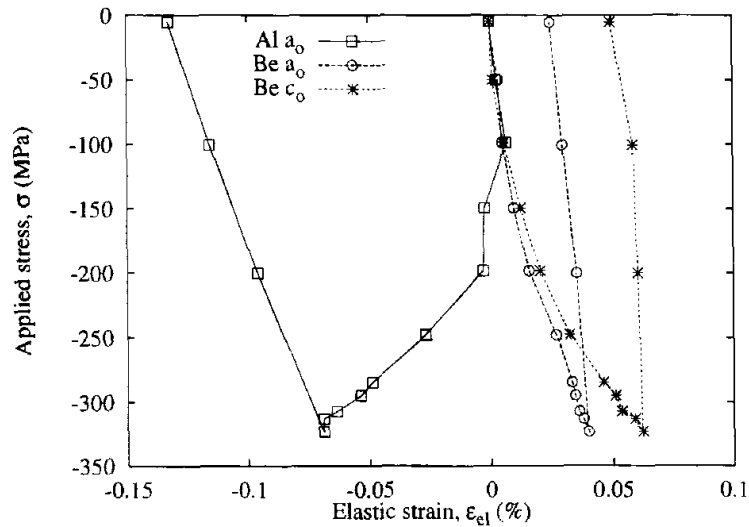


Fig. 7: Strains perpendicular to the loading direction

Be curves deflect downwards, and the Al curve deflects in the opposite direction. It can be inferred that Be is beginning to yield, which transfers some of the load back to the Al phase.

Both phases unload along a line which has approximately the same slope as their initial loading curves. The residual strains upon unloading in both phases are tensile: 3.2×10^{-4} for Be a_o , 1.9×10^{-4} for Be c_o and 2.7×10^{-4} for Al a_o .

Perpendicular to the loading direction (Fig. 7), upon initial loading, both phases are in tension, as expected. At approximately -100 MPa, however, the stress-strain curve for the Al phase begins to deflect in the opposite direction, and by -150 MPa, the Al phase exhibits a compressive strain. Aluminum continues to load in compression up to the maximum applied stress of -323 MPa, where its compressive strain is -6.9×10^{-4} . As before, both phases unload along a line which has approximately the same slope as their initial loading curves. Since Al is already in compression when unloading begins, it goes further into compression upon unloading, reaching a final compressive strain of -1.3×10^{-3} . The residual strain in Be upon unloading is tensile: 2.5×10^{-4} for Be a_o and 5.0×10^{-4} for Be c_o .

CONCLUSIONS

The co-deformation behavior of BeAl was measured using neutron diffraction. Parallel to the loading direction, BeAl behaves as expected for a two phase composite, in which one phase is substantially stronger than the other. The Al phase begins to yield in the range of -100 MPa, evidenced by the change in slope of its $\sigma_{app} - \epsilon_{el}$ curve. The Be phase begins to deform plastically at an applied stress in the range of -200 to -250 MPa, most likely due to its fine grain size and the morphological constraints of the composite. The solid solution of Ag in Al probably has a minimal strengthening effect, but the strength of the Al is enhanced by its fine grain size. Therefore the Al can bear a higher proportion of the applied load and maintain this load even once the Be begins to yield. Upon unloading, the residual strain in both phases is negligible ($\leq 3.2 \times 10^{-4}$).

Perpendicular to the loading direction, the Al is in compression at applied compressive

stresses above -150 MPa. This may be due to the morphological constraint inherent in the composite. The value of ν for Al is a factor of 10 greater than that for Be, and the elastic modulus of Be is more than four times that of Al. The Al is highly constrained by the Be, which essentially does not expand perpendicular to the loading direction. Upon unloading, the Al retains a compressive residual strain, and the Be retains a much smaller tensile residual strain.

REFERENCES

- [1] David C. Van Aken and Hamish L. Fraser. The microstructures of rapidly solidified hyper-eutectic Al-Be alloys. *Acta Metallurgica et Materialia*, 33(6):963–974, June 1985.
- [2] B. A. Mueller, L. E. Tanner, and J. H. Perepezko. Microstructure development in undercooled Al-Be powders. *Materials Science and Engineering A*, A150:123–132, 1992.
- [3] J. L. Murray and D. J. Kahan. The Al-Be system. *Bulletin of Alloy Phase Diagrams*, 4(1):50–55, 1983.
- [4] Michael T. Hutchings and Aaron D. Krawitz, editors. *Measurement of residual and applied stress using neutron diffraction*, volume 216. Kluwer Academic Publishers, Boston, 1992.
- [5] Ismail C. Noyan and Jerome B. Cohen. *Residual Stress: Measurement by Diffraction and Interpretation*. Springer-Verlag, New York, 1987.
- [6] A. J. Allen, M. T. Hutchings, C. G. Windsor, and C. Andreanni. Neutron diffraction methods for the study of residual stress fields. *Advances in Physics*, 34(4):445–473, 1985.
- [7] R. B. Von Dreele, J. D. Jorgensen, and C. G. Windsor. Rietveld refinement with spallation neutron powder diffraction data. *Journal of Applied Crystallography*, 15:581–589, 1982.
- [8] Allen C. Larson and Robert B. Von Dreele. General structure analysis system (GSAS). Technical Report LA-UR 86-748, Los Alamos National Laboratory, 1986.
- [9] D. S. Kupperman, S. Majumdar, and J. P. Singh. Neutron diffraction NDE for advanced composites. *Transactions of the ASME*, 112(2):198–201, April 1990.
- [10] G. L. Povirk, M. G. Stout, M. Bourke, J. A. Goldstone, A. C. Lawson, M. Lovato, S. R. MacEwen, S. R. Nutt, and A. Needleman. Mechanically induced residual stresses in Al/SiC composites. *Scripta Metallurgica et Materialia*, 25(8):1883–1888, 1991.
- [11] G. L. Povirk, M. G. Stout, M. Bourke, J. A. Goldstone, A. C. Lawson, M. Lovato, S. R. MacEwen, S. R. Nutt, and A. Needleman. Thermally and mechanically induced residual strains in Al-SiC composites. *Acta Metallurgica et Materialia*, 40(9):2391–2412, September 1992.

- [12] M. A. M. Bourke, J. A. Goldstone, N. Shi, J. E. Allison, M. G. Stout, and A. C. Lawson. Measurement and prediction of strain in individual phases of a 2219Al/TiC/15p-T6 composite during loading. *Scripta Metallurgica et Materialia*, 29(6):771-776, September 1993.
- [13] D. C. Dunand, D. Mari, M. A. M. Bourke, and J. A. Roberts. NiTi and NiTi-TiC composites. IV. neutron diffraction study of twinning and shape-memory recovery. *Metallurgical Transactions A*, 27A(9):2820-2836, September 1996.
- [14] M. A. M. Bourke, J. A. Goldstone, M. G. Stout, A. C. Lawson, and J. E. Allison. Strain measurement in individual phases of an Al/TiC composite during mechanical loading. In E. V. Barrera and I. Dutta, editors, *Residual Stresses in Composites: Measurement, Modeling & Effects on Thermo-Mechanical Behavior, 21-25 February 1993*, pages 67-77, Denver, Colorado, 1993. The Minerals, Metals & Materials Society, Warrendale, Pennsylvania.
- [15] David H. Carter, Andrew C. McGeorge, Loren A. Jacobson, and Paul W. Stanek. Age hardening in beryllium-aluminum-silver alloys. *Acta Materialia*, 44(11):4311-4315, 1996.
- [16] David H. Carter, Paul W. Stanek, and Loren A. Jacobson. Beryllium/aluminum composites. In David Hui, editor, *Proceedings of the First International Conference on Composites Engineering, ICCE/1, 28-31 August, 1994*, pages 83-84. International Community for Composites Engineering (ICCE), 1994.
- [17] David H. Carter, Loren A. Jacobson, and Paul W. Stanek. Mechanical behavior of beryllium-aluminum composites. In Anoush Poursartip and Ken Street, editors, *Proceedings of the Tenth International Conference on Composite Materials, 14-18 August, 1995*, volume II: Metal Matrix Composites, pages 401-408, Whistler, British Columbia, Canada, 1995. Woodhead Publishing Limited, Cambridge, England.

GENERATION OF ELECTRET STATE IN COMPOSITE POLYMERIC MATERIALS BY FRICTION

A. I. Sviridenok¹, A. F. Klimovich² and V. N. Kestelman³

¹*Research Center of Resource Saving, Sovetskaya Str. 10, Grodno, 230023, Belarus*

²*Institute of Mechanic of Metal-Polymeric System of Academy of Science of Republic Belarus,
Gomel, 246028, Kirova 32A, Belarus*

³*KVN International, Inc., 632 Jamie Circle, King of Prussia, Pa 19406, USA*

SUMMARY: During operation of metalopolymeric frictional systems, a triboelectret state is generated in dielectric polymer materials due to intensive electrophysical processes. As it follows from the analysis of the energy balance at friction, a part of mechanical energy is used to generate a triboelectret state in polymers during the run-in stage, and maintains the same at steady operation. The following topics are discussed: generation of electret state, effect of electret state on friction and wear, electret-triboloelectrification superposition in the course of polymer friction. Electret state resulted from the fabrication pre-history of the materials, processing technology, etc. Mechanical activation of powder is accompanied by increasing its structural imperfection, density of surface states, and, as a result, by higher parameters of electret state. The experimentation conducted allowed to establish that presence of a filler in electret state in a composite affects polymer electrification in the course of frictional interaction with metal. Depending on the vector's direction of field intensity created by electret filler's particles, the field generated by triboelectrification can be either weakened or strengthened, i.e. the principle of electret-triboelectrification superposition is realized. The parameters of frictional interaction can be controlled.

KEYWORDS: friction, wear, electret, electrostatic interaction, electrization, triboelectrification, superposition, bearings.

INTRODUCTION

Intense electrophysical processes in dielectric materials employed in metal-polymer friction pairs generate their triboelectret state. It is strongly governed by the electrostatic interactions between contacting surfaces and the magnitude of the adhesion component of the force of friction.

GENERATION OF TRIBOELECTRETS AND THEIR EFFECT ON FRICTION AND WEAR

The analysis of the energy balance in friction indicates that a portion of the mechanical energy goes to generate the triboelectret state in a polymer during the run-in and to maintain it in the stationary conditions of friction. Indications of the appearance of the charge $1-10 \mu\text{C}/\text{m}^2$ in specimens subjected to friction; persistence of the charge up to 160 days and the presence of a

spectrum of thermally stimulated currents (TSC) have allowed to identify the electret state of polymers during friction in fluids, such as dielectrics and electrolytes [1,3]. It has been noted that friction in fluids with various electric conductivity increases the general effect of adsorption processes upon the magnitude of the generated charge more than the electric resistance of the medium. The appearing electret state (ES), in its turn, affects the chemophysical processes in friction of polymers. In particular, the adsorption processes evolve primarily on the surface electrically active centers of solids, therefore, the appearing electret state makes polymers more reactive in tribochemical processes [2].

Appearance of the ES in traditional polymer electrets may be attributed to the accumulation of charges due to the injection and polarization caused by orientation of dipoles. It has required to study the electret effect in nonpolar (HDPE) and polar (PVC) polymers. In order to monitor the effect of temperature upon the ES kinetics the friction test would be discontinued after a certain fixed temperature is reached in the friction zone.

The analysis of TSC-graphs of HDPE coatings (Fig. 1) proves that two trapping levels exist with a corresponding low temperature peak within the range $T = 348\text{--}358\text{ K}$ and a high temperature peak within the range $T = 388\text{--}403\text{ K}$. The depth of traps (the activation energy) has been estimated for the first level using the 'initial rise' technique [3] which turned out to be within the range $1.07\text{--}1.8\text{ eV}$ ($10.33\text{--}173.7\text{ kJ/mol}$) in response to the temperature T in the friction zone. Trapping centers in polyethylene are known to appear when the activation energy is within the estimated range causing structural modifications.

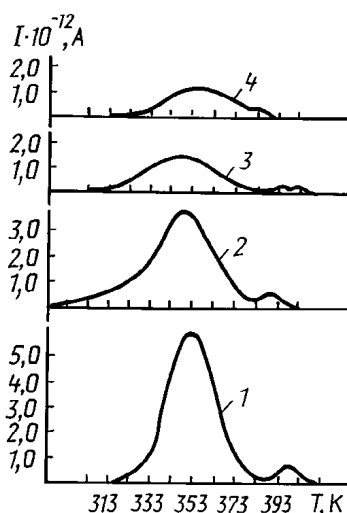


Fig. 1: TSC diagrams of HDPE coatings after friction against steel counterbody ($p = 0.2\text{ MPa}$, $v = 1.0\text{ m/s}$) at temperature in friction zone: 1, 323 K; 2, 333; 3, 353; 4, 373 K.

Thus, considering that polyethylene is nonpolar, the TSC magnitudes are positive and the position of the peaks on the temperature scale correspond to the relaxation transitions and estimated activation energy levels, so it can be asserted that generation of ES in PE is due to the injection processes. The observed TSC spectra in polyethylene are caused by the charge liberation when separate links, segments and larger kinetic units are displaced [4].

Unlike the nonpolar partially crystalline PE, a negative polarity peak within the glass transition temperature range T_g in the TSC spectrum of the amorphous polar PVC (Fig. 2)

proves that in this case the ES is generated by the injection of charge carriers from the metallic counterbody assisted by dipole polarization. The negative peak ($T=343\text{--}348\text{ K}$) within the glass transition range (T_g of PVC is 345 K) is due to the molecular mobility, the amorphous phase and the dipole segment α -process. The positive peak observed above T_g , i.e. at $358\text{--}363\text{ K}$, is caused by the relaxation of space charges injected during friction due to the ohmic conductivity. Each relaxation process has its typical duration which depends upon the temperature according to the known Eqn. 1 of Boltzmann-Arenius:

$$\tau_i = B_i \exp(V_i / kT) \quad (1)$$

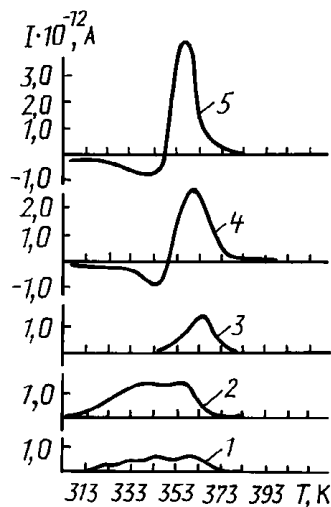


Fig. 2: TSC diagrams of PVC coatings after friction ($p = 0.2\text{ MPa}$, $v = 1.0\text{ m/s}$) at temperature in friction zone: 1, 303 ; 2, 313; 3, 323; 4, 333; 5, 343 K..

The relationship between the effective volume of the kinetic unit W_k and factor B is expressed by the Eqn. 2:

$$W_k = [B^6 (6kT/\rho)^3]^{1/5} \quad (2)$$

Based on the TSC-diagrams the parameters of relaxation (according to Fig. 2) for the negative peak have been determined using Eqns. (1) and (2). Table 1 shows the results. Their analysis indicates that the estimated parameters correspond to the λ -process of relaxation. The relaxation time according to [5] is $\tau_i = 10^2 \text{--} 10^4\text{ s}$ at $T = 300\text{ K}$, the activation time is $V_i = 30\text{--}50\text{ kJ/mol}$, the kinetic unit volume is $W_k = 10^{-23} \text{--} 10^{-24}\text{ M}^3$. Also, according to the negative peak position corresponding to the glass transition temperature on the scale (Fig. 2, curve 4), absence of the negative peak in the experiments, once they were suspended before this temperature is reached, (Fig. 2, curves 1–3), proves that the α -process of relaxation takes place in this case. Apparently, the observed abnormality is caused by the specific friction effects when both macro- and microvolumes of contacting bodies get involved with their sizes after friction transfer reaching $10^{-19} \text{--} 10^{-20}\text{ m}^3$. It is accompanied by the orientation and

elongation of molecular chains in the direction of friction. Hence, the negative peak on the TSC-graphs of PVC specimens is due to the α -process of relaxation in friction with greater parameters usually because of dispersion and orientation by friction.

Table 1: Parameters of relaxation in PVC coatings subjected to friction.

Temperature in contact zone T_c , K	Activation energy U_i , kJ/mol	Relaxation time τ at $T=300$ k, s	Dimensional factor V , s	Kinetic unit volume W_k , m^3
333	69.9	13217	$7.2 \cdot 10^{-9}$	$4.1 \cdot 10^{-23}$
343	59.8	9013	$2.8 \cdot 10^{-7}$	$4.3 \cdot 10^{-22}$
353	63.7	8715	$7 \cdot 10^{-8}$	$6.4 \cdot 10^{-23}$
* Activation energy is determined by the 'initial rise technique'.				

Thus, the electret state in PVC coatings in a direct couple of friction on the steel counterbody appears in the following way: when members come into contact and go apart the charge carries are injected into the polymer and localize over the trapping centers or surface states. As the temperature of the contacting bodies increases the molecules are liberated and dipole groups get oriented in the direction of friction and in the injected charge field. The friction process is known to be accompanied by the orientation of segments of the molecules of the polar groups in the main and transferred material in the direction of the force of friction which may cause polarization. It is caused by the mechanical (the effect of the normal and tangential forces) and electrostatic (the inner field effect produced by electrization) factors. The degree of this effect upon polarization depends upon the structures and physical behavior of contacting materials [3]. The TSC-graphs (Fig. 2) allow to conclude that the parameters of the negative (dipole) peak governed by the numbers of oriented dipole groups, are determined primarily by the space charge magnitude injected into polymer by friction. It means that the orientation of dipole groups in PVC is produced by the internal field created by injected charge carriers (the electrostatic factor) and the orientation produced by friction.

It has been earlier demonstrated that current inversion, as a general regularity of polymers triboelectrification, proves the intricacy of these processes and their adequate relationships with the chemophysical processes in polymer surface layers. The TSC-graphs for PVC coatings during various stages of the electrification (Fig. 3) indicate that the moments of time before and after inversion coincide with the earlier established temperature effects in the friction zone upon the ES generation in friction (Fig. 2, curves 1,2 and 4,5), because the temperature in the contact zone (Fig. 3, curve 1) $T_h=306$ K corresponds to that in experiments 1 and 2 (Fig. 2, curves 1,2); $T_h=346$ K (Fig. 3, curve 3) correspond to the temperature in experiment 5 (Fig. 2, curve 5).

Table 2: ESCD (σ , $\mu\text{C}/\text{m}^2$) of HDPE coatings triboelectrified at various friction velocities in couple with dielectric counterbody (relative humidity 65–75%).

v, m/s	Counterbody material					
	PCA		HDPE		PTFE	
	n_{1-}/n_{1+}	σ_{1-}/σ_{1+}	n_{2-}/n_{2+}	σ_{2-}/σ_{2+}	n_{3-}/n_{3+}	σ_{3-}/σ_{3+}
0.3	100/0	57/-	36/64	6/11	71.29	20/5
0.5	100/0	47/-	22/78	10/17	67/33	28/11
0.8	100/0	60/-	71/29	11/5	50/50	28/13
1.1	100/0	46/-	86/14	14/2	80/20	31/19
1.4	100/0	58/-	100/0	8/-	0/100	-/9

Note. All PCA specimens were positively charged.

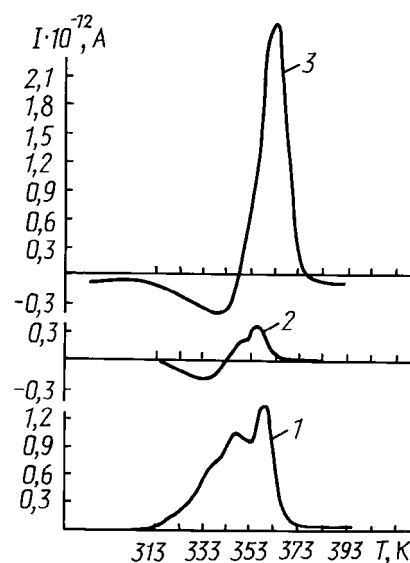


Fig. 3: TSC diagrams of PVC coatings for different stages of triboelectrification process: 1, prior to electrification current inversion; 2, moment of inversion; 3, after inversion.

A typical feature of the TSC spectrum at the moment of inversion is a significant reduction (5–10 times) of the intensity of the positive peak at 353–363 K. The notion ‘the moment of inversion’ is conventional, only the moment of approaching to such inversion can be implied in experiments. Proceeding from the temperature in the contact zone, then $T_k=328$ K (Fig. 3, curve 2) is an intermediate temperature for experiments 3 and 4 (Fig. 2), when T_k magnitudes are equal to 323 and 333 K, respectively, the pattern of TSC-graph 2 (Fig. 3) can be considered intermediate between graphs 3 and 4 (Fig. 2). Yet, a significant reduction of the positive peak intensity at 353–363 K proves that both the surface layers (e.g., desorption) and the bulk of the polymer experience strong transformations [10]. Hence, the tribological behavior closely relates to the appearance and relaxation of ES in a polymer.

The positive peak at 343 K (Fig. 2, 3, curves 1,2) should be noted separately. The analysis indicates that it occurs in the case when the friction zone is much less heated than the glass transition temperature. Apparently this peak is due to depolarization under the effect of the

field of injected charges when the thermally stimulated discharge appears, it has nothing to do with structural modifications of the polymer during electrification and electretization.

Triboelectretization in the contact between two dielectrics (polymer-polymer) deserves interest. High density polyethylene (HDPE) was tested in the form of coatings 350–400 μm made of the polyethylene powder melt by pressing it at 5 MPa during 0.3 ks at 473 K to aluminum foil substrates. The dielectric counterbody was made from polycapromamide (PCA), HDPE and polytetrafluorethylene (PTFE). The original roughness of rollers 0.7–0.45 μm was prepared with abrasive paper. The tests were configured as a shaft on a partial insert at a nominal pressure 0.1 MPa, the friction torque, the temperature of the specimen and current parameters were registered synchronously. The wear rate of coatings and rollers were evaluated by weighing after continuous operation during 1.8 ks. The air relative humidity varied within 65–75%. The effective surface charge density (ESCD) characterizing the degree of triboelectrification was measured using the compensation technique with the help of a vibrating electrode. The thermally stimulated depolarization current (TSC) of the coatings was registered using aluminum electrodes at a linear heating rate 2.5 deg/min. The results were averaged relative to the air humidity variations.

The results have allowed to establish (Table 2) that the magnitude and the polarity of the residual, hence the generated tribocharge on the coatings strongly depend upon the dielectric behavior of the counterbody material and the friction mode. The HDPE coatings in contact with the polar PCA at the friction velocities used become negatively charged. The same coatings in contact with the nonpolar PTFE and HDPE acquire an unstable residual tribocharge: the specimens may become both positively and negatively charged under the same friction conditions. Table 2 demonstrates that the growing friction velocities change the ratio between the negatively and positively charged specimens and between the mean ESCD magnitudes. The dominating charge polarity changes from positive to negative when the counterbody is HDPE and vice versa when it is PTFE. The ESCD inverts at friction velocities 0.5–0.8 and 1.1–1.4 m/s, respectively. The mean ESCD magnitudes change most extremely in contact with PCA, HDPE and PTFE as the friction velocities grow (passing through the maximum) satisfying the relationships $\sigma_{1-} > \sigma_{3-} > \sigma_{2-}$; $\sigma_{2+} \approx \sigma_{3+}$.

The above friction couples differ by the friction coefficients, the temperature of specimens and the wear rates (Table 3). The above parameters are typically the minimum for HDPE – PCA systems and the maximum for HDPE – PTFE systems. Tables 2 and 3 show that higher wear rates and higher friction velocities accelerate the charge inversion.

Table 3: Tribological characteristics of the HDPE – dielectric friction pairs ($p = 0.1$ MPa, $v = 0.8$ m/s, $t = 1.8$ ks).

Counterbody material	T, K	Friction coefficient	Wear rate I_g , kg/(m ² m)	
			HDPE coating	polymer roller-counterbody
PCA	305	0.15	$1.72 \cdot 10^{-7}$	$1.65 \cdot 10^{-7}$
HDPE	333	0.21	$6.92 \cdot 10^{-7}$	$4.20 \cdot 10^{-6}$
PTFE	346	0.24	$5.50 \cdot 10^{-6}$	$3.72 \cdot 10^{-5}$

Since these polymers have different work functions, different surface (water adsorption) and frictional behavior, it can be assumed that the charge inversion is due to the change of the dominating charging mechanism when the friction velocity is altered.

It has been demonstrated above that the polymer electrets are a classic example of disordered systems. Also, the effects play a substantial role in the polymer electrets. friction of polymers can be assumed as an integral process accompanied by a wide variety of electrophysical phenomena. Apparently, they interact with a possible feedback, self-control and self-restoration [11,12].

Possibilities of the appearance of an autoregulating system in the process of evolution and relaxation of the electret states of polymers in friction is a worthwhile study. Therefore, the cascading (intermittent) friction mode was used for experimentation with the electrophysical parameters. The experiment was configured as follows: HDPE films 300–320 μm produced by hot pressing were subjected to the cyclic friction at $p = 0.1$ MPa and $v = 1$ m/s during variable time periods t in the cascading mode with the interval τ between cycles. Common techniques were applied to check the parameters of the electret states of coatings after friction by measuring the effective surface charge density (ESCD) and thermally stimulated currents (TSC). Initially the effect of friction duration upon triboelectrification were studied. The specimens were subjected to friction during one cycle lasting 60, 300, 600 and $1.2 \cdot 10^9$ s. The TSC spectra of the coatings manifested two typical peaks: the low temperature one in the range of 303 K and the high temperature one in the range 383–403 K, the high temperature peak tending to bifurcate as the friction extends.

A different pattern is observed when the number of cycles is varied together with the intervals between them. The increasing number of cycles reduces the high temperature peak, i.e. the electret charge as the variations of the ESCD evidence it under different friction conditions. As the interval is increased the ESCD grows noticeably. It can be explained by the fact that continuous and concurrent electrification processes produce the electret charge with consecutive appearance of the space charge domain (SCD), because the existing electron states in the SCD field are ionized, the emission phenomena occur and the charges are relaxed. Such relaxation primarily occurs in the interval between the cycles: the charges in the fast surface states are the first to reduce followed by those in the slow states. The charge relaxation becomes faster as the interval grows. Subsequent friction cycles cause the filling of the vacant high-energy traps and the ESCD goes up.

So, it can be concluded that such unsteady systems are capable to undergo self-organization when collective, cooperating.

CONCLUSION

Application of the basic postulates of the electrical theory of adhesion to the explanation of the regularities of electrification of polymers in friction and conclusions of the electron theory of disordered systems and surface states have allowed to verify the mechanism of electrification. The presence of surface states and their attraction of electrons injected from the metallic counterbody when the contact is broken produce an electrical charge on the surface of the polymer specimen. The triboelectrical field of the surface charge produces charge redistribution in the surface region producing the spatial charge region. A double electrical layer appears along the polymer – metal boundary. The charge density and the structure of the layer are governed by the characteristics of the surface states.

The mechanism of electretization of polymers in friction seems to be the following: during electrification a space charge and a spatial charge region appear causing polarization of a polymer material in the field and (with the account of injected charges) an electret state is generated. The parameters of the state are conditioned by the free injected charge carriers and polarization. The triboelectret state significantly affects the frictional characteristics of polymers.

REFERENCES

1. Guzenkov S.I. Soviet Journal of Friction and Wear, vol. 11, no 1, pp. 151-154, 1990.
2. Belyi V.A., A.F. Klimovich, V.S. Mironov. Proc. of the BSSR Academy of Science, vol. 26, no 1, pp. 39-42, 1982.
3. Lushchejkin G.A.. Polymer Electrets (in Russian), Moscow, 1976.
4. Bartenev G.M.. Strength and Mechanism of Failure of Polymers (in Russian), Moscow, 1984.
5. Bartenev G.M., and Yu.V. Zemnev. Course of Physics of Polymers(in Russian), Leningrad, 1972.
6. Sviridenok A.I.. Tribology Int., vol. 24, no 1, pp. 37-44, February 1991.
7. Polymers in Friction Units of Machines and Instruments/ Ed. by A.V. Chichinadze (in Russian), Moscow, 1988.
8. Margis D.. J.Mater.Sci., vol. 20, pp. 3041-73, 1985.
9. Briscoe B.J., K.Fridrich (ed.).Friction and Wear of Polymer Composites. Elsevier, Amsterdam, Ch.2,p.25, 1986.
10. Klimovich A.F., and V.S. Mironov. Soviet Journal of Friction and Wear, vol. 2, no 4, pp. 113-117, 1981.
11. Kostetskii B.N., M.G. Nosovskii, and L.I. Bershadskii. Surface Strength of Materials in Friction (in Russian), Kiev, 1976.
12. Gershman I.S., and N.A. Bushe. Journal of Friction and Wear, vol. 16, no 1, pp. 41-48, 1995.
13. Harper W.R.. Contact and Frictional Electrification, Oxford, 371 pp., 1967.
14. Belyi V.A., A.I. Sviridenok, M.I. Petrokovets, and V.G. Savkin. Friction and Wear in Polymer-Based Material. Pergamon Press, N.Y., 1982.
15. Deryagin B.V., N.A. Krotova, and Yu.A. Khrustalev. Adhesion of Solids. Moscow, 1973.

16. Balachandran W.. Tribology in Particulate Technology. Ed. by B.J. Briscoe and M.J. Adams. Adam Hilgen, pp. 135-154, 1987.
17. Vallbrandt I., U. Brjukner, and E. Linke. Proc. of Symposium on Mechanochemistry and Mechanoemission of Solids (in Russian), Tallinn, pp. 46-47, 1981.
18. Guzenkov S.I., Yu.V. Gromyko, and A.F. Klimovich. Soviet Journal of Friction and Wear, vol. 8, no 1, pp. 107–110, 1987.
19. Electrets (English translation), Moscow, 1983.
20. Gromyko Yu.V., and A.F. Klimovich. Proc. of BSSR Acad. of Sci., vol. XXXIII, no 6, pp. 531-534, 1989.
21. Mironov V.S., and A.F. Klimovich. Proc. of BSSR Acad. of Sci., vol. 30, no 8, pp. 724-727, 1986.
22. Vannikov A.V., V.K. Matveev, V.P. Sichkarev, and A.P. Tyutnev. Radiation Effects in Polymers. Electrical Properties, (in Russian), Moscow, 1982.
23. Silin A.A.. Friction and Its Role in The Progress of Technology (in Russian), 176 pp., Moscow, 1983.
24. Klimovich A.F., and V.S. Mironov. Soviet Journal of Friction and Wear, vol. 2, no 4, pp. 113-117, 1981.
25. Pleskachevskii Yu.M., V.V. Smirnov, and V.M. Makarenko. Introduction into Radiation Science of Polymer Composites (in Russian), 191 pp., Minsk, 1991.

THE FLOW BEHAVIOUR OF COMPOSITES CONTAINING CUT, ALIGNED FIBRES

D. T. Steel and W. J. Clegg

Department of Materials, Cambridge University, Pembroke Street, Cambridge CB2 3QZ, UK

SUMMARY: The possibility of improving the formability of aligned fibre composites by cutting the fibres into controlled lengths using a laser has been investigated. It is shown that the ease with which the composite may be deformed in tension is substantially improved. It is found that the composite deforms primarily by the growth of the slots introduced by the laser cutting process and that the way in which this growth occurs is dependent upon the details of the slot pattern.

KEYWORDS: formability, processing, aligned fibres

INTRODUCTION

Long fibre thermoplastic composites can be formed using relatively low cost techniques such as diaphragm forming [1], rubber forming [2], and stamp forming [3]. However, in more complex shapes, such as those requiring a reverse or double curvature, fibre wrinkling, component buckling [1,3,4] and thickness variations [1,5] often occur during the forming process, particularly at high forming rates.

The occurrence of these features is principally associated with the inextensible nature of the fibres [6-8] restricting tensile flow in the direction of the fibres [9]. Under compression the fibres can buckle and become misaligned [3,9]. In a component such as a U-channel the strains on one face of the laminate are different to those on the opposing face so that shear is required between the individual plies, normally taking place within resin rich areas between the individual lamina. However, with a reverse or double curvature, such as a hemisphere, additional shearing between the individual fibres must also take place within a single ply [10]. While this allows the laminate to conform to the specimen geometry these processes often result in undesirable thickness variations in the component [1,5].

The superior properties of long fibre composites require not only long fibres but also that the fibres are aligned along the tensile axis. Misalignments of only a few degrees can cause a substantial reduction in the properties. It is more difficult to try to align discontinuous fibres, for instance by extrusion, than it is to cut aligned continuous fibres in the form of pre-preg, so allowing tensile deformation in the direction of the fibres. A number of methods for doing this have been tried [8,10]. In this study the flow behaviour and formability of a thermoplastic polymer containing uniaxially aligned carbon fibres cut into shorter lengths using a laser has been investigated.

EXPERIMENTAL PROCEDURES

Fibre Cutting

The material used was a poly (ether ether ketone) containing a volume fraction of 0.61 of continuous and uniaxially aligned carbon fibres (ICI plc, APC-2). The fibres were cut into controlled lengths by moving a sheet of the prepreg material below a laser, giving a pattern of elongated holes. The geometry of these could be varied by changing the rate at which the material was moved, the length of time for which the laser was on and the interval between successive firings of the laser [11].

The main features of the geometry of the hole array are shown in Fig. 1(a). The material is cut into strips each with a length l , in this case either 20 or 50 mm and with a width, D , approximately equal to the length of the slot formed by the laser, typically $160\ \mu\text{m}$. The adjacent strip is similarly cut except that the slot is displaced by a distance P_y in the direction of the fibres. After a number of strips have been cut, the position of the slot is level with the original slot, the distance between the two being P_x . The very small offset between the holes on the diagonal line gives the appearance of lines of slots a distance P_x apart in the transverse direction, and P_y apart in the direction parallel to the fibres, as shown in Fig. 1(b).

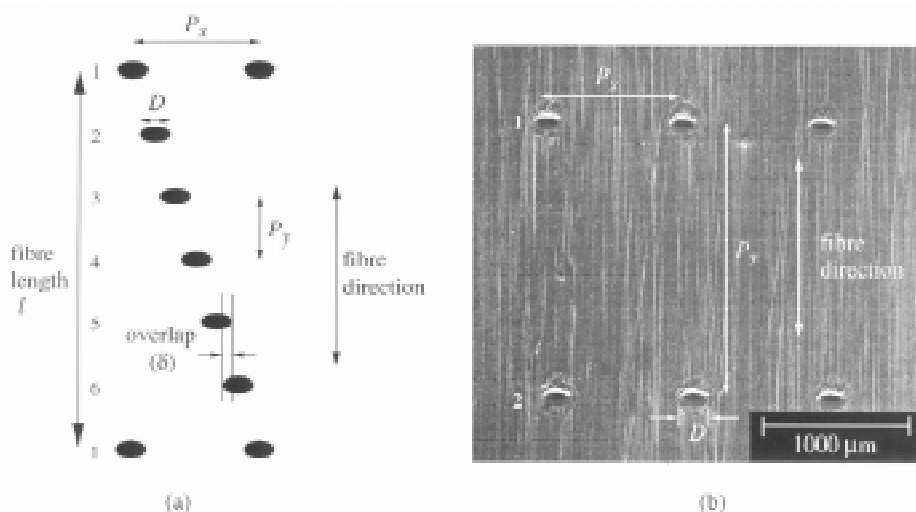


Fig. 1: Showing (a) a schematic arrangement of the laser cut slots. Note that the material is made up essentially of relatively long strips of fibres, each strip of width, D . (b) shows the appearance of an actual array. Note that it appears to be a rectangular array of slots.

The pattern must also ensure that all the fibres are cut. To minimise the possibility of any continuous fibres remaining due to any fibre misalignment, there is an overlap between the holes, δ . The slots do not have a uniform size through the thickness of the prepreg as the laser energy is absorbed by the material, so the mean diameter of the hole on the surface of the prepreg on which the laser is incident is typically twice that on the lower surface [12].

Specimen Production

Strips of the pre-prep 420 mm long and 75 mm wide were perforated in the gauge section of each sample. Samples with mean fibre lengths of 20 and 50 mm were made, with perforated gauge lengths of 40 and 100 mm respectively.

The perforated strips of pre-preg were butt-jointed together using a soldering iron to give plies with typical dimensions of 450 x 420 mm. 8-ply laminates were consolidated in an autoclave heated to 380°C at a pressure of 1.05 MPa for 20 minutes. The plies in the laminate were stacked with the pre-preg surfaces on which the laser was first incident, uppermost, taking care to ensure that the holes in neighbouring plies did not overlap.

Mechanical Testing

Tensile drawing was carried out on a 10 kN servo-hydraulic machine at strain-rates between 4.2×10^{-4} and $4.2 \times 10^{-2} \text{ s}^{-1}$. Tests were carried out on both continuous and laser cut material. Tensile drawing tests were carried out at temperatures of 380°C and 340°C using a radiant bulb furnace with six quartz iodine infra-red lamps fitted within a water cooled stainless steel case giving a uniform heated length on the sample of approximately 110 mm.

To study the overall tensile flow behaviour of the composite and its variation with fibre length some samples were strained to failure. Some samples were deformed to smaller strains to investigate any microstructural changes occurring during straining.

RESULTS AND DISCUSSION

Flow Behaviour

Typical stress/strain curves for samples containing 20 mm long fibres and 50 mm fibres drawn at 380°C at strain-rates between 4.16×10^{-4} and $4.16 \times 10^{-2} \text{ s}^{-1}$ are shown in Fig. 2(a) and (b) respectively. It can be seen that the stress rises approximately linearly with increasing strain until some peak stress is reached, after which the stress falls. This is consistent with tensile drawing experiments carried out elsewhere on materials containing aligned fibres cut into shorter lengths, but by different methods to that used here [8,13]. Reducing the strain-rate decreased the magnitude of this peak stress. Similar behaviour was observed at 340°C. However, the peak stresses were higher than those at 380°C at equivalent strain rates.

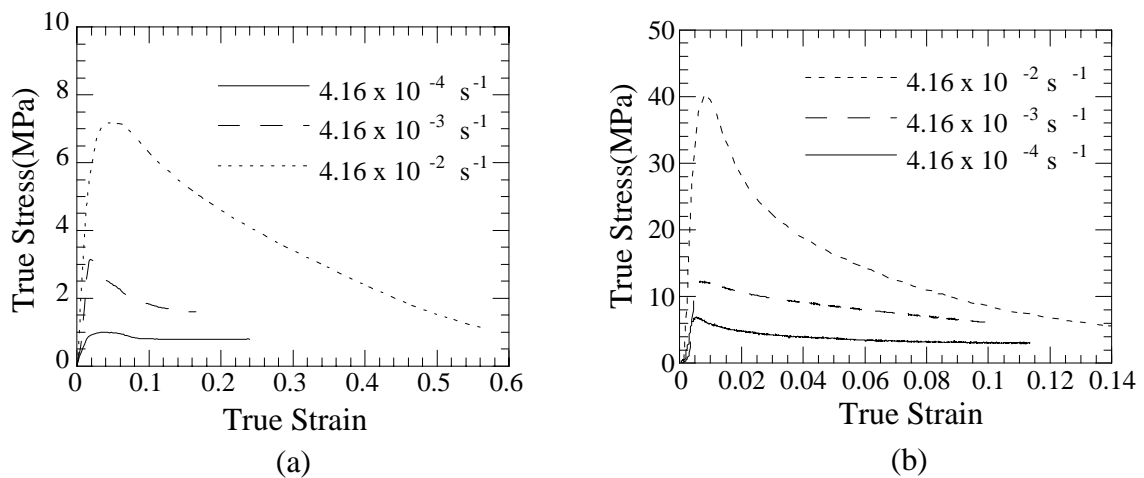


Fig. 2: Showing the variation in flow stress with strain-rate for the composite containing fibres with a mean length of (a) 20 mm, and (b) 50 mm, drawn at 380 °C.

The tensile drawing behaviour of the continuous fibre material is shown in Fig. 3. The stress rises rapidly to a peak at approximately 800 MPa, at which point the fibres break. At high strain-rates the stress immediately drops to zero but at lower rates the broken fibres are held in the matrix and the composite can be drawn to a limited extent. However, the peak stress in the unperforated composite is more than twenty times higher than that observed in the perforated material.

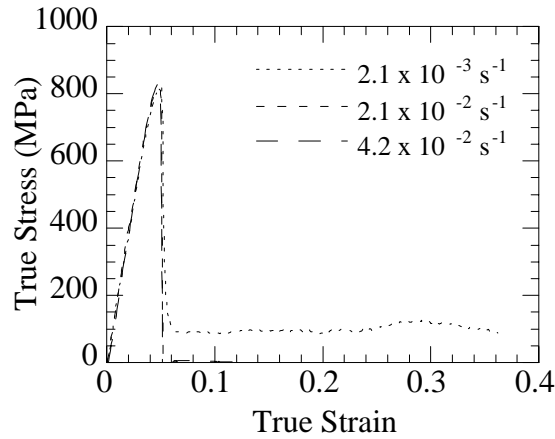


Fig. 3: Showing the variation in flow stress for the composite containing continuous fibres drawn at 380 °C.

The flow behaviour of a Newtonian viscous fluid containing a given volume fraction of discontinuous fibres, V_f has been considered by Byron-Pipes *et al* [7]. Using a shear-lag approach, they showed that the applied stress, σ_y , at the point where the stress in the matrix is equal to the shear yield stress, τ_y , would be given by

$$\sigma_y = \frac{l}{d} \tau_y V_f \quad (1)$$

where l and d are the mean length and the diameter of the fibres respectively and V_f is the volume fraction of the fibres.

To compare these ideas with the observations here, the shear yield stress of the unreinforced resin at 380°C was measured by capillary rheometry. The values obtained at the equivalent tensile strain-rates to those used in the experiments are given in Table 1, together with the corresponding peak stresses for the materials containing 20 and 50 mm fibres. Setting V_f to 0.61, d to 7 μm and l to either 20 or 50 mm, as appropriate, allows the values for the tensile yield stress to be calculated from Equation (1) for the different materials. From Fig. 4, it can be seen that the predictions give good agreement with the experimental observations, suggesting that at the peak stress the material is essentially behaving as a uniform array of discontinuous fibres, in which the interfacial shear stresses are just approaching the flow stress of the polymer, allowing uniform flow to occur.

Table 1: Showing the stress required to give flow of poly (ether ether ketone) at different strain-rates.

Tensile strain-rate (s ⁻¹)	Polymer flow stress (Pa)
4.16 10 ⁻²	3652
4.16 10 ⁻³	1386
4.16 10 ⁻⁴	526

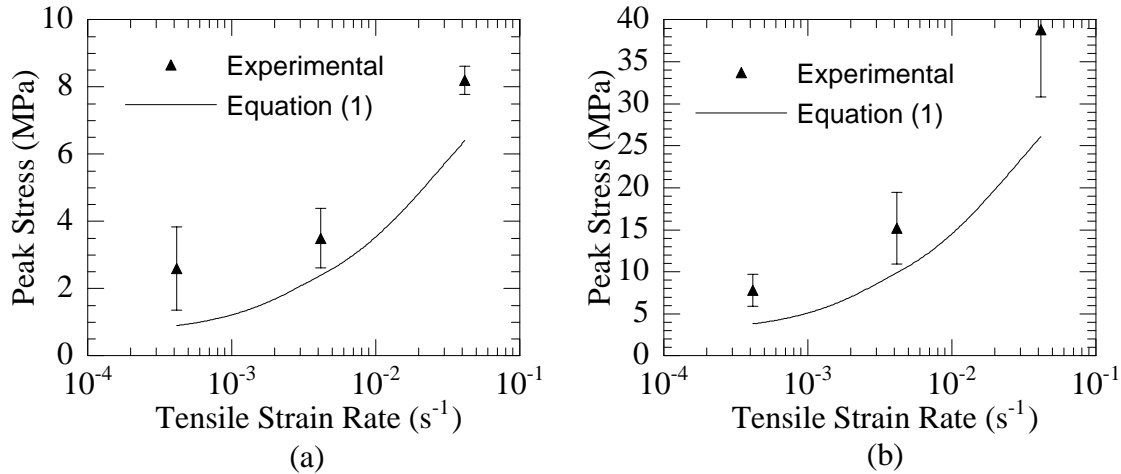


Fig. 4: Showing the predictions of Equation 1 compared with the experimental results for composites containing fibres with a mean length of (a) 20 mm and (b) 50 mm.

The decrease in the flow stress in Fig. 2, has been observed elsewhere and was attributed to local thinning occurring in the sample followed by eventual tearing and failure [8]. Examination of the samples after testing showed that there was rarely any observable macroscopic necking, although after strains of typically 0.04 the fibres did tend to come loose from the sample. The flow stress however had already substantially decreased in all cases.

However, as can be seen in Figs 5(a) and (b), it was clear that large voids had opened up in the sample. It was unambiguously established that these holes had grown from those introduced by the laser cutting process because the fibres at the surfaces of the holes had swollen ends, which are a characteristic of the laser perforation process [12, 14].

Fig. 5(a) shows a sample deformed to a strain below that at which the peak stress was reached and it can be seen that the perforations have all strained uniformly. However at a strain just above that where the peak stress is reached, Fig. 5(b), it can be seen that the holes begin to grow at different rates. Both micrographs have been taken from the surfaces of the specimens and have not in this case been filled with resin. Clearly the presence of a normal pressure might be expected to force resin into the holes. However given that the holes were filled with resin before tensile drawing, it is unlikely that it should prevent this growth. This has been confirmed [8] by similar observations in materials that have been diaphragm formed. Clearly these holes are likely to have deleterious effects on the mechanical properties of formed material.

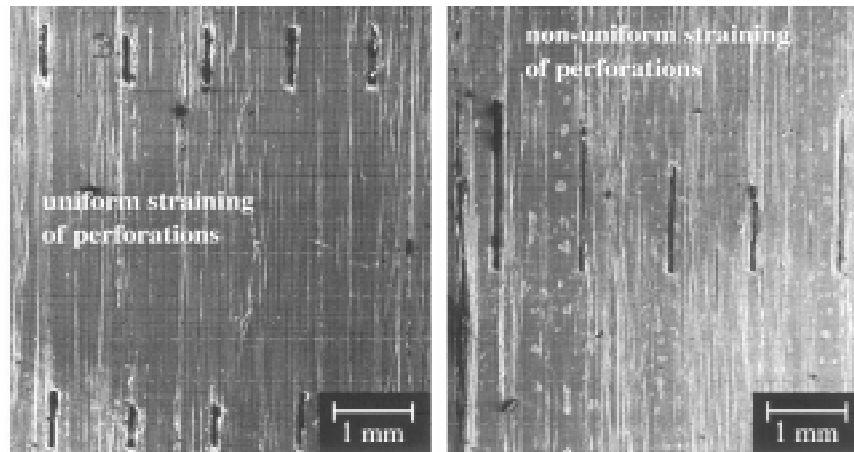


Fig. 5: Showing the holes growing in a sample containing fibres with a mean length of 50mm, deformed at 340 °C to a strain (a) just below that at which the peak stress is reached and (b) just above that at which the peak stress is reached.

One way in which such voids can grow is by the shear of adjacent strips of fibres each of width D , as shown in Fig. 1(a), past one another, so that all the deformation is concentrated in a very narrow region between the strips. If this were the case, it would be expected that the overall displacement of the sample would be equal to the extension of the laser cut slots in a strip of the sample with a width of the slot. Each sample containing 50 mm fibres had twenty-three rows of perforations along the gauge length, each a distance P_y apart (for 20 mm material there were twenty-one rows of perforations). Bearing in mind that the mean fibre length is half the gauge length, each strip of fibres in the 50 mm material covers twelve rows of holes, each row a distance P_y apart, before another hole cuts that strip. This means that if the sample displacement is due entirely to the growth of the holes, it should be equal to the displacement measured from two sets of holes, each twelve rows apart (Fig. 6).

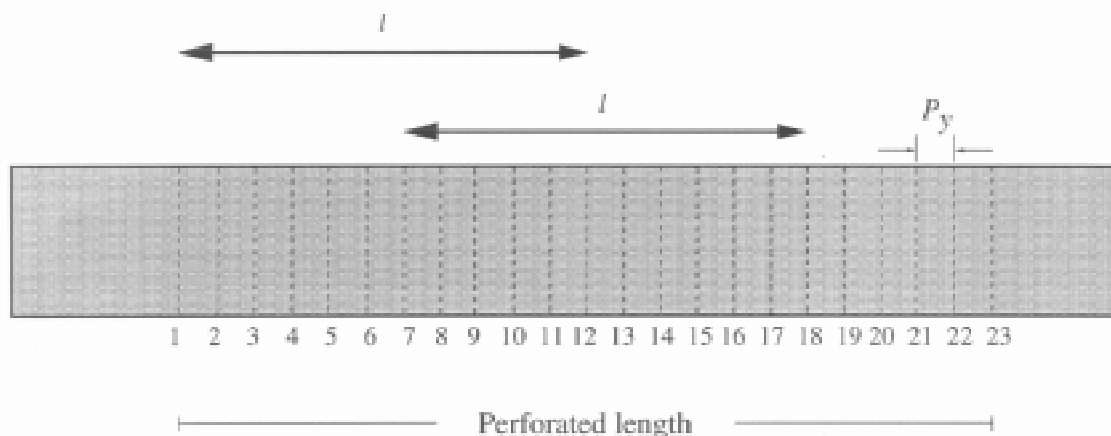


Fig. 6: Schematic of a sample showing the rows of laser cut slots for a mean fibre length of 50 mm.

For both sets of specimens the average hole size per line was measured and added to the corresponding average hole size twelve rows along. It was assumed that the groups of fibres between the respective row of perforations were all moving as one unit. Table 2(a) and (b)

show the net opening of the holes for each of the rows as numbered in Fig. 6 for specimens strained to just below and just above the peak stress respectively and the row numbers that correspond to the end of a given strip of fibres.

Table 2(a): Sum of hole openings for samples strained to just below the peak stress.

Row No.	1,12,23	2,13	3,14	4,15	5,16	6,17	7,18	8,19	9,20	10,21	11,22	Mean
Hole opening (mm)	0.44	0.52	0.56	0.52	0.50	0.46	0.49	0.47	0.57	0.52	0.48	0.50

Table 2(b): Sum of hole openings for samples strained to just above the peak stress.

Row No.	1,12,23	2,13	3,14	4,15	5,16	6,17	7,18	8,19	9,20	10,21	11,22	Mean
Hole opening (mm)	2.27	2.45	2.64	2.75	2.91	2.74	2.47	2.73	2.63	2.42	2.45	2.59

The total displacement for the sample strained to just below the peak stress was 0.95 mm, approximately double that measured from the elongation of the holes, if this were caused by shear between the adjacent strips of cut fibres. For the sample strained to above the peak stress, the total displacement was 3.4 mm, whereas that measured from the elongation of the holes was 2.6 mm. Clearly once the peak stress has been reached, the majority of the displacement is caused by shear in very narrow regions between the adjacent strips of fibres. The decreasing flow stress might then be interpreted in terms of some shear thinning effect. This is entirely consistent with the idea that flow occurs once the shear stress of the matrix has reached its flow stress. Indeed one might expect that flow could occur nowhere else apart from within these thin zones between the strips.

However the observation that substantial hole growth can occur before the peak stress shows that not only is there another way in which the specimen can irreversibly deform, but also that there is another mechanism by which the holes can grow. So far we have assumed that the body is made up simply of cut strips of fibres stuck together. However this neglects the overlap region which was introduced to minimise the possibility of any intact fibres remaining.

The existence of the overlap region introduces a zone between laser cut slots in adjacent strips of material, marked in Fig. 7(a) as ABCD. These zones exist right across the width of the material, so that deformation of the material within these zones gives rise to a macroscopic deformation of the sample, as shown in Fig. 7(b). Such a deformation would be expected to give rise to holes which have grown at an angle to the tensile axis, as shown in Fig. 7(b) and this was observed, as shown in Fig. 8.

The experimental observations suggest that this mode of deformation predominates at lower applied stresses, before the peak stress is reached. The initial length of these fibres is given by P_y in Fig. 1(a). In both cases, this is about 0.1 that of the mean fibre length. Using equation 1, the yield stress of the regions due to the overlap is less than that elsewhere in the

material by a factor of 10, so that flow of these regions would be predicted to occur before that of the surrounding material, consistent with the observations.

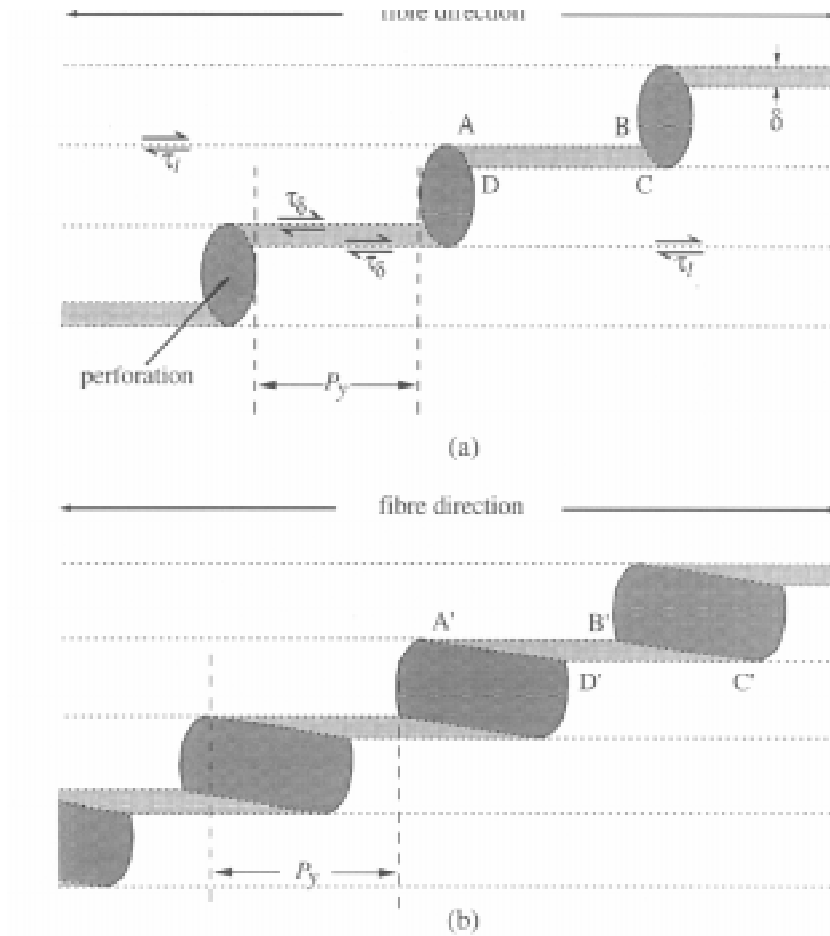


Fig. 7: Showing an array of holes containing an overlap to minimise the possibility of any fibres remaining uncut. This introduces regions such as that marked ABCD in (a) which can deform to A'B'C'D' without any deformation of the immediately surrounding material, as shown in (b). Compare this with Fig. 8.

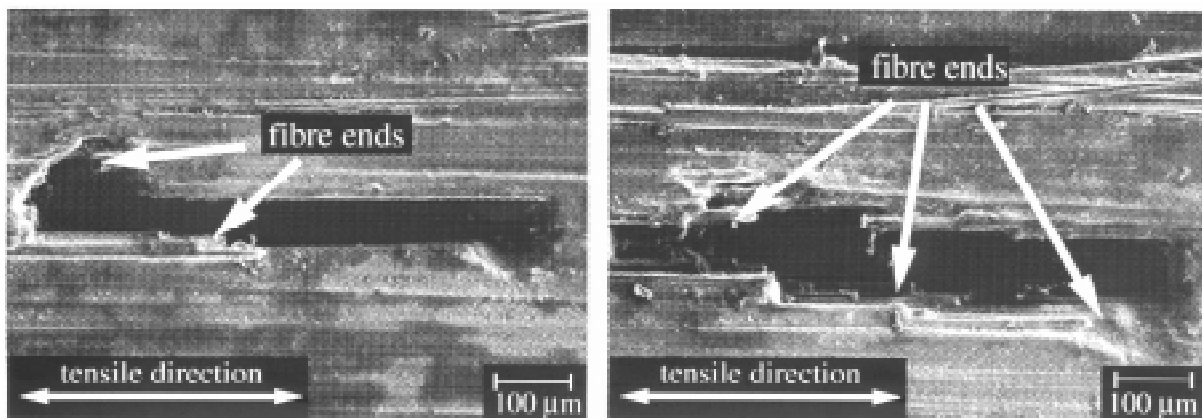


Fig. 8: Showing elongated holes which appear to have deformed in a manner similar to that in Fig. 7(b).

Both mechanisms give rise to hole elongation. The difference between the two is that where the overlap region is unimportant, the total displacement due to hole elongation is obtained by summing the contribution from every twelfth row of holes (in this case). Where hole overlap is important, the displacement will need to be summed from every row of holes, see Fig. 6. Of course the relative contribution from the two mechanisms cannot be simply separated and more detailed measurements are now underway to investigate this further.

CONCLUSIONS

Tensile drawing experiments on a thermoplastic polymer containing 61% of carbon fibres by volume has demonstrated that the laser cutting approach allows the material to be drawn in tension much more easily than material containing continuous fibres. The magnitudes of the stresses required to draw the cut fibre material are close to those predicted for a fluid containing a given volume fraction of discontinuous fibres. It has been shown that deformation of the sample can occur in two ways. At lower stresses this occurs by the deformation of zones between the laser drilled slots. After the peak stress, this occurs predominantly by the movement of adjacent strips of material, whose thickness is equal to the length of a laser drilled slot. Both processes result in the formation of large elongated voids.

ACKNOWLEDGEMENTS

The work forms part of a project involving Integrated Materials Technology, T&N Technology, DRA Farnborough and the University of Cambridge. Thanks are due to T&N Technology for financial support for one of us (DTS).

REFERENCES

1. P.J. Mallon, C.M. O'Brádaigh and R.B. Pipes, *Polymeric Diaphragm Forming of Complex-Curvature Thermoplastic Composite Parts*, Composites, Vol. 20(No. 1) (1989), pp. 48-56.
2. L.M.J. Robroek, *Development of The Rubber Forming Technique to Realize Fabric Reinforced Thermoplastic Products*, in 38th International SAMPE Symposium (1993), pp. 2032-2044.
3. W. Soll and T.G. Gutowski, *Forming Thermoplastic Composite Parts*, SAMPE Journal, (May/June) (1988), pp. 15-19.
4. M.A. Keane, and P.J. Mallon, *A Study into the Forming of Advanced Thermoplastic Composite Laminates in Diaphragm Forming*, in Flow Processes In Composite Materials, 3rd International Conference. (1994), University College, Galway, Ireland, (eds.), pp. 496-408.
5. R.K. Okine, *Analysis of Forming Parts From Advanced Thermoplastic Composite Sheet Materials*, SAMPE Journal, Vol. 25(No. 3) (1989), pp. 9-19.
6. I.Y. Chang and J.F. Pratte, *LDF Thermoplastic Composites Technology*, Journal of Thermoplastic Materials, Vol. 4(July) (1991), pp. 227-252.

7. R.B. Pipes, W.S. Hearle, A.J. Beaussart and A.M. Sastry, *A Constitutive Relation for the Viscous Flow of an Orientated Fiber Assembly*, Journal of Composite Materials, Vol. 25(September) (1991), pp. 1204-1217.
8. R.K. Okine, D.H. Edison and N.K. Little, *Properties and Formability of A Novel Advanced Thermoplastic Composite Sheet Product*, in 32nd International SAMPE Symposium (1987), pp. 1413-1421.
9. M. Hou, and K. Friedrich, *Stamp Forming of Continuous Carbon Fibre/Polypropylene Composites*, Composites Manufacturing, Vol. 2(No. 1) (1991), pp. 3-9.
10. R.K. Okine, *A Formable Advanced Thermoplastic Composite Sheet Based on an Excess Filament Length Concept*, Journal of Thermoplastic Composite Materials, Vol. 5(April) (1992), pp. 152-165.
11. R.A. Ford, *Improved Composite Materials and Method For Making Them*, Patent No. WO96/01177 (1996).
12. T.J. Matthams, D.J. Bray and T.W. Clyne, *A Microperforation Process for Improving the Formability of Thermoplastic Composites and its Effect on Mechanical Properties*, in ECCM-7 (1996), London, Vol. 1, Woodhead Publishing Ltd, pp. 229-237.
13. J. Schuster and K. Friedrich, *The Fatigue Behaviour of Thermoformed Discontinuous Aligned Fiber Composites*, in ICCM-10 (1995), Whistler, British Columbia, Canada, Vol. 1, pp. 593-600.
14. D.T. Steel and W.J. Clegg, *The Flow Behaviour and Formability of Microperforated Composites Containing Aligned Fibres*, in ECCM-7 (1996), London, Vol. 1, Woodhead Publishing Ltd, pp. 239-245.

A STUDY ON THERMO-OXIDATIVE STABILITY OF NON-MDA PMR POLYIMIDE COMPOSITES

Xiang Bao Chen, Ying Fu and Ping Li

Beijing Institute of Aeronautical Materials, P. O. Box 81, Beijing 100095, China

SUMMARY: Two kinds of diamine monomers, BAPP and BABE, were used in PMR polyimides instead of MDA to develop NON-MDA polyimide systems. Thermo-oxidative stability and elevated-temperature mechanical properties of graphite fiber reinforced NON-MDA polyimide composites were evaluated to be compared with PMR-15 composite. The results showed that the NON-MDA polyimide composites have similar mechanical properties and thermo-oxidative stability to that of PMR-15 composite, thus BAPP and BABE have the potentiality of replacing MDA to be used in PMR polyimide composites.

KEYWORDS: PMR polyimide composite, thermo-oxidative stability, mechanical property

INTRODUCTION

The in-situ of polymerization of monomer reactants(PMR) polyimide resins which first developed at the NASA Lewis Research Center [1] have been used in aircraft engines for its high temperature mechanical properties and processability [2]. PMR-15 is of the best known PMR polyimide synthesized from three monomers, MDA, NE and BTDE. PMR-15 has a number of unique performances, including easy processing, good mechanical properties, excellent retention of mechanical properties at elevated temperatures (288 ~ 316°C) [3], however, its notable shortcomings are inadequate resin flow for complicated composite structures' fabrication and a suspected carcinogen from the use of MDA [4], so it is severely limited in the applications.

The purpose of this study was to determine the effects of replacing the MDA monomer in PMR-15 with other two aromatic diamine monomers BAPP and BABE on composite high-temperature mechanical properties and thermo-oxidative stability.

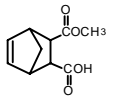
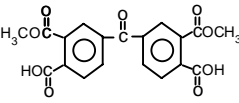
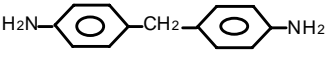
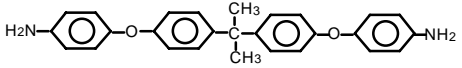
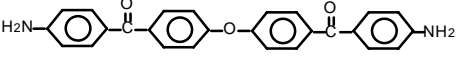
EXPERIMENTAL

The monomers used in this study are shown in table 1. The BTDE/NE was prepared by refluxing a suspension of BTDA/NA in anhydrous ethyl until the BTDA/NA dissolved and then continued heating at the reflux temperature for an additional two hours to result to a 50 wt% BTDE/NE ethyl solution. The PMR resin solutions were prepared at room temperature by adding the diamine monomers(MDA, BAPP, or BABE) to the BTDE/NE solution to maintain 50 wt% solids. All of the resin formulated molecular weights are about 1500.

AS4 graphite fiber prepreg tapes were made by solution impregnation, which calculated to give composites having approximately 60 vol% fiber. The tapes were cut into 26 cm by 18 cm

plies and stacked unidirectional 16 plies thick. The stack was placed into a matched metal die and cured on a hot molding press, figure 1 showed the cure cycle. 1.5 MPa pressures were used for NON-MDA systems: LP-15(BAPP) and LF-15(BABE), and 2.5 MPa pressures for PMR-15. The postcures were carried out in the air circulating oven at 330 for 16 hours.

Table 1- Monomers used for polyimide synthesis

Structure	Name	Abbreviation
	monomethyl ester of endo-5-norbornene-2,3-dicarboxylic acid	NE
	dimethyl ester of 3,3'-4,4'-benzophenonetetracarboxylic acid	BTDE
	4,4'-methylenedianiline	MDA
	2,2'-bis(4-aminophenoxyphenyl)-propane	BAPP
	4,4'-bis(aminobenzoyl)diphen-ether	BABE

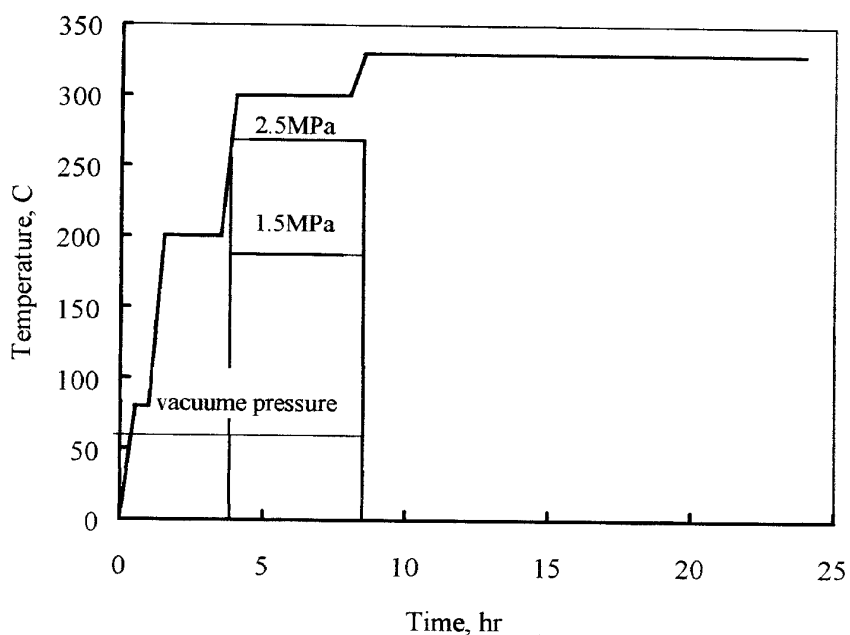


Fig.1: Cure cycle used for laminate processing.

Isothermal exposure of the specimens was performed in air circulating oven. Flexural and interlaminar shear tests were carried out before and after exposure to 260, 280 and 300. Flexural strength tests were performed in accordance with ASTM D-790, interlaminar shear strength tests were performed in accordance with ASTM D-2344. Elevated temperature tests were conducted in an environmental heating chamber following at the test temperature. Composite weight loss measurements were performed after exposure to 260, 280 and 300. Glass transition temperatures (T_g) were determined by dynamic mechanical analysis (DMA).

RESULTS AND DISCUSSION

The composite weight loss characteristics after exposure in air at 260, 280 and 300 are shown in Fig. 2. It is seen that all systems have a similar weight loss for exposure to air at 260 and 280 beyond 300 hours. After 1000 hours of exposure, LP-15 and LF-15 composites have higher weight loss (1.27wt% at 260 and 2.25wt% at 280) than that of PMR-15 (1.06wt% at 260 and 1.34wt% at 280), and there is still not apparent difference between LP-15, LF-15, and PMR-15 composites.

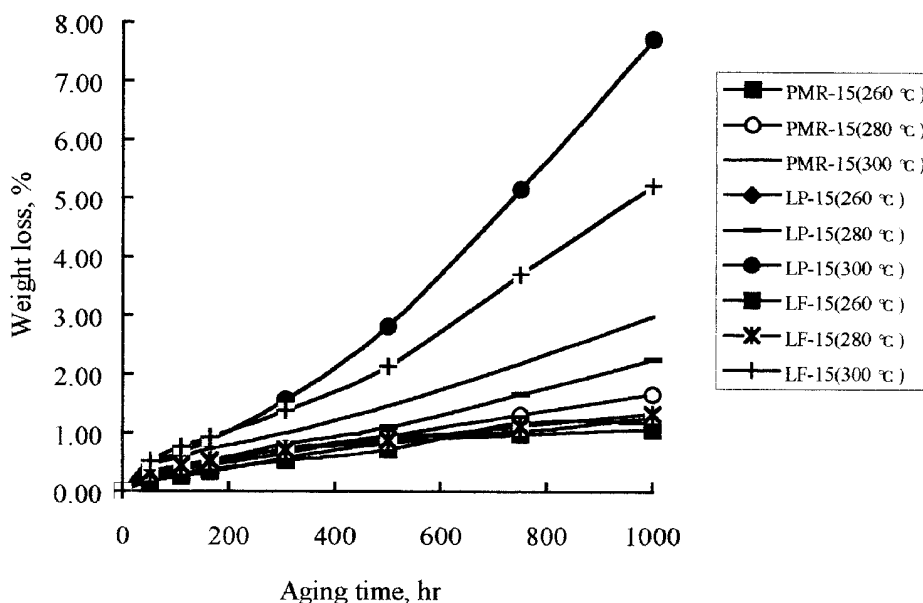


Fig.2: Weight loss of the composites with aging time at 260, 280 and 300.

Fig. 3 showed the mechanical property retention of the composites after 1000 hours aging tests at different temperatures. We can see that after exposure 1000 hours at 260 and 280, the interlaminar shear strength and flexural strength retention of all systems are higher than 90%; but after exposure 1000 hours at 300, the retention of interlaminar shear strength and flexural strength of LP-15 and LF-15 composites is much lower than that of PMR-15 composite. thus LP-15 and LF-15 composites have a similar thermo-oxidative stability to that of PMR-15 composite up to 280.

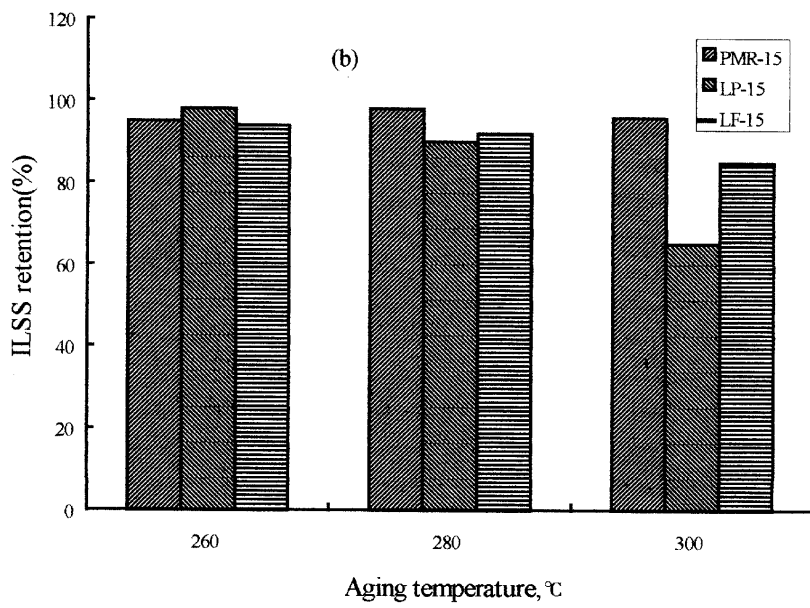
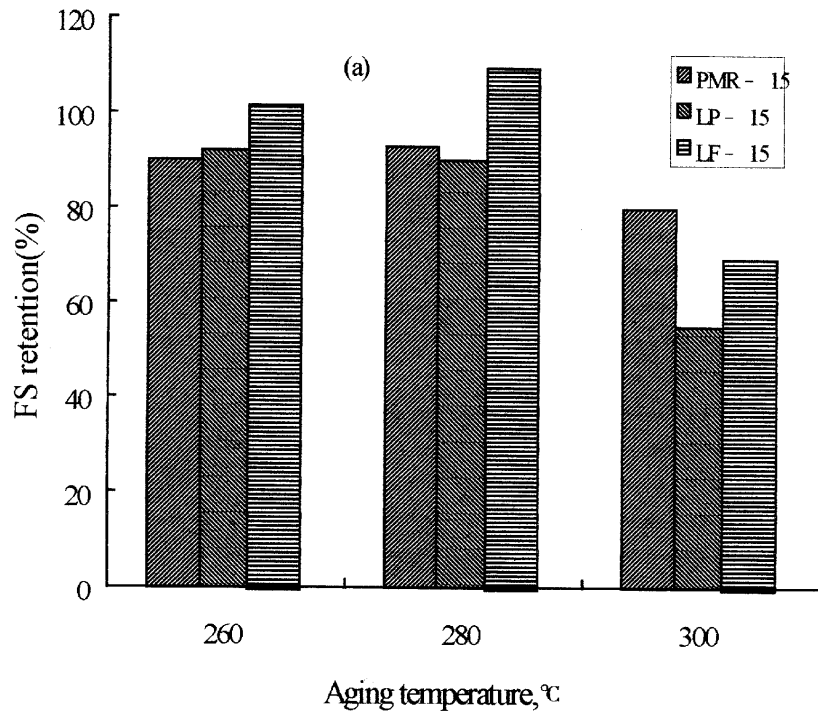


Fig.3: The FS(a) and ILSS(b) of composites after 1000 hr. aging at 260, 280 and 300°C.

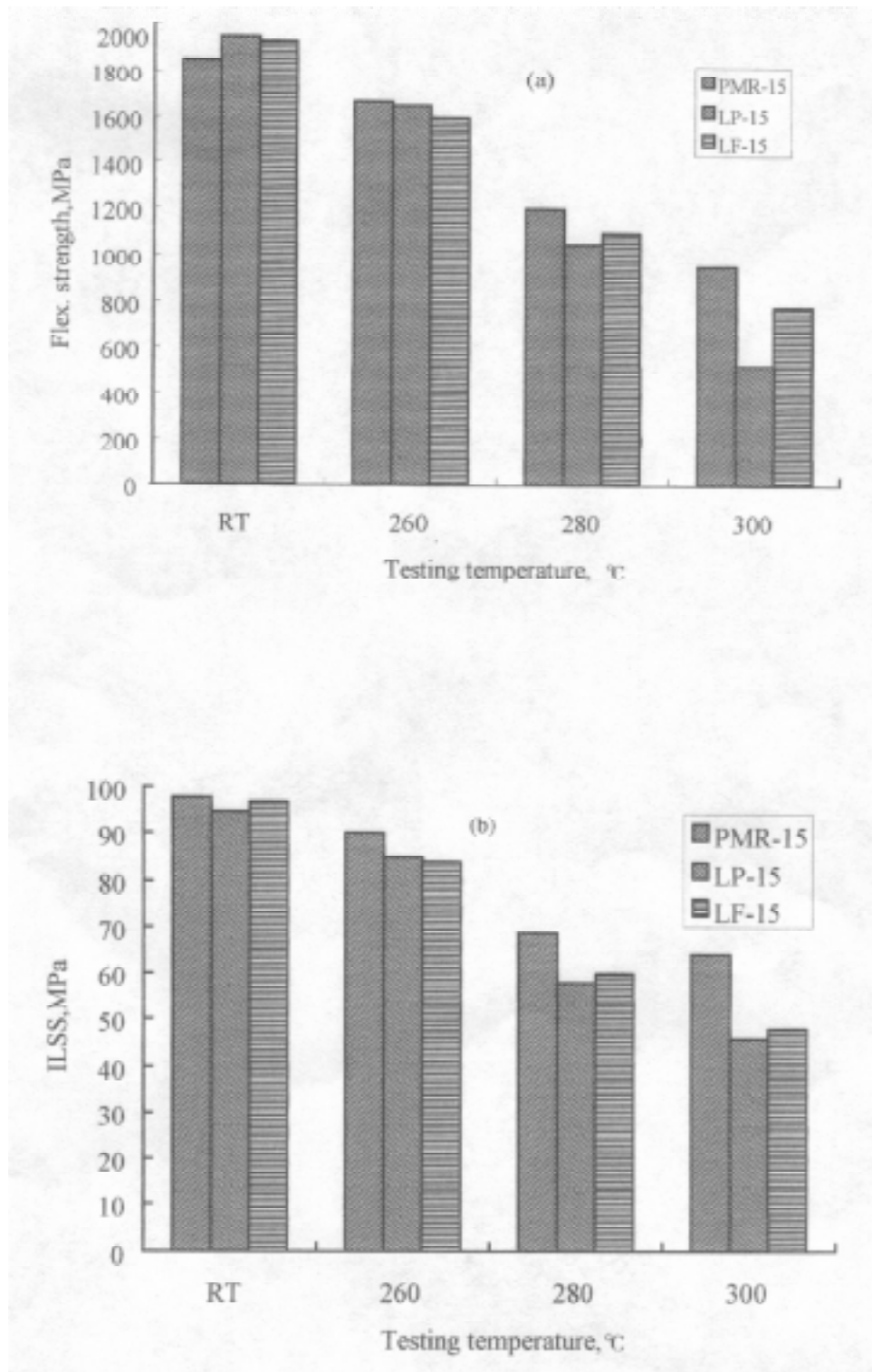


Fig.4: FS(a) and ILSS(b) of the composites at different temperatures.

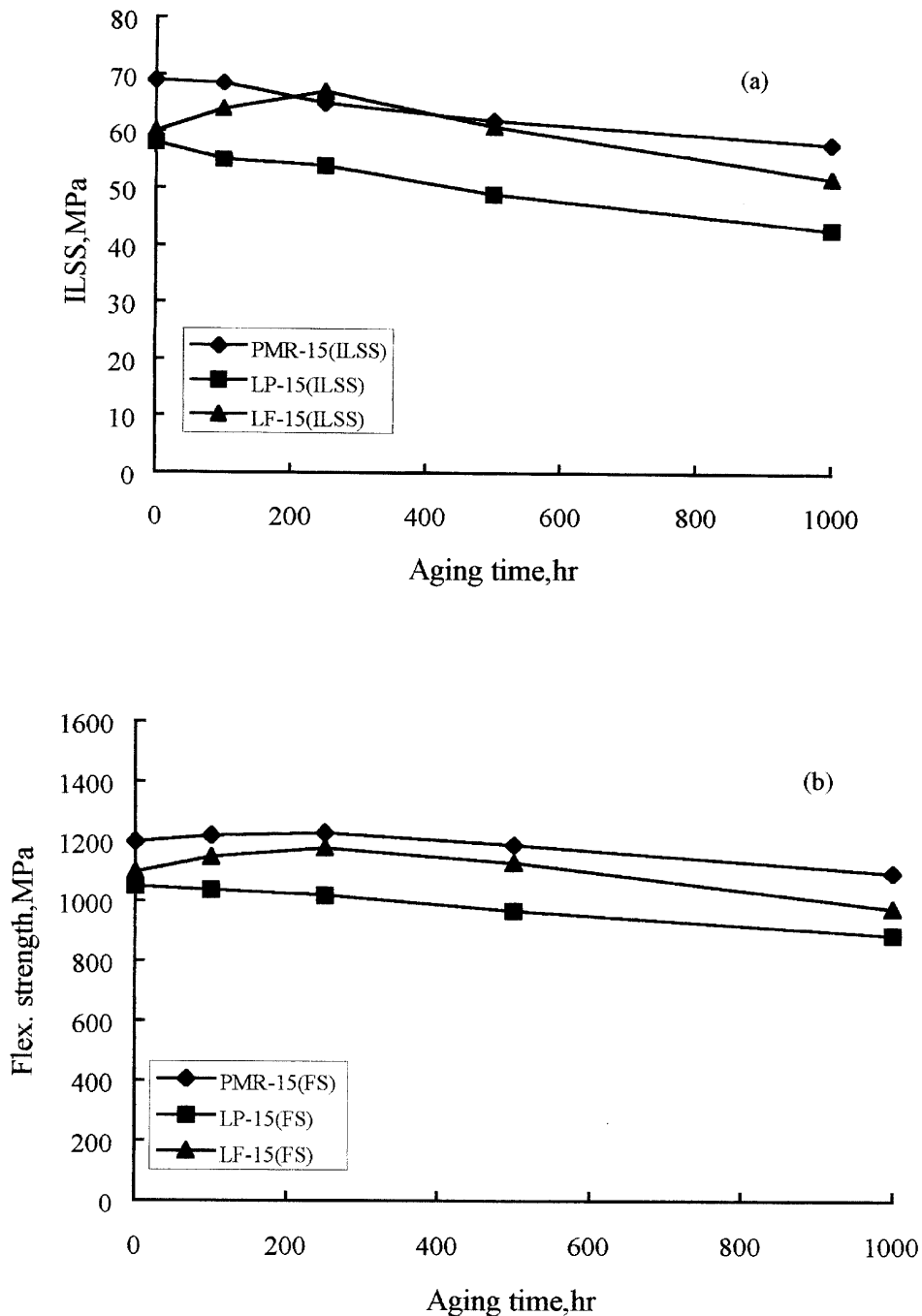


Fig.5: Variation of 280ILSS(a) and FS(b) of the composites with exposing time at 280.

Fig. 4 showed the mechanical properties of LP-15, LF-15, and PMR-15 composites at room temperature, 260, 280 and 300. The LP-15 and LF-15 composites exhibit the high room temperature flexural strength and 260 interlaminar shear strength and flexural strength retention values, and at 280 the interlaminar shear strength and flexural strength retention are still higher than 60% and 55% respectively. But at 300 the LP-15 and LF-15 composites have a lower property retention, this can be attributed to their lower Tg(LP-15: 318; LF-15: 332 and PMR-15: 343). Fig. 5 showed the variation of interlaminar shear strength and flexural

strength characteristics of the composites after exposure and tested in air at 280. The results exhibit that the flexural properties at 280 of LF-15 and LP-15 composites are similar to that of PMR-15 composites. After 1000 hours of exposure to air at 280, all systems have a very high flexural strength retention (>85%), the LP-15 composite exhibits lower interlaminar shear strength and flexural strength retention, but PMR-15 shows the best interlaminar shear strength and flexural strength retention characteristics.

CONCLUSIONS

LP-15 and LF-15 have similar mechanical properties, and thermo-oxidative stability to that of PMR-15 and offer excellent potential as PMR-15 replacements for use at temperatures up to 280. Thus BAPP and BABE have the potentiality of replacing MDA to be used in PMR polyimide composites.

REFERENCES

1. T.T. Seratini, P. Delvigs, and G.R. Lightsey, *J. Appl. Polym. Sci.*, 16, 905 , 1972.
2. R.H. Pater, *SAMPE Journal*, Vol.30, No.5, 29, 1994.
3. E. Delaney, F. Ried, T. Uong, J. Beale, K. Hirschbuehler and A. Leone-Bay, *SAMPE J.*, 28(1), 31, 1992.
4. Michael A. Meador, 40th International SAMPE Symposium, 268, 1995.

THE APPLICATION OF POSITRON ANNIHILATION METHODS FOR INVESTIGATION AND TESTING OF COMPOSITES

S.A. Tishin¹, V.A. Tishin², V.N. Kestelman³

¹*Institute of Electronics, Academy of Science, 10 Alleya Paradov, Tashkent, 700000, Uzbekistan*

²*Mitsar-A Inc., 59 Parkentskaya Street, Tashkent, 700070, Uzbekistan*

³*KVN International Inc., 632 Jamie Circle, King of Prussia, Pa 19406, USA*

SUMMARY: It is shown that the use positron annihilation methods allowed to investigate the properties of components and composites with different fillers and matrix. The methods was also used for analysis of microdefects in disordered polymers, for study of polymer modification and for diagnostics of polymer composites.

KEYWORDS: positron annihilation, microdefects, polymer modification, silica powder, diagnostics, microstructure, phase transition, diffusion

INTRODUCTION

The purposes of this article are: 1) to analyze the mechanism of formation and decay of a positronium atom in fine powder silicas and to use the positron annihilation for study of structure peculiarities, 2) to use positron annihilation for diagnostics of polymer composites.

RESULTS AND DISCUSSION

Investigation of Fine Power Silicas Composites

The surface modification of fine powder silicas by the organic compounds allows us to use them as selective adsorbents, catalysts or active fillers for polymer systems [1,2].

The complicated structure of the surface layer of silica modified by inoculated organic and inorganic groups is still very interesting topic [3-12].

Positron annihilation experiments

The observation of positron annihilation (PA) has been conducted by two principal methods: measuring the life time (LT) and spectra and the angular correlation of annihilation radiation (ACAR), to which has been added the measurement of probability of a three-photon annihilation (TFA). The application of a set of experimental measuring techniques is a principle particular to this work, as the interpretation of complicated polycomponent annihilation spectra in fine powder substances is difficult. The comparison of LT, ACAR and

TFA results permits us to define more precisely the annihilation mechanism and consequently to make well founded conclusions about the properties of the substances under study.

Mathematical treatment of spectra has been carried out by means of the computer programs POSITRON FIT, RESOLUTION and ACAR FIT [13].

Samples

Fine modified silicas [2] obtained by substitution of surface groups by organic compounds of a different nature as well as alumo- and titanoaerosil samples obtained by combined high-temperature hydrolysis of titanium (or aluminum) vapour and silicon chlorides have been investigated. Some experimental characteristics are in Table 1.

Table 1: Specific surface area (S), structure and concentration of inoculated groups (a) of fine powder silica samples.

Grades of Silica	Structure of Surface	$S \cdot 10^{-3}, m^2/kg$	a, nmol/g
Aerosil, A-175	$\equiv Si-OH$	175	0.30-0.35*
Aerosil, A-300	$\equiv Si-OH$	300	0.60*
Aerosil, modified by diethyleneglycol, ADEG	$\equiv Si-O-CH_2-CH_2-OH$	300	0.70-0.80
Aminoethoxyaerosil, AEA	$ \begin{array}{c} O-C_2H_5 \\ \\ \equiv Si-O-CH_2-CH_2-NH_2 \\ \\ O-C_2H_5 \end{array} $	300	0.70
Aminopropylaerosil, APA	$\equiv Si-O-Si-O-(CH_2)_3-NH_2$	300	0.50
Butosil, B-2	$\equiv Si-O-(CH_2)_3-CH_3$	300	0.70
Titanoaerosil, TAS-20	$\equiv Si-O-Ti \equiv$	108	0.20**
Alumoaerosil, A-A-8	$\equiv Si-O-Al \equiv$	256	0.08**

* Concentration of silanol groups

** Mass part of titanium and aluminium oxides

Experimental data

The quick positrons emitted from the source ^{22}Na are thermalized in the volume of silica microparticles. The thermal positrons can annihilate by means of quasi-elastic collisions with atoms and molecules (free positrons) and by means of formation of localized states in structure defects of atomic size.

An effective mechanism of slowing down positrons at energies of a few eV is the formation of a positronium atom - bound state of positron and electron. With spin orientation it is possible to form para-positronium p-Ps (self-annihilation time 0.125 ns 2γ -decay), and ortho-positronium o-Ps (self-annihilation time of 140 ns, 3γ -decay in vacuum). The ratio of probability of the formation of para- and ortho-Ps is 1:3 because of different statistical weights. However, as a result of Ps interaction with atoms and molecules of the media, Ps characteristics (LT and its kinetic energy) are changed.

Characteristics of positronium are traditionally of great interest for studying fine powder samples of silicas [3-12]. Changes of o-Ps LT and the formation of a narrow component of the ACAR curve can be detected easily.

The experimental results of LT, ACAR spectra and of TFA probability are in Tables 2-3. The computer-fitted results of a four-component analysis with a fixed value of the shortest-lived component ($\tau_1 = 0.120$ ns) and associated similarly [12] with annihilation of p-Ps are listed in the Tables. Annihilation characteristics for the silica samples changed with dispersion degree and with the state of the microparticle surface. The most considerable changes have been observed for aluminosilicates and titanosilicates. However, samples modified by organic combinations are also clearly different in comparison with the experimental error by its annihilation spectra.

Table 2: Characteristics of lifetime positron spectra: life time (τ_s , τ_I , τ_L) and intensities (I_s , I_I , I_L) of short-lived, intermediate and long-lived components.

Samples	τ_s ± 0.006 ns	τ_I ± 0.07 ns	τ_L ± 1.5 ns	I_s ± 0.70 %	I_I ± 0.70 %	I_L ± 0.18 %
A-175	0.409	1.73	70.9	78.11	10.12	11.77
A-300	0.417	2.14	69.0	79.54	6.38	14.08
ADEG	0.421	1.71	66.6	69.95	18.20	11.86
AEA	0.419	1.87	66.7	78.83	10.16	11.01
APA	0.424	1.93	69.1	76.70	11.35	11.95
B-2	0.417	1.95	67.3	74.15	9.95	15.90
TAS-20	0.366	1.37	71.1	95.89	2.02	2.09
A-A-B	0.429	1.88	69.0	89.35	4.89	5.67
Amorphous quartz	0.429	1.62	-	58.59	41.41	-

Among the three time components well distinguished for silica powder the origin of the longest-lived component is studied the most [3, 4, 6, 8]. That component is formed as a result of ortho-positron annihilation in the volume between silica grains [3-6, 9]. The decay in high vacuum occurs not only by means of 3γ -self-annihilation but also by means of 2γ -annihilation [11, 12]. Because of the interactions with the microparticle surface LT of o-Ps is shortened up to 130 ns [11]. If the pores between the particles are filled up with the gas, LT

of oPs decreased more as a result of interactions with gas molecules. In this work the measurements are carried out in air, for which it is known [9] that the most important mechanism of LT shortening is ortho-para conversion at an in-elastic collision of a positronium with a molecule of oxygen.

As a result of conversion, LT of o-Ps in the pores is decreased up to 70 ns and as it can be seen from Table 2 LT does not depend practically on specific surface area and surface state. The state and the particle surface are very important. The changes of intensities of positronium components of annihilation spectra are in Table 2. The samples with different surfaces are united in two groups. The first group is the silica on the base of A-300 with different organophylic surfaces. First, it should be noted that an increase in intensity of o-Ps annihilation in the pores between grains for butosil (B-2) takes place in this group. A corresponding increase of the intensity of the narrow component of the ACAR curve and of the TFA probability for this sample has been observed. The similar change in angle spectra have been found earlier [10] at the dehydration of the surface of fine powder silicas. So it can be proposed, that most values of I_L, I_N and $P_{3\gamma}$ in B-2 are due to hydrophobic properties of its surface.

Table 3: Total probability of positronium formation (P_o), intensity of narrow component of angular distribution (I_N^1) obtained by characteristics of positron lifetime and probability of three-photons annihilation ($P_{3\gamma}$), as well as intensities of intermediate component (I_I) normalized to the sum of ortho-positroniums components (I_I+I_L) and probability of three-photons annihilation.

Samples	$P_{3\gamma}+0.1$ %	$P_o+1.2$ %	$I_N^1+0.5$ %	$\frac{I_I}{I_I+I_L}$	$\frac{I_I}{P_{3\gamma}}$
A-175	7.3	30.7	19.4	0.46	1.37
A-300	8.5	30.3	21.7	0.31	0.75
ADEG	6.0	40.7	22.0	0.60	3.03
AEA	6.0	28.5	18.1	0.48	1.70
AAPA	6.8	31.5	19.7	0.49	1.67
B-2	10.1	36.9	25.1	0.39	0.88
TAS-20	1.5	5.7	2.5	0.47	1.33
A-A-8	3.3	16.5	9.2	0.47	1.92

An alternative possible reason of the effect observed is the change of probability of positronium formation with the chemical nature of inoculated groups. In this group the decrease of the positronium quantity with modification by polar amino-containing groups is observed. The polarity is higher, the probability of positronium formation on the surface is lower and less positronium atoms escaped in the pores between the particles. Such a

correlation of probability of positronium formation with polarity is observed, for example, in polymers [14].

A special position is occupied by the sample modified by diethylenglycol (ADEG) for which I_L and $P_3\gamma$ have the lower values, but maximum value of I_I . This effect is caused by the largest probability of formation and capture of positronium atoms on the surface among silicas studied. This sample is likely to be characterized by the formation of a more complicated and extended structure of the surface layer formed by groups inoculated and by water molecules absorbed. Additional hydration of the ADEG surface is connected with the presence of the mobile hydroxyl end group and occurs in decreasing the τ_1 value which approaches to that characteristic of annihilation in water and in increasing I_I because of a larger probability of positronium formation in water.

In accordance with [3, 9, 11], the decrease of I_L , $P_3\gamma$ values with the increase of grain size (the samples of A-175 and A-300) is observed. However, the anomalously great decrease of contribution of positronium components to spectra for alumo- and titanoaerosills can not be explained by the changes of particle discursiveness (Table 1).

In our opinion the effect observed can be connected with the decay of positronium atoms while passing the surface on acid centers or according to the model of formation of positronium on the surface with the high potential barrier for the electron escape. For the latter the inhibition of positronium formation is connected with the energy limitation of the possibility of forcing out electron from the surface, necessary for the formation of positronium.

There is no common opinion on the origin of the intermediate component of LT in the fine powder silica samples. Earlier there were ideas more theoretically and experimentally substantiated according to which the positronium formation occurs inside the particles and then as a result of diffusion a number of o-Ps atoms can come out into a free volume between particles. The escape probability can be determined by the microparticle radius, LT and coefficient of positronium diffusion [3]. Later it was experimentally found that the intensity of the intermediate component (and the intensity of narrow positronium component of ACAR) is varied depending on the state of the particle surface [5, 8, 11, 12]. In addition, it should be noted that the LT value observed in the amorphous quartz (1,1-1,8 ns) is less than the τ_1 value registered in the experiments and that the τ_1 value depends on the surface area and state (Table 2).

Thus, there are reasons to suppose that the intermediate component is due to both annihilation inside the particles and annihilation on its surface. Inner centers of capture are more likely to be formed on the boundary of primary submicroparticles (by the size of 10 nm), adhering during high-temperature hydrolysis with the formation of the secondary particle-agglomerates [1]. Hence, the characteristics of the intermediate component of the LT spectrum are an integral sum from positronium annihilation on the internal (difficult for the other larger atomic and molecular probes) and external surface of silica microparticles.

In accordance with the diffusion model the increase of particles size in alumo- and titanoaerosills must lead to the increase of a contribution to the intermediate component (annihilation in volume defects of packing of molecular size). Values of I_I and I_L are substantially decreased for those samples. There is no reason to suppose that the whole effect of inhibition can be explained by the changes of the Ore gap boundaries or by parameters of a

positronium spur as disperse samples of Al_2O_3 , e.g., are characterized by a not lower probability of the positronium formation [6, 9]. So there are also reasons to connect the considerable decrease of I_I in those samples with the influence of hidden surface - with the Ps decay on acid centers on the internal boundary of submicroparticles.

The comparison of positronium LT with the TFA probability permits us to estimate the total probability P_o of positronium formation in the samples studied. The values of P_o are in Table 3. It can be seen that the changes of probability of Ps formation differ from the character of the changes of I_L , I_N and $P_{3\gamma}$ values. That underlines the differences noted above, in annihilation mechanisms, depending on the surface state or molecular inclusions of metal oxide.

The contribution of annihilation on the surface can be estimated by the I_I value normalized to the total intensity of o-Ps components in the LT spectra $I_I/(I_I + I_L)$ or by taking into account that 3 -decay of o-Ps is not completely registered by LT spectra and that the TFA probability gives the more complete information about positronium annihilation in free volume between the particles, to $P_{3\gamma}$. Values normalized are in Table 3. According to that parameter titanioaerosils and butosil are characterized by the least surface annihilation contribution and ADEG by the most one. Those results are approximate because the small contribution of volume annihilation is not subtracted from the I_I value.

The values of the intensity of the narrow component ACAR are also listed in Table 3. Estimates have been obtained by approximation, that three annihilation channels contribute to a narrow component: (1) self-annihilation of p-Ps in pores - as precise measurements [8] have shown the width of this component is determined by the energy of positronium emitted from the silica surface which is not thermalized within the short time of a para-state lifetime; (2) annihilation of p-Ps in defects and on the particle surface - this component must be approximately one third from I_I value of lifetime spectrum and also, as the first one, can not be very narrow (because of the formation of the localized state); (3) annihilation as a result of ortho-para conversion on oxygen, which gives the more narrow distribution because a part of positronium is thermalized by elastic collision with walls and gas molecules.

The values obtained are in a good agreement with the results of angular spectrum measurements (Table 3). The experimental data qualitatively justify the annihilation model suggested. The exceeding of the value calculated by 2-3% in comparison with the experimental one can be explained by the inadequacy of a three Gaussian model by which the angular spectrum has been approximated.

POSITRON DIAGNOSTICS OF POLYMER COMPOSITES

The correlation of the probability of positronium formation and its annihilation characteristics with microstructure properties of polymer composites is discussed. The results obtained allow to make the conclusion about efficiency of this method at analysis microdefects in disordered polymer (5...20 nm) which are inaccessible or difficult for the other analytical methods.

Observation of Phase Transition in Thermoelastoplasts

The present work investigates the temperature dependencies of positronium component lifetime τ_L butadien-sturene thermoelastoplasts (TEP) and in samples of polybutadiene (PB)

and polystyrene (PS) [15]. Unique technological properties of TEP make it necessary to study their microstructure by different methods.

Commercial samples of styrene-butadiene-styrene block copolymers, obtained by the method of solution polymerization on the presence of lithium-organic compounds, were investigated. The mass content of styrene in the TEP was 25%.

It is known that butadiene styrene TEPs possess a two phases segregation structure. According to mechanical factors TEPs are similar to laces filled elastomers. Comparing $\tau_L=f(T)$ dependencies for these samples it should be noted that in TEPs there are two fractures one of which corresponds to the glass transition of polybutadiene matrix (-100°C) and the second one to the glass transition of polystyrene blocks ($+90^\circ\text{C}$). In the temperature dependence in PB, PS there is one glass transition.

The T_g for both PS and PB blocks increases in comparison to T_g of corresponding polymers. This effect cannot be explained by mutual penetration of PB and PS phases. The T_g increase in PS is connected with the formation of the more ordered structure in microblocks PS in TEP. The T_g increase for PB blocks can be explained by the influence of the intermediated phase.

Annihilation in Polymers with Carbon-black

Annihilation spectra in samples of polybutadiene rubber with different content (up to 50 mass fraction) and type of carbon (the mean of particle diameter being 30 and 180 nm for PM-100 and PM-15 types, respectively) were measured [16].

The changes of intermediate and long-time components intensity (I_d) of the time spectrum depending in the content and type of carbon black were found. I_d change in the spectrum filled by PM-15 is well described by the Eqn.1 obtained under assumption of additive contribution of positron annihilation in the filled and polymer:

$$I_d = I_d^0 \left(1 - \frac{KC}{1 + KC}\right); \quad K = \frac{V_n}{1 - V_n}; \quad C = \frac{a_n}{a_p} = 2.45 \quad (1)$$

where: I_d^0 is the intensity of long-time component in pure rubber; V_n is the filled volumetric fraction; a_n , a_p are positron absorption coefficients in a filler and a polymer respectively.

Concentration dependence I_d for the samples filled by highly dispersed black PM-100 is also well described by the above ratio. In this case $C = 5.50$, i.e. twice as high as additive value. Increase of C can be due to positronium atom trapping by black particles (in samples with PM-15 trapping is negligible as black concentration does not exceed $2 \cdot 10^{-14} \text{ cm}^{-3}$).

The efficiency of positron diagnostics application for the study of elastomeric matrix in the systems with carbon-black content is determined by the ratio of diffusion length and the distance between the trapping centers, i.e. carbon particles. In the case of sample filling by carbon black of PM-100 type diffusion length is 15-30 nm taking into account high concentration of particles even for low levels of filling, the diffusion effects in these samples can be easily found. For samples with PM-15 carbon black trapping effects can be observed under content of 0.7-0.8 mass fraction.

Observation of modification of epoxides

The temperature dependencies of the rate of counting in maximum of angular distribution of annihilation photons in samples of epoxipiperidine polymer (sample 1) modified by silicon rubber (sample 2) and blocked diisocyanates (sample 3) have been measured [17].

Two temperature transitions related to glass transition in densely packed globular (T_g^2) and loosened interglobular regions (T_g^1) have been discovered. The position and intensity of transitions are found to be largely dependent on the modifiers availability.

The maximum has been observed at temperature range $T_g^1+50^\circ\text{C}$ on temperature curves and it can be caused by the relaxation of microcavities [18]. The relaxation effect occurs at temperature $T_g^2+80^\circ\text{C}$ too.

Table 4: Temperatures ($^\circ\text{C}$) of glass transitions and relaxation maximums in epoxide polymers.

Samples	T_g^1	T_g^2	T_n^1	T_n^2
1	42	130	87	-
2	35	115	82	185
3	37	93	83	170

On the basis of the results obtained it may be concluded the improvement of physical and mechanical properties at modification caused not only by increasing the facing density but by lowering the degree of heterogeneity structure of epoxide composites, as well.

CONCLUSION

Positron annihilation can be widely used as sensitive tool for the investigation of components and their interaction in composites, for study of physic-mechanical properties and structure of composites and polymers for diagnostics of polymer composites.

REFERENCES

1. Iler R.K, The chemistry of silica, Wiley-Interscience Publication, London 1979.
2. Chuiko A.A. and Gorlov U.I., Khimiya poverchnosty kremnezema, Naukova dumka, Kiev, 1991.
3. Brandt W. and Paulin R., Phys.Rev.Lett., 1968, # 21, pp. 193-201.
4. Steld F.R. and Varlashkin P.G., Phys.Rev.B, 1972, #5, pp. 4265-4269.
5. Debowska M., Swiatkowski W. and Wasolowski J., Acta Phys. Polon, 1977, # 51A, pp. 195-196.

6. Sen P. and Sen C., *Il Nuovo Cim.*, 1975, # 29B , pp. 124-127.
7. Hsu F.N., Shao J., Hulett L.D., Rosseel T.M. and Dale J.M., in *Positron Annihilation, ICPA-8*, World Scientific, Singapore, 1988, pp. 840-843.
8. Chang T., *Positron annihilation, ICPA-8*, World Scientific, Singapore, 1988, p. 150.
9. Sen P. and Patro A.P., *Il Nuovo Cim.*, 1969, # 64B, pp. 324-325.
10. Steld F.R. and Varlashkin P.G., *Phys. Rev. B*, 1973, # 7 , pp. 3394-3395.
11. Chang T.B., Deng J.K., Akahane T., Chiba T. and Kakimoto M., *Positron Annihilation, ICPA-7*, World Scientific, Singapore, 1985, pp. 974-976.
12. VenKateswaran K., Cheng K.L. and Jean Y.C, *J. Phys.Chem.*, 1984, # 88, pp. 2465-2469.
13. Kirkegaard P., Pedersen N.E. and Eldrup M., *PATFIT 88| A Data Processing System for Positron Annihilation Spectra on Main- frame and Personal Computers*, Denmark, Risom-2740, 1988.
14. Arifov P., Vasserman S. and Tishin S., *Phys. Stat. Sol.*, 1987, # 102a, pp. 565-568.
15. Arifov P., Vasserman S., Dontsov A., Tishin S. *Dokl. AN SSSR*, 1984, # 277, pp. 889-893.
16. Arifov P., Vasserman S., Tishin S. in *Positron Annihilation ICPA-7*, World Scientific Publishers, Singapore, 1985, pp. 787-790.
17. Tishin S., Tishin V. and Shipilevskiy B., *Plaste und Kautschuk*, 1991, # 2, pp. 45-51.

NONLINEAR VISCOELASTIC CHARACTERIZATION OF FILLED ELASTOMER COMPOSITES

J. D. Brown¹, S. S. Sternstein¹, and L. Yanyo²

¹*Center for Composite Materials and Structures, Rensselaer Polytechnic Institute,
110 8th Street, Troy, NY 12180, USA*

²*Thomas Lord Research Center, Lord Corporation
405 Gregson Drive, Cary, NC 27511, USA*

SUMMARY: Filled elastomers exhibit highly nonlinear viscoelastic behavior as demonstrated by a large dynamic strain amplitude dependence of the dynamic moduli. Dynamic testing has been performed over a range of dynamic amplitudes on a variety of filled elastomers. Also, stress-strain curves were generated from constant strain rate tests at 4 rates, with static offsets. Static offsets have minimal effect on both dynamic and stress-strain curves. Frequency dependence is greatest at the lowest dynamic amplitudes and minimal for high dynamic amplitudes. The ramp and storage moduli closely mirror one another at corresponding strain amplitudes. The normalized moduli of a group of natural rubber/carbon blacks is similar, suggesting that surface area and structure influence the magnitude of the reinforcing mechanism, but not the general behavior. The data suggest that a strain rate activated structural change in the filler is occurring, which is viscously coupled to the elastomeric matrix.

KEYWORDS: filled elastomer, nonlinear viscoelasticity, storage and loss modulus, strain rate, damping

INTRODUCTION

The presence of fillers in elastomers serves to enhance many properties, notably dynamic mechanical behavior. Unfilled elastomers exhibit the classical Gaussian behavior in that they have linear shear stress-strain curves, and have low stiffness and low damping. The filler serves to dramatically increase both stiffness and damping. The dynamic behavior of filled elastomers is highly nonlinear and not well understood.

A number of engineering applications require quantitative damping information for the proper performance of the design. One example is the lead-lag damper of a rotorcraft. This is the damper which provides in-plane damping and is critical to the performance of the helicopter.

EXPERIMENTAL

Payne [1,2] was the first to perform dynamic mechanical characterization on carbon black reinforced vulcanizates by testing samples of cylinders 2.54 cm high by 0.8 cm radius in shear in which the shear plane was parallel to the circular cross-section. This is an imperfect test

geometry since the sample is subject to a highly nonuniform strain field (not uniform shear) and the modulus thus obtained is actually an apparent modulus.

Materials

The dynamic behavior of a number of filled elastomers was measured. Proprietary samples were provided by Lord Corporation, and included natural rubber (NR) reinforced with carbon black at four filler levels, 11 silicone reinforced with silica, and two blends. In addition, Lord Corporation provided a set of natural rubber samples reinforced with one of four different carbon blacks at 15, 45, and 75 phr (parts per hundred rubber). Table 1 shows the four carbon blacks and their respective surface area and structure. There are four combinations of high and low surface area and structure.

Table I: Area and structure of carbon blacks to reinforce natural rubber.

Filler	Area by Iodine	Structure by DBP	Filler Levels
Vulcan 5H	81	150	15, 45, 69
Sterling 5550	82	72	15, 45, 75
Sterling 4620	20	126	15, 45, 75
Sterling NS-1 V-4655	28	64	15, 45, 75

Sample Geometry

The sample geometry is critical to the quality of the data. Elastomers have nonlinear behavior in tension/compression, with rapidly increasing modulus in compression, and decreasing modulus in tension. Simple shear behavior is symmetrical about the undeformed state.

End effects can significantly affect the data if an improper geometry is used. A sample of low aspect ratio (loaded surface to free surface area ratio) will have significant end effects and a dramatically reduced apparent modulus, even at infinitesimal strains [3]. For the testing in this research, a concentric cylinder geometry was used (Fig. 1). The elastomer is bonded to two cylinders, an inner and an outer, resulting in an integrated sample/fixture. The annular geometry has no edges in the circumferential direction and hence an “infinite” aspect ratio. The aspect ratio is 8 in the height to thickness, and radius to thickness is sufficient to minimize end effects and produce a nearly homogeneous strain field [3].

It is particularly important to have a homogeneous strain field when measuring nonlinear material behavior, otherwise the nonlinear material response will be obscured by the nonuniform strain field, making it difficult, if not impossible, to extract the material nonlinear behavior.

An additional feature of the concentric cylinder/annulus geometry is that it enables two orthogonal shears (axial and torsional) to be imposed on the sample, either or both being any combination of static and dynamic shear components.

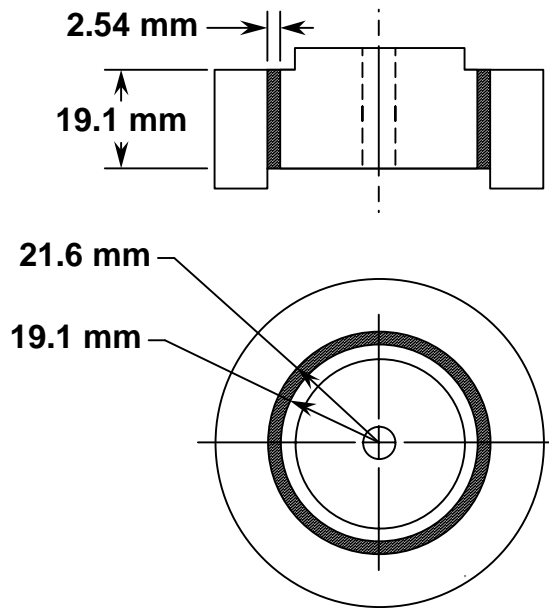


Fig. 1: Sample geometry used for dynamic testing.

Dynamic Testing

The integrated sample/fixture is mounted to two fixtures which are inserted into collets on an Instron 1321 biaxial (torsion/tension) servohydraulic testing machine.

The Instron is linked to a Dynalyzer (an FFT based dynamic analyzer), which produces a digitally generated reference signal which is transmitted to the controlling channel and receives load and displacement transducer signals from the selected channels. The Dynalyzer performs a Fourier analysis on these signals with respect to the reference signal to determine the phase angle between them. The static components of the load and displacement signals are rejected as well as any harmonics that may be present. The Dynalyzer computes the storage and loss modulus, displacement and force signal amplitudes, and transmits them digitally to a PC. Calibration constants, machine compliance and electronic phase shift corrections are handled in software provided with the Dynalyzer.

The maximum dynamic range is attained by performing a test in dynamic torsion load control. The sizing of the Instron and the load cells is such that the capability of the machine to control in load is much better than in stroke control for very low dynamic amplitudes.

Dynamic moduli are recorded at each frequency in a sweep, where a sweep consists of a fixed dynamic load amplitude, performed at 21 frequencies from 0.1 to 10 Hz, evenly spaced on a log scale. The dynamic amplitude was increased from the lowest to the highest amplitude. The lowest load amplitude was determined from minimal acceptable load resolution. The highest load amplitude was determined from either the maximum possible load at that scale or from the LVDT displacement transducer maximum scale if the sample was soft.

Orthogonal static offset tests were performed on the elastomers by imposing dynamic loading in the torsional mode with static axial displacement. In addition, parallel shear offsets were performed by performing dynamic displacement in torsion with static angular displacement. It is not possible to obtain as low a dynamic amplitude in this manner since displacement control cannot be controlled with good resolution at very small displacements.

Ramp Testing

Stress-strain curves are generated by a constant strain rate test controlled by a computer. Both ramp time and amplitude can be chosen. For this study, ramps were performed up to 5 percent shear strain in 2, 20, 200, and 2000 seconds, corresponding to strain rates from $2.5 \cdot 10^{-2}$ to $2.5 \cdot 10^{-5}$ per second.

All samples were ramped to 10 percent shear strain at the nominal rate of $2.5 \cdot 10^{-3}$ per second prior to the test ramps. After the initial conditioning ramp, 10 minutes were allowed to elapse before initiating the fastest ramp. After the first ramp, a static offset of 1 percent shear strain was set, and 10 minutes were allowed to elapse before initiating the next ramp. This sequence was repeated up to 5 percent static shear strain. Subsequent ramp tests at lower rates were carried out in the same fashion, always with a 10 minute elapsed time between tests.

RESULTS

Dynamic mechanical testing was performed on all samples. Representative data will be shown to illustrate general features common to most or all of the samples.

Dynamic Results

The dynamic response of the natural rubber/carbon black in Fig. 2 shows the typical qualitative features that all filled elastomers exhibit. The storage modulus is highest at the smallest dynamic amplitudes and monotonically decreases to some limiting value at high dynamic amplitudes. The loss modulus curves show the typical loss peak which occurs at approximately the same dynamic amplitude range where the storage modulus is most rapidly decreasing.

To more clearly show that this behavior is typical of filled elastomers, the storage and loss modulus of a silicone filled with silica is shown in Fig. 3.

As stated above, the storage and loss modulus show qualitatively the same behavior as the natural rubber/carbon black, albeit with different magnitudes. The silicone/silica sample appears to have an asymmetrical loss peak whereas the NR/carbon black has a symmetrical loss peak. In addition, the ratio of the low amplitude modulus to the modulus at high amplitude reaches 16 to 1 (at 0.1 Hz) for the silicone rubber sample.

Another feature common to both systems is that the frequency dependence is greatest at the smallest dynamic amplitudes. For both systems, as the dynamic amplitude increases, the three curves shown (0.1, 1.0, and 10 Hz) converge. This is particularly so for the storage modulus, but also is apparent in the loss behavior as well.

The effect of static offset, either parallel or orthogonal, is important to the understanding of the behavior of elastomers under dynamic conditions. For both the storage and loss moduli, the effect of static offset is to reduce the moduli somewhat, but it is far less than the effect of dynamic amplitude, and can be considered a second order effect. Fig. 4 shows the effect of a parallel static offset on the storage and loss modulus of a NR/carbon black at dynamic amplitude of 0.025. Similarly, the effect of an orthogonal static offset on the dynamic moduli is small.

Payne constructed a plot of the loss peak versus the change in storage modulus for a number of natural rubbers filled with carbon black [1]. This same plot has been constructed for all of the data on NR/carbon blacks and silicone/silica samples for this research and is shown in Fig. 5.

The Payne curve in Fig. 5 does not indicate where a particular elastomer will lie, merely that there is an overall correlation between the loss peak and the storage modulus. To determine where a particular elastomer lies on the Payne curve, a filler effectiveness curve is necessary. Such a curve is shown in Fig. 6 for a series of NR/carbon blacks.

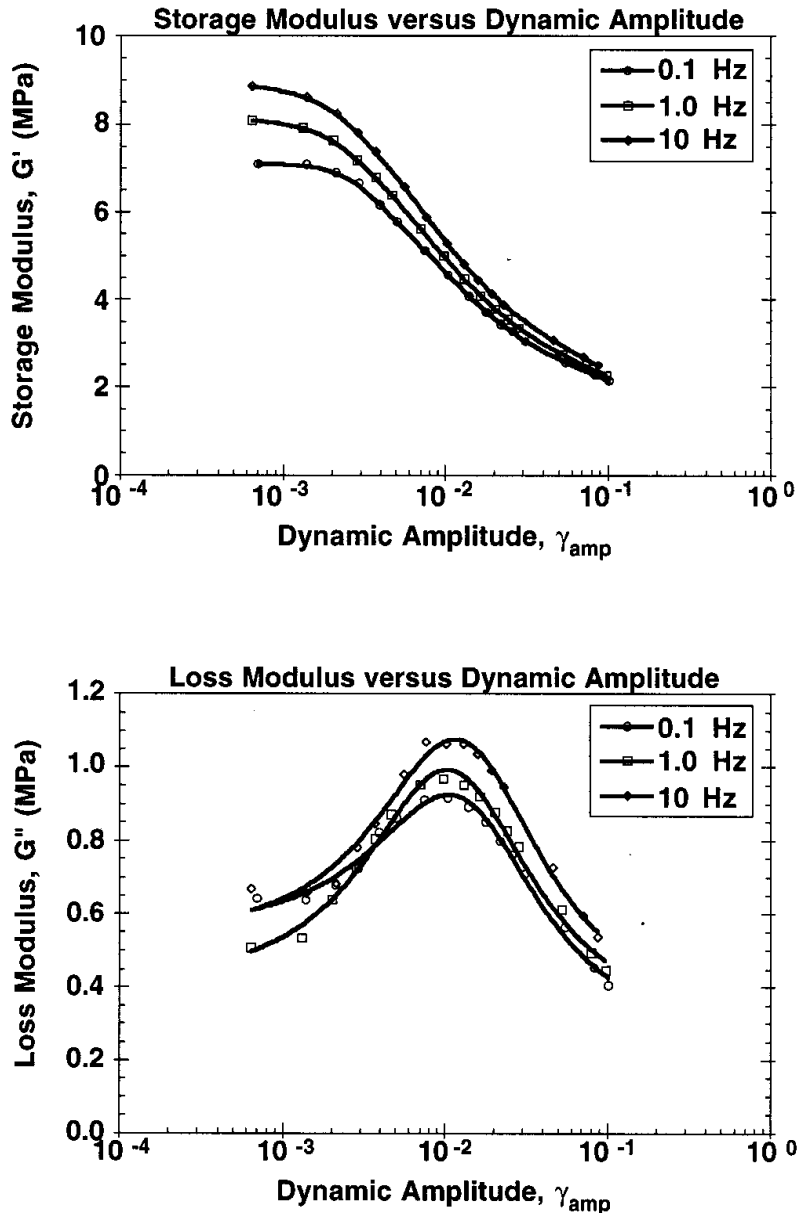


Fig. 2: Storage and loss moduli versus dynamic amplitude for a highly filled natural rubber/carbon black elastomer system.

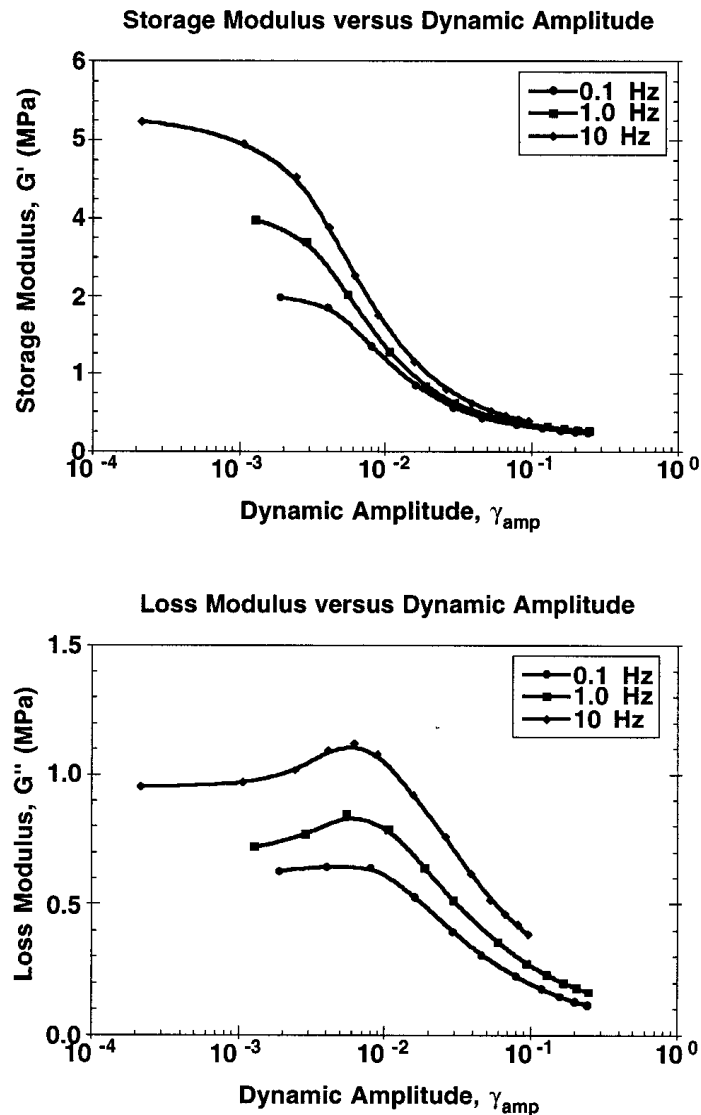


Fig. 3: Storage and loss modulus of a silicone filled with silica.

The filler effectiveness curve shows the pronounced nonlinear dependence on filler content for all four fillers. The effect of surface area is clearly stronger than that of the structure. The Vulcan 5H and the ST 5550 have nearly the same surface area, but different structures, yet their change in moduli is fairly close. The ST 4620 and the SNS1 V-4655 have low surface areas and different structures and again their behavior is similar.

Harmonic Paradox

If the nonlinear dynamic amplitude dependence is merely a manifestation of a nonlinear stress-strain curve, then the presence of a static offset should have a significant effect on the dynamic moduli. However, the data show that this is not the case. In addition, the harmonics of the response are 25 to 35 decibels below the fundamental, indicating that the response is in fact, “linear.” This presents a “harmonic paradox,” in which the material exhibits pronounced nonlinear amplitude dependence, yet has a “linear” response to the sinusoidal excitation. This suggests that a series of stress-strain curves at various static offsets would be illuminating.

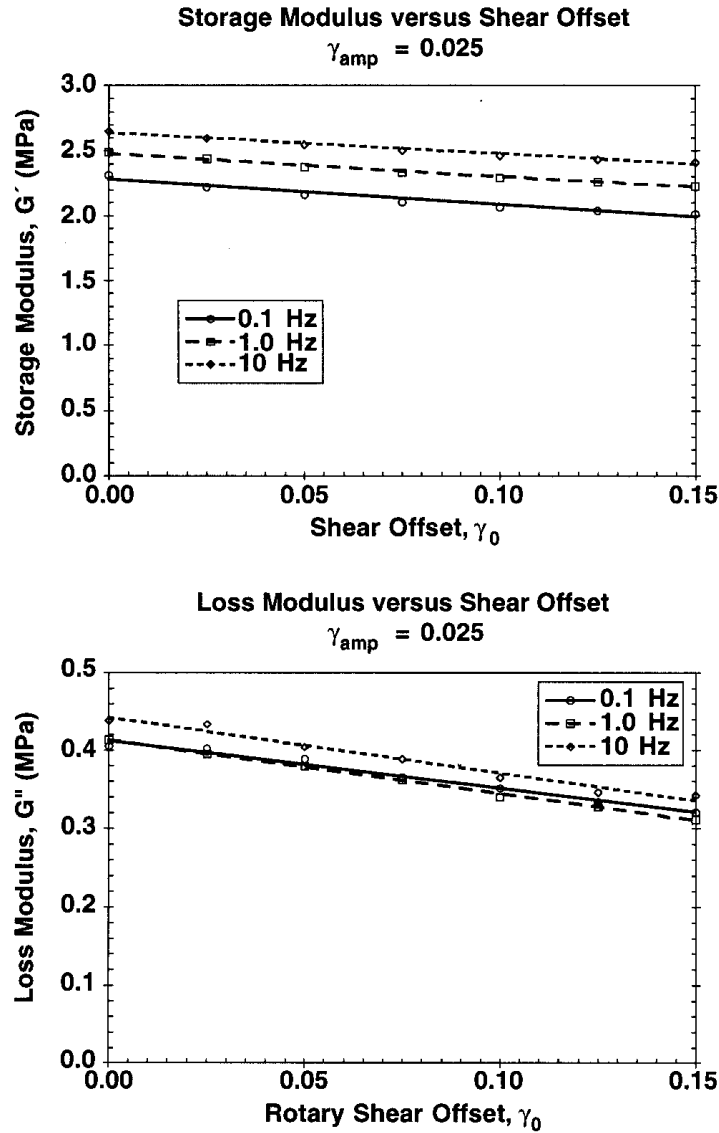


Fig. 4: Effect of parallel static offset on the dynamic moduli of an NR/carbon black filled elastomer.

Stress-Strain Results

The stress-strain response with static offsets of a natural rubber filled with carbon black (Vulcan 5H, 69 phr) is shown in Fig. 7.

The effect of a static offset on the stress-strain response is negligible. The material responds as if there were no offset. The initial modulus of a nonlinear elastic material would be a function of the total strain level, and would therefore be dependent on the static strain level.

The instantaneous modulus of the elastomers in the constant strain rate test further illuminates their dynamic response. As seen in Fig. 8, there is considerable agreement between the storage modulus and the ramp modulus at a fixed nominal rate for a highly filled natural rubber with carbon black. It is important to note that for dynamic results, the strain rate is not

constant and is an “average” of rates from 0 to some maximum, and that on the next half-cycle varies from 0 to the negative of the maximum value. In addition, the nominal slewing rate of the dynamic test varies proportionately with dynamic amplitude. Despite these differences, the similarities in the two curves is striking.

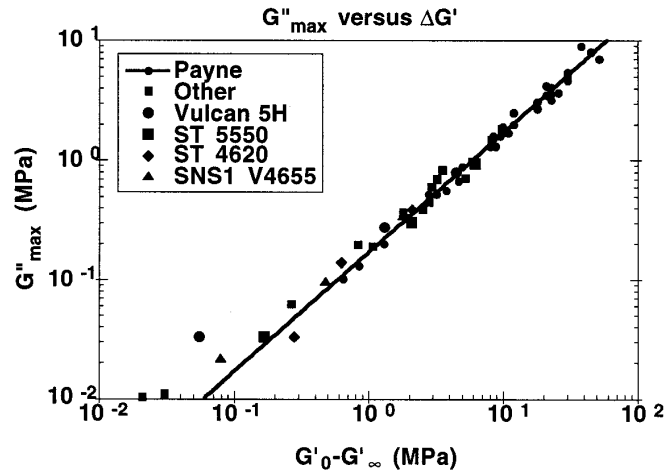


Fig. 5: Loss peak versus change in storage modulus for Payne[1] and present work.

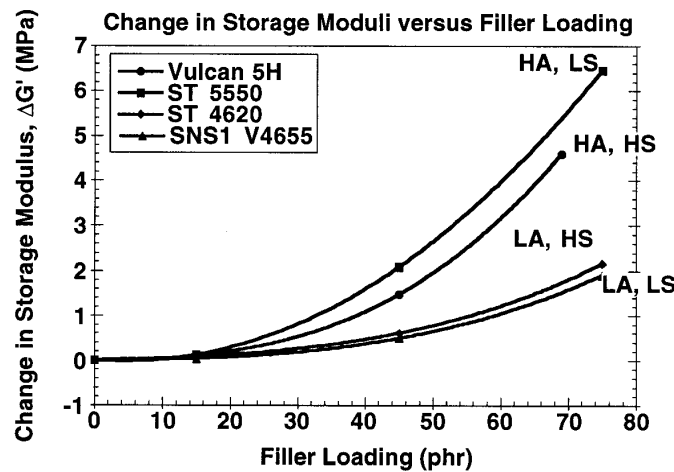


Fig. 6: Filler effectiveness curves for carbon blacks in NR. Legend: HA, high area; LA, low area; HS, high structure; LS, low structure.

DISCUSSION

All of the elastomers tested (30 in all) show qualitatively the same phenomena. They show the storage modulus at low dynamic amplitude decreasing markedly with increasing dynamic amplitude. The loss peak occurs at approximately the same dynamic amplitude range in which the marked change in storage modulus occurs.

The extent of the change in the storage modulus and the strength of the loss peak are clearly related to the filler level. The changes in the dynamic moduli increase nonlinearly with filler content, with the most rapid increase occurring in the high filler content range.

The presence of a static offset, either parallel or orthogonal, has a minimal second order effect on the dynamic moduli. The effect that is seen is most pronounced for the storage modulus at low dynamic amplitudes, and near the peak for the loss modulus. Since a static offset does not alter significantly the dynamic response, it appears that it cannot be due to merely a nonlinear stress-strain response. This observation led to a critical experiment in which the stress-strain response and the effect of static offsets on that response were tested.

The stress-strain response of filled elastomers show a marked nonlinearity with a high modulus at the outset, and a terminal modulus which is significantly lower. The initial modulus is highly strain rate dependent, whereas the terminal modulus is nearly strain rate independent (Fig. 9). This mirrors the frequency dependence which is greatest at low dynamic amplitudes and minimal at high dynamic amplitudes.

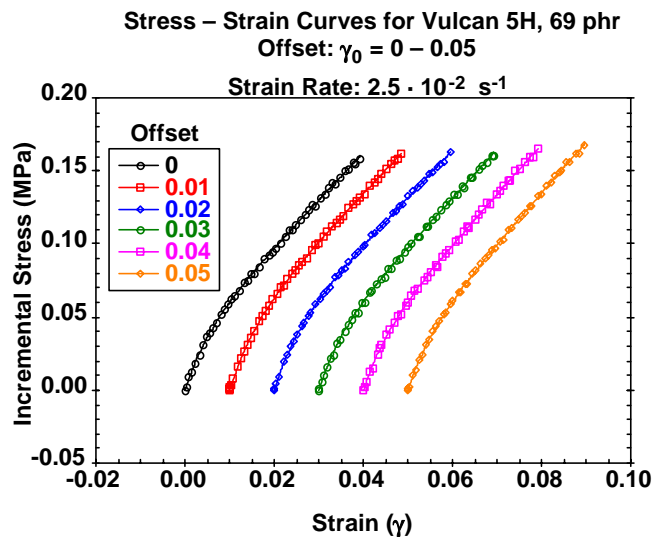


Fig. 7: Stress-strain curves for NR/carbon black with static offsets.

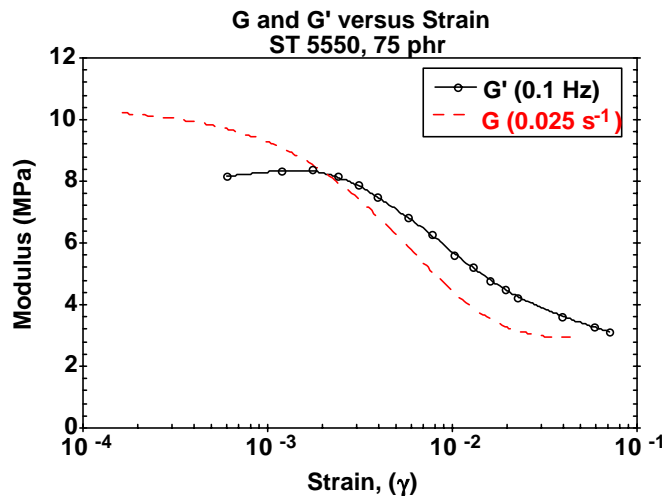


Fig. 8: Comparison of storage modulus, G' (at 1 Hz) and ramp modulus at nominal strain rate of $2.5 \cdot 10^{-2}$ per second.

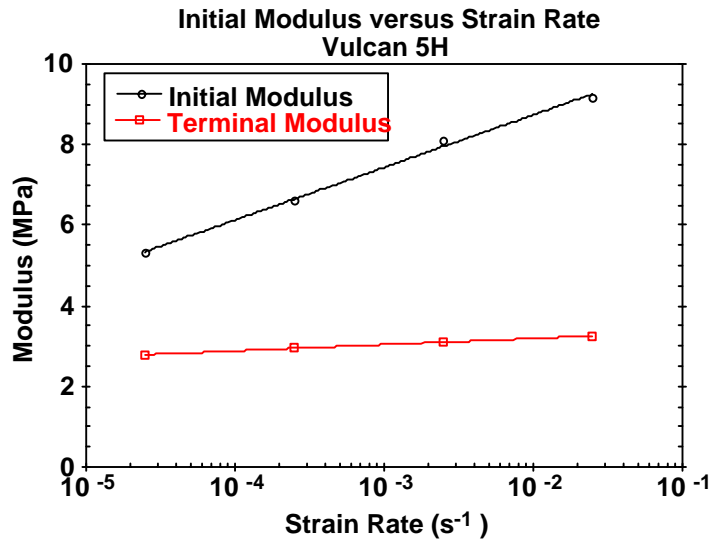


Fig. 9: Initial and terminal modulus from a stress-strain curve taken at $2.5 \cdot 10^{-2}$ per second strain rate.

The ramp modulus can be normalized so that its value is 1 at its maximum and 0 at its minimum, according to Eqn 1.

$$G_{\text{norm}} = \frac{G - G_{\text{min}}}{G_{\text{max}} - G_{\text{min}}} \quad (1)$$

This normalized modulus is then a measure of the proportion of modulus change remaining. A plot of normalized modulus versus strain amplitude is seen in Fig. 10. Despite the large differences in filler systems, the normalized moduli show remarkable agreement. The specific filler used in an elastomer will dramatically affect the magnitude of the response but not the general behavior of it.

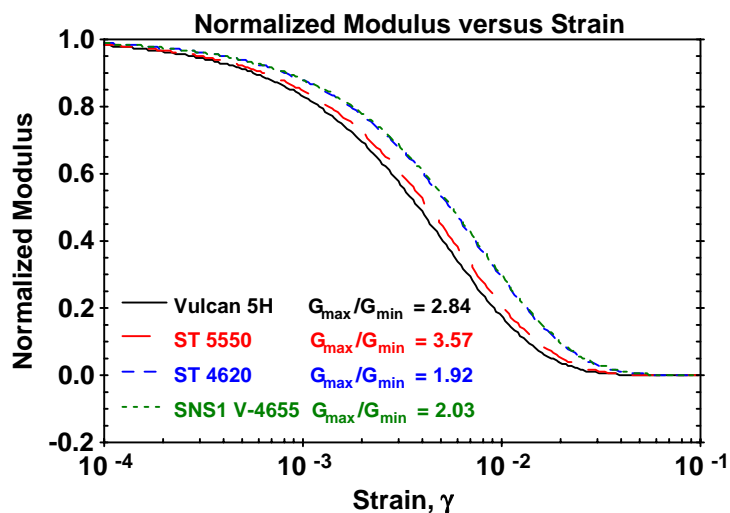


Fig. 10: Normalized modulus versus strain amplitude for the series of carbon blacks (highly filled).

These results suggest that a strain rate activated structural change of filler is occurring and that it is viscously coupled to the matrix. There is a material state that is determined by strain rate and is the result of an equilibrium between breakdown and reformation processes. In the case of dynamic tests, some “average” strain rate controls the steady-state structure or material state. The ramp tests indicate that the material rapidly equilibrates to the current strain rate, independent of the static strain level.

CONCLUSIONS

Dynamic testing has been performed over a 3 decade range of dynamic amplitudes on a variety of filled elastomers. Stress-strain curves were generated from constant strain rate tests covering 3 decades. Static offsets were found to have minimal effect on both dynamic and stress-strain behavior. The ramp and storage moduli closely mirror one another at corresponding strain amplitudes. The data suggest that a strain rate activated structural change in the filler is occurring, and is viscously coupled to the elastomeric matrix. The results cannot be explained by a nonlinear elastic network theory.

ACKNOWLEDGMENTS

The authors wish to thank the Lord Corporation for providing the samples and for support of this work.

REFERENCES

1. Payne, A. R., “The Dynamic Properties of Carbon Black-Loaded Natural Rubber Vulcanizates,” *Journal of Applied Polymer Science*, 6(19):57–63 (1962).
2. Payne, A. R. and Watson, W. F., “Carbon black structure in rubber,” *Rubber Chemistry and Technology*, 36:147–155 (1963).
3. Rivlin, R. S. and Saunders, D. W., “Cylindrical Shear Mountings,” *Transactions I. R. I.*, 296–306 (1949).

“GOOD VIBRATIONS”, THE SCIENCE AND APPLICATION OF INTRINSICALLY DAMPED COMPOSITE MATERIALS

I.D. Grant, A. Lowe and S. Thomas

Structural Materials Centre, DERA, Farnborough, Hampshire, GU14 6TD, UK.

SUMMARY: The work presented in this paper shows how the viscoelastic properties of an epoxy resin system can be modified to produce an Intrinsically Damped Composite (IDC) material. Through the addition of chain extension modifiers peak loss factors of up to 0.4 have been achieved compared to 0.005 for traditional Glass Reinforced Epoxy (GRE) materials. Both Dynamic Mechanical Analysis and Vibroacoustic measurement techniques were used to determine the loss factors of the IDC materials. The DMA technique was less sensitive to changes in damping due to fibre orientations. In conclusion some potential areas of application for these novel composite materials are described.

KEYWORDS: viscoelastic, damping, vibrations, DMA, flexibilised epoxy, CFRP, GRP

INTRODUCTION

One of the principal benefits offered by composite materials is the ability to tailor their mechanical properties for different applications. One area which is only just being investigated is the ability of composite materials to provide considerable reductions in the level of vibration and noise generated by a structure. Through careful choice of fibre angle it is possible to achieve some increase in the vibrational loss factor of a composite material. This usually requires a high proportion of fibres orientated at $\pm 45^\circ$ which results in a considerable reduction in mechanical properties in the 0° and 90° directions. One approach to overcome this limitation is to use alternative fibres which possess intrinsically higher levels of damping. Investigations of this type have been carried out by Yu and Song at the US Army Natick Research Labs [1-3] and have concentrated on the damping levels achieved by using Kevlar 29 and Spectra for ballistic protection. Other workers have investigated the benefits gained through the use of interleaving in angle-ply carbon fibre epoxy laminates [4]. All these techniques do show some improvements, but none of them have achieved loss factors greater than 0.05 for a composite material at frequencies above 10 Hz. Some workers [5] have speculated that the only way to achieve high loss factors would be through modifying the resin system and this is the approach which is described here.

Currently a wide range of resins are used for fibre consolidation in composite materials including Polyesters, Vinyl Esters, Phenolics and Epoxies. All these resin systems exhibit viscoelastic properties, but only when heated well above room temperature i.e. 80°C to 230°C . The viscoelastic region is often referred to as the glass transition temperature (T_g) and is characterised by an increase in loss factor ($\tan \delta$) and a reduction in the Young's

Modulus (E' or E''). Generally composite materials such as GRP have a loss factor of 0.005 which is only marginally superior to that of mild steel with a value of 0.0001. Through careful resin chemistry it is possible to enter the viscoelastic region at a much lower temperature and consequently achieve much higher levels of damping. Intrinsically Damped Composite (IDC) materials containing 4 ply $0/90^\circ$ woven XAS carbon fibre and consolidated with highly damped epoxy resin systems have shown loss factors of up to 0.4.

Obviously there is a trade off between the level of damping which is achieved and the mechanical properties, however, for many class 2 or secondary type structures these limitations can be overcome. Furthermore, if careful thought is given to the vibroacoustic environment a structure may experience during its life time, considerable cost savings can be made by using these composite materials in the early design phase, rather than adding additional parasitic damping whilst in service. This paper will describe the work carried out by the UK Defence Evaluation and Research Agency (DERA) in formulating these highly damped epoxy resin systems, providing information on their dynamic mechanical characteristics and typical areas of application.

COMPOSITE MATERIAL FABRICATION

The time and effort required to develop a completely new matrix system with enhanced damping properties would be immense. Consequently, the approach taken was to use proprietary resins and chain modifiers with the aim of reducing both development and eventual unit production costs.

At an early stage a decision was made to focus resources on studying only epoxy based systems, since flexibilised epoxy resins are widely used for industrial flooring and also in the electronics industry for the encapsulation of electronic devices. Chain modifiers manufactured by two independent suppliers have been investigated in combination with standard bisphenol A epoxy resins. The assessment of candidate matrix systems has been made by considering the mechanical performance and the processibility of the resin systems concurrently. Since many of the most effective flexibilising additives are highly viscous it was necessary to make some performance trade-offs to arrive at a viable practical solution. The resins investigated in this report have been designated R1816, R1818 and RF69.

Economic and environmental pressures have increased the attractiveness of using closed mould and filament winding techniques to fabricate composites. To be readily processed using these production methods, a matrix system must have a low viscosity, long pot life and only require moderate post curing. Such considerations are equally important for highly damped composites, and careful attention has been made to address these issues early in the resin development stage.

Viscosity measurements were performed on a Brookfield viscometer immediately after mixing together the matrix components. The pot life measurements are values of the useable life of a resin system when stored in a typical 2 litre laminating bucket, based on experience gained from manufacturing laminates using the various resins. In all cases the ambient temperature was 22°C . A summary of results is shown Table 1; note the comparison with a typical resin used for Resin Transfer Moulding (RTM) of components:

The RF69 system has been successfully processed using RTM and filament winding. Vosper

Thornycroft Ltd (UK) have fabricated a 30 mm thick composite using RF69 and the Seaman Composite Resin Injection Moulding Process (SCRIMP) with few processing difficulties. Attempts were made to RTM using the R1816, however these efforts were unsuccessful due to a combination of the high viscosity and the extremely short pot life.

Table 1: Processing Properties of Viscoelastic Resin Systems

Resin Type	Viscosity (Pa s)	Pot life (Hours)
RF69	1.2	~ 6
R1816	4.6	~ 1
R1818	4.6	~ 2.5
Derakane 8084	0.5	~ 1

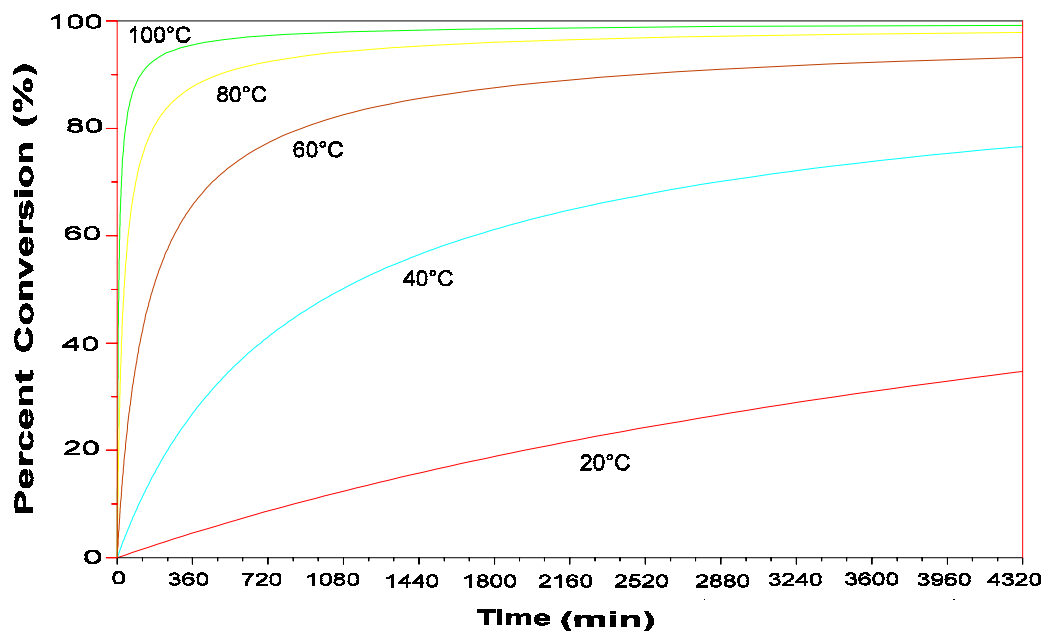


Fig 1: DSC Plot of Percentage Cure State v Post Cure Time at Different Temperatures for RF69.

An analysis of the cure kinetics of the RF69 resin has been performed from results measured on a Thermal Analysis (TA) 2920 Differential Scanning Calorimeter (DSC). DSC tests were conducted from -20°C to 250°C using a $10^{\circ}\text{C}/\text{min}$ ramp rate. These measurements were then used in conjunction with a kinetics analysis package (B&D kinetics) to predict the time required to post cure the matrix at various temperatures, see Fig. 1.

It should be noted that the conditions within the DSC are not wholly representative of those found in a 2mm thick laminate where larger amounts of resin will be reacting with less opportunity for the transfer of heat from the laminate. However, the effect of this will be to underestimate the time taken for the resin to cure. The data presented above shows that not only does the RF69 resin system have a relatively low viscosity and long pot-life, but it can also be satisfactorily post cured at moderate temperatures, over a short period of time.

The IDC materials used for Dynamic Mechanical Analysis and Vibroacoustic Measurements have all been manufactured using hand lay up or RTM techniques. To allow a direct comparison of results, spacers were used during hand lay-up to ensure that the panel thickness remained constant (i.e. to maintain a volume fraction of 40% fibre by weight). All laminates were cured at room temperature for 24 hours followed by a post cure at 60°C for 3 days (4320 min).

DYNAMIC MECHANICAL ANALYSIS (DMA)

Dynamic Mechanical Analysis (DMA) provides a convenient method of testing large numbers of resin formulations and composite systems quickly and simply. Test samples were cut from hand layed up laminates panels made from 4 plies of plain weave Courtaulds XAS carbon fibre and tested in three point bending using a Netzsch 242 DMA. Specimen dimensions were approximately 1.8 x 12.0 mm and measurements were made on a sample holder with a free bending length of 40 mm and at a frequency of 10 Hz.

Figs 2 & 3 show the results for 3 highly damped composite laminates measured in both 0/90° and ±45° fibre orientations. When measured at 0/90° the R1816, R1818 and RF69 exhibited a loss factor ($\tan \delta$) of approximately 0.45. However, as the temperature increased this rapidly fell to around 0.1. This represents a 1-2 order of magnitude improvement compared to a traditional carbon fibre composite material.

If we compare the data presented in Figs 2 and 3 then as expected the Young's Modulus for the 0/90° fibre orientation is approximately 4 times that in the ±45° direction. However, the values for $\tan \delta$ are similar in magnitude, irrespective of the fibre orientation. The peak values of $\tan \delta$ appear to be actually higher for the 0/90° laminates, although for the ±45° specimens the peak is broader. These results do not comply with the analytical model previously described by the authors [6] however, there are a number of potential explanations.

In a composite laminate damping occurs as a mixture of two mechanisms. One relies on damping between the fibre and resin within the laminate plies and the other on damping between the plies. Measurements made on the DMA are achieved by cyclic flexure of the composite beam samples in three point bending at constant amplitude and frequency. Damping in a flexural mode is largely due to shear effects between plies in a laminate which is analogous to constrained layer damping [7] and is dominated by inter-ply effects. Thus the damping performance measured on the DMA is less sensitive to the properties of the individual plies than on the effect of shear in the matrix between the plies. Due to the higher stiffness of the 0/90° plies, the amount of energy that can be transferred into the matrix may be proportionally higher than for the ±45° plies thus leading to the higher value of peak $\tan \delta$.

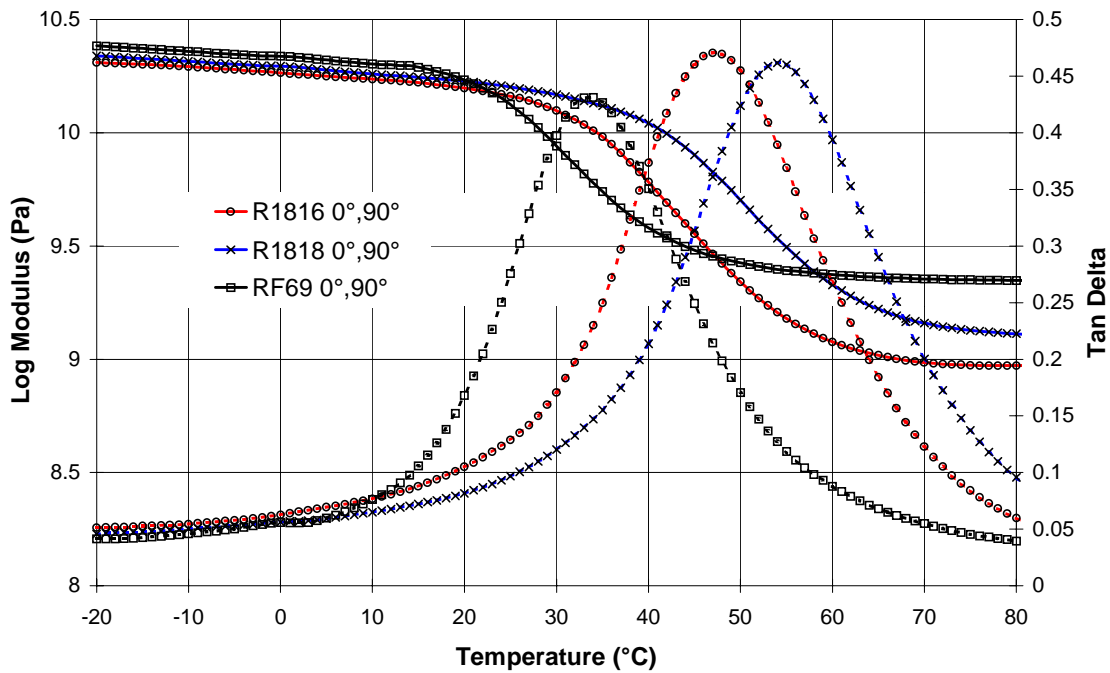


Fig 2: DMA performance of $0/90^\circ$ plain weave carbon fibre, consolidated with a range of highly damped epoxy resin systems.

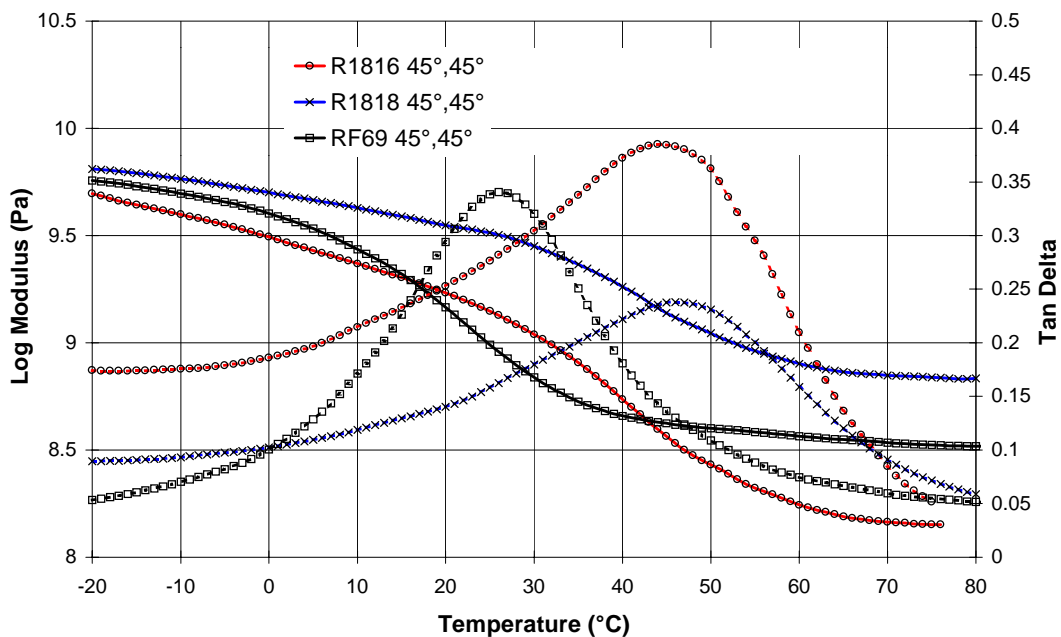


Fig 3: DMA performance of $\pm 45^\circ$ plain weave carbon fibre, consolidated with a range of highly damped epoxy resin systems.

An alternative view is given by the theoretical studies carried out by Sun and Gibson [8] on predicting the material damping of laminated polymer matrix composites. Here they used classical lamination theory to show that when beams with a very small fibre length to diameter (L/d) ratio are numerically analysed there is very little difference in the value of tan

δ for different fibre orientations. It is only when L/d ratios >5000 are achieved that significant differences between fibres orientations are shown. If we make a gross simplification of the mechanisms occurring in an IDC composite material and liken the fibre tows to the individual fibres described in the work of Sun and Gibson. Then it is conceivable that the L/d ratio of the 40 mm long beams used by the DMA are too short to characterise the effects of fibre orientation.

A further consideration when using the DMA is to remember that it does not measure the damping due to longitudinal waves. It might be expected that the longitudinal waves are dependent on the damping performance of the sum of the individual plies (i.e. shear effects within the plies) and rather less due to the shear effects between plies. If this is the case the $\pm 45^\circ$ beam would be much more effective at damping longitudinal waves when compared with the $0/90^\circ$ beam due to the higher in-plane stiffness of the $0/90^\circ$ fibres. It is therefore necessary to establish the most dominant type of vibration in potential applications so that a correct value for the damping performance can be applied i.e. have multiple values for $\tan \delta$, one for flexural and the other for longitudinal vibration modes. A more representative technique for determining damping performance is given by full size beam measurements as presented below.

VIBROACOUSTIC MEASUREMENTS

To demonstrate the more representative loss factors generated by this technique the vibroacoustic performance of a plain weave E-Glass/Cycom 919 epoxy (GRE) composite material has been compared with an IDC XAS Carbon/RF69 material. The analysis was carried out using a hammer with a force gauge mounted on the head and a laser accelerometer as shown schematically in Fig. 4. The signals from these two transducers were then analysed and the Fourier spectrum of each calculated. The output spectrum was then divided by the input spectrum to give the transfer function. The composite beams were cut to dimensions $215 \times 37 \times 3.5$ mm, with the fibres orientated at $\pm 45^\circ$.

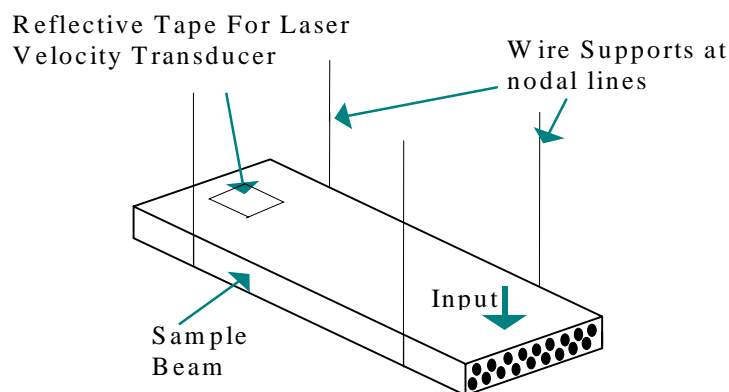


Fig 4: Schematic diagram of vibroacoustic measurement technique.

The transfer function for a given beam sample will give the resonant frequencies of that beam. Then by taking the half power points of the modes the loss factor can be calculated. With

further knowledge of the beam using the following beam equation [9] it is possible to calculate the Young's Modulus.

$$f_1 = \frac{\pi}{2l^2} \sqrt{\frac{YK^2}{\rho}} \quad (1)$$

Where :

f	=	<i>fundamental frequency</i>
l	=	<i>Length of beam</i>
K	=	<i>Radius of gyration</i>
Y	=	<i>Young's Modulus</i>
a	=	<i>Beam Thickness</i>
ρ	=	<i>Density</i>

$$K = a/\sqrt{12} \quad (2)$$

To prevent any interference from the mountings and the transducers a Bruel and Kjar Laser Velocity Transducer was used and a small Dytran hammer was selected to excite the structure. The signal processing was performed using a Bruel and Kjar spectrum analyser 2035 in two channel mode. The beam samples were supported by wire loops at the nodal lines for the fundamental mode to reduce interactions between the supports and the beam. All tests were conducted in the flexural mode. The frequencies for the first four modes of each of the two resin types were taken and the loss factors calculated, see Figures 5 & 6.

As we can see from the loss factors presented in *Fig. 5* this technique gives a value of between 0.005 and 0.01 for the standard E-Glass/Cycom 919 sample. This provides confidence in this test method as these values conform to the loss factors traditionally quoted for GRE. The Young's Modulus for this material is specified by Cytec as 26 GPa and analysis via the vibroacoustic method gives a value of approximately 24 GPa. If we now examine the data for the IDC material presented in *Fig. 6* we can see that the loss factor for the $\pm 45^\circ$ and $0/90^\circ$ fibre orientations are approximately 0.2 and 0.1 respectively. These data conform to the theoretical models presented in Refs 6 & 8 where the $\pm 45^\circ$ fibre orientation imparts greater shear into the resin system thus introducing a higher level of viscoelastic response. However, there is some discrepancy in the values of Young's Modulus which are considerably lower than the 23 GPa given by the DMA measurements and the 27 GPa value calculated from tensile tests. One explanation may be the inferior quality of these early hand layed up laminates compared to the test samples used for the DMA measurements which were produced by RTM technology. Clearly further testing is required before the definitive technique for characterising the damping properties of composite materials can be specified but until then care should be taken to describe the test conditions and excitation mode when quoting loss factors.

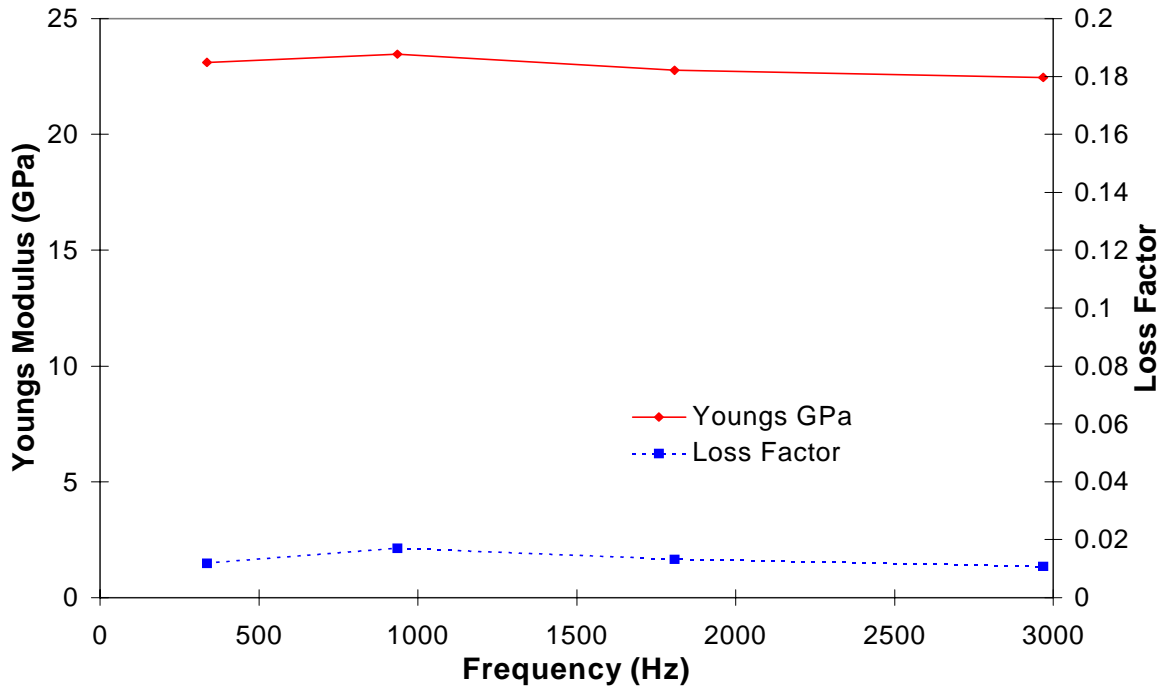


Fig. 5: Loss Factor and Young's Modulus for standard GRE composite material. 0°/90°

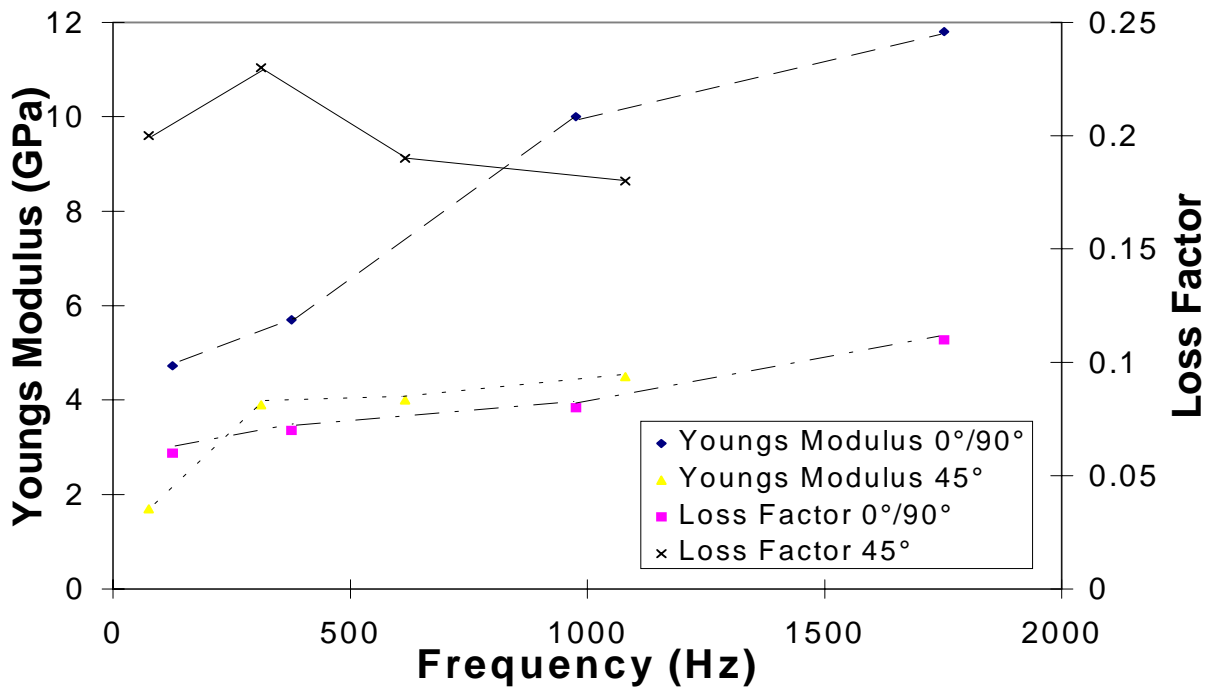


Fig. 6: Loss Factor and Young's Modulus for Carbon Fibre IDC material.

APPLICATIONS

There are a wide range of applications for viscoelastically tuned IDC materials many of the papers listed in the reference section show the potential benefits to be gained in ballistic impact performance but a number of other examples are given below:

Currently many deep water oil and gas platform operators are replacing their existing sea water pipe systems with pipework manufactured from filament wound Glass Reinforced Epoxy (GRE) composite materials. If these pipes are exposed to a continuous flow rate greater than 5 ms^{-1} then cavitation erosion can occur at bends and fittings. Work carried out by SINTEF in Holland [10] showed that under accelerated testing GRE had an erosion incubation time of 1.7 hours at a flow rate of 50 ms^{-1} compared to >30 hours for a 6Mo steel. It is known that the erosion resistance of a composite material is resin dependant and relies on its capacity to resist the impact energy imparted by the collapsing cavitation bubbles. Consequently, if the first layers of a pipe were wound in E-glass/RF69 IDC material this could overcome the additional expense of using an internal thermoplastic liner. In addition potential benefits could be gained in reduced noise, vibration transmission and hence fatigue damage to connected equipment due to the higher levels of structural damping. A more extreme cavitation environment is produced by composite marine propellers and IDC materials are currently being developed to provide erosion and impact protection under these conditions.

Another area associated with the oil and gas industry is the protection of drilling riser arrays from clashing damage. This problem became more significant as exploration companies began developing oil fields at depths greater than 1000 metres. Initial investigations considered the use of a polyurethane coating, but these proved to be too brittle to resist repeated impact. Consequently, a filament wound polyester fibre/RF69 is currently being evaluated.

One of the most significant areas of application for IDC materials is in the reduction of radiated noise from machinery rafts. These are used in marine applications for the siting of diesel generators, gearboxes, engines etc. Currently they are manufactured from steel or aluminium and are then isolated from the machinery and deck via rubber isolation mounts. By constructing the space frame structure from box sections filament wound at $\pm 45^\circ$ from T300/RF69 IDC material vibrational power transmission levels have been reduced by between 10 to 20 dB across a broad frequency range.

CONCLUSIONS

A range of Intrinsically Damped Composite (IDC) materials have been produced containing XAS/T300 carbon fibres and consolidated with a highly modified bisphenol A epoxy resin system. Dynamic mechanical characterisation has revealed that highly damped thermoset resin systems can produce much higher loss factors than previously shown by techniques such as interleaving. Due to the compromise made between Young's Modulus and Loss Factor these materials are more suitable for use in secondary structures. Additional work is required to broaden the temperature range over which the high levels of loss are produced.

Two techniques were used to dynamically characterise the IDC materials. Generally it was found that the Dynamic Mechanical Analysis (DMA) was less sensitive in measuring the

changes in loss factor due to fibre direction than a more global vibrating beam method. Also the level of loss predicted by the DMA was higher than that found on larger scale samples. Consequently great care must be taken when quoting loss factors for composite materials to ensure the test technique and mode of excitation (i.e. Flexural or Longitudinal) are stated.

ACKNOWLEDGEMENTS

The authors would like to acknowledge the United Kingdom Ministry of Defence for funding this project and the encouragement provided by Mrs C Solen and Dr R Leung.

© Crown Copyright/DERA 1997.

Reproduced with the permission of the Controller of Her Britannic Majesty's Stationery Office.

REFERENCES

1. Yu J Z, Ko F K, Song J W, "The Effect of Fiber Orientation on the Dynamic Mechanical Behaviour of Kevlar Fiber Reinforced Composites", *Proceedings of ICCM-10*, Whistler, B.C., Canada, August 1995, Vol VI, pp 431-438.
2. Ko F K, Lei C, Rahman A, Shaker M, Zavaliangos, Yu J Z, Song J W, "Viscoelastic Properties of Advanced Polymer Composites for Ballistic Protective Applications", *Technical Report/Natick/TR-94/035* (1993).
3. Lee B L, Song J W, Ward J E, "Failure of Spectra Polyethylene Fiber-Reinforced Composites under Ballistic Impact Loading", *Journal of Composite Materials*, Vol 28, No. 13/1994, pp 1202-1226.
4. Liao F, Su A, Hsu T, "Vibration Damping of Interleaved Carbon Fibre-Epoxy Composite Beams", *Journal of Materials*, Vol 28, No. 18/1994, pp 1840-1854.
5. Benchechou B, White R G, "Fatigue of Highly Damped Carbon Fibre Reinforced Plastic Panels at High Temperature", *Proceedings of ICCM-10*, Whistler, B.C., Canada, August 1995, Vol I, pp 657-664.
6. House J R, Grant I D, "Viscoelastic Composite Materials for Noise and Damage Tolerance", *Advanced Performance Materials*, Vol 3, No. 3/4 (1996), pp295-307.
7. Beranek L L, Ver I L, "*Noise and Vibration Control Engineering*", published by John Wiley & Sons, 1992, ISBN 0-471-61751-2.
8. Sun C T, WU J K, Gibson R F, "Prediction of Material Damping of Laminated Polymer Matrix Composites", *Journal of Materials Science*, Vol 22 (1987), pp1006-1012.
9. Olson H F, "*Elements of Acoustical Engineering*" D Van Nostrand & Company, inc.
10. Lindheim T, "Erosion Performance of Glass Fibre Reinforced Plastics (GRP)", *Proceedings of l'Institute Francais du Petrole Composite Materials in the Petroleum Industry Conference*, 3-4 Nov 1994, Paris.

SUBJECT INDEX

6061	154	centrifugal shs process	546
a vortex method	154	ceramic yield	573
Al ₂ O _{3p}	607	ceramic/metal joining	661
Al ₂ O ₃ steel composite pipe	546	CF/Al-4.5Cu composites	672
accelerated aging	698	CFRM	126
acoustic emission	585	CFRP	792
activation energy for creep	221	citric acid	384
age hardening	250	coated copper	597
aging effects	337	coefficient of friction	290
Al alloys	63	coefficient of thermal expansion	290
Al and Mg alloy matrix composites	578	cold roll	532
Al/SiC	565	combustion synthesis	438
Al ₂ O ₃	63	compatibility	643
Al ₂ O ₃ particles	527	composite	154
Al ₂ O ₃ -Al ₃ Ti	438	composite material	457
Al-based metal matrix composites	90	composites	365, 597
AlCuMgAg alloy	274	compressive loading	467
aligned fibres	755	compressive strength	438, 653
Al-Li/SiC composites	348	conductive plastics composite	727
Al-MMCs	143	constrained plastic flow	1
Al-Ti intermetallic	63	continuous fibre reinforced MMC	134
alumina	290	continuous fibre reinforcement	391
alumina borate whisker	108, 612	cooling rate	311, 672
alumina short fibre	585	copper matrix composites	290
aluminium	736	corrosion resistant composites	90
aluminium alloy	709	crack bridging	260
aluminium matrix composites	134	crack deflection	374
aluminium metal matrix composites	250	crack growth	356
aluminum	24, 113, 154, 505, 643	crack initiation	10, 215
aluminum alloy	182, 198	crack opening displacement	260
aluminum carbide	337	crack propagation	10
aluminum flakes	727	cracking	418
aluminum matrix	101, 418	creep	300
aluminum matrix composite	108, 612	creep exponent	221
aluminum nitride	486	creep of MMC	221
amorphization	101	critical current	384
anneal	532	cruciform sample	317
		crystalline	101
bearings	746	c-scan	719
beryllium	736	current enhancement joining	661
beryllium alloys	736	cynamic fracture	327
bolt connector	134		
bond strength	119, 374	d ₀₀₂	643
brazing	113	damage	238, 300, 348, 365, 409
bridging	374	damage model	143
buckling	467	damping	585, 781, 792
		decohesion	409
carbide precipitation	399	deformation	1
carbon diffusion	399	deformation mechanisms	479
carbon fibres	221	diagnostics	772
carbon/epoxy	719	diamond coated tools	205
casting welding	617	diffusion	772
cavitation	300	dilatation	585
cementation process fractograph	597	directional solidification	311
centrifugal force	546	discontinuously reinforced metal matrix composites	43

dislocation	612	grain boundary precipitates	418
dislocations and whisker	10	graphite	290, 617
dispersal materials	495	graphite particles	597
DMA	792	graphite-reinforced metal matrix composites	90
doping	63	GRP	792
drilling	205		
dry sliding wear	709	hardening	63
ductility	418, 429	hardness	80, 290, 597, 607
		heat treatment	63, 399
effective aspect ratio	15	heat-treatment,	709
elastic deformation	578	high strain rate	198
elastic limits	578	high strain rate superplasticity	486
elastic shielding	374	high temperature	550
electret	746	hipping	43
electrization	746	homogeneous distribution	627
electrochemical composite deposition	495	hot extrusion	627
electrochemical plating	495	hot hardness	653
electromagnetic interference (EMI)	727	hot press	653
electron beam	637	hot rolling	154
electron irradiation	101	hot workability	418
electrostatic interaction	746	hybrid	126
elongation	527	hybrid metal matrix composites	327
energy absorption	260	hybrid MMC	164
eutectic microstructure	637		
extrusion	505	image analysis	719
extrusion particulate	617	in situ composite	637
		indentation fracture toughness	653
failure	300	induced	101
failure mechanisms	365	infiltration processing	274
failure of composites	365	injection molding	727
fatigue	356, 365	insert	126
fatigue behaviour	134	in-situ	356, 565
fatigue crack growth	374	in-situ SEM	539
fatigue crack propagation	556	in-situ TEM	539
fatigue fracture surface	556	interaction between crack	10
fatigue life	365	interface	15, 24, 126, 238, 374, 672, 698
FEM	143	interface diffusion	661
fiber/matrix reaction	399	interface modelling	661
fibre/matrix interface	391	interface properties	317
filled elastomer	781	interface reaction	661
finite element method	457, 565	interfacial debonding	260
finite element modelling	32	interfacial reaction	337
flexibilised epoxy	792	interfacial reaction layer	447
flexural strength	653	interfacial reactions	688
forging	143	interfacial shear stress	447
form a metallic composite	230	interlayer	113
formability	755	intermetallic compounds	182
forming test	198	intermetallic phases	119
foundry technique	290	internal stresses	32, 565
fracture	311, 344, 409, 539	interphase debonding	429
fracture process	520		
fracture toughness	337	joining interface	108
fragmentation	238	joining mechanism	661
friction	678, 746	joint strength	108
friction coefficient	75		
		keying in	215
generalized self-consistent finite element		kinking	467
iterative averaging method	429		
generalized shear-lag model	15	lanthanum hexaboride	637
global	238	laser processing	80

Lc(002)	643	neutron diffraction	565
liquid metal infiltration	274	NiAlp/Al composites	678
liquid metal processing	43	nickel	182
load sharing	238	nickel composite coatings	495
load transfer	15	nickel electrolytic	495
local	238	nickel-nickel aluminide multilayer composites	192
local strain distribution	1	nitriding	80
longitudinal	238	nonequilibrium Al alloys	90
macroscopic properties	429	nonlinear viscoelasticity	781
magnesium	585	non-uniformity	698
magnesium alloy	539	normal interface separation	374
magnesium alloy AS41	221	notch fracture toughness	327
magnesium base composites	511	object grating technique	1
magnesium matrix composite	221, 486	onion- structure	643
magnesium-based metal matrix composites	688	optical microscopy	418
matrix cracking	391	optimal die	627
matrix materials	495	oxidation	53
mechanical alloying	250	oxidization	101
mechanical behavior at high temperature	520	parametric investigation	429
mechanical behaviour	215	particle	113
mechanical properties	182, 311, 511	particle content	578
mechanical property	532, 765	particle cracking	409
mechanical property estimation	578	particle reinforced metal matrix composites	678
mechanics	348	particle reinforcement	511
Meissner effect	384	particle-reinforced MMCs	409
melt pool	80	particulate	418
melt-stirring method	486, 627	particulate dispersion strengthening	505
mesoscopic damage mechanisms	429	particulate reinforced	284
metal flow	75	particulate reinforced composites	337
metal laminate composites	119	particulates	688
metal matrix composite	1, 24, 198, 274, 317, 356	perform	688
	520, 532	phase strains	565
metal matrix composites	15, 32, 63, 205, 238, 284	phase transition	772
	311, 365, 447, 479, 505, 539, 617, 627	pin-on-disc	709
metal matrix composites dilution	698	pitch-based carbon fibers	643
metal module casting,	527	plastic deformation	550
metal-ceramic laminates	260	plastic zone	260
metal-matrix	53	plasticity	238
metal-matrix composites	709	PMR polyimide composite	765
microcrack	539	polymer modification	772
microcracking	337	positron annihilation	772
microdefects	772	post-treatment	192
microhardness of coatings	495	powder alloying	80
microstructure	511, 520, 612, 772	powder diffraction package	384
microstructures	174	powder extrusion	532
microvoids	348	powders plating and rolling method	230
milling	205	precursor	573
misalignment angle	15	processing	182, 755
MMC	182, 300, 399, 467	processing map	143
modulus	578	pure aluminum	532
moisture absorption	719	pyrolysis	573
molybdenum disilicide silicon carbide composites	653	quantitative analysis	578
MoSi ₂	391	radial	643
mullite	391	random	643
nano-particles	495	reaction	63, 182
necking	260	reaction hardening	24
neturon diffraction	736		

reaction sintering	653	superplasticity	154, 479
reaction squeeze cast	164	superposition	746
reinforcement shape	300	surface layer	101
residual strength	365		
residual stress	317, 612	TEM	418
residual stresses	32, 565	tensile	539
residual tensile strength	447	tensile properties	174, 274
room and high temperature strength	164	tensile strength	527
rupture	418	tensile stress	597
		tensile test	198
Saffil fibre	709	thermal cycling	447, 585
Saffil preform	274	thermal expansion	53, 391
scanning electron microscopy	391	thermal explosive synthesis	192
seamless pipe	617	thermal mechanical property	284
seizure,	597	thermal mismatch	612
selective reinforcement	126, 134	thermal stresses	32, 565, 585
SEM	418	thermo-elasto-viscoplasticity	457
semi-solid state	108	thermomechanical coupling	457
shear failure	374	thermo-oxidative stability	765
sheet-composite rolling	75	Ti-6242	317
sialon	391	Ti-6Al-4V alloy	80
SiC	154	TiO ₂	63
SiC fiber	399	titanium	182, 238
SiC particle	53, 101, 198, 532	titanium alloy based MMC	447
SiC particles volume fraction	556	titanium carbide	486
SiC powder	505	titanium dioxide	24
SiC whisker	539	titanium matrix	365, 399, 467
SiC _p	607	toughness	327
SiCp/Al composites	174, 215, 678	transform moire method	230
SiCw/6061Al composite	10	transmission electron microscopy	24
silica powder	772	transmission electron microscopy (TEM)	
silicon carbide	113, 238, 550	straining techniques	10
silicone carbide	698	transverse properties	317
Si-N=C=N unit	573	triboelectrification	746
single-fiber	238	tribology	597
sintering treatments	119	Tsai-Halpin model	511
SiO ₂	101	turning	205
slight interfacial reaction	215	twin	612
slip line field	260	two-step process	126
sodium	24		
solid particles	495	unmixing-mising scheme	457
solidification	672	unsealed can	505
spinel	337		
squeeze cast	539	value	607
squeeze casting	24, 53, 174, 182, 274, 438, 527, 627, 688	vibrations	792
		viscoelastic	792
squeeze infiltration method	327	void measurement	719
stability map	143	void nucleation and growth	429
static fracture toughness	327	voids	719
storage and loss modulus	781		
strain analysis of interface	230	wear	678, 746
strain rate	781	wear behaviour	290
strengthening	429	wear behaviour of coatings	495
strengthening mechanisms	438	wear mechanism	205
stress relaxation	585, 612	wear rate	597
structure of coatings	495	wear resistance	80, 164, 527, 607
subgrains	418	wear resistance behavior	678
subsurface zone	205	wear resisting material	505
suitable cutting tool materials	205	wetting activated by exothermic interfacial	
superplastic forming	198	reactions	43

whisker	550	YBCO/Ag	384
whiskers	15	yield stress	597
work hardening	260		
		zirconium diboride	637
x-rays	32	ZL102	527
		Zn-Al composite	607
YBCO	384		